

JAC: Jena Atomic Calculator

— User Guide, Compendium & Theoretical Background —

<https://github.com/OpenJAC/JAC.jl>

Reference: S. Fritzsche, Computer Physics Communications 240, 1 (2019)

Stephan Fritzsche

Helmholtz-Institut Jena &

Theoretisch-Physikalisches Institut, Friedrich-Schiller-Universität Jena, Fröbelstieg 3, D-07743 Jena, Germany

(Email: s.fritzsche@gsi.de, phone: +49-3641-947606)

Monday 8th May, 2023

Atomic representations

- Configuration-based expansions
- Restricted active spaces (layer-by-layer)
- CI+perturbation theory; Gamov states
- Approximate Green functions, ...

Processes & properties

- Transition probabilities
- Excitation, ionization & recombination
- Auger, DR, Rayleigh-Compton, multi- γ
- Hyperfine & Zeeman splitting; plasma
- Isotope shifts, Lande & form factors

Atomic cascades

- Average single-configuration approach
- Multiple-configuration approach
- Incorporation of shake-up & shake-off
- Ion & electron distributions, ...

Symbolic Racah algebra

- Wigner symbols, special values
- Symmetries & recursions
- Symbolic sum rule evaluation
- Spherical harmonics & tensors

Interactive High-Level Language

JAC

Jena Atomic Calculator

A Julia implementation for atomic computations.

*Open-source applications
in physics, science and
technology.*

Atomic responses

- Field-induced processes & ionization
- High-harmonic generation
- Particle-impact processes
- Charge exchange

Time evolution

- Liouville equation for statistical tensors & atomic density matrices
- Atoms in intense light pulses
- Angle & polarization-dep. observables

Atomic descriptors

- Feature transform. & machine learning
- Bi-spectra of electronic densities
- Subshell & coupling descriptors
- Atomic fragments & effective charges

Semi-empirical estimates

- Weak-field ionization rates
- Asymptotic behaviour & formulas
- Stopping powers
- Plasma Stark broadening, ...

Contents

| | |
|---|-----------|
| 1. Overview about JAC. Structure of this User Guide | 21 |
| 1.1. Computational atomic physics: Challenges & difficulties | 21 |
| 1.2. Goals of the JAC toolbox | 23 |
| 1.3. Frequent terms and notations in using JAC | 29 |
| 1.4. A quick overview about the amplitudes, level properties and processes handled by JAC | 34 |
| 1.5. Remarks on the implementation | 37 |
| 1.6. Brief comparison of JAC with other existing codes | 42 |
| 1.7. To-do's, next steps & desired features of the JAC program | 52 |
| 1.7.a. To-do lists | 52 |
| 1.7.b. Discussion about (further) implementations | 54 |
| 1.7.c. Desired medium- and long-term features of the JAC program | 54 |
| 2. Dirac's hydrogenic atom | 57 |
| 2.1. Energies and wave functions | 57 |
| 2.2. Coulomb-Green function | 64 |
| 2.3. Matrix elements with Dirac orbitals | 65 |
| 2.3.a. Matrix elements with radial orbitals | 65 |
| 2.3.b. Matrix elements including the angular part of Dirac orbitals | 66 |
| 2.4. Frequently applied expansions, transformations and identities in atomic theory | 67 |
| 2.4.a. Partial-wave expansions of free electrons | 67 |
| 2.4.b. Expansions including spherical harmonics | 68 |
| 2.4.c. Radial grid transformations | 69 |
| 2.4.d. Useful idendities | 71 |
| 2.5. Frequently occurring radial integrals | 71 |

Contents

| | | |
|-----------|--|-----------|
| 2.6. | B-splines | 73 |
| 2.7. | Generation of continuum orbitals | 76 |
| 2.7.a. | Spherical Bessel orbitals | 77 |
| 2.7.b. | Non-relativistic Coulomb orbitals | 77 |
| 2.7.c. | Asymptotically-correct relativistic Coulomb orbitals | 78 |
| 2.7.d. | Continuum orbitals in an atomic potential: Galerkin method | 78 |
| 2.7.e. | Normalization and phase of continuum orbitals | 79 |
| 2.8. | Dirac equation with an axially-symmetric potential | 82 |
| 2.9. | Volkov solutions | 83 |
| 2.10. | Nuclear models and potentials | 84 |
| 2.10.a. | Coulomb potential; point-like nuclei | 84 |
| 2.10.b. | Shell-like nuclei | 85 |
| 2.10.c. | Uniform nuclear model | 85 |
| 2.10.d. | Helm's uniform-uniform nuclear model | 87 |
| 2.10.e. | Helm's nuclear-depression model | 87 |
| 2.10.f. | Fermi nuclear model | 88 |
| 2.10.g. | Deformed Fermi nuclear model | 90 |
| 2.10.h. | Z-scaling of atomic energies, rates and properties | 90 |
| 3. | Many-electron atomic interactions, state functions, density operators and statistical tensors | 93 |
| 3.1. | Electron-electron interaction | 93 |
| 3.2. | Atomic potentials | 98 |
| 3.2.a. | In JAC implemented potentials | 98 |
| 3.2.b. | Further atomic potentials, not yet considered in JAC | 100 |
| 3.3. | Construction of symmetry-adapted CSF basis | 106 |
| 3.4. | Spin-angular coefficients for symmetry-adapted CSF | 108 |
| 3.4.a. | Quasi-spin formalism in jj -coupling | 108 |
| 3.4.b. | Reduced matrix elements of unit tensors | 110 |
| 3.4.c. | Spin-angular coefficients for symmetric two-particle operators | 111 |
| 3.4.d. | Computation of spin-angular coefficients for symmetry-adapted CSF | 111 |
| 3.5. | Dirac-Hartree-Fock method | 113 |

| | | |
|-----------|---|------------|
| 3.6. | Atomic estimates of quantum-electrodynamic (QED) corrections | 115 |
| 3.6.a. | QED model operators & model potentials | 115 |
| 3.6.b. | In JAC implemented QED estimates | 119 |
| 3.7. | Unitary $jjJ - LSJ$ transformation of atomic states | 120 |
| 3.7.a. | Transformation matrices from jjJ - to LSJ -coupling | 120 |
| 3.7.b. | Re-coupling coefficients | 123 |
| 3.7.c. | In JAC implemented $jjJ - LSJ$ transformation | 126 |
| 3.8. | Atomic interaction amplitudes | 128 |
| 3.9. | Atomic density operators and matrices | 132 |
| 3.9.a. | Single-electron reduced density matrix | 132 |
| 3.9.b. | Atomic density matrix formalism | 132 |
| 3.10. | Parity- and time-violating atomic interactions | 134 |
| 3.10.a. | Interactions beyond the standard model | 134 |
| 3.10.b. | Parity-violating (P-odd, T-even) interactions | 136 |
| 3.10.c. | Time-reversal violating (P-odd, T-odd) interactions | 139 |
| 3.10.d. | Time-reversal violating atomic electric-dipole moments | 140 |
| 3.11. | Elements from atomic spectroscopy | 143 |
| 3.11.a. | Line shifts and profiles | 143 |
| 3.11.b. | Atomic target distributions | 145 |
| 3.11.c. | Manipulation of light beams | 146 |
| 3.11.d. | Miscellaneous | 146 |
| 4. | Atomic representations | 149 |
| 4.1. | In JAC implemented atomic representations | 153 |
| 4.1.a. | Mean-field basis (<code>Atomic</code>) | 153 |
| 4.1.b. | Configuration interaction (CI) expansions (<code>Atomic</code>) | 153 |
| 4.1.c. | Restricted active space (RAS) expansions (<code>Atomic</code>) | 154 |
| 4.1.d. | Approximate many-electron Green function for atomic levels (<code>GreenFunction</code>) | 155 |
| 4.2. | In JAC partly-implemented atomic representations | 161 |
| 4.2.a. | Multi-configuration Dirac-Hartree-Fock (MCDHF) expansions (<code>Atomic</code>) | 161 |
| 4.2.b. | Combined configuration interaction & perturbation theory (CI-PT) expansions (...) | 163 |

Contents

| | |
|--|------------|
| 4.2.c. Fast configuration interaction & perturbation theory (FCI-PT) expansions (....) | 165 |
| 4.3. Further atomic representations, not yet considered in JAC | 167 |
| 4.3.a. Many-body perturbation theory | 167 |
| 4.3.b. Complex-scaling method | 170 |
| 4.3.c. Many-electron scattering functions | 171 |
| 4.3.d. Berggren expansion method | 172 |
| 4.3.e. Convergent close-coupling (CCC) method | 174 |
| 4.3.f. Density-matrix renormalization group (DMRG) method | 175 |
| 4.4. Other representations, related to JAC | 178 |
| 4.4.a. Analytical screened hydrogen models | 178 |
| 4.4.b. Natural-orbital functional theory (NOFT) | 178 |
| 4.4.c. Density funtional theory (DFT) | 178 |
| 4.4.d. Relativistic coupled-cluster (RCC) theory | 179 |
| 4.4.e. Miscellaneous methods for the representation of many-electron systems | 181 |
| 4.4.f. Wigner distribution of quantum systems | 182 |
| 4.4.g. Transformation of atomic into qubit Hamiltonians | 183 |
| 4.4.h. qumodes | 191 |
| 4.5. Numerical methods for large-scale atomic computations | 193 |
| 4.5.a. Matrix diagonalization | 193 |
| 5. Atomic interactions with the radiation field | 195 |
| 5.1. Wave equations & optical fields | 195 |
| 5.1.a. Homogeneous wave equation | 195 |
| 5.1.b. Plane-wave radiation | 196 |
| 5.1.c. Polarization of plane waves in classical electrodynamics | 199 |
| 5.1.d. Atom-light interaction in the electric-dipole approximation | 201 |
| 5.2. Representation and parametrization of photons in atomic theory | 201 |
| 5.2.a. Stokes parametrization and density matrix of a photon | 201 |
| 5.2.b. Pure polarization states of photons | 204 |
| 5.2.c. Spherical tensors of polarization vectors | 208 |

| | | |
|-----------|--|------------|
| 5.3. | Multipole decomposition of the radiation field | 210 |
| 5.3.a. | Elements from the theory of multipole transitions | 210 |
| 5.3.b. | Single-electron (reduced) multipole-transition matrix elements | 212 |
| 5.3.c. | Many-electron (reduced) multipole emission and absorption amplitudes | 213 |
| 5.4. | Electromagnetic light pulses | 214 |
| 5.4.a. | High-intensity pulses | 214 |
| 5.4.b. | Pulse shapes and optical cycles | 215 |
| 5.4.c. | Maximum pulse intensity | 216 |
| 5.4.d. | Bichromatic laser fields | 217 |
| 5.5. | Light-field forces (optical forces) | 218 |
| 5.6. | Elements from modern optics | 219 |
| 6. | Atomic amplitudes | 221 |
| 6.1. | In JAC implemented amplitudes | 221 |
| 6.1.a. | Dipole amplitudes (<code>MultipoleMoment</code>) | 221 |
| 6.1.b. | Electro-magnetic multipole transition amplitudes (<code>MultipoleMoment</code> , <code>Radiative</code>) | 221 |
| 6.1.c. | Electro-magnetic multipole-moment amplitudes (<code>MultipoleMoment</code>) | 222 |
| 6.1.d. | Momentum transfer amplitudes (<code>FormFactor</code>) | 224 |
| 6.2. | In JAC partly-implemented amplitudes | 225 |
| 6.2.a. | Parity non-conservation amplitudes (<code>ParityNonConservation</code>) | 225 |
| 6.2.b. | Schiff-moment amplitudes (<code>ParityNonConservation</code>) | 226 |
| 6.3. | Further amplitudes, not yet considered in JAC | 227 |
| 6.3.a. | Anapole-moment amplitudes (<code>ParityNonConservation</code>) | 227 |
| 6.3.b. | Scalar-pseudo-scalar amplitudes | 227 |
| 6.3.c. | Tensor-pseudo-tensor amplitudes | 228 |
| 6.3.d. | Nuclear magnetic-quadrupole-moment amplitudes due to internal B -field | 229 |
| 6.4. | Composed many-electron amplitudes, not yet considered in JAC | 230 |
| 6.4.a. | Parity-violating (non-diagonal, second-order) amplitudes | 230 |
| 6.4.b. | Charge-parity-violating (diagonal, second-order) amplitudes | 230 |
| 6.4.c. | Electric-dipole moment enhancement factor | 230 |

| | |
|--|------------|
| 7. Atomic properties | 231 |
| 7.1. In JAC implemented level properties | 231 |
| 7.1.a. Transition probabilities for a single multiplet (<code>Einstein</code>) | 231 |
| 7.1.b. Hyperfine parameters and hyperfine representations (<code>Hfs</code>) | 232 |
| 7.1.c. Isotope-shift parameters (<code>IsotopeShift</code>) | 239 |
| 7.1.d. Lande g_J factors and Zeeman splitting of fine-structure levels (<code>LandeZeeman</code>) | 247 |
| 7.1.e. Lande g_F factors and Zeeman splitting of hyperfine levels (<code>LandeZeeman</code>) | 250 |
| 7.1.f. Atomic form factors (<code>FormFactor</code>) | 251 |
| 7.1.g. One- and two-particle reduced density matrices & natural orbitals (<code>ReducedDensityMatrix</code>) | 257 |
| 7.1.h. Energy shifts in plasma environments (<code>PlasmaShift</code>) | 263 |
| 7.1.i. Level-dependent fluorescence and Auger yields (<code>DecayYield</code>) | 270 |
| 7.2. In JAC partly-implemented level properties | 272 |
| 7.2.a. Scattering amplitudes and scattering factors (<code>FormFactor</code>) | 272 |
| 7.2.b. Multipole polarizabilities (<code>MultipolePolarizability</code>) | 273 |
| 7.2.c. Photoemission in external magnetic fields (<code>MagneticFieldInduced</code>) | 273 |
| 7.2.d. Sensitivity of level energies with regard to variations of α (<code>AlphaVariation</code>) | 276 |
| 7.3. Further properties, not yet considered in JAC | 278 |
| 7.3.a. Information measures for quantum states | 278 |
| 7.3.b. Electron localization function (ELF) | 279 |
| 7.3.c. Stark shifts and (dc) ionization rates in static electric fields | 280 |
| 7.3.d. Frequency-dependent (ac) Stark shifts (<code>AcStarkShift</code>) | 283 |
| 7.3.e. Intensity-dependent quasi-energies and dressed (Floquet) states in slowly varying laser fields | 291 |
| 7.3.f. Atomic polarizabilities | 293 |
| 7.3.g. Hyperpolarizability | 301 |
| 7.3.h. Black-body radiation shifts | 302 |
| 7.3.i. Dispersion coefficients | 303 |
| 7.3.j. Fano profiles of continuum-embedded resonances | 308 |
| 7.3.k. Stark splitting in crystal field | 309 |
| 7.4. Other topics closely related to atomic properties | 311 |
| 7.4.a. Laser cooling, precision spectroscopy and quantum control | 311 |
| 7.4.b. Atomic clocks | 312 |

| | | |
|-----------|--|------------|
| 7.4.c. | Atomic partition functions | 318 |
| 7.4.d. | Quantum similarity measures & similarity indices for pairs of atoms and ions | 318 |
| 7.4.e. | Atom-atom and atom-ion interaction potentials | 319 |
| 7.4.f. | Dispersive interactions in liquids and solids | 326 |
| 7.4.g. | Mean excitation energy of atomic ions & stopping powers | 327 |
| 7.4.h. | Transport coefficients for ion mobility and diffusion in gases | 328 |
| 7.4.i. | Polarizability and optical absorbance of nanoparticles | 329 |
| 7.4.j. | Radiative opacities in cold plasma | 331 |
| 7.4.k. | Plasma diagnostics | 342 |
| 7.4.l. | Radial distribution functions for plasma and liquid models | 347 |
| 7.4.m. | Average-atom model for warm-dense matter | 348 |
| 7.4.n. | X-ray Thomson scattering for warm-dense matter | 352 |
| 7.4.o. | Equation-of-state relations for astro physics and condensed matter | 353 |
| 7.4.p. | Radiation damage of DNA by electron impact | 353 |
| 7.4.q. | Binding energies and quantum defects of Rydberg atoms | 354 |
| 7.4.r. | Radiative transitions and form factors of Rydberg atoms | 358 |
| 7.4.s. | Endohedrally confined atoms | 359 |
| 7.4.t. | Exotic atoms and ions | 360 |
| 7.4.u. | Precision spectroscopy of hydrogen-like and few-electron ions | 361 |
| 7.4.v. | Spectroscopy of lanthanides and actinides: Open <i>f</i> -shell elements | 362 |
| 7.4.w. | Spectroscopy of (super-) heavy elements | 363 |
| 7.4.x. | Electronic structure and properties of quantum dots | 365 |
| 8. | Atomic processes | 369 |
| 8.1. | In JAC implemented processes | 369 |
| 8.1.a. | Photoemission. Transition probabilities (<i>PhotoEmission</i>) | 369 |
| 8.1.b. | Photoexcitation (<i>PhotoExcitation</i>) | 376 |
| 8.1.c. | Atomic photoionization (<i>PhotoIonization</i>) | 384 |
| 8.1.d. | Radiative recombination (<i>PhotoRecombination</i>) | 393 |
| 8.1.e. | Auger and autoionization processes (<i>AutoIonization</i>) | 406 |
| 8.1.f. | Dielectronic recombination (<i>Dielectronic</i>) | 412 |

Contents

| | | |
|--------|--|-----|
| 8.1.g. | Photoexcitation & fluorescence (PhotoExcitationFluores) | 422 |
| 8.1.h. | Photoexcitation & autoionization (PhotoExcitationAutoion) | 425 |
| 8.1.i. | Rayleigh & Compton scattering of light (RayleighCompton) | 431 |
| 8.1.j. | Multi-photon excitation and decay (MultiPhotonDeExcitation) | 438 |
| 8.1.k. | Double-Auger decay (DoubleAutoIonization) | 449 |
| 8.1.l. | Photo-double ionization (PhotoDoubleIonization) | 450 |
| 8.1.m. | Radiative-Auger decay (RadiativeAuger) | 453 |
| 8.1.n. | Electron-impact (de-) excitation. Collision strengths (ImpactExcitation) | 455 |
| 8.1.o. | Electron-impact ionization (ImpactIonization) | 459 |
| 8.1.p. | Photoabsorption | 461 |
| 8.1.q. | Hyperfine-induced transitions (Hfs) | 463 |
| 8.2. | In JAC partly-implemented processes | 464 |
| 8.2.a. | Multi-photon & multi-color ionization (MultiPhotonIonization) | 464 |
| 8.2.b. | Coulomb excitation (CoulombExcitation) | 467 |
| 8.2.c. | Photoionization & fluorescence (PhotoIonizationFluor) | 476 |
| 8.2.d. | Photoionization & autoionization (PhotoIonizationAutoIon) | 477 |
| 8.2.e. | Dielectronic recombination & fluorescence (DielectronicFluores) | 478 |
| 8.2.f. | Electron-impact excitation & autoionization (ImpactExcitationAutoIon) | 478 |
| 8.2.g. | Multi-photon double ionization (MultiPhotonDoubleIon) | 479 |
| 8.2.h. | Multiple photoionization or photodetachment | 479 |
| 8.2.i. | Internal conversion (InternalConversion) | 479 |
| 8.2.j. | Nuclear electron capture and β^\pm decay | 482 |
| 8.3. | Further processes, not yet considered in JAC | 485 |
| 8.3.a. | Coulomb ionization (CoulombIonization) | 485 |
| 8.3.b. | Bremsstrahlung (BremsStrahlung) | 486 |
| 8.3.c. | Inverse bremsstrahlung | 486 |
| 8.3.d. | Radiative recombination & fluorescence | 487 |
| 8.3.e. | Resonant two-color (two-photon, single-electron) ionization | 487 |
| 8.3.f. | Interference of multi-photon ionization channels (MultiPhotonInterference) | 487 |
| 8.3.g. | Two-color multi-photon interference ionization (TwoColorInterferenceIon) | 489 |
| 8.3.h. | Two-photon above-threshold ionization (ATI) (TwoColorInterferenceIon) | 489 |

| | | |
|--------|---|-----|
| 8.3.i. | Photon-stimulated Auger decay (PSAD) | 490 |
| 8.3.j. | Positron-annihilation-induced autoionization | 490 |
| 8.3.k. | Resonant excitation with sequential double autoionization (RESDA): | 491 |
| 8.3.l. | Resonant excitation with direct double autoionization (REDDA): | 492 |
| 8.3.m. | Radiative double electron capture | 493 |
| 8.3.n. | Generalized oscillator strengths (GOS) | 493 |
| 8.3.o. | Nuclear excitations due to electronic transitions and capture | 494 |
| 8.3.p. | Electron-impact multiple ionization | 496 |
| 8.3.q. | Three-body recombination | 496 |
| 8.3.r. | Elastic scattering of electrons and ions | 497 |
| 8.3.s. | Negative-continuum dielectronic recombination | 499 |
| 8.3.t. | Inter-Coulombic capture and decay | 500 |
| 8.4. | More processes, not yet considered in JAC | 501 |
| 8.4.a. | Nonradiative electron capture (NRC) | 501 |
| 8.4.b. | Vacuum-electron capture | 503 |
| 8.4.c. | Positron-bound-electron pair annihilation with single-photon emission (PairAnnihilation1Photon) | 504 |
| 8.4.d. | Positron-bound-electron pair annihilation with two-photon emission (PairAnnihilation2Photon) | 504 |
| 8.4.e. | Positron-bound-electron pair production by a photon (PairProduction) | 506 |
| 8.4.f. | Pair production in intense laser fields | 506 |
| 8.4.g. | Thomson scattering | 508 |
| 8.5. | Other topics related to atomic processes | 512 |
| 8.5.a. | Atomic databases from the literature | 512 |
| 8.5.b. | Codes from astro and plasma physics that require atomic data input | 513 |
| 8.5.c. | Electro-magnetic transients & light curves from astrophysical matter clouds | 517 |
| 8.5.d. | Absorption and emission spectra of distinct astrophysical objects | 530 |
| 8.5.e. | Supernovae and kilonovae observations | 534 |
| 8.5.f. | Radiation transport in astrophysical and hydrodynamical environments | 535 |
| 8.5.g. | Plasma light sources for nanolithography | 538 |
| 8.5.h. | Laser-induced fluorescence spectroscopy (LIFS) in flames | 539 |
| 8.5.i. | Synthetic spectra for laser-induced breakdown spectroscopy (LIBS) | 540 |
| 8.5.j. | Laser-produced plasma | 541 |

Contents

| | |
|---|------------|
| 8.5.k. Laser wake-field acceleration (LWFA) of particles | 545 |
| 8.5.l. Fusion research | 546 |
| 8.5.m. Mass attenuation coefficients | 546 |
| 8.5.n. Associated and Penning ionization in low-energy atom-atom collisions | 547 |
| 8.5.o. X-ray absorption of solid-state materials | 547 |
| 8.5.p. X-ray magnetic circular dichroism (XMCD) | 550 |
| 8.5.q. Coherent x-ray scattering at high intensities | 551 |
| 8.5.r. X-ray quantum optics | 553 |
| 8.5.s. Gamma-factory project | 555 |
| 8.5.t. Spin-waves and spin-wave engineering (magnomics) | 556 |
| 8.5.u. Hollow atom and ion formation | 557 |
| 8.5.v. Decay of medical radioactive isotopes | 558 |
| 8.5.w. Universal shape function for charged-particle impact ionization | 558 |
| 8.5.x. Configuration-averaged energies and cross sections | 560 |
| 9. Atomic cascades | 561 |
| 9.1. Cascade computations and cascade simulations | 564 |
| 9.2. In JAC implemented cascade schemes | 570 |
| 9.2.a. Decay cascades | 570 |
| 9.2.b. Photoionization step of a cascade | 570 |
| 9.2.c. Photoexcitation step of a cascade | 571 |
| 9.2.d. Hollow-ion cascades | 572 |
| 9.2.e. Radiative recombination cascade | 572 |
| 9.2.f. Dielectronic recombination cascade | 572 |
| 9.2.g. Electron-capture step of a cascade | 572 |
| 9.2.h. Ion impact step of a cascade | 573 |
| 9.3. In JAC implemented cascade approaches | 574 |
| 9.3.a. Average single-configuration approach (AverageSCA), based on a common set of orbitals (<i>Cascade</i>) | 574 |
| 9.3.b. Single-configuration approach (SCA) with individual sets of orbitals (<i>Cascade</i>) | 575 |
| 9.4. In JAC partly-implemented cascade approaches | 576 |
| 9.4.a. User-grouped multi-configuration approach (UserMCA; <i>Cascade</i>) | 576 |

| | |
|---|------------|
| 9.4.b. Multi-configuration approach with shake transitions (ShakedMCA; Cascade) | 577 |
| 9.5. In JAC implemented cascade simulations | 578 |
| 9.5.a. Ion distributions (Cascade) | 578 |
| 9.5.b. Final-level distributions (Cascade) | 579 |
| 9.5.c. Photon intensity spectra (Cascade) | 579 |
| 9.5.d. Electron-ion coincidence spectroscopy (Cascade) | 579 |
| 9.6. In JAC partly-implemented cascade simulations | 580 |
| 9.6.a. Absorption cross sections (Cascade) | 580 |
| 9.6.b. DR plasma rate coefficient (Cascade) | 580 |
| 9.6.c. Electron intensity spectra (Cascade) | 580 |
| 10. Collision- and field-induced atomic responses | 581 |
| 10.1. Interaction with external particles and fields. Notations | 581 |
| 10.1.a. Atoms interacting with external particles | 581 |
| 10.1.b. Atoms in time-harmonic (Floquet) fields | 582 |
| 10.1.c. Atoms in intense radiation fields | 582 |
| 10.1.d. Atoms in few-cycle pulses | 586 |
| 10.1.e. Atoms forming local plasma | 589 |
| 10.2. In JAC considered ion-atom collisional responses | 590 |
| 10.2.a. Semi-classical ion-atom collisions [theoretical background] | 590 |
| 10.3. In JAC considered high harmonic (HH) responses | 593 |
| 10.3.a. High-harmonic generation HHG [phenomenology] | 593 |
| 10.3.b. High-harmonic generation in the strong-field approximation [theoretical background] | 606 |
| 10.3.c. High harmonic spectra from localized target clouds [partly-implemented in JAC] | 609 |
| 10.3.d. Phase matching in high-harmonic generation from extended target clouds [partly-implemented] | 609 |
| 10.3.e. Far-field phase distributions [not yet implemented] | 610 |
| 10.3.f. Far-field intensity distributions [not yet implemented] | 610 |
| 10.4. In JAC considered above-threshold ionization (ATI) processes | 611 |
| 10.4.a. ATI in the strong-field approximation [phenomenology] | 611 |
| 10.4.b. ATI in the strong-field approximation [theoretical background] | 612 |

Contents

| | |
|--|------------|
| 10.5. In JAC considered non-sequential double ionization (NSDI) processes | 614 |
| 10.5.a. NSDI in the strong-field approximation [phenomenology] | 614 |
| 10.5.b. NSDI in the strong-field approximation [theoretical background] | 614 |
| 10.6. In JAC considered collisional-radiative (CR) models | 616 |
| 10.6.a. Simple CR models [phenomenology] | 616 |
| 10.6.b. CR models [theoretical background] | 617 |
| 10.7. Atomic responses not yet considered in JAC | 618 |
| 10.7.a. Floquet theory [theoretical background] | 618 |
| 10.7.b. Two-color sideband formation in atomic photoionization [theoretical background] | 620 |
| 10.7.c. Phase control of atomic photoionization in multi-color fields [theoretical background] | 621 |
| 10.7.d. Amplified spontaneous emission (ASE) & superfluorescence (SF) | 622 |
| 10.7.e. Two-color streaking in atomic photoionization | 622 |
| 10.8. Theoretical background to atomic responses considered above | 624 |
| 10.8.a. Strong-field approximation (SFA) [background] | 624 |
| 10.8.b. Rotating-frame approximation [background] | 653 |
| 10.8.c. Kramers-Henneberger frame [background] | 654 |
| 10.8.d. Guo-Aberg-Crasemann (GAC) theory [background] | 655 |
| 10.8.e. Twisted light beams [background] | 655 |
| 11. Time-evolution of many-electron atomic state functions and density matrices | 657 |
| 11.1. Time-dependent approximations of many-electron states | 657 |
| 11.2. Time-dependent statistical tensors | 662 |
| 11.3. Time-integration of statistical tensors | 663 |
| 11.4. Time evolution of statistical tensors. Formalism | 664 |
| 11.4.a. Liouville equation for the atomic density matrix | 664 |
| 11.4.b. Time-dependent statistical tensors of atomic lines | 665 |
| 11.5. Observables to be derived from time-dependent statistical tensors | 666 |
| 12. Atomic descriptors | 667 |
| 12.1. In JAC implemented atomic descriptors | 670 |

| | |
|---|------------|
| 12.2. In JAC partly-implemented atomic descriptors | 670 |
| 12.2.a. Descriptors for electronic densities (<code>Descriptor</code>) | 670 |
| 12.2.b. Descriptors for pairs of atomic levels | 672 |
| 12.3. Methods of machine learning | 672 |
| 12.3.a. Supervised learning methods | 674 |
| 12.3.b. Neural network (NN) methods | 675 |
| 12.3.c. autoencoder methods | 676 |
| 12.3.d. Other methods | 676 |
| 12.4. Feature transformations & applications of machine learning | 677 |
| 12.4.a. Feature transformation and engineering | 677 |
| 12.4.b. Applications in molecular physics | 678 |
| 12.4.c. Applications in solid-state physics and material science | 682 |
| 12.4.d. Other applications | 685 |
| 13. Semiempirical estimates | 687 |
| 13.1. In JAC implemented estimates for atomic properties and data | 687 |
| 13.1.a. Data from the periodic table of elements (<code>PeriodicTable</code>) | 687 |
| 13.1.b. Isotope data (<code>PeriodicTable</code>) | 687 |
| 13.1.c. Binding energies of inner- and valance-shell electrons (<code>PeriodicTable</code>) | 688 |
| 13.1.d. Atomic radii, susceptibilities and polarizabilities (<code>PeriodicTable</code>) | 688 |
| 13.2. In JAC partly-implemented estimates for atomic properties and data | 689 |
| 13.2.a. Weak-field ionization of effective one-electron atoms | 689 |
| 13.2.b. Tunnel ionization rates | 690 |
| 13.2.c. Electron-impact ionization. Cross sections | 692 |
| 13.2.d. Charge-exchange cross sections | 696 |
| 13.3. Further estimates on atomic properties, not yet considered in JAC | 700 |
| 13.3.a. Electron and positron stopping powers (<code>StoppingPower</code>) | 700 |
| 13.3.b. Stopping power of multiply-charged ions | 701 |
| 13.3.c. Stark broadening of spectral lines in plasma | 703 |
| 13.3.d. Atomic electron-momentum densities | 706 |

Contents

| | |
|---|------------|
| 14. Beams of light and particles | 707 |
| 14.1. Helmholtz wave equation | 707 |
| 14.2. Symmetries of light beams | 710 |
| 14.2.a. Orbital and spin angular momentum | 710 |
| 14.2.b. Torus-knot angular momentum | 712 |
| 14.2.c. Chirality of beams | 715 |
| 14.3. Light beams | 717 |
| 14.3.a. Gaussian beams | 718 |
| 14.3.b. Vortex beams. Characterization and properties | 719 |
| 14.3.c. Vortex beams. Generation & manipulation | 722 |
| 14.3.d. Hermite-Gaussian beams | 726 |
| 14.3.e. Laguerre-Gaussian beams | 727 |
| 14.3.f. Ince-Gaussian beams | 729 |
| 14.3.g. Bessel-Gauss beams | 731 |
| 14.3.h. Bessel beams | 732 |
| 14.3.i. Airy beams | 738 |
| 14.3.j. Necklace ring beams | 738 |
| 14.3.k. Lattices of OAM beams | 738 |
| 14.3.l. Light beams with non-integer OAM | 739 |
| 14.3.m. Vector beams | 739 |
| 14.3.n. Traktor beams | 742 |
| 14.3.o. Polarization radiation | 742 |
| 14.3.p. X-waves | 743 |
| 14.3.q. Optical forces of vortex beams | 744 |
| 14.3.r. Application of optical (vortex) beams | 745 |
| 14.4. Electron beams | 747 |
| 14.4.a. Gaussian electron beams | 747 |
| 14.4.b. Vortex electron beams | 747 |
| 14.4.c. Generation of vortex electron beams | 748 |
| 14.4.d. Laguerre-Gaussian electron beams | 750 |
| 14.4.e. Bessel electron beams | 752 |

| | |
|--|------------|
| 14.4.f. Airy electron beams | 753 |
| 14.4.g. Application of twisted electron beams | 753 |
| 14.5. Quantum technologies | 754 |
| 14.5.a. Elements from quantum optics | 754 |
| 14.5.b. Spontaneous parametric down-conversion (SPDC) | 756 |
| 14.5.c. Boson sampling | 761 |
| 14.5.d. Quantum imaging | 763 |
| 14.5.e. Other technologies | 763 |
| 15. Symbolic evaluation of expressions from Racah's algebra | 765 |
| 15.1. Racah's algebra in atomic and many-body physics | 765 |
| 15.1.a. Advantages of using Racah's algebra | 765 |
| 15.1.b. Frequently applied symbols and functions from Racah's algebra | 767 |
| 15.1.c. Symmetries of the Wigner $3n-j$ symbols, rotation matrices and spherical harmonics | 771 |
| 15.1.d. Expansions of the Wigner $3n-j$ symbols, rotation matrices and spherical harmonics | 773 |
| 15.2. In JAC implemented symbolic evaluations of Racah algebra expressions | 777 |
| 15.2.a. Strategies in the symbolic evaluation of expressions from Racah's algebra | 777 |
| 15.3. In JAC partly-implemented symbolic evaluations of Racah algebra expressions | 780 |
| 15.3.a. Recursive relations for the Wigner $3n-j$ symbols and rotation matrices | 780 |
| 15.3.b. Special values of the Wigner $3n-j$ symbols and rotation matrices | 782 |
| 15.3.c. Orthogonality and sum rules of the Wigner $3n-j$ symbols | 786 |
| 15.4. Symbolic evaluations of Racah algebra expressions not yet considered in JAC | 793 |
| 15.4.a. Orthogonality, completeness and integral representation of the Wigner rotation matrices: | 793 |
| 15.4.b. Sum rules for spherical harmonics | 795 |
| 15.4.c. Integrals involving spherical harmonics | 796 |
| 16. References | 799 |
| Index | 816 |

A few remarks about this User Guide & Compendium ahead:

- **Goals of this User Guide & Compendium:** While a large (huge) number of publications have contributed to the progress in atomic physics and theory over the years, they have lead also to different research fields as well as rather diverse designations and notations, with many of them hard to resolve in detail. — With this Compendium, we aim to establish a common language in which the results are easier communicated and (hopefully) applied by others researchers. Indeed, such a common language must aim to comprise (1) precise and analogue designations for (the same or) analogue physical quantities; (2) the same or obviously modified mathematical syntax in formulas for the same physics; and (3) quite similar but still distinguishable (mathematical) symbols for similar but distinguishable quantities.
While this goal is rather ambitious and hard to achieve in practice, I shall explain below some of the concepts and difficulties below, which I tried to (partly) overcome in this Compendium on computational atomic physics.
- **Goals of this User Guide & Compendium:** First, this Compendium contains all expressions and formulas that are implemented in JAC as well as many more. Such a compilation will make it explicit which of the *physics* is (partly) implemented already within the toolbox, and which other topics are close to an implementation. Apart from those topics *not yet considered in JAC*, most chapters of this Compendium therefore contain basic information also from other research fields that might benefit from this toolbox. Overall, however, no attempt is made (and I wouldn't feel able) to provide further details about these fields; nonetheless, we hope to capture curiosity and, perhaps, find new supporters of JAC by this way.
- **Symbols and formulas:** A good deal of (modern) research papers are quite difficult to follow because quantities are either not explained at all or because little care is taken about (additional) assumptions, their dependencies or simply because of an overload of notations. Moreover, the (parametric) dependencies of physical quantities are often not shown, or authors are not even aware about them. Here, we aim to (partly) overcome these missing dependences and the overloading of designated or alias name and symbols. In a good number of research papers, indeed, the same symbols have different (and by far no obvious) meaning, or different symbols are used for the same quantity, either within the same or from one to the next publication by the same authors.
- **Symbols and formulas:** In physics, there is a wide belief that symbols can be used quite freely, as long as they are properly explained. While this is *formally* true from a technical viewpoint, such a carelessness can indeed hamper considerably the work of other people, and will make certain case studies unfeasible. Of course, we can write Newton's famous law for a 1-dimensional motion either: $m \ddot{x} = F$ or $x \ddot{F} = m$, if all the symbols are carefully introduced. However, such a freedom is of little help since a careful introduction of all entities becomes elaborate with increasing complexity, and one might even not be fully aware of the precise definition of all quantities at most of the times. From a physical viewpoint, strictly speaking, a re-definition of symbols requires knowledge about *all* assumptions that were made prior to

their first use. I guess, hardly anyone will spontaneously be able to recall most or, at least, most of these assumptions about the quantities as they appear in some derivation or discussion. — This Compendium therefore aims to make assumptions about as well as the notations and dependencies of various entities in atomic physics (much) more explicit, than what is typically found in most research papers. No claim is made that this is always done in a *wise* and final manner.

- **Expressions and formulas:** This Compendium provides first of all a compilation of expressions and formulae, with less focus on their detailed derivation. In fact, many of the underlying derivations are lengthy enough, so that they are not or only rarely repeated by other researchers in the field. Of course, this Compilation should not discourage young people to re-think and re-do certain derivations in good detail, and sometimes with their very own success to find *new* insights into physics. Nonethlesse, such derivations will be made less often as the size and complexity of (intermediate) expressions increase. Many of the formulas below are (simply) taken from the literature, adapted in their notations and/or checked for their consistent use in the literature. (In some other cases, I was earlier involved myself in the derivations.) No claim is made that all these formulas are correct or correctly ‘translated’ into the chosen notation. Both, misprints and misunderstandings are readily possible; despite of all these difficulties, the search for common and appropriate notations for all physical quantities has taken enormous effort but is considered as ‘main prize’ of this Compendium.
- **Parametric dependence of amplitudes and derived quantities:** From the viewpoint of elementary mathematics, we easily accept expressions such as

$$f(x, y; a) = \int_b^\infty dz g(x, y; a) h(y, z; b) \quad \text{for } b > 0,$$

as long as we know which values the explicit variables x, y, z and the parameters a, b may take. We even accept such epxressions if the detailed derivation of this formula is not known at a given time. Nonetheless, the physical intepretation of such formulas is quite easy as long as the *dependencies* are clear. In physics, in contrast, we all-too-often find formulas, in which the dependencies cannot be resolved by the reader, and sometimes also by the authors themselves. An *educated guess* is then needed to resolve the expression. For example, the radiative recombination (RR) plasma rate coefficient describes the rate of an ion to recombine by (direct) photoemission for one particle per *unit* volume. For a plasma with electron temperature T_e , this rate coefficient is often written as

$$\alpha^{(\text{RR})} = \int_0^\infty dE E \sigma^{(\text{RR})} \exp\left(-\frac{E}{T_e}\right)$$

without telling much about the cross section $\sigma^{(\text{RR})}$, nor its dependencies or about the energy E that appear here in this expression. Moreover, in which ‘units’ should all these entities be utilized ? — A more detailed analysis of the radiative recombination process will reveal that the RR plasma rate coefficient depends parametrically on the temperature of the plasma T_e and the initial (ground) level ($\alpha_i J_i$) of the

ion, while the (set of) final states of the recombined ion determine the approximation that is used in a particular computation. Moreover, the structure of the radiation field (multipole fields) needs to be specified but is typically restricted to the electric-dipole component. A more explicit notation with all entities in atomic units [1] then reads as

$$\Downarrow$$

$$\alpha^{(\text{RR})}(T_e; \alpha_i \mathbb{J}_i) = \frac{4}{\sqrt{2\pi m} T_e^{3/2}} \int_0^\infty dE E \left[\sum_{\alpha_f \mathbb{J}_f, \mathbb{M}} \sigma^{(\text{RR})}(E; \alpha_i \mathbb{J}_i \rightarrow \alpha_f \mathbb{J}_f; \mathbb{M}) \right] \exp\left(-\frac{E}{T_e}\right) \quad [\text{a.u.}] ,$$

and where the major complexity now arises from determining the relevant final levels ($\alpha_f \mathbb{J}_f$) and all the associated cross sections. Here, $(\alpha_i \mathbb{J}_i)$ refers to the initial N electron bound level of the ions that recombines into any bound $N + 1$ electron level. While it is sometimes still mentioned that the ions are initially taken in their ground level, I haven't seen serious discussions how the summation over the $N + 1$ electron *resonances* ($\alpha_f \mathbb{J}_f$) should be made in practice. Although, no doubts, several codes perform reasonable approximations to this (multiple-infinite) summation over all final states, the overall structure of these rate coefficients and, in particular, the truncation of the final states will usually remain intransparent. Such a simple example shows that better insight into the physics is often already obtained if the dependencies are made explicit.

- **Hierarchy of approximations and prior assumptions:** Many (frequently) applied expressions in atomic physics are obtained, once a series of different assumptions and approximation were made before. While such an hierarchy of approximations is crucial for a successful description of physics, not all approximations are necessarily consistent with each other and, hence, may weaken some derivations significantly. By showing the assumptions made for an expression, the risk of computational pitfalls will be reduced.
- **Same designation, different physics:** There is little misunderstanding of scientific terms (and notation) possible if the subjects, where these terms are used, are sufficiently separate from each other. The use of scientific terms becomes however more problematic if there exist both, overlap and differences in their meaning and detailed designation. The use of (common) short designations and symbols then cause quickly confusion. This confusion can be (partly) overcome if the notations are made more explicit, and as done extensively in this Compendium. The opposite, different designations but the same physics, is easier to resolve but still requires extra effort. Likely, some readers may feel the partly redundant notations in this Compendium a little point for their own work but may still benefit, if they need to understand and apply expressions from neighboring fields.

1. Overview about JAC. Structure of this User Guide

1.1. Computational atomic physics: Challenges & difficulties

Contemporary challenges of computational atomic physics:

- (i) Developement of (practical) many-body techniques which account for all relevant electron-electron correlation contributions, and which can be improved systematically. These many-body techniques can be based on both, extended quantum electro-dynamical (QED) but also much simpler approximations, whenever *ab-initio* computations become unfeasible. Since the fine-structure constant and, hence (almost) all inner-atomic interactions, is known with very high accuracy, emphasis should be placed first of all on a detailed and much better understanding of many-electron effects in the behaviour and response of atoms and ions.
- (ii) Support of atomic spectroscopy to make time-consuming experiments necessary just as benchmarks of atomic theory but no longer in order to collect data for other research areas. This support requires the treatment of a (very) large number of atomic properties, processes and responses, and just as the JAC toolbox is aiming for, cf. section 1.2. It also requests for a critical evaluation of computational methods as well as a careful estimate of theoretical uncertainties in atomic computations.
- (iii) Highly-accurate predictions for various fundamental physics studies (and experiments) in exploring “new physics”. When compared to high-energy physics, such atomic experiments are performed at rather low costs, although they may still provide hints towards new concepts and interactions in physics owing to their (extremely) high accuracy. By using systematically-enlarged representations of atomic states, small remaining deviations between theory and experiment may indicate fundamental processes that are still omitted from theory. This approach has been utilized, for instance, in studying parity-nonconserving interactions, for atomic clocks as well as in the search of variations of the fine-structure constant.
- (iv) Electron dynamics in intense and spatially-structured light fields. While a first generation of these studies have often been successfully performed without considering much of the electronic structure of the target atoms, forthcoming experiments will reveal further details about the strong-field interaction, only if the time-dependent wave functions of the atoms and ions are taken into account. Such studies of atoms in intense fields make it also necessary to deal with time-dependent atomic density matrices at different level of sophistication.

1. Overview about JAC. Structure of this User Guide

- (v) Diagnostics in astro (and plasma) physics in order to support large space missions and to improve our understanding of the Universe; in fact, more than 99 % of all visible matter in the Universe is expected in a plasma states and subject to conditions that can hardly be re-produced in the laboratory.
- (vi) Use of [machine-learning techniques](#) to quickly generate large data sets for astrophysical observations and for the dynamical evolution of complex atomic (and molecular) systems.

Difficulties for the implementation and use of atomic theory:

- I have been involved in the computation of atomic properties and processes for more than two decades. During this time, I had to follow through various theoretical (and experimental) studies, from research papers to *ad-hoc* compilations of formulas to conference contributions. Frankly speaking, I found myself struggling on certain details again and again. Often, there has been taken little care by the authors about notations and the dependence of physical in the formulas, or more generally about the reader. In practice, a few lines in such texts can literally turn into several pages of precise mathematics (notations).
- **Difficulties for applying atomic theory:** From the recent study of $\gtrsim 250$ papers, that have been screened or analyzed for the implementation of JAC, the following observations were made:
 - (1) Although the *physics* is reasonably clear in a large fraction of papers, the notations (and formulas) can often not be resolved in good detail;
 - (2) Use of *ad-hoc* notations (and names) that do *not* properly support a consistent 'physics picture';
 - (3) Missing bindings of arguments and indices in formulas, for instance:
 - + Polarizability:
 - + Opacities:
 - (4) Assumptions and limitations (of given expressions) are often not mentioned or are incomplete, i.e. these expressions are valid only for special cases that are not transparent for the reader;
 - (5) Hierarchy of approximations is often not explained (and sometimes not even justified) from the viewpoint of physics;
 - (6) Reasoning in the derivation of formulas is not made explicit (enough) with regard to the underlying assumptions.

1.2. Goals of the JAC toolbox

Goals, purpose and use of JAC:

- The Jena Atomic Calculator (JAC) provides tools for performing atomic (structure) calculations at various degrees of complexity and sophistication. This toolbox has been designed to calculate not only **atomic level structures and properties** [g-factors, hyperfine and isotope-shift parameters, etc.] or **transition amplitudes between bound-state levels** [dipole operator, parity non-conservation, etc.] but also a large number of atomic processes including **(atomic) transition probabilities**, Auger rates, photoionization cross sections, radiative and dielectronic recombination rates as well as cross sections and parameters for many other (elementary) processes.
- Apart from **interactive (atomic) computations**, JAC also facilitates the simulation of **atomic cascades**, **atomic responses**, the **time-evolution of statistical tensors**, the **symbolic simplification of expressions from Racah's algebra** as well as various **semi-empirical estimates** of atomic properties. Indeed, JAC provides a diverse and wide-ranging, yet consistent set of methods which can be applied in different fields of atomic physics and elsewhere. In addition, the JAC module has been designed to readily support the display of level energies, electron and photon spectra, radial orbitals and several others entities.
- **Central features of JAC:** Figure 1.1 below displays a few central features of the JAC program that helps integrate different atomic processes within a single computational toolbox in order to ensure good self-consistency of all generated data.
- **Goals of JAC:** For many (modern) application of atomic structure theory, it is crucial indeed to integrate different atomic processes within a single computational toolbox in order to ensure good self-consistency of all generated data. JAC here aims to provide a very flexible user interface for different computational tasks, including a simple communication between the different parts of the program. In the past, sophisticated user interfaces often hampered the application of codes for people other than the authors (and sometimes even for them). **JAC aims to combines the strengths of previous atomic (structure) codes and to clearly enlarge the range of applications.**
- **Goals of JAC:** Since many methods for dealing computationally with quantum many-particle physics have first been applied to atoms and ions, JAC aims to retain and to advance this knowledge, and to make it usable by future AMO scientists. In JAC, the treatment of the electron continuum follows those of the FAC code but also goes well beyond it.
- **Goal of the JAC:** The JAC toolbox and its extensive User Guide aims to lower the barrier in developing new numerical methods in atomic physics. It provides a convenient and very flexible environment for use and code development, verification and analysis. The JAC toolbox differs from many other atomic structure programs whose codes are often difficult to decipher.
- **Domain-specific atomic language:** During the past decades, the demands to atomic structure and collision theory have distinctly changed from the accurate computation of level energies and properties towards (massive) applications in astro, plasma and various places elsewhere.

1. Overview about JAC. Structure of this User Guide

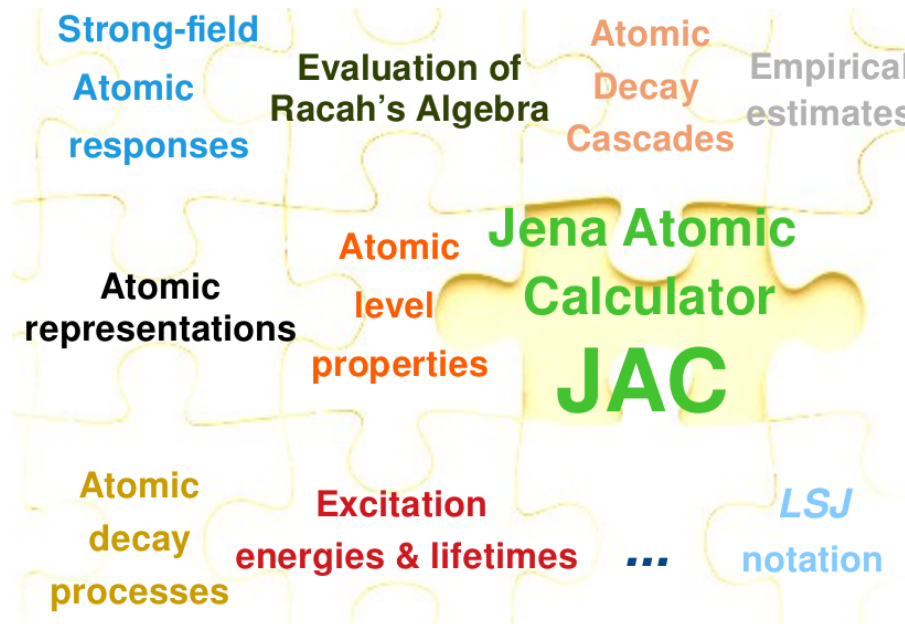


Figure 1.1.: Overview of the JAC toolbox for calculating atomic and ionic structures, processes and cascades, based on Dirac's equation and the MCDHF method. This toolbox facilitates a variety of relativistic computations as briefly shown in this jigsaw puzzle; from Fritzsche (2022).

These demands make it desirable to develop a domain-specific and descriptive language, which not only reveal the underlying formalism but also avoids most technical details. Apart from a concise syntax, close to the formulation of atomic physics problems, such a domain-specific language should support access to different models and approximations as well as the decomposition of a given task into well-designed steps, similar to writing pseudo-code; cf. Figure 1.2.

- **Domain-specific atomic language:** The design of JAC aims for several requirements that appear quite opposite to most previous — either FORTRAN or C — codes. These requirements refer to extending the code in a simple manner, a rapid proto-typing or the use of graphical interfaces. Moreover, such a language should as well support a transparent communication *with* and *within* the code, independent of the shell structure of the atoms or any particular application. By using Julia with its deliberate language design, JAC therefore aims to bring over productivity and performance also to atomic physics.
- **Promise of the JAC toolbox:** At present, this toolbox is perhaps the best educational resource in the field of (relativistic) atomic structure

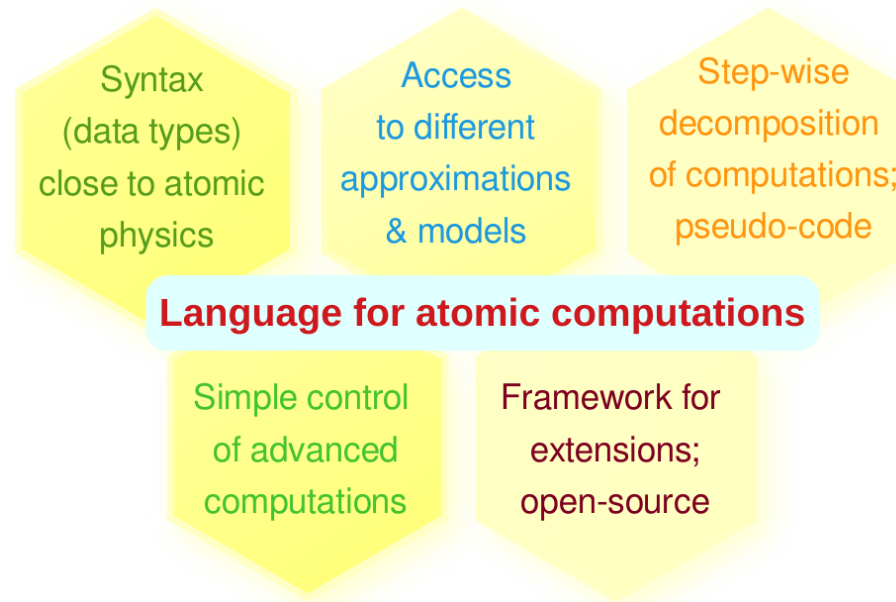


Figure 1.2.: Requirements for establishing a domain-specific and *descriptive* atomic language as it is implemented in JAC; from Fritzsche (2022).

theory; apart from the source code, a good number of Jupyter Notebooks help the user to explore the implementation stepwise and to exploit and analyze additional approximations.

- In order to support these goals, several **types of computation** are distinguished within the JAC toolbox, and which are summarized below.
- **To find (the details about) individual features of the JAC program, see the index or search for keywords/phrases in this User Guide.**
- **Design of JAC:** The design of these tools has been based on an analysis of typical user requirements and a hierarchical structure of the code.
- With the design and development of JAC, we also aim to identify (emerging) problems from AMO science and to support rapid scientific progress for the AMO community.
- **Theoretical background of JAC:** Since the theoretical background and data, implemented in JAC, have been extracted from quite many sources, we also hope to develop JAC as a **repository of previous experience with electronic structure calculations of atoms in different environments**, and that is to be further refined, expanded and developed here.

1. Overview about JAC. Structure of this User Guide

- **Use of JAC:** Applications of the JAC toolbox range from simple estimates for various atomic properties and processes upto full-scale atomic simulations. Since performance is crucial for many applications, the goal is to demonstrate performance comparable FAC, GRASP, RATIP and other atomic structure codes.
- **Use of JAC:** The source code, an extensive documentation as well as a number of tutorials and examples are available from our Web site <https://www.github.com/sfritzsche/JAC.jl>.
- **Comparison with other computational communities:** When compared to astro and particle physics, and even if compared to quantum chemistry, the AMO community has placed less emphasis over the last decades in developing and maintaining robust und user-friendly software tools for its own applications and for those in related fields.
- **Estimates of theoretical uncertainties:** Although the uncertainty quantification of computationally-generated data is still a great challenge for theoretical (many-particle) physics, uncertainty estimates are crucial for assessing the quality of predictions and for discriminating different models. An evaluation of the uncertainties is therefore an important part of atomic computations.
- **Estimates of theoretical uncertainties:** There are two major strategies in order to estimate the uncertainty of theoretical (computed) atomic data: (1) By enlarging and monitoring the size of state vector representations or (2) by deriving upper uncertainty limits for the computed results. Until the present, however, the second approach has been found less useful in practice, mainly because of the large (or often even huge) uncertainty bounds that are obtained eventually.

Types of computations:

- In the JAC toolbox, different types of computations are distinguished and can be easily controlled by the user without much prior knowledge about the code. Here, these different types of computations are briefly summarized, while all further details are given below in this User Guide.
- **Atomic computations, based on a set of explicitly specified electron configurations:** A typical computation, that is based on explicitly specified electron configurations, refers to level energies, atomic states or to either **one (or several) atomic properties** (for selected or all levels from a given multiplet). In addition, these atomic computations can provide also the rates and cross sections of just **one selected atomic process**. For all further details about the call and control of these computations, see the supported amplitudes, properties and processes in Sections 6–8 below.
- **Computation of atomic representations:** JAC supports the automatic generation of various atomic representations, such as an atomic *mean-field*, configuration-interaction as well as restricted active-space (RAS) expansions. In particular, the RAS computations refer to the

automatic and stepwise representation of atomic state functions and level energies due to a user-specified (and, hence, restricted) active space of orbitals as well as due to a given number and/or kind of virtual excitations to be included. Such RAS computations are internally always performed *stepwise* in JAC by utilizing the self-consistent field (orbitals) from some prior step. See Section 4 for all further details about atomic representations.

- **Interactive computations:** In an interactive computation, the functions/methods of the JAC program are applied interactively, either directly within the REPL or by just writing a short JULIA script, in order to compute energies, expansion coefficients, transition matrices, rates, cross sections, etc. An interactive computation typically first prepares and generates (instances of) different data structures of JAC, such as orbitals, (configuration-state) bases, multiplets, and later applies these computed data in subsequent steps in order to obtain the desired information. Of course, all methods from JAC and its submodules can be utilized also interactively, although some specialized methods are typically available and help facilitate the computations. Like most other JULIA functions, the functions and methods from the JAC toolbox can be seen as (high-level) language elements in order to perform atomic computations at various degrees of sophistication.
- **Atomic cascade computations and simulations:** A cascade computation typically refers to three or more charge states of an atom that are connected to each other by different atomic processes, such as photoionization, Auger emission, radiative transitions, etc. Different (cascade) schemes and approaches have been predefined in JAC in order to deal with atomic cascades. The user has to specify the particular atomic processes that are taken into account for the individual steps of the cascade. Apart from cascade computations, (cascade) simulations make then use of a pre-calculated list of (many-electron) amplitudes, rates and/or cross sections in order to derive different ion, photon and/or electron distributions and spectra. In Jac, cascade computations and cascade simulations are always handled independently. See section ?? for further details about these cascade computations and simulations.
- **Atomic responses:** Atomic response computations (will) provide access to various responses of atoms and ions to some incident (beam of) light pulses and particles, such as strong-field induced ionization processes, high-harmonic generation and others. For these responses, almost no detailed atomic structure has been considered in the past, although these details will become relevant as more elaborate and accurate measurements are to be carried out. Only a rather restricted number of such response computations are supported so far. See section 10 for all further details.
- **Time evolution of statistical tensors in (intense) light pulses:** In JAC, a time evolution of statistical tensors always proceeds within a pre-specified set of sublevels $\{|\alpha JM\rangle\}$, i.e. within a pre-defined subspace of the many-electron Hilbert space; all further (decay) processes that lead the system eventually out of this subspace must be treated by loss rates. Although such a time evolution can deal with pulses of different shape, strength and duration, it is assumed that they are weak enough in order not to disturb the level structure and level sequence of the atoms substantially in their neutral or ionic stage, i.e. that every selected sublevel can still be characterized by its (total) energy and symmetry. However, such time-evolutions of statistical tensors has not yet been implemented in detail so far. Note that no attempt is made (nor planned) in JAC in order to solve the time-dependent (many-electron) Schrödinger equation explicitly.

1. Overview about JAC. Structure of this User Guide

- **Symbolic simplification of expressions from Racah's algebra:** Such expressions can often be simplified by applying well-selected algebraic transformation from the theory of angular momentum. These transformations may generally include any number of Wigner n-j symbols of different kind as well as (various integrals over) the spherical harmonics, the Wigner rotation matrices and the Kronecker and triangular deltas. In practice, the complexity of Racah expressions increases very rapidly as more Wigner symbols, spherical harmonics and/or rotation matrices are involved. In JAC, a symbolic evaluation of these expressions can be performed, based on a sizeable set of special values, orthogonality relations and sum rules, including rules with a (multiple) summation over dummy indices, cf. the monography by Varshalovich et al (1988) and section 15 for further details about such symbolic simplifications.
- **Atomic descriptors:** In building models for machine learning, the definition of proper (atomic) descriptors or feature transformations is central for predicting the physical properties and behaviour of atoms and ions; here, we shall provide various of such descriptors useful for atomic physics. See section 12 for further details about atomic descriptors.
- **Semi-empirical estimates of atomic properties, cross sections, asymptotic behaviour, etc.:** A semi-empirical ‘estimate’ of atomic data refers either to some simplified model computation or to the evaluation of fit functions in order to **provide those atomic data which cannot be generated so easily by *ab-initio* computations.** These semi-empirical estimates are typically built on — more or less — sophisticated models and external parameter optimizations. However, only a very few of such estimates have been implemented so far, and no attempt is made to extend this type of computation, if such data are not essential for other applications of JAC. See section 13 for further details.

1.3. Frequent terms and notations in using JAC

Glossary:

- **Angular coefficient:** Reduced many-electron matrix elements (amplitudes) can usually be decomposed into a sum of *angular coefficient* \times *interaction strength*, and where latter refers to standard one- and two-particle due to the character of the (many-electron) operator. The (pure) angular coefficients are presently calculated by means of the ANCO program (Gaigalas *et al.*, 2001); cf. section 3.8.
- **Atomic shell model:** This model, in which electrons fill a (more or less) regular list of atomic shells or make transitions (quantum jumps) between different shells, is **key and guidance for calculating the electronic structure of atoms, ions and molecules, and most of their properties.**
- **Atomic-state function (ASF):** In the multiconfiguration Dirac-Hartree-Fock method, an atomic state function is written as linear combination of configuration state functions (CSF) with well adapted symmetry, cf. section 4. This is analogue to the non-relativistic Hartree-Fock method with symmetry-adapted functions.
- **Basis:** In JAC, a many-electron basis is specified in terms of a CSF list and the radial orbitals of all (equivalent) electrons that occur in this list. Moreover, each CSF is specified uniquely by a proper set of quantum numbers. In JAC, the (so-called) **seniority scheme** is applied for the unique classification of the CSF and the evaluation of all matrix elements.
- **Cascade:** A cascade typically includes ions of an element in three or more charge states that are connected to each other by different atomic processes, such as photoionization, Auger emission or radiative transitions. A quantum modelling of a cascade requires to follow all possible *pathways* that the ions leads eventually into some stable ground state. In JAC, we distinguish between different *cascade scheme* (photoionization cascades, decay cascades) and *cascade approaches* to account for different computational models in dealing with the pathways.
- **Cascade simulation:** A cascade simulation makes use of a pre-calculated list of (many-electron) amplitudes, rates and/or cross sections in order to derive different ion, photon and/or electron distributions and spectra, and which can be compared directly to experiment. In JAC, cascade computations and cascade simulations are always handled independently.
- **Channel:** For most atomic lines, different (quantum) channels need to be distinguished due to the symmetry properties of the multipoles or of partial waves in the decomposition of the many-electron levels and/or matrix elements.
- **Configuration interaction (CI) expansion:** Refers to a CI representation of ASF.

1. Overview about JAC. Structure of this User Guide

- **Electron configuration:** Describes the occupation of shells within the atomic shell model, for instance, $1s^2 2s^2 2p^6 3s^2$. In JAC, closed-shell configurations can be abbreviated by using the noble gases or selected close-shell atoms with a closed ground-state configuration. For example, the valence-shell excited configurations of aluminium-like atoms can be given as [Ne] $3s^2 3p$, [Ne] $3s 3p^2$, or [Mg] $3d$.
 - **Configuration-state function (CSF):** These symmetry-adapted many-electron (basis) states are constructed as antisymmetrized product of one-particle states but coupled to well-defined total angular momentum and parity. In JAC, CSF are typically abbreviated by $|\gamma \mathbb{J}M\rangle \equiv |\gamma J^P M\rangle$.
 - **Electro-magnetic property (EmProperty):** A (data) **struct** of JAC to maintain internally the same property (rates, cross sections) in Coulomb and Babushkin gauge for the coupling of the radiation field.
 - **Envelope:** A (data) **struct** of JAC to deal with an (externally-defined) pulse-shape function $f(t)$ in the time-evolution of statistical tensors. The user can select from a (small) library of such pulse-shape function due to different parametrization, and where an integer number of optical cycles is ensured for the sake of numerical stability.
 - **Green function expansion:** A (data) **struct** of JAC to compute an approximate (many-electron) Green function representation of an atom or ion, based on a user-specified set of reference configuration. Such a representation is provided by JAC by a list of Green function channels::`ArrayAtomicState.GreenChannel` ,1; cf. section 4.1.d.
 - **Hyperfine level:** Analogon to an ASF but with well-defined total angular momentum and parity $\mathbb{F} = F^P$: $\alpha\mathbb{F}$, and where α refers to all further quantum numbers that are needed for a uniques specification. These hyperfine levels are typically expanded in terms of electronic ASF and not directly in CSF.
 - **Hyperfine multiplet:** Analogon to a level multiplet but taken as group of hyperfine level. Such a hyperfine multiplet can refer to either a single electronic level or to one or several electron configurations.
 - **Level (notation):** $|\alpha\mathbb{J}\rangle \equiv |\alpha J^P\rangle$; $|\alpha\mathbb{J}M\rangle \equiv |\alpha J^P M\rangle$.
- Here, the multi-index α formally refers to all additional quantum numbers that are needed for the unique specification of any given many-electron level or state. — In this User Guide, for instance, we shall often use $(\alpha_i \mathbb{J}_i)$ and $(\alpha_f \mathbb{J}_f)$ below in order to refer to the initial and final-ionic bound levels of some atomic amplitude and process.
- **Level key:** A (data) **struct** of JAC that help identifying a level by its symmetry, energy and some further property. These level keys facilitate the implementation of cascade simulations.
 - **Level symmetry:** A (data) **struct** of JAC to represent $\mathbb{J} = J^P$ in terms of its total angular momentum J and parity P .

- **Line:** A (transition) line refers to an atomic transition that is characterized in terms of a well-defined initial and final level; these lines frequently occur in the computation of atomic properties, such as cross sections or rates, angular distribution parameters. Typically, a line contains various channels (sublines), for instance, due to occurrence of multipoles or of partial waves in the decomposition of the many-electron levels and/or matrix elements.
- **Line key:** A (data) **struct** of JAC that help identifying a (transition) line by the keys of the initial and final level, its transition energy, decay strength, etc. These line keys facilitate the implementation of cascade simulations.
- **Mean field:** A (data) **struct** of JAC to compute a mean-field basis for an atom or ion, by starting from a set of user-specified reference configurations.
- **Multi-photon process:** Non-linear multi-photon absorption and emission processes occur in sufficiently intense field, including two-photon absorption and emission as well as higher-order processes; cf. section [refMultiPhotonDeExcitation](#).
- **Multiplet:** Atomic levels are naturally *grouped together* into (so-called fine-structure) mutiplets; most often, this term just refers to all fine-structure levels of one or a few given configurations. More generally, a multiplet can refer to any group of atomic levels, for instance, in order to groups levels with the same total angular momentum J and/or parity P , the fine-structure levels of nearby-in-energy or overlapping configurations, etc.
- **Multipole:** In JAC, the standard notations is used for the E1 (electric-dipole), M1 (magnetic-dipole), E2 (electric-quadrupole), etc. (field) components; they are briefly referred to a ***multipoles*** \mathbb{M} of the radiation field. A multipole \mathbb{M} is internally characterized by its multipolarity L and its (boolean) character *electric* (= `true/false`).
- **Multipole components (fields) of the radiation field:** These multipole fields occur at many different places in atomic theory due to the electron-photon interaction, though often within slightly different contexts.
- **Multipole transition operator** $\mathbb{O}^{(\mathbb{M})}$: Transition operator in absorption and emission processes due to the interaction with the specified multipole component of the radiation field; these operators frequently occurs in summations $\sum_{\mathbb{M}} \dots$ over such operators and/or the associated transition amplitudes (matrix elements).
- **Multipole moment operator** $\mathbb{Q}^{(\mathbb{M})}$: These operators describe the frequency-independent (part of the) interaction with a multipole component of the radiation field.
- **Nuclear model:** The nuclear charge distribution can be modelled by different – more or less – realistic models, including a point-like, uniform or Fermi-distributed nuclear charge.
- **Orbital:** In atomic physics, an orbital typically refers to a one-electron function in some radial-spherical representation and, often, only the radial function is meant (radial orbital). In the relativistic theory, moreover, one needs to distinguish between the large and small components of the orbital, as the occur for Dirac's equation in a central-field potential.

1. Overview about JAC. Structure of this User Guide

- **Pathway:** In contrast to an (atomic) line, that is characterized by an initial- and a final-level (from the corresponding multiplets), a pathway describe a sequence of three or more levels, and which are often connected via different atomic processes. These levels are usually referred to as initial, (one or several) intermediate as well as the final level of the pathway. Pathways occur naturally in dielectronic recombination of ions, in various excitation-ionization or excitation-autoioization processes and in photoionization and decay cascades.
- **Plasma model:** In JAC support is provided for a number of simple plasma models (Debye-Hückel, ion-sphere, ...) that can be applied in order to determine plasma shifts of atomic energies and rates.
- **Polarization:** Several atomic properties and processes depend on the polarization of the incident radiation field, which often need to be specified in terms of Stokes parameters.
- **Potential:** A (data) **struct** of JAC to represent a (spherically-symmetric) atomic potential.
- **Probability propagation:** Process to propagate the occupation of the initial levels through some – photoionization or decay – cascade in order to determine final, photon and/or electron distribution. Such a probability propagation can done either stepwise or by means of Monte-Carlo techniques.
- **QED model:** In JAC, two simplified models can be applied to estimate the dominant QED contributions to atomic level energies and wave functions: (i) **QedPetersburg** to apply a self-energy model operator from the St. Petersburg group; (2) **QedSydney** to make use of a *radiative* potential of the Sydney group.
- **Racah expression:** Such (Racah) expressions may generally include any number of Wigner $n-j$ symbols of different kind as well as (various integrals over) the spherical harmonics, the Wigner rotation matrices and the Kronecker and triangular deltas. Obviously, the complexity of a Racah expression increases very rapidly as more Wigner symbols are involved.
- **Radial grid:** In JAC, all radial orbital functions are always represented on a (radial) grid, i.e. only the grid representation of these functions is eventually applied in the evaluation of all (single- and many-electron) matrix elements. In JAC, either an *exponential* grid, suitable for bound-state computations, or a *logarithmic-linear* grid, that still increases exponentially in the inner part and linearly in the outer part, can be selected by the user. A logarithmic-linear grid is suitable especially for collision processes and for dealing with electrons within the continuum.
- **RAS expansion:** An expansion of an ASF for a given restricted-active space of orbitals (and symmetries).
- **Relativistic angular-momentum quantum number:** $\kappa = \pm(j + 1/2)$ for $\ell = j \pm 1/2$ carries information about both, the total angular momentum j and the parity $(-1)^\ell$ of the (single-electron) wavefunction.
- **Representation:** A (data) **struct** of JAC to specify an atomic state representation, i.e. a representation of atomic state vectors; different representations are supported by the program.

- Resonances or scattering (atomic) states with a single free electron: $|\alpha\mathbb{J}, \varepsilon\kappa\rangle \mathbb{J}_t \rangle \equiv |(\alpha J^P, \varepsilon\kappa) J_t^{P_t}\rangle$
describes a many-electron scattering wave with a single free electron in the partial wave $|\epsilon\kappa\rangle$, and where \mathbb{J}_t denotes the overall symmetry of the many-electron scattering state (level).
- **Settings:** In JAC, the control of most, if not all, computations is made by specially-designed **Settings**, and which are associated with particular amplitudes, properties and processes. These settings are used in JAC in order to specify all details about the requested computation; these settings also enable one, for instance, to select individual levels or lines as well as various physical and technical parameters, such as the multipoles, gauges, etc.
- **Sharing:** A particular energy ratio of two photons (and/or electron) in multi-photon or multi-electron processes. Such sharings are given as percentages, while the energies themselves usually depend on the particular transitions.
- **Shells and subshells:** Shells and subshells are the building blocks of the atomic shell model. In the relativistic theory, each non-relativistic $n\ell$ -shell (apart from the ns -shells) splits into two relativistic subshells due to $j = \ell \pm 1/2$. In JAC, the shell and subshell notations are therefore used in order to refer to electron configurations, configuration state functions (CSF), or to the orbitals of equivalent electrons. In JAC, there are special data struct's available to easily deal with and communicate the (sub-) shell occupation of levels and wave functions.
- **Statistical tensor:** Spherical tensors $\rho_{kq}(\alpha\mathbb{J})$ that are associated with atomic levels and that help characterize the *polarization* and *alignment* of atoms and ions; these statistical tensor have well-defined symmetry properties.
- **Stokes parameter (EmStokes):** A (data) **struct** of JAC to describe the Stokes parameter for the polarization of emitted photons or electrons.
- **Target model:** A (abstract data) **struct** of JAC to represent an atomic target (cloud), for instance, for high-harmonic generation processes.
- **Tensor component:** Individual component of a statistical tensor, applied for the time-evolution of many-electron density matrices.
- **Transition amplitude:** Transition amplitudes refer to the many-electron matrix elements that provide access to all observables. The atomic structure and collision theory of many-electron atoms and ions is most naturally built upon such transition amplitudes (matrix elements).
- **Wigner $n-j$ symbol:** The Wigner symbols are all related to the recoupling of angular momenta; they occur very frequently in the recoupling of matrix elements as well as the decomposition of angular distributions and the polarization of emitted photons and electrons.

1.4. A quick overview about the amplitudes, level properties and processes handled by JAC

In JAC (partly) implemented amplitudes:

- In JAC, several many-electron (reduced) amplitudes are readily accessible. Further details about the call of these amplitudes can be found below in this User Guide or interactively by `?<module>.amplitude`.

| Amplitude | Call within JAC | Brief explanation |
|--|---------------------------------|--|
| $\langle \alpha J \ T^{(1)} \ \beta J' \rangle, \langle \alpha J \ T^{(2)} \ \beta J' \rangle$ | Hfs.amplitude | Amplitude for the hyperfine interaction with the magnetic-dipole and electric-quadrupole field of the nucleus. |
| $\langle \alpha J \ N^{(1)} \ \beta J' \rangle$ | LandeZeeman.amplitude | Amplitude for the interaction with an external magnetic field. |
| $\langle \alpha_f J_f \ O^{(\mathbb{M}, \text{emission})} \ \alpha_i J_i \rangle$ | PhotonEmission.amplitude | Transition amplitude for the emission of a multipole (\mathbb{M}) photon. |
| $\langle \alpha_f J_f \ O^{(\mathbb{M}, \text{absorption})} \ \alpha_i J_i \rangle$ | PhotonEmission.amplitude | Transition amplitude for the absorption of a multipole (\mathbb{M}) photon. |
| $\langle (\alpha_f J_f, \varepsilon \kappa) J_t \ O^{(\mathbb{M}, \text{photoionization})} \ \alpha_i J_i \rangle$ | PhotoIonization.amplitude | Photoionization amplitude for the absorption of a multipole (\mathbb{M}) photon and the release of an electron into the partial wave $ \varepsilon \kappa\rangle$. |
| $\langle \alpha_f J_f \ O^{(\mathbb{M}, \text{recombination})} \ (\alpha_i J_i, \varepsilon \kappa) J_t \rangle$ | PhotoRecombination.amplitude | Photorecombination amplitude for the emission of a multipole (\mathbb{M}) photon and the capture of an electron that comes <i>in</i> the partial wave $ \varepsilon \kappa\rangle$. |
| $\langle (\alpha_f J_f, \varepsilon \kappa) J_t \ V^{(\text{Auger})} \ \alpha_i J_i \rangle$ | Auger.amplitude | Auger transition amplitude due to the electron-electron interaction and the release of an electron into the partial wave $ \varepsilon \kappa\rangle$. |
| $\langle \alpha_f J_f \ \sum \exp i \mathbf{q} \cdot \mathbf{r}_i \ \alpha_i J_i \rangle$ | FormFactor.amplitude | Amplitude for a momentum transfer \mathbf{q} with an external particle or photon field. |
| $\langle \alpha_f J_f \ H^{(\text{weak-charge})} \ \alpha_i J_i \rangle$ | PNC.weakChargeAmplitude | Amplitude for the nuclear-spin independent Hamiltonian of the (P -odd, T -even) interaction; here PNC stand for ParityNonConservation. |
| $\langle \alpha_f J_f \ H^{(\text{Schiff-moment})} \ \alpha_i J_i \rangle$ | PNC.schiffMomentAmplitude | Amplitude for the nuclear Schiff moment of the (P -odd, T -odd) interaction. |
| $\langle \alpha_f J_f \ H^{(\text{scalar-pseudo-scalar})} \ \alpha_i J_i \rangle$ | PNC.scalarPseudoScalarAmplitude | Amplitude for the scalar-pseudo-scalar (P -odd, T -odd) interaction. |

In JAC (partly) implemented atomic level properties:

- In JAC implemented or partly-implemented atomic properties. For these properties, different parameters (observables) can usually be obtained by performing an `Atomic.Computation(..., properties=[id1, id2, ...])`, and if one or more of the given identifiers below are specified for this computation. For each of these properties, moreover, the corresponding (default) `Settings` can be readily overwritten by the user in order to control the computations.

| Property | id | Brief explanation. |
|---|------------------------|---|
| $ \alpha\mathbb{J}\rangle \rightarrow \alpha(J)\mathbb{F}\rangle$ | HFS | Hyperfine splitting of an atomic level into hyperfine (sub-) levels with total angular momentum $F = I - J , \dots, I + J - 1, I + J$; hyperfine A and B coefficients; hyperfine energies and interaction constants; representation of atomic hyperfine levels in a IJF -coupled basis. |
| $ \alpha\mathbb{J}\rangle \rightarrow \alpha JM\rangle$ | LandeJ | Zeeman splitting of an atomic level into Zeeman (sub-) levels; Lande $g_J \equiv g(\alpha\mathbb{J})$ and $g_F \equiv g(\alpha\mathbb{F})$ factors for the atomic and hyperfine levels. |
| $K^{(\text{MS})}, F$ | Isotope | Isotope shift of an atomic level for two isotopes with mass numbers A, A' : $\Delta E^{AA'} = E(\alpha\mathbb{J}; A) - E(\alpha\mathbb{J}; A')$; mass-shift parameter $K^{(\text{MS})}(\alpha\mathbb{J})$ and field-shift parameter $F(\alpha\mathbb{J}; A)$. |
| α -variations | AlphaX | Differential sensitivity of an atomic level $(\beta\mathbb{J})$ with regard to variation of the fine-structure constant; $\Delta E(\delta\alpha; \beta\mathbb{J}), \Delta q(\delta\alpha; \beta\mathbb{J}), K(\beta\mathbb{J})$. |
| $F(q; \alpha\mathbb{J})$ | FormF | Standard and modified atomic form factor of an atomic level $(\alpha\mathbb{J})$ with a spherical-symmetric charge distribution. |
| $\omega(\alpha\mathbb{J}) + a(\alpha\mathbb{J}) = 1$ | Yields | Fluorescence & Auger decay yields of an atomic level, or averaged over an electron configuration. |
| $\alpha^{(K, \text{acStark})}(\omega; \beta\mathbb{J}) \dots$ | | Static (dc) and frequency-dependent (ac Stark) polarizabilities. |
| $E(\alpha\mathbb{J}; \text{plasma model})$ | Plasma | Plasma shift of an atomic level as obtained for different but commonly-applied plasma models. |
| $ \alpha_i\mathbb{J}_i\rangle \rightarrow \alpha_f\mathbb{J}_f\rangle + \hbar\omega$ | EinsteinX ^a | Photon emission from an atom or ion; Einstein A and B coefficients and oscillator strength between levels $ \alpha_i\mathbb{J}_i\rangle \rightarrow \alpha_f\mathbb{J}_f\rangle$ that belong to a single multiplet (representation). |

^a Although the Einstein coefficients are not the property of a single level, we here still support a quick computation of these coefficients by means of the `Einstein` module for pairs of levels that are part of the same multiplet, i.e. given within a single CSF basis.

1. Overview about JAC. Structure of this User Guide

In JAC (partly) implemented atomic processes:

- In JAC implemented or partly-implemented atomic processes. For just *one* of the listed process at a given time, different parameters (observables) can usually be obtained by performing an `Atomic.Computation(..., process=id)`, and if the corresponding identifier is specified. For this selected process, moreover, the corresponding (default) `Settings` can be overwritten by the user in order to control the computations.

| Process | id | Brief explanation |
|--|---------------|---|
| $A^* \rightarrow A^{(*)} + \hbar\omega$ | Radiative | Photon emission from an atom or ion; transition probabilities; oscillator strengths; angular distributions. |
| $A + \hbar\omega \rightarrow A^*$ | PhotoExc | Photoexcitation of an atom or ion; alignment parameters; statistical tensors. |
| $A + \hbar\omega \rightarrow A^{+*} + e_p^-$ | PhotoIon | Photoionization of an atom or ion; cross sections; angular parameters; statistical tensors. |
| $A^{q+} + e^- \rightarrow A^{(q-1)+} + \hbar\omega$ | Rec | Photorecombination of an atom or ion; recombination cross sections; angular parameters. |
| $A^{q+*} \rightarrow A^{(q+1)+(*)} + e_a^-$ | Auger | Auger emission (autoionization) of an atom or ion; rates; angular and polarization parameters. |
| $A^{q+} + e^- \rightarrow A^{(q-1)+*} \rightarrow A^{(q-1)+(*)} + \hbar\omega$ | Dierec | Dielectronic recombination (DR) of an atom or ion; resonance strengths. |
| $A + \hbar\omega_i \rightarrow A^* \rightarrow A^{(*)} + \hbar\omega_f$ | PhotoExcFluor | Photoexcitation of an atom or ion with subsequent fluorescence emission. |
| $A + \hbar\omega \rightarrow A^* \rightarrow A^{(*)} + e_a^-$ | PhotoExcAuto | Photoexcitation & subsequent autoionization of an atom or ion. |
| $A + \hbar\omega_i \rightarrow A^{(*)} + \hbar\omega_f$ | Compton | Rayleigh or Compton scattering of photons at an atom or ion; angle-differential and total cross sections. |
| $A + n\hbar\omega \rightarrow A^* \quad \text{or}$ $A^* \rightarrow A^* + n\hbar\omega$ | MultiPhotonDE | Multi-photon (de-) excitation of an atom or ion, including two-photon absorption and emission, bi-color two-photon absorption, etc. |
| $A + Z_p \rightarrow A^* + Z_p$ | CoulExc | Coulomb excitation of an atom or ion by fast, heavy ions; energy-differential, partial and total Coulomb excitation cross sections. |
| $A + \hbar\omega \rightarrow A^* + e_p^- \rightarrow A^{(*)} + e_p^- + \hbar\omega'$ | PhotoIonFluor | Photoionization of an atom or ion with subsequent fluorescence emission. |
| $A + \hbar\omega \rightarrow A^* + e_p^- \rightarrow A^{(*)} + e_p^- + e_a^-$ | PhotoIonAuto | Photoionization of an atom or ion with subsequent autoionization. |
| $A^{q+} + e^- \rightarrow A^{(q-1)+*} \rightarrow A^{(q-1)+(*)} + \hbar\omega \rightarrow A^{(q-1)+} + \hbar\omega + \hbar\omega'$ | DierecFluor | Dielectronic recombination of an atom or ion with subsequent fluorescence. |

| Process | id | Brief explanation |
|--|----------------|---|
| $e_s^- + A \rightarrow A^* + e_s^-'$ | Eimex | Electron-impact excitation of an atom or ion; collision strength. |
| $A + e_s^- \rightarrow A^* + e_s^-' \rightarrow A^{+(*)} + e_s^-' + e_a^-$ | EimexAuto | Electron-impact excitation and subsequent autoionization of an atom or ion. |
| $A^{q+*} \rightarrow A^{(q+1)+(*)} + (e_a^- + \hbar\omega)$ | RadAuger | Radiative-Auger (autoionization) of an atom or ion. |
| $A + n\hbar\omega \rightarrow A^{(*)} + e_p^-$ | MultiIon | Multi-photon ionization of an atom or ion. |
| $A + n\hbar\omega \rightarrow A^{(*)} + e_{p_1}^- + e_{p_1}^-$ | MultiDoubleIon | Multi-photon double ionization of an atom or ion. |
| $A^{q+[\text{nucleus}^*]} \rightarrow A^{(q+1)+*} + e_c^-$ | Conversion | Internal conversion, i.e. electron emission due to nuclear de-excitation. |

- **Applications of the JAC toolbox:** Figure 1.3 displays selected applications of the JAC toolbox for predicting the properties and processes of atoms and ions, though not all of these processes have yet been implemented in full detail (as indicated by grey color).

1.5. Remarks on the implementation

Why Julia ?

- Here, we just recall some of our own experiences as well as a few remarks from the literature **why JULIA have been found very helpful for developing the JAC program**. Some of these arguments are directly adapted from the work of Bezanson *et al.* (2017, 2018).
- **Productivity:** JULIA is a language for scientific computing that offers many of the features of productivity languages, namely rapid development cycles; exploratory programming without having to worry about types or memory management; reflective and meta-programming; and language extensibility via multiple dispatch (Bezanson *et al.*, 2018).
- **Productivity *versus* performance:** JULIA is often said to stand for the combination of productivity and performance through a careful language design and carefully chosen technologies; it never enforces the user to resort to C or Fortran for fast computations. — Moreover, JULIA's design allows for gradual learning of modern concepts in scientific computing; from a manner familiar to many users and towards well-structured and high-performance code.
- **Productivity *versus* performance:** JULIA's productivity features include: dynamic typing, automatic memory management, rich type annotations, and multiple dispatch. JULIA also supports some control of the memory layout and just-in-time compilation in order to eliminate much of the overhead of these features above (Bezanson *et al.*, 2018).

1. Overview about JAC. Structure of this User Guide

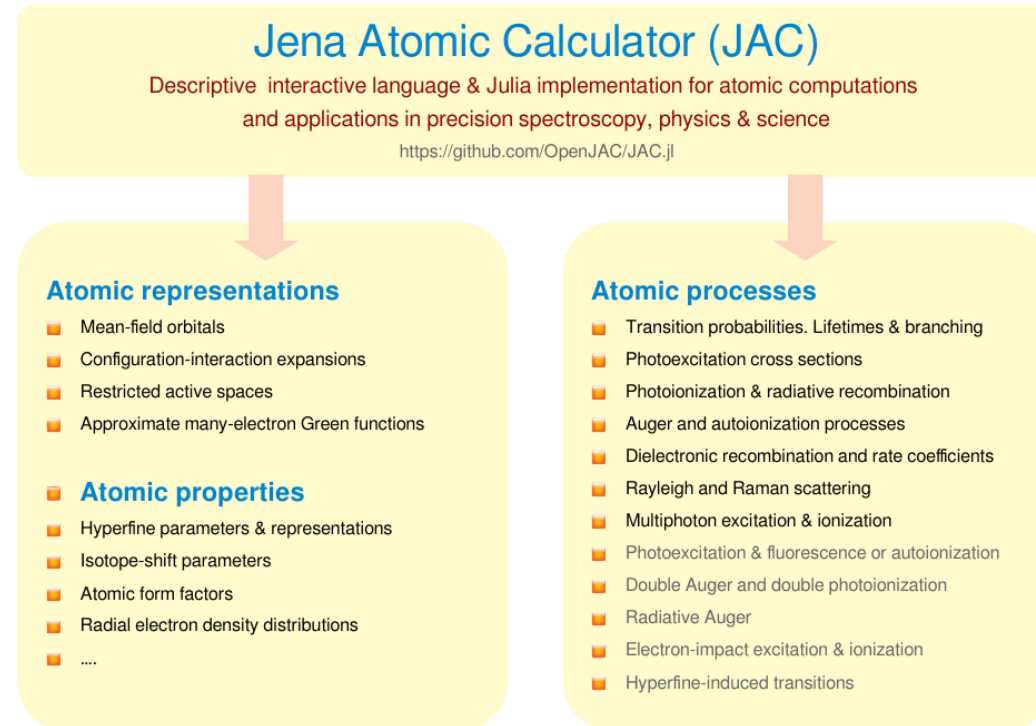


Figure 1.3.: Selected applications of the JAC toolbox to generate atomic representations or to compute properties and processes; from Fritzsche (2022).

- Productivity *versus* performance: Julia promises scientific programmers the ease of a productivity language at the speed of a performance language.
- Productivity *versus* performance: JULIA aims to decrease the natural gap that usually occurs between productivity and performance languages by providing **productivity features like dynamic typing, garbage collection, and multiple dispatch** but with a type-specializing just-in-time compiler and good control of the the layout of data structure in memory.
- Productivity & language design: Julia includes a number of (modern) features that are common to many productivity languages, namely dynamic types, optional type annotations, reflection, dynamic code loading as well as garbage collection (Bezanson *et al.*, 2018).
- Productivity: In JULIA, it is sometimes believed that **class-based methods are not scientifically powerful enough in order to express full**

abstraction in scientific computing.

- **Performance:** A key to performance in JULIA refers to the synergy between language design, implementation techniques and programming style so that a rather small team of language implementers could create an efficient implementation/compiler (Bezanson *et al.*, 2018).
- **Performance:** There exist helpful macros, such as `@timing function_call(parameters)` or `@benchmark function_call(parameters)` in order to analyze the performance of the program and to find (and resolve) bottlenecks.
- **Performance & LAPACK:** All of LAPACK is available in JULIA, not just the most common functions. LAPACK wrappers are fully implemented by `ccall` and can be called directly from the Julia prompt.
- **Performance and parallelization:** One of the central motivation to built JULIA was the design of a parallel computing language. Therefore, JULIA provides different facilities for parallelism. Two important concepts are *remote calls* and *remote references*; cf. `@parallel`. In contrast, vectorization is in JULIA NOT considered as a pre-requisite for performance.
- **High-level languages:** Most traditional high-level languages are hampered by the overhead from the interpreter, and which typically results into (much) more run-time processing of what is strictly necessary. One of these hindrances is (missing) type information, and which then results in the request for supporting vectorization. JULIA is a 'verb'-based language in contrast to most object-oriented 'noun'-based language, in which the generic functions play a more important role than the datatypes.
- **Multiple dispatch:** This concept refers to the dynamically selected implementation and to running the right code at the right time. This is achieved by overloading by means of multiple-argument function, a very powerful abstraction. Multiple dispatch makes it easier to structure the programs close to the underlying science.
- **Multiple dispatch:** At run-time, a function call is dispatched to the most specific method applicable to the types of its arguments. JULIA's type annotations can be attached also to datatype declarations and checked whenever typed fields are assigned to. Moreover, multiple dispatch help the programmers to extend the core languages' functionalities to their particular needs.
- **Multiple dispatch** obviously reduces the needs for argument checking at the begin of a function. The overloading of functions by multiple dispatch is also called *ad-hoc polymorphism*. Instead of encapsulating data-specific methods inside classes, JULIA's multiple dispatch is a paradigm in which methods are defined on combinations of data types (classes). JULIA demonstrates that this paradigm is remarkably well-suited for numerical computing.
- **Multiple dispatch** is perhaps the most prominent feature of JULIA's design and is crucial for the performance of the language and its ability to inline code efficiently. Another promise of multiple dispatch is that it can be used to extend existing behavior with new features.
- **JULIA's type system:** To a large extent, JULIA code can be implemented without any mentioning of types (in contrast to C and Fortran), and which are derived by data-flow inference. JULIA's expressive type system supports an aggressive code specialization against run-time types and also allows the use of optional type annotations.

1. Overview about JAC. Structure of this User Guide

- JULIA's type system: User's own types are also first class in JULIA, that is there is no meaningful distinction between built-in and user-defined types. There are mutable and (default: immutable) composite types.
- JULIA's type system: JULIA distinguishes between concrete data types, that can be instantiated, and abstract types, that can (only) be extended by subtypes in order to built up an hierarchy of such types.
- JULIA's type system *versus* object oriented programming: JULIA's design does not support the class-based object-oriented programming style, that is familiar from Java, and it also lacks the usual encapsulation going back to Smalltalk: Instead, all fields of a (data) struct are public and can be accessed freely within the code.
- Julia's type system: This type system is known as one of its strongest features, when compared with many other compute languages. In Julia, all types are said to be *first-class* and are utilized to select the code dynamically by means of (so-called) multiple dispatch. While abstract data types are used to establish a hierarchy of relationships between data and actions, and are applied in order to model *behavior*, the actual data are always kept by concrete types, either as primitive and composite types. Moreover, abstract and concrete types can be both *parametric* to further enhance the dynamic code allocation. All these rather general concepts are also well adopted in JAC to facilitate the communication *with* as well as the data transfer *within* the program. Frankly speaking, these data structures form the basic language elements in order to specify and describe the desired computations.
- Data type stability: In JULIA, users are always encouraged to make their programs, whenever possible, type stable. Much of the efficiency of a JULIA code relies on being type stable and on devirtualization and inlining.
- Name space and code selection: JULIA name space allows for the use of the same vocabulary in different circumstances, and which makes programs easier to read. In particular, it uses the same mechanism of code selection at the lowest and highest levels and is therefore able to select the right method, either already at compile time or later at run time.
- Use of macros: A macro is a function that runs at parse time. It takes symbolic expressions in and returns transformed expressions out, which are inserted into the code for later compilation. The output of macros is often *inlined* into the code.
- Optimization in JULIA: The JULIA compiler is built on three strategies that are still performed on a high-level intermediate representation of the code, while all native code generation is later delegated to the LLVM compiler infrastructure. These optimization strategies are: (1) method inlining which devirtualizes multi-dispatched calls and inlines the call target; (2) object unboxing to avoid heap allocation; and (3) method specialization where code is special cased to its actual argument types (Bezanson *et al.*, 2018).

Requests in building large software packages:

- The design and implementation of large software packages makes it advisable to follow some *common* rules and requests for those, who wish or need to contribute. For the design of good physics software, the following (and some further) requests were given by Post and Kendall (2004).
- **Physical models:** In general, better physics is more important than better computer science. It is recommended to use modern but well-proven computer-science techniques, and a '**physics code**' should not be a computer-science research project. Instead, one should use best engineering practices to improve quality rather than processes. Emphasis should be given to improvements of useful physics capabilities. Do not use the latest computer-science features; let the new ideas mature first. **Better physics is the most important product of the code.**
- **Code development and evolution:** The scale of code-development can become truly immense; a good overview/quantitative database about (previously) successful software projects in some given field is typically required for good estimation for resources and schedules. **It is easy to loose motivation on a project that last years and which has few incremental deliveries. Continues replacement of code modules is recommended as better tools and techniques are developed.** Every code development typically proceeds in steps: First develop a core capability (with a small team) and let this small core be tested by users and, if successful, add further capabilities (so-called incremental delivery).
- **Success criteria:** One of the important success criteria is the costumer focus. — **What do the user really need ?**
- **Code specification:** Some flexibility in the requirement specification phase is essential because it is difficult to predict when (or if) a new algorithm/approach will be available. **There is a need to pursue multiple approaches for algorithms and modules near to the critical path.** If one approach is not feasible, another one can be used.
- **External users and developers:** The validation of physics models is a critical issue for all extended software packages and need to be done with regard to authoritative reference data.
- **Documentation** should be intended to cover all needs of the beginner through to the expert user, who wishes to expand the capabilities of some tools.
- **Demands on programs for electronic-structure calculations:** In practice, modern electronic structure calculations pose enormous challenges to create complex but yet robust software. In atomic physics, there is still an increasing demand for accurate large-scale computations of (atomic) processes and cascades. These demands comes along with an escalating size and complexity of the applied computational models, and they have been fueled by computers of moderate cost, on which large and complex simulations have become ever more possible.

1. Overview about JAC. Structure of this User Guide

- **Computational infrastructure:** Though various (highly) specialized language implementation are known in different research areas of physics, such as software tools from CERN, most scientific communities do not have the resources that are necessary to build and maintain their own computational infrastructure.

1.6. Brief comparison of JAC with other existing codes

We here compile some rather (incomplete) information about other existing atomic structure codes for the computation of level energies, transition rates, cross sections, etc. We just remind to some of their special features and briefly summarize how these codes differ from the implementation of the JAC toolbox. These codes are ordered chronologically how they first occurred (or were published) in the literature.

MUONIC ATOMIC CASCADE (Akylas and Vogel, 1978):

- MUONIC ATOMIC CASCADE,
- **MOUNIC ATOM CASCADE:** Akylas and Vogel (1978) describe a code for the calculation of muonic x-ray spectra following the capture of an muon by an atom. This code starts from a given (initial) distribution of shells ($n\ell$), into which the muon is initially captured. The program then calculates the radiative (multipole) and Auger transitions rates. From these rates, a list of x-ray lines and intensities is printed that support experimentalist in identifying the observed peaks. All computations in the MOUNIC ATOM CASCADE code are based on Dirac's (single-muon) energies but, otherwise, applies a non-relativistic theory for the computation of all amplitudes and rates. For the calculations of x-ray intensities, moreover, the code neglects all contributions due to the remaining, though certainly less important bound electrons. This is a rather old Fortran IV code that appears and whose write-up appears is very difficult to understand as well.
- **MOUNIC ATOM CASCADE:** The distortion of the electronic wave functions by the muon is simulated purely non-relativistic by using an effective charge Z . Furthermore, the treatment of the (electron) Auger emission is simplified by means of some penetration model (that deals with the different radial extent of the muonic and radial wave functions). All electronic shells beyond the M shell and multipoles beyond octupoles are then neglected.

CATS (Cowan: 'Theory of Atomic Spectra', 1980):

- **CATS code:** The Cats code is based on Cowan's original atomic structure code and has been employed in the calculation of a large number of level energies and absorption oscillator strengths. It enables one to readily scale the strength of the radial integrals in order to bring the theoretical level structures into better agreement with experimental observations.

- CATS, the Cowan Atomic Structure code, relies on a semi-relativistic self-consistent potential and makes use of either a nonlocal Hartree-Fock (HF) or local Hartree-Fock-Slater (HFS) approach in order to deal with the exchange interaction.
- **Level energies & ASF:** Since the late 1960s, Cowan's HFX code has set some – well-approved – standard for many experimentalists and has, together with his well-known textbook, helped many (atomic) physicist to understand and make use of atomic structure theory. While these earlier developments are highly appreciated (and are still utilized for various applications), **CATS has several severe limitations in the layout and implementation of the code, which are hard to overcome.** The same applies also for the approximate computation of various atomic properties, such at transition probabilities, photo-excitation and ionization cross sections and Auger rates.
- Cowan's code has been found a mature tool for identifying new lines, especially if additional information is available from experimental observations in order to support further empirical adjustments of energies and ASF.
- **Display of data & spectra:** Several tools and facility-programs have been developed for CATS in order to display the computed data and to compare them with each other and with experiment. The success of some of these tools has or will motivate us for developing some graphical interfaces for the display of (radial) orbitals, line spectra, etc. also for the JAC toolbox.

MCDFME (Desclaux *et al.*, 1975; Indelicato 2000 and later):

- **MCDFME code:** The Multi-configuration Dirac-Fock and General-Matrix-Element code by Desclaux and Indelicato includes one-electron one-loop corrections (self-energy and vacuum polarization) and two-loop one-electron corrections (two-loop self-energy, mixed self-energy as well as vacuum polarization diagrams, Källen-Sabry potential contributions).
- **MCDFME code:** This code also includes vacuum-polarization due to the electronic potential, retardation beyond the Breit interaction and the effect from the electron-electron interaction on the self-energy evaluated within the so-called **Welton method.** From the comparison with the model operator approach by Shabaev and co-workers, a relative difference of $\leq 0.01\%$ was found for $Z = 18$.

GRASP (Grant *et al.*, 1980; Jönsson *et al.*, 2013; Fischer *et al.*, 2018):

- **Level energies & ASF:** GRASP has originally been developed since the late 1960s in order to provide level energies and eigenvectors for quite general open-shell atoms. Much emphasize during the last two decades was placed upon the systematic improvement of these energies and representations. While we also provide such level energies and atomic state functions by the JAC toolbox, we *do not* intent (at present) to facilitate such extensive wave function expansions. Instead, **approximate level energies and ASF are mainly considered as the technical preposition** in order to describe further atomic properties and processes. With the computation of restricted-active space

1. Overview about JAC. Structure of this User Guide

(RAS) representation of atomic ASF, however, we shall provide in JAC useful features for a (more or less) systematic improvement of such (*ab-initio*) ASF representations.

- **Transition probabilities & oscillator strength:** Apart from the level energies, GRASP has been extensively applied in order to compute and tabulate transition probabilities for many atoms, ions and isoelectronic sequences throughout the periodic table of elements. **With JAC, we provide analogue or even simpler tools for such computations.** Moreover, (the many-electron amplitudes that arise from) the coupling of the radiation field provides the natural *building blocks* for a large number of other atomic processes, cf. section 8 on atomic processes below.
- **Selected advantages of JAC:**
 - The use of the JULIA language clearly facilitates the coding and maintenance of the JAC code, when compared to previous Fortran codes.
 - JAC enables one to handle a much larger number of atomic properties and processes, the computation and simulation of atomic cascades as well as several other types of computation.
 - SCF fields can be generated in JAC at different levels of complexity, including several (local) mean-field potentials as well as, in the future, the average-level and extended average-level schemes.
 - JAC supports a much larger flexibility in handling the output data and, in particular, does not know any relevant limitation with regard to the length of filenames (in contrast, for instance, to 24 letters in grasp2K).

RMATRX (Berrington *et al.*, 1995):

- The Belfast RMATRIX code is readily available and used by a (small) group of users, and with an updated version from 2020. Already the 1995 version was based on a number of previous versions and included various extensions by the Opacity Project and the Iron Project team.
- Various parallel R-matrix codes have been developed as well from modified versions of the serial RMATRIX code, the non-exchange R-matrix programs and the Dirac Atomic R-matrix Code (DARC).
- Calculations with the RMATRIX code can be either in *LS*-coupling, or in an intermediate-coupling scheme by including terms of the Breit-Pauli Hamiltonian.

LADW (Los Alamos Atomic Physics, 2000 and later):

- **LADW:** The Los Alamos Distorted-Wave code, has been developed by Sampson and co-workers; it has been further utilized and partly incorporated into the (so-called) LASER code.

- Interface to Los Alamos Atomic Physics Codes is some gateway to the set of atomic physics codes developed at the Los Alamos National Laboratory. These codes include the well known Hartree-Fock method Cowan, developed at LANL, as well as electron-impact excitation cross sections by using the distorted wave approximation (DWA).

HULLAC (Bar-Shalom *et al.*, 2001):

- **HULLAC:** The Hebrew University Lawrence Livermore Atomic Code (HULLAC, Bar-Shalom *et al.* 2001) is a computational platform for atomic structures and cross sections that help modelling emission spectra as well as atomic processes in plasma; this code is based on a parametric potential method and has been applied to many medium and heavy elements.
- **HULLAC:** This code applies fully relativistic orbitals to calculate atomic energy levels and radiative transition probabilities. These orbitals are obtained as solution of the Dirac equation with a local and parametrized central-field potential $U(r)$ to represent the nucleus and the spherically averaged interaction with all other electrons in the atom. The central-field potential is optimized such that energy levels of the ground state and a few low-lying excited states agree with the NIST (or related) tables. Although such a semi-empirical optimization procedure requires less computational resources, it hampers a systematic improvement of the results.
- **HULLAC** has been developed as an integrated code for calculating the atomic structure and cross sections for collisional and radiative atomic processes, based on the relativistic configuration interaction method.
- In HULLAC, all collisional cross sections are calculated in the distorted wave approximation with special emphasis on efficiency.

RATIP (Fritzsche, 2001 and 2012):

- **Relativistic CI (RELCI):** While RATIP has always used the SCF computations and orbitals from the GRASP code, it also supports relativistic configuration-interaction (CI) computations. For several years, it also helped define a new standard for performing the angular integration (angular coefficients; cf. Gaigalas *et al.*, 2002). These angular coefficients are presently utilized in JAC by an interface to the Fortran modules of RATIP.
- **Atomic properties and processes:** RATIP was (one of) the first codes that made use of GRASP's systematically improved wave functions in order to compute a good number of atomic properties and processes, such as relaxed-orbital transition probabilities (REOS; Fritzsche and Froese Fischer 1999), Auger rates, photoionization cross sections and angular parameters, radiative and dielectronic recombination rates, electron-impact excitation cross sections, and several others. The experience with RATIP has been found central for the development of JAC and has find its continuation here.

Elsepa and Eccpa (Salvat *et al.*, 2005, 2022):

- **ELSEPA:** facilitates the computation of differential cross sections, total cross sections and transport cross sections for the (single) elastic scattering of electrons and positrons by neutral atoms, positive ions as well as randomly oriented molecules. Moreover, this code help compute scattering amplitudes and spin-polarization functions for projectiles with kinetic energies $E_{\text{kin}} \lesssim 5 \text{ MeV}$ by means of a conventional relativistic Dirac partial-wave analysis.
- **ELSEPA code:** This Fortran code calculates accurate differential cross sections for electrons and positrons by means of the relativistic (Dirac) partial-wave method and for arbitrarily screened atomic potentials.
- The calculations are performed by means of relativistic (Dirac) partial wave analysis for an effective local central-interaction potential. The scattering by molecules is described by making use of an *independent-atom* approximation, i.e. by adding coherently the waves scattered from all the atoms in the molecule as well as by performing an average over random orientations of the molecule.
- For high kinetic energies, however, the convergence of the partial-wave series becomes slow and is then replaced by some approximate factorization method. ELSEPA has been found useful to explore the sensitivity of differential cross sections for different choices of the (static) interaction potential.
- **ECCPA program:** The ECCPA program computes **differential cross sections for elastic collisions** of charged particles (electrons, positrons, muons, antimuons, protons, antiprotons, and alphas) with neutral atoms (Salvat *et al.*, 2022). For the target, a static-field is assumed with a screened Coulomb potential that is expressed as a sum of Yukawa terms. The parameters of these Yukawa potentials is obtained from either a Thomas-Fermi model or self-consistent Dirac-Hartree-Fock-Slater calculations.
- **ECCPA code:** This Fortran program provides differential cross sections for the elastic scattering of charged particles by using either (1) the method of classical trajectories, (2) a first Born approximation, (3) the partial-wave expansion method with phase shifts obtained from the Born and WKB approximations and/or (4) the eikonal approximation. The differential cross sections can be obtained both, in the center-of-mass and the laboratory frames and visualized by means of provided plotting functions. ECCPA is therefore suitable to explore of the classical trajectory method and various quantum approximations (Salvat *et al.*, 2022).

GEANT4 (Amako *et al.*, 2005):

- **GEANT4** is an object-oriented toolkit for analyzing and simulating the passage of particles through matter; this toolbox provides a **variety of semi-empirical models in order to simulate the underlying electromagnetic and hadronic interactions**. GEANT4 combines theoretical models with experimental data or parameterizations of such data.

- **GEANT4** is especially based on a number of separate packages in order to deal with the electromagnetic interactions of (either) electrons, muons, positrons, photons, hadrons and ions as well as for dealing with specific energy ranges of the processes that are taken into account by this toolbox.
- **Implemented processes:** The electro-magnetic packages of the GEANT4 toolbox include: multiple scattering, ionization, Bremsstrahlung, positron annihilation, photo-electric effect, Compton and Rayleigh scattering, pair production, synchrotron and transition radiation, Cherenkov effect, refraction, reflection, absorption, scintillation, fluorescence as well as Auger electron emission (Amako *et al.*, 2005). **Less attention has been placed however on the electronic structure of atoms and ions.** However, it is not obvious how easily this toolbox can be applied in order to predict the spectra and behaviour of individual atoms and ions.
- **GEANT4** mainly covers the energy range from 1 keV to 10 PeV; for these energies, the **atomic electrons are treated as *quasi-free* particles which, apart from photoelectrons, is often a really crude approximation.** For all these processes, moreover, GEANT4 always considers *fixed* atomic nuclei with no recoil momentum.

BSR (Zatsarinny 2006):

- **BSR code:** The B-spline R-matrix (BSR) method and the accompanying code was developed by Zatsarinny and coworkers; this code computes **photoionization and electron-impact excitation amplitudes**. From these many-electron amplitudes, the cross sections and other experimentally observable parameters can be obtained. Apart from these amplitudes, the BSR code also support simple bound-state computations for the energies and oscillator strengths.
- The BSR code solves the close-coupling equations in coordinate space and, thus, is complementary to the usual convergent close-coupling (CCC) computations for electron-ion collisions in momentum space. The BSR code applies a finite-element (B-spline) rather than a finite-difference approach in order to compute the Hamiltonian matrix elements in the inner region.
- The BSR code supports the **use of non-orthogonal sets of one-electron orbitals** in order to account for the term-dependence of the valence orbitals. This enables one to apply an economical and flexible construction of both, bound-state wave functions and scattering states and, hence, the treatment of electron-impact single-ionization as well as photon-driven double ionization processes. Still, setting up the Hamiltonian matrix can be (very) expensive for complex targets, and the large number of resonances may require to deal with many thousands of collision energies separately; this makes it difficult to include details from the asymptotic region.
- The (published) BSR code is a serial non-relativistic version that can be applied also for (semi-relativistic) Breit-Pauli computations. A relativistic DBSR as well as MPI-parallelized versions exists and has been applied by a small group of people (Zatsarinny, 2020; <https://github.com/zatsaroi>).

1. Overview about JAC. Structure of this User Guide

FAC (Gu 2008):

- **FAC** is a well-known relativistic atomic structure code based on the (standard) Dirac-Fock-Slater method and on some fit of free parameters in order to define the atomic potentials.
- **Level energies & wave functions:** When compared to GRASP, the simplified and more object-oriented treatment of wave functions in the FAC code has partly stimulated us in developing the JAC program. While JAC enable the user to perform also systematically improved computational models, the support of some first and perhaps rather simple approximation has been found crucial and need to be supported, for example, for dealing with cascades and time-evolutions. **Angular integration:** FAC makes use of the angular coefficients by Gaigalas *et al.* (2001), which is based on quasi-spin space and the coupling of second-quantized operators.
- **Single-multipole approximation:** Although FAC supports different multipoles in the computation of decay rates and (photoionization) cross sections, it does not support interference contributions from different multipoles, i.e. the summation of amplitudes from different multipoles. Moreover, it remains unclear how easily the contributions from different multipole fields could be added together due to different phases (phase conventions) and prefactors.
- **Simulation of atomic processes:** Several features of the FAC code have stimulated and have been adapted to the JAC program. Many atomic processes, which are supported by FAC, can now be handled, and often more readily, within JAC
- **Electron-impact excitation and ionization:** In FAC, the implemented (first-Born) distorted-wave approximation for the electron-impact excitation and ionization cross sections is very similar to a number of previous implementation used in astro- and plasma physics.
- **Selected advantages of JAC:**
 - JAC is (almost) completely programmed within the Julia language, and this simplifies the further extension of the code;
 - JAC always applies a relativistic representation of all one-electron orbitals in terms of their large and small components;
 - JAC also supports both, the Dirac-Coulomb and well as Dirac-Coulomb-Breit Hamiltonians.

tRecX (Scrinzi 2010):

- **TRECX code:** This code provides a general framework for solving initial-value problems of the form

$$\frac{\partial}{\partial t} \Psi = \mathbb{L}[\Psi, t] + \Phi(t)$$

for any number of spatial dimensions and for different coordinate systems. While the main emphasis was placed on some *linear* evolution operators \mathbb{L} , non-linear operators can be used as well.

AUTOSTRUCTURE (Badnell, 2011):

- AUTOSTRUCTURE is a rather general atomic code for the description of free-bound electron and photon collision processes, based on the original SUPERSTRUCTURE code bei Eissner and coworkers.
- AUTOSTRUCTURE supports efficient computations of dielectronic recombination cross sections and rates, especially if large numbers of highly-excited states are involved in the radiative stabilization of an atom or ion.
- The code applies the Breit-Pauli distorted wave method for the electron-impact excitation of atomic ions in order to support problems that are impractical or even impossible for more sophisticated methods.
- AUTOSTRUCTURE mainly computes (Maxwell-averaged) effective collision strengths at temperatures with a broad ionic abundance, rather than the detailed collision strengths at all the energies.
- **AUTOSTRUCTURE:** This code applies Slater determinants and an explicit coupling of angular momenta (without the concept of parentage). In this code, therefore, first an uncoupled Slater basis is formed before further transformations are to either *LS* or *LSJ* coupling.

LASER (Fontes *et al.*, 2015):

- **LASER:** The Los Alamos SuitE of Relativistic atomic physics code, comprises various codes for fundamental atomic structure calculations as well as for various processes, such as photoexcitation, electron-impact excitation and ionization, photoionization and autoionization, within a consistent framework. It may help develop atomic physics models in either configuration-average and fine-structure modes, and by including a proper self-consistency. This suite of code has been developed for more than 20 years.
- **Applications of the code:** The LASER code has been applied to the collisional-radiative modeling of plasma, for line identifications in plasma spectroscopy and for testing relativistic atomic and quantum electro-dynamics (QED) theories. The code also has been utilized for feasibility studies of collisional-radiative modeling of non-LTE (optically thin) gold plasmas for and to questions from inertial confinement fusion.
- **Approximations:** LASER mainly employs the semi-relativistic theory, similar to or by directly applying Cowan's atomic structure code (CATS). All bound-electron wavefunctions are obtained from the semi-relativistic approach in CATS, while the continuum-electron orbitals are obtained as solutions of Schrödinger's equation from some specialized routines. In the LASER code, the bound and continuum radial wave

1. Overview about JAC. Structure of this User Guide

functions are typically single-component orbital functions associated with the Schrödinger equation, rather than two- or four-component spinors associated with the Dirac equation.

- **Features:** Cross sections and other properties can be calculated with the LASER code for five fundamental processes: photo-excitation, photo-ionization, electron-impact excitation and ionization and autoionization. The code supports the IPCRESS (Independent of Platform and Can be Read by Existing Software Subroutines) random-access binary file format that is used to store large amounts of data, and which can be ported to almost any platform.

[QEDMOD \(Shabaev *et al.*, 2015\):](#)

- **Self-energy model operator, $\hbar^{(QED)}$:** Computes the matrix elements of a model QED operator $\hbar^{(QED)}$ that accounts for the Lamb shift in accurate atomic-structure calculations. However, there arises various technical difficulties with QEDMOD, which make a direct application of the code and its combination with GRASP or JAC rather cumbersome.
- **Effective QED Hamiltonian:** The QEDMOD code provides one-electron matrix elements that, in principle, can be added directly to any CI matrix and, hence, to the computation of level energies and multiplets. For the vacuum polarization, it includes automatically both, the Uehling and Wichmann-Kroll terms.
- **Selected advantages of JAC:** A simplified version of the effective QED Hamiltonian from QEDMOD has been implemented also in JAC.

[ARC \(Sibalec *et al.*, 2017\):](#)

- **ALKALI RYDBERG CALCULATOR (ARC; Sibalec *et al.*, 2017):** ARC 3.0 is a modular and object-oriented Python library that combines (semi-empirical) algorithms and data in order to calculate different properties of Rydberg-excited alkali and di-valent atoms. It also supports methods for working with atom-surface interactions, for modeling ultracold atoms in optical lattices and for calculating valence-electron wave functions and dynamic polarizabilities.
- **ALKALI RYDBERG CALCULATOR:** This modular and reusable code provides a (Python) package of routines for calculating single- and two-atom properties, such as level diagrams, interactions and transition strengths for alkali and divalent atoms.

[PYSCF \(Smith *et al.*, 2018\):](#)

- **PySCF & Psi4NumPy:** PySCF is a (typical) quantum chemistry package that, like many other codes, favors performance over readability. In contrast, the Psi4NumPy project prioritize readable and clear code; it is optimized for certain computationally intensive operations but

is less optimal for any other operations beyond the central core routines. The Psi4NumPy project aims to lower the barrier to implementing and understanding quantum chemical methods (Smith *et al.*, 2018).

QUANTICS (Worth, 2019):

- **QUANTICS toolbox:** For small molecules, this code help solve the time-independent Schrödinger equation as well as the (time-dependent) Liouville-von Neumann equation by propagating density matrices. The package comprises various auxiliary programs to set-up calculations and to analyse different outputs.
- QUANTICS has been promoted as a community code of the UK Collaborative Computational Project for Quantum Dynamics (CCPQ) and of the European E-CAM project, an e-infrastructure for software development by the Centre European de Calcul Atomique et Moléculaire (CECAM).

1.7. To-do's, next steps & desired features of the JAC program

Encouragement for external users and developers:

- While we (will further) develop JAC for applications that are requested explicitly by selected users, here I shall compile a number of **desired features which will make JAC even more powerful and/or easy to use**. For these *additional features*, I wish to encourage collaboration with external developers. In particular, I welcome all help from outside if the overall style of the program is maintained and if some prior consensus exist how to add and implement additional features.
- New code developments may concern incremental improvements but also multiple approaches for selected algorithms and modules in order to provide well-defined alternatives, for instance, if some particular approach does not work properly under certain circumstances.
- Emphasis will first be placed upon those applications that receive good attention by the community.

1.7.a. To-do lists

Urgent to-do's:

- Design and development of a robust continuum solver.
- Design and development of a module for the computation of electron-impact excitation cross sections.
- Design and implementation of a DHF self-consistent-field that include the full exchange interaction into the MCDHF equations.
- **Use of JAC on remote clusters:** Work out some prototype example how 'job scripts' (similar to those from examples) can be exportet and handled at remote cluster computers and how to re-import the results later on.
- **Documenter.jl:** How to establish an alternative and web-based documentation of JAC.

Short-term to-do's:

- Implement ... `Jac.modify("level energies: interactive", multiplet::Multiplet)`

- Implement ... `Jac.display("level energies: HFS", multiplets::HFSMultiplet[...])`
- Implement ... `Jac.display("level energies", multiplets::Multiplet[...])`
- Implement ... `Jac.display("configuration list: from basis", basis::Basis)`
- **Alternative diagonalization procedures:** We shall look for and establish 1-2 further diagonalization procedures that work with the same input/output data or very similar as `Jac.diagonalize("matrix: Julia, eigfact", matrix::ArrayFloat64,2)` ... but allows to just find certain low-lying eigenstates or certain bands of eigenstates.

Medium- and long-term to-do's:

- Implement ... `Jac.apply("restrictions: CSF list", csfs::CsfR[...], basis::Basis)` ... to apply a number of restrictions interactively to a list of CSF. The procedure might proceed in three steps: (i) by taking and applying a restriction to a given CSF list; (ii) showing the number of CSF to be deleted from the given list; and (iii) making this restrictions explicit. The user would then be requested to enter one restriction after the other, and until the reduction process is terminated by the user. A `csfList::ArrayCsfR,1` is returned. — Here we might adopt especially the form of restrictions from the RATIP program.
- Implement ... `Jac.apply("biorthogonal transformation", mpltA::Multiplet, mpltB::Multiplet, grid::Radial.Grid)`
- Compute and extract the Fano parameters and line-shapes for a given set of autoionizing resonances.
- **Atoms in plasma environments:** Implement 2-3 plasma models in order to deal with atoms in a few (averaged but) different plasma environments. This usually works via some effective `Jac.InteractionStrength.XL_plasma_ionSphere(L::Int64, a::Orbital, b::Orbital, c::Orbital, d::Orbital, lambda::Float64)` that depends on some particular model and plasma parameters; cf. Saha and Fritzsch, PRE (2004). This will likely require also the set-up of a corresponding Hamiltonian matrix: `Jac.compute("matrix: plasma, ion-sphere model", settings::Plama.Settings, basis::Basis)`.

1. Overview about JAC. Structure of this User Guide

1.7.b. Discussion about (further) implementations

Issues that need to be discussed:

- Parallelization and performance of the code: How can one make the code parallel without that the user need to know and provide much information about the cluster that is used for the computations.
- Modern input forms in scientific computing: Which modern formats do exist ?? Which simple graphical (applet) features exist ? How useful can be to mael.jl ??

1.7.c. Desired medium- and long-term features of the JAC program

Plotting and visualization:

- Implement ... Jac.plot("spectrum: oscillator strength over energy, emission", lines::RadiativeLine[...]; widths=value::Float64) and Jac.plot("spectrum: oscillator strength over energy, absorption", lines::RadiativeLine[...]; widths=value::Float64)
- Implement ... Jac.plot("spectrum: transition rates over energy, Gaussian", lines::RadiativeLine[...]; widths=value::Float64) and Jac.plot("spectrum: transition rates over energy, Lorentzian", lines::RadiativeLine[...]; widths=value::Float64)
- Visualize the convergence of energies or other results as function of the size of the computation and/or model space.
- Visualize the level structure of a given multiplet, for instance, by displaying the level energies in different colors for different (leading) configurations or groups of such configurations.
- Plot energy diagrams for an atomic cascade together with its major decay pathes; here, it would be highly desirable to be able to 'zoom' into such a energy diagram in order to easily understand how the levels form different configurations *group* together.

More physics in Jac ?

- Atomic spectra: Evaluate and display the photoabsorption spectra from calculated photoexcitation and photoionization cross sections.

➤ Computation of approximate single-electron properties:

- Subshell-dependent differential and total photoionization cross sections; cf. Eichler and Meyerhof (1995, Eqs. 9.34 and 9.47).
- Non-relativistic total K-shell or subshell radiative recombination cross sections by using the Stobbe cross section; cf. Eichler & Meyerhof (1995, Eqs. 9.49–9.50)

➤ Collisional-radiative models: Such collisional-radiative models have been frequently applied to describe the evolution of plasma and to derive information for plasma diagnostics. JAC can provide many (if not all) of the rates and cross sections that are needed in order to built-up such models for selected (plasma) environments.

➤ Electron-momentum distributions: Provide the expectation values $\langle p^k \rangle$, $k = -2, \dots, 4$ of the single-electron radial momentals, i.e. the radial orbitals in momentum space. These expectation values are frequently applied in crystallography and in studying Compton profiles; cf. Koga and Thakkar (1996), Eq. (10-11). In the first instance, these expectation values could be readily provided as semi-empirical values by following the work above.

2. Dirac's hydrogenic atom

2.1. Energies and wave functions

Notations & application in Jac:

- In JAC, non-relativistic hydrogenic orbitals can be easily generated by a call to `JAC.HydrogenicIon.radialOrbital()`.
- JAC also provides approximate radial (relativistic bound-state) orbitals by just applying the kinetic-balance condition to the corresponding non-relativistic radial orbital and by re-normalizing it afterwards.

Dirac's (one-electron) energies:

- Relativistic bound-state energy spectrum: For electrons with principal quantum number n and angular-momentum quantum number κ , the relativistic bound-state energy spectrum is given by

$$\varepsilon_{n\kappa} = mc^2 W_{n\kappa} = \frac{mc^2}{\sqrt{\left[1 + \left(\frac{\alpha Z}{n' + s}\right)\right]}}$$

where α is the fine-structure constant, $n' = n - |\kappa| = 0, 1, 2, \dots$ is the number of nodes, and $s = \sqrt{\kappa^2 - (\alpha Z)^2}$, respectively.

- Since $W_{n\kappa} < 1$, it can be expanded in terms of (αZ) and written as

$$W_{n\kappa} = 1 - \frac{1}{2} \frac{(\alpha Z)^2}{n^2} - \frac{1}{2} \frac{(\alpha Z)^4}{n^3} \left(\frac{1}{j + 1/2} - \frac{3}{4n} \right) - \dots$$

where the second term, multiplied with mc^2 , represents the nonrelativistic binding energy of a hydrogenic atom.

2. Dirac's hydrogenic atom

- For a given (principal) shell n , the eigenvalues are the same for equal values of j but are different for equal values of ℓ . For a given value of ℓ , the spin-orbit splitting between states with $j = \ell + 1/2$ and $j = \ell - 1/2$ gives rise to the **fine-structure in the spectrum of hydrogen-like atoms**. The equation above shows that the relativistic corrections to the one-electron energies decreases rapidly with n . The relativistic correction to the non-relativistic energy is therefore important, especially for highly-charged ions with rather large Z .
- **Number of nodes in relativistic orbitals:** The large component $P_{n\kappa}(r)$ has $n - \ell - 1$ nodes, as in the non-relativistic case, while the small component $Q_{n\kappa}(r)$ has $n - \ell - 1$ nodes for $\kappa < 0$ but $n - \ell$ nodes for $\kappa > 0$, respectively.
- **Asymptotic behavior of relativistic solutions in a spherical-symmetric potential $V(r)$:** In a spherical-symmetric potential with $V(r \rightarrow \infty) = 0$, the radial Dirac spinors behave as

$$\begin{aligned} P_{n\kappa}(r \rightarrow 0) &= r^\gamma, & Q_{n\kappa}(r \rightarrow 0) &= \frac{c(\kappa + \gamma)}{Z} r^\gamma, & \gamma &= \sqrt{\kappa^2 - \frac{Z^2}{c^2}} \\ P_{n\kappa}(r \rightarrow \infty) &= e^{-\lambda r}, & Q_{n\kappa}(r \rightarrow \infty) &= \frac{c^2 - E}{c^2 + E} e^{-\lambda r}, & \lambda &= \sqrt{c^2 - \frac{E^2}{c^2}}. \end{aligned}$$

- **Kinetically-balanced basis sets:** For a given number of single-component radial basis functions $g_i(r)$, a kinetically-balanced radial basis set can be formed by the two-component functions $(g_i(r), 0)$ and $(0, D^+ g_i(r))$ with

$$D = \frac{1}{2mc} \left(-\frac{d}{dr} + \frac{\kappa}{r} \right).$$

However, this construction is not symmetric in the positive- and negative-energy states and causes numerical problems, especially if the negative-energy continuum contributes significantly to some property. In the **dual-kinetic-balance (DKB) approach**, the radial basis set is used instead as $(g_i(r), D^+ g_i(r))$ and $(-D g_i(r), g_i(r))$, and the efficiency of this method has been shown in various QED computations.

Non-relativistic radial orbitals:

- **Radial orbital functions $P(r)$:** These functions in the non-relativistic orbital $\psi(r, \vartheta, \varphi) = \frac{P(r)}{r} Y_{\ell m}(\vartheta, \varphi)$ is known to obey the *radial Schrödinger equation* and belongs to either the discrete part of the spectrum with the (negative) energies $E_n = -\frac{Z^2}{2n^2}$ a.u. < 0 (bound states), or to the continuous part for all energies $E > 0$ (the so-called *free-electron* or *continuum* states).

- Radial orbital functions $P(r)$: An analytic solution of the radial functions $P(r)$ in terms of the confluent hypergeometric function $F(\alpha, \beta; x)$ are known for both, the bound-states

$$P_{n\ell}(r) = r^{l+1} \frac{1}{(2\ell+1)!} \sqrt{\frac{(n+\ell)!}{(n-\ell-1)! 2n}} \left(\frac{2Z}{n}\right)^{3/2+\ell} e^{-\frac{Zr}{n}} F\left(-(n-\ell-1), 2\ell+2; \frac{2Zr}{n}\right)$$

as well as for the *continuum* ($E > 0$) with $k = \sqrt{2E}$ and $n' = Z/k$

$$P_{E\ell}(r) = \frac{2\sqrt{Z}}{\sqrt{1 - e^{-2\pi n'}}} \left[\prod_{s=1}^{\ell} \sqrt{s^2 + n'^2} \right] \frac{(2kr)^l}{(2\ell+1)!} e^{-ikr} F(in' + \ell + 1, 2\ell + 2, 2ikr).$$

- These radial orbitals for bound and continuum electrons are normalized due to the conditions:

$$\int_0^\infty dr r^2 R_{n\ell}^2(r) = \int_0^\infty dr P_{n\ell}^2(r) = 1 \quad \text{for having a single particle per bound state}$$

$$\int_0^\infty dr P_{E\ell}^*(r) P_{E'\ell}(r) = \delta(E - E') \quad \text{for representing one particle per unit energy.}$$

- Hydrogenic 1s density in position space: For nonrelativistic hydrogenic ions, the 1s wave function in position space and the associated density distribution are given by

$$\psi_{1s,m=0}(r) = \sqrt{\frac{Z^3}{\pi}} \exp(-Zr), \quad \rho(r) = \frac{Z^3}{\pi} \exp(-2Zr)$$

$$\langle r \rangle = \frac{3}{2Z}, \quad \langle r^2 \rangle = \frac{3}{Z^2}, \quad \delta r = \sqrt{\langle r^2 \rangle - \langle r \rangle^2} = \sqrt{\frac{3}{2Z}} \approx \frac{0.8660}{Z}.$$

- Hydrogenic 1s wave function in momentum space: For nonrelativistic hydrogenic ions, the 1s wave function in momentum space and the

2. Dirac's hydrogenic atom

associated momentum distribution are given by

$$\begin{aligned}\psi_{1s,m=0}(p) &= \frac{1}{\pi} \left(\frac{2}{Z} \right)^{3/2} \left[\left(\frac{p}{Z} \right)^2 + 1 \right]^{-2}, & \pi(p) &= \frac{8}{\pi^2 Z^3} \left[\left(\frac{p}{Z} \right)^2 + 1 \right]^{-4} \\ \langle p \rangle &= \int_0^\infty dp 4\pi p^3 \pi(p) = \frac{8Z}{3\pi} \approx 0.848826 Z, & \langle p^2 \rangle &= \int_0^\infty dp 4\pi p^4 \pi(p) = Z^2 \\ \delta p &= \sqrt{\langle p^2 \rangle - \langle p \rangle^2} = \frac{Z}{3\pi} \sqrt{9\pi^2 - 64} \approx 0.5287 Z.\end{aligned}$$

➤ Radial orbitals for (Rydberg) orbitals with maximum ℓ

$$P_{n,\ell=n-1} = \frac{1}{\sqrt{(2n)!} r} \left(\frac{2Z}{na_o} \right)^{3/2} e^{-Zr/na_o} \left(\frac{2Zr}{na_o} \right)^{n-1}$$

➤ Nonrelativistic *versus* relativistic (hydrogenic) orbitals: Relativistic orbitals for ions of given Z are generally (i) contracted towards to nucleus, (ii) have no exact zeros in the electron density due to shifted zeros of the large and small components and (iii) exhibit a charge density with a smaller gradient near to the origin as well as for large r .

Non-relativistic orbitals in momentum representation:

➤ Wave function in momentum representation: These wave functions are often written in terms of the wave vector $\mathbf{k} = (k, \vartheta_k, \varphi_k) = \mathbf{p}/\hbar$ and the spherical Bessel functions $j_\ell(z) = \sqrt{\pi/2z} J_{\ell+1/2}(z)$

$$G(\mathbf{k}) = \frac{1}{(2\pi)^{3/2}} \int d^3r \exp(-i\mathbf{k} \cdot \mathbf{r}) \psi(\mathbf{r})$$

$$G_{n\ell m}(\mathbf{k}) = g_{n\ell}(k) Y_{\ell m}(\vartheta_k, \varphi_k), \quad g_{n\ell}(k) = (-i)^\ell \sqrt{\frac{2}{\pi}} \int_0^\infty dr r P_{n\ell}(r) j_\ell(kr), \quad \int_0^\infty dk k^2 g_{n'\ell}^*(k) g_{n\ell}(k) = \delta_{n'n}.$$

- **Hydrogenic orbitals in momentum representation:** The hydrogenic orbitals in momentum representation can be written in terms of the Gegenbauer polynomials C_n^ℓ and the reduced momentum coordinate $x = n k a_o / Z$ as

$$\begin{aligned} g_{n\ell}(k) &= \left(\frac{a_o}{Z} \right)^{3/2} \left[\frac{2}{\pi} \frac{(n-\ell-1)!}{(n+\ell)!} \right]^{1/2} n^2 2^{2(\ell+1)} \ell! \frac{(-ix)^\ell}{(x^2+1)^{\ell+2}} C_{n-\ell-1}^{\ell+1} \left(\frac{x^2-1}{x^2+1} \right) \\ C_{n-\ell-1}^{\ell+1} \left(\frac{x^2-1}{x^2+1} \right) &= \frac{(2n+\ell+n)!}{n! (2\ell+1)!} F \left(-n; n+2\ell+2; \ell+3/2; \frac{1}{x^2+1} \right). \end{aligned}$$

Relativistic radial orbitals:

- **Radial orbital functions $P(r)$, $Q(r)$:** Analogue to the non-relativistic case, the solution $\psi(\mathbf{r})$ of the Dirac equation can be separated for a spherical potential into a radial and angular part

$$\psi_{\kappa m}(r, \vartheta, \varphi) = \frac{1}{r} \begin{pmatrix} P(r) \Omega_{\kappa m}(\vartheta, \varphi) \\ i Q(r) \Omega_{-\kappa m}(\vartheta, \varphi) \end{pmatrix},$$

where $\Omega_{\kappa m}(\vartheta, \varphi)$ denotes a standard Dirac spin-orbital function, and where $\kappa = \pm(j + 1/2)$ for $\ell = j \pm 1/2$ is called the *relativistic angular-momentum quantum number*.

- **Relativistic angular-momentum quantum number:** Owing to the definition of $\kappa = \pm 1, \pm 2, \dots$, this *relativistic quantum number carries information about both, the total angular momentum j and the parity $(-1)^\ell$ of the orbital function.*
- **Angular-momentum operator with eigenvalues κ :** In the spherical spinors, there occur generally two values of ℓ for each j : $\ell = j \pm 1/2$, and for spinors with different parity. Instead of the quantum numbers j, ℓ , it is possible to introduce the (relativistic) angular momentum operator

$$k = -2\mathbf{l} \cdot \mathbf{s} - 1, \quad k \Omega_{\kappa m}(\vartheta, \varphi) = k \Omega_{j\ell m}(\vartheta, \varphi) = \kappa \Omega_{\kappa m}(\vartheta, \varphi).$$

- **Large & small component:** The radial part of a relativistic wavefunctions is given by the two functions $P(r)$ and $Q(r)$, and which are often called the *large* and *small* components.

2. Dirac's hydrogenic atom

- **Dirac spin-orbital:** As usual, the Dirac spin-orbitals can be written in terms of the spin-1/2 Pauli spinors χ_{\pm} and the spherical harmonics by

$$\Omega_{\kappa m}(\vartheta, \varphi) = \sum_{m_\ell} \langle \ell m_l, 1/2, m - m_\ell | jm \rangle Y_{\ell m_\ell}(\vartheta, \varphi) \chi_{m-m_\ell}, \quad \int d\Omega \Omega_{\kappa m}^*(\vartheta, \varphi) \Omega_{\kappa' m'}(\vartheta, \varphi) = \delta_{\kappa, \kappa'} \delta_{mm'}.$$

$$Q(r) = \frac{1}{2mc} \left(\frac{d}{dr} + \frac{\kappa}{r} \right) P(r).$$

The two-component angular-momentum function $\Omega_{\kappa m}(\vartheta, \varphi)$ are often also referred to as **spherical spinors**.

Dirac equation in an axially-symmetric potential:

- **Dirac equation in an axially-symmetric potential:** In a homogeneous magnetic field $\mathbf{B} \parallel \mathbf{e}_z$, a relativistic electron follows the stationary Dirac equation with the standard notation of the Dirac matrices α, β (Volchkova *et al.*, 2020)

$$\mathbb{h}^{(\text{Dirac})} \psi(\mathbf{r}) = (\boldsymbol{\alpha} \cdot \mathbf{p} + \beta + V(r, \vartheta)) \psi(\mathbf{r}) = \varepsilon \psi(\mathbf{r}), \quad [\mathbb{h}^{(\text{Dirac})}, \mathbf{j}] \neq 0, \quad [\mathbb{h}^{(\text{Dirac})}, j_z] = 0$$

$$\psi(\mathbf{r}) = \frac{1}{r} \begin{pmatrix} P_1(r, \vartheta) e^{i\varphi(m-1/2)} \\ P_2(r, \vartheta) e^{i\varphi(m+1/2)} \\ i Q_1(r, \vartheta) e^{i\varphi(m-1/2)} \\ i Q_2(r, \vartheta) e^{i\varphi(m+1/2)} \end{pmatrix}$$

and where m is the eigenvalue to J_z .

- **Dirac equation in an axially-symmetric potential:** With the notations from above, the Dirac equation simplifies for the states of well-defined magnetic projection m to (Volchkova *et al.*, 2020)

$$\mathbb{h}_m \phi(r, \vartheta) = \left[\begin{pmatrix} 1 & D_M \\ -D_M & -1 \end{pmatrix} + V(r, \vartheta) \right] \phi(r, \vartheta) = \varepsilon \phi(r, \vartheta) = \varepsilon \begin{pmatrix} P_1(r, \vartheta) \\ P_2(r, \vartheta) \\ Q_1(r, \vartheta) \\ Q_2(r, \vartheta) \end{pmatrix}$$

$$D_m = (\sigma_z \cos \vartheta + \sigma_x \sin \vartheta) \left(\frac{\partial}{\partial r} - \frac{1}{r} \right) + \frac{1}{r} (\sigma_x \cos \vartheta - \sigma_z \sin \vartheta) \frac{\partial}{\partial \vartheta} + \frac{1}{r \sin \vartheta} (i M \sigma_y + \sigma_x),$$

and where the four components P_1, P_2, Q_1, Q_2 can be – as usual – expanded in B-splines, and by taking kinetic balance into account. Obviously, only the φ -dependence can be separated explicitly in this case, although the parity of these one-electron states is conserved as well.

2.2. Coulomb-Green function

Relativistic radial Coulomb-Greens function:

- Radial Green function of the Dirac equation: Following Yerokhin and Shabaev (1999, appendix D), the radial Green function of the Dirac equation for electrons with the angular-momentum symmetry κ can be written in the form:

$$G_\kappa(\omega, r_1, r_2) = -\frac{1}{W_\kappa(\omega)} \left[\phi_\kappa^\infty(\omega, r_1) \phi_\kappa^{0^T}(\omega, r_2) \Theta(r_1 - r_2) + \phi_\kappa^0(\omega, r_1) \phi_\kappa^{\infty^T}(\omega, r_2) \Theta(r_2 - r_1) \right]$$

where $\phi_\kappa^0(\omega, r)$ and $\phi_\kappa^\infty(\omega, r)$ are solutions of the radial Dirac equation, bounded at the origin and at the infinity, and where $W_\kappa(\omega)$ is the Wronskian.

- The functions $\phi_\kappa^0(\omega, r)$ and $\phi_\kappa^\infty(\omega, r)$ can be calculated in terms of the Whittaker functions of the first and second kind, although special care has to be taken.

2.3. Matrix elements with Dirac orbitals

2.3.a. Matrix elements with radial orbitals

Matrix elements with non-relativistic radial orbitals:

➤ Special non-relativistic r^k expectation values: The following expectation values are displayed by Marxer (1991)

$$\begin{aligned}\langle r^{-1} \rangle &= \frac{Z}{a_o n^2}, & \langle r^{-2} \rangle &= \frac{2 Z^2}{2(\ell+1) n^3} \\ \langle r^{-4} \rangle &= \frac{16 Z^4}{n^5} \left[3n^2 - \ell(\ell+1) \frac{(2\ell-2)!}{(2\ell+3)!} \right] \\ \langle r^{-6} \rangle &= \left[\frac{Z}{a_o} \right]^6 \frac{35n^4 - n^2 [30\ell(\ell+1) - 25] + 3(\ell-1)\ell(\ell+1)(\ell+2)}{8n^7 (\ell-3/2)(\ell-1)(\ell-1/2)\ell(\ell+1/2)(\ell+1)(\ell+3/2)(\ell+2)(\ell+5/2)} \\ \langle r^{-k-2} \rangle &= \left[\frac{Z}{a_o} \right]^{k+2} \frac{1}{n^{k+3} \ell^{k+1}} \mathcal{P}_{k,\ell} \left(\frac{n}{\ell} \right), & \mathcal{P}_{k,\ell}(x) &= \frac{(2\ell)^{k+1} (2\ell-k)!}{(2\ell+1)!} {}_3F_2(-k, k+1, \ell+1-\ell x; 1, 2\ell+2; 1)\end{aligned}$$

➤ Pasternack-Kramers rekursion relation: For $k \leq 0$, the r^{-k} expectation values of any $(n\ell)$ level fullfill the relation (Marxer 1991)

$$\begin{aligned}\langle r^{-k-2} \rangle &= \frac{4}{(2\ell+1)^2 - k^2} \left[\left(\frac{2k-1}{k} \right) \frac{Z}{a_o} \langle r^{-k-1} \rangle - \left(\frac{k-1}{k} \right) \frac{Z^2}{n^2 a_o^2} \langle r^{-k} \rangle \right] \\ \langle r^k \rangle &= \frac{(2\ell+k+2)!}{(2\ell-k-1)!} \left[\frac{n a_o}{2Z} \right]^{2k+3} \langle r^{-k-3} \rangle\end{aligned}$$

From this relation, explicit formulas for low principal quantum number n can be computed rather easily.

2. Dirac's hydrogenic atom

Matrix elements with relativistic Dirac wavefunctions:

- An analytical expression of the matrix elements with operators $r^k e^{-sr}$ can be found (also) for Dirac's relativistic wavefunctions. In order to derive such expressions, it is typically more convenient first to re-write the standard representation of the hydrogenic functions in terms of a series expansion in r as it was suggested originally by Rose (1961).
- An expression for the corresponding matrix element is given by:

$$\begin{aligned} \langle n\kappa | r^k e^{-\sigma r} | n'\kappa' \rangle &= \int_0^\infty dr e^{-\sigma r} (P_{n\kappa}(r) P_{n'\kappa'}(r) + Q_{n\kappa}(r) Q_{n'\kappa'}(r)) \\ &= N_{n\kappa} N_{n'\kappa'} \sum_{\nu=0}^{n-|\kappa|} \sum_{\nu'=0}^{n'-|\kappa'|} (c_{n\kappa,\nu}^+ c_{n'\kappa',\nu'}^+ + c_{n\kappa,\nu}^- c_{n'\kappa',\nu'}^-) \frac{q^{s+\nu-1} q'^{s'+\nu'-1}}{(q+q'+\sigma)^{1+\nu+\nu'+s+s'+k}} \Gamma(\nu + \nu' + k + s + s' + 1), \\ c_{n\kappa,\nu}^\pm &= \left(1 \pm \sqrt{1 - q^2}\right)^{1/2} \frac{((-n + |\kappa|)_\nu \, 2^\nu)}{\nu! (2s+1)_\nu} [(\nu - n + |\kappa|) \pm (\alpha Z/q - \kappa)] \end{aligned}$$

with $(a)_\nu$ being the Pochhammer symbol and where the parameters q , s and the normalization factor $N_{n\kappa}$ were defined above.

2.3.b. Matrix elements including the angular part of Dirac orbitals

Matrix elements of spherical tensors:

- Matrix elements of the \mathbb{C}^K tensors: In the nonrelativistic theory, we have

$$\langle \ell_a \| \mathbb{C}^{(K)} \| \ell_b \rangle = (-1)^{\ell_a} [\ell_a, \ell_b]^{1/2} \begin{pmatrix} \ell_a & K & \ell_b \\ 0 & 0 & 0 \end{pmatrix}, \quad (\mathbb{C}^{(k_1)} \mathbb{C}^{(k_2)})^{(K)} = (-1)^K [K]^{1/2} \begin{pmatrix} k_1 & K & k_2 \\ 0 & 0 & 0 \end{pmatrix} \mathbb{C}^{(K)},$$

where, in the last expression, $\mathbb{C}^{(k_1)}$, $\mathbb{C}^{(k_2)}$ must act upon the same electron (coordinates).

- Matrix elements of the \mathbb{C}^K tensors: Gaidamauskas *et al.* (2011) use the following definition:

$$\langle \kappa_a \| \mathbb{C}^{(K)} \| \kappa_b \rangle = (-1)^{j_a + 1/2} [j_a, j_b]^{1/2} \begin{pmatrix} j_a & K & j_b \\ 1/2 & 0 & -1/2 \end{pmatrix} \delta_{\ell_a+\ell_b+1, \text{even}}$$

2.4. Frequently applied expansions, transformations and identities in atomic theory

2.4.a. Partial-wave expansions of free electrons

Partial-wave expansion:

- Partial-wave components of a plane-wave electron: The computation of partial (and total) ionization cross sections often requires an integration over all possible angles $\Omega_p = (\vartheta_p, \varphi_p)$ of the photoelectrons, emitted in 4π . In practice, this integration over Ω_p can be carried out rather easily by making use of the *decomposition* of the free-electron wavefunction $|\mathbf{p} m_s\rangle$ into *partial-wave* components.
- In practice, however, this expansion generally depends on the choice of the quantization axis.
- If the quantization axis is taken along \mathbf{e}_z , this expansion is given by

$$|\mathbf{p} m_s\rangle = \sum_{\kappa m} i^\ell e^{-i\Delta_\kappa} \langle lm_\ell, 1/2 m_s | jm \rangle Y_{\ell m_\ell}^*(\vartheta_p, \varphi_p) |\varepsilon \kappa m\rangle,$$

and where the summation runs over all partial waves, $\kappa = \pm 1, \pm 2, \dots$ as well as $m = -j, \dots, j$. In this expansion, moreover, Δ_κ is the Coulomb phase shift, and the (nonrelativistic orbital angular momentum) quantum number ℓ just distinguishes the parity of the partial waves.

2.4.b. Expansions including spherical harmonics

Expansions including the spherical harmonics:

- Expansion of a plane-wave in terms of spherical Bessel functions:

$$e^{i\mathbf{k}\cdot\mathbf{r}} = 4\pi \sum_{\ell m} i^\ell j_\ell(kr) Y_{\ell m}^*(\hat{k}) Y_{\ell m}^*(\hat{r}).$$

- Multipole expansion of the (transverse-gauge) plane-wave vector potential:

$$\mathbf{A}^{(\text{transverse})}(\mathbf{r}, \omega) = 4\pi \sum_{LM} \sum_{p=0,1} i^{L-p} \left(\mathbf{Y}_{LM}^{(p)}(\hat{k}) \cdot \boldsymbol{\epsilon} \right) \mathbf{a}_{LM}^{(p)}(\mathbf{r}),$$

where the vector functions $\mathbf{a}_{LM}^{(p)}(\mathbf{r})$ are referred to as **multipole potentials**, and where only terms with $p = 0$ (magnetic) and $p = 1$ (electric) contribute, since $\mathbf{Y}_{LM}^{(-1)}(\hat{k})$ is orthogonal to $\boldsymbol{\epsilon}$.

- Laplace expansion of the $1/|\mathbf{r} - \mathbf{r}'|$ Coulomb interaction: ... together with the kernel

$$\frac{1}{r_{12}} = \frac{4\pi}{r_>} \sum_{k=0}^{\infty} [k]^{-1} \left(\frac{r_<}{r_>} \right)^k \sum_{q=-k}^k Y_{kq}(\vartheta_1, \varphi_1) Y_{kq}^*(\vartheta_2, \varphi_2), \quad U_k^{(\text{Coulomb})} = \frac{r_<^k}{r_>^{k+1}}.$$

- (Laplace) expansion of the $e^{-\lambda|\mathbf{r}-\mathbf{r}'|}/|\mathbf{r}-\mathbf{r}'|$ screened Yukawa-type interaction: ... together with the kernel

$$\frac{e^{-\lambda r_{12}}}{r_{12}} = 4\pi \lambda \sum_{k=0}^{\infty} J_k(\lambda r_<) K_k(\lambda r_>) \sum_{q=-k}^K Y_{kq}(\vartheta_1, \varphi_1) Y_{kq}^*(\vartheta_2, \varphi_2), \quad U_k^{(\text{Yukawa})} = [k] \lambda J_k(\lambda r_<) K_k(\lambda r_>),$$

and where $J_k(x)$, $K_k(x)$ are the regular and irregular modified Bessel functions which are regular at zero and infinity, respectively. In practice, Yukawa-screened functionals are quite easy to handle in fully numerical approaches owing to the given factorization of the individual terms in the expansion. It can therefore be implemented into atomic and molecular structure codes rather similar to the Coulomb interaction.

➤ Multipole expansion with two vectors $\mathbf{r}, \mathbf{r}' \ll R$: For this expansion, one finds (Patil and Tang, 2000)

$$\begin{aligned} \frac{1}{|\mathbf{R} - \mathbf{r} + \mathbf{r}'|} &= \sum_{\ell \ell' m} a(\ell, \ell', m) \frac{r^\ell r'^{\ell'}}{R^{\ell+\ell'+1}} Y_{\ell m}(\vartheta, \varphi) Y_{\ell', -m}(\vartheta', \varphi') \\ a(\ell, \ell', m) &= \frac{4\pi (-1)^{\ell'} (\ell + \ell')!}{[(2\ell + 1)(2\ell' + 1)(\ell + m)!(\ell - m)!(\ell' + m)!(\ell' - m)!]^{1/2}} \\ \frac{1}{|\mathbf{R} - \mathbf{r} + \mathbf{r}'|} &= \sum_{\ell \ell'} \left(\frac{r^\ell r'^{\ell'}}{R^{\ell+\ell'+1}} \right) \frac{4\pi (-1)^{\ell'} (\ell + \ell')!}{[(2\ell + 1)(2\ell' + 1)]^{1/2}} \sum_m \frac{Y_{\ell m}(\vartheta, \varphi) Y_{\ell', -m}(\vartheta', \varphi')}{[(\ell + m)!(\ell - m)!(\ell' + m)!(\ell' - m)!]} \\ \Delta \left(\frac{1}{|\mathbf{R} - \mathbf{r} + \mathbf{r}'|} \right) &= \Delta' \left(\frac{1}{|\mathbf{R} - \mathbf{r} + \mathbf{r}'|} \right) = 0, \quad R \gg r, r'. \end{aligned}$$

➤ Addition theorem for Legendre polynomials:

$$\begin{aligned} P_\ell(\cos \vartheta) &= \left(\frac{4\pi}{2\ell + 1} \right)^{1/2} Y_{\ell 0}(\vartheta, \varphi) \\ P_{\ell+\ell'}(\cos \vartheta) &= \left(\frac{4\pi}{2\ell + 2\ell' + 1} \right)^{1/2} \left[\frac{1}{(2\ell + 2\ell')!} \right]^{1/2} \left[\frac{4\pi (2\ell + 2\ell' + 1)!}{(2\ell + 1)!(2\ell' + 1)!} \right]^{1/2} \frac{\ell! \ell'!}{(\ell + \ell')!} \\ &\quad \times \sum_m \frac{(\ell + \ell')!}{(\ell - m)!(\ell' + m)!} \left[\frac{(2\ell)!(\ell - m)!(2\ell')!(\ell' + m)!}{(\ell + m)!(\ell' - m)!} \right]^{1/2} Y_{\ell m}(\vartheta, \varphi) Y_{\ell', -m}(\vartheta', \varphi'). \end{aligned}$$

2.4.c. Radial grid transformations

Radial grids:

- Radial grids for atomic computations: Various types of (radial) grid transformation $t = t(r)$ have been applied in the literature in order to adapt the physics, that need to be described, to an *equi-distant* grid. For bound-state (SCF) computations, one often applies a **logarithmic transformation** $t(r) \propto \ln(r)$ to account for the singularity of the potential at the origin. In a **logarithmic-linear transformation** $t(r) = c_1 \ln(r) + c_2 r$, one combines a exponential increase of the step-size near to the origin with a (nearly) linear behavior for large r . In the HULLAC and FAC codes, moreover, a **logarithmic-square-root transformation** $t(r) = c_1 \ln(r) + c_2 \sqrt{r}$ has been applied, which ensures that approximately the same number of grid points occurs for each oscillation of the continuum waves . When compared to the logarithmic-linear transformation, the logarithmic-square-root transformation covers for a given number of points a larger radial extent. This may have advantages for multiply- and highly-charged ions, though no detailed analysis has been made in the literature.

2.4.d. Useful identities

Useful identities:

- Derivative of the spherical Bessel functions:

$$j_{n-1}(z) = \frac{n+1}{z} j_n(z) + j'_n(z), \quad j_{n+1}(z) = \frac{n}{z} j_n(z) - j'_n(z)$$

2.5. Frequently occurring radial integrals

Notation & applications in Jac:

- In JAC, all these radial integrals can be directly computed by a call to some function from the `RadialIntegrals` module.

Functions $Y^k(r; ab)$ and $Z^k(r; ab)$:

- Nonrelativistic functions $Y^k(r; ab)$ and $Z^k(r; ab)$: These two function naturally arises from the derivative of the (two-electron) Slater integrals and appear very frequently in all atomic structure calculations. For radial orbitals with quantum numbers $a = (n_a, \kappa_a)$, $b = \dots$, these functions are given by

$$Y^k(r; ab) = r \int_0^\infty ds \frac{r_-^k}{r_+^{k+1}} P_a(s) P_b(s) = \int_0^r ds \left(\frac{s}{r}\right)^k P_a(s) P_b(s) + \int_r^\infty ds \left(\frac{r}{s}\right)^{k+1} P_a(s) P_b(s)$$

$$Z^k(r; ab) = \int_0^r ds \left(\frac{s}{r}\right)^k P_a(s) P_b(s).$$

Indeed, the fast and accurate calculation of $Y^k(r; ab)$ depends on $Z^k(r; ab)$, i.e. the first part in the definition above.

2. Dirac's hydrogenic atom

➤ **Solutions of the $Y^k(r; ab)$ and $Z^k(r; ab)$ functions:** It was originally suggested by Hartree that the $Y^k(r; ab)$ and $Z^k(r; ab)$ integrals can be determined by simultaneously solving a pair of differential equations with boundary conditions

$$\begin{aligned} \frac{d}{dr} Z^k(r; ab) &= P_a(r) P_b(r) - \frac{k}{r} Z^k(r; ab), & Z^k(0; ab) &= 0 \\ \frac{d}{dr} Y^k(r; ab) &= \frac{1}{r} [(k+1) Y^k(r; ab) - (2k+1) Z^k(r; ab)], & Y^k(r \rightarrow \infty; ab) &= Z^k(r \rightarrow \infty; ab) \end{aligned}$$

Grant's radial integrals for the coupling of the radiation field:

➤ Grant (1988) defines the following radial integrals that frequently occur in the coupling of the radiation field

$$\begin{aligned} I_L^o(q; ab) &= \int_0^\infty dr j_L(qr) [P_a Q_b] = \int_0^\infty dr j_L(qr) [P_a(r) Q_b(r)] \\ I_L^\pm(q; ab) &= \int_0^\infty dr j_L(qr) [P_a Q_b \pm Q_a P_b] \\ J_L(q; ab) &= \int_0^\infty dr j_L(qr) [P_a P_b + Q_a Q_b] \end{aligned}$$

➤ These integrals are useful also if the spherical Bessel function occurs in the integrant as $j_L(qr)/qr$, and where the following recursion relations can be used:

$$\frac{j_L(x)}{x} = \frac{1}{2L+1} [j_{L-1}(x) + j_{L+1}(x)].$$

➤ Following Najjari (2022), we also define the two integrals:

$$J_L^{(P)}(q; ab) = \int_0^\infty dr j_L(qr) [P_a P_b], \quad J_L^{(Q)}(q; ab) = \int_0^\infty dr j_L(qr) [Q_a Q_b].$$

Further radial integrals for different one-electron spherical tensor operators:

- In the treatment of the electron nucleus (hyperfine) interaction and the interaction with an external magnetic field, some radial integrals occur frequently:

$$I_L^{[r]}(ab) \equiv [r^L]_{ab} = \int_0^\infty dr r^L [P_a Q_b + Q_a P_b]$$

$$J_L^{} (ab) = \langle r^L \rangle_{ab} \equiv \int_0^\infty dr r^L [P_a P_b + Q_a Q_b]$$

- Vinti-Integral: In the treatment of the (relativistic) mass shift, the (so-called) Vinti-Integrals occur

$$R^{(\text{Vinti})}(a, b) = \int_0^\infty dr P_a \left[\frac{d}{dr} - \frac{\kappa_a(\kappa_a + 1) - \kappa_b(\kappa_b + 1)}{2r} \right] P_b + \int_0^\infty dr Q_a \left[\frac{d}{dr} - \frac{-\kappa_a(-\kappa_a + 1) + \kappa_b(-\kappa_b + 1)}{2r} \right] Q_b.$$

2.6. B-splines

Properties of B-splines:

- Use of B-splines: Finite basis sets of piecewise polynomials, so-called B-splines, have been shown useful in atomic physics, quantum chemistry and elsewhere. For these basis sets, the atom or ions is virtually placed in a sufficiently large cavity, and the wavefunctions are expanded in terms of the given functions.
- A B-spline (basis spline) is a spline function with a minimal support and which can be used to express all spline function of any given as a finite linear combination.
- In physics, B-splines are often utilized for curve-fitting and in order to fit derivatives to experimental data.
- Knot sequence: A sequence of (radial) grid points $\{t_1, t_2, \dots, t_m\}$ with $t_1 \leq t_2 \leq \dots \leq t_m$.

2. Dirac's hydrogenic atom

➤ **Set of B-splines:** Set of piecewise polynomial functions of order k , the so-called B-splines:

$$\left\{ B_1^{(k)}(x), B_2^{(k)}(x), \dots, B_n^{(k)}(x) \right\}, \quad B_i^{(1)}(x) = \begin{cases} 1 & \text{for } t_i \leq x \leq t_{i+1} \\ 0 & \text{otherwise,} \end{cases} \quad i = 1, 2, \dots, m-1.$$

➤ Recursion relation for the generation of B-splines:

$$B_i^{(k)}(x) = \frac{x - t_i}{t_{i+k-1} - t_i} B_i^{(k-1)}(x) + \frac{t_{i+k} - x}{t_{i+k} - t_{i+1}} B_{i+1}^{(k-1)}(x) \quad i = 1, 2, \dots, m-k$$

The number of B-splines $n = m - k$ ($k < m$) is determined by the order k and the number of knots m . For B-splines of a given order, it is therefore sufficient to use the notation $B_i^{(k)}(x)$

- Each B-spline is non-negative and is non-zero only for: $B_i(x) > 0$ for $t_i < x < t_{i+k}$ and $B_i(x) = 0$ for $x < t_i$, $x > t_{i+k}$. — Essentially, the B-spline $B_i(x)$ starts at t_i and ends at t_{i+k} with only positive values in between.
- **Use of B-splines in pseudo-code summations:** The first and last B-spline are often omitted in bound- and pseudo-state computations in order to fulfill the proper boundary conditions: $Q_{n\kappa}(0) = 0$ ($\kappa < 0$) and $P_{n\kappa}(0) = 0$ ($\kappa > 0$) as well as $P_{n\kappa}(r_{\max}) = P_{n\kappa}(r_{\min}) = 0$. Such a construction avoids the appearance of non-physical (*spurious*) states that may hamper the computations.
- **Dirac-Hartree-Fock matrix equations for a given set of core-orbitals within a finite box of radius R :** For a given set of (frozen) core orbitals and the one-particle symmetry κ , the Dirac-Hartree-Fock matrix equations for the two components $P(r)$, $Q(r)$ in a finite basis set can be

written as (Beloy and Derivianko, 2008)

$$\begin{aligned}
 P(r) &= \sum_i^N p_i g_i^L(r); & Q(r) &= \sum_i^N q_i g_i^S(r) \\
 \left(V_{ij}^{(\text{DHF})} \right) &= \left(V_{ij}^{(\text{DHF: direct})} \right) + \left(V_{ij}^{(\text{DHF exchange})} \right) \\
 \left(V_{ij}^{(\text{DHF: direct})} \right) &= \sum_{a \in \text{core}} (2j_a + 1) \int_0^R dr v_o(r; a, a) [g_i^L(r) g_j^L(r) + g_i^S(r) g_j^S(r)] \\
 \left(V_{ij}^{(\text{DHF: exchange})} \right) &= - \sum_{a \in \text{core}} \sum_k (2j_a + 1) \begin{Bmatrix} j & j_a & k \\ -1/2 & 1/2 & 0 \end{Bmatrix}^2 \int_0^R dr v_k(r; a, j) [g_i^L(r) P_a(r) + g_i^S(r) Q_a(r)] \\
 v_k(r; b, a) &= \int_0^R ds \frac{r_{\leq}^k}{r_{>}^{k+1}} [P_a(s) P_b(s) + Q_a(s) Q_b(s)].
 \end{aligned}$$

Application of B-splines:

- Application of B splines for constructing single- and many-electron basis sets are nowadays widely employed in computational atomic and molecular physics.
- **B-splines:** For a B-spline representation of single-electron orbitals, only the low-lying orbitals will usually contribute significantly to the many-electron wave function. More generally, the configuration mixing between two configuration states is inversely proportional to the energy interval between them. It is therefore said sometimes that a B-spline representation of the single-electron orbitals provide an effective and natural way in order to adopt the basis to the problem of interest.
- **B-splines in relativistic theory:** In contrast to the nonrelativistic theory, the use of B-splines in relativistic computations is often accompanied by the occurrence of spurious states (Shabaev *et al.*, 2004). In a Coulomb potential, spurious states appear especially for $\kappa > 0$ as the lowest bound states but with rather nonphysical energies.

2.7. Generation of continuum orbitals

Simple approximations in Jac:

- For a first estimate of continuum processes, we have implemented a number of (rather) simple approximations/methods for the continuum orbitals that occur frequently at various places in the program. In JAC, the particular method can be selected by (re-) defining the global variable `JAC_CONT SOLUTION` by a proper call to `Jac.define("method: continuum; ...")`.
- Approximations implemented in JAC:
 - (a) spherical Bessel functions;
 - (b) non-relativistic Coulomb waves for the large component of the continuum orbital, together with the kinetic-balance condition to obtain a small component;
 - (c) asymptotically correct, relativistic Coulomb orbital;
 - (d) Galerkin method to solve for continuum orbitals within a B-spline basis and for a given atomic potential.
- In JAC, spherical Bessel orbitals are generated if the global constant `JAC_CONT SOLUTION = ContBessel`; cf. `JAC.define()` and section 2.7.a.
- In JAC, a free nonrelativistic Coulomb orbitals are generated if the global constant is `JAC_CONT SOLUTION = NonrelativisticCoulomb`; cf. `JAC.define()` and section 2.7.b. Not available at present.
- In JAC, asymptotically-correct relativistic Coulomb orbitals are generated for a potential with a Coulombic tail, if the global constant `JAC_CONT SOLUTION = AsymptoticCoulomb`; cf. `JAC.define()` and section 2.7.c.
- In JAC, a B-spline representation of the relativistic orbital $\varepsilon\kappa$ in a given local potential are generated if the global constant `JAC_CONT SOLUTION = BsplineGalerkin`; cf. `JAC.define()` and section 2.7.d.
- In JAC, different normalization methods can be selected for all continuum orbitals; a pure-sine normalization for `JAC_CONT NORMALIZATION = PureSine`, an asymptotic Coulomb normalization for `JAC_CONT NORMALIZATION = CoulombSine`, or a WKB-type normalization for multiply and highly-charged ions for `JAC_CONT NORMALIZATION = OngRussek`; cf. `JAC.define()`.
- At present, no attempt has yet been made to incorporate the exchange interaction of the continuum and bound-state orbitals.

2.7.a. Spherical Bessel orbitals

Implementation and numerical details:

- Generating equation and solutions: The spherical Bessel functions $j_\ell(|\mathbf{k}|r)$ obey the (non-relativistic) *free* radial Schrödinger equation for positive energies $\varepsilon > 0$, and the corresponding wave number $k = \sqrt{2\varepsilon}$, $\rho = kr$ and for well-defined orbital angular momentum ℓ

$$R_{\varepsilon\ell}(r) = \frac{P_{\varepsilon\ell}}{r} = N j_\ell(|\mathbf{k}|r) = N j_\ell(\sqrt{2\varepsilon} r) \iff j_\ell''(\rho) + 2 \frac{j_\ell'(\rho)}{\rho} + \left(1 - \frac{\ell(\ell+1)}{\rho^2}\right) j_\ell(\rho) = 0.$$

- While the large component of such a continuum (Bessel) orbital $|\varepsilon\ell\rangle$ are represented by the Bessel function $P = N r j_\ell(|\mathbf{k}|r)$ above, the **small components** are here obtained from the kinetic-balance condition.

2.7.b. Non-relativistic Coulomb orbitals

Implementation and numerical details:

- The non-relativistic Coulomb orbitals $|\varepsilon\ell\rangle$ are known analytically for $\varepsilon > 0$ and can be utilized to represent the large components of a relativistic orbital with this (given kinetic) energy, while the **small components** are here obtained again from the kinetic-balance condition.
- Non-relativistic free Coulomb waves: The free solutions with $\varepsilon > 0$ to the radial Schrödinger equation with a central-field potential $V(r)$ with Coulombic tail satisfy the boundary condition:

$$P_{\varepsilon\ell}(0) = 0; \quad P_{\varepsilon\ell}(r \rightarrow \infty) \simeq \sqrt{\frac{2}{\pi k}} \sin \left(kr + \frac{\bar{Z}}{k} \ln(2kr) - \frac{\ell\pi}{2} + \sigma_\ell^{(\text{Coulomb})} + \delta_\ell \right),$$

where $k^2 = 2\varepsilon$, $\bar{Z} = Z - N$ is the effective charge as seen by the free electron at large distance and $\sigma_\ell^{(\text{Coulomb})} = \arg \Gamma(\ell + 1 - i\bar{Z}/k)$ is the (well-known) **Coulomb phase**. Note that this solution is normalized on the energy scale.

- See section 2.1 for a representation of a non-relativistic Coulomb orbital with positive energy $\varepsilon > 0$. This approach does not yet work properly since there is no hypergeometric function with complex arguments available in JULIA.

2.7.c. Asymptotically-correct relativistic Coulomb orbitals

Implementation and numerical details:

- **Relativistic free-Coulomb waves:** The free solutions to the radial Dirac equation in a spherical potential with Coulombic tail satisfy the boundary conditions (Åberg and Howat, 1982; Eqs. (19.29-30))

$$\begin{aligned}
 P_{\varepsilon\kappa}(0) &= Q_{\varepsilon\kappa}(0) = 0 \\
 P_{\varepsilon\kappa}(r \rightarrow \infty) &\simeq \sqrt{\frac{\varepsilon + 2c^2}{\pi c^2 k}} \cos [\theta_\kappa(\varepsilon) + \delta_\kappa(\varepsilon)], & Q_{\varepsilon\kappa}(r \rightarrow \infty) &\simeq -\sqrt{\frac{\varepsilon}{\pi c^2 k}} \sin [\theta_\kappa(\varepsilon) + \delta_\kappa(\varepsilon)] \\
 \theta_\kappa(\varepsilon) &= kr + y \ln(2kr) - \arg \Gamma(\bar{\gamma} + iy) - \frac{1}{2}\pi\bar{\gamma} + \eta, & k^2 &= 2\varepsilon + \frac{\varepsilon}{c^2} \\
 \bar{\gamma} &= +\left(\kappa^2 - \frac{\bar{Z}^2}{c^2}\right)^{1/2}, & y &= \frac{\bar{Z}(\varepsilon + c^2)}{c^2 k} & \exp(2i\eta) &= -\frac{\kappa - iy/(\varepsilon + c^2)}{\bar{\gamma} + iy}.
 \end{aligned}$$

- The phase-shift δ_κ is the non-Coulombic phase shift and is set to $\delta_\kappa = 0$ for a pure Coulombic potential.

2.7.d. Continuum orbitals in an atomic potential: Galerkin method

Implementation and numerical details:

- One advantage of using B-splines is that solutions of the Schrödinger or Dirac equation can be found for any energy $\varepsilon > 0$ by properly adopting r_{\max} .
- While both the Schrödinger and Dirac equations have formally a solution for any positive energy $\varepsilon > 0$, a diagonalization in a B-spline representation provides only a discrete set of solutions due to the boundary condition $P(r_{\max}) = Q(r_{\max}) = 0$, and where r_{\max} here denotes the size of the *numerical box*.

- **Galerkin method:** This method determines an approximate solution of the generalized eigenvalue equations

$$\sum_i \langle B_i | (\mathbb{H} - \varepsilon) | B_j \rangle c_j = \sum_i A_{ij} c_j = 0, \quad A_{ij} = \langle B_i | (\mathbb{H} - \varepsilon) | B_j \rangle = H_{ij} - \varepsilon S_{ij}.$$

- **Galerkin method:** A possible approximation to this generalized eigenvalue problem is to compute the smallest eigenvalue of $\mathbf{A} \cdot \mathbf{c} = \lambda \mathbf{c}$, a more accurate solution follows from a minimization of $|A\psi|^2$ under the constraint $|\psi|^2 = 1$. This variational problem is mathematically equivalent to find the smallest eigenvalue of the matrix $A^+ A : \mathbf{A}^+ \mathbf{A} \cdot \mathbf{c} = a \mathbf{c}$. — The eigenvector of the smallest eigenvalue $a_i > 0$ is then the requested (approximate) solution of the eigenvalue problem above.

2.7.e. Normalization and phase of continuum orbitals

Pure sine behaviour at large r :

- **Pure sine behaviour:** The free radial Schrödinger equation without an external potential always satisfies the asymptotic pure sine behaviour $\sim \sin(kr + \varphi)$. A very similar asymptotic form $\sim \sin(kr - \ell\pi/2 + \varphi)$ also applies for all partial-wave solutions $\ell \geq 0$ and positive energy $\varepsilon > 0$ for the standard radial Schrödinger equation with just a centrifugal potential $\sim 1/r^2$.
- **Normalization for a pure sine behaviour:** For this normalization, the large component is assumed to be given with $k = \sqrt{2\varepsilon}$ by

$$P(r \approx r_{\max}) = \sqrt{\frac{2}{\pi k}} \begin{cases} \sin(kr + \varphi) & \text{for } \ell = 0 \\ \sin(kr - \frac{\ell\pi}{2} + \varphi) & \text{for } \ell > 0. \end{cases}$$

With this behaviour, the normalization constant N and the phase φ can be obtained by means of the logarithmic derivative P/P' .

Asymptotic Coulomb behaviour at large r :

- **Normalization for an asymptotic Coulomb behaviour:** For this normalization, the large and small components are assumed to be described for all r -values by the asymptotic behaviour as shown in subsection 2.7.c. With this assumption, the normalization constant N and the phase φ can again be obtained by means of the logarithmic derivative P'/P .
- Instead of the logarithmic derivative P'/P , one can of course also apply the ratio Q/P ; this option is currently hard-coded in JAC but need to be further tested.

Normalization for multiply-charged ions due to Ong and Russek (1973):

- This normalization scheme has not yet been implemented and tested so far.
- Normalization on energy scale: Continuum orbital functions are often normalized on an energy scale, $\langle \varepsilon\kappa | \varepsilon'\kappa' \rangle = \delta(\varepsilon - \varepsilon') = \delta(E - E')$, and where E, E' are the free-electron energies *inclusive* the rest mass energy, i.e. $E > mc^2$.
- WKB ansatz for the large component $P_{\varepsilon\kappa}(r)$: If $V(r)$ is an atomic central-field potential of the ionic core and if we make use of the ansatz below for the large component in the Dirac equation, a second-order ODE can be derived for the function $\phi(r)$, cf. Ong and Russek (1978)

$$P_{\varepsilon\kappa}(r) = A \sqrt{\frac{E - V(r) + c^2}{c(d\phi/dr)}} \cos \phi(r),$$

$$-\left(\frac{d\phi}{dr}\right)^2 + \frac{(E - V)^2 - c^4}{c^2} - \frac{\kappa(\kappa + 1)}{r^2} + \left(\frac{d\phi}{dr}\right)^{1/2} \frac{d^2}{dr^2} \left(\frac{d\phi}{dr}\right)^{-1/2} - (E - V + c^2)^{1/2} \frac{d^2}{dr^2} (E - V + c^2)^{-1/2} + \frac{\kappa}{r} \frac{dV/dr}{E - V + c^2} = 0.$$

- WKB approximation: If the last three terms are neglected in the equation above, an approximate solution to this ODE is given by
- $$\left(\frac{d\phi}{dr}\right)^2 \approx \frac{(E - V)^2 - c^4}{c^2} - \frac{\kappa(\kappa + 1)}{r^2}, \quad P_{\varepsilon\kappa}(r) \approx \frac{A \sqrt{E - V + c^2}}{[(E - V)^2 - c^4 - c^2 \kappa(\kappa + 1)/r^2]^{1/4}} \cos \phi(r).$$
- Normalization and phase of the WKB solution at some finite value r_o : Following Ong and Russek (1978, Eq. 12), one can introduce an auxiliary potential $U(r)$, from which the normalization constant $A(r_o)$ and the phase $\phi(r_o)$ at some finite radius r_o is obtained by

$$U(r) = \frac{c}{2} \frac{(E - V) \frac{dV}{dr} - c^2 \kappa(\kappa + 1)/r^3}{[(E - V)^2 - c^4 - c^2 \kappa(\kappa + 1)/r^2]^{3/2}} P_{\varepsilon\kappa}(r) - c \frac{\frac{dP_{\varepsilon\kappa}}{dr} + \frac{dV/dr}{2(E - V + 2c^2)} P_{\varepsilon\kappa}(r)}{[(E - V)^2 - c^4 - c^2 \kappa(\kappa + 1)/r^2]^{1/2}}$$

$$A(r_o) = \sqrt{\frac{[(E - V)^2 - c^4 - c^2 \kappa(\kappa + 1)/r^2]^{1/2}}{E - V + c^2}} (P_{\varepsilon\kappa}^2 + U^2) \Big|_{r=r_o}, \quad \phi(r_o) = \text{atan2}(U, P_{\varepsilon\kappa}) \Big|_{r=r_o}.$$

- Normalization and phase of the asymptotic wave function $P_{\varepsilon\kappa}(r)$: The normalization of $A(r_o)$ can be used to normalize also the large (and small) component $P_{\varepsilon\kappa}(r)$. For $V(r_o) \approx 0$ and $\phi(r) \approx kr + \delta_\kappa(\varepsilon)$ and if C is the normalization constant so that $CP_{\varepsilon\kappa}$ has the correct asymptotic amplitude, one finally obtains

$$C = \frac{1}{A} \sqrt{\frac{(E + c^2) c d\phi/dr}{\pi c^2 k (E - V + c^2)}} \approx \frac{1}{A \sqrt{\pi c}}, \quad \delta_\kappa(\varepsilon) \approx \phi(r) - kr.$$

2.8. Dirac equation with an axially-symmetric potential

Separation of the Dirac equation:

➤ **Dirac equation with an axially symmetric potential:** For an axially-symmetric potential $V(r, \vartheta)$, the total angular momentum \mathbf{j} is no longer conserved, while the projection j_z is conserved and still commutes with the Hamiltonian: $[j_z, \mathbb{H}^{(\text{Dirac: axially})}] = 0$. Therefore, only the φ -dependence can be separated by the ansatz (Rozenbaum *et al.*, 2014)

$$\mathbb{H}^{(\text{Dirac: axially})} \psi(\mathbf{r}) = [c(\boldsymbol{\alpha} \cdot \mathbf{p}) + mc^2 \beta + V^{(\text{nuc})}(r) + V(r, \vartheta)] \psi(\mathbf{r}) = E \psi(\mathbf{r}); \quad \psi(\mathbf{r}) = \frac{1}{r} \begin{pmatrix} P_1(r, \vartheta) e^{i(m_j - \frac{1}{2})\varphi} \\ P_2(r, \vartheta) e^{i(m_j + \frac{1}{2})\varphi} \\ iQ_1(r, \vartheta) e^{i(m_j - \frac{1}{2})\varphi} \\ iQ_2(r, \vartheta) e^{i(m_j + \frac{1}{2})\varphi} \end{pmatrix}$$

$$\mathbb{H}^{(\text{axially})} \phi(r, \vartheta) = E \phi(\mathbf{r}); \quad \phi(\mathbf{r}) = \begin{pmatrix} P_1(r, \vartheta) \\ P_2(r, \vartheta) \\ Q_1(r, \vartheta) \\ Q_2(r, \vartheta) \end{pmatrix}$$

$$\langle \phi_a | \phi_b \rangle = \int_0^\infty dr \int_0^\pi d\vartheta \sin \vartheta (P_{a,1} P_{b,1} + P_{a,2} P_{b,2} + Q_{a,1} Q_{b,1} + Q_{a,2} Q_{b,2}), \quad \phi(r \rightarrow 0, \vartheta) = 0.$$

The particular form of $\mathbb{H}^{(\text{axially})}$ depends of course on $V(r, \vartheta)$ and, hence, the external field(s) of interest.

➤ **Dirac equation for an external electric field:** For an axially-symmetric potential $V(r, \vartheta)$ due to an external electric field and the definition of the four-component spinor $\phi(r, \vartheta)$ from above, the four-component Dirac equation can be written in spherical coordinates as (Rozenbaum

et al., 2014)

$$\begin{aligned} \mathbb{H}^{(\text{axially: electric})} &= \begin{pmatrix} mc^2 + V & c D^{(e)} \\ -c D^{(e)} & -mc^2 + V \end{pmatrix}, & V &= V^{(\text{nuc})} + V(r, \vartheta), & D^{(e)+} &= -D^{(e)} \\ D^{(e)} &= (\sigma_z \cos \vartheta + \sigma_x \sin \vartheta) \left(\frac{\partial}{\partial r} - \frac{1}{r} \right) + \frac{1}{r} (\sigma_x \cos \vartheta - \sigma_z \sin \vartheta) \frac{\partial}{\partial \vartheta} + \frac{1}{r \sin \vartheta} \left(i m_j \sigma_y + \frac{\sigma_x}{2} \right). \end{aligned}$$

➤ **Dirac equation for an external magnetic field:** For an axially-symmetric potential $V(r, \vartheta)$ due to an external magnetic field and the definition of the four-component spinor $\phi(r, \vartheta)$ from above, the four-component Dirac equation can be written in spherical coordinates as

$$\begin{aligned} \mathbb{H}^{(\text{axially: magnetic})} &= \begin{pmatrix} mc^2 + V^{(\text{nuc})} & c(D^{(e)} + D^{(m)}) \\ -c(D^{(e)} + D^{(m)}) & -mc^2 + V^{(\text{nuc})} \end{pmatrix} \\ D^{(m)} &= -\frac{e}{2c} \mathcal{B} r \sin \vartheta i \sigma_y, & D^{(m)+} &= -D^{(m)}. \end{aligned}$$

2.9. Volkov solutions

Volkov states:

- **Standard Volkov solutions:** Volkov wave functions describe the motion of a charged particle in an intense monochromatic laser field; the standard form can be applied in a field without spatial dependence (dipole approximation) or if the plane-wave field have all a well-defined propagation direction.
- **Generalized Volkov solutions:** The standard Volkov solutions are valid for monochromatic plane-wave radiation. Rosenberg and Zhou (1993) worked out (generalized) Volkov states for a wider class of plane-wave field which do not propagate along the same direction. This generalization allows in principle also to construct Volkov states for pulses, i.e. em fields that are localized in space and time. The nonrelativistic form of these solutions are essentially exact, i.e. errors occur only at the order $(v/c)^2$, as for all nonrelativistic theories. The

2. Dirac's hydrogenic atom

lowest nonrelativistic order $\sim (v/c)^2$ also accounts for the recoil of the charged particle due to the exchange of photon momentum but should be omitted from a consistent nonrelativistic treatment.

2.10. Nuclear models and potentials

Nuclear models and radii:

- **Compilation of root-mean-square (rms) radii:** Angeli and Marinova (2013) have published a compilation of the root-mean-square (rms) radii for more than 900 isotopes, most of them radioactive. Refined experimental (and partly theoretical) techniques helped enlarge the knowledge of the nuclear size for many isotopes within the nuclear chart. Indeed, detailed measurements of nuclear radii have been performed along many isotope sequences of the periodic table with special emphasis close to magic numbers. Often, these measurements serve a benchmark for nuclear structure calculations.
- **Determination of nuclear charge distributions:** A plenty of microscopic nuclear models have been developed and applied in order to obtain realistic nuclear charge distributions by starting from a set of effective interactions (Hamiltonians). In these models, the shape, size and distribution of the nuclear density is typically obtained from the self-consistent set of Hartree-Fock-Bogoliubov (HFB) equations, or methods beyond. The (so-called) effective Skyrme interaction has been applied with different sets of parameter that help to adjust energies and radii to experimental data in a broad range of nuclei. While the SLY4 parameters set was fitted for describing neutron-rich nuclei, the UNEDF1 set makes use also of bound-state energies, radii and single-particle energies for nuclei across the nuclear chart.

2.10.a. Coulomb potential; point-like nuclei

Potential:

- **Coulomb potential in space and momentum representation:** For a point-like nucleus, the space and momentum representation of the Coulomb potential can be written as

$$V^{(\text{Coulomb})}(r) = -\frac{\alpha Z}{r}, \quad V^{(\text{Coulomb})}(q) = -4\pi \frac{\alpha Z}{q^2}.$$

2.10.b. Shell-like nuclei

Potential:

- Potential of shell-like nucleus in space and momentum representation: For a (jellium) shell-like nucleus with radius $R = \sqrt{\langle r^2 \rangle}$, the space and momentum representation of the Coulomb potential can be written as

$$V^{(\text{shell})}(r) = \begin{cases} -\frac{\alpha Z}{R} & r < R \\ -\frac{\alpha Z}{r} & r \geq R \end{cases} \quad V^{(\text{shell})}(q) = -4\pi \frac{\alpha Z}{q^2} \frac{\sin R q}{R q}.$$

2.10.c. Uniform nuclear model

Uniform charge distribution and potential:

- Uniform nuclear-charge distribution: For a nucleus with radius R , charge Z and mass number A , the nuclear charge distribution and potential is given for $r \leq R$ by

$$\rho^{(\text{uniform})}(r) = \frac{3Z}{4\pi R^3}, \quad \phi^{(\text{uniform})}(r) = \begin{cases} \frac{Ze}{2R} \left[3 - \left(\frac{r}{R} \right)^2 \right] & \text{if } r \leq R \\ \frac{Ze}{R} & \text{if } r > R \end{cases}$$

$$R = R_n \sqrt{\frac{1 + (5s^2/2R_n^2)}{1 + (3s^2/4R_n^2)}}, \quad R_n = 1.07 \times 10^{-15} A^{1/3} \text{ m}, \quad s = 2.0 \times 10^{-15} \text{ m}.$$

- Form factor for nuclei with uniform nuclear-charge distribution:

$$F^{(\text{uniform})}(q; R) \equiv 4\pi \int_0^\infty dr r^2 \frac{\sin(qr)}{qr} \rho^{(\text{uniform})}(r) = \frac{3Z}{(qR)^3} [\sin(qR) - qR \cos(qR)].$$

2. Dirac's hydrogenic atom

➤ **Potential of uniform nucleus in space and momentum representation:** For a nucleus with constant charge distribution in a sphere of radius R , the space and momentum representation of the Coulomb potential can be written as (Oreshkina, 2022)

$$V^{(\text{uniform})}(r) = \begin{cases} -\frac{\alpha Z}{R} \left[\frac{3}{2} - \frac{3}{2} \left(\frac{r}{R} \right)^2 \right] & r < R \\ -\frac{\alpha Z}{r} & r \geq R \end{cases} \quad V^{(\text{uniform})}(q) = -4\pi \frac{\alpha Z}{q^2} \frac{3(\sin Rq - Rq \cos Rq)}{(Rq)^3}.$$

Often, a radius $R = \sqrt{5/3 \langle r^2 \rangle}$ is applied.

2.10.d. Helm's uniform-uniform nuclear model

Uniform-uniform charge distribution and potential:

- Helm's uniform-uniform nuclear-charge distribution: An alternative realistic nuclear-charge distribution can be expressed as convolution of two uniform distributions $\rho_1^{(\text{uniform})}$, $\rho_2^{(\text{uniform})}$ with nuclear radii $R_1 > R_2$ and normalization constant N (Salvat *et al.*, 2005)

$$\rho^{(\text{Helm})} = Z N \int d^3\mathbf{r}' \rho_1^{(\text{uniform})}(\mathbf{r}') \rho_2^{(\text{uniform})}(\mathbf{r} - \mathbf{r}')$$

$$\phi^{(\text{Helm})} = \begin{cases} N & \text{if } r \leq R_1 - R_2 \\ N \frac{[(r + R_1)^2 - R_2^2 + 2rR_1][(r - R_1)^2 - R_2^2]^2}{32r^3R_2^3} + \frac{[(r + R_2)^2 - R_1^2 + 2rR_2][(r - R_2)^2 - R_1^2]^2}{32r^3R_1^3} & \text{if } R_1 - R_2 \leq r \leq R_1 + R_2 \\ 0 & \text{if } r > R_1 + R_2 \end{cases}$$

- The normalization constant N of Helm's uniform-uniform nuclear-charge distribution and the corresponding electrostatic potential $\phi^{(\text{Helm})}$ need to be determined numerically.

2.10.e. Helm's nuclear-depression model

Distribution and potential for central nuclear depression:

- Central depression of the nuclear density: In (super-) heavy nuclei with $Z \gtrsim 100$, a central depression of the nuclear density is caused by the Coulomb repulsion of the Z protons, i.e. the nuclear charge distribution slightly rise from the centre towards the surface region. Although this nuclear suppression is further affected by the (detailed) nuclear shell structure, it leads to an estimated decrease of up to 7.5 % of the nuclear matter density at the center of the nucleus (Friedrich *et al.*, 1986).
- Helm model: A quantitative relation between the nuclear electromagnetic form factor and the nuclear charge distribution has been established by means of the folding (Helm) model. In this Helm model, the nuclear charge density is described by means of a convolution of a square-well distribution $\rho^{(\text{square-well})} = \rho_o \Theta(R_d - r)$, with diffraction radius R_d , and a Gaussian distribution $\rho^{(\text{Gaussian})} = \rho(r, \sigma)$.
- Nuclear charge distribution:

$$\rho^{(\text{Helm})} = \rho^{(\text{square-well})} \rho^{(\text{Gaussian})} = (1 + w r^2) \rho^{(\text{homogeneous})} \exp\left(-\frac{r^2}{2\sigma^2}\right)$$

2. Dirac's hydrogenic atom

➤ **Modified Helm model:** Since the rise of the nuclear density near to the origin is proportional to r^2 , a modified modified Helm model has been suggested by Friedrich *et al.* (1986) in terms of the weight w whose value follows from the normalization $\int dr \rho^{(\text{Helm})} = 1$. With this weight parameter, the nuclear charge distribution is often written as:

$$\rho^{(\text{modified Helm})} = \frac{(1 + w r^2)}{1 + w \langle r^2 \rangle^{(\text{homogeneous})}} \rho^{(\text{homogeneous})} \exp\left(-\frac{r^2}{2\sigma^2}\right).$$

2.10.f. Fermi nuclear model

Fermi charge distribution and potential:

➤ **Fermi model:** For a nucleus with *root-mean-square* (rms) radius $R = \sqrt{\langle r^2 \rangle}$

$$\rho(r, R) = \frac{N}{1 + \exp[(r - c)/a]}, \quad \int dr r^2 \rho(r, R) = 1$$

where the **thickness parameter** a is often chosen as $a = 2.3/4 \ln 3$.

➤ **Fermi nuclear-charge distribution:** For a nucleus with *half-density* density R_n , the Fermi distribution is uniform in the center and falls off smoothly at the surface of the nucleus from 0.9 to 0.1 of the central density within a skin of thickness t

$$\rho^{(\text{Fermi})} = \frac{\rho_o}{\exp[(r - R_n)/z] + 1}, \quad z = \frac{t}{(4 \ln 3)} = 0.546 \times 10^{-15} \text{ m}$$

➤ The normalization constant ρ_o of the Fermi nuclear-charge distribution and the corresponding electrostatic potential $\phi^{(\text{Fermi})}$ need to be determined numerically.

➤ With high accuracy, the parameters N and c can be obtained from the analytical formulas

$$N = \frac{3}{4\pi c^3} \left(1 + \frac{\pi^2 a^2}{c^2}\right)^{-1}, \quad c = \sqrt{\frac{5}{3} \langle r^2 \rangle - \frac{7}{3} \pi^2 a^2}.$$

➤ **Potential of Fermi-distributed nucleus in space and momentum representation:** For a nucleus with a Fermi-distributed charge of skin thickness a and half-density radius c , the space and momentum representation of the potential can be written as (Oreshkina, 2022)

$$V^{(\text{Fermi})}(r < c) = -\frac{\alpha Z}{r N^{(\text{Fermi})}} \left\{ 6 \left(\frac{a}{c}\right)^3 \left[S_3\left(\frac{r-c}{a}\right) - S_3\left(-\frac{c}{a}\right) \right] + \frac{r}{c} \left[\frac{3}{2} + \frac{\pi^2}{2} \left(\frac{a}{c}\right)^2 - 3 \left(\frac{a}{c}\right)^2 S_2\left(\frac{r-c}{a}\right) \right] - \frac{1}{2} \left(\frac{r}{c}\right)^3 \right\}$$

$$V^{(\text{Fermi})}(r \geq c) = -\frac{\alpha Z}{r N^{(\text{Fermi})}} \left\{ N^{(\text{Fermi})} + 6 \left(\frac{a}{c}\right)^3 S_3\left(\frac{c-r}{a}\right) + 3 \left(\frac{a}{c}\right)^2 \frac{r}{c} S_2\left(\frac{c-r}{a}\right) \right\}$$

$$N^{(\text{Fermi})} = 1 + \pi^2 \left(\frac{a}{c}\right)^2 - 6 \left(\frac{a}{c}\right)^3 S_3\left(-\frac{c}{a}\right), \quad S_k(x) = \sum_{n=1}^{\infty} \frac{(-1)^n}{k^n} \exp(nx)$$

$$V^{(\text{Fermi})}(q) = V^{(\text{Coulomb})}(q) \left(1 + \frac{V^{(\text{A})}(q)}{N^{(\text{Fermi})}} + \frac{V^{(\text{B})}(q)}{N^{(\text{Fermi})}} \right)$$

$$V^{(\text{A})}(q) = -\frac{c^2 + a^2 \pi^2}{c^2} + \frac{1}{(cq)^2} \left(\frac{a^2 q^2 \pi^2 - 6}{2} \frac{\cos(cq)}{cq} + \frac{a^2 q^2 \pi^2 + 6}{2} \frac{\sin(cq)}{cq} \right)$$

$$V^{(\text{B})}(q) = 6 \left(\frac{a}{c}\right)^2 \cos(cq) \left[\frac{1}{2(aq)^2} + \frac{\pi^2}{6} - \frac{\pi}{2(aq)} \coth(\pi aq) \right] + 6 \left(\frac{a}{c}\right)^2 \frac{\sin(cq)}{cq} \left[-\frac{1}{2(aq)^2} + \frac{\pi}{6} + \frac{\pi^2}{2} \frac{1}{\sinh^2(\pi aq)} \right]$$

$$+ 6 \left(\frac{a}{c}\right)^3 (aq)^2 \sum_{n=1}^{\infty} \frac{2n^2 + (aq)^2}{n^3 [n^2 + (aq)^2]^2} \exp\left(-\frac{nc}{a}\right).$$

Nuclear potential:

2. Dirac's hydrogenic atom

➤ Potential of extended nucleus:

$$\mathbb{V}^{(\text{nuc})}(r; R) = -4\pi \alpha Z \int_0^\infty dr' r'^2 \frac{\rho(r', R)}{r'} = -\frac{4\pi \alpha Z}{r} \int_0^r dr' r'^2 \rho(r', R) - 4\pi \alpha Z \int_r^\infty dr' r' \rho(r', R), \quad r' = \max(r, r').$$

2.10.g. Deformed Fermi nuclear model

Fermi charge distribution and potential:

➤ Nuclear density of a deformed Fermi model: A deformed nuclear density is given by (Kozhedub *et al.*, 2008)

$$\rho(\mathbf{r}) = \frac{N}{1 + \exp\left(\frac{r-c}{a}\right)}, \quad c = c_o \left(1 + \sum_{\ell m} \beta_{\ell m} Y_{\ell m}(\vartheta, \varphi)\right),$$

and where N is a normalization constant in order to ensure $\int d^3r \rho(\mathbf{r}) = 1$.

2.10.h. Z -scaling of atomic energies, rates and properties

Simple Z -scaling:

➤ Z -scaling of atomic energies, energy splittings and rates for hydrogenic ions: The analytical treatment of hydrogenic ions readily allows to extract the Z -scaling of energies, energy splittings and rates. These scalings enable one to quickly check for the relevance of interactions and processes under quite different circumstances. A few of such scalings are given by:

| Observable | scaling | observable | scaling |
|-------------------|-----------------------|-------------------------------|-----------------------------|
| Transition energy | $(\alpha Z)^2$ | Fine-structure splitting | $(\alpha Z)^4$ |
| Lamb shift | $\alpha (\alpha Z)^4$ | Hyperfine-structure splitting | $\alpha (\alpha Z)^3 m/m_p$ |

- **Scaling laws for ionization and scattering cross sections:** For hydrogenic ions and from observations, the following scaling laws has been found and are frequently applied for first applications

$$\sigma^{(\text{photoionization})} \propto \frac{Z^{4-5}}{(\hbar \omega)^{7/2}}; \quad \sigma^{(\text{Compton})} \propto \frac{Z}{(\hbar \omega)^2}; \quad \sigma^{(\text{pair production})} \propto Z^2 \ln(\hbar \omega).$$

3. Many-electron atomic interactions, state functions, density operators and statistical tensors

3.1. Electron-electron interaction

Background & notations:

- In the (non-relativistic) limit of a rather slow motion of the electrons, each electron pair just interact by the instantaneous Coulomb repulsion

$$\frac{1}{r_{12}} \equiv \frac{1}{|\mathbf{r}_1 - \mathbf{r}_2|}.$$

Already this quite simple (interaction) operator results mathematically in various complications and is generally **the major source of electron-electron correlations in all many-electron computations**.

- For moving charges, Maxwell's theory also predicts both, **current-current** and **retarded interactions**, to which we briefly refer as **Breit interactions** in atomic physics. — These relativistic contributions to the electron-electron interactions must be added to the electro-static Coulomb repulsion.
- An effective (relativistic) operator for the electron-electron interaction can be formally derived from QED in perturbation theory with regard to the number of virtually exchanged photons (Sapirstein 1987, Grant und Quiney 1988), while the same expressions can be obtained also from heuristic arguments as given, for example, by Bethe and Salpeter (1957) und Johnson (1995).
- In practice, the **computation of the electron-electron interaction usually requires the largest effort in all electronic-structure codes** and, therefore, deserves special consideration. In atomic physics, a considerable simplification is usually achieved if all electron-electron interaction operators are represented as spherical tensors.

3. Many-electron atomic interactions, state functions, density operators and statistical tensors

- For two electrons in orbitals a, b and with energies $\varepsilon_a, \varepsilon_b$, the **interaction energy** can be written as difference of a direct and exchange **matrix element** of the potential

$$\mathbb{V}^{(\text{tr})} = -\frac{1}{2\pi} \int \frac{d^3k}{k^2 - \omega^2} e^{i\mathbf{k}\cdot(\mathbf{r}_1-\mathbf{r}_2)} \sum_{i,j=1}^3 \left[\delta_{ij} - \frac{k_i k_j}{k^2} \right] \alpha_{1i} \alpha_{2j}$$

where α_{1i} is the i -th component of the $\boldsymbol{\alpha}$ matrix (vector) of the electron at position \mathbf{r}_1 and

$$\omega = \begin{cases} 0 & \text{direct matrix element} \\ \frac{|\epsilon_a - \epsilon_b|}{c} & \text{exchange matrix element} \end{cases}$$

refers to the momentum of the exchanged photon.

- The **exchange matrix elements of the potential** $\mathbb{V}^{(\text{tr})}$ is generally complex; while the *real* part describes an energy shift due to this transverse interaction, the *imaginary* part represents a rate for the decay $a \rightarrow b$ for $\epsilon_a > \epsilon_b$ or $b \rightarrow a$ vice versa.
- Frequency-independent Breit interaction: For $\omega \rightarrow 0$, the transversal Breit interaction gives rise to the **frequency-independent Breit interaction**

$$b_{12}^o = -\frac{1}{2r_{12}} \left[\boldsymbol{\alpha}_1 \cdot \boldsymbol{\alpha}_2 + \frac{(\boldsymbol{\alpha}_1 \cdot \mathbf{r}_{12})(\boldsymbol{\alpha}_2 \cdot \mathbf{r}_{12})}{r_{12}^2} \right],$$

which neglects all contributions $\sim \alpha^4 Z^3$ (as well as of higher order in αZ).

- Typically, the explicit energy-dependence of the transverse interaction [upon the energy difference of the two electrons] gives rather tiny corrections, so that, in practice, often no difference is made between the transversal and zero-frequency Breit interaction.
- **Gaunt interaction:** The first term of the zero-frequency Breit interaction (operator) is known also as Gaunt interaction (Gaunt 1929). This term describes the current-current interaction due to the motion of the electrons and contributes about 90 % of the total Breit interaction for closed-shell atoms.
- For many elements of the periodic table, the corrections due to the Breit interaction are usually small, when compared with the dominant Coulomb repulsion. This applies especially for the Breit contributions to the electron-electron correlation.
- For describing most processes, it is sufficient, if at all, to include the Breit interaction perturbatively in lowest order. Formally, however, both terms

$$v_{12} = \frac{1}{r_{12}} + b_{12} \quad \iff \quad \mathbb{V}^{(e-e)} = \mathbb{V}^{(\text{Coulomb})} + \mathbb{V}^{(\text{Breit})}$$

are equivalent, and they should be treated simply together for all (super-) heavy elements.

- In JAC, only the frequency-independent Breit interaction is currently implemented.

Effective interaction strength $X^{(L)}(abcd)$ of scalar electron-electron interactions:

- All operators of the (scalar) electron-electron interaction can be generally represented as spherical tensors in the form:

$$g_{12} \equiv g(\mathbf{r}_1, \mathbf{r}_2) = \sum_L g_L(r_1, r_2) (\mathbb{T}^{(L)}(\vartheta_1, \varphi_1) \cdot \mathbb{T}^{(L)}(\vartheta_2, \varphi_2))$$

$$\langle n_a \kappa_a m_a(1) n_b \kappa_b m_b(2) | g_{12} | n_c \kappa_c m_c(1) n_d \kappa_d m_d(2) \rangle = \sum_{LM} (-1)^{L-M+j_a-m_a+j_b-m_b} \begin{pmatrix} j_a & L & j_c \\ -m_a & M & m_c \end{pmatrix} \begin{pmatrix} j_b & L & j_d \\ -m_b & -M & m_d \end{pmatrix} X^{(L)}(abcd),$$

leading to a simple **factorization of the two-electron matrix elements**, and where the magnetic quantum numbers (i.e. the angular dependence) of the matrix elements only occurs in the phase and the Wigner $3-j$ symbols.

- Effective interaction strength $X^{(L)}(abcd)$ of order L : The strengths $X^{(L)}(abcd)$ describe the physical interaction and are specific for every operator. They are often used as the **building blocks in order to handle the electron-electron interactions efficiently in electronic structure computations**.

Effective interaction strength $X^{(L, \text{Coulomb})}(abcd)$ of the Coulomb repulsion:

- Coulomb repulsion: The decomposition of the Coulomb operator is given by:

$$\frac{1}{r_{12}} = \sum_{L=0}^{\infty} U_L(r, s) P_L(\cos(\vartheta)) = \sum_{L=0}^{\infty} U_L(r, s) (\mathbb{C}^{(L)}(\vartheta_1, \varphi_1) \cdot \mathbb{C}^{(L)}(\vartheta_2, \varphi_2)), \quad U_L(r, s) = \begin{cases} \frac{r^L}{s^{L+1}} & r < s \\ \frac{s^L}{r^{L+1}} & r > s. \end{cases}$$

In this expansion, $P_L(x)$ denotes a Legendre-polynomial and $\vartheta = \mathbf{r} \cdot \mathbf{s}/rs$ the angle between the two electron coordinates.

3. Many-electron atomic interactions, state functions, density operators and statistical tensors

➤ Effective interaction strength of the Coulomb repulsion:

$$X^{(L, \text{Coulomb})}(abcd) = \delta(j_a, j_c, L) \delta(j_b, j_d, L) \Pi^e(\kappa_a, \kappa_c, L) \Pi^e(\kappa_b, \kappa_d, L) (-1)^L \langle \kappa_a \| \mathbb{C}^{(L)} \| \kappa_c \rangle \langle \kappa_b \| \mathbb{C}^{(L)} \| \kappa_d \rangle R^L(abcd),$$

$$\delta(j_a, j_b, j_c) = \begin{cases} 1 & |j_a - j_b| \leq j_c \leq |j_a + j_b| \text{ and cyclic interchanged} \\ 0 & \text{otherwise,} \end{cases}$$

and where $\Pi^e(\kappa, \kappa', L)$ represent the angular momentum and parity selection rules.

Effective interaction strength $X^{(L, \text{Breit})}(abcd)$ of the Breit interaction:

➤ Effective interaction strength of the zero-frequency Breit: For the zero-frequency interaction, we find

$$X^{(L, \text{Breit})}(abcd) = (-1)^L \langle \kappa_a \| \mathbb{C}^{(L)} \| \kappa_c \rangle \langle \kappa_b \| \mathbb{C}^{(L)} \| \kappa_d \rangle \left[\Pi^o(\kappa_a, \kappa_c, L-1) \Pi^o(\kappa_b, \kappa_d, L+1) \sum_{\mu=1}^8 s_{\mu}^L(abcd) S_{\mu}^L(abcd) + \sum_{\nu=L-1}^{L+1} \Pi^o(\kappa_a, \kappa_c, \nu) \Pi^o(\kappa_b, \kappa_d, \nu) \sum_{\mu=1}^4 t_{\mu}^{\nu, L}(abcd) T_{\mu}^{\nu}(abcd) \right].$$

$$\Pi^o(\kappa_a, \kappa_b, L) = \begin{cases} 1 & \text{if } l_a + l_b + L \text{ odd} \\ 0 & \text{otherwise.} \end{cases}$$

➤ The constant coefficients s_{μ}^L and $t_{\mu}^{\nu, L}$ just depend on the angular quantum numbers $\{\kappa_a, \kappa_b, \kappa_c, \kappa_d, \nu, L\}$ and are displayed, for example, by Grant (1988; tables 3 and 4, and where we here use $t_{\mu}^{\nu, L} \equiv r_{\mu}^{\nu, L}$).

Table 3.1.: Definition of the integrales $S_\mu^\nu(abcd)$ und $T_\mu^\nu(abcd)$

| | | |
|--|--|--|
| $S_1^\nu(abcd) = S^\nu[ac \parallel bd]$ | $S_2^\nu(abcd) = S^\nu[bd \parallel ac]$ | $T_1^\nu(abcd) = T^\nu[ac \parallel bd]$ |
| $S_3^\nu(abcd) = S^\nu[ca \parallel db]$ | $S_4^\nu(abcd) = S^\nu[db \parallel ca]$ | $T_2^\nu(abcd) = T^\nu[ca \parallel db]$ |
| $S_5^\nu(abcd) = S^\nu[ac \parallel db]$ | $S_6^\nu(abcd) = S^\nu[db \parallel ac]$ | $T_3^\nu(abcd) = T^\nu[ac \parallel db]$ |
| $S_7^\nu(abcd) = S^\nu[ca \parallel bd]$ | $S_8^\nu(abcd) = S^\nu[bd \parallel ca]$ | $T_4^\nu(abcd) = T^\nu[ca \parallel bd]$ |

➤ The radial integrals $S_\mu^\nu(abcd)$ and $T_\mu^\nu(abcd)$ are different (linear) combinations of the two integrals [cf. table 3.1]

$$S^\nu[ac \parallel bd] = \int_0^\infty dr \int_0^\infty ds P_a(r) Q_c(r) \frac{1}{2} [W_{\nu-1, \nu+1, \nu}(r, s; \omega_{ac}) + W_{\nu-1, \nu+1, \nu}(r, s; \omega_{bd})] P_b(s) Q_d(s)$$

$$T^\nu[ac \parallel bd] = \int_0^\infty dr \int_0^\infty ds P_a(r) Q_c(r) \frac{1}{2} [V_\nu(r, s; \omega_{ac}) + V_\nu(r, s; \omega_{bd})] P_b(s) Q_d(s)$$

$$V_\nu(r, s; \omega) = \begin{cases} -(2\nu + 1) j_\nu(\omega r) n_\nu(\omega s) & r < s \\ -(2\nu + 1) j_\nu(\omega s) n_\nu(\omega r) & r > s \end{cases}$$

$$W_{\nu-1, \nu+1, \nu}(r, s; \omega) = \begin{cases} -(2\nu + 1) j_{\nu-1}(\omega r) n_{\nu+1}(\omega s) + \left(\frac{2\nu+1}{\omega}\right)^2 \frac{r^{\nu-1}}{s^{\nu+2}} & r < s \\ -(2\nu + 1) \omega j_{\nu-1}(\omega s) n_{\nu+1}(\omega r) & r > s \end{cases}.$$

➤ In these expressions, $j_\nu(\omega r)$ and $n_\nu(\omega r)$ denote the spherical Bessel functions, and $\omega_{ac} = |\epsilon_a - \epsilon_c|$ the difference of the corresponding single-particle energies.

3.2. Atomic potentials

Parametrized many-electron densities:

- Thomas-Fermi-Moliere (TFM) electron density: A useful analytical model for the spherical symmetric electron density follows from a simple parametrization of the Thomas-Fermi (TF) screening function $\chi^{(\text{TFM})}(r)$ and its substitution into the Poisson equation (Salvat *et al.*, 2005)

$$\chi^{(\text{TFM})}(r) = \sum_{i=1}^3 A_i \exp\left(\frac{a_i r}{b}\right), \quad A_1 = 0.1, \quad A_2 = 0.55, \quad A_3 = 0.35, \quad a_1 = 6, \quad a_2 = 1.2, \quad a_3 = 0.3$$

$$b = \frac{(3\pi)^{2/3}}{2^{7/3}} \frac{\hbar^2}{m e^2 Z^{1/3}} = \frac{0.88534 a_o}{Z^{1/3}}$$

$$\rho^{(\text{TFM, electrons})}(r) = \frac{Z}{4\pi r} \sum_{i=1}^3 A_i a_i^2 \exp(a_i r).$$

- Thomas-Fermi-Dirac (TFD) electron density: The TFD theory also accounts for the exchange term of the electron gas and leads again to a differential equation that need to be solved numerically for each individual atom or ion. A parametrized form for an approximated TFD screening function $\chi^{(\text{TFD})}$ has been suggested in the literature but results in a rather lengthy and cumbersome expansion.

3.2.a. In JAC implemented potentials

Atomic potentials:

- Core-Hartree potential:

$$V^{(\text{core-Hartree})}(r) = \int_0^\infty dr' \frac{\rho_c(r')}{r_>}, \quad r_> = \max(r, r'), \quad \rho_c(r) = \sum_a (P_a^2(r) + Q_a^2(r)),$$

and where the summation runs over all *core* orbitals of electron configurations. This potential is applied if just a single valence electron occurs (alkali atoms). In JAC, this potential can be obtained for a given level from `Jac.computePotentialCoreHartree(grid::Radial.Grid, level::Level)`.

➤ Dirac-Fock-Slater potential:

$$V^{(\text{DFS})}(r) = \int_0^\infty dr' \frac{\rho_t(r')}{r_>} - \left(\frac{3}{4\pi^2 r^2} \rho_t(r) \right)^{1/3}, \quad r_> = \max(r, r'), \quad \rho_t(r) = \sum_a (P_a^2(r) + Q_a^2(r)),$$

and where the summation runs over *all* orbitals (electrons). In JAC, this potential can be obtained for a given level from `Jac.computePotentialDFS(grid::Radial.Grid, level::Level)`.

➤ Hartree potential:

$$V^{(\text{Hartree})}(r) = - \sum_a \bar{q}_a r Y_{aa}^0(r)$$

where \bar{q}_a is the generalized occupation number, and where the summation runs over all orbitals here. In JAC, this potential can be obtained for a given level from `Jac.computePotentialHartree(grid::Radial.Grid, level::Level)`.

➤ Hartree-Slater potential:

$$V^{(\text{HS})}(r) = - \sum_a \bar{q}_a Y_{aa}^0(r) + \frac{3}{2} \left(\frac{3}{4\pi^2 r^2} \rho(r) \right)^{1/3} \frac{r}{2} \quad \rho(r) = \sum_a \bar{q}_a (P_a^2(r) + Q_a^2(r)),$$

and where the summation runs over *all* orbitals. In JAC, this potential can be obtained for a given level from `Jac.computePotentialDFS(grid::Radial.Grid, level::Level)`.

➤ Kohn-Sham potential:

$$V^{(\text{Kohn-Sham})}(r) = \int_0^\infty dr' \frac{\rho_t(r')}{r_>} - \frac{2}{3r} \left(\frac{81}{32\pi^2} r \rho_t(r) \right)^{1/3}, \quad r_> = \max(r, r'), \quad \rho_t(r) = \sum_a (P_a^2(r) + Q_a^2(r)),$$

and where the summation runs over *all* orbitals (electrons). In JAC, this potential can be obtained for a given level from `Jac.computePotentialKohnSham(grid::Radial.Grid, level::Level)`.

3. Many-electron atomic interactions, state functions, density operators and statistical tensors

- Dirac-Fock-Slater-plus-Core-Polarization (DFS+CPOL) potential: (Migdalek & Baylis, 1979; Palmeri & Quinet, 2021)

$$V^{(\text{DFS+CPOL})}(r) = \int_0^\infty dr' \frac{\rho_t(r')}{r'} - \left(\frac{3}{4\pi^2 r^2} \rho_t(r) \right)^{1/3} + V_p(r) \delta_{val}, \quad r' = \max(r, r'), \quad \rho_t(r) = \sum_a (P_a^2(r) + Q_a^2(r))$$

$$V_p(r) = -\frac{\alpha_d r^2}{2 (r^2 + r_c^2)^3}, \quad \delta_{val} = \begin{cases} 1 & \text{valence electrons} \\ 0 & \text{core electrons,} \end{cases}$$

where the summation runs over all orbitals (electrons) and where $V_p(r)$ is the core-polarization potential (Migdalek and Baylis, 1979) that just acts upon the valence electrons. In the core-polarization potential, α_d is the core polarizability and r_c the core radius, two external parameters. In JAC, this potential can be obtained for a given level from `Jac.computePotentialDFSwCP(cp::CorePolarization, grid::Radial.Grid, level::Level)`.

- Atomic potential of many-electron atoms: Starting from the effective potential with the asymptotic behaviour $V^{(\text{eff})}(r \rightarrow \infty) \propto a/r$ in the single-electron Schrödinger equation, the well-known centrifugal term $\propto \ell(\ell + 1)/r^2$ forms a positive barrier especially for $\ell \geq 2$. This makes the effective potential $V^{(\text{eff})}(r)$ to a two-well potential, and where the inner well is determined by the mean electron-electron interaction, while the outer well remains mostly hydrogenic. Small variations in the shape of this double-well potential may then lead to rather large changes in the localization of bound electrons, and this makes singly- and multiply-charged ions sometimes (very) sensitive to the orbital relaxation due to the ionization process. For open-shell configurations, moreover, different terms of a given configuration might be differently sensitive to such relaxation contributions.
- Atomic potential of many-electron atoms: If a collapse of electron localization occurs due to different wells of the effective potentials, the wave functions cannot be approximated so easily by configuration mixing as the potential wells strongly effect the inter-electron (exchange) interactions.

3.2.b. Further atomic potentials, not yet considered in JAC

Atomic potentials:

- Modified Dirac-Fock potential: For a closed-shell N -electron atom, a modified Dirac-Fock potential has been defined for the (outgoing)

electron by Derevianko *et al.* (1999) as

$$V(r) = \sum_b (2j_b + 1) \frac{Y_0(r, bb)}{r} - V^{(\text{exchange})}(r), \quad V^{(\text{exchange})}(r) = \frac{V^{(\text{direct})}(r)}{N}.$$

In this potential, the function $Y_0(r, bb)/r$ is the Hartree screening potential for an electron in subshell b , and all generated orbitals are orthonormal to each other if the bound electrons are generated self-consistently in this potential. All continuum orbitals can then be generated in the same potential.

➤ Tietz (1954) potential:

$$V^{(\text{Tietz})}(r) = -\frac{\alpha Z}{r} \phi(x), \quad \phi(x) = \frac{1}{(1 + (\pi/8)^{2/3} x)^2}, \quad x = \frac{r Z^{1/3}}{\mu}, \quad \mu = \left(\frac{3\pi}{4}\right)^{2/3} \approx 0.8853.$$

➤ Modified-Tietz potential: (Neuffer and Commins, 1977)

$$V^{(\text{modified-Tietz})}(r) = -\frac{\alpha}{r} \left(1 + \frac{(Z-1)}{(1+tr)^2} e^{-\gamma r}\right)$$

where γ and t are parameters adjusted to fit the low-lying spectra of the atoms under consideration. Johnson *et al.* (1985) tabulate these parameters for rhubidium, cesium, gold and thallium.

➤ extended-Hartree potential: The extended-Hartree potential has been defined by Gu (2008) and is based on the $Y^k(r, ab)$ function as

3. Many-electron atomic interactions, state functions, density operators and statistical tensors

well as various direct and exchange coefficients, as they arise from the energy average of a given (non-relativistic) configuration.

$$V^{(\text{extended-Hartree})}(r) = \frac{1}{r \sum_a q_a \rho_a(r)} \left\{ \sum_{ab} q_a (q_b - \delta_{ab}) Y^0(r; bb) \rho_a(r) + \sum_a q_a (q_a - 1) \sum_{k>0} f_k(a, a) Y^k(r; aa) \rho_a(r) \right.$$

$$\left. + \sum_{a \neq b} \sum_k q_a q_b g_k(a, b) Y^k(r; ab) \rho_{ab}(r) \right\}$$

$$E^{(\text{extended-Hartree})} = \frac{1}{2} \sum_a q_a \langle a | V^{(\text{extended-Hartree})} | a \rangle = \frac{1}{2} \sum_a q_a \int dr V^{(\text{extended-Hartree})}(r) \rho_{aa}(r)$$

$$f_k(a, b) = - \left(1 + \frac{1}{2j_a} \right) \begin{pmatrix} j_a & k & j_b \\ -\frac{1}{2} & 0 & \frac{1}{2} \end{pmatrix}^2, \quad g_k(a, b) = - \left(\begin{pmatrix} j_a & k & j_b \\ -\frac{1}{2} & 0 & \frac{1}{2} \end{pmatrix}^2, \quad \rho_{ab} = P_a(r), P_b(r) + Q_a(r), Q_b(r). \right)$$

For a single configuration, this potential is chosen so that it just contributes with $E^{(\text{extended-Hartree})}$ as electron-electron part to the averaged DHF energy; here, the factor 1/2 occurs due to the double counting of electron pairs in the summation over electron shells in the potential $V^{(\text{extended-Hartree})}(r)$ and which has the correct asymptotic behavior for $r \rightarrow \infty$.

➤ Green-potential: (Green *et al.*, 1969)

$$V^{(\text{Green})}(r) = -\frac{\alpha}{r} \left(1 + \frac{(Z-1)}{[H(e^{r/d} - 1) + 1]} \right)$$

where $H = d(Z-1)^{1/3}$ and d is an adjustable parameter. Johnson *et al.* (1985) apply this type of potential but leave d and H adjustable; they also tabulate these parameters for rhubidium, cesium, gold and thallium.

➤ Norcross (1973) potential:

$$V^{(\text{Norcross})}(r) = V^{(\text{Thomas-Fermi})}(\lambda, r) - \frac{\alpha}{2r^4} \alpha_d \left(1 - e^{-(r/r_c)^6} \right) - \frac{\alpha}{2r^6} (\alpha_q - 6\beta a_o) \left(1 - e^{-(r/r_c)^{10}} \right)$$

where $V^{(\text{Thomas-Fermi})}(\lambda, r)$ is a Thomas-Fermi type potential with an adjustable parameter λ . The second and third terms correct for the polarization of the core; α_d is the electric-dipole polarizability of the core, α_q is the electric-quadrupole polarizability of the core and βa_o a dynamical correction to the quadrupole polarizability. Johnson *et al.* (1985) tabulate these parameters for rhubidium, cesium, gold and thallium.

- **Variationally-optimized spherical potential for given Hamiltonian:** Talman and Shadwick (1976) derived a formal expression for a spherical potential that is variationally optimal for a given Hamiltonian. For this, they considered a given spherical potential $V(r)$, for which (1) the single-electron Schrödinger is solved equation and (2) an associated N -electron Hamiltonian is formed. The potential $V_H(r)$ is then varied to minimize the ground-state energy of the Hamiltonian. These derivations give rise to a **formal integral equation for the difference $V(r) - V_H(r)$** , and which can be interpreted as an equation for an effective central exchange potential. Overall, however, this equation seem to be of **little practical use**, since no explicit expression for the optimized spherical potential is obtained. It is shown only that such an optimized potential behaves like $-e/r$ (for neutral atoms), i.e. that any electron of the atom moves asymptotically ($r \rightarrow \infty$) in the Coulomb potential of the residual ion — likely, as expected by most atomic physicists.
- **Atomic potential for helium:** For atomic helium, a simple central potential is written as

$$V(r) = -\frac{1}{r} - \frac{(1 + \lambda r)}{r} e^{-2\lambda r};$$

it has the corrects asymptotic behaviour $V(r \rightarrow 0) \sim -2/r$ and $V(r \rightarrow \infty) \sim -1/r$. The parameter $\lambda = 1.688$ ensures that the lowest $1s$ eigenenergy reproduces the ionization potential of helium (~ 0.903 a.u.)

- **Simple analytical exchange potential:** A simple exchange-correlation potential from the literature reads (in atomic units) as function of the electron density at position \mathbf{r} as

$$V^{(\text{xc})}(\mathbf{r}) = -\frac{0.611}{R(\mathbf{r})} - 0.0333 \ln \left(1 + \frac{11.1}{R(\mathbf{r})} \right), \quad R(\mathbf{r}) = \left(\frac{3}{4\pi n(\mathbf{r})} \right)$$

Thomas-Fermi theory:

- **Thomas-Fermi density and equation:** The TF model of atoms and ions assumes that the electronic charge density $\rho(r)$ [in atomic units] is continuous and finite in the interval $[0, r_o]$; this charge density is related to the (dimensionless) **Thomas-Fermi potential** $\psi(x)$ with the

3. Many-electron atomic interactions, state functions, density operators and statistical tensors

ion boundary $x_o = x_o(r_o)$ by (Dmitrieva *et al.*, 1982)

$$\begin{aligned} \rho^{(\text{Thomas-Fermi})}(x) &= \frac{32 Z^2}{9 \pi^3} \left[\frac{\psi(x)}{x} \right]^{3/2} = \frac{32 Z^2}{9 \pi^3} \frac{\psi''(x)}{x}, & x &= \left(\frac{128 Z}{9 \pi^2} \right)^{1/3} r = \frac{r}{\mu} \\ \psi''(x) &= \frac{\psi^{3/2}(x)}{\sqrt{x}}, & \psi(0) &= 1, & \psi(x_o) &= 0, & x_o \psi'(x_o) &= -1 + \frac{N}{Z}. \end{aligned}$$

For neutral atoms, we have $x_o \rightarrow \infty$, and both $\psi(x)$ and the ion boundary x_o just depend on the parameter $N/Z \leq 1$.

- **Thomas-Fermi electron density and distribution function:** For a spherical-symmetric Thomas-Fermi atom, the electron density is given in terms of the Thomas-Fermi distribution function $f^{(\text{TF})}(x)$ as

$$n^{(\text{TF})}(r) = Z^2 f^{(\text{TF})}(x = r/r^{(\text{TF})}), \quad f^{(\text{TF})}(x) = \frac{1}{4\pi b^3} \left(\frac{\chi(x)}{x} \right)^{3/2}, \quad r^{(\text{TF})} = \frac{b}{\sqrt[3]{Z}}, \quad b = \left(\frac{9\pi^2}{128} \right)^{1/3}.$$

- **Multipole moments of the Thomas-Fermi density:** The multipole moments of the charge density can then be expressed as

$$\langle r^k \rangle^{(\text{Thomas-Fermi})} = \int d^3r r^k \rho^{(\text{Thomas-Fermi})}(r) = \left(\frac{9\pi^2}{128} \right)^{k/3} Z^{\frac{3-k}{3}} \int_0^{x_o} dx \psi^{3/2}(x) x^{k+1/2}$$

- **Thomas-Fermi expectation value $\langle 1/r \rangle^{(\text{Thomas-Fermi})}$ for neutral atoms:** An expansion of the Thomas-Fermi density can be utilized to express the $\langle r^{-1} \rangle$ expectation value (multipole moment) by three just three terms (Dmitrieva *et al.*, 1982)

$$\langle r^{-1} \rangle^{(\text{Thomas-Fermi})} = 1.7937 Z^{4/3} - Z + 0.44983 Z^{2/3}.$$

In comparison with Hartree-Fock calculations, it was shown that this expectation value provides a reliable estimate within a few percent for all neutral atoms with $Z \gtrsim 10$.

- **Thomas–Fermi–Moliere (TFM) screening function:** Moliere first applied a screening function as derived from the Thomas-Fermi model with the parameters

$$A_1 = 0.10, \quad A_2 = 0.55, \quad A_3 = 0.35, \quad a_1 = \frac{6.0}{b}, \quad a_2 = \frac{1.2}{b}, \quad a_3 = \frac{0.3}{b}, \quad b \equiv \frac{(3\pi)^{2/3} \hbar^2}{2^{7/3} m e^2} Z^{-1/3} = 0.88534 Z^{-1/3} a_o,$$

and where b is the Thomas–Fermi radius. The TFM screening function agrees closely with the Thomas-Fermi screening function in the region $r \lesssim 6b$ (Salvat *et al.*, 2022).

3.3. Construction of symmetry-adapted CSF basis

Definition of symmetry-adapted CSF:

- **Coefficients of fractional parentage (CFP):** A set of CFP is defined for each subshell occupation $(n\kappa)^w$; these coefficients are defined in order to ensure that all shell-state functions are antisymmetric and, hence, satisfy the Pauli exclusion principle. The CFP coefficients play an crucial role in the theory of many-electron atoms but are not needed in the quasi-spin formalism.
- **Factorization of CSF:** For a single subshell $(n\kappa)$, aCSF simply factorizes into a radial and a spin-angular part with well-defined seniority ν and (subshell) total angular momentum $\mathbb{J}M$

$$|(n\kappa)^w \alpha \nu \mathbb{J}M\rangle = \prod_{j=1}^w R_{n\kappa}(r_i) |\kappa^w \alpha \nu \mathbb{J}M\rangle, \quad R_{n\kappa}(r) = \frac{1}{r} \begin{pmatrix} P(r) \\ Q(r) \end{pmatrix},$$

and where $|\kappa^w \alpha \nu \mathbb{J}M\rangle$ refers to a spin-angular subshell state that only involves angular variables of all w equivalent electrons in this subshell.

- **Quasispin of relativistic subshell states:** Analogue to the construction of non-relativistic shell states, a quasi-spin quantum number and its projection can be assigned to each relativistic subshell state $|\kappa^w \alpha \nu \mathbb{J}M\rangle$ by

$$Q = \left(\frac{2j+1}{2} - \nu \right), \quad M_Q = \frac{1}{2} \left(w - \frac{2j+1}{2} \right)$$

With this notation, a **relativistic subshell state of w equivalent electrons** can be written in either seniority or quasi-spin notation:
 $|(n\kappa)^w \alpha \nu \mathbb{J}M\rangle = |(n\kappa) \alpha Q M_Q \mathbb{J}M\rangle$.

Excitation schemes for the constructing a many-electron CSF basis:

- Several (de-) excitation schemes for the construction of non-relativistic configuration lists are defined within JAC in order to facilitate the set-up of (lists of) CSF bases with selectec total symmetry \mathbb{J} . These bases are required specially for the computation of cascades and/or approximate many-electron Green functions.
- In JAC, various excitation schemes are distinguished by the (abstract) scheme::Basics.AbstractExcitationScheme, and which is used for the construction of systematically enlarged basis sets, the computation of approximate Green functions as well as for the generation of atomic cascades.

- (De-) excitation of a single electron from a given set of (non-relativistic) configurations (`DeExciteSingleElectron`): This scheme includes all excitations and de-excitations of a single electron from a given list of (nonrelativistic bound-electron) configurations. Here, of course, the number of electrons of the newly generated configurations is the *same* as given by the configuration, while up to *one* free electron occur in each CSF for representing N -electron scattering levels.

$$\text{Example: } 1s^2 2s^2 2p^6 \rightarrow \left\{ \begin{array}{l} 1s2s^22p^6(ns + np + nd + \dots) \\ 1s^22s2p^6(ns + np + nd + \dots) \\ 1s^22s^22p^5(ns + np + nd + \dots) \end{array} \right\}$$

- (De-) excitation of two electrons from a given set of (non-relativistic) configurations (`DeExciteTwoElectrons`): Similar as above, this scheme includes all excitations and de-excitations of up to *two* electrons from the given list of (bound-electron) configurations and, hence, allows up to *two* free electrons for representing the N -electron scattering levels.

$$\text{Example: } 1s^2 2s^2 2p^6 \rightarrow \left\{ \begin{array}{l} 1s2s^22p^6(ns + np + nd + \dots) + 2s^22p^6 nl n'l' \\ 1s^22s2p^6(ns + np + nd + \dots) + 1s^22p^6 nl n'l' \\ 1s2s2p^6 nl n'l' \\ \dots \end{array} \right\}$$

- Add a single electron to a given set of configurations (`AddSingleElectronWithoutHoles`): This scheme generates all configurations with one additional electron to the given set of configurations but without any replacement from the occupied orbitals.

$$\text{Example: } 1s^2 2s^2 2p^6 \rightarrow \{ 1s^2 2s^2 2p^6(ns + np + nd + \dots) \}$$

Configuration state function generators (CSFG):

- Configuration state function generators (CSFG): Li *et al.* (2023) made use of (so-called) CSFG to reduce the computational load of relativistic CI calculations. This concept has been partly implemented also into GRASP2018 and applied to atoms and correlation models of increasing complexity. With these CSFG, a reduction of CPU time with factors between 10 and 14 have been achieved for the largest CI calculations. In selected cases, where condensed expansions have been generated prior to the computations, even slightly larger reduction of CPU time has been achieved.

3.4. Spin-angular coefficients for symmetry-adapted CSF

Approaches for the evaluation of matrix elements with symmetry-adapted CSF:

- **Evaluation of many-electron matrix elements:** The efficient decomposition and computation of many-electron matrix elements is essential for most atomic-structure calculations. It often decides how much electron-electron correlation can be taken into account, and how accurate predictions can be made for some particular atomic property of process. Therefore, various approaches have been worked out in the past in order to decompose the matrix elements for (symmetric) one- and two-particles operators between open-shell and symmetry-adapted configuration state functions.
- **Fano's scheme for evaluating many-electron matrix elements:** Fano's decomposition of open-shell matrix elements, that applies the coefficients of fractional parentage (CFP) and the seniority of the antisymmetric subshell states, has been widely used in configuration-interaction and multi-configuration calculations, both in LS - and jj -coupling. This scheme was used, for instance, in all earlier versions of the ATSP and GRASP suites of atomic-struture programs. However, although Fano's procedure provides an elegant decomposition of the matrix elements, it does not exploit the full power of Racah's algebra (Gaigalas *et al.*, 2001).
- **Quasi-spin formalism:** If second quantization is applied within a *coupled tensorial form*, a further reduction of matrix elements can be found by using the quasi-spin formalism. This formalism is based on the theory of angular momentum, together with Wick's theorem, and enables one to replace the coefficients of fractional parentage (CFP) by *completely-reduced* CFP as well as completely reduced matrix elements of the operators $W^{(k_q k_l k_s)}$ in LS -coupling or $W^{(k_q k_j)}$ in jj -coupling, respectively. Gaigalas *et al.* (2000) worked out these completely reduced matrix elements for all subshell with $j \leq 9/2$, and as sufficient for most relativistic computations.
- **Quasi-spin formalism:** The use of this formalism is crucial for all systematically-enlarged MCDF studies on open d - and f -shell elements, for which single, double and (sometimes even) triple excitation are required in order to account for all major correlations. These requirements refer to most heavy and super-heavy elements ($Z \geq 104$), and for which virtual excitations into $j = 9/2$ subshells are often inevitable.

3.4.a. Quasi-spin formalism in jj -coupling

Matrix elements between antisymmetric subshell states:

- **Antisymmetrized subshell states:** In the relativistic theory, each electron shell nl (apart from $1s$) is known to split into two subshells with $j = \ell \pm 1/2 = \ell_{\pm}$, and which also affects the representation of the relativistic configuration state function. Instead of the antisymmetric,

LS -coupled shell states $|n\ell^N \alpha LSJ\rangle$, one then has to deal with the antisymmetrized (product) functions $|(n\ell) j_1^{N_1} j_2^{N_2} \alpha_1 J_1 \alpha_2 J_2 J\rangle$. Here, ℓ just denotes the parity of the configuration state but no longer to the orbital angular momenta of the equivalent electrons as in the non-relativistic theory.

- **Phase convention:** Various phase convention can be found in the literature, and they often hamper a comparison of different approaches. In JAC, we make use of the so-called *standard phase system*, i.e. the phase system due to Fano and Racah.
- **Quasi-spin notation for subshell states:** A subshell state of N equivalent electrons with quasi-spin Q and total angular momentum J is written as

$$|(n\ell) j^N \alpha \nu J\rangle = |(n\ell) j^N \alpha Q J\rangle = |(n\ell) j \alpha Q J; M_Q\rangle \quad \begin{cases} Q = (\frac{2j+1}{2} - \nu)/2 \\ M_Q = (N - \frac{2j+1}{2})/2 \end{cases}$$

and where α refers to all additional quantum numbers that are needed for a unique classification of all subshell states.

- **Quasi-spin momentum of subshell states versus seniority:** For some subshell $(n\ell j) \equiv (n\kappa)$, the quasispin momentum Q of some subshell $(n\ell j) \equiv (n\kappa)$ help encode the seniority quantum number ν by $Q = (\frac{2j+1}{2} - \nu)/2$, while its *z-component* depends on the electron occupation N of this subshell state by $M_Q = (N - \frac{2j+1}{2})/2$.
- **Wigner-Eckart theorem in quasi-spin space:** The Wigner-Eckart theorem can be applied with regard to the quasi-spin for the subshell states $|(n\ell) j^N \alpha Q J\rangle$ in quite the same way as for angular momentum J , and in order to separate the occupation from the coupling of angular momenta of the equivalent electrons

$$\begin{aligned} \langle j^N \alpha Q J M_Q | | A_{m_q}^{(qj)} | | j^N \alpha' Q' J' M'_Q \rangle &= -[Q]^{-1/2} \langle Q' M'_Q, q m_q | Q M_Q \rangle \langle j \alpha Q J | | A^{(qj)} | | j \alpha' Q' J' \rangle \\ &= (-1)^{Q-M_Q} \begin{pmatrix} Q & q & Q' \\ -M_Q & m_q & M'_Q \end{pmatrix} \langle j \alpha Q J | | A^{(qj)} | | j \alpha' Q' J' \rangle. \end{aligned}$$

Here, $A_{m_q}^{(qj)}$ refers to any spherical tensor with quasi-spin q and projection m_q . This equation also gives the relation between the (usual) reduced matrix element of the antisymmetric subshell states on the left-hand side to the *completely-reduced* matrix elements $\langle j \alpha Q J | | A^{(qj)} | | j' \alpha' Q' J' \rangle$ of the operator $A^{(qj)}$ on the right-hand side.

- **Completely reduced matrix elements:** Since the Wigner-Eckart theorem help separate the occupation N from the physical interaction of any symmetric (interaction) operator, the completely-reduced matrix element are independent of N for all subshell terms; this occupation then just occurs in either the Clebsch-Gordan coefficient $\langle Q' M'_Q, q m_q | Q M_Q \rangle$ or, equally, the Wigner 3-j symbol $\begin{pmatrix} Q & q & Q' \\ -M_Q & m_q & M'_Q \end{pmatrix}$.

3. Many-electron atomic interactions, state functions, density operators and statistical tensors

Obviously, this further (complete) reduction of the matrix elements decreases the size of all *internal* tabulations, especially for all subshells with $j \geq 7/2$.

- **Symmetry of the (completely-) reduced coefficients of fractional parentage:** The following symmetry of the completely-reduced CFP can be utilized to reduce the size of tabulations and, hence, to simplify the implementation of angular coefficients in atomic-structure calculations:

$$\langle (n\ell) j \alpha Q J | | a^{(qj)} | | (n\ell) j \alpha' Q' J' \rangle = (-1)^{Q-Q'+J-J'+j-1/2} \langle (n\ell) j \alpha' Q' J' | | a^{(qj)} | | (n\ell) j \alpha Q J \rangle .$$

3.4.b. Reduced matrix elements of unit tensors

Matrix elements of irreducible tensor operators:

- **Matrix elements of coupled quasi-spin creation & annihilation operators:** By applying the Wigner-Eckart theorem in quasi-spin space, the (sub-) matrix elements of the creation & annihilation operators $a_{m_q}^{(qj)}$ can be written as

$$\langle (n\ell) j^N \alpha Q J | | a_{m_q}^{(qj)} | | (n\ell) j^N \alpha' Q' J' \rangle = -[Q]^{-1/2} \langle Q'M'_Q, q m_q | Q M_Q \rangle \langle (n\ell) j \alpha Q J | | a^{(qj)} | | (n\ell) j \alpha' Q' J' \rangle .$$

The matrix elements $\langle (n\ell) j \alpha Q J | | a^{(qj)} | | (n\ell) j \alpha' Q' J' \rangle$ are also referred to as the *completely-reduced CFP*.

- **Matrix elements of two coupled quasi-spin creation & annihilation operators:** The (sub-) matrix elements of the simplest compound tensor operator of type $[a_{m_{q1}}^{(qj)} \times a_{m_{q2}}^{(qj)}]^{(k_j)}$ defines the completely reduced matrix elements of the *double* tensor $W^{(k_q k_j)}$ by

$$\begin{aligned} & \left\langle (n\ell) j^N \alpha Q J \left| \left[a_{m_{q1}}^{(qj)} \times a_{m_{q2}}^{(qj)} \right]^{(k_j)} \right| (n\ell) j^{N'} \alpha' Q' J' \right\rangle \\ &= \sum_{k_q, m_q} [Q]^{-1/2} \langle q m_{q1}, q m_{q2} | k_q m_q \rangle \langle Q'M'_Q, k_q m_q | Q M_Q \rangle \langle (n\ell) j \alpha Q J | | W^{(k_q k_j)} | | (n\ell) j \alpha' Q' J' \rangle \end{aligned}$$

Here, the subshell quantum numbers $(n\ell) j = (n\ell j)$ indicate that the matrix elements are defined only between (subshell) states of the same subshell.

- Reduced matrix element of the tensor operator $W^{(k_q k_j)}(n_j, n_j) = [a^{(qj)} \times a^{(qj)}]^{(k_q k_j)}$ in quasi-spin space: The matrix elements of the tensor operator $W^{(k_q k_j)}(n_j, n_j)$ can be readily expressed in terms of the fully reduced coefficients of fractional parentage $\langle j \alpha Q J || a^{qj} || j \alpha' Q' J' \rangle$ by:

$$\begin{aligned} \langle (n\ell) j \alpha Q J || W^{(k_q k_j)} || (n\ell) j \alpha' Q' J' \rangle &= (-1)^{Q+J+Q'+J'+k_q+k_j} [k_q, k_j]^{1/2} \sum_{\alpha'' Q'' J''} \left\{ \begin{matrix} q & q & k_q \\ Q' & Q & Q'' \end{matrix} \right\} \left\{ \begin{matrix} j & j & k_j \\ J' & J & J'' \end{matrix} \right\} \\ &\quad \times \langle (n\ell) j \alpha Q J || a^{(qj)} || (n\ell) j \alpha'' Q'' J'' \rangle \langle (n\ell) j \alpha'' Q'' J'' || a^{(qj)} || (n\ell) j \alpha' Q' J' \rangle. \end{aligned}$$

This decomposition shows that the completely-reduced matrix CFP on the right hand side of the relation above are independent of the occupation number of the subshell states and, thus, the number of matrix elements that need to be stored.

- Reduced matrix element of the tensor operator $W^{(k_q k_j)}(n_j, n_j) = [a^{(qj)} \times a^{(qj)}]^{(k_q k_j)}$ in quasi-spin space: Gaigalas *et al.* (2000) displays the reduced coefficients of fractional parentage and the completely reduced matrix elements of the tensor $W^{(k_q k_j)}(n_j, n_j)$ for all subshells with $j = 1/2, \dots, 9/2$. These coefficients and matrix elements are frequently needed in relativistic atomic-structure calculations in order to carry out the integration over the spin-angular variables in most standard approaches, such as the multiconfiguration Dirac-Fock method or many-body perturbation theory.

3.4.c. Spin-angular coefficients for symmetric two-particle operators

...:

➤

3.4.d. Computation of spin-angular coefficients for symmetry-adapted CSF

Program components to calculate spin-angular coefficients:

- **ANCO module:** Gaigalas *et al.* (2001) provide a program for pure angular momentum coefficients of scalar one- and two-particle operators. This program has been written in Fortran 90/95 and is based on techniques of second quantization, irreducible tensorial operators, quasi-spin

3. Many-electron atomic interactions, state functions, density operators and statistical tensors

and the theory of angular momentum. It has been implemented originally within the RATIP program and later partly ported to GRASP2K and its subsequent versions, in order to support large-scale relativistic atomic-structure calculations.

- **ANCO module:** This module provide *pure* angular coefficients that only depend on the rank k of the coefficients but not on details of the effective interaction strengths. These coefficients can be utilized equally well to calculate the Coulomb and/or Breit interaction contributions to the Hamiltonian or electron-electron interaction matrix. However, the effective interaction strengths for the Coulomb and Breit interaction obey different selection rules and make (each) just use of certain subsets of the full set of coefficients $V_{rs}^k(abcd)$.

3.5. Dirac-Hartree-Fock method

Remarks:

- **DHF equations:** The solutions of the DHF equations are often not unique because the DHF equations are *invariant* with regard to orbital rotations, i.e. unique only up to some unitary transformation. These unitary transformation changes the radial functions, but leaves the (total) wave function and energy invariant. This non-uniqueness of the DHF method can often be resolved by either placing some additional constraints upon the occupation numbers of the orbitals, or by minimizing the energy of the lowest orbital of each single-electron symmetry κ . Moreover, Koopman's theorem enables one to construct a symmetric energy matrix $(\varepsilon_{n\kappa, n'\kappa'})$ and to separately optimize the extreme values of this matrix (Froese Fischer *et al.*, 2016).
- **DHF equations:** Various methods have been worked out to solve the set of coupled DHF equations (coupled integro-differential equations). Instead of solving these integro-differential equations directly, an **iterative procedure is often applied in which the exchange interaction and the off-diagonal energy parameters are treated as non-homogeneous terms** (and obtained from the last iteration), and where the equations are simply solved as a boundary-value problem. In finite-difference methods, moreover, all the radial functions are typically described on either a logarithmic or logarithmic-linear mesh.
- **Hartree-Dirac-Fock potential:** A very particular choice of a central-field potential in all many-electron computations refer to the Hartree-Fock potential for closed-shell atoms or ions. This is a non-local potential that can be defined by its action upon any orbital as

$$V^{(\text{HF})} \phi_a(\mathbf{r}) = \sum_b \int d^3\mathbf{r}' \frac{e^2}{|\mathbf{r} - \mathbf{r}'|} [\phi_b^*(\mathbf{r}') \phi_b(\mathbf{r}') \phi_a(\mathbf{r}) - \phi_b^*(\mathbf{r}') \phi_a(\mathbf{r}') \phi_b(\mathbf{r})]$$

and where the summation over $b = (n_b, \kappa_b, m_b)$ runs over all occupied orbitals in the closed-shell core.

- **Hartree-Dirac-Fock potential for a spherical-symmetric atom:** For a spherical-symmetric core, the radial part of an orbital function $R_a(r) = \begin{pmatrix} P_a(r) \\ Q_a(r) \end{pmatrix}$ can be expressed in terms of its *large* and *small* component, and the integration over all spherical coordinates can be performed analytically. In this representation, the Hartree-Fock potential can be written also in terms of the **Hartree screening function $v_L(r; a, b)$** as

$$V^{(\text{HF})} R_a(r) = \sum_{n_b \kappa_b} [j_b] \left\{ v_o(r; b, b) R_a(r) - \sum_L \frac{\langle \kappa_b \|C^{(L)}\| \kappa_a \rangle}{[j_a, j_b]} v_L(r; b, a) R_b(r) \right\}.$$

3. Many-electron atomic interactions, state functions, density operators and statistical tensors

➤ Hartree screening function $v_L(r; a, b)$:

$$v_k(r; a, b) = e^2 \int_0^\infty dr' \frac{r_{\leq}^k}{r_{>}^{k+1}} [P_a(r') P_b(r') + Q_a(r') Q_b(r')], \quad r_{<} = \min(r, r'), \quad r_{>} = \max(r, r')$$

➤ Total energy of a closed-shell atom: For the Dirac-Coulomb Hamiltonian $\mathbb{H}^{(DC)}$ and a closed-shell configuration, the total energy can be readily expressed in terms of the one-electron integrals $I(a, a)$ and the two-electron Slater integrals $R^k(abcd)$ as well as the occupation numbers q_a of all (occupied) subshells

$$\begin{aligned} E^{(\text{closed-shell})} &= \sum_a q_a I(a, a) + \sum_a \frac{q_a (q_a - 1)}{2} \left[R^0(aa, aa) - \frac{[j_a]}{2 j_a} \sum_{k=2}^{2\ell_a} \langle \kappa_a \| C^{(k)} \| \kappa_a \rangle^2 R^k(aa, aa) \right] \\ &\quad + \sum_{a, b>a} q_a q_b \left[R^0(ab, ab) - \sum_{k=|\ell_a - \ell_b|}^{\ell_a + \ell_b} \langle \kappa_a \| C^{(k)} \| \kappa_b \rangle^2 R^k(ab, ba) \right] \end{aligned}$$

➤ Frozen-core Dirac-Hartree-Fock method: If a single valence electron moves in the potential of a frozen closed-shell core, i.e. if the relaxation of the core is neglected, the potential of the core electrons just enter the (single-electron) radial equation by $\mathbb{V}(r) = \mathbb{V}^{(nuc)}(r) + \mathbb{V}^{(direct)} + \mathbb{V}^{(exchange)}$, and with the matrix elements

$$\langle v | \mathbb{V}^{(direct)} | v \rangle = \sum_{c \in \text{core}} [j_c] R^0(vc, vc), \quad \langle v | \mathbb{V}^{(exchange)} | v \rangle = - \sum_{c \in \text{core}} \sum_k [j_c] \begin{pmatrix} j_c & k & j_v \\ 1/2 & 0 & -1/2 \end{pmatrix}^2 R^k(vc, cv).$$

3.6. Atomic estimates of quantum-electrodynamic (QED) corrections

3.6.a. QED model operators & model potentials

Background & notations:

- Various proposals have been made in the literature to incorporate the (radiative) quantum-electrodynamic corrections by different model potentials into correlated many-electron methods, such as the MCDHF, many-body perturbation or coupled-cluster theories.
- Effective single-electron QED Hamiltonian: To a good approximation, these QED corrections can be incorporated into the (many-electron) representation $\{c_r(\alpha\mathbb{J})\}$ of some level $(\alpha\mathbb{J})$ by means of a local single-electron QED Hamiltonian. This Hamiltonian can be separated into two parts

$$\mathbb{h}^{(\text{QED})} = \mathbb{h}^{(\text{SE})} + \mathbb{h}^{(\text{VP})},$$

the self-energy (SE) and vacuum-polarization (VP) Hamiltonians, and which are often written in terms of (effective) potentials.

- Vacuum-polarization: The vacuum-polarization is given by a *local* potential and can be further splitted into an Uehling and a Wichmann-Kroll potential; this local potential is rather straightforward to calculate and has already been applied in many applications in the past.
- Self-energy Hamiltonian $\mathbb{h}^{(\text{SE})}$: Such a Hamiltonian can be generally represented as sum of a local and non-local potential. These potentials are typically based on *ab initio* calculations of the diagonal and nondiagonal matrix elements of the one-loop QED operator with H-like wave functions (Shabaev *et al.*, 2013).
- Shabaev and coworkers (2013) have shown that the QED corrections can be systematically incorporated into an effective Hamiltonian that acts in the space of Slater determinants, if these determinants are built from one-electron positive-energy states only and if the total (many-electron binding) energies of the system are smaller than the pair-creation energy. This effective QED Hamiltonian can then be added to the Dirac-Coulomb-Breit Hamiltonian.
- Beyond QED model Hamiltonians: Explicit calculations of radiative corrections are extremely sophisticated and time-consuming for many-electron systems, if the standard QED perturbation theory is to be applied. Until the present, such detailed QED computations can be carried out only for highly-charged, few-electron ions and by still making use of an effective screening potential (instead of the complete perturbation expansion for all electron-electron pairs).

3. Many-electron atomic interactions, state functions, density operators and statistical tensors

- **QED in electronic and muonic atoms:** For normal atoms and ions, the vacuum polarization and self-energy are usually comparable with each other, though often with different sign. In muonic atoms, in contrast, the vacuum polarization dominates over the self-energy contributions that are either neglected or just estimated by simplified methods.

Vacuum polarization potentials:

- **Uehling potential:** This potential is the dominant part of the VP and can be obtained from the direct numerical integration of the well-known formula

$$V^{(\text{Uehling})}(r) = -\alpha Z \frac{2\alpha}{3\pi} \int_0^\infty dr' 4\pi r' \rho(r') \int_1^\infty dt \left(1 + \frac{1}{2t^2}\right) \frac{\sqrt{t^2 - 1}}{t^2} \frac{e^{-2m|r-r'|t} - e^{-2m(r+r')t}}{4mr t},$$

and where $Z \rho(r)$ denotes the density of the nuclear charge distribution, if normalized to $\int dV \rho(r) = 1$.

- **Approximate Uehling potential:** The Uehling potential can be calculated also by an approximate formula for a point-like nucleus (Flambaum and Ginges, 2005)

$$V^{(\text{simplified Uehling})}(r) = \frac{2\alpha}{3\pi} V_{\text{nuc}}(r) \int_1^\infty dt \left(1 + \frac{1}{2t^2}\right) \frac{\sqrt{t^2 - 1}}{t^2} e^{-2mr t}.$$

- **Wichmann-Kroll potential:** A detailed evaluation of the Wichmann-Kroll potential is (much) more sophisticated but can be estimated again to a rather good accuracy by the approximate formula for a point-like nucleus and with the classical radius r_c (Flambaum and Ginges, 2005)

$$V^{(\text{simplified WK})}(r) = -\frac{2\alpha}{3\pi} V(r) \frac{0.092 Z^2 \alpha^2}{1 + (1.62 r/r_c)^4}.$$

- The Wichmann-Kroll correction is generally small and gives a $\sim 1\%$ contribution to the VP shifts only for $Z \gtrsim 80$ (Flaumbaum and Ginges, 2005).

Local self-energy potentials:

- Shabaev *et al.* (2013) suggest a local but independent part of the self-energy potential for each symmetry block κ of the one-electron orbitals of the form

$$V_{\kappa}^{(\text{local SE})}(r) = A_{\kappa} \exp\left(-\frac{2\pi r}{\lambda_C}\right) = A_{\kappa} \exp\left(-\frac{r}{\alpha}\right),$$

where the constants A_{κ} are chosen to reproduce the SE shift for the lowest (one-electron, H-like) energy of each given κ symmetry, and where $\lambda_C = h/m c$ is the Compton wavelength of the electron.

- These local contributions can also be cast be into the form

$$V^{(\text{local SE})}(r) = \sum_{\kappa} A_{\kappa} P_{\kappa} \exp\left(-\frac{2\pi r}{\lambda_c}\right), \quad \langle a | P_{\kappa} | b \rangle = \delta_{\kappa, \kappa_a} \delta_{\kappa, \kappa_b}.$$

- **Self-energy interaction strength:** Following the discussion with Volotka (2019), a (single-electron) local self-energy interaction strength for the (local) potential above can be written

$$\langle a | h^{(\text{local SE})} | a \rangle = \left[\frac{\langle n_g \kappa | h^{(\text{local SE})} | n_g \kappa \rangle}{\langle n_g \kappa | \exp\left(-\frac{r}{\alpha}\right) | n_g \kappa \rangle} \right]_{\text{hydrogenic}} \langle a | \exp\left(-\frac{r}{\alpha}\right) | a \rangle, \quad \langle a | h^{(\text{local SE})} | b \rangle = 0 \quad \text{for } a \neq b,$$

where $|n_g \kappa\rangle = \{1s_{1/2}, 2p_{1/2}, 2p_{3/2}, 3d_{3/2}, \dots\}$ refers to the lowest hydrogenic orbitals of symmetry κ and nuclear charge Z . For a non-diagonal self-energy potential, the representation of the one-electron matrix elements will be more difficult and are presently not considered in JAC.

- **Self-energy interaction strength:** Shabaev *et al.* (2013) have tabulated values for $\langle n_g \kappa | h^{(\text{local SE})} | n_g \kappa \rangle_{\text{hydrogenic}}$ for selected nuclear charges, which can be readily applied in order to compute the self-energy interactions strengths for general many-electron atoms and ions.

Radiative potentials:

- **Radiative potential:** Flambaum and Ginges (2005) suggest an approximate expression for a (so-called) **radiative potential** which can be utilized in order to estimate the radiative corrections in strong Coulomb fields to the energies and electric-dipole transition amplitudes in atomic (many-electron) computation. This (alternative) potential is said to give good QED estimates with an accuracy of just a few percent but has been mainly tested and applied to (neutral) cesium only.
- **Radiative potential:** Flambaum and Ginges (2005) decompose this radiative potential into five terms which are explained either above or below:

$$V^{(\text{total QED})} = V^{(\text{simplified Uehling})} + V^{(\text{magnetic form})} + V^{(\text{electric form})} + V^{(\text{low frequency})} + V^{(\text{simplified WK})}.$$

- **Magnetic form-factor potential:** For the magnetic form-factor contribution, Flambaum and Ginges (2005) give

$$V^{(\text{magnetic form})} = \frac{\alpha}{4\pi m} i \boldsymbol{\gamma} \cdot \boldsymbol{\nabla} \left[V(r) \left(\int_1^\infty dt \frac{\exp(-2mr t)}{t^2 \sqrt{t^2 - 1}} - 1 \right) \right],$$

and where $\boldsymbol{\gamma} = (\gamma_1, \gamma_2, \gamma_3)$ is the vector of gamma matrices.

- **Low-frequency potential to the electric form-factor:** Flambaum and Ginges (2005) suggest the (low-frequency) expression

$$V^{(\text{low frequency})} = - \frac{B(Z)}{e} Z^4 \alpha^5 mc^2 \exp\left(\frac{Zr}{a_o}\right), \quad B(Z) = 0.074 + 0.35 Z \alpha,$$

with the Bohr radius a_o and where the function $B(Z)$ has been fitted in order to reproduce the radiative energy shifts for p -levels of selected heavy elements. This term should be used with some care however.

- **Electric form-factor potential (including high-frequency contributions):** Flambaum and Ginges (2005) display a final expression for the electric form-factor contribution

$$V^{(\text{electric form})}(r) = - A(Z, r) \frac{\alpha}{\pi} V(r) \int_1^\infty dt \frac{\exp(-2mr t)}{\sqrt{t^2 - 1}} \left[\left(1 - \frac{1}{2t^2}\right) [\ln(t^2 - 1) + 4 \ln(1/Z\alpha + 0.5)] - \frac{3}{2} + \frac{1}{t^2} \right].$$

Here, the function $A(Z, r) = (1.071 - 1.976 x^2 - 2.128 x^3 + 0.169 x^4) m r / (m r + 0.07 Z^2 \alpha^2)$, has been suggested with $x = (Z - 80) \alpha$. The detailed form of $A(Z, r)$ was found by fitting the radiative shifts for the high Coulomb s levels from the literature. **This term should be used with good care again.**

- Note that this local potential by Flambaum and Ginges (2005) was optimized for weakly bound valence states of heavy neutral atoms and may be less accurate for strongly bound ionic or even core-hole states.

3.6.b. In JAC implemented QED estimates

Models & applications:

- In JAC, the radiative QED corrections can be incorporated into the computation and representation of the wave functions if `AsfSettings(..)` is initialized with `qedModel = QedPetersburg()` or `qedModel = QedSydney()`. This singleton data types tell JAC how the estimates for the vacuum polarization and the (local) self-energy contributions are incorporated into the Hamiltonian matrix, cf. below.
- In JAC, use `qedModel = NoneQed()` in `AsfSettings(..)` if no QED estimates are to be included; this is also the default.

Implementation:

- **QedPetersburg model:** Here, we simply add to all matrix elements $\langle a \parallel h^{(1\text{-particle})} \parallel b \rangle$ in the many-electron Hamiltonian matrix the (single-electron) matrix elements

$$\langle a \parallel h^{(\text{QED})} \parallel b \rangle = \langle a \parallel h^{(\text{local SE})} \parallel b \rangle + \langle a \parallel h^{(\text{simplified Uehling})} \parallel b \rangle.$$

- **QedSydney model:** Analogues, here we add to all matrix elements $\langle a \parallel h^{(1\text{-particle})} \parallel b \rangle$ in the many-electron Hamiltonian matrix the (single-electron) matrix elements

$$\langle a \parallel h^{(\text{QED})} \parallel b \rangle = \langle a \parallel h^{(\text{magnetic form})} \parallel b \rangle + \langle a \parallel h^{(\text{electric form})} \parallel b \rangle + \langle a \parallel h^{(\text{low frequency})} \parallel b \rangle + \langle a \parallel h^{(\text{simplified Uehling})} \parallel b \rangle.$$

3. Many-electron atomic interactions, state functions, density operators and statistical tensors

- **Effective QED operator** With the definitions from above, the total QED operator for a many-electron atom includes of course a summation over all atomic electrons:

$$\mathbb{H}^{(\text{QED})} = \mathbb{H}^{(\text{SE})} + \mathbb{H}^{(\text{VP})} = \sum_j \mathbb{h}_j^{(\text{QED})} = \sum_j \left(\mathbb{h}_j^{(\text{SE})} + \mathbb{h}_j^{(\text{VP})} \right),$$

where the $\mathbb{h}_j^{(\text{SE})}$ and $\mathbb{h}_j^{(\text{VP})}$ refers to the one-electron operators for electron j .

3.7. Unitary $jjJ - LSJ$ transformation of atomic states

3.7.a. Transformation matrices from jjJ - to LSJ -coupling

Atomic coupling schemes:

- **Coupling schemes:** Atomic and ionic levels are usually identified and labeled by means of quantum numbers of an appropriate coupling scheme. However, these quantum numbers are well-conserved only for a pure coupling of symmetry-adapted many-electron state, and which is realized only (rather) approximately in Nature.
- **LSJ - and jjJ coupling** are nowadays the two most frequently applied coupling schemes in atomic theory.
- As usual in quantum mechanics, the transformation from one to another orthonormal basis (i.e. the representation of atomic levels in a particular coupling scheme) is simply given by a unitary matrix, although it is generally not easy to evaluate this transformation matrix for arbitrary shell structures of atoms and ions.
- **LSJ -notation:** In atomic spectroscopy, the standard LSJ -notation of the levels is frequently applied for classifying the low-lying level structures of atoms or ions.
- **Labeling of levels:** Atomic energy levels are often labeled by means of their leading LSJ -coupled CSF in a wave function expansion. However, special care need to be taken, if the same CSF occurs largest in the expansion of two levels, since then, the classification is no longer unique.
- The lack of providing a fast and proper spectroscopic notation in relativistic computations may hamper the spectroscopic level classification of medium and heavy elements as well as the interpretation and analysis of inner-shell processes.

$jjJ - LSJ$ transformation of subshell states:

- **Unique subshell order:** Since each non-relativistic $n\ell$ -shell (apart from the ns shells) split into two relativistic subshells with $j = \ell \pm 1/2$, the order of these subshell is relevant for the transformation of the many-electron basis and is always fixed in JAC to $n\ell_{j=\ell-1/2}$, $n\ell_{j=\ell+1/2}$. For the np - and nd -shells, for example, we always assume the sequence $np_{1/2}$, $np_{3/2}$ and $nd_{3/2}$, $nd_{5/2}$ in all formulas below.
- **Non-relativistic subshell states:** In the transformation of the non-relativistic shell states $|n\ell^N \alpha\nu LS\rangle$, we generally have to consider the product of two (relativistic) subshell states $\left| n\kappa^{-\bar{N}} \bar{\nu}J, n\kappa^{+\bar{N}} \bar{\nu}J \right\rangle$, and with $\bar{N} + \bar{N} = N$. Here, the + and - on top of the quantum numbers just refer to the relativistic subshells with $j = \ell \pm 1/2$.
- The transformation between the (sub-) shell states in jjJ - and LSJ -coupling can be expressed with real Fourier coefficients as

$$\begin{aligned} \left\langle (n\kappa^{-\bar{N}} \bar{\nu}J, n\kappa^{+\bar{N}} \bar{\nu}J) J \right\rangle &= \sum_{\alpha\nu LS} |n\ell^N \alpha\nu LSJ\rangle \left\langle n\ell^N \alpha\nu LSJ | (n\kappa^{-\bar{N}} \bar{\nu}J, n\kappa^{+\bar{N}} \bar{\nu}J) J \right\rangle, \quad N \equiv \bar{N} + \bar{N} \\ \left\langle n\ell^N \alpha\nu LSJ | (n\kappa^{-\bar{N}} \bar{\nu}J, n\kappa^{+\bar{N}} \bar{\nu}J) J \right\rangle &= \left\langle (n\kappa^{-\bar{N}} \bar{\nu}J, n\kappa^{+\bar{N}} \bar{\nu}J) J | n\ell^N \alpha\nu LSJ \right\rangle. \end{aligned}$$

- The evaluation of the (unitary) transformation does generally not involve the radial (orbital) functions but depends only on the spin-angular functions.
- Although the notation of the non-relativistic and relativistic (sub-) shell states is quite similar in jjJ - and LSJ -coupling, these states generally belong to different irreducible representations of the SO_3 rotation group. This can be seen already from the splitting of each non-relativistic shell into two subshells as outlined above.

Transformation of atomic states:

- **LSJ -coupled, non-relativistic CSF:**

$$|\gamma^{(\text{NR})} LSJ\rangle = |((. ((((n_1 \ell_1^{N_1} \alpha_1 \nu_1 L_1 S_1), (n_2 \ell_2^{N_2} \alpha_2 \nu_2 L_2 S_2)) L_{12} S_{12}, (n_3 \ell_3^{N_3} \alpha_3 \nu_3 L_3 S_3)) L_{123} S_{123}, \dots) LS) J\rangle$$

3. Many-electron atomic interactions, state functions, density operators and statistical tensors

➤ *jjJ*-coupled, relativistic CSF:

$$|\gamma^{(R)} J\rangle = \left| \left(\cdot \left(\left(\left((n_1 \bar{\kappa}_1^{-N_1} \bar{\nu}_1^- J_1), (n_1 \bar{\kappa}_1^+ \bar{N}_1^+ \bar{\nu}_1^+ J_1) \right)^+ X_1, (n_2 \bar{\kappa}_2^{-N_2} \bar{\nu}_2^- J_2) \right) \bar{X}_2, (n_2 \bar{\kappa}_2^+ \bar{N}_2^+ \bar{\nu}_2^+ J_2) \right)^+ X_2, \dots \right) J \right\rangle$$

➤ To determine the explicit transformation matrix for going from one to another (many-electron) basis, of course, all these quantum numbers above play an important role in practice. For the sake of simplicity, however, it is sufficient to just re-call that the *jj*-coupled CSF basis spans a (finite) part $\mathcal{H}^{(\text{finite})}$ of the N -electron Hilbert space and that the matrix $(\langle \gamma^{(NR)} LSJ | \gamma^{(R)} J \rangle)$ just represent the (usual) Fourier coefficients for the expansion of an atomic state with respect to the basis $\{|\gamma^{(NR)} LSJ\rangle\}$ in $\mathcal{H}^{(\text{finite})}$.

➤ Representation of atomic state functions:

$$|\psi_\alpha\rangle = \sum_r c_r^{(R)}(\alpha) |\gamma_r^{(R)} J\rangle = \sum_t c_t^{(NR)}(\alpha) |\gamma_t^{(NR)}(L_t, \beta, S_t) J\rangle$$

➤ Formal construction of the *jjJ* → *LSJ* transformation matrix: If we denote the basis states of the (standard) product basis of the (subshell) states in *jjJ*- and *LSJ*-coupling by the $|\text{standard} - \text{jjJ}\rangle$ and $|\text{standard} - \text{LSJ}\rangle$, the transformation of a relativistic CSF can be formally written as

$$\begin{aligned} |\gamma_r^{(R)} J\rangle &= \sum_{\text{standard-jjJ}} |\text{standard} - \text{jjJ}\rangle \langle \text{standard} - \text{jjJ} | \gamma_r^{(R)} J\rangle \\ &= \sum_{\substack{\text{standard-jjJ} \\ \text{standard-LSJ} \\ \text{atomic-LSJ}}} |\gamma_t^{(NR)}(L_t, S_t) JP\rangle \langle \gamma_t^{(NR)}(L_t, S_t) JP | \text{standard} - \text{LSJ}\rangle \langle \text{standard} - \text{LSJ} | \text{standard} - \text{jjJ}\rangle \langle \text{standard} - \text{jjJ} | \gamma_r^{(R)} J\rangle \\ &= \sum_{Q_p, Q_r} |\gamma_t^{(NR)}(L_t, S_t) J\rangle \times [\text{LSJ} - \text{recoupling}] \times [\text{product of LSJ} - \text{jjJ matrix elements}] \times [\text{jjJ} - \text{recoupling}] \end{aligned}$$

Here, a summation over $\text{standard} - \text{jjJ}$, $\text{standard} - \text{LSJ}$, ... implies a summation over all quantum numbers that are not bound due to given values at the left-hand-side of the expression. In the last line, in particular, the summation runs over the (product basis) quantum numbers $Q_p = [(\alpha_1 \nu_1 L_1 S_1), (\alpha_2 \nu_2 L_2 S_2), \dots]$ as well as over the (re-coupling) quantum numbers as defined by the [LSJ-recoupling] and [jjJ-recoupling] recoupling coefficients, $Q_p = [J_1, J_2, J_{12}, J_3, J_{123}, \dots, T_1, T_2, T_{12}, T_3, T_{123}, \dots]$ with $\delta_{J_1, T_1} \delta_{J_2, T_2} \delta_{J_{12}, T_{12}} \dots$.

➤ Re-coupling from the LSJ -product to the (L_t, S_t) J -coupled basis:

$$\begin{aligned} \left\langle \gamma_t^{(\text{NR})}(L_t S_t) J \mid \text{standard} - \text{LS} \right\rangle &\equiv [\text{LSJ} - \text{recoupling}] \\ &= \langle (.(((L_1, L_2) L_{12}, L_3) L_{123}, \dots) L_t, (.((S_1, S_2) S_{12}, S_3) S_{123}, \dots) S_t) J \mid (.(((L_1, S_1) T_1, (L_2, S_2) T_2) T_{12}, (L_3, S_3) T_3) T_{123}, \dots) J \rangle \end{aligned}$$

➤ Re-coupling from the jjJ -product to the jXJ -coupled basis:

$$\begin{aligned} \langle \text{standard} - jj \mid \gamma_r^{(\text{R})} J \rangle &\equiv [jjJ - \text{recoupling}] \\ &= \left\langle \left(. \left(\left((\bar{J}_1, \bar{J}_1) J_1, (\bar{J}_2, \bar{J}_2) J_2 \right) J_{12}, (\bar{J}_3, \bar{J}_3) J_3 \right), J_{123}, \dots \right) J \mid \left(. \left(\left(((\bar{J}_1, \bar{J}_1) \bar{X}_1, \bar{J}_2) \bar{X}_2, \bar{J}_3 \right) \bar{X}_2, \bar{J}_3 \right) \bar{X}_3, \dots \right) J \right\rangle \end{aligned}$$

➤ In practice, the summation over such large sets of quantum numbers is often replaced by a (simpler or even single) summation over the allowed and predefined sets of quantum numbers.

3.7.b. Re-coupling coefficients

Zero open shell:

➤ CSF with *no* open shell are the same in the jjJ - and LSJ -coupling scheme,

$$|\gamma_r^{(\text{R, closed})} J = 0^+ \rangle \equiv |\gamma_r^{(\text{NR, closed})} J = 0^+ \rangle$$

and can be simply replaced with their (expansion) coefficients in the expansion of the wave function.

Single open shell:

➤ Re-coupling from the LSJ -product to the (L_t, S_t) J -coupled basis:

$$[\text{LSJ} - \text{recoupling}] = \langle (L_1, S_1) J \mid (L_1, S_1) J \rangle = 1.$$

3. Many-electron atomic interactions, state functions, density operators and statistical tensors

➤ Re-coupling from the jjJ -product to the jXJ -coupled basis:

$$[\text{jjJ} - \text{recoupling}] = \left\langle (\bar{J}_1, \overset{+}{J}_1) J \mid (\bar{J}_1, \overset{+}{J}_1) J \right\rangle = 1.$$

Two open shells:

➤ Re-coupling from the LSJ -product to the $(L_t, S_t)J$ -coupled basis:

$$\begin{aligned} [\text{LSJ} - \text{recoupling}] &= \langle ((L_1, L_2) L_{12}, (S_1, S_2) S_{12}) J \mid ((L_1, S_1) T_1, (L_2, S_2) T_2) J \rangle \\ &= (-1)^{L_1 + S_1 - T_1 + L_2 + S_2 - T_2 + L_{12} + S_{12} - J} \sqrt{[T_1, T_2, L_{12}, S_{12}]} \begin{Bmatrix} L_1 & S_1 & T_1 \\ L_2 & S_2 & T_2 \\ L_{12} & S_{12} & J \end{Bmatrix}, \quad Q_r = [T_1, T_2]. \end{aligned}$$

➤ Re-coupling from the jjJ -product to the jXJ -coupled basis:

$$\begin{aligned} [\text{jjJ} - \text{recoupling}] &= \left\langle \left((\bar{J}_1, \overset{+}{J}_1) J_1, (\bar{J}_2, \overset{+}{J}_2) J_2 \right) J \mid \left(((\bar{J}_1, \overset{+}{J}_1) \overset{+}{X}_1, \bar{J}_2), \bar{X}_2, \overset{+}{J}_2 \right) J \right\rangle \\ &= (-1)^{\bar{J}_2 + \overset{+}{J}_2 + J_1 + J} \delta(\bar{J}_1, \overset{+}{J}_1, J_1) \delta_{J_1 \overset{+}{X}_1} \sqrt{[J_2, \bar{X}_2]} \begin{Bmatrix} J_1 & \bar{J}_2 & \bar{X}_2 \\ \overset{+}{J}_2 & J & J_2 \end{Bmatrix}, \quad Q_r = [J_1, J_2]. \end{aligned}$$

➤ The summation over Q_r also implies all further quantum numbers that are needed in order to distinguish different subshell states in jjJ and to LSJ product basis, respectively. In JAC, this summation is performed by (1) applying the standard coupling $L \oplus S = T_{\text{low}}, \dots, T_{\text{up}}$ and (2) by a summation over the corresponding subshell states from a internally (defined) list. An explicit summation over J_1, J_2 can be omitted because of orthogonality, and which gives rise to the Kronecker factors $\delta_{T_1, J_1}, \delta_{T_2, J_2}$.

Three open shells:

➤ Re-coupling from the LSJ -product to the $(L_t, S_t)J$ -coupled basis: (Kosheleva 2020)

$$\begin{aligned} [\text{LSJ} - \text{recoupling}] &= \langle (((L_1, L_2) L_{12}, L_3) L_{123}, ((S_1, S_2) S_{12}, S_3) S_{123}) J | (((L_1, S_1) T_1, (L_2, S_2) T_2) T_{12}, (L_3, S_3) T_3) J \rangle \\ &= (-1)^{L_1 + S_1 - T_1 + L_2 + S_2 + L_3 - L_{123} + S_3 - S_{123} - J - 2T_{12}} \sqrt{[L_{12}, L_{123}, S_{12}, S_{123}, T_1, T_2, T_3, T_{12}]} \\ &\quad \times \left\{ \begin{matrix} L_2 & L_1 & L_{12} \\ S_2 & S_1 & S_{12} \\ T_2 & T_1 & T_{12} \end{matrix} \right\} \left\{ \begin{matrix} J & L_{123} & S_{123} \\ T_3 & L_3 & S_3 \\ T_{12} & L_{12} & S_{12} \end{matrix} \right\}, \quad Q_r = [T_1, T_2, T_{12}, T_3]. \end{aligned}$$

➤ Re-coupling from the jjJ -product to the jXJ -coupled basis:

$$\begin{aligned} [\text{jjJ} - \text{recoupling}] &= \left\langle \left(((\bar{J}_1, \dot{J}_1) J_1, (\bar{J}_2, \dot{J}_2) J_2) J_{12} (\bar{J}_3, \dot{J}_3) J_3 \right) J \mid \left((((\bar{J}_1, \dot{J}_1) \dot{X}_1, \bar{J}_2) \bar{X}_2, (\dot{J}_2, \dot{J}_3) \dot{X}_2, (\bar{J}_3, \dot{J}_3) \bar{X}_3, \dot{J}_3) J \right) J \right\rangle \\ &= (-1)^{2\dot{X}_1 + \bar{J}_2 + \dot{J}_2 + J_2 + 2J_{12} + \bar{J}_3 + \dot{J}_3 + J_3} \sqrt{[J_2, \bar{X}_2, J_3, \bar{X}_3]} \left\{ \begin{matrix} \bar{J}_2 & \dot{J}_2 & J_2 \\ J_{12} & \dot{X}_1 & \bar{X}_2 \end{matrix} \right\} \left\{ \begin{matrix} \bar{J}_3 & \dot{J}_3 & J_3 \\ J & J_{12} & \bar{X}_3 \end{matrix} \right\}, \\ &\quad Q_r = [J_1, J_2, J_{12}, J_3]. \end{aligned}$$

➤ The summation over Q_r also implies all further quantum numbers that are needed in order to distinguish different subshell states in jjJ and to LSJ product basis, respectively. In JAC, this summation is performed by (1) applying the standard coupling $L \oplus S = T_{\text{low}}, \dots, T_{\text{up}}$ and (2) by a summation over the corresponding subshell states from a internally (defined) list. An explicit summation over J_1, J_2, J_3 can be omitted because of orthogonality, and which gives rise to the Kronecker factors $\delta_{T_1, J_1}, \delta_{T_2, J_2}, \delta_{T_3, J_3}$

3.7.c. In JAC implemented $jjJ - LSJ$ transformation

Transformation, notations & application:

- Representation $c_s^{(\text{NR})}(\alpha)$ of atomic states.

$$|\psi_\alpha\rangle = \sum_t c_t^{(\text{NR})}(\alpha) |\gamma_t^{(\text{NR})} LS J\rangle = \sum_r c_r^{(\text{R})}(\alpha) |\gamma_r^{(\text{R})} J\rangle$$

- Unique label: $(\dots ((n_1\ell_1)^{N_1-2S_1+1}L_1; (n_2\ell_2)^{N_2-2S_2+1}L_2)^{2S_{12}+1}L_{12}, (n_3\ell_3)^{N_3-2S_3+1}L_3 \dots)^{2S+1}L_J$

Such a label is assigned to each selected level, for instance, by printing

$$[(n_1\ell_1)^{N_1-2S_1+1}L_1]^{2S_{12}+1}L_{12} : [(n_2\ell_2)^{N_2-2S_2+1}L_2]^{2S_{123}+1}L_{123} : \dots$$

- In JAC, a $jjJ - LSJ$ transformation is performed for all selected levels if `jjLS = LSjjSettings(true, ...)` is set in `AsfSettings()`.
- In JAC, the LSJ -coupled expansion of selected levels is printed by default after the diagonalization of the (many-electron) Hamiltonian matrix.
- Apart from the LSJ assignment to atomic levels, JAC can rather easily support also the full transformation of the wave functions, if required for (nonrelativistic) computations. This is achieved by setting the cut-off parameter to *zero* in `LSjjSettings(...)`.
- A proper LSJ spectroscopic notation has been found useful in order to explain the excitation and decay properties of individual levels, at least qualitatively.
- The $jjJ - LSJ$ transformation of the (jjJ -coupled) CSF is supported for all shell structures with (up to) two open shells, including open **s-, p-, d-shells**. Further work is required to fully implement also transformation of open *f*-shells.

Implementation of $jjJ - LSJ$ transformation:

- Internally, a $jj - LS$ transformation of selected levels from a given multiplet is carried out by the following steps:
 - 1) Generation of a non-relativistic shell list for the given multiplet, based on a proper relativistic subshell list. The program terminates with an error message if the relativistic subshells of the given multiplet are ordered in *non-standard order*, for example, ..., $2p_{3/2}$, $2p_{1/2}$, ... or similar.
 - 2) Extract all non-relativistic configurations that contribute to the given multiplet and generate a corresponding set of nonrelativistic CSF states; define an instance of a nonrelativistic basis.

- 3) Expand (in turn) each relativistic CSF into the non-relativistic basis and add their contributions to the (nonrelativistic) eigenvectors. This expansion is made independently of CSF with zero-, one-, two-, ... open (nonrelativistic) shells.
- 4) Check and print the LSJ expansion of all selected levels in a neat format with respect to the (nonrelativistic) configurations as well as CSF.

```
"""
'struct LS_jj_qn' ... defines a struct for the generalized quantum numbers (qn) of a LS_jj matrix element.
+ NN      ::Int64   ... occupation w = NN
+ QQ      ::Int64   ... subshell total quasispin 2*Q = nu
+ LL      ::Int64   ... subshell total angular momentum 2*L
+ SS      ::Int64   ... subshell total angular momentum 2*S
+ JJ      ::Int64   ... subshell total angular momentum 2*J
+ Nm      ::Int64   ... subshell Nm
+ Qm      ::Int64   ... subshell quantum number 2*Qm = nu^-_
+ Jm      ::Int64   ... subshell quantum number 2*Jm
+ Qp      ::Int64   ... subshell quantum number 2*Qp = nu^+
+ Jp      ::Int64   ... subshell quantum number 2*Jp
"""

```

3.8. Atomic interaction amplitudes

Concept of interaction amplitudes:

- **Hamiltonian matrix:** The (scalar) Hamiltonian matrix elements in section ?? below describe the interaction energy between two ASF $|\alpha JM\rangle$ and $|\alpha' J'M'\rangle$, and these Hamiltonian matrix elements are perhaps the most simplest (many-electron) **interaction amplitudes in atomic structure theory**: $\langle \psi_\alpha | \mathbb{H} | \psi_{\alpha'} \rangle = \langle \alpha JM \| \mathbb{H} \| \alpha' J'M' \rangle = \sum_{rs} c_r^*(\alpha) H_{rs} c_s(\alpha') \delta_{JJ'} \delta_{MM'} \delta_{PP'}$.
- In relativistic atomic structure theory, in particular, $E_\alpha = \langle \alpha J \| \mathbb{H}^{(DCB)} \| \alpha J \rangle \approx \langle \alpha J \| \mathbb{H}^{(DC)} \| \alpha J \rangle$ is the total energy of a given level (αJ) .
- **Many-electron interaction amplitudes:** Using time-dependent perturbation theory and Fermi's Golden rule, most atomic level and transition properties can be expressed rather **similarly as matrix elements of a (so-called) transition or *interaction* operator \mathbb{T} :**

$$\langle \psi_\alpha | \mathbb{T} | \psi_\beta \rangle = \sum_{rs} c_r^*(\alpha) T_{rs} c_s(\beta).$$

- **Reduced matrix elements:** More often than not, the transition operator \mathbb{T} can be expressed in terms of **spherical tensor operators of rank K** , and, perhaps, with magnetic projections $Q = -K, -K+1, \dots, K$, respectively. These spherical tensor operators transform under rotations like the spherical harmonics $Y_{KQ}(\vartheta, \varphi)$: $\mathbb{T} = \sum_{KQ} a(K, Q) \mathbb{T}_Q^{(K)}$. – Instead of the complete matrix elements, that include the magnetic projections M of the given atomic or configuration states as well as of the tensor operators, one often makes then use of the reduced matrix elements by applying the **Wigner-Eckart theorem**:

$$T_{Q, rs}^{(K)} \equiv \left\langle \alpha_r J_r M_r \left| \mathbb{T}_Q^{(K)} \right| \alpha_s J_s M_s \right\rangle = \langle J_r M_r, KQ | J_s M_s \rangle \langle \alpha_r J_r \| \mathbb{T}^{(K)} \| \alpha_s J_s \rangle.$$

- Although these reduced transition amplitudes are frequently utilized in the literature, for instance in order to discuss and analyze various atomic processes, **not many codes make explicit use of these amplitudes as the *natural* building blocks** for describing the level structure and properties of (open-shell) atoms and ions. – More often than not, **a prior decomposition of these transition amplitudes** into various types of one- and two-particle (reduced) matrix elements or even directly into radial integrals is made well before any implementation or coding is considered. **This prior decompositon has seriously hampered the modelling of complex processes** and is still the reason, why most atomic structure codes support the computation of just a few properties, cross sections and rates.
- Indeed, the different techniques, which are employed in the decomposition of the many-electron amplitudes, as well as the large number of definitions (and notations) of angular- or radial-type integrals in the literature has hampered not only the comparison of different codes

during the last decades but made it difficult also to (re-) use these entities for other properties than those considered by the original program developers.

- In JAC, we attempt to overcome this situation and to make consequent use of the many-electron amplitudes $\langle \alpha_r \mathbb{J}_r M_r | \mathbb{T}_Q^{(K)} | \alpha_s \mathbb{J}_s M_s \rangle$ and/or $\langle \alpha_r \mathbb{J}_r \| \mathbb{T}^{(K)} \| \alpha_s \mathbb{J}_s \rangle$ as the central building blocks for describing the interaction among the electrons as well as with external particles and fields.
- The concept of these interaction amplitudes has helped to simplify and maintain the code. — Moreover, it (will hopefully) enable us to exploit the many-electron interaction and transition amplitudes also in second- and higher-order processes, once an appropriate (intermediate) basis $\{\psi_\nu(PJM) \equiv |\alpha_\nu \mathbb{J}_\nu M_\nu\rangle, \nu = 1, \dots, n_\nu\}$ has been constructed for modelling some given process.

Reduced matrix elements of spherical tensor operators for two CSF:

- For two CSF of well-defined symmetry, the reduced matrix elements of spherical tensor operators take always the form

$$\langle \gamma_r P_r J_r \| \mathbb{T}^{(K)} \| \gamma_s P_s J_s \rangle = \sum_t u(a_t b_t; K) X(a_t b_t; K), \quad \mathbb{T}^{(K)} = \sum_j \mathbb{t}^{(K)}(j; \dots) \quad \dots \text{one part. operators}$$

$$\langle \gamma_r P_r J_r \| \mathbb{T}^{(K)} \| \gamma_s P_s J_s \rangle = \sum_t v(L_t; a_t b_t c_t d_t; K) X^{L_t}(a_t b_t c_t d_t; K), \quad \mathbb{T}^{(K)} = \sum_{i < j} \mathbb{T}^{(K)}(i, j; \dots) \quad \dots \text{symmetric two part. operators},$$

and where $X(a_t b_t; K)$ and $X^{L_t}(a_t b_t c_t d_t; K)$ are one- and two-particle (effective) interaction strengths, cf. section 3.1. These interaction strengths are specific to the particular transition or interaction operator under consideration, and special care has to be taken that the same phase convention applies, if different interaction amplitudes are to be combined with each other.

- In practice, there are two steps in the computation of the transition amplitudes above for any pair of CSF, which need to be performed separately: The (pure) angular coefficients are usually calculated by means of some proper program, for instance ANCO (Gaigalas *et al.*, 2001), for either a pair or a whole set of CSF, and all the non-vanishing coefficients are then returned together to the calling routine. For these coefficients, the associated one- or two-particle interaction strengths are evaluated and summed up to form the requested matrix element T_{rs} of the transition matrix.
- To decrease the computational effort, these (one- and two-particle) interaction strength are often also *stored* and *re-utilized* in various applications, a feature which has not yet been considered in JAC.
- A similar decomposition of the many-electron matrix elements (amplitudes) as for the Hamiltonian matrix elements into a sum of *angular coefficient* \times *interaction strength* can be made for every physically relevant (interaction) amplitude, independent of the particular rank of

3. Many-electron atomic interactions, state functions, density operators and statistical tensors

the corresponding interaction operator. Since most atomic processes can be traced back to just a (very) few of such interaction or transition amplitudes, we made use of them as the *building blocks* in the design and implementation of the JAC tools.

Electron-electron interaction:

- The interaction among the electrons is described by the scalar operator that occurs in the Dirac-Coulomb-Breit Hamiltonian; cf. section 3.1

$$\mathbb{V}^{(e-e)} = \mathbb{V}^{(\text{Coulomb})} + \mathbb{V}^{(\text{Breit})} = \sum_{i < j} \left(\frac{1}{r_{ij}} + b_{ij} \right).$$

- The Dirac-Coulomb-Breit Hamiltonian gives rise to the (reduced) interaction amplitudes

$$\langle \gamma_r P_r J_r \parallel \mathbb{V}^{(e-e)} \parallel \gamma_s P_s J_s \rangle = \langle \gamma_r P_r J_r \parallel \mathbb{V}^{(\text{Coulomb})} \parallel \gamma_s P_s J_s \rangle + \langle \gamma_r P_r J_r \parallel \mathbb{V}^{(\text{Breit})} \parallel \gamma_s P_s J_s \rangle.$$

For scalar operators, the full and reduced matrix elements coincide with each other and need not to be distinguished, since the Clebsch-Gordan coefficient in the Wigner-Eckert theorem then simply evaluates to $\langle J_r M_r, 00 | J_s M_s \rangle = \delta_{J_r J_s} \delta_{M_r M_s}$ for $K = Q = 0$.

- Since the Coulomb and Breit interaction operators are both scalar operators and since they contribute *additively* to the total electron-electron interaction, the same (pure) angular coefficients $v(L_t; a_t b_t c_t d_t; K = 0)$ occur in the decomposition of the amplitudes above, although different angular and parity selection rules apply for the various interaction strengths themselves, cf. section 3.1. In the computation of these amplitudes, the Breit interaction can therefore be added quite easily to the (usual) instantaneous Coulomb repulsion, if this appears appropriate for some particular process:

$$X^{(L)}(abcd) = X^{(L, \text{Coulomb})}(abcd) + X^{(L, \text{Breit})}(abcd).$$

- The electron-electron interaction amplitudes above are indeed utilized (and calculated) in many components of the JAC tools.

Electron-photon interaction:

- The (relativistic) interaction of an electron with the radiation field is central for describing all photo-excitation, ionization, emission and capture processes.
- The electron-photon interaction is described by the one-particle operator: $\mathcal{R}_\lambda(\mathbf{k}) = \sum_i \boldsymbol{\alpha}_i \cdot \mathcal{A}_{\lambda,i}(\mathbf{k})$; cf. chapter 5 below.

Electron-nucleus (hyperfine) interactions:

- For a nuclear spin $I > 0$, the hyperfine interaction describes the interplay of each atomic electron with the electric and magnetic (multipole) fields of the nucleus, apart from the dominant (electric-monopole) field of the nucleus due to its nuclear charge Ze .
- The two dominant contributions to the hyperfine interaction arise from the nuclear magnetic-dipole field $\mathbf{A} = \frac{\mu \times \mathbf{r}}{r^3}$ and the electric-quadrupole field $\Phi(r) = \sum_{ij} \frac{r_i r_j}{2r^5} Q_{ij}$, while all higher magnetic and electric multipole fields, that may in principle occur for nuclei with spin $I > 1$, are typically negligible.

3.9. Atomic density operators and matrices

3.9.a. Single-electron reduced density matrix

First-order reduced density matrix:

- First-order reduced density matrix: This single-electron density matrix is known also as **generalized density function** and is given in terms of the N -electron wave function $\Psi(\mathbf{q}_1, \dots, \mathbf{q}_N)$ by

$$\rho^{(1)}(\mathbf{q}_1, \mathbf{q}'_1) = N \int d\mathbf{q}_2 \dots d\mathbf{q}_N \Psi(\mathbf{q}_1, \dots, \mathbf{q}_N) \Psi^*(\mathbf{q}'_1, \dots, \mathbf{q}'_N)$$

From this first-order reduced density matrix, the (spin-less) electron density is simply obtained by the summation over all spin projections for $\mathbf{q}_1 = \mathbf{q}'_1$, and is usually normalized to number of electron of the system

$$\rho(\mathbf{r}_1) = \sum_{\sigma_1} \rho^{(1)}(\mathbf{q}_1, \mathbf{q}'_1), \quad \int d\mathbf{r} \rho(\mathbf{r}) = \int dr d\vartheta d\varphi r^2 \sin \vartheta \rho(\mathbf{r}) = N.$$

3.9.b. Atomic density matrix formalism

Motivation

- Density matrix formalism: In this formalism, the state of a physical system is characterized by means of statistical operators ρ which describe a single system or an ensemble of equally prepared **collision systems** in either a **pure quantum state** or in a **mixture of different states with any given degree of coherence**.
- The great benefit of using the (atomic) density matrix theory is that it enables one to “accompany” such an ensemble through one or several steps of excitation, decay and/or collision process, **and without loss of quantum-mechanical information**.
- Transition operators R of the density-matrix elements If one starts from a well-specified initial state of the system, as described by the operator ρ_i , all information about the atomic interactions, that govern the process, simply resides in the (so-called) **transition operators** R , and the final state operator just follows from the well-known relation: $\rho_f = R \rho_i R^+$.

- **Building blocks:** The electron-photon, electron-electron interaction and electron-nucleus interaction amplitudes from above are the building blocks to form the (scattering or) transition matrix for all atomic processes of interest and, hence, the density matrices of the system at the various steps of some particular excitation or decay process.
- For scattering states with a single electron in the continuum, these interaction amplitudes can be readily calculated by means of the JAC tools.
- Apart from the efficient computation of these building blocks, one also requires a simple book-keeping of these amplitudes in order to set-up the (atomic) density matrices at the various steps. To facilitate this handling and the book-keeping of these amplitudes, they are typically provided in JAC by some (amplitude) array, and together with all quantum numbers that are needed for their unique classification.
- The prior computation of the many-electron amplitudes enables one to start directly from the amplitudes (for one or several elementary processes) and to combine them into an appropriate form, in order to support the prediction of different atomic properties and parameters.
- **Set-up of the density matrix:** In practice, the computation of all interaction amplitudes is performed within three steps: (i) the generation of all necessary bound-state wave functions, (ii) the evaluation of the transition amplitudes between bound states and scattering states in the continuum, and (iii) the set-up and handling of the density matrices, i.e. by applying the formulas from chapter 8.

Density operator of an atom in level (αJ) :

- **Mixed states of a level (αJ) :** For an atom in a well-defined and isolated level (αJ) , a general mixed state with regard to its magnetic subspace (i.e. its projections M) can always be written as

$$\hat{\rho} = \sum_{MM'} c_{MM'} |\alpha JM\rangle \langle \alpha JM'|.$$

- **Statistical tensor:** Often, it is most convenient to represent the intermediate state of the ions in terms of its so-called statistical tensors

$$\rho_{kq}(\alpha J) = \sum_{MM'} (-1)^{J-M'} \langle JM, J(-M') | kq \rangle \langle \alpha JM | \rho | \alpha JM' \rangle .$$

and which are non-zero only for $0 \leq k \leq 2J$ and $-k \leq q \leq k$. These statistical tensors transform like the spherical harmonics.

- Although both, the (reduced, mixed) density matrix and the statistical tensors of some level (αJ) are mathematically equivalent, the latter form can be transformed more easily and analogue to the spherical harmonics of rank k under a rotation of the coordinates.

3. Many-electron atomic interactions, state functions, density operators and statistical tensors

- (Initial) polarization state of an atom: The polarization state of the initial atom can be characterized by the statistical tensors $\rho_{kq}^{\mathbf{n}_t}(\alpha_i \mathbb{J}_i)$, if defined with regard to the axis of the (target) polarization $\mathbf{n}_t = (\vartheta_t, \varphi_t)$. While the odd-rank tensors $k = 1, 3, \dots$ are known to characterize the orientation of the target atom, the even-rank tensors $k = 2, 4, \dots$ describe its alignment. The maximal rank of these tensors is limited by the condition $k \leq 2J$.

3.10. Parity- and time-violating atomic interactions

3.10.a. Interactions beyond the standard model

Standard electro-weak model:

- The success of the standard electro-weak model of elementary particles is indeed extraordinary. It has been tested by many physical processes that cover more than ten orders of magnitude in momentum transfer. The standard model also correctly predicted the existence of new particles, such as the neutral Z boson.
- The standard model is sometimes understood also as a low-energy manifestation of a more complete theory that, perhaps, unifies the four forces. Many well-motivated extensions to the standard model have been proposed, such as supersymmetric, technicolour and left-right symmetric models, and they often predictr physical phenomena quite different from those of the standard model.
- CP symmetry: This symmetry refers to the combined symmetry of charge conjugation C and parity P.
- Violation of CP symmetry: The violation of CP symmetry was first discovered in 1964 in decays of the neutral K mesons, and this violation is taken into account by the standard electro-weak model by just a single complex phase in the quark-mixing matrix (the so-called Kobayashi-Maskawa mechanism).
- Various extensions of the standard model, such as supersymmetry, predict considerably larger EDM of the particles. Any observation of these EDM would therefore lead unambiguously to a hint of *new physics*.
- In addition, the standard model of particle physics is sometimes said to violate time-reversal (T) invariance, but again only through just a single phase in the Cabibbo-Kobayashi-Maskawa matrix, that mixes the quark flavors.
- For a rather long time, K mesons remained the only system in which CP-violation wwere observed explicitly. In 2001, however, the BaBar and Belle collaborations detected CP violation also for neutral B mesons, although this is still consistent with the predictions of the standard model.

- **CPT symmetry:** The (mathematical) structure of most gauge theories suggest that the combined symmetry of charge conjugation C , parity change P and time-reversal violation T has to be conserved.
- **If CPT is conserved,** as suggested by gauge theories, then CP-violation must be strictly accompanied by T (time-reversal) violation. Until the present, however, there has been no (undisputed) direct observation of T violation and its detection is of fundamental interest by itself. A direct detection of T-violation may shed further light also on the origin of CP-violation.
- **Permanent electric dipole moment (EDM)** The measurement of a per of neutrons, atoms, or molecule would show explicit evidence of T-violation.
- **New physics:** theories in physics beyond the standard model predict new sources of T-violation and these sources may lead to EDM that are many orders of magnitude larger than those from the standard model. This may allow EDM measurements by means of current experiments. Already the parameter space of quite popular extensions of the standard model, such as supersymmetry, multi-Higgs models, and left-right symmetric models, are strongly restricted by current measurements.
- **Schiff theorem:** If an external electric field acts upon a neutral atom, that consists out of non-relativistic point-like charged particles with some EDM and that only interact via electrostatic forces with each other, the field is screened exactly at each particle. This screening arises due to the polarization of the atomic electrons by the external field. Therefore, an external electric field cannot induce an atomic EDM. As shown by Schiff, however, this **shielding is incomplete if magnetic or finite-size effects are taken into account**, and this may give rise in principle to an atomic EDM.

High-precision measurements on fundamental symmetries of atoms:

- **Atomic high-precision experiments:** High-precision measurements on the (violation of fundamental) symmetries in atoms are suitable to test the standard model of elementary particles and to search for new physics beyond it. Such precision experiments in atomic physics complement measurements in high-energy physics.
- Indeed, atomic experiments have played an important role in the verification of the standard model for more than 30 years ago already. While the first evidence for neutral-weak currents, i.e. the existence of the neutral Z boson, was discovered in neutrino scattering, a parity violation was first established in atomic experiments, and before it was later observed also in high-energy electron scattering.
- Today, **atomic physics plays a major role in the search for new physics beyond the standard model.**
- **PNC measurements for cesium:** For example, the cesium measurement on parity non-conservation in atomic physics have been found in excellent agreement with the standard model.

3. Many-electron atomic interactions, state functions, density operators and statistical tensors

- **Atomic PNC measurements:** Instead of more and more accurate PNC measurements and computations, it appears useful today to perform such measurements for different isotopes of the same atom, since the ratio of the PNC signals for two different isotopes is rather insensitive to the details of the electron structure. For such measurements, the largest uncertainty to the PNC amplitudes arise from the unknown neutron distribution of the isotopes (Roberts *et al.*, 2014).

3.10.b. Parity-violating (**P-odd, T-even**) interactions

Motivation:

- **Parity non-conservation (PNC) effects:** These effects arise in atoms largely due to the exchange of Z^0 -bosons between the atomic electrons and the nucleus.
- The exchange of Z^0 bosons is formally described by the Weinberg-Salam theory and leads to (observable) phenomena, such as circular dichroism and optical rotation, and which have been investigated in order to detect P-violation in cesium, thallium, bismut and plumbum.
- There is also another contribution to atomic parity violation due to the exchange of Z^0 bosons between each pair of electrons; however, this effect is negligibly small for heavy atoms and well suppressed by a factor $10^{-3} \dots 10^{-4}$. This contribution is usually neglected in most PNC studies.
- PNC effects in atoms can be caused also by nuclear moments, i.e. by parity-violating electromagnetic form factors that occur in addition to the usual nuclear magnetic-dipole and electric-quadrupole moments (form factors).
- **Rare-earth atoms:** Several PNC experiments in rare-earth atoms have been suggested for close-lying levels of opposite parity in order to enhance the PNC effects. Moreover, rare-earth often have various stable isotopes and, hence, the dependence on atomic theory can be removed by taking ratios of the measured PNC contributions for different isotopes.
- **Enhancement of PNC signals:** Several physical factors can contribute to an enhancement (or suppression) of the measured parity-violating signal for selected atomic transitions: (i) The PNC amplitude is expected to scale slightly faster than Z^3 with the nuclear charge of the ions and make heavy elements even more favorable; and (ii) the existence of close-lying levels of different parity. For the alkaline-earth elements, there are often levels with a splitting $\sim 10 \text{ cm}^{-1}$ which need to be compared to the well-studied $6s - 7s$ PNC transition in Cs with a splitting $\sim 104 \text{ cm}^{-1}$ (Roberts *et al.*, 2014).

Nuclear-spin independent P-odd electron-nucleus interactions:

- Nuclear-spin independent Hamiltonian: For non-relativistic nucleons, the nuclear-spin independent Hamiltonian for the P-odd electron-nucleus interaction is given by the effective single-electron operator

$$\mathbb{H}^{(\text{weak-charge})} = -\frac{G}{\sqrt{2}} \gamma_5 [Z C_{1p} \rho_p(r) + N C_{1n} \rho_n(r)] ,$$

where Z and N are the number of protons and neutrons, and where the proton and neutron densities are normalized to unity, $\int dr \rho_p(r) = 1 = \int dr \rho_n(r)$.

- If the proton and neutron densities coincide, $\rho_p = \rho_n \equiv \rho$, the nuclear-spin independent Hamiltonian simplifies and can be described in terms of a nuclear weak-charge Q_W ,

$$\mathbb{H}^{(\text{weak-charge})} = -\frac{G}{2\sqrt{2}} \gamma_5 Q_W \rho .$$

- Nuclear weak charge Q_W : This charge is very close to the neutron number and is in lowest order in the electro-weak interaction given by

$$Q_W = -N + Z(1 - 4 \sin^2 \theta_W) \approx -N .$$

This value for Q_W is modified however by radiative corrections.

- The nuclear-spin independent electron-neutron interaction is a scalar that mixes levels (states) with the same total electron angular momentum but different parity.
- For heavy atoms, the nuclear-spin independent interaction due to the nuclear weak-charge gives the dominant contribution to parity violation, when compared to other mechanisms.

Nuclear-spin dependent P-odd electron-nucleus interactions:

- **P-odd interactions that depend on the nuclear spin I :** There are different interactions that depend on the nuclear spin I due to:
i) the neutral weak current; ii) hyperfine-induced neutral currents; or iii) the nuclear anapole moment.
- **Spin-dependent electron-nucleus interactions:** The dominating contribution in heavy atoms comes from the nuclear anapole moment (κ_a), while smaller contributions still arise from the Z_0 exchange due to spin-dependent electron-nucleus weak interactions (κ_z) as well as the interaction of the weak charge (κ_Q) with the magnetic hyperfine interaction (Roberts *et al.*, 2014).
- **Interaction with the nuclear anapole:** The anapole moment gives typically the dominant nuclear-spin dependent P-odd electron-nucleus interaction. The nuclear anapole moment arises from P-odd interactions inside the nucleus. These interactions manifest themselves in atoms through a slightly modified electro-magnetic interaction of the nucleus with atomic electrons.
- The anapole moment κ_a increases with the atomic mass number, $\kappa_a \propto A^{2/3}$ and, thus, dominates in heavy atoms, when compared to other nuclear-spin dependent mechanisms listed above.
- **Hamiltonian for the electron-anapole (-moment) interaction:** For an external nucleon with orbital angular momentum ℓ , the Hamiltonian is given by (Dzuba *et al.*, 2009)

$$\mathbb{H}^{(\text{anapole})} = \frac{G}{\sqrt{2}} \kappa_a \frac{K}{I(I+1)} \boldsymbol{\alpha} \cdot \mathbf{I} \rho(r), \quad K = (I + 1/2) (-1)^{I+1/2-\ell}.$$

Anapole moment:

- **Anapole moment:** The anapole moment arises from P-odd, T-even nuclear moments (i.e. parity-violating nuclear forces) and usually requires less accurate atomic structure calculations. This may simplify the search for favorable conditions and atomic systems.
- The notion of the anapole moment was introduced by Zel'dovich just after the discovery of parity violation.
- However, an **nuclear anapole moment was unambiguously detected only 30 years later**. In 1997, a group at Boulder measured a nuclear anapole moment in ^{133}Cs to an accuracy of 14 % in an atomic experiment. This is considered as the first observation of an electromagnetic moment that violates fundamental discrete symmetries (Ginges and Flambaum, 2003).

- A P-odd, T-even anapole moment of the nucleus arises due to the presence of a parity violating weak interaction between nucleons.
- The anapole moment is directed along the nuclear spin \mathbf{I} : $\langle \mathbf{a} \rangle = -\pi \langle r^2 \mathbf{j} \rangle = a \mathbf{I}/I$. Since the current vector \mathbf{j} changes its sign under reflection of coordinates, but not the spin \mathbf{I} , **an anapole moment need to violate parity but not time-reversal symmetry**.

3.10.c. Time-reversal violating (P-odd, T-odd) interactions

Motivation:

- **Time-reversal symmetry:** Many physical systems and processes are asymmetric under time-reversal. In classical mechanics, for example, a velocity reverses its direction under time reversal, $v \rightarrow -v$, while an acceleration does not. This time-reversal asymmetry is often associated with some energy dissipation and, hence, with the second law of thermodynamics. Without dissipation, the laws of mechanics are usually considered to be invariant with regard to time-reversal.
- In nuclei, P-odd and T-odd nuclear moments can arise due to an intrinsic EDM of the nucleons, or due to P-odd and T-odd nuclear forces. The P-odd and T-odd nuclear forces induce larger nuclear moments than a single nucleon EDM.
- Various P-odd and T-odd interactions can be considered, especially for heavy atoms and ions. These interaction include the **tensor-pseudotensor electron-nucleon (e-N) interaction**, the **scalar-pseudoscalar (e-N) interaction**, the **nuclear Schiff moment** and the **interaction of the electron EDM with the internal nuclear magnetic field of the atom**.
- An atomic EDM can be induced if the nucleus possesses P-odd and T-odd nuclear moments.

P-odd & T-odd Hamiltonians due to electron-nucleus interactions:

- The expressions for $\mathbb{H}^{(\text{scalar-pseudoscalar})}$ and $\mathbb{H}^{(\text{weak charge})}$ as well as $\mathbb{H}^{(\mathbf{I}-\text{independent})}$ are quite similar.
- These electron-nucleus interactions mixes atomic states of opposite parity and induces a static electric-dipole moments in atoms.

P-odd & T-odd nuclear moments:

- The operators $\mathbb{H}^{(\text{scalar-pseudoscalar})}$ and $\mathbb{H}^{(\text{tensor})}$ have both electronic and nuclear components. While these Hamiltonians are overall scalar, the electronic and nuclear operators can be of any (equal) rank. To obtain any non-zero matrix element, therefore, the triangle rule for coupling of angular momenta imposes restrictions on the angular momenta of the electron and nuclear states.

3. Many-electron atomic interactions, state functions, density operators and statistical tensors

- Nuclear moments that violate parity and time-reversal invariance: electric dipole, magnetic quadrupole, electric octupole. For an nuclear electric-dipole moment, the Hamiltonian must be of the form $\mathbb{H}^{(\text{Schiff moment})}$ in order to mix electron states of opposite parity.
- Nuclear electric-dipole (Schiff) moments: If \mathbf{S} is nuclear Schiff moment, the associated P-odd and T-odd Hamiltonian is given by

$$\mathbb{H}^{(\text{Schiff-moment})} = -e \phi^{(\text{Schiff-moment})} = -4\pi e \mathbf{S} \cdot \nabla \delta(r).$$

Here $\phi^{(\text{Schiff-moment})}$ is the electrostatic potential of the nucleus that corresponds to a P-odd and T-odd charge distribution.

- Nuclear magnetic-quadrupole moments (MQM): A general expression for the nuclear MQM can be constructed in terms of the total angular momentum of the system I ,

$$M_{ij} = -e \frac{3}{2} \frac{M}{I(2I-1)} \left[I_i I_j + I_j I_i - \frac{2}{3} I(I+1) \delta_{ij} \right].$$

The quantity M is conventionally referred to as the nuclear MQM and is defined as the maximum projection of M_{ij} upon the nuclear axis, $M = M_{zz}$. The magnetic quadrupole moment violates parity and time-reversal invariance.

3.10.d. Time-reversal violating atomic electric-dipole moments

Motivation:

- A non-zero electric-dipole moment (EDM) of atoms require P-odd and T-odd interactions, either among the nucleons or the electrons and the nucleus.
- Therefore, the **null measurements of EDM in atoms** place severe restrictions upon new sources of **CP-violation** that often arise in models beyond the standard model, such as supersymmetry.
- The nuclear EDM exceeds the EDM of single nucleons by one to two orders of magnitude. P-odd and T-odd nuclear forces generate all P-odd and T-odd nuclear moments, such as the Schiff and MQM moments. These nuclear moments can be 10-to-100 times larger than those generated by the presence of a nucleon EDM.
- In the standard model, an atomic EDM is suppressed by many orders when compared to predictions from (so-called) *new theories*. Therefore, the detection of an EDM would be **unambiguous evidence of new physics**, even if it contributes only weakly to a very small signal in atomic parity violation.

- An atomic EDM can arise from various P-odd and T-odd mechanisms (Ginges and Flambaum, 2004): i) an intrinsic EDM of an electron; ii) a P-odd and T-odd electron-nucleon interaction; iii) an intrinsic EDM of an external nucleon; iv) a P-odd and T-odd nucleon-nucleon interaction.
- Until the present, no permanent EDMs in neutrons, atoms or molecules have been detected.
- The best limits on the electron electric dipole moment is presently derived from measurements of atomic EDM.

Physics of the atomic EDM:

- An atomic EDM is associated with an atomic level $|\alpha J\rangle$ and arises due to the admixture of levels (states) $|\nu J_\nu\rangle$ with opposite-parity wave functions. This atomic EDM has the form

$$d^{(\text{atomic EDM})} = 2 \sum_{\nu} \frac{\langle \alpha J | D | \nu J_\nu \rangle \langle \nu J_\nu | H^{(\text{PT})} | \alpha J \rangle}{E_{\alpha} - E_{\nu}} = d^{(\text{atomic EDM})} \frac{\mathbf{F}}{F},$$

where D is the electric dipole operator, $H^{(\text{PT})}$ the P-odd and T-odd operator that mixes $|\alpha J\rangle$ with the set of wave functions $|\alpha_\nu J_\nu\rangle$, and F is the total angular momentum of the atom corresponding to the state $|\alpha J\rangle$.

- A typical EDM experiment is performed in parallel electric and magnetic fields and can be described by the Hamiltonian

$$H^{(\text{em field})} = -\mu \cdot \mathbf{B} - \mathbf{d} \cdot \mathbf{E}.$$

- A linear Stark shift is measured by observing the change in frequency when the electric field is reversed, since it is sensitive to the P-odd and T-odd term $\mathbf{E} \cdot \mathbf{B}$.
- Interaction Hamiltonian of the electron EDM with an internal atomic electric field \mathbf{E}^{int} : The Hamiltonian for interaction of the electron EDM with internal atomic electric field \mathbf{E}^{int} can be written as (Dzuba and Flambaum, 2009)

$$H^{\text{eEDM-electric}} = -d_e \sum_{i=1}^N (\gamma_o - 1)_i \Sigma_i \cdot \mathbf{E}^{\text{int}}, \quad \Sigma_i = \begin{pmatrix} \sigma_i & 0 \\ 0 & \sigma_i \end{pmatrix}.$$

- Atomic EDM: An atomic EDM can be caused by the interaction of the electron EDM (if it exists) with either the internal electric field of the atom or the scalar-pseudoscalar electron-nucleon (T-odd, P-odd) interaction; an EDM of atoms in their ground state is then given by

$$\mathbf{d}_{\text{atom}} = 2 \sum_{\nu} \frac{\langle 0 | D | \nu \rangle \langle \nu | H^{\text{eEDM-..}} | 0 \rangle}{E_o - E_{\nu}}$$

3. Many-electron atomic interactions, state functions, density operators and statistical tensors

where $|0\rangle$ is the atomic ground state, $\mathbb{D} = -e \sum_i \mathbf{r}_i$ is the electric-dipole operator and $\mathbb{H}^{e\text{EDM}-..}$ the (P-odd, T-odd) interaction operator. Here, the summation need formally to be performed over the complete many-electron spectrum of the intermediate levels ν with total energies E_ν .

- Measurements of EDMs in paramagnetic atoms, i.e. for a total electron angular momentum $J \neq 0$, are most sensitive to leptonic sources of P- and T-violation, and especially the electron EDM.
- In contrast, measurements of EDM in diamagnetic systems with zero total electron angular momentum are most sensitive to P-odd and T-odd mechanisms in the hadronic sector.

3.11. Elements from atomic spectroscopy

3.11.a. Line shifts and profiles

Line profiles in atomic spectroscopy:

- **Experimental photon energy distribution:** In order to fit the observed spectra to Fano's formula, the experimental photon energy distribution (window function) need usually to be taken into account. This experimental window function can often be represented by Gaussian with a full-width-at-half maximum (FWHM) according to the experimental energy spread. Therefore, the Fano profile has to be convoluted with a Gaussian. Analogue convolutions are known from the Voigt line profiles in the emission spectroscopy of hot gases which also includes the convolution of a Lorentzian with a Gaussian line curve.
- **Convolution of a Lorentzian and Gaussian line profile:** The Voigt profile arises from the convolution of a Lorentzian and Gaussian line profile with the Lorentzian and Gaussian FWHM Δ_L and Δ_G

$$L(E) = \frac{2A}{\pi} \frac{\Delta_L}{4(E - E_r)^2 + \Delta_L^2}, \quad G(E) = \frac{2}{\Delta_G} \sqrt{\frac{\ln 2}{\pi}} \exp\left[-\frac{4(\ln 2) E^2}{\Delta_G^2}\right], \quad \int dE L(E) = A, \quad \int dE G(E) = 1$$

$$V(E) = \int_{-\infty}^{\infty} dE' L(E') G(E' - E) = A \frac{4\sqrt{\ln 2}}{\pi^{3/2} \Delta_G} \int_{-\infty}^{\infty} dE' \frac{\Delta_L}{4(E' - E_r)^2 + \Delta_L^2} \exp\left[-\frac{4(\ln 2)(E - E')^2}{\Delta_G^2}\right].$$

- **Convolution of a Lorentzian and a Gaussian line profile:** The convolution of a Lorentzian profile with a Gaussian function generally results in a **Faddeeva function that can be utilized for a fast and accurate evaluation of the convolution, e.g., in peak fitting routines** (Schippers 2018). With the following definitions, the Voigt profile can be expressed in terms of the Faddeeva function as

$$\begin{aligned} t &= \frac{2\sqrt{\ln 2}(E' - E)}{\Delta_G}, & x &= \frac{2\sqrt{\ln 2}(E_r - E)}{\Delta_G}, & y &= \frac{\Delta_L \sqrt{\ln 2}}{\Delta_G}, & z &= x + iy \\ V(E) &= A \frac{2\sqrt{\ln 2}}{\Delta_G \sqrt{\pi}} \frac{1}{\pi} \int_{-\infty}^{\infty} dt \frac{y e^{-t^2}}{(t - x)^2 + y^2} dt = A \frac{2\sqrt{\ln 2}}{\Delta_G \sqrt{\pi}} \Re[w(z)], & \int dEV(E) &= A \end{aligned}$$

3. Many-electron atomic interactions, state functions, density operators and statistical tensors

➤ **Faddeeva function $w(z)$:** The Faddeeva function is a scaled complex error function which, for $\Im z = y > 0$, is defined as (Schippers 2018)

$$w(z) = e^{-z^2} \operatorname{erfc}(-iz) = \frac{i}{\pi} \int_{-\infty}^{\infty} dt \frac{e^{-t^2}}{z-t}, \quad \Re[w(z)] = \frac{1}{\pi} \int_{-\infty}^{\infty} dt \frac{ye^{-t^2}}{(t-x)^2 + y^2}, \quad \Im[w(z)] = \frac{-1}{\pi} \int_{-\infty}^{\infty} dt \frac{(t-x)e^{-t^2}}{(t-x)^2 + y^2}.$$

$\Re[w(x+iy)]$ and $\Im[w(x+iy)]$ can be displayed as functions of the scaled energy x for different ratios y of Lorentzian and Gaussian widths.

➤ **Convolution of a Fano and a Gaussian line profile:** One can re-define the Fano line profile from above in a slightly different form with either $|q| > 1$ or negative $|q| < 1$ peak area and with the same definition of t , x and y as above. This definition of the Fano profile is consistent with the theoretical treatment of the atomic photoabsorption cross section. For the convolution of a Fano and a Gaussian line profile, this gives rise to (Schippers 2018):

$$\begin{aligned} F(E) &= \left| \frac{A}{q^2 - 1} \right| \frac{2}{\Delta_L \pi} \left[\frac{(q+\epsilon)^2}{1+\epsilon^2} - 1 \right], \quad \lim_{q \rightarrow \infty} F(E) \rightarrow L(E) \quad \int dE F(E) dE = A, . \\ C(E) &= \int_{-\infty}^{\infty} dE' F(E') G(E' - E) = \left| \frac{A}{q^2 - 1} \right| \frac{2}{\Delta_L \pi} \left[\frac{1}{\sqrt{\pi}} \int_{-\infty}^{\infty} dt \frac{[qy + (t-x)]^2 e^{-t^2}}{(t-x)^2 + y^2} dt - 1 \right] = \left| \frac{A}{q^2 - 1} \right| \frac{2\sqrt{\ln 2}}{\Delta_G \sqrt{\pi}} \left\{ (q^2 - 1) \Re(w) - 2q \Im(w) \right\}. \end{aligned}$$

Doppler-shifted transition frequencies:

➤ **Doppler shift of atomic transition frequency ν_o :** If the atom moves with velocity \mathbf{v} under the angle $\vartheta = \angle(\mathbf{v}, \text{atom-observer, line of sight})$ with regard to the observer (or, *vice versa*, the observer w.r.t the atom), the atomic line appears for the observed *Doppler-shifted* at frequency

$$\nu = \frac{\nu_o}{\gamma(1 - \beta \cos \vartheta)} = \nu_o \sqrt{1 - \beta^2} (1 - \beta \cos \vartheta)^{-1}, \quad \beta = \frac{v}{c}, \quad \gamma = (1 - \beta^2)^{-1/2}.$$

➤ **Uncertainty estimation of a *Doppler-shifted* frequency:** To estimate how the uncertainties in β and ϑ , the following partial derivatives

are needed:

$$\begin{aligned}\Delta \nu &= \left| \frac{\partial \nu}{\partial \beta} \right| \Delta \beta + \left| \frac{\partial \nu}{\partial \vartheta} \right| \Delta \vartheta, & \frac{\partial \nu}{\partial \beta} &= \nu_o \frac{\gamma(1 - \beta)}{(1 - \beta \cos \vartheta)^2}, & \frac{\partial \nu}{\partial \vartheta} &= -\nu_o \frac{\beta \sin \vartheta}{\gamma(1 - \beta \cos \vartheta)^2} \\ \left| \frac{\partial \nu}{\partial \beta} \right| \frac{\Delta \beta}{\nu} &= \frac{\gamma \beta(1 - \beta)}{(1 - \beta \cos \vartheta)} \frac{\Delta \beta}{\beta}\end{aligned}$$

The second line just displays the frequency ratio $\Delta \nu/\nu$ due to an uncertain (normalized) velocity $\Delta \beta/\beta$ of the atoms.

- **Mean Doppler frequency of an atomic transition:** If photons are observed from atoms with relative velocity v and both, in forward ($\vartheta = 0 \pm \delta_o$) and backward directions ($\vartheta = \pi \pm \delta_\pi$) with overall small misalignments, the mean Doppler-shifted frequency can be defined in terms of the *averaged* frequency in both directions

$$\langle \nu \rangle = \frac{\nu_o}{2\gamma} \left[\frac{1}{(1 - \beta \cos \delta_o)} + \frac{1}{(1 - \beta \cos(\pi + \delta_\pi))} \right] = \left[\frac{1}{(1 - \beta \cos \delta_o)} + \frac{1}{(1 + \beta \cos \delta_\pi)} \right] \approx \frac{\nu_o \gamma}{2} \quad \text{for } \delta_o = \delta_\pi = 0.$$

3.11.b. Atomic target distributions

Target distributions:

- **Gaussian target distribution:** A localized but macroscopic target can be described by a Gaussian probability distribution that is centred with width σ around the impact parameter \mathbf{b}_0 with regard to the beam axis. Then the probability distribution is given by

$$f(\mathbf{b}; \mathbf{b}_0) = \frac{1}{2\pi\sigma^2} e^{-\frac{(\mathbf{b}-\mathbf{b}_0)^2}{2\sigma^2}} = \frac{1}{2\pi\sigma^2} e^{-\frac{b^2 + b_0^2 - 2b b_0 \cos \phi_b}{2\sigma^2}}.$$

3.11.c. Manipulation of light beams

Optical elements:

- **Half-wave plate *versus* mirror:** A half-wave plate reverses the spin angular momentum, i.e. the circular polarization of an incident light beam. A half-wave plate can therefore be seen as the **angular variant of a mirror** which reverses the linear momentum of the light (reflection). A similar analogy in the response to an incident light beam exists also for the Doppler shift: If the mirror moves with velocity \mathbf{v} , an incident photon experiences a linear momentum transfer \mathbf{q} and a **linear (Doppler) shift** $\Delta E = \mathbf{q} \cdot \mathbf{v}$, while photons transmitted through a rotating half-wave plate with angular velocity $\boldsymbol{\Omega}$ experience an angular momentum transfer \mathbf{Q} and an **angular Doppler shift** $\Delta E = \mathbf{Q} \cdot \boldsymbol{\Omega}$. Both, the linear and angular Doppler shift can be related to a broken symmetry (invariance) in the light-matter interaction due to the motion of the medium.
- **Jones' matrix formalism:** In classical optics, the propagation of beams through optical elements, such as polarizers, wave plates, etc. are often described by Jones' matrix formalism and by making use of a basis of well-defined spin angular momentum (e.g., linear or circular polarization).

3.11.d. Miscellaneous

Experimental features & conditions:

- **Resonant behaviour:** A resonance generally refers to a drastic change in the intensity of some signal, while the energy (or some other parameter) changes only little. In quantum physics, resonances in the intensity pattern are often accompanied by some – more or less strong – interference of different quantum amplitudes.
- **Energy calibration of photon-ion merged-beams measurements:** Since the ions move opposite to the photon beam, the (photon) energy needs to be Doppler corrected within the framework of the ion. If $E^{(\text{lab})}$ is the photon energy in the laboratory and $\theta \simeq 180^\circ$ the angle between the beams, the Doppler-shifted energy is:

$$E^{(\text{merged-beam})} = \frac{E^{(\text{lab})}}{\gamma(1 + \cos\theta)}, \quad \gamma = \frac{1}{\sqrt{1 - \beta^2}}, \quad v = \beta c.$$

- Energy calibration of photon-ion merged-beams measurements: The ion velocity v can be derived from the acceleration voltage $U^{(\text{acceleration})}$ via the kinetic energy $E^{(\text{kin})}$ of the ions as well as their mass $M^{(\text{ion})}$ and their Lorentz factor γ as (Müller *et al.*, 2018)

$$E^{(\text{kin})} = qe U^{(\text{acceleration})} = (\gamma - 1) M^{(\text{ion})} \quad \rightarrow \quad \beta = \sqrt{1 - \frac{1}{(1+x)^2}}, \quad x = \frac{qe U^{(\text{acceleration})}}{M^{(\text{ion})} c^2}$$

$$E^{(\text{merged-beam})} = \frac{E^{(\text{lab})}}{(1+x) + \sqrt{2x+x^2} \cos\theta} \quad \rightarrow \quad E^{(\text{lab})} \left[(1+x) + \sqrt{x} \sqrt{2+x} \right] \quad \text{for } \theta \approx 180^\circ.$$

- Madelung ordering *versus* Coulomb ordering of shells: While the Coulomb order of (sub-) shells follow from the hydrogenic solutions $n\ell$, $\ell = 0, \dots, n-1$, $n = 1, 2, \dots$, the Madelung order describes the shell order as it is filled by the elements from the periodic table

$1s, 2s, 2p, 3s, 3p, 4s, 3d, 4p, 5s, 4d, 5p, 6s, 4f, 5d, 6p, 7s, 5f, 6d, \dots$

- Cauchy moments: For an atomic level (αJ) with energy E_o and oscillator strength $f_{\nu o}$ to neighboured levels $(\alpha_\nu J_\nu)$ with excitation energies $\Delta E_{\nu o}$, the Cauchy moment is defined by (Mitroy *et al.*, 2010)

$$S(-q) = \sum_\nu \frac{f_{\nu o}}{(\Delta E_{\nu o})^q}.$$

The Cauchy moments appear in atomic physics as various places: $S(0) = N$, i.e. the number of electrons (Thomas-Reiche-Kuhn sum rule), while $S(-3)$ is related to the non-adiabatic polarizabilities.

- Voigt function: The Voigt function is defined by

$$K(a, x) = \frac{k(\nu)}{k_o} = \frac{a}{\pi} \int_{-\infty}^{+\infty} dt \frac{e^{-t^2}}{a^2 + (x-t)^2}.$$

- Several numerical methods for the computation of the Voigt integral are known from the literature as, for instance, the algorithm by Humlíček.

Rate coefficients $\alpha(T)$:

- Rate coefficients $\alpha(T)$: The rate coefficient of a capture or transfer process [in cm^3/s] is generally temperature-dependent and obtained by averaging the energy-dependent cross section $\sigma_{fi}(E)$ over a Maxwellian velocity distribution (Babb *et al.*, 2017)

$$\alpha(T) = \left(\frac{8}{m \pi i} \right)^{1/2} \left(\frac{1}{k_B T} \right)^{3/2} \int_0^\infty dE E \sigma_{fi}(E) \exp\left(-\frac{E}{k_B T}\right), \quad k_B = 1.380 \times 10^{-23} \text{ J K}^{-1}.$$

Here, m refers to the (reduced) electron mass-

- Quasi-rate $R(E)$: An effective energy-dependent rate of a capture or transfer process from state $i \rightarrow f$ can be obtained from the relationship (Babb *et al.*, 2017)

$$R_{fi}(E) = v \sigma_{fi}(E) = \sqrt{2E/m} \sigma_{fi}(E) \quad [\text{in } \text{cm}^3 \text{ s}^{-1}]$$

and can be used for estimating the rate coefficients $\alpha(T)$ of the given process if the energy E of the incident particles is converted into a temperature T .

4. Atomic representations

Methods, characterization & applications. An overview:

- Post-HF methods: Moller-Plesset (Rayleigh-Schrödinger) perturbation theory, configuration interaction (CI) expansions, coupled cluster (CC) theory, convergent close-coupling.
- Various *ab-initio* many-electron methods have been developed during the last decades to accurately describe the level structure and properties of atoms and ions with a relatively simple shell structure, such as the configurations interaction (CI), many-body perturbation theory (MBPT), coupled-cluster (CC) theory, correlation potential (CP) or multiconfigurational Dirac-Fock (MCDF) methods. These *ab-initio* methods are frequently applied for atoms and ions with just a (very) few valence electrons above a closed-shell core but cannot be applied so easily to systems with more than, say, four valence electrons.
- Weak or dynamic correlations: These correlation can be captured in a systematic fashion by various post-HF methods. More often than not, these weak correlations are built upon a single Slater determinant, although a multi-reference formulation also exist for most of these methods. In single-reference methods, however, very large expansions are often needed in order to retrieve the strong (static) correlation.
- Static *versus* dynamic correlations: This distinction is mainly made in quantum chemistry in order to separate the correlation contributions of energetically-nearby and often delocalized orbitals with large fractional occupation from those orbitals with a small-to-tiny contribution. Here, the second-order Moller-Plesset perturbation theory is often seen as the simplest and cheapest way to incorporate dynamic electron correlations. While dynamic correlations are often treated by single-reference methods, these methods are known to work not well for the static correlations.
- Size-consistency of (molecular) wave functions: For two noninteracting subsystems, the total wavefunction should be separable and the total energy additive. While the coupled-cluster method is always size-consistent because of its exponential wavefunction ansatz, a typical configuration-interaction wave function with k virtual excitations is usually not size-consistent for $N > k$ electrons in the system.
- An independent optimization of the wave functions for level groups of different total symmetry J still ensures that parts of the electron relaxation of the electron density is taken into account. Of course, an independent variation finally also results in a set of orbitals which, for a given level group, are not orthogonal to the orbitals of any other group.

4. Atomic representations

- In the study of transition probabilities and other atomic processes, this **relaxation of the electron density** causes technical problems but, otherwise, often yields results that are in better agreement with experiments.
- **Atomic resonances:** Since inner-shell hole states lay — by its very nature — high up embedded within the continuum of the next higher charge state, these atomic states have to be treated as **resonances**. From scattering theory, several (formal) approaches, such as the K-matrix , exist in order to treat the interaction among different resonances or decay channels properly. Up to the present, it remains **open whether and to which extent such sophisticated scattering approaches can be properly implemented into many-electron structure codes and how well they are suitable also for open-shell systems.**
- **Description of scattering states:** The size of the CSF expansions often increases very rapidly if the atomic bound-state density is *coupled* to the electron continuum, since the presence of one (or more) electrons in the continuum automatically leads to extra open shells. Such an *additional* increase of the CSF expansion and, hence, of the computations practically occurs in the study of all ionization, autoionization and scattering processes.
- Less attention was paid overall the years to the **calculation of atomic properties other than line strength, hyperfine structures or isotopes shifts**. With the **JAC tools**, we here wish to provide a simple access to the computation of (relativistic) atomic transition, ionization and **capture properties**, including the description of scattering states with one or more electrons in the continuum, and along with many other features of these tools.
- **CSF basis:** In practice, the **definition of a physically appropriate basis turns out to be less simple**. In particular, the difficulties in calculating *open-shell* atoms and ions have long been underrated. The first (successful) structure calculations of a few simple atoms and ions in the sixties and seventies quickly led to the **popular fallacy, that it would take only a bit more effort and computational power in order to theoretically predict the structure and properties of atoms in rather arbitrary configurations**.
- We know much better now: **Many atomic properties have been found to depend rather sensitive on the correlated motion of the electrons and, thus, on the shell structures of the atoms and ions**. Although much larger computations are feasible today, most open-shell atoms are yet not well understood. In fact, the *real* challenge when dealing with open-shell structures concerns the very rapidly growing wave function expansions, if one or several open shells are already involved within the reference configuration(s).
- **Many-particle states close to the particle emission threshold:** These states often display unusual properties, such as **halo and Borromean structures, clusterization** phenomena, or cusps in various observables. This behaviour arises due to the strong coupling of (quasi-) bound states to the continuum.
- **Complex eigenvalue Schrödinger equation (CESE) method:** The SE with a complex or non-hermitian potential has been studied at various places, especially in order to describe resonance states.

- **Variational 2-p RDM method:** This method has been applied in studying the (strong) correlations in quantum dots, quantum phase transitions, or even in metal-to-insulator transitions.
- **Wave functions *versus* density functional theory:** Wavefunction-based methods are very frequently applied in quantum chemistry, and especially for small quantum systems, despite of their very unfavorable scaling of the computational costs. DFT offers instead a much better trade-off between computational efficiency and accuracy, since it is just based on the electron density. However, **DFT can be built also upon one- and few-particle RDM to keep the computational costs feasible but by removing some of the drawbacks of standard DFT.**

Elements from atomic representation theory:

- **Atomic state function (ASF):** Similar to the well-known – non-relativistic and symmetry-adapted – Hartree-Fock (HF) method, in which the state of an atom or ion is approximated by a single (symmetry-adapted) Slater determinant, an **atomic state function** is written in the CI or multi-configuration Dirac-Hartree-Fock (MCDHF) method as **linear combination of configuration state functions (CSF) with well adapted symmetry**

$$|\alpha \text{ } JM\rangle \equiv \psi_\alpha(JM) = \sum_{r=1}^{n_c} c_r(\alpha) |\gamma_r PJM\rangle .$$

In this ansatz, n_c is the number of CSF, $\mathbb{J} \equiv J^P$ the total angular momentum and parity of the state, and α refers to all (further) quantum numbers that are needed to specify the state uniquely. Moreover, $\{c_r(\alpha)\}$ denotes the representation of the atomic state in the given basis.

- **Secular equation:** For a given CSF basis, the representation of an atomic state above (i.e. the mixing coefficients $\mathbf{c}(\alpha) \equiv (c_1(\alpha), c_2(\alpha), \dots, c_{n_c}(\alpha))$) is obtained by solving the **secular equation**

$$\det(\mathbf{H} - E_\alpha^{(n_c)} \mathbf{I}) = 0 , \quad \mathbf{H} = (H_{rs}) = (\langle \gamma_r PJM | \mathbb{H} | \gamma_s \bar{P} \bar{J} \bar{M} \rangle \delta_{P\bar{P}} \delta_{J\bar{J}} \delta_{M\bar{M}})$$

and where $E_\alpha^{(n_c)}(PJ)$ denotes the eigenvalue.

- **Hamiltonian matrix:** This matrix is **block-diagonal in the total parity and angular momentum of the atom**, and this is independent of the particular choice of the electron-electron interaction in the Hamiltonian.
- **Hamiltonian matrix:** Since the **Hamiltonian matrix is real and symmetric**, all atomic states are orthogonal for $E_\alpha \neq E_\beta$ or can be chosen in this way for $E_\alpha = E_\beta$. In practice, an efficient decomposition of the many-electron matrix elements H_{rs} in the Hamiltonian matrix above is central to every implementation of the CI or related method.

4. Atomic representations

- **Hamiltonian matrix:** Owing to the symmetry of the Hamiltonian, the computational effort of the MCDHF method can be reduced by a rather large factor (> 10), if the various (total) angular momenta and parities $J = J^P$ of the atomic states of interest are considered independently.
- **Hamiltonian matrix:** Formally, the number of basis states and, hence, the size of the Hamiltonian matrix grows exponentially with the number of electrons as well as the size of the active space; cf. section 4.1.c.
- **Choice of atomic Hamiltonian:** The decision about the atomic Hamiltonian operator, that is utilized in a particular CI or MCDHF computation, is often made on the basis of (1) the nuclear charge, (2) the charge state of the atom or ion, (3) its particular **shell structure** as well as (4) the atomic property under consideration. Further relativistic and radiative corrections to the (total energies of the) atomic levels can be added in various (effective) approximations.
- **Spin-angular integrals:** For symmetry-adapted CSF, the integration over the spin-angular variables of all N electrons can be performed algebraically and enables one to write the Hamiltonian matrix elements always in the form (Grant, 1989)

$$H_{rs} = \sum_t u_{rs}(a_t b_t) \langle a_t \| h_D \| b_t \rangle + \sum_t v_{rs}^{(L_t)}(a_t b_t c_t d_t) X^{(L_t)}(a_t b_t c_t d_t).$$

In this expansion, $u_{rs}(ab)$ and $v_{rs}^{(L_t)}(abcd)$ are one- and two-particle (scalar) angular coefficients, while the $X^{(L)}(abcd)$ describe the effective interaction strengths of (formally) the four electrons a, b, c, d that are involved in the interaction. As usual, we here abbreviate the one-particle quantum numbers $a = (n_a, \kappa_a)$, $b = (n_b, \kappa_b)$, ... to have a compact notation for the subshells of equivalent electrons.

- **Reduced one-electron matrix elements of the Dirac Hamiltonian:** As usual, the reduced matrix elements of the (one-electron) Dirac Hamiltonian,

$$\langle a \| h_D \| b \rangle = \delta_{\kappa_a \kappa_b} \int_0^\infty dr \left[c Q_a \left(\frac{d}{dr} + \frac{\kappa_a}{r} \right) P_b + c P_a \left(-\frac{d}{dr} + \frac{\kappa_a}{r} \right) Q_b - 2c^2 Q_a Q_b + V_{\text{nuc}}(r) (P_a P_b + Q_a Q_b) \right],$$

describe the kinetic and potential energy of an electron in subshell a and can be expressed in terms of the *large* and *small* (radial) components, $P_a(r)$ and $Q_a(r)$, of the corresponding one-electron orbital functions.

- These reduced matrix elements can be considered as the one-particle *analogua* to the effective interaction strength $X^{(L)}(abcd)$ as discussed above in section 3.1 for the electron-electron interaction.
- **Restricted active spaces:** In most standard all-electron implementations of the CI method and beyond, the electrons are often divided into (closed) core-shell and valence electrons, and with virtual excitations only included for the valence electrons within a restricted active orbital space.

4.1. In JAC implemented atomic representations

4.1.a. Mean-field basis (Atomic)

Use:

- Using JAC: Generate an `AtomicRepresentation(..., MeanFieldBasis(meanFieldSettings))` for a given set of reference configurations and given settings; cf. `? MeanFieldSettings` or `MeanFieldSettings()`.
- Using JAC, see also the functions: `Basics.generate()`.

4.1.b. Configuration interaction (CI) expansions (Atomic)

Use:

- Using JAC: Generate an `AtomicRepresentation(..., CiExpansion(orbitals, excitations, ciSettings))` for a given set of reference configurations as well as given orbitals, excitation and settings; cf. `? CiSettings` or `CiSettings()`. The dictionary of (fixed) orbitals can be generated, for instance, by a `MeanFieldBasis` expansion from Section 4.1.a.
- Using JAC: The virtual excitations to be included with regard to the reference configurations can be defined by `RasStep(seFrom=..., seTo=..., deFrom=..., deTo=, ..., frozen=...)`, where all optional parameters refer to shell lists in order to specify single excitations (se) from → to, double excitations (de) from → to as well as the list of frozen shells.
- Using JAC, see also the functions: `Basics.generate()`.

Difficulties with large CI computations:

- Bottleneck of large CI computations: For large CI calculations with symmetry-adapted CSF, the main computational effort arises from the set-up of the Hamiltonian matrix, while the compute time for the diagonalization increases less quickly with the size of the matrix, if only the low-lying levels are needed. The set-up of the Hamiltonian matrix can be more efficient by using so-called configuration state function generators (CSFG) since – parts of – the spin-angular integration can be re-used more easily. The efficiency of CSFG mainly refers to and arises from an intelligent reordering of the (typically) generated CSF lists.

4. Atomic representations

4.1.c. Restricted active space (RAS) expansions (Atomic)

Use & notations:

- **Restricted active space (RAS) method:** This method includes the *correlated* motion of the bound electrons in a (much) more systematic fashion; it is based either one mean-field DHF or MCDHF solutions of the one-electron orbitals *and* a restricted active space that is formed by a subset of occupied and virtual orbitals. The idea of the RAS method is to account for an excitation of the *active* electrons from the outer shells (into a number of predefined *unoccupied* orbitals), while some ‘electronic core’ remains often fixed in the set-up of the RAS self-consistent field (RAS-SCF) computations.
- **Using JAC:** Generate an `Atomic.Representation(..., RasExpansion(LevelSymmetry(...), NoElectrons, steps, rasSettings))` for a given set of reference configurations as well as a specified level symmetry, number of electrons, the requested (list of excitation) steps and settings; cf. `? RasSettings` or `RasSettings()`.
- **Using JAC:** The individual steps of the RAS computations are defined by `RasStep(seFrom=..., seTo=..., deFrom=..., deTo=..., frozen=...)`, where all optional parameters refer to shell lists in order to specify single excitations (se) from → to, double excitations (de) from → to as well as the list of frozen shells.
- **Using JAC, see also the functions:** `Basics.generate()`.
- **Classes of virtual excitations:** It is often useful to divide the virtual excitations of the active electrons into different *classes*, namely single (S), double (D), triple (T), ... excitations, in dependence of how many electrons are *to be replaced* with regard to the set of reference configurations. While single and double excitations are typically treated quite equally, because of Brillouin’s theorem for the Dirac-Hartree-Fock approximation, the triple and higher excitations are typically less important and, if considered at all, are incorporated only for/within the valence shells.
- **Implementation of the (RAS-SCF) method:** The RAS and SCF parts are often implemented by means of a two-step cycle to (1) re-optimize the self-consistent field and (2) to enlarge the (layers of) shells in the representation of the atomic state vectors.
- **Computation of level energies:** Different computational schemes have been applied to choose an restrictive active space for atomic level computations. If just the separation of the low-lying level energies are of interest, a closed core is often treated as *inactive*, and electron-electron correlations are considered only among the outer valence electrons. These valence-valence correlation scheme assumes a strict cancellation of all core-correlation contributions to the different levels. While this scheme often appears justified for core-core correlations, it is often less suitable for core-valence (CV) contributions, i.e. the polarization of the ionic core due to the valence electrons.

- **Core polarization:** To incorporate CV correlations, CSF with orbital replacements $a \rightarrow r$ or even $ab \rightarrow cr$ need to be taken into account, and where a, b, c refer to core orbitals and r to either valence or excited orbitals. Several systematically-enlarged case studies have been carried out, which basically include all core-valence excitations up to a maximally-occupied correlation layer. Although the separation energies are often improved by including these core-valence correlations, the separation of core and valence orbitals is much less obvious. For atom or ion, this separation need to be explore in further detail, in particular, if accurate excitation energies are needed.

4.1.d. Approximate many-electron Green function for atomic levels (GreenFunction)

Formal representation & notations:

- **Formal quantum notation:** $[\{E_{\nu_1}, |\psi_{\nu_1}(\beta_1 \mathbb{J}_1)\rangle\}, \{E_{\nu_2}, |\psi_{\nu_2}(\beta_2 \mathbb{J}_2)\rangle\}, \dots] \longrightarrow \mathbb{G}(E) = \sum_{\nu_1 \nu_2 \dots} \frac{|\psi_{\nu_i}(\beta_i \mathbb{J}_i)\rangle \langle \psi_{\nu_i}(\beta_i \mathbb{J}_i)|}{E - E_{\nu_i}} .$
- **Spectral (many-electron) Green function representation for the levels of one or several (given) configurations:** Such a representation refers to just one or several lists of many-electron levels $\{E_{\nu_i}, |\psi_{\nu_i}(\beta_i \mathbb{J}_i)\rangle, \nu_i = 1, \dots, \nu_i^{(\max)}\}$, $\mathbb{J}_i \in \mathbb{J}^{(\max)}$ from a list of total symmetries $\mathbb{J}^{(\max)} = [\mathbb{J}_1, J_{sym}, \dots]$ and with up to $n = n^{(\max)}$ electrons within the continuum, i.e. with $n = 0, \dots, n^{(\max)}$ free (unbound) electrons.
- **Classification of Green functions:** Each Green function is classified by the (maximum) number of free electrons and a pre-specified (*de-excitation scheme*) that is to be applied in order to generate from a list of given configurations all those (nonrelativistic) configurations that are to be considered in the many-electron (CSF) basis of the Green function representation.
- **Classification of the many-electron Green functions:** In JAC, the major classification of Green function representations is based on the number of free electrons in the continuum. The many-electron basis must hereby include both, bound-type CSF as well as CSF with up to the maximum number of free electrons, and this CSF basis should be constructed in a systematic manner. **At present, we restrict ourselves to Green function representations with at least $N - 1$ bound electrons and, hence, just up to a single electron in the continuum.**
- **Green function channel:** A channel refers to the set of atomic levels $\{E_{\nu_i}, |\psi_{\nu_i}(\beta_i \mathbb{J}_i)\rangle\}$, all with same total symmetry \mathbb{J}_i . Each Green function representation typically contains several (Green function) channels.
- **Atomic levels in a Green function representation:** The levels in such a many-electron representation formally belong to both, the bound-state spectrum of the atom ($E_{\nu_i} < 0$) as well as to the continuum spectrum (scattering states) with 1, 2, ... electrons in the continuum. All these levels are constructed from a single set of one-electron orbitals, and which has to be properly chosen to represent reasonably well the bound-state levels of the given configurations.

4. Atomic representations

➤ ‘Infinities’ in Green function representations: Already a single-electron Green function generally implies three *infinities* due to the electron’s spatial degrees of freedom, and which are often treated numerically by restricting the principal quantum number $n^{(\max)}$ and the angular momentum quantum numbers $j^{(\max)}$, $m_j^{(\max)}$. An N -fold multiple of such infinities arise for N -electron Green functions and make their approximation a real challenge. In JAC, approximation many-electron Green functions are restricted by:

- orbitals with a principal quantum number $n^{(\max)}$ which applies for to all κ symmetry blocks;
- a specified list of orbital angular momenta $[\ell_1, \ell_2, \dots]$ for the virtual excitations and the generation of all non-relativistic configurations;
- the coupling of the N orbitals to total symmetries J_1, J_2, \dots .

Each of these total symmetries represent a many-electron continuum, and in which the Hamiltonian is still diagonal.

➤ Many-particle Green functions: In atomic and many-particle physics, Green functions often occur as *propagators* to formally represent the (integration over the) complete spectrum of the underlying Hamiltonian. While these functions appear crucial for describing second- and higher-order perturbation processes, they have hardly been considered and classified for complex atoms. In JAC, we show such how relativistic (many-electron) Green functions can be approximated and systematically improved for few- and many-electron atoms and ions.

➤ Many-particle Green functions: In most second- and higher-order computations, the summation (integration) over the complete spectrum of the system remains the most challenging part of all numerical computations owing to large (infinite) number of terms and the occurrence of *free-free* matrix elements in the construction of the intermediate states. The (infinite) summation over the spectrum can be *captured* by means of an approximate Green function.

➤ Approximate (many-electron) Green function: Taking a *pragmatic* viewpoint, an approximate (many-electron) Green function of an atom or ion refers to any properly truncated spectral decomposition

$$G_E(\mathbf{x}_1, \mathbf{x}_2, \dots; \mathbf{x}'_1, \mathbf{x}'_2, \dots) \equiv G_E(\mathbf{X}; \mathbf{X}') = \sum_{\nu} \frac{\langle \mathbf{X} | \alpha_{\nu} J_{\nu} M_{\nu} \rangle \langle \alpha_{\nu} J_{\nu} M_{\nu} | \mathbf{X}' \rangle}{E_{\nu} - E},$$

that is based on relativistic and approximate, many-electron ASF $\langle \mathbf{X} | \alpha_{\nu} J_{\nu} M_{\nu} \rangle$ in position space $\mathbf{X} = \mathbf{x}_1, \mathbf{x}_2, \dots$. This compact notation resembles the (one-electron) Green function above but enables us to readily include the coupling (fine-structure) of the electrons and to enlarge the many-electron Green functions in a systematic manner without any change in the underlying classification of the atomic levels.

➤ Complexity of the (many-electron) Green function: The (pragmatic) definition of the many-electron Green function above “moves” the inherent complexity with the summation and evaluation of transition amplitudes into the construction of the symmetry-adopted CSF bases, their diagonalization as well as the computation of the (so-called) angular coefficients. Apart from the truncation of the $3N$ quantum numbers in the summation above, the term *approximate* also refers to the representation of the ASF $\langle \mathbf{X} | \alpha_{\nu} J_{\nu} M_{\nu} \rangle$ as well as to the detailed pole structure (in the complex plane) in order to account for (additional) boundary conditions.

- **Complexity of the (many-electron) Green function:** Indeed, any well truncated summation can be seen as an approximate many-electron Green function as long as the asymptotic behaviour (of the electron waves with positive energy), the symmetry and *completeness* of the ASF in this expansion can be properly explained. While the one-electron orbitals are readily generated for any (self-consistent) central-field potential, the symmetry of the atomic states $|\alpha_\nu, \mathbb{J}_\nu M_\nu\rangle$ arises, as usual, from the diagonalization of a properly chosen Hamiltonian matrix, and whose set-up and computation may significantly be simplified by using a symmetry-adopted basis of CSF. The “completeness” of the (various spectra of) ASF is of course elusive but can be explained quite similar as for any restricted or complete active-space method. Finally, the asymptotic behaviour of the atomic states for $r_N \rightarrow \infty$ is mainly relevant for the (auto-) ionization and electron capture processes.
- **Channels of the (many-electron) Green function:** If we approximate the (many-electron) Green function by means of a (finite) number of symmetry channels, i.e. properly constructed *sets* of many-electron ASF with well-defined symmetry \mathbb{J} and energetic order, we can select those subspaces (of the many-electron Hilbert space) as appropriate for a particular application. Obviously, this selection and construction of the subspaces requires some physical understanding of the underlying atomic process.
- **(De-) Excitation schemes for (many-electron) Green function:** For most processes, this construction can be made by specifying suitable *schemes* (classes) of virtual excitations or de-excitations with regard to some reference configurations (or states), and are often based on the atomic shell model and the concept of (non-relativistic) electron configurations. These use of reference configurations readily indicates which of the electrons are excited by some process and how many of them may be released into the continuum.
- **Classification of the (many-electron) Green function:** With the assumptions above, each approximate Green function can be classified also in terms of the (maximum) number of free electrons as well as a pre-specified *excitation scheme*. This scheme is then applied in order to generate all (non-relativistic) configurations that are considered in the associated many-electron (CSF) basis.
- **Approaches for constructing approximate (many-electron) Green functions:** Three such approaches are presently designed and (partly) supported by the JAC toolbox. They are based on a:
 - (a) Diagonal CSF basis without any configuration interaction (`SingleCSFwithoutCI`): This is a fast, though very rough, approximation, in which each CSF with total symmetry \mathbb{J} just represents a single level $E_\nu^{(\mathbb{J}_i)}, |\alpha_\nu^{(\mathbb{J}_i)}\rangle$ of the spectrum. In this simple approximation, however, only the diagonal matrix elements of the Hamiltonian need to be computed.
 - (b) Basis that includes configuration interactions only between bound-state orbitals (`CoreSpaceCI`): For each channel \mathbb{J} , a full Hamiltonian matrix is diagonalized for all those CSF that are built only from bound-state orbitals, while just the diagonal matrix elements are estimated for computed for all other CSF with at least *one* free electron, $\varepsilon > 0$.
 - (c) Full Hamiltonian, but where the electron-electron interaction is damped (`DampedSpaceCI`) in the radial coordinate r by a user-specified convergence factor $e^{-\tau r}$. This convergence factor applies to both, the bound and free-electron orbitals. For a proper choice of τ ,

4. Atomic representations

however, this factor mainly affects the interaction with the continuum (and between pseudo-state which are embedded *within* the continuum). The use of such a *damping function* in the Slater integrals (and, possibly also in the Breit integrals — although this has not been realized so far) ensures that the bound-bound, bound-free and free-free interactions are formally treated on equal footings. Further approaches for the (generation of the) Green function channels might be considered in the future if the need arises due to newly emerging applications.

Use:

- Approximate many-electron Green functions play an essential role in studying all second- and higher-order perturbation processes as well as for various dynamic processes in atomic systems. For many-electron atoms and ions, however, the construction of proper Green function approximations is still rare in the literature because of their complexity and the required computational resources. More often than not, Green functions have mainly been used in the past in order to describe either single-electron or quasi-single-electron atoms.
- Using JAC: Generate an `AtomicRepresentation(..., GreenExpansion(approach::Atomic.AbstractGreenApproach, scheme::Basics.AbstractExcitationScheme, levelSymmetries, NoElectrons, greenSettings))` for a given set of reference configurations as well as a specified (Green function) approach, excitation scheme, (list of) level symmetries, number of electrons and settings; cf. `? GreenSettings` or `GreenSettings()`.
- Using JAC: The `approach::Atomic.AbstractGreenApproach` determines how and to which extent correlations among the bound and continuum electrons are taken into account into the Green function representation.
- Using JAC: The `scheme::Basics.AbstractExcitationScheme` determines how and to which extent excitations from the reference configurations into the specified *active* set of orbitals are included into the representation.
- In JAC, further details about the requested Green function can be specified by the maximum principle quantum number $n^{(\max)}$ and a list of orbital angular momenta $[\ell_1, \ell_2, \dots]$ that are allowed within the given (de-) excitation scheme in order to generate the many-electron (CSF) basis. These parameters have to be specified in `GreenSettings(..)`.
- In JAC, the output of a Green (function) expansion is a list of `GreenChannel`'s, i.e. a list of multiplets that are suitable for numerical computations and/or summation over many-electron levels..
- Using JAC, see also the functions: `Basics.generate()`.
- Using JAC: Perform an `Atomic.Computation(..., properties=[Green, ...], configs=[..], greenSettings=GreenFunction.Settings(..), ...)` or call directly functions from the module `GreenFunction`.

- **Green function approaches:** Several approaches are distinguished in JAC in order to determine how the set of many-electron levels $\{E_{\nu_i}, |\psi_{\nu_i}(\beta_i \mathbb{J}_i)\rangle\}$ are to be generated and how much of the electron-electron interaction is to be taken into account in order to represent *both*, the bound and continuum spectra of the atom or ion:
 - (a) **Diagonal CSF basis without configuration interaction (SingleCSFWITHOUTCI):** This is a fast though very rough approximation, in which each CSF with total symmetry $\mathbb{J}_i(\beta_i \mathbb{J}_i)$ also just represents a single level (ψ_{ν_i}) of the spectrum. This approximation fully omits all configuration interactions within the CSF basis (of a fixed \mathbb{J}_i symmetry).
 - (b) **Configuration interaction only between bound-state orbitals (CoreSpaceCI):** This approach diagonalizes (in turn) the Hamiltonian matrices of symmetry $(\beta_i \mathbb{J}_i)$ by including the electron-electron interaction only between bound-state orbitals, while their interaction with and among the free electrons are neglected.
 - (c) **Damped configuration-interaction approach (DampedCI):** This approach again diagonalizes the Hamiltonian matrices of symmetry $(\beta_i \mathbb{J}_i)$ by **including the electron-electron interaction for all pairs of electrons but damped by some exponential factor $e^{-\tau r}$** . The use of such a *damping function* in the Slater integrals (and, possibly the Breit integrals – although this has not been realized so far) ensures that the bound-bound, bound-free and free-free interactions are treated equally without that a *continuation* of the continuum orbitals for $r \rightarrow \infty$ need to be considered in the numerical evaluation of the radial integrals.
- **(De-) Excitation schemes of electrons for the representation of approximate Green functions:** Since many-electron Green functions are very complex entities with many ‘infinities’ involved already within their formal definition, **further control about the generation of such Green function approximations is obtained by specifying a proper (de-) excitation scheme of the electrons** with regard to the given configurations:
 - (i) **(De-) excitation of a single electron from a given set of (nonrelativistic) configurations (DeExciteSingleElectron):** Cf. section 3.3
 - (*) Further (de-) excitation schemes will be implemented as the needs arises in selected applications.

Green functions for scattering processes:

- **Green functions for the study of scattering processes:** Formally, most scattering processes can be analyzed by solving the Schrödinger equation for some given many-electron Hamiltonian \mathbb{H} , the collision energy E and by including the proper scattering boundary conditions

$$\mathbb{H} |\Psi^+\rangle = E |\Psi^+\rangle.$$
- **Lippman-Schwinger representation:** A formal solution to the Schrödinger equation above is given by the Lippman-Schwinger equation which provides an integral form of the scattering wave function $|\Psi^+\rangle$ in terms of the initial state $|\Psi_o\rangle$ and the many-electron Green

4. Atomic representations

function $\mathbb{G}^+(E)$ (cf. Tong *et al.*, 2009)

$$|\Psi^+\rangle = |\Psi_o\rangle + \frac{1}{E - \mathbb{H} + i\eta} \mathbb{V} |\Psi_o\rangle + \dots = |\Psi_o\rangle + \mathbb{G}^+(E) \mathbb{V} |\Psi_o\rangle + \dots .$$

Here, $\eta > 0$ is a small positive infinitesimal which ensures that the boundary conditions of an outgoing wave are properly taken into account, and where a (radiative) loss rate can be incorporated into the representation of $|\Psi^+\rangle$ by means of a complex energy E .

- **Green function with optical potential:** The Green function of the scattering system with total scattering energy E can be formally written as

$$\mathbb{G}^+(E) = \sum_{\nu} \frac{|\psi_{\nu}\rangle \langle \psi_{\nu}|}{E - E_{\nu} + i\eta},$$

and where the summation runs over all (generalized) eigenfunctions of the Hamiltonian \mathbb{H} . This Green function can be utilized also for many scattering and dynamical processes if just a proper (sub-) set of many-electron levels $\{E_{\nu}, |\psi_{\nu}\rangle\}$ is taken into account.

- **Optical potential:** If a proper optical potential is added to the (inner-) atomic potential, the outgoing wave is formally absorbed due to the occurrence of complex single-electron energies. Tong *et al.* (2009) suggest an energy-dependent optical potential of the form

$$V^{(\text{optical})}(r; \varepsilon) = \begin{cases} 0 & \text{for } r < r_c \\ V_o \left(\frac{r - r_c}{r_{\max} - r_c} \right) & \text{for } r \geq r_c \end{cases}, \quad \frac{\varepsilon^{1/2}}{r - r_c} < V_o < \varepsilon^{1/2} (r_{\max} - r_c),$$

and where the optical potential becomes *nonzero* at r_c . However, little experience exists so far how the parameters r_c , r_{\max} , ε need to be chosen in order to obtain a realistic representation of the Green function, and how useful such an approximation is in different physical contexts.

- **Diagonalization of the Hamiltonian matrix with an optical potential:** For an optical potential, the **Hamiltonian matrix is no longer hermitian but symmetric complex**, and it generally includes both diagonal and off-diagonal matrix elements due to the electron-electron interaction. From the diagonalization of the Hamiltonian matrix in a CSF basis with well-defined total symmetry \mathbb{J}_i , one then obtains the eigenenergies $\{E_{\nu}\}$ and (atomic) eigenvectors $\{E_{\nu_i}, |\psi_{\nu_i}\rangle\}$, but which need to be calculated just once.

4.2. In JAC partly-implemented atomic representations

4.2.a. Multi-configuration Dirac-Hartree-Fock (MCDHF) expansions (Atomic)

Use & notations:

- Multi-configuration Dirac-Hartree-Fock (MCDHF) method: This method has been found a versatile tool for calculating the level structure and approximate wave functions for atoms and ions of all elements across the periodic table. In contrast to the CI method above, both the radial (one-electron) functions as well as the expansion coefficients $\{c_r(\alpha), r = 1, \dots, n_c\}$ are optimized simultaneously on the basis of the Dirac-Coulomb Hamiltonian.
- Using JAC: Generate an `Atomic.Representation(..., McdhfExpansion(ciSettings))` for a given set of reference configurations and given settings; cf. `? McdhfSettings` or `McdhfSettings()`.
- Using JAC, see also the functions: `Basics.generate()`.
- Steps for practical MCDHF computations: In the MCDHF method and in JAC as well, the atomic bound states are typically generated by a series of steps:
 - Definition of the nuclear parameters as well as the angular structure (and extent) of the CSF basis $\{|\gamma PJM\rangle\}$ in the MCDHF ansatz;
 - Algebraic evaluation and computation of the spin-angular integrals (the so-called angular coefficients), based on standard techniques from Racah's algebra;
 - Generation or collection of proper radial start orbitals and self-consistent field (SCF) calculations, based on the Dirac-Coulomb Hamiltonian;
 - Configuration interaction (CI) calculations in order to incorporate further relativistic contributions into the Hamiltonian matrix and/or to enlarge the CSF basis beyond the given SCF model.

Often, these four steps are repeated at several stages by systematically enlarging the one-electron (active) orbital space.

- Radiative corrections: There are two dominant corrections for all medium and heavy elements which arise from QED; cf. section 3.6. When compared to missing correlation contributions, these QED corrections are relevant only if the inner-shell electrons of these elements are involved in some (atomic) property or process, and they are often negligible otherwise, at least as the present level of computational accuracy.

4. Atomic representations

- **Other MCDHF codes:** During the last decades, a number of codes have became available, which implement the MCDHF method for free atoms and ions and which provide the approximate energies and wave functions for atomic bound states. For example, GRASP2K and later versions of the former Oxford package (Jönsson *et al.* 2013, 2018) now facilitate large-scale computations and supports wave function expansion of up to or beyond a million CSF as required for many open-shell atoms.
- **MCDHF method:** In this variational method, both the radial (single-electron) **orbital functions and the mixing coefficients are optimized on a (predefined) energy expression**. Often, this energy expression is given by a weighted sum of expectation values of some atomic Hamiltonian with regard to a geometrically-selected set of basis states for the atom or ion of interest. The systematic enlargement of this many-electron basis requires however to use non-spectroscopic (virtual) orbital functions, which just represent 'corrections' to the atomic state functions and which cannot be interpreted physically and independent of the chosen many-electron basis. In atomic and molecular physics, these corrections mainly arise from the **cusp condition** due to the singularities in the (pairwise) electron-electron interaction.
- **MCDHF method:** The introduction and use of systematically-enlarged wave function expansions have significantly improved the performance of the MCDHF method. More often than not, these expansions are based on (all) single and double (SD) excitations from a multi-reference (MR) set of generating configurations or expansions into a restrictive set of active orbitals; cf. section refsect:representation-RAS.

4.2.b. Combined configuration interaction & perturbation theory (CI-PT) expansions (...)

Formal representation:

- **Combined CI-PT method:** While the **diagonalization of the many-electron Hamiltonian matrix** is perhaps the simplest way to take electronic correlations into account, only very few core excitations can typically be included by the CI method. In practice, further correlations between the valence and core electrons can be calculated and incorporated into the CI matrix by means of many-body perturbation theory (MBPT). Of course, no correlations between the core and valence electrons are included if excitations from the core are prohibited.
- **CI-PT method:** In this method, most of the weakly-correlated many-electron basis states (usually with rather high excitation energy) are not directly included into the diagonalization of the CI matrix but are treated instead perturbatively (Dzuba *et al.*, 2017). This approach significantly reduces the size of the CI matrix and, hence, removes one of the major limitations of this method for any larger number of valence electrons.
- **CI+MBPT calculations:** The CI+MBPT method tries to combine the complementary strengths of the two methods. In particular, this combination requires a **proper partitioning of the orbital space into core electrons, that are kept inert, and valence electron**. With such a partitioning, the valence-valence correlations are treated by the CI methods, while the core-valence and core-core correlations are computed by means of MBPT techniques. In the CI computations, moreover, additional corrections can be included perturbatively in first or higher order in order to obtain well-correlated wave functions.
- **Partitioning of CI spaces:** In the CI-PT method, all CSF $\{|\gamma_r \mathbb{J} M\rangle, r = 1, \dots, N_c\}$ as many-electron basis are assumed to be ordered in energy and divided into the (CI) model space P with $r = 1, \dots, N_p$ CSF and a complementary space Q with $N_q = N_c - N_p$ CSF, and for $r = N_p + 1, \dots, N_c$. The CI matrix ($H_{rs} \equiv \langle \gamma_r \mathbb{J}_r M_r | H | \gamma_s \mathbb{J}_s M_s \rangle, r, s = 1, \dots, N_p$) is diagonalized only within the P space, while all off-diagonal matrix elements from the Q space are neglected.
- **Effective CI matrix:** For the coupling between the P and Q spaces, all off-diagonal matrix elements ($H_{rs}, r = 1, \dots, N_p, s = N_p + 1, \dots, N_c$) as well as all diagonal matrix elements ($H_{ss}, s = N_p + 1, \dots, N_c$) are taken into account explicitly in terms of an **effective CI matrix with modified matrix elements**:

$$H_{rs} \longrightarrow H_{rs} + \sum_k \frac{\langle r | H | k \rangle \langle k | H | s \rangle}{(E - E_k)}, \quad N_p < k \leq N_p + N_Q.$$

In these matrix elements, E formally refers to the (exact) energy from the many-electron SE. Owing to the overall symmetry of the Hamiltonian, this effective CI matrix can be computed and solved independently for each level symmetry \mathbb{J} of interest.

4. Atomic representations

- **Iteration of the effective CI matrix:** Since the exact energy E is not known, it need to be initially replaced by some proper approximation $E \rightarrow E^{(0)}$ and, hence, the **set-up and diagonalization of the effective CI matrix need to be solved iteratively**, using the CI energy $E^{(t)}$, $t = 0, \dots$ from the previous iteration. If more than one level of symmetry J is required, this iteration of the effective CI matrix need to be done separately because of the different energies $E^{(t)}(\alpha J) \rightarrow E(\alpha J)$, making the approach much less efficient. Moreover, the **use of different energies $E(\alpha J)$ in the effective CI matrix results in ASF that are not quite orthogonal to each other**.
- **CI+MBPT method for open d-shell elements:** A combination of configuration interaction and many-body perturbation theory (CI+MBPT) has been applied to accurately treat neutral thallium as a three-valence-electron atom. The same method might be utilized for four- and even five-valence-electron systems, although these computations become less accurate as more (open-shell) electrons are involved. The extension of the CI+MBPT method towards particle-hole interactions might help improve the accuracy of such level energy calculations.
- **Energy correction from the Q space:** In second-order perturbation theory, the (energy) correction to a level (αJ) is given by (Kozlov *et al.*, 2022)

$$\Delta E(\alpha J) = \sum_{\nu} \frac{\langle \alpha J | P \mathbb{H} Q | \alpha_{\nu} J_{\nu} \rangle \langle \alpha_{\nu} J_{\nu} | Q \mathbb{H} P | \alpha J \rangle}{E(\alpha J) - E_{\nu}}$$

and where $(\alpha_{\nu} J_{\nu})$ are states from the complementary Q space.

Use & notations:

- **Using JAC:** Perform an `Atomic.Computation(.., properties=[Green, ..], configs=[..], greenSettings=GreenFunction.Settings(..), ..)` or call directly functions from the module `GreenFunction`.
- **In JAC, we provide**
- The CI-PT method can be easily applied if: (i) only a few low-lying levels are required with a large projection within the chosen P space already, (ii) all many-electron CSF are ordered in terms of their energy and (iii) if there is a reasonable *energy gap* between the CSF included directly into the CI matrix and those treated perturbatively. In practice, these conditions mean that the perturbative summation over the high-energy CSF must overall result in a rather small correction; the method fails if these conditions are not fulfilled.
- **Parallelization:** Since the summation over the high-energy CSF is very time-consuming but need to be performed independently for each matrix element, the CI-PT method is very suitable for parallel computations.

Applications:

- Such a combined CI and perturbation theory (CI-PT) treatment has been applied especially for (super-) heavy elements and multiply-charged ions with open p , d - and f -shells. Because of the particular shell structure, many of these multiply- and highly-charged ions have optical transitions near to their ground level and might be sensitive to **physics beyond the standard model**. This refers to possible variations of the fine-structure constant or violations of the (local) Lorenz invariance and Einstein equivalence principle as well as to potential interactions with dark matter.
- Two multiply-charged ions have been considered in the search for time variations of the fine-structure constant; these are Ir¹⁷⁺ ions with a $4f^{13} 5s$ and Ho¹⁴⁺ ions with a $4f^6 5s$ ground configuration.
- Dzuba *et al.* (2017) apply the V^{N-M} approximation in order to generate the initial Dirac-Hartree-Fock basis for the CI-PT procedure. In this approximation, only the core-shell electrons are included into the Dirac-Hartree-Fock, while all valence-shell are treated a *virtual* at this step of the computation. However, the set-up of the CI matrices then follows the standard procedure by using the orbitals from the Dirac-Hartree-Fock orbitals from the single-electron basis.
- Owing to the effective completeness of B-splines, Dzuba and Johnson (1998) showed for the low-lying levels of barium that a combined CI-MBPT method may significantly improve the convergence and numerical accuracy of many-electron computations.

4.2.c. Fast configuration interaction & perturbation theory (FCI-PT) expansions (. . .)

Formal representation:

- **Fast CI:** Dzuba *et al.* (2019) suggest a further modification to the CI-PT method from above which is termed fast configuration interaction (fast CI). In this modification, the denominator in the perturbative sum of the CI-PT method is approximated by $|E - E_k| \approx |E - E_c|$, where E_c denotes some mean configuration energy of the basis state $|k\rangle$. This approximation enables one to re-write the summation as

$$\sum_k \frac{\langle r | H | k \rangle \langle k | H | s \rangle}{(E - E_k)} \approx \sum_{\text{configurations}} \frac{1}{E - E_c} \sum_{k_c} \langle r | H | k_c \rangle \langle k_c | H | s \rangle, \quad N_p < k \leq N_p + N_Q.$$

- While, at the first glance, this seem to make not much difference to the CI-PT method, it can considerably accelerate the computation of the second summation $\sum_{k_c} \langle r | H | k_c \rangle \langle k_c | H | s \rangle$. Such a simplification is possible for the evaluation of the many-electron matrix elements, since all the matrix elements can be traced back to a rather small number of radial integrals *times* some angular coefficients which only depend on the configuration but not on the detailed coupling of the basis states. Moreover, the mean configuration energy can also be expressed in terms of simple radial matrix elements or computed numerically just from the trace of the corresponding submatrix.

4. Atomic representations

- A similar reduction in computation time might be obtained however by a careful arrangement of the many-electron basis states $|k\rangle$ and by the re-use of angular coefficients and radial integrals.

Use & notations:

- Using JAC: Perform an `Atomic.Computation(.., properties=[Green, ..], configs=[..], greenSettings=GreenFunction.Settings(..), ..)` or call directly functions from the module `GreenFunction`.
- In JAC, we provide
- Because of the rapid increase in the computational costs, a reasonable active space can be applied in (standard) CI expansions only for a moderate number of (active) valence electrons, often not more than for 3-4 valence electrons above of closed shells otherwise.

4.3. Further atomic representations, not yet considered in JAC

4.3.a. Many-body perturbation theory

Formal representation:

- **Decomposition of the Hamiltonian operator:** The standard perturbation theory starts from a suitable decomposition of the total Hamiltonian \mathbb{H} , and where solutions to \mathbb{H}_o are supposed to be known for a complete set of many-particle states.

$$\mathbb{H} = H_o + V, \quad \mathbb{H}_o \phi_n^{(0)} = E_n^{(0)} \phi_n^{(0)}, \quad V_{mn} = \langle \phi_m^{(0)} | V | \phi_n^{(0)} \rangle.$$

- Expansion for energies and wave functions:

$$E_n = E_n^{(0)} + E_n^{(1)} + E_n^{(2)} + \dots; \quad \phi_n = \phi_n^{(0)} + \phi_n^{(1)} + \dots$$

$$E_n^{(1)} = V_{mn}, \quad \phi_n^{(1)} = \sum_{m \neq n} \frac{\langle \phi_m^{(0)} \rangle V_{mn}}{E_n^{(0)} - E_m^{(0)}} \\ E_n^{(2)} = \sum_{m \neq n} \frac{V_{nm} V_{mn}}{E_n^{(0)} - E_m^{(0)}}, \quad \phi_n^{(2)} = \sum_{m, p \neq n} \frac{\langle \phi_m^{(0)} \rangle V_{mp} V_{pn}}{(E_n^{(0)} - E_m^{(0)}) (E_n^{(0)} - E_p^{(0)})} - E_n^{(1)} \sum_m \frac{\langle \phi_m^{(0)} \rangle V_{mn}}{(E_n^{(0)} - E_m^{(0)})^2}.$$

In general, however, it is by far not easy to apply the formalism above to many-electron system due to the degeneracy of the zero-order solutions and a rather sophisticated book-keeping.

- **Basic steps of many-body perturbation theory (MBPT):** If we assume the decomposition from above and can express the **unperturbed Hamiltonian \mathbb{H} as a symmetric one-particle operator**, the solutions to \mathbb{H} are given by (orthogonormal) Slater determinants $\{\Phi_a\}$

$$\mathbb{H} = H_o + V, \quad \mathbb{H}_o = \sum_i h_o(\mathbf{r}_i), \quad \mathbb{H}_o \Phi_a = E_a^{(0)} \Phi_a, \quad \langle \Phi_a | \Phi_b \rangle = \delta_{ab}.$$

- **Slater determinants Φ_a** can be readily built from the one-electron functions ϕ_k : $h_o \phi_k = \varepsilon \phi_k$.

- **Goal of MBPT:** Solutions of the Schrödinger equation $H \Psi_a = E_a \Psi_a$ for a finite number $a = 1, \dots, d$ of atomic states.

4. Atomic representations

- **Model space:** $\mathcal{M} = \text{span}\{\Phi_a, a = 1, \dots, d\}$; all other solutions Φ_r of \mathbb{H}_o with $\Phi_r \notin \mathcal{M}$ lay in the (complementary) space that is orthogonal to \mathcal{M} .
- **1-dimensional model space:** For a 1-dimensional model space with the two projectors $P = |\Phi_a\rangle\langle\Phi_a|$ and $Q = 1 - |\Phi_a\rangle\langle\Phi_a| = \sum_{r \neq a} |\Phi_r\rangle\langle\Phi_r|$, the energy corrections and wave function can be written as

$$|\Psi_a\rangle = |\Phi_a\rangle + |\Psi_a^{(1)}\rangle + |\Psi_a^{(2)}\rangle + \dots, \quad E = E^{(0)} + E^{(1)} + E^{(2)} + \dots$$

- **Projection operator:** Obviously, the projection operator commutes with \mathbb{H}_o ; if Ψ_a is known, Φ_a just refers to the projection of the exact solution upon the model space. More general, the projection operator fullfil the standard relations:

$$P = \sum_{a \in \mathcal{M}} |\Phi_a\rangle\langle\Phi_a|, \quad Q = 1 - P = \sum_{r \notin \mathcal{M}} |\Phi_r\rangle\langle\Phi_r|, \quad \Phi_a = P\Psi_a$$

$$P = P^+ = P^2, \quad PQ = QP = 0, \quad [P, \mathbb{H}_o] = [Q, \mathbb{H}_o] = 0$$

- **Wave operator (Möller, 1945):** One can formally define the (opposite) operator Ω that maps the state in the model space upon the exact state, although Ω and P are not *inverse* operators.

$$\Psi_a = \Omega \Phi_a$$

- **Generalized Bloch equation:** Using the definitions above and the (so-called) intermediate normalization, the Schrödinger equation can be

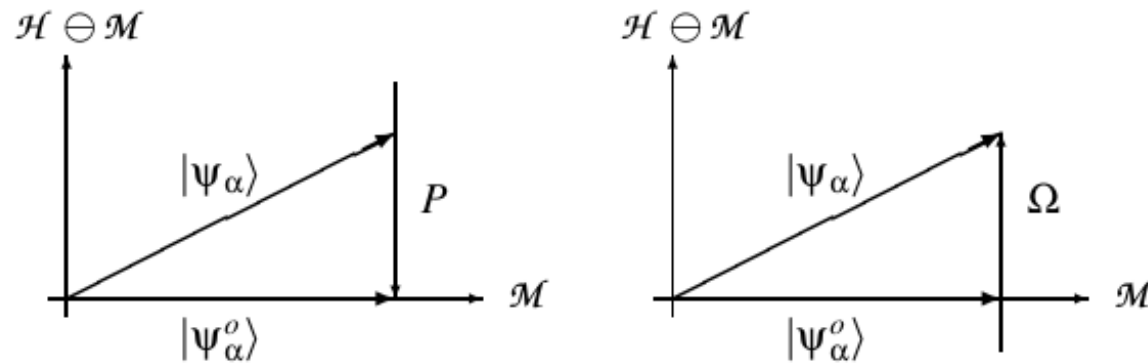


Figure 4.1.: Simplified representation of the operators P and Ω in IN. The projector P transforms a d -dimensional space $\{\Phi_a, a = 1, \dots, d\}$ of the Hilbert space into the model space \mathcal{M} of the same dimension. The wave operator Ω reverses this transformation. Note, however, that P and Ω are **not inverse operators**.

re-formulated as operator equation (Lindgren and Morrison, 1978):

$$\begin{aligned}
 \langle \Psi_a | \Phi_a \rangle &= \langle \Phi_a | \Phi_a \rangle = 1 \iff P = P \Omega P \\
 \cdot \Omega P | &\quad \Omega P \mathbb{H}_o \Psi^a + \Omega P V \Psi_a = E_a \Omega P \Psi_a \\
 - \mathbb{H}_o \Omega P \Psi_a + V \Omega P \Psi_a &= E_a \Omega P \Psi_a \\
 (\Omega \mathbb{H}_o - \mathbb{H}_o \Omega) P \Psi_a + (\Omega P V \Omega P - V \Omega P) \Psi_a &= 0 \quad \forall a = 1, \dots, d \\
 [\Omega, \mathbb{H}_o] P &= (V \Omega - \Omega P V \Omega) P
 \end{aligned}$$

For the states of interest $\{\Psi_a, a = 1, \dots, d\}$, this equation is completely equivalent to Schrödinger's equation. Instead an equation for the wave function, we now have an (operator) equation for the wave operator Ω .

4. Atomic representations

➤ Expansion of the wave operator: $\Omega = 1 + \Omega^{(1)} + \Omega^{(2)} + \dots$ gives rise to

$$[\Omega^{(1)}, H_o] P = Q V P$$

$$[\Omega^{(2)}, H_o] P = Q V \Omega^{(1)} P - \Omega^{(1)} V P$$

⋮

$$[\Omega^{(n)}, H_o] P = Q V \Omega^{(n-1)} P - \sum_m^{n-1} \Omega^{(n-m)} V \Omega^{(m-1)} P$$

➤ Second quantization: The operators H_o, V, Ω, \dots can be written also quite easily in second quantization and can be utilized for the (complex) coefficients $x_j^{i(1)}$ and $x_{kl}^{ij(1)}$

$$\Omega^{(1)} = \sum_{ij} a_i^+ a_j x_j^{i(1)} + \sum_{ijkl} a_i^+ a_j^+ a_k a_l x_{kl}^{ij(1)}$$

4.3.b. Complex-scaling method

Formal representation:

➤ Complex scaling: This scaling method is based on the global rotation of all radial coordinates $\vartheta, r \rightarrow r e^{i\vartheta}$. This rotation generally transforms hermitian into non-hermitian Hamiltonians whose (bound) eigenstates then describe both, bound and resonant states of the quantum system. The resonant states have complex energies whose imaginary part describe the width (lifetime) of the resonances (with regard to autoionization).

Use & notations:

➤ Boundary conditions become irrelevant: Since a complex-scaled function vanishes for $r \rightarrow \infty$, a representation of the resonances can be obtained by diagonalizing the rotated Hamiltonian within a square-integrable basis, and without taking special care of the boundary conditions.

- **Rotation of the Hamiltonian:** A rotation of the radial coordinates by an angle ϑ is possible only, if the potential is (so-called) *dilatation-analytic*. While this is the case for any reasonable atomic Hamiltonian, this property is not necessarily fulfilled for pseudo- or polarization potentials, which can either be nonanalytical or even diverge within the complex plane for small values of ϑ (Fossez *et al.*, 2015).
- **Exterior complex scaling:** The (so-called) infinite-range exterior complex scaling method provides an efficient tool for modelling an absorbing boundary in (time-dependent) many-electron calculations, such as many-electron atoms in an intense laser pulse. The exterior complex scaling is based on the transformation: $r \rightarrow z(r) = R + r e^{i\vartheta}$.

4.3.c. Many-electron scattering functions

Formal representation:

- **Scattering functions within the vicinity of an isolated resonance:** For a given (positive) energy E of the stationary Schrödinger equation with Hamiltonian $\mathbb{H} = \mathbb{H}_o + \mathbb{V}$, the exact scattering solution in the vicinity of an isolated resonance can be written as superposition of a localized component $|\psi_o\rangle$ and unbound components $|\phi(\mathbf{r}; E)\rangle$ as (Nicolaides and Themelis, 1992)

$$(\mathbb{H} - E) |\psi(\mathbf{r}; E)\rangle = 0,$$

$$\mathbb{H} |\psi_o\rangle = E_o |\psi_o\rangle$$

$$\begin{aligned} |\psi(\mathbf{r}; E)\rangle &= a(E) |\psi_o\rangle + \int dE' b(E'; E) \phi(\mathbf{r}; E') \\ &= a(E) \left(|\psi_o\rangle + \mathcal{P} \int dE' \frac{|\phi(\mathbf{r}; E)\rangle \langle \phi(\mathbf{r}; E)| \mathbb{H} | \psi_o\rangle}{E - E'} + c(E) |\phi(\mathbf{r}; E)\rangle \langle \phi(\mathbf{r}; E)| \mathbb{H} | \psi_o\rangle \right) \\ E &= E_o + \mathcal{P} \int dE' \frac{|\langle \phi(\mathbf{r}; E) | \mathbb{H} | \psi_o\rangle|^2}{E - E'} + c(E) |\langle \phi(\mathbf{r}; E) | \mathbb{H} | \psi_o\rangle|^2 \end{aligned}$$

Here, E is a real number on the positive energy axis and not an eigenvalue.

4.3.d. Berggren expansion method

Formal representation:

- Berggren expansion method (BEM): In this single-particle method, (complex-energy) resonance states are described by a particular completeness relation for bound, decaying and scattering states, first introduced by Berggren in 1968. Because of the quasi-localized nature of the single-particle states, the BEM method does not require a precise treatment of the boundary conditions at infinity.
- Completeness relation of Berggren ensembles: A (single-particle) Berggren ensemble satisfies for each partial wave κ the relation

$$\sum_{n \in b,d} |u_{n\kappa}\rangle \langle u_{n\kappa}| + \int_{\mathcal{L}_\kappa^+} |u_{\varepsilon\kappa}\rangle \langle u_{\varepsilon\kappa}| = 1.$$

Here, $|u_{n\kappa}\rangle$ are the radial wave functions of the bound (b) and decaying (d) states, while $|u_{\varepsilon\kappa}\rangle$ represent scattering states, and \mathcal{L}_κ^+ denotes the contour that encompasses the decaying states in the fourth quadrant of the complex ϵ -plane.

- Coupled-channel formalism: A Berggren ensemble represents a single-particle spectrum in the vicinity of some resonance and can be combined quite easily with the coupled-channel method in order to describe (resonant) behaviour in nuclei, atoms and molecules.

Use & notations:

- Berggren ensemble: This ensemble refers to the single-particle spectrum of a Hamiltonian with complex eigenvalues; it generally contains bound (b), decaying (d), and scattering (s) single-particle states along the contour \mathcal{L}_κ^+ for each partial wave κ .
- Slater determinants built from a Berggren ensemble: The Berggren single-particle states can be also utilized to construct a many-particle basis, in which the (many-particle) Hamiltonian is diagonalized. This scheme has so far been applied especially in nuclear-structure theory in order to describe the behaviour of valence nucleons outside of a closed core. Since the contour of the Berggren ensemble is discretized, the same applies also to the many-body basis that is spanned from this ensemble.
- Gamow shell model (GSM): This model is an extension of the traditional nuclear shell model with complex-energy single-particle states. In this model, a single-particle Berggren basis is generated in a finite-depth potential, independent for each partial wave κ , and then comprises Gamow (or resonant) discrete states as well as the nonresonant scattering continuum.

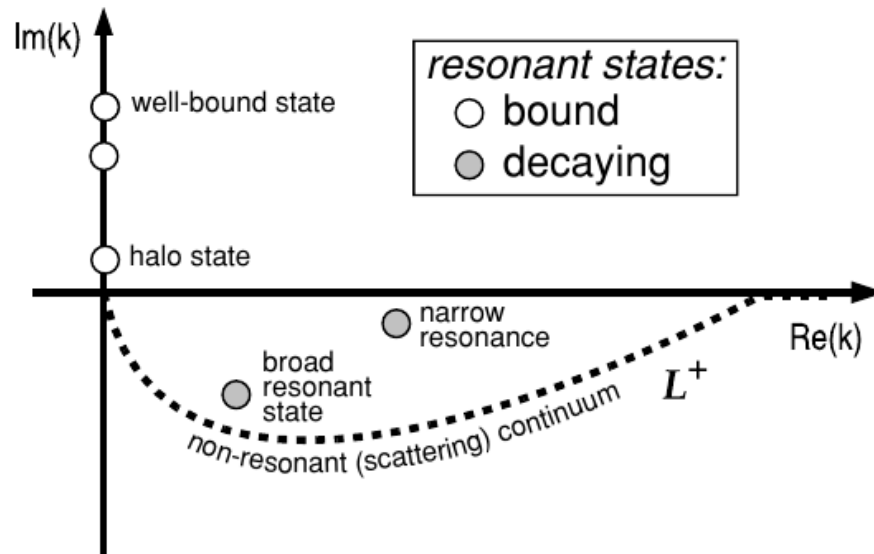


Figure 4.2.: Illustration of the Berggren ensemble in the complex k -plane. While the bound states are all located on the positive imaginary axis, the weakly bound halo states lay close to the origin and the positive-energy resonant states in the fourth quadrant. All states with a small imaginary part can be interpreted as resonances. The complex- k shells on the contour L^+ represent the nonresonant scattering continuum. From Rotureau *et al.* (2009).

- **Complex-energy Gamow shell model (GSM):** The structure and representation of weakly bound and unbound nuclear states close to **particle drip lines** has attracted much recent interest in nuclear physics. A proper treatment of these states goes beyond the traditional shell model, which makes only use of localized states, but requires to allow particle emission. The GSM enables one to describe resonant and nonresonant many-body states on equal footing (Jaganathan *et al.*, 2017).

Applications:

- Fossez *et al.* (2015) applied the Berggren expansion method to parts of the unbound spectrum of dipolar molecules and achieved both, a much higher accuracy for the representation of the weakly-bound as well as the unbound resonance states.
- **Structure of light nuclei:** Light nuclei have been traditionally applied to test microscopic nuclear structure models. The work by Lane (1955)

4. Atomic representations

and Kurath (1956) on p -shell nuclei have become a cornerstone of nuclear structure theory and provided great guidance to analyzing the wealth of spectroscopic data on energy levels, electromagnetic transitions, nuclear moments, and various particle decays during the past decades (Jaganathan *et al.* 2017).

4.3.e. Convergent close-coupling (CCC) method

Formal representation:

- **Coupled-channel equations:** For scattering problems, the convergent close-coupling method refers to a reformulation of the SE in terms of an **infinite set of coupled-channel equations**. This reformulation assumes a complete set of target states.
- The Convergent Close-Coupling (CCC) method has been worked out originally in order to compute accurate cross sections for the scattering of light projectiles on (quasi-) one- and two-electron targets. In the original representation of this method, the scattering wavefunctions are often given in momentum space and are based on the Lippmann-Schwinger equation.
- **Advantages of the CCC method:** This method enables one to treat the many-particle continuum systematically by means of square-integrable functions. In particular, the CCC starts from an expansion of the target into a complete set of orthogonal L^2 functions to span the Hilbert space.

Use & notations:

- **Difficulties with the CCC method** The continuum channels at *intermediate* energies are particularly important and need to be well represented in their coupling to other channels.
- **Convergence:** Convergence in the scattering amplitudes can (and need to be) shown as the size of the square-integrable functions increases.

4.3.f. Density-matrix renormalization group (DMRG) method

Formal representation:

- **Ab-initio DMRG method:** This method can be described either in terms of the renormalization group and renormalized operators, and as it was formulated originally, *or* by means of **matrix product states and matrix product operators (MPS & MPO)**, a more recent language. These two languages use different vocabularies and appear to be quite different in their formulation (Chan *et al.*, 2016).
- **Use of MPS & MPO language:** The power of this language consists in new perspectives and algorithms, rather than in just re-writing the original renormalization group operator (RGO) language. For example, the algebra of the MPS & MPO language provides various new operations beyond the scalar computation of expectation values, and which can be utilized for instance to describe time evolutions.
- **Matrix product state (MPS):** For a given quantum many-particle system, the MPS generally refer to some **low-rank decomposition of the full interaction matrix**. In atomic physics and quantum chemistry, this matrix is **known also as the (full) configuration-interaction matrix or tensor**.
- In atomic physics and elsewhere, the **DMRG method provides a nonperturbative scheme that is useful to replace the (full) configuration interaction method in restricted active spaces**.
- The DMRG method has attracted increasing interest in quantum chemistry during the past two decades.
- **Density-matrix renormalization group (DMRG):** This method can be applied to generate approximate many-particle wave functions and energies with well-defined uncertainties. Apart from the accuracy of the state vectors, the DMRG methods provides a simple access to operators and their expectation values in second-quantized form.
- **Density-matrix renormalization group (DMRG):** This method can be applied to generate approximate many-particle wave functions and energies with well-defined uncertainties. Apart from the accuracy of the state vectors, the DMRG methods provides a simple access to operators and their expectation values in second-quantized form.

Use & notations:

- **Matrix product ansatz:** The power of the DMRG method mainly arise from the **matrix product ansatz** which enables one to express the low entanglement nature of one- or few-dimensional low-energy quantum eigenstates, including the ground-state (Chan *et al.*, 2016).
- **Dimension of MPS:** The (virtual) dimension of the MPS designates the rank of the decomposition and, hence, the dimension of many-body Hilbert subspace that is taken into account. In the DMRG method, this dimension can be increased systematically until numerical convergence is reached (Wouters and van Neck, 2014).

4. Atomic representations

- **Left- and right-bases:** To support a simple translation from the renormalization-group operators to the MPS & MPO language (and back, if requested), emphasis must be placed to the relation between the left- and right-bases *and* the tensors in the MPS & MPO language. Moreover, these relations need to be worked out for (i) the renormalized wavefunctions, (ii) the representation of the Hamiltonian, (iii) the minimization of energies as well as (iv) for the evaluation of expectation values within these two schemes.
- **Difficulties in 2D and 3D:** The DMRG has difficulties with achieving good accuracy for two- and three-dimensional systems since the need of computational resources increase more or less exponentially with system size. From a detailed comparison of 1D and 2D lattices, it was recognized that this behaviour is **closely related to scaling of entanglement in many-body states** as described, for instance, by the area laws (Schollwöck 2011).

Matrix product states:

- **Matrix product states (MPS):** These product states refer to a particular wavefunction representation that help define the variational space of the DMRG. For an orthonormal Fock-space basis $\{|n_1 n_2 \cdots n_K\rangle\}$ of K orbitals (including spin labels), an atomic wave function is written in **occupation representation** as

$$|\psi\rangle = \sum_{n_1 n_2 \cdots n_K} \psi^{n_1 n_2 \cdots n_K} |n_1 n_2 \cdots n_K\rangle .$$

For a fixed particle number N , moreover, we have the condition

$$\psi^{n_1 n_2 \cdots n_K} = \begin{cases} \psi^{n_1 n_2 \cdots n_K} & \sum_{k=1}^K n_k = N \\ 0 & \text{else.} \end{cases}$$

- **MPS amplitudes:** For any state of the atom or ion, the wavefunction amplitude can be written

$$\psi^{n_1 n_2 \cdots n_K} = \sum_{\{\alpha_k\}} A_{\alpha_1}^{n_1}[1] A_{\alpha_1 \alpha_2}^{n_2}[2] \cdots A_{\alpha_{K-1}}^{n_K}[K]$$

as a product of $M \times M$ matrices $A^{n_k}[k]$, of equal dimension, apart from the $1 \times M$ leftmost and $M \times 1$ rightmost matrices. This particular construction of the MPS ensures that the matrix product always results in the *scalar* amplitude $\psi^{n_1 n_2 \cdots n_K}$. In a non-relativistic formulation, moreover, the dimension of these matrices is $2 \times M \times M$ if the spin-index of the (spin-) orbitals is taken into account.

- **MPS bond dimension M :** The number of renormalized states gives rise to the dimension M of the matrices and makes the representation of the state with increasing M more flexible. **For bound-state systems, it can be assumed that the matrices $A^{n_k}[k]$ are all real.**

- **Graphical representation of MPS:** A general wavefunction amplitude can always be represented graphically as a tensor with K legs, while the MPS as a whole is just represented by a connected set of 2-index and 3-index tensors, each associated with a certain site. In addition, graphical rules can be derived to contract the tensors in various ways.
- **DMRG sweep algorithm:** The MPS & MPO language also suggests a new formulation of the *ab-initio* DMRG sweep algorithm itself (Chan *et al.*, 2016).

Applications:

- The entanglement perspective of the DMRG method made it possible to extent its application towards new fields, such as matrix product operator representations, the time-evolution of atoms and molecules, infinite systems, systems at finite temperatures as well as towards higher-dimensions. In addition, the language of matrix product and tensor network states is nowadays quite widely applied to reason about the structure of many-particle quantum states (Chan *et al.*, 2016).
- Earlier *ab-initio* DMRG applications in quantum chemistry have mainly focused upon level and excitation energies as well as reduced density matrices, which can be computed stepwise by running through all orbitals.
- **1D spin chains:** The DMRG method has been found a versatile tool especially for simulating the static and dynamical behaviour of strongly correlated 1D quantum lattice systems (Schollwöck 2011). The use of MPS, in particular, has lead to a much deeper understanding of the DMRG method itself including both, its great potential and limitations.
- For such 1D spin chains, the accuracy of DMRG simulations has been found limited only by machine precision, rather independent of the particular choice of Hamiltonian.
- **Application of 1D spin chains:** 1D and 2D strongly-correlated systems have applications in condensed matter physics, such as for studying spin chains and ladders, high-temperature superconductance of frustrated magnets in low spatial dimensions and at several places elsewhere. These spin chains have found interest also in exploring ultra-cold gases in optical lattices.
- **Applications in nuclear physics:** The DMRG method (may) enable configuration interaction studies of weakly bound and unbound strongly-interacting complex systems, which cannot be treated by any direct diagonalization because of the prohibitively large Fock space (Rotureau *et al.* 2009). Any theoretical description of such states requires a rigorous treatment of the many-body correlations in the presence of decay channels and a scattering continuum.
- **Applications to nonequilibrium systems:** While most of the previous DMRG studies were focused on equilibrium properties in strongly-correlated closed quantum systems with a hermitian density matrix, nonequilibrium systems with non-hermitian and non-symmetric density matrices can also be treated, though with rather mixed success.

4.4. Other representations, related to JAC

4.4.a. Analytical screened hydrogen models

Screened hydrogen models:

- **Effective nuclear charge model:** A single effective charge $Z^{(\text{eff})}$ ensures that a complete and orthonormal one-electron basis is used. Such a basis also supports the second-quantized representation of wave functions beyond the analytical approximation. Skoromnik *et al.* (2022) showed that an analytical zeroth-order approximation can be formulated, on which perturbation theory can be built. They predict total energies with roughly the same accuracy for all atoms or ions, although their presentation of the corrections appear quite cumbersome and not in line with the standard theory.

4.4.b. Natural-orbital functional theory (NOFT)

Natural-orbital functionals:

- **Scope of the theory:** The natural-orbital functional theory (NOFT) has been developed as alternative to both, the density functional theory (DF) and to a large variety of wavefunction-based methods. In NOFT, the electronic structure of atoms or molecules is described by **natural orbitals (NO)** and their **occupation numbers (ON)**. The use of approximate NO functionals has been found both, more accurate than DFT computations and to scale (much) better in their computational costs than correlated wavefunction representations.

4.4.c. Density funtional theory (DFT)

Formal representation:

- **Hohenberg-Kohn theorem:** Hohenberg and Kohn showed that all ground-state properties of atoms, molecules, etc. are uniquely determined by the electron density alone. In particular, **there exist a unique universal functional of the electron density that can be utilized in order to obtain the ground state energy and density.**

- **Kohn-Sham theorem:** The universal functional of the electron density can be re-written as a sum of kinetic energies of noninteracting (so-called Kohn-Sham) particles *and* some **exchange-correlation functional**. This representation enables one to represent the electron density by means of a single (Kohn-Sham) Slater determinant, even if the exact form of the exchange-correlation functional remains unknown.
- **Hohenberg-Kohn theorem:** This theorem tells that the energy of any (finite quantum) system can be written as a functional of the **electron density**, the well-known basis of Density Function Theory (DFT). Various approximate density functionals have been developed and explored with regard to different physical and chemical properties. For instance, concepts from DFT have been applied in order to obtain **chemical reactivity indices** and to characterize the chemical reactions of molecular systems in terms of perturbations (distortions) of the electron density.
- **Approximate exchange-correlation functionals:** Many approximate semi-empirical exchange-correlation functionals have been proposed in the literature with different strengths and complexity.
- **Strength and weaknesses of DFT:** Since the exact exchange-correlation functional remains unknown, not all correlation can usually be retrieved by the DFT method. Indeed, **DFT has been found good in capturing dynamic correlations**, i.e. if the main physics can be described by means of the single Slater determinant, **but it often fails for strong correlations** for which multireference methods are then required.

Applications:

- Today, the simple Kohn-Sham representation of DFT is the basis for its great success for different – and partly very complex – systems, such as clusters, biomolecules and nanostructures.

4.4.d. Relativistic coupled-cluster (RCC) theory

Formal representation:

- **All-order techniques:** One of the most popular all-order technique is the **CC approach** in which correlation contributions are **classified due to the number of excited particles rather than by the order of the perturbation**.
- **All-order techniques:** From many-body and coupled-cluster (CC) computations, one knows that only certain classes of correlation diagrams need to be incorporated to all orders in order to obtain very accurate results.

Applications:

- In practice, most CC computations include just single and pair correlations to all orders but neglect triple and higher correlations, though selected triple and quadrupole excitations might be included (Dzuba and Johnson, 1998).

4.4.e. Miscellaneous methods for the representation of many-electron systems

Eigenvector continuation techniques:

➤ **Eigenvector continuation:** Demol *et al.* (2020) mention the method of eigenvector continuation as an efficient and reliable tool for the **resummation of wave function expansions**; although this text is quite difficult to follow, the method is said to be robust and based on simple mathematical principles. If, in particular, a quantum system is described by the Hamiltonian $H \equiv H(1)$, that smoothly depend on a single parameter $H(c)$, the **power of the eigenvector continuation method** refers to (Demol *et al.*, 2020):

1. There exist formally a parameter regime $0 \leq c \leq c_e \leq 1$ for which the many-body problem is easier to solve than for the target value $c = 1$.
2. The stability of the eigenvectors of $H(c)$ with regard to variations of c remains for the many-body state of interest ($c = 1$) within a low-dimensional manifold of the full A -body Hilbert space when c is changed from $[0, c_e] \rightarrow 1$.

Krylov space:

➤ **Krylov space:** For a given Hamiltonian \mathbb{H} and some (approximate eigen-) state $|v_o\rangle$, an associated $L+1$ dimensional Krylov space (of \mathbb{H} over $|v_o\rangle$) is defined by applying \mathbb{H} successively to the previous state,

$$\mathcal{K}^{(L)}(|v_o\rangle) = \text{span}(|v_o\rangle, \mathbb{H}|v_o\rangle, \mathbb{H}^2|v_o\rangle, \dots, \mathbb{H}^L|v_o\rangle).$$

For such a Krylov space, the lowest-energy state in $\mathcal{K}^{(L)}(|v_o\rangle)$ can be obtained much simpler than by an explicit diagonalization of the (tridiagonal) Hamiltonian matrix. It can be readily seen that the Hamiltonian matrix for the Krylov space is tridiagonal

$$\mathbb{H}|v_n\rangle = b_n|v_{n-1}\rangle + a_n|v_n\rangle + b_{n+1}|v_{n+1}\rangle,$$

or that $\mathbb{H}|v_n\rangle$ is orthogonal to all basis states except of $|v_n\rangle$ and $|v_{n\pm 1}\rangle$. This tridiagonalization of \mathbb{H} is also the essence of the Lanczos method (Koch, 2019). For many-electron systems, unfortunately, the Hamiltonian \mathbb{H} cannot be applied so easily to any given state $|v\rangle$.

➤ **Spectral functions:** The Lanczos method gives good approximations to the largest and smallest eigenvalues but not for the bulk of the spectrum (Koch, 2019). It is therefore ill-suited for the representation of the excited states. The Hamiltonian matrix in the Krylov-space representation $\mathcal{K}^{(L)}(|v_o\rangle)$ can however be used to express the so-called Lehmann representation

$$G_c(z) = \left\langle \Psi_c \left| \frac{1}{z - \mathbb{H}} \right| \Psi_c \right\rangle = \sum_{n=0}^L \frac{\langle \Psi_c | \Psi_n \rangle \langle \Psi_n | \Psi_c \rangle}{z - E_n},$$

4. Atomic representations

and which appears to be straighforward to calculate, provided the tridiagonal Hamiltonian matrix in the Krylov space is known (Koch, 2019).

Direct quantum dynamics:

- **Direct quantum dynamics:** Direct dynamical methods refer to a **branch of molecular-dynamical simulations** that combines and applies methods from quantum chemistry in order to calculate potential energy surfaces and their derivatives for a particular nuclear geometry. Although these energy surfaces are usually computed *on-the-fly*, some intermediate results are stored in databases to help re-cycle the expensive quantum chemical computations. First applications of direct quantum dynamics were performed already in the 1970s using the local gradient in order to generate approximate Born-Oppenheimer trajectories during chemical reactions. The propagation of the wave functions was later improved by using a local Hessian matrix, and which typically allows for larger step sizes in the propagation. **Direct quantum dynamic methods are today often integrated into quantum chemistry programs and are as easy to apply as *static* methods for any system that remains feasible.**
- **Direct quantum dynamics:** Nowadays, **(direct) quantum dynamics is a key technique for molecular dynamics simulations** in order to understand different physico-chemical processes at (ultra-) short time scales. These techniques are for instance applied to interprete experiments in femto-chemistry. In contrast to other classical and semi-classical simulations, quantum-dynamics methods suppose the prior knowledge of the (whole) potential energy function in order to solve the time-dependent Schrödinger equation for the nuclear motion (Lasorne *et al.*, 2007). Since accurate potential energy surfaces (PES) cannot be calculated globally for more than, say, five or six degrees of freedom, they are then often combined with classical mechanics and the use of the Car-Parinello method.

4.4.f. Wigner distribution of quantum systems

Formal representation:

- **Wigner distribution:** The Wigner distribution for describing the (quantum) state of a physical system has found its application from statistical mechanics to modern optics, to electrical engineering, and even up to seismology (Mirhosseini *et al.*, 2016). In physics, the Wigner distribution help combine concepts from phase-space statistical mechanics with quantum physics. It describes a quasi-probability distribution whose regions of *negative values* indicate wave-like behavior.
- **Wigner distribution:** A system with periodic boundaries and unknown density matrix ρ , that depends on a single (discrete) azimuthal angle φ_o , can be approximated by a N-dimensional state space $\{|\ell\rangle, |\ell| \leq N\}$, spanned by the orbital-angular-momentum eigenvectors

$|\ell\rangle$. In this finite-dimensional sub-space, the (discrete) Wigner distribution function is given by (Mirhosseini *et al.*, 2016)

$$W(\varphi_o, \ell) = \frac{1}{2N+1} \sum_{\varphi=-N}^N \exp\left(-\frac{4\pi i}{2N+1} \ell \varphi\right) \langle \varphi_o - \varphi | \rho | \varphi_o + \varphi \rangle, \quad \varphi_o \in \{-N, \dots, N\}.$$

For this discretization, one can define *angular* states via a discrete Fourier transform of the OAM states above by

$$|\varphi_o; N\rangle = \frac{1}{\sqrt{2N+1}} \sum_{\ell=-N}^N \exp\left(-\frac{2\pi i}{2N+1} \varphi_o \ell\right) |\ell\rangle, \quad |\varphi_o + 2N+1\rangle = |\varphi_o\rangle.$$

Analogue angular states have been introduced in the literature for expressing angular-momentum operators in a finite basis. Such a representation is needed, for example, for extending the BB-84 QKD protocol to the OAM basis or for violation of Bell inequalities with angular variables (Mirhosseini *et al.*, 2016). For incoherent mixtures of quantum states, it can be shown that the corresponding Wigner distribution is always positive and does not indicate any wave interference.

4.4.g. Transformation of atomic into qubit Hamiltonians

Formal representation:

➤

Quantum hardware and algorithms for atomic physics:

- **Atomic computations & quantum computing:** Quantum computing may affect atomic computations due to: (1) Running atomic computations on quantum hardware and (2) Transformation of atomic Hamiltonians into qubit Hamiltonians and quantum circuits [cf. McClean *et al.* (2019) and the code OPENFERMIUM].
- **Qubit transformation of atomic Hamiltonians:** Once the problem has been recast in the second quantized, it needs to be mapped upon qubits. While electrons are indistinguishable fermions, qubit representations have to be distinguishable in order to support useful computations.

4. Atomic representations

- **Qubit transformation:** Several transformations, such as the Jordan-Wigner (JW), Bravyi-Kitaev (BK), and Bravyi-Kitaev super fast (BKSF) transformations, are known today to support the mapping of indistinguishable fermions to distinguishable qubits. These transformations also take the antisymmetry (particle statistics) of the electronic wave functions into account. In particular, the **Jordan-Wigner transformation directly returns an equivalent ‘qubit operator’ for the atomic Hamiltonian.**
- **Atomic Hamiltonian in second quantization:**

$$\mathbb{H} = \sum_{ij} h_{ij} a_i^+ a_j + \frac{1}{2} \sum_{ijkl} h_{ijkl} a_i^+ a_j^+ a_k a_l.$$

The one- and two-particle amplitudes h_{ij} , h_{ijkl} are usually computed classically and are provided as input to the quantum simulations.

- **Jordan-Wigner transformation:** This transformation help re-write the electronic Hamiltonian as a sum over products of Pauli spin operators, i.e. as a series of qubit gates. To do so, the individual terms of the Hamiltonian are converted into unitary gates. In the Jordan-Wigner transformation, a single fermionic creation or annihilation operator is represented by $\mathcal{O}(n)$ qubit operations. Even if the individual terms of the electronic Hamiltonian **do not** commute with each other (as usual), a Trotter decomposition and sequential execution of the corresponding gate operations will eventually support an approximate unitary propagator.
- **Jordan-Wigner transformation:** To encode the occupation-number (Fock-space) basis, one can simply replace the antisymmetric many-electron basis by the corresponding multi-qubit state

$$|f_1, f_2, \dots, f_n\rangle \implies |q_1\rangle \otimes |q_2\rangle \otimes \dots \otimes |q_n\rangle, \quad f_i = q_i \in \{0, 1\}.$$

In this transformation, one qubit is used to encode one occupation number. To represent the corresponding (qubit) creation and annihilation operators in the qubit basis, we can use the Pauli matrices as

$$\begin{aligned} q^+ |0\rangle &= |1\rangle, & q^+ |1\rangle &= 0, & q^- |1\rangle &= |0\rangle, & q^- |0\rangle &= 0, \\ q^+ |1\rangle \langle 0| &= \frac{1}{2} (\sigma_x - i\sigma_y), & q^- |0\rangle \langle 0| &= \frac{1}{2} (\sigma_x + i\sigma_y). \end{aligned}$$

Here, the mutual anti-commutation of the three Pauli matrices ensures that q^\pm anti-commutes also with σ_z . This eventually enables one to represent the (electronic) creation and annihilation operators a^\pm by the corresponding qubit operators q^\pm .

- **Jordan-Wigner transformation:** Typical quantum computers manipulate the state of a N -qubit register by a sequence of Pauli matrices X_q , Y_q , Z_q ; $q = 1..N$. For fermionic quantum many-particle systems, the creation and annihilation operators can be mapped onto Pauli

matrices via the Jordan-Wigner transformation

$$a_k^+ \quad \rightarrow \quad \frac{1}{2} \left[\prod_{j=1}^{n-1} -Z_j \right] (X_k - i Y_k), \quad a_k \quad \rightarrow \quad \frac{1}{2} \left[\prod_{j=1}^{n-1} -Z_j \right] (X_k + i Y_k).$$

The antisymmetry under permutation of the fermionic coordinates is not required and irrelevant for the qubits, since the qubits refer to distinguishable particles.

- **Bravyi-Kitaev transformation:** This transformation provides a more efficient mapping of electronic Hamiltonians upon qubit Hamiltonians than the Jordan-Wigner transformation. It represents single fermionic creation or annihilation operator by $\mathcal{O}(\log n)$ qubit operations.
- **Quantum computing** is known as a rapidly growing discipline that aims for the discovery of exponentially faster quantum algorithms than the best-known classical algorithms. However, one first needs to know and control the required resources in order to realize such algorithms.
- **Resources of quantum computing:** In pure-state quantum computations, entanglement is often considered as a necessary resource in order to achieve an exponential speed-up in the computations. Although this seems not to be true for mixed-state quantum computations, until the present, it is largely unclear which entities help quantify the resource in such a computational model. Moreover, there is no simple relationship known between different resources for mixed-state quantum computations.
- **Experimental quantum simulator:** To experimentally demonstrate a quantum speedup, one needs to: (i) specify a quantum device that efficiently solves a sampling task, which is obviously hard to solve for classical computers; (ii) verify the speed-up and solution. **This verification has been found a crucial, though often still missing issue in demonstrating quantum speedup.**
- **Application of quantum simulations:** Modern simulations make use of **approximate quantum optimization algorithms, quantum annealing or the sampling from computationally expensive probability distributions**. Similar techniques may be applied also to tackle problems in quantum chemistry, machine learning or even at stock markets.
- **Quantum simulations:** At present, rather large-scale quantum simulations are the most promising application of quantum computers within the foreseeable future, and with direct applications in quantum chemistry and condensed matter. In contrast to the standard **qubit representation** of most quantum protocols, the simulation of fermionic many-particle systems is a great challenge, since all fermionic operator must be transformed into a representation of distinguishable qubits. In atomic or molecular physics, a useful quantum simulation protocol (algorithm) should be able to reliably predict energy spectra, reaction rates, correlation functions or other (atomic and molecular) properties. Such quantum simulation protocols will become superior to classical computers, if larger systems can be calculated than currently accessible by (classical) calculations.

4. Atomic representations

- **Lie-Trotter-Suzuki decomposition:** If the Hamiltonian of a composed quantum system H_s can be written as a sum of local terms, then the time evolution for a single time step can always be decomposed as

$$H_s = \sum_j h_j \quad \Rightarrow \quad \exp(-i H_s \delta t) = \prod_j \exp(-i h_j \delta t) + \mathcal{O}(\delta t^2).$$

In this decomposition, the number of terms in the Hamiltonian scales polynomially in atomic physics and quantum chemistry with the number of electrons owing to the two-body nature of the electron-electron interaction.

- **Quantum simulations of molecular hydrogen:** O’Malley *et al.* (2016) applied a programmable array of superconducting qubits in order to estimate the energy surface of molecular hydrogen using two distinct quantum algorithms. In particular, they applied the unitary coupled cluster method based on some variational quantum eigensolver. They also demonstrated experimentally the Trotterization and quantum phase estimation for quantum-chemical calculations. Such quantum simulation of atomic and molecular energies will advance the fields of material science, catalysis or pharmaceutic.
- **Spin Hamiltonian for molecular hydrogen:** The spin Hamiltonian for molecular hydrogen in a minimal (STO-6G) basis has been derived by using the Bravyi-Kitaev transformation and has been given as (O’Malley *et al.*, 2016)

$$\mathbb{H}^{(H_2, \text{mininal basis})} = f_0 \mathbb{1} + f_1 Z_0 + f_2 Z_1 + f_3 Z_2 + f_4 Z_0 Z_1 + f_5 Z_1 Z_3 + f_6 \mathbf{X}_0 Z_1 \mathbf{X}_2 + f_7 \mathbf{Y}_0 Z_1 \mathbf{Y}_2 + \dots \quad \text{6 other terms},$$

where, again, f_i depend on the fixed bond length.

- **Unitary coupled-cluster (UCC):** UCC has been found a promising model to implement quantum chemistry tasks on quantum computers. Recent developments include extended strategies for pair-excitation and for the efficient representation of fermionic systems. If i, j, k, \dots refer to general — occupied and unoccupied — spin-orbitals, the basic building blocks of UCC are the unitary operators,

$$U_{ij}(c) = \exp\left(-\frac{c}{2} G_{ij}\right)$$

$$G_{ij} = (a_i^+ a_j - a_j^+ a_i), \quad G_{ijkl} = (a_i^+ a_j a_k^+ a_l - \text{h.c.}), \quad \dots$$

and where the G_{ij} , G_{ijkl} generate N -body excitations. These generators can be constructed, once a list of indices is given.

- **Mapping of fermionic creation and annihilation operators upon qubits:** In a basis of spin-orbitals, the fermionic creation and annihilation operators do increase or decrease the occupation not only by 1 but must ensure also a phase factor due to the position of the spin-orbital.

These two properties must be preserved by the mapping upon qubits

$$\begin{aligned} a_p &= Q_p \otimes Z_{p-1} \otimes \dots \otimes Z_1, & a_p^+ &= Q_p^+ \otimes Z_{p-1} \otimes \dots \otimes Z_1 \\ Q &= |0\rangle\langle 1| = \frac{1}{2} (X + iY), & Q^+ &= |1\rangle\langle 0| = \frac{1}{2} (X - iY), \end{aligned}$$

and where Q, Q^+ change the occupation of the target qubit while the string of Z operators recover the phase factor $(-1)^{\sum_{i=1}^{p-1} f_i}$ due to the antisymmetry of the fermionic wave function.

- **Quantum network:** For any large-scale quantum network, quantum gates need to be efficiently combined by optical channels. If the gate operations are provided and realized by neutral atoms in an optical cavity, the enhanced light-matter interaction in such cavities can be applied to achieve a strong coupling of the matter qubits with flying photonic qubits. This combination has been discussed as a long-term goal in designing quantum networks.
- **Noisy intermediate-scale quantum (NISQ) devices:** Preskill (2018) termed the name **noisy intermediate-scale quantum devices** in order to describe the present generation of quantum devices. In particular, he pointed out that it is presently highly unclear of whether these NISQ devices will be able to outperform classical computers on any useful task. There is a large (huge) gap between showing (so-called) **quantum supremacy** of a device with, say, more than around 50 qubit and solving some useful task. The question remains open of what will near-term quantum computers be useful for ? (McArdle *et al.*, 2020).
- **Noisy intermediate-scale quantum (NISQ) era:** Today, quantum computing is said to be in the NISQ era in which circuits/devices operate on just a few qubits with non-negligible noise and no error correction. This era is characterized by hybrid quantum-classical algorithms, such as variational quantum algorithms (VQA).
- **Promise of quantum computers:** For the simulation of quantum many-particle systems, quantum computers aim (and promise) to reduce the computational effort and complexity from exponential to polynomial. A quantum computer with about 100 completely error-corrected qubits are sufficient to surpass nuclear and electronic structure calculations. Until the present, however, quantum devices are limited to typically 10-20 noisy qubits, on which all simulation algorithms suffer from decoherence as well as gate and measurement errors.
- **Quantum computers and quantum chemistry:** Elementary tasks from quantum chemistry and magnetism have been solved with 2–6 noisy qubits by applying the phase estimation or the variational quantum eigensolver (VQE) algorithms. Different quantum simulator platforms are publicly available and can be utilized by means of software tools, such as PYQUIL, XACC, OPENQASM or OPENFERMION. There is also several cloud access and cloud services available in order to provide quantum computing devices and algorithms to a broader scientific community.

4. Atomic representations

- **Eyring equation:** If the energies are known with the chemical accuracy $1.6 \cdot 10^{-3}$ Hartree, the chemical reaction rate at room temperature can be predicted (within about an order of magnitude) by using the Eyring equation

$$R \propto \exp\left(-\frac{\Delta E}{kT}\right),$$

for a system at temperature T and with the energy difference ΔE between the reactant and product states.

- **Simulation of atomic systems at quantum computers:** Atomic computations on quantum computers require first of all to map the operators for the indistinguishable fermions to operators which act upon distinguishable qubits. The requirement refers to a map from the fermionic Fock space to the \mathbb{C}^{2^N} Hilbert space of an N -qubit system so that every state of the atom can be represented by a corresponding qubit state. This mapping is most readily made by using second quantization. qubits such that every fermionic state can be represented by a
- **Jordan-Wigner basis:** In the Jordan-Wigner basis, every Slater determinant from the electronic system (as it occurs in a full-CI representation) refers to one of the computational basis states. Therefore, a proper N -qubit register can store the full-CI or any restricted wave function of the atom efficiently.
- **Alternative mapping of fermionic creation and annihilation operators upon qubits:** A number of mappings have been developed that support a similar locality of the qubit operations as given by the fermionic Hamiltonian. These qubits require a large number of qubits than in the Jordan-Wigner basis. In particular, Verstraete and Cirac (2005) eliminated the strings of Z operators from the qubit creation and annihilation operators by doubling the number of qubits.

Quantum algorithms:

- **Universal quantum computer:** No universal quantum computer is likely be demonstrated within the near or foreseeable future. Instead, various sub-universal models of quantum computing, such as Boson Sampling have been suggested and need next to developed towards their full quantum regime. These sub-universal models may enable one to demonstrate a quantum speedup, although under certain – more or less strict – assumptions with regard to their complexity.
- **Variational quantum eigensolver (VQE):** O’Malley *et al.* (2016) applied an experimental QVE to demonstrate a first scalable quantum simulation of molecular energies that were performed on quantum hardware. The QVE only requires short state preparation and measurement sequences and can perhaps be used without the overhead of error correction.
- **Quantum computational supremacy:** Fault-tolerant quantum computing can speed-up significantly the solutions of various NP-hard problems, such as the factorization of prime numbers, search algorithms, linear-algebra and various others. While, until to the present, most

realizations of multi-qubit realizations are fragile and suffer from noise and sub-universal behaviour, newly emerging quantum processors are expected to be developed and to be powerful enough in order to outperform classical computers for selected tasks, known also as **quantum computational supremacy** (Killoran *et al.*, 2019).

- **Quantum computational supremacy:** Quantum supremacy refers to the expected speedup of quantum computers that promise to outperform their classical pendants. Quantum supremacy has been used also to characterize the speedup of various quantum simulator experiments, which now gradually escape the regime of classical simulations. In practice, however, many quantum simulators lack an efficient verification and validation of the obtained observations, when compared to their expected outcome.
- **Quantum variational eigensolver (VQE):** This quantum algorithm enables one to approximate the eigenenergies of large matrices with current or near-term quantum hardware. This algorithm applies the variational principle to the expectation values of some parameterized quantum circuit $U(q)$, based on some qubit Hamiltonian \mathbb{H} , and optimizes these parameters q by means of a classical optimization algorithm,

$$\min_q (\langle \mathbb{H} \rangle_{U(q)}) \equiv \min_q (\langle 0 | U^+(q) \mathbb{H} U(q) | 0 \rangle) .$$

The original VQE algorithm has meanwhile inspired several other variational quantum algorithms, with special emphasis on various quantum machine learning, quantum optics or quantum chemical and many-body physics models.

- **Variational quantum algorithms (VQA):** Variational quantum algorithms are presently seen as the most promising class of algorithms in order to realize near-term quantum computers. While the field of these quantum algorithms evolve quite rapidly, no standard scheme is however known until the present for developing new algorithms. Recent work on developing new algorithms was mainly based on heuristic arguments, quite analogue to classical computing. Examples of VQA refer to the **variational quantum eigensolver (VQE)** or the **quantum approximate optimization algorithm (QAOA)**.
- **Applications of VQA:** VQA algorithms show promises and might be used in quantum chemistry, materials science, finance and quantum machine learning.

Boson sampling:

- **Boson sampling:** Boson sampling was originally proposed by Aaronson and Arkhipov and provides a non-universal model for linear-optical quantum computation. In practice, boson sampling requires (i) high-performance quantum light sources, (ii) efficient single-photon detectors as well as (iii) the realization of large-scale photonic circuits with low loss rates. All three ingredients are very essential for building universal, photon-based quantum computation.

4. Atomic representations

- Gaussian boson sampling (GBS): GBS exploits especially squeezed vacuum states as input for non-classical light sources with the aim to increase the multiphoton click probability at the output. GBS therefore relies on coherent superposition of the photon numbers.
- Boson Sampling: Boson Sampling is formally based on ∞ -dimensional Hilbert spaces, even if it only requires single-mode Gaussian states and measurements. Although Gaussian state preparations and measurements are well understood theoretically, they still need to be implemented with sufficient quality and at sufficiently large scales.
- Fock-state boson sampling: In Fock-state boson sampling, there is no phase relation between single photons.

Photon-based quantum computations:

➤

Continuous variable (CV) model of quantum computing:

- Continuous variable (CV) model of quantum computing: In the CV model, the basic (information-processing) unit is an infinite-dimensional bosonic mode as it can be realized and manipulated with light. While such a CV model of quantum computing retains the major features from the standard qubit model, it promises simpler implementations for various bosonic systems, such as photons, electromagnetic fields, trapped atoms, harmonic oscillators or Bose-Einstein condensates. More generally, a CV model of quantum computing may facilitate quantum computations and simulations for all those systems where continuous quantum operators are naturally occurring, such as position and momentum.
- Systems based on continuous variables (CV): Many quantum systems have (also) spatial degrees of freedom and, hence, are intrinsically continuous. With these systems, an infinite-dimensional Hilbert space is associated, and any representation in such a space is very different from a discrete qubit representation. Indeed, the CV model of quantum computing got its name from the continuous spectra of the quantum operators associated with spatial degrees of freedom and which offers a paradigm for quantum computations.
- Qubits versus continuous variables (CV): It can be shown that every qubit-based computation can be realized also by means of CV representations. This makes the CV model of quantum computing a powerful extension of the familiar qubit model.
- Systems based on continuous variables (CV): Perhaps, the most simple CV system is the 1D bosonic harmonic oscillator which can be defined either by its (canonical) mode operators a and a^\dagger with $[a, a^\dagger] = \mathbb{1}$ or, equivalently, by its the position and momentum –

(quadrature) operators

$$\hat{x} = \sqrt{\frac{\hbar}{2}} (a + a^+), \quad \hat{p} = -i \sqrt{\frac{\hbar}{2}} (a - a^+), \quad [\hat{x}, \hat{p}] = i\hbar \mathbb{1}.$$

In a optical fibre or waveguide, for instance, a fixed harmonic oscillator mode can be considered (drawn) as a single 'wire' in a quantum circuit, and these modes are the fundamental units of CV quantum computers.

Software tools for qubit transformations:

- **OPENFERMION:** This is an open-source software library in Python for simulation of fermionic and bosonic models. It aims to provide a (preliminary) interface for translating the atomic or quantum chemistry specification of problems into a (qubit) representation, suitable for quantum hardware. The goal is to specify a quantum circuit for solving or studying electronic structure problems, and without that the user need to have *domain expertise* in quantum information theory.
- **OPENFERMION:** This toolbox provides some preliminary functionality for developing (new) quantum algorithms for solving electronic-structure problems. Until the present, however, efficient algorithms for atomic physics and quantum chemistry are still a challenge and their implementation on quantum hardware remains a rather formidable task. This toolbox also aims to facilitate the communication between quantum-chemistry and quantum-information community.
- **STRAWBERRY FIELDS:** This Python package refers to an open-source software architecture for photonic quantum computing. It is based on the new quantum programming language **Blackbird** and is especially designed for dealing with CV models of quantum computing. This package makes us of different circuit decompositions from quantum photonics, such as the Williamson, Bloch-Messiah or Clements decompositions (Killoran *et al.*, 2019). STRAWBERRY FIELDS can be utilized either as Python package or as a browser-based interface for the set-up of quantum circuits.
- **Decompositions of STRAWBERRY FIELDS:** Several decompositions are realized, including: (a) the Williamson decomposition to decompose arbitrary Gaussian states into some symplectic transformation that can be applied on thermal states, (b) the Bloch-Messiah decomposition for modelling interferometers and single-mode squeezing as well as (c) the Clements decomposition for representing multi-mode linear interferometers in terms of arrays of beamsplitters and rotations of fixed depth.

4.4.h. qumodes

4. Atomic representations

Formal representation:

- **Representation of qumodes:** In a CV model and with the vacuum state $|0\rangle$, each qumode can be written in terms of the quadrature states

$$|\psi\rangle = \int dx \psi(x) |x\rangle, \quad \hat{x} |x\rangle = x |x\rangle, \quad x \in \mathbb{R}$$

$$|\psi\rangle = \exp(-i \mathbb{H} t) |0\rangle,$$

and where \mathbb{H} is a bosonic Hamiltonian, i.e. a function of the mode operators a, a^+ and of the time t ; the quadrature states are a sub-class of the so-called Gaussian states of qumodes.

- **Gaussian states:** For these states, the Hamiltonian \mathbb{H} is at most quadratic in a, a^+ . Gaussian single-qumode states can be parametrized by two complex variables, a **displacement parameter** $\alpha \in \mathbb{C}$ and a **squeezing parameter** $z \in \mathbb{C}$.

4.5. Numerical methods for large-scale atomic computations

4.5.a. Matrix diagonalization

Lanczos method:

- **Block Lanczos method:** The block Lanczos method help solve multiple eigenvalue problems and has been used as general eigenvalue solver. When compared to Lanczos original methods, it accelerates the convergence of the Lanczos iterations when a large number of the low-lying eigenvalues are required.
- **Lanczos method:** The Lanczos method is one of the most powerful methods to compute the lowest eigenstates of a sparse matrix. In this method, the eigenvalues of the Hamiltonian matrix (H_{ij}) are approximated by the eigenvalues of the associated Krylov subspace (Shimizu *et al.*, 2019)

$$\mathbb{K}^{l_m}(H; \mathbf{v}_1) = \{\mathbf{v}_1, H\mathbf{v}_1, H^2\mathbf{v}_1, H^3\mathbf{v}_1, \dots, H^{l_m-1}\mathbf{v}_1\}$$

with \mathbf{v}_1 being an arbitrary initial vector. The few lowest eigenvalues converge typically very fast and the necessary number of iterations l_m , that is needed for convergence, is much smaller than the dimension of H itself.

- **Block Lanczos method:** The block Lanczos method reduces the number of iterations (and, hence, the elapse time) when many eigenvalues are required. In this method, however, the number of the Lanczos vectors increases more rapidly than in the original method, together with the cost of their reorthogonalization. Shimizu *et al.* (2019) therefore propose to combine the block Lanczos method with the thick restart method to reduce the cost of the reorthogonalization.

5. Atomic interactions with the radiation field

5.1. Wave equations & optical fields

5.1.a. Homogeneous wave equation

General solutions:

- **Monochromatic plane-wave light:** Monochromatic plane-wave light is uniquely determined by either the electric (**E**) or magnetic (**B**) field. Without restriction, we here consider a plane-wave along $\mathbf{k} \parallel \mathbf{e}_z$.
- **Waves that propagate along the wave vector $\pm \mathbf{k}$:** We consider the homogenous wave equation (for $\psi = \{\mathbf{E}, \mathbf{B}, \Phi, \mathbf{A}, \dots\}$) with the known solution (proof by substitution and by means of the chain rule), whose wave fronts propagate along $\pm \mathbf{k}$

$$\square \psi(\mathbf{r}, t) = 0 \quad \psi(\mathbf{r}, t) = \psi_+(\mathbf{k} \cdot \mathbf{r} + \omega t) + \underbrace{\psi_- (\mathbf{k} \cdot \mathbf{r} - \omega t)}_{\text{phase}}$$

for arbitrary functions $\psi_{\pm}(\mathbf{k} \cdot \mathbf{r} \pm \omega t)$, and if they fulfill the dispersion relation $\omega = (\pm) c k$.

- **(Complex) monochromatic plane waves:** If we restrict ourselves to periodic (harmonic) solutions, two obvious solutions are

$$\psi(\mathbf{r}, t) = A_- e^{i(\mathbf{k} \cdot \mathbf{r} - \omega t)} \quad \text{or} \quad \psi(\mathbf{r}, t) = A_+ e^{i(\mathbf{k} \cdot \mathbf{r} + \omega t)}$$

$$\psi = \text{const.} \quad \text{for} \quad t = t_o \quad \iff \quad \mathbf{k} \cdot \mathbf{r} = \text{const.}$$

Here, the vector **k** is called the wave or propagation vector and ω the frequency of the plane waves.

5.1.b. Plane-wave radiation

Plane-wave solutions:

➤ **Plane waves:** Plane waves always propagate into the direction of the wave vector and can be written as

$$\mathbf{E}(\mathbf{r}, t) = \mathbf{E}_o e^{i(\mathbf{k} \cdot \mathbf{r} - \omega t)}, \quad \mathbf{B}(\mathbf{r}, t) = \mathbf{B}_o e^{i(\tilde{\mathbf{k}} \cdot \mathbf{r} - \tilde{\omega} t)}$$

However, since the em field must satisfy not only the homogenous wave equation $\square \psi = 0$ but also Maxwell's equations for the coupling of the \mathbf{E} - und \mathbf{B} fields

$$\text{rot } \mathbf{E} = -\frac{\partial \mathbf{B}}{\partial t} \iff i(\mathbf{k} \times \mathbf{E}_o) e^{i(\mathbf{k} \cdot \mathbf{r} - \omega t)} = i\tilde{\omega} \mathbf{B}_o e^{i(\tilde{\mathbf{k}} \cdot \mathbf{r} - \tilde{\omega} t)}, \quad \omega = \tilde{\omega}; \quad \mathbf{k} = \tilde{\mathbf{k}}; \quad \mathbf{k} \times \mathbf{E}_o = \omega \mathbf{B}_o.$$

Of course, this Maxwell equation need to be fulfilled for all times and places.

➤ If we use of the three other Maxwell equations, we furthermore obtain:

$$\text{div } \mathbf{E} = 0 \implies \mathbf{k} \cdot \mathbf{E}_o = 0$$

$$\text{div } \mathbf{B} = 0 \implies \mathbf{k} \cdot \mathbf{B}_o = 0$$

$$\text{rot } \mathbf{B} = \frac{1}{c^2} \frac{\partial \mathbf{E}}{\partial t} \implies \mathbf{k} \times \mathbf{B}_o = -\frac{\omega}{c^2} \mathbf{E}_o \implies (\mathbf{k} \times \mathbf{B}_o)^2 = k^2 B_o^2 = \frac{\omega^2}{c^4} E_o^2 \implies E_o^2 = c^2 B_o^2.$$

Therefore, the **three vectors** \mathbf{E}_o , \mathbf{B}_o , \mathbf{k} form (up to any even permutation) an orthogonal and right-handed **system**, i.e. the vectors \mathbf{E} and \mathbf{B} are perpendicular on \mathbf{k} for plane waves.

➤ **Vector potential:**

$$\mathbf{A}(\mathbf{r}, t) = \mathbf{A}_{\pm} e^{i(\mathbf{k} \cdot \mathbf{r} \pm \omega t)} = \sum_{\lambda} A_{o,\lambda} \mathbf{e}_{\lambda} e^{i(\mathbf{k} \cdot \mathbf{r} \pm \omega t)}$$

➤ **Equation of a plane:** For plane waves, all spatial points \mathbf{r} with $\mathbf{k} \cdot \mathbf{r} = \text{const.}$ have the same value at any time $t = t_o$.

➤ **Wave crest:** The wave crest of a plane wave is $A_{\pm} e^{i(\mathbf{k} \cdot \mathbf{r} \pm \omega t)}$ and propagates into the direction $\pm \mathbf{k}$.

- **Monochromatic light field:** Most simply, a classical monochromatic light field with frequency $\omega > 0$, (complex) envelope or field amplitude $\mathcal{E}(t)$ and polarization \mathbf{u} (complex unit vector) is given by

$$\mathbf{\mathcal{E}}(t) = \frac{1}{2} \mathcal{E}(t) \mathbf{u} e^{-i\omega t} + \text{c.c.}$$

- **(Time-averaged) Poynting vector & intensity:** For a plane electro-magnetic wave, the (time-averaged) Poynting vector is given by

$$\mathbf{S} = \frac{c}{8\pi} \mathcal{E}_o^2 \mathbf{e}_k, \quad I = |\mathbf{S}| = \frac{c}{8\pi} \mathcal{E}_o^2 \quad \dots \text{ intensity}$$

$$\mathbf{u}^* \cdot \mathbf{u} = 1, \quad \mathbf{u}^* \times \mathbf{u} = i P_3 \mathbf{e}_k,$$

and where the **degree of circular polarization P_3** coincides with the third Stokes parameter (right-circularly polarized $P_3 = 1$, left-circularly polarized $P_3 = -1$ and linearly-polarized $P_3 = 0$). Obviously, a *real* polarization vector \mathbf{u} refers to $P_3 = 0$ and to a linear polarization for a (pure) plane-wave from above. Moreover, the degree of circular polarization can be described also in terms of the **eccentricity ϵ of the polarization ellipse** by $|P_3| = 2\sqrt{1 - \epsilon^2} / (2 - \epsilon^2)$.

- **Electric-field of a superposition of two plane waves:** With the (real) wave vectors $\mathbf{k}_1, \mathbf{k}_2$ and the (complex) polarization vectors $\mathbf{u}_1, \mathbf{u}_2$, the electric field of a plane electromagnetic wave is given by:

$$\mathbf{\mathcal{E}}(\mathbf{r}, t) = \frac{1}{2} [\mathcal{E}_1 \mathbf{u}_1 e^{i(\mathbf{k}_1 \cdot \mathbf{r} - \omega_1 t)} + \mathcal{E}_2 \mathbf{u}_2 e^{i(\mathbf{k}_2 \cdot \mathbf{r} - \omega_2 t)}] + \text{c.c.}$$

- **Electric-field of a *standing* plane waves:** For $\mathbf{k}_1 = -\mathbf{k}_2 = \mathbf{k}$, $\omega_1 = \omega_2 = \omega$, $\mathbf{u}_1 = \mathbf{u}_2 = \mathbf{u}$, $\mathcal{E}_1 = \mathcal{E}_2 = \frac{\mathcal{E}}{2}$ in the superposition of two plane waves above, the electric field becomes

$$\begin{aligned} \mathbf{\mathcal{E}}(\mathbf{r}, t) &= \frac{1}{2} \left[\frac{\mathcal{E}}{2} \mathbf{u} e^{i(\mathbf{k} \cdot \mathbf{r} - \omega t)} + \frac{\mathcal{E}}{2} \mathbf{u} e^{i(\mathbf{k} \cdot \mathbf{r} - \omega t)} \right] + \text{c.c.} = \frac{1}{2} \mathcal{E} \mathbf{u} e^{-i\omega t} \left[\frac{e^{i\mathbf{k} \cdot \mathbf{r}} - e^{-i\mathbf{k} \cdot \mathbf{r}}}{2} \right] + \text{c.c.} \\ &= \cos(\mathbf{k} \cdot \mathbf{r}) \left[\frac{1}{2} \mathcal{E} \mathbf{u} e^{-i\omega t} + \text{c.c.} \right] = \cos(\mathbf{k} \cdot \mathbf{r}) \bar{\mathcal{E}}(t) \end{aligned}$$

5. Atomic interactions with the radiation field

Here, the factor $\cos(\mathbf{k} \cdot \mathbf{r})$ shows the *standing wave*, while $\bar{\mathcal{E}}(t)$ refers to some time-harmonic electric field, i.e. an uniformly oscillating field. This standing wave can be interpreted also as 1D optical lattice (Beloy 2009).

Conserved properties of plane waves with $\mathbf{k} \parallel \mathbf{e}_z$:

➤ (Linear) momentum:

$$p_k = -i \partial_k, \quad p_{x,y} \mathbf{A}(\mathbf{r}, t) = 0, \quad p_z \mathbf{A}(\mathbf{r}, t) = k_z.$$

➤ Orbital angular momentum:

$$\ell_z = -i(x \partial_y - y \partial_x) = -i \frac{\partial}{\partial \varphi}, \quad \ell_z \mathbf{A} = 0.$$

➤ Spin (of photons):

$$s_z = -i \begin{pmatrix} 0 & 1 & 0 \\ -1 & 0 & 0 \\ 0 & 0 & 0 \end{pmatrix}, \quad s_z \mathbf{A} = \lambda \mathbf{A}.$$

➤ Total angular momentum:

$$j_z = \ell_z + s_z, \quad j_z \mathbf{A} = \lambda \mathbf{A}.$$

➤ For plane waves, the (four) good quantum numbers refer to $\mathbf{p} = (p_x, p_y, p_z)$ and λ_c .

5.1.c. Polarization of plane waves in classical electrodynamics

Polarization of plane-waves beams:

- Apart from the (well-defined) frequency of plane-wave photons, each photon has generally a spin angular momentum \hbar that can be (partly) aligned in parallel or antiparallel to the direction of propagation. A full alignment of all photon spins gives then rise to a circularly-polarized light beam.
- A beam with a circularly-polarized planar wavefront has an azimuthal component of the Poynting vector that is proportional to the radial intensity gradient, even if it has no orbital angular momentum. This gives rise to a finite value, if integrated over the total cross-section of the beam.
- **Polarization of the electric field:** Polarization is an additional property of (em) waves that describes the orientation of their oscillations; by convention, the polarization $-1 \leq p \leq 1$ refers to the electric field. The polarization of light is associated with the spin-angular momentum (density) of the em wave.
- The polarisation is said to be linear if $p = 0$, and is left- or right-circular for $p = -1$ and $p = +1$, respectively. For all other values of $-1 < p < 1$, the wave is said to be elliptically polarized. Sometimes, one also refers to the chirality or handedness of the waves in order to denote the left- or right-circular polarization of the light beam.
- Vector potential of a circularly-polarized plane wave:

$$\mathbf{A}(\mathbf{r}, t) = \mathbf{e}_\lambda e^{i(kz - \omega t)}; \quad \mathbf{e}_\lambda = (\mathbf{e}_x + i\lambda \mathbf{e}_y) \quad \begin{cases} \lambda = +1 & \text{left circular} \\ \lambda = -1 & \text{right circular} \end{cases}$$

- Spin angular momentum (SAM): The circular polarization of light is usually associated with a well-defined SAM.
 - Complex spherical unit vectors \mathbf{e}_\pm :
- | | | |
|--|--------|--|
| $\mathbf{e}_\pm = \frac{1}{\sqrt{2}} (\mathbf{e}_x \pm i\mathbf{e}_y)$ | \iff | $\mathbf{e}_x = \frac{1}{\sqrt{2}} (\mathbf{e}_+ + \mathbf{e}_-)$ $\mathbf{e}_y = \frac{-i}{\sqrt{2}} (\mathbf{e}_+ - \mathbf{e}_-).$ |
|--|--------|--|
- Complex electric field $\mathbf{E}^{(c)} = (E_x^{(c)}, E_y^{(c)}, 0)$: Although a complex notation of em fields is often very convenient, the transverse, real

5. Atomic interactions with the radiation field

electric field is given by

$$\left. \begin{aligned} E_x^{(c)} &= |E_x^{(c)}| e^{i\gamma} \\ E_y^{(c)} &= |E_y^{(c)}| e^{i(\gamma+\delta)} \end{aligned} \right\} \quad \mathbf{E}^{(c)} = \Re[(E_x^{(c)} \mathbf{e}_x + E_y^{(c)} \mathbf{e}_y) e^{i(kz - \omega t)}] = E_x \mathbf{e}_x + E_y \mathbf{e}_y$$

$$E_x = |E_x^{(c)}| \cos(kz - \omega t + \gamma), \quad E_y = |E_y^{(c)}| \cos(kz - \omega t + \gamma + \underbrace{\delta}_{!!}) \dots \text{real.}$$

- **Relative phase δ to distinguish different polarization:** This relative phase δ refers to the complex field amplitudes $E_x^{(c)}$ and $E_y^{(c)}$
- **Linear polarization along the angle α :** For $\delta = n\pi$ ($n \in \mathbb{N}$)

$$\mathbf{E}^{(c)} = (|E_x^{(c)}| \mathbf{e}_x \pm |E_y^{(c)}| \mathbf{e}_y) \cos(kz - \omega t + \gamma) = |\mathbf{E}^{(c)}| \mathbf{e}_\alpha \cos(kz - \omega t + \gamma)$$

$$|\mathbf{E}^{(c)}| = \sqrt{|E_x^{(c)}|^2 + |E_y^{(c)}|^2}, \quad \tan \alpha = \pm \frac{|E_y^{(c)}|}{|E_x^{(c)}|} \quad \dots \left\{ \begin{array}{ll} (+) & n = \text{gerade} \\ (-) & n = \text{ungerade} \end{array} \right.$$

$$\mathbf{e}_\alpha = \cos \alpha \mathbf{e}_x + \sin \alpha \mathbf{e}_y$$

The angle α denotes the (polarization-) direction of \mathbf{E} with regard to the x -axis.

- **General monochromatic plane wave:** Any plane wave can always be written as superposition of two components
- **Poynting vector of a elliptically-polarized plane-wave beam:** The intensity of a laser field is defined by the cycle-averaged Poynting vector. For an elliptically polarized plane-wave laser field $\mathbf{A}(t) = A_o/\sqrt{1 + \varepsilon^2} [\cos(\omega t) \mathbf{e}_x + \varepsilon \sin(\omega t) \mathbf{e}_y]$ with the ellipticity parameter $0 \leq \varepsilon \leq 1$, the Poynting vector only has a z -component and, thus, the intensity is a measure for the energy flow into the propagation direction of the beam. This intensity is given by $I = A_o^2 \omega^2 / 8\pi \alpha = \mathcal{E}_o^2 / 8\pi \alpha$.

5.1.d. Atom-light interaction in the electric-dipole approximation

Atom-light interaction operator:

- **Electric-dipole approximation to the atom-light interaction:** In the electric-dipole approximation, the interaction operator between an atom and the light field can be expressed in terms of the electric-dipole operator \mathbb{D} of the atom and the electric field $\mathcal{E}(t)$ by

$$\mathbb{H}^{(E1)} = -\mathcal{E} \cdot \mathbb{D} = -\frac{1}{2} \mathcal{E}(t) \mathbf{u} \cdot \mathbb{D} e^{-i\omega t} - \frac{1}{2} \mathcal{E}^*(t) \mathbf{u}^* \cdot \mathbb{D} e^{i\omega t}.$$

5.2. Representation and parametrization of photons in atomic theory

5.2.a. Stokes parametrization and density matrix of a photon

Stokes parameters:

- **Stokes parameters:** These parameters provide a simple and alternative characterization for the polarization of plane waves and are given in terms of three real parameters that describe the polarization state of (transversal) electromagnetic radiation.
- **Stokes parameters P_1 , P_2 , P_3 :** The first two Stokes parameters quantify the *relative* asymmetries between intensities I_χ of light that is linearly polarized under different angles χ with regard to the reaction plane: $P_1 = (I_o - I_{90})/(I_o + I_{90})$ and $P_2 = (I_{45} - I_{135})/(I_{45} + I_{135})$. The parameter P_3 reflects the degree of circular polarization of the emitted photons.
- The Stokes parameters were defined by George Gabriel Stokes in 1852 as a mathematically convenient alternative to the more common description of incoherent or partly polarized radiation in terms of its total intensity I , the degree of polarization P , and the orientation of the (so-called) polarization ellipse.
- **Degree of polarization:** The polarization state of the photon is said to be *pure* if they obey the Stokes parameters obey the restriction $\sum_{i=1}^3 P_i^2 = 1$.
- **Degree of linear polarization:** The parameter $P_\ell = \sqrt{P_1^2 + P_2^2}$ is called the **degree of linear polarization**.

Table 5.1.: Stokes parametrization of photons for selected polarization of photons with $\mathbf{k} \parallel \mathbf{e}_z$.

| Selected photon polarization | P_1 | P_2 | P_3 |
|------------------------------|-------|-------|-------|
| unpolarized | 0 | 0 | 0 |
| polarized along x -axis | 1 | 0 | 0 |
| polarized along y -axis | -1 | 0 | 0 |
| right-circularly polarized | 0 | 0 | 1 |
| left-circularly polarized | 0 | 0 | -1 |

- Stokes parameters $P_3 = P_c$: Photons with $\lambda = +1$ are called **right-circularly polarized photons**, and photons with $\lambda = -1$ are called **left-circularly polarized photons**.
- Note that the notation in optics is often opposite to that used in quantum electrodynamics for historical reasons.

Alternative representation of polarized photons:

- Instead of the Stokes parameters P_1 and P_2 , it is often convenient for the analysis of different experimental situations to use the degree of linear polarization P_ℓ and the direction of the principal axis of the polarization ellipse φ_0 .
- **Polarization ellipse:** If, in the chosen coordinate frame, the x -axis is directed along the principal axis of a polarized photon beam ($\varphi_0 = 0^\circ$), the Stokes parameter P_1 takes the largest value $|P_1| = P_\ell$, while the Stokes parameter P_2 vanishes. This easily shows that the Stokes parameters P_1 and P_2 depend on the choice of the x -axis even if the z -axis is fixed along the beam, while the degree of linear polarization P_ℓ remains invariant.
- **Polarization ellipse:** It is often convenient to introduce the angle φ_0 by the relations

$$\cos 2\varphi_0 = \frac{P_1}{P_\ell}, \quad \sin 2\varphi_0 = \frac{P_2}{P_\ell}$$

- **Probability for measuring a linearly polarized photon along φ in the xy -plane:** For a density matrix with given P_ℓ , φ_0 Balashov *et al.*

(2001) shows the probability distribution

$$W(\varphi) = \frac{1}{2}(1 + P_\ell \cos 2(\varphi - \varphi_0))$$

for measuring linearly-polarized photon along φ in the xy -plane.

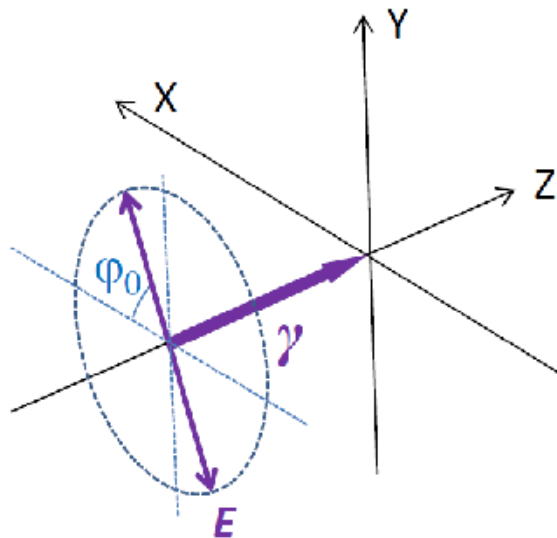


Figure 5.1.: Laboratory coordinate system.

- Angle of the polarization vector: The angle φ_0 indicates the *principal axis of the polarization ellipse* of the photon beam. It describes the direction of the axis (with regard to the x -axis) which the intensity of the transmitted photon beam is the largest, while it is lowest intensity perpendicular to this direction.

Photon density matrix:

- Photon density matrix in helicity representation: Most naturally, the spin state of an incident photon is expressed within its **helicity representation**

$$\rho_\gamma = \sum_{\lambda \lambda'} c_{\lambda \lambda'} |\mathbf{k} \lambda\rangle \langle \mathbf{k} \lambda'|,$$

where the helicity λ is the spin projection of the photon upon the direction of its propagation, i.e. along the momentum or wave vector \mathbf{k} .

- Since for a photon (with intrinsic spin $s \equiv 1$) the helicity just takes the values $\lambda = \pm 1$, only three real parameters are required to describe the spin state of the photons. These parameters in the photon density matrix are closely connected to the Stokes parameters of light (Rose, 1961)

$$(c_{\lambda \lambda'}) = \langle \mathbf{k} \lambda | \rho_\gamma | \mathbf{k} \lambda' \rangle = \frac{1}{2} \begin{pmatrix} 1 + P_3 & P_1 - iP_2 \\ P_1 + iP_2 & 1 - P_3 \end{pmatrix}.$$

Note that this definition differs from those in Balashov *et al.* (2005) by a factor -1 for the P_1 and P_2 parameters because of the different convention of the spherical unit vectors \mathbf{e}_\pm .

5.2.b. Pure polarization states of photons

Linearly-polarized plane-wave photons with $\mathbf{k} \parallel \mathbf{e}_z$:

- In this section, we consider **pure polarization states** of an incoming photon, i.e. light with a photon density matrix $P_1^2 + P_2^2 + P_3^2 = 1$, and which is thus equivalent to a density-matrix with $\rho^2 = \rho$.
- With this restriction in mind, **any polarized state of a transverse photon** can be described by the linear combination

$$|\mathbf{e}\rangle = g_+ \mathbf{e}_+ + g_- \mathbf{e}_-,$$

where \mathbf{e}_λ ($\lambda = \pm$) are the **unit polarization vectors** within the circular basis, and with $|g_+|^2 + |g_-|^2 = 1$.

➤ The state of a linearly-polarized photon along some given direction φ_0 in the $x - y$ plane can be written in the form

$$|\mathbf{e}_{\varphi_0}\rangle = -\frac{1}{\sqrt{2}} (e^{-i\varphi_0} \mathbf{e}_+ - e^{i\varphi_0} \mathbf{e}_-) .$$

➤ Pure linearly-polarized light with $P_\ell = 1$: $|g_+| = |g_-|$.

Elliptically-polarized plane-wave photons with $\mathbf{k} \parallel \mathbf{e}_z$:

➤ Photon density matrix in terms of the g_{\pm} coefficients: With these notations, an arbitrarily polarized pure state of a (transversal) photon can be expressed in terms of the g_{\pm} coefficients by either a 2×2 matrix or by means of the corresponding Stokes parameters:

$$\langle \mathbf{k}\lambda | \rho | \mathbf{k}\lambda' \rangle = \begin{pmatrix} |g_+|^2 & g_+ g_-^* \\ g_+^* g_- & |g_-|^2 \end{pmatrix}, \quad P_1 = -2 \Re(g_+ g_-^*), \quad P_2 = 2 \Im(g_+ g_-^*), \quad P_3 = |g_+|^2 - |g_-|^2.$$

➤ Polarization ellipse: The linear polarization can be characterized also by P_ℓ and φ_0 with

$$P_\ell = 2|g_+ g_-^*| = 2|g_+| |g_-| \cos 2\varphi_0 = -\frac{\Re(g_+ g_-^*)}{|g_+ g_-^*|}, \quad \sin 2\varphi_0 = -\frac{\Im(g_+ g_-^*)}{|g_+ g_-^*|}.$$

These simple relations can be used to also find the g_{\pm} -coefficients for given parameters P_ℓ and φ_0 .

➤ Fully-polarized light with $P_\ell \neq 1$:

$$\text{for } |g_+| > |g_-| : \quad |g_+| = \frac{1}{2} (\sqrt{1+P_\ell} + \sqrt{1-P_\ell}), \quad |g_-| = \frac{1}{2} (\sqrt{1+P_\ell} - \sqrt{1-P_\ell})$$

$$\text{for } |g_+| < |g_-| : \quad |g_+| = \frac{1}{2} (\sqrt{1+P_\ell} - \sqrt{1-P_\ell}), \quad |g_-| = \frac{1}{2} (\sqrt{1+P_\ell} + \sqrt{1-P_\ell})$$

➤ The relative phase of the coefficients: $g_+ = |g_+| e^{i\xi_+}$; $g_- = |g_-| e^{i\xi_-}$ can be found from the equation: $\xi_- - \xi_+ = 2\varphi_0 + \pi$.

➤ Polarization vectors $\boldsymbol{\epsilon}_1, \boldsymbol{\epsilon}_2$ of elliptical-polarized plane-wave radiation: An alternative representation of the polarization vector is given by:

$$\boldsymbol{\epsilon}_j = \left(\mathbf{e}_x \cos\left(\frac{\xi_j}{2}\right) + i \mathbf{e}_y \sin\left(\frac{\xi_j}{2}\right) \exp\left(\frac{i\eta_j}{2}\right) \right), \quad \boldsymbol{\epsilon}_j^* = \left(\mathbf{e}_x \cos\left(\frac{\xi_j}{2}\right) - i \mathbf{e}_y \sin\left(\frac{\xi_j}{2}\right) \exp\left(\frac{-i\eta_j}{2}\right) \right), \quad j = 1, 2.$$

5. Atomic interactions with the radiation field

- Two elliptically-polarized beams with the same angular momentum but opposite helicity: The easiest way to describe such a superposition is $\xi_1 = \xi_2 = \pi/2$, $\eta_1 = \eta_2 = 0$, and this leads to

$$\epsilon_1 = \epsilon_2 \equiv \epsilon, \quad \epsilon_1^* = \epsilon_2^* \equiv \epsilon^*, \quad \epsilon \cdot \epsilon^* = 1, \quad \epsilon \cdot \epsilon = \epsilon^* \cdot \epsilon^* = 0.$$

- Two elliptically-polarized beams with the same helicity and opposite angular momentum: These beams are described by $\xi_1 = -\xi_2 = \pi/2$, $\eta_1 = \eta_2 = 0$, and the two polarization vectors then fulfill

$$\epsilon_1 = \epsilon_2^* \equiv \epsilon, \quad \epsilon_1^* = \epsilon_2 \equiv \epsilon^*, \quad \epsilon \cdot \epsilon^* = 1, \quad \epsilon \cdot \epsilon = \epsilon^* \cdot \epsilon^* = 0.$$

Beams of fully-polarized light with $\mathbf{k} \nparallel \mathbf{e}_z$:

- Sequences of completely polarized light pulses: In experiments, one often considers a sequence of (fully polarized) photon pulses, which propagate however into different directions.
- Hierarchy of angles in defining the em pulses: For such a sequence of pulses, all angles are defined with respect to a fixed laboratory frame $\Sigma = (x, y, z)$, and where we assume all coordinate systems to be properly ‘right-handed’.
- In the (primed) coordinates Σ' as associated with some given pulse, the polarization coefficients are assumed to be:

$$g_+ = 1, \quad g_- = 0 \quad (\text{for ‘helicity : +1’})$$

$$g_+ = 0, \quad g_- = 1 \quad (\text{for ‘helicity : -1’})$$

$$g_+ = -\frac{1}{\sqrt{2}} e^{-i\phi_0}, \quad g_- = \frac{1}{\sqrt{2}} e^{i\phi_0} \quad (\text{for ‘linear’ and given } \phi_0).$$

- First pulse: The wave vector of the first pulse always defines the z -axis and its linear polarization (ϕ_0) the x -axis of the fixed frame Σ , i.e. the first pulse defines the $x - z$ scattering plane. For a circularly polarized pulse, the x -axis is defined indirectly due to the definition of subsequent pulses (see below); it need not to be defined explicitly if there is only a single, circularly-polarized pulse.

➤ Parameters of the first pulse:

$$\phi_1 = 0; \quad \theta_1 = 0; \quad (\phi_1 = 0 \quad \text{for circularly polarized light})$$

➤ **Polarization vectors for circularly-polarized light:** In the helicity representation of the density matrix or polarization tensors, the photons have well-defined spin projection along their propagation direction, $\lambda = \mathbf{s} \cdot \mathbf{k}/s k = \pm 1$. In this representation, the polarization vectors are given by

$$\mathbf{u}_{\lambda=\pm 1} = \sum_{\sigma=0,\pm 1} e^{-i\sigma\varphi} d_{\sigma\lambda}^{(1)} \mathbf{e}_\sigma,$$

where \mathbf{e}_σ are the spherical unit vectors and $d_{\sigma\lambda}^{(1)}$ the small Wigner rotation matrix.

5.2.c. Spherical tensors of polarization vectors

Spherical tensors:

- Relation between linear and circular polarization vectors: Using the convention by Rose, the polarization vectors fulfill with the azimuthal angle $\phi^{(\text{linear})} = \angle(\mathbf{u}^{(\text{linear})}, \mathbf{e}_x)$ the (standard) relation:

$$\mathbf{u}^{(\text{linear})} = \frac{1}{\sqrt{2}} \sum_{\lambda} e^{-i\lambda\phi^{(\text{linear})}} \mathbf{u}_{\lambda}.$$

- Spherical tensor $[\mathbf{u}^* \otimes \mathbf{u}]_q^{(K)}$: The compound spherical tensor of the (complex) polarization vectors can be written in terms of its spherical tensor components of \mathbf{u}

$$[\mathbf{u}^* \otimes \mathbf{u}]_q^{(K)} = \sum_{r,s=0,\pm 1} (-1)^{q+s} \sqrt{2K+1} \begin{pmatrix} 1 & K & 1 \\ r & -q & s \end{pmatrix} u_r u_{-s}^*$$

and, hence, is related also to the cartesian (vector) components $\mathbf{u} = (u_x, u_y, u_z)$ of the polarization vector.

- Tensor products of the polarization vector: The tensorial products of the polarization vector can be evaluated in terms of the unit vectors of the coordinates and the electro-magnetic field as

$$[\mathbf{u}^* \otimes \mathbf{u}]_0^{(0)} = -\frac{1}{3} (\mathbf{u}^* \cdot \mathbf{u}) = -\frac{1}{3}$$

$$[\mathbf{u}^* \otimes \mathbf{u}]_0^{(1)} = -\frac{i}{\sqrt{2}} (\mathbf{u}^* \times \mathbf{u}) \cdot \mathbf{e}_z = \frac{P_3}{\sqrt{2}} (\mathbf{e}_k \cdot \mathbf{e}_z) = \frac{P_3}{\sqrt{2}} \cos \vartheta_k$$

$$[\mathbf{u}^* \otimes \mathbf{u}]_0^{(2)} = \frac{1}{\sqrt{6}} [3(\mathbf{u}^* \cdot \mathbf{e}_z)(\mathbf{u} \cdot \mathbf{e}_z) - (\mathbf{u}^* \cdot \mathbf{u})] = \frac{1}{\sqrt{6}} [3|\mathbf{u} \cdot \mathbf{e}_z|^2 - 1] = \frac{1}{\sqrt{6}} [3 \cos^2 \vartheta_u - 1].$$

Here, ϑ_k is the angle of the \mathbf{k} -vector with regard to the z -axis, ϑ_u the angle of the polarization direction with regard to the z -axis. Often, however, other parameters are chosen characterize the polarizabilities and (ac) Stark shifts.

- Polarization tensor approach: Irreducible polarization tensors have been defined in the past in order to analyze the polarization properties of the elastically scattered light in the resonant-scattering approximation. These polarization tensors enable one to explore the polarization

of the scattered light, even if the incident radiation is polarized itself. For a more realistic treatment beyond the resonant-scattering approximation, the irreducible polarization tensors need to be combined with the density matrix theory.

- **Polarization tensor $T_{kq}^{(E1,E1)}$ in the helicity representation:** In the helicity representation of the polarization vectors, the polarization tensor $T_{kq}^{(E1,E1)}$ for head-on collisions of partially-stripped ions with photon ($\vartheta_f = \pi, \varphi = 0$) can be written as

$$\begin{aligned} T_{kq}^{(E1,E1)}(\mathbf{k}_i, \mathbf{u}_{\lambda_i}; \mathbf{k}_f, \mathbf{u}_{\lambda_f}) &= \frac{3}{8\pi} \sum_{\sigma\sigma'} \left[\langle 1\sigma, 1\sigma' | kq \rangle (-1)^{\sigma'} e^{i(\sigma\varphi_f + \sigma'\varphi_i)} d_{\sigma, \lambda_f}^{(1)}(\vartheta_f) d_{-\sigma', \lambda_i}^{(1)}(\vartheta_i) \right] \\ &= -\frac{3}{8\pi} \sum_{\sigma} \langle 1\sigma, 1\lambda_i | kq \rangle e^{i\sigma\varphi_f} d_{-\sigma', \lambda}^{(1)}(\vartheta_f). \end{aligned}$$

- **Polarization vector of twisted beams:** Since the polarization vector of such beams depend on its individual plane-wave components, it must depend explicitly not only on the helicity λ of its plane-wave component but also on the angles ϑ_k, φ_k . A useful parametrization of the polarization vector is then given by

$$\mathbf{u}(\mathbf{k}, \lambda) = \frac{e^{i\lambda\varphi_k}}{\sqrt{2}} \begin{pmatrix} \cos \vartheta_k \cos \varphi_k - i\lambda \sin \varphi_k \\ \cos \vartheta_k \sin \varphi_k - i\lambda \cos \varphi_k \\ -\sin \varphi_k \end{pmatrix}, \quad \mathbf{u}(\mathbf{k}, \lambda; \vartheta_k \rightarrow 0) = \begin{pmatrix} 1 \\ i\lambda \\ 0 \end{pmatrix}$$

which fulfills the transversality condition $\mathbf{k} \cdot \mathbf{u}(\mathbf{k}, \lambda) = 0$ and goes for $\vartheta_k \rightarrow 0$ over into the usual polarization vectors for circularly polarized plane waves.

- **Polarization vector of twisted beams:** The polarization vector $\mathbf{u}(\mathbf{k}, \lambda)$ is an eigenvector of the z-component $j_z = l_z + s_z$ of the total angular momentum operator with eigenvalues $m_j = m + \lambda$. With the standard definition of Bessel beams, therefore, the Bessel modes are also eigenfunctions of the total angular momentum projection: $j_z \mathbf{A}^{(\text{Bessel})} = (m + \lambda) \mathbf{A}^{(\text{Bessel})}$.

5.3. Multipole decomposition of the radiation field

5.3.a. Elements from the theory of multipole transitions

Electron-photon interaction:

- **Electron-photon interaction operator:** To account for different gauges in the interaction with monochromatic, plane-wave light, this (interaction) operator can be written in terms of the wave vector \mathbf{k} and the (complex) polarization vector \mathbf{u} as

$$R(\mathbf{k}, \mathbf{u}) = \boldsymbol{\alpha} \cdot (\mathbf{u} + G \mathbf{k}) e^{i\mathbf{k}\cdot\mathbf{r}} - G e^{i\mathbf{k}\cdot\mathbf{r}} = 4\pi \sum_{pLM} i^{L-|p|} \left[\mathbf{u} \cdot \mathbf{Y}_{LM}^{(p)}(\vartheta_k, \varphi_k) \right] a_{LM}^{(p)}(r)$$

Here, the gauge parameter can be set to $G = 0$ for the Coulomb (velocity) gauge and to $G = \sqrt{(L+1)/L}$ for the Babushkin (length) gauge. Moreover, $\mathbf{Y}_{LM}^{(p)}(\vartheta_k, \varphi_k)$ are the vector spherical harmonics and $a_{LM}^{(p)}(r)$ are the electric ($p = 1$), magnetic ($p = 0$) and longitudinal ($p = -1$) multipole components of the radiation field (or briefly, multipole fields).

- Orthogonality of the vector spherical harmonics:

$$\int d\Omega_k \left[\mathbf{u}^* \cdot \mathbf{Y}_{LM}^{(p)}(\vartheta_k, \varphi_k) \right] \left[\mathbf{u} \cdot \mathbf{Y}_{L'M'}^{(p')*}(\vartheta_k, \varphi_k) \right] = \delta_{pp'} \delta_{LL'} \delta_{MM'},$$

Transition amplitudes:

- Johnson (2008) provide a systematic decomposition of the transition amplitudes into multipole components.
- **Transition amplitudes due to a transverse-gauge vector potential $\mathbf{A}^{(\text{transverse})}(\mathbf{r}, \omega)$:** For a single-electron atom, the transition amplitude from state $a = |n_a \kappa_a m_a\rangle \rightarrow b = |n_b \kappa_b m_b\rangle$ due to the interaction with a plane-wave radiation field with the transverse-gauge vector potential $\mathbf{A}^{(\text{transverse})}(\mathbf{r}, \omega) = \epsilon e^{i\mathbf{k}\cdot\mathbf{r}}$, with $\epsilon \cdot \mathbf{e}_z = 0$ is

$$T_{ba} = \int d^3\mathbf{r} \psi_b^* \boldsymbol{\alpha} \cdot \mathbf{A}^{(\text{transverse})}(\mathbf{r}, \omega) \psi_a.$$

Multipole potentials:

- Plane-wave multipole potentials $\mathbf{a}_{LM}^{(p)}(\mathbf{r})$: In the **multipole expansion** of the plane-wave vector potential, the multipole potentials satisfy both, the Helmholtz equation and **transversality condition**

$$\nabla^2 \mathbf{a}_{LM}^{(p)} + k^2 \mathbf{a}_{LM}^{(p)} = 0, \quad \nabla \cdot \mathbf{a}_{LM}^{(p)} = 0 \quad p = 0, 1.$$

- The multipole potentials $\mathbf{a}_{LM}^{(p)}$ with $p = 0$ are the magnetic multipole potentials and with $p = 1$ the electric multipole potentials.
- **Electron-multipole interaction operator:** The interaction operator $\boldsymbol{\alpha} \cdot \mathbf{a}_{LM}^{(p)}$ is an irreducible tensor operator of rank L and parity $(-1)^{L+1-p}$.
- The **multipole expansion of the (transverse-gauge) plane-wave vector potential** still contains all information about the polarization and propagation direction of the photons.
- **Representation of the multipole potentials:** Using the well-known identities of the spherical Bessel functions, the multipole potentials $\mathbf{a}_{LM}^{(p)}$ can be expressed as (Johnson, 2007)

$$\mathbf{a}_{LM}^{(0)}(\mathbf{r}) = j_L(kr) \mathbf{Y}_{LM}^{(0)}(\mathbf{r}), \quad \mathbf{a}_{LM}^{(1)}(\mathbf{r}) = \left[j'_L(kr) + \frac{j_L(kr)}{kr} \right] \mathbf{Y}_{LM}^{(1)}(\mathbf{r}) + \sqrt{L(L+1)} \frac{j_L(kr)}{kr} \mathbf{Y}_{LM}^{(-1)}(\mathbf{r}).$$

- **Spherical-wave decomposition of the photon field:** The spherical-wave decomposition of the photon field can be written for photons with well-defined wave vector \mathbf{k} and helicity $\lambda = \pm 1$ as

$$\mathbf{u}_{\mathbf{k}\lambda} = \sqrt{2\pi} \sum_{LM} i^L \sqrt{2L+1} D_{M\lambda}^{(L)}(\varphi_k, \vartheta_k, 0) \sum_{p=0,1} (i\lambda)^p \mathbf{a}_{LM}^{(p)}(\mathbf{r}),$$

and where the $\mathbf{a}_{LM}^{(p)}(\mathbf{r})$ refer to the magnetic ($p = 0$) and electric ($p = 1$) multipole components of the radiation fields

$$\mathbf{a}_{LM}^{(0)}(\mathbf{r}) = j_L(kr) \mathbf{Y}_{L,L,M}^{(0)}(\mathbf{r}), \quad \mathbf{a}_{LM}^{(1)}(\mathbf{r}) = j_{L-1}(kr) \sqrt{\frac{L+1}{2L+1}} \mathbf{Y}_{L,L-1,M}^{(1)}(\mathbf{r}) - j_{L+1}(kr) \sqrt{\frac{L}{2L+1}} \mathbf{Y}_{L,L+1,M}^{(1)}(\mathbf{r}).$$

5.3.b. Single-electron (reduced) multipole-transition matrix elements

Johnson's single-electron reduced multipole-transition matrix elements:

- **Transverse (velocity) gauge:** Johnson (2007, section 6.3) derives the reduced multipole-transition matrix elements for $\mathbb{M} = (L, p)$ and $q = \omega/c$ as:

$$\langle a \parallel \mathbb{t}^{(\mathbb{M}, \text{magnetic})}(\omega) \parallel b \rangle = \langle -\kappa_a \parallel \mathbb{C}^{(L)} \parallel \kappa_b \rangle \int_0^\infty dr \frac{\kappa_a + \kappa_b}{L+1} j_L(qr) [P_a Q_b + Q_a P_b]$$

$$\langle a \parallel \mathbb{t}^{(\mathbb{M}, \text{electric})}(\omega) \parallel b \rangle = \langle \kappa_a \parallel \mathbb{C}^{(L)} \parallel \kappa_b \rangle \int_0^\infty dr \left\{ -\frac{\kappa_a - \kappa_b}{L+1} \left[j'_L(qr) + \frac{j_L(qr)}{qr} \right] [P_a Q_b + Q_a P_b] + L \frac{j_L(qr)}{qr} [P_a Q_b - Q_a P_b] \right\}.$$

- **Length gauge:** While the reduced multipole-transition matrix elements are the same in length gauge, Johnson (2007, section 6.3) derives the reduced multipole-transition matrix elements in length gauge as:

$$\begin{aligned} & \langle a \parallel \mathbb{t}^{(\mathbb{M}, \text{electric})}(\omega) \parallel b \rangle \\ &= \langle \kappa_a \parallel \mathbb{C}^{(L)} \parallel \kappa_b \rangle \int_0^\infty dr \left\{ j_L(qr) [P_a P_b + Q_a Q_b] + j_{L+1}(qr) \left[\frac{\kappa_a - \kappa_b}{L+1} [P_a Q_b + Q_a P_b] + [P_a Q_b - Q_a P_b] \right] \right\}. \end{aligned}$$

Johnson's frequency-dependent multipole-moment operators:

- **Multipole-moment matrix elements:** Following Johnson (2007), the reduced multipole-moment matrix elements can be calculate for the reduced multipole-transition matrix elements

$$\langle a \parallel \mathbb{q}^{(\mathbb{M})}(\omega) \parallel b \rangle = \frac{(2L+1)!!}{q^L} \langle a \parallel \mathbb{t}^{(\mathbb{M})}(\omega) \parallel b \rangle.$$

5.3.c. Many-electron (reduced) multipole emission and absorption amplitudes

JAC's (standard) multipole amplitudes for photon absorption and emission:

- Mutipole (absorption) amplitude $|\alpha_i \mathbb{J}_i\rangle + \hbar\omega(\mathbb{M}, \lambda) \rightarrow |\alpha_f \mathbb{J}_f\rangle$: For the absorption of a photon with energy ω , well-defined multipolarity (angular momentum) L and helicity $\lambda = \pm 1$, we always use the notation

$$\langle \alpha_f \mathbb{J}_f | \mathbb{O}^{(\mathbb{M}, \text{absorption})}(\omega) | \alpha_i \mathbb{J}_i \rangle.$$

- Photon emission: from an atom or ion $|\alpha_i \mathbb{J}_i\rangle \longrightarrow |\alpha_f \mathbb{J}_f\rangle + \hbar\omega(\mathbb{M})$.
- Care has to be taken about the many-electron multipole amplitudes which appear in many expressions. While we need formally to distinguish between the absorption a_L^λ and emission operators $a_L^{\lambda+}$ operators, all (one- and many-electron) multipole-transition matrix elements are always evaluated *in absorption*.
- For any photon emission process, this would then require to 'interchange' the sequence *final-state — operator — initial-state* explicitly. This is a (very) high price however in such a large software project, since such an interchange affects the intuitive description of many processes in terms of initial-intermediate-final levels as well as still possibly other subsequent (final) states/levels.

5.4. Electromagnetic light pulses

5.4.a. High-intensity pulses

Matter in intense fields:

- The exposure of atoms and matter to high-intensity laser fields is known to give rise to **high-harmonic generation**, **above-threshold ionization** and well as **laser-induced dissociation** and **plasma formation**, and which are all fundamentally different from processes in the weak-field regime.
- These phenomena are often outside of what is described by (standard) atomic-structure methods since the external field, that acts upon the electrons in typical strong-field experiments, is then comparable to the Coulomb potential of the nucleus.
- **Pump-probe experiments:** In these experiments, two short pulses are typically required. While the pump pulse starts the reaction, the probe pulse investigates the state of the system after a defined time delay. These measurements are repeated several times with increasing time delays in order to finally obtain a **molecular movie**.
- If the level structure of the atoms is not affected by the (moderately intense) laser pulses, the time-dependent density matrix may allow to model the (time-dependent) level occupation and coherences of an atom and, eventually, all the photoexcitation and ionization processes.
- **Two-color absorption in strong laser fields:** The simultaneous absorption of a single high-frequency photon in a strong optical laser field generally leads to equally spaced sideband peaks in the photoelectron spectra due to the (additional) absorption or emission of several laser photons. This (XUV + IR) two-color absorption has been first observed in high-order harmonic generation by overlapping high harmonics with the fundamental laser frequency. With a femtosecond XUV pulse from a FEL, the two-color absorption in strong laser fields can be explored without the contributions from neighbouring harmonics (Gramajo *et al.*, 2017).
- **Two-color absorption in strong laser fields:** Two different interaction regimes can be distinguished for the interaction of atoms with a combined and overlapping XUV and IR pulses owing to their relative pulse duration: (i) If the XUV pulse duration $\tau^{(\text{XUV})} \gtrsim \tau^{(\text{IR})}$ is longer than the IR pulse, the intensity of the sideband peaks in the photoelectron spectrum directly reflect the intensity of the IR laser; (ii) for $\tau^{(\text{XUV})} \ll \tau^{(\text{IR})}$, in contrast, the photoelectron spectrum acts as a *streak camera* and reflects the shape and duration of an IR laser pulse. Moreover, variations of the polarization state of the XUV and/or IR laser fields gives generally rise to **dichroic effects in the photoelectron spectrum** (Gramajo *et al.*, 2017).
- **Normalized vector potential a_o :** For a time-harmonic light field with the electric-field amplitude \mathcal{E}_o and frequency ω , the (frequency-)

normalized amplitude of the vector potential can be expressed by the amplitude

$$a_o = \frac{e \mathcal{E}_o}{m \omega c} = 0.85 \times \lambda [\mu\text{m}] \times \sqrt{I [\times 10^{18} \text{ W cm}^{-2}]}; \quad I \propto a_o^2 \propto \mathcal{E}_o^2$$

For $a_o \approx 1$, the field is strong enough to accelerate electrons to relativistic velocity and then requires to account for both, the electric and magnetic fields.

- **Normalized laser amplitude:** In strong-field physics, the amplitude of the laser field is typically obtained by $a_o = 0.68 I [10^{18} \text{ W cm}^{-2}]$. In such fields, the electrons are considered to be relativistic if $a_o \gg 1$.

5.4.b. Pulse shapes and optical cycles

Pulse shaping in physics and science:

- Pulse shaping is frequently used in physics, science and technology. Pulse shaping generally refers to the process of changing the waveform of a (transmitted) pulse, for instance, in order to make a transmitted signal better suited for a particular communication channel. In telecommunication, for example, pulse shaping is essential in order to ensure that the signal fit to a given frequency band.
- In femtosecond physics and chemistry, pulse shaping describes a technology for generating nearly arbitrary pulses with user defined, ultrafast optical waveforms, and by controlling its phase, amplitude, and polarization. Here, the most widely applied technique is Fourier transform pulse shaping.

Frequently applied pulse shapes for time-dependent atomic computations:

- In pump- and/or pump-probe experiments, all (symmetric) light pulses are typically defined in terms of a central frequency ω and a (delay) time T_d for the arrival of the pulse center with regard to same reference time $t_0 = 0$. Moreover, the shape function is always normalized to $\max[f_s(t)] = \max[f(t)/f_o] = 1$ and, hence, the intensity of the em field must be captured properly by the constant f_o .
- In JAC, the following (symmetric) shapes of the em pulses have been pre-defined: "sin^2", "sin^2: plateau", "sin^2: cycles" and "gaussian" facilitate the description of experimentally specified pulses. Further pulses shapes might be added if the need arises from the side of experiment.
- It is important to ensure that the pulse-shape function $f_s(t)$ (envelope) just contains an integer number of optical cycles. Therefore, one often starts with an \sin^2 envelope. For example, an envelope function $\sin^2 10T$ pulse refers to a pulse with 10 optical cycles.

5. Atomic interactions with the radiation field

- **Laser pulse:** In time-resolved computations, the laser-atom interaction can be described either by a **smooth** or a **square pulse with envelope** (Gharibnejab *et al.*, (2020))

$$\mathcal{E}(t) = \begin{cases} \mathcal{E}_o \sin^2\left(\frac{\pi t}{T}\right) \mathbf{e}_z & 0 \leq t < T \\ 0 & \text{otherwise} \end{cases}, \quad \mathcal{E}(t) = \begin{cases} \mathcal{E}_o \mathbf{e}_z & 0 \leq t < T \\ 0 & \text{otherwise} \end{cases}$$

- **Vector potential of laser pulses in velocity gauges:** For a smooth or square pulse and $\phi^{(\text{CEP})} = 0$, the vector potential in the interval $0 \leq t < T$ is (Gharibnejab *et al.*, 2020)

$$A(t) = c \mathcal{E}_o \left(\frac{\sin^2(a^+ t/2)}{2 a^+} - \frac{\sin^2(a^- t/2)}{2 a^-} - \frac{\sin^2(\omega t/2)}{\omega} \right), \quad a^+ = \frac{2\pi}{T} + \omega, \quad a^- = \frac{2\pi}{T} - \omega \quad \text{smooth pulse}$$

$$A(t) = -c \int_0^t d\tau \mathcal{E}(\tau) = -2c \mathcal{E}_o \frac{\sin^2(\omega t/2)}{\omega} \quad \text{square pulse}$$

- In time-dependent studies, various findings about the relative timing and the convergence of numerical results with regard to the step size are independent of the particular type of the laser pulse, i.e. are similar for smooth and square pulse.

- **Length *versus* velocity gauge:** In length gauge, the interaction with the external electro-magnetic field is local and gives rise to a straightforward time evolution due to the given Hamiltonian. In the velocity gauge, in contrast, the Hamiltonian is hermitian and the interaction is *non-local*. In realistic problems, therefore, the choice of the gauge can make significant differences in dependence of the given wavelength. This dependence is also a direct consequence which (high) angular momenta are relevant for the coupling of the radiation field to the electrons.

5.4.c. Maximum pulse intensity

Vector potential:

- **Amplitude of the vector potential:** This amplitude need to be derived from the (maximum) intensity of a laser pulses that is typically given in W/cm^2 . In general, this relation between intensity and amplitude is non-trivial since the relationship between intensity and the electric field depends also slightly on the polarization of the pulse. A simple relation only occurs for a linearly-polarized laser beam.

- **Average intensity of a pulse:** If only the average intensity is given, the conversion factor depends also on the particular pulse-shape function. In practice, however, experimentalists rarely know the intensity accurately and, hence, a simplified normalization procedure can normally be used.
- **Vector potential of a single pulse:** The interaction of the electrons with the electric field of the incident pulse of frequency ω , duration T , carrier envelope phase ϕ and with linear polarization along \mathbf{e}_p is often described in terms of the vector potential

$$\mathbf{A}(t) = A_o \sin^2\left(\frac{\pi t}{T}\right) \sin(\omega t + \phi) \mathbf{e}_p, \quad A_o = \frac{1}{\omega} \sqrt{\frac{I}{I_o}},$$

and where $I_o = 3.5 \cdot 10^{16}$ W/cm².

Intensity and pulse geometry:

- The atomic unit of electric field is $m_e^2 e^5 / \hbar^4 = 5.1422 \cdot 10^9$ V/cm. From this we have: E_0 [a.u.] = $5.34 \cdot 10^{-9} \sqrt{I}$ [W/cm²].

5.4.d. Bichromatic laser fields

Bichromatic laser fields:

- **Bichromatic laser fields:** Of some special interests in light-atom interaction studies are fields with two components of commensurate frequencies; for instance, the fundamental component ω and one of its low harmonics 2ω or 3ω . Moreover, these two components are in general out of phase by some angle ϕ .
- **Linearly-polarized bichromatic fields:** For such a field, the electric field can be written in a quite general form as

$$E(t) = F(t) \left[\cos(\omega t + \phi_1^{(cep)}) + \eta \cos(2\omega t + \phi_2^{(cep)}) \right]$$

with frequencies ω of the fundamental radiation and 2ω due to the second harmonic. Here, the same envelope function $F(t)$ is applied for both, the fundamental and the second harmonic, while the ratio of the corresponding amplitudes is specified by the real parameter η ($\eta > 0$). The carrier-envelope phases (CEP) are here denoted by $\phi_1^{(cep)}$ and $\phi_2^{(cep)}$, respectively.

5. Atomic interactions with the radiation field

- Time-dependent electric field in two-color experiments: In two-color experiments, the field is often approximated by (DiFraia *et al.*, 2019)

$$\mathcal{E}(t) = \sqrt{I_\omega(t)} \cos \omega t + \sqrt{I_{2\omega}(t)} \cos(2\omega t - \phi), \quad \boldsymbol{\mathcal{E}}(t) = \mathcal{E}(t) \mathbf{e}_z,$$

and where $I_\omega(t)$, $I_{2\omega}(t)$ are the envelopes of the two pulses and ϕ the relative phase between the $\omega - 2\omega$ pulses. In this definition, the larger ϕ as more the 2ω pulse is delayed.

- Fritzsche and Hofbrucker (2022); NZ; xp-2022.njp-fritzsche-biharmonic.pdf
- **Biharmonic fields:** Biharmonic fields are generally formed as superposition of two beam components with different color, polarization, and sometimes even of different pulse structure. For the sake of simplicity, one often considers the superposition of two vector potentials, one with fundamental frequency ω and another from its second harmonic

$$\mathbf{A}(\mathbf{r}, t) = A_0^{(\omega)} \mathbf{A}^{(\omega)}(\mathbf{r}, t) + e^{i\Phi} A_0^{(2\omega)} \mathbf{A}^{(2\omega)}(\mathbf{r}, t), \quad \mathbf{A}^{(n\omega)}(\mathbf{r}, t) = \boldsymbol{\epsilon}^{(n\omega)} e^{-in\omega t + i\mathbf{k}^{(n\omega)} \cdot \mathbf{r}},$$

which both propagate along the quantization axis, $\mathbf{k} \parallel \mathbf{e}_z$. This form clearly distinguishes the field amplitudes (intensities) $A_0^{(n\omega)}$ ($n = 1, 2$) right from the beginning from the spatially and time-dependent vector potentials. The field amplitude $A_0^{(n\omega)}$ determine both, the flux $F^{(n\omega)} = (A_0^{(n\omega)})^2$ and the intensity $I^{(n\omega)} = n\omega F^{(n\omega)} = n\omega (A_0^{(n\omega)})^2$ of the corresponding component.

5.5. Light-field forces (optical forces)

Light-field forces:

- **Multipole fields:** Because of their quite strong suppression, the electric-quadrupole (E2) contributions to the optical forces of laser light have rarely been considered, especially for electric-dipole allowed transitions. A few quantum-optical studies have been made only for two-level atoms and without any account of their spatial degrees of freedom. However, these E2 contributions have led to a number of applications in atom trapping and cooling, atom optics, the creation of atomic Bose-Einstein condensates, atom lasers, atoms in optical lattices as well as for quantum simulators (Lembessis and Babiker, 2013).

5.6. Elements from modern optics

Singular optics:

- **Singular optics:** This field of modern optics makes use of wavefront dislocations and phase singularities.
- **Singular optics:** The subject of singular optics are light fields with an intricate knot structure in their field line, fields with optical vortices and (so-called) C-lines as well as light fields with spirals, umbilics, ribbons and Möbius strips in their polarization. These light fields give rise to many different phenomena if they are coupled with space-dependent birefringent elements.
- **Characterization of single photons:** Single photons and photonic qubits form the foundation many optical quantum information techniques, such as teleportation, repeaters, quantum computation or cryptography. In these applications, it is often desirable to have photons in a well-defined pure mode. While the spatial modes of photons have been characterized experimentally, the temporal modes of photons are more difficult to resolve (Qin *et al.*, 2015). Further insight into the quality of photon preparation techniques can be obtained by analyzing the time-dependent photon counting autocorrelation statistics, though this method does not give information about the phase coherence between different segments of the temporal mode of the photons.
- **Selective reflection (SR):** SR of resonant optical radiation from interfaces of atomic vapor and gas cells was first observed by Wood in 1909 and later revisited in the 1970s, when narrow-linewidth tunable cw lasers became available. Today, the SR technique has become a powerful tool for studying the van der Waals (vdW) interaction of atoms with a dielectric window of the cell, and which leads to a redshift of the SR frequency. Optical spectroscopy with atomic vapor and cells with nanometric-thickness is an alternative technique for obtaining information about atom-surface processes.

Spontaneous parametric down-conversion:

- **Spontaneous parametric down-conversion (SPDC):** SPDC refers to the generation of two low-frequency photons, when a (strong) pump field interacts with a nonlinear crystal. The SPDC process has been found a reliable source of entangled photons, and where the photon pair is generally entangled not only in their polarization but also with regard to their spatial degrees of freedom. While most applications of SPDC make presently use of the entangled polarization state, the spatial entanglement occurs has gained increasing attention. The spatial entanglement of photon pairs occurs in some (infinite-dimensional) Hilbert space and is a very promising feature for applying SPDC for quantum information tasks.

Interaction-free measurements:

5. Atomic interactions with the radiation field

- **Interaction-free measurements:** Such measurements have been suggested by White *et al.* (1998) by utilizing the complementary wave-like and particle-like character of photons. Several such interaction-free measurements schemes have been explored and support the optical imaging of photosensitive objects. In these schemes, less light need to be absorbed or scattered by the object, when compared to classical expectations.
- **Quantum imaging:** In 1993, Elitzur and Vaidman showed that any classical or quantum object (photon) can affect the interference of a single quantum particle with itself, even if the particle and object never directly interact with each other. This possibility to detect an object without having ever interacted with it has led to the term **interaction-free imaging**. Such an interaction-free imaging may advance the study of biological systems that often suffer by power-induced optical damage.

Quantum imaging:

- **Ghost imaging:** Ghost imaging refers to correlated photon imaging, whereby an image is formed from light that has never interacted with the object. **In ghost imaging experiments, two entangled or correlated light fields are produced.** One of these fields illuminates the object, while the other field is just measured by a spatially resolving detector. In quantum ghost imaging, the entangled photons are often generated by spontaneous parametric down-conversion.

6. Atomic amplitudes

6.1. In JAC implemented amplitudes

6.1.a. Dipole amplitudes (MultipoleMoment)

Amplitude, notations & application:

- Formal quantum notation: $\langle \alpha_f \mathbb{J}_f \| \mathbb{D} \| \alpha_i \mathbb{J}_i \rangle = \langle \alpha_f \mathbb{J}_f \| \sum_i \mathbf{r}_i \| \alpha_i \mathbb{J}_i \rangle$ for $P_f \neq P_i$
- Note that the full dipole operator is often defined by: $\mathbb{D}' = -|e| \mathbb{D}$.
- Using JAC: Call `MultipoleMoment.dipoleAmplitude(levelf::Level, leveli::Level)` or `(levelf::Level, leveli::Level; display=true)`, if the value of the amplitude needs to be printed to screen.

6.1.b. Electro-magnetic multipole transition amplitudes (MultipoleMoment, Radiative)

Amplitude, notations & application:

- Formal quantum notation:

$$\begin{aligned}\langle \alpha_f \mathbb{J}_f \| \mathbb{O}^{(\mathbb{M}, \text{emission})}(\omega) \| \alpha_i \mathbb{J}_i \rangle &= \left\langle \alpha_i \mathbb{J}_i \left\| \sum_{k=1}^N \boldsymbol{\alpha}_k a_{k,L}^p \right\| \alpha_f \mathbb{J}_f \right\rangle^* \equiv \langle \alpha_i \mathbb{J}_i \| \mathbb{O}^{(\mathbb{M}, \text{absorption})}(\omega) \| \alpha_f \mathbb{J}_f \rangle^* \\ \langle \alpha_f \mathbb{J}_f \| \mathbb{T}^{(\mathbb{M}, \text{absorption})}(\omega) \| \alpha_i \mathbb{J}_i \rangle\end{aligned}$$

6. Atomic amplitudes

which retains the right order of the initial and final levels with regard to absorption or emission and which can be obtained from `Jac.Radiative.amplitude()`; cf. section 5.3.c.

- Using JAC: Call `Radiative.amplitude("absorption", Mp::Multipole, gauge::EmGauge, omega::Float64, level_f::Level, level_i::Level)` or `("absorption", Mp::Multipole, gauge::EmGauge, omega::Float64, level_f::Level, level_i::Level; display=true)`, if the value of the amplitude needs to be printed to screen.
- Using JAC: Call `MultipoleMoment.transitionAmplitude(Mp::Multipole, gauge::EmGauge, omega::Float64, level_f::Level, level_i::Level)` or `(Mp::Multipole, gauge::EmGauge, omega::Float64, level_f::Level, level_i::Level; display=true)`, if the value of the amplitude needs to be printed to screen.

Further remarks:

- A multipole $\mathbb{M} \equiv (L, p) \equiv (L, \text{electric/magnetic}) = E1, M1, E2, \dots$ hereby contains all information about its multipolarity (angular momentum) L and type *magnetic* ($p = 0$) or *electric* ($p = 1$), respectively.
- In the module `Radiative`, the multipole-transition amplitudes can be calculated in one of the gauge = {Coulomb, Babushkin, Magnetic} as appropriate for electric- and magnetic-multipole transitions.
- **Johnson's multipole-transition operators:** Following Johnson (2007), the electron-photon interaction with the multipole fields (\mathbb{M}) can be expressed in terms of a dimensionless multipole-transition operator $\mathbb{T}_M^{(\mathbb{M})}(\omega) = \sum_j \mathbb{t}_M^{(\mathbb{M})}(\mathbf{r}_j; \omega)$, an irreducible tensor operator, whose reduced (single-electron) matrix elements are given in Section 5.3.b. The amplitudes to these operators always describe the absorption of a photon with a given multipolarity.
- Johnson's (2007) multipole-transition amplitudes can be calculated in one of the gauge = {Velocity, Length, Magnetic} as appropriate for electric- and magnetic-multipole transitions.

6.1.c. Electro-magnetic multipole-moment amplitudes (MultipoleMoment)

Amplitude, notations & application:

- Formal quantum notation:

$$\langle \alpha_f \mathbb{J}_f \| \mathbb{Q}^{(\mathbb{M})}(\omega) \| \alpha_i \mathbb{J}_i \rangle$$

- Using JAC: Call `MultipoleMoment.amplitude(Mp::Multipole, gauge::EmGauge, omega::Float64, levelf::Level, leveli::Level)` or `(Mp::Multipole, gauge::EmGauge, omega::Float64, levelf::Level, leveli::Level; display=true)`, if the value of the amplitude needs to be printed to screen.

Further remarks:

- **Johnson's multipole-moment operator:** Johnson (2007) also defines a frequency-dependent (irreducible tensor) multipole-moment operator

$$\mathbb{Q}_M^{(\mathbb{M})}(\omega) = \sum_j \mathfrak{q}_M^{(\mathbb{M})}(\mathbf{r}_j; \omega) \equiv \frac{(2L+1)!!}{(\omega/c)^L} \sum_j \mathfrak{k}_M^{(\mathbb{M})}(\mathbf{r}_j; \omega)$$

- These amplitudes are calculated by a call to (Johnson's) multipole-transition amplitudes from above [cf. section 6.1.b] but by taking the frequency-dependence into account.
- Electric multipole-moment amplitudes can be calculated in one of the `gauge = {Velocity, Length, Magnetic}` as appropriate for electric- and magnetic-multipole transitions.
- **Unit of the transition dipole moment:** The transition dipole moment is often given in units of $1 \text{ D} = 0.393456 e a_o$, and where e is the unsigned electric charge.

6.1.d. Momentum transfer amplitudes (FormFactor)

Amplitude, notations & application:

- Formal quantum notation: $\left\langle \alpha_f J_f \middle| \sum_j \exp(i \mathbf{q} \cdot \mathbf{r}_j) \middle| \alpha_i J_i \right\rangle =$ selection rules
- Using JAC: Call `FormFactor.amplitude(levelf::Level, leveli::Level, ...)` or `(levelf::Level, leveli::Level, ...; display=true)`, if the value of the amplitude needs to be printed to screen.

Further remarks:

- The (single-electron) momentum transfer amplitude help describe inelastic scattering processss and is closely related also to the (so-called) generalized oscillator strength.
- The (one-electron) momentum-transfer operator $T^{(1)}(\mathbf{q}) = \sum_{j=1}^N \exp(i \mathbf{q} \cdot \mathbf{r}_j)$ can be utilized in order to express the standard form factor for an atom in a given sublevel $|\alpha JM\rangle$ in terms of an (many-electron) expectation value; cf. 7.1.f.

6.2. In JAC partly-implemented amplitudes

6.2.a. Parity non-conservation amplitudes (ParityNonConservation)

Amplitude, notations & application:

- Formal quantum notation: $\langle \alpha_f J_f \| H^{(\text{weak-charge})} \| \alpha_i J_i \rangle$
- Using JAC: Call `ParityNonConservation.weakChargeAmplitude(levelf::Level, leveli::Level, model::Nuclear.Model)` or `(levelf::Level, leveli::Level, model::Nuclear.Model; display=true)`, if the value of the amplitude needs to be printed to screen.

Further remarks:

- Parity non-conservation (PNC) effects arises in atoms mainly because of the exchange of Z^0 -bosons between atomic electrons and the nucleus. Various observables due to this parity non-conserving interactions can be described in terms of a **nuclear-spin independent Hamiltonian** $H^{(\text{weak-charge})}$, an effective single-electron operator, if non-relativistic nucleons can be assumed, cf. section 3.10.b.
- Especially, if the **proton and neutron densities coincide**, $\rho_p = \rho_n = \rho$, the general nuclear-spin independent Hamiltonian simplifies and can be described in terms of a single nuclear- weak charge Q_W ,

$$H^{(\text{weak-charge})} = -\frac{G}{2\sqrt{2}} Q_W \sum_j \gamma_{5,j} \rho(r_j),$$

where $G = 2.22 \cdot 10^{-14}$ a.u. is the Fermi constant, $\rho(r)$ is the normalized nuclear density with $\int dV \rho(\mathbf{r}) = 1$, and $Q_W \approx -N + Z(1 - 4 \sin^2 \theta_W)$ is the nuclear weak charge with θ_W being the Weinberg angle.

6.2.b. Schiff-moment amplitudes (ParityNonConservation)

Amplitude, notations & application:

- Formal quantum notation: $\langle \alpha_f J_f \parallel H^{(\text{Schiff-moment})} \parallel \alpha_i J_i \rangle = \langle \alpha_f J_f \parallel H^{(\text{Schiff-moment})} \parallel \alpha_i J_i \rangle \delta_{J_f, J_i} \quad P_f \neq P_i$
- Using JAC: Call `ParityNonConservation.schiffMomentAmplitude(levelf::Level, leveli::Level, model::Nuclear.Model)` or `(levelf::Level, leveli::Level, model::Nuclear.Model; display=true)`, if the value of the amplitude needs to be printed to screen.

Further remarks:

- Nuclear electric-dipole (Schiff) moments: If \mathbf{S} is the P-odd and T-odd nuclear Schiff moment, the associated P-odd and T-odd Hamiltonian is given by (Dzuba *et al.*, 2009)

$$H^{(\text{Schiff-moment})} = -e \phi^{(\text{Schiff-moment})} = -4\pi e \mathbf{S} \cdot \nabla \delta(r) = -\frac{3 S^{(\text{SM})} (\mathbf{I}/I) \cdot \mathbf{r}}{R} \rho(r)$$

where $S^{(\text{SM})} (\mathbf{I}/I)$ is the Schiff-moment vector, i.e. the product of the coupling constant $S^{(\text{SM})}$ and the nuclear spin \mathbf{I} , and $R = \int_0^\infty dr r^4 \rho(r)$. Moreover, $\phi^{(\text{Schiff-moment})}$ is the electrostatic potential of the nucleus corresponding to a P-odd and T-odd charge distribution; cf. section 3.10.c.

- Nuclear quadrupole moment: For nuclei with spin $I \geq 1$, the (size of the) quadrupole moment characterizes the *non-spherical* nuclear charge distribution. Such nuclei with a quadrupole (or even octupole) deformation may help for measuring the (nuclear) Schiff moments. A Schiff moment arises from a time-reversal and parity violating nucleon-nucleon interaction and has been proposed in the search for new (meta-) physics. The Schiff moment can be enhanced for deformed nuclei.

6.3. Further amplitudes, not yet considered in JAC

6.3.a. Anapole-moment amplitudes (ParityNonConservation)

Amplitude, notations & application:

- Formal quantum notation: $\langle \alpha_f \mathbb{J}_f \parallel \mathbb{H}^{(\text{anapole-moment})} \parallel \alpha_i \mathbb{J}_i \rangle$

Further remarks:

- A P-odd, T-even **anapole moment** of the nucleus was first introduced by Zel'dovich and arises due to the presence of a parity-violating weak interaction between nucleons, cf. section 3.10.b. The anapole moment is directed along the nuclear spin \mathbf{I} , gives typically the **dominant nuclear-spin dependent electron-nucleus interaction** and manifests itself in terms of a slightly modified electro-magnetic interaction between the nucleus and the atomic electrons.
- Hamiltonian for the interaction of the electrons with the nuclear anapole moment: This Hamiltonian has the form (Dzuba *et al.*, 2009)

$$\mathbb{H}^{(\text{anapole-moment})} = \frac{G}{\sqrt{2}} (I + 1/2) (-1)^{I+1/2-\ell_N} \kappa_{\text{AM}} \sum_j \frac{\mathbf{I} \cdot \boldsymbol{\alpha}_j}{I(I+1)} \rho(r_j),$$

where $G = 2.22 \cdot 10^{-14}$ a.u. is the Fermi constant, I is the nuclear spin, ℓ_N the orbital angular momentum of the outermost nucleon and κ_{AM} is a dimensionless coupling constants for ...

6.3.b. Scalar-pseudo-scalar amplitudes

Amplitude, notations & application:

- Formal quantum notation: $\langle \alpha_f \mathbb{J}_f \parallel \mathbb{H}^{(\text{scalar-pseudo-scalar})} \parallel \alpha_i \mathbb{J}_i \rangle$

6. Atomic amplitudes

Further remarks:

- Hamiltonian for the P-odd, T-odd scalar-pseudo-scalar interaction: In coordinate representation, this Hamiltonian can be written as (Dzuba *et al.*, 2009)

$$\mathbb{H}^{(\text{scalar-pseudo-scalar})} = -\frac{G}{\sqrt{2}} \frac{1}{2m_p c} C_s \sum_j \left[\gamma_0 \frac{d\rho(r)}{dr} \right]_j$$

where G is the Fermi constant, m_p is the nucleon mass, C_s is a (isotope and) nuclear-state dependent constant, and where $\left[\gamma_0 \frac{d\rho(r)}{dr} \right]$ is a scalar term that arises from the scalar product of the ∇ -vector with an particularly averaged spin-vector of the nucleus.

6.3.c. Tensor-pseudo-tensor amplitudes

Amplitude, notations & application:

- Formal quantum notation: $\langle \alpha_f J_f \parallel \mathbb{H}^{(\text{tensor-pseudo-tensor})} \parallel \alpha_i J_i \rangle$

Further remarks:

- Hamiltonian for the P-odd, T-odd tensor-pseudo-tensor interaction: In coordinate representation, this Hamiltonian can be written as (Dzuba *et al.*, 2009)

$$\mathbb{H}^{(\text{tensor-pseudo-tensor})} = i\sqrt{2} G C_t \sum_j [\gamma \rho(r)]_j$$

where G is the Fermi constant, C_t is a (isotope and) nuclear-state dependent constant, and where $[\gamma \rho(r)]$ is a scalar term that arises from the scalar product of the γ -vector with an averaged spin-vector of the nucleus.

- Total P-odd, T-odd electron-nucleus interaction Hamiltonian: $\mathbb{H}^{(\text{P-odd, T-odd electron-nucleus})} = \mathbb{H}^{(\text{tensor-pseudo-tensor})} + \mathbb{H}^{(\text{tensor-pseudo-tensor})}$

6.3.d. Nuclear magnetic-quadrupole-moment amplitudes due to internal B -field

Amplitude, notations & application:

- Formal quantum notation: $\langle \alpha_f \mathbb{J}_f \parallel \mathbb{H}^{(\text{nuclear-MQM})} \parallel \alpha_i \mathbb{J}_i \rangle$

Further remarks:

- This interaction (Hamiltonian) arise from the interaction of the electron EDM d_e with the electro-magnetic fields of the nucleus as seen by the electron. If the treatment is restricted to second order, only the interaction of the electron EDM with the magnetic field \mathbf{B} , which is created by the nuclear magnetic-dipole moment, need to be taken into account.
- Nuclear-MQM Hamiltonian: In coordinate representation, this Hamiltonian can be written as (Dzuba *et al.*, 2009)

$$\mathbb{H}^{(\text{nuclear-MQM})} = -i d_e \boldsymbol{\gamma} \cdot \mathbf{B} = -i d_e \sum_j \boldsymbol{\gamma}_j \cdot \left[\nabla_j \times \frac{\mathbf{M} \times \mathbf{r}_j}{r_{>j}^3} + \dots \right]$$

6.4. Composed many-electron amplitudes, not yet considered in JAC

6.4.a. Parity-violating (non-diagonal, second-order) amplitudes

Amplitude, notations & application:

- **Parity violation:** The (effective) parity-violating interaction is caused by the exchange of Z_0 bosons between the atomic electrons and the nucleus. The parity-violating interaction typically results in non-vanishing off-diagonal electric-dipole matrix element between two atomic states of the same parity; cf. section 3.10.b.

6.4.b. Charge-parity-violating (diagonal, second-order) amplitudes

Amplitude, notations & application:

- **Charge-parity violation:** An intrinsic electron electric dipole moment d_e leads to CP-violation in atoms and also induces an **atomic electric dipole moment**, cf. section 3.10.d.

6.4.c. Electric-dipole moment enhancement factor

Amplitude, notations & application:

- An intrinsic electric-dipole moment (EDM) of the electron can enhance the EDM of the atom. In heavy atoms, in particular, an induced atomic EDM can be strongly enhanced, when compared to the electron EDM itself.
- A typical goal is to find the atomic EDM $d_{\text{atom}} = |\mathbf{d}_{\text{atom}}| \equiv d_{\text{atom}} |\mathbf{F}/F|$, where $\mathbf{F} = \mathbf{I} + \mathbf{J}$ is the total angular momentum of an atomic (hyperfine) level.
- The value of the atomic EDM, compared to the electron EDM, is expressed by means of an enhancement factor $K = d_{\text{atom}}/d_e$, and which increases with nuclear charge Z faster than Z^3 .

7. Atomic properties

7.1. In JAC implemented level properties

7.1.a. Transition probabilities for a single multiplet (Einstein)

Properties, notations & application:

- Photon emission: from an atom or ion $A^* \rightarrow A^{(*)} + \hbar\omega$
- Formal quantum notation: $|\alpha_i J_i\rangle \rightarrow |\alpha_f J_f\rangle + \hbar\omega$
- Using JAC: Perform an `Atomic.Computation(..., properties=[EinsteinX, ...], configs=[...], einsteinSettings=Einstein.Settings(...), ...)` or call directly functions from the module `Einstein`.
- In the JAC program, the transition probabilities, oscillator strength (in emission) and radiative lifetimes are calculated and tabulated by default for all selected transitions from a given single multiplet (i.e. list of configurations). Apart from the multipoles, the user can also specify an overall shift in the photon energies as well as a minimum and maximum transition energy, for which transitions are taken into account.
- In the `Einstein` module, the emission (transition) amplitudes $\langle \alpha_f J_f | O^{(M, \text{emission})} | \alpha_i J_i \rangle$ or absorption amplitudes $\langle \alpha_f J_f | O^{(M, \text{absorption})} | \alpha_i J_i \rangle$ can be obtained directly by call of the function `Jac.Einstein.amplitude()`.

Further remarks:

- Einstein A and B coefficients and oscillator strength for levels (αJ) from a single multiplet are frequently needed for various applications and in different contexts.

7. Atomic properties

- Although these coefficients are *no* (single) level property, the Einstein module still supports the computation of these coefficients for levels from a single multiplet, and which is generated by a single CSF basis.
- Although the Einstein module does not allow to include relaxation effects, this module helps obtain either a quick estimate of the Einstein coefficients between levels from just a few configurations or to deal with cascade computations.
- JAC's standard multipole amplitudes for photon emission: Although all (one- and many-electron) matrix elements are always evaluated in absorption within the JAC toolbox, we keep the intuitive description of the matrix elements as *final-state – operator – initial-state*, cf. section 5.3.c.

7.1.b. Hyperfine parameters and hyperfine representations (Hfs)

Properties, notations & application:

- Hyperfine splitting of an atomic level into hyperfine (sub-) levels: $|\alpha J\rangle \rightarrow |\alpha(J) F\rangle, \quad F = |I - J|, \dots, I + J - 1, I + J$.
- Formal quantum notation: $|\alpha J\rangle \rightarrow |\alpha F\rangle \equiv |(I, \alpha' J) F\rangle \equiv |\alpha(IJ) F\rangle \equiv |\alpha(IJP) F\rangle$ or
 $|\alpha JM_J\rangle \rightarrow |\alpha FM\rangle \equiv |(I, \alpha' J) FM\rangle \equiv |\alpha(IJ) FM\rangle \equiv |\alpha(IJP) FM\rangle$.
- Using JAC: Perform an `Atomic.Computation(.., properties=[HFS, ..], configs=[..], hfsSettings=Hfs.Settings(..), ..)` or call directly functions from the module `Hfs`. The Boolean values `calcT1` and `calcT2` in `Hfs.Settings` determine which parts of the hyperfine Hamiltonian are taken into account into the computations.
- In the JAC program, the hyperfine A and B coefficients as well as the (electric) hyperfine amplitudes $\langle \alpha J \| T^{(1)} \| \alpha J \rangle, \langle \alpha J \| T^{(2)} \| \alpha J \rangle$ are calculated and tabulated by default for all selected levels together with the energy shifts ΔE_F of the hyperfine levels with regard to the (electronic) level energy $E_{\alpha J}$.
- In JAC, the hyperfine amplitudes $\langle \beta_r J_r \| T^{(1)} \| \beta_s J_s \rangle$ and $\langle \beta_r J_r \| T^{(2)} \| \beta_s J_s \rangle$ can be obtained from the function `Jac.Hfs.amplitude()`.
- In JAC, moreover, an explicit representation of a hyperfine multiplet is obtained by diagonalizing the Hamiltonian $\mathbb{H} = \mathbb{H}^{(DCB)} + \mathbb{H}^{(hfs)}$ within the atomic hyperfine IJF -coupled basis if `calcIJFExpansion=true` is set in `Hfs.Settings`.
- In JAC, all the (hyperfine) level energies $E_{\alpha F}$ and the energies relative to the lowest (hyperfine) level are tabulated if `printDeltaEF=true` in `Hfs.Settings`.

- In JAC, all (diagonal and nondiagonal) hyperfine amplitudes are calculated and tabulated explicitly if `calcNondiagonal=true` in `Hfs.Settings`.

Further remarks:

- For a nucleus with *non-zero* spin $I > 0$, a hyperfine splitting of (all) atomic levels generally occurs since each atomic electron also interacts with the electric and magnetic (multipole) fields of the nucleus. This is sometimes described also as the interaction of the magnetic moments of the electrons and nucleus.
- In atomic physics, this interaction is better known as '**hyperfine interaction**' whose two dominant contributions arise from the nuclear magnetic-dipole field $\mathbf{A} = \frac{\boldsymbol{\mu} \times \mathbf{r}}{r^3}$ and the electric-quadrupole field $\Phi(r) = \sum_{ij} \frac{r_i r_j}{2r^5} Q_{ij}$, respectively. In these expressions, $\boldsymbol{\mu}$ is the nuclear magnetic moment operator and Q_{ij} , $i, j = 1..3$ are the Cartesian components of the nuclear quadrupole operator.
- **Hyperfine interaction operator:** The (hyperfine) interaction of an atomic electron with the magnetic-dipole moment of the nucleus is given in relativistic units by

$$\mathbb{h}^{(\text{hfs})} = |e| \boldsymbol{\alpha} \cdot \mathbf{A}(\mathbf{r}) = \frac{|e|}{4\pi} \frac{\boldsymbol{\mu} \cdot (\mathbf{r} \times \boldsymbol{\alpha})}{r^3} F(r), \quad \boldsymbol{\mu} = \frac{\mu \mathbf{I}}{I},$$

and where the factor $F(r)$ is the magnetization distribution, and for a point nucleus $F(r) = 1$.

- Apart from the hyperfine parameters $A(\alpha J)$ and $B(\alpha J)$, we also provide in JAC a representation of the atomic hyperfine levels that can be utilized, for instance, to compute **hyperfine quenched transitions probabilities**.
- **Scaling of nuclear moments:** If all, the nuclear moments, nuclear spins and hyperfine parameters are known for another isotope or isomer, the nuclear moments are often scaled by

$$\mu = \mu^{(\text{ref})} \frac{A I}{A^{(\text{ref})} I^{(\text{ref})}}, \quad Q = Q^{(\text{ref})} \frac{B}{B^{(\text{ref})}}.$$

- **Relation between the hyperfine B parameter and the nuclear quadrupole moment:** This linear relation is determined by the electric-field gradient (EFG) q (in a.u. = Hartree / a_o^2) and given by

$$Q [b] = \frac{B [\text{MHz}]}{234.9648867 q [\text{a.u.}]}$$

The hyperfine B parameters are often very accurately known from experiment.

Hyperfine interaction Hamiltonian:

- Relativistic hyperfine interaction Hamiltonian: For many-electron systems, this Hamiltonian can be written as

$$H^{(\text{hfs})} = \sum_K \mathbb{W}^{(K)} \cdot \mathbb{T}^{(K)}$$

where $\mathbb{W}^{(K)}$ and $\mathbb{T}^{(K)}$ represent the spherical tensor operators of rank K that occur in the nucleonic and electronic sectors, respectively.

- Reduced nuclear matrix elements: These matrix elements are determined geometrically by

$$\langle I \parallel \mathbb{W}^{(1)} \parallel I \rangle = \mu_I \sqrt{\frac{I+1}{I}}, \quad \langle I \parallel \mathbb{W}^{(2)} \parallel I \rangle = \frac{Q}{2} \sqrt{\frac{(I+1)(2I+3)}{I(2I-1)}},$$

while, in contrast, the corresponding electronic amplitudes require detailed atomic structure calculations.

- Values of nuclear magnetic dipole and electric quadrupole moments can be found in the compilation by Stone (2005).
- Electronic tensor operators: For an N -electron atom or ion, these tensor operators are given by (Andersson and Jönsson, 2008)

$$\mathbb{T}^{(1)} = \sum_j^N \mathbb{t}^{(1)}(j) = \sum_j^N -i\sqrt{2}\alpha \frac{(\alpha_j \mathbb{C}^{(1)}(j))^{(1)}}{r_j^2} \quad \text{interaction with the magnetic - dipole field}$$

$$\mathbb{T}^{(2)} = \sum_j^N \mathbb{t}^{(2)}(j) = \sum_j^N -\frac{\mathbb{C}^{(2)}(j)}{r_j^3} \quad \text{interaction with the electric - quadrupole field,}$$

and where α is the fine-structure constant, α_j the vector of Dirac matrices of the j -th electron, and the $\mathbb{C}^{(K)}$ are (normalized) spherical tensors as before.

- Empirical hyperfine-interaction Hamiltonian: From an empirical viewpoint, the hyperfine-interaction Hamiltonian can be parametrized in terms of the hyperfine constants $A^{(\text{hfs})}$, $B^{(\text{hfs})}$ as well as the total nuclear and electronic angular momenta as

$$\mathbb{H}^{(\text{hfs})} = \hbar A^{(\text{hfs})} \mathbf{I} \cdot \mathbf{J} + \hbar B^{(\text{hfs})} \frac{6(\mathbf{I} \cdot \mathbf{J})^2 + 3\mathbf{I} \cdot \mathbf{J} - 2\mathbf{I}^2 \mathbf{J}^2}{2I(2I-1)2J(2J-1)}.$$

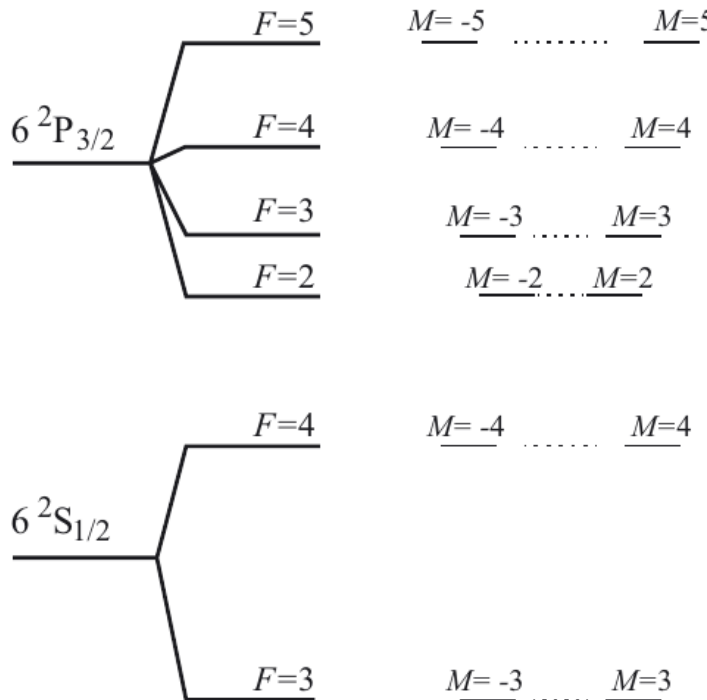


Figure 7.1.: Fine-structure and hyperfine-structure (energy) levels as associated with the $6s\ 2^S_{1/2} - 6p\ 2^P_{3/2}\ D_2$ line of atomic cesium; taken from Kien *et al.* (2013).

Here, of course, the hyperfine constants $A^{(\text{hfs})}$, $B^{(\text{hfs})}$ depend on the atomic level of interest. Moreover, this empirical Hamiltonian neglects the coupling of hyperfine levels from different (fine-structure) levels with some total angular momenta \mathbf{J} .

➤ Diagonal matrix elements of $\mathbb{H}^{(\text{hfs})}$ in a hyperfine-coupled basis: Obviously, the empirical Hamiltonian $\mathbb{H}^{(\text{hfs})}$ is diagonal with regard to

7. Atomic properties

F, M_f in a hyperfine-coupled basis $\{|\alpha(IJ)FM_F\rangle\}$, and these diagonal matrix elements are given by

$$\begin{aligned}\langle \alpha(IJ)FM_F | \mathbb{H}^{(\text{hfs})} | \alpha(IJ)FM_F \rangle &= \frac{\hbar}{2} A^{(\text{hfs})} G + \hbar B^{(\text{hfs})} \frac{3/2 G(G+1) - 2I(I+1)J(J+1)}{2I(2I-1)2J(2J-1)} \\ G &= F(F+1) - I(I+1) - J(J+1).\end{aligned}$$

Atomic (hyperfine) IJF -coupled basis:

➤ This (geometrically fixed) basis is obtained by the standard coupling of the nuclear states $|IM_I\rangle$ and the ASF $|\alpha JM_J\rangle$

$$|\alpha(I, J)FM\rangle \equiv |(I, \alpha' J)FM\rangle = \sum_{M_I M_J} |IM_I\rangle |\alpha' JM_J\rangle \langle IM_I, JM_J| FM\rangle.$$

➤ The atomic (hyperfine) IJF -coupled basis, also called the IJF -coupled ASF basis, is applied internally to represent all hyperfine levels, see below.

Atomic hyperfine amplitudes and levels:

➤ **Atomic hyperfine levels:** For the combined system ‘nucleus+electrons’, the atomic hyperfine states (magnetic sub-levels) can be formed as linear combination

$$|\alpha FM\rangle = \sum_{r=1} \tilde{c}_r(\alpha) |(I, \beta_r J_r)FM\rangle$$

of hyperfine (basis) states $|(I, \beta_r J_r)FM\rangle$ of the same total angular momentum F and (the same electronic) parity P , and where $\{\tilde{c}_r(\alpha)\}$ denotes the representation of these states in the **atomic hyperfine-coupled basis** (Johnson, 2010).

➤ Analogue as for the ASF $|\alpha J\rangle$ in the standard MCDF ansatz, the representation $\{\tilde{c}_r(\alpha)\}$ of an atomic hyperfine state is obtained by diagonalizing the Hamiltonian $\mathbb{H} = \mathbb{H}^{(\text{DFB})} + \mathbb{H}^{(\text{hfs})}$ of the combined system ‘nucleus+electrons’ in either the IJF -coupled CSF or ASF basis.

- In the *IJF*-coupled ASF basis, we can make use of $\mathbb{H}^{(\text{DFB})} |(I, \beta_r \mathbb{J}_r) \mathbb{F} M\rangle = E(\beta_r \mathbb{J}_r) |(I, \beta_r \mathbb{J}_r) \mathbb{F} M\rangle \equiv E_{\beta_r \mathbb{J}_r} |(I, \beta_r \mathbb{J}_r) \mathbb{F} M\rangle$.
- For the hyperfine part of the Hamiltonian, the (reduced) matrix elements can be written after some standard angular momentum algebra as

$$\begin{aligned} \langle (I, \beta_r \mathbb{J}_r) \mathbb{F} M | H^{(\text{hfs})} | (I, \beta_s \mathbb{J}_s) \mathbb{F}' M' \rangle &= \delta_{MM'} \langle (I, \beta_r \mathbb{J}_r) \mathbb{F} | H^{(\text{hfs})} | (I, \beta_s \mathbb{J}_s) \mathbb{F}' \rangle \\ &= \delta_{MM'} \delta_{\mathbb{F}\mathbb{F}'} (-1)^{I+J_r+F} \sum_K \left\{ \begin{matrix} I & J_r & F \\ J_s & I & K \end{matrix} \right\} \langle \beta_r \mathbb{J}_r \| \mathbb{T}^{(K)} \| \beta_s \mathbb{J}_s \rangle \langle I \| \mathbb{W}^{(K)} \| I \rangle, \end{aligned}$$

with $\delta_{\mathbb{F}\mathbb{F}'} = \delta_{PP'} \delta_{FF'}$, and if all nuclear excitations are ignored right from the beginning.

- **Hyperfine amplitudes:** These amplitudes refer to the (reduced) electronic matrix elements $\langle \beta_r \mathbb{J}_r \| \mathbb{T}^{(K)} \| \beta_s \mathbb{J}_s \rangle$. In the JAC program, we compute the **hyperfine amplitudes for both, the magnetic-dipole and the electric-quadrupole operators** of the electron-nucleus interaction.
- These hyperfine amplitudes are utilized to set-up and diagonalize the Hamiltonian matrix within the **atomic *IJF*-coupled basis** for $\mathbb{H} = \mathbb{H}^{(\text{DCB})} + \mathbb{H}^{(\text{hfs})}$ in order to determine the representation $\{\tilde{c}_r(\alpha)\}$ of the atomic hyperfine states.

Hyperfine energies and interaction constants:

- **Hyperfine interaction constants:** Usually the hyperfine splitting is considered independently for each atomic level $(\alpha \mathbb{J})$ and without the need to specify all the hyperfine level energies $E_{\alpha \mathbb{F}}$ explicitly. Instead, the energy splitting of an atomic level $(\alpha \mathbb{J})$ into hyperfine levels $(\alpha \mathbb{F})$ can be expressed conveniently in terms of the (hyperfine interaction) constants

$$A(\alpha \mathbb{J}) = \frac{\mu_I}{I} \frac{1}{\sqrt{J(J+1)}} \langle \alpha \mathbb{J} \| \mathbb{T}^{(1)} \| \alpha \mathbb{J} \rangle, \quad B(\alpha \mathbb{J}) = 2Q \sqrt{\frac{J(2J-1)}{(J+1)(2J+3)}} \langle \alpha \mathbb{J} \| \mathbb{T}^{(2)} \| \alpha \mathbb{J} \rangle$$

- **Hyperfine energy splitting:** With these constants, the hyperfine energy shifts with regard to the electronic level energy $E(\alpha \mathbb{J})$ is given by

$$\Delta E_F = \frac{A(\alpha \mathbb{J}) C}{2} + B(\alpha \mathbb{J}) \frac{3/4 C(C+1) - I(I+1) J(J+1)}{2I(2I-1) J(2J-1)}, \quad C = F(F+1) - J(J+1) - I(I+1).$$

Nuclear magnetic shielding:

- **Hyperfine puzzle:** From g -factor measurements of few-electron ions, the nuclear magnetic moments can be derived, if one relies on QED calculations. However, some discrepancy was reported between recent measurements of the hyperfine splitting in hydrogen- and lithium-like bismuth as well as accurate theoretical prediction (taking the known nuclear moment into account). This so-called ‘hyperfine-puzzle’ was resolved by a new value of the magnetic moment of ^{209}Bi . These studies showed also that the uncertainty of the (known) magnetic moments of nuclei might be underestimated significantly.
- **Total magnetic moment from measurements:** In most experiments, the observed total magnetic moment is given by the nuclear magnetic moment *times* a shielding constant. This simple relation enables one to measure the nuclear magnetic moment in high-precision Penning-trap measurements, **provided the shielding constant are well enough known.**

7.1.c. Isotope-shift parameters (IsotopeShift)

Properties, notations & application:

- Isotope shift of an atomic level for two isotopes A, A' with nuclear masses $M < M'$: $E(\alpha\mathbb{J}; A) \rightarrow E(\alpha\mathbb{J}; A')$.
- Formal quantum notation: $\Delta E(\alpha\mathbb{J}; A, A') = \frac{M' - M}{M M'} K^{(\text{MS})} + F \delta \langle r^2 \rangle$... for each level $((\alpha\mathbb{J}))$.
- Importance of the mass- and field-shift contributions to the isotope shift: These two contributions dominate for different elements and charge states: While the mass-shift contribution is most relevant for low- Z ions, heavy elements are dominated by the field-shift contributions due to the finite nuclear size.
- Standard parametrization of the isotope (energy) shift of an atomic level $(\alpha\mathbb{J})$ for isotope A : The standard parametrization just distinguishes between the *mass shift* and *field shift* of any atomic level $(\alpha\mathbb{J})$ with regard to some reference isotope A_o with mass M_o because of the recoil of the (overall) ion and the change in the nuclear (atomic) potential, if additional neutrons are *added* to A_o ($M < M_o$):

$$\Delta E^{(\text{IS})}(\alpha\mathbb{J}; A, A_o; \text{nuclear model}) = \frac{1}{M} K^{(\text{MS})}(\alpha\mathbb{J}; \text{nuclear model}) + \langle r^2 \rangle F(\alpha\mathbb{J}; \text{nuclear model}) \quad \Delta E^{(\text{IS})}(A_o) \equiv 0$$

In this standard parametrization, the units are: $[K^{(\text{MS})}] = \text{GHz u}$ and the nuclear masses $M = A u$ are simply taken as mass numbers; $[F] = \text{MHz/fm}^2$ and the mean radii $\langle r^2 \rangle = \langle R^2 \rangle \text{ fm}^2$ are taken in terms of their (squared) tabulated values.

The nuclear mean-square radius $\langle r^2 \rangle = \langle R^2 \rangle \text{ fm}^2$ can be determined by different nuclear techniques and is communicated within the literature. Indeed, almost all nuclear radii are tabulated in Fermi (fm).

- Using JAC: Perform an `Atomic.Computation(..., properties=[Isotope, ...], configs=[...], isotopeSettings=IsotopeShift.Settings(...), ...)` with `calcNMS=true`, `calcNMS=true` or `calcF=true` and/or call directly functions from the module `IsotopeShift` in order to include the various contribution of the recoil Hamiltonian.
- In JAC, we calculate and tabulate by default the (relativistic) mass-shift parameters $K^{(\text{MS})}, K^{(\text{NMS})}, K^{(\text{SMS})}$ and the field-shift parameter F for all selected levels. The field-shift parameters are calculated by two methods: i) The evaluation of the Hamiltonian matrix element; ii) by using the (difference of the) electronic density in the region of the nucleus.
- Isotope shift of atomic transitions: Similar to the level energies, the isotope shift of a transition with (emission) energy $E(\alpha_i\mathbb{J}_i \rightarrow$

7. Atomic properties

$\alpha_f \mathbb{J}_f, A) = E(\alpha_i \mathbb{J}_i, A) - E(\alpha_f \mathbb{J}_f, A)$ for two isotopes A, A' can be parametrized by

$$\begin{aligned}\Delta E^{(\text{IS})}(\alpha_i \mathbb{J}_i \rightarrow \alpha_f \mathbb{J}_f; A, A') \\ &= E(\alpha_i \mathbb{J}_i \rightarrow \alpha_f \mathbb{J}_f; A) - E(\alpha_i \mathbb{J}_i \rightarrow \alpha_f \mathbb{J}_f; A') \\ &= \Delta E^{(\text{IS})}(\alpha_i \mathbb{J}_i; A, A') - \Delta E^{(\text{IS})}(\alpha_f \mathbb{J}_f; A, A') = \Delta E^{(\text{MS})}(\alpha_i \mathbb{J}_i \rightarrow \alpha_f \mathbb{J}_f; A, A') + \Delta E^{(\text{FS})}(\alpha_i \mathbb{J}_i \rightarrow \alpha_f \mathbb{J}_f; A, A')\end{aligned}$$

This isotope shift is called **normal**, if the transition energy is larger for the heavier isotope, $\Delta E^{(\text{IS})}(\alpha_i \mathbb{J}_i \rightarrow \alpha_f \mathbb{J}_f; A, A') > 0$ for $A > A'$, and this convention is usually made if isotope shifts are presented and discussed. However, not all the observed isotope shifts are ‘normal’ in this sense but also $\Delta E^{(\text{IS})}(\alpha_i \mathbb{J}_i \rightarrow \alpha_f \mathbb{J}_f; A, A') < 0$ have been observed for selected atomic transitions.

- **Parametrization of the isotope shift for transition energies:** The isotope shift of an atomic transition above immediately leads to the parametrization

$$\begin{aligned}\Delta E^{(\text{IS})}(\alpha_i \mathbb{J}_i \rightarrow \alpha_f \mathbb{J}_f; A, A') \\ &= \frac{M' - M}{M M'} \left(K_i^{(\text{MS})} - K_f^{(\text{MS})} \right) + (F_i - F_f) \delta \langle r^2 \rangle \equiv \frac{M' - M}{M M'} \left(K_i^{(\text{MS})} - K_f^{(\text{MS})} \right) + (F_i - F_f) [\langle R^2 \rangle - \langle R'^2 \rangle]\end{aligned}$$

- **Application of high-resolution atomic laser spectroscopy:** High-resolution spectroscopy of individual atomic transitions can be utilized to derive fundamental nuclear parameters of ground-state nuclei and long-lived isomers, if the hyperfine splittings and the isotope shift of a chain of isotopes is measured. In particular, the combination of the Isotope Separation On-Line (ISOL) technique with high-resolution laser spectroscopy has been found helpful to *enrich* (the information) about the nuclear chart away from the valley of beta-stability and towards the short-lived radioisotopes of an isotopic chain.
- **Non-relativistic mass shift Hamiltonian:** The (total non-relativistic) mass-shift contribution to each atomic level energy arises from the conservation of the total momentum and consists of two parts: The (so-called) **normal mass shift (NMS)** and the **specific mass shift (SMS)**

$$\mathbb{H}^{(\text{MS, nr})} = \mathbb{H}^{(\text{NMS, nr})} + \mathbb{H}^{(\text{SMS, nr})} = \frac{1}{2M} \sum_j \mathbf{p}_j^2 + \frac{1}{2M} \sum_{i \neq j} \mathbf{p}_i \cdot \mathbf{p}_j.$$

While the normal mass shift operator is obviously a one-particle operator, the specific mass shift is a two-particle operator. The sum of these two parts is known also as the (non-relativistic) **total recoil operator**.

- **Odd-even staggering of charge radii:** The nuclear charge radii of stable isotopes are well known to roughly scale $r \propto A^{1/3}$ with their atomic mass number. For a chain of isotopes from the same element, moreover, isotopes with an odd number of neutrons are typically slightly smaller in size than their neighbours with an even neutron number. This **odd-even staggering of the nuclear charge radii** has been confirmed over wide ranges of the nuclear chart, although the (size of) variations of these radii vary with the number of protons and neutrons (Groote *et al.*, 2020). The prediction of this odd-even staggering is one of the challenges of contemporary nuclear theory.
- **Local minima in charge radii:** With only one notable exception for $N = 20$, a local minimum or *kink* in the charge radii has always been found at all shell closures. Phenomenologically, such local minima are typically associated with a minimum in pairing and higher-order correlations or deformation in the literature (Bissel *et al.*, 2016).
- **Odd-odd self-conjugate ($N = Z$) nuclei:** These nuclei provide an ideal test ground for studying proton-neutron pairings. For these nuclei, the charge independence of the nucleon-nucleon interaction suggests symmetry in isospin between protons and neutrons, though violations of this symmetry have been reported as well.
- **Magic nuclei:** New magic numbers have been found by means of radioactive beam facilities for nuclei far from stability. For these nuclei, the traditional shell closures partly disappear. For calcium at the proton-shell closure $Z = 20$, the isotopic chain has been studied especially for the doubly-magic isotopes $^{40,48}\text{Ca}$ at the $N = 20$ and 28 neutron shell closures. The charge radii of the calcium chain has been studied for a long time by many-body nuclear theory.
- **Charge radii along isotopic or isotonic chains:** A kink in the nuclear radii are found at all shell closures, although there exist no simple relation between the depth of the kink and the magic number. Different many-body nuclear methods have been developed to explain this kink in terms of spin-orbit interactions, pair correlations, the particle-vibrational coupling or (so-called) vibrational correlations of the ground state. In the calcium chain at $N = 28$, a prominent kink occurs that is comparable to the nickel chain at $N = 56$, $Z = 28$, another doubly-magic nucleus. In the calcium chain at $N = 20$, in contrast, only a smooth variation of charge radii has been observed.

Relativistic recoil (Hamilton) operator:

- **Recoil Hamiltonian:** Within the lowest-order relativistic approximation ($\sim v^2/c^2$) and in first order of m/M for a nucleus with mass M , the recoil corrections are given by means of the (recoil) Hamiltonian (Tupitsyn *et al.*, 2003):

$$\mathbb{H}^{(\text{recoil})}(M) = \frac{1}{2M} \sum_{ij} \left[\mathbf{p}_i \cdot \mathbf{p}_j - \frac{\alpha Z}{r_i} \left(\boldsymbol{\alpha}_i + \frac{(\boldsymbol{\alpha}_i \cdot \mathbf{r}_i) \mathbf{r}_i}{r_i^2} \right) \cdot \mathbf{p}_j \right] = \frac{\mathbb{H}^{(\text{recoil, w/o M})}}{M}$$

7. Atomic properties

The expectation value of $\mathbb{H}^{(\text{recoil})}(M)$ for relativistic eigenfunction (levels) of $\mathbb{H}^{(\text{DCB})}$ then provides the **recoil correction for the level energy ($\alpha \mathbb{J}$) in first order of m/M** . Usually, the factor $1/M$ is taken out from the Hamiltonian and is treated independently in the parametrization.

- **Decomposition of the relativistic recoil Hamiltonian:** Similar as in the non-relativistic theory, the (relativistic) recoil operator above can be written as (Tupitsyn *et al.*, 2003; Gaidamauskas *et al.*, 2011)

$$\begin{aligned}
\mathbb{H}^{(\text{recoil})}(M) &= \mathbb{H}^{(\text{NMS, relativistic})} + \mathbb{H}^{(\text{SMS, relativistic})} \\
&= \frac{1}{2M} \sum_i \left[\mathbf{p}_i^2 - \frac{\alpha Z}{r_i} \left(\boldsymbol{\alpha}_i + \frac{(\boldsymbol{\alpha}_i \cdot \mathbf{r}_i) \mathbf{r}_i}{r_i^2} \right) \cdot \mathbf{p}_i \right] + \frac{1}{2M} \sum_{i \neq j} \left[\mathbf{p}_i \cdot \mathbf{p}_j - \frac{\alpha Z}{r_i} \left(\boldsymbol{\alpha}_i + \frac{(\boldsymbol{\alpha}_i \cdot \mathbf{r}_i) \mathbf{r}_i}{r_i^2} \right) \cdot \mathbf{p}_j \right] \\
&= \frac{1}{2M} \sum_i \left[\mathbf{p}_i^2 - \frac{\alpha Z}{r_i} \boldsymbol{\alpha}_i \cdot \mathbf{p}_i - \frac{\alpha Z}{r_i} (\boldsymbol{\alpha}_i \cdot \mathbb{C}_i^{(1)}) \mathbb{C}_i^{(1)} \cdot \mathbf{p}_i \right] + \frac{1}{2M} \sum_{i \neq j} \left[\mathbf{p}_i \cdot \mathbf{p}_j - \frac{\alpha Z}{r_i} \boldsymbol{\alpha}_i \cdot \mathbf{p}_j - \frac{\alpha Z}{r_i} (\boldsymbol{\alpha}_i \cdot \mathbb{C}_i^{(1)}) \mathbb{C}_i^{(1)} \cdot \mathbf{p}_j \right] \\
&= \frac{1}{M} (\mathbb{H}^{(\text{NMS})} + \mathbb{H}^{(\text{SMS, A})} + \mathbb{H}^{(\text{SMS, B})} + \mathbb{H}^{(\text{SMS, C})})
\end{aligned}$$

- **Relativistic correction to the recoil energy:** This correction is typically strongly overestimated if relativistic wave functions are applied together with the nonrelativistic recoil operator.
- **Relativistic theory of nuclear recoil contributions:** The full relativistic theory can be formulated only within the framework of quantum electrodynamics. Such a theory was first formulated by Shabaev (1985), where the complete αZ -dependence of the recoil corrections to an energy level ($\alpha \mathbb{J}$) was derived in first order of m/M .

Reduced one-electron matrix elements of the recoil (Hamilton) operator:

- **Recoil Hamiltonian:** While the normal mass-shift Hamiltonian is a one-particle operator, the specific mass-shift is a (symmetric) two-particle operator

$$\mathbb{H}^{(\text{NMS})} = \sum_j \mathbb{h}^{(\text{NMS})}(\mathbf{r}_j), \quad \mathbb{H}^{(\text{SMS, k})} = \sum_{i \neq j} \mathbb{h}^{(\text{SMS, k})}(\mathbf{r}_i, \mathbf{r}_j) = \sum_{i \neq j} g(r_i, k) g(r_j, k) \left(\mathbb{T}_i^{(1)} \cdot \mathbb{T}_j^{(1)} \right), \quad k = A, B, C.$$

The particular tensorial structure of the two-particle specific mass-shift Hamiltonian ensures that the reduced (one-electron) matrix elements can be expressed in terms of the **first-rank effective interaction strength $X^{(1; \text{SMS, k})}$** that are specified below for $k = A, B, C$.

- Reduced one-electron matrix element for the normal mass-shift: With the definition of the angular coefficients in GRASP, this one-electron matrix element is given with $P' = \frac{\partial P}{\partial r}$ (Gaidamauskas *et al.*, 2011)

$$\begin{aligned} \langle a \parallel h^{(NMS)} \parallel b \rangle &= \delta_{\kappa_a, \kappa_b} \frac{1}{2} \int_0^\infty dr \left(P'_a P'_b + Q'_a Q'_b + \frac{\ell_b (\ell_b + 1) P_a P_b + (2j_b - 1) 2j_b Q_a Q_b}{r^2} \right. \\ &\quad \left. - (2\alpha Z) \frac{Q_a P'_b + Q_b P'_a}{r} - (\alpha Z) \left(\frac{\kappa_b - 1}{r^2} \right) (Q_a P_b + Q_b P_a) \right). \end{aligned}$$

Parametrization of the isotope shift:

- Mass shift $\Delta E^{(MS)}(\alpha_i \mathbb{J}_i \rightarrow \alpha_f \mathbb{J}_f; A, A')$ of atomic transitions for a pair (A, A') of isotopes: The mass shift of an atomic emission line $i \rightarrow f$ is typically expressed in terms of the mass-shift parameters of the upper and lower level by

$$\begin{aligned} \Delta E^{(MS)}(\alpha_i \mathbb{J}_i \rightarrow \alpha_f \mathbb{J}_f; A, A') &= \left(\frac{M' - M}{M M'} \right) (K^{(MS)}(\alpha_i \mathbb{J}_i) - K^{(MS)}(\alpha_f \mathbb{J}_f)) \\ &= \left(\frac{M' - M}{M M'} \right) (K^{(NMS)}(\alpha_i \mathbb{J}_i) - K^{(NMS)}(\alpha_f \mathbb{J}_f) + K^{(SMS)}(\alpha_i \mathbb{J}_i) - K^{(SMS)}(\alpha_f \mathbb{J}_f)). \end{aligned}$$

- Mass shift of two isotopes: Within lowest order of m/M , the (isotope) mass shift for an atomic level $(\alpha \mathbb{J})$ is determined by the difference of the expectation values of $\mathbb{H}^{(recoil)}(M)$ for two different isotopes:

$$\begin{aligned} \Delta E^{(MS)}(M, M') &= \langle \alpha \mathbb{J} | \mathbb{H}^{(recoil)}(M) - \mathbb{H}^{(recoil)}(M') | \alpha \mathbb{J} \rangle = \frac{M' - M}{M M'} K^{(MS)} \\ K^{(MS)} &= \langle \alpha \mathbb{J} | \mathbb{H}^{(recoil; w/o M)} | \alpha \mathbb{J} \rangle = \langle \alpha \mathbb{J} \parallel \mathbb{H}^{(recoil; w/o M)} \parallel \alpha \mathbb{J} \rangle \neq K^{(MS)}(A, A'), \end{aligned}$$

and where the Wigner-Eckardt theorem is used here in a special form that is consistent with GRASP and that is utilized for the implementation of corresponding angular coefficients.

- The conversion factor between the mass-shift parameters $K^{(MS)}$ in the frequently applied units is:

$$K^{(MS)}/[\text{GHz u}] = 3609.4824 K^{(MS)}/[\text{a.u.}].$$

7. Atomic properties

➤ **Field shift of two isotopes:** is caused by their different nuclear charge distributions and can be parametrized by:

$$\begin{aligned}\Delta E^{(\text{FS})}(\alpha\mathbb{J}; A, A') &= \left\langle \alpha\mathbb{J} \left| \sum_{j=1}^N (\mathbb{V}^{(\text{nuc})}(r_j; A) - \mathbb{V}^{(\text{nuc})}(r_j; A')) \right| \alpha\mathbb{J} \right\rangle = \left\langle \alpha\mathbb{J} \left\| \sum_{j=1}^N \delta \mathbb{V}^{(\text{nuc})}(r_j; A, A') \right\| \alpha\mathbb{J} \right\rangle \\ &= F \delta \langle r^2 \rangle = F (\langle R^2 \rangle - \langle R'^2 \rangle) \\ F &= \frac{\left\langle \alpha\mathbb{J} \left| \sum_j \delta \mathbb{V}^{(\text{nuc})}(r_j; A, A') \right| \alpha\mathbb{J} \right\rangle}{\langle R^2 \rangle - \langle R'^2 \rangle}\end{aligned}$$

where $\delta \langle r^2 \rangle = \langle R^2 \rangle - \langle R'^2 \rangle$ is the difference of the *mean-square* charge radii of the two isotopes with masses A, A' .

➤ **Field shift $\Delta E^{(\text{FS})}(\alpha\mathbb{J}, A, A')$ of an atomic level ($\alpha\mathbb{J}$) for a pair (A, A') of isotopes:** Since the field shift arises from the different nuclear charge distributions of the isotopes A, A' , it can be simply obtained as difference of the total energies of two separate SCF computations. However, these shifts are quite small, when compared to the total level energies, and such differences are therefore very sensitive to the numerical implementation of the total energies as well as to the parametrization of the nuclear charge distributions. Alternatively, the field shifts can be obtained from first-order perturbation theory by

$$\Delta E^{(\text{FS})}(\alpha\mathbb{J}; A, A') = \int d^3\mathbf{r} \rho(\mathbf{r}; \alpha\mathbb{J}) [\mathbb{V}^{(\text{nuc})}(\mathbf{r}; A) - \mathbb{V}^{(\text{nuc})}(\mathbf{r}; A')], \quad F = \frac{\Delta E^{(\text{FS})}(\alpha\mathbb{J}; A, A')}{\langle R^2 \rangle - \langle R'^2 \rangle}$$

where $\rho(\mathbf{r}; \alpha\mathbb{J})$ is the *electronic density of level ($\alpha\mathbb{J}$)* for either the (reference) isotope A or A' , and $\mathbb{V}^{(\text{nuc})}(\mathbf{r}; A), \mathbb{V}^{(\text{nuc})}(\mathbf{r}; A')$ are the (nuclear) potentials that arise from the nuclear charge distributions of the isotopes A, A' . For deformed nuclei, the electronic density is not spherical symmetric and $\rho(\mathbf{r}; \alpha\mathbb{J})$ then refers to the averaged electron density, e.g. as obtained from the averaged magnetic components M of the magnetic substates ($\alpha\mathbb{J}M$).

➤ **Electronic density of level ($\alpha\mathbb{J}$) near the origin:** Near to the origin ($r \rightarrow 0$), the electronic density is spherical symmetric to a very good approximation and can be expressed as a even-polynomial function (Ekman *et al.*, 2019)

$$\rho(\mathbf{r}; \alpha\mathbb{J}) \approx b(r) = \sum_{k=0,2,4,6} b_k(\alpha\mathbb{J}) r^k = b_0(\alpha\mathbb{J}) + b_2(\alpha\mathbb{J}) r^2 + b_4(\alpha\mathbb{J}) r^4 + b_6(\alpha\mathbb{J}) r^6,$$

due to the decomposition of the many-electron wave function into (orthonormal) orbitals. Here, the restriction to $k_{\max} = 6$ is made for practical purposes and because of the (spherical) approximation, the numerical stability as well as, to a very large extent, the accuracy of the experimental data that are available for such field shifts.

- **Field-shift parameters of level $(\alpha\mathbb{J})$:** The expansion of the electronic density for $r \rightarrow 0$ can be substituted into the first-order perturbative expression for $\Delta E^{(\text{FS})}(\alpha\mathbb{J}; A, A')$ and the terms sorted due to powers of r^k as (Ekman *et al.*, 2019)

$$\begin{aligned}\Delta E^{(\text{FS})}(\alpha\mathbb{J}, A, A') &\approx \sum_{k=0,2,4,6} F_k(\alpha\mathbb{J}) \left(\langle r^{k+2} \rangle^A - \langle r^{k+2} \rangle^{A'} \right) \equiv \sum_{k=0,2,4,6} F_k(\alpha\mathbb{J}) \langle r^{k+2} \rangle^{A,A'} \\ F_k(\alpha\mathbb{J}) &= \frac{4\pi Z b_k(\alpha\mathbb{J})}{(k+2)(k+3)}, & \langle r^{k+2} \rangle^A &= \frac{1}{Z} \int d^3 \mathbf{r} r^{k+2} \rho^{(\text{nuc})}(r; A).\end{aligned}$$

Here, the $F_k(\alpha\mathbb{J})$ are the field-shift parameters of level $(\alpha\mathbb{J})$, and the nuclear charge Z arise in the nuclear moments due to the normalization of the nuclear density $\int d^3 \mathbf{r} \rho^{(\text{nuc})} = 1$. Of course, analogous relations for the field-shift energies $\Delta E^{(\text{FS})}(\alpha_i\mathbb{J}_i \rightarrow \alpha_f\mathbb{J}_f; A, A')$ and field-shift parameter $F_k(\alpha_i\mathbb{J}_i \rightarrow \alpha_f\mathbb{J}_f)$ in terms of modified expansion coefficients $b_k(\alpha_i\mathbb{J}_i \rightarrow \alpha_f\mathbb{J}_f)$ can be formulated for atomic (emission) lines $(\alpha_i\mathbb{J}_i \rightarrow \alpha_f\mathbb{J}_f)$ by just taking the according differences, although this makes the notation more cumbersome.

The parametrization of the field shift applies for all spherically-symmetric nuclear potentials $\mathbb{V}^{(\text{nuc})}(r; A)$ and, hence, **for all spherically-symmetric nuclear charge densities $\rho^{(\text{nuc})} = \rho^{(\text{nuc})}(r; A)$** as well as for **deformed nuclei with total spin $I = 0$** . Moreover, this parametrization is expected to work even for **deformed nuclei with $I \neq 0$** , since the electronic density depends only weakly on small deformations of the nuclear density.

- **Modified field-shift parameter of level $(\alpha\mathbb{J})$:** A single electron-density coefficient $b_0(\alpha\mathbb{J})$ occurs for a *constant* electronic density inside of the nuclear charge distribution. All other coefficients $b_0(\alpha\mathbb{J}), k > 0$ therefore describe (more or less) small variations of the electronic density *within* the nucleus. The different relevance of these coefficients therefore suggests a slightly modified parametrization

$$\begin{aligned}\Delta E^{(\text{FS})}(\alpha\mathbb{J}; A, A') &\approx F_0(\alpha\mathbb{J}) \delta \langle r^2 \rangle^{A,A'} + F_2(\alpha\mathbb{J}) \delta \langle r^4 \rangle^{A,A'} + F_4(\alpha\mathbb{J}) \delta \langle r^6 \rangle^{A,A'} + F_6(\alpha\mathbb{J}) \delta \langle r^8 \rangle^{A,A'} \\ &= \delta \langle r^2 \rangle^{A,A'} \left(F_0(\alpha\mathbb{J}) + F_2(\alpha\mathbb{J}) \frac{\delta \langle r^4 \rangle^{A,A'}}{\delta \langle r^2 \rangle^{A,A'}} + F_4(\alpha\mathbb{J}) \frac{\delta \langle r^6 \rangle^{A,A'}}{\delta \langle r^2 \rangle^{A,A'}} + F_6(\alpha\mathbb{J}) \frac{\delta \langle r^8 \rangle^{A,A'}}{\delta \langle r^2 \rangle^{A,A'}} \right) \equiv F_{\text{mod}}(\alpha\mathbb{J}) \delta \langle r^2 \rangle^{A,A'}.\end{aligned}$$

- **Electronic-density coefficients $b_k(\alpha\mathbb{J})$:** Since these coefficients refer to a spherically-symmetric electronic charge density, they can be readily obtained by either calculating the mean occupation numbers of all CSF, which are involved in the wave function expansion of level $((\alpha\mathbb{J}))$ or, equivalently by calculating the expectation value $\langle \alpha\mathbb{J} | \delta^{(\text{N-electron})}(\mathbf{r}) | \alpha\mathbb{J} \rangle$ of the zero-rank operator $\delta^{(\text{N-electron})}(\mathbf{r})$ and by

7. Atomic properties

making use of the corresponding angular coefficients. Indeed, these zero-rank coefficients are the same as they occur also in the computation of the normal mass shift (matrix elements).

Boson-field (isotope) shift parameters:

- **Scalar-boson-field Hamiltonian:** In quantum-field theory, an additional contribution to the electron-nucleus interaction may arise from massive (hypothetical) boson particles of mass m_ϕ . This additional interaction can be expressed in terms of the mass $M = A u$ and nuclear charge Z of the isotope by means of the (many-electron) Hamiltonian (Surzhykov 2020)

$$H^{(\text{boson field})} = \sum_i^N -\alpha^{(\text{boson field})} (A - Z) \hbar c \frac{e^{-m_\phi r_i c/\hbar}}{r_i}$$

In this definition of $H^{(\text{boson field})}$, the (new-physics) **boson-field coupling constant is dimensionless**, and the proper dimension of the Hamiltonian arise from $[\frac{\hbar c}{r}] = [\frac{\text{kg}\cdot\text{m}}{\text{s}^2}] = [\text{J}]$.

Non-linear King plots:

- **King plots:** The standard parametrization of isotope shifts assumes that the isotope-shift parameter $K(\alpha J; \text{nuclear model})$ and $F(\alpha J; \text{nuclear model})$ do not depend on the isotope A , neither their mass nor the nuclear model. Then, the dependence on the atomic level can be eliminated by taking the ratio of this parametrization for two atomic transitions. With this assumption in mind, this ratio refer to a linear dependence, i.e. the King plot is by definition *linear*. — How come non-linearities into play for the King plot ?? ... Explain in further details how such King plots are constructed in detail.
- **Nonlinear King plot:** Nonlinear King plots can arise from quite different sources, for instance, from higher-order terms in standard atomic theory, higher-order terms in the expansion of the nuclear potential, a nuclear deformation, the nuclear polarizability, or due to new (meta-) physics. However, first a proper atomic theory need to be developed before one could (successfully) speculate about new physics.
- **Non-linear King plot:** A non-linear King plot arises from the breakdown of the standard parametrization of the atomic isotope shifts and has been emphasized recently in the search of new physics. However, a non-linear King plot can arise from quite different sources, including the uncertainties of nuclear charge radii or second- and higher-order terms in the parametrization of the isotope shifts of atomic lines.
- **King plot:** The King plot as a useful tool for analyzing and interpreting isotope-shift measurements was first introduced by King in 1963 and is **simply based on the standard parametrization of the isotope shift in terms of the a mass- and field-shift**. If this parametrization is applied to two independent atomic transition, the $\delta \langle R^2 \rangle$ dependence on the nuclear radius can be eliminated from the isotope shifts, and

all experimental points must follow a linear trend that is solely determined by the mass- and field-shift parameters of the two transitions. Any non-linearity of the King plot therefore directly questions the standard parametrization.

- **King plot:** Recent measurements on the isotope shifts of strontium and ytterbium ions have reduced the experimental uncertainties so much that the ‘linearity’ was broken by several standard deviations. While the experimental uncertainties might have been underrated in these measurements, it seems desirable to re-analyze the foundation of the standard parametrization based on atomic perturbation theory and beyond the empirical treatment of — more or less — *ad-hoc* introduced terms.

Isotope shifts due to nuclear deformations:

- **Isotope shifts due to nuclear deformations:** Kozhedub *et al.* (2008) investigated the isotope shifts to the level energies that (may) arise from some nuclear deformation. In particular, they derived for these shifts approximate formulas that account for the nuclear size and deformation. They combined these formulas with numerical estimates in order to re-analyze the nuclear corrections to the binding energies of hydrogen- and lithium-like ^{238}U ions. However, several details in this analysis remain rather unclear. For heavy ions, up to the present, the most accurate isotope shifts are known for the hydrogen- and lithium-like ^{238}U ions.

7.1.d. Lande g_J factors and Zeeman splitting of fine-structure levels (LandeZeeman)

Properties, notations & application (not yet fully implemented):

- Zeeman splitting of an atomic level into Zeeman (sub-) levels: $|\alpha J\rangle \rightarrow |\alpha JM\rangle, M = -J, \dots, J-1, +J$.
- Formal quantum notation: $|\alpha JM\rangle$.
- Using JAC: Perform an `Atomic.Computation(.., properties=[LandeJ, ..], configs=[..], zeemanSettings=LandeZeeman.Settings(..), ..)` with `calcLandeJ=true` or call directly functions from the module `LandeZeeman`.
- In JAC, we calculate and tabulate by default the Lande $g_J \equiv g(\alpha J)$ factors for the selected fine-structure levels.
- In the JAC program, the Zeeman amplitudes $\langle \beta_r J_r \| N^{(1)} \| \beta_s J_s \rangle$ and $\langle \beta_r J_r \| \Delta N^{(1)} \| \beta_s J_s \rangle$ can be obtained from the function `Jac.LandeZeeman.amplitude()`.

Further remarks:

- The Zeeman effect describes the (level) splitting of an atomic level $|\alpha J\rangle$ into its sub-levels $|\alpha JM\rangle$ in the presence of a static magnetic field.
- The various components $|\alpha JM\rangle$ of a Zeeman-splitted line usually have different intensities, and with some of them possibly even forbidden within the dipole approximation.
- The energy splitting of the Zeeman sub-levels depends of course on the magnetic field strength. — Therefore, the Zeeman effect has been applied for measuring magnetic field strengths, e.g. in astrophysics at the surface of the Sun or in laboratory plasmas.

Zeeman Hamiltonian $\mathbb{H}^{(\text{mag})}$:

- If the z -axis is chosen along the magnetic field $\mathbf{B} \parallel \mathbf{e}_z$ and if we neglect diamagnetic contributions, the magnetic (Zeeman) Hamiltonian can be written in terms of spherical tensors (Andersson and Jönsson, 2008)

$$\mathbb{H}^{(\text{mag})} = \left(\mathbb{N}_0^{(1)} + \Delta \mathbb{N}_0^{(1, \text{QED})} \right) B$$

$$\mathbb{N}^{(1)} = \sum_j^N \mathbb{n}^{(1)}(j) = \sum_j^N -i \frac{\sqrt{2}}{2\alpha} r_j (\boldsymbol{\alpha}_j \mathbb{C}^{(1)}(j))^{(1)}$$

$$\Delta \mathbb{N}^{(1)} = \sum_j^N \Delta \mathbb{n}^{(1)}(j) = \sum_j^N \frac{g_s - 2}{2} \beta_j \boldsymbol{\Sigma}_j, \quad \boldsymbol{\Sigma} = \begin{pmatrix} \boldsymbol{\sigma} & 0 \\ 0 & \boldsymbol{\sigma} \end{pmatrix},$$

and where the second term in the magnetic Hamiltonian above is (so-called) Schwinger's QED correction. Here, $g_s = 2.00232$ is the g -factor of the electron, including some leading QED corrections.

- **Total Hamiltonian:** For a moderate magnetic \mathcal{B} -field, one considers the total Hamiltonian $\mathbb{H}^{(\text{DC})} + \mathbb{H}^{(\text{mag})}$ whose matrix is diaognal in P, M but no longer in the total angular momentum quantum number J . In practice, one usually starts from a given ASF basis, in which $\mathbb{H}^{(\text{DC})}$ is already diagonal, and then diagonalized the total Hamiltonian matrix in very moderate basis of atomic state functions. For a non-zero nuclear spin, however, the hyperfine and Zeeman splitting is often comparable and the Hamiltonian $\mathbb{H}^{(\text{DC})} + \mathbb{H}^{(\text{mag})} + \mathbb{H}^{(\text{hfs})}$ need then to be diagonalized in some given ASF basis. In this case, only the parity and M_F are diagonal, i.e. good quantum numbers.

Lande factor $g_J \equiv g(\alpha\mathbb{J})$ and Zeeman splitting of an electronic level ($\alpha\mathbb{J}$) :

- **g -factors of atomic fine and hyperfine levels:** In the classical vector coupling model, the g -factors simply follow from the coupling rules of the angular momenta and are given by:

$$g_J = 1 + \frac{J(J+1) - L(L+1) + S(S+1)}{2J(J+1)}$$

$$g_F = g_J \frac{F(F+1) + J(J+1) - I(I+1)}{2F(F+1)} + g_I \frac{F(F+1) - J(J+1) + I(I+1)}{2F(F+1)},$$

and where the second relation can be used to obtain g_I , provided that g_J and g_F is known.

- **Zeeman splitting of an atomic level ($\alpha\mathbb{J}$):** If the energy splitting due to the magnetic field is small, when compared with the fine-structure splitting, it can be expressed in first-order perturbation theory by

$$\begin{aligned} \Delta E^{(\text{mag})}(\alpha\mathbb{J}M) &= E(\alpha\mathbb{J}M) - E(\alpha\mathbb{J}, M=0) \\ &= \langle \alpha\mathbb{J}M | N_0^{(1)} + \Delta N_0^{(1, \text{QED})} | \alpha\mathbb{J}M \rangle = (-1)^{J-M} \begin{pmatrix} J & 1 & J \\ -M & 0 & M \end{pmatrix} \sqrt{2J+1} \langle \alpha\mathbb{J} | N^{(1)} + \Delta N^{(1, \text{QED})} | \alpha\mathbb{J} \rangle B \\ &= \frac{M}{\sqrt{J(J+1)}} \langle \alpha\mathbb{J} | N^{(1)} + \Delta N^{(1, \text{QED})} | \alpha\mathbb{J} \rangle B \end{aligned}$$

and with regard to the unperturbed energy $E(\alpha\mathbb{J}, M=0) = E(\alpha\mathbb{J}, B=0)$.

- **Lande g_J factor of an atomic level ($\alpha\mathbb{J}$):** Usually, the dependence on the M quantum number is factored out and the energy splitting is expressed for a single level ($\alpha\mathbb{J}$) in terms of its Lande factor $g_J \equiv g(\alpha\mathbb{J})$

$$\Delta E^{(\text{mag})}(\alpha\mathbb{J}M) = g(\alpha\mathbb{J}) M \frac{B}{2}, \quad g(\alpha\mathbb{J}) \equiv g_J = 2 \frac{\langle \alpha\mathbb{J} | N^{(1)} + \Delta N^{(1, \text{QED})} | \alpha\mathbb{J} \rangle}{\sqrt{J(J+1)}}$$

7. Atomic properties

7.1.e. Lande g_F factors and Zeeman splitting of hyperfine levels (LandeZeeman)

Properties, notations & application (not yet fully implemented):

- Zeeman splitting of an atomic hyperfine level into Zeeman (sub-) levels: $|\alpha(J)\mathbb{F}\rangle \longrightarrow |\alpha(J)\mathbb{F}M\rangle, M = -F, \dots, F-1, +F$.
- Formal quantum notation: $|\alpha(J)\mathbb{F}M\rangle$.
- Using JAC: Perform an `Atomic.Computation(.., properties=[LandeJ, ...], configs=[..], zeemanSettings=LandeZeeman.Settings(..), ..)` with `calcLandeF=true` or call directly functions from the module `LandeZeeman`.
- In JAC, we calculate and tabulate by default the Lande $g_F \equiv g(\alpha\mathbb{F})$ factors for the selected hyperfine-structure levels.

Further remarks:

- The Lande g -factor (also known as g value or dimensionless magnetic moment) is a **dimensionless entity that characterizes the gyromagnetic ratio of an atomic or hyperfine level**. The Lande g -factor is basically a proportionality constant how efficient a particle, spin or quantum state with given total angular momentum s contributes to the splitting in an external magnetic field B .

Lande factor $g_F \equiv g(\alpha\mathbb{F})$ of an hyperfine level ($\alpha\mathbb{F}$) :

- Zeeman splitting of an hyperfine level ($\alpha\mathbb{F}$): If the energy splitting due to the magnetic field is small, when compared with the hyperfine-

splitting, it can be expressed in first-order perturbation theory in terms of the reduced electronic Zeeman amplitudes by

$$\begin{aligned}
 \Delta E^{(\text{mag})}(\alpha\mathbb{F}M) &= E(\alpha\mathbb{F}M) - E(\alpha\mathbb{F}, M=0) \\
 &= \left\langle (I, \alpha\mathbb{J}) FM \left| \mathbb{N}_0^{(1)} + \Delta \mathbb{N}_0^{(1, \text{QED})} \right| (I, \alpha\mathbb{J}) FM \right\rangle \\
 &= M \frac{F(F+1) + J(J+1) - I(I+1)}{2F(F+1)} \frac{\left\langle \alpha\mathbb{J} \left\| \mathbb{N}_0^{(1)} + \Delta \mathbb{N}_0^{(1, \text{QED})} \right\| \alpha\mathbb{J} \right\rangle}{\sqrt{J(J+1)}} \\
 &= M \frac{F(F+1) + J(J+1) - I(I+1)}{2F(F+1)} g(\alpha\mathbb{J}) \frac{B}{2},
 \end{aligned}$$

and expressed with regard to the unperturbed hyperfine energy $E(\alpha\mathbb{F}, M=0) = E(\alpha\mathbb{F}, B=0)$.

➤ Lande factor $g_F \equiv g(\alpha\mathbb{F})$ and Zeeman energy splitting of an hyperfine level $(\alpha\mathbb{F})$:

$$g(\alpha\mathbb{F}) = \frac{F(F+1) + J(J+1) - I(I+1)}{2F(F+1)} g(\alpha\mathbb{J}) \implies \Delta E^{(\text{mag})}(\alpha\mathbb{F}M) = g(\alpha\mathbb{F}) M \frac{B}{2}$$

7.1.f. Atomic form factors (FormFactor)

Properties, notations & application:

- Form factor $F(q; \alpha\mathbb{J})$ of an atom in level $(\alpha\mathbb{J})$ with an (assumed) spherical-symmetric charge distribution:.
- Formal quantum notation: $F^{(\text{standard})}(q; \alpha\mathbb{J})$, $F^{(\text{modified})}(q; \alpha\mathbb{J})$, $J^{(\text{covariant: } \mu)}(q; i \rightarrow f)$, $\mu = 0..3$.
- Using JAC: Perform an `Atomic.Computation(.., configs=[..], FormFactor.Settings(..), ..)` or call directly functions from the module `FormFactor`.
- In JAC, the standard and modified form factors are calculated and tabulated by default for all selected levels in `FormFactor.Settings` and for all specified q -values [in a.u.]; the default values of the momentum transfer are $q = 0.1, 1.0, 10.0$ a.u.

7. Atomic properties

- **Atomic form factor:** In atomic physics, the form factors are generally taken as fast approximation to the (scattering) amplitude in forward direction at $\vartheta \simeq 0$, if an incident quantum wave is scattered by an isolated atom with spherical-symmetric charge distribution.
- **Momentum transfer:** Most easily, the atomic form factor can be written as function of the momentum transfer $q = |\mathbf{q}|$, and which is closely related to the scattering angle: $\hbar q = 2k \sin(\vartheta/2) = \frac{2}{\lambda} \sin(\vartheta/2)$.
- **Momentum-transfer variable:** Instead of the momentum transfer q , some tabulations of x-ray scattering amplitude make use also of the (so-called) momentum-transfer variable $x = [\sin(\vartheta/2)] / \lambda [A]$ with $\lambda [A] = 12.398520/E$ [keV].
- **Atomic form factor for different particles:** In practice, of course, the definition of the atomic form factor depends on both, the particular scattering (elastic or inelastic) as well as the type of incident radiation, such as photons, electrons or neutrons. As usual, we here restrict ourselves to the **atomic form factor for the elastic (x-ray) scattering of photons**.
- **Atomic form factor:** The (so-called) **form-factor approach to the scattering amplitude is primarily valid for small angles** and has been found more tractable also for quite extensive systems, although it neglects the interelectronic motion.
- **Application of form factors:** The elastic scattering of photons by atoms, ions or molecules has been found important in many fields of physics, such as crystallography, plasma physics and astrophysics. For high-photon energies well above the K-shell threshold energy of the atom or ion, both the standard form factor (FF) or the modified form factor (MFF) approximations are widely applied and were found moderately successful in estimating the scattering cross sections. However, **both form factor approximations typically fail for small photon energies**.
- **Application of x-ray form factors:** Reliable (complex) x-ray form factors [$\Re(f)$, $\Im(f)$] and photoelectric attenuation coefficient $\sigma^{(\text{photoelectric})}$ are frequently applied in crystallography, radiation safety, medical diagnosis, XAS and at several places elsewhere. Despite of their frequent use, however, theoretical data differ by more than a factor 2 for several elements and photon energies between 1 to 3 keV. Discrepancies often arise from the smoothing of edge structures, the use of nonrelativistic wave functions in the computation of form factors or the missing convergence of the computations (Chantler *et al.*, 2000).
- **Complex x-ray form factor f :** The complex form factor f is the fundamental parameter for many optical devices, such as mirrors, lenses, filters and coatings. This form factor enables one to derive the refractive index, permittivity as well as the scattering and attenuation coefficients of a given material. For high enough photon energies, the x-ray form factor can be predicted more readily based on the atomic form factor and the dominance of inner-shell photoionization processes.
- **Complex x-ray form factor f for > 1 keV photons:** For photon energies $\gtrsim 1$ keV, the x-ray form factor f is dominated by photoabsorption and coherent elastic scattering. For energies $\gtrsim 10$ keV, moreover, inelastic Compton scattering becomes relevant, especially for low- Z elements (for hydrogen, the inelastic scattering already dominates $\gtrsim 5$ keV). For even higher photon energies $\gtrsim 1$ MeV, nuclear absorption

and scattering processes (may) strongly contribute, such as pair production, Delbrück scattering as mediated by the nucleus or even resonant nuclear excitations (nuclear Thomson scattering).

Definition of atomic form factors:

- **Standard atomic form factor:** For an atom in level $(\alpha \mathbb{J})$ with a spherically-symmetric charge distribution $\rho(r)$, the standard atomic form factor is given by

$$F^{(\text{standard})}(q; \alpha \mathbb{J}) = 4\pi \int dr r^2 \rho(r) \frac{\sin(qr)}{qr} = \frac{1}{2J+1} \sum_M \langle \alpha \mathbb{J} M | \mathbb{T}^{(1\text{-particle})}(\mathbf{q}) | \alpha \mathbb{J} M \rangle.$$

It is equal to the Fourier transform of the charge density $\rho(r)$, if the charge density is just normalized to the number of bound electrons: $4\pi \int dr r^2 \rho(r) = N$. The second equivalence still need to be worked out in detail since $\mathbb{T}^{(1\text{-particle})}(\mathbf{q})$ is a general (symmetric) one-particle operator but without definite rank.

- As seen from above, this standard form factor can be expressed also as (averaged many-electron) expectation value of the single-electron momentum-transfer operator $\mathbb{T}^{(1\text{-particle})}(\mathbf{q}) = \sum_{j=1}^N \exp(i \mathbf{q} \cdot \mathbf{r}_j)$ for a given sublevel $|\alpha \mathbb{J} M = 0\rangle$.
- **Modified atomic form factor:** For an atom or ion with a spherically-symmetric charge distribution, a modified atomic form factor can be defined via the charge distributions of the individual (sub-) shells of the element

$$F^{(\text{modified})}(q; \alpha \mathbb{J}) = 4\pi \sum_{i=1}^N \int dr r^2 \rho_i(r) \frac{\sin(qr)}{qr} \frac{mc^2}{\varepsilon'_i - V(r)},$$

and where $\rho_i(r)$ is the charge density of the i -th electron, $\varepsilon'_i = \varepsilon_i + mc^2$ its energy (including the rest mass) and $V(r)$ the (full) atomic potential of the i -th electron as seen at position r . Here, the summation is taken over all electrons, and the charge distribution must fullfill again the constraint that $4\pi \sum_i \int dr r^2 \rho_i(r) = N$ is equal to the number of bound electrons.

- **Covariant atomic form factor:** The covariant (4-vector) atomic form factor $J^{(\text{covariant: } \mu)}(q; i \rightarrow f)$, $\mu = 0..3$ naturally arises in the

S-matrix formalism of atomic collisions as the (3-dimensional) Fourier transform of the transition current (Najjari, 2022)

$$\begin{aligned}
 J^{(\text{covariant: } \mu)}(q; i \rightarrow f) &= \int d^3r e^{i\mathbf{q}\cdot\mathbf{r}} \bar{\psi}_f(\mathbf{r}) \gamma^\mu \psi_i(\mathbf{r}) \equiv \int d^3r e^{i\mathbf{q}\cdot\mathbf{r}} \psi_f^+(\mathbf{r}) \gamma_0 \gamma^\mu \psi_i(\mathbf{r}) \\
 &= 4\pi \sum_{LM} i^L Y_{LM}^*(\hat{\mathbf{q}}) \int d^3r j_L(qr) Y_{LM}(\hat{\mathbf{r}}) \bar{\psi}_f(\mathbf{r}) \gamma^\mu \psi_i(\mathbf{r}) = 4\pi \sum_{LM} i^L Y_{LM}^*(\hat{\mathbf{q}}) \mathcal{J}_{LM}^\mu(q) \\
 \mathcal{J}_{LM}^\mu(q) &= \int d^3r j_L(qr) Y_{LM}(\hat{\mathbf{r}}) \psi_f^+(\mathbf{r}) \gamma_0 \gamma^\mu \psi_i(\mathbf{r}),
 \end{aligned}$$

and where γ^μ, γ_0 are the standard Dirac matrices and $\bar{\psi} = \psi^+ \gamma_0$.

Covariant atomic form factor:

- **Covariant atomic form factor:** The covariant (4-vector) atomic form factor $J^{(\text{covariant: } \mu)}(\mathbf{q}; i \rightarrow f), \mu = 0..3$ is defined as (3-dimensional) Fourier transform of the (4-vector) transition current (Najjari, 2022)

$$\begin{aligned}
 J^{(\text{covariant: } \mu)}(\mathbf{q}; i \rightarrow f) &= \int d^3r e^{i\mathbf{q}\cdot\mathbf{r}} \psi_f^+(\mathbf{r}) \gamma_0 \gamma^\mu \psi_i(\mathbf{r}) = 4\pi \sum_{LM} i^L Y_{LM}^*(\hat{\mathbf{q}}) \mathcal{J}_{LM}^\mu(q) \\
 \mathcal{J}_{LM}^\mu(q) &= \int d^3r j_L(qr) Y_{LM}(\hat{\mathbf{r}}) \psi_f^+(\mathbf{r}) \gamma_0 \gamma^\mu \psi_i(\mathbf{r}).
 \end{aligned}$$

- **Time-like form factor component:**

$$\mathcal{J}_{LM}^0(q) = \int d^3r j_L(qr) Y_{LM}(\hat{\mathbf{r}}) \psi_f^+(\mathbf{r}) \psi_i(\mathbf{r}) = \left\langle \kappa_f m_f \left| Y_M^{(L)} \right| \kappa_i m_i \right\rangle J^{(P)}(q; fi) + \left\langle -\kappa_f m_f \left| Y_M^{(L)} \right| -\kappa_i m_i \right\rangle J^{(Q)}(q; fi).$$

- **Space-like form factor components:** For $k = 1..3$ and $\boldsymbol{\alpha} = (\alpha_x, \alpha_y, \alpha_z) \equiv (\alpha_1, \alpha_2, \alpha_3)$, these space-like components of the covariant

7. Atomic properties

atomic form factor are given by

$$\begin{aligned}\mathcal{J}_{LM}^k(q) \equiv \mathcal{J}_{LM}^k(q) &= \int d^3 r j_L(qr) Y_{LM}(\hat{\mathbf{r}}) \psi_f^+(\mathbf{r}) \alpha_k \psi_i(\mathbf{r}) \\ &= \left\langle \kappa_f m_f \left| Y_M^{(L)} \sigma_k \right| -\kappa_i m_i \right\rangle I_L^o(q; fi) + \left\langle -\kappa_f m_f \left| Y_M^{(L)} \sigma_k \right| \kappa_i m_i \right\rangle I_L^o(q; if).\end{aligned}$$

➤ Angular-dependent matrix elements:

$$\begin{aligned}\left\langle \kappa_f m_f \left| Y_M^{(L)} \right| \kappa_i m_i \right\rangle &= \int d\hat{\mathbf{r}} \Omega_{\kappa_f m_f}^+ Y_{LM}(\hat{\mathbf{r}}) \Omega_{\kappa_i m_i} \\ &= \frac{[L, \ell_i]^{1/2}}{\sqrt{4\pi} [\ell_f]^{1/2}} \langle \ell_i 0, L 0 | \ell_f 0 \rangle \sum_{m_s} \langle \ell_f, m_f - m; 1/2, m_s | j_f m_f \rangle \langle \ell_i, m_i - m_s; 1/2, m_s | j_i m_i \rangle \langle \ell_i, m_i - m_s; LM | \ell_f, m_f - m_s \rangle \\ \left\langle \kappa_f m_f \left| Y_M^{(L)} \sigma_x \right| -\kappa_i m_i \right\rangle &= \int d\hat{\mathbf{r}} \Omega_{\kappa_f m_f}^+ Y_{LM}(\hat{\mathbf{r}}) \alpha_x \Omega_{\kappa_i m_i} \\ &= \frac{[L, \ell_i]^{1/2}}{\sqrt{4\pi} [\ell_f]^{1/2}} \langle \ell_i 0, L 0 | \ell_f 0 \rangle \sum_{m_s} \langle \ell_f, m_f + m_s; 1/2, -m_s | j_f m_f \rangle \langle \ell_i, m_i - m_s; 1/2, m_s | j_i m_i \rangle \langle \ell_i, m_i - m_s; LM | \ell_f, m_f + m_s \rangle \\ \left\langle \kappa_f m_f \left| Y_M^{(L)} \sigma_y \right| -\kappa_i m_i \right\rangle &= \int d\hat{\mathbf{r}} \Omega_{\kappa_f m_f}^+ Y_{LM}(\hat{\mathbf{r}}) \alpha_y \Omega_{\kappa_i m_i} \\ &= 2i \frac{[L, \ell_i]^{1/2}}{\sqrt{4\pi} [\ell_f]^{1/2}} \langle \ell_i 0, L 0 | \ell_f 0 \rangle \sum_{m_s} m_s \langle \ell_f, m_f + m_s; 1/2, -m_s | j_f m_f \rangle \langle \ell_i, m_i - m_s; 1/2, m_s | j_i m_i \rangle \langle \ell_i, m_i - m_s; LM | \ell_f, m_f + m_s \rangle \\ \left\langle \kappa_f m_f \left| Y_M^{(L)} \sigma_z \right| -\kappa_i m_i \right\rangle &= \int d\hat{\mathbf{r}} \Omega_{\kappa_f m_f}^+ Y_{LM}(\hat{\mathbf{r}}) \alpha_z \Omega_{\kappa_i m_i} \\ &= 2 \frac{[L, \ell_i]^{1/2}}{\sqrt{4\pi} [\ell_f]^{1/2}} \langle \ell_i 0, L 0 | \ell_f 0 \rangle \sum_{m_s} m_s \langle \ell_f, m_f - m_s; 1/2, m_s | j_f m_f \rangle \langle \ell_i, m_i - m_s; 1/2, m_s | j_i m_i \rangle \langle \ell_i, m_i - m_s; LM | \ell_f, m_f - m_s \rangle\end{aligned}$$

7.1.g. One- and two-particle reduced density matrices & natural orbitals (ReducedDensityMatrix)

Properties, notations & application:

- One-particle reduced density matrix (1p RDM) $\rho^{(1p)}$: of an atom in level (αJ) .
- Two-particle reduced density matrix (2p RDM) $\rho^{(2p)}$ of an atom in level (αJ) .
- Natural orbitals $\phi_{n\kappa}^{(NO)}(r)$ of an atom in level (αJ) .
- Radial electron-density distribution $D(r) \equiv r^2 \rho(r)$ of an atom in level (αJ) represents the probability to find an electron in the interval $[r, r + dr]$ from the nucleus, averaged over all directions.
- Pairwise orbital interaction I_{pq} of orbitals p, q of an atom in level (αJ) .
- Using JAC: Perform an `Atomic.Computation(..., configs=[...], propertySettings= ReducedDensityMatrix.Settings(...), ...)` or call directly functions from the module `ReducedDensityMatrix`.
- In JAC, the natural orbitals are calculated and tabulated by default for all selected levels in `ReducedDensityMatrix.Settings`. The 1p and 2p RDM as well as the pairwise orbital interaction are calculated and printed if the corresponding flags has been set to true.

k-particle reduced density matrices:

- One- and two-particle RDM: The occupation-number operators $n_{p,q} \equiv a_p^+ a_q$, $a_{pq,rs} \equiv a_p^+ a_q^+ a_r a_s$, etc. obviously conserve the particle number and can be utilized to defined the one- and two-particle RDM by:

$$\rho^{(1p)} = (\rho_{p,q}^{(1p)}) = (\langle \Psi | n_{p,q} | \Psi \rangle), \quad \rho^{(2p)} = (\rho_{pq,rs}^{(2p)}) = (\langle \Psi | n_{pq,rs} | \Psi \rangle), \quad \text{etc.}$$

- Total energy in terms of the 1p and 2p RDM: The energy of an atom or ion can be written in terms of the 1p and 2p RDM as (Kong and Valeev, 2011)

$$E = \sum_{pq} \langle p | h | q \rangle \rho_{p,q}^{(1p)} + \frac{1}{4} \sum_{pqrs} \langle pq | v | rs \rangle \rho_{pq,rs}^{(2p)}.$$

7. Atomic properties

In fact, only the 2p RDM is needed in order to compute the energy and many other properties, since the matrix elements of the 1p RDM can always be obtained as partial trace from the 2p RDM.

- **Diagonal of the 1p RDM:** Since the RDM are by construction *diagonal* for uncorrelated (product) states, the diagonal of the 1p RDM $\rho_{pp}^{(1p)}$ is expected to be dominant also for all *weakly* correlated states.
- **Diagonal matrix elements of the 1p and 2p RDM:** If a pure state ψ is expanded into a basis, the diagonal matrix elements of the 1p RDM simplify to

$$\rho_{pp}^{(1p)} = \langle \Psi | n_{p,p} | \Psi \rangle = \sum_i c_i^2 \langle i | n_{p,p} | i \rangle = \sum_i \omega_i n_p(i) = \bar{n}_p$$

$$\rho_{pp,rr}^{(2p)} = \langle \Psi | n_{pp,rr} | \Psi \rangle = \sum_i c_i^2 \langle i | n_{pp,rr} | i \rangle = \sum_i \omega_i n_p(i) n_r(i) = \overline{n_p n_r}$$

where $n_p(i) \in [0, 1]$ is the occupation number of orbital p in the basis state i , ω_i the weight of the basis state, \bar{n}_p the mean occupation number of orbital p and $\overline{n_p n_r}$ the mean occupation number of the orbital pair (pr) .

- **Wave functions versus 2p RDM:** The wave function of a many-electron quantum system comprises much more information of what is needed in order to calculate its total energy as well as the expectation values of most observables. For example, the ground-state energy can be determined variationally from a functional of the 2p RDM, and which scales polynomially with the number of electrons N .
- **Spectral representation of the 1p RDM:** The 1p RDM is hermitian and has a spectral representation

$$\rho^{(1p)}(\mathbf{x}, \mathbf{x}') = \sum_p n_p \phi_p^{(NO)}(\mathbf{x}) \phi_p^{(NO)*}(\mathbf{x}')$$

where the eigenvalues n_p are called the natural occupation numbers and the eigenfunctions $\phi_p^{(NO)}(\mathbf{x}) = \phi_p^{(NO)}(\mathbf{r}, \sigma)$ the natural spin-orbitals. Often, the convention is made that the indices p, q, r, s pertain to natural spin-orbitals and a, b, c, d to any other one-electron orbital functions. For a properly normalized 1p RDM, moreover, the following conditions are satisfied (Pernal and Giesbertz, 2015):

$$\int d\mathbf{x} \phi_p^{(NO)+}(\mathbf{x}) \phi_q^{(NO)}(\mathbf{x}) = \delta_{pq} \quad \forall p, q, \quad 0 \leq n_p \leq 1 \quad \forall p, \quad \sum_p n_p = N.$$

For these conditions, Coleman (1963) proved that there exists an ensemble of N -electron antisymmetric wave functions that all yield the given $\rho^{(1p)}(\mathbf{x}, \mathbf{x}')$.

- **Spherical-averaged 1p RDM:** For closed-shell systems, contour-plots of the spherically-averaged 1p RDM

$$\rho^{(1p)}(r, r') = \frac{1}{4\pi} \int_0^{2\pi} d\varphi \int d\vartheta \sin\vartheta \rho(\mathbf{r}, \mathbf{r}') |_{\vartheta=\vartheta', \varphi=\varphi'}$$

have been discussed in the literature. This averaging procedure obviously omits the off-diagonal angular part ($\vartheta \neq \vartheta'$, $\varphi \neq \varphi'$) and, thus, does not include information about the angular (nodal) structure of the natural orbitals $\phi^{(NO)}(\mathbf{r})$. To resolve this information, Smider and Smith Jr. (1993) suggested to replace this 2-dimensional integration by a full 4-dimensional integration.

- **Spin-averaged 1p and 2p RDM:** In second-quantization and by using the occupation-number operator $n_{p\sigma} = a_{p\sigma}^+ a_{p\sigma}$ for an electron with spin component σ in orbital p , the spin-averaged 1p and 2p RDM are given by

$$\rho_{pq}^{(1p: w/o spin)} = \sum_{\sigma} \langle \Psi | n_{p\sigma} | \Psi \rangle = \sum_{\sigma} \langle \Psi | a_{p\sigma}^+ a_{p\sigma} | \Psi \rangle, \quad \rho_{pq}^{(2p: w/o spin)} = \sum_{\sigma, \sigma'} \langle \Psi | n_{p\sigma} n_{q\sigma'} | \Psi \rangle.$$

Again, the reduced density matrix elements are non-zero only if the orbital p and q are occupied in the wave function $|\Psi\rangle$. The elements of the spin-averaged 1p RDM $\rho^{(1p: w/o spin)}$ are contained also in the off-diagonal matrix elements of the spin-averaged 2p RDM $\rho^{(2p)}$, and the elements of the 2p-RDM $\rho^{(2p: w/o spin)}$ are in the diagonal matrix elements of $\rho^{(2p)}$ (Rissler *et al.*, 2011).

Natural orbitals:

- **Natural orbitals:** These orbitals are defined as the one-electron orbital functions that diagonalize the block-diagonal one-particle reduced density matrix $\mathbf{C}^+ \boldsymbol{\rho}_{n'n}^{(\kappa)} \mathbf{C} = \tilde{\boldsymbol{\rho}}$. The natural orbitals are then obtained as linear combination

$$\tilde{R}_{n\kappa}(r) = \sum_{n'} C_{n',n}^{(\kappa)} R_{n'\kappa}(r),$$

and the eigenvalues $\tilde{\rho}_{nn} = \tilde{q}_n^{(\kappa)}$ is interpreted as the occupation numbers of the natural orbital $(n\kappa)$.

Orbital interactions:

- **Orbital interaction I_{pq} :** For a given (atomic) level, the orbital interaction I_{pq} between the orbitals p and q can be defined by following concepts from quantum information theory and by using especially the von Neumann entropy (Rissler *et al.*, 2011). This orbital interaction has been analyzed for different molecular (chemical) bonds.

7. Atomic properties

- **Orbital interaction:** In atomic and molecular physics, a strong orbital or configuration interaction is often observed when the orbitals have a similar energy and/or matching spatial distribution, and sometimes also a comparable occupation. These and similar arguments are often used to select restricted-active (orbital) spaces.

Shannon entropy:

- **Shannon entropy of electronic states:** The Shannon entropy of electronic states reflect as function of the spatial coordinates the localization or delocalization of electrons and has been applied as alternative for studying the dispersion in systems. This entropy has been used to study the electronic probability density and the localization density.
- **Shannon information entropy:** While Shannon's information entropy has been frequently used in communication theory for measuring the uncertainty of information, it has been applied also for analyzing the state of quantum systems. Examples for such studies refer to the dynamics of particles in a 2-dim infinite potential, a hyperbolic double-well potential, Dirac-delta like potentials or simple two-electron systems as well as to cold interacting bosons in a trap.
- **Shannon information entropy versus Heisenberg's uncertainty:** The Shannon entropy gives rise to an uncertainty relation that is related to Heisenberg's uncertainty but may support a simpler access for determining the position (uncertainty) of particles or the degree of delocalization.
- **Shannon information entropy of atoms and molecules:** The Shannon information entropy has been calculated for several complex atoms and molecules as an alternative in order to learn more about their electronic structure. Hereby, this entropy sheds light upon special electronic correlations and the delocalization of the probability density. Shannons entropy was used also to characterize avoided crossings, if excited hydrogen atoms are considered in parallel magnetic and electric field. Shannon's entropy can be readily determined with wave functions that are given in position or momentum space.

Radial electron-density distributions:

- **Radial electron density distribution:** The electron density can be readily obtained from the N -electron wave function as expectation value of the many-electron $\delta^{(N\text{-electron})}(\mathbf{r})$ operator

$$\rho(\mathbf{r}) = N \int d\mathbf{q}_1 d\mathbf{q}_2 \dots d\mathbf{q}_N \Psi^*(\mathbf{q}_1, \dots, \mathbf{q}_N) \delta^{(N\text{-electron})}(\mathbf{r}) \Psi(\mathbf{q}_1, \dots, \mathbf{q}_N).$$

- Many-electron $\delta^{(\text{N-electron})}(\mathbf{r})$ operator: This operator probes whether all electrons are at a given position $(\mathbf{r}_1, \mathbf{r}_2, \dots, \mathbf{r}_N)$ in space and can be expressed in terms of the single-electron operators as:

$$\begin{aligned}\delta(\mathbf{r} - \mathbf{r}_j) &= \frac{1}{r^2 \sin \vartheta} \delta(r - r_j) \delta(\vartheta - \vartheta_j) \delta(\varphi - \varphi_j) = \frac{1}{r^2} \delta(r - r_j) \sum_{\ell m} Y_{\ell m}(\vartheta, \varphi) Y_{\ell m}^*(\vartheta_j, \varphi_j) \\ \delta(\mathbf{r})^{(\text{N-electron})} &= \sum_{j=1}^N \delta(\mathbf{r} - \mathbf{r}_j) = \frac{1}{r^2} \sum_{j=1}^N \delta(r - r_j) \left[\sum_{\ell m} Y_{\ell m}(\vartheta, \varphi) Y_{\ell m}^*(\vartheta_j, \varphi_j) \right].\end{aligned}$$

- Single-electron $\delta(\mathbf{r})$ operator in second quantization: In the relativistic theory, this single-electron operator can be expressed also in second quantization in terms of the creation and annihilation operators with regard to the relativistic subshell $(n\kappa)$ basis

$$\delta(\mathbf{r} - \mathbf{r}_j) = \sum_{\kappa} \sqrt{2j+1} \sum_{ab} [a_{n_a \kappa}^+ a_{n_b \kappa}]^{(0)} [P_{n_a \kappa}(r) P_{n_b \kappa}(r) + Q_{n_a \kappa}(r) Q_{n_b \kappa}(r)].$$

- Radial electron-density distribution of a single level $(\alpha\mathbb{J})$: This distribution represents the probability to find an electron in the interval $[r, r + dr]$ from the nucleus, averaged over all directions:

$$D(r) \equiv r^2 \rho(r) = \sum_a q_a (P_a^2(r) + Q_a^2(r)), \quad \int_0^\infty dr D(r) = \int_0^\infty dr r^2 \rho(r) = \sum_a q_a = N.$$

7. Atomic properties

➤ Many-electron $\delta^{(\text{N-electron})}(\mathbf{r})$ operator in second quantization:

$$\begin{aligned}
 \delta(\mathbf{r})^{\text{N-electron}} &= \sum_{pq} d_{pq}(r) a_p^+ a_q \\
 &= \sum_{pq} \delta_{\kappa_p \kappa_q} \delta_{m_p m_q} [P_p(r) P_q(r) + Q_p(r) Q_q(r)] a_p^+ a_q = \sum_{n_a n_b}^{\text{(occ)}} \sum_{\kappa} [P_{n_a \kappa}(r) P_{n_b \kappa}(r) + Q_{n_a \kappa}(r) Q_{n_b \kappa}(r)] a_a^+ a_b \\
 &= \delta_0^{(0)} = - \sum_j \sqrt{2j+1} \sum_{n_a n_b, \kappa}^{\text{(occ)}} (a_{n_a \kappa}^+ a_{n_b \kappa})_0^{(0)} [P_a(r) P_b(r) + Q_a(r) Q_b(r)] \\
 (a_{n_p \kappa}^+ a_{n_q \kappa})_0^{(0)} &= - \frac{1}{\sqrt{2j+1}} \sum_m a_{n_p \kappa m} a_{n_q \kappa m},
 \end{aligned}$$

and where the Kronecker deltas here reflect the orthogonality of the one-electron orbitals. The expectation value of the radial density operator also provides the radial density distribution $D(r) = r^2 \rho(r) = 4\pi r^2 \rho(\mathbf{r})$. In the last line, moreover, the orbital creation and annihilation operators have been coupled to a zero-rank irreducible tensor.

➤ One-electron reduced matrix elements of the radial density operator:

$$\langle a \| \delta(\mathbf{r}) \| b \rangle = \delta_{\kappa_a \kappa_b} [P_a(r) P_b(r) + Q_a(r) Q_b(r)].$$

Coherence, entanglement, etc.:

- Entanglement of electron orbitals: In quantum information, two partites are said to share information as more they are entangled with each other. Therefore, entanglement measures can be utilized also to established quantitative measures for the orbital interaction, for instance based on the von Neumann entropy S .
- Quantum coherence: This term often just refers to some superpositions of (a set of) orthogonal states; if the superposition is made explicit for the state of some natural or tailored quantum system, the quantum coherence is said to be revealed.

7.1.h. Energy shifts in plasma environments (PlasmaShift)

Properties, notations & application:

- Plasma shift of an atomic level: $E(\alpha\mathbb{J}) \longrightarrow E(\alpha\mathbb{J}; \text{plasma model and parameters})$.
- Formal quantum notation: $\Delta E^{(\text{plasma})}(\alpha\mathbb{J}) = E(\alpha\mathbb{J}; \text{plasma model and parameters}) - E(\alpha\mathbb{J}; \text{unperturbed})$.
- Spectral line shifts: The interaction between the plasma and the bound electrons of an ion embedded into the plasma alters the ionic structure and transition properties. Therefore, a plasma environment generally results in spectral line shifts, line broadening and changes in the line shapes, when compared with the free ion.
- For realistic plasma conditions, the number of bound states of the ions often becomes finite and the electrons less tightly bound by the nucleus, if the plasma coupling parameter increases.
- Using JAC: Perform an `Atomic.Computation(.., properties=[Plasma, ...], configs=[...], plasmaSettings=PlasmaShift.Settings(..), ...)` or call directly functions from the module `PlasmaShift`.
- In JAC, the plasma (energy) shifts are calculated and tabulated by default for a Debye-Hückel plasma model with screening parameter $\lambda = 0.25$. Hereby, the Debye-Hückel interaction is incorporated only in first-order perturbation theory within the CI matrix.
- Plasma: More than 95 % of the visible matter in the universe are likely made of plasma, i.e. a mixture of electrons, atoms as well as positive and negative ions.
- Ions in plasma: In a plasma, the atomic central field is modified by the neighbored ions and the free plasma electrons and, hence, all atomic data become affected as the density of the plasma increases.

High-density plasma:

- Relativistic corrections to the plasma screening may become necessary for a detailed analysis of atomic spectra, especially if lines of multiply-charged ions are used in some spectral analysis.
- Collisional-radiative model: The effects of the plasma-environment can be further taken into account also by kinetic *or* collisional-radiative models, and where the energy shifts are often introduced by semi-empirically formulas, such as the formula by Stewart and Pyatt.
- Application of simple plasma models: Apart from plasma diagnostics, a proper treatment of a (plasma) screening potential has been found useful also in other areas of physics, such as nuclear and elementary particle physics, solid state physics, or even the design of nanostructures.

7. Atomic properties

- **Strongly-coupled plasma:** For a **strongly-coupled dense plasma**, the (averaged) electrostatic energy between neighbouring particles in the plasma exceeds their thermal energy. The coupling parameter $\Gamma = q^2/4\pi\epsilon_0 R_0 kT > 1$ is used in order to characterize such a strongly-coupled plasma. This **coupling parameter Γ simply describes the ratio of the electrostatic and the thermal energy of the plasma particles, and where $R_o = (3/4 \pi n_e)^{1/3}$.**
- **Laser-induced plasma with $\Gamma \gg 1$:** Strongly-coupled plasma obeys generally classical statistics and has been observed for a large number of experimental and astrophysical conditions. In the laboratory, for instance, laser-induced plasma with $\Gamma \gg 1$ has been investigated in high-compression fusion experiments. Such a laser-produced plasma provides a very typical example of a high-density, strongly-coupled plasma with electronic densities well beyond 10^{24} cm^{-3} .
- Theoretical (plasma) models for hot and dense plasma are necessary to simulate its properties, such as the equation of state, radiative transfer coefficients or the conduction coefficients in plasma. These properties are relevant for inertial confinement fusion and astrophysics.
- **Average-atom (AA) model:** The AA model has been utilized to describe the electronic structure of hot and dense plasmas. This model was developed in order to describe **bound electrons in terms of the (atomic) shell model, and to deal with the free electrons within the Thomas-Fermi statistical model**.
- **Plasma models:** Plasma screening effects have been investigated extensively by employing various analytical models, such as the ion sphere, Debye-Hückel, Stewart-Pyatt as well as Ecker-Kröll models.
- **Diagnostics of high-density plasma:** The density of laboratory plasma has been analyzed by measuring the field-induced broadening of spectral lines; this diagnostics has been used for analyzing inertial confinement fusion experiments as well as in other plasma environments. However, such line broadening measurements are affected also by several systematic and instrumental effects, such as the assumptions about the radiative background in a given spectrum (Gu and Beiersdorfer, 2020). — In contrast, **line-shift measurements are less sensitive on the radiation background and offer a useful and complementary alternative for plasma diagnostics**. This requires that the density-dependent shifts are well enough understood to rely on it in the analysis.

Frequently applied plasma models in atomic structure calculations:

- **Debye-Hückel versus the ion-sphere model:** These two plasma models are valid for quite different plasma conditions. If we define the mean ion-sphere radius as $R_s = \left[\frac{3(Z-N^{(\text{bound})})}{4\pi n_e} \right]^{1/3}$ and the screening radius R_d , the Debye-Hückel model is valid for $R_d \gg R_s$, while the ion-sphere model applies for $R_d \ll R_s$. Both models fail however in the intermediate region. Gu and Beiersdorfer (2020) point out that the Debye-Hückel model is rather poor and likely only valid for $R_d \gg R_s$. In contrast, the ion sphere model appears to be a reasonable

approximation if just shifts of excitation and transition energies are to be considered. The total plasma potential as seen by the bound electrons is given by the sum of the (isolated) ionic potential and the (free-electron plasma) potential due to the free electrons

$$V(r) = V^{(\text{ion})}(r) + V_f(r).$$

- **Debye-Hückel (screening) model:** This model is suitable at low density and high temperature, and for which the Debye length R_d is (much) larger than the size of the ions. In this case, it appears justified to screen the total atomic potential, for instance in a mean-field Dirac-Hartree-Slater potential, instead of screening the interelectronic Coulomb interactions and the nuclear potential separately. For a given screening length R_d (Debye length), this gives rise to free-electron plasma potential $V_f(r) = V^{(\text{ion})}(\exp(-r/R_D) - 1)$, and where $V^{(\text{ion})}(r \rightarrow \infty) = -(Z - N^{(\text{bound})} + 1)/r$.
- **Debye-Hückel model:** This model has been commonly used in order to incorporate plasma effects into atomic structure calculations. However, the **validity of this model remains rather questionable** because it is valid only when the *correlation* time of the ion is much longer than the lifetime of excited atomic states. Therefore, **this perturbative approach is at best valid for weakly-coupled plasmas and should not be applied for modeling of high-density plasmas.**
- **Coulomb interaction in the Debye-Hückel model:** In this model, the (pairwise) Coulomb interaction among the charged particles is modified (screened) for an ion with nuclear charge Z to

$$V^{(\text{DH})}(r, \lambda) = -\sum_i^N \frac{Ze^{-\lambda r_i}}{r_i} + \sum_{i>j}^N \frac{e^{-\lambda r_{ij}}}{r_{ij}} = \sum_i^N V^{(\text{e-n, DH})}(r_i, \lambda) + \sum_{i>j}^N V^{(\text{e-e, DH})}(r_{ij}, \lambda).$$

Here, N is the number of bound electrons in the ion, r_i is the distance of the i -th electron from the nucleus, and r_{ij} the distance between the electrons i and j .

- **Plasma screening parameter λ :** This parameter is the inverse of the Debye shielding length for a certain plasma environment and can be readily expressed in terms of the electron density n_e and the temperature T_e of the plasma by:

$$\lambda = \left[\frac{4\pi n_e}{k T_e} \right]^{\frac{1}{2}}.$$

- **Debye-Hückel model:** To obtain the modified two-particle integrals due the plasma screening, we can write

$$V^{(\text{e-e, DH})}(r_{ij}, \lambda) = -\lambda \sum_{l=0}^{\infty} (2l+1) j_l(i\lambda r_<) h_l^1(i\lambda r_>) P_l(\cos\theta)$$

7. Atomic properties

in terms of the *larger* ($r_> = \max(r_i, r_j)$) and *smaller* radii ($r_< = \min(r_i, r_j)$) of the one-particle radii r_i and r_j , respectively, and where j_l denotes a spherical Bessel function and h_l^1 a Hankel function of the first kind.

- **Debye-Hückel plasma potential:** The many-body interaction between the (atomic) electrons and the (neutral) plasma outside of the atom can be modeled effectively by the Debye-Hückel potential that just depends on two parameters, the radius R_D of the Debye sphere and the Debye length D . This length $D = 1.4048 (kT/n_e)^{1/2} a_o$ can be expressed in terms of the temperature kT [eV] and the electron density n_e [10^{22} cm^{-3}] of the outside plasma and is given in atomic units [a_o]. The Debye length characterizes the screening of the electrons by the plasma. Without a plasma, the density is $n_e \rightarrow 0$ and $D \rightarrow \infty$ or $\exp(r/D) \rightarrow 1$, respectively. The Debye screening therefore modifies the attractive nuclear interaction due to the (neutral) plasma outside.
- **Debye-Hückel plasma potential:** The Debye radius R_D and length D help to write the Debye-Hückel plasma potential as (Chang *et al.*, 2022)

$$V^{(\text{DH})} = \begin{cases} -Z e^2 \left(\frac{1}{r} - \frac{1}{D+r_D} \right) & r \leq R_D \\ -Z e^2 \frac{D \exp(R_D/D)}{D+R_D} \frac{\exp(r/D)}{r} & r > R_D \end{cases}$$

For $R_D \rightarrow 0$, the Debye-Hückel plasma potential reduced to $- \frac{Z}{r} \exp(r/D)$.

- **Stewart-Pyatt plasma model:** This model applies to rather a wide range of plasma temperature and density parameters since it interpolates between the two limits of the ion-sphere and Debye-Hückel model. It is therefore considered to be more realistic for different applications. In the Stewart-Pyatt model, the free-electron plasma potential $V_f(r)$ is obtained from a second-order differential equation, based on the Thomas-Fermi theory.
- **Ion-sphere model:** This model applies especially for high-density and low-temperature plasma. For these conditions, the free-electron plasma potential of the free electron can be written as (Gu and Beiersdorfer, 2020);

$$V_f(r) = 4\pi \left[\frac{1}{r} \int_0^r dr' (r')^2 \rho_f(r') + \int_r^{R_s} dr' r' \rho_f(r') \right], \quad R_s = \left[\frac{3(Z - N^{(\text{bound})})}{4\pi n_e} \right]^{1/3}$$

and where the radial density $\rho_f(r)$ of the free electron is assumed to follow the Fermi-Dirac distribution, for which the chemical potential is determined implicitly by the neutrality of charge within the ion-sphere radius R_s . For high-enough temperatures, the free-electron plasma

potential can be simplified to

$$V_f = \frac{Z - N^{(\text{bound})}}{2 R_s} \left[3 - \left(\frac{r}{R_s} \right)^2 \right], \quad R_s = \left[\frac{3(Z - N^{(\text{bound})})}{4\pi n_e} \right]^{1/3}.$$

- Nonrelativistic functions $Y^k(r; ab)$ and $Z^k(r; ab)$ for a Debye-Hückel potential: Jiao *et al.* (2019) reformulated the frequently-applied $Z^k(r; ab)$ and $Y^k(r; ab)$ for atoms and ions in a Debye-Hückel potential, i.e. for weakly-coupled plasmas. In this reformulation, use is made of the Gegenbauer expansion in order to decompose the screened interelectronic Coulomb potential.
- Electron-electron interaction in a Debye-Hückel plasma: For atoms in a screened Debye-Hückel plasma, the Coulomb operator $\mathbb{V}^{(\text{Coulomb})}$ has to be replaced by (Jiao *et al.*, 2019)

$$\mathbb{V}^{(\text{e-e, DH})} = \frac{e^{-\lambda r_{12}}}{r_{12}} = \sum_{k=0}^{\infty} (2k+1) \frac{I_{k+\frac{1}{2}}(\lambda r_<)}{\sqrt{r_<}} \frac{K_{k+\frac{1}{2}}(\lambda r_>)}{\sqrt{r_>}} P_k(\cos \vartheta_{12}),$$

where λ is the screening parameter and I_α and K_α are the modified (but not spherical) Bessel functions of the first and second kind.

- Solutions of the $Y^k(r; ab)$ and $Z^k(r; ab)$ functions: For atoms in a screened Debye-Hückel potential, the pair of differential equations can be written (Jiao *et al.*, 2019)

$$\begin{aligned} \frac{d}{dr} Z^k(r; \lambda, ab) &= \left[\frac{k+1}{r} - \lambda \frac{K_{k+3/2}(\lambda r)}{K_{k+\frac{1}{2}}(\lambda r)} \right] Z^k(r; \lambda, ab) + (2k+1) I_{k+\frac{1}{2}}(\lambda r) K_{k+\frac{1}{2}}(\lambda r) P_a(r) P_b(r), \\ \frac{d}{dr} Y^k(r; \lambda, ab) &= \left[\frac{k+1}{r} - \lambda \frac{K_{k+3/2}(\lambda r)}{K_{k+\frac{1}{2}}(\lambda r)} \right] Y^k(r; \lambda, ab) - \lambda \left[\frac{I_{k+3/2}(\lambda r)}{I_{k+\frac{1}{2}}(\lambda r)} + \frac{K_{k+3/2}(\lambda r)}{K_{k+\frac{1}{2}}(\lambda r)} \right] Z^k(r; \lambda, ab) \end{aligned}$$

and with the same boundary conditions $Z^k(0; \lambda, ab) = 0$, $Y^k(r \rightarrow \infty; ab) = Z^k(r \rightarrow \infty; ab)$ for all finite λ . It is therefore convenient to calculate $Z^k(r; \lambda, ab)$ by an outward integration from $r = 0$ and then to obtain $Y^k(r; \lambda, ab)$ by an inward integration from $r \approx \infty$.

- Debye-Hückel model: While the Debye-Hückel screening of the electron-nucleus interaction usually destabilizes the binding of the electron, the screening of the electron-electron repulsion counteracts this trend.
- Debye-Hückel model and beyond: For weakly coupled plasma, the classical static Debye-Hückel model is often used to define the interaction potential between charged particles. This potential becomes unreliable when the velocity of the projectile electron becomes comparable or

7. Atomic properties

even larger than the velocity of the plasma electrons since the projectile electron then polarizes the surrounding plasma electrons (Jung, 1997).

- Saha and Fritzsche (2006) demonstrated for beryllium-like ions that the Debye-Hückel screening (if applicable) should be incorporated into both, the electron-nucleus and electron-electron interaction in order to obtain reliable results for the plasma shifts.
- **Ion-sphere model:** In this model, the ion is typically enclosed in a spherically symmetric cell that contains the exact number of electrons in order to ensure neutrality. In the ion-sphere model, one needs to define an electron-density distribution that either obeys self-consistency equations or need to make some simple hypothesis, such as an uniform density within the cell.

Plasma in oscillating electric fields:

- **Plasma in oscillating electric fields:** The collective movement of plasma particles, such as the electron plasma waves (Langmuir oscillations) or ion plasma waves, is mainly determined by the plasma creation and/or heating device but lead also to quite significant fields (Peyrusse 1977).

Free-electron distributions in plasma:

- In a plasma, the free-electron (radial) density $n_e(r)$ can follow different distributions:
- **Maxwell-Boltzmann distribution:** The Maxwell-Boltzmann statistics has been often applied to describe the free-electron distribution but is not well justified for high-density or low-temperature plasma.
- **Fermi-Dirac distribution:** This distribution is preferable if the free electrons are degenerate

$$n_e(r) = \frac{4}{\sqrt{\pi}} \int_{r_o}^{\infty} dr \frac{\sqrt{r}}{e^{r - r_o - \mu/kT_e} + 1} = 2\lambda_{\text{th}}^{-3} \mathcal{F}_{1/2} \left(-\frac{V(r)}{kT_e} + \frac{\mu}{kT_e}; -\frac{V(r)}{kT_e} \right).$$

Here μ is the chemical potential of the plasma, $\mathcal{F}_{1/2}(x, y)$ the incomplete Fermi-Dirac integral and $\lambda_{\text{th}} = \sqrt{2\pi/kT_e}$ the thermal de-Broglie thermal wavelength.

- **Uniform electron-gas distribution:** This distribution considers a sphere of radius $R_o = (3/4\pi n_e)^{1/3}$ around the ion with N_b bound electrons, in which the ionic charge is completely neutralized by the additional $N_f = Z - N_b$ free electrons. Although all electrons inside of the sphere will strongly interact with the embedded ion, the free electrons are here assumed to be distributed uniformly. With this assumption

in mind, the electrostatic potential for the bound electrons with radial coordinate r is given by

$$V^{(\text{IS})}(\mathbf{r}; \mathbf{R}_0) = \begin{cases} -\frac{Z}{r} + \frac{Z-N_b}{2R_0} \left[3 - \left(\frac{r}{R_0} \right)^2 \right] & \text{for } r \leq R_0 \\ 0 & \text{for } r > R_0. \end{cases}$$

In this potential above, the first term describes the interaction of the bound electron with the nucleus, while the second (repulsive) term arises from the plasma background and always causes a shift of all the level energies towards the continuum.

- Collision-induced localization: The plasma environment typically leads to a broadening of the momentum distribution of free electrons and partly also to its localization. Indeed, random collisions of the continuum electron with particles from the plasma environment may result in a loss of coherence of the outgoing, photoionized electrons when leaving the parent ions. Such a collision-induced localization resembles the Anderson localization of randomly scattered electrons in solids as well as the dynamical localization of Rydberg electrons in plasma.
- Collision-induced localization: The collision-induced energy and momentum broadening of stationary states can reduce also the lifetime of the bound states. At a given plasma temperature, the momentum broadening increases with the plasma density or, in other words, the electron localization is more pronounced in a dense plasma.

Gordon-Kim theory:

- In the Gordon-Kim theory (1972), the total energy of the system consists out of the direct Coulomb potential energy, the exchange Coulomb potential energy, the kinetic energy as well as the correlation energy. The direct Coulomb potential energy is calculated by integrating the Coulomb potential for the (approximated) electron density, while the other contributions to the total energy were calculated by using a temperature-dependent local density functional (LDA) approach.

7.1.i. Level-dependent fluorescence and Auger yields (DecayYield)

Properties, notations & application:

➤ Fluorescence *versus* Auger decay of an (excited) atomic level: $A^{q+*} \rightarrow \begin{bmatrix} A^{q+(*)} + \hbar\omega \\ A^{(q+1)+(*)} + e_a^- \\ \dots \end{bmatrix}$.

The corresponding **level-specific or configuration-averaged fluorescence and Auger yields** just describe the fraction of atoms in a particular level or configuration that decay either by fluorescence *or* Auger electron emission.

➤ Formal quantum notation: $|\alpha_J\rangle \rightarrow \begin{bmatrix} \{ |\alpha_r J_r\rangle + \hbar\omega(\{\mathbb{M}\}) \} \\ \{ |\alpha_a J_a\rangle + |\varepsilon \kappa\rangle \} \\ \dots \end{bmatrix}$.

- Using JAC: Perform an `Atomic.Computation(.., properties=[Yields, ...], configs=[..], yieldSettings=DecayYield.Settings(..), ...)` or call directly functions from the module `DecayYield`.
- In JAC, we calculate and tabulate by default the fluorescence yields $\omega_r(\alpha J)$ and Auger yields $\omega_a(\alpha J)$ for all selected levels.
- In JAC, the computation of all fluorescence and Auger yields is always traced back to single-step cascade computations. Therefore, the same (cascade) approaches `{ AverageSCA, SCA, ... }` can be applied as in cascade computations, cf. section 9.1. The particular approach, that is to be applied in the given computation above, need to be specified however as `String` in the `DecayYield.Settings("AverageSCA", ...)`.
- In JAC, the explicit settings of the underlying `Cascade.Computation` can be overwritten in the function `Cascade.determineSteps()`; no attempt has been made so far to support such control features directly by means of the `DecayYield.Settings(...)`.
- **Fluorescence yields $\omega_r(\alpha J)$:** This yield typically represents the probability of an inner-shell (core) hole to be filled under photon emission, in contrast and competition with other nonradiative processes.
- **Auger yields $\omega_a(\alpha J)$:** This yield describes the **(complementary) probability for an inner-shell hole level** to decay by electron emission, hence: $\omega_r(\alpha J) + \omega_a(\alpha J) = 1$. The Auger yield is sometimes further partitioned into an Auger and Coster-Kronig yield: $\omega_a(\alpha J) = \omega^{(Auger)}(\alpha J) + \omega^{(Coster-Kronig)}(\alpha J)$.

- If not explicitly overwritten within the code [cf. the module **Cascade**], only the electric-dipole (E1) transitions and the **Coulomb interaction** $\Psi^{(\text{Coulomb})}$ are taken into account in the evaluation of all Auger and radiative transition amplitudes and rates.
- More often than not, the fluorescence and Auger yields are computed and analyzed for either K - or L -shell (holes) states, and for which usually no distinction need to be made for the different fine-structure levels ($\alpha\mathbb{J}$) that arise only due to the couplings of the valence shells.
- **Typically, it is completely sufficient to include only electric-dipole decay channels**, although other multipoles could be incorporated explicitly in the computations, as far this is supported by the underlying cascade approach, or invoked explicitly within the code.
- **Fluorescence yield:** Hasoglu *et al.* (2006) have shown that the fluorescence yield of K -shell vacancy configurations, is level-dependent, i.e. might depend especially on the particular term and level. In this case, fine-structure resolved calculations need to be performed.

7.2. In JAC partly-implemented level properties

7.2.a. Scattering amplitudes and scattering factors (FormFactor)

Properties, notations & application:

- Scattering amplitude $S(q; \alpha \mathbb{J})$ of an atomic level with supposed spherical-symmetric charge distribution:.
- Formal quantum notation: .

Anomalous scattering factors:

- Coherent Rayleigh scattering factor: This scattering factor characterizes the (complex) scattering amplitude in forward direction and is obtained by:

$$\frac{1}{2} \sum_{\varepsilon_i, \varepsilon_f} M(\varepsilon_i, \mathbf{k}_i, \varepsilon_f, \mathbf{k}_f = \mathbf{k}_i),$$

i.e. as average over the polarization (states) of the incident photon and by a summation over the polarization of the scattered photon.

- Using the modified form factor for describing the scattering in forward-scattering angle $\vartheta \approx 0$, the real $g'(\omega)$ and imaginary $g''(\omega)$ anomalous scattering factors can be approximately defined in terms of the photoionization cross sections and oscillator strength (Zhou *et al.*, 1990). This formally requires a summation over the complete spectrum of the atom, although the major contributions arise from just a few resonances.
- Anomalous scattering factor: The real $g'(\omega)$ and imaginary $g''(\omega)$ anomalous scattering factors are frequently employed in order to express the coherent (Rayleigh) scattering factor $G(\omega)$ for incident photons with energy $\hbar\omega$.
- Coherent Rayleigh scattering factor: For incident photons with energies $\hbar\omega$, the coherent (Rayleigh) scattering factor in forward direction has been written as (Zhou *et al.*, 1990)

$$G(\omega) = F(0) + g'(\omega) + i g''(\omega),$$

where $F(0) = N$ is the atomic form factor. Therefore, the (Rayleigh) scattering amplitude and scattering factor can be expressed also in terms of the standard (atomic) form factor (FF) or the modified form factor (MFF).

Incoherent scattering function $S(\mathbf{q})$:

- Incoherent scattering function:
- Incoherent scattering function: This scattering function can be expressed in terms of the generalized atomic form factor

$$S(\mathbf{q}; \alpha_o \mathbb{J}_o M_o) = \sum_{e \neq o} |F^{(\text{generalized})}(q; \alpha_e \mathbb{J}_e M_e; \alpha_o \mathbb{J}_o M_o)|^2 = \langle \alpha_o \mathbb{J}_o | \mathbb{T}^{(2)}(\mathbf{q}) | \alpha_o \mathbb{J}_o \rangle - |F^{(\text{standard})}(q; \alpha_o \mathbb{J}_o)|^2.$$

but where the summation over e includes all discrete levels as well as an integration over the continuum. In the second equivalence, the two-electron momentum-transfer operator $\mathbb{T}^{(2)}(\mathbf{q}) = \sum_{m,n=1}^N \exp[i \mathbf{q} \cdot (\mathbf{r}_m - \mathbf{r}_n)]$ occurs, but then just requires to compute the expectation value of this operator with regard for the ground state $|\alpha_o \mathbb{J}_o M_o\rangle$.

7.2.b. Multipole polarizabilities (MultipolePolarizability)

Remarks & notations:

- Frequency-dependent (ac 2^L -multipole) polarizability: For an atomic level $(\beta \mathbb{J})$ with energy E_o , the frequency-dependent (ac 2^L -multipole) polarizability is given by (Porsey *et al.*, 2018)

$$\alpha^{(\mathbb{M})}(\omega, \beta \mathbb{J}) = \frac{L+1}{L} \frac{2L+1}{[(2L+1)!!]^2} (\alpha \omega)^{2L-2} \sum_{\nu} \frac{(E_{\nu} - E_o) |\langle \alpha_{\nu} \mathbb{J}_{\nu} | \mathbb{T}^{(\mathbb{M})} | \beta \mathbb{J} \rangle|^2}{(E_{\nu} - E_o)^2 - \omega^2}$$

where $\mathbb{T}^{(\mathbb{M})}$ is the corresponding multipole operator for E1, M1, ... transitions.

7.2.c. Photoemission in external magnetic fields (MagneticFieldInduced)

Remarks & notations:

- Magnetic-field induced transitions (MIT): These induced transitions occur when an external magnetic field mixes levels with different total angular momenta \mathbb{J} .

7. Atomic properties

- **Transition rates for magnetic-field & hyperfine-induced transitions:** These transition rates are calculated as a sum over (reduced, unperturbed and single-photon) emission amplitudes between fine- or hyperfine-structure levels, respectively, and weighted by the representation of the corresponding expansion coefficients. Special care has to be taken if the radiative widths of the (hyperfine) levels becomes comparable with the level splitting which, at least in principle, then requires a common treatment of both, the hyperfine and magnetic-field interactions. The corresponding changes in the line intensities is also known as **radiation damping** in the literature.
- **Application of MIT:** Hyperfine & magnetic-field induced transitions have been investigated for different atomic systems both, theoretically and experimentally. In plasma diagnostics, these transitions may help in the determination of electron densities, isotope compositions as well as magnetic fields. A proper implementation of these induced transitions also help analyze spectra from electron-beam ion trap (EBIT) sources as well as the spectra of magnetic stars.
- **Application of MIT:** MIT may help in plasma diagnostics in order to determine the local strength of magnetic fields in plasmas, especially if the transitions is otherwise a forbidden atomic line.

Amplitudes and rates:

- **Magnetic-field induced transitions (MIT):** In an external magnetic field, the direction of the \mathcal{B} -field is typically chosen as quantization axis. For this particular choice, only states with the same parity and magnetic quantum number M_J , but with different total angular momentum J from different J will mix with each other

$$|\alpha PM; \mathcal{B}\rangle \equiv |\psi_\alpha(PM)\rangle = \sum_{\bar{\beta}=1} c_{\bar{\beta}}(\alpha; \mathcal{B}) |\bar{\beta} JM, \mathcal{B}=0\rangle, \quad c_{\bar{\beta}}(\alpha; \mathcal{B}) = \frac{\langle \bar{\beta} PM; \mathcal{B}=0 | H^{(\mathcal{B}-\text{field})} | \alpha PM; \mathcal{B} \rangle}{E(\bar{\beta} PM; \mathcal{B}=0) - E(\alpha PM; \mathcal{B})}$$

and where $\bar{\beta} = (\beta J_\beta)$ and the mixing coefficients $c_{\bar{\beta}}(\alpha; \mathcal{B})$ are here given in first-order perturbation theory.

- **Oscillator strength for transitions between hyperfine levels:** If the (off-diagonal) hyperfine interaction is negligible between neighboured fine-structure levels (αJ) , the absorption oscillator strengths for the electric-dipole transitions between two hyperfine levels $\alpha_i(IJ_i) \mathbb{F}_i \rightarrow \alpha_f(IJ_f) \mathbb{F}_f$ can be expressed in terms of the transition energy $\Delta E = (E(\alpha_i(IJ_i) \mathbb{F}_i) - E(\alpha_f(IJ_f) \mathbb{F}_f))$ and the associated fine-structure

amplitudes by

$$\begin{aligned} gf(\alpha_i(IJ_i) \mathbb{F}_i \rightarrow \alpha_f(IJ_f) \mathbb{F}_f) &= \frac{2}{3} \Delta E \left| \langle \alpha_f(IJ_f) \mathbb{F}_f \parallel \mathbb{O}^{(E1, \text{absorption})} \parallel \alpha_i(IJ_i) \mathbb{F}_i \rangle \right|^2 \\ &= \frac{2}{3} \Delta E (2F_i + 1) (2F_f + 1) \begin{Bmatrix} J_i & I & F_i \\ F_f & 1 & J_f \end{Bmatrix} \left| \langle \alpha_i \mathbb{J}_i \parallel \mathbb{O}^{(E1, \text{absorption})} \parallel \alpha_f \mathbb{J}_f \rangle \right|^2. \end{aligned}$$

In this case, the distribution of the oscillator strength among the hyperfine-resolved transitions is just determined geometrically by the Wigner 6-j symbol, i.e. due to the $(IJ)F$ coupling of the nuclear spin and the total electronic angular momentum.

- **Oscillator strength for transitions between hyperfine levels:** If, more generally, the hyperfine coupling between neighboured fine-structure levels $\{|\alpha \mathbb{J}\rangle\}$ is not negligible, the expansion coefficients $c_{\bar{\beta}}(\alpha \mathcal{B})$ of the hyperfine levels in the given ASF basis need to be taken into account. Then, the absorption oscillator strength for the electric-dipole transitions between two hyperfine levels $\alpha_i(IJ_i) \mathbb{F}_i \rightarrow \alpha_f(IJ_f) \mathbb{F}_f$ can still be written in terms of the associated fine-structure E1 transition amplitudes as (Andersson *et al.*, 2006)

$$\begin{aligned} gf(\alpha_i \mathbb{F}_i \rightarrow \alpha_f \mathbb{F}_f; \mathcal{B}) &= \frac{2}{3} \Delta E \left| \sum_{\bar{\beta}_i} \sum_{\bar{\beta}_f} c_{\bar{\beta}_i}(\alpha_i; \mathcal{B}) c_{\bar{\beta}_f}(\alpha_f; \mathcal{B}) \langle \beta_i(IJ_i) \mathbb{F}_i \parallel \mathbb{O}^{(E1, \text{absorption})} \parallel \beta_f(I, J_f) \mathbb{F}_f \rangle \right|^2 \\ &= \frac{2}{3} \Delta E (2F_i + 1) (2F_f + 1) \left| \sum_{\beta_i J_i} \sum_{\beta_f J_f} c_{\bar{\beta}_i}(\alpha_i; \mathcal{B}) c_{\bar{\beta}_f}(\alpha_f; \mathcal{B}) \begin{Bmatrix} J_i & I & F_i \\ F_f & 1 & J_f \end{Bmatrix} \langle \beta_i \mathbb{J}_i \parallel \mathbb{O}^{(E1, \text{absorption})} \parallel \beta_f \mathbb{J}_f \rangle \right|^2. \end{aligned}$$

Here, the summation runs over all fine-structure levels in the representation of the initial and final hyperfine levels. Moreover, interferences occurs if different terms in this summation are of similar size, and this may lead to a sizeable redistribution of the oscillator strengths from the different fine-structure transitions, which can be formed between selected fine-structure levels in the ASF representations above.

7.2.d. Sensitivity of level energies with regard to variations of α (AlphaVariation)

Properties, notations & application (not yet fully implemented):

- Differential sensitivity parameter $\Delta q(\delta\alpha; \beta\mathbb{J})$ of an atomic level: For an atomic level $(\beta\mathbb{J})$, the level energy depends of course on the fine-structure constant α . Therefore, an energy shift arises for any variation $\delta\alpha = \alpha - \alpha_o$ of the fine-structure constant and for a non-zero differential sensitivity parameter $\Delta q(\delta\alpha; \beta\mathbb{J})$:

$$\Delta E(\delta\alpha; \beta\mathbb{J}) = \Delta q(\delta\alpha; \beta\mathbb{J}) \left[\left(\frac{\alpha}{\alpha_o} \right)^2 - 1 \right],$$

and where α_o is the (current) reference value of the fine-structure constant.

- Formal quantum notation: $\Delta E(\delta\alpha; \beta\mathbb{J})$, $\Delta q(\delta\alpha; \beta\mathbb{J})$, $K(\beta\mathbb{J})$.
- Using JAC: Perform an `Atomic.Computation(.., properties=[AlphaVar, ..], configs=[..], alphaSettings=AlphaVariation.Settings(..), ..)` or call directly functions from the module `AlphaVariation`.
- In JAC, we calculate and tabulate by default the differential sensitivity parameter $\Delta q(\delta\alpha; \beta\mathbb{J})$ and the enhancement factor $K(\beta\mathbb{J})$ for all selected levels.

Further remarks:

- Fine-structure constant α : The dimensionless constant α becomes dynamical, i.e. explicitly time-dependent, in a number of (quantum-field) theories that go beyond the standard model and general relativity.
- Search for variations of fundamental constants: This search is closely related to several, so-far still unexplained phenomena of the Universe, such as the nature of dark matter.
- From the individual level-dependent sensitivity parameters $\Delta q(\delta\alpha; \beta\mathbb{J})$ and enhancement factors $K(\beta\mathbb{J})$, the analogue values for any atomic transition can be simply obtained by taking the sum of the corresponding level parameters.
- Experimentally, a variation of α are currently measured by monitoring for two ions the ratio of (two) clock frequencies with quite different values of K .

- **Current limits on the time variation of α :** Currently, the best laboratory limit of $\dot{\alpha}$ was obtained from a comparison of the frequency ratio $\text{Al}^+ / \text{Hg}^+$ over the course of *one* year. This ratio is sensitive to variations in α because these two optical transitions have quite different sensitivity coefficients with regard to time-variations in the ‘current’ value of the fine-structure constant α_o (Berengut *et al.*, 2012)

$$q = \frac{d\omega}{dx} |_{x=0}, \quad x = \frac{\alpha^2}{\alpha_o^2} - 1,$$

- **Limits on the time variation of α :** Various proposals have been made in the literature to limit the time variations of α more tightly, provided that the frequency ratio can be measured with similar accuracy as for $\text{Al}^+ / \text{Hg}^+$ clock transitions. This is possible for clock transitions with a much higher sensitivity q , as expected for the optical transitions of the Tl^+ clock, for multiply-charged Te, Po, and Ce ions as well as for the ^{229}Th nuclear clock, which all have a rather large sensitivity to the variation of α .

Enhancement and sensitivity of atomic levels with regard to variations of $\delta\alpha$:

- **Enhancement of energy shifts due to $\delta\alpha$ variations:** The sensitivity of an atomic level energy $E(\beta\mathbb{J}; \alpha)$ on $\delta\alpha$ can be re-written also in terms of the dimensionless enhancement factor $K = 2\Delta q/\Delta E$ as:

$$\frac{E(\beta\mathbb{J}; \alpha) - E(\beta\mathbb{J}; \alpha_o)}{E(\beta\mathbb{J}; \alpha_o)} = K \frac{\alpha - \alpha_o}{\alpha_o} = K \frac{\delta\alpha}{\alpha_o}$$

- The reasons for $\delta\alpha$ variations can be of different type, such as temporal, spatial, slow drift, or of oscillatory nature, and it can depend on the gravity-potential or others reasons. The theoretical reasoning about such changes is typically outside of atomic theory.

7.3. Further properties, not yet considered in JAC

7.3.a. Information measures for quantum states

Information measures:

- **Information measures for quantum states:** Several information measures have been suggested and explored for atomic states (levels), including those by Shannon and Fisher. They are sometimes considered as additional atomic properties with applications in quantum information and technology. For hydrogenic ions and states, many of these information measures can be evaluated analytically with — both, nonrelativistic and relativistic — position-space wave functions, whereas this is not so easily done with momentum-space wave functions (Katriel and Sen, 2010).
- **Shannon information entropy:** The Shannon entropies present global information measures for any probability distribution as obtained in different representations. A well-localized distribution results into a small information entropy, whereas de-localized distributions have larger entropies.
- **Shannon information entropy S :** For a bound system with electronic density $\rho(\mathbf{r})$ and momentum density $\pi(\mathbf{p})$, the Shannon information entropy in position and momentum space is given by

$$S^{(position)} = - \int d^3\mathbf{r} \rho(\mathbf{r}) \ln [\rho(\mathbf{r})], \quad S^{(momentum)} = - \int d^3\mathbf{p} \pi(\mathbf{p}) \ln [\pi(\mathbf{p})],$$

and where both densities, $\rho(\mathbf{r})$ and $\pi(\mathbf{p})$, are assumed to be normalized to unity.

- **Renyi entropy:** The Renyi entropy is a generalization of the Shannon entropy and is usually defined in position space (Katriel and Sen, 2010)

$$H_a^{(\text{Renyi})} = \frac{1}{1-a} \log \left(\int_0^\infty dr 4\pi r^2 [\rho(r)]^a \right)$$

$$a = \frac{1}{1-s}, \quad b = \frac{1}{1+s}, \quad -1 \leq s \leq 1.$$

The detailed definition and use of this Renyi entropy in physics is however still unclear.

- **Information measures:** A number of information-theoretic measures have been proposed to characterize the three-dimensional geometry of bound systems by means of their nonrelativistic wave functions. These measures include the Shannon, Renyi and Tsallis entropies, the Fisher information as well as measures for the non-uniformity of the electron density.

7.3.b. Electron localization function (ELF)

Remarks & notations:

- **Electron localization function (ELF):** Becke and Edgecombe (1990) derived a simple *localization function* in order to reveal the atomic shell structure as well as the core, binding and lone electron pairs in simple molecules. This localization function is an orbital-independent measure and based on the Hartree-Fock pair probability. Such a concept of localized electron groups is quite different from the typically delocalized Hartree-Fock orbitals; it supports a descriptive chemistry and may thus help identify and distinguish, for instance, between σ - and π -electrons systems.
- **Localization versus Hartree-Fock theory:** The canonical HF orbitals can be transformed unitarily due to different prescriptions and by leaving the total HF energy unchanged. However, these transformations are generally not unique and can even result in qualitatively different ‘bondings’ of the electrons. In fact, Hartree-Fock theory is defined by its single-electron density matrices, which are invariant with regard to unitary orbital transformations. Therefore, any meaningful definition of electron localization must be sought in the (two-electron) density matrix itself and not in the orbitals (Becke and Edgecombe, 1990).
- **Electron localization function (ELF):** The ELF depends on the total electronic density, its gradient as well as the kinetic energy density. For all noble gases, this function completely reveals their expected shell structure. The ELF is closely related also to density-functional theory which asserts the total electronic density as the fundamental variable of many-electron theory. Moreover, since the probability density ρ_σ is nonnegative, it can be shown that the spherically-averaged pair probability D_σ must vanish for one-electron systems as well as in multi-electron systems that is dominated by a single, localized spin orbital.
- **Electron localization function (ELF):** Becke and Edgecombe (1990) propose a localization function in terms of the spherically-averaged pair probability D_σ and an analogue density D_σ^o of a uniform electron gas with a spin density equal to the local value of $\rho_\sigma(\mathbf{r})$

$$\text{ELF} = \left[1 + \left(\frac{D_\sigma}{D_\sigma^o} \right)^2 \right]^{-1}, \quad D_\sigma^o = \frac{3}{5} (6\pi^2)^{2/3} \rho_\sigma^{5/3}, \quad 0 \leq \text{ELF} \leq 1.$$

7. Atomic properties

Of course, the ratio D_σ / D_σ^o refers to a dimension-less localization index that is calibrated with regard to the uniform-density electron gas. Here, the upper limit $\text{ELF} = 1$ correspond to a perfect localization, while a value $\text{ELF} = 1/2$ refers to a electron-gas like pair probability.

- **Electron localization function (ELF):** In (quantum) chemistry, the ELF has been found a valuable alternative in the description and interpretation of chemical bindings.

7.3.c. Stark shifts and (dc) ionization rates in static electric fields

Remarks & notations:

- **Stark shift:** The Stark shift of an atomic level generally refers to the change of its level energy in an external electric field. Apart from the dc Stark shift in static fields, the frequency-dependent (ac) Stark shift in a monochromatic light field has attracted much recent attention. The dc Stark shift was first observed by Stark in 1913, and detailed measurements were restricted indeed for a rather long time (until $\sim 1960s$) to such static electric fields. The frequency-dependent (ac) Stark shift due to laser irradiation was first observed by Bonch-Bruevich and coworkers in 1969.
- **Static (dc) Stark shift:** When an atom or molecule is exposed to a (constant) external electric field $\mathcal{E} \neq \mathcal{E}(t)$, its discrete level spectrum turns into a **spectrum of resonances with complex energies**. These energies are the eigenvalues of a non-Hermitian Hamiltonian (Schrödinger equation), and whose eigenfunctions are asymptotically outgoing-waves. The shift and broadening of the (discrete) bound energies are also known as **LoSurdo-Stark effect** (Nicolaides and Themelis, 1992).
- **Static (dc, electric-dipole) Stark Shift:** An atom in the level (αJM) in a homogeneous static (dc) electric-dipole field $\mathcal{E} = \mathcal{E} \mathbf{e}_z$ experiences a shift due to the coupling to the induced electric-dipole moment

$$\Delta E^{(\text{dc Stark})}(\mathcal{E}; \alpha JM) \propto -\frac{1}{2} \alpha^{(\text{static})}(\alpha JM) \mathcal{E}^2 = -\frac{1}{2} \alpha^{(\text{ac E1})}(\omega = 0; \alpha JM) \mathcal{E}^2,$$

and which is **quadratic in the electric field**. Here, $\alpha^{(\text{static})}(\alpha J)$ is also called the **static electric-dipole polarizability**. Similarly, for an atom in the hyperfine level $(\alpha(IJ)\mathbb{F})$, the static (dc) Stark Shift is quadratic

$$\Delta E^{(\text{dc Stark})}(\mathcal{E}; \alpha \mathbb{F}) \propto -\frac{1}{2} \alpha^{(\text{ac E1})}(\omega = 0; \alpha \mathbb{F}) \mathcal{E}^2,$$

and is often briefly referred to as **quadratic Stark shift**.

- **Static (dc) Stark shift:** In a static external electric field $\mathbf{E} \parallel \mathbf{e}_z$, a degenerate level $|\alpha\mathbb{J}\rangle$ with energy E_o generally splits into $(2J+1)$ states

$$E(\mathcal{E}; \alpha\mathbb{J}) = E_o + \Delta E^{(\text{dc Stark})}(\mathcal{E}; \alpha\mathbb{J}M)$$

since each magnetic sublevel may acquire a different energy shift $\Delta E^{(\text{dc Stark})}(\mathcal{E}; \alpha\mathbb{J}_o M)$. These shifts are quite small as all field strengths in the laboratory are typically small when compared to the atomic fields. Typical (dc) Stark shifts do not exceed 1 Kayser = 1/cm, although these shifts can be much larger ($\sim 10^2 \dots 10^4$) than most natural line widths.

- **Perturbation expansions of the static (dc) Stark shift:** Since, even for an arbitrarily weak dc field, all atomic states become unstable with regard to *ionization*, **all perturbation (series) expansions are divergent**. In these expansions, in fact, the first terms in the series often decrease before they start to diverge; therefore, a summation should be done only up to the smallest term. At least for (non-relativistic) hydrogenic atoms, dc Stark shifts calculations are fairly well understood and are in good agreement with experiment, cf. Delone and Krainov (1999).
- **Static electric-quadrupole (dc) Stark shift & electric-quadrupole Hamiltonian:** A gradient of a static (external) electric field \mathbf{E} interacts of course with the (induced) quadrupole moment of the atom and gives rise to a static electric-quadrupole (dc) Stark shift. This interaction can be described by the Hamiltonian

$$\mathbb{H}^{(\text{dc EQM})} = (\nabla \mathcal{E})^{(2)} \cdot Q^{(2)} = \sum_{q=-2}^2 (-1)^q (\nabla \mathcal{E})_q^{(2)} Q_{-q}^{(2)},$$

where $(\nabla \mathcal{E})^{(2)}$ is the vector gradient at the position of the atom (a second-rank tensor) and $Q^{(2)}$ the quadrupole tensor of the atom. In the frame of the principal axis of the induced charge distribution (quadrupole tensor), the Hamiltonian $\mathbb{H}^{(\text{dc EQM})}$ can be expressed in terms of just three spherical tensor components $Q_2^{(2)}, Q_0^{(2)}, Q_{-2}^{(2)}$ or, equivalently, **two real parameters which characterize the strength and asymmetry of the field gradient**. The **static electric-quadrupole (dc) Stark shift**, or briefly electric-quadrupole shift, of an atomic fine-structure level $|\alpha\mathbb{J}M\rangle$ or hyperfine level $|\alpha(IJ)\mathbb{F}M\rangle$ is then obtained by

$$\langle \alpha\mathbb{J}M | \mathbb{H}^{(\text{dc EQM})} | \alpha\mathbb{J}M \rangle, \quad \langle \alpha(IJ)\mathbb{F}M | \mathbb{H}^{(\text{dc EQM})} | \alpha(IJ)\mathbb{F}M \rangle,$$

and can be really expressed in terms of the strength and asymmetry parameters of the Hamiltonian, the Euler angles to convert the principal-axis into the laboratory frame (that defines the quantization axis) as well as the reduced matrix elements $\langle \alpha\mathbb{J} \parallel Q^{(2)} \parallel \alpha\mathbb{J} \rangle$ of the quadrupole tensor with regard to the level of interest.

7. Atomic properties

- **Static (dc) Stark shift measurements:** In the laboratory, static electric fields are often limited to $\lesssim 10^5$ V/cm and, hence, are much smaller than the inner-atomic fields $\sim 10^9$ V/cm. Therefore, almost all (dc) Stark shifts refer to rather small corrections to the level energies and can be readily calculated perturbatively, if these corrections are considered at all in applications.
- **Relation between static (dc) and frequency-dependent (ac) polarizabilities:** The static (dc) and frequency-dependent (ac) — scalar, vector and tensor — polarizabilities are usually related to each other by the simple replacement

$$\frac{1}{\Delta E} \quad \longleftrightarrow \quad \frac{\Delta E}{(\Delta E)^2 - \omega^2}.$$

- **Static (dc) Stark shift *versus* ionization:** If the dc electric field is weak, when compared with the atomic field seen by the electrons, the **ionization width** (imaginary part of the total energy) is much smaller than the quadratic (dc) Stark shift. For such weak fields, therefore, a well-defined (dc) Stark shift is observed for all level energies. However, such a distinct (dc) Stark shift is no longer true if the dc field becomes comparable to field of the valence electrons, and which then leads to a rapid ionization. For hydrogenic ions with energy $E_n = Z^2/n^2$, the dc electric field become in a 1D ionization model equal to the Coulomb field for

$$\mathcal{E}(n) = \frac{E_n^2}{4Z} = \frac{Z^3}{16n^4}.$$

More generally, however, this critical field strength depends on both, n and ℓ , in a more rigorous numerical treatment (for instance, in parabolic coordinates).

- **Static Stark effect:** For a static and homogeneous electric field \mathcal{E}_o , a Rydberg level $(n\ell)$ splits by the linear Stark effect into $2n - 1$ equi-spaced sublevels with energy shifts

$$\Delta E_{n_1 n_2 m} = \frac{3}{2} n (n_1 - n_2) \frac{e a_o \mathcal{E}_o}{Z}, \quad n = n_1 + n_2 + |m| + 1,$$

and where n_1, n_2, m are the parabolic quantum numbers.

Neutral atoms in static (dc) fields:

- **Complex-eigenvalue Schrödinger equation:** The system "neutral atom + static (dc) field" defines a rather complicated many-electron problem. Because of the (additional) time-independent field, the discrete spectrum of the atom changes into a resonance spectrum whose

states are obtained as solutions of a complex-eigenvalue Schrödinger equation

$$(H - z_o) \psi = 0, \quad H = H^{(\text{atom})} + \sum_i \mathcal{E} \cdot \mathbf{r}_i, \quad z_o = E_o + \Delta(\mathcal{E}) - \frac{i}{2} \Gamma(\mathcal{E}).$$

- **Solution of the complex eigenvalue equation:** This equation can be solved in terms of square-integrable function spaces, if the transformation $\rho = r e^{i\theta}$ is applied.
- This coordinate rotation for ρ has been applied to the Hamiltonian operators for the computation of the LoSurdo-Stark ground-state resonance of hydrogen atoms, and the solution was achieved by **direct diagonalization of the non-Hermitian Hamiltonian on a large square-integrable basis set**. However, such a direct diagonalization of the non-Hermitian Hamiltonian matrix is quite unrealistic for the decaying states of many-electron atoms and molecules.

Static (dc) Stark shifts for hydrogenic ions:

- **Static (dc) Stark shift for hydrogenic ions:** For non-relativistic hydrogenic ions, the quadratic (second-order, dc) Stark shift can be evaluated analytically in terms of the principal and orbital quantum numbers and are given by Delone and Krainov (1999) as

$$\begin{aligned} \Delta E^{(\text{dc Stark})}(\mathcal{E}; n\ell m) &= -\frac{1}{2} \left[\alpha^{(\text{scalar})}(n\ell) + \alpha^{(\text{tensor})}(n\ell) \frac{3m^2 - j(j+1)}{j(2j-1)} \right] \\ \alpha^{(\text{scalar})}(n\ell) &= n^6 + \frac{7}{4} n^4 (\ell^2 + \ell + 2) \text{ a.u.}, \quad \alpha^{(\text{tensor})}(n\ell) = -\frac{1}{4/2\ell + 3} n^4 (3n^2 + 11\ell^2 + 11\ell - 9) \text{ a.u.} \end{aligned}$$

Both, the scalar and tensor parts of the polarizabilities are of the same order, although the tensor part vanishes for $\ell = 0$.

7.3.d. Frequency-dependent (ac) Stark shifts (AcStarkShift)

Remarks & notations:

- **Frequency-dependent (ac) Stark shift:** The **frequency-dependent, dynamic Stark shift** is caused by the interaction of an atom with the electro-magnetic field; it can be induced by a laser pulses but also by a single-photon wave packet.

7. Atomic properties

- (ac) Stark shifts: An intense light field also shifts the energy levels of the atom. In a time-harmonic laser field, **these frequency-dependent (ac) Stark shifts generally depend on the frequency, intensity and polarization of the incident light as well as the atomic levels of interest.**
- Role of frequency-dependent (ac) Stark shifts: Modern laser fields readily become comparable or even exceed the atomic field strength $\sim 10^9 \text{ V/cm}$. Therefore, the interaction with such lasers often leads to remarkable changes in the separation and sequence of levels and also requires to develop non-perturbative computational methods. Even for quite large (ac) Stark shifts, however, the level broadening often remains moderate and keeps the concept of atomic levels in many experiments alive.
- Static (dc) *versus* frequency-dependent (ac) Stark shifts: In general, the dc and ac Stark shifts of atomic levels differ quite drastically from each other. While a weak static field simply shifts the energy levels, (1) a time-harmonic (ac) field also splits even non-degenerate states into (quasi-) energy states that are shifted with regard to the unperturbed level and that are separated by the frequency of the light field (formation of side bands). Despite of these shifts, however, (2) some atomic transitions frequencies are apparently not shifted for a certain frequency and intensity of the incident light; these (so-called) **magic wavelength** (frequencies) usually occur for different pairs of hyperfine levels of an atomic bound-state transitions. (3) For short few-cycle pulses, both the concept of quasi-energy levels (sidebands) as well as a well-defined (ac) Stark shifts gets lost.
- Frequency-dependent (ac) Stark shift of atomic levels: For time-harmonic electro-magnetic fields with well-defined frequency ω and field strength \mathcal{E} , each atomic level is shifted by the (ac) Stark shift $\Delta E^{(\text{acStark})}(\omega; \alpha JM)$ to its **quasi-energy** and is accompanied by a **spectrum of quasi-harmonics, $E^{(\text{quasi-energy})} \pm k\omega$ (sidebands)**. Of course, this frequency-dependent (ac) Stark shift and the strength of the sidebands depend on the strength and frequency of the incident field. Therefore, there is a clear difference in the level structure of atoms for a static and time-harmonic electric field.
- Frequency-dependent (ac) Stark shift of atoms in weak, high-frequency fields: At high laser frequencies, e.g. for $\hbar\omega \gg \Delta E_{\nu,\nu'}$ much larger than the separation energy to neighboured atomic states, only one quasi-harmonic ($k = 0$) can be excited, and this simply leads to the observed (ac) Stark shift $\Delta E^{(\text{acStark})}(\omega; \alpha JM)$ of atomic levels. To a very good approximation, this frequency-dependent (ac) Stark shift is proportional to the square of the field strength (amplitude), $\Delta E^{(\text{acStark})}(\omega; \alpha J) \propto \mathcal{E}^2$ and is equal also to the (classical vibrational) energy of a free electron for a harmonic and linearly-polarized electric field, $E^{(\text{vibration})} = \mathcal{E}^2/(4\omega^2)$. **For such weak, high-frequency fields, indeed, the atomic level structure is similar to a static (dc) field.** In such a weak field, moreover, most atoms experience a negative shift of their ground state energy, i.e. the ionization potential slightly increases or, in other words, the atoms are slightly stronger bound in a weak, high-frequency fields.
- (ac) Stark shifts in intense laser fields: The concept of well-defined (ac Stark) level shifts, however, get lost – more or less completely, when the oscillation amplitude of a (free) electron in a laser field, $a = \mathcal{E}/\omega$, becomes comparable or even larger than the size of the atom. For such fields, the known level structure of the atom breaks down and the **electron dynamics must be described by methods from strong-field**

theory, such as the strong-field approximation. While this strong-field regime is nowadays easily reached for low, infrared laser frequencies, much less is known about this breakdown for optical frequencies and moderate-to-high laser intensities.

- **Magic wavelength:** In atom trapping, this concepts refers to the search and use of a laser (field) with proper frequency and intensity, for which the ground and excited state of the trapped atom experience an equal frequency-dependent (ac) Stark shift. Such a laser then leaves the atomic transition basically unaffected. Obviously, such a **magic wavelength requires a proper choice of the frequency and intensity of the laser as well as a proper pair of magnetic sub-levels of the atom.**
- **Magic wavelength:** The ac Stark shift of a clock transition is mainly determined by the frequency-dependent (ac electric-dipole) polarizabilities of the clock states. The (so-called) **magic wavelengths** of a clock transition can be determined by finding the frequencies where the (ac E1) polarizabilities of the two clocks states are the same.
- **Trapping of atoms:** For atom trapping, **far-off resonant laser fields are often applied** in order to ensure low scattering rates and, hence, rather long coherence times.
- **Application of frequency-dependent (ac) Stark shifts:** These shifts are required to efficiently encode, process and store quantum information in atomic systems by using resonant or near-resonant light. Since neutral atoms only weakly couple to their environments, the coherent manipulation of atomic states might be robust enough against external perturbations. In the past, however, most previous computations were performed only for static (dc) Stark shifts.
- **Importance of the frequency-dependent (ac) Stark shift for ionization processes:** The frequency-dependent (ac) Stark shift is relevant for different research fields in physics and beyond because of: (1) an increase of the ionization potential of *dressed* atoms, that may become comparable or even exceed the photon energy (of the external field) and that may strongly affect the tunnel ionization behaviour and rate; (2) the modified threshold intensity (barrier suppression) at which all atoms are basically ionized, although this ionization is often achieved already at the front of the laser pulse.

Ionization regimes in time-varying electro-magnetic fields:

- Keldish adiabacity parameter γ_K : Different strong-field ionization mechanisms can be distinguished for different laser frequencies ω_L , (electric) field strength $\mathcal{E}_o = |\mathcal{E}_o|$ as well as atomic ionization potentials I_p . They are often distinguished by the **Keldish adiabacity parameter**, $\gamma_K = \omega \sqrt{2I_p}/\mathcal{E}_o$.
- Multiphoton regime, $\gamma_K \gg 1$: This regime is realized at high laser frequency and low or moderate field strength, and it gives rise to a power law for the ionization rate, $\Gamma \propto \mathcal{E}_o^n$.
- Tunnel regime, $\gamma_K \ll 1$: This regime occurs at low laser frequency and a high-field strength, and it gives rise to an **exponential dependence of Γ on \mathcal{E}_o** . In the tunnel regime, the ionization is often considered as a quasi-static process due to the low frequency, and the total ionization yield is obtained as **integral over the time-dependent field strength**:

$$A = 1 - \exp \left[1 - \int_{-\infty}^{\infty} dt \Gamma(\mathcal{E}_o(t)) \right].$$

- **Atomic structure computations:** In the tunnel regime, atomic structure computation can provide reliable predictions for both, the Stark shifts in an (quasi-static) electric field as well as for the ionization rates.
- **Ammosov-Delone-Krainov (ADK) formula:** This formula for the ionization rate has often been used for many-electron atoms and has been extended also towards molecules.
- **Quasi-static regime:** For $\gamma_K \ll 1$, one often further distinguishes between the **tunnel ionization** and the **above-barrier ionization** due to the **(semi-classical) field strength** $\mathcal{E}^{(\text{above-barrier})} = I_p^2/4$. From a simplified classical viewpoint, the electron can leave the atom without tunneling for $\mathcal{E}_o > E^{(\text{above-barrier})}$ owing to the suppression of the (atomic) Coulomb potential. In practice, however, this *barrier* is not sharp since an (scattered) outgoing electron is still partly reflected even for a classical suppressed barrier.
- **(Quasi-) Static ionization rates:** Within the tunneling regime, a variety of semiempirical expressions exist for the static ionization rates $\Gamma(\mathcal{E}_o)$. Many of them are based on Landau's seminal formula for the ionization rate of the hydrogen atom in its ground state, such as the ADK rule.
- **Limitations of the ADK rate:** A more rigorous treatment of the static ionization rates is often preferable, since the ADK and similar formulas neglect both, the exchange interaction and correlation effects, and **rather little is known so far how well these semi-empirical formulas work quantitatively**.

Computation of second-order (ac) Stark shifts:

- Perturbation expansions for the frequency-dependent (ac) Stark shift: Most often, the frequency-dependent (ac) Stark shift of a level ($\alpha\mathbb{J}$) with energy E_o is described in second-order perturbation theory and within the electric-dipole approximation due to the absorption and re-emission of a laser photon. A necessary condition for such a perturbative treatment can be given in terms of the laser frequency ω , the field strength \mathcal{E} , the energy separation $|E_o - E_\nu|$ from neighboured levels ($\alpha_\nu\mathbb{J}_\nu$) as well as the associated dipole matrix elements $\langle \alpha_\nu\mathbb{J}_\nu | \mathbb{D} | \alpha\mathbb{J} \rangle$

$$|\langle \alpha_\nu\mathbb{J}_\nu | \mathbb{D} | \alpha\mathbb{J} \rangle | \mathcal{E} \ll |\omega - \omega_{nm}|, \quad \iff \quad \begin{cases} |\langle \alpha_\nu\mathbb{J}_\nu | \mathbb{D} | \alpha\mathbb{J} \rangle | \mathcal{E} \ll \omega \\ |\langle \alpha_\nu\mathbb{J}_\nu | \mathbb{D} | \alpha\mathbb{J} \rangle | \mathcal{E} \ll |E_o - E_\nu|. \end{cases} \quad \text{or}$$

Obviously, the perturbation by the field (with strength \mathcal{E}) must neither exceed the laser frequency nor the energy separation to neighboured levels.

- Second-order (ac) Stark shift of a non-degenerate atomic state $|\alpha\mathbb{J}M\rangle$: For a light field $\mathbf{E}(t) = \mathcal{E} \mathbf{u}(t)$ with \mathcal{E} = (complex) constant far from resonance, the second-order (ac) Stark shift of a level $|\alpha\mathbb{J}M\rangle$ with energy E_o is given in electric-dipole approximation by

$$\Delta E^{(\text{ac Stark})}(\omega; \alpha_o\mathbb{J}_o M_o) = -\frac{|\mathcal{E}|^2}{4} \sum_\nu \Re \left(\frac{|\langle \alpha_\nu\mathbb{J}_\nu M_\nu | \mathbf{u} \cdot \mathbb{D} | \alpha\mathbb{J}M \rangle|^2}{E_\nu - E_o - \omega - i\Gamma_{\nu o}/2} + \frac{|\langle \alpha\mathbb{J}M | \mathbf{u} \cdot \mathbb{D} | \alpha_\nu\mathbb{J}_\nu M_\nu \rangle|^2}{E_\nu - E_o + \omega + i\Gamma_{\nu o}/2} \right),$$

and where $\Gamma_{\nu o} = \Gamma_\nu + \Gamma_o$ is the sum of the spontaneous decay widths of these two levels. The states $|\alpha\mathbb{J}M\rangle$ and $|\alpha_\nu\mathbb{J}_\nu M_\nu\rangle$ here refer to the *unperturbed* states with energies E_o and E_ν , respectively. Here, the frequency-dependent (ac) Stark shift is given in the electric-dipole approximation due to the use of the dipole operator \mathbb{D} .

- Second-order (ac) Stark shift of a hyperfine state $|\alpha(IJ)\mathbb{F}M\rangle$: The (ac) Stark shift of a hyperfine state $|\alpha(IJ)\mathbb{F}M\rangle$ can be expressed in terms of the reduced tensorial (frequency-dependent, ac) polarizabilities as

$$\Delta E^{(\text{ac Stark})}(\omega; \alpha(IJ)\mathbb{F}M) = \frac{|\mathcal{E}|^2}{4} \sum_{K=0,1,2} (-1)^K [\mathbf{u}^* \otimes \mathbf{u}]_0^{(K)} (-1)^{F-M} \begin{pmatrix} F & K & F \\ -M & 0 & M \end{pmatrix} \alpha^{(K)}(\omega; \alpha(IJ)\mathbb{F}).$$

Here, the *scalar* (character of the) energy shift is ensured by the Wigner 3-j symbol which selects the $q = 0$ components of the three tensor products due to $-M + q + M = 0$. Moreover, the $\alpha^{(K)}$ are referred to also as reduced tensorial (ac) polarizabilities.

7. Atomic properties

- **Second-order (ac) Stark shift of hyperfine state $|\alpha(IJ)\mathbb{F}M\rangle$:** For a given geometry of the wave vector \mathbf{k} and polarization vectors as well as a given quantization axis (z -axis), the frequency-dependent (ac) Stark shift can be parametrized in terms of the (conventional) scalar, vector and tensor (frequency-dependent) polarizabilities of a given hyperfine level $(\alpha(IJ)\mathbb{F})$

$$\begin{aligned}\Delta E^{(\text{ac Stark})}(\omega; \alpha(IJ)\mathbb{F}M) &= \frac{\mathcal{E}^2}{4} \left[\alpha^{(\text{scalar})}(\alpha(IJ_o)\mathbb{F}) + P_3 \cos \vartheta_k \frac{M}{2F} \alpha^{(\text{vector})}(\omega; \alpha(IJ)\mathbb{F}) \right. \\ &\quad \left. + \left(\frac{3 \cos^2 \vartheta_p - 1}{2} \right) \frac{3M^2 - F(F+1)}{F(2F-1)} \alpha^{(\text{tensor})}(\omega; \alpha(IJ)\mathbb{F}) \right] \\ &= \frac{\mathcal{E}^2}{4} \alpha^{(\text{ac E1})}(\omega; \alpha(IJ)\mathbb{F}M) \\ \alpha^{(\text{ac E1})}(\omega; \alpha(IJ)\mathbb{F}M) &= \alpha^{(\text{scalar})}(\omega; \alpha(IJ)\mathbb{F}) + P_3 \cos \vartheta_k \frac{M}{2F} \alpha^{(\text{vector})}(\omega; \alpha(IJ)\mathbb{F}) \\ &\quad + \left(\frac{3 \cos^2 \vartheta_p - 1}{2} \right) \frac{3M^2 - F(F+1)}{F(2F-1)} \alpha^{(\text{tensor})}(\omega; \alpha(IJ)\mathbb{F}).\end{aligned}$$

However, these expressions only apply if J is a good quantum number for the hyperfine levels under consideration. The same relation remains valid, if the scalar, vector and tensor polarizabilities contains 3rd and higher-order contributions in the perturbative treatment of the (ac) Stark shift, for instance, due to the hyperfine interaction to the polarizabilities, cf section 7.3.f.

- **Frequency-dependent (ac) clock shift:** For a clock (absorption) transition $\alpha_i F_i M_i \rightarrow \alpha_f F_f M_f$ between two hyperfine magnetic substates, the total (frequency-dependent, ac) Stark shift is simply the difference of the individual shifts and is given by

$$\Delta \nu = \frac{1}{\pi} [\Delta E^{(\text{ac Stark})}(\omega; \alpha_f F_f M_f) - \Delta E^{(\text{ac Stark})}(\omega; \alpha_i F_i M_i)] = \frac{1}{\pi} \frac{|\mathcal{E}|^2}{4} [\alpha^{(\text{ac E1})}(\omega; \alpha_f \mathbb{F}_f M_f) - \alpha^{(\text{ac E1})}(\omega; \alpha_i \mathbb{F}_i M_i)]$$

- **Comparison of polarizabilities & (ac) Stark shifts:** Since both, the frequency-dependent polarizabilities & (ac) Stark shifts depend on the fine-structure level or hyperfine levels as well as the frequency and polarization of the incident light, great care has to be taken to compare such data from the literature. In many numerical computations, moreover, the resonance wavelengths and reduced matrix elements are often taken from different sources. Missing information about the underlying formalism as well as the application of semi-empirical data often hamper a direct comparison of the underlying polarizabilities.

(ac) Stark shift Hamiltonian:

- Second-order (ac) Hamiltonian shift operator in electric-dipole approximation: The (ac) Stark shift of a non-degenerate atomic state $|\alpha JM\rangle$ with unperturbed energy E_o can be expressed also as expectation value of an (ac) Stark shift Hamiltonian

$$\begin{aligned} \mathbb{H}^{(\text{ac Stark})} &= \frac{|\mathcal{E}|^2}{4} [(\mathbf{u}^* \cdot \mathbf{opD}) \mathbb{R}_+ (\mathbf{u} \cdot \mathbb{D}) + (\mathbf{u} \cdot \mathbb{D}) \mathbb{R}_- (\mathbf{u}^* \cdot \mathbb{D})], & \Delta E^{(\text{ac Stark})}(\omega, \alpha JM) &= \langle \alpha JM | \mathbb{H}^{(\text{ac Stark})} | \alpha JM \rangle \\ \mathbb{R}_+ &= - \sum_{\nu} \Re \left(\frac{1}{E_{\nu} - E_o - \omega - i\Gamma_{\nu o}/2} \right) |\alpha_{\nu} JM_{\nu}\rangle \langle \alpha_{\nu} JM_{\nu}| \\ \mathbb{R}_- &= - \sum_{\nu} \Re \left(\frac{1}{E_{\nu} - E_o + \omega + i\Gamma_{\nu o}/2} \right) |\alpha_{\nu} JM_{\nu}\rangle \langle \alpha_{\nu} JM_{\nu}|. \end{aligned}$$

Although this (ac) Stark shift Hamiltonian is adopted from the shift of a nondegenerate level, it is often assumed that $\mathbb{H}^{(\text{ac Stark})}$ can be applied generally, i.e. for degenerate levels as well as for the interaction among nondegenerate and degenerate levels. This assumption is consistent with the expression that is obtained in second-order perturbation theory with the perturbation $\mathbb{H}^{(\text{E1})}$ for the electric-field interaction.

- Relation between reduced tensorial and conventional tensorial polarizabilities: The diagonal matrix elements of $\mathbb{H}^{(\text{ac Stark})}$ of a given fine-structure level (αJ) can be expressed also in terms of the (cartesian) vector products of the polarization and total angular momentum operators as well as the *conventional frequency-dependent scalar, vector and tensor polarizabilites* of the given fine-structure level by (cf. Kien *et al.*, 2013)

$$\begin{aligned} &\langle \alpha J | \mathbb{H}^{(\text{ac Stark})} | \alpha J \rangle \\ &= \frac{|\mathcal{E}|^2}{4} \left(\alpha^{(\text{scalar})}(\omega; \alpha J) - i \alpha^{(\text{vector})}(\omega; \alpha J) \frac{[\mathbf{u}^* \times \mathbf{u}] \cdot \mathbf{J}}{2J} + \alpha^{(\text{tensor})}(\omega; \alpha J) \frac{3[(\mathbf{u}^* \cdot \mathbf{J})(\mathbf{u} \cdot \mathbf{J}) + (\mathbf{u} \cdot \mathbf{J})(\mathbf{u}^* \cdot \mathbf{J}) - 2\mathbf{J}^2]}{2J(2J-1)} \right) \end{aligned}$$

7. Atomic properties

$$\begin{aligned}\alpha^{(\text{scalar})}(\omega; \alpha\mathbb{J}) &= \frac{1}{\sqrt{3(2J+1)}} \alpha^{(0)}(\omega; \alpha\mathbb{J}), & \alpha^{(\text{vector})}(\omega; \alpha\mathbb{J}) &= -\sqrt{\frac{2J}{(J+1)(2J+1)}} \alpha^{(1)}(\omega; \alpha\mathbb{J}) \\ \alpha^{(\text{tensor})}(\omega; \alpha\mathbb{J}) &= \sqrt{\frac{2J(2J-1)}{3(J+1)(2J+1)(2J+3)}} \alpha^{(2)}(\omega; \alpha\mathbb{J}).\end{aligned}$$

Here, the $\alpha^{(K)}(\omega; \alpha\mathbb{J})$ are referred to as the reduced tensorial polarizability of the fine-structure level $(\alpha\mathbb{J})$.

- **Combined hyperfine and (ac) Stark shift interaction:** For a non-zero nuclear spin I , each (fine-structure) state $|\alpha\mathbb{J}M\rangle$ is disturbed by both, the hyperfine interaction with the nucleus and the classical light field of the laser. This can be described perturbatively by the **combined interaction Hamiltonian**

$$\mathbb{H}^{(\text{hfs} + \text{Stark})} = \mathbb{H}^{(\text{hfs})} + \mathbb{H}^{(\text{ac Stark})},$$

and for which the Hamiltonian matrix can be calculated and diagonalized in the (unperturbed) hyperfine basis $\{|\alpha(IJ)FM_F\rangle\}$.

- **Matrix elements of $\mathbb{H}^{(\text{ac Stark})}$ in an (unperturbed) hyperfine basis:** In an (unperturbed) hyperfine basis $\{|\alpha FM\rangle \equiv |\alpha(IJ)FM\rangle\}$ of an electronic level $(\alpha\mathbb{J})$, these maxtrix elements are given by (Kien *et al.*, 2013)

$$\begin{aligned}&\langle \alpha FM | \mathbb{H}^{(\text{ac Stark})} | \alpha' F' M' \rangle \\ &= \frac{|\mathcal{E}|^2}{4} \sum_{K=0,1,2, q} [\alpha^{(K)}(\omega; \alpha\mathbb{J})] [\mathbf{u}^* \otimes \mathbf{u}]_q^{(K)} (-1)^{J+I+K+q-M} \sqrt{(2F+1)(2F'+1)} \begin{pmatrix} F & K & F' \\ M & q & -M' \end{pmatrix} \begin{Bmatrix} F & K & F' \\ J & I & J \end{Bmatrix},\end{aligned}$$

and where $\alpha^{(K)}(\omega; \alpha\mathbb{J})$ is refered to as the **reduced tensorial and frequency-dependent (or dynamical) polarizabilities of the atom in its fine-structure level $(\alpha\mathbb{J})$** . These tensorial polarizabilities comprise the reduced scalar ($K = 0$), vector ($K = 1$) and tensor ($K = 2$) polarizabilities, and these reduced polarizabilities also just represent the real parts of the complex polarizability. The corresponding **imaginary parts of the polarizability are related to the (Rayleigh) scattering rate** of an atom in its fine-structure level $(\alpha\mathbb{J})$.

- **Matrix elements of $\mathbb{H}^{(\text{hfs} + \text{Stark})}$ in an (unperturbed) hyperfine basis:** In general, $\mathbb{H}^{(\text{ac Stark})}$ is neither diagonal in F nor M . Therefore, the combined Hamiltonian $\mathbb{H}^{(\text{hfs} + \text{Stark})}$ need to be diagonalized in order to determine the eigenvectors and energies of an atom in a hyperfine basis. However, if the (ac) Stark shift of the (hyperfine) levels is small, when compared to the hyperfine splitting, one can neglect the mixing

with other hyperfine levels and just calculate the diagonal matrix element $\langle \alpha F M | \mathbb{H}^{(\text{ac Stark})} | \alpha F M \rangle$ to estimate this frequency-dependent (ac) Stark shift.

Rayleigh-Schrödinger expansion of ac-Stark shifted levels:

- **Atoms and ions in intense laser field:** The perturbative description of the ac Stark shift of atoms (atomic levels) in fields with intensity $I \gtrsim 10^{13} \text{ W/cm}^2$ has found continuous interest. For such fields, it is usually not sufficient to restrict the perturbation theory to second order.
- **Perturbative description of multiphoton ionization experiments:** Although, perturbation theory is often considered inadequate for the analysis of multiphoton ionization experiments with atoms and ions, rather little is still known about the breakdown of perturbation theory. Therefore, a perturbative treatment of the many-electron atom in intense fields is still of interest for various scenarios and intensities.
- **m -th order perturbation states of atoms + field:** For a given (electric-) field operator \mathcal{E} , the atom-field interaction is $V = \mathbf{r} \cdot \mathbf{E}$. The m -th order perturbed state of the overall system 'atom + field' is then a linear combination of product states with just $N - k$ photons (Pan *et al.*, 1988)

$$|\psi_m\rangle = \sum_{k=-m}^m |\phi_{m,k}(\mathbf{r})|N-k\rangle .$$

Here, N is the occupation number of the photon field and k runs in steps of 2.

7.3.e. Intensity-dependent quasi-energies and dressed (Floquet) states in slowly varying laser fields

Remarks & notations:

- **Dressed atomic states:** In a laser pulse of slowly varying intensity, the dressed atomic states follow adiabatically the temporal evolution of the intensity during the passage of the pulse. The slow variation of the intensity then results into fairly slow changes in the (coefficients of the) superposition of the dressed states when compared with the optical period of the laser.
- **Dressed atomic states:** The dressed states of atoms in an (ac) field of constant intensity and frequency refer to particular quasi-stationary solutions of the time-dependent Schrödinger equation.

7. Atomic properties

- **Quasi-stationary wave function of dressed states:** For sufficiently slow variations of the laser intensity, each dressed state can be written in the **Floquet form**, i.e. by means of a space-independent complex exponential *multiplied* by a time-harmonic function that oscillates with the same (optical) period as the incident field.
- **Floquet ansatz:** The Floquet ansatz generally enables one to adopt the (time-independent) **dressed-state approach to pulses with a sufficiently slowly varying field intensity**, and where the time-dependence is captured by slow changes in the coefficients of the superposition.
- **Floquet ansatz:** The Floquet ansatz and eigenvalue problem has been applied especially in order to calculate the quasi-energy spectrum of atomic hydrogen and of hydrogenic ions within the dipole approximation and by neglecting spontaneous decay.
- **Floquet ansatz:** This ansatz might not be suitable for long-range polarization potentials as well as for multi-electron systems (Potvliege, 1998).
- **Floquet equations:** If the incident field is expanded in terms of a Fourier series, the time-dependent Schrödinger equation can be decomposed and re-written as a system of time-independent equations, the (so-called) **Floquet equations**. For multi-photon ionization, this system should be solved together with the radiation (Siegert) boundary conditions.
- **Floquet equations:** The (complex) eigenvalues of the Floquet equations provide both, the **quasienergies of the dressed states and the resonance poles of the scattering amplitudes for laser-assisted scattering**.
- **Floquet approximation:** This approximation is typically adequate for infrared laser pulses as well as for atoms in either the ground or some Rydberg level. It has been found inappropriate for UV laser frequencies and for low-lying excited levels because of avoided crossings between the dressed levels and the large non-ponderomotive (ac) Stark shifts at such high frequencies.
- **Widths of quasi-energies:** The computation of the widths of quasi-energies often requires to go beyond first-order perturbation theory.
- **Moderately intense and time-varying laser pulses:** If the laser pulses are neither ultra-intense nor ultra-short, they can usually be modeled as a rapidly oscillating electric field, though with a well-defined and slowly varying envelope (field amplitude). For such quasi-constant ac-fields, the behaviour of atoms can be described in terms of **superpositions of dressed bound states that decay under the emission of photoelectrons**.

7.3.f. Atomic polarizabilities

Remarks & notations:

- **Atomic polarizabilities and hyperpolarizabilities:** The polarizability of an atom in level (αJ) generally describes its *response* to the radiation field in second-order perturbation theory, i.e. due to the absorption and re-emission of a laser photon. In contrast, the **hyperpolarizabilities refer to contributions from a perturbation expansion in third or higher order of the radiation field**. This counting of the number of ‘electron-field’ interactions need to be distinguished from these perturbation expansions in which either the hyperfine interaction and/or some magnetic field is incorporated, in addition to the radiation field in second order, and which are often also referred to as ‘third-order expansions’.
- **Frequency-dependent (ac) polarizabilities:** For a sufficiently weak time-harmonic (ac) electric field, the frequency-dependent (ac) polarizability of an atomic state $|\alpha JM\rangle$ also depends on the magnetic quantum number M , although just in a geometrical manner. This M -dependent part is associated with the (so-called) **vector and tensor polarizability**, while the **scalar polarizability** just refers to the atomic level (αJ) . The simple analytically form of the M -dependent components of the polarizabilities results of course from the (JM) symmetry of the unperturbed levels; the vector component vanishes for $J = 0$, and the tensor component for $J = 0, 1/2$. The vector polarizability is sometimes also referred to as **axial (asymmetric) polarizability** and arises for ac fields with a circularly-polarized (field) component. In general, the ratio of the scalar, vector and tensor polarizabilities are also frequency-dependent, and a detailed analysis often requires rather lengthy computations.
- **Frequency-dependent (ac E1) polarizability $\alpha^{(\text{ac E1})}(\omega)$:** The frequency-dependent (ac E1) polarizability describes the response of atoms or nanoobjects to an (external) electromagnetic disturbance, if this field is much weaker than the (internal) atomic field: $E \ll E^{(\text{atomic})} = m^2 e^5 / \hbar^4 \approx 5.14 \cdot 10^9 \text{ V/cm}$, and if the wavelength of the field is much larger than the size of the object (Astapenko 2013).
- **Methods for calculating atomic polarizabilities:** Three broad classes of methods have been used in the literature, in addition to various combinations of these methods: (1) *Ab-initio* calculations are typically based on the **summation over all relevant states of the (many-electron) spectrum**, and where each contribution is determined individually; (2) direct solution of some inhomogenous Schrödinger equation that include the frequency-dependent electric field in an effective manner into its inhomogeneous parts, and for which quite a number of different strategies were developed; (3) use of experimentally determined oscillator strengths together with estimates from class (1).
- **Precise computations of atomic polarizabilities:** For many-electron atoms, precise computations of atomic polarizabilities require at least a careful treatment of valence-valence correlations as well as the — direct or implicit — summation over the whole many-electron spectrum that can be reached by electric-dipole transitions. Here, core-valence and core-core correlations may also contribute quite significantly.

7. Atomic properties

- **Precise computations of atomic polarizabilities:** Valence-valence correlations are usually taken into account by the configuration interaction (CI) method, while core-valence and core-core correlations have been treated by a combined CI+MBPT method in order to construct an effective Hamiltonian for the CI computations in the valence space (Porsev *et al.* 2018).
- **Static *versus* dynamic polarizability:** While the (real) static polarizability characterizes the response of an atom to a constant electric field, the (complex) dynamic polarizability describes the response to an oscillating field and exhibits a rather strong frequency-dependence. The dynamic polarizability provides especially information about the resonance behavior of atoms and molecules. Moreover, the imaginary part describes the absorption and scattering of light, while the real part of the dynamic polarizability gives rise to Stark shifts, which are primarily utilized for constructing optical dipole traps in various geometries.
- **Units of atomic polarizabilities:** In atomic units, the polarizabilities of an atomic level have the dimension of a volume and values of $\alpha(\omega; \alpha\mathbb{J})$ are usually given in a_o^3 . In measurements, the units \AA^3 , $\text{kHz} / (\text{kV cm}^{-1})^2$, cm^3 / mol as well as the SI unit $\text{C m}^2 / \text{N}$ have been applied in the literature.
- **Typical frequency-dependence of atomic polarizabilities:** Figure 7.2 displays a typical dependence of the polarizability of atomic ground states on the frequency of the external (incident laser) field. Resonances in the (frequency-dependent, ac) polarizability occur especially near to the excitation energies of single-photon (electric-dipole) transitions to neighbouring levels.
- **Frequency-dependent (ac) polarizabilities at high laser frequencies:** At high frequencies of the incident light, the (bound) electrons of an atom can no longer follow the external field and, hence, their response (polarizability) decreases. From the second-order perturbation expansions, it can be readily seen that the scalar polarizability of an atomic level ($\alpha\mathbb{J}$) in a linearly-polarized laser field decreases $\sim \omega^{-2}$, while the vector and tensor polarizabilities vanish even faster

$$\alpha^{(\text{scalar})}(\omega > E_o; \alpha\mathbb{J}) \rightarrow -\frac{1}{\omega^2}, \quad \alpha^{(\text{vector})}(\omega > E_o; \alpha\mathbb{J}) \rightarrow \frac{1}{\omega^k} \quad (k > 2), \quad \alpha^{(\text{tensor})}(\omega > E_o; \alpha\mathbb{J}) \rightarrow \frac{1}{\omega^4}.$$

For the vector polarizabilities, moreover, the asymptotic behaviour for large ω depends on the atomic state of interest.

- **Schiff theorem & atomic dipole moment:** Because of its spherical symmetry, the dipole moment of an atom is *zero* without an external field (Schiff theorem); therefore, any **induced dipole moment** is a direct measure for the disturbance of an atom by a field. For low-enough field strengths, this response of an atom to electromagnetic field can be simply characterized by its polarizability.
- **Induced dipole moment of an atom in an external field:** For an atom in an external field $\mathcal{E} = \Re [\mathcal{E}_o e^{-i\omega t}] \mathbf{e}_z$, the induced electric-dipole moment \mathbf{p} is related to its frequency-dependent polarizability by

$$\mathbf{p} = \frac{1}{2} (\alpha^{(\text{ac E1})}(\omega; \beta\mathbb{J}) \mathcal{E}_o e^{-i\omega t} + \alpha^{(\text{ac E1})*}(\omega; \beta\mathbb{J}) \mathcal{E}_o^* e^{i\omega t}).$$

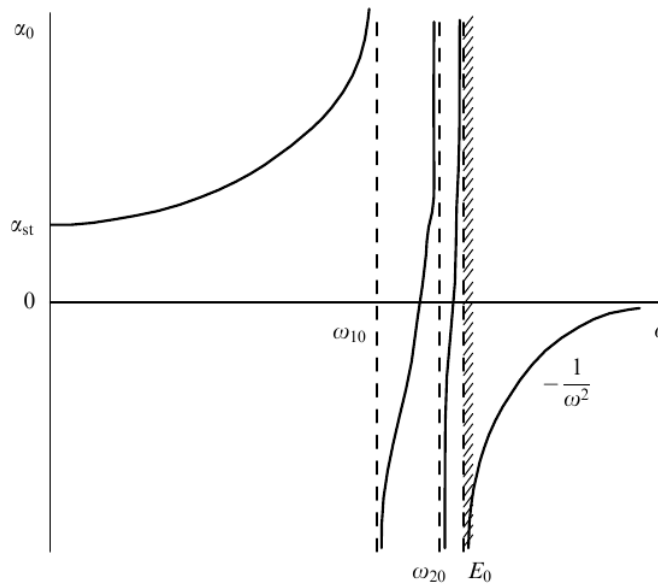


Figure 7.2.: Typical frequency dependence of the (ac) polarizability of atomic ground levels; from Krainov and Delone (1999).

- **Macroscopic view:** Mathematically, the dynamic polarizability $\alpha(\omega)$ can be expressed by a second-rank tensor (α_{ij}) that connects the induced dipole moment \mathbf{d} of the atom with the strength of the external electric field \mathcal{E} at frequency ω , and which, for spherically symmetrical systems, simplifies to a scalar

$$d_i = \sum_j \alpha_{ij} E_j(\omega), \quad \alpha_{ij}(\omega) = \alpha(\omega) \delta_{ij} \quad \rightarrow \quad \mathbf{d}(\omega) = \alpha(\omega) \mathbf{E}.$$

- **Shielding of external fields:** For weak fields, the induced – electric or magnetic – dipole moments are proportional to the applied field and give rise to secondary fields with the same spatial symmetry as the externally applied field. Therefore, any applied multipole field is typically shielded (or enhanced) near to the nucleus by some factor that is specific for the given atom or ion.
- **Dielectric constant K of a gas:** An atomic or molecular gas is often characterized by its dielectric constant K which is closely related to

7. Atomic properties

the atomic number density N_d and (scalar electric-dipole) polarizability of the ground level ($\beta\mathbb{J}$) of the atom

$$\alpha^{(\text{scalar E1})}(\beta\mathbb{J}) = \alpha^{(\text{scalar E1})}(\omega = 0; \beta\mathbb{J}) = \frac{K - 1}{4\pi N_d}.$$

This relation has also been applied in order to measure polarizabilities with relative uncertainties $\sim 0.1\%$ for rare-gas atoms as well as for nitrogen and oxygen.

- **Clausius-Mossotti relation:** For a system embedded into a medium, the dynamic polarizability of atoms also defines the **dielectric permittivity** $\varepsilon(\omega)$ of a medium with **number density** n_a of atoms, and if the medium just consists out of a single type of atoms

$$\frac{\varepsilon(\omega) - 1}{\varepsilon(\omega) + 2} = \pi n_a \alpha(\omega).$$

- **Frequency-dependent refractive index** $n(\omega)$ of a gas: The refractive index $n(\omega)$ of a gas with number density N_d is also related to the polarizability of the ground level ($\beta\mathbb{J}$) by

$$\alpha^{(\text{scalar E1})}(\omega; \beta\mathbb{J}) = \frac{n(\omega) - 1}{2\pi N_d}.$$

- **Electric-dipole and magnetic-dipole susceptibility:** The susceptibility $\chi^{(\text{electric, magnetic})}$ is generally a (dimensionless) proportionality constant that characterizes the induced polarization of a medium in response to an applied electric or magnetic field. The greater the susceptibility, the greater the response of the material to an applied field.
- **Electric susceptibility** $\chi_e \equiv \chi^{(\text{electric})}$: A proportionality **constant or tensor which relates the induced dielectric polarization density** \mathbf{P} **to the applied field** and which is very closely related to the (ground-state) atomic or molecular polarizability $\alpha^{(\text{ac:E1})}(\beta\mathbb{J})$:

$$\mathbf{P} = \varepsilon_0 \chi_e \mathbf{E}, \quad \mathbf{p} = \varepsilon_0 \alpha^{(\text{ac:E1})}(\beta\mathbb{J}) \mathbf{E}_{\text{local}}$$

Here \mathbf{p} refers to the induced atomic or molecular electric-dipole moment. Analogue expressions also exist for the magnetic susceptibility $\chi^{(\text{magnetic})}$, the magnetic field \mathbf{B} and the magnetization \mathbf{M} as well as for the magnetic-dipole moment \mathbf{m} .

- Relation of frequency-dependent (ac) polarizabilities & Cauchy moments: The static (dc) and frequency-dependent (ac) polarizabilities are related to each other by means of the Cauchy moments $S(-q)$ by (Mitroy *et al.*, 2010)

$$\alpha^{(\text{scalar E1})}(\omega; \alpha_o \mathbb{J}_o) = \alpha^{(\text{scalar E1})}(\omega = 0; \alpha_o \mathbb{J}_o) + \omega^2 S(-4) + \omega^4 S(-6) + \dots$$

Moreover, $S(-3)$ is related to the non-adiabatic polarizabilities.

- Application of atomic polarizabilities: Atomic polarizabilities are closely related to a number of macroscopic properties of gases and materials, such as the dielectric constant and the refractive index. At the microscopic scale, the formation of alkaline-earth anions and the (short term) binding of positrons by many-electron atoms can be largely explained by polarization-type interactions, i.e. in terms of atomic polarizabilities. Indeed, many textbooks of electro-magnetic theory study in quite detail the electrical polarizabilities of differently shaped macroscopic bodies, and for which only the (macroscopic) dielectric constant and the conductivity of the materials are then occur in the formalism.
- Application of atomic polarizabilities: Accurate atomic polarizabilities are needed also for quantum information processing as well as for precise optical cooling and trapping techniques.
- Application of atomic polarizabilities for atomic clocks: Precise estimates of atomic polarizabilities are needed especially for the next-generation of atomic clocks, and which will likely be based on optical transitions. Indeed, the uncertainties of atomic clocks are seriously limited by (unknown) atomic levels shifts due to (ac) Stark shifts and thermal (BBR) fluctuations of the environment. A more detailed theory of the BBR shifts also need to relate the definition of the time unit to the thermodynamics of the radiation field.
- Application of dynamical polarizabilities: Both, the real and imaginary parts of the dynamical polarizabilities are crucial to achieve good control about the – external and internal – atomic degrees of freedom of ultracold atom (clouds).
- High frequency limit of the dynamic polarizability: For $\hbar\omega \gg I_p$ and an atom or ion with N electrons

$$\alpha(\omega \rightarrow \infty) = -\frac{e^2 N}{m \omega^2}.$$

In this limit, the high frequency dynamic polarizability is real, negative and decreases quadratically with the frequency ω .

- Resonance approximation to the dynamic polarizability: At the atomic resonances, the summation over the spectrum can be restricted within the frequency interval $\omega - \omega_{n0} \lesssim \Gamma_n$ near to the resonance n with energy E_n and width Γ_n to a single term

$$\alpha^{(\text{resonant})}(\omega) = \frac{e^2}{m \omega_{n0}} \frac{f_{n0}}{\omega_{n0} - \omega - i \Gamma_{n0}/2}.$$

7. Atomic properties

At the resonances, therefore, the dynamic polarizability is generally complex with either a positive negative real part.

Frequency-dependent (ac) polarizabilities of a fine-structure level ($\beta\mathbb{J}$) :

- Frequency-dependent (ac) polarizability of an atomic state $|\alpha\mathbb{J}M\rangle$: In a frequency-dependent (ac) electric field $\mathcal{E}(t) = \mathcal{E}(t)\mathbf{e}_z$, the (frequency-dependent, electric-dipole) polarizability of an atom in the state $|\alpha\mathbb{J}M\rangle$ is given in terms of the electric-dipole matrix elements by

$$\alpha(\omega; \alpha\mathbb{J}M) = \sum_{\alpha_\nu\mathbb{J}_\nu M_\nu} |\langle \alpha_\nu\mathbb{J}_\nu m_\nu | \mathbb{D} | \alpha\mathbb{J}M \rangle|^2 \left[\frac{1}{(E_n - E_k) + \omega} + \frac{1}{(E_n - E_k) - \omega} \right],$$

and where the summation is taken over all possible E1 transitions of the level $|\alpha\mathbb{J}M\rangle$.

- Scalar *versus* vector and tensor polarizability: For an effective closed-shell atom in the (ground) level ($\beta\mathbb{J}$) with energy E_o , the scalar atomic polarizability can be expressed in terms of the absorption oscillator strength to any other level from the (many-electron) spectrum by (Mitroy *et al.*, 2010)

$$\alpha^{(\text{scalar E1})}(\omega; \beta\mathbb{J} = 0) = \sum_\nu \frac{f_{o\nu}}{(E_\nu - E_o)^2} = \sum_\nu \frac{2}{3(J+1)} \frac{|\langle \alpha_\nu\mathbb{J}_\nu | \mathbb{O}^{(\text{E1, absorption})} | \beta\mathbb{J} \rangle|^2}{(E_\nu - E_o)}.$$

For an atom in a level with $J > 0$, the frequency-dependent polarizability also depends on the projection M by

$$\alpha^{(\text{E1})}(\omega; \beta\mathbb{J}M) = \alpha^{(\text{scalar E1})}(\omega; \beta\mathbb{J}M) + \alpha^{(\text{tensor E1})}(\omega; \alpha_o\mathbb{J}_o M_o) \frac{3M^2 - J(J+1)}{J(2J-1)}$$

The tensor polarizability $\alpha^{(\text{tensor E1})}(\beta\mathbb{J}M) = \alpha^{(\text{tensor E1})}(\omega = 0; \beta\mathbb{J}M)$ is defined by

$$\alpha^{(\text{tensor E1})}(\beta\mathbb{J}M) = 4 \left(\frac{5J(2J-1)}{6(J+1)(2J+1)(2J+3)} \right)^{1/2} \sum_\nu (-1)^{J+J_\nu} \begin{Bmatrix} J & 1 & J_\nu \\ 1 & J & 2 \end{Bmatrix} \frac{|\langle \alpha_\nu\mathbb{J}_\nu | \mathbb{O}^{(\text{E1, absorption})} | \beta\mathbb{J} \rangle|^2}{(E_\nu - E_o)}.$$

The last expression shows that spherically-symmetric fine-structure levels with $J \leq 1/2$ only have a scalar polarizability, while the corresponding hyperfine levels generally still depend on F, M_F . The relation between the polarizabilities for fine-structure and hyperfine levels depend on the size of the frequency-dependent (ac) Stark shifts relative to the hyperfine splitting, and accurate prediction may require theories of different sophistication (Mitroy *et al.*, 2010).

- Non-relativistic limit of the frequency-dependent (ac) polarizability: In the non-relativistic limit, the (ac) polarizability is simply related to the number of electrons N of the atom due to the Thomas-Reiche-Kuhn sum rule for the oscillator strengths

$$\alpha^{(\text{ac E1})}(i\omega, \beta\mathbb{J}) \sim \sum_{\nu} \frac{f(\alpha_{\nu}\mathbb{J}_{\nu} \rightarrow \beta\mathbb{J})}{\omega^2} = \frac{N}{\omega^2}.$$

7. Atomic properties

Frequency-dependent (ac) polarizabilities of a hyperfine level ($\beta(IJ)\mathbb{F}$) :

- Reduced tensorial (frequency-dependent, ac) polarizability of hyperfine level ($\alpha(IJ)\mathbb{F}$) : In second-order electric-dipole approximation, and if the (non-diagonal) hyperfine interaction is negligible, the reduced tensorial (frequency-dependent ac) polarizability of a hyperfine level ($\alpha(IJ)\mathbb{F}$) with level energy E_o is given by (Beloy 2009)

$$\alpha^{(K)}(\omega; \beta(IJ)\mathbb{F})$$

$$= (-1)^{I-J+F} [F] [K]^{1/2} \left\{ \begin{matrix} F & K & F \\ J & I & J \end{matrix} \right\} \sum_{\alpha_\nu \mathbb{J}_\nu} \left\{ \begin{matrix} J & K & J \\ 1 & J_\nu & 1 \end{matrix} \right\} \langle \beta \mathbb{J} \| \mathbb{D} \| \alpha_\nu \mathbb{J}_\nu \rangle \langle \alpha_\nu \mathbb{J}_\nu \| \mathbb{D} \| \beta \mathbb{J} \rangle \left[\frac{1}{E_o - E_\nu + \omega} + \frac{(-1)^K}{E_o - E_\nu - \omega} \right],$$

and where \mathbb{D} denotes the electric-dipole operator.

- Conventional scalar, vector and tensor (frequency-dependent, ac) polarizabilities of hyperfine level ($\alpha(IJ)\mathbb{F}$) : The conventional scalar, vector and tensor polarizabilities can be expressed in terms of the reduced tensorial (frequency-dependent, ac) polarizability of a hyperfine level ($\beta(IJ)\mathbb{F}$) by

$$\alpha^{(\text{scalar})}(\omega; \beta(IJ)\mathbb{F}) = \frac{1}{\sqrt{3(2F+1)}} \alpha^{(0)}(\omega; \beta(IJ)\mathbb{F})$$

$$\alpha^{(\text{vector})}(\omega; \beta(IJ)\mathbb{F}) = -\sqrt{\frac{2F}{(2F+1)(F+1)}} \alpha^{(1)}(\omega; \beta(IJ)\mathbb{F})$$

$$\alpha^{(\text{tensor})}(\omega; \beta(IJ)\mathbb{F}) = -\sqrt{\frac{2F(2F-1)}{3(2F+1)(F+1)(2F+3)}} \alpha^{(2)}(\omega; \beta(IJ)\mathbb{F}).$$

Frequency-dependent (ac) polarizabilities for hydrogenic ions:

- Frequency-dependent polarizabilities for hydrogenic ions: For non-relativistic hydrogenic ions, the frequency-dependent polarizabilities can be evaluated analytically in the low- and high-frequency limit, i.e. far from atomic resonances. A few such relations in terms of the

principal and orbital quantum numbers are given by Delone and Krainov (1999)

$$\alpha^{(\text{scalar})}(\omega \ll E_n, n\ell) = -\frac{n^6 \ell \omega}{8} (55n^2 + 26\ell^2 + 26\ell + 169) \text{ a.u.}$$

$$\alpha^{(\text{scalar})}(\omega \gg E_n, n, \ell = 0) = -\frac{1}{\omega^2} - \frac{4}{3n^2 \omega^4} \text{ a.u.},$$

$$\alpha^{(\text{vector})}(\omega \gg E_n, n, \ell = 1) = -\frac{2\sqrt{2}(n^2 - 1)}{9n^5 \omega^{11/2}} \text{ a.u.},$$

$$\alpha^{(\text{tensor})}(\omega \gg E_n, n, \ell = 1) = \frac{1}{\omega^2} - \frac{4}{15n^3 \omega^4} \text{ a.u.},$$

$$\alpha^{(\text{scalar})}(\omega \gg E_n, n, \ell = 1) = -\frac{1}{\omega^2} - \frac{2\sqrt{2}(n^2 - 1)}{9n^5 \omega^{11/2}} \text{ a.u.}$$

$$\alpha^{(\text{vector})}(\omega \gg E_n, n, \ell \geq 2) = -\frac{2\sqrt{2}(n^2 - 1)}{9n^5 \omega^{11/2}} \text{ a.u.}$$

$$\alpha^{(\text{tensor})}(\omega \gg E_n, n, \ell \geq 2) = -\frac{4}{n^7 (\ell + 1) (2\ell + 1) (2\ell + 3) \omega^4} \text{ a.u.}$$

Further relations of this kind can be found in this reference and in the literature; they mainly show that the corrections to the asymptotic values of the polarizabilities rapidly decrease as the principal quantum number (Rydberg states) or the frequency of the external field increases. Moreover, the scalar polarizabilities usually dominate for all hydrogenic ions.

7.3.g. Hyperpolarizability

Remarks & notations:

- The **hyperpolarizability of atoms** describe a nonlinear-optical property of matter and is closely related to the second-order electric susceptibility (per unit volume).
- **Hyperpolarizability:** The hyperpolarizability of an atom or ions can be deduced experimentally, for instance, by observing the Kerr effect in gases. However, the experimental uncertainties in these measurements are often large.
- **Accuracy of static hyperpolarizabilities:** Any accurate calculation of the static hyperpolarizabilities of atoms in some state $|\beta JM\rangle$ is still a great challenge for atomic theory, and this even applies to the simplest atoms, such as lithium with only three electrons. As reported in the literature, both the choice of the basis set (grid) as well as the electronic correlations can have a large effects upon the (accuracy of the) computed hyperpolarizabilities.

7. Atomic properties

- Hyperpolarizability of closed-shell atoms: For a neutral, closed-shell atom in its ground state $|\beta^1S_0\rangle$, the energy (level) shift in the presence of a homogeneous static electric field of strength F is given by (Kassimi and Thakkar, 1994)

$$E(F; \beta\mathbb{J}) - E_o = -\alpha \frac{F^2}{2!} - \gamma_2 \frac{F^4}{4!} - \gamma_4 \frac{F^6}{6!} - \gamma_6 \frac{F^8}{8!} - \dots,$$

where α is the (static) dipole polarizability and γ_k , $k = 2, 4, \dots$ the hyperpolarizability parameters of the atom.

- Induced dipole moment $d = |\mathbf{d}|$: In the same field static field F , the dipole moment is then given by

$$d(F; \beta\mathbb{J}) = \alpha F + \gamma_2 \frac{F^3}{3!} + \gamma_4 \frac{F^5}{5!} + \dots$$

- Finite-field procedure: In the computational procedure, the polarizabilities and hyperpolarizabilities are obtained from energy and/or dipole moment calculations of the atom in the presence of an electric fields of various strengths, and by using truncations of the given expansion above.

7.3.h. Black-body radiation shifts

Remarks & notations:

- Black-body radiation (BBR) shift: An atom at finite temperature interacts with (Planck's) black-body radiation background due to the virtual absorption and emission of photons with temperature-dependent wavelengths. This interaction leads to a (tiny) shift of the atomic levels, known as BBR shift. These BBR shifts have to be analyzed for atomic clocks in order to estimate, for instance, the influence of the cosmic microwave background radiation (CMBR) in various space missions. The uncertainties in the estimated BBR shifts contribute to the uncertainty budget of the present-day atomic clocks. The BBR shifts are typically estimated by applying a multipole expansion of the electro-magnetic background field and by just considering the E1 multipole component of the field. Other multipole components of the electro-magnetic field, such as the M1 and E2 multipole fields, are expected to become relevant for the next-generation atomic clocks.
- CMBR: Even in intergalactic space, an isolated atom is still subject to the cosmic microwave background. The uncertainties in the blackbody radiation shift may impose limits on the accuracy of the best atomic clocks.
- Radiation studies: From radiation studies it is known that objects emit radiation whose wavelength depends on its temperature. At room temperature, objects emit radiation with wavelengths in the infrared region of the electro-magnetic spectrum.

- **Black-body radiation Hamiltonian $\mathbb{H}^{(BBR)}$** : In Coulomb gauge, the interaction of the atomic electrons with the propagating background field with vector potential $\mathbf{A}(\mathbf{r}, \omega)$ is described by the Hamiltonian

$$\mathbb{H}^{(BBR)} = \sum_j -c \boldsymbol{\alpha}_j \cdot \mathbf{A}(\mathbf{r}_j, \omega) = \sum_j -c (\boldsymbol{\alpha}_j \cdot \mathbf{u}) e^{i \mathbf{k} \cdot \mathbf{r}_j},$$

and where ω , \mathbf{k} and \mathbf{u} are the frequency, wave vector and the polarization vector of the background field, respectively.

- **Black-body radiation (BBR) shift:** From the Hamiltonian $\mathbb{H}^{(BBR)}$, the frequency shift of a level $(\alpha \mathbb{J})$ with (unperturbed) energy E_o is given by

$$\Delta E^{(BBR)}(T; \alpha \mathbb{J}) = \frac{1}{2} \sum_{\nu} \int d\omega |\langle \alpha_{\nu} \mathbb{J}_{\nu} | \mathbb{H}^{(BBR)} | \alpha \mathbb{J} \rangle|^2 \left(\frac{E_o - E_{\nu}}{(E_o - E_{\nu})^2 - \omega^2} \right).$$

Here, the decomposition and evaluation of the matrix elements $\langle \alpha_{\nu} \mathbb{J}_{\nu} | \mathbb{H}^{(BBR)} | \alpha \mathbb{J} \rangle$ follows the standard decompositon of the interaction of electrons with the (plane-wave) radiation field but requires to include the spectral energy density from the background field.

- **Blackbody radiation (BBR) shift:** For a time-independent environment, the BBR shift is given at temperature T in terms of the polarizability α_o by (Berengut *et al.*, 2012)

$$\delta E = -\frac{1}{2} (831.9 \text{ V/m})^2 \left[\frac{T[K]}{300} \right]^4 \alpha_o (1 + \eta)$$

and where η refers to some dynamic correction due to the frequency distribution of the atom.

7.3.i. Dispersion coefficients

Remarks & notations:

- **Lennard-Jones model:** This model refers to a **mathematically simplified potential** for describing the interaction between a pair of neutral atoms or molecules at different distances. It was first proposed in 1924 by John Lennard-Jones. Especially, the long-range interactions between atoms and molecules play a prominent role in the **low-energy and low-temperature collision experiments**.
- **Dispersion coefficients C_n :** The interaction of atoms at large interatomic distances, for instance for cold gases in a cold traps, is usually described in terms of **dispersion (van der Waals) coefficients C_n** .

7. Atomic properties

- **Alkaline-earth dimers:** For two alkaline-earth atoms in their ground state, the long-range potential as function of the internuclear distance R can be written as (Porsev and Derivianko, 2006)

$$V(R) = -\frac{C_6}{R^6} - \frac{C_8}{R^8} - \frac{C_{10}}{R^{10}} - \dots$$

- **London's model of dispersion:** For two atoms at internuclear distance R and with given electron distributions, the dispersion arises from the interaction of the induced dipoles. For two (single-active) electrons with position \mathbf{r}_A at atom A and \mathbf{r}_B at atom B , the electron at \mathbf{r}_A causes multipole moments with respect to nucleus A and, similarly, the electron at \mathbf{r}_B multipole moments with respect to nucleus B . The energy shifts due to the interaction between these multipole moments can be evaluated by second-order perturbation theory and by using the *static* approximation. This approximatinon leads to the expansion above but with explicitly given dispersion coefficients (Johnson, 2011)

$$C_6(A, B) = \frac{\alpha_A \alpha_B \langle \mathbf{p}^2 \rangle_A \langle \mathbf{p}^2 \rangle_B}{\alpha_B \langle \mathbf{p}^2 \rangle_A + \alpha_A \langle \mathbf{p}^2 \rangle_B}$$

$$C_8(A, B) = \frac{3}{2} \frac{\alpha_A \alpha_B (\langle \mathbf{p}^2 \rangle_A \langle \mathbf{Q}^2 \rangle_B + \langle \mathbf{Q}^2 \rangle_A \langle \mathbf{p}^2 \rangle_B)}{\alpha_B \langle \mathbf{p}^2 \rangle_A + \alpha_A \langle \mathbf{p}^2 \rangle_B}$$

$$C_{10}(A, B) = 2 \frac{\alpha_A \alpha_B (\langle \mathbf{p}^2 \rangle_A \langle \mathbf{T}^2 \rangle_B + \langle \mathbf{T}^2 \rangle_A \langle \mathbf{p}^2 \rangle_B)}{\alpha_B \langle \mathbf{p}^2 \rangle_A + \alpha_A \langle \mathbf{p}^2 \rangle_B} + \frac{21}{5} \frac{\alpha_A \alpha_B \langle \mathbf{Q}^2 \rangle_A \langle \mathbf{Q}^2 \rangle_B}{\alpha_B \langle \mathbf{p}^2 \rangle_A + \alpha_A \langle \mathbf{p}^2 \rangle_B}$$

and where $\langle \mathbf{p}^2 \rangle$, $\langle \mathbf{Q}^2 \rangle$, $\langle \mathbf{T}^2 \rangle$ are the expectation values of the squared dipole, quadrupole and octupole moments, respectively.

- **Atom-surface interactions:** Near to a (metallic) surface, a neutral atom interacts with its *image* via the dipole-dipole interaction, and which leads to small shifts of the atomic energy levels. If λ is the wavelength of a resonance transition and if the quantization axis is taken perpendicular to the surface, the interaction potential for an atom in level (a) near to the surface at $z < \lambda/2\pi$ can be expressed in the van-der-Waals form (Robertson *et al.*, 2020)

$$V^{(\text{atom-surface})}(z) = -\frac{C_3(a)}{z^3} = -\frac{1}{4\pi \epsilon_0} \sum_b \frac{[n(\omega_{ab})]^2 - 1}{[n(\omega_{ab})]^2 + 1} \cdot \frac{|d_x(ab)|^2 + |d_y(ab)|^2 - 2|d_z(ab)|^2}{16 z^3}.$$

Here, $n(\omega_{ab})$ refers to the frequency-dependent refraction index of the surface at the resonant frequencies ω_{ab} of the atom and $d_k(ab)$, $k =$

x, y, z to the corresponding dipole-moment matrix elements. Obviously, different levels of the atom will lead to different C_3 dispersion coefficients.

- **Dipsersion energy of atoms and molecules:** For two atoms A and B at a distance R , the standard expansion of the dispersion energy

$$E^{\text{(dispersion: two-body)}} = - \sum_{n=6,8,10,\dots} \frac{C_n^{(\text{AB})}}{R^n}$$

is obtained from second-order perturbation theory of the inner-atomic interactions. In this expansion, the coefficient C_6 captures the induced-dipole-induced-dipole interactions (fluctuations), C_8 the induced-dipole-induced-quadrupole interactions, C_{10} the sum of the induced-dipole-induced-octupole *plus* the induced-quadrupole-induced-quadrupole interactions, and so on (Jones *et al.*, 2013). There exist further two-body interactions that first occur in third-order perturbation theory and that start with terms $\mathcal{O}(R^{-11})$. For nonspherical molecules, moreover, there also exist additional interaction terms that start with terms $\mathcal{O}(R^{-7})$. These additional terms are (almost) negligible for nearly spherical molecules, such as water and others.

Atomic computation of dispersion coefficients:

- Atom-wall coefficient, C_3 : For an atom in a spherically-symmetric ground state $|\beta JM\rangle$, the dispersion coefficient C_3 of the Lennar-Jones interaction between an atom and a perfectly conducting wall is given by (Derivianko *et al.*, 1999)

$$C_3 = \frac{1}{4\pi} \int_0^\infty d\omega \alpha^{(ac E1)}(i\omega; \beta JM) = \frac{1}{12} \langle \beta JM | \mathbf{R} \cdot \mathbf{R} | \beta JM \rangle, \quad \mathbf{R} = \sum_{i=1}^N \mathbf{r}_i.$$

- Van-der-Waals coefficient, C_6 : For an atom in a spherically-symmetric ground state $|\beta JM\rangle$, the dispersion coefficient C_6 of the Lennar-Jones interaction can be expressed as integral over the frequency-dependent (ac) electric-dipole polarizability (Derivianko *et al.*, 1999)

$$C_6 = \frac{3}{\pi} \int_0^\infty d\omega [\alpha^{(ac E1)}(i\omega; \beta JM)]^2.$$

- Van-der-Waals coefficient, C_6 : Since the van-der-Waals coefficients C_6 contains the electric-dipole matrix element upto fourth power, these dipole amplitudes must usually be calculated with high accuracy.
- Long-range interaction of two atoms: For two atoms a and b in spherical-symmetric ground states $|\beta_a J_a M_a\rangle$ and $|\beta_b J_b M_b\rangle$, the long-range interaction can be written with $k' = n - k - 1$ as (Porsev and Derivianko, 2006)

$$V(R) = - \sum_{n=3} \frac{C_{2n}^{ab}}{R^{2n}}, \quad C_{2n}^{ab} = \frac{(2n-2)!}{2\pi} \sum_{k=1}^{n-2} \frac{1}{(2k)!(2k')!} \int_0^\infty d\omega \alpha_k^{(ac E1)}(i\omega; \beta_a J_a M_a) \alpha_{k'}^{(ac E1)}(i\omega; \beta_b J_b M_b),$$

and where $\alpha_k^{(ac E1)}(i\omega; \alpha_c J_c M_c)$ is the 2^k -pole frequency-dependent (ac electric-dipole) polarizability of each atom a, b .

- Dispersion coefficients $C_n^{(AB)}$ of mixtures: For mixed interactions of atomic pairs (AB) , a simple rule is often applied:

$$C_n^{(AB)} = \sqrt{C_n^{(A)} C_n^{(B)}}.$$

- Van-der-Waals coefficients C_{12} and C_{14} : The high-order dispersion coefficients, i.e. the van der Waals coefficients C_{12} and C_{14} are usually not so easily available for most systems of interest. They can be approximated from the low-order dispersion coefficients C_{12} and C_6, C_8, C_{10} by using certain dimensionless ratios of such coefficients as discussed for instance by Douketis *et al.* (1982).

Dispersion coefficients in chemical computations:

- **Dispersion corrections to DFT calculations:** It has been found (very) important to incorporate dispersion corrections into (typical) DFT computations, especially if chemical processes and reaction pathes are to be considered. Different approaches to account for dispersion corrections include van-der-Waals functionals, dispersion-corrected effective-core potentials, the parameterization of meta-GGA functionals or, simply, the *posteriori* addition of a dispersion energy to the DFT energy (Johnson, 2011).
- **Grimme's DFT approaches to dispersion:** Several suggestions have been made by Grimme and coworkers to obtain dispersion coefficients for molecular environments from the ionization potentials, polarizabilities of the elements and some empirical constants. These suggestions are mainly motivated by the (so-called) **London model**. In a recent work of Grimme and coworkers, the dispersion coefficients were computed for each pair of atoms separately by using the Casimir-Polder formula for a number of reference molecules, and by adding some dependence on the coordination number. These dispersion coefficients then vary smoothly along a considered **reaction coordinate** and are sensitive also to changes in the hybridization, atomic volume as well as the atomic charge and oxidation state of the compound. Such dispersion models can then be combined with Hartree-Fock and/or exchange-correlation DFT calculations.
- **Hirshfeld scaling of polarizabilities:** The effective atom-in-molecule polarizabilities of each atom α_i are often evaluated by using the proportionality between the polarizability and volume as well as the free-atomic polarizabilities $\alpha_i^{(\text{free})}$ from available tabulations:

$$\alpha_i = \left(\frac{\langle r^3 \rangle_i}{\langle r^3 \rangle_i^{(\text{free})}} \right) \alpha_i^{(\text{free})}.$$

While this Hirshfeld volume-based scaling is a reasonable approximation to determine the atom-in-molecule polarizabilities in various (neutral) molecular environments, the approach breaks down for ions. For instance, if the ionic polarizabilities are obtained from the neutral-atom values multiplied by a ratio of atomic volumes, the ionic C_6 dispersion coefficients are drastically overestimated. In general, the volume-scaling approach overestimates the polarizability and dispersion coefficients of cations and underestimates these values for anions (Johnson, 2011).

Noble-gas dimers:

- **Helium dimers, He_2 :** The helium dimer He_2 is weakly bound by van-der-Waals forces that just support a single molecular (bound) state with tiny binding energy of $\sim 10^{-7}$ eV. It has an average bond length of ~ 52 Å and oscillates to distances of more than 200 Å, being thus the largest known (ground-state) diatomic molecule. While the He_2 dimer has been theoretically discussed since the 1920s, it has been observed experimentally in the early 1990s.

7. Atomic properties

- **Helium dimers, He_2 :** In a semi-classical treatment of the He_2 dimer, the outer classical turning point is estimated to about 14 Å, almost 4 times smaller than its average size. This shows that He_2 can be seen as a quantum halo system that spends most of the time in the classically forbidden region.

7.3.j. Fano profiles of continuum-embedded resonances

Remarks & notations:

- **Fano resonances in physics:** In physics, a **Fano resonance** generally refers to a resonant scattering process (**phenomenon**) that gives rise to an asymmetric line-shape in the energy of scattered (emitted) particles due to the interference between a constant background and a resonant scattering amplitude. Fano-type resonances can be found across many areas of physics and engineering because resonant scattering is a rather ubiquitous wave phenomenon.
- **Fano resonances in atomic physics:** In atomic physics, the background amplitude often arises from the direct (ionization) amplitude of an electron to the continuum, while the resonant amplitude arises from the (indirect) coupling of the atom to a discrete, localized state that is embedded into the continuum.
- **Photoionization near to resonances:** The photoionization cross section near to an isolated resonance at energy E_r is best described by Fano's formula. In this formula, the resonant cross section is characterized by the resonance width Γ , the asymmetry parameter q and the non-resonant background cross section σ_b . Using this formula, the cross sections peaks at $E_{\max} = E_r + \frac{1}{2} \Gamma/q$ with $\sigma_{\max} = \sigma_b (1 + q^2)$ and reaches zero at $E_r - \frac{1}{2} \Gamma q$.

7.3.k. Stark splitting in crystal field

Remarks & notations:

- **Atomic line emission from ionic crystals:** Embedded rare-earth ions in ionic crystals, such as Er^{3+} , are known to exhibit very sharp absorption and emission lines. In selected cases, these lines can be as narrow as the lines of free ions, and quite in contrast to the rather broad spectra of most defects in crystals, such as nitrogen centers.
- **Application of doped erbium ions:** Apart from data communications, erbium oxides are considered also as primary candidate in nuclear fusion devices in order to reduce the tritium permeation barriers in the blanket system of tokamaks and stellarators.

Crystal-field Hamiltonian & splitting of atomic levels:

- **Crystal-field Hamiltonian $\mathbb{H}^{(\text{crystal field})}$:** If the N_c surrounding ions of the crystal are treated as point charges $\{Z_c\}$ at given (fixed) positions $\{\mathbf{R}_c = (R_c, \vartheta_c, \varphi_c)\}$, the crystal-field interaction Hamiltonian of an embedded atom or ion with N electrons can be written in atomic units in the form (Gaigalas and Kato, 2020)

$$\mathbb{H}^{(\text{crystal field})} = - \sum_{c=1}^{N_c} \sum_{j=1}^N \frac{Z_c}{|\mathbf{R}_c - \mathbf{r}_j|} = \sum_{c=1}^{N_c} \sum_{j=1}^N \sum_{k=0}^{\infty} \sum_{q=-k}^k (-1)^{q+1} \sqrt{\frac{4\pi}{2k+1}} B_k(r_j; R_c, Z_c) C_q^{(k)}(\vartheta_j, \varphi_j) Y_{k,-q}(\vartheta_c, \varphi_c)$$

$$B_k(r; R, Z) = Z \begin{cases} \frac{r^k}{R^{k+1}} & r \leq R \\ \frac{R^k}{r^{k+1}} & r > R. \end{cases}$$

The charges and positions of the surrounding ions are the physical parameters N_c , Z_1 , $\mathbf{R}_1 = (R_1, \vartheta_1, \varphi_1)$, Z_2 , $\mathbf{R}_2 = (R_2, \vartheta_2, \varphi_2)$, ... that determine the (additional) *crystal field*, and that must be given explicitly for each compound of interest.

- **Splitting of atomic levels in a crystal field:** For degenerate atomic levels with total angular momentum $J \neq 0$, the splitting in the electric

7. Atomic properties

(Stark) field of the crystal can be calculated in first-order perturbation theory from the matrix elements (Gaigalas and Kato, 2020)

$$\begin{aligned} & \langle \alpha J M_J \| \mathbb{H}^{(\text{crystal field})} \| \alpha' J' M'_J \rangle \\ &= \sum_{c=1}^{N_c} \sum_{k=0}^{j_a+j_b} \sum_{q=-k}^k \sum_{rs} \sum_{ab} c_r c_s (-1)^{J-M_J} \begin{pmatrix} J & k & J' \\ -M_J & q & M'_J \end{pmatrix} \sqrt{2J+1} d_{ab}^k(r, s) \langle \kappa_a \| C^{(k)} \| \kappa_b \rangle (-1)^{q+1} Z_c \sqrt{\frac{4\pi}{2k+1}} \\ & \quad \times Y_{k,-q}(\vartheta_c, \varphi_c) \left[\int_0^{R_c} dr \frac{r^k}{R_c^{k+1}} (P_a P_b + Q_a Q_b) + \int_{R_c}^{\infty} dr \frac{R_c^k}{r^{k+1}} (P_a P_b + Q_a Q_b) \right] \\ & \langle \kappa_a \| C^{(k)} \| \kappa_b \rangle = (-1)^{j_a-1/2} \sqrt{2j_b+1} \begin{pmatrix} j_a & k & j_b \\ 1/2 & 0 & -1/2 \end{pmatrix} \pi(\ell_a, \ell_b, k). \end{aligned}$$

Here $P_a(r)$ and $Q_a(r)$ are the large and small components of the relativistic one-electron radial wave function, and $d_{ab}^k(r, s)$ the spin-angular coefficients due to the decomposition of the matrix elements of the rank-1 Hamiltonian $\mathbb{H}^{(\text{crystal field})}$.

- **Splitting of atomic levels in a crystal field:** In general, each degenerate level (αJ) splits into a number of sublevels, while $J = 0$ levels are only shifted. The number of non-degenerate sublevels depend on the symmetry of the surrounding ions (crystal field) and follows directly from the diagonalization of the $\mathbb{H}^{(\text{crystal field})}$ Hamiltonian matrix

$$|\beta\rangle = \sum_{r=1}^{N_{\text{csf}}} \sum_{-M_r}^{M_r} c_{r,M_r}(\beta) |\gamma_r J_r M_r\rangle.$$

These (sub-) levels of a multiplet in a crystal field have no longer a well-defined total angular momentum nor projection, J, M , although they can often be related to fine-structure levels of the free atom or ion.

Classification and characterization of crystal fields:

- **Characterization of the crystal field:** While the ion of interest is always assumed to be at the origin of the coordinates, the position of the crystal atoms need to be specified in spherical coordinates $\{\mathbf{R}_c = (R_c, \vartheta_c, \varphi_c)\}$. These coordinates can be given explicitly as a list of point $[(R_1, \vartheta_1, \varphi_1), (R_2, \vartheta_2, \varphi_2), \dots]$ or ...

7.4. Other topics closely related to atomic properties

7.4.a. Laser cooling, precision spectroscopy and quantum control

Quantum logic spectroscopy:

- **Quantum logic spectroscopy:** Quantum logic is typically implemented by a laser-induced coupling of the internal and external degrees of freedom of two ions, namely the **spectroscopy** and the **logic** ion. By making use of appropriate laser pulses, the **information about the internal state of the spectroscopic ion can then be transferred from the spectroscopic to the logic ion**.
- **Logic ion:** Simply speaking, the logic ion can be viewed as both, a remote control and a sensitive quantum sensor for the internal and external state of the spectroscopy ion.
- **Quantum-logic techniques:** Many limitations of precision spectroscopy can be overcome if simple quantum-logic techniques are used and **if the spectroscopic and logic ion is controlled together**. In this technique, especially, the readily-controllable logic ion provides sympathetic cooling, internal state preparation and detection of the ion with an interesting spectroscopic transition.
- **Realization of quantum logic spectroscopy:** Such a quantum-logical transfer scheme can be realized with two ions in a linear Paul trap.
- **Application of quantum logic spectroscopy:** Possible applications of quantum logic spectroscopy refer to the unprecedentedly high resolution spectroscopy of a wide range of sympathetically cooled atoms and molecules with special spectroscopic properties, such as an improved sensitivity to a variation of fundamental physics constants, or to tests of QED via precision spectroscopy.

Laser cooling and precision spectroscopy:

- **Laser-cooling techniques:** The recent development of laser-cooling techniques made cold and ultra-cold atomic samples available for optical spectroscopy. This development nowadays allows for long interrogation times and significantly reduced Doppler shifts; they give rise also to an unprecedented uncertainty in atomic clocks, exceeding one part in 10^{-15} .
- **Coherent control of external and internal degrees of freedom:** In 1995, a controlled-NOT (CNOT) gate between a trapped atomic ion and its motional mode in the trap was first realized experimentally. Since then, the **coherent control over the internal and external degrees of freedom in an atomic system** has been demonstrated.
- **Coherent control of external and internal degrees of freedom:** Laser spectroscopy helped develop methods to simultaneously **control both, the internal electronic and the motional degrees of freedom of individual atoms, molecules and singly-charged ions in traps with high accuracy**.

7. Atomic properties

- **Precision spectroscopy of atoms and ions:** Most laser spectroscopy with clouds of trapped ions have explored a rather small class of atoms and atomic ions, including hydrogen, the alkali and alkaline-earth atoms and ions as well as few other species (Schmöger *et al.*, 2015). These atoms and ions usually have electronic transitions that are suited for laser cooling and that help localize the atoms for precision spectroscopy.
- **Application of precision spectroscopy:** In quantum information processing with trapped ions, precision spectroscopy has lead to new applications, such as teleportation, error-correction as well as the implementation of the Deutsch-Jozsa and semi-classical Fourier transformation algorithms.
- **Coulomb crystals:** A signature for trapped and well-localized ions is the formation of Coulomb crystals, i.e. **spatially ordered ensembles of mutually repelling ions that are confined in a common external trapping potential**. Such Coulomb crystals form when the thermal kinetic energy of the ions becomes (much) smaller than the ion-ion electrostatic energy.
- **Sympathetic cooling:** If atoms and ions do not have a direct cooling transition, **sympathetic cooling by use of co-trapped ions has been found a successful strategy in the past for singly and doubly charged atoms and molecules**.

7.4.b. Atomic clocks

Concepts and criteria of atomic clocks:

- **Atomic clock:** An atomic clock is typically based on an electron transition of either microwave, optical or ultraviolet frequency, and which serves as frequency standard for its time-keeping element.
- **Definition of the second:** The transition between the hyperfine levels of cesium in its [Xe] $6s\ ^2S_{1/2}$ ground level was first proposed by Essen and Parry for the definition of the time unit [sec]. As **primary frequency standard**, the second is today defined by 9,192,631,770 oscillations of a light pulse with $6s\ ^2S_{1/2}\ F = 1/2 \rightarrow 3/2$ transition frequency of cesium. Standard atomic clocks must ensure this accuracy irrespective of their locations or the particular time of measurement. While the cesium clock is a microwave clock, **modern clocks are preferred to operate at optical frequencies**, i.e. at frequencies which are about five orders of magnitude higher and which are based on much narrower optical reference transitions.
- **Criteria for atomic clocks:** Three important criteria for an atomic clock refer to (1) a transition frequency that can be easily probed by some (rather) short-acting stable local oscillator; (2) a transition with a narrow natural linewidth; (3) a suitable technology for counting frequencies. Here, the suitability of a given atomic line is often characterized by a **quality factor** $Q = \nu/\delta\nu$, which should be large. Apart

from this quality factor of an atomic transition, however, one needs also to consider the limitations of the line with regard to reproducibility and stability. Here, the **stability of an atomic transition** measures the variability of the frequency standard as function of time. The three relevant factors of atomic clock transitions (accuracy, stability and reproducibility) generally depend also on the experimental set-up and the extent to which environmental perturbations can be controlled. In the optical domain, frequency combs are applied as references to ensure high stability and accuracy of the optical clocks.

- **Optical atomic clocks:** Recent developments in the **set-up and control of optical atomic clocks** has improved their precision by a factor of **1000** in less than two decades.
- **Challenges to atomic-clock developments:** The control of the thermal motions of the atoms and ions, trapped in some oscillating electro-magnetic field, often introduces the largest systematic uncertainties to the overall uncertainty budget. For clocks, which are operated at room temperature, the velocity distribution of the atoms causes **Doppler shifts due to the residual thermal or micromotion of the ions**.
- **Classes of systematic uncertainties:** (1) **Instrumental uncertainties** arise from the construction of the traps and instruments, while (2) **external uncertainties** are caused by the incomplete control of the external – electro-magnetic stray or gravitational – fields. The second class of uncertainties can be further controlled by both, a proper choice of the clock transitions and a detailed understanding how these transitions are affected by electro-magnetic fields. This control in terms of choosing the atomic clock transitions usually requires a detailed analysis of the trapping electric and magnetic fields as well as of all laser fields that act upon the trapped atoms or ions. This analysis must include also a careful treatment of the – linear and quadratic – Zeeman and (ac) Stark shifts.

Shifts of atomic clock transitions:

- **Magic wavelength:** Often, the trap lasers of the optical lattice clock are operated at the (so-called) *magic* wavelength at which the electric-dipole polarizabilities of the (two) clock levels are the same in order to ensure a (nearly) zero ac Stark shift of the clock transition.
- **Magic wavelengths:** The need in precise (ac) polarizabilities arises especially from the study of atomic clocks and the search for **magic wavelengths** for developing optical frequency standards. At the magic wavelength (of some proper transition), the frequency-dependent polarizabilities of the lower and upper (atomic) state are the same and, hence, the (ac) Stark shift of the transition frequency just vanishes. Such magic wavelengths cannot be found for every atomic transitions, at least not for acceptable experimental conditions.
- **Light shifts for clock levels:** The frequency of an atomic clock can be affected by (i) the thermal bath of blackbody radiation (BBR), (ii) the electric-quadrupole coupling of the ions to the trapping field and with other residual electro-magnetic fields, (iii) by ambient magnetic fields as well as (iv) through various Stark shifts (Yudin *et al.*, 2014).
- **BBR shifts of clock transitions:** The probing of the clock transition by a laser leads to clock shifts due to the ac Stark effect. These shifts are proportional to the E1 polarizability like the BBR shift, but is strongly suppressed with $\propto 1/\tilde{Z}^6$ for highly-charged ions.

7. Atomic properties

- **E1 versus M1 contributions to the BBR shift:** While the E1 contribution usually dominates the BBR shift of most atomic levels, M1 clock transitions are mainly affected by the thermal \mathbf{B} -field fluctuations which couple to M1 transition moments (Yudin *et al.*, 2014).
- **Electric-quadrupole (E2) shift:** The gradients of the trapping and residual electric fields also couple to the quadrupole moments of the clock states. For $J = 1/2$ clock states, the electric-quadrupole moment vanishes due to the angular selection rules.
- **Shifts of atomic clock transitions for HCI:** Taken from Berengut *et al.* (2012).

| Contribution to the shift | Scaling |
|---------------------------|--|
| Second-order Stark shift | $\sim / (Z^{(\text{eff})})^4$ |
| Blackbody shift | $\sim / (Z^{(\text{eff})})^4$ |
| Second-order Zeeman shift | suppressed due to large energy denominators. |
| Electric-quadrupole shift | $\sim / (Z^{(\text{eff})})^2$ |
| Fine structure | $\sim Z^2 (Z^{(\text{eff})})^2 / (Z_{\text{ion}} + 1)$ |
| Hyperfine A coefficient | $\sim Z (Z^{(\text{eff})})^2 / (Z_{\text{ion}} + 1)$ |

Classes and realization of atomic clocks:

- **Classes of atomic clocks:** There are currently two types of optical atomic clocks under development: (i) based on neutral atoms in optical lattices or (ii) based on a single trapped ion. For both types, a similar uncertainty have been reached, namely: 2.1×10^{-18} for a Sr neutral atom clock (Nicholson *et al.*, 2015) and 3.2×10^{-18} for a Yb^+ trapped ion clock (Huntemann *et al.*, 2016), that have been operated on a particular electric-octupole (E3) transition.
- **Classes of atomic clocks:** Modern optical clocks are either based on (1) neutral atoms, which are trapped and cooled in some magnetic-optical trap (MOT); or (2) singly- and multiply-charged ions in a Paul-type trap. There has been a remarkable progress (and competition) along both of these research lines, and it is undecided until now which particular scheme will become the primary frequency standard of the next-generation atomic clocks.
- **Accuracy and stability of optical atomic clocks:** The accuracy and stability of optical atomic clocks has been advanced significantly over the past ten years. The systematic uncertainty of the Sr optical lattice clock has been reduced to 2.1×10^{-18} in (so-called) fractional frequency units. A similar small (systematic) uncertainty of 3.2×10^{-18} was reported also for a single-trapped ion atomic clock, based on an electric-octupole transition in Yb^+ .

- **Optical clocks:** Optical clocks that operate at an accuracy level of a few parts per 10^{-18} will be sufficient to measure subtle relativistic effects and to become sensitive to the geodesic gravitational potential difference of Earth or to set upper limits on possible temporal or spatial variations of fundamental constants.
- **Single-ion optical clocks:** Because of limitations for having a proper spectroscopic transition, single-ion optical clocks, which are based on the isotopes of aluminium and boron, have not been realized in the past.
- **Single-ion mercury clock:** Recently, an optical clock, that is based on a forbidden transition in a single mercury ion, has achieved an uncertainty of 7.2×10^{-17} . This clearly exceeds the performance of the best cesium fountain standards.
- **Atomic clocks based on singly-charged ions:** During the past two decades, detailed clock studies and developments have been performed for the ions: $^{27}\text{Al}^+$, $^{40}\text{Ca}^+$, $^{43}\text{Ca}^+$, $^{87}\text{Sr}^+$, $^{88}\text{Sr}^+$, $^{115}\text{In}^+$, $^{171}\text{Yb}^+$, $^{173}\text{Yb}^+$, $^{199}\text{Hg}^+$, and $^{201}\text{Hg}^+$, respectively.
- **Atomic clocks based on forbidden optical transitions:** Single-photon $ns^2 \ ^1S_0 - nsnp \ ^3P_0$ transitions among the low-lying levels of alkaline atoms are strictly forbidden because of selection rules. However, these lines can be readily quenched by weak electric and magnetic fields and may serve a reference transition for new frequency standards. Moreover, these transitions are ideal in the sense that their line widths can be perfectly tuned by the strength of the applied fields.
- **Optical-clock ions:** The singly-ionized alkaline-earth ions (Ca^+ , Sr^+ , Ba^+) have been proposed for establishing **optical-frequency standards** because of the long lifetime of the low-lying $nd \ ^2D_{3/2,5/2}$ ($n = 3, 4, 5$) levels. A large number of measurements and theoretical computations have been performed on these ions and include a detailed analysis of the single-photon magnetic-dipole (M1) and electric-quadrupole (E2) channels as well as (less often to) their $nd \ ^2D_{3/2,5/2} \rightarrow (n+1)s \ ^2S_{1/2} + 2\gamma$ two-photon decay.
- **Proposals for a neutral Yb atomic clock:** The $4f^{14} 6s^2 \ ^1S_0 - 4f^{14} 6s 6p \ ^3P_0$ transition in neutral Yb can be induced by hyperfine mixing in isotopes with nuclear spin $I \neq 0$ and has served already as some frequency standard. However, neutral Yb has still another and very interesting $4f^{14} 6s 6p \ ^3P_0 - 4f^{13} 6s^2 5d$ ($J = 2$) electric-quadrupole (E2) transition at an easily accessible wavelength of 1695 nm, which might be suitable as well for the development of another frequency standard in this atom (Safranova *et al.*, 2018).
- **^{229m}Th nuclear clock:** Thorium has one exceptional nuclear state that is known for the last 40 years and that has a very low energy of presumably below 10 eV. The currently assumed excitation energy of this isomeric state is 7.8 ± 0.5 eV, or correspondingly 159 ± 11 nm or ~ 1900 THz. **This isomeric state conceptually allows for a direct laser excitation of the nucleus by using solid-state laser technology.** This state has therefore been **proposed for the development of a nuclear clock of extremely high stability** owing to the expected high resilience against external influences and its radiative lifetime in the range of minutes to hours (von der Wense *et al.*, 2017).
- **^{229m}Th nuclear clock:** Von der Wense *et al.* (2017) propose a different approach for the excitation of ^{229m}Th that allows for a **direct laser excitation of this transition without the prior request to know the transition energy accurately.** This approach makes use of the fast

7. Atomic properties

(lifetime of $\sim 10 \mu s$) nonradiative internal conversion decay channel of neutral thorium for the isomer detection. The internal conversion transfers the nuclear excitation energy to the electron cloud and, hence, results in the ejection of a (valence-shell) electron.

- **Atomic clocks based on multiply and highly-charged ions:** For highly-charged ions, the hyperfine transitions are often in or near to the optical region, in contrast to the present microwave cesium standard. Very narrow optical lines can be found especially within the ground configurations or near to the ground levels of multiply and highly-charged ions, and if all (electric-) dipole or even quadrupole transitions are forbidden. Such ions can also be considered for optical frequency standards because they are often different in their (low-lying) level structure as well as sensitivity to the environmental perturbations.
- **Atomic clocks based on hyperfine-induced transitions in highly-charged ions:** Magnetic-dipole hyperfine-induced transitions in highly-charged ions may serve as reference transition because of their reduced *size* that is $\sim (Z - N)^{-1}$ for N -electron ions with nuclear charge Z . Such a reduced size also leads to reduced blackbody radiation (BBR), quadratic Zeeman, frequency-dependent (ac) Stark and static electric-quadrupole shifts in these ions.
- **Atomic clocks with highly-charged ions:** Optical E1, M1 and E2 transitions among low-lying atomic levels also occur for highly-charged ions due to level crossings along selected isoelectronic sequences. In HCl, such clock transitions may have the advantage that systematic effects, such thermal shifts, can be reduced when compared with existing optical atomic clocks.
- **^{229}Th isotopes:** Among all known isotopes from the nuclear chart, the thorium isotope ^{229}Th has a isomeric state with the lowest excitation energy of about $7.8 \pm 0.5 \text{ eV}$. This rather low energy might allow a direct optical excitation by today's laser technology, once the excitation energy is sufficiently well known. The isomeric state decays via three main channels to its ^{229}Th ground nucleus, namely, internal conversion, γ decay as well as bound internal conversion, but whose strengths sensitively depend on the charge state of ^{229}Th . For neutral ^{229m}Th atoms, Seiferle *et al.* (2017) measured a half-life of $7 \pm 1 \mu s$ owing to internal conversion. From theoretical predictions, a half-life of $\sim 10^4 \text{ s}$ is expected for the nuclear (M1) photon decay. Obviously, the large internal conversion coefficient $\sim 10^9$ makes the observation of photon emissions very difficult for neutral ^{229m}Th atoms. If internal conversion is forbidden, Indeed, ^{229m}Th is (theoretically) expected to live up to 10^9 times longer.
- **^{229}Th isotopes:** The low excitation energy of the ^{229m}Th state makes singly- or mulitply-charged ^{229}Th ions a promising candidate for a nuclear optical clock that may outperform today's atomic clock technology (Seiferle *et al.*, 2017). Because of this low excitation energy, various proposals have been made in order to use this isotope for searching dark matter, gravitational waves as well as for geodesy. Moreover, the ultra-high sensitivity of a ^{229}Th may help reveal variations in the fundamental constants.

Applications of atomic clocks:

- **Atomic clock:** Atomic clocks are the most accurate time and frequency standards; they are frequently applied as **primary standards for international time distribution services**, to control the wave frequency of television broadcasts as well as to operate the global navigation satellite systems such as GPS.
- **Application of atomic clocks:** Various applications of atomic clocks are now in reach or have already been realized owing to the improved precision and the high stability of these clocks. These applications include: (1) the study of many-body physics and quantum simulations; (2) relativistic geodesy; (3) very-long baseline interferometry; (4) searches for the variation of the fundamental constants; (5) searches for dark matter candidates; (6) tests of the Lorentz invariance and several others. Further improvement of clock precision is needed for several of these applications.
- **Application of atomic clocks:** Modern atomic clocks require precisely-known transition frequencies and, hence, can be utilized as well in order to probe the temporal and spatial variations of many fundamental physical constants. Such measurements at (atomic) low energies form a valuable alternative to experiments in high-energy physics but require a careful treatment and precise predictions from relativistic atomic structure theory.
- **Global positioning system (GPS):** Atomic clocks are essential for the global positioning system (GPS) where multiple such devices are onboard of each GPS satellite, and which must provide the time to within 100 billionths (10^{-7}) of a second. Atomic clocks are applied also in radio astronomy, meteorology, telecommunications as well as for military services.
- **Atomic clocks for gravitational wave detection:** These and further ideas and applications, such as the use of atomic clocks for gravitational wave detection, will require even more precise clocks in the future.

7.4.c. Atomic partition functions

Motivation:

- The atomic partition function $U(T)$ includes a summation over all bound levels of the atom and is defined as

$$U(T) = \sum_j g_j \exp\left(-\frac{E_j}{kt}\right).$$

7.4.d. Quantum similarity measures & similarity indices for pairs of atoms and ions

Quantum similarity measures:

- **Quantum similarity measures (QSM):** A number of such similarity measures has been worked out formally in the early 1980s by Carbo and coworkers (1980, 2004). These similarity measures and (so-called) similarity indices for pairs of atoms or molecules are mainly based on the (overlap of the) electron density distribution of two *distinguishable* quantum systems. When applied to isolated atoms, these measures can help analyze the chemical periodicity in the periodic table of elements.
- **Quantum similarity measure:** For two quantum systems with (spinless, electron) densities $\rho^{(A)}(\mathbf{r})$, $\rho^{(B)}(\mathbf{r})$ and a separation operator $\Omega(\mathbf{r}_1, \mathbf{r}_2)$, Carbo *et al.* (1980) define such a similarity measure by

$$Z^{(A,B)}(\Omega) = \int d\mathbf{r}_1 d\mathbf{r}_2 \rho^{(A)}(\mathbf{r}_1) \Omega(\mathbf{r}_1, \mathbf{r}_2) \rho^{(B)}(\mathbf{r}_2).$$

Often, the separation operator $\Omega(\mathbf{r}_1, \mathbf{r}_2) = \delta(\mathbf{r}_1 - \mathbf{r}_2)$ is chosen which *reduces* the double integration to a ‘overlap’ integral of the two electron densities. For $\Omega(\mathbf{r}_1, \mathbf{r}_2) = \frac{1}{|\mathbf{r}_1 - \mathbf{r}_2|}$, in contrast, a Coulomb-interaction integral is obtained.

- **Quantum similarity index:** A *normalized* similarity measure, known as similarity index, is obtained by

$$I^{(A,B)}(\Omega) = \frac{Z^{(A,B)}(\Omega)}{\sqrt{Z^{(A,A)}(\Omega)} \sqrt{Z^{(B,B)}(\Omega)}}, \quad 0 \leq I^{(A,B)}(\Omega) \leq 1.$$

Both, the quantum similarity measure and similarity index can be evaluated quite easily by using proper densities of ions, atoms or molecules.

- **Application of QSM:** These measures can be used to provide compact information about (pairs of) molecules with regard to their shape and extent of the electron density. Moreover, these measures might be used as **atomic and molecular descriptors** in order to predict molecular structures and reactivities. Various modifications have been suggested for the quantum similarity measures from above by using different separation operators or reactivity-motivated densities.

7.4.e. Atom-atom and atom-ion interaction potentials

Theory of interatomic forces:

- **Interatomic forces and potentials:** Accurate interatomic potentials are of fundamental importance for understanding and modelling the static and dynamic properties of gases, liquids or even solids.
- **Interatomic forces:** While the theory of interatomic forces has been developed over the last four decades, fast and reasonably reliable predictions are often still not so easily available, especially if a whole range of intermolecular separations (distances) need to be considered.
- **Interatomic forces:** A good **knowledge of the interatomic forces in (closed-shell) molecules has been found a key especially for understanding the behavior of various systems**, such as the geometry and stability of molecular solids, the properties of liquids and their phase transitions as well as for collisions between molecules in gases or in molecular beams.
- **Interatomic forces:** The (attractive) interatomic interaction is **dominated by correlation or dispersion effects at large internuclear distances R** , where perturbation theory gives rise to a series expansion R^{-2n} , $n \geq 3$. However, this perturbation series is known to be asymptotically divergent and is best truncated to its smallest term, following the work of Dalgarno and Lewis.
- **Intermolecular interaction:** The (inter-molecular) interaction energies are often partitioned into the SCF parts of the individual atoms and the correlation energy of the molecule as a whole. For atoms, the SCF computation can be carried out quite easily, while the correlation energies need to be obtained semi-empirically by means of standard long range multipolar expansion (Douketis *et al.*, 1982).
- **Interatomic interactions:** In material science, two key quantities in the modeling of van-der-Waals (vdW) interactions between atoms are the electric-dipole polarizability α and the so-called vdW radius $R^{(\text{vdW})}$. Usually, these two quantities have to be determined independently. However, Fedorov *et al.* (2018) derived a quantum-mechanical relation $R^{(\text{vdW})} \approx 2.54 \alpha^{1/7}$ a.u., which is quite different from the classical

7. Atomic properties

behaviour $R^{(\text{vdW})} \approx \text{const. } \alpha^{1/3}$, based on hard-sphere atoms. As pointed out by these authors, this simple relation can be applied for 72 chemical elements between hydrogen and uranium, and can be extended also to vdW-bonded heteronuclear dimers consisting of atoms A and B. Moreover, this relation might be used to relate the geometric parameter in the Lennard-Jones and other semi-empirical potentials to the electric polarizability.

- **Ion-atom interactions at cold temperatures:** At cold temperatures of just a few Kelvin or even lower, ion-atom interactions are often affected by (i) rapid energy variations in the potentials as induced by long-range polarization contributions; (ii) the generally large number of contributing partial waves; and (iii) a rather sensitive dependence of the interatomic interactions upon the details of the short-range potential. Further difficulties may arise from (iv) other weak interactions, such as hyperfine interactions and other.
- **Application of interatomic forces:** While the scattering of charged particles has already a rather long history, collisions of ions and neutral particles at ultracold temperatures has emerged only recently as an exciting (new) field in AMO physics.

Interatomic potentials:

- **Different theoretical approaches:** Different regions of the molecular potential curves have been investigated by different theoretical methods. Perturbation theory has been applied, in particular, to describe the long-range attraction, and where the first- and second-order perturbation energies are often approximated by just the first few terms in a multipole-series expansion of the Coulomb interaction between the molecules.
- **Failure of perturbation theory:** A perturbative treatment of interatomic potentials fails to describe the potential at short and intermediate distances since it: (i) does not include exchange interactions between the electrons, (ii) diverges for strong interatomic interactions, and (iii) because a multipole expansion generally fails when the electron distributions overlap each other.
- **Intermediate distance:** At intermediate distances, i.e. in the region of the minimum of the intermolecular potential, only SCF computations typically predict the potentials reasonably well if the molecule does not form strong chemical bonds.
- **Experimental interatomic potential:** Because of the difficulties in obtaining good interatomic potentials, many accurate such potentials have been determined experimentally by combining data from beam scattering experiments, virial and transport coefficient measurements as well as liquid and solid state properties. In practise, however, the interatomic potentials are still best probed in the intermediate regions.
- **Analytic interaction potentials:** Analytic interatomic potentials have been widely applied in organic chemistry for estimating the minimum energy structures of (energy) surfaces, grain boundaries and others. These analytic potentials are known also as bond-order, semi-empirical or even classical potentials. All analytic potentials are defined by some functional form of the interatomic interactions, and whose parameters are fitted to data from selected databases (Andrienko *et al.*, 2016).
- **Properties of analytic interaction potentials:** Following Brenner (2010), an analytic potential needs to be:

- **Flexible:** ... to account for a relatively wide range of structures from the fitting database;
- **Accurate:** ... able to accurately reproduce quantities such as energies, bond lengths, elastic constant, and related properties entering a fitting database.
- **Transferable:** ... able to reproduce related properties that are not yet included in the fitting database.
- **Computationally efficient:** ... so that it is tractable for a desired calculation, given the available computing resources.

➤ **Interaction between two spherical-symmetric atoms at large distance R :** For two spherical-symmetric atoms, the dominant interaction at large distance R is usually given in terms of **dispersion coefficients**. If atom A is at the origin with an electron at \mathbf{r} (relative to the nucleus of A) and atom B at the position $(0, 0, R)$ on the z -axis with an electron at \mathbf{r}' (relative to the nucleus of B), the perturbing interaction can be written as

$$V^{(\text{perturbation})} = \frac{1}{R} - \frac{1}{|\mathbf{R} - \mathbf{r}|} - \frac{1}{|\mathbf{R} + \mathbf{r}'|} + \frac{1}{|\mathbf{R} - \mathbf{r} + \mathbf{r}'|}$$

If there are more than one electron at some atom, the corresponding term(s) must be formally added for all pairs of electron coordinates. In the perturbation above, the last term is crucial as it requires a more advanced multipole expansion, cf. 2.4.b

➤ **Modified Buckingham potential:** Already 1941, Heller suggested a modified Buckingham potential by including a R^{-10} dispersion term

$$V^{(\text{mod. Buckingham})} = A e^{-bR} - \frac{C_6}{R^6} - \frac{C_8}{R^8} - \frac{C_{10}}{R^{10}}.$$

➤ **Molecules with ionic bonds:** For ionic bonds, **the summation over the ionic neighbours can then be carried out using the standard techniques**; hereby, the total interaction energy is often called the **crystal energy** and can be expressed in terms of the nearest-neighbor distance R as

$$V(R) = -\frac{\alpha^{(\text{Madelung})}}{R} + n_s V_s(R),$$

where n_s is the number of nearest neighbours and $V_s(R)$ a short-range potential as worked out by Gordon and Kim (1974). From $V(R)$, one can obtain the equilibrium internuclear distances, the dissociation energies to the free ions, the nearest-neighbor separations R , the cohesive energies D , or the bulk modulus for these crystals.

➤ **Di-atomic interaction potential:** Within the single-active electron approximation, the inter-atomic interaction arise from the interaction between the active (valence) electrons and their interaction with the *screened* nuclei. If \mathbf{r}_1 and \mathbf{r}_2 are the coordinates of the two active

7. Atomic properties

electrons of a di-atomic molecule, relative to their nuclei, the interaction potential at the internuclear distance R can be described in terms of a **multipolar expansion** as (Robertson *et al.*, 2020)

$$V(R) = \sum_{k_1, k_2=1}^{\infty} \frac{V_{k_1, k_2}(\mathbf{r}_1, \mathbf{r}_2)}{R^{k_1+k_2+1}}$$

$$V_{k_1, k_2}(\mathbf{r}_1, \mathbf{r}_2) = \frac{(-1)^{k_2} 4\pi}{\sqrt{(2k_1+1)(2k_2+1)}} \sum_p \sqrt{\binom{k_1+k_2}{k_1+p} \binom{k_1+k_2}{k_2+p}} r_1^{k_1} r_2^{k_2} Y_{k_1, p}(\vartheta_1, \varphi_1) Y_{k_2, -p}(\vartheta_2, \varphi_2).$$

Here, the quantization axis is taken along the internuclear distance, and $\binom{n}{m}$ are binomial coefficients and $Y_{k, p}(\vartheta, \varphi)$ spherical harmonics. The terms with $k_1 + k_2 = 2, 3, 4, \dots$ refer to the dipole-dipole, dipole-quadrupole, quadrupole-quadrupole, etc. interactions. From these potentials, expressions of the C_6 dispersion coefficient can be derived for large R (Robertson *et al.*, 2020).

Quantum Drude oscillator (QDO) model:

- **Quantum Drude oscillator (QDO) model:** The classical Drude oscillator model approximates the interaction of an atom with another system by just replacing the response of all (external) individual electrons by just a single negatively-charged (light) quasi-electron that is harmonically bound to a positively-charged heavy quasi-nucleus. This classical model therefore provides a very simple access to the many-body dipole polarization. **The QDO model extends this concept to a coarse-grained description of the electronic structure of surrounding particles.** It enables one to deal with the many-body multipole polarization and the dispersion interactions beyond the dipole approximation, but can still be solved with linear scaling in system size (Jones *et al.*, 2013).

Gordon-Kim (1972) theory for atom-atom interactions:

- **Gordon-Kim model:** Gordon and Kim (1972) developed a model in order to calculate the interaction between closed-shell atoms, ions and molecules. In this model, the **electron density of the system is taken as the sum of the two separate densities**, and the non-Coulombic part of the interaction potential is calculated from this density by using energy expressions from the free-electron gas.
- **Assumptions of the Gordon-Kim theory:** Three basic assumptions were made by Gordon and Kim (1972):
 - i) No rearrangement or distortion of the separate atomic densities occurs when the two atoms are brought together and, hence, **the total electron density is just the sum of the two (spherically symmetric) atomic densities**. This assumption neglects of course the rearrangement

of the electron density and therefore restricts the theory to systems with a strong chemical bond, including covalent chemical bonds and to interatomic distances that are smaller than about half of the equilibrium separation.

- ii) The interatomic interaction can be evaluated from the combined atomic density, including the Coulomb interactions between all charges.
- iii) Gordon and Kim applied originally Hartree-Fock wave-functions in order to obtain the electron densities of the separate atoms, although other, and perhaps more accurate, wave functions should work as well.

- **Total interaction of the two (atomic) charge distributions:** The total energy includes the **contributions from the kinetic, exchange and correlation energies as well as the (direct) Coulomb interactions energy**. Below, we briefly summarize how these contributions can be calculated by just using atomic wave functions.
- **Total interaction of the two (atomic) charge distributions:** Apart from the Coulomb interaction of the two (atomic) charge distributions, the **kinetic, exchange and correlation energy contributions to the total interaction energy are obtained from the electron density and the free-electron gas approximation**.
- **Uniform electron gas model:** The regions around the nuclei (in which the density varies rather rapidly) do overall not contribute much to the interaction energy, even if they strongly affect the total energy. These contributions to the total energy cancel out if the atomic energies are subtracted. **Only the outer regions of the atoms, in which the atomic densities overlap, contribute significantly to the interaction energy**. For these reasons, the uniform electron gas model should be reasonably accurate (Gordon and Kim, 1972).
- **Application of the Gordon-Kim potential:** The rather simple Gordon-Kim potential have been used, for example, in the treatment of ionic compounds such as alkali-halide and alkaline-earth-dihalide molecules in order to predict (surprisingly) accurate molecular properties (Kim and Gordon, 1974). In this work, Gordon and Kim made the following two basic assumptions in addition to those assumptions already made for their pair potentials: (a) the systems are made of free ions; (b) the interactions of ions are pairwise additive, i.e. the total interaction is the sum of all the pair interactions, neglecting the many-body interactions.
- **Coulomb interaction of the two (atomic) charge distributions:** For two separated atoms with nuclear charges Z_a and Z_b and with (total)

7. Atomic properties

atomic density $\rho = \rho_a + \rho_b$, the total Coulombic interaction energy but without the energies of the infinitely separated atoms is

$$\begin{aligned}
V^{(\text{Coulomb})} &= \frac{Z_a Z_b}{R} + \int d^3r_1 d^3r_2 \frac{\rho_a(\mathbf{r}_1) \rho_b(\mathbf{r}_2)}{r_{12}} - Z_b \int d^3r_1 \frac{\rho_a(\mathbf{r}_1)}{r_{1b}} - Z_a \int d^3r_2 \frac{\rho_b(\mathbf{r}_2)}{r_{2a}} \\
&= \int_0^\infty dr_1 r_1^2 \rho_a(r_1) \int_0^\infty dr_2 r_2^2 \rho_b(r_2) \int_0^{2\pi} d\varphi_1 \int_0^{2\pi} d\varphi_2 \int_0^\pi d\vartheta_1 \sin \vartheta_1 \int_0^\pi d\vartheta_2 \sin \vartheta_2 \left(\frac{1}{R} + \frac{1}{r_{12}} - \frac{1}{r_{1b}} - \frac{1}{r_{2a}} \right) \\
&= \int_0^\infty dr_1 r_1^2 \rho_a(r_1) \int_0^\infty dr_2 r_2^2 \rho_b(r_2) \times (4\pi)^2 I(R, r_1, r_2),
\end{aligned}$$

where (in the upper line) the first term on the right-hand side represents the repulsion between nuclei, the second term the electron-electron repulsion, and where the third and fourth terms include attractions between the electrons of the atom with the *other* nucleus.

- **Coulomb interaction of the two (atomic) charge distributions:** In the final expression, moreover, the atomic densities are to be assumed spherically symmetric (which is the case for closed-shell atoms), so that ρ_a and ρ_b just depend on the radial distances from their own atomic nucleus.
- **Coulomb interaction of the two (atomic) charge distributions:** The integral $I(R, r_1, r_2)$ depend on the charges of the two atoms and can be expressed as

$$I(R, r_1, r_2) = \begin{cases} \frac{1}{R} + F(R, r_1, r_2) - \frac{4}{R + r_1 + |R - r_1|} & \text{for homo-nuclear pairs of atoms} \\ \frac{1}{R} + F(R, r_1, r_2) - \frac{2}{R + r_1 + |R - r_1|} - \frac{2}{R + r_2 + |R - r_2|} & \text{for hetero-nuclear pairs of atoms} \\ \frac{Z_a Z_b + 1}{(Z_a - 1)(Z_b + 1) R} + F(R, r_1, r_2) - \frac{2 Z_b}{(Z_b + 1)(R + r_1 + |R - r_1|)} - \frac{2 Z_a}{(Z_a - 1)(R + r_2 + |R - r_2|)} & \text{for ion pairs,} \end{cases}$$

if we utilize for the electron densities of the ion pair in the last line $\int d^3\mathbf{r} \rho_a(\mathbf{r}) = Z_a - 1$, $\int d^3\mathbf{r} \rho_b(\mathbf{r}) = Z_b + 1$.

- **Charge-density expectation values:** The expression above contains the $\langle r_{12}^{-1}; R \rangle$ expectation value of which the two charge densities depends (parametrically) upon the internuclear separation R , and which can be evaluated analytically for two spherical-symmetric charge

distributions:

$$F(R, r_1, r_2) = \langle r_{12}^{-1} \rangle = \begin{cases} \frac{2}{R + r_1 + |R - r_1|} & \text{for } r_2 < |R - r_1| \\ \frac{1}{2} \left(\frac{1}{r_1} + \frac{1}{r_2} \right) - \frac{R}{4r_1 r_2} - \frac{(r_1 - r_2)^2}{4R r_1 r_2} & \text{for } |R - r_1| < r_2 < R + r_1 \\ \frac{1}{r_2} & \text{for } r_2 > R + r_1. \end{cases}$$

- **Total Coulomb interaction:** With these three expressions, the total Coulomb interaction can be obtained from the just two-dimensional integral over the radial coordinates r_1 and r_2 . This integral from above can be carried out numerically by using a Gauss-Laguerre quadrature. Despite the piecewise form of the integrand, it appears continuous and well behaved. Gordon and Kim (1972) note that the numerical quadrature for the Coulomb interaction converges easily and that 24×24 points generally gives rise to a four-figure accuracy.
- **Kinetic and exchange energy:** The contributions to the total interaction energy due to the (kinetic) motion of the electrons and their exchange interaction is derived from expressions for the free-electron gas. To this end, one integrates the electron density contribution from the electron gas over the molecular volume and subtracts the atomic contributions.
- **Total energy density from electron gas:** Gordon and Kim (1972) define the total energy density functional for the electron gas as

$$E^{(\text{total})}(\rho) = E^{(\text{HF})}(\rho) + E^{(\text{correlation})}(\rho), \quad E^{(\text{HF})}(\rho) = \frac{3}{10} (3\pi^2)^{2/3} \rho^{2/3} - \frac{3}{4} \left(\frac{3}{\pi} \right)^{1/3} \rho^{1/3},$$

and where additional corrections can be made for the correlation energy $E^{(\text{correlation})}$.

- **Total electron gas contribution:** The electron-gas contribution to the interatomic interaction is

$$V^{(\text{total})} = \int d^3\mathbf{r} \{ [\rho_a(\mathbf{r}_a) + \rho_b(\mathbf{r}_b)] E^{(\text{total})}(\rho_a + \rho_b) - \rho_a(\mathbf{r}_a) E^{(\text{total})}(\rho_a) - \rho_b(\mathbf{r}_b) E^{(\text{total})}(\rho_b) \}$$

Obviously, the total interatomic potential is the sum of the Coulomb terms above and these electron gas terms.

7.4.f. Dispersive interactions in liquids and solids

Dispersive interactions in molecular-dynamics and Monte-Carlo simulations:

- **Dispersive interactions:** Dispersive forces and interactions in media often refer to contributions due to intermolecular interactions, and which that arise from the polarization of one (of the) atoms in the fluctuating but instantaneous multipole field of other atoms. Therefore, dispersive interactions exist between each pair, triple, etc. of atoms or ions.
- **Dispersive interactions:** For dense-phase and solid-state systems, full quantum mechanical calculations of the interaction energy are generally not feasible and, hence, require to describe the interactions by means of interatomic or intermolecular potentials; cf. section 7.4.e.
- **Dispersive interactions:** In principle, the dispersive interactions in media can be captured also by first-principles simulations, for instance, based on density functional theories (DFT). Although such simulations are quite promising, reliable results are obtained only for systems with covalent bonding, while difficulties arise when dealing with dispersion interactions.
- **Dispersion coefficients:** Expressions for the dispersion coefficients can be derived from perturbation theory; however, the theory of intermolecular interaction also shows clearly that the dispersive interactions in media are generally not pair-additive. Apart from the two-particle interactions, the three-body terms are known to play a significant role in the thermodynamics of condensed phases.
- **Application of dispersive interactions:** Apart from inert-gas or crystallized solids of various organic molecules, the dispersive interactions are typically small, though not negligible. Reasonable estimates of the magnitude of the dispersion interaction are therefore necessary for many solid-state studies, such as the cohesion of matter, the behaviour of ionic crystals, for molecular liquids, the adsorption on surfaces or in porous media (Pellenq and Nicholson, 1998).
- **Application of dispersive interactions:** In Monte-Carlo and molecular-dynamics simulations, for example, a reasonable accurate potential energy function is required and need to be based on quantum-mechanical estimates, even if the dynamics of the particles is described classically.

Two-body dispersive interactions:

- **Long-range dispersive interactions:** If we consider two interacting neutral atoms, time-dependent perturbation theory gives rise to a long-range dispersive interaction due to charge fluctuations of the interacting species.
- **Multipole expansion:** For two spherically symmetric atoms or molecules A and B , that are separated by a distance R , a multipole expansion

is given by (Pellenq and Nicholson, 1998)

$$V^{(\text{dispersion, AB})}(R) = - \left[\frac{C_6}{R_6} + \frac{C_8}{R_8} + \frac{C_{10}}{R_{10}} + \dots \right].$$

- In this expansion, the dispersion coefficient C_6 describes the interaction between two instantaneous dipoles, C_8 the interaction between a quadrupole and a dipole and C_{10} both, the interaction between an octopole and a dipole as well as between two quadrupoles.

Three-body dispersive interactions:

- In the multipole expansion, the terms with three species A , B and C are obtained from perturbation theory at in third and higher orders. For such a triplet, the total dispersion energy is however non-additive:

$$V^{(\text{dispersion})} = V^{(\text{dispersion, AB})} + V^{(\text{dispersion, BC})} + V^{(\text{dispersion, CA})} + V^{(\text{dispersion, ABC})} + \dots$$

where $V^{(\text{dispersion, ABC})}$ represents a sum of several terms describing the three-body interaction.

7.4.g. Mean excitation energy of atomic ions & stopping powers

Mean excitation energy of atomic ions:

- Application of mean excitation energies of atoms and ions: Such mean excitation energies $E(Z; N)$ if ions might be helpful for simple models in the time evolution of plasmas, warm dense matter or complex biochemical structures. In all these systems, energy is often pumped in by the stopping power of fast ions. The characteristic energy transfer is given by the stopping power, i.e. the energy deposit by the projectile per unit length of the projectile trajectory. For ions with velocity v and the material density $n(x)$, the stopping power is

7. Atomic properties

related to the (so-called) **stopping cross section** $S(v)$ by

$$-\frac{dE(v)}{dx} = n(x) S(v) = \frac{4\pi e^4 n(x) [Z^{(\text{projectile})}]^2 Z^{(\text{target})}}{m v^2} L(v)$$

$$L(v) = \sum_{j=0} [Z^{(\text{projectile})}]^j L_j \approx L_o^{(\text{Bethe})}(v) + Z^{(\text{projectile})} L_1^{(\text{Lindhard})}(v) + [Z^{(\text{projectile})}]^2 L_2^{(\text{Bloch})}(v)$$

$$L_o^{(\text{Bethe})}(v) = \ln \frac{2m v^2}{I_o} - \frac{C}{Z^{(\text{projectile})}}.$$

In these expressions, $L(v)$ is the so-called **stopping number which includes terms from different contributors**. The Bethe term $L_o^{(\text{Bethe})}(v)$ is usually the most relevant contribution to the stopping number. Moreover, I_o is the mean excitation energy of an element for a given charge state.

- **Mean excitation energy of an element for a given charge state:** The mean energy tells how easily an atomic or molecular target can absorb kinetic energy from the projectile; this mean energy depends on the target but not on the projectile. It can be expressed as the weighted sum (integral) of all relevant oscillator strength of the target in the given charge state

$$\ln I_o = \frac{\int dE \ln E \frac{df}{dE}}{\int dE \frac{df}{dE}}.$$

Because of the oscillator strength, it should be possible to re-express this mean energy in second-order perturbation theory by an approximate summation over the complete spectrum (Sauer *et al.*, 2015). This would be a useful application of JAC.

7.4.h. Transport coefficients for ion mobility and diffusion in gases

Transport coefficients in gases:

- **Ion-mobility spectrometry (IMS):** The IMS is an analytical technique that is used to separate and identify ionized molecules in the gas phase, based on their mobility within a carrier buffer gas.
- **Ion-mobility spectrometry (IMS):** IMS has been heavily employed for military or security purposes, such as detecting drugs and explosives, but also for the analysis of both, small and large biomolecules.

- **Ion mobility K :** The ion mobility is defined as the proportionality factor between the drift velocity v_d of the ions and the applied electric field \mathcal{E} : $v_d = K\mathcal{E}$. These ion mobilities are usually reported as (standard) reduced (ion) mobilities for a standard gas density n_0 , i.e. for standard temperature $T = 273$ K and pressure $p_o = 1013$ hPa.
- **Ion mobility K :** Ion mobilities also help in analysis of collision broadening in ion cyclotron resonance, the study of ion-molecule reactions as a function of electric field strength in flow-drift tubes, and especially the use of mobility data to test or determine ion-neutral interaction potentials.
- **Ion mobility K :** While the reduced ion mobility just refers to the standard density, the ion mobility is still temperature dependent $K_o = K \frac{n}{n_o} == K \frac{T_o}{T} \frac{p}{p_o}$.
- **Kinetic theory of ion mobility in neutral gases:** Viehland and Mason (1978) present the first rigorous kinetic theory of ion mobility in neutral gases which is valid for electric fields of arbitrary strength and without restriction to the ion-neutral mass ratio or interaction potential. These results proved to be useful in a number of applications: the calculation of low-field ion mobilities in high-temperature gases, if measurements as function of electric field strength were made before in low-temperature gases.

7.4.i. Polarizability and optical absorbance of nanoparticles

Optical properties of nanoparticles:

- **Color of nanoparticles:** Noble-metal nanoparticles with a size, that is comparable to the wavelength of the incident light, show characteristic colors owing to the strong absorption and scattering of light in the visible region.
- **Localized surface plasmon resonance (LSPR).** The LSPR are often explained as collective oscillation of free electrons in the nanoparticle that are induced by the electro-magnetic waves. Therefore, the color of the absorbed light can be tuned by the size, shape, materials as well as the surrounding environment of the nanoparticles, and with applications in chemistry, physics and biomedical fields.
- **Surface-to-volume ratio:** Nanoparticles with a size below 10 nm have extremely high surface-to-volume ratios and, thus, substantially different optical properties, when compared to large nanoparticles or to the bulk material. These optical properties also depend on the atomistic structure of the nanoparticles.
- **Discrete dipole approximation (DDA):** This classical discrete dipole approximation and various variants of this method has been applied extensively for studying plasmonic nanoparticles. However, since the DDA makes usually use of the bulk dielectric constant, it cannot so easily be applied to quantum-sized nanoparticles.

Methods for calculating the polarizability of nanoparticles:

- **Polarizability of a discretized medium:** The polarizability of a discretized medium is in general proportional to its volume.
- **Polarizability of the i-th atom α_i :** In a given nanoparticle, the polarizability of the i-th atom α_i can be approximated by multiplying the polarizability of the free atom $\alpha^{(\text{free})}$ with the relative volume (ratio), i.e. by dividing the effective volume $V^{(\text{eff})}$ by the volume of the free atom $V^{(\text{free})}$,

$$\alpha_i = \frac{V^{(\text{eff})}}{V^{(\text{free})}} \alpha^{(\text{free})} = \frac{V^{(\text{eff})}}{V^{(\text{free})}} \frac{e^2}{m} \sum_{\nu} \frac{f_{\nu o}}{\omega_{\nu o}^2 - \omega^2 - i\omega\delta}$$

where $\omega_{\nu o}$ is the n-th absorption frequency (with regard to the ground level), $f_{\nu o}$ its oscillator strength and where the **frequency shift δ** depends on the coordination factor within the nanoparticle.

- **Optical absorbance of nanoparticles:** The optical absorbance of the nanoparticle is obtained from the total polarizability of all atoms $i = 1\dots N$ by

$$\sigma^{(\text{absorption})} = \frac{4\pi\omega}{c} \Im\{\alpha^{(\text{total})}(\omega)\} = \frac{4\pi\omega}{c} \Im \left\{ \sum_i^N \alpha_i^{(\text{ac E1})}(\omega) \right\}.$$

7.4.j. Radiative opacities in cold plasma

Properties, notations & application:

- Contributions to the radiative opacity of an atom or ion in its ground-state configuration or a number of low-lying configurations are given by:

$$A^{q+} + \hbar\omega \rightarrow \begin{bmatrix} A^{q+*} & \text{photoabsorption} \\ A^{(q+1)+*} & \text{photoionization} \\ A^{q+} + \hbar\omega' & \text{photonscattering} \\ \dots & \end{bmatrix}.$$

- Formal quantum notation: $|\alpha_i J_i\rangle + \hbar\omega(\{\mathbb{M}\}) \rightarrow \begin{bmatrix} |\alpha_f J_f\rangle \\ |\alpha_f J_f\rangle + |\varepsilon \kappa\rangle \\ \dots \end{bmatrix}.$

- Using JAC: Perform a `Cascade.Computation(Cascade.Computation(); name=.., nuclearModel=.., grid=.., approach=.., scheme=Cascade.ExpansionOpacityScheme(..), initialConfigs=[..])` or call directly functions from the module `Cascade`. Cf. Section 9.
- Fraction of transmitted radiation: The fraction of the incident radiation with incident frequency ω , that is transmitted through a medium (plasma), can be expressed by means of the spectral opacity $\kappa(\omega)$ [or $\kappa'(u)$] as:

$$F(\omega) = \exp(-\rho \kappa L)$$

where L refers to the path length of the light through the medium (plasma) and ρ to its mass density. This fraction of the transmitted radiation can be readily determined also experimentally. Often, the spectral opacities is expressed also as $\kappa'(u)$ in terms of the temperature-normalized photon energy. From the spectra opacity $\kappa(\omega; T, \rho, ..)$, and *mean* opacity $\kappa^{(\text{mean})}(T, \rho, ..)$ can be derived.

- Opacity: The — spectral and mean — opacities of a (plasma) medium characterizes the transport of radiation through matter. Opacity computations generally require atomic data for a large number of processes involving the absorption and scattering of radiation (Seaton 1987).

7. Atomic properties

- **Role of opacity calculations:** The opacity quantifies how photons are absorbed or re-scattered by the plasma ions, while traveling through the plasma. The opacity of different ion sources is needed for understanding the radiation transport in different plasma environments, such as stellar interiors, fusion devices and short-wavelength plasma light sources.
- **Role of opacity computations:** Opacity computations generally imply the accurate knowledge of different atomic data, such as level energies, oscillator strength, photoionization cross sections and several other properties. These data are generally needed for all ionic species in the plasma. In practice, moreover, one also requires an adequate equation of state in order to determine the ionization fractions and level populations of the ions as well as information about line broadening mechanisms.
- **Presentation of radiative opacities:** The radiative opacity is often analysed and displayed either as function of the mass density at given temperature or as function of temperature at given mass density.
- **Grey opacity schemes:** In such (grey) opacity schemes, the value of the opacity is typically adjusted to reproduce the color of the emission. This is often done in (almost all) radiation transport simulations. In contrast to the iron-group elements, however, the opacities of the actinides are expected to be roughly 10 times larger.
- **Sources of opacity:** For a high optical depth of the plasma and LTE conditions, the primary source of opacity for a given sort of ions is its number of lines per unit wavelength, rather than strong individual transitions. Therefore, the precision of transition energies and oscillator strength appears less relevant in those environments, in which the level density is sufficiently high to sustain a LTE and a high optical depth.
- **Opacities of dense plasma:** Johnson and Nilsen (2020) calculated the opacity of dense plasmas for light elements within the average-atom model. From this model, other plasma properties can be derived as well, such as the chemical potential, average ionic charge, free electron density, bound and continuum wave functions or the occupation numbers. All these properties are based on computations of the photo-induced bound-free and free-free transitions in the plasma. The average-atom properties and opacities can be extended also to plasma with more than one ionic species, for example, boron nitride, polystyrene or various compositions of H, He C plasma.
- **Optical properties of plasma:** The optical properties of a plasma often refer to its dielectric constants, the indices of refraction as well as absorption coefficients. All these properties can be computed by means of the average-atom approximation. An average-atom version of the Kubo-Greenwood formula can be derived from the linear response of such an atom to a harmonic electric field, and from which frequency-dependent electric conductivity of the plasma can be computed quite easily (Johnson *et al.*, 2006). Moreover, the frequency-dependent dielectric function can be determined from the conductivity by using the Kramers-Kronig dispersion relations and, hence, the index of refraction and absorption coefficient of the plasma. The conductivity is related to the imaginary part of the relative dielectric function and, thus, the entire complex dielectric function can be obtained from the Kubo-Greenwood (KG) formula.

Light propagation in plasma:

- **Spectral intensity $I(\vartheta, \varphi; \lambda)$:** The (spectral) light intensity of a plasma or light source describes the amount of electro-magnetic radiation with wavelengths between $\lambda \dots \lambda + d\lambda$ that passes in the time interval dt through the area dA into the solid angle $d\Omega = \sin \vartheta d\vartheta d\varphi$ (Pettini 2018),

$$W(\lambda) d\lambda = I(\vartheta, \varphi; \lambda) d\lambda dt dA \cos \vartheta \sin \vartheta d\vartheta d\varphi = I(\vartheta, \varphi; \lambda) d\Omega d\lambda dt dA \cos \vartheta.$$

In astrophysics, the spectral intensity is often measured in units: $\text{erg s}^{-1} \text{cm}^{-2} \text{\AA}^{-1} \text{sr}^{-1}$.

- **Spectral and total energy density $W(\lambda)$:** The spectral energy density $w(\lambda)$ refers to the energy per unit volume that is contained in the radiation field with wavelengths between $\lambda \dots \lambda + d\lambda$, and from which the **total energy density $w(\lambda)$** is easily obtained

$$w(\lambda) d\lambda = \frac{d\lambda}{c} \int d\Omega I(\vartheta, \varphi; \lambda) = \frac{4\pi}{c} J(\lambda) d\lambda \quad \Rightarrow \quad w = \int_0^\infty d\lambda w(\lambda),$$

and where $J(\lambda)$ is the angle-averaged spectral intensity.

- **Photon mean free path:** In a plasma or gas, photons from a light beam with spectral intensity $I(\vartheta, \varphi; \lambda)$ are absorbed or scattered along its differential path ds through the medium (of given density ρ and spectral opacity $\kappa(\omega)$). This attenuation of the spectral intensity $I(\vartheta, \varphi; \lambda)$ is given by

$$dI(..; \lambda) = -\mu I(..; \lambda) ds = -\kappa(\omega) \rho I(..; \lambda) ds, \quad \mu = \frac{1}{\kappa(\omega) \rho} = \frac{1}{\sigma(\lambda) n}$$

where μ is the attenuation coefficient, σ the interaction (absorption) cross section and n the number density of particles within the plasma.

- **Optical depth of photons $\tau(\lambda)$:** $\tau(\lambda) = \int_0^s ds \kappa(\omega) \rho$.

- **Optical depth:** The optical depth integrates the opacity along an optical path in the medium

$$\tau(l; t) = \int_0^l ds \kappa(s(\mathbf{r}), t; \mathbf{n}, \omega)$$

and essentially measures the mean number of photon interactions along its trajectory $\mathbf{r}_1 = \mathbf{r}(s=0)$ to $\mathbf{r}_2 = \mathbf{r}(s=l)$.

Definition of spectral and mean radiative opacities:

- Temperature-normalized photon energy $u(\omega)$: Opacities are often expressed in terms of the temperature-normalized photon energy $u = \frac{\hbar\omega}{k_B T}$, or temperature-normalized photon frequency.
- Spectral opacity $\kappa(\omega)$: For plasma in a local thermodynamic equilibrium at temperature T and mass density ρ , the (radiative) spectral opacity $\kappa(\omega)$ is given by (Cheng and Jiaolong, 2008)

$$\rho \kappa(\omega) = [\mu^{(\text{bound-bound})}(\omega) + \mu^{(\text{bound-free})}(\omega) + \mu^{(\text{free-free})}(\omega)] \left(1 - \exp\left(\frac{\hbar\omega}{k_B T}\right)\right) + \mu^{(\text{scattering})}(\omega),$$

where $\mu^{(\text{bound-bound})}$, $\mu^{(\text{bound-free})}$, $\mu^{(\text{free-free})}$ and $\mu^{(\text{scattering})}$ are the absorption coefficients due to bound-bound, bound-free, free-free as well as the scattering processes, respectively.

- Spectral opacity $\kappa(\omega)$: The total spectral opacity $\kappa(\omega)$ can be calculated as the sum of different contributions due to:
 (i) photo-excitation $\kappa^{(\text{bound-bound})}$, (ii) photo-ionization $\kappa^{(\text{bound-free})}$, (iii) inverse Bremsstrahlung $\kappa^{(\text{free-free})}$ as well as (iv) photon scattering $\kappa^{(\text{scattering})}$.

$$\kappa(\omega) = \kappa^{(\text{bound-bound})}(\omega) + \kappa^{(\text{bound-free})}(\omega) + \kappa^{(\text{free-free})}(\omega) \quad \left[\frac{\text{cm}^2}{\text{g}} \right]$$

$$\kappa'(\omega) = \kappa(\omega) \left(1 - \exp\left(-\frac{\hbar\omega}{k_B T}\right)\right) + \kappa^{(\text{scattering})}(\omega)$$

- Free-free opacity contributions: The free-free transitions refer to the (inverse) Bremsstrahlung due to emitted radiation, if a free electron slows down in the electromagnetic field of an ion.
- Assumptions for deriving the spectral opacity $\kappa(\omega)$: Two assumptions are typically made in order to obtain the (radiative) spectral opacity $\kappa(\omega)$ of a plasma: (i) All quantum states of a degenerate level are equally populated and (ii) the levels with different energy E are populated due to a Boltzmann statistics $\sim \exp(-E/kT)$.

- **Expansion opacity:** Most atomic computations are nowadays based on the formalism by Karp *et al.* (1977):

$$\begin{aligned}\kappa^{(\text{expansion: bound-bound})} &= \frac{1}{\rho c t_{\text{obs}}} \sum_{\ell} \frac{\lambda_{\ell}}{\Delta\lambda} (1 - e^{-\tau_{\ell}}) \quad \equiv \kappa(\lambda, \Delta\lambda; T; \rho t_{\text{obs}}, [\text{level population}]) \\ &= \kappa(u, \Delta\lambda; T; \rho t_{\text{obs}}, [\text{level population}]) = \kappa(\omega, \Delta\omega; T; \rho t_{\text{obs}}, [\text{level population}]) \quad \left[\frac{\text{cm}^2}{\text{g}} \right] \\ \tau_{\ell} &= \frac{\pi e^2}{m c} f_{\ell} n_{\ell} \lambda_{\ell} t = \frac{\pi e^2}{m c} \left(\frac{n \lambda_{\ell} t}{g_o} \right) g_{\ell} f_{\ell} e^{-E_{\ell}/k_B T}.\end{aligned}$$

In this expansion opacity, ρ and t_{obs} refers to the density and (observation) time after the merger, while the summation runs over all lines ℓ in some (arbitrarily) chosen wavelength bin ($\Delta\lambda$), and where λ_{ℓ} is the transition wavelength and τ_{ℓ} the (so-called) Sobolev optical line depth. Moreover, g_{ℓ} , E_{ℓ} , f_{ℓ} refer to the statistical weight and the energy of the lower level as well as the oscillator strength of the transition.

- **Validity of the expansion opacity:** The expansion opacity can be used only if the frequency change of a photon is large. When compared to the thermal width of the spectral lines, and, in turn, when compared large compared with the thermal width of the spectral lines. With these assumptions, the expansion opacity can be defined as monochromatic. The frequency change as seen by the target atoms is first of all proportional to its mean free path. The assumption of thermal equilibrium arises from the enhanced interaction of the photons with the spectral lines.
- **Expansion opacity formalism:** For a homologously expanding ejecta with density ρ , the expansion opacity at time t_e after the explosion is given by

$$\kappa^{(\text{expansion})}(\Delta\lambda) = \frac{1}{\rho c t_{\text{obs}}} \sum_k \frac{\lambda_k}{\Delta\lambda} (1 - e^{-\tau_k}), \quad \tau_k = \left(\frac{\pi e^2}{m c} \right) n_k t_e f_k \lambda_k$$

where n_k refers to the occupation of the lower level and f_k to the corresponding oscillator strength.

- **Number density n_{ℓ} :** For the number density n_{ℓ} of levels at temperature T , a Boltzmann distribution $n_{\ell} = \frac{g_{\ell}}{g_o} n \exp(-E_{\ell}/kT)$ is often assumed, and where g_o just refers to the statistical weight of the ground level. In the original formulation by Karp *et al.* (1977), moreover, the number density n_e is calculated from the Saha equations by assuming an LTE.

7. Atomic properties

- **Rosseland mean opacity:** The radiative transfer in a plasma is mainly controlled by the Rosseland mean opacity and is often expressed in terms of the temperature-normalized photon energy u

$$\frac{1}{\kappa^{(\text{Rosseland})}} = \left[\frac{dB}{dT} \right]^{-1} \left[\int_0^\infty d\omega \frac{1}{[\kappa(\omega; T; ..)]} \frac{\partial B(\omega; T)}{\partial T} \right] = \int_0^\infty du \frac{1}{[\kappa(u; ..)]} \times g(u), \quad g(u) = \frac{15}{4\pi^4} u^4 \frac{\exp(-u)}{[1 - \exp(-u)]^2}.$$

- **Rosseland mean opacity:** The Rosseland opacity is defined as average of the energy density $W^{(\text{Rosseland})}(u)$, given in terms of the temperature-normalized photon energy, and divided by the expansion opacity $\kappa(u; ..)$

$$\frac{1}{\kappa^{(\text{Rosseland})}} = \int_0^\infty du \frac{W^{(\text{Rosseland})}}{\kappa^{(\text{expansion})}(u; ..)}, \quad W^{(\text{Rosseland})} = \frac{15}{4\pi^4} \frac{u^4 e^{-u}}{(1 - e^{-u})^2}.$$

$$\kappa^{(\text{Rosseland})} = \kappa^{(\text{Rosseland})}(u, \Delta\lambda; T; \rho t_{\text{obs}}, [\text{level population}]).$$

- **Rosseland mean opacity $\kappa^{(\text{Rosseland})}$:** The Rosseland opacity is the relevant quantity for describing the radiation transport in the solar convection zone.

- **Spectral *versus* Rosseland mean opacity:** Although the Rosseland opacity can be easily determined from the spectral opacity (Seaton 1987), special care is required since: (i) $\kappa^{(\text{Rosseland})} = 0$, if $\kappa(\omega) = 0$ over a finite range of frequencies; therefore, all missing contributions should be further plugged into $\kappa(\omega)$ before the averaging is made. (ii) $\kappa^{(\text{Rosseland})}$ is not additive with regard to terms from different atomic processes.

- **Rosseland mean opacity:** The contribution of strong lines upon the Rosseland mean opacity is typically small because the widths of the lines is small, when compared the separation of lines, and only a (small) fraction of the photons is eventually absorbed by the strong lines.

- **Planck mean opacity:** Similarly, the Planck mean opacity is defined as average over the energy density $W^{(\text{Planck})}(u)$ by:

$$\frac{1}{\kappa^{(\text{Planck})}} = \int_0^\infty du W^{(\text{Planck})} [\kappa^{(\text{expansion})}(u; ..) - \kappa^{(\text{scattering})}(u)]^{-1}; \quad W^{(\text{Planck})} = \frac{15}{\pi^4} \frac{u^3 e^{-u}}{(1 - e^{-u})}, \quad u = \frac{\hbar\omega}{k_B T}.$$

$$\kappa^{(\text{Planck})} = \kappa^{(\text{Planck})}(u, \Delta\lambda; T; \rho t_{\text{obs}}, [\text{level population}]).$$

- **Planck mean opacities at different temperatures:** The opacity does generally not depend much on the temperature of the ejecta of matter clouds. If the density and time is kept constant, the Planck mean opacities agree within a factor of 1.5 with each other for different temperatures.

- **Rosseland *versus* Planck mean opacities:** The spectrally-resolved Rosseland and Planck mean opacities of iron plasmas at different temperatures between a few to a few hundred eV have been found useful in studying the evolution of stars, such as the Sun. These studies refer to both, stellar envelopes as well as their interiors.
- **Gray opacity:** The (so-called) gray opacity just results from the Thomson-scattering opacity, $\kappa^{(\text{Thomson})} = 0.4(\bar{Z}/A) \text{ cm}^2/\text{g}$, i.e. if one assumes a fully ionized material (medium) with $\bar{Z} = Z$. Here, A is the atomic weight and one often simply applies $\bar{Z}/A \approx 1/2$ for most elements.

Radiative opacities computations:

- **Opacity computations:** help extract valuable information about a plasma, including the fractional distribution of different charge states and whether the plasma is within a local thermodynamic equilibrium (or not) as well as about the temperature gradient within a plasma.
- **Early opacity computations:** These computations have often used data obtained from simple atomic models. However, already Simon (1982) suggested that such simple estimates are too small by factor of 2-3 for all elements heavier than helium.
- **Opacity of r-process elements:** Among other r-process elements, the lanthanide elements are expected to have rather high optical and NIR opacities. Therefore, if lanthanides occur in some astrophysical environment, a rather red and faint emission is expected from the ejecta of neutron-star mergers, while the emission spectra are (expected to be) blue and bright for lanthanide-free ejecta ('blue kilonova').
- **Opacity Project:** This project is an international collaboration of about 25 scientists from 6 countries which started around 1982. The atomic data from this project are available in the TOPbase database, while the spectral opacities and Rosseland mean opacities are available from the OPServer at the Ohio Supercomputer Center.
- **Opacity Project:** This project is perhaps a pioneering example of what is nowadays known as **collaborative big-data science** (Mendoza 2018). This project involved the computation of large data sets by several internationally distributed research groups, which were then compiled and stringently evaluated before they became part of TOPbase.
- **Opacity Project:** The Opacity Project entailed extensive calculations of photoionization cross sections for all bound states of an atom or ion with $n \leq n_o$. In this project, the photoionization cross sections were computed for nearly 200 atoms and ions, with focus upon the astrophysical abundant elements.
- **Opacity Project:** Up to the present, the precision of the opacity computations from the Opacity Project, and even the newer OPLIB tables from Los Alamos, has raised recurrent debates which are fueled by recent comparisons between theory, laboratory experiments as well as solar and stellar observations (Mendoza 2018).

Radiative opacities computations for light and iron-group elements:

- **Computation of low- Z opacities:** A low- Z opacity model, which starts from the detailed computation of all atomic data, has been found to agree quite well with experimental measurements of the spectral opacity of aluminium at temperature $T \approx 40$ eV, and for different plasma densities.
- **Opacity of light elements ($Z < 30$):** The atomic properties of light elements are known reasonably well from experiment and many previous computations. In particular, Kurucz (1993) and Kurucz and Bell (1995) provide an extensive list of lines (with about 42 million lines and 500,000 line shifts) mainly from the iron group elements. These lists were generated by using the CATS code (Cowan 1981) and by tuning the theoretical energies semi-empirically in order to reproduce the extensive database of observed experimental level energies.
- **Opacities of iron-group elements:** Detailed supernova calculations suggest that blue-wavelengths bound-bound transitions from complex iron group elements dominate in a given frequency band over other contributions to the opacity, such as the electron-scattering, free-free, and photoionization contributions to the overall opacity. In the blue and ultra-violet region, indeed, millions of lines may contribute to the bound-bound opacity, and they often appear as a pseudo-continuum, if these lines are Doppler-broadened due to the differential velocities of the remnants.

Radiative opacities computation for lanthanides:

- **Opacity of lanthanides:** Barnes and Kasen (2013) applied the line data from the VALD database in order to study the opacity of the lanthanides and to demonstrate that these heavy elements may exhibit a much larger opacity. At present, however, the limitations of VALD does not allow to compute reliable r -process opacities over the wavelength and temperature range as required by realistic transport calculation. In particular, **VALD contains almost no lines with wavelengths greater than $1\text{ }\mu\text{m}$ (or < 1.2 eV)** and, hence, cannot be applied to compute sensible infrared opacities or emissivities of the neutron-star merger.
- **Opacity of lanthanides:** A detailed modelling of the radiative properties of lanthanides and other high- Z ions will be a long-term endeavor because of the (large) number of electrons and the shell structure of the lanthanides as well as most elements beyond.
- **Opacity calculations for the lanthanides:** For $T \approx 5,000$ K, Tanaka *et al.* (2019) predict the largest Planck mean opacities among all lanthanide elements for Pr, Nd, and Pm ($Z = 59, 60$, and 61). For all elements with even more $4f$ electrons, these Planck mean opacities then become smaller because the energy-level density decreases near to the ground level. More generally, the temperature dependence of the Planck mean opacity has been found asymmetric with regard to half-filled shells, while the number of levels is symmetric with regard to a half-filled occupation and is determined *geometrically*. See also Fig. 7.3.

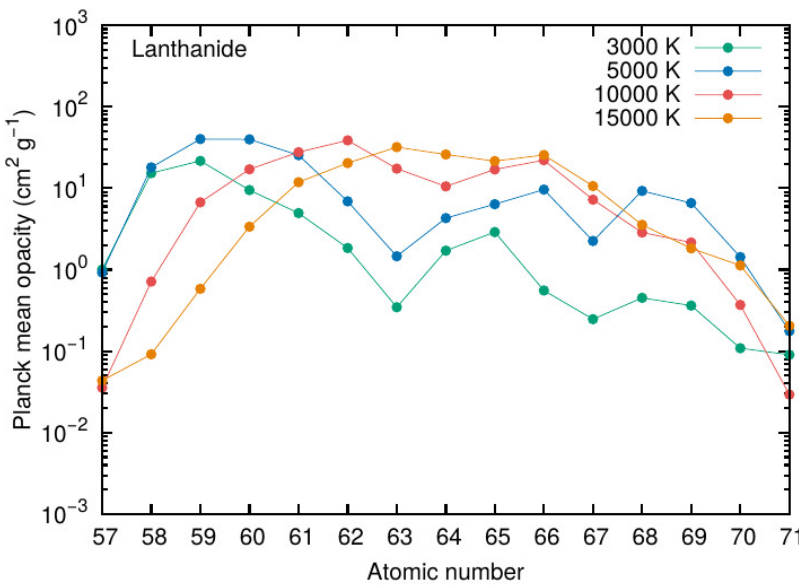


Figure 7.3.: Planck mean opacities of lanthanide elements as a function of atomic number and for selected temperatures. For lower temperature ($T < 5,000\text{K}$), the opacity decrease with the nuclear charge Z , while the opacities are largest for elements with a half-filled f -shell at temperatures $T > 10,000\text{K}$; taken from Tanaka *et al.* (2020).

- **Opacities for neutron-star mergers:** Kasen *et al.* (2013) calculated the opacity of the expanding ejecta from neutron-star mergers with line data from AUTOSTRUCTURE. These authors assumed a local thermodynamic equilibrium (LTE) and that **ions with a similar shell structure will have also similar properties**, an assumption which has not been approved so far.

Radiative opacities computation for actinides and heavy elements:

- **Opacity for U^{2+} ions:** Silva *et al.* (2022) concluded from detailed levels and oscillator-strength calculations that the opacity of U III is about an order of magnitude greater than the opacity of Nd III due to a higher density of levels in the case of the actinide. In this work, the expansion opacity of Nd III and U III was calculated individually for each ion by just assuming a cloud of those ions, a thermal population of excited states and by just comparing the density of bound-bound transitions and the opacity.

Measurement of radiative opacities:

- **Laboratory plasma:** All plasmas, that are produced in the laboratory, are generally quite far from local thermodynamic equilibrium (LTE). Therefore, the ion distribution of such laboratory plasma cannot be described by the usual Saha-Boltzmann equations, neither for selected ions nor for dealing with different charge states of the ions.
- **Z-pinch experiments:** In the laboratory, one often has a **steady-state plasma, far from equilibrium, that is formed by x-ray radiation from a Z-pinch**. In such plasma, the (incident) ambient radiation field is important in addition to the electron-collisional processes in order to determine the excitation and ionization dynamics. **Such photoionized plasmas are believed to occur also in various astrophysical situations;** in fact, Z-pinch experiments allow for the first time to compare numerical models of photoionized plasmas with experiment (Rose *et al.*, 2004).
- **Opacity measurements by Z-pinch radiation:** There are several benefits in resorting to Z-pinch radiation for opacity measurements, including relatively large cm-scale lateral sample sizes and the relatively long 3-5 ns duration of the experiments.
- **Uniform plasma density:** For a uniform density, the transmission of the sample is usually measured

$$T(\omega) = \frac{I(\omega)}{I_o} = \exp(-\rho L \kappa(\omega)),$$

and where $I(\omega)$ is the attenuated intensity of the probe (backlighter) radiation and I_o the reference intensity. **This transmission is related also to opacity by the Beer-Lambert law if the re-absorption can be neglected within the homogeneous plasma.** Here, ρ is the density of the material and L its thickness.

- **Tachocline of the Sun:** This (hyper-) surface refers to the **boundary between the convective and the radiative zone of the Sun and is determined by the spectral opacity of the plasma in this region.** The opacities of the Sun have been recently explored as the Z-machine at Sandia National Laboratory.
- **Tachocline of the Sun:** In the tachocline region, iron is responsible for about 25% of the total opacity. In 2005, a measurement of the opacity in the spectral region between 7 and 12.7 Å gave rise to values that are 30 to 400 % than those from the (best) codes.

Role of opacities for astrophysics:

- **Application of radiative opacities:** The radiative opacity of a plasma is of great significance for various research fields, such as astro and stellar physics, inertial confinement fusion or the development of x-ray lasers. Therefore, the (so-called) **Opacity Project** calculated mean — and often rather approximate — opacities for most astrophysically abundant elements. This project also led to a database of opacities.

- **Application of opacities:** Opacities are frequently applied in various research fields, such as the standard solar model (SSM), helio and astero-seismology, non-LTE 3D hydrodynamic photospheric modeling, nuclear reaction rates, solar neutrino observations, computational atomic physics as well as in plasma experiments (Mendoza 2018).
- **Effective (expansion) opacities:** In an expanding object, the frequency of photons suffers from a continuous Doppler shift with regard to the rest frame of the material, similar to the redshift of photons in the expanding Universe. Therefore, each photon has also an increased probability for interacting with an atomic line. Karp *et al.* (1977) showed that this enhanced interaction with the spectral lines of atoms and ions can be taken into account by just replacing the ordinary static opacity by an effective opacity, also known as the expansion opacity, and by applying diffusion theory.
- **Radiative opacity of iron plasma:** Since the radiative opacity of iron plasmas at high temperatures is important for astrophysics, various experiments have been carried out to accurately measure their radiative opacity during recent decades.
- **Planck mean opacities at different temperatures:** Spectral opacities are required for the modeling of astrophysically relevant plasmas under local thermodynamic equilibrium (LTE) conditions. For the computation of these opacities, the atomic structure calculations should be carried out for many (or even all) fine-structure levels and by including electronic correlations.

Average-atom model:

- **Average-atom model:** Typically opacity computations have considered a total of up to 10^8 radiative lines. Since these computations cannot so easily be extended towards high- Z elements, the average-atom model has been found a valuable alternative.
- **Average-atom model:** The average-atom is not a real entity with an integer number of bound electrons but a rather fictitious quantum system with a non-integer number of electrons. These electrons are distributed continuously among the shells in order to handle the average occupation of the shells in a (astro-physical) plasma. The main difficulty arises from finding an approximate average-atom potential, from which a set of one-electron wavefunctions are obtained by the solution of the corresponding wave equation.
- **Average-atom model:** The average-atom model predicts an increase of the low- Z opacities that has been found in line with observations of stellar pulsations. Because of the known sensitivity of the Rosseland mean opacity with regard to some "window" in the photoabsorption spectrum, however, this averaged method may be potentially inaccurate.
- **Validation of the average-atom model:** The validation of the average-atom model for plasma in different density and temperature regimes is (still) important since this model has been widely applied in radiation-hydrodynamic simulations of laboratory plasmas, and where the rate equations are coupled to the hydrodynamics both through collisional processes and through the radiation field.

7.4.k. Plasma diagnostics

Remarks and classification:

- **Physical parameters of plasma:** However, in order to determine the relevant physical parameters that describe both, the astrophysical and laboratory plasmas, i.e. its electron temperature, density distribution, ion and element abundances, etc., we need to compare the observed data to a theoretical model spectra.
- **Energy exchange:** In a plasma, in general, any collision between particles cause energy exchange and changes in the state distribution changes.
- **Laboratory *versus* astrophysical plasma:** Laboratory plasmas can differ from astrophysical sources in various ways:
 - Laboratory plasmas can be (very) short-lived so that they do not reach any statistical equilibrium.
 - Although much larger densities occur in laboratory plasma, when compared to typical astrophysical sources, by far not all lines are optically thick in such a plasma and, in particular, the **re-bound and free-free transitions (continuum radiation)** remain usually optically thin.
 - In laboratory plasma, most atomic levels are often collisionally rather than radiatively dominated.
 - The (large) density of laboratory plasma can dramatically affect the line profiles, and this should/need to be taken into account in the radiative-transfer calculations.
- **Non-local thermodynamic equilibrium (NLTE):** NLTE exists in a wide variety of astrophysical and laboratory-created plasmas. Examples of NLTE astronomical plasmas are the stellar corona, interstellar nebulae and some other low-density ionized plasmas. In the laboratory, NLTE exists in laser-produced plasmas, tokamaks and Z-pinch based experiments.
- **Stratification of the plasma:** In order to calculate synthetic spectra from laboratory plasma or expanding stars, one first needs to determine the stratification of the plasma temperature, density and velocity. This **stratification of the plasma** can be either obtained from some hydrodynamic code or from some simplified self-similar analytic model.
- **Role of helium-like ions for plasma physics:** The intensity ratio of spectral lines from helium-like ions are important for plasma diagnostics and, especially, in order to derive the electron densities and temperatures in plasma. This diagnostics is frequently applied both, in astrophysics and fusion research. Unfortunately, however, there are quite different spectroscopic notations in use in the literature for helium-like ions, which (may) hamper the quick comparison. Only rather recently, a more standard notation [cf. NIST data tables] has began to become more popular in the field.

- **Plasma as an ideal gas:** At low temperatures, a plasma is either only partly ionized or in a rather degenerate (Fermi) state. At these temperatures, the plasma is weakly coupled and can often be modeled as an ideal gas. The same applies at (very) high temperatures where the plasma resembles an ideal gas with negligible interactions among the particles. However, the ideal gas approximation does not apply for plasma in an intermediate temperature regime.
- **Plasma heating by primary electrons:** Fast electron in a plasma produce additional electrons which, again, contribute to the heating as well as electron-impact excitation and ionization. The energy distribution of the secondary electrons with energies ε_s as function of the primary electron energy ε_p has been modeled as (Kozma and Fransson, 1992)

$$p(\varepsilon_s; \varepsilon_p) = \frac{1}{J \arctan \left[\frac{\varepsilon_p - I_p}{2J} \right] \left[1 + \left(\frac{\varepsilon_s}{J} \right)^2 \right]}$$

and where J is an element-specific parameter that describes an cut-off for the release of the second electron. This cut-off J has been measured for selected elements and charge states and were determined to $J(\text{HeI}) = 15.8$ eV, $J(\text{NeI}) = 24.2$ eV and $J(\text{ArI}) = 10.0$ eV. For all other elements, Kozma and Fransson (1992) simply use $J(\text{others}) = 0.6 I_p$.

Techniques from plasma diagnostics:

- **X-ray Thomson scattering for plasma diagnostics:** In dense or compressed matter with electron densities of solids or beyond, intense x-ray can replace optical sources and can be used for plasma diagnostics.
- **X-ray interferogram for plasma diagnostics:** X-ray interferograms have been widely applied in plasma diagnostics in order to analyze and to interprete the index of refraction n as well as the electron density distribution of the plasma. While the simple free-electron model predicts an index of refraction $n < 1$, indices $n > 1$ have been observed in interferograms of an Al plasma as produced by a 14.7 nm nickel-like Pd soft x-ray laser at the Lawrence Livermore National Laboratory laser facility (Johnson *et al.*, 2006). A similar behavior was found for an Al plasma produced by a 13.9 nm nickel-like Ag laser and has been attributed to the influence of bound electrons on the optical properties of the plasma.

Interpretation of line spectra:

- **Line spectra:** More often than not, any detailed interpretation of the line spectra from laboratory plasmas and astrophysical sources has been found a great challenge since it often requires to go often beyond a local thermodynamical equilibrium (LTE) approach. If no equilibrium is reached, the spatially-dependent photon emission and absorption then need to be taken into account in the solution of the rate equations throughout the emitting medium.

7. Atomic properties

- **Line spectra:** X-ray satellites, such as CHANDRA and XMM-NEWTON have provided large amounts of high-resolution line spectra from astronomical objects, and with many of them in NLTE.
- **Astrophysical missions for x-ray emissions:** The X-ray observatories Chandra (NASA), Hinode (NASA) or XMM-Newton (ESA) were launched in order to collect high resolution x-ray spectra from various cosmic sources. From these spectra, information about the charge state distribution, temperature and relative elemental abundances can be derived, if accurate radiative and dielectronic recombination data are available.
- **Thermonuclear fusion devices:** Beryllium and boron are two key elements in the (edge) plasma of thermonuclear fusion devices. While boron is released by plasma-wall interaction processes from boronized graphites, beryllium is the suggested wall material for ITER. To model the transport in such plasma, various elastic and inelastic cross sections are required to understand the energy transport and particle loss in the plasma. Liu *et al.* (2010) studied the radiative charge-transfer process for electron energies between $10^{-5} - 0.1$ eV/u by using an optical potential method and for $0.1 - 100$ eV/u by means of a semiclassical method.

Diagnostics of astrophysical plasma:

- **Plasma in different astrophysical objects:** Hot plasmas are present in the universe in a variety of astrophysical objects, from stellar coronae to the birth of stars and up to the intergalactic medium in clusters of galaxies. The high-quality data, that have been obtained during the last few decades from space observatories like EINSTEIN, ROSAT, ASCA and SAX, enabled one to study in great detail the physical condition of several astrophysical plasmas.
- **Solar corona plasma:** The solar corona plasma is low-density plasma and is believed to be dominated by the spontaneous decay and radiative recombination. For these two processes, the corresponding decay rates are much higher than the collisional decay and three-body recombination and, hence, the plasma is not in a local thermodynamic equilibrium and cannot be described by Saha or Boltzmann equations.
- **Static stellar atmospheres:** In the standard models of static stellar atmospheres, the atomic (or ionic) populations, the radiation field, the temperature and density are calculated self-consistently by means of rate equations and radiative transfer equations but owing to certain constraints, such as statistical equilibrium, radiative equilibrium or a hydrostatic equilibrium.

Diagnostics of laboratory plasma:

- **Heat transfer:** For ITER, various concepts have been developed to reduce the peak heat at the plasma-facing components of the tokamak. Indeed, much of the current experimental and theoretical work in fusion research now focus on the question of how the heat from the plasma need to be transferred to the walls of the main and divertor chambers.

- **Heat transfer:** To analyse this heat transfer and to enroll the relative importance of the primary atomic processes, simple quasi-analytic models and refined rate coefficients and cross sections have been utilized. Important heat transfer processes refer to the radiation losses through bremsstrahlung, impurity radiation losses from the plasma edge, the charge exchange and radiation losses from hydrogen in outer layers as well as to radiation losses due to impurities in the divertor plasma.
- **Heat transfer:** In large fusion devices, such as ITER, most of the heating power strikes the divertor plate and results in a high peak-heat loads of all plasma-facing components.
- **Heat transfer:** The ITER divertor has been designed in order to enhance the charge exchange processes, hydrogen and impurity line radiation, ionization, or elastic collisions between the recycling gas and the plasma in the diverted plasma and, hence, to spread out the heat and momentum transfer over the device.
- **Simulation of emission spectra:** To simulate the emission spectra from laboratory plasma, special attention has been placed on the coupling between the ionic population and the transfer of line radiation through the plasma. Often, this coupling is taken into account iteratively by deriving the level population from the temperature, density as well as the velocity profile of a plasma. While the ion population in the plasma is computed from linearized rate equation, the **line transfer is calculated within the (so-called) core saturation approximation and with a complete frequency redistribution** (Peyrusse 1992).

Diagnostics of tungsten plasma:

- **Tungsten@ITER:** Atomic physics has been crucial for understanding the plasma-energy balance and for diagnostic development. In particular, tungsten is nowadays very frequently used on present-day tokamaks in preparation for ITER.
- **Tungsten@ITER:** Tungsten has become of high importance since it will be a major constituent of ITER plasmas. Tungsten will be applied as plasma-facing component that is able to withstand high heat loads and with a lower tritium retention than other possible materials.
- **ITER Core Imaging X-ray Spectrometer (CIXS):** The CIXS has been designed to measure the ion temperature and the motion of ITER's plasma core, based especially on the x-ray emission of neon-like W^{64+} ions (Beiersdorfer *et al.*, 2015). The emission from tungsten will be measured by extreme ultraviolet (EUV) and optical spectrometers in order to determine its concentration in the plasma and to assess the power loss and the sputtering rate of tungsten.
- **Spectra of multiply-charged tungsten:** Extensive magnetic fusion plasma studies on the spectra of multiply-charged tungsten have been carried out at the Livermore electron beam ion trap, the Sustained Spheromak Physics Experiment (SSPX), the National Spherical Torus Experiment (NSTX) and the Alcator C-mod tokamak.

7. Atomic properties

- **Ionization balance calculations:** There is currently a need for reliable ionization balance calculations since the CIXS will provide radial profiles of the ion abundance in ITER which can be used in order to extract the ion transport parameters. These parameters refer to the radial ion diffusion coefficient and the inward pinch velocities, when compared to accurate ionization balance calculations. Such ionization balance calculations are still highly non-trivial for tungsten.

Diagnostics of lanthanide ions:

- Lanthanide ions have very complex spectra owing to the presence of the open $4f$ shell that can be resolved only by high-resolution laboratory studies. Tchang-Brillet *et al.* (2018) have performed a systematic comparison and analysis of such high-resolution spectra for several lanthanide ions in the vacuum ultra-violet (VUV) region, including especially the fourth and fifth spectra and partially also the third spectra.
- The radiative properties of the lanthanide ions have numerous applications in solid-state laser materials, photonics and the lighting industry. Radiative transitions of lanthanide ions were observed in doped crystals and in solution with small shifts relative to those of the free ions.
- **Emission spectra from multiply-charged lanthanide ions:** First investigations of the spectral intensities within the ground-state $4f^n$ configurations of the trivalent lanthanides in solution have been carried out by Carnall *et al.* in the early 1960s and were supported also by calculations of transition probabilities by Judd and Ofelt.
- **Emission spectra from multiply-charged lanthanide ions:** The bright emission spectra from highly-charged ions of lanthanide elements ($Z = 57 - 71$) are known to appear in the extreme ultraviolet (EUV) or soft x-ray wavelength range due to $n = 4 - 4$ transitions of lanthanide ions in the wavelength range of 5–12 nm. These emission spectra are typically strongly affected by relativistic effects and multi-electron correlations. Likely, these emission spectra will play an important role in application to the next generation light sources for EUV lithography.
- **Emission spectra from multiply-charged lanthanide ions:** Suzuki *et al.* (2018) have systematically observed extreme ultraviolet (EUV) spectra from the highly-charged ions of nine lanthanide elements with nuclear charge $Z = 60 \dots 70$ in optically thin plasmas as produced in the Large Helical Device (LHD). The wavelengths of the main peaks in the quasi-continuum features were found to agree well previously measured singlet transitions of Pd-like ions as well as with the discrete spectral lines from Cu-like and Ag-like ions.
- **Emission spectra from multiply-charged lanthanide ions:** Charge-separated EUV spectra from Sm, Gd, Dy, Er and Yb have recently been observed also in electron beam ion trap (EBIT) facilities at higher electron beam energies (Suzuki *et al.*, 2018).
- **Hubble Space Telescope:** In astrophysics, observations with the Hubble Space Telescope of spectra of chemically peculiar stars have proven the presence of lanthanide ions up to doubly-charged ions. More recently, the shortly delayed observation of gravitational waves and

the emission of electromagnetic waves during a neutron-star merger have renewed the interest for radiative properties of higher-charged lanthanide ions.

7.4.1. Radial distribution functions for plasma and liquid models

General remarks:

- **Distribution function for plasma:** The radial distribution function for a plasma is often required and need to be calculated. In these computations, quantum effects have to be taken into account for small inter-particle separations, either by using a modified path-integral technique or, equivalently, by a summation over states, together with the assumption that the charged particles interact via a shielded Coulomb potential.
- **Distribution function for plasma:** General expressions for the radial distribution function in an electron-ion plasma outside of thermal equilibrium have been obtained in the literature in first-order of the plasma parameters.
- **Distribution functions for fluids:** Radial distribution function and static structure factors have been computed at several places in the literature. The radial distribution function can be utilized to characterize a fluid, for instance in terms of the pronounced maxima at some inter-particle distance, and followed by successive minima and maxima with reduced amplitudes.
- **Ion-electron plasma:** A plasma or a liquid metal are two fundamental examples for a mixture of ions and electrons that mainly interact via the Coulomb force. The properties of such admixtures in thermal equilibrium just depend on the temperature $T = 1/k_B \beta$ and density of nuclei n_o as well as the atomic number Z_a of these ions.
- **Ion-electron plasma:** In practice, it is difficult to describe the plasma dynamics since the ions and plasma just depend on each other: i) The internal structure of an ion need to be determined for the given plasma and ii) the plasma, i.e. the external distribution of the ions and electrons, requires to know the potential between them.

Quantal hypernetted-chain approximation:

- **Hypernetted-chain equation:** In statistical mechanics, the hypernetted-chain equation arises as a closure relation in order to solve the Ornstein-Zernike equation, i.e. a relation between the direct and total correlation functions. The hypernetted-chain equation is commonly applied in fluid theory in order to obtain, e.g. expressions for the radial distribution function.
- The hypernetted-chain approximation is an integral-equation method from statistical physics that arises from the theory of liquids.

7. Atomic properties

- A quantal version of the hypernetted-chain equation (QHNC) was derived in the literature by using the density-functional method, and extended to treat a liquid metal and a plasma as an ion-electron mixture.
- Hou *et al.* (2015) combined the average-atom model with the [hypernetted chain approximation](#) (to a so-called AAHNC approximation) in order to describe the electronic and ionic structure in the WDM regime.

7.4.m. Average-atom model for warm-dense matter

Warm-dense matter:

- **Warm-dense matter (WDM):** This term generally refers to some state of matter under plasma conditions, and which can range from condensed matter to [weakly-coupled plasmas with typical temperatures from a few to a few hundred eV as well as with densities from a few hundredths to about a hundred times of the solid density](#).
- **Model of WDM:** In modeling WDM, great challenges arise from the partial ionization of the plasma, the degeneracy of the electron states, the bound-state level shifts, the pressure ionization in plasma as well as the strong coupling of the ion-ion pairs that must all be taken into account self-consistently.
- **Equation of state:** A good understanding of the properties and behaviour of WDM, such as the equation of state, its radiati opacity or the transport properties, has been found important, for modeling for example astrophysical objects or inertial confinement fusion experiments (Hou *et al.*, 2015).
- **Electronic structure of impurities:** Studies on the electronic structure of impurities within an electron gas have been performed in the literature as function of their density and temperature. For these investigations, one need to know the [dependence of screening effects on the plasma parameters](#).
- **Friedel oscillations:** Especially at low temperatures and metallic densities, the electron density of a plasma often exhibits Friedel oscillations, similar as known also from solid-state physics.

Opacity of warm-dense matter:

- **Kubo-Greenwood formula for the photoabsorption cross section within the average-atom model:** Within the independent-particle linear-response approximation and the average-atom model, the Kubo-Greenwood formula for the photoabsorption cross section is given by (Piron

and Blenski, 2017)

$$\sigma^{(\text{photoabsorption})} = \frac{4\pi^2 \alpha \hbar \omega g_{\text{spin}}}{3} \sum_{jk} [f(\varepsilon_i) - f(\varepsilon_k)] |\langle \phi_i | \mathbf{r} | \phi_k \rangle|^2 \delta(\hbar \omega - \hbar \omega_{ik})$$

where $f(\varepsilon)$ is the Fermi-Dirac distribution, g_{spin} the spin degeneracy factor, \mathbf{r} the single-electron position operator, and where the summation over j, k runs over all bound and continuum orbitals. Only within this approximation, the photoabsorption cross section factorizes into three contributions due to bound-bound, bound-free and free-free matrix elements. Practically all opacity calculations rely on such a decomposition.

Average-atom model for WDM simulations:

- **Average-atom model:** In this model, the plasma is divided into neutral cells with each Z electrons, which are centered around a nucleus of charge Z . Using the plasma density and the atomic weight, the Wigner–Seitz (WS) radius can be readily obtained. For hot plasma, the average-atom model often leads to rather a small number of bound states that can be formed inside of the Wigner–Seitz cell.
- **Average-atom (AA) model:** This model divides the plasma into separate **neutral Wigner-Seitz cells with a nucleus of charge Z and Z free electrons**. Various versions of the AA model have been implemented in plasma physics for describing warm- and hot-dense matter and plasma.
- **Self-consistent ion-sphere model:** In this model, the Schrödinger equation is solved for all bound and free-electron states and, hence, for the electron number density. For a Fermi-Dirac distribution with chemical potential μ , this number density is given by:

$$n(\mathbf{r}) = \sum_i |\psi_i(\mathbf{r})|^2 f(\varepsilon_i; \mu).$$

- Fermi-Dirac function for chemical potential μ :

$$f(\varepsilon; \mu) = \left[\exp\left(\frac{\varepsilon - \mu}{T}\right) + 1 \right]^{-1}.$$

- **Wigner-Seitz sphere:** In plasma physics, the radius $R^{(\text{WS})}$ of the Wigner-Seitz sphere is readily given by

$$R^{(\text{WS})} = \left[\frac{3}{4\pi \rho^{(\text{medium})}} \right]^{1/3}.$$

7. Atomic properties

- **Average-atom (AA) model:** In the AA model, each ion or atom is described within a finite (ion) sphere and by using a central-field approximation for the bound electrons. For heavy atoms and ions, a (radial) Dirac equation can be applied but where the potential $V(r)$ need again to be calculated self-consistently.
- **Electron density in the AA model:** For an isolated atom or ion, the electron density is calculated in the AA model in order to include the level broadening of the energy levels within a plasma environment. This density is applied also for studying the temperature and density effects upon the electron distributions within a statistical way.
- **Radial potential in the AA model:** A radial potential in terms of the bound-electron radial density $\rho_b(r)$ and uniform electron density $\rho_{e,0} = \rho(r_b)$ has been given by (Hou *et al.*, 2015)

$$V(r) = -\frac{Z}{r} + \int d^3r' \frac{\rho_b(r')}{|\mathbf{r} - \mathbf{r}'|} + V_{xc}[\rho_b(r) + \rho_{e,0}] - V_{xc}(\rho_{e,0}) - \frac{\rho_{e,0}}{\beta} \int d^3r' C_{ee}(|\mathbf{r} - \mathbf{r}'|) h_{ie}(r') - \frac{\rho_{i,0}}{\beta} \int d^3r' C_{ie}(|\mathbf{r} - \mathbf{r}'|) h_{ii}(r')$$

but need to be better analyzed in order to understand its validity and limitations. Here, the first four terms constitute the **contributions from a single ion**: **electron-nucleus interaction, the electro-static repulsion with the other bound electrons as well as the exchange and correlation potential**, which are often evaluated by using some local density approximation. The last two terms in this expression represent the **interaction of the ion with the surrounding free electrons and with the other ions**.

- **Application of the average-atom model:** The average-atom model has been found useful for describing dense-plasma within a statistical framework. This model facilitates to compute dense-plasma opacities and conductivities, several thermodynamic properties and the equation of state. It has been applied also to estimate broadband radiative properties of dense plasmas. The average-atom model can be considered also for partially to fully ionized and moderately coupled plasmas with any degeneracy.
- **Assumptions of self-consistent ion-sphere model:** The SCF ion-sphere model is generally based on the assumptions that (i) the SCF potential is zero for $r \geq R^{(WS)}$, (ii) the charge density outside the Wigner-Seitz sphere is neutral (zero) due to a constant homogeneous positive ion distribution and that (iii) the exchange-correlation potential is also zero for $r \geq R^{(WS)}$. The first assumption (i) requires outside $R^{(WS)}$ a nearly constant electron density equal to its asymptotic value for $r \rightarrow \infty$. The assumption (iii) requests that $V^{(\text{direct})}(R^{(WS)}) = V^{(xc)}(n(R^{(WS)})$. Moreover, the chemical potential μ is found from the neutrality condition for the total charge inside the Wigner-Seitz sphere.
- **Electron number density in terms of the one-electron orbitals:** By assuming the standard normalization for the bound and continuum

orbitals (per unit energy), the electron number density $n(\mathbf{r})$ can be written in terms of the radial orbitals as

$$\begin{aligned} n(\mathbf{r}) &= n^{(\text{bound})}(\mathbf{r}) + n^{(\text{free})}(\mathbf{r}) \\ n^{(\text{bound})}(\mathbf{r}) &= \sum_{n\ell} f(\varepsilon_{n\ell}; \mu) \frac{2(2\ell+1)}{4\pi} P_{n\ell}^2(r), \quad n^{(\text{free})}(\mathbf{r}) = \text{analogue.} \end{aligned}$$

The neutrality condition of the total charge inside of the Wigner-Seitz sphere involves the summation over the bound- and free-electron part of the spectrum. For the free-electron spectrum, special care should be taken with regard to the asymptotic behaviour, which does not occur for a finite basis-set representation.

Spectral emission from plasma in a non-local thermodynamic equilibrium (NLTE):

- **NLTE versus LTE:** In a non-local thermodynamic equilibrium (NLTE), in which the levels of each configuration are still considered to be in LTE, the population N_a of a given electron configuration follows as solution of a system of rate equations

$$\frac{\partial N_a}{\partial t} = -N_a \sum_b R_{ab} + \sum_b R_{ba} N_b,$$

and where R_{ab} is a global (averaged) transition rate that connects the configurations a and b .

- **NLTE versus LTE:** Many collisional-radiative models, that are applied for a realistic modelling of NLTE line emission, often account for several individual levels explicitly, that occur in the spectroscopic observations, while the levels of other configurations are simply lumped together. These **superlevels** have no spectroscopic meaning but are included to just describe the population kinetics.

Conductivity, dielectric function, index of refraction:

- **Complex dielectric function:** The complex dielectric function is related to the complex conductivity $\sigma(\omega)$ through the relation (and within the free-electron limit)

$$\epsilon_r(\omega) = 1 + i \frac{4\pi \sigma(\omega)}{\omega}, \quad \epsilon_r \rightarrow 1 - \frac{4\pi n_e e^2}{m \omega^2}.$$

7. Atomic properties

- **Index of refraction:** The complex index of refraction is related to the relative dielectric function ϵ_r by $n + i\kappa = \sqrt{\epsilon_r}$. This leads to the following expressions

$$n(\omega) = \sqrt{\frac{\sqrt{[\Re \epsilon_r(\omega)]^2 + [\Im \epsilon_r(\omega)]^2} + \Re \epsilon_r(\omega)}{2}}, \quad \kappa(\omega) = \sqrt{\frac{\sqrt{[\Re \epsilon_r(\omega)]^2 + [\Im \epsilon_r(\omega)]^2} - \Re \epsilon_r(\omega)}{2}}.$$

7.4.n. X-ray Thomson scattering for warm-dense matter

X-ray Thomson scattering:

- **X-ray Thomson scattering:** Temperature, density and the distribution of ionization states are important parameters to characterize dense plasma. X-ray Thomson scattering refer to measurements in which x-rays penetrate dense or compressed matter and are analyzed how the transmitted radiation depend on the plasma parameters above. Moreover, x-ray scattering has been applicable as tool to resolve the equation of state or the structure factors of two-component dense plasma.
- **Thomson scattering:** Originally, Thomson scattering was observed in 1906 and referred to the (elastic) scattering of optical light from free electrons. The frequency of the scattered light remains unchanged if the electron velocity does not change. In dense plasma, high x-ray probe energies of $E \sim 10$ keV are needed to penetrate through dense plasma with densities $\rho \lesssim 10^{-26}$ cm⁻³. Thomson scattering has been used as plasma-diagnostic technique in order to measure collective and noncollective phenomena in laboratory plasma. Typically, the scattered (transmitted) radiation is measured with detectors at a distance that is much larger than the extent of the plasma. Especially, various XFEL laser facilities have been applied recently to probe dense plasmas produced in compressed matter experiments.
- **Classical Thomson scattering cross section:** With the classical electron radius, the (classical) Thomson scattering cross section is (photon-) energy independent and can be written as

$$\sigma^{(\text{Thomson})} = r_e^2 = 0.665 \times 10^{-24} \text{ cm}^2.$$

This cross section need to be modified for high-energy γ -ray photons, strong magnetic fields and/or under intense radiation.

7.4.o. Equation-of-state relations for astro physics and condensed matter

Equation-of-state:

- **Equation-of-state relations:** More often than not, the equation-of-state just refers to some particular pressure-density or pressure-temperature relation for matter under (more or less) extreme conditions.
- **Equation-of-state relations:** When the atomic density is rather low, we can deal with isolated atoms that are in equilibrium with the surrounding free electrons, while the statistical or Thomas-Fermi-Dirac model has been found useful at (very high density).

Lberman's self-consistent model:

- **Lberman model:** Liberman (1979) describes a model for condensed matter in which the ions surrounding a particular atom are replaced by a positive charge distribution that is constant outside of a sphere containing the atom and zero inside. This model enables one to separate the quantities that pertain to the atom from those of the electron gas (in which the atom is imbedded) and, hence, to derive the desired equation-of-state data.
- **Lberman model:** The model assumes that there are locally sufficient electrons near to the atom in order to give overall electrical neutrality together with the (required) electrical neutrality inside the sphere.
- **Lberman model:** Instead of a – more natural – polyhedral cell, and which are surrounded by other identical cells, a nearly equivalent spherical cell is assumed in Liberman's model, and surrounded by a uniform electron gas. The density of this electron gas is the same as the mean density of ionic charges. Therefore, the electron gas outside will neither alter the charge distribution inside the cell (if its density is correctly chosen), nor will the atom affect the electron gas outside of the cell.

7.4.p. Radiation damage of DNA by electron impact

Radiation damage of DNA:

- **Radiation damage:** This term often refers to the damage of biological material on rather short time scales, i.e. reactions and processes that occur within ns or even less following the interaction of high-energetic light or particles with a living cell. These initial events may ultimately lead to the collapse of such cells. In practice, they result in the death of the individual cells within hours or days but may affect the matter also on much longer time scales.

7. Atomic properties

- **Low-energy electrons (LEE) that interact with the DNA:** The absorption of high-energetic photons by biological matter often leads to low-energy electrons (LEE) that interact with the DNA. These LEE can cause specific resonant processes and may lead eventually either to single- or double-strand breaks in DNA materials, to the damage of its molecular components and possibly even to biological apoptosis (Bacarelli *et al.*, 2011).
- **Energy deposition by LEE:** Several theoretical and computational approaches have been developed in order to explore the molecular processes that occur in the various steps of the energy deposition by LEE.
- **Radiative background on Earth:** In general, any exposure of living beings to high-energy radiation (photon or particles) may result into serious effects, although everybody is typically exposed to some constant dosage of high-energy radiation due to natural radio-activity as well as medical treatments. Indeed, a constant background of low-intensity but high-energy radiation is found all over the Earth and arises from cosmic radiation and radioactive ^{222}Rn isotopes as α -decay product of radioactive uranium isotopes on earth (Bacarelli *et al.*, 2011).

Electron-molecule dynamics:

- **Computation of electron-impact processes:** To understand the electron-impact of bio-molecules, a quite sizeable computational machinery need to be developed. The multiple inelastic scattering of these electrons typically result in a re-distribution in the energy content and may then lead to a fragmentation as well as the excitation of various vibrational modes.

7.4.q. Binding energies and quantum defects of Rydberg atoms

Rydberg matter:

- **Application of Rydberg matter:** In Rydberg matter, the strong interaction between individual Rydberg atoms leads to a number of exciting applications in quantum information science, quantum simulation and ultracold chemistry (Weber *et al.*, 2017). All these applications benefit from the quite simple fine-tuning of the strength and the angular dependence of Rydberg interactions, if appropriate Rydberg states are chosen and/or external electric and magnetic fields are applied.
- **Rydberg matter:** Rydberg atoms are explored for several decades along with the progress in laser technology. If two (neutral) atoms are well separated with negligible overlap of their wave functions, they will mainly interact via their electrostatic interaction due to their (induced) dipoles. This interaction can be most readily described by means of a chosen multipole expansion in spherical coordinates, and by making especially use of the leading dipole-dipole interaction term. For well-separated atoms, this dipole-dipole term also causes the widely-studied van-der-Waals interaction in gases and fluids.

- **Rydberg blockade:** Near to an excited Rydberg atom, the so-called **Rydberg blockade prevents other atoms to be excited to the same Rydberg level by using a given laser (frequency)**. This blockade has been observed in ultracold atomic ensembles within the frozen Rydberg-gas regime, both in bulk ensembles as well as in small systems, in which only a single excitation becomes possible (Weber *et al.*, 2017).
- **Rydberg dressing:** This term refers to modifications in the interaction of ultracold atoms in their ground state, if a small admixture of Rydberg atoms are located nearby. By choosing a particular Rydberg state, the anisotropy of the Rydberg interaction can then be mapped upon the – normally isotropic – interaction of the ultracold atoms.
- **Interaction Hamiltonian of two Rydberg atoms:** In the Born-Oppenheimer approximation, the corresponding two-atomic Hamiltonian

$$\mathbb{H}(R) = \mathbb{H}^{(\text{atoms})} + \mathbb{H}^{(\text{dipole-dipole})}(R)$$

where $\mathbb{H}^{(\text{atoms})}$ is determined by the energies of the unperturbed Rydberg states, while $\mathbb{H}^{(\text{dipole-dipole})}(R)$ describes the interaction of the two Rydberg electrons, the interaction among the ionic cores as well as the interaction between each Rydberg electron with the other ion core. The interaction Hamiltonian $\mathbb{H}^{(\text{dipole-dipole})}(R)$ is usually written in a multipole expansion.

- **Short- *versus* long-range interactions:** In the past, the short-range interactions have been controlled in various experiments, while the long-range interactions could not be steered to easily in many-particle physics. An easy access to the long-range interactions will open new avenues for many-body physics. Rydberg atoms are particularly well suited to this goal because the van-der-Waals forces between them are many orders of magnitude larger than those between ground-state atoms (Schauß *et al.*, 2012).
- **Rydberg blockade:** A dipole blockade of two interacting atoms prevents the simultaneous Rydberg excitation of two close-by atoms. This Rydberg blockade can be utilized to implement fast two-qubit quantum gates.

Scaling of Rydberg atoms:

7. Atomic properties

- Scaling of Rydberg atoms: (Lebedev and Beigman, 1998)

| Property | Scaling | Short explanation |
|----------------------|--|---|
| Radius | $r_n \sim \frac{n^2}{Z} a_o$ | Radius of a Rydberg atom as defined by its (Rydberg) electron. |
| Geometric area | $A_n \sim \pi \frac{n^4}{Z^2} a_o^2$ | Geometric cross section of a Rydberg atom. |
| Period of electron | $T_n \sim \frac{n^3}{Z^2} 2\pi \frac{a_o}{v_o}$ | Period of an electron in a semi-classical interpretation, and where $v_o = 2.188 \cdot 10^8 \text{ cm s}^{-1}$ is the mean velocity of a $1s$ electron in hydrogen. |
| Velocity | $v_n \sim \frac{Z}{n} v_o$ | Velocity of the Rydberg electron that is much smaller than the velocity of the ionic core electrons. |
| Energy | $E_n = -\frac{Z^2}{2n^2}$ Hartree | From these level energies, the ionization potential I_n as well as the transition frequency $\omega_{n,n\pm 1}$ and wavelength $\lambda_{n,n\pm 1}$ to neighbored levels can be easily derived. |
| Statistical weight | $g_n = 2 \sum_{\ell=0}^{n-1} g_\ell = 2n^2$ | Number of (magnetic) substates of shell n . |
| Density of states | $\rho(E_n) = \frac{n^5}{Z^2} \text{ Rydberg}^{-1} = \frac{2m^{3/2} Z^3 e^6}{\hbar^3 (2 E_n)^{5/2}}$ | Density of states per unit energy interval |
| Transition frequency | $\omega_{n,n\pm 1} \approx \frac{Z^2}{\hbar n^3}$ Hartree | Characteristic transition energy between neighbored levels. |
| Transition frequency | $\omega_{n,J \rightarrow J'} \approx \frac{\alpha^2 Z^4}{2\hbar n^3 \ell(\ell+1)}$ Hartree | Characteristic transition energy between fine-structure levels of the same shell n . |
| Fine structure | $E_{nJ} = -\frac{Z^2}{2n^2}$ Hartree + $E_{nJ}^{(1)}$ $E_{nJ}^{(1)} = -\frac{\alpha^2 Z^4}{2n^3} \left(\frac{1}{j+1/2} - \frac{3}{4n} \right)$ | Characteristic fine-structure splitting of Rydberg electrons. |
| Radiative lifetime | $\tau_n \approx \frac{n^5}{3A_0 Z^4 \ln(n/1.1)}$ $A_0 = \frac{8\alpha^3 (v_o/a_o)}{3\pi \sqrt{3}}$ | Radiative lifetime of a Rydberg electron in shell n , avaraged over all magnetic substates $ \ell m\rangle$. This averaged lifetime is based on all $n\ell \rightarrow n', \ell' \pm 1$ transitions, and where $A_0 \approx 7.9 \cdot 10^9 \text{ s}^{-1}$ refer to the characteristic Einstein coefficients for $2p \rightarrow 1s$ transition in hydrogen. |

- Radiative lifetime of Rydberg electrons: In Rydberg atoms, the most efficient $n\ell \rightarrow n', \ell' \pm 1$ transitions occur for low n' because of the energy scaling of the transition rates $\sim (\Delta E)^3$ and to neighbored levels with $n' = n - 1$. Therefore, the radiative lifetime of Rydberg electrons increases drastically with n and becomes larger than 10 sec for $n \gtrsim 100$.
- Binding energies and quantum defects of Rydberg atoms: For a Rydberg atom with N electrons in its ionic core, the binding energy of

the Rydberg electron is given by

$$E_{n\ell} = -\frac{(Z-N)^2}{2(n-\delta)^2}, \quad n \gg 1.$$

- **$N+1$ -electron Hamiltonian for Rydberg atoms:** For an ionic core with N electrons, the non-relativistic $N+1$ electron Hamiltonian can be written as

$$H = H_o + V = H^{(\text{ionic core})} + \frac{p^2}{2} - \frac{(Z-N)^2}{r} + \sum_{j=1}^N \left(\frac{1}{|\mathbf{r} - \mathbf{r}_i|} - \frac{1}{r} \right)$$

$$\rho^{(\text{ionic core})}(r \gg 1) = A r^{2u} e^{-2ar}, \quad a = \sqrt{2E_s}, \quad u = \frac{Z-N+1}{a} - 1,$$

where E_s is the binding energy of the least-bound core electron and A the coefficient of the asymptotic density of the core ion.

- **Penetration energy for Rydberg atoms:** The (so-called) penetration energy refers to the first-order energy shift that arises from the perturbation V in the $N+1$ -electron Hamiltonian above (Lebedev and Beigman, 1998)

$$E^{(\text{penetration})} = \int d^3r d^3r' |\psi(\mathbf{r})|^2 \left[\frac{1}{|\mathbf{r} - \mathbf{r}'|} - \frac{1}{r} \right] \rho^{(\text{ionic core})}(r') = \int d^3r |\psi(\mathbf{r})|^2 V^{(\text{penetration})}(r)$$

$$\approx - \left(\frac{2\pi A}{a^3} \right) \frac{2^{2\ell} (Z-N)^{2\ell+3} (n+\ell)! \Gamma(2\ell+2+2u)}{n^{2\ell+4} (n-\ell-1)! (2\ell+1)! \Gamma(2\ell+2)}$$

$$\times \left[2(2u+1) + 2a \frac{(2\ell+2+2u)}{2a + 2(Z-N)/(\ell+1)} \right] \left(2a + \frac{2(Z-N)}{\ell+1} \right)^{-2\ell-2-2u}$$

$$\approx - \left(\frac{\pi A}{a^3} \right) \left[\frac{(n+\ell)! (\ell+1)^{2u} (Z-N)^{2\ell+3}}{n^{2\ell+4} (n-\ell-1)! (2\ell+1)!} \right] \left[\ell + 2 + 3u - \frac{(Z-N)}{a} \right] \left(a + \frac{(Z-N)}{\ell+1} \right)^{-(2\ell+2+2u)} \quad \text{for large } \ell.$$

Here, $\psi(\mathbf{r})$ describes the hydrogenic wave function of the Rydberg electron for an ionic core of charge $Z-N$ with a charge density $\rho^{(\text{ionic core})}(r)$.

7.4.r. Radiative transitions and form factors of Rydberg atoms

Oscillator strength and radial integrals of hydrogenic ions:

- Relation between oscillator strength and radial integrals: The absorption oscillator strength between two hydrogenic levels $f(n\ell \rightarrow n'\ell')$ can be readily expressed in terms of the energies (in Hartree) and the radial integrals $\langle n\ell | r | n'\ell' \rangle$ as

$$f(n\ell \rightarrow n'\ell') = \frac{2}{3} \frac{\max(\ell, \ell')}{2\ell + 1} \frac{E_{n'\ell'} - E_{n\ell}}{\text{Hartree}} |\langle n'\ell' | r | n\ell \rangle|^2, \quad \langle n'\ell' | r | n\ell \rangle = \int_0^\infty dr P_{n'\ell'}(r) r P_{n\ell}(r)$$

- Radial transition integral with hydrogenic wave functions for bound-bound transitions: For $n' \neq n$, one finds (Lebedev and Beigman, 1998)

$$\begin{aligned} \langle n'\ell' | r | n\ell \rangle &= \frac{a_o}{Z} \frac{(-1)^{n'-\ell} (4nn')^{\ell+1} (n-n')^{n+n'-2\ell-2}}{4(2\ell-1)! (n+n')^{n+n'}} \left[\frac{(n+\ell)! (n'+\ell-1)!}{(n'-\ell)! (n-\ell-1)!} \right]^{1/2} \\ &\times \left\{ F \left(-n+\ell+1; -n'+\ell; 2\ell; -\frac{4nn'}{(n-n')^2} \right) - \left(\frac{n-n'}{n+n'} \right)^2 F \left(-n+\ell-1; -n'+\ell; 2\ell; -\frac{4nn'}{(n-n')^2} \right) \right\} \end{aligned}$$

$$\langle n, \ell-1 | r | n\ell \rangle = \frac{a_0}{Z} \frac{3n \sqrt{n^2 - \ell^2}}{2}$$

$$\sum_{n'} |\langle n', \ell-1 | r | n\ell \rangle|^2 = \sum_{n'} |\langle n', \ell+1 | r | n\ell \rangle|^2 = \frac{a_o^2}{2Z^2} n^2 (5n^2 + 1 - 3\ell(\ell+1)).$$

- Radial transition integral with hydrogenic wave functions for bound-free transitions: With the generalized principal quantum number $\nu = \sqrt{Z^2/\varepsilon}$ (from the non-relativistic theory: $\varepsilon_n = -Z^2/n^2$ for bound electrons), these bound-free transition matrix elements can be

written as (Lebedev and Beigman, 1998) as

$$\begin{aligned} \langle \varepsilon \ell' | r | n\ell \rangle &= \frac{a_o}{2} \frac{\nu^2}{Z^2} c_o \frac{\exp(-2\nu \arctan(\frac{n}{\nu}))}{\sqrt{1 - e^{-2\pi\nu}}} \left[\frac{4\nu n}{n^2 + \nu^2} \right]^{\ell_>+1} (1 - z)^{(\ell_>+1-\nu)/2} \\ &\quad \times \prod_{s=1}^{\ell'} \sqrt{s^2 + \nu^2} \left[F(\ell_> + 1 - i\nu, -n + \ell + 1, 2\ell_>, z) - \frac{1}{1-z} F(\ell - i\nu, -n + \ell_> + 1, 2\ell_>, z) \right] \\ \ell_> &= \max(\ell, \ell'), \quad \nu^2 = \frac{Z^2}{\epsilon}, \quad z = \frac{4i\nu}{(n + i\nu)^2}, \quad \ell' = \ell \pm 1 \\ c_o &= \frac{i^{\ell_>-\ell} (-1)^{n-\ell_>}}{4(2\ell_>+1)!} \left[\frac{(n+\ell)!}{(n-\ell-1)!} \right]^{1/2}. \end{aligned}$$

- **Collisions of Rydberg atoms:** The collision of Rydberg atoms and ions with electrons at different velocity as well as with neutral atoms has attracted much interest in astrophysics and elsewhere (Lebedev and Beigman, 1998). Unfortunately, however, the language in this field is quite different from what is used in atomic-structure theory, and will first require a honest discussion to overcome the quite technical language presented that often occurs so far.

7.4.s. Endohedrally confined atoms

Endohedrally confined atoms:

- **Endohedrally confined atoms, A@C₆₀:** Experimentally, atoms can be inserted into the fullerene cage by applying rather high pressures and temperature like in a *brute-force* implantation. Under these conditions, one of the carbon-carbon bonds of the C₆₀ cage may break and allow the atom to enter the cage, forming a stable endohedral system. Endohedrally confined atoms exhibit interesting features and may have potential applications in superconductivity material science or for developing quantum technologies.
- **Metallofullerenes:** La@C₆₀ is one of the synthesized metallofullerenes that may exhibit large relativistic splittings. Other known and experimentally isolated metallofullerenes are Be@C₆₀ and Ba@C₆₀.

7.4.t. Exotic atoms and ions

Muonic atoms and ions:

- **Muonic atoms:** When a muon is captured by the nucleus, it generally forms a hydrogen-like muonic ion, although it often remains still surrounded by other atomic electrons.
- **Muonic hydrogen:** In muonic hydrogen, the electron is replaced by a muon μ with a 200 times larger mass. This large mass results in orbits that are 200 times closer to the nucleus, when compared to the electron in regular hydrogen.
- **Muonic hydrogen:** Because of the finite extent of the proton, muons in their s -state have therefore some enhanced probability to be inside the proton, and where it sees also a slightly reduced electric charge of the proton. Therefore, the muon is less bound as larger the proton is.
- **Transition energies in muonic atoms:** Measurements of the transition energies in muonic atoms help determine nuclear parameters, such as charge radii, quadrupole moments and magnetic hyperfine constants. One of the most precise measurements of the nuclear root-mean-square radius by means of muonic atoms refer to the radius of ^{208}Pb at the 0.2 % level.
- **Muonic atoms:** In muonic atoms, the effective Bohr radius of the bound muon is reduced by more than an order of magnitude (or even a factor ~ 200 for its ground state), increasing the (charge) density by more than three orders of magnitude and, hence, the overlap of the muon with the nucleus. Therefore, QED contributions play a very crucial role in the spectroscopy of muonic hydrogen.
- **Nuclear polarization:** Atomic precision spectroscopy provides access also to the (internal) nuclear dynamics since the electronic motion leads to a polarization of the nucleus, and which can be expressed in terms of real or virtual nuclear electromagnetic excitations. Such a polarization plays an important role in muonic atoms but also contributes to the binding energies (ionization potentials) of highly-charged ions.

Coulomb capture of muons:

- **Frequently considered ℓ -subshell distributions for the capture of muons:** Several types of initial distributions have been considered in the past years, together with the fit parameters a, b (Hartmann *et al.*, 1982)
 1. Statistical distribution: $P^{(\text{initial})}(n_o\ell) \propto (2\ell + 1)$
 2. Modified statistical distribution: $P^{(\text{initial})}(n_o\ell) \propto (2\ell + 1) \exp(a\ell)$
 3. Uniform distribution: $P^{(\text{initial})}(n_o\ell) \propto \text{const.}$
 4. Linear distribution: $P^{(\text{initial})}(n_o\ell) \propto 1 + b\ell; \quad P^{(\text{initial})}(n_o\ell) \propto \ell$.

X-ray cascades from muonic atoms:

- **X-ray intensities from muon capture:** Typically, the observed x-ray intensities are compared to cascade computations in which the captured muon is initially distributed by $P^{(\text{initial})}(n_o\ell)$ into a fixed shell n_o but for different subshells $(n_o\ell)$. These initial distributions are often adjusted rather arbitrarily in order to achieve reasonable agreement between experiment and calculation for the observed x-ray lines. These distributions can then be compared also to those for the Coulomb capture but where further assumptions about the cascade must be made. Until the present, all these simulations and comparisons seem to follow rather simple models.
- **Muonic cascade computations:** Even if only electromagnetic interactions are assumed for the cascade, several difficulties occur in the associated cascade calculations (Hartmann *et al.*, 1982)
 - (i) The number of electrons, that are available for autoionization (electron emission) during the various steps of a cascade, is not well known.
 - (ii) Little is known about the role of the electronic screening during the radiative stabilization of the muons. In some early stage of the cascade, in particular, a number of second-order electron emission processes may occur and may modify significantly the subsequent x-ray emission.
 - (iii) All Auger rate calculations are performed in a rather simple **penetration model**, since parts of the electron density lie inside of the muon orbit, this model might not be enough.

7.4.u. Precision spectroscopy of hydrogen-like and few-electron ions

Spectroscopy:

- **Precision spectroscopy of helium-like ions:** The spectroscopy of highly-charged helium-like ions currently provides (one of) the most stringent high- Z tests of different QED contributions, including virtual two- and three-photon exchange terms. For Ti^{20+} ions, however, a significant 3σ discrepancy was found by Gillaspy and coworkers (Gillaspy, 2014) with regard to advanced computations, and quite in contrast to some earlier measurement by Kubicek *et al.* (2010).
- **Precision spectroscopy of helium-like ions:** For medium and highly-charged helium-like ions, a fundamental systematic error may possibly arise from double charge exchange (DCX) since this *double capture* may give rise to satellite shifts of the observed lines shapes (Gillaspy,

7. Atomic properties

2014). So far, very little effort has been undertaken to explore these DCX contributions, though it might apply to a wide range of experiments with helium-like ad few-electron ions.

- **Precision spectroscopy of helium-like ions:** In an EBIT, helium-like ions are produced from a (neutral) gas that is injected into the trap. Hereby, the excitation of the considered resonance transition can proceed via different channels: (i) the electron-impact excitation of already helium-like ions, (ii) the electron capture into initially hydrogen-like ions or (iii) by various higher-order excitation and/or capture processes. Under typical EBIT condition, the electron-impact excitation is usually dominant by a factor 3 or more, and this factor has been estimated to be rather independent for a wide range of gas-injection pressures (Gillaspy, 2014).
- **Precision spectroscopy of helium-like ions:** Apart from the single-electron capture, the capture of two electrons (or the *so-called* double-charge exchange) is not negligible and might affect the spectroscopy of some considered x-ray (resonance) line. Since the Einstein coefficient $A_{ik} \propto \omega_{ik}^3 \propto n^{-3}$ scale inversely with the third power of the principal quantum number, electrons in rather high- n shells may survive the radiative decay cascade of the other electron by staying in some outer shell, although these excited electrons than give rise to small line shifts that are not so easy to detect.

Highly-charged ions in storage rings:

- **Production of bare uranium ions at GSI Darmstadt:** A four-step procedure is applied at GSI Darmstadt to produce bare uranium ions in the ESR: (1) the ion source gives initially rise to U^{4+} ions; (2) the acceleration to 1.4 MeV/u and collision with a N_2 gas target yields U^{28+} ions; (3) further acceleration to 11 MeV/u and collision with a C solid target yields U^{73+} ions; (4) further acceleration to > 300 MeV/u and collision with a Cu solid target (stripper foil) finally results into the U^{92+} ions.
- **Ions in storage rings:** An excellent vacuum system with an ultra-high vacuum (UHV) of better 10^{-11} mbar is usually required in order to store (keep) the ions for minutes and longer. In addition, ion cooling is generally needed in order to enhance the phase space density of the ions.

7.4.v. Spectroscopy of lanthanides and actinides: Open *f*-shell elements

Spectroscopy of lanthanides:

- **Laser spectroscopy of atomic promethium ($Z = 61$):** Promethium differs from other elements by its radioactive nature and complex atomic spectrum, which make measurements to a real challenge. Along its isotopic chain, moreover, a strong deformation of the nuclei (wrt. a

spherical shape) is expected for the neutron-deficient isotopes. For the neutron-rich isotopes, moreover, a shape transition is predicted for the neutron numbers $N > 88$. Long-lived Pm isotopes in relevant quantities can be produced today by modern cyclotrons, if tuned to the proper activity.

Spectroscopy of actinides:

- **Laser spectroscopy of atomic actinium ($Z = 89$):** Actinium is the first element of the actinide series; its longest-lived isotope ^{227}Ac has a half-life time of $\tau_{1/2} \approx 22$ years and is found in trace amounts due to the decay of natural ^{235}U . Various actinium isotopes have been produced in nuclear reactors and applied in radiotherapy, thermoelectric devices, tomography and elsewhere. The isotope ^{225}Ac is an α -emitter and has a half-life $\tau_{1/2} \approx 10$ days. ^{227}Ac has been applied also as tracer for deep sea-water circulation (Zhang *et al.*, 2020).
- **Difficulties with open f -shell elements:** Apart from (i) strong relativistic and quantum-electrodynamical (QED) contributions to the level structure in all medium and heavy elements, difficulties arise especially from (ii) the nearly-degenerate and overlapping configurations, beside the spectroscopic nominated one, as well as (iii) the large *number* of electrons. All these difficulties have to be taken into account in *ab-initio* computations for explaining the low-lying levels of such elements. Therefore, the excitation energies and properties of open f -shell elements are not (yet) well understood, even if quite large computations have become feasible today.

7.4.w. Spectroscopy of (super-) heavy elements

Super-heavy nuclei:

- **Radioactive isotopes & island of stability:** All nuclei with $Z > 98$ have typically rather short lifetimes from fractions of a second to, say, hundreds of days. For the super-heavy nuclei ($Z > 104$), in contrast, an **island of stability** has been hypothetically proposed several decades ago, mainly based on quite limited nuclear structure computations at that time. In particular, the **double-magic flerium nucleus with $Z = 114$ and $N = 184$** is expected to be more stable (than other super-heavy nuclei), because both protons and neutrons form closed shells for this isotope. Such a **weakly-stable island may include also the elements Ubn, Ubh as well as some other isotopes**. — In practice, however, no (nearly-) stable super-heavy nuclei are nowadays expected anymore.
- **Magic numbers:** For spherical, super-heavy nuclei, the **magic neutron number $N = 184$** is supposed quite generally, while several **magic proton numbers $Z = 114, 120, 126$** are still discussed in the literature. Further magic number from the literature are: $Z = 122$ and $N = 172, 178, 182, 194$, respectively.

7. Atomic properties

- **Neutron-poor isotopes:** Until the present, all synthesized superheavy nuclei ($Z > 104$) are neutron-poor, i.e. with significantly less neutrons than expected for reasonably stable nuclei. For example, the heaviest synthesized flerium isotope, ^{292}Fl , still miss 6 neutrons to the (expected) $N = 184$. In general, a larger neutron number help compensate the strong Coulomb repulsion among the protons.
- **Oganesson (Og):** At present, oganesson (Og, $Z = 118$) is the heaviest element in the Periodic Table that belongs to the noble gases (group 18) and completes the seventh period of elements. Only a very few Og nuclei have been successfully produced by (nuclear) collisions and gave rise to the half-life estimate $0.69_{-0.22}^{+0.64}$ ms for ^{294}Og . Simulations have shown that Og, at room temperatures, is expected to be a solid with melting point of ≈ 325 K (Smits *et al.*, 2020).
- **7p shell elements:** Since around 2000, the six elements Nh, Fl, Mc, Lv, Ts and Og have been added to the periodic table, all with a partly (or total) filled 7p shell in the 7-th period. All presently known isotopes of these elements are short-living and are created individually with typical production rates of one (or a few) atom per week, and sometimes even less. All these elements are characterized by (very) strong relativistic effects. For example, flerium (Fl) is expected to be inert due to a closed $7p_{1/2}$ subshell and its large separation from the $7p_{3/2}$ subshell.
- **Production of super-heavy elements:** The production rate of (super-) heavy elements at nuclear reactor typically decreases with increasing Z because of (i) the limited neutron flux and (ii) fast fission processes. While milligram probes can still be breded for californium (Cf, $Z = 98$), only nanogram probes were made available for fermium (Fm, $Z = 100$). For all element *beyond* fermium in the periodic table, on-line reactions are needed, as available at large accelerator facilities. To achieve projectile currents of μA , these accelerator need to be combined with thin-target production techniques (Laatiaoui and Raeder, 2022).

Laser spectroscopy of (super-) heavy elements:

- **Laser spectroscopy for (super-) heavy elements:** While laser spectroscopy offers great precision $\sim \mu\text{eV}$, it usually requires prior knowledge about the level structure and allowed transitions of the elements that need to be synthesized by nuclear fusion reactions at large accelerator facilities.
- **Isotope shifts of superheavy elements ($Z > 104$):** Until the present, isotope shifts have been measured for the (heavy) elements Pu, Am, Cm and No, while no experimental data are available near to flerium or other super-heavy isotopes.
- **Laser spectroscopy for (super-) heavy elements:** Chhetri *et al.* (2018) applied laser spectroscopy on an atom-at-a-time scale in order to probe the optical spectrum of **neutral nobelium near the ionization threshold**. These measurements pave the way for high-precision spectroscopy of the atomic properties of heavy elements and also provide a benchmark for state-of-the-art atomic computations, including many-body, relativistic and QED contributions at an equal footing.

- Theoretical ionization potentials for (super-) heavy elements: For neutral nobelium, in particular the intermediate Hamiltonian Fock-space coupled-cluster (IHFSCC) and configuration interaction with linearized single-double coupled-cluster computations were found to agree within $\sim 2\%$ with the observed ionization potential, while larger deviations occur for the $7s6d\ ^3D_3$ excitation energy.

7.4.x. Electronic structure and properties of quantum dots

Electronic-structure calculations:

- Electronic structures of the quantum dots: Quite similar to atoms, the structures of quantum dots is often described in terms of single-particle states as well as the Coulomb interaction between these states.
- Electronic structures of quantum dots: In addition to quantum dots of different size (and number of electrons), these dot structures have been studied especially with regard to external perturbations, such as electron-phonon interactions, a magnetic or electric field, or for their dependence on the temperature, impurity and pressure. Various models were developed in order to understand the role of different confinement potentials, including disk-like (cylindrical), rectangular, spherical-harmonic, non-spherical oscillator, ring-shaped oscillator or ring-shaped non-spherical oscillator confinement potentials.
- Oscillator strength and radiative lifetimes of excitons: The decay of excitons via photon emission competes with the recombination of (free-) electron-hole pairs. A typical photoluminescence decay is *non-exponential* with typical time constants from nanosecond (ns) to millisecond (ms). The non-exponential decay of the photoluminescence signal can be hereby discussed in terms of the size inhomogeneity of the Si nanostructures as well as the presence of nonradiative relaxation channels. In a non-uniform quantum wire, for example, an exciton near to some thinner part of the wire shows a faster luminescence decay but may also first relax back nonradiatively to some thicker part of wire, and where it may subsequently decay slower by luminescence.
- Electronic structures of the quantum dots: The DFT and other *ab-initio* methods, that have been found useful for large molecules, do often not describe well the multiply-excited states of quantum dots. In contrast to atoms and molecules, multiply-excited quantum dots can lose their energy not only through radiative or nonradiative processes but also by phonon emissions to the surrounding (semiconductor) lattice. Such phonon relaxation processes involves initial and final states with an equal number of electron-holes pairs (Lehtonen *et al.*, 2008).
- Fock-Darwin energy levels: For an conduction-band electron in an external magnetic field, whose motion is confined in a two-dimensional

7. Atomic properties

parabolic well with axis $\mathbf{e}_z \parallel \mathcal{B}$, the Hamiltonian is given in the effective-mass approximation by

$$\mathbb{H} = -\frac{1}{2m^{(\text{eff})}} \left(\mathbf{p} - \frac{e}{c} \mathbf{A} \right)^2 + \frac{m^{(\text{eff})} \omega_o^2 r^2}{2} = \frac{\mathbf{p}^2}{2m^{(\text{eff})}} + \frac{m^{(\text{eff})}}{2} \left(\omega_o^2 + \frac{\omega_c^2}{4} \right) r^2 - \frac{\omega_c l_z}{2},$$

and where \mathbf{r} is the position and \mathbf{p} the momentum of the confined electron, while l_z is the projection of its angular momentum upon the field direction. For a constant magnetic field $\mathcal{B} = \text{rot } \mathbf{A}$, one can assume $\mathbf{A} = \mathcal{B}/2(y, -x, 0)$ and the cyclotron frequency $\omega_c = e\mathcal{B}/(m^{(\text{eff})} c)$. The energies and eigenstates of this Hamiltonian were determined analytically by Fock and Darwin long before the use of nanostructures.

➤ **Fock-Darwin energies:** The Hamiltonian above can be expressed also as [sum of two independent harmonic oscillators with the characteristic frequencies](#) and with energies

$$\begin{aligned} \omega_{\pm} &= \sqrt{\omega_o^2 + \frac{\omega_c^2}{4}} \pm \frac{\omega_c}{2}, & \Omega^2 &= \omega_o^2 + \frac{\omega_c^2}{4} \\ \epsilon(n_+ n_-) &= \hbar\omega_+ \left(n_+ + \frac{1}{2} \right) + \hbar\omega_- \left(n_- + \frac{1}{2} \right) \\ \epsilon(n, m) &= \hbar\Omega(n + 1) - \frac{\hbar\omega_c m}{2}, & n &= n_- + n_+, & m &= n_- - n_+, \end{aligned}$$

Obviously, these energy levels are degenerate in the absence of a magnetic field $\omega_+ = \omega_- = \omega_o$, whereas a strong magnetic field ($\omega \gg \omega_o$) leads to the formation of [Landau levels](#), approximately separated by the cyclotron energy $\hbar\omega_+ \approx \hbar\omega_c$. Often, the energies are displayed as function of the magnetic field.

➤ **Quantum dots in external magnetic fields:** Maksym and Chakraborty (1990) studied the energies of interacting electrons if the quantum dot obeys an external magnetic field. Although the excitation energy are of course a function of the magnetic field, they crucially depend also on the interelectronic interaction. For a quadratic confinement potential, for instance, the optical excitation energies of the many-body system are very much the same as those of a single electron.

Charge transport in quantum dots:

- Methods for chargetransport in quantum dot computations: To describe the charge transport in quantum dots in first-order perturbation theory, the Pauli (classical), first-order Redfield, first-order von Neumann master equations as well as some particular form of the Lindblad equation have been applied (Kirsanskas *et al.*, 2017). Other methods are the numerical-renormalization group, non-equilibrium Green's functions, and master equation based approaches. In practice, however, such charge transport computations are quite complex, and especially if phenomena like Coulomb blockade occur.

Simulation of impurities and nanostructure:

- Low-dimensional nano structures: Modern technologies enable one to fabricate low-dimensional nanostructures, such as quantum wells, quantum wires and quantum dots, in which the charge carriers (electrons or holes) are confined either in one-, two- and even within three-dimensions. Quantum dots are hereby often referred to as artificial atoms because of their similar shell structure and discrete energy levels.
- Quantum dots embedded into bulk materials: If quantum dots are embedded into bulk material, they occur as defects and perturb the periodicity of the surrounding solid-state material. Two classes of methods are applied in order to describe the electronic structure of such *embedded* quantum dots (Lehtonen *et al.*, 2008): (1) Molecular-type electronic structure calculation as developed for free-standing quantum dots; (2) so-called effective-mass approximations (EMA). Both of these classes have their pros and cons, and are complementary to each other. EMA calculations have difficulties to describe the properties of (quite) small quantum dots because their *atomic* character directly affect the optical properties; however, they are suitable to describe large quantum dots whose properties are mainly determined by the *confinement*. EMA methods can be applied also to model the transition from large quantum dots towards bulk material by using smoothly larger and shallower confinement potentials.
- Hydrogenic impurity in spherical quantum dots: In the effective mass approximation, the nonrelativistic Hamiltonian for a hydrogenic impurity at the center of a quantum dot is given by (Yakar *et al.*, 2013)

$$H_o = -\frac{\hbar^2 \nabla^2}{2m^*} - \frac{k e^2}{\epsilon r} + V^{(\text{confinement})}(r), \quad V^{(\text{confinement})}(r) = \begin{cases} 0 & r < R \\ \infty & r \geq R, \end{cases}$$

and where k , m^* and ϵ are the electric constant, effective mass of electron and the dielectric constant of medium, respectively, and where $V^{(\text{confinement})}(r)$ refers to a spherical confining potential well. The eigenvalues of this Hamiltonian are then further modified by adding

7. Atomic properties

the relativistic contributions due to the mass-velocity, Darwin as well as spin-orbit terms; all these relativistic terms have been calculated perturbatively since they small.

Applications of quantum dots:

- **Low-dimensional nano structures:** These structures have attracted recent interest because of their properties and potential applications in physics, chemistry and engineering. They are promising structures for developing semiconductor microelectronic and optoelectronic devices, such as electro-optic modulators, inter-band lasers and inter-sub band long wavelength detectors. In particular, quantum dots have been explored extensively, both experimentally and theoretically.

8. Atomic processes

8.1. In JAC implemented processes

8.1.a. Photoemission. Transition probabilities (PhotoEmission)

Process, notation & application:

- Photoemission: from an atom or ion $A^* \rightarrow A^{(*)} + \hbar\omega$
- Quantum notations used in the formulas below: $|\alpha_i \mathbb{J}_i\rangle \rightarrow |\alpha_f \mathbb{J}_f\rangle + \hbar\omega(\{\mathbb{M}\})$
- JAC's standard multipole amplitudes for photon emission: Although all (one- and many-electron) electron-photon interaction matrix elements are always evaluated in *absorption* within JAC, we wish and need to retain the intuitive description of matrix elements as they are typically applied in quantum mechanics: $\langle \text{final state} | \text{operator} | \text{initial state} \rangle$. In JAC, we therefore introduce an explicit and independent notation for a *standard (reduced) emission as well as absorption multipole matrix element*

$$\langle \alpha_f \mathbb{J}_f \parallel \mathbb{O}^{(\mathbb{M}, \text{emission})} \parallel \alpha_i \mathbb{J}_i \rangle = \left\langle \alpha_i \mathbb{J}_i \left\| \sum_{k=1}^N \boldsymbol{\alpha}_k a_{k,L}^p \right\| \alpha_f \mathbb{J}_f \right\rangle^* \equiv \langle \alpha_i \mathbb{J}_i \parallel \mathbb{O}^{(\mathbb{M}, \text{absorption})} \parallel \alpha_f \mathbb{J}_f \rangle^*$$

which retains the right order and can be obtained from `Jac.PhotoEmission.amplitude()`; cf. section 5.3.c. A multipole $\mathbb{M} \equiv (L, p) = E1, M1, E2, \dots$ hereby contains all information about its multipolarity (angular momentum) L and type *magnetic* ($p = 0$) or *electric* ($p = 1$).

- Using JAC: Perform an `Atomic.Computation(..., processSettings=PhotoEmission.Settings(...), ...)` or call directly functions from the module `PhotoEmission`.

8. Atomic processes

- In JAC, the transition probabilities and radiative lifetimes are tabulated by default for all selected transitions $i \rightarrow f$.
- In JAC, the anisotropy (structure) parameters $f_k(\alpha_i \mathbb{J}_i, \alpha_f \mathbb{J}_f)$ are calculated and tabulated if the flag `calcAnisotropy = true` is set in `PhotoEmission.Settings`.

Transition probabilities and oscillator strengths:

- **Transition probability and oscillator strength:** With the notation of the (standard reduced) emission multipole matrix element from above, the transition probability (Einstein A and B coefficients) and oscillator strengths are given by

$$A(i \rightarrow f) = \frac{8\pi \alpha \omega}{2J_i + 1} \sum_{\mathbb{M}} |\langle \alpha_f \mathbb{J}_f \parallel \mathbb{O}^{(\mathbb{M}, \text{emission})} \parallel \alpha_i \mathbb{J}_i \rangle|^2, \quad B(i \rightarrow f) = \frac{g_f}{g_i} B(f \rightarrow i) = \frac{\pi^2 c^3}{\hbar \omega_{if}^3} A(i \rightarrow f)$$

$$f(i \rightarrow f) = \frac{2\omega}{3(2J_i + 1)} \sum_{\mathbb{M}} |\langle \alpha_f \mathbb{J}_f \parallel \mathbb{O}^{(\mathbb{M}, \text{emission})} \parallel \alpha_i \mathbb{J}_i \rangle|^2 = \frac{c}{12\pi\omega} A(i \rightarrow f),$$

and where the sum over $\mathbb{M} = E1, M1, E2, \dots$ runs over all requested multipoles in a given computation.

- **Oscillator strength versus the strength of photoionization (autoionizing) resonances:** For a single photoionization resonance, that arise from the excitation of an inner-shell electron, the photoionization resonance strength $S(i \rightarrow n) \equiv \sum_f S(i \rightarrow n \rightarrow f)$ is proportional to the (emission) oscillator strength as $f(n \rightarrow i)$ (Müller *et al.*, 2018):

$$S(i \rightarrow n) = \int dE_\omega \sigma^{(\text{photoionization})} = \frac{h e^2}{4\epsilon_0 m c} f(n \rightarrow i) = 109.761 \text{ Mb eV } f(n \rightarrow i)$$

$$f(n \rightarrow i) = S(i \rightarrow n) \times 9.1107 \cdot 10^{-3} (\text{Mb eV})^{-1}.$$

Therefore, if the absolute photoionization cross section can be measured experimentally, **this (simple) relation enables one to derive the emission and absorption oscillator strength**. For a multiple ionization of the intermediate resonance n , the relation still holds, if $S(i \rightarrow n) = S^{(1e)}(i \rightarrow n) + S^{(2e)}(i \rightarrow n) + \dots$ refers to the sum of the corresponding photoionization resonance strengths.

- **Absorption oscillator strength versus Einstein A coefficient:** Following the 2014 CODATA values, the relation between the absorption oscillator strength and the Einstein A coefficient is

$$f(i \rightarrow n) = 1.4992 \cdot 10^{-14} \text{ s/nm}^2 \times \lambda_{ni}^2 \frac{g_n}{g_i} A(n \rightarrow i).$$

- Spontaneous *versus* stimulated process: For a generic transition process $i \rightarrow f$, the rate $A^{(\text{stimulated})}(a \rightarrow b)$ of the stimulated process is related to the rate $A^{(\text{spontaneous})}(a \rightarrow b)$ of the spontaneous process [in SI units] by

$$A^{(\text{stimulated})}(i \rightarrow f) = A^{(\text{spontaneous})}(i \rightarrow f) \frac{\pi^2 \hbar^2 c^2}{E_{ab}^3} I \text{ [W/cm}^2\text{]}, \quad A^{(\text{absorption})}(f \rightarrow i) = A^{(\text{stimulated})}(i \rightarrow f) \frac{g_i}{g_f}.$$

- Wavelength *versus* resonance or transition energy: Following the 2014 CODATA values, the relation between the wavelength and energy is

$$\lambda_{if} = \frac{hc}{E_{\text{res}}} = \frac{1239.8419739 \text{ nm eV}}{E_{\text{res}}}.$$

- Lifetime *versus* resonance widths: Following the 2014 CODATA values, the relation between the lifetime τ [s] and widths Γ [eV] is

$$\tau = \frac{\hbar}{\Gamma} = \frac{6.582119514 \cdot 10^{-16} \text{ eV s}}{\Gamma \text{ [eV]}}.$$

- Line strength conversion: For wavelengths λ [\AA] (NIST Atomic Spectra Database), the conversion between gA [1/s] and S is given by

$$S = 3.707342 \times 10^{-14} \lambda^3 g_f A \quad (\text{E1})$$

$$S = 8.928970 \times 10^{-19} \lambda^5 g_f A \quad (\text{M1})$$

- Conversion between matrix elements and Einstein A coefficients: Biswas *et al.* (2018) list the following conversion formulas for the lowest multipole transitions

$$g_f \lambda^3 A^{(\text{E1})}(f \rightarrow i) = 2.0261 \times 10^{18} \langle i | \mathbb{O}^{(\text{E1, emission})} | f \rangle, \quad g_f \lambda^5 A^{(\text{E2})}(f \rightarrow i) = 1.1199 \times 10^{18} \langle i | \mathbb{O}^{(\text{E2, emission})} | f \rangle$$

$$g_f \lambda^3 A^{(\text{M1})}(f \rightarrow i) = 2.697 \times 10^{13} \langle i | \mathbb{O}^{(\text{M1, emission})} | f \rangle, \quad g_i f_{ik} = 1.4991938 \times 10^{-16} g_f \lambda^2 A^{(\text{E1})}(f \rightarrow i).$$

Electric-dipole transitions including core-polarization potential:

- Fine-structure calculations with core-polarization potentials: Since the 1970s, a core-polarization potential has been occasionally included into the SCF in order to improve the atomic level and fine-structure calculations. In these computations, a core-polarization potential is typically added only for the valence electron, in addition to the Dirac-Fock-Slater potential for the core- and valence-shell electrons. However, this **core-polarization potential must be ‘corrected for’ in all transition probability calculations** in order to make proper use of such improved wave functions.
- Core-polarization correction to the nonrelativistic electric-dipole operator: Migdalek and Baylis (1979) derived a modified electric-dipole operator, in which the position operator \mathbf{r}_i of the i -th electron need to be replaced:

$$\mathbf{r} \rightarrow \mathbf{r} \left[1 - \frac{\alpha_d}{(r^2 + r_c^2)^{3/2}} \right].$$

- Quasi-relativistic electric-dipole amplitude: To account for the core-polarization of the atomic potential also in the representation of the electric-dipole (E1) operator, the E1 transition amplitude need to be modified as:

$$\left\langle \alpha_f \mathbb{J}_f \left| \sum_j \mathbf{r}_j \right| \alpha_i \mathbb{J}_i \right\rangle \rightarrow \left\langle \alpha_f \mathbb{J}_f \left| \sum_j \mathbf{r}_j \left[1 - \frac{\alpha_d}{(r^2 + r_c^2)^{3/2}} \right] \right| \alpha_i \mathbb{J}_i \right\rangle.$$

- Reduced quasi-relativistic E1 one-electron amplitude: ... need still to be found/worked out.
- In JAC, the core-polarization corrected E1 amplitude can be calculated by the function `PhotoEmission.amplitude("E1 with core-polarization emission", cp::CorePolarization, omega, finalLevel, initialLevel, grid; ...)`. Here, the core-polarization `cp::CorePolarization` need to be specified and the same as in the associated SCF computations; cf. `AsfSettings`.
- In JAC, the core-polarization is taken into account if the logical flag `doApply = true` is set for the `CorePolarization` (type), together with the proper polarizability α_d , the core-radius r_d as well as the valence shells.

Angular distribution and anisotropy parameters of the fluorescence radiation:

- The fluorescence (radiation) from an excited atom is characterized not only by its frequency $\hbar\omega$ but also by the **angular distribution and polarization of the emitted radiation**. Both of these properties of the emitted photons depend on the sublevel occupation of the excited atom or ion and, hence, on its reduced statistical tensors $\mathcal{A}_{kj}(\alpha_i \mathbb{J}_i)$ which **reflect the prior excitation process**.

- **Angular distribution of the photoemission from initially unpolarized but aligned atoms:** For initially unpolarized but aligned atoms, the angular distribution of the (characteristic) fluorescence radiation is given in perturbation theory by:

$$W(\vartheta) = \frac{W_o}{4\pi} \left(1 + \sum_{k=2,4,\dots} f_k(\alpha_i \mathbb{J}_i \rightarrow \alpha_f \mathbb{J}_f) \mathcal{A}_{k0}(\alpha_i \mathbb{J}_i) P_k(\cos\vartheta) \right),$$

where W_o is the total decay rate and ϑ the angle of the photons with regard to the alignment axis (quantization axis).

- **Anisotropy (structure) parameters $f_k(\alpha_i \mathbb{J}_i \rightarrow \alpha_f \mathbb{J}_f)$:** In the angular distribution above, the **anisotropy (or structure) parameters $f_k(\alpha_i \mathbb{J}_i \rightarrow \alpha_f \mathbb{J}_f)$** are independent of the particular excitation process of the level ($\alpha_i \mathbb{J}_i$) and merely reflects the electronic structure of the ion in the two levels that are involved in the fluorescence

$$\begin{aligned} f_k(\alpha_i \mathbb{J}_i, \alpha_f \mathbb{J}_f) &= \left[\sum_{\mathbb{M}} \left| \langle \alpha_i \mathbb{J}_i \parallel \mathbb{O}^{(\mathbb{M}, \text{emission})} \parallel \alpha_f \mathbb{J}_f \rangle \right|^2 \right]^{-1} \frac{\sqrt{2J_i + 1}}{2} \sum_{\mathbb{M}\mathbb{M}'} i^{L'+p'-L-p} (-1)^{J_f+J_i+1+k} [L, L']^{1/2} \langle L1, L' - 1 | k0 \rangle \\ &\times \left(1 + (-1)^{L+p+L'+p'-k} \right) \left\{ \begin{matrix} L & L' & k \\ J_i & J_i & J_f \end{matrix} \right\} \langle \alpha_f \mathbb{J}_f \parallel \mathbb{O}^{(\mathbb{M}, \text{emission})} \parallel \alpha_i \mathbb{J}_i \rangle \langle \alpha_f \mathbb{J}_f \parallel \mathbb{O}^{(\mathbb{M}', \text{emission})} \parallel \alpha_i \mathbb{J}_i \rangle^*. \end{aligned}$$

Of course, there is usually one multipole term that dominates the radiative decay (fluorescence) for any given pair of initial and final-bound states.

Semi-empirical calculations of transition probabilities:

- Since level energies in semi-empirical computations are based on experimental energies, one hopes that they represent better predictions than purely *ab-initio* values. The consistency between the observed intensities and calculated gA values for electric-dipole transitions can be used also as criterion for the reliability of level and transition identifications.
- Semi-empirical calculations of transition probabilities are often performed by using Cowan's code and, especially, the components RCN/RCN2/RCG/RCE. In a first step, Hartree-Fock calculations of radial integrals are carried out, including relativistic corrections (HFR) to generate all required atomic orbitals and average energies of configurations. The diagonalization of the Hamiltonian matrix then leads to approximate energy values and eigenvectors of levels in intermediate coupling.
- When, in addition, also experimental energies are available, RCE is run to perform an iterative least-squares fit with the aim to minimize the differences between the calculated and experimental energies, and where the radial integrals are applied as fitting parameters. The

mean error of such a fit is defined by $\Delta E = \sqrt{\sum_i (E_i^{(\text{exp})} - E_i^{(\text{calc})})^2 / (N_i - N_p)}$, where N_i is the number of experimentally known energies and N_p the number of free parameters.

Unresolved transition arrays (UTA):

- **Unresolved transition arrays:** The UTA approach has become the method of choice in order to calculate the radiative properties of high- Z elements. Within this approach, a group of lines (i.e. a so-called array), which belongs to the same pair of electron configurations, are treated globally by a Gaussian distributions whose width and position are given by analytical formulae.
- The UTA approach has been used to identify various characteristic unresolved spectral features present in the spectra of various kinds of hot plasmas.
- **super-transition array method (STA):** The UTA approach is computationally efficient and accurate for plasma conditions where the line broadening is such, that individual line profiles merge. This approach has been further extended to a group of arrays in the so-called super-transition array method (STA) where set of arrays are treated globally.
- **Resolved transition arrays (RTA):** The RTA method was proposed to overcome the shortcoming of the UTA method that just a few transitions often dominate the spectral emission distribution of the array. This RTA method improves on the UTA approach by resolving the transition array into individual lines by using random lines but without performing an explicit atomic structure calculation.
- **UTA approach:** The UTA approach describes a set of radiative transitions between levels from two configurations, which just differ in the displacement of one electron. This approach applies

$$\mu^{(n)} = \frac{\sum_{ab} N_a A_{ab} E_{ab}^n}{\sum_{ab} N_a A_{ab}},$$

where N_a is the population of level a from the initial configuration, E_{ab} is the transition energy and A_{ab} the corresponding radiative rate. The subtlety of the UTA method is to calculate directly the first moments μ_1, μ_2, \dots (or even $\mu^{(3)}$) by operator techniques instead of detailed calculating all the individual atomic quantities E_{ab}, A_{ab} explicitly. From these moments, one then derives the energy position $\mu^{(1)}$ and the variance $\sigma^2 = \mu^{(2)} - (\mu^{(1)})^2$ of the (more or less Gaussian) spectral profile of each UTA. In these computations, one usually assumes local thermodynamical equilibrium (LTE) for the level population and neglects the Boltzmann factors $\exp(-E/kT)$ for all levels of a given configuration. This approximation is consistent with a partial LTE distribution for nearly degenerate levels (when compared with $k_B T$).

- **Spectral distribution of the UTA:** These two moments can be utilized together with the variance $\sigma^2 = \mu^{(2)} - (\mu^{(1)})^2$ in order to define the spectral distribution of the UTA

$$f(\mathcal{E}) = \frac{1}{\sigma \sqrt{\pi}} \exp \left[-\frac{(\mathcal{E} - \mu^{(1)})^2}{2\sigma^2} \right].$$

- **UTA method:** By avoiding the explicit calculation of the properties of each line, that belongs to a given array, the UTA method enables one to account for a large number of transitions for a rather low computational cost.
- Overall, however, the use of such UTA appears quite tedious, and the application of the formulas as derived by Bauche-Arnould and coworkers (1985, 1988) partly lost its importance as more powerful computers became available.

Fractional occupation number (FON) approach:

- **Fractional occupation number (FON) approach:** The FON approach involves the prescription of **single but fictitious configuration with FONs for each (n, κ) subshell in order to represent an entire set of physical configurations within a given model**. This fictitious configuration is used to first generate a single set of bound wave functions. Second, integer occupation numbers are then combined with the (averaged) wave functions in order to describe all the physical configurations that are enumerated in a particular model (Sampson *et al.*, 2009).

Two-electron one-photon transitions (TEOP):

- Two-electron one-photon transitions were postulated almost 100 years ago and are well-known from the optical region.
- In the early 1970s, Wölfli *et al.* reported results for nickel and iron, for which high-energetic satellites arose due to two-electron one-photon transitions. In these experiments, two vacancies in the K-shell were simultaneously filled by two L-shell electrons under the emission of a energetic single photon.
- Since the interaction with the electro-magnetic field is governed by an one-electron operator, the contribution of two-electron one-photon (TEOP) transitions can usually be ignored in comparison to other, E1 allowed one-electron transitions.

8.1.b. Photoexcitation (PhotoExcitation)

Process, notation & application:

- Photoexcitation of an atom or ion: $A + \hbar\omega \rightarrow A^*$
- Quantum notations used in the formulas below: $|\alpha_i J_i\rangle + \hbar\omega(\mathbf{k}, \lambda) \rightarrow |\alpha_f J_f\rangle, \quad \lambda = \pm 1.$
- Using JAC: Perform an `Atomic.Computation(..., processSettings=PhotoExcitation.Settings(...), ...)` or call directly functions from the module `PhotoExcitation`.
- In JAC, the photoexcitation cross sections are calculated by default for resonant and completely linearly-polarized plane-wave radiation.
- In JAC, the photoexcitation cross sections are calculated also for plane-wave radiation with given Stokes parameters (P_1, P_2, P_3) if the flag `calcStokes = true` are set in `PhotoExcitation.Settings` and if the Stokes parameters are given explicitly by the field `PhotoExcitation.Settings.stokes`.
- In JAC, the statistical tensors $\rho_{kq}(\alpha_f J_f)$ and the alignment parameters $\mathcal{A}_{kq}(\alpha_f J_f)$ are calculated and tabulated for initially unpolarized atoms and plane-wave photons with given Stokes parameters, if the flag `calcTensors = true` is set in `PhotoExcitation.Settings` and if the Stokes parameters are given explicitly by the field `PhotoExcitation.Settings.stokes`. The default Stokes parameters are $(P_1, P_2, P_3) = (0, 0, 0)$.

Photoexcitation cross sections:

- Total photoexcitation cross section for *zero linewidth*: For *initially unpolarized atoms* and incident photons with given (photon) density matrix $\langle \mathbf{k}\lambda | \rho_\gamma | \mathbf{k}\lambda' \rangle$, the total photoexcitation cross section can be most easily defined in the *limit of a zero linewidth* as

$$\begin{aligned} \sigma(\omega; \alpha_i J_i \rightarrow \alpha_f J_f) &= \frac{4\pi^2\alpha}{\omega(2J_i+1)} \sum_{M_i M_f, \lambda \lambda'} \langle \mathbf{k}\lambda | \rho_\gamma | \mathbf{k}\lambda' \rangle \langle \alpha_f J_f M_f | \mathbb{T}^{(\text{photoabsorption})}(\mathbf{k}, \lambda) | \alpha_i J_i M_i \rangle \\ &\quad \times \langle \alpha_f J_f M_f | \mathbb{T}^{(\text{photoabsorption})}(\mathbf{k}, \lambda') | \alpha_i J_i M_i \rangle^* \delta(\omega + E_i - E_f), \end{aligned}$$

and where $\mathbb{T}^{(\text{photoabsorption})}(\mathbf{k}, \lambda)$ formally describes the electron-photon interaction operator for absorbing a photon $\hbar\omega(\mathbf{k}, \lambda)$.

- Total photoexcitation cross section for finite linewidth: In order to allow for a finite natural width Γ_f of the excited level, we just need to replace the $\delta(\omega + E_i - E_f)$ function in the expression above by a (Lorentzian) spectral distribution

$$\begin{aligned}\sigma(\omega; \alpha_i \mathbb{J}_i \rightarrow \alpha_f \mathbb{J}_f) &= \frac{4\pi^2\alpha}{\omega(2J_i+1)} \sum_{M_i M_f, \lambda \lambda'} \langle \mathbf{k} \lambda | \rho_\gamma | \mathbf{k} \lambda' \rangle \langle \alpha_f \mathbb{J}_f M_f | \mathbb{T}^{(\text{photoabsorption})}(\mathbf{k}, \lambda) | \alpha_i \mathbb{J}_i M_i \rangle \\ &\quad \times \langle \alpha_f \mathbb{J}_f M_f | \mathbb{T}^{(\text{photoabsorption})}(\mathbf{k}, \lambda') | \alpha_i \mathbb{J}_i M_i \rangle^* \frac{1}{\pi} \frac{\Gamma_f/2}{(\omega + E_i - E_f)^2 + \Gamma_f^2/4}.\end{aligned}$$

- Photoexcitation cross sections for initially unpolarized atoms: For incident plane-wave photons with (photon) density matrix $(c_{\lambda \lambda'}) = \frac{1}{2} \begin{pmatrix} 1 + P_3 & P_1 - iP_2 \\ P_1 + iP_2 & 1 - P_3 \end{pmatrix}$, which are resonant to the given transition $(\alpha_i \mathbb{J}_i) \rightarrow (\alpha_f \mathbb{J}_f)$, the total photoexcitation cross section is

$$\sigma(\omega; \alpha_i \mathbb{J}_i \rightarrow \alpha_f \mathbb{J}_f; \omega) = \frac{2\pi^3\alpha}{\omega(2J_i+1)} \sum_{\mathbb{M}, \lambda} c_{\lambda \lambda} |\langle \alpha_f \mathbb{J}_f | \mathbb{O}^{(\mathbb{M}, \text{photoabsorption})}(\lambda) | \alpha_i \mathbb{J}_i \rangle|^2 \times \begin{cases} \delta(E_i + \omega - E_f) \\ \frac{1}{\pi} \frac{\Gamma_f/2}{(E_i + \omega - E_f)^2 + \Gamma_f^2/4} \end{cases}.$$

- Photoexcitation cross sections for initially unpolarized atoms and linear-polarized, circularly-polarized or unpolarized incident photons: For the resonant excitation with unpolarized or completely linearly-polarized or circularly-polarized plane-wave photons, the total photoexcitation cross section is given by

$$\sigma(\omega; \alpha_i \mathbb{J}_i \rightarrow \alpha_f \mathbb{J}_f) = \frac{8\pi^3\alpha}{\omega(2J_i+1)} \sum_{\mathbb{M}} |\langle \alpha_f \mathbb{J}_f | \mathbb{O}^{(\mathbb{M}, \text{photoabsorption})}(\lambda) | \alpha_i \mathbb{J}_i \rangle|^2 \times \begin{cases} \delta(E_i + \omega - E_f) \\ \frac{1}{\pi} \frac{\Gamma_f/2}{(E_i + \omega - E_f)^2 + \Gamma_f^2/4} \end{cases}.$$

Final-level statistical tensors and alignment parameters:

- Statistical tensors: Instead of the (final-level) density matrix, it is often more convenient to describe the population of the magnetic sublevels in terms of (so-called) statistical tensors of the atom or ion

$$\rho_{kq}(\alpha_f \mathbb{J}_f) = \sum_{M_f M'_f} (-1)^{J_f - M'_f} \langle J_f M_f, J_f (-M'_f) | kq \rangle \langle \alpha_f \mathbb{J}_f M_f | \rho | \alpha_f \mathbb{J}_f M'_f \rangle,$$

and which are non-zero only for $0 \leq k \leq 2J_f$ and $-k \leq q \leq k$.

8. Atomic processes

- **Reduced statistical tensors or alignment parameters:** The reduced statistical tensors of the excited levels are called **alignment parameters** of the excited atom and are defined by

$$\mathcal{A}_{kq}(\alpha_f \mathbb{J}_f) = \frac{\rho_{kq}(\alpha_f \mathbb{J}_f)}{\rho_{00}(\alpha_f \mathbb{J}_f)}.$$

Photoexcitation by plane-wave photons:

- Since the observation and details of the photoexcitation and subsequent photoemission may crucially depend on the detailed properties of the incident photon field, we here collect some further information for **photon fields (beams)** with **well-defined properties**.
- **Vector potential for a plane-wave light field:** As usual, the relativistic electron-photon interaction operator $R = \sum_j \boldsymbol{\alpha}_j \mathbf{A}^{(\text{plane-wave})}(\mathbf{r}_j)$ is given in terms of the Dirac matrices $\boldsymbol{\alpha}_q$ of the q^{th} particle and the vector potential $\mathbf{A}^{(\text{plane-wave})}(\mathbf{r}_q)$. For an incident plane-wave radiation with wave vector \mathbf{k} , polarization vector $\mathbf{e}_{\mathbf{k},\lambda}$ and with helicity $\lambda = \pm 1$, the vector potential can be written in Coulomb gauge as:

$$\mathbf{A}^{(\text{plane-wave})}(\mathbf{r}) = \mathbf{e}_{\mathbf{k},\lambda} e^{i\mathbf{k}\cdot\mathbf{r}}.$$

- **Multipole operators of the electron-photon interaction:** For the analysis of atomic photo-excitation and ionization processes, it is generally convenient to expand the vector potential $\mathbf{A}^{(\text{plane-wave})}(\mathbf{r})$ in terms of its electric and magnetic multipole fields. If the (plane-wave) field propagates along $\mathbf{n}_k = \mathbf{k}/k = (\vartheta_k, \varphi_k, 0) \nparallel \mathbf{e}_z$, this expansion is given by:

$$\mathbf{e}_{\mathbf{k},\lambda} e^{i\mathbf{k}\cdot\mathbf{r}} = \sqrt{2\pi} \sum_{LM} \sum_{p=0,1} i^L [L]^{1/2} (i\lambda)^p D_{M\lambda}^{(L)}(\varphi_k, \theta_k, 0) \mathbf{a}_{LM}^{(p)}(\mathbf{r}) \equiv \sqrt{2\pi} \sum_{MM} i^L [L]^{1/2} (i\lambda)^p D_{M\lambda}^{(L)}(\varphi_k, \theta_k, 0) \mathbf{a}_M^{(M)}(\mathbf{r}).$$

Here, $[L] = 2L + 1$, $D_{M\lambda}^{(L)}$ is the Wigner rotation matrix, while $\mathbf{a}_{LM}^{(p)}(\mathbf{r})$ refers to magnetic ($p = 0$) and electric ($p = 1$) multipole components of the vector potential; these components are constructed as irreducible tensors of rank L and enable one to evaluate the overall transition amplitude $\mathcal{M}_{fi}^{(\text{plane-wave})}$ in terms of the *multipole* amplitudes.

- **Transition amplitudes of the multipole fields (*multipole* amplitudes):** Using the expansion for the plane-wave vector potential from above and by making use of the Wigner-Eckart theorem, the transition amplitudes of the multipole fields can be written in terms of (many-electron)

reduced matrix elements as

$$\begin{aligned} \mathcal{M}_{fi}^{(\text{plane-wave})} &= \sqrt{2\pi} \sum_{MM} i^L \frac{[L]^{1/2}}{[J_f]^{1/2}} (i\lambda)^p D_{M\lambda}^{(L)}(\varphi_k, \vartheta_k, 0) \langle J_i M_i, LM | J_f M_f \rangle \langle \alpha_f J_f \| \mathbb{O}^{(\mathbb{M}, \text{absorption})} \| \alpha_i J_i \rangle, \\ \langle \alpha_f J_f \| \mathbb{O}^{(\mathbb{M}, \text{absorption})} \| \alpha_i J_i \rangle &\equiv \left\langle \alpha_f J_f \left\| \sum_j \boldsymbol{\alpha}_j \mathbf{a}_L^{(p)}(\mathbf{r}_j) \right\| \alpha_i J_i \right\rangle \equiv \langle \alpha_f J_f \| H_\gamma(pL) \| \alpha_i J_i \rangle. \end{aligned}$$

These (reduced) matrix element does *neither* depend on the projections of the angular momenta of an atom and photon *nor* the particular choice of the quantization axis *nor* the propagation direction \mathbf{n}_k . These multipole amplitudes solely reflect the electronic structure of an atom and its coupling to a particular multipole component (pL) of the radiation field.

Photoexcitation by twisted light:

- Photoexcitation by twisted light: $\hbar\omega^{(\text{twist})} + A \longrightarrow A^*$.
- Photo-induced processes with twisted light: Since the helical phase structure of twisted beams causes a non-uniform intensity profile and a rather complex energy flow, many photo-induced atomic processes are modified in twisted light. This applies to both, the photo-excitation and ionization as well as to Rayleigh, Raman and Compton scattering processes. For example, the use of twisted (vortex light) may help reduce the light shift of bound-state transitions and, hence, to control electric dipole-forbidden (atomic) clock transitions.
- Photoexcitation by twisted light: For different atomic targets, the ratio of partial photoexcitation cross sections of different multipole components of the radiation field, depend phenomenologically quite sensitive on the topological charge ℓ and further parameters of the incident light. In particular, the (photoexcitation) cross section ratios may differ for incident twisted light significantly from the corresponding ratios for incident plane waves.
- Photoexcitation of boron-like ions: For the $2p\ ^2P_{1/2} - 3d\ ^2D_{3/2}$ transition in boron-like ions, it was shown that the relative magnetic dipole (M1) and electric quadrupole (E2) contributions strongly depend on the particular position of the target ions with regard to the beam axis.
- Schulz *et al.* (2019) analyzed the $3s3p\ ^3P_1 - 3s3p\ ^1P_1$ excitation of a neutral Mg atoms for both, an incident plane-wave and Bessel beam. While the E2 and M1 multipole transition contribute roughly equally for incident plane-wave radiation, the (relative) strength of the E2 multipole transition can be enhanced by almost an order of magnitude if the target is excited by a Bessel beam with topological charge $m = 2$, and independent of the size of the target cloud.

8. Atomic processes

- The investigations by Markgraf-Scholz *et al.* (2014) showed that the sublevel population of the excited atoms differ quite substantially when compared with the excitation by a plane-wave (Gaussian) beam. These changes in the sublevel population is expected to be observable in experiments by measuring, for instance, the linear polarization of the subsequent fluorescence radiation.

Do the selection rules differ for twisted light ?:

- **Selection rules for atomic transitions:** These rules tell which atomic transitions are possible for a given multipole decomposition of the radiation field. For different light fields, of course, different atomic fine-structure transitions can be excited, while the atom appears — more or less — *transparent* with regard to all other multipole components. In optical (low-frequency) fields, moreover, the electric-dipole component is far dominant so that all other allowed multipole transitions are usually negligible. However, the relative importance of the different multipoles change with the photon frequency and if more subtle properties are considered for the (subsequent) photon or electron emission. In general, the strength of the atomic multipole excitation hereby also depends on **geometrical (weight) factors** due to the coupling of a given multipole field in the particular decomposition.
- **Selection rules for atomic transitions:** Here, let us start explicitly from the QN of the light beams. and let us point out: **Twisted light does not change the selection rules but only the multipole decomposition of these radiation field is quite different.**
- **Selection rules for atomic transitions:** The selection rules are also independent of the particular atom, even if their interaction with the twisted beam will lead to different observations. For their analysis, Duan *et al.* (2019) expand a Bessel beam into its multipole components from which the total transition amplitude is obtained as weighted sum of multipole amplitudes.
- **Multipole expansions of light fields:** Any incident (and practically relevant) light field can be readily expanded in terms of its multipole fields

$$\begin{aligned} \mathbf{A}(\mathbf{r}; \text{geometry \& polarization}) &= \sum_{\mathbb{M}, M} w(\mathbf{r}; \mathbb{M}, M; \text{geometry \& polarization}) a_M^{(\mathbb{M})}(\mathbf{r}) \\ &= \sum_{pLM} w(\mathbf{r}, p, L, M; \text{geometry \& polarization}) a_{LM}^{(p)}(\mathbf{r}) \end{aligned}$$

where the first line is the notation in JAC, and the second the frequently applied notation in the literature, cf Rose (1964) and Johnson (2007). For transverse fields, the multipole components refer explicitly to either magnetic ($p = 0$) or electric fields ($p = 1$). These multipole fields fullfill the eigenvalue equation of a well-defined (total) angular momentum: $\mathbf{j}^2 a_{LM}^{(p)} = L(L+1) a_{LM}^{(p)}$, $j_z a_{LM}^{(p)} = M a_{LM}^{(p)}$.

For the light field, we can therefore write

$$j_z \mathbf{A}(\mathbf{r}; \text{geometry \& polarization}) = \sum_{\mathbb{M}, M} M w(\mathbf{r}, \mathbb{M}, M; \text{geometry \& polarization}) a_M^{(\mathbb{M})}(\mathbf{r}).$$

Therefore, the light field will be an eigenfunction if the summation over M just selects one particular value M' : $w(\mathbf{r}, \mathbb{M}, M) = w(\mathbf{r}, \mathbb{M}, M') \delta_{MM'}$, a value which can vary also locally within the radiation field.

Photoexcitation by photons from a Bessel beam:

- The photoexcitation of atoms by a Bessel beam has been investigated for low- Z hydrogen-like ions by Markgraf-Scholz *et al.* (2014) who calculated the *partial* (subshell) cross sections and the alignment of the excited states, if the beam interacts especially with a macroscopic target of hydrogen-like ions.
- Vector potential for twisted Bessel beams: For an incident Bessel beam, the vector potential $\mathbf{A}^{(\text{Bessel})}(\mathbf{r})$ is given by (Schulz *et al.*, 2019)

$$\mathbf{A}^{(\text{Bessel})}(\mathbf{r}) \equiv \mathbf{A}_{\varkappa m k_z \lambda}^{(\text{Bessel})}(\mathbf{r}) = \int \frac{d^2 \mathbf{k}_\perp}{(2\pi)^2} \mathbf{e}_{\mathbf{k}, \lambda} e^{i \mathbf{k} \cdot \mathbf{r}} a_{\varkappa m}(\mathbf{k}_\perp) e^{-i \mathbf{k}_\perp \cdot \mathbf{b}}, \quad a_{\varkappa m}(\mathbf{k}_\perp) = e^{im\varphi_k} \frac{2\pi}{k_\perp} \delta(k_\perp - \varkappa).$$

This vector potential represents *Bessel* photons with well-defined helicity λ , a longitudinal component k_z of the wave vector and the projection m of the total angular momentum (TAM) upon the light propagation axis (z -axis). These Bessel photons also have a well-defined (absolute) value of the transverse momentum $|\mathbf{k}_\perp| = \varkappa$ and are, hence, monochromatic with $\omega = k/\alpha = \sqrt{k_z^2 + \varkappa^2}/\alpha$.

- Transition amplitude for twisted Bessel beams: The expression above expands the vector potential of *Bessel* beam photons in terms of (a coherent superposition of) plane waves $\mathbf{e}_{\mathbf{k}, \lambda} e^{i \mathbf{k} \cdot \mathbf{r}}$, whose wave vectors \mathbf{k} are uniformly distributed upon the surface of a cone with a polar opening angle $\theta_k = \arctan(\varkappa/k_z)$. Using the standard expansion of these plane waves in terms of multipoles and by inserting $\mathbf{A}_{\varkappa m k_z \lambda}^{(\text{Bessel})}(\mathbf{r})$, one finds after some algebra the amplitude for the transition $|\alpha_i J_i M_i\rangle + \gamma^{(\text{Bessel})} \rightarrow |\alpha_f J_f M_f\rangle$ induced by photons from a Bessel beam (Schultz *et al.*, 2020)

$$\mathcal{M}_{fi}^{(\text{Bessel})} = \sqrt{\frac{1}{[J_f]}} \sum_{\mathbb{M} M} i^{L+M} [L]^{1/2} (i\lambda)^p d_{M\lambda}^{(L)}(\theta_k) J_{m-M}(\varkappa b) e^{i(m-M)\varphi_b} \langle J_i M_i, LM | J_f M_f \rangle \langle \alpha_f J_f \| \mathbb{O}^{(\mathbb{M}, \text{absorption})} \| \alpha_i J_i \rangle.$$

Similar as for plane waves, the transition amplitude $\mathcal{M}_{fi}^{(\text{Bessel})}$ is now written as a sum of reduced matrix elements $\langle \alpha_f J_f \| \mathbb{O}^{(\mathbb{M}, \text{absorption})} \| \alpha_i J_i \rangle$ that are weighted by some additional geometric (angular) factors. For Bessel photons, these weight factors depend on the opening angle θ_k and the TAM projection m of the beam as well as on the impact parameter of an atom b ; they enter the amplitude above in particular through the small Wigner function $d_{M\lambda}^{(L)}(\theta_k)$ and the Bessel function $J_{m-M}(b\varkappa)$.

8. Atomic processes

- **Excitation rate for twisted Bessel beams:** The total rate for the excitation of atoms by Bessel light is obtained as usual by taking the average (summation) over the magnetic quantum numbers of the initial and final states,

$$A_{fi}^{(\text{Bessel})}(\theta_k; \lambda, b) = \frac{2\pi}{[J_i] \alpha^2} \sum_{M_i M_f} \left| \mathcal{M}_{fi}^{(\text{Bessel})} \right|^2 = \sum_{\mathbb{M}} A_{fi}^{(\text{Bessel})}(\mathbb{M}) = \sum_{pL} \sum_M \left| d_{M\lambda}^{(L)}(\theta_k) J_{m-M}(b\kappa) \right|^2 A_{fi}^{(\text{plane-wave})}(pL).$$

- **Excitation rate for twisted Bessel beams:** Similar to $A_{fi}^{(\text{plane-wave})}$, the rate $A_{fi}^{(\text{Bessel})}(\theta_k; \lambda, b)$ is still a sum of partial rates of allowed multipole transitions (\mathbb{M}). Moreover, each partial rate $A_{fi}^{(\text{Bessel})}(\mathbb{M})$ is a product of the corresponding plane-wave contribution *times* a geometrical term that describes the properties of the Bessel beam as well as the position of the target atom. This decomposition ensures that the relative contributions of the various multipole amplitudes (\mathbb{M}) to the total rate of the $|\alpha_i \mathbb{J}_i\rangle + \gamma^{(\text{Bessel})} \rightarrow |\alpha_f \mathbb{J}_f\rangle$ transition will change if the parameters of the (twisted) Bessel light, such as θ_k , κ , λ , ..., are modified
- **Excitation rate for Bessel-beam photons & Gaussian target:** Making use of the Gaussian target distribution with widths σ centered at b_0 , the photoexcitation rate can be written as:

$$A_{fi}^{(\text{Bessel})}(\theta_k; \lambda, \mathbf{b}_0; \sigma) = \sum_{\mathbb{M}} \sum_M \left| d_{M\lambda}^{(L)}(\theta_k) \right|^2 \mathcal{J}_{m-M}(b_0; \sigma) A_{fi}^{(\text{plane-wave})}(\mathbb{M})$$

$$\mathcal{J}_{m-M}(b_0, \sigma) = \int \frac{d\mathbf{b}}{(2\pi)^2} f(\mathbf{b}; \mathbf{b}_0) |J_{m-M}(\kappa b)|^2 = \frac{1}{(2\pi)^2 \sigma^2} \int_0^\infty db b I_0 \left(\frac{b b_0}{\sigma^2} \right) |J_{m-M}(\kappa b)|^2 e^{-\frac{b^2 + b_0^2}{2\sigma^2}},$$

and where I_0 is the modified Bessel function of the first kind. Similar as before, the partial multipole rates in this rate expression are given by the product of the corresponding plane-wave rates $A_{fi}^{(\text{plane-wave})}(\mathbb{M})$ *times* a weight function that depends on the properties of twisted beam as well as the geometry and the distribution of the target, but which does not depend on the electronic structure of the atoms.

- **Excitation rate for plane-wave *versus* Bessel beams:** While, for plane-wave radiation and initially unpolarized atoms, the partial multipole rates are entirely determined by the electronic structure of the target atom, the corresponding partial multipole rates $A_{fi}^{(\text{Bessel})}(\mathbb{M})(\theta_k; \lambda, \mathbf{b}_0; \sigma)$ also depend on the (geometrical) properties of the radiation as well as the position of the atom with regard to the beam axis for twisted light. For instance, we can consider how the (relative) strength of multipoles is affected by properties of the twisted light by taking the probability ratio (Schulz *et al.*, 2019)

$$\frac{A_{fi}^{(\text{Bessel})}(\mathbb{M}_1)}{A_{fi}^{(\text{Bessel})}(\mathbb{M}_2)} = \mathcal{R}(\mathbb{M}_1 \mathbb{M}_2; m, \kappa b) \frac{A_{fi}^{(\text{plane-wave})}(\mathbb{M}_1)}{A_{fi}^{(\text{plane-wave})}(\mathbb{M}_2)},$$

$$\mathcal{R}(\mathbb{M}_1 \mathbb{M}_2; m, \kappa b) = \frac{\sum_M \left| d_{M\lambda}^{(L_1)}(\theta_k) J_{m-M}(b\kappa) \right|^2}{\sum_M \left| d_{M\lambda}^{(L_2)}(\theta_k) J_{m-M}(b\kappa) \right|^2}.$$

In this factorization, the first term just describes the geometry of the electron-photon interaction which depends on the TAM projection m and the opening angle θ_k of the Bessel beam as well as on the position of the target atom. This will become even more obvious if the dependence is made more explicit.

8.1.c. Atomic photoionization (PhotoIonization)

Process, notation & application:

- Photoionization of an atom or ion: $A + \hbar\omega \rightarrow A^{+*} + e_p^-$
- Quantum notations used in the formulas below: $|\alpha_i J_i\rangle + \hbar\omega(M) \rightarrow |\alpha_f J_f\rangle + e_p^-(\mathbf{p}, m_s)$ or
 $|\alpha_i J_i\rangle + \hbar\omega(M) \rightarrow |\alpha_f J_f\rangle + \{e_p^-(\varepsilon \kappa)\}$.
- Using JAC: Perform an `Atomic.Computation(..., processSettings=PhotoIonization.Settings(...), ...)` or call directly functions from the module `PhotoIonization`.
- In JAC, the total photoionization cross sections $\sigma^{(\text{photoionization})(\omega; \alpha_i J_i \rightarrow \alpha_f J_f)}$ are calculated and tabulated by default, while the partial cross sections into the final magnetic substates $|\alpha_f J_f M_f\rangle$ with well-defined projection M_f are printed only if the flag `calcPartialCs = true` is set in `PhotoIonization.Settings`.
- In JAC, the statistical tensors of the photoion are calculated and tabulated for the photoionization of initially unpolarized atoms by plane-wave photons with given Stokes parameters, if the flag `calcTensors` is set in `PhotoIonization.Settings` and if the Stokes parameters (P_1, P_2, P_3) are provided explicitly by `Ionization.Settings.stokes`.
- Using JAC: Perform an `Atomic.Computation(..., processSettings = PlasmaShift.PhotoSettings(...), ...)` or call directly functions from the modules `PhotoIonization` and `PlasmaShift`. Until the present, however, only a Debye-Hückel plasma model is supported in JAC, and where the Debye-Hückel screening of the electron-nucleus and electron-electron interaction is incorporated only in first-order perturbation theory into the CI matrix.
- In JAC, the reduced photoionization amplitudes (matrix elements) are the main *building blocks* in order to represent and discuss most photoionization properties as they arise from the interaction of atoms and ions with the radiation field.
- **Quantization axis:** While the magnetic quantum numbers of the photoion and electron refer to the adopted *quantization axis* of the overall system (z -axis), the **helicity λ of the photon** is *always* defined with regard to the wave vector \mathbf{k} of the photon, i.e. with regard to the direction of the incident photons.
- **Quantization axis:** In practice, a proper quantization axis has to be chosen for the computation of all photoionization processes; hereby, one often needs to take into account **the geometry of the underlying experiment**. For instance, in order to describe the alignment of the photoion for its (photo-) ionization by *unpolarized* light, it is most convenient to adopt the quantization axis along the incoming photon momentum: $\mathbf{k} \parallel z$.

- **Fano's propensity rule for photoionization:** According to this (propensity) rule, the dipole transition to the partial wave with larger orbital angular momentum $\ell_c = \ell_i + 1$ is usually dominant, and the photoemission group delay is then approximately given by $\tau^{(\text{Wigner})} = \frac{d\sigma_{\ell_c}}{dE}$. Here, ℓ_c, ℓ_i refer to the partial waves of the active electron.
- **Electron-electron correlations:** Interesting correlation effects with regard to the exchange interaction, interchannel coupling, relaxation and polarization of the incident photons and/or photoelectrons often occurs in the vicinity of the photoionization threshold.
- **Circular dichroism (CD) of photoelectrons:** Studies on the CD of photoelectrons have been performed not only in basic research on the spin control and magnetism of different target material but also in (bio-)chemistry and material science. In their simplest form, the CD is measured by using circularly-polarized optical lasers or synchrotron radiation sources, and combined with high-resolution angle-resolved electron spectroscopy.
- **Dichroism:** A dichroism in the photoelectron emission is conventionally related to a change in the polarization of the incident light, while the initial polarization state of the target is kept fixed in most of these measurements.
- **Giant resonances:** The $4d$ ionization of xenon and barium are both characterized by a broad (and delayed) absorption peak with a widths of approximately 50 eV above of the $4d$ ionization threshold, a so-called **giant resonance**. Photoelectron spectroscopy measurements in this region have shown that a significant fraction of this strong absorption arises for xenon and barium due to the formation of – valence-shell excited – autoionizing resonances.

Photoionization amplitude:

- **Emission of an electron with well-defined asymptotic momentum \mathbf{p} and spin projection m_s :** If the atom undergoes the transition $|\alpha_i \mathbb{J}_i M_i\rangle \rightarrow |\alpha_f \mathbb{J}_f M_f\rangle$ during the photoionization process, the transition amplitude for the absorption of a photon with wave vector \mathbf{k} and helicity $\lambda = \pm 1$ is given by:

$$\mathcal{M}(M_f, m_s, \lambda, M_i) = \left(\frac{4\pi^2 \alpha}{\omega} \right)^{1/2} \left\langle \alpha_f \mathbb{J}_f M_f, \mathbf{p} m_s \left| \sum_{j=1}^N \boldsymbol{\alpha}_j \mathbf{u}_\lambda e^{i\mathbf{k}\cdot\mathbf{r}_j} \right| \alpha_i \mathbb{J}_i M_i \right\rangle.$$

- **Population of the magnetic sublevels $|\alpha_f \mathbb{J}_f M_f\rangle$ of the photoion:** This population depends (of course) on the spin projection λ of the incident photons as well as the magnetic quantum numbers M_f of the final state of the photoion, while one need to average over the initial sublevels as well as the spin projections of the emitted electron.

8. Atomic processes

- (Reduced many-electron) photoionization amplitude: For both, a partial-wave decomposition of the outgoing photoelectron *and* a multipole expansion of the electron-photon interaction, the reduced photoionization amplitude describes the contribution of individual multipole components of the radiation field to the formation of a scattering state $|\langle \alpha_f J_f, \varepsilon \kappa \rangle J_t\rangle$ with well-defined total symmetry and asymptotic energy ε of the outgoing photoelectron; this reduced amplitude is related to the photoabsorption amplitude by:

$$\langle (\alpha_f J_f, \varepsilon \kappa) J_t | \mathbb{O}^{(\mathbb{M}, \text{photoionization})} | \alpha_i J_i \rangle = i^{-\ell} \exp(i \Delta_\kappa) \langle (\alpha_f J_f, \varepsilon \kappa) J_t | \mathbb{O}^{(\mathbb{M}, \text{absorption})} | \alpha_i J_i \rangle.$$

Here, the photoionization amplitude also accounts for the proper phase Δ_κ (or the asymptotic boundary condition) of the outgoing electron.

- In JAC, the reduced photoionization amplitudes (matrix elements) above are the main *building blocks* in order to represent and discuss most photoionization properties as they arise from the interaction of atoms and ions with the radiation field.

Partial and total photoionization cross sections:

- Partial photoionization cross sections for the photoionization of an initially unpolarized atom: For the photoionization of an initially unpolarized atom from level $(\alpha_i J_i) \rightarrow |\alpha_f J_f M_f\rangle$ by unpolarized plane-wave photons with wave vector $\mathbf{k} \parallel \mathbf{e}_z$ (quantization axis), the partial cross sections can be expressed as:

$$\begin{aligned} \sigma(\omega; \alpha_i J_i \rightarrow \alpha_f J_f M_f) &= \frac{1}{2(2J_i + 1)} \sum_{M_i \lambda m_s} \int d\Omega_p |\mathcal{M}(M_f, m_s, \lambda, M_i)|^2 \\ &= \frac{4\pi^2 \alpha}{2\omega(2J_i + 1)} \sum_{M_i} \sum_{\lambda} \sum_{km} \sum_{JJ'M} \langle J_f M_f jm | JM \rangle \langle J_f M_f jm | J' M \rangle \left\langle (\alpha_f J_f, \varepsilon \kappa) J_t M \left| \sum_{j=1}^N \alpha_j \mathbf{u}_\lambda e^{i \mathbf{k} \cdot \mathbf{r}_j} \right| \alpha_i J_i M_i \right\rangle \\ &\quad \times \left\langle (\alpha_f J_f, \varepsilon \kappa) J_t M \left| \sum_{j=1}^N \alpha_j \mathbf{u}_\lambda e^{i \mathbf{k} \cdot \mathbf{r}_j} \right| \alpha_i J_i M_i \right\rangle^*. \end{aligned}$$

Here, the integration over all emission angles $\Omega_p = (\vartheta_p, \varphi_p)$ of the photoelectron results into a *incoherent* summation over the partial waves of the many-electron scattering states with different κ -symmetries of the photoelectron.

- Partial photoionization cross sections for the photoionization of initially unpolarized atoms by unpolarized plane-wave photons: For unpolarized atoms and unpolarized incident plane-wave photons, the partial cross sections from above can be simplified and expressed as:

$$\begin{aligned} \sigma(\omega; \alpha_i \mathbb{J}_i \rightarrow \alpha_f J_f M_f) &= \frac{8\pi^3 \alpha}{2\omega(2J_i+1)} \sum_{t\lambda} \sum_{\kappa} \sum_{JJ'} \sum_{\mathbb{M}\mathbb{M}'} i^{L-L'} (i\lambda)^p (-i\lambda)^{p'} (-1)^{L+L'} \sqrt{(2L+1)(2L'+1)(2J+1)(2J'+1)} \\ &\quad \times \langle L'\lambda, J_f M_f | t, \lambda + M_f \rangle \langle L\lambda, J_f M_f | t, \lambda + M_f \rangle \left\{ \begin{array}{ccc} j & J' & J_f \\ J & J_i & L \\ J_f & L' & t \end{array} \right\} \\ &\quad \times \langle (\alpha_f \mathbb{J}_f, \varepsilon\kappa) \mathbb{J} \| \mathbb{O}^{(\mathbb{M}, \text{photoionization})} \| \alpha_i \mathbb{J}_i \rangle \langle (\alpha_f \mathbb{J}_f, \varepsilon\kappa) \mathbb{J}' \| \mathbb{O}^{(\mathbb{M}', \text{photoionization})} \| \alpha_i \mathbb{J}_i \rangle^*. \end{aligned}$$

- Total photoionization cross sections for the photoionization of initially unpolarized atoms by unpolarized plane-wave photons: For the photoionization of an initially unpolarized atom from level $(\alpha_i \mathbb{J}_i) \rightarrow |\alpha_f \mathbb{J}_f\rangle$ by unpolarized plane-wave photons with wave vector $\mathbf{k} \parallel \mathbf{e}_z$, the total cross sections can be expressed as:

$$\sigma(\omega; \alpha_i \mathbb{J}_i \rightarrow \alpha_f \mathbb{J}_f) = \sum_{M_f} \sigma(\omega; \alpha_i \mathbb{J}_i \rightarrow \alpha_f \mathbb{J}_f M_f) = \frac{4\pi^2 \alpha \omega}{2(2J_i+1)} \sum_{\kappa} \sum_{\mathbb{J}} |\langle (\alpha_f \mathbb{J}_f, \varepsilon\kappa) \mathbb{J} \| \mathbb{O}^{(\mathbb{M}, \text{photoionization})} \| \alpha_i \mathbb{J}_i \rangle|^2.$$

In JAC, the summation over $\kappa \mathbb{J}$ refers to the summation over all photoionization channels of a given photoionization line between fine-structure levels: $(\alpha_i \mathbb{J}_i \rightarrow \alpha_f \mathbb{J}_f)$.

Final-state density matrix 'photoion + photoelectron':

- Final-state density matrix of the 'photoion + photoelectron': The final-state density matrix of the overall system 'photoion + photoelectron' is generally not very useful and only needed for entanglement studies and related topics. Here, we just collect some formulas but further work will be required in order to find the proper expression of the density matrix for incident light with different polarization properties.
- Final-state density matrix of the 'photoion + photoelectron': After the absorption of the photon, we have a free electron with asymptotic linear momentum \mathbf{p} and with spin projection m_s , while the photoion is left in a (magnetic) fine-structure state $|\alpha_f \mathbb{J}_f M_f\rangle$. Using a basis with well-defined (angular) momenta J_i and J_f of the initial and the residual ion as well as the asymptotic linear momentum \mathbf{p} and spin

8. Atomic processes

projection m_s of the ejected electron, the final-state density matrix can be written as

$$\begin{aligned} & \langle \alpha_f J_f M_f, \mathbf{p} m_s | \rho_f | \alpha_f J_f M'_f, \mathbf{p} m'_s \rangle \\ &= \sum_{M_i M'_i, \lambda \lambda'} c_{\lambda \lambda'} \left\langle \alpha_f J_f M_f, \mathbf{p} m_s \left| \hat{\mathcal{R}} \right| \alpha_i J_i M_i, \mathbf{k} \lambda \right\rangle \langle \alpha_i J_i M_i, \mathbf{k} \lambda | \rho_i | \alpha_i J_i M'_i, \mathbf{k} \lambda' \rangle \left\langle \alpha_i J_i M'_i, \mathbf{k} \lambda' \left| \hat{\mathcal{R}}^\dagger \right| \alpha_f J_f M'_f, \mathbf{p} m'_s \right\rangle \end{aligned}$$

where $R = \sum_j \boldsymbol{\alpha}_j \cdot \mathbf{u}_\lambda e^{i \mathbf{k} \cdot \mathbf{r}_j}$ represents the electron-photon interaction.

Angular distribution of photoelectrons:

- **Measurement operator for angular distributions:** If the detector is neither sensitive to the spin state of the photoelectron nor to those of the residual photoion, a proper measurement (projection) operator is obtained if we sum over the electron spin projections m_s as well as the magnetic quantum numbers M_f of the ion. In the density matrix formalism, this projection operator for measuring the angular distribution of the emitted photoelectrons therefore is:

$$P = \sum_{M_f m_s} |\alpha_f J_f M_f, \mathbf{p} m_s \rangle \langle \alpha_f J_f M_f, \mathbf{p} m_s|, \quad \mathbf{p} = \mathbf{p}(\vartheta, \varphi)$$

With this measurement operator, the well-known **angular distribution of the photoelectrons** is just the normal trace of the final-state density matrix:

$$W(\vartheta) \equiv \text{Tr}(P \rho_f) = \sum_{M_f m_s} \langle \alpha_f J_f M_f, \mathbf{p} m_s | \rho_f | \alpha_f J_f M_f, \mathbf{p} m_s \rangle.$$

- **Photoionization of closed-shell atoms:** Derevianko *et al.* (1999) provide a detailed study of the photoionization cross sections and angular distributions of all rare-gas atoms up to xenon and by going beyond the typical dipole approximation. In particular, these authors include all corrections $\mathcal{O}(ka)$ and $\mathcal{O}(k^2 a^2)$ where k is the modulus of the wave vector and a the radius of the ionized subshell. While, within the electric-dipole approximation, the photoelectron angular distribution for the photoionization by linearly or unpolarized light is characterized by a single (anisotropy) parameter β , the $\mathcal{O}(ka)$ corrections are characterized by two parameters γ and δ , and the $\mathcal{O}(k^2 a^2)$ corrections by even three parameters λ, μ, ν with the constraint $\lambda + \mu + \nu = 0$ as well as a correction $\Delta \beta$ to the dipole parameter.
- **Angle-differential photoionization cross section for closed-shell atoms:** For the photoionization of an electron from an initially closed

subshell by linearly-polarized light, the angle-differential photoionization cross section is given by (Derevianko *et al.*, 1999)

$$\frac{d\sigma}{d\Omega}(\vartheta, \varphi) = \frac{\sigma_o}{4\pi} \{ 1 + (\beta + \Delta\beta) P_2(\cos \vartheta) + (\delta + \gamma \cos^2 \vartheta) \sin \vartheta \cos \varphi + \lambda P_2(\cos \vartheta) \cos 2\varphi + \mu \cos 2\varphi + \nu (1 + \cos 2\varphi) P_4(\cos \vartheta) \}$$

with $\lambda + \mu + \nu = 0$, and where (ϑ, φ) are the polar angles of the outgoing photoelectrons. This expansion applies, if the quantization axis is chosen along the polarization, $\mathbf{u} \parallel \mathbf{e}_z$, and $\mathbf{e}_x \parallel \mathbf{k}$ along the photon propagation. This expression also includes the standard angular distribution of photoelectron, $1 + \beta P_2(\cos \vartheta)$ in the electric-dipole approximation, where β results from the interference of (electric-dipole) amplitudes for different partial waves of the outgoing electron. Derevianko *et al.* (1999) discuss also briefly which interferences due to the various multipole components of the radiation field give rise to all other anisotropy parameters, while expressions are given only in one-electron notation as appropriate for hydrogenic and closed-shell systems. No attempt has been made to derive expressions for open-shell atoms. Derevianko *et al.* (1999) found the non-dipole angular parameters rather insensitive with regard to details of the chosen potential $V(r)$.

- Formulas of the (non-) dipole anisotropy parameters for closed-shell atoms: All dipole and non-dipole anisotropy parameters can be readily expressed in terms of the (reduced) multipole transition amplitudes. Derevianko *et al.* (1999) provide tables and graphs of the seven angular distribution parameters, calculated within the relativistic independent-particle approximation (IPA). Results are shown for electron energies between 20-5000 eV for all subshells of the rare gas atoms He, Ne, Ar, Kr and Xe. For Ar and Kr, moreover, comparison is made for selected parameters with results from the random-phase approximation in order to illustrate the influence of electron correlations.

Reduced statistical tensors of the photoion for plane-wave incident radiation:

- Statistical tensors of the photoion in level $(\alpha_f \mathbb{J}_f)$ after the photoionization of unpolarized atoms by unpolarized plane-wave photons: If the incident light propagates along the x -axis (here used as quantization axis because of its frequent use in experimental discussions) and if the photoelectron remains unobserved, the statistical tensors are given by Kämpfer *et al.* (2016)

$$\begin{aligned} \rho_{kq}(\alpha_f \mathbb{J}_f) &= \frac{\pi}{2J_i + 1} \delta_{q0} \sum_{\mathbb{M}\mathbb{M}'} \sum_{\kappa} \sum_{JJ'} \sum_{\lambda=\pm 1} i^{L+p-L'-p'} \lambda^{p+p'} [L, L', J, J']^{1/2} (-1)^{J+J'+J_f+J_i+j+1} \langle L\lambda, L'(-\lambda) | kq \rangle \left\{ \begin{matrix} J_f & j & J' \\ J & k & J_f \end{matrix} \right\} \left\{ \begin{matrix} J' & J_i & L' \\ L & k & J \end{matrix} \right\} \\ &\times \langle (\alpha_f \mathbb{J}_f, \varepsilon\kappa) \mathbb{J} \left| \mathbb{O}^{(\mathbb{M}, \text{photoionization})} \right| \alpha_i \mathbb{J}_i \rangle \langle (\alpha_f \mathbb{J}_f, \varepsilon\kappa) \mathbb{J}' \left| \mathbb{O}^{(\mathbb{M}', \text{photoionization})} \right| \alpha_i \mathbb{J}_i \rangle^*. \end{aligned}$$

- Statistical tensors of the photoion in level $(\alpha_f \mathbb{J}_f)$ after the photoionization of unpolarized atoms by plane-wave photons with given density matrix $(c_{\lambda\lambda})$: If, more generally, the incident plane-wave light propagates along the z -axis and refers to photons with well-defined (photon)

8. Atomic processes

density matrix ($c_{\lambda\lambda'}$) or Stokes parameters (P_1, P_2, P_3), the statistical tensors are given by (Sharma *et al.*, 2010)

$$\begin{aligned} \rho_{kq}(\alpha_f J_f) &= \frac{\pi}{2J_i + 1} \sum_{\mathbb{M}\mathbb{M}'} \sum_{\kappa J J'} \sum_{\lambda\lambda'} [\delta_{\lambda\lambda'}(1 + \lambda P_3) + (1 - \delta_{\lambda\lambda'}) (P_1 - i\lambda P_2)] i^{L-L'+p-p'} \lambda^p (\lambda')^{p'} [L, L', J, J']^{1/2} \\ &\times (-1)^{(J+J'+J_f+J_i+j+1)} \langle L\lambda L'(-\lambda') | kq \rangle \left\{ \begin{matrix} J_f & j & J' \\ J & k & J_f \end{matrix} \right\} \left\{ \begin{matrix} J' & J_i & L' \\ L & k & J \end{matrix} \right\} \\ &\times \langle (\alpha_f J_f, \varepsilon\kappa) J \left| \mathbb{O}^{(\mathbb{M}, \text{photoionization})} \right| \alpha_i J_i \rangle \langle (\alpha_f J_f, \varepsilon\kappa) J' \left| \mathbb{O}^{(\mathbb{M}', \text{photoionization})} \right| \alpha_i J_i \rangle^*. \end{aligned}$$

- In JAC, the statistical tensors of the photoion are calculated and tabulated for the photoionization of unpolarized atoms by plane-wave photons with given Stokes parameters, if the proper information is provided by the PhotoIonization.Settings.

Time-resolved photoionization:

- **Time-resolved photoionization experiments:** During the last two decades, experiments with subfemto-second resolution enabled one to study the electron dynamics of atoms. Examples refer to the observation of time-resolved autoionizing resonances, the decay of core vacancies or the (relative) delay time of emitted photoelectrons. All these relaxation processes usually occur within tens of attoseconds in dependence of the excitation energy and the electronic structure of the atomic targets. Following Heisenberg's uncertainty principle, of course, a natural trade-off exist between the temporal and spectral resolution, though resolution can be tuned to either the time or frequency domain. In the time domain, such spectroscopic studies have largely benefitted from the high-resolution frequency combs that are based on phase-stable femtosecond pulse trains.
- **Time-resolved photoionization experiments:** Isinger *et al.* (2017) used the high-order harmonic spectrum in order to analyze the interplay between high-resolution photoelectron spectroscopy and attosecond dynamics. This analysis enabled them to disentangle the direct $2s$ ionization of neon from ionization-excitation processes of two $2p$ electrons (shake-up processes) by utilizing a phase-stable interferences between attosecond pulses in the pulse train. The $2s - 2p$ time delay derived from this detailed analysis agrees well with theoretical predictions based on the Wigner time. Here, the observation of the shake processes also provided an explanation to the discrepancy with earlier observations by Schultze *et al.* (2010).
- **Wigner (time) delay:** The photoionization time delay or Wigner delay refers to the delay of the group velocity of the electronic wave packet as created by the absorption of xuv radiation. This Wigner delay can be obtained quite readily by taking the derivative of the

scattering phase of the outgoing electron wave. — An additional time delay arises from the interaction of the laser probe field with the Coulomb potential, and this can be calculated accurately at high kinetic energies from either the asymptotic form of the wave function or by classical trajectories (Isinger *et al.*, 2017).

- **Time-resolved photoionization:** The measured time delays in (time-resolved) photoionization experiments general consists of different parts which need to be considered separately, and often also within different theoretical frameworks. Apart from the **quantum-mechanical Eisenbud-Wigner-Smith (EWS) delay**, which arises from the group delay of the photoelectron wave packet, the interaction of the electrons with the additional laser field, e.g. the ir streaking field, has to be taken into account as well. The EWS delay practically refers to changes in the phase of the outgoing wave packets and require a careful treatment of the inter-electronic correlations in the photoionization process. Both contributions are assumed to be strictly additive with (sub-) attosecond precision and can therefore be determined independently of each other.
- **Time-resolved photoionization:** In attosecond-streaking experiments, the photoionization of a bound electron arises from the interaction of atoms with two light fields, an isolated attosecond pulse in the extreme ultraviolet (xuv) range of the spectrum and a streaking ir field

$$\mathcal{E}(t) = \mathcal{E}^{(\text{xuv})}(t) + \mathcal{E}^{(\text{ir})}(t).$$

The time-resolved information about the photoionization of single electrons are obtained by varying the temporal overlap between the xuv and ir fields. Theoretically, the xuv is usually weak and treated perturbatively, while the ir streaking field is moderately strong, although not strong enough to modify the ionization. However, the ir field strongly affects the motion of the quasi-free electron, once it is released from the atom (Feist *et al.*, 2014).

- **Eisenbud-Wigner-Smith (EWS) delay:** The EWS time for the photoionization of atom from the initial level ($\alpha_i \mathbb{J}_i$) to the final level ($\alpha_f \mathbb{J}_f$) of the residual photoion is given by the energy derivative of the (single-electron) photoionization amplitude

$$t^{(\text{EWS})} = \frac{\partial}{\partial \varepsilon} \langle \alpha_f \mathbb{J}_f, \mathbf{p} m_s | \mathbb{O}^{(\text{E1, photoionization})} | \alpha_i \mathbb{J}_i \rangle,$$

and where $\mathbf{p} = \mathbf{p}(\varepsilon, \vartheta, \varphi)$ is the asymptotic momentum of the emitted electron. In this notation, (ϑ, φ) just refers to the direction of the outgoing electron wave and E1 to the electric-dipole approximation. Details of this (single-electron) photoionization amplitude depend on the polarization of the incident xuv photons and how the inter-electronic correlations are taken into account.

Photoionization by twisted light:

8. Atomic processes

➤ Photoionization by twisted light:



8.1.d. Radiative recombination (PhotoRecombination)

Process, notation & application:

- Radiative recombination or photorecombination of an atom or ion: $A^{q+} + e^- \longrightarrow A^{(q-1)+} + \hbar\omega$
- Quantum notations used in the formulas below: $|\alpha_i J_i\rangle + |\varepsilon\kappa\rangle \longrightarrow |\alpha_f J_f\rangle + \{\hbar\omega(M)\}$ or $|\alpha_i J_i\rangle + |\mathbf{p} m_s\rangle \longrightarrow |\alpha_f J_f\rangle + \{\hbar\omega(M)\}$.
- Using JAC: Perform an `Atomic.Computation(..., processSettings=PhotoRecombination.Settings(...), ...)` or call directly functions from the module `PhotoRecombination`.
- In JAC, the total radiative recombination cross sections are calculated and tabulated by default for all selected recombination lines.
- In JAC, the (reduced) photorecombination amplitudes are the building blocks in order to obtain most of the properties below.
- In JAC, the anisotropy parameters $\beta_\nu^{(RR)}$, $\nu = 1, \dots, 4$ are calculated and tabulated for all selected photorecombination lines if the flag `calcAnisotropy = true` is set in `PhotoRecombination.Settings`.
- In JAC, the statistical tensors for the recombination of unpolarized ions with unpolarized plane-wave electrons are calculated and tabulated if the flag `calcTensors = true` is set in `PhotoRecombination.Settings`.
- Radiative recombination (RR): The photorecombination of ions is known also as radiative recombination (RR) or radiative electron capture (REC) in the literature.
- Radiative recombination (RR): The RR can be viewed as the time-reversed photoionization process, and which occurs very frequently in stellar and laboratory plasmas as well as in ion-trap and storage-ring experiments.
- RR in storage rings: If a highly-charged ion circulates in a storage ring, it may capture electrons from rest-gas atoms in the ring and will then be misbent by subsequent steering magnets. Therefore, the radiative recombination or electron capture typically results in a loss of the ion from the ring, and where the lifetime is just proportional to the inverse product of the capture cross section and target pressure.
- Magnetic sublevel population $|\alpha_f J_f M_f\rangle$ of the recombined ion: The radiative recombination amplitude from below can be utilized to describe the (magnetic) sublevel population of the recombined ion. In the framework of density matrix theory, this sublevel population of the ionic (or atomic) states is described most conveniently in terms of the *statistical tensors* $\rho_{kj}(\alpha_f J_f)$ of the recombined ion in its final level $(\alpha_f J_f)$.

8. Atomic processes

- **Importance of RR in astrophysics:** The radiative recombination of multiply-charged ions has been found important for estimating the ionization equilibrium and thermal balance in gaseous nebulas and fusion plasma. For these applications, simple scaling rules of the RR cross sections as function of the continuum electron energy, atomic number and/or ionic species can be helpful (Kim and Pratt, 1983), if plasmas of different different temperatures, charge states and ion species are considered.
- **RR of bare ions:** The RR process has attracted much interest from the very beginning of quantum mechanics and even before, where it has been treated semi-classically. Already in 1923, Kramers used semi-classical arguments in order to estimate the cross section for the RR of initially bare ions into high- n subshells. Several other authors also obtained approximate expressions for the RR cross sections of initially bare ions; for instance, the Bethe-Salpeter analytical formula provides an approximate cross section for the recombination into the ground and low-excited levels. Katkov and Strakhovenko (1978) later derived for initially bare ions another approximate expression for the RR cross section $\sigma^{(\text{RR})}(\varepsilon; \text{bare} \rightarrow n)$ into any given shell n . Approximate expressions are known in the literature also for the total RR cross section $\sigma^{(\text{RR, total})}(\varepsilon; \text{bare} \rightarrow \sum_n n)$.

Photorecombination amplitude:

- **Photorecombination amplitude:** In first-order perturbation theory, most RR properties can be traced back to the evaluation of the (reduced photon emission) matrix elements between levels with well-defined total angular momentum

$$\langle \alpha_f J_f \parallel O^{(\mathbb{M}, \text{photorecombination})} \parallel (\alpha_i J_i, \varepsilon\kappa) J_t \rangle \equiv \langle \alpha_f J_f \parallel O^{(\mathbb{M}, \text{RR})} \parallel (\alpha_i J_i, \varepsilon\kappa) J_t \rangle = \langle (\alpha_i J_i, \varepsilon\kappa) J_t \parallel O^{(\mathbb{M}, \text{photoionization})} \parallel \alpha_f J_f \rangle^*,$$

and which describes just the capture of a free electron with (asymptotic) kinetic energy ε and angular momentum κ under the – simultaneous – emission of a photon with multipolarity $\mathbb{M} = (L, p)$.

Total recombination cross sections and rate coefficients:

- **Total recombination cross section:** If the density of states and the principle of detailed balance between the capture and the (photo-) ionization of an electron is taken into account, the total RR cross section for a projectile ion with $\gamma \neq 1$ reads as

$$\sigma^{(\text{RR})}(\varepsilon; \alpha_i J_i \rightarrow \alpha_f J_f) = \frac{8\alpha^3 \pi^3 \omega}{(2J_i + 1)} \frac{1}{\beta^2 \gamma^2} \left[\sum_{\mathbb{M} J_\kappa} |\langle \alpha_f J_f \parallel O^{(\mathbb{M}, \text{RR})} \parallel (\alpha_i J_i, \varepsilon\kappa) J_t \rangle|^2 \right], \quad \omega = \varepsilon + E_i - E_f,$$

and where $\beta = v/c$ and $\gamma = \sqrt{1 - \beta^2}$ arise from the Lorentz transformation in going from the projectile into the laboratory frame.

- **Milne relation between photoionization and RR cross sections:** The R-matrix approach enables one to treat both, the direct as well as resonance contributions to the total photoionization cross section for ions in some initial level ($\alpha_i \mathbb{J}_i$). By using the principle of detailed balance (Milne relation), this approach therefore enables one to deal simultaneously with the RR and DR contributions to the overall (electron capture) plasma rate coefficient, although usually in the level-resolved form. The Milne relation between the cross sections are given (in Rydberg units) by

$$\sigma^{(\text{electron capture})}(\varepsilon; \alpha_f \mathbb{J}_f \rightarrow \alpha_i \mathbb{J}_i) = \frac{\alpha^2}{4} \frac{g_f}{g_i} \frac{(\varepsilon + I_p)^2}{\varepsilon} \sigma^{(\text{photoionization})}(\varepsilon; \alpha_i \mathbb{J}_i \rightarrow \alpha_f \mathbb{J}_f)$$

and where the statistical factors g_i, g_f refer to the ion before capture and the residual photoion, respectively.

Angular distribution of emitted photons:

- **Angular distribution of emitted photons:** For initially unpolarized ions and unpolarized incident plane-wave electrons, the angular distribution of the emitted recombination photons can be readily obtained from the final-state density matrix by taking the trace $\text{Tr}(P_{\mathbf{k}} \rho_f)$ with regard to the measurement (projection operator) of plane-wave photons:

$$W^{(\text{RR})}(\theta, \varepsilon; \alpha_i \mathbb{J}_i \rightarrow \alpha_f \mathbb{J}_f) = \frac{\sigma^{(\text{RR})}}{4\pi} \left(1 + \sum_{\nu=1} P_{\nu}(\cos \vartheta) \beta_{\nu}^{(\text{RR})}(\varepsilon; \alpha_i \mathbb{J}_i \rightarrow \alpha_f \mathbb{J}_f) \right).$$

- **Anisotropy parameters of the emitted photons:**

$$\begin{aligned} \beta_{\nu}^{(\text{RR})}(\varepsilon; \alpha_i \mathbb{J}_i \rightarrow \alpha_f \mathbb{J}_f) &= -\frac{1}{2N} \sum_{\mathbb{J}\mathbb{J}'\kappa\kappa'} \sum_{\mathbb{M}\mathbb{M}'} i^{L+p-L'-p'} (-1)^{J_i-1/2-J_f} [L, L', \ell, \ell', j, j', J, J']^{1/2} \langle \ell 0, \ell' 0 | \nu 0 \rangle \langle L 1, L' - 1 | \nu 0 \rangle \left(1 + (-1)^{L+p+L'+p'-\nu} \right) \\ &\quad \times \begin{Bmatrix} J & J' & \nu \\ L' & L & J_f \end{Bmatrix} \begin{Bmatrix} J & J' & \nu \\ j' & j & J_i \end{Bmatrix} \begin{Bmatrix} j & j' & \nu \\ \ell' & \ell & 1/2 \end{Bmatrix} \langle \alpha_f \mathbb{J}_f \| \mathbb{O}^{(\mathbb{M}, \text{RR})} \| (\alpha_i \mathbb{J}_i, \varepsilon \kappa) \mathbb{J} \rangle^* \langle \alpha_f \mathbb{J}_f \| \mathbb{O}^{(\mathbb{M}', \text{RR})} \| (\alpha_i \mathbb{J}_i, \varepsilon \kappa') \mathbb{J}' \rangle \\ N &= \left[\sum_{\mathbb{J}\kappa\mathbb{M}} \left| \langle \alpha_f \mathbb{J}_f \| \mathbb{O}^{(\mathbb{M}, \text{RR})} \| (\alpha_i \mathbb{J}_i, \varepsilon \kappa) \mathbb{J} \rangle \right|^2 \right]. \end{aligned}$$

8. Atomic processes

Final-state density matrix of the ‘recombined ion + photon’:

- Final-state density matrix of the ‘recombined ion + photon’: For an unpolarized ion with nuclear spin $I = 0$ and for unpolarized plane-wave electrons, the final-state density matrix can be expressed as:

$$\begin{aligned} & \langle \alpha_f \mathbb{J}_f M_f, \mathbf{k} \lambda | \rho_f | \alpha_f \mathbb{J}_f M'_f, \mathbf{k} \lambda' \rangle \\ &= \frac{8\pi}{2(2J_i + 1)} \sum_{\mathbb{M}\mathbb{M}'} \sum_{JJ'} \sum_{\kappa\kappa'} \sum_{\nu\mu_1\mu_2 ss'} D_{\mu_1\mu_2}^{(\nu)}(\mathbf{k} \rightarrow \mathbf{e}_z) i^{L'-L} (i\lambda')^{\pi'} (-i\lambda)^{\pi} (-1)^{1/2+J_i+J'+L+s+s'-M'_f} [\ell, \ell', L, L', j, j', J, J', s]^{1/2} \\ & \quad \times [s'] \left\{ \begin{array}{ccc} j' & 1/2 & \ell' \\ \ell & s & j \end{array} \right\} \left\{ \begin{array}{ccc} j' & J_i & J' \\ J & s & j \end{array} \right\} \left\{ \begin{array}{ccc} J & L & J_f \\ \nu & s' & L' \end{array} \right\} \left\{ \begin{array}{ccc} J & J' & s \\ J_f & s & L' \end{array} \right\} \langle \ell' 0, \ell 0 | s 0 \rangle \langle J_f M_f, s' (-M'_f) | \nu \mu_1 \rangle \\ & \quad \times \langle s 0, s' M'_f | J_f M'_f \rangle \langle L' \lambda', L (-\lambda) | \nu \mu_2 \rangle \langle \alpha_f \mathbb{J}_f \| \mathbb{O}^{(\mathbb{M}, \text{RR})} \| (\alpha_i \mathbb{J}_i, \varepsilon \kappa) \mathbb{J} \rangle \langle \alpha_f \mathbb{J}_f \| \mathbb{O}^{(\mathbb{M}'', \text{RR})} \| (\alpha_i \mathbb{J}_i, \varepsilon \kappa') \mathbb{J}' \rangle^*. \end{aligned}$$

- In JAC, no attempt has been made so far to implement the density matrix of the overall system ‘recombined ion + photon’ because of its little relevance for practical computations. However, this density matrix could be implemented quite easily by using the photorecombination amplitudes from above.

(Reduced) Statistical tensors of the recombined ion in the level $(\alpha_f \mathbb{J}_f)$:

- Statistical tensors $\rho_{k0}(\alpha_f \mathbb{J}_f)$ of the final ion following the recombination of unpolarized ions with unpolarized plane-wave electrons: If the electron has the kinetic energy ε and if the quantization axis is adopted along the incoming electron momentum $\mathbf{p} \parallel \mathbf{e}_z$, the statistical tensors of the recombined ion in level $(\alpha_f \mathbb{J}_f)$ are given by

$$\begin{aligned} \rho_{k0}(\varepsilon; \alpha_f \mathbb{J}_f) &= \frac{32\pi^3}{2J_i + 1} \sum_{\mathbb{M}} \sum_{\mathbb{J}\mathbb{J}'\kappa\kappa'} [\ell, \ell', j, j', J, J']^{1/2} (-1)^{J_i+L-J_f+J-J'-1/2} \langle \ell 0, \ell' 0 | k 0 \rangle \left\{ \begin{array}{ccc} j & j' & k \\ \ell' & \ell & 1/2 \end{array} \right\} \left\{ \begin{array}{ccc} j & j' & k \\ J' & J & J_i \end{array} \right\} \left\{ \begin{array}{ccc} J & J' & k \\ J_f & J_f & L \end{array} \right\} \\ & \quad \langle \alpha_f \mathbb{J}_f \| \mathbb{O}^{(\mathbb{M}, \text{RR})} \| (\alpha_i \mathbb{J}_i, \varepsilon \kappa) \mathbb{J} \rangle^* \langle \alpha_f \mathbb{J}_f \| \mathbb{O}^{(\mathbb{M}, \text{RR})} \| (\alpha_i \mathbb{J}_i, \varepsilon \kappa') \mathbb{J}' \rangle. \end{aligned}$$

8. Atomic processes

Here, the summation over \mathbb{M} refers to the multipoles of the radiation field and $(\mathbb{J}\kappa)$, $(\mathbb{J}'\kappa')$ to summations over all photorecombination channels, i.e. all the many-electron continua $|\langle \alpha_i \mathbb{J}_i, \varepsilon \kappa \rangle \mathbb{J} \rangle$ of the initial ion.

- **Reduced statistical tensors:** Instead of using the statistical tensors $\rho_{k0}(\alpha_f \mathbb{J}_f)$ of the (photo-) recombined ion, it is often more convenient to describe the sublevel population of the residual ions in terms of the (so-called) *reduced* tensors:

$$\mathcal{A}_{k0}(\varepsilon; \alpha_f \mathbb{J}_f) = \frac{\rho_{k0}(\varepsilon; \alpha_f \mathbb{J}_f)}{\rho_{00}(\varepsilon; \alpha_f \mathbb{J}_f)},$$

which are directly related to the RR cross sections $\sigma^{(RR)}(\varepsilon; \alpha_i \mathbb{J}_i \rightarrow \alpha_f \mathbb{J}_f M_f)$ for the electron capture into an ionic sublevel $|\alpha_f \mathbb{J}_f M_f\rangle$.

Photorecombination or radiative recombination plasma rate coefficient:

- **Level-resolved RR plasma rate coefficient:** The level-resolved RR plasma rate coefficient is obtained from the convolution of the RR cross section for an ion $\sigma^{(RR)}(\varepsilon; \alpha_i \mathbb{J}_i \rightarrow \alpha_f \mathbb{J}_f)$, initially in the level $(\alpha_i \mathbb{J}_i)$, and for an isotropic Maxwellian distribution function of the free electrons in the plasma

$$\alpha^{(RR)}(T_e; i \rightarrow f) = \frac{4}{\sqrt{2\pi m} T_e^{3/2}} \int_0^\infty d\varepsilon \varepsilon \sigma^{(RR)}(\varepsilon; \alpha_i \mathbb{J}_i \rightarrow \alpha_f \mathbb{J}_f) \exp\left(-\frac{\varepsilon}{T_e}\right).$$

- **Shell-resolved RR plasma rate coefficient:** The shell-resolved RR plasma rate coefficient is obtained from the convolution of the RR cross section for an ion $\sigma^{(RR)}(\varepsilon; i \rightarrow \{f\})$, initially in the level $(\alpha_i \mathbb{J}_i)$, and for an isotropic Maxwellian distribution function of the free electrons in the plasma

$$\alpha^{(RR)}(T_e; i \rightarrow (i, n\ell)) = \frac{4}{\sqrt{2\pi m} T_e^{3/2}} \int_0^\infty d\varepsilon \varepsilon \left[\sum_{\{\alpha_f \mathbb{J}_f\}} \sigma^{(RR)}(\varepsilon; \alpha_i \mathbb{J}_i \rightarrow \alpha_f \mathbb{J}_f) \right] \exp\left(-\frac{\varepsilon}{T_e}\right), \quad \{\alpha_f \mathbb{J}_f\} \equiv \{(\alpha_i \mathbb{J}_i, \kappa' s) \alpha_f \mathbb{J}_f\}.$$

- **Total RR plasma rate coefficient:** The total RR plasma rate coefficient is obtained from the convolution of the RR cross section for an ion, initially in the level $(\alpha_i \mathbb{J}_i)$, and the capture into any excited shell $(n\ell)$ as well as for an isotropic Maxwellian distribution function of the free electrons in the plasma

$$\alpha^{(RR)}(T_e; \alpha_i \mathbb{J}_i) = \frac{4}{\sqrt{2\pi m} T_e^{3/2}} \int_0^\infty d\varepsilon \varepsilon \left[\sum_{\alpha_f \mathbb{J}_f} \sigma^{(RR)}(\varepsilon; \alpha_i \mathbb{J}_i \rightarrow \alpha_f \mathbb{J}_f) \right] \exp\left(-\frac{\varepsilon}{T_e}\right).$$

- **Total RR + DR plasma rate coefficients:** Various approaches have been developed to calculate combined RR + DR plasma rate coefficients; these approaches are often based on the R-matrix formalism, exterior complex scaling, the close-coupling approximation as well as various hybrid theories. The total RR + DR plasma rate coefficients are important for solar- and astrophysics and have mainly been calculated at various electron temperatures by using the Maxwell velocity distribution function.
- **Application of RR plasma rate coefficients:** Shell-resolved and total radiative recombination plasma rate coefficients are often needed to estimate the ionization equilibrium and thermal balance in different terrestrial and astrophysical plasma. In fusion reactors, these plasma rate coefficients help model the contributions of impurity ions of heavy elements. The RR rate coefficients are therefore needed for the further development of fusion facilities and its plasma diagnostics; a need and effort which has led also to the (so-called) **Tungsten Program**.
- **Fit of RR plasma rate coefficients:** Verner and Ferland (1996) applied the formula

$$\alpha^{(RR)}(T_e; \alpha_i \mathbb{J}_i) = \frac{a}{\left[\sqrt{\frac{T_e}{T_o}} \left(1 + \sqrt{\frac{T_e}{T_0}} \right)^{1-b} \left(1 + \sqrt{\frac{T_e}{T_1}} \right)^{1+b} \right]}$$

to fit the RR plasma rate coefficients in terms of the parameters T_0, T_1 [in eV], a [in $10^{-11} \text{ cm}^3/\text{s}$] and b (dimensionless). This formula ensures the correct asymptotic behavior of the RR plasma rate coefficients at low and high temperatures: $\alpha^{(RR)}(T_e) \propto 1/\sqrt{T_e}$ for $T_e \ll T_0, T_1$ and $\alpha^{(RR)}(T_e) \propto 1/\sqrt{T_e^3}$ for $T_e \gg T_0, T_1$. This formulas is said to reproduce the plasma rate coefficients better than a few percent in the temperature range $10^{-5} \dots 10^{+5}$ eV, if fitted to the correct data.

- **Relativistic Maxwell-Boltzmann distribution:** In the relativistic (kinetic) theory, the electrons follow the (normalized) distribution

$$f(E) dE = \frac{E \sqrt{E^2 - 1}}{\Theta \exp(-\Theta)} K_2(1/\Theta) \exp\left(\frac{E - 1}{\Theta}\right) dE, \quad \Theta = \frac{k_B T}{m c^2}$$

where E refers to the total electron energy [in units $m c^2$], including the rest energy, and $K_2(x)$ is the modified Bessel function of second order. In the RR plasma rate coefficients, such a relativistic distribution of electron can be readily accounted for by using the relation (Trzhaskovskaya *et al.*, 2010)

$$\begin{aligned} \alpha^{(RR: relativistic)}(T_e; \alpha_i \mathbb{J}_i) &= \frac{\sqrt{\pi/2} \Theta}{K_2(1/\Theta) \exp(-\Theta)} \alpha^{(RR)}(T_e; \alpha_i \mathbb{J}_i) = F^{(\text{rel})}(\Theta) \alpha^{(RR)}(T_e; \alpha_i \mathbb{J}_i) \\ F^{(\text{rel})}(\Theta) &\approx \frac{1}{\left(1 + \frac{15}{8} \Theta + \frac{105}{128} \Theta^2 + \dots \right)}, \quad \text{for } \Theta \lesssim 1 \end{aligned}$$

8. Atomic processes

This factor is usually disregarded in almost all computations (Trzhaskovskaya *et al.*, 2010).

Photorecombination (or RR) of bare ions:

➤ Radiative recombination of bare ions: Four entities are often used to characterize the RR of bare ions (Kotelnikov and Milstein, 2019):

$$\sigma^{(\text{RR})}(\varepsilon; \text{bare} \rightarrow \sum_n n) = \sum_n \sigma^{(\text{RR; total})}(\varepsilon; \text{bare} \rightarrow n) \quad \text{total cross section}$$

$$\kappa^{(\text{RR})}(\varepsilon; \text{bare} \rightarrow \sum_n n) = \sum_n \hbar \omega_n \sigma^{(\text{RR})}(\varepsilon; \text{bare} \rightarrow n) \quad \text{total effective radiation}$$

$$\alpha^{(\text{RR})}(f_e; \text{bare}) = \int d\varepsilon \sigma^{(\text{RR})}(\varepsilon; \text{bare} \rightarrow \sum_n n) f_e(\varepsilon) \quad \text{RR plasma rate coefficient}$$

$$q^{(\text{RR})}(f_e; \text{bare}) = \int d\varepsilon \kappa^{(\text{RR})}(\varepsilon; \text{bare} \rightarrow n) f_e(\varepsilon) \quad \text{RR plasma emission coefficient ,}$$

where $\omega_n = \varepsilon + Z^2/(2n^2)$ [in a.u.] is the photon frequency (energy), Z the nuclear charge and $f_e(\varepsilon)$ refers to the electron energy distribution in the plasma.

➤ Radiative recombination *versus* photoionization: Since these processes are *time-reversed* to each other, they are closely related. For the RR of an ions with an electron of energy ε , the cross sections obey the principle of detailed balance

$$\sigma^{(\text{RR})}(\varepsilon; \text{bare} \rightarrow n) = \frac{\omega_n^2}{c^2} \sigma^{(\text{photoionization})}(\omega; n \rightarrow \text{bare}), \quad \omega_n = \varepsilon + Z^2/(2n^2) \quad [\text{a.u.}]$$

➤ Radiative recombination *versus* photoionization cross section for hydrogen-like ions in the ground level: The photoionization cross section of hydrogen-like ions in the $1s$ ground level can be expressed quite readily for photon energies near to the threshold $\omega \approx Z^2/n^2$ as well as for large energies $\omega \gg Z^2/n^2$ as (Kotelnikov and Milstein, 2019; here, e is the Euler constant)

$$\sigma^{(\text{PI})}(\omega \approx Z^2/n^2; 1s \rightarrow \varepsilon) = \frac{2^9 \pi^2 \alpha a_o^2}{3 e^4 Z^2}, \quad \sigma^{(\text{PI})}(\omega \gg Z^2/n^2; 1s \rightarrow \varepsilon) = \frac{2^8 \pi \alpha a_o^2}{3 Z^2} \left(\frac{Z^2}{2\omega} \right)^{7/2}$$

$$\sigma^{(\text{RR})}(\varepsilon \approx 0 \ll Z^2/2; \text{bare} \rightarrow 1s) = \frac{2^8 \pi^2 \alpha^3 a_o^2}{3 e^4} \frac{Z^2}{2\varepsilon}, \quad \sigma^{(\text{RR})}(\varepsilon \gg Z^2/2; \text{bare} \rightarrow 1s) = \dots a_o^2.$$

8. Atomic processes

- **Stobbe formula for the shell-resolved cross section:** For the radiative capture of an electron with the scaled (hydrogenic) energy $\varepsilon_o = \frac{2\varepsilon}{Z^2}$, the (non-relativistic) recombination cross section for the capture into the subshell (nl) can be expressed in terms of this energy ε_o and the (absorption, $Z = 1$) oscillator strengths $f(n\ell \rightarrow \varepsilon_o)$ of neutral hydrogen:

$$\begin{aligned}\sigma^{(\text{RR, Stobbe})}(\varepsilon_o; n\ell) &= 2\pi^2 \alpha^3 a_o^2 (2\ell + 1) \frac{1}{\varepsilon_o} \left(\varepsilon_o + \frac{1}{n^2} \right)^2 f(n\ell \rightarrow \varepsilon_o) \\ &= 9.165 \cdot 10^{-21} \text{ cm}^2 \frac{1}{\varepsilon_o (\varepsilon_o + 1)^2} \frac{\exp\left(-\frac{4 \arctan \sqrt{\varepsilon_o}}{\sqrt{\varepsilon_o}}\right)}{1 - e^{-2\pi/\sqrt{\varepsilon_o}}}, \quad \text{for RR into the } 1s \text{ shell} \\ f(n\ell \rightarrow \varepsilon_o) &= \frac{1}{3(2\ell + 1)} \left(\varepsilon_o + \frac{1}{n^2} \right) [(2\ell + 1) |\langle \varepsilon_o, \ell + 1 | r | n\ell \rangle|^2 + \ell |\langle \varepsilon_o, \ell - 1 | r | n\ell \rangle|^2].\end{aligned}$$

The scaled (hydrogenic) energy $\varepsilon_o = 2\varepsilon/Z^2 = 1/n_+^2$ can be seen also as generalization of the (squared inverse of the) principal quantum number for the free electron in the continuum.

- **RR cross section for the electron capture into the $1s$ ground-level of initially bare ions:** The (non-relativistic) exact cross section for the capture into the $1s$ ground level of initially bare ions was derived by Stobbe in terms of the (so-called) **Sommerfeld parameter** $\eta = Z/v = \sqrt{Z^2/(2\varepsilon)}$ with the ($1s$) velocity in [a.u.]

$$\sigma^{(\text{RR, Stobbe})}(\varepsilon; \text{bare} \rightarrow 1s) = \frac{2^8 \pi^2 \alpha^3 a_o^2}{3} \frac{\eta^6 e^{-4\eta \arctan(1/\eta)}}{(1 - e^{-2\pi\eta})(\eta^2 + 1)^2}, \quad \eta = \sqrt{\frac{Z^2}{2\varepsilon}}, \quad \varepsilon \text{ [Hartree]}.$$

- **Shell-resolved RR cross section for the electron capture into the shell $n = 1, \dots, 4$ of initially bare ions:** For the radiative recombination of initially bare ions into any level of shell n , both a semi-classical as well as exact formula is known for the total RR cross sections

(cf. Kotelnikov and Milstein, 2019)

$$\begin{aligned}\sigma^{(\text{RR, Kramers})}(\varepsilon; \text{bare} \rightarrow n) &= \frac{32\pi\alpha^3a_o^2}{3\sqrt{3}} \frac{\eta^4}{n(\eta^2+n^2)}, & \eta &= \sqrt{\frac{Z^2}{2\varepsilon}}, & \varepsilon &[\text{Hartree}]. \\ \sigma^{(\text{RR, Katkov \& Strakhovenko})}(\varepsilon; \text{bare} \rightarrow n) &= \frac{2^8\pi^2\alpha^3a_o^2}{3} \frac{\eta^6 e^{-4\eta} \arctan(1/\eta)}{(1 - e^{-2\pi\eta})(\eta^2 + n^2)^2} S_n(\eta) \\ S_1 &= 1, & S_2 &= 2 + \frac{3}{x_2} + \frac{1}{x_2^2}, & S_3 &= 3 + \frac{14}{x_3} + \frac{19}{x_3^2} + \frac{8}{x_3^3} + \frac{1}{x_3^4}, \\ S_4 &= 4 + \frac{38}{x_4} + \frac{346}{3x_4^2} + \frac{409}{3x_4^3} + \frac{622}{9x_4^4} + \frac{43}{9x_4^5} + \frac{1}{x_4^6}, & x_n &= \frac{n^2 + \eta^2}{4\eta^2}.\end{aligned}$$

From this expression $\sigma^{(\text{RR, Katkov \& Strakhovenko})}(\varepsilon; \text{bare} \rightarrow n)$, the two (approximate) formulas above by Stobbe and Kramers can be derived.

- **Total RR cross section for the electron capture into any shell n of initially bare ions:** The approximate expressions for the RR into a given shell n of initially bare ions give rise also to different total RR cross section for the electron capture into any shell n

$$\begin{aligned}\sigma^{(\text{RR, total, Kramers})}(\varepsilon; \text{bare} \rightarrow \sum_n n) &= \frac{32\pi\alpha^3a_o^2}{3\sqrt{3}} \sum_{n=1}^{\infty} \frac{\eta^4}{n(n^2 + \eta^2)} \approx \frac{16\pi\alpha^3a_o^2}{3\sqrt{3}} \eta^2 \ln(1 + \eta^2), & \eta &= \sqrt{\frac{Z^2}{2\varepsilon}} \gg 1 \\ \sigma^{(\text{RR, total, Bell \& Bell})}(\varepsilon; \text{bare} \rightarrow \sum_n n) &= \frac{32\pi\alpha^3a_o^2}{3\sqrt{3}} [\ln(\eta) + 0.1402 + 0.5250\eta^{-2/3}], & \eta &\gg 1.\end{aligned}$$

The latter fit formula by Bell and Bell (1981) is said to be accurate within 3.3 % for $\eta \geq 10$ and even better then 1 % for $\eta \geq 50$.

- **Partial and total RR cross section for relativistic electrons:** For relativistic electrons, the partial and total RR cross section decreases very rapidly with the (free-) electron energy ε . The main contribution to the total cross section is then given by capture into the ground level.
- **Bound-bound and bound-free matrix elements:** For $Z = 1$, the matrix elements $\langle n'\ell' | r | n\ell \rangle$ and $\langle \varepsilon_o\ell' | r | n\ell \rangle$ for atomic hydrogen can

8. Atomic processes

be generated recursively in terms of the quantum numbers and scaled hydrogenic energy by (Schippers, 2020):

$$\begin{aligned}
 A(n\ell) &= \frac{\sqrt{(n+\ell)(n-\ell)}}{n\ell}, & B(k\ell) &= \frac{\sqrt{k^2 + \ell^2}}{k\ell}, & \nu &= \frac{1}{\sqrt{\varepsilon_o}} = Z \frac{\text{Hartree}}{\sqrt{2\varepsilon}} \\
 \langle n'\ell - 1 | r | n\ell \rangle &= \frac{(4n'n)^{n'+2}}{4} \frac{(n-n')^{n-n'-2}}{(n+n')^{n+n'-2}} \left[\frac{(n+n')!}{(n-n'-1)!(2n'-1)!} \right]^{1/2} \\
 2\ell A(n',\ell) \langle n',\ell - 1 | r | n\ell \rangle &= (2\ell + 1) A(n,\ell + 1) \langle n'\ell | r | n,\ell + 1 \rangle + A(n',\ell + 1) \langle n'\ell + 1 | r | n\ell \rangle \\
 2\ell A(n,\ell) \langle n'\ell | r | n\ell \rangle &= A(n,\ell + 1) \langle n'\ell | r | n,\ell + 1 \rangle + (2\ell + 1) A(n',\ell + 1) \langle n',\ell + 1 | r | n\ell \rangle \\
 \langle \varepsilon_o \ell | r | n, \ell - 1 \rangle &= \frac{\nu^2}{4\sqrt{2}} \left(\frac{4n\nu}{\nu^2 + n^2} \right)^{n+2} \left[\frac{\prod_{s=1}^n (s^2 + \nu^2)}{(2n-1)!} \right]^{1/2} \frac{\exp(-2\nu \arctan(n/\nu))}{\sqrt{1 - e^{-2\pi\nu}}} \\
 2\ell A(n,\ell) \langle \varepsilon_o \ell | r | n, \ell - 1 \rangle &= (2\ell + 1) B(\nu, \ell + 1) \langle \varepsilon_o \ell | r | n\ell \rangle + A(n, \ell + 1) \langle \varepsilon_o \ell | r | n, \ell + 1 \rangle \\
 2\ell B(k,\ell) \langle \varepsilon_o, \ell - 1 | r | n\ell \rangle &= B(\nu, \ell + 1) \langle \varepsilon_o, \ell + 1 | r | n\ell \rangle + (2\ell + 1) A(n, \ell + 1) \langle \varepsilon_o \ell | r | n, \ell + 1 \rangle .
 \end{aligned}$$

- **Application of radiative recombination of bare and highly-charged ions:** Particle accelerators, plasma physics, astrophysics and antimatter production. In storage rings, the electron cooling of protons and highly-charged ions also lead to the recombination of ions and to their loss from the beam. In general, however, the **radiative recombination competes with other free-free and free-bound (transition) processes, such as bremsstrahlung, dielectronic recombination, electron-impact excitation and ionization processes, and others.**

Photorecombination of ions with twisted electrons:

- **Angular distribution and linear polarization of photons:** Expressions have been derived for the angular distribution and the linear polarization of the emitted photons following the capture of twisted electrons into the ground state of (bare) ions. These expressions showed that the angular and polarization distributions are sensitive to both, the transverse momentum and the topological charge of the incident electron beam.

- Photorecombination with twisted electrons from a Bessel beam: For (twisted) Bessel electrons with well-defined values of the linear momentum p_z and with topological charge $m = 0, \pm 1, \pm 2$, i.e. with well-defined projection of the OAM upon the propagation direction, the initial-state wave function is given by:

$$\psi^{(\text{Bessel})}(\mathbf{r}; i) \equiv \psi_{\varkappa m p_z}^{(\text{Bessel})}(\mathbf{r}) = \int \frac{d^2 \mathbf{p}_\perp}{(2\pi)^2} a_{\varkappa m}(\mathbf{p}_\perp) e^{i(\mathbf{p}_\perp \cdot \mathbf{r}_\perp + p_z z)},$$

and where $a_{\varkappa m}(\mathbf{p}_\perp)$ refer to the Fourier coefficients that include also the transverse momentum profile of the beam.

- Final bound-state wave functions:

$$\psi_f(\mathbf{r} - \mathbf{b}_\perp; f) = e^{-i\mathbf{p} \cdot \mathbf{b}_\perp} \psi(\mathbf{r}; f).$$

8.1.e. Auger and autoionization processes (AutoIonization)

Process, notation & application:

- Auger emission (autoionization) of an atom or ion: $A^{q+*} \rightarrow A^{(q+1)+(*)} + e_a^-$
- Quantum notations used in the formulas below: $|\alpha_i J_i\rangle \rightarrow |\alpha_f J_f\rangle + \{|\varepsilon\kappa\rangle\}$.
- Using JAC: Perform an `Atomic.Computation(.., processSettings=AutoIonization.Settings(..), ..)` or call directly functions from the module `Auger`.
- In JAC, the particular kind of the Auger operator $\mathbb{V}^{(\text{Auger})}$ can be specified by selecting `AutoIonization.Settings.operator::AbstractEeInteraction = (CoulombInteraction(), BreitInteraction(), CoulombBreit(), ...)`.
- In JAC, the Auger rates and (Auger) lifetimes are tabulated by default for all selected (Auger) transitions.
- In JAC, the intrinsic anisotropy parameters are calculated and tabulated if the flag `calcAnisotropy = true` is set in `AutoIonization.Settings`.
- Using JAC: Perform an `Atomic.Computation(.., processSettings = PlasmaShift.AutoIonizationSettings(..), ..)` or call directly functions from the modules `AutoIonization` and `PlasmaShift`. Until the present, however, only a Debye-Hückel plasma model is supported, and where the Debye-Hückel screening of the electron-nucleus and electron-electron interaction is incorporated only in first-order perturbation theory within the CI matrix.
- Calculation of Auger properties: In JAC, we generally support the computation of nonradiative (Auger) rates, relative Auger intensities and intrinsic angular anisotropy parameters. To this end, first the (reduced) Auger amplitudes are calculated for all selected pairs of initial and final levels and, later, these amplitudes are combined into Auger rates, intrinsic anisotropy or spin-polarization parameters.
- Additional control features for autoionization computations: Since the number of possible Auger transitions often increases very rapidly, especially if several inner-shell holes and/or valence electrons occur, JAC provides several additional control features for reducing the complexity of the computations: Apart from (1) the selection of individual Auger lines, these features include (2) the definition of an **energy threshold (i.e. a minimum energy) of the free electron** as well as (3) a **maximum angular momentum** (negative κ -symmetry quantum number; $\kappa_{\max} = 3 \rightsquigarrow \ell_{\max} = 2$) for the partial waves of the outgoing electron. A proper use of (3) mainly affects the number of the scattering states, that are taken into account, and can be chosen independently of the formally allowed scattering states of the residual ion.
- Additional control features for autoionization computations: The features (2) and (3) from above are in line with the **common experience that partial waves with high angular momenta do either not contribute at all** (i.e. have *zero* Auger amplitudes in most computational

models) or are simply negligible. In addition, JAC supports (4) the use of an overall energy shift of all Auger transition energies which can be specified interactively.

- **Energetic condition for autoionization:** An autoionization of an (inner-shell) excited bound state can occur (only) if the initial level is energetically embedded into the *continuum* of the next higher charge state.
- **Inner-atomic interactions:** Formally, an electron emission from such an *embedded* resonance (level) arise due to its coupling to one or several scattering states of the residual ion with one (or more) free electrons in the continuum. All these states are degenerate with the initial state. Often, the number of the possible scattering states $|\langle \alpha_f \mathbb{J}_f, \varepsilon \kappa | \alpha_t \mathbb{J}_t \rangle|$ of a system increases rapidly since the free electrons may couple in quite different ways to the bound-state electrons from the final (Auger) ions.
- **Coulomb versus Breit interaction:** While the Coulomb repulsion in the Auger amplitude below is typically sufficient in order to describe the autoionization of light and medium elements, the Breit interaction has been found important for electron emission and capture processes of highly-charged ions.
- **Simplification of the transition operator $\mathbb{H} - E$:** The restriction to the electron-electron interaction in the computation (evaluation) of the Auger amplitudes is quite standard in all presently available Auger codes, even if the orbital functions of the resonant scattering level ($\alpha_t \mathbb{J}_t$) and the initial bound state ($\alpha_i \mathbb{J}_i$) are not quite orthogonal to each other.
- **Interchannel interaction:** Apart from a very few case studies on the $K - LL$ and $K - LM$ spectra of noble gases (Tulkki *et al.*, 1989; Fritzsche *et al.*, 1992), more often than not, both the interchannel interactions as well as the nonorthogonality is neglected in the evaluation of the many-electron Auger amplitudes.
- **Reaction plane of the Auger emission:** For a prior photo-absorption or particle impact, the reaction plane is usually defined by the directions of the incident photon (particle) beam and the emitted Auger electron.
- **Application of Auger electron spectroscopy (AES):** AES is nowadays a tool to measure element specific inner-shell excitations.

Autoionization amplitudes:

- **Autoionization amplitude:** Following Åberg and Howat (1982), the Auger transition amplitude for the autoionization of an excited bound state $|\alpha_i \mathbb{J}_i M_i\rangle$ into the final scattering state $|\alpha_t \mathbb{J}_t M_t\rangle$, built from an ion in the final level ($\alpha_f \mathbb{J}_f$), can be expressed most generally as

$$\begin{aligned} \langle (\alpha_f \mathbb{J}_f, \varepsilon \kappa) \mathbb{J}_t M_t | \mathbb{V}^{(\text{Auger})} | \alpha_i \mathbb{J}_i M_i \rangle &= \langle (\alpha_f \mathbb{J}_f, \varepsilon \kappa) \mathbb{J}_t | \mathbb{V}^{(\text{Auger})} | \alpha_i \mathbb{J}_i \rangle \delta_{J_i, J_t} \delta_{M_i, M_t} \delta_{P_i, P_t} \\ &= \langle (\alpha_f \mathbb{J}_f, \varepsilon \kappa) \mathbb{J}_t | \mathbb{H} - E | \alpha_i \mathbb{J}_i \rangle \delta_{J_i, J_t} \delta_{M_i, M_t} \delta_{P_i, P_t}. \end{aligned}$$

8. Atomic processes

This amplitude is independent of the projection M_i of the initial state owing to the rotational symmetry of free atoms and the scalar character of the Hamiltonian and/or interelectronic interaction.

- Final scattering states $|\alpha_t \mathbb{J}_t M_t\rangle \equiv |(\alpha_f \mathbb{J}_f, \varepsilon \kappa) \mathbb{J}_t M_t\rangle$: In an autoionization process, these final scattering states arise from the coupling of the final state $|\alpha_f \mathbb{J}_f M_f\rangle$ of the ion with well-defined symmetry with the partial-wave $|\varepsilon \kappa m_j\rangle$ of the outgoing electron with energy ε and (one-electron) angular momentum $\kappa = \kappa(j, l)$ as well as magnetic projection m_j .
- Simplification of the transition operator $\mathbb{H} - E$: In JAC, as in most other tools for computing autoionization processes, a common set of orthonormal orbitals is often supposed for the representation of the initial ($\alpha_i \mathbb{J}_i$) and final (ionic) bound levels ($\alpha_f \mathbb{J}_f$) in the evaluation of the autoionizatiaon amplitudes. In this case, the Auger transition operator $\mathbb{V}^{(\text{Auger})} \equiv \mathbb{H} - E \approx \mathbb{V}^{(e-e)}$ simplifies to the electron-electron interaction operator, while the (reduced) Auger amplitude becomes

$$\langle (\alpha_f \mathbb{J}_f, \varepsilon \kappa) \mathbb{J}_t \parallel \mathbb{V}^{(\text{Auger})} \parallel \alpha_i \mathbb{J}_i \rangle \simeq i^\ell \exp(-i \Delta_\kappa) \langle (\alpha_f \mathbb{J}_f, \varepsilon \kappa) \mathbb{J}_t \parallel \mathbb{V}^{(e-e)} \parallel \alpha_i \mathbb{J}_i \rangle \delta_{J_i, J_t} \delta_{M_i, M_t} \delta_{P_i, P_t}.$$

Here, the autoionization amplitudes also accounts for the proper phase (or asymptotic boundary condition) for the *incoming* free electron, if the autoionization is considered as scattering process.

- Auger transition operator: Within the framework of the Dirac-Coulomb-Breit Hamiltonian, the interelectronic interaction is the sum of the Coulomb repulsion and Breit interaction, $\mathbb{V}^{(e-e)} = \mathbb{V}^{(\text{Coulomb})} + \mathbb{V}^{(\text{Breit})} \simeq \mathbb{V}^{(\text{Coulomb})}$, although it is often approximated by just the Coulomb part.
- Phase of the autoionization amplitudes: In the scattering approach to the Auger emission (Åberg and Howat, 1982), the free electron appears as an incoming wave whose phase directly contributes to the overall phase of the Auger amplitude:
 $e^{i\ell} \exp(-i \Delta_\kappa) \langle (\alpha_f \mathbb{J}_f, \varepsilon \kappa) \mathbb{J}_t \parallel \mathbb{V}^{(\text{Auger})} \parallel \alpha_i \mathbb{J}_i \rangle$.
- Evaluation of the autoionization amplitudes: Until the present, the standard Racah algebra techniques (Grant, 1988) are always applied in order to evaluate the many-electron Auger amplitudes, independent of how the radial orbitals of the intial and final bound states were generated before.

Auger rates:

- Auger rates: If the (continuum) interaction between the different autoionization channels is neglected, the Auger rates are simply given by

$$A(i \rightarrow f) = 2\pi \sum_{\kappa} |\langle (\alpha_f \mathbb{J}_f, \varepsilon \kappa) \mathbb{J}_t \parallel \mathbb{V}^{(\text{Auger})} \parallel \alpha_i \mathbb{J}_i \rangle|^2,$$

where the summation runs over all partial waves $|\varepsilon\kappa\rangle$ that fulfill the triangular rule $\delta(J_f, j, J_i)$ and where the transition operator $\mathbb{V}^{(\text{Auger})}$ still need to be specified due to the (computational) framework and additional approximations that are made in practice.

- In JAC, the Auger rates and (Auger) lifetimes are tabulated by default for all selected (Auger) transitions.
- **Auger rates:** The Auger rates are known to be rather independent of the atomic number or the charge state of the ion, but they strongly increases as the kinetic energies of the emitted electrons decrease. This increase of the (autoionization) rates mainly arise from the large overlap between the outgoing continuum waves and the bound orbitals of the ion. For similar reasons, the Auger transitions with the smallest (allowed) difference in the principal quantum numbers $\Delta n = n_i - n_f$ of the bound orbital are usually favoured of multiply excited ions.

Angular distribution of Auger electrons:

- **Angular distribution of emitted electrons:** If the (inner-shell) excited ion in level $(\alpha_i \mathbb{J}_i)$ is fully characterized by the reduced statistical tensors $\mathcal{A}_{kq}(\alpha_i \mathbb{J}_i)$ and if only Auger electrons are detected, the angular distribution of the emitted electrons from the Auger transition $(\alpha_i \mathbb{J}_i \rightarrow \alpha_f \mathbb{J}_f)$ can be expressed in the general form (Balashov *et al.* 2000, equation 3.10)

$$W(\vartheta, \varphi; \alpha_i \mathbb{J}_i \rightarrow \alpha_f \mathbb{J}_f) = \frac{A(i \rightarrow f)}{4\pi} \left[1 + \sum_{k=2,4,\dots}^{k_{\max}} \sqrt{\frac{4\pi}{2k+1}} \alpha_k(\alpha_i \mathbb{J}_i \rightarrow \alpha_f \mathbb{J}_f) \sum_{q=-k}^k \mathcal{A}_{kq}(\alpha_i \mathbb{J}_i) Y_{kq}(\vartheta, \varphi) \right],$$

and where $\alpha_k(\alpha_i \mathbb{J}_i \rightarrow \alpha_f \mathbb{J}_f)$ designates the (so-called) **intrinsic anisotropy parameters** of the electron emission

$$\begin{aligned} \alpha_k(\alpha_i \mathbb{J}_i \rightarrow \alpha_f \mathbb{J}_f) &= \left[\sum_{\kappa} \langle (\alpha_f \mathbb{J}_f, \varepsilon \kappa) \mathbb{J}_i \parallel \mathbb{V}^{(\text{Auger})} \parallel \alpha_i \mathbb{J}_i \rangle \right]^{-1} (-1)^{J_i+J_f+k-1/2} \sqrt{2J_i+1} \sum_{\kappa\kappa'} [\ell, \ell', j, j']^{1/2} \langle \ell 0, \ell' 0 \mid k 0 \rangle \\ &\quad \times \begin{Bmatrix} J_i & j & J_f \\ j' & J_i & k \end{Bmatrix} \begin{Bmatrix} \ell & j & 1/2 \\ j' & \ell' & k \end{Bmatrix} \langle (\alpha_f \mathbb{J}_f, \varepsilon \kappa) \mathbb{J}_i \parallel \mathbb{V}^{(\text{Auger})} \parallel \alpha_i \mathbb{J}_i \rangle \langle (\alpha_f \mathbb{J}_f, \varepsilon \kappa') \mathbb{J}_i \parallel \mathbb{V}^{(\text{Auger})} \parallel \alpha_i \mathbb{J}_i \rangle^*. \end{aligned}$$

- **Anisotropy parameters $\alpha_k(\alpha_i \mathbb{J}_i \rightarrow \alpha_f \mathbb{J}_f)$:** Here, the factor $A(i \rightarrow f)$ is the total probability of the Auger transition $(\alpha_i \mathbb{J}_i \rightarrow \alpha_f \mathbb{J}_f)$, integrated over all ejection angles. The **anisotropy parameters** $\alpha_k(\alpha_i \mathbb{J}_i \rightarrow \alpha_f \mathbb{J}_f)$ contain all information about the dynamics of the **decay**, while the tensors $\mathcal{A}_{kq}(\alpha_i \mathbb{J}_i)$ just describe the polarization properties of the atom in its initial level.

8. Atomic processes

- Angular distribution of emitted Auger electrons averaged over several final levels: If the final levels cannot be resolved by the detector, the total angular distribution of the Auger electrons is obtained by the incoherent sum of the angular distributions for all the unresolved final levels:

$$W(\vartheta, \varphi; \alpha_i \mathbb{J}_i \rightarrow \{\alpha_f \mathbb{J}_f\}) = \sum_{\alpha_f \mathbb{J}_f} W(\vartheta, \varphi; \alpha_i \mathbb{J}_i \rightarrow \alpha_f \mathbb{J}_f).$$

In this case, the angular distribution can be expressed also by means of an **average anisotropy parameter** within the electric-dipole approximation. Here, the electric-dipole approximation ensures the factorization of the anisotropy parameters β_2 ,

$$\bar{\beta}_2 = \frac{\sum_{\alpha_f \mathbb{J}_f} \beta_2(i \rightarrow f) A(i \rightarrow f)}{\sum_{\alpha_f \mathbb{J}_f} A(i \rightarrow f)}, \quad \beta_2(i \rightarrow f) = \alpha_2(\alpha_i \mathbb{J}_i \rightarrow \alpha_f \mathbb{J}_f) A_{20}(\alpha_i \mathbb{J}_i).$$

Spin polarization of Auger electrons:

- Polarization vector **P** of Auger electrons: The spin polarization of Auger electrons is usually described by an polarization vector $\mathbf{P} = (P_1, P_2, P_3)$ whose three components can be expressed in terms of the statistical tensors $\rho_{kj}(\alpha_i \mathbb{J}_i)$ of the initial level as well as the intrinsic anisotropy parameters of the considered Auger transition.
- Coordinates used for characterizing the spin polarization: Two coordinate systems, $S(XYZ)$ and $S'(X'Y'Z')$ are often employed in order to characterize the spin polarization of Auger electrons; cf. the figure below and Kabachnik *et al.* (2007).

Two-electron single Auger emission (TESA):

- Observation of TESA lines: Non-resonant three-electron Auger transitions have been suggested several decades ago, although clear evidence for such TESA transition were found in Ar only with very low intensity relative to the normal Auger lines.
- Observation of TESA lines: The observed TESA transitions usually start with the creation of a double vacancy, i.e. with two vacancies in an inner shell, and which are filled simultaneously by two outer-shell electrons, while the released energy is passed to a third emitted electron. In practice, however, such inner-shell double vacancies are normally at energies above the minimum fourfold ionization energy and can easily be filled also by two separate successive (two-electron) Auger transitions involving four electrons in total.

- Two-electron single Auger (TESA) emission: In this process, an ion with two inner-shell holes is filled by two-electron whose excess energy is given to a single Auger electron. TESA is a resonant process that is readily recognized by the (large) kinetic energy of the emitted electron.

8.1.f. Dielectronic recombination (Dielectronic)

Process, notation & application:

- Dielectronic recombination (DR) of an atom or ion: $A^{q+} + e^- \rightarrow A^{(q-1)+*} \rightarrow A^{(q-1)+(*)} + \hbar\omega$
- Quantum notations used in the formulas below: $|\alpha_i J_i\rangle + |\varepsilon \kappa\rangle \rightarrow |\alpha_d J_d\rangle \rightarrow |\alpha_f J_f\rangle + \{\hbar\omega(M)\}$ or $|\alpha_i J_i\rangle + |\mathbf{p}_i m_i\rangle \rightarrow |\alpha_d J_d\rangle \rightarrow |\alpha_f J_f\rangle + \{\hbar\omega(M)\}$
- Using JAC: Perform an `Atomic.Computation(.., processSettings=Dielectronic.Settings(..), ..)` or call directly functions from the module `Dielectronic`.
- In JAC, both the individual $S(E_d; i \rightarrow d \rightarrow f)$ and total resonance strengths $S(E_d; i \rightarrow d)$ are calculated and tabulated by default for all selected pathways of the initial-, intermediate- and final-state configurations of the DR process.
- In JAC, the electron capture (inverse Auger) and radiative amplitudes and rates are always computed by the corresponding modules `Auger` and `PhotoEmission`; because of the size of the configuration expansions, single-electron excitations with $n \gtrsim 6..8$ can often not be treated by the code in the current form.
- Dielectronic recombination (DR) is the dominant electron-ion recombination process in many astrophysical and laboratory plasmas. This process also determines the level population and the ionization balance of most plasma, both in high- and low-temperature plasmas. Since DR can often take place via many intermediate (doubly-excited) resonances, it may affect the plasma dynamics and spectral analysis over a wide range of electron densities. Burgess (1964) was one of the first who recognized the importance of dielectronic recombination for many plasmas and who derived first approximate formulas for the DR plasma rate coefficient.
- Two-step process: In most computations, the dielectronic recombination of a N -electron target ion in the (initial) level $(\alpha_i J_i)$ is handled as a two-step process, in which first an electron is captured resonantly from the continuum into a $[(N+1)\text{-electron}]$ resonance level $(\alpha_d J_d)$ embedded into the continuum of the initial ion and with often two or more excited electrons. In a second step, this excited level $(\alpha_d J_d)$ then either decays radiatively by the emission of photons to some (final) level $(\alpha_f J_f)$ below of the ionization threshold of the ion. Quite likely, however, the excited ion returns by autoionization back into the initial charge stage before the radiative stabilization.
- Demands of DR computations: Apart from the computation of accurate electron-capture or Auger rates, helpful calculations of DR spectra critically depends on the simple control (and handling) of all the — radiative and non-radiative — decay branches of the resonantly excited ion. In JAC, all these branches are treated equally within the `Dielectronic` module, although further restriction upon the final states in the radiative stabilization could be introduced quite readily.

- **DR cross section for an isolated resonance:** For a narrow (non-overlapping DR) resonance, the DR cross section due to the electron capture into the intermediate resonance level d with energy E_d at the nearby (center-of-mass) electron-ion energy E can be factorized in terms of the resonance strength $S(E_d; i \rightarrow d)$ and a Lorentzian line-shape function $L(E; d)$ with $\int dE L(E; d) = 1$ and as

$$\begin{aligned}\sigma^{(\text{DR})}(E \simeq E_d; i \rightarrow d) &= S(i \rightarrow d) L(E; d) \\ &= 4.95 \times 10^{-30} [\text{cm}^2 \text{ eV}^2 \text{ s}] \frac{g_d}{2 g_i E_d} \frac{A_a(d \rightarrow i) \left[\sum_f A_r(d \rightarrow f) \right]}{\sum_{i'} A_a(d \rightarrow i') + \sum_{f'} A_r(d \rightarrow f')} \cdot L(E; d), \quad E_d \text{ in [eV]}, \quad A \text{ in } [\text{s}^{-1}].\end{aligned}$$

Here the summations over f' refer to all final states of the recombined ion, f to all final states below the first ionization limit and i' to all states of the initial ion, into which the intermediate ion can (re-) autoionize.

- **Excitation into high-lying (Rydberg) orbitals:** The need for an *efficient* handling of all (excited) ionic levels arises especially in all those DR studies, in which (single-electron) excitations with quite large principal quantum numbers occur in the low-lying DR resonances. For such highly-excited resonance levels $(\alpha_d \mathbb{J}_d)$, the radiative transition probabilities need to be computed to all the lower-lying levels.
- **Scattering states $|\langle \alpha_i \mathbb{J}_i, \varepsilon \kappa \rangle, \mathbb{J}_d M_d \rangle$:** In practice, the number of possible scattering states $|\langle \alpha_i \mathbb{J}_i, \varepsilon \kappa \rangle, \mathbb{J}_d M_d \rangle$ of the recombined ion often increases very rapidly, since the free electron $|\varepsilon \kappa\rangle$ may couple in many different ways to the bound-state electrons of the initial ion. This increase is analogue to and follows from the electron capture (autoionization) process that is part of the dielectronic recombination.
- **Enhanced DR cross sections in external electric fields:** The DR cross sections for the capture into intermediate, high-energy Rydberg resonances are often enhanced owing to the ℓ -mixing of the associated Rydberg levels. This behaviour has been verified both, experimentally and theoretically. However, a reduced influence of this mixing is expected for (rather) high- Z ions because of the strong scaling of the radiative rates with Z and because less ℓ -states are (then) take part in the recombination at some given electron energy.
- **Unified treatment:** Since the **radiative recombination often strongly increases close to the threshold**, the isolated-resonance approach is formally no longer valid in this case and should be better replaced by some unified treatment of the radiative and non-radiative decay pathes for the capture of low-energy electrons.
- **Dielectronic recombination of W^{20+} ions:** For the DR of W^{20+} ions, Schippers *et al.* (2011) found many (strong) resonances near to the threshold ($\varepsilon = E_d - E_i < 1$ eV), and which also affect the DR plasma rate coefficient at much higher temperatures. For plasma temperatures $100 \leq T_e \leq 300$ eV, these rate coefficients were found larger by a factor of 4 than those used (until then) in the modeling of magnetic fusion plasmas.
- **DR rates for lithium-like Ni^{25+} ions:** Schippers *et al.* (2000) measured the absolute DR rates for initially Ni^{25+} ions in their $1s^2 2s \ ^2S_{1/2}$ ground state with high-energy resolution at the Heidelberg heavy-ion storage ring TSR. For these ions, the considered (center-of-mass)

8. Atomic processes

energy range 0-130 eV of the free electrons covers all $\Delta n = 0$ core excitations. The lowest Rydberg states which are energetically allowed are the capture into $n = 13$ for $2s_{1/2} \rightarrow 2p_{1/2}$ and $n = 11$ for $2s_{1/2} \rightarrow 2p_{3/2}$ excitations. Schippers *et al.* (2000) display the resonance strengths of the individually resolved $2p_{1/2,3/2} nl$ resonances as obtained from a fit of Gaussian line shapes to the observed resonance structures. In addition, Schippers *et al.* (2000, Table I) also list the resonance position and resonance strength for about 30 resonances.

- **Dielectronic recombination:** The DR process is normally important at rather high electron energies and temperatures since it requires to excite the target states to (Rydberg-type) resonances. However, DR resonances may occur also at very low kinetic energies, and when the position of the resonances become very crucial.
- **Importance of dielectronic recombination (DR):** DR is known to play a significant role in all high-temperature plasma since it affects its temperature, charge distribution and level population. DR often disturbs also the measurements of the electron temperature in the plasma diagnostics, since it results in unresolvable satellites that may modify the shape and intensity of the observed lines.
- **Importance of dielectronic recombination (DR):** In fusion plasma, the DR of multiply and highly charged ions contribute significantly to the (radiation) energy loss from the plasma. While, for example, tungsten will be used as divertor material at the International Thermonuclear Experimental Reactor (ITER), a rather small fraction of 10^{-4} of tungsten ions within the core plasma will already result in a large radiation loss and, possibly, the flameout of fusion.
- **DR resonances with one Rydberg-excited electron:** To estimate the DR resonance energies with one Rydberg-excited electron, the well-known **Rydberg formula** can be used

$$E(\alpha_d \mathbb{J}_d; n\ell) = E^{(\text{core excitation})} - R \frac{q^2}{n^2}.$$

where $E^{(\text{core excitation})}$ refers to the excitation energy of the ionic core with charge $q+$ of the initial ion and $R = 13.60569$ eV to the Rydberg constant. While this simple formula works reasonably well for high- n electrons, it is inadequate for the capture into low- n shells.

- **Electron-ion recombination *versus* photoionization:** If the photoionization cross section $\sigma^{(\text{photoionization})}$ is given as function of the photo-electron energy, the recombination cross section can be obtained directly by using the Milne relation

$$\sigma^{(\text{recombination})} = \sigma^{(\text{photoionization})} \frac{2J_i + 1}{2J_f + 1} \frac{(\hbar\omega)^2}{16 \pi^4 m^2 c^2 v^2},$$

and where v is the velocity of the photoelectron.

Strength of dielectronic recombination (DR) resonances:

- **Partial resonance strength:** If the interference between the radiative and dielectronic (nonradiative) capture of the electron is negligible in the field of the target, the dielectronic recombination of an ion from an initial, via the isolated resonance state and into any final state of the (recombined) atom, $i \rightarrow d \rightarrow f$ can be characterized by a (so-called) **resonance strength**. This strength can be solely expressed in terms of the Auger and radiative rates of the resonant state d as well as its (half-) widths Γ_d by

$$S(i \rightarrow d \rightarrow f) \equiv \int_{-\infty}^{\infty} dE \sigma^{(\text{DR})}(E) = \frac{2\pi^2 \hbar}{k_i^2} \frac{A_a(i \rightarrow d) A_r(d \rightarrow f)}{\Gamma_d} = \frac{\pi^2 \hbar}{k_i^2} \frac{(2J_d + 1)}{(2J_i + 1)} \frac{A_a(d \rightarrow i) A_r(d \rightarrow f)}{\Gamma_d}.$$

In this expression, k_i is wave number of the incident electron, $A_a(d \rightarrow i)$ the (inverse) Auger rate for the electron capture from the initial level ($\alpha_i J_i$) into the (doubly-excited) resonance level ($\alpha_d J_d$), and $A_r(d \rightarrow f)$ the rate for the radiative stabilization into the state ($\alpha_f J_f$). The resonance strength $S(i \rightarrow d \rightarrow f)$ refers to the area *under* the energy-dependent differential DR cross sections and is typically given in units of: [cm² eV].

- **Total resonance strength:** At storage rings, the radiative stabilization of the ions into some final level ($\alpha_f J_f$) via the (intermediate) resonance level ($\alpha_d J_d$) is often not observed explicitly and, hence, the radiative rate for the individual transition $d \rightarrow f$ in the resonance strength above has to be replaced by the total radiative rate of the (doubly-excited) resonance level ($\alpha_d J_d$):

$$A_r(d \rightarrow f) \rightarrow \sum_f A_r(d \rightarrow f) \implies S(i \rightarrow d \rightarrow f) \rightarrow S(i \rightarrow d) = \sum_f S(i \rightarrow d \rightarrow f).$$

In JAC, both the partial $S(i \rightarrow d \rightarrow f)$ and total resonance strengths $S(i \rightarrow d)$ are calculated and tabulated by default for all selected pathways of the initial- intermediate- and final-state configurations of the DR process.

- **Total resonance strength:** The use of the total resonance strength $S(i \rightarrow d)$ is appropriate, especially if the energy-dependent DR cross section has a Lorentzian profile

$$\sigma^{(\text{DR})}(E \propto E_d) = \frac{S(i \rightarrow d)}{\pi} \frac{\Gamma/2}{(E_r - E)^2 + \Gamma^2/4} = S(i \rightarrow d) L(E; d)$$

around the resonance energy $E_r = E_d - E_i$ as well as a **natural width less or comparable to the energy spread of the electron beam**. In general, this condition is well fulfilled for most $\Delta n \geq 1$ resonances (with an excitation of a bound electron from the shell $n_i \rightarrow n_f$, for which the total widths are small in most cases), but the same condition can usually be utilized also for the $\Delta n = 0$ lines if the shape of the resonances is not to be analyzed in detail.

8. Atomic processes

- **Total resonance strength:** As seen from the (total) strength below, the experimentally observed strength of the dielectronic recombination for a given resonance level ($\alpha_d \mathbb{J}_d$) is proportional to the (inverse) Auger rate $A_a(i \rightarrow d)$ as well as the (total) radiative rate $\sum_r A_r(d \rightarrow f)$.
- **Total width of the resonance level ($\alpha_d \mathbb{J}_d$):** The total width Γ_d is determined by all possible decay channels of the resonance level ($\alpha_d \mathbb{J}_d$) and is given in first-order perturbation theory by

$$\Gamma_d = \hbar \left(\sum_i A_a(d \rightarrow i) + \sum_f A_r(d \rightarrow f) \right),$$

i.e. by taking the sum over all the individual Auger and radiative rates (widths) of the intermediate level ($\alpha_d \mathbb{J}_d$).

- **Principle of kinetic balance:** The capture and (inverse) Auger rates $A_a(i \rightarrow d) = g_i/g_d A_a(d \rightarrow i)$ are proportional to each other owing to the principle of kinetic balance, and where the g 's refer to the statistical factors of the initial and intermediate resonance levels.
- **Dielectronic capture versus Auger rate:** The dielectronic capture and the time-reversed Auger rates are related to each other by the principle of detailed balance:

$$A_{dc}(i \rightarrow d) = \frac{2 J_d + 1}{2(J_i + 1)} A_a(d \rightarrow i), \quad S^{(\text{DR})}(E; i \rightarrow d \rightarrow f) = \frac{2\pi^2}{p^2} \frac{1}{2} \frac{2 J_d + 1}{2(J_i + 1)} \frac{A_a(d \rightarrow i) A_r(d \rightarrow f)}{\Gamma_d}.$$

Here, the factors $\frac{2\pi^2}{p^2}$ refers to the phase-space density and $1/2$ to the spin-degeneracy of the initially free electron.

- **Threshold behaviour:** Owing to the energy of the incident electron [cf. the factor $1/k_i^2$ above], the resonance strength increases rapidly towards the threshold of the dielectronic recombination and makes the process rather sensitive to low kinetic energies of the incoming electrons.
- **Dominance of autoionization:** For most light and medium elements with just a single autoionization channel of the doubly-excited ions, the resonance strength of the dielectronic recombination is mainly determined by the radiative widths of the resonance levels, since the photon emission from the resonance level ($\alpha_d \mathbb{J}_d$) is then much slower than its autoionization and, hence, $A_a A_r / (A_a + A_r) \approx A_r$.
- **Treatment of radiative rates:** To obtain the total radiative rate of the intermediate resonance ($\alpha_d \mathbb{J}_d$), i.e. in order to facilitate the summation over all lower levels (f), a (very) large number of transition rates have often to be computed with quite comparable quality. For this reason, the computation of DR spectra may become quite tedious if either: (1) resonances are considered that are far away from the threshold, or if (2) a large number of excited levels of the ($N + 1$)-electron ion just occur below of the threshold.

- **Application of DR resonance strength for highly-charged ions:** Since the resonant electron capture is particularly efficient in multiply-charged ions, DR has been found important for understanding of the physics of outer planetary atmospheres, interstellar clouds as well as efficient (radiative) cooling mechanism in astrophysical and laboratory plasmas.

Branching fractions for dielectronic recombination ...:

- **Radiative branching fraction for dielectronic recombination:** For the dielectronic recombination of an ion via well-defined resonance states, $\alpha_i \mathbb{J}_i \rightarrow \{\alpha_d \mathbb{J}_d\}$, the **radiative branching fraction of the resonance level** $\alpha_d \mathbb{J}_d$ is

$$b(\alpha_d \mathbb{J}_d) = \frac{\sum_{f<0} A_r(\alpha_d \mathbb{J}_d \rightarrow \alpha_f \mathbb{J}_f) + \sum_{f>0} A_r(\alpha_d \mathbb{J}_d \rightarrow \alpha_f \mathbb{J}_f) b(\alpha_f \mathbb{J}_f)}{\sum_{i'<d} A_a(\alpha_d \mathbb{J}_d \rightarrow \alpha_{i'} \mathbb{J}_{i'}) + \sum_{f<0} A_r(\alpha_d \mathbb{J}_d \rightarrow \alpha_f \mathbb{J}_f) + \sum_{f>0} A_r(\alpha_d \mathbb{J}_d \rightarrow \alpha_f \mathbb{J}_f)},$$

where A_r and A_a refer to radiative and Auger rates, and where $f < 0$ refers to all final $N+1$ -electron levels of the recombined ion (below of its autoionization threshold), $f > 0$ to all $N+1$ -electron above the autoionization threshold, and i' to N -electron levels that are allowed for (re-) autoionization. Moreover, since the radiative rates are usually much smaller than the autoionization rates, these radiative branching fractions can be approximated by

$$b(\alpha_d \mathbb{J}_d) = \frac{\sum_{f<0} A_r(\alpha_d \mathbb{J}_d \rightarrow \alpha_f \mathbb{J}_f)}{\sum_{i'<d} A_a(\alpha_d \mathbb{J}_d \rightarrow \alpha_{i'} \mathbb{J}_{i'}) + \sum_{f<0} A_r(\alpha_d \mathbb{J}_d \rightarrow \alpha_f \mathbb{J}_f)}.$$

This approximation has been found useful even if the decay to low-lying autoionizing levels is not negligible. Moreover, **since the radiative rates scale with the third power of the transition energies**, $A_r \propto (E_d - E_f)^3$, it is often enough to include only a subset of low-lying final levels ($\alpha_f \mathbb{J}_f$) in order to estimate a reasonable DR strength or branching fraction.

DR rate coefficients:

- **DR plasma rate coefficient:** In a plasma, the electron-ion (dielectronic) recombination is temperature-dependent because of the (Maxwell) distribution of the free electron that are captured by the ion. For a single ion per unit volume in the initial level $i = (\alpha_i \mathbb{J}_i)$, the DR plasma rate coefficient

$$\alpha^{(\text{DR})}(T_e; i) = \frac{4}{T_e^{3/2} \sqrt{2\pi m}} \int_0^\infty dE E \sigma^{(\text{DR})}(E; i \rightarrow \{d\}) \exp\left(-\frac{E}{k_B T_e}\right) \left[\frac{\text{cm}^3}{\text{s}}\right].$$

8. Atomic processes

describes the explicit *rate* to recombine at plasma temperature T_e due to the dielectronic recombination with a Maxwell-distributed electron.

- **DR plasma rate coefficient:** Since for δ -like DR resonances, the cross section is $\sigma^{(\text{DR})}(E; i \rightarrow \{d\}) = \sum_d S(i \rightarrow d) \delta(E - \varepsilon_i) = \sum_d S(i \rightarrow d) \delta(E - E_d + E_i)$, the plasma rate coefficient can be readily expressed as a sum over partial DR rate coefficients $\alpha^{(\text{DR})}(T_e; i \rightarrow d)$

$$\begin{aligned} \alpha^{(\text{DR})}(T_e; i) &= \sum_d \alpha^{(\text{DR})}(T_e; i \rightarrow d) \\ \alpha^{(\text{DR})}(T_e; i \rightarrow d) &= \frac{4}{(k_B T_e)^{3/2} \sqrt{2\pi m}} (E_d - E_i) S(i \rightarrow d) \exp\left(-\frac{E_d - E_i}{k_B T_e}\right) \left[\frac{\text{cm}^3}{\text{s}}\right], \end{aligned}$$

and as associated with the electron capture into the resonance level $\alpha_d \mathbb{J}_d$. Here, $\varepsilon_i = E_d - E_i$ is the energy of the initially free electron. Although the summation over d formally runs over all — valence and inner-shell excited — resonances of the [($N+1$)-electron] recombined ion, it can be readily truncated due to the temperature-dependent factor $\exp\left(-\frac{E_d - E_i}{k_B T_e}\right)$.

- **Accuracy of DR plasma rate coefficients:** Reasonably accurate predictions of DR plasma rate coefficients still remain a challenge for atomic theory. Serious difficulties often arise from (i) the proper representations of all levels involved, (ii) the crucial, though not obvious, role of different resonances for certain plasma temperature and (iii) the quite large number of resonances that (may) contribute to the plasma rate coefficient. For ions of medium and heavy elements, moreover, (iv) the relevance of the auto-ionizing and radiative transitions can no longer be derived from just term- or configuration-averaged transition rates but typically requires more detailed treatment of all fine-structure transitions.
- **Future requirements on DR plasma rate coefficients:** To support forthcoming observations in astrophysics and plasma diagnostics, the following requirements have been discussed briefly (Badnell *et al.*, 2003) but not much explored in detail:
 - (i) Computation of rate coefficients for different stable and meta-stable initial levels;
 - (ii) study of partial rate coefficients for certain groups of final levels, if not all the recombined ions will return to their ionic ground-state level;
 - (iii) further information about the Auger rates to those levels i' , into which the re-combined ion can re-autoionize after the electron capture.
- Various data and tables are available internally.

DR plasma rate coefficients:

- **DR plasma rate coefficient:** The DR plasma rate coefficient is (electron) temperature-dependent and describes, for the resonant capture of a single electron by an ion in the initial state i (per unit volume), the rate to recombine due to dielectronic recombination

$$\alpha^{(\text{DR})}(T_e; i) = \frac{4}{T_e^{3/2} \sqrt{2\pi m}} \int_0^\infty dE E \sigma^{(\text{DR})}(E; i \rightarrow \{d\}) \exp\left(-\frac{E}{T_e}\right) \left[\frac{\text{cm}^3}{\text{s}} \right].$$

- **DR plasma rate coefficient in isolated resonance approximation:** For a single resonance, the dielectronic recombination cross section is $\sigma^{(\text{DR})}(E; i \rightarrow d) = S(i \rightarrow d) \delta(E - E_d)$, and the plasma rate coefficient then becomes

$$\alpha^{(\text{DR})}(T_e; i \rightarrow d) = \frac{4}{T_e^{3/2} \sqrt{2\pi m}} E_d S(i \rightarrow d) \exp\left(-\frac{E_d}{T_e}\right) \left[\frac{\text{cm}^3}{\text{s}} \right].$$

- **Plasma rate coefficients:** Most (RR and DR) plasma rate coefficients of multiply charged ions are based today on computations. Although sizeable progress has been made, the accurate prediction of DR resonance positions still remains a challenge for atomic theory because of their sensitivity to (strong) correlations between the ionic core as well as the excited and the captured electron. Sometimes, the accuracy of calculated DR resonances are still better for $\Delta n = 0$ core excitations, as they are known to be less affected by correlations. In practice, however, even rather small or medium-sized uncertainties in the low-energy DR resonances can lead to large discrepancies in the theoretically predicted plasma rate coefficients (Schippers *et al.*, 2004). Therefore, different theoretical methods and implementations need always to be benchmarked by accurate experimental DR rate coefficients in order to extract useful data for astrophysical relevant ions.
- **Application of DR plasma rate coefficients:** DR rate coefficients are needed to determine the ionization balance of high-temperature plasmas; they are also needed for plasma diagnostics.
- **DR processes for multiply-charged ions:** Burgess (1964) was likely the first who recognized the role of dielectronic recombination processes for astrophysics and, especially, for the charge state distribution and the temperature in atomic plasmas. Up to the present, however, accurate calculations of the low-lying DR resonance positions and strengths are still a challenge for atomic theory.

DR plasma rate coefficient for plasma modelling:

- **Cosmic atomic plasma:** Cosmic plasmas are often divided into two broad classes: (i) Photoionized plasmas are found in planetary nebulae, x-ray binaries, cold nova shells as well as active galactic nuclei; (ii) collisionally-ionized plasmas in the Sun, stars, supernova remnants and galaxies (Savin, 2007).
- **DR plasma rate coefficient for plasma modelling:** Several approximations and hierarchies have been used over the decades to account for the DR in plasma from simple estimates to more sophisticated computations of the DR plasma rate coefficients. However, the complexity of

8. Atomic processes

these computations may become enormous already for ions with still rather simple (ground-state) shell structures. Nowadays, it becomes for instance necessary to deal with the ions of medium and heavy elements. For these elements, the competition between autoionizing and radiative transitions can no longer be derived from just (a partitioning of) term-resolved dielectronic recombination data over the individual fine-structure levels.

- **Modern requirements on plasma rate coefficients:** (i) Recombination data are needed not only for ground-state levels but also for (initially) metastable levels of ions; (ii) Such recombination data are required also for groups of final states of the recombined ion since not all of these ions will decay successively down to their ground level; (iii) the final states of the recombined ion must be treated individually, and sometime handled for just certain intermediate resonance levels; (iv) recombination data into metastable and still autoionizing levels of the recombined ion might be of interest as well (although not many such levels will exist in practice; Badnell *et al.*, 2003).
- **DR plasma rate coefficients & plasma density:** The plasma rate coefficients is generally derived by using perturbation theory for the non-radiative capture of an electron and, hence, is suitable for the low-density plasmas. If multiplied with a given plasma density, these coefficients directly give the overall rate of all ions to recombine due to DR. These coefficients are expected to change, if micro-fields of the plasma, external electric fields or some collisional mixing of the ionic levels occur. For high-density plasmas of low- Z ions, moreover, further density effect, need to be included into the calculation of the DR plasma rate coefficient.
- **Dynamic finite-density plasmas:** This term refers to plasma in which the plasma parameters (electron temperature T_e and density n_e) changes within the lifetime of the metastable levels of the plasma ions. Such dynamic plasmas occur in fusion for plasma impurities near to the contacted surfaces. In such dynamic plasma, ions in the metastable states can also recombine and, hence, these long-living levels must be included quite similar to the ionic ground states into the modeling. Such models, that take metastable levels into account, are sometimes called also **generalized collisional-radiative (GCR) models**. Another challenge in dealing with dynamic finite-density plasmas arises from finite-density effects, since recombined ions in stabilized (excited) levels will no longer always decay back radiatively to their ground state but may be collisionally excited and/or ionized before.

Angle-differential DR photon emission cross section:

- **Angle-differential DR photon emission cross section:** For the pathway $i \rightarrow d \rightarrow f$, the angle-differential cross section for the photon emission into a solid angle Ω just depends on the polar angle ϑ with regard to the incident electron beam and can be parametrized in

terms of a (dipole) anisotropy parameter $\beta(i \rightarrow d \rightarrow f)$ as:

$$\frac{d\sigma^{(\text{DR})}(E; i \rightarrow d \rightarrow f)}{d\Omega^{(\text{photon})}} = \frac{\sigma^{(\text{DR})}(E; i \rightarrow d \rightarrow f)}{4\pi} [1 + \beta(i \rightarrow d \rightarrow f) P_2(\cos \vartheta)]$$

$$W(\vartheta) = [1 + \beta(i \rightarrow d \rightarrow f) P_2(\cos \vartheta)], \quad W(90^\circ) = \frac{3}{3 - P^{(\text{DR})}}$$

In practice, this angular dependence of the radiative stabilization of the ion also requires to modify the resonance strength by $S^{(\text{DR})}(E; i \rightarrow d \rightarrow f) \rightarrow S^{(\text{DR})}(E; i \rightarrow d \rightarrow f) [1 + \beta(i \rightarrow d \rightarrow f) P_2(\cos \vartheta)]$. Moreover, $P^{(\text{DR})}$ is the linear polarization of the DR x-rays.

➤ (Dipole) anisotropy parameter for the photon emission in DR: For an incident electron beam $\parallel \mathbf{e}_z$, the (dipole) anisotropy parameter $\beta(i \rightarrow d \rightarrow f)$ can be written as (Harman *et al.*, 2019)

$$\beta(i \rightarrow d \rightarrow f) = \frac{(-1)^{(1+J_d+J_f)} P^{(2)}(\alpha_i \mathbb{J}_i, \alpha_d \mathbb{J}_d)}{P^{(0)}(\alpha_i \mathbb{J}_i, \alpha_d \mathbb{J}_d)} \sqrt{\frac{3}{2} (2J_d + 1)} \left\{ \begin{matrix} 1 & 1 & 2 \\ J_d & J_d & J_f \end{matrix} \right\}$$

$$P^{(L)}(\alpha_i \mathbb{J}_i, \alpha_d \mathbb{J}_d) = \sum_{\kappa \kappa'} (-1)^{J_i + J_d + L - 1/2} i^{\ell - \ell'} \cos(\Delta_\kappa - \Delta_{\kappa'}) [j, j', \ell, \ell', L]^{1/2} \left(\begin{matrix} \ell & \ell' & L \\ 0 & 0 & 0 \end{matrix} \right) \left\{ \begin{matrix} j' & j & L \\ \ell & \ell' & \frac{1}{2} \end{matrix} \right\} \left\{ \begin{matrix} J_d & J_d & L \\ j & j' & J_i \end{matrix} \right\}$$

$$\times \langle \alpha_d \mathbb{J}_d | \mathbb{V}^{(\text{Auger})} | (\alpha_i \mathbb{J}_i; \varepsilon \kappa) \mathbb{J}_d \rangle \langle \alpha_d \mathbb{J}_d | \mathbb{V}^{(\text{Auger})} | (\alpha_i \mathbb{J}_i; \varepsilon \kappa') \mathbb{J}_d \rangle^*$$

8.1.g. Photoexcitation & fluorescence (PhotoExcitationFluores)

Process, notation & application:

- Photoexcitation of an atom or ion with subsequent fluorescence emission: $A + \hbar\omega_i \rightarrow A^* \rightarrow A^{(*)} + \hbar\omega_f$
- Quantum notations used in the formulas below: $|\alpha_i J_i\rangle + \hbar\omega(\mathbf{k}_i \parallel \mathbf{e}_z; \mathbf{P}_i; \{\mathbb{M}\}) \rightarrow |\alpha_e J_e\rangle \rightarrow |\alpha_f J_f\rangle + \hbar\omega_f(\Omega; \mathbf{P}_f); \{\mathbb{M}\}$
- Using JAC: Perform an `Atomic.Computation(..., processSettings=PhotoExcitationFluores.Settings(...), ...)` or call directly functions from the module `PhotoExcitationFluores`.
- In JAC, the statistical tensors $\rho_{kq}(\alpha_e J_e)$ of the intermediate excited level are calculated (and tabulated) by the module `PhotoExcitation`. These tensors are then internally utilized in order to describe the photoexcitation & fluorescence process.
- In JAC, the reduced density matrix of a fluorescence photon can be calculated for selected solid angles $\{\Omega_1 = (\vartheta_1, \varphi_1), \Omega_2 = (\vartheta_2, \varphi_2), \dots\}$ if the logical flag `calcPhotonDm=true` is set in `PhotoExcitationFluores.Settings()`, and if one or more solid angles are specified explicitly. Hereby, it is assumed that the atoms and the incident plane-wave photons are initially unpolarized.
- In JAC, the angular distribution and Stokes parameters of the fluorescence photon can be calculated for selected solid angles $\{\Omega_1 = (\vartheta_1, \varphi_1), \Omega_2 = (\vartheta_2, \varphi_2), \dots\}$ if the logical flags `calcAngular=true` and `calcStokes=true` are set in `PhotoExcitationFluores.Settings()`, and if one or more solid angles are specified explicitly. Again, it is assumed that the atoms and the incident plane-wave photons are initially unpolarized.
- In JAC, the alignment parameters of the (intermediate) excited level $\mathcal{A}_{kq}(\alpha_e J_e)$ is be calculated and tabulated by the module `PhotoExcitation`, while the structure functions $f_k(\alpha_e J_e, \alpha_f J_f)$ are internally obtained by using the module `PhotoEmission`.
- The photoexcitation and (subsequent) fluorescence emission from atoms and ions has been investigated in good detail in the literature for both, incident plane-wave radiation as well as for twisted Bessel and Laguerre-Gaussian beams.
- Since the properties of the photoexcited atoms can be calculated by the module `PhotoExcitation` and the properties of the radiative emission by the module `Radiative`, here we shall focus only upon properties that are specific to the overall photoexcitation & fluorescence process, such as the angular distribution or density matrix of the fluorescence photons.

Density matrix of the fluorescence photon $\hbar\omega_f(\Omega)$:

- (Reduced) density matrix of the fluorescence photons for the photoemission from a (pre-) aligned or oriented atom in the excited level $(\alpha_e \mathbb{J}_e)$: If the excited atom in the level $(\alpha_e \mathbb{J}_e)$ is described by the statistical tensors $\rho_{kq}(\alpha_e \mathbb{J}_e)$, the (reduced) density matrix of the photons emitted under the angle $\Omega_f = (\vartheta_f, \varphi_f)$ with regard to the propagation direction of the incident plane-wave radiation $\mathbf{k}_i \parallel \mathbf{e}_z$ can be expressed as:

$$\begin{aligned} \langle \mathbf{k}_f \lambda | \rho_{\omega_f} | \mathbf{k}_f \lambda' \rangle &= 2\pi \sum_{k, qq'} \sum_{\mathbb{M} \mathbb{M}'} D_{-qq'}^{(k)}(\varphi_f, \vartheta_f, 0) \rho_{kq}(\alpha_e \mathbb{J}_e) i^{L'+p'-L-p} \lambda^p (\lambda')^{p'} \sqrt{2L+1} \sqrt{2L'+1} (-1)^{J_f + J_e + k + q + 1} \\ &\times \langle L\lambda, L'(-\lambda') | k(-q') \rangle \left\{ \begin{matrix} L & L' & k \\ J_e & J_e & J_f \end{matrix} \right\} \langle \alpha_f \mathbb{J}_f \| \mathbb{O}^{(\mathbb{M}, \text{emission})}(\omega_f) \| \alpha_e \mathbb{J}_e \rangle \langle \alpha_f \mathbb{J}_f \| \mathbb{O}^{(\mathbb{M}', \text{emission})}(\omega_f) \| \alpha_e \mathbb{J}_e \rangle^*. \end{aligned}$$

- In JAC, the reduced density matrix of a fluorescence photon can be calculated at all selected solid angles $\Omega_1 = (\vartheta_1, \varphi_1), \dots$, see above.

Angular distribution and Stokes parameters of the fluorescence photon $\hbar\omega_f(\Omega; \mathbf{P})$:

- Angular distribution of the fluorescence light for the photoemission from a (pre-) aligned or oriented atom: Most generally, the angular distribution can be obtained from the photon density matrix above by a summation over the two polarization states:

$$W(\vartheta, \varphi) = \sum_{\lambda} \langle \mathbf{k}_f \lambda | \rho_{\omega_f} | \mathbf{k}_f \lambda \rangle.$$

- Using the expressions from above, this angular distribution can be readily calculated as well at all selected solid angles: $\Omega_1 = (\vartheta_1, \varphi_1), \dots$, see above.

- Angular distribution of the fluorescence light for initially unpolarized atoms: For initially unpolarized atoms and unpolarized photons in the photoexcitation process, the angular distribution is given by the same formulas as for the photoemission (alone), i.e. in terms of the alignment parameters $\mathcal{A}_{k0}(\alpha_e \mathbb{J}_e)$ and the structure function of the (intermediate) excited level $(\alpha_e \mathbb{J}_e)$:

$$W(\vartheta) = \frac{W_o}{4\pi} \left(1 + \sum_{k=2,4,\dots} f_k(\alpha_e \mathbb{J}_e, \alpha_f \mathbb{J}_f) \mathcal{A}_{k0}(\alpha_e \mathbb{J}_e) P_k(\cos \vartheta) \right).$$

8. Atomic processes

➤ Stokes parameters $\mathbf{P} = (P_1, P_2, P_3)$ of the fluorescence light: The three Stokes parameters $\mathbf{P} = (P_1, P_2, P_3)$, that characterize the polarization properties of the emitted photons, are given by:

$$P_1(\vartheta, \varphi) = -\frac{\langle \mathbf{k}_f, \lambda = +1 | \rho_{\omega_f} | \mathbf{k}_f, \lambda' = -1 \rangle + \langle \mathbf{k}_f, \lambda = -1 | \rho_{\omega_f} | \mathbf{k}_f, \lambda' = +1 \rangle}{\langle \mathbf{k}_f, \lambda = +1 | \rho_{\omega_f} | \mathbf{k}_f, \lambda' = +1 \rangle + \langle \mathbf{k}_f, \lambda = -1 | \rho_{\omega_f} | \mathbf{k}_f, \lambda' = -1 \rangle}$$

$$P_2(\vartheta, \varphi) = i \frac{\langle \mathbf{k}_f, \lambda = -1 | \rho_{\omega_f} | \mathbf{k}_f, \lambda' = +1 \rangle - \langle \mathbf{k}_f, \lambda = +1 | \rho_{\omega_f} | \mathbf{k}_f, \lambda' = -1 \rangle}{\langle \mathbf{k}_f, \lambda = +1 | \rho_{\omega_f} | \mathbf{k}_f, \lambda' = +1 \rangle + \langle \mathbf{k}_f, \lambda = -1 | \rho_{\omega_f} | \mathbf{k}_f, \lambda' = -1 \rangle}$$

$$P_3(\vartheta, \varphi) = \frac{\langle \mathbf{k}_f, \lambda = +1 | \rho_{\omega_f} | \mathbf{k}_f, \lambda' = -1 \rangle - \langle \mathbf{k}_f, \lambda = -1 | \rho_{\omega_f} | \mathbf{k}_f, \lambda' = -1 \rangle}{\langle \mathbf{k}_f, \lambda = +1 | \rho_{\omega_f} | \mathbf{k}_f, \lambda' = +1 \rangle + \langle \mathbf{k}_f, \lambda = -1 | \rho_{\omega_f} | \mathbf{k}_f, \lambda' = -1 \rangle}.$$

➤ In JAC, no attempt has been made so far to evaluate and display these Stokes parameters explicitly as function of the emission angles, although this can be readily done since the (reduced) photon density matrix is accessible; see above.

8.1.h. Photoexcitation & autoionization (PhotoExcitationAutoion)

Process, notation & application:

- Photoexcitation & autoionization of an atom or ion: $A + \hbar\omega \rightarrow A^* \rightarrow A^{(*)} + e_a^-$
- Quantum notations used in the formulas below: $|\alpha_i \mathbb{J}_i\rangle + \hbar\omega(\mathbf{k}_i \parallel \mathbf{e}_z, \mathbf{P}_i; \{\mathbb{M}\}) \rightarrow |\alpha_e \mathbb{J}_e\rangle \rightarrow |\alpha_f \mathbb{J}_f\rangle + |\varepsilon \kappa\rangle$
- Using JAC: Perform an `Atomic.Computation(.., processSettings=PhotoExcitationAutoion.Settings(..), ..)` or call directly functions from the module `PhotoExcitationAutoion`.
- In JAC, the partial photoexcitation & autoionization cross sections $\sigma(i \rightarrow e \rightarrow f)$ are calculated and tabulated if the direct photoionization cross sections $\sigma^{(\text{photionization})}(i \rightarrow f)$ can be assumed to be negligible.
- In JAC, the Fano parameters of the (total) photoionization cross sections at the given resonances $(\alpha_i \mathbb{J}_i \rightarrow \alpha_e \mathbb{J}_e \rightarrow \alpha_f \mathbb{J}_f)$ can be calculated if the logical flags `calcFano=true` is set in `PhotoExcitationAutoion.Settings()`. This feature has not yet been properly implemented. Here, it is assumed that each resonance is sufficiently well isolated from other resonances.
- In JAC, the angular distribution of the emitted (Auger) electrons can be calculated for all selected solid angles $\{\Omega_1 = (\vartheta_1, \varphi_1), \Omega_2 = (\vartheta_2, \varphi_2), \dots\}$ if the logical flags `calcAngular=true` is set in `PhotoExcitationAutoion.Settings()`, and if one or more solid angles are specified explicitly. Hereby, it is assumed that the atoms and the incident plane-wave photons are initially unpolarized.
- The photoexcitation and (subsequent) autoionization of atoms and ions has been explored in good detail, either as the dominant (photo-)ionization process within the vicinity of a certain resonant excitation process or simply as competitive process to atomic photoionization.
- **Resonances in atomic photoionization:** Such resonances have been investigated for a (very) long time as function of the frequency of the incoming light. Such resonances in the total cross sections are of particular interest since they are a **clear signature of the internal structure of many-electron atoms and ions**. Apart from the *direct* photoionization, an inner-shell excitation enable the atom to emit electrons along different ‘quantum pathes’.
- Often, the photoexcitation & autoionization can be considered independently from the *direct* photoionization, and this then leads to an independent **total photoexcitation & autoionization cross sections**.
- If the direct photoionization is assumed to be negligible (or, at least, independent), the photoexcitation & autoionization is the time-reversed process to the dielectronic recombination.

8. Atomic processes

- **Fano profile in photoionization cross sections:** For a sufficient high resolution of the photoionization cross section, the interference between the direct and the excitation & autoionization amplitudes leads to the formation of Fano profiles with either a constructive or destructive superposition of the quantum amplitudes.
- In JAC, no attempt has been made so far to calculate the Fano profiles explicitly for selected resonances, although this will be possible quite readily by combining proper calls to functions from the modules `PhotoIonization`, `PhotoExcitation` as well as `Auger`.
- **R-matrix theory for photoionization:** Since the R-matrix method formally include a close-coupling expansion of the final scattering states, it is well suited for all photoionization studies. In practice, however, most R-matrix applications just refer to excitations of (sub-) valence electrons owing to the size of the required basis. So far, little emphasis has been paid to inner-shell photoexcitation-autoionization processes.
- **Resonance *versus* spectator decay of inner-shell hole states in atomic photoionization** For inner-shell excitations, both the resonance and spectator decay of the inner-shell hole states need to be treated on equal footing.

Fano profiles in photoionization cross sections:

- **Fano's parametrization:** For an isolated resonance $(\alpha_i \mathbb{J}_i \rightarrow \alpha_e \mathbb{J}_e \rightarrow \alpha_f \mathbb{J}_f)$, the total photoionization cross section of the resonant level $(\alpha_e \mathbb{J}_e)$ can be (formally) parametrized in the vicinity of this resonance by the energy-dependent cross section

$$\sigma^{(\text{PI, total})}(\omega; \alpha_i \mathbb{J}_i \rightarrow \alpha_f \mathbb{J}_f) = \sigma^{(\text{EA})}(\omega; \alpha_i \mathbb{J}_i \rightarrow \alpha_e \mathbb{J}_e \rightarrow \alpha_f \mathbb{J}_f) \frac{(q + \epsilon)^2}{1 + \epsilon^2} + \sigma^{(\text{DPI})}(\omega; \alpha_i \mathbb{J}_i \rightarrow \alpha_f \mathbb{J}_f), \quad \epsilon = \frac{\omega - E_e + E_i}{\Gamma_e/2},$$

where $\sigma^{(\text{DPI})}(\omega; \alpha_i \mathbb{J}_i \rightarrow \alpha_f \mathbb{J}_f)$ is the direct photoionization cross section and $\sigma^{(\text{EA})}(\omega; \alpha_i \mathbb{J}_i \rightarrow \alpha_e \mathbb{J}_e \rightarrow \alpha_f \mathbb{J}_f)$ the cross section due to the photoexcitation & autoionization of the resonance. Moreover, $\epsilon = (\omega - E_e)/(\Gamma_e/2)$ refers to the detuning of the incident photon energy $\hbar\omega$ from the resonance energy E_e , in units of the half-width $(\Gamma_e/2)$ of the resonance.

- **Fano q parameter:** This parameter determines the overall profile of the cross section, ranging from a near-Lorentzian ($q \rightarrow \infty$), to a window-like ($q \rightarrow 0$), and up to a completely asymmetric resonance ($q \rightarrow \pm 1$).
- **Resonant photoexcitation & ionization cross section:** Another important parameter, that help characterize the minimum in a (resonant photoexcitation) cross section $\sigma(E)$ is the ratio: $\rho^2 = \sigma^{(\text{EA})}(E_e) / (\sigma^{(\text{EA})}(E_e) + \sigma^{(\text{DPI})}(E_e))$.
- **Resonant photoexcitation & ionization cross section for fine-structure splitted resonances $(\alpha_e \mathbb{J}_e, \alpha'_e \mathbb{J}'_e)$:** Based on generalized expressions for the partial cross sections in the vicinity of a fine-structure splitted isolated resonance $(\alpha_e \mathbb{J}_e, \alpha'_e \mathbb{J}'_e)$, it was shown analytically for $\rho^2 \rightarrow \infty$ that any two groups of partial cross sections for the excitation & autoionization via neighboured fine-structure levels mirror each

other (Liu and Starace, 1999), i.e. an increase in one of the cross section is matched by a decrease in the other. The summation of the fine-structure resolved partial cross sections gives then rise for $E_e \approx E'_e = E$ to the total cross section

$$\sigma^{(\text{PI, total})}(E; \alpha_i \mathbb{J}_i \rightarrow \alpha_f \mathbb{J}_f) = (\sigma^{(\text{EA})}(E; \alpha_i \mathbb{J}_i \rightarrow \alpha_e \mathbb{J}_e \rightarrow \alpha_f \mathbb{J}_f) + \sigma^{(\text{DPI})}(E; \alpha_i \mathbb{J}_i \rightarrow \alpha_f \mathbb{J}_f)) \left(1 + \frac{\rho^2 q^2}{1 + \epsilon^2}\right).$$

- For $\rho^2 \rightarrow \infty$, the asymmetric energy dependence cancels each other and results in a symmetric Lorentzian profile. In the extreme case for $\rho^2 \rightarrow 1$, in contrast, the sum of two partial cross sections mimic each other and exhibits a single-channel like behavior.

Total photoionization amplitude and cross sections across the resonance level ($\alpha_e \mathbb{J}_e$) :

- The photoexcitation and (subsequent) autoionization of atoms and ions obviously contributes to the photoionization and, hence, to its amplitudes and cross sections.
- Total photoionization amplitudes across the isolated resonance level ($\alpha_e \mathbb{J}_e$) :

$$\begin{aligned} \mathcal{M}^{(\text{PI, total})}(\omega; (\alpha_f \mathbb{J}_f, \varepsilon\kappa) \mathbb{J}_t, \alpha_e \mathbb{J}_e, \alpha_i \mathbb{J}_i) \\ = \sum_{\mathbb{M}} \left[\langle (\alpha_f \mathbb{J}_f, \varepsilon\kappa) \mathbb{J}_t \parallel \mathbb{O}^{(\mathbb{M}, \text{photoionization})} \parallel \alpha_i \mathbb{J}_i \rangle + \frac{\langle (\alpha_f \mathbb{J}_f, \varepsilon\kappa) \mathbb{J}_t \parallel \mathbb{O}^{(\text{Auger})} \parallel \alpha_e \mathbb{J}_e \rangle \langle \alpha_e \mathbb{J}_e \parallel \mathbb{O}^{(\mathbb{M}, \text{absorption})} \parallel \alpha_i \mathbb{J}_i \rangle}{E_i + \omega - E_e + i\Gamma_e/2} \right]. \end{aligned}$$

In this notation of the resonant photoionization, we assume the photoelectron to escape by means of the partial wave $|\varepsilon\kappa\rangle$ with kinetic energy $\varepsilon = E_i + \omega - E_f$ and with well-defined angular momentum and parity. — Apart from the *direct* photoionization amplitude (first term in [...]), the total photoionization amplitude also contains the photoexcitation & autoionization amplitudes (second term in [...]).

- **Total photoionization cross section:** From these amplitudes, the total photoionization cross section (intensity) is obtained as before by the summation over all the possible scattering states of the final system ‘photoion + electron’:

$$\sigma^{(\text{PI, total})}(\omega; \alpha_i \mathbb{J}_i \rightarrow \alpha_f \mathbb{J}_f) = \frac{4\pi^2 \alpha \omega}{3(2J_i + 1)} \sum_{\alpha_e \mathbb{J}_e \kappa \mathbb{J}_t} \left| \sum_{\alpha_e \mathbb{J}_e} \mathcal{M}(\omega; (\alpha_f \mathbb{J}_f, \varepsilon\kappa) \mathbb{J}_t, \alpha_e \mathbb{J}_e, \alpha_i \mathbb{J}_i) \right|^2,$$

The total photoionization cross section here includes the summation over all relevant resonances as well as the summation over the partial waves of the photoelectron and the total angular momenta and parities of the total scattering states $|\alpha_t \mathbb{J}_t\rangle$.

8. Atomic processes

- **Resonance behaviour of all observables:** Although all of the (reduced many-electron) matrix elements are basically energy-independent, at least across or nearby of some given resonance, the excitation-autoionization contribution (second term or the summation over the various resonance levels $\sum_{\alpha_e \mathbb{J}_e}$) will lead to either a **constructive or destructive interference pattern in practically almost all observables**, owing to the energy-dependent nominator and the relative phases of the individual amplitudes.
- **Resonant Auger spectroscopy** Special ‘resonances’ in the photoionization cross sections are used in resonant Auger spectroscopy. In this spectroscopy, an inner-shell electron is first excited to some (unoccupied) valence shell, leaving the atom in a well-defined hole state. In a second step, these hole states then autoionize, and this completes the photoionization process.
- In JAC, no attempt has yet been made to calculate and tabulate the resonant photoionization cross sections or angular anisotropy parameters, although this will be possible since all required many-electron matrix elements are internally available.

Angular distribution of resonantly emitted Auger electrons:

- **Auger electron angular distribution from a resonantly-excited level ($\alpha_e \mathbb{J}_e$):** Of course, the angular distribution of the emitted Auger electrons critically depend on the (properties of the) prior excitation process; in the **PhotoExcitationAutoion** module, we assume a prior photoexcitation of atoms or ions for calculating all subsequent properties of the Auger electrons. We here also assume that the direct photoionization is negligible near to the considered resonance level ($\alpha_e \mathbb{J}_e$).
- **Auger electron angular distribution from a resonantly-excited level ($\alpha_e \mathbb{J}_e$):** If the resonantly-excited level ($\alpha_e \mathbb{J}_e$) is axially symmetric along the z -axis of the atom or ion, $\mathcal{A}_{kq}(\alpha_e \mathbb{J}_e) \sim \delta_{q,0}$, the angular distribution only depends on the angle ϑ between the symmetry (z -) axis and the linear momentum of the ejected electron. Then, the angular distribution simplifies to

$$W(\vartheta; \alpha_e \mathbb{J}_e \rightarrow \alpha_f \mathbb{J}_f) = \frac{A_a(e \rightarrow f)}{4\pi} \left[1 + \sum_{k=2,4,\dots}^{k_{\max}} \alpha_k(\alpha_e \mathbb{J}_e \rightarrow \alpha_f \mathbb{J}_f) \mathcal{A}_{k0}(\alpha_e \mathbb{J}_e) P_k(\cos \vartheta) \right],$$

and where the rate $A_a(e \rightarrow f)$ is often used to compare the autoionization of level ($\alpha_e \mathbb{J}_e$) to different final levels ($\alpha_f \mathbb{J}_f$).

- In JAC, no attempt has been made so far to tabulate the angular distribution $W(\vartheta; \alpha_e \mathbb{J}_e \rightarrow \alpha_f \mathbb{J}_f)$ explicitly for selected scenarios; cf. section 8.1.e.
- **Photoexcitation of initially unpolarized atoms within the dipole approximation:** For the photoexcitation of initially unpolarized atoms the Auger angular distribution further simplifies within the electric-dipole approximation to

$$W(\vartheta; \alpha_e \mathbb{J}_e \rightarrow \alpha_f \mathbb{J}_f) = \frac{A_a(e \rightarrow f)}{4\pi} [1 + \beta_2(e \rightarrow f) P_2(\cos \vartheta)] \equiv \frac{A_a(e \rightarrow f)}{4\pi} [1 + \alpha_2(\alpha_e \mathbb{J}_e \rightarrow \alpha_f \mathbb{J}_f) \mathcal{A}_{20}(\alpha_e \mathbb{J}_e) P_2(\cos \vartheta)].$$

In this case, the overall form of the angular distribution for the photo-induced Auger emission coincides with those for the (direct) photoelectron emission, although the asymmetry parameter β is now a product of two factors: $\beta_2(e \rightarrow f) = \alpha_2(\alpha_e \mathbb{J}_e \rightarrow \alpha_f \mathbb{J}_f) \mathcal{A}_{20}(\alpha_e \mathbb{J}_e)$. However, this factorization of the β_2 anisotropy parameter is only valid if the excited level ($\alpha_e \mathbb{J}_e$) is (sufficiently) well isolated and fully characterized by its (single) alignment parameter $\mathcal{A}_{20}(\alpha_e \mathbb{J}_e)$.

- **The angular distribution of the emitted Auger electrons is sensitive to the phase difference between the Auger amplitudes**, in contrast to the total probability $A_a(e \rightarrow f)$. Since the coefficients are symmetric with regard to an interchange $\kappa \leftrightarrow \kappa'$ in the summation of the angular distribution, this distribution is invariant also with respect to the inversion: $\vartheta \rightarrow \pi - \vartheta$, $\varphi \rightarrow \varphi + \pi$, simply because it only contains the spherical harmonics of even rank.
- **Intrinsic Auger anisotropy parameters:** For a single decay channel, the anisotropy parameters $\alpha_k(\alpha_e \mathbb{J}_e \rightarrow \alpha_f \mathbb{J}_f)$ reduces to some pure algebraic value, independent of any Auger amplitude (single partial wave with fixed κ)

$$\alpha_k(\alpha_e \mathbb{J}_e \rightarrow \alpha_f \mathbb{J}_f) = (-1)^{J_e+J_f+k-1/2} \sqrt{2J_e+1} [\ell, j] \langle l0, l0 | k0 \rangle \begin{Bmatrix} J_e & j & J_f \\ j & J_e & k \end{Bmatrix} \begin{Bmatrix} \ell & j & 1/2 \\ j & \ell & k \end{Bmatrix}.$$

This case occurs, for example, if the final level has total angular momentum $J_f = 0$.

- **Auger angular distribution of an axially-symmetric initial level ($\alpha_e \mathbb{J}_e$) with well-defined alignment:** The Auger angular distribution for an axially-symmetric initial level ($\alpha_e \mathbb{J}_e$) has been widely applied for analyzing experimental data. If the alignment of the initial level is known (as, for example, in resonant Auger processes with a photoexcitation of initially unpolarized atoms), this expression of the angular distribution can be utilized to determine experimentally the intrinsic anisotropy parameter $\alpha_2(\alpha_e \mathbb{J}_e \rightarrow \alpha_f \mathbb{J}_f)$ and, thus, information about the Auger amplitudes including their phases.

Spin polarization of resonantly emitted Auger electrons:

- **Spin polarization of Auger electrons:** The spin polarization of Auger electrons is usually described by an polarization vector \mathbf{P} . The three components of \mathbf{P} can be expressed in terms of the statistical tensors of the photo-excited level as well as the intrinsic anisotropy parameters of the considered Auger transition.
- **Spin polarization of Auger electrons:** Two coordinate systems, $S(XYZ)$ and $S'(X'Y'Z')$, are often employed in order to characterize the spin polarization of Auger electrons; cf. the figure below and Kabachnik *et al.* (2007).
- **(Longitudinal) spin component of the emitted Auger electrons:** If the photo-excited level ($\alpha_e \mathbb{J}_e$) is produced by photoabsorption of unpolarized target atoms with monochromatic plane-wave photons, the (longitudinal) spin component of the emitted Auger electrons along

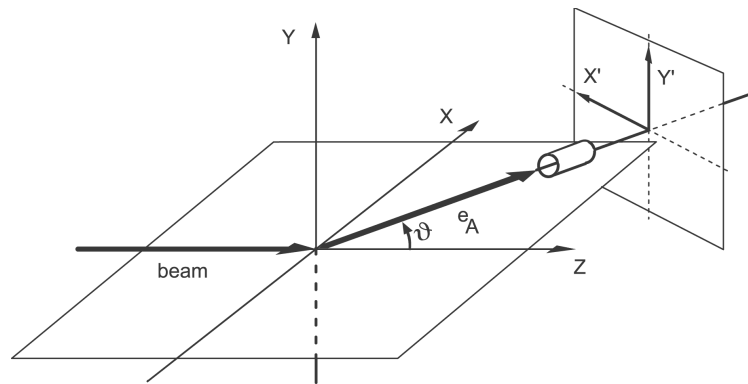


Figure 8.1.: The coordinate systems that are usually utilized for describing the Auger electron spin polarization. From Kabachnik *et al.* (2007).

their propagation direction can be written as:

$$P_{z'} = \frac{\mathcal{A}_{10}(\alpha_e \mathbb{J}_e) \delta_1 \cos \vartheta}{1 + \alpha_2(\alpha_e \mathbb{J}_e \rightarrow \alpha_f \mathbb{J}_f) \mathcal{A}_{20}(\alpha_e \mathbb{J}_e) P_2(\cos \vartheta)}.$$

- **Transverse spin component:** The transverse spin component within the $(x - z)$ reaction plane $P_{x'}$ and the transverse component perpendicular to the reaction plane $P_{y'}$ take the form

$$P_{x'} = \frac{\mathcal{A}_{10}(\alpha_e \mathbb{J}_e) \xi_1 \sin \vartheta}{1 + \alpha_2(\alpha_e \mathbb{J}_e \rightarrow \alpha_f \mathbb{J}_f) \mathcal{A}_{20}(\alpha_e \mathbb{J}_e) P_2(\cos \vartheta)}, \quad P_{y'} = P_y = \frac{\mathcal{A}_{20}(\alpha_e \mathbb{J}_e) \xi_2 \sin 2\vartheta}{1 + \alpha_2(\alpha_e \mathbb{J}_e \rightarrow \alpha_f \mathbb{J}_f) \mathcal{A}_{20}(\alpha_e \mathbb{J}_e) P_2(\cos \vartheta)},$$

- **Photoionization by unpolarized or linearly polarized light:** For the photoionization by unpolarized or linearly polarized light, the photoion is aligned along the beam direction *or* photon polarization direction, respectively. From the expressions above for the components of the spin-polarization vector, it follows then that the spin of the Auger electron can be oriented only perpendicular to the (reaction) plane that contains the alignment axis and the electron emission direction. This has been called **dynamic polarization** (Klar 1980, Kabachnik 1981).
- **For the photoionization by circularly-polarized light, the photon ion is not only aligned but also oriented.** In this case, the spin components of the Auger electrons in the reaction plane do not vanish. This is an example of an **polarization transfer** process (Klar 1980).

8.1.i. Rayleigh & Compton scattering of light (RayleighCompton)

Process, notation & application:

- Rayleigh or Compton scattering of photons at an atom or ion: $A + \hbar\omega_i \longrightarrow A^{(*)} + \hbar\omega_f$... including $\omega_i = \omega_f$.
- Quantum notations used in the formulas below: $|\alpha_i J_i M_i\rangle + \hbar\omega_i(\mathbf{k}_i, \mathbf{P}_i; \{\mathbb{M}_i\}) \longrightarrow |\alpha_f J_f M_f\rangle + \hbar\omega_f(\mathbf{k}_f, \mathbf{P}_f; \{\mathbb{M}_f\})$
 $\omega_i = \omega_f$... for elastic Rayleigh scattering.
- Using JAC: Perform an `Atomic.Computation(..., processSettings=RayleighCompton.Settings(...), ...)` or call directly functions from the module `RayleighCompton`.
- In JAC, the total elastic Rayleigh scattering cross sections are calculated and tabulated by default for all selected levels $(\alpha_i J_i)$.
- In JAC, the angle-differential cross sections of the elastically (Rayleigh) scattered photons can be calculated for selected initial levels $(\alpha_i J_i)$ and for the solid angles $\{\Omega_1 = (\vartheta_1, \varphi_1), \Omega_2 = (\vartheta_2, \varphi_2), \dots\}$ if the logical flags `calcAngular=true` is set in `RayleighCompton.Settings()`, and if one or more solid angles are specified explicitly. Here, it is assumed that the atoms and the incident plane-wave photons are initially unpolarized.
- In JAC, the Stokes parameters of the elastically (Rayleigh) scattered photons can be calculated for selected intial levels $(\alpha_i J_i)$ and for the solid angles $\{\Omega_1 = (\vartheta_1, \varphi_1), \Omega_2 = (\vartheta_2, \varphi_2), \dots\}$ if the logical flags `calcStokes=true` is set in `RayleighCompton.Settings()`, and if one or more solid angles are specified explicitly. Again, it is assumed that the atoms and the incident plane-wave photons are initially unpolarized.
- In JAC, the Green function (channels) have to be calculated before and passed to the computations by `RayleighCompton.Settings(..., green=greenFunction)`.
- Rayleigh scattering: The elastic scattering of light by bound electrons of an atom or ion is commonly known as *Rayleigh* scattering; this scattering process has been found a versatile tool for studying the electronic structure of atoms and their (chemical) environment.
- Rayleigh scattering: The Rayleigh scattering of incident light by the atomic electrons is the **dominant elastic scattering mechanism for all photon energies below 2 MeV**, while the nuclear Thomson, nuclear resonance and low-energy Delbrück (virtual pair) scattering processes are negligible for these photon energies.
- Rayleigh scattering: First theoretical investigations on the elastic scattering of photons by bound electrons date back to the mid-1930s. While initially rather simple approximations were applied, for instance based on atomic form factors, a more rigorous quantum-electrodynamical (QED) approach was developed later in terms of the relativistic second-order S-matrix amplitude.

8. Atomic processes

- **Rayleigh scattering:** Experimentally, the Rayleigh scattering (also known as coherent scattering) has attracted also recent interest owing to ongoing developments and the availability of x-ray polarization detectors as well as hard x-ray synchrotron and FEL sources.
- **Compton scattering:** The **inelastic (Compton or Raman) scattering of light** on atoms, ions or molecules is associated in contrast with an (de-) excitation of the target and has also been explored since the 1920s, both experimentally and theoretically.
- **QED treatment of Rayleigh scattering:** Volotka *et al.* (2016) recently developed and implemented a rigorous quantum-electrodynamical approach for the elastic scattering of (high-energetic) photons by helium-like ions. These computations for the Rayleigh scattering of light by a (single) closed K -shell showed that **QED and many-electron contributions do typically not exceed 2 %**, when compared to an independent-particle approximation.
- **Rayleigh scattering from heavy elements:** Smith (1987) studied the anomalous x-ray scattering from medium and heavy elements and found that the commonly applied electric-dipole approximation overestimates the **relativistic reduction of the elastic scattering cross sections** by more than a factor of 2; instead, higher multipole and retardation terms need to be taken into account into the dispersion analysis in order to resolve the discrepancy with experiments. Moreover, it was formally shown that the commonly applied electric-dipole approximation is incomplete to first order in v^2/c^2 for the relativistic contributions.
- **Compton profile measurements for atoms and molecules:** The new generation of synchrotrons facilitate accurate Compton profile measurements for atoms and molecules. With x-ray FEL, moreover, non-linear processes, including the Compton effect, can be studied for atoms.
- **Compton scattering of many-electron atoms:** In the Compton scattering of light at elementary particles, the frequency change of the scattered photons follows from the energy and momentum conservation in the center-of-mass system and is often discussed in terms of the recoil of the target particle. A straight relativistic derivation gives then rise to the **Klein–Nishina formula for the angular distribution of the scattered photons**. This simple derivation fails however for the scattering by (many-electron) atoms and ions since the change in the frequency and momentum also depend on the properties of the target (medium). This influence of the target is usually encoded in the dynamic structure factor (Crowley and Gregori, 2013). In many-electron systems, the recoil might be taken up by different parts of the target, such as the whole atom (Rayleigh scattering) or even the whole crystal (Bragg scattering, Mossbauer effect). **For the scattering of light on many-particle systems, the distinction between Compton and Thomson scattering gets partly lost.**

Second-order Rayleigh-Compton scattering amplitudes:

- **Rayleigh-Compton scattering amplitude for photons with well-defined polarization:** In second-order perturbation theory, the elastic Rayleigh and inelastic Compton process can be described in terms of the **two-photon transition amplitudes** for a transition from sub-states $|\alpha_i \mathbb{J}_i M_i\rangle \rightarrow |\alpha_f \mathbb{J}_f M_f\rangle$ owing to the absorption and emission of photons with well-defined wave vectors $\mathbf{k}_{i,f}$ and polarization vectors

$\mathbf{u}_{i,f}$. This amplitude is given in terms of the electron-photon interaction operator by (Jahrsetz *et al.*, 2015)

$$\begin{aligned} \mathcal{M}_{fi}^{(\text{Compton})}(\mathbf{k}_f, \mathbf{u}_f, \mathbf{k}_i, \mathbf{u}_i; \alpha_i \mathbb{J}_i M_i \rightarrow \alpha_f \mathbb{J}_f M_f) &= \sum_{\alpha_\nu \mathbb{J}_\nu M_\nu} \left[\frac{\langle \alpha_f \mathbb{J}_f M_f | \hat{R}^\dagger(\mathbf{k}_f, \mathbf{u}_f) | \alpha_\nu \mathbb{J}_\nu M_\nu \rangle \langle \alpha_\nu \mathbb{J}_\nu M_\nu | \hat{R}(\mathbf{k}_i, \mathbf{u}_i) | \alpha_i \mathbb{J}_i M_i \rangle}{E_i + \omega_i - E_\nu} \right. \\ &\quad \left. + \frac{\langle \alpha_f \mathbb{J}_f M_f | \hat{R}(\mathbf{k}_i, \mathbf{u}_i) | \alpha_\nu \mathbb{J}_\nu M_\nu \rangle \langle \alpha_\nu \mathbb{J}_\nu M_\nu | \hat{R}^\dagger(\mathbf{k}_f, \mathbf{u}_f) | \alpha_i \mathbb{J}_i M_i \rangle}{E_i - \omega_f - E_\nu} \right]. \end{aligned}$$

Here, the energies of the — incident and scattered — photons are related to each other and to the energies of the initial and final states of the atoms or ions by $\omega_f = \omega_i - E_f + E_i$. While these second-order amplitudes can be written down quite readily, they are less useful for practical computations, since they are based on different representations of the atomic and photon state(s). Therefore, one first need to perform a multipole expansion of the electron-photon interaction operators together with a number of algebraic simplifications in order to make such computations feasible.

- **Time-dependent perturbation theory:** Because of the time-ordering in (time-dependent) perturbation theory, there are two contributions to this second-order amplitude in order to account for the (formal) *absorption-emission* and *emission-absorption* contributions of the two photons.
- **Rayleigh-Compton scattering amplitude for photons with well-defined polarization:** The twp-photon Rayleigh-Compton amplitudes from above can be re-written in terms of two-photon amplitudes with well-defined helicity and multipolarity by making use of the irreducible tensors $W_q^{(K)}(\mathbf{k}_f, \mathbf{u}_f, \mathbf{k}_i, \mathbf{u}_i; \alpha_i \mathbb{J}_i \rightarrow \alpha_f \mathbb{J}_f)$ of rank k or, equivalently, the so-called angular-polarization tensor and the reduced Rayleigh-Compton scattering amplitude $U^{(\text{K, Compton})}(\alpha_f \mathbb{J}_f, \mathbb{M}_2, \mathbb{J}_\nu, \omega, \mathbb{M}_1, \alpha_i \mathbb{J}_i)$ (Surzhykov *et al.* (2011))

$$\begin{aligned} \mathcal{M}_{fi}^{(\text{Compton})}(\mathbf{k}_f, \mathbf{u}_f, \mathbf{k}_i, \mathbf{u}_i; \alpha_i \mathbb{J}_i \rightarrow \alpha_f \mathbb{J}_f) &= \sum_{Kq} \sqrt{2k+1} \langle Kq | J_f M_f | J_i M_i \rangle W_q^{(K)}(\mathbf{k}_f, \mathbf{u}_f, \mathbf{k}_i, \mathbf{u}_i; \alpha_i \mathbb{J}_i \rightarrow \alpha_f \mathbb{J}_f) \\ W_q^{(K)}(\mathbf{k}_f, \mathbf{u}_f, \mathbf{k}_i, \mathbf{u}_i; \alpha_i \mathbb{J}_i \rightarrow \alpha_f \mathbb{J}_f) &= \sum_{\mathbb{M}_1 \mathbb{M}_2} \frac{(4\pi)^2}{\sqrt{2j_i+1}} (-1)^{p_1+p_2} i^{L_1+p_1-L_2-p_2} T_q^{(K)}(\mathbf{k}_f, \mathbf{u}_f, \mathbb{M}_2 \mathbf{k}_i, \mathbf{u}_i, \mathbb{M}_1) \\ &\quad \times \sum_{J_\nu} (U^{(\text{K, Compton})}(\alpha_f \mathbb{J}_f, \mathbb{M}_2, \mathbb{J}_\nu, \omega_i, \mathbb{M}_1, \alpha_i \mathbb{J}_i) + (-1)^{L_1+L_2+K} U^{(\text{K, Compton})}(\alpha_i \mathbb{J}_i, \mathbb{M}_1, \mathbb{J}_\nu, -\omega_f, \mathbb{M}_2, \alpha_f \mathbb{J}_f)). \end{aligned}$$

8. Atomic processes

➤ Angular-polarization tensor:

$$T_q^{(K)}(\mathbf{k}_f, \mathbf{u}_f, \mathbb{M}_2 \mathbf{k}_i, \mathbf{u}_i, \mathbb{M}_1) = \dots$$

➤ Reduced Rayleigh-Compton scattering amplitude:

$$U^{(K, \text{Compton})}(\alpha_f \mathbb{J}_f, \mathbb{M}_2, \mathbb{J}_\nu, \omega, \mathbb{M}_1, \alpha_i \mathbb{J}_i) = \sum_{\alpha_\nu} \begin{Bmatrix} L_i & L_f & K \\ J_f & J_i & J_\nu \end{Bmatrix} \frac{\langle \alpha_f \mathbb{J}_f \parallel \mathbb{O}^{(\mathbb{M}_2, \text{emission})} \parallel \alpha_\nu \mathbb{J}_\nu \rangle \langle \alpha_\nu \mathbb{J}_\nu \parallel \mathbb{O}^{(\mathbb{M}_1, \text{absorption})} \parallel \alpha_i \mathbb{J}_i \rangle}{E_i + \omega - E_\nu}.$$

➤ Rayleigh-Compton scattering amplitude for photons with well-defined helicity and multipolarity:

$$\mathcal{M}^{(\text{Compton})}(\mathbb{M}_2, \lambda_2, \mathbb{M}_1, \lambda_1; \alpha_i \mathbb{J}_i \rightarrow \alpha_f \mathbb{J}_f) = \sum_{Kq, J_\nu} (U^{(K, \text{Compton})}(\alpha_f \mathbb{J}_f, \mathbb{M}_2, \mathbb{J}_\nu, \omega, \mathbb{M}_1, \alpha_i \mathbb{J}_i) + \dots \quad ??).$$

Total and angle-differential Rayleigh-Compton scattering cross sections:

➤ Total cross section for the Rayleigh-Compton scattering of unpolarized light by initially unpolarized atoms: The total cross section is obtained if the angle-differential cross section (below) is integrated over all directions of the outgoing photons:

$$\sigma^{(\text{Compton})}(\omega_i; \alpha_i \mathbb{J}_i \rightarrow \alpha_f \mathbb{J}_f) = \int d\Omega \frac{d\sigma^{(\text{Compton})}}{d\Omega}(\vartheta; \omega_i) = \frac{\omega_f}{2\omega_i} \int d\Omega \sum_{Kq} \sum_{\mathbf{u}_i \mathbf{u}_f} |W_q^{(K)}(\mathbf{k}_f, \mathbf{u}_f, \mathbf{k}_i, \mathbf{u}_i; \alpha_i \mathbb{J}_i \rightarrow \alpha_f \mathbb{J}_f)|^2.$$

➤ Angle-differential cross section for the Compton scattering of unpolarized light by initially unpolarized atoms: For unpolarized incident plane-wave photons and if the polarization of the scattered photons as well as the magnetic sublevel population of the residual ions remain both unobserved, the angle-differential cross section is given by

$$\begin{aligned} \frac{d\sigma^{(\text{Compton})}}{d\Omega}(\vartheta; \omega_i) \\ = \frac{\omega_f}{2\omega_i} \frac{1}{2J_i + 1} \sum_{\lambda_i \lambda'_i} \sum_{\lambda_f \lambda'_f} c_{\lambda_i \lambda'_i} \mathcal{M}^{(\text{Compton})}(\mathbb{M}_2, \lambda_f, \omega_i, \mathbb{M}_1, \lambda_i; \alpha_i \mathbb{J}_i \rightarrow \alpha_f \mathbb{J}_f) \mathcal{M}^{(\text{Compton})*}(\mathbb{M}_2, \lambda'_f, \omega_i, \mathbb{M}_1, \lambda'_i; \alpha_i \mathbb{J}_i \rightarrow \alpha_f \mathbb{J}_f). \end{aligned}$$

Unfortunately, there is no simple parametrization of this angle-differential cross section $\frac{d\sigma^{(\text{Compton})}}{d\Omega}(\vartheta; \omega_i)$.

- Angle-differential cross section for the Rayleigh scattering of unpolarized light by initially unpolarized atoms: The angle-differential Rayleigh cross sections can be obtained from the formulas above by using $|\alpha_f \mathbb{J}_f\rangle \equiv |\alpha_i \mathbb{J}_i\rangle$ in the two-photon amplitudes and irreducible tensors.

Polarization of the scattered photon:

- Polarization of Rayleigh scattered light: In general, the polarization properties of Rayleigh scattered light depend on the ratio of the Rayleigh amplitudes \mathcal{M}_{\parallel} for the scattering parallel to the polarization of the incident light and \mathcal{M}_{\perp} for the scattering perpendicular to it: $S = \mathcal{M}_{\parallel} / \mathcal{M}_{\perp}$. This ratio generally depends on the energy ω of the incident radiation, the scattering angle ϑ as well as the electronic structure of the target atom.
- Polarization of Rayleigh scattered light: For closed-shell atoms, the amplitude ratio $S = \mathcal{M}_{\parallel} / \mathcal{M}_{\perp}$ can be utilized to express the Stokes parameter of the scattered radiation in terms of the Stokes parameter of the incident light; these relations are given by (Strnat *et al.*, 2020)

$$\begin{aligned} P_1^{(\text{final})} &= \frac{|S|^2 (P_1^{(\text{initial})} + 1) - (1 - P_1^{(\text{initial})})}{|S|^2 (P_1^{(\text{initial})} + 1) + (1 - P_1^{(\text{initial})})}, & P_2^{(\text{final})} &= \frac{2 P_2^{(\text{initial})} \Re(S) + 2 P_3^{(\text{initial})} \Im(S)}{|S|^2 (P_1^{(\text{initial})} + 1) + (1 - P_1^{(\text{initial})})}, \\ P_3^{(\text{final})} &= \frac{2 P_3^{(\text{initial})} \Re(S) - 2 P_2^{(\text{initial})} \Im(S)}{|S|^2 (P_1^{(\text{initial})} + 1) + (1 - P_1^{(\text{initial})})}, \end{aligned}$$

- Rayleigh scattering of x-ray photons by closed-shell atoms: Strnat *et al.* (2020) analyze the linear polarization of Rayleigh scattered light by closed-shell atoms, if the incident light is taken to be linearly-polarized. For closed-shell atoms, such an analysis can be performed independent of the (particular values of) Rayleigh scattering amplitudes, if the linear polarization of the scattered light is measured both, at the azimuthal angles 0° and 45° with regard to the polarization of the incident (synchrotron) radiation.
- Compton polarimetry: New solid-state photon detectors have been developed for efficient Compton polarimetry; they are position-sensitive x-ray detectors that help, for instance, analyze the linear polarization of photons in the radiative electron capture from the subsequent Ly α_1 emission.

Dellbrück scattering:

- **Dellbrück scattering:** refers to the elastic scattering of (energetic) photons $\hbar\omega$ off the Coulomb field of nuclei owing to the formation of virtual electron-positron pairs from a vacuum. Dellbrück scattering cross sections scale $\sim Z^4$ with the fourth power of the nuclear charge and has been measured experimentally. However, the Dellbrück scattering amplitudes are difficult to calculate because of the four interacting vortices, and preliminary Dellbrück scattering amplitudes exist so far only at a fairly coarse grid in photon energies and scattering angles (Koga and Hayakawa, 2017). The Dellbrück scattering gives rise to just one contribution to the scattering amplitude, in addition to the Rayleigh, nuclear Thomson and giant dipole resonance contributions. All these contributions need to be summed up coherently and compared together with experiment.

Elastic light scattering by relativistic ions:

- **Elastic light scattering by relativistic ions:** The resonant elastic scattering of light by a partially stripped ion can be written schematically as

$$|\alpha_i J_i\rangle + \gamma_i(\mathbf{k}_i, \mathbf{u}_i) \longrightarrow |\alpha_\nu J_\nu\rangle \longrightarrow |\alpha_i J_i\rangle + \gamma_f(\mathbf{k}_f, \mathbf{u}_f)$$

and where the initial and final ionic states are taken to be the same. Apart from the wave vectors $\mathbf{k}_i, \mathbf{k}_f$, the incident and scattered photons are characterized here by their polarization vectors $\mathbf{u}_i, \mathbf{u}_f$. To analyze this scattering in further detail, a coordinate system (xyz) need to be chosen explicitly.

- **Elastic scattering amplitude in electric-dipole approximation:** If the incident photon propagates along the z -axis, $\mathbf{k}_i \parallel \mathbf{e}_z$ and by using $\mathbf{k}_f = (k_f, \vartheta_f, \varphi_f)$, the elastic scattering amplitude in electric-dipole approximation can be written as (Volotka *et al.*, 2021)

$$\begin{aligned} \mathcal{M}^{(\text{resonant: E1})}(\mathbf{u}_i, \mathbf{u}_f; i \rightarrow \nu \rightarrow f) &= \frac{8\pi (-1)^{2J_i}}{\sqrt{2J_i + 1}} L(\omega_i; J_\nu) \sum_{kq} (-1)^k \sqrt{2k + 1} \langle kq, J_i M_f | J_i M_i \rangle \left\{ \begin{array}{ccc} 1 & 1 & k \\ J_i & J_i & J_\nu \end{array} \right\} T_{kq}^{(\text{E1,E1})}(\mathbf{k}_i, \mathbf{u}_i; \mathbf{k}_f, \mathbf{u}_f) \\ L(\omega_i; J_\nu) &= \frac{2J_i + 1}{2\omega_i} \frac{\Gamma_\nu/2}{E_\nu - E_i - \omega_i - i\Gamma_\nu/2}, \quad T_{kq}^{(\text{E1,E1})}(\mathbf{k}_i, \mathbf{u}_i; \mathbf{k}_f, \mathbf{u}_f) = [\mathbf{u}_f^* \otimes \mathbf{u}_i]_q^{(k)}. \end{aligned}$$

Here, the polarization tensor $T_{kq}^{(\text{E1,E1})}(\mathbf{k}_i, \mathbf{u}_i; \mathbf{k}_f, \mathbf{u}_f)$ just depends on the properties of the incident and scattered photons but *does* neither depend on the nuclear charge Z , nor the wave functions of the atomic levels, nor the energies of the photons themselves.

Stimulated Compton scattering:

- **Stimulated Compton scattering:** Dondera *et al.* (2017) modeled the stimulated Raman scattering of ultrashort laser pulses with frequencies of $300 \text{ eV} \lesssim \hbar\omega_0 \lesssim 1.5 \text{ keV}$ and peak intensity $3.51 \times 10^{16} \text{ W cm}^{-2}$ for a hydrogen ($1s$) target. Numerical results were obtained by solving the time-dependent SE as well in second-order perturbation theory. However, the presentation of the formalism is hard to follow in any detail, especially when the contributions of the $\mathbf{A} \cdot \mathbf{p}$ and \mathbf{A}^2 terms are compared and discussed. Non-dipole effects may play a crucial role, if incident photon energies of several 100 eV and beyond are considered.

8.1.j. Multi-photon excitation and decay (MultiPhotonDeExcitation)

Process, notation & application:

- Multi-photon excitation of an atom or ion: $A + n \hbar\omega \longrightarrow A^*$
- Multi-photon decay of an atom or ion: $A^* \longrightarrow A^{(*)} + n \hbar\omega$

- Quantum notations used in the formulas below:

$$|\alpha_i J_i\rangle + \hbar\omega_1(\mathbf{k}_1, \lambda_1; \{M_1\}) + \hbar\omega_2(\mathbf{k}_2, \lambda_2; \{M_2\}) + \dots + \hbar\omega_n(\mathbf{k}_n, \lambda_n; \{M_n\}) \longrightarrow |\alpha_f J_f\rangle \quad \text{or}$$

$$|\alpha_i J_i\rangle \longrightarrow |\alpha_f J_f\rangle + \hbar\omega_1(\mathbf{k}_1, \lambda_1; \{M_1\}) + \hbar\omega_2(\mathbf{k}_2, \lambda_2; \{M_2\}) + \dots + \hbar\omega_n(\mathbf{k}_n, \lambda_n; \{M_n\})$$

- Using JAC: Perform an `Atomic.Computation(.., processSettings=MultiPhotonDeExcitation.Settings(..), ...)` or call directly functions from the module `MultiPhotonDeExcitation`.
- In JAC, only the initial and final levels are tabulated by default, together with their symmetry and total transition energy, while some proper flags must be set in `MultiPhotonDeExcitation.Settings` in order to obtain any other rate or cross section information.
- In JAC, different multi-photon (de-) excitation processes are distinguished in `MultiPhotonDeExcitation.Settings(..)` by an (abstract) type `process::AbstractMultiPhotonExcProcess` that (currently) takes the values `TwoPhotonAbsorptionMonochromatic(..)`, `TwoPhotonEmission(..)`,
- In JAC, different multi-photon properties are distinguished for each `process::AbstractMultiPhotonExcProcess` by choosing one or several `properties::Array{AbstractMultiPhotonExcProperty, 1}`. The currently defined subtypes of `AbstractMultiPhotonExcProperty` are: `TotalCsLinear()`, `TotalCsRightCircular()`, `TotalCsLeftCircular()`, ..., although only particular properties can be chosen for each multi-photon (de-) excitation process; cf. docstrings.
- In JAC, the Green function (channels) have to be calculated before and passed to the computations by `MultiPhotonDeExcitation.Settings(.., green=greenFunction)`.
- Two-photon decay: In the past, the two-photon decay of few-electron ions $|\alpha_i J_i\rangle \longrightarrow |\alpha_f J_f\rangle + \hbar\omega_1 + \hbar\omega_2$ has often been considered, both experimentally and theoretically. For this two-photon decay, the total decay rate, the spectral (energy) distribution as well as the angle-angle correlation function of the emitted photons have been explored in quite detail.

Monochromatic two-photon absorption amplitude, density matrix and total rate:

- Two-photon absorption of monochromatic light (from the same beam) of an atom or ion: $A + 2\hbar\omega \rightarrow A^*$.
- Quantum notations used in the formulas below: $|\alpha_i J_i\rangle + \hbar\omega(\mathbf{k}, \lambda_1; \{\mathbb{M}_1\}) + \hbar\omega(\mathbf{k}, \lambda_2; \{\mathbb{M}_2\}) \rightarrow |\alpha_f J_f\rangle, E_f - E_i = 2\hbar\omega$.
- Final-state density matrix of the excited atom following the absorption of two monochromatic and coplanar photons: For a two-photon excitation ($\alpha_i J_i \rightarrow \alpha_f J_f$) of an atom or ion by (two) monochromatic and equally-polarized photons (usually from the same beam) with $\mathbf{k} \parallel \mathbf{e}_z$, the final-state density matrix $\langle \alpha_f J_f M_f | \rho_f | \alpha_f J_f M'_f \rangle$ of the excited atom can be expressed in terms of the initial-state density matrix $\langle \alpha_i J_i M_i | \rho_i | \alpha_i J_i M'_i \rangle$, the photon density matrices $c_{\lambda\lambda'}$ of the two photons as well as the two-photon transition amplitudes in the helicity basis by (Hofbrucker 2020):

$$\begin{aligned}
& \langle \alpha_f J_f M_f | \rho_f | \alpha_f J_f M'_f \rangle \\
&= \sum_{\lambda_1 \lambda'_1, \lambda_2 \lambda'_2, M_i M'_i} c_{\lambda_1 \lambda'_1} c_{\lambda_2 \lambda'_2} \langle \alpha_i J_i M_i | \rho_i | \alpha_i J_i M'_i \rangle \mathcal{M}(\mathbf{k}, \lambda_2, \lambda_1; \alpha_i J_i M_i \rightarrow \alpha_f J_f M_f) \mathcal{M}^*(\mathbf{k}, \lambda'_2, \lambda'_1; \alpha_i J_i M'_i \rightarrow \alpha_f J_f M_f) \\
& \quad \mathcal{M}(\mathbf{k}, \lambda_2, \lambda_1; \alpha_i J_i M_i \rightarrow \alpha_f J_f M_f) \\
&= \sum_{\alpha_\nu J_\nu M_\nu} \frac{\langle \alpha_f J_f M_f | R(\mathbf{k}, \mathbf{u}_{\lambda_2}) | \alpha_\nu J_\nu M_\nu \rangle \langle \alpha_\nu J_\nu M_\nu | R(\mathbf{k}, \mathbf{u}_{\lambda_1}) | \alpha_i J_i M_i \rangle}{E_i + \omega - E_\nu} \\
&= 2\pi \sum_{Kq} \sum_{\mathbb{M}_1 \mathbb{M}_2, J_\nu} i^{L_1 - p_1 + L_2 - p_2} (-\lambda_1)^{p_1} (-\lambda_2)^{p_2} (-1)^{J_f - M_f + K - q} \sqrt{[L_1, L_2]} [K] \begin{pmatrix} K & J_f & J_i \\ q & -M_f & M_i \end{pmatrix} \begin{pmatrix} L_1 & L_2 & K \\ \lambda_1 & \lambda_2 & -q \end{pmatrix} \\
& \quad \times \mathcal{U}^{(K, \text{absorption})}(\alpha_f J_f, \mathbb{M}_2, J_\nu, \omega, \mathbb{M}_1, \alpha_i J_i).
\end{aligned}$$

Since we assume $\mathbf{k} \parallel \mathbf{e}_z$, we here have $\vartheta = \varphi = 0$ and, hence, no angles are mentioned explicitly in the decomposition of the transition amplitude $\mathcal{M}(\mathbf{k}, \lambda_2, \lambda_1; \alpha_i J_i M_i \rightarrow \alpha_f J_f M_f)$.

8. Atomic processes

➤ Reduced two-photon absorption amplitude for *equal* photons:

$$\mathcal{U}^{(K, 2\gamma \text{ absorption})}(\alpha_f \mathbb{J}_f, \omega_2, \mathbb{M}_2, \mathbb{J}_\nu, \omega_1, \mathbb{M}_1, \alpha_i \mathbb{J}_i) = \begin{Bmatrix} J_i & J_f & K \\ L_2 & L_1 & J_\nu \end{Bmatrix} \sum_{\alpha_\nu} \frac{\langle \alpha_f \mathbb{J}_f | \mathbb{O}^{(\mathbb{M}_2, \text{ absorption})} | \alpha_\nu \mathbb{J}_\nu \rangle \langle \alpha_\nu \mathbb{J}_\nu | \mathbb{O}^{(\mathbb{M}_1, \text{ absorption})} | \alpha_i \mathbb{J}_i \rangle}{E_i + \omega_1 - E_\nu}.$$

In the reduced amplitude $\mathcal{U}^{(K, 2\gamma \text{ absorption})}(\alpha_f \mathbb{J}_f, \mathbb{M}_2, \mathbb{J}_\nu, \omega, \mathbb{M}_1, \alpha_i \mathbb{J}_i)$ above, the summation α_ν runs over all the atomic states of given symmetry \mathbb{J}_ν , i.e. over all the ASF as provided by the **Green function channel with symmtry \mathbb{J}_ν** .

➤ **Total two-photon absorption cross sections for initially unpolarized atoms:** For initially unpolarized atoms, the two-photon absorption cross section for the atomic excitation (transition) ($\alpha_i \mathbb{J}_i \rightarrow \alpha_f \mathbb{J}_f$) and for the absorption of two arbitrary but equally-polarized photons with $c_{\lambda\lambda'} = c_{\lambda\lambda'}(P_1, P_2, P_3)$ is given by (Hofbrucker 2020):

$$\begin{aligned} & \sigma^{(2\gamma \text{ absorption})}(\alpha_i \mathbb{J}_i + 2\gamma \rightarrow \alpha_f \mathbb{J}_f) \\ &= \frac{8\pi^3 \alpha^2}{\omega^2 [J_i]} \sum_{M_f} \langle \alpha_f \mathbb{J}_f M_f | \rho_f | \alpha_f \mathbb{J}_f M_f \rangle \\ &= \frac{8\pi^3 \alpha^2}{\omega^2 [J_i]} \sum_{M_i M'_i M_f} \sum_{\lambda_1 \lambda'_1, \lambda_2 \lambda'_2} c_{\lambda_1 \lambda'_1} c_{\lambda_2 \lambda'_2} \mathcal{M}(\mathbf{k}, \lambda_2, \lambda_1; \alpha_i \mathbb{J}_i M_i \rightarrow \alpha_f \mathbb{J}_f M_f) \mathcal{M}^*(\mathbf{k}, \lambda'_2, \lambda'_1; \alpha_i \mathbb{J}_i M'_i \rightarrow \alpha_f \mathbb{J}_f M_f) \\ &= \frac{32\pi^5 \alpha^2}{\omega^2 [J_i]} \sum_{\lambda_1 \lambda'_1, \lambda_2 \lambda'_2} c_{\lambda_1 \lambda'_1} c_{\lambda_2 \lambda'_2} \sum_{Kq} \sum_{\mathbb{M}_1 \mathbb{M}_2, \mathbb{J}_\nu} i^{L_1 - p_1 + L_2 - p_2} (-\lambda_1)^{p_1} (-\lambda_2)^{p_2} \sqrt{[L_1, L_2]} \begin{Bmatrix} L_1 & L_2 & K \\ \lambda_1 & \lambda_2 & -q \end{Bmatrix} [K] \\ &\quad \times \left\{ \sum_{\mathbb{M}'_1 \mathbb{M}'_2, \mathbb{J}'_\nu} (-i)^{L'_1 - p'_1 + L'_2 - p'_2} (-\lambda'_1)^{p'_1} (-\lambda'_2)^{p'_2} \sqrt{[L'_1, L'_2]} \begin{Bmatrix} L'_1 & L'_2 & K \\ \lambda'_1 & \lambda'_2 & -q \end{Bmatrix} \right. \\ &\quad \times \left. \mathcal{U}^{(K, 2\gamma \text{ absorption})}(\alpha_f \mathbb{J}_f, \mathbb{M}_2, \mathbb{J}_\nu, \omega, \mathbb{M}_1, \alpha_i \mathbb{J}_i) [\mathcal{U}^{(K, 2\gamma \text{ absorption})}(\alpha_f \mathbb{J}_f, \mathbb{M}'_2, \mathbb{J}'_\nu, \omega, \mathbb{M}'_1, \alpha_i \mathbb{J}_i)]^* \right\}. \end{aligned}$$

- Two-photon absorption cross section for initially unpolarized atoms and for linearly-polarized photons: For linear-polarization ($P_1 = 1$), the total two-photon amplitude contains a full summation over λ_1 , λ_2 , and the two-photon absorption cross section becomes (Hofbrucker 2020):

$$\sigma^{(2\gamma \text{ absorption, linear})}(\alpha_i \mathbb{J}_i + 2\gamma \rightarrow \alpha_f \mathbb{J}_f) = \frac{8\pi^5 \alpha^2}{\omega^2 [J_i]} \sum_{Kq} \left| \sum_{\lambda_1 \lambda_2} \sum_{\mathbb{M}_1 \mathbb{M}_2 \mathbb{J}_\nu} i^{L_1-p_1+L_2-p_2} (-\lambda_1)^{p_1} (-\lambda_2)^{p_2} [L_1, L_2]^{1/2} \begin{pmatrix} L_1 & L_2 & K \\ \lambda_1 & \lambda_2 & -q \end{pmatrix} [K] \mathcal{U}^{(K, 2\gamma \text{ absorption})}(\alpha_f \mathbb{J}_f, \mathbb{M}_2, \mathbb{J}_\nu, \omega, \mathbb{M}_1, \alpha_i \mathbb{J}_i) \right|^2.$$

- Two-photon absorption cross section for initially unpolarized atoms and for right-circularly polarized photons: For right-circularly polarized light ($P_3 = -1$), the two-photon absorption cross section is given by

$$\sigma^{(2\gamma \text{ absorption, } \circlearrowright)}(\alpha_i \mathbb{J}_i + 2\gamma \rightarrow \alpha_f \mathbb{J}_f) = \frac{8\pi^5 \alpha^2}{\omega^2 [J_i]} \sum_{Kq} \left| \sum_{\mathbb{M}_1 \mathbb{M}_2 \mathbb{J}_\nu} i^{L_1-p_1+L_2-p_2} [L_1, L_2]^{1/2} [K] \begin{pmatrix} L_1 & L_2 & K \\ 1 & 1 & -q \end{pmatrix} \mathcal{U}^{(K, 2\gamma \text{ absorption})}(\alpha_f \mathbb{J}_f, \mathbb{M}_2, \mathbb{J}_\nu, \omega, \mathbb{M}_1, \alpha_i \mathbb{J}_i) \right|^2.$$

- Two-photon absorption cross section for initially unpolarized atoms and for unpolarized photons: For unpolarized light ($P_1 = P_2 = P_3 = 0$), the summation over λ_1 , λ_2 occurs *outside* of the modulus (of the amplitude), and the two-photon absorption cross section becomes

$$\sigma^{(2\gamma \text{ absorption, unpolarized})}(\alpha_i \mathbb{J}_i + 2\gamma \rightarrow \alpha_f \mathbb{J}_f) = \frac{8\pi^5 \alpha^2}{\omega^2 [J_i]} \sum_{Kq} \sum_{\lambda_1 \lambda_2} \left| \sum_{\mathbb{M}_1 \mathbb{M}_2 \mathbb{J}_\nu} i^{L_1-p_1+L_2-p_2} (-\lambda_1)^{p_1} (-\lambda_2)^{p_2} [L_1, L_2]^{1/2} [K] \begin{pmatrix} L_1 & L_2 & K \\ \lambda_1 & \lambda_2 & -q \end{pmatrix} \mathcal{U}^{(K, 2\gamma \text{ absorption})}(\alpha_f \mathbb{J}_f, \mathbb{M}_2, \mathbb{J}_\nu, \omega, \mathbb{M}_1, \alpha_i \mathbb{J}_i) \right|^2.$$

Bichromatic two-photon absorption amplitude, density matrix and total rate:

- Two-photon absorption of bichromatic light (from differently oriented beams) of an atom or ion: $A + \hbar\omega_1 + \hbar\omega_2 \longrightarrow A^*$.
- Quantum notations used in the formulas below:

$$|\alpha_i \mathbb{J}_i\rangle + \hbar\omega_1(\mathbf{k}_1, \lambda_1; \{\mathbb{M}_1\}) + \hbar\omega_2(\mathbf{k}_2, \lambda_2; \{\mathbb{M}_2\}) \longrightarrow |\alpha_f \mathbb{J}_f\rangle, \quad E_f - E_i = \hbar(\omega_1 + \omega_2).$$

8. Atomic processes

- Final-state density matrix of the excited atom following the absorption of two *non-equivalent* photons: For a two-photon excitation ($\alpha_i \mathbb{J}_i \rightarrow \alpha_f \mathbb{J}_f$) of an atom or ion by two photons $\gamma_1 = (\omega_1, \mathbf{k}_1, \lambda_1; \{\mathbb{M}_1\})$ and $\gamma_2 = (\omega_2, \mathbf{k}_2, \lambda_2; \{\mathbb{M}_2\})$ with well-defined frequency, propagation direction and helicity (as well as for a given set of multipolarities), the final-state density matrix $\langle \alpha_f \mathbb{J}_f M_f | \rho_f | \alpha_f \mathbb{J}_f M'_f \rangle$ of the excited atom can be expressed in terms of the initial-state density matrix $\langle \alpha_i \mathbb{J}_i M_i | \rho_i | \alpha_i \mathbb{J}_i M'_i \rangle$, the directions $\mathbf{k}_1 = \mathbf{k}_1(\omega_1, \vartheta_1, \varphi_1)$, $\mathbf{k}_2 = \mathbf{k}_2(\omega_2, \vartheta_2, \varphi_2)$, the photon density matrices $c_{\lambda_1 \lambda'_1}$ and $c_{\lambda_2 \lambda'_2}$ of the two photons as well as the two-photon transition amplitudes in the

helicity basis by (Hofbrucker 2020):

$$\begin{aligned}
 & \langle \alpha_f \mathbb{J}_f M_f | \rho_f | \alpha_f \mathbb{J}_f M'_f \rangle \\
 = & \sum_{\lambda_1 \lambda'_1, \lambda_2 \lambda'_2, M_i M'_i} c_{\lambda_1 \lambda'_1} c_{\lambda_2 \lambda'_2} \langle \alpha_i \mathbb{J}_i M_i | \rho_i | \alpha_i \mathbb{J}_i M'_i \rangle \mathcal{M}(\mathbf{k}_2, \lambda_2, \mathbf{k}_1, \lambda_1; \alpha_i \mathbb{J}_i M_i \rightarrow \alpha_f \mathbb{J}_f M_f) \mathcal{M}^*(\mathbf{k}_2, \lambda'_2, \mathbf{k}_1, \lambda'_1; \alpha_i \mathbb{J}_i M'_i \rightarrow \alpha_f \mathbb{J}_f M'_f) \\
 & \mathcal{M}(\mathbf{k}_2, \lambda_2, \mathbf{k}_1, \lambda_1; \alpha_i \mathbb{J}_i M_i \rightarrow \alpha_f \mathbb{J}_f M_f) \\
 = & \sum_{\alpha_\nu \mathbb{J}_\nu M_\nu} \frac{\langle \alpha_f \mathbb{J}_f M_f | R(\mathbf{k}_2, \mathbf{u}_{\lambda_2}) | \alpha_\nu \mathbb{J}_\nu M_\nu \rangle \langle \alpha_\nu \mathbb{J}_\nu M_\nu | R(\mathbf{k}_1, \mathbf{u}_{\lambda_1}) | \alpha_i \mathbb{J}_i M_i \rangle}{E_i + \omega_1 - E_\nu} \\
 & + \sum_{\alpha_\nu \mathbb{J}_\nu M_\nu} \frac{\langle \alpha_f \mathbb{J}_f M_f | R(\mathbf{k}_1, \mathbf{u}_{\lambda_1}) | \alpha_\nu \mathbb{J}_\nu M_\nu \rangle \langle \alpha_\nu \mathbb{J}_\nu M_\nu | R(\mathbf{k}_2, \mathbf{u}_{\lambda_2}) | \alpha_i \mathbb{J}_i M_i \rangle}{E_i + \omega_2 - E_\nu} \\
 = & \pi \sum_{Kq} \sum_{\mathbb{M}_1 \mathbb{M}_2, \mathbb{J}_\nu} \sum_{M_1 M_2} i^{L_1 - p_1 + L_2 - p_2} (-\lambda_1)^{p_1} (-\lambda_2)^{p_2} (-1)^{J_f - M_f + K - q} \sqrt{[L_1, L_2]} [K] \begin{pmatrix} K & J_f & J_i \\ q & -M_f & M_i \end{pmatrix} \begin{pmatrix} L_1 & L_2 & K \\ M_1 & M_2 & -q \end{pmatrix} \\
 & \times D_{M_1, \lambda_1}^{(L_1)}(\vartheta_1, \varphi_1) D_{M_2, \lambda_2}^{(L_2)}(\vartheta_2, \varphi_2) \\
 & \times \left(\begin{Bmatrix} J_i & J_f & K \\ L_2 & L_1 & J_\nu \end{Bmatrix} \sum_{\alpha_\nu} \frac{\langle \alpha_f \mathbb{J}_f \| \mathbb{O}^{(\mathbb{M}_2, \text{absorption})} \| \alpha_\nu \mathbb{J}_\nu \rangle \langle \alpha_\nu \mathbb{J}_\nu \| \mathbb{O}^{(\mathbb{M}_1, \text{absorption})} \| \alpha_i \mathbb{J}_i \rangle}{E_i + \omega_1 - E_\nu} \right. \\
 & \quad \left. + (-1)^{L_1 + L_2 + K} \begin{Bmatrix} J_i & J_f & K \\ L_1 & L_2 & J_\nu \end{Bmatrix} \frac{\langle \alpha_f \mathbb{J}_f \| \mathbb{O}^{(\mathbb{M}_1, \text{absorption})} \| \alpha_\nu \mathbb{J}_\nu \rangle \langle \alpha_\nu \mathbb{J}_\nu \| \mathbb{O}^{(\mathbb{M}_2, \text{absorption})} \| \alpha_i \mathbb{J}_i \rangle}{E_i + \omega_2 - E_\nu} \right) \\
 = & \pi \sum_{Kq} \sum_{\mathbb{M}_1 \mathbb{M}_2, \mathbb{J}_\nu} \sum_{M_1 M_2} i^{L_1 - p_1 + L_2 - p_2} (-\lambda_1)^{p_1} (-\lambda_2)^{p_2} (-1)^{J_f - M_f + K - q} \sqrt{[L_1, L_2]} [K] \begin{pmatrix} K & J_f & J_i \\ q & -M_f & M_i \end{pmatrix} \begin{pmatrix} L_1 & L_2 & K \\ M_1 & M_2 & -q \end{pmatrix} \\
 & \times D_{M_1, \lambda_1}^{(L_1)}(\vartheta_1, \varphi_1) D_{M_2, \lambda_2}^{(L_2)}(\vartheta_2, \varphi_2) \mathcal{U}^{(K, \gamma + \gamma' \text{ absorption})}(\alpha_f \mathbb{J}_f, \omega_2, \mathbb{M}_2, \mathbb{J}_\nu, \omega_1, \mathbb{M}_1, \alpha_i \mathbb{J}_i)
 \end{aligned}$$

8. Atomic processes

➤ Reduced two-photon absorption amplitude for two *non-equivalent* photons:

$$\begin{aligned} & \mathcal{U}^{(K, \gamma+\gamma' \text{ absorption})}(\alpha_f \mathbb{J}_f, \omega_2, \mathbb{M}_2, \mathbb{J}_\nu, \omega_1, \mathbb{M}_1, \alpha_i \mathbb{J}_i) \\ &= \mathcal{U}^{(K, 2\gamma \text{ absorption})}(\alpha_f \mathbb{J}_f, \omega_2, \mathbb{M}_2, \mathbb{J}_\nu, \omega_1, \mathbb{M}_1, \alpha_i \mathbb{J}_i) + (-1)^{L_1+L_2+K} \mathcal{U}^{(K, 2\gamma \text{ absorption})}(\alpha_f \mathbb{J}_f, \omega_1, \mathbb{M}_1, \mathbb{J}_\nu, \omega_2, \mathbb{M}_2, \alpha_i \mathbb{J}_i). \end{aligned}$$

➤ Total two-photon absorption cross sections for initially unpolarized atoms: For initially unpolarized atoms, the two-photon absorption cross section for the excitation $(\alpha_i \mathbb{J}_i \rightarrow \alpha_f \mathbb{J}_f)$ and for the absorption of two photons with well-defined frequencies ω_1, ω_2 , propagation directions $(\vartheta_1, \varphi_1), (\vartheta_2, \varphi_2)$ and photon density matrices $c_{\lambda_s \lambda'_s} = c_{\lambda_s \lambda'_s}(P_1, P_2, P_3)$, $s = 1, 2$ is given by (Hofbrucker 2020):

$$\begin{aligned} & \sigma^{(\gamma+\gamma' \text{ absorption})}(\alpha_i \mathbb{J}_i + \gamma_1 + \gamma_2 \rightarrow \alpha_f \mathbb{J}_f) \\ &= \frac{8\pi^3 \alpha^2}{\omega^2 [J_i]} \sum_{M_f} \langle \alpha_f \mathbb{J}_f M_f | \rho_f | \alpha_f \mathbb{J}_f M_f \rangle \\ &= \frac{8\pi^3 \alpha^2}{\omega^2 [J_i]} \sum_{M_i M'_i M_f} \sum_{\lambda_1 \lambda'_1, \lambda_2 \lambda'_2} c_{\lambda_1 \lambda'_1} c_{\lambda_2 \lambda'_2} \mathcal{M}(\mathbf{k}_2, \lambda_2, \mathbf{k}_1, \lambda_1; \alpha_i \mathbb{J}_i M_i \rightarrow \alpha_f \mathbb{J}_f M_f) \mathcal{M}^*(\mathbf{k}_2, \lambda'_2, \mathbf{k}_1, \lambda'_1; \alpha_i \mathbb{J}_i M'_i \rightarrow \alpha_f \mathbb{J}_f M_f) \\ &= \frac{8\pi^5 \alpha^2}{\omega^2 [J_i]} \sum_{\lambda_1 \lambda'_1, \lambda_2 \lambda'_2} c_{\lambda_1 \lambda'_1} c_{\lambda_2 \lambda'_2} \sum_{Kq} \sum_{\mathbb{M}_1 \mathbb{M}_2, \mathbb{J}_\nu} \sum_{M_1 M_2} i^{L_1-p_1+L_2-p_2} (-\lambda_1)^{p_1} (-\lambda_2)^{p_2} \sqrt{[L_1, L_2]} \begin{pmatrix} L_1 & L_2 & K \\ M_1 & M_2 & -q \end{pmatrix} [K] \\ & \quad \times \left\{ \sum_{\mathbb{M}'_1 \mathbb{M}'_2, \mathbb{J}'_\nu} \sum_{M'_1 M'_2} (-i)^{L'_1-p'_1+L'_2-p'_2} (-\lambda'_1)^{p'_1} (-\lambda'_2)^{p'_2} \sqrt{[L'_1, L'_2]} \begin{pmatrix} L'_1 & L'_2 & K \\ M'_1 & M'_2 & -q \end{pmatrix} \right. \\ & \quad \times D_{M_1, \lambda_1}^{(L_1)}(\vartheta_1, \varphi_1) D_{M_2, \lambda_2}^{(L_2)}(\vartheta_2, \varphi_2) [D_{M'_1, \lambda'_1}^{(L'_1)}(\vartheta_1, \varphi_1) D_{M'_2, \lambda'_2}^{(L'_2)}(\vartheta_2, \varphi_2)]^* \\ & \quad \times \left. \mathcal{U}^{(K, \gamma+\gamma' \text{ absorption})}(\alpha_f \mathbb{J}_f, \omega_2, \mathbb{M}_2, \mathbb{J}_\nu, \omega_1, \mathbb{M}_1, \alpha_i \mathbb{J}_i) [\mathcal{U}^{(K, \gamma+\gamma' \text{ absorption})}(\alpha_f \mathbb{J}_f, \omega_2, \mathbb{M}'_2, \mathbb{J}'_\nu, \omega_1, \mathbb{M}'_1, \alpha_i \mathbb{J}_i)]^* \right\}. \end{aligned}$$

➤ Total two-photon absorption cross sections for initially unpolarized atoms and for photons from co-linear beams: For initially unpolarized atoms, the two-photon absorption cross section for the excitation $(\alpha_i \mathbb{J}_i \rightarrow \alpha_f \mathbb{J}_f)$ and for the absorption of two photons with well-defined

frequency ω_1, ω_2 , propagation directions $(\vartheta_1, \varphi_1) = (\vartheta_2, \varphi_2) = (0, 0) \parallel \mathbf{e}_z$, and photon density matrices $c_{\lambda_s \lambda'_s} = c_{\lambda_s \lambda'_s}(P_1, P_2, P_3)$, $s = 1, 2$ is given by (Hofbrucker 2020)

??

- Total two-photon absorption cross sections for photons from perpendicular beams: For initially unpolarized atoms, the two-photon absorption cross section for the excitation $(\alpha_i \mathbb{J}_i \rightarrow \alpha_f \mathbb{J}_f)$ and for the absorption of two photons with well-defined frequencies ω_1, ω_2 , propagation directions $(\vartheta_1, \varphi_1) = (0, 0) \parallel \mathbf{e}_z$ and $(\vartheta_2, \varphi_2) = (\pi/2, 0) \parallel \mathbf{e}_x$, and photon density matrices $c_{\lambda_s \lambda'_s} = c_{\lambda_s \lambda'_s}(P_1, P_2, P_3)$, $s = 1, 2$ is given by (Hofbrucker 2020)

??

- : Surzhykov *et al.* (2018) studied the two-photon absorption of few-electron ions by using second-order perturbation theory and Dirac's relativistic equation. General expressions for the excitation cross sections and rates are derived that include all high-order multipole terms in the expansion of the electron-photon interaction. Detailed computations were carried out for the two-photon absorption of hydrogen-, helium-, and berylliumlike ions and are compared with the available theoretical and experimental data.

Two-photon decay amplitude, density matrix and total rate:

- Two-photon emission of an atom or ion: $A^* \longrightarrow A + \hbar \omega_1 + \hbar \omega_2$

- Quantum notations used in the formulas below:

$$|\alpha_i \mathbb{J}_i\rangle \longrightarrow |\alpha_f \mathbb{J}_f\rangle + \hbar \omega(\mathbf{k}_1, \lambda_1; \{\mathbb{M}_1\}) + \hbar \omega(\mathbf{k}_2, \lambda_2; \{\mathbb{M}_2\}), \quad E_i - E_f = \hbar(\omega_1 + \omega_2).$$

- Final-state density matrix of the de-excited atom *plus* the two emitted photons in the helicity basis: For the two-photon decay $(\alpha_i \mathbb{J}_i \rightarrow \alpha_f \mathbb{J}_f)$ of an initially-excited atom or ion in level $(\alpha_i \mathbb{J}_i)$, the total final-state density matrix $\langle \alpha_f \mathbb{J}_f M_f | \rho_f | \alpha_f \mathbb{J}_f M'_f \rangle$ of the atom *plus* the two photons with well-defined wave vectors $\mathbf{k}_1, \mathbf{k}_2$ and helicities λ_1, λ_2 can be expressed in terms of the initial-state density matrix $\langle \alpha_i \mathbb{J}_i M_i | \rho_i | \alpha_i \mathbb{J}_i M'_i \rangle$ of the atom as well as the two-photon emission amplitudes in the helicity basis as (Hofbrucker 2020):

$$\langle \alpha_f \mathbb{J}_f M_f, \mathbf{k}_1 \lambda_1, \mathbf{k}_2 \lambda_2 | \rho_f | \alpha_f \mathbb{J}_f M'_f, \mathbf{k}_1 \lambda'_1, \mathbf{k}_2 \lambda'_2 \rangle$$

$$= \sum_{M_i M'_i} \langle \alpha_i \mathbb{J}_i M_i | \rho_i | \alpha_i \mathbb{J}_i M'_i \rangle \mathcal{M}(\mathbf{k}_2, \lambda_2, \mathbf{k}_1, \lambda_1; \alpha_i \mathbb{J}_i M_i \rightarrow \alpha_f \mathbb{J}_f M_f) \mathcal{M}^*(\mathbf{k}_2, \lambda'_2, \mathbf{k}_1, \lambda'_1; \alpha_i \mathbb{J}_i M'_i \rightarrow \alpha_f \mathbb{J}_f M'_f)$$

$$\begin{aligned}
& \mathcal{M}(\mathbf{k}_2, \lambda_2, \mathbf{k}_1, \lambda_1; \alpha_i \mathbb{J}_i M_i \rightarrow \alpha_f \mathbb{J}_f M_f) \\
&= \sum_{\alpha_\nu \mathbb{J}_\nu M_\nu} \left(\frac{\langle \alpha_f \mathbb{J}_f M_f | R(\mathbf{k}_2, \mathbf{u}_{\lambda_2}) | \alpha_\nu \mathbb{J}_\nu M_\nu \rangle \langle \alpha_\nu \mathbb{J}_\nu M_\nu | R(\mathbf{k}_1, \mathbf{u}_{\lambda_1}) | \alpha_i \mathbb{J}_i M_i \rangle}{E_i + \omega_1 - E_\nu} \right. \\
&\quad \left. + \frac{\langle \alpha_f \mathbb{J}_f M_f | R(\mathbf{k}_1, \mathbf{u}_{\lambda_1}) | \alpha_\nu \mathbb{J}_\nu M_\nu \rangle \langle \alpha_\nu \mathbb{J}_\nu M_\nu | R(\mathbf{k}_2, \mathbf{u}_{\lambda_2}) | \alpha_i \mathbb{J}_i M_i \rangle}{E_i + \omega_2 - E_\nu} \right) \\
&= \pi \sum_{Kq} \sum_{\mathbb{M}_1 \mathbb{M}_2, \mathbb{J}_\nu} \sum_{M_1 M_2} i^{L_1-p_1+L_2-p_2} (-\lambda_1)^{p_1} (-\lambda_2)^{p_2} (-1)^{J_f-M_f+K-q} [K] \begin{pmatrix} K & J_f & J_i \\ q & -M_f & M_i \end{pmatrix} \begin{pmatrix} L_1 & L_2 & K \\ M_1 & M_2 & -q \end{pmatrix} D_{M_1, \lambda_1}^{(L_1)}(\vartheta_1, \varphi_1) \\
&\quad \times D_{M_2, \lambda_2}^{(L_2)}(\vartheta_2, \varphi_2) \left[\mathcal{U}^{(K, \gamma+\gamma' \text{ emission})}(\alpha_f \mathbb{J}_f, \omega_2, \mathbb{M}_2, \mathbb{J}_\nu, \omega_1, \mathbb{M}_1, \alpha_i \mathbb{J}_i) + (-1)^{L_1+L_2+K} \mathcal{U}^{(K, \gamma+\gamma' \text{ emission})}(\alpha_f \mathbb{J}_f, \omega_1, \mathbb{M}_1, \mathbb{J}_\nu, \omega_2, \mathbb{M}_2, \alpha_i \mathbb{J}_i) \right].
\end{aligned}$$

➤ Reduced two-photon emission amplitude for two *non-equivalent* photons: (Hofbrucker 2020)

$$\mathcal{U}^{(K, \gamma+\gamma' \text{ emission})}(\alpha_f \mathbb{J}_f, \omega_2, \mathbb{M}_2, \mathbb{J}_\nu, \omega_1, \mathbb{M}_1, \alpha_i \mathbb{J}_i) = \begin{Bmatrix} J_i & J_f & K \\ L_2 & L_1 & J_\nu \end{Bmatrix} \sum_{\alpha_\nu} \frac{\langle \alpha_f \mathbb{J}_f \| \mathbb{O}^{(\mathbb{M}_2, \text{ emission})} \| \alpha_\nu \mathbb{J}_\nu \rangle \langle \alpha_\nu \mathbb{J}_\nu \| \mathbb{O}^{(\mathbb{M}_1, \text{ emission})} \| \alpha_i \mathbb{J}_i \rangle}{E_i + \omega_1 - E_\nu}.$$

In the reduced amplitude $\mathcal{U}^{(K, \gamma+\gamma' \text{ emission})}(\alpha_f \mathbb{J}_f, \mathbb{M}_2, \mathbb{J}_\nu, \omega_1, \mathbb{M}_1, \alpha_i \mathbb{J}_i)$ above, the summation α_ν runs again over all the atomic states of given symmetry \mathbb{J}_ν , i.e. over all the ASF as provided by the [Green function channel with symmtry \$\mathbb{J}_\nu\$](#) .

➤ Two-photon angle-angle-differential emission rate for initially unpolarized atoms: For the two-photon decay $(\alpha_i \mathbb{J}_i \rightarrow \alpha_f \mathbb{J}_f)$ of an initially unpolarized atom or ion in $(\alpha_i \mathbb{J}_i)$, and if neither the polarization of the photons nor the polarization of the atom is observed, the

angle-angle-differential emission rate, can be written as

$$\begin{aligned}
 & \frac{d^2 W^{(\gamma+\gamma' \text{ emission})}}{d\Omega_1 d\Omega_1} (\omega_1; \alpha_i \mathbb{J}_i \rightarrow \alpha_f \mathbb{J}_f) \\
 &= \frac{\alpha^2}{(2\pi)^3} \omega_1 \omega_2 d\omega_1 \sum_{M_f} \sum_{\lambda_1, \lambda_2} \langle \alpha_f \mathbb{J}_f M_f, \mathbf{k}_1 \lambda_1, \mathbf{k}_2 \lambda_2 | \rho_f | \alpha_f \mathbb{J}_f M_f, \mathbf{k}_1 \lambda_1, \mathbf{k}_2 \lambda_2 \rangle \\
 &= \frac{\alpha^2}{8\pi^3 [J_i]} \omega_1 \omega_2 d\omega_1 \sum_{\lambda_1 \lambda_2, Kq} [K] \\
 &\quad \times \sum_{\mathbb{M}_1 \mathbb{M}_2, \mathbb{J}_\nu} \sum_{M_1 M_2} i^{L_1-p_1+L_2-p_2} (-\lambda_1)^{p_1} (-\lambda_2)^{p_2} [L_1, L_2]^{1/2} \begin{pmatrix} L_1 & L_2 & K \\ M_1 & M_2 & -q \end{pmatrix} D_{M_1, \lambda_1}^{(L_1)}(\vartheta_1, \varphi_1) D_{M_2, \lambda_2}^{(L_2)}(\vartheta_2, \varphi_2) \\
 &\quad \times \left\{ \sum_{\mathbb{M}'_1 \mathbb{M}'_2, \mathbb{J}'_\nu} \sum_{M'_1 M'_2} (-i)^{L'_1-p'_1+L'_2-p'_2} (-\lambda'_1)^{p'_1} (-\lambda'_2)^{p'_2} [L'_1, L'_2]^{1/2} \begin{pmatrix} L'_1 & L'_2 & K \\ M'_1 & M'_2 & -q \end{pmatrix} [D_{M'_1, \lambda'_1}^{(L'_1)}(\vartheta_1, \varphi_1) D_{M'_2, \lambda'_2}^{(L'_2)}(\vartheta_2, \varphi_2)]^* \right. \\
 &\quad \times \left[\mathcal{U}^{(K, \gamma+\gamma' \text{ emission})}(\alpha_f \mathbb{J}_f, \omega_2, \mathbb{M}_2, \mathbb{J}_\nu, \omega_1, \mathbb{M}_1, \alpha_i \mathbb{J}_i) + (-1)^{L_1+L_2+K} \mathcal{U}^{(K, \gamma+\gamma' \text{ emission})}(\alpha_f \mathbb{J}_f, \omega_1, \mathbb{M}_1, \mathbb{J}_\nu, \omega_2, \mathbb{M}_2, \alpha_i \mathbb{J}_i) \right] \\
 &\quad \left. \times \left[\mathcal{U}^{(K, \gamma+\gamma' \text{ emission})}(\alpha_f \mathbb{J}_f, \omega_2, \mathbb{M}'_2, \mathbb{J}'_\nu, \omega_1, \mathbb{M}'_1, \alpha_i \mathbb{J}_i) + (-1)^{L_1+L_2+K} \mathcal{U}^{(K, \gamma+\gamma' \text{ emission})}(\alpha_f \mathbb{J}_f, \omega_1, \mathbb{M}'_1, \mathbb{J}'_\nu, \omega_2, \mathbb{M}'_2, \alpha_i \mathbb{J}_i) \right]^* \right\}.
 \end{aligned}$$

➤ Two-photon energy-differential emission rate for initially unpolarized atoms: For the two-photon decay $(\alpha_i \mathbb{J}_i \rightarrow \alpha_f \mathbb{J}_f)$ of an initially unpolarized atom, the energy-differential emission rate can be written as

$$\begin{aligned}
 & \frac{dW^{(\gamma+\gamma' \text{ emission})}}{d\omega_1} (\omega_1; \alpha_i \mathbb{J}_i \rightarrow \alpha_f \mathbb{J}_f) \\
 &= \frac{2\pi\alpha^2}{[J_i]} \omega_1 \omega_2 \sum_{\mathbb{M}_1 \mathbb{M}_2 \mathbb{J}_\nu} \left| \mathcal{U}^{(K, \gamma+\gamma' \text{ emission})}(\alpha_f \mathbb{J}_f, \omega_1, \mathbb{M}_1, \mathbb{J}_\nu, \omega_2, \mathbb{M}_2, \alpha_i \mathbb{J}_i) + (-1)^{L_1+L_2+K} \mathcal{U}^{(K, \gamma+\gamma' \text{ emission})}(\alpha_f \mathbb{J}_f, \omega_2, \mathbb{M}_2, \mathbb{J}_\nu, \omega_1, \mathbb{M}_1, \alpha_i \mathbb{J}_i) \right|^2
 \end{aligned}$$

8. Atomic processes

➤ Total two-photon decay rate:

$$W^{(\gamma+\gamma' \text{ emission, total})} (\alpha_i \mathbb{J}_i \rightarrow \alpha_f \mathbb{J}_f) = \int d\omega_1 \frac{dW^{(\gamma+\gamma' \text{ emission})}}{d\omega_1} (\omega_1; \alpha_i \mathbb{J}_i \rightarrow \alpha_f \mathbb{J}_f).$$

8.1.k. Double-Auger decay (DoubleAutoIonization)

Process, notation & application:

- Simultaneous double Auger electron emission (autoionization) of an atom or ion: $A^{q+*} \rightarrow A^{(q+2)+(*)} + (e_{a_1}^- + e_{a_2}^-)$
- Quantum notations used in the formulas below: $|\alpha_i \mathbb{J}_i\rangle \rightarrow |\alpha_f \mathbb{J}_f\rangle + |\varepsilon_1 \kappa_1\rangle + |\varepsilon_2 \kappa_2\rangle$
- Using JAC: Perform an `Atomic.Computation(..., processSettings=DoubleAutoIonization.Settings(), ...)` or call directly functions from the module `DoubleAutoIonization`.
- In JAC, the total double-Auger rates calculated and tabulated by defaults for all selected transitions $(\alpha_i \mathbb{J}_i \rightarrow \alpha_f \mathbb{J}_f)$.
- In JAC, the Green function (channels) have to be calculated before and passed to the computations by `DoubleAutoIonization.Settings(..., green=greenFunction)`.
- In JAC, the excitation scheme `:Basics.AbstractExcitationScheme` determines how and to which extent excitations from the initial configuration(s) are included into the representation of the Green function by specifying the active set of orbitals as well as the number of virtual excitations.
- **Double Auger decay:** An autoionization of an atom or ion may occur also via the simultaneous emission of two electrons which just share the overall excess energy.
- **Double Auger decay:** The *direct* double Auger (DA) emission has been found an important second-order process, in which two electrons are ejected simultaneously from an inner-shell excited atom. A first evidence of the direct DA was found in *K*-shell photoionization experiments of neon with photon energies between 867 and 913 eV by Krause and coworkers (~1965) as well as for argon.
- **Double Auger decay:** Data from direct multiple Auger emission processes, such as double Auger rates, are required to model the interaction of x-rays with matter.
- **Double Auger decay:** For the decay of a neon 1s-hole, Carlson and Krause (1965) already found an about 8 % portion of Ne^{3+} ions owing to the simultaneous double Auger decay. This large portion of the double Auger process occurs quite in contrast to the $\lesssim 1\%$ prediction from a simple shake-off model.
- **Double Auger decay of Ar:** Viefhaus *et al.* (2004) observed the direct $L_{23} - \text{MMM}$ double Auger decay following the photoionization of a 2p electron of argon by angle-resolved electron-electron coincidence spectroscopy. The measured energy and angular distributions of the (two) emitted electrons provide insight into the inter-electronic interaction. Further studies were performed also on the double Auger decay of the Ar ($2p \rightarrow 3d, 4s$) satellite levels by using multi-electron coincidence techniques. Finally, double Auger spectra were recorded also by following the 1s photoionization of argon and by measuring the recoil energy of the ions.

8. Atomic processes

- **$L_{23}MMM$ double Auger transitions in argon:** Viefhaus *et al.* (2004) observed the direct $L_{23}MMM$ double Auger transition by angle-resolved electron-electron coincidence spectroscopy, following the photoionization of a $2p$ electron in argon. The double Auger spectrum shows a continuous intensity distribution and is said to be responsible for about 20 % of the observed Auger electron intensity.
- **Double and triple Auger process:** While matrix elements have been partly discussed for the double Auger emission of electron, no reliable predictions are available yet for the triple Auger processes.

Total and differential double autoionization cross sections:

- **Double Auger rate:** In second-order of perturbation theory, the (direct) double Auger rate is given by (with $\mathbb{J}_\nu = \mathbb{J}_i \delta_{i\nu}$)

$$A^{(\text{DA})}(i \rightarrow f) = 2\pi \int_0^{E_i - E_f} d\varepsilon_1 \sum_{\kappa_1 \kappa_2} \left| \sum_{\alpha_\nu \mathbb{J}_\nu \mathbb{J}_x} \frac{\langle ((\alpha_f \mathbb{J}_f, \varepsilon_1 \kappa_1) \mathbb{J}_x, \varepsilon_2 \kappa_2) \mathbb{J}_i \| \mathbb{V}^{(\text{Auger})} \| \alpha_\nu \mathbb{J}_\nu \rangle \langle \alpha_\nu \mathbb{J}_\nu \| \mathbb{V}^{(\text{Auger})} \| \alpha_i \mathbb{J}_i \rangle}{E_i - E_\nu} \right|^2$$

$$|\varepsilon_1 \kappa_1\rangle = \sum_r c_r |n_r \kappa_1\rangle, \quad |\varepsilon_2 \kappa_2\rangle = \sum_s c_s |n_s \kappa_s\rangle.$$

8.1.I. Photo-double ionization (PhotoDoubleIonization)

Process, notation & application:

- Simultaneous double photoionization of an atom or ion: $A^{q+} + \hbar\omega \rightarrow A^{(q+2)+(*)} + (e_{p_1}^- + e_{p_2}^-)$
- Quantum notations used in the formulas below: $|\alpha_i \mathbb{J}_i\rangle + \hbar\omega(\{\mathbb{M}\}) \rightarrow |\alpha_f \mathbb{J}_f\rangle + |\varepsilon_1 \kappa_1\rangle + |\varepsilon_2 \kappa_2\rangle$
- Using JAC: Perform an `Atomic.Computation(..., processSettings = PhotoDoubleIonization.Settings(), ...)` or call directly functions from the module `PhotoDoubleIonization`.
- In JAC, the total photo-double ionization cross sections are calculated and tabulated by defaults for all selected transitions $(\alpha_i \mathbb{J}_i \rightarrow \alpha_f \mathbb{J}_f)$.

- In JAC, the Green function (channels) have to be calculated before and passed to the computations by `PhotoDoubleIonization.Settings(..., green=greenFunction)`.
- In JAC, the excitation scheme `:Basics.AbstractExcitationScheme` determines how and to which extent excitations are included from the reference configurations in order to generate an active set of orbitals for the representation of the Green function.
- **Photo-double ionization:** Single-photon double ionization, or shortly photo-double ionization, refers to the simultaneous emission of two electrons from an atom or molecule due to the interaction with a photon field; this process requires an inter-electronic interaction and, hence, can be applied to study correlation contributions. Therefore, photo-double ionization measurements for medium-to-heavy elements may allow testing relativistic correlation contributions in a hitherto unexplored region.
- **(Direct) photo-double ionization of atoms:** The (single-photon) photo-double ionization of atoms and ions has attracted interest during the last decades as it often contributes to the ionization of atoms and ions at synchrotrons and FEL.
- **Photo-double ionization (PDI):** Single-photon double ionization (PDI) of atoms and molecules provides new insights into electron-electron correlations and how this affects the angular distributions of the two (outgoing) electrons.
- **(Direct) photo-double ionization of atoms:** The recent advancements of free electron lasers (FEL) has lead to intense short pulses with rather high photon energies, and which may help investigate the (direct) photo-double ionization process for multiply charged ions. Further progress with single-photon double ionization experiments will depend on the future advancements in developing high-brilliant synchrotron or HHG radiation sources as well as efficient coincidence techniques.
- **Single-photon multiple ionization:** The direct multiple ionization of atoms and ions by single photons is perhaps the simplest many-body process. Such a simultaneous release of two or more electrons is caused by interelectronic correlations and is very different from the (typical) inner-shell photoexcitation or photoionization of atoms and their subsequent autoionization. Therefore, the direct photo-double (multiple) ionization is very sensitive to details of the electron-electron interaction, and this applies especially for negative ions.
- **Direct multiple ionization:** While a direct multiple photoionization has been observed for both, positive and negative ions, a clear separation of the direct and sequential ionization processes is often difficult.

Photo-double ionization of helium and helium-like ions:

- **Photo-double ionization measurements of helium:** For atomic helium, the full differential electron dynamics has been obtained by measuring the Coulomb fragments in coincidence as well as by extensive closed-coupling cross section computations. Nowadays, the photo-double ionization of helium is overall considered as a solved problem.

8. Atomic processes

- **Photo-double ionization of helium:** Most studies on the photo-double ionization has been performed for atomic helium, both theoretically and experimentally. In particular, the ratio of the double-to-single photoionization cross sections $R(\hbar\omega) = \sigma^{++} / \sigma^+$ has been analyzed as function of the incident photon energy $\hbar\omega$. For energies near to the photo-double ionization threshold (~ 79 eV), Wannier's theory has been found applicable. At the maximum of the cross section ratio around $\hbar\omega \approx 200$ eV, more elaborate many-body techniques, such as the close-coupling formalism, are needed and make accurate predictions of the cross section ratio $R(\hbar\omega)$ difficult.
- **PDI of helium:** PDI has been extensively studied for helium and has led to good agreement between experiment and theory and, virtually, to rather a complete understanding of the double ionization dynamics for this simple system.

Photo-double ionization of complex atoms:

- **Photo-double ionization of complex atoms:** K -shell photo-double ionization experiments have been performed for several light and medium elements up to atomic silver. Often, these K -shell photo-double ionization cross section ratios are compared with those of the corresponding helium-like ion. For such medium and heavy systems, however, photoionization cross section calculations should account for, in addition to correlations, also relativistic contributions to the photo-double ionization amplitudes (Yerokhin and Surzhykov, 2011).

Angle-differential and total cross sections:

- **Photo-double ionization amplitude:** In many-electron notation, these amplitudes can be written as

$$\begin{aligned} \mathcal{M}^{(\text{PDI})}(\omega; \alpha_i \mathbb{J}_i \rightarrow \alpha_f \mathbb{J}_f; \varepsilon_1 \kappa_1, \varepsilon_2 \kappa_2, \mathbb{J}_t) &= \sum_{\alpha_\nu \mathbb{J}_\nu \mathbb{J}_x} \frac{\langle ((\alpha_f \mathbb{J}_f, \varepsilon_1 \kappa_1) \mathbb{J}_x, \varepsilon_2 \kappa_2) \mathbb{J}_t \parallel \mathbb{V}^{(e-e)} \parallel \alpha_\nu \mathbb{J}_\nu \rangle \langle \alpha_\nu \mathbb{J}_\nu \parallel \mathbb{O}^{(\mathbb{M}, \text{absorption})} \parallel \alpha_i \mathbb{J}_i \rangle}{E_i + \omega - E_\nu (1 - i 0)} \\ &+ \sum_{\alpha_\nu \mathbb{J}_\nu \mathbb{J}_x} \frac{\langle ((\alpha_f \mathbb{J}_f, \varepsilon_1 \kappa_1) \mathbb{J}_x, \varepsilon_2 \kappa_2) \mathbb{J}_t \parallel \mathbb{O}^{(\mathbb{M}, \text{absorption})} \parallel \alpha_\nu \mathbb{J}_\nu \rangle \langle \alpha_\nu \mathbb{J}_\nu \parallel \mathbb{V}^{(ee)} \parallel \alpha_i \mathbb{J}_i \rangle}{E_i + \omega - E_\nu (1 - i 0)}. \end{aligned}$$

- **Energy-differential photo-double ionization cross section:**

$$\frac{d\sigma^{(\text{PDI})}}{d\varepsilon_1}(\omega; \alpha_i \mathbb{J}_i \rightarrow \alpha_f \mathbb{J}_f; \varepsilon_1) = \frac{4\pi^2\alpha}{\omega} \sum_{\kappa_1 \kappa_2 \mathbb{J}_t} |\mathcal{M}^{(\text{PDI})}(\omega; \alpha_i \mathbb{J}_i \rightarrow \alpha_f \mathbb{J}_f; \varepsilon_1 \kappa_1, \varepsilon_2 \kappa_2, \mathbb{J}_t)|^2.$$

Final-state density matrix:

- **Final-state density matrix:** The final-state density matrix of the ‘photoion + two free electrons’ can be expressed in terms of the statistical tensors of the total initial state ‘atom + incident photon’ as well as the reduced photo-double ionization amplitudes (Berakdar and Kabachnik, 2005)

$$\rho_{kq}(\alpha_f \mathbb{J}_f, \alpha'_f \mathbb{J}'_f) = \sum_{k_o q_o, k_\gamma q_\gamma} [k_o, k_\gamma]^{1/2} \langle k_o q_o, k_\gamma q_\gamma | kq \rangle \begin{Bmatrix} J_o & 1 & J \\ J_o & 1 & J' \\ k_o & k_\gamma & k \end{Bmatrix} \rho_{k_o q_o}(\alpha_i \mathbb{J}_i) \rho^\gamma(P_1, P_2, P_3) \\ \times \langle \alpha \mathbb{J} \| \mathbb{O}^{(PDI)} \| \alpha_o \mathbb{J}_o \rangle \langle \alpha' \mathbb{J}' \| \mathbb{O}^{(PDI)} \| \alpha_o \mathbb{J}_o \rangle^*.$$

Photo-triple ionization:

- **Photo-triple photoionization (PTI):** PTI refers to the absorption of a single photon under the simultaneous ejection of three atomic electrons. First PTI experiments on atomic lithium were performed by Wehlitz *et al.* (1998); these authors proposed that PTI is reasonably well described by the photo-double ionization of the two inner-shell electrons, together with a shake-off of an outer electron. These arguments are expected to be valid for sufficient excess energy of the (initial) two-electron emission, and which must at least exceed the $2s$ binding energy. Another approach was taken by Pattard and Burgdörfer (2001), who suggested a half-collision model, in which one of the primary ejected $1s$ electron collides with the $2s$ electron on its way out.
- **Photo-triple ionization (PTI):** Various theoretical method and detailed measurements need to be explored to better understand the limits of the approximations that are necessary due to predominant role of the interelectronic interactions.

8.1.m. Radiative-Auger decay (RadiativeAuger)

Process, notation & application:

8. Atomic processes

- Radiative-Auger (autoionization) of an atom or ion: $A^{q+*} \longrightarrow A^{(q+1)+,(*)} + (e_a^- + \hbar\omega)$
- Quantum notations used in the formulas below: $|\alpha_i J_i\rangle \longrightarrow |\alpha_f J_f\rangle + \hbar\omega(M) + |\varepsilon_a \kappa_a\rangle$
- The radiative Auger process results in the simultaneous emission of an electron and photon, and mainly occurs for inner-shell excited atoms and ions. There are no characteristic electron or photon lines associated with this process, since the transition energy is shared between the photon and the electron.

8.1.n. Electron-impact (de-) excitation. Collision strengths (ImpactExcitation)

Process, notation & application:

- Electron-impact excitation of an atom or ion: $e_s^- + A \rightarrow A^* + e_s^-'$
- Quantum notations used in the formulas below: $|\alpha_i \mathbb{J}_i\rangle + |\varepsilon_i \kappa_i\rangle \rightarrow |\alpha_f \mathbb{J}_f\rangle + |\varepsilon_f \kappa_f\rangle$ or $|\alpha_i \mathbb{J}_i\rangle + |\mathbf{p}_i m_i\rangle \rightarrow |\alpha_f \mathbb{J}_f\rangle + |\mathbf{p}_f m_f\rangle$
- Electron-impact excitation is formally an inelastic scattering process in which a free incident electron $|\varepsilon_i \kappa_i\rangle$ is scattered at the atom and leaves as final electron $|\varepsilon_f \kappa_f\rangle$.
- Electron-impact ionization cross sections are required in different field, for example, for calculating level populations and spectral line intensities of non-local-thermodynamic-equilibrium (non-LTE) plasmas.

Computation of electron-impact processes:

- Approaches for electron-impact excitation cross sections: Different approaches have been implemented and applied in order to compute electron-impact cross sections for atoms and ions. Two main approaches refer to (1) the use of the first-order Born approximation and (2) the close-coupling approximation. The close-coupling (CC) equations enable one to incorporate, at least partly, the coupling of the different excitation channels due to the impact of free electrons as well as resonances in the cross sections. To a good approximation, such CC equations are implemented in various R-matrix codes; cf. the BSR code.
- First-Born approximation: The second (standard) method for the computation of electron-impact excitation cross sections apply the first-order Born approximation and **assumes that the excitation into different (excited) states are independent of each other**. Apart from the (simple) plane-wave first-Born approximation, the Coulomb- or distorted-wave (DW) Born approximation accounts for the modification of the emitted electron waves due to the Coulomb *or* the effective many-electron potential of the excited atom or ion. In particular, the DW Born approximation includes the realistic electronic structure of the atoms and provides significantly better results than all simpler versions of the (first-) Born approximation.
- Plane-wave Born cross sections for EIE: For neutral atoms, scaled plane-wave Born cross sections for EIE become comparable with other *ab-initio* methods, such as the convergent close-coupling method. However, such scaling methods are applicable only to dipole-allowed excitations, since they are all based on three properties: (i) the ionization energy, (ii) the excitation energy as well as (iii) the dipole oscillator strength. These properties are obtained by accurate *ab-initio* methods and, thus, are free from adjustable parameters (Kim, 2001). However, these scaled cross sections do not account for the resonances often found near to the excitation thresholds.

8. Atomic processes

- The electron-impact excitation of atoms is often described in first-order Born approximation, in which one can easily distinguish individual excitation channels. This approximation neglects however the coupling of the *continuum channels*, but which can later be incorporated perturbatively.
- **Distorted-wave Born approximation (DWBA):** We here make use of the DWBA that accounts for the distortion of the continuum orbitals due to (local) potential of the nucleus and all the electrons of the target. The DWBA typically gives better results than the *pure* Born or the Coulomb-Born approximation. The current implementation is similar to the codes by Zhang *et al.*(1989) as well as to the FAC code (Gu 2008).
- **EIE of multiply charged ions:** The EUV emissions from multiply charged ions have been found relevant in studying various astrophysical and laboratory plasmas, such as laser-produced plasmas, fusion devices and electron beam ion traps (EBITs). In such plasma, the observed EUV lines may unveil information about plasma electron temperature, ion density and/or chemical composition.
- For a reliable evaluation of plasma parameters, such as temperature, density or level populations, the excitation cross sections need to be known quite accurately.
- **Computational methods for electron-impact excitation & ionization:** Three methods are commonly used in the literature to calculate electron-impact excitation and ionization cross sections: i) Coulomb-Born (CB) approximation, where the continuum orbital just represent a free electron in a Coulomb potential; ii) distorted-wave (DW) approximation that includes a more realistic potential for the continuum orbitals; iii) close-coupling (CC) approximation. **In the first two approximations, all excitation channels are treated independently and give overall rise to a scattering matrix which is not necessarily unitary.**
- **Electron-impact excitation code:** Zhang *et al.* (1989) suggested a rapid approach for calculating collisions strengths and electron-impact cross sections, with focus upon multiply and highly charged ions. These collision data are needed especially for modeling high-temperature plasma. When compared with a purely non-relativistic treatment, the number of radial matrix elements increases roughly by a factor of 10 within the relativistic (atomic) theory. Typically, the collision strengths need to be known for several impact-electron energies as well as for indeed many initial and final partial waves of the free (scattered) electron.
- **Electron-impact excitation in plasma diagnostics:** In plasma-diagnostics measurements, the population of the excited states, relevant for plasma diagnostics, is largely driven by the direct electron-impact excitation of the ground and low-lying metastable states, and followed by their radiative decay.
- **Effective collision strengths:** For an atomic transition $i \rightarrow f$, the effective collision strength is defined by

$$\Omega_{if}^{(\text{eff})} = \frac{1}{k T_e} \int_0^\infty d\varepsilon \Omega_{if}(\varepsilon) \exp\left(\frac{\varepsilon}{k T_e}\right),$$

where T_e is the electron temperature and ε is the kinetic energy of the scattered electron in its final state.

Collision strength and cross sections:

- **Collision strength:** The name *collision strength* was first suggested by Seaton (1953). For a given (atomic target) transition $\alpha_i \mathbb{J}_i \rightarrow \alpha_f \mathbb{J}_f$, the collision strength is related to the cross section Q by

$$\Omega(\alpha_i \mathbb{J}_i, \alpha_f \mathbb{J}_f) = \frac{4\pi g_i}{\lambda_i^2} Q(\alpha_i \mathbb{J}_i, \alpha_f \mathbb{J}_f),$$

if the continuum orbitals are normalized per unit energy. The statistical weight g_i of level $|\alpha_i \mathbb{J}_i\rangle$ ensures the detailed-balance relation $\Omega(\alpha_i \mathbb{J}_i, \alpha_f \mathbb{J}_f) = \Omega(\alpha_f \mathbb{J}_f, \alpha_i \mathbb{J}_i)$.

- **Collision strength:** If $|\varepsilon_i, \kappa_i\rangle$ and $|\varepsilon_f, \kappa_f\rangle$ denote the partial waves of the incident and scattered electrons, the collision strength is given by

$$\Omega_{if} = 2 \sum_{\kappa_i, \kappa_f} \sum_{\mathbb{J}_t} [J_t] \left| \langle (\mathbb{J}_f, \epsilon_f, \kappa_f) \mathbb{J}_t M_t | V^{(e-e)} | (\mathbb{J}_i, \epsilon_i, \kappa_i) \mathbb{J}_t M_t \rangle \right|^2.$$

- **Electron-impact cross section versus collision strength:** The relation between the electron-impact cross section and collision strength with wave functions normalized on Rydbergs is given by (Zhang *et al.*, 1990)

$$Q = \frac{\pi a_o^2}{k_i^2 (2J_i + 1)} \Omega.$$

- In the JAC program, the standard decomposition of the electron-electron interaction matrix elements is utilized to compute the collision strength.
- **Normalization of continuum orbitals:** A continuum orbital is said to be **normalized per unit energy** if it has an asymptotic amplitude $\sqrt{k/\varepsilon}$ (or, $\sqrt{2/k}$ in the non-relativistic limit) or, equivalently, if it fulfills, equivalently,

$$\int dr [P_\varepsilon(r) P_{\varepsilon'}(r) + Q_\varepsilon(r) Q_{\varepsilon'}(r)] = \pi \delta(\varepsilon - \varepsilon').$$

- For electron-impact processes, the collision strength $\Omega(\alpha_i \mathbb{J}_i, \alpha_f \mathbb{J}_f)$ is typically of the order of unity, though still large variation may still occur owing to its dependence on the particular ion as well as the transition and impact energy. Therefore, it is usually not justified to assume $\Omega = 1$ as sometimes done in astrophysical codes.

8. Atomic processes

- **Simplification for heavy ions with open d - and f -shells:** For heavy and ionized atoms with open d - and f -shells, the fine-structure of just (mixed) single initial- and final-state configurations may give rise to thousands of (fine-structure) transitions, for which the radial integrals often depend only weakly on the transition energy. For such transition arrays, the total cross section computations can be simplified considerably by either neglecting the weak dependence of the radial integrals or by some simple interpolation.
- Accurate calculations of electron-impact excitation of atom and ions are overall still a challenge for contemporary electronic methods, such as convergent close-coupling, R-matrix close-coupling or time-dependent close-coupling scheme, and even by using the largest (parallel) computers.

Electron-impact excitation of magnetic sublevels:

- **Electron-impact excitation by an incident electron beam:** If the electron-impact is made by a *beam* of electrons, the excited target atoms are generally **aligned** and the subsequently emitted radiation becomes polarized. This alignment of the (electron-impact) excited atoms can be either expressed in terms of the atomic density matrix or by means of magnetic sublevel dependent cross sections. Both schemes require **electron-impact transition amplitudes** with well-defined angular momenta of the initial and final-bound states as well the coupling of the partial waves to define scattering states of proper symmetry.
- **Electron-impact excitation by an incident electron beam:** Theoretical computations of the alignment and magnetic sublevel-dependent electron-impact cross sections can be applied, for instance, to beam-plasma interactions in solar flares, for the diagnostics tokamak plasmas, or to analyze experiments with electron-beam-ion-traps (EBIT).

Collisional-excitation rate coefficients:

- The rate coefficient of collisional excitation is given by
- **Electron-impact excitation plasma rate coefficients:** These plasma rate coefficients can be obtained as usual from the cross section and the convolution about the electron distribution in the plasma by (Malker and Sharma, 2022)

$$\alpha^{(\text{EIE})}(T; \alpha_i \mathbb{J}_i \rightarrow \alpha_f \mathbb{J}_f) = 2 \sqrt{\frac{2}{\pi m}} (kT)^{-3/2} \int_{E_{if}}^{\infty} dE E \sigma^{(\text{EIE})}(E; \alpha_i \mathbb{J}_i \rightarrow \alpha_f \mathbb{J}_f) \exp\left(\frac{E}{kT}\right),$$

and where $E_{if} = E_f - E_i$ refers to the excitation energy of the transition $\alpha_i \mathbb{J}_i \rightarrow \alpha_f \mathbb{J}_f$. Here, a Maxwellian electron energy probability function is used to average the cross sections.

$$\alpha^{(\text{impact:excitation})} = \int_{\Delta E}^{\infty} dv f(v) \sigma^{(\text{impact-excitation})}(v)$$

where $f(v)$ is velocity distribution of electrons which is typically assumed to have a Maxwellian distribution with electron temperature T_e , $\sigma^{(\text{impact-excitation})}(\alpha_i \mathbb{J}_i, \alpha_f \mathbb{J}_f)$ is the electron-impact excitation cross-section from level $i \rightarrow f$ at velocity v , and $\Delta E = E_f - E_i$ is the excitation energy.

- For a given energy of the incident electrons, the collisional-excitation rate coefficient can be expressed also as

$$\alpha^{(\text{impact-excitation})} = \sqrt{\frac{\pi}{E}} \int_{\Delta E}^{\infty} dE E \sigma^{(\text{impact-excitation})}(E) \exp\left(-\frac{E}{T_e}\right).$$

8.1.o. Electron-impact ionization (ImpactIonization)

Process, notation & application:

- Electron-impact ionization of an atom or ion: $e_s^- + A \rightarrow A^* + e_s^-' + e^-$
- Quantum notations used in the formulas below: $|\alpha_i \mathbb{J}_i\rangle + |\varepsilon_i \kappa_i\rangle \rightarrow |\alpha_f \mathbb{J}_f\rangle + |\varepsilon_f \kappa_f\rangle + |\varepsilon_c \kappa_c\rangle$ where $|\varepsilon_c \kappa_c\rangle$ is the initially bound *atomic* electron.
- The electron-impact ionization process is important in all (high-temperature) plasma, both in astro and plasma physics, and elsewhere. It is the inverse process to the three-body recombination, $A + e_i^- \longleftrightarrow A^+ + e_f^- + e_c^-$.
- We refer to the three *free* electrons, that are involved in this process, as **incident**, **(final-) scattered** and **(additionally released) continuum electron**, and with the corresponding indices above.
- **Electron-impact ionization (EII) cross sections:** In the distorted-wave approximation, the differential (in energy) electron-impact ionization cross sections can be obtained from the formulas of the electron-impact excitation cross section, if the excited bound electron is replaced by another continuum electron. Unfortunately, such a replacement increases the number of ionization channels considerably, since now formally two *free* electrons need to be coupled to the final state of the residual ion and since a summation has to be made over all (total) angular momenta of the scattering states with two free electrons. Here, a clean notation for all incoming and outgoing electron waves is crucial to retain the application of such electron-impact ionization for different physical scenarios. Until the present, most derivation have been made with specific assumptions about the electron-impact ionization cross sections, and often in a rather intransparent notation.

8. Atomic processes

- **Quantum *versus* empirical EII cross sections:** Owing to the complexity of quantum EII cross sections, we first implement a few (semi-)empirical approximations to the EII cross sections that are based on the work by Kim and coworkers (2000, 2001). See Section 13.2.c for the empirical computation of EII cross sections.

Quantum cross sections:

- **Electron-impact ionization cross section:** These cross sections are obtained rather similarly as the electron-impact excitation cross sections but by allowing an ionizing transition between fine-structure levels $\alpha_i \mathbb{J}_i(N) \rightarrow \alpha_f \mathbb{J}_f(N-1)$ (Fontes *et al.* 2015)

$$\sigma^{(\text{ionization})}(\alpha_i \mathbb{J}_i, \alpha_f \mathbb{J}_f) = \frac{8}{k_i^2 g_i} \sum_{\mathbb{J}_c, \mathbb{J}_t} (2J_s + 1) \sum_{\kappa_i \kappa_f \kappa_e} \int_0^{\varepsilon_i - I_p} \varepsilon' |\langle ((\alpha_f \mathbb{J}_f, \epsilon_c \kappa_c) \mathbb{J}_c), \epsilon_f \kappa_f \rangle \mathbb{J}_t \| V^{(e-e)} \| (\alpha_i \mathbb{J}_i, \epsilon_i \kappa_i) \mathbb{J}_t \rangle|^2$$

- This cross section contains a summation over all possible values \mathbb{J}_t of the initial ion and the (incoming) incident electron in the partial wave $|\varepsilon_i \kappa_i\rangle$.

8.1.p. Photoabsorption

Process, notation & application:

- Photoexcitation of an atom or ion: $A + \hbar\omega \rightarrow \begin{cases} A^* \\ A^{+,*} e_p^- \\ \text{photonscattering, QED, ...} \end{cases}$
- Quantum notations used in the formulas below: $|\alpha_i \mathbb{J}_i\rangle + \hbar\omega(\mathbf{k}, \lambda) \rightarrow |\alpha_f \mathbb{J}_f\rangle, \quad \lambda = \pm 1$
 $|\alpha_i \mathbb{J}_i\rangle + \hbar\omega(\mathbf{k}, \lambda) \rightarrow |(\alpha_f \mathbb{J}_f, \varepsilon \kappa) \mathbb{J}_t\rangle$
- Using JAC: Perform a `Cascade.Computation(..., ..., processSettings=PhotoExcitation.Settings(...), ...)`.
- Photoabsorption is more general than photoexcitation or photoionization alone and may include various – more or less – weak processes, such as light scattering, photo-assisted ionization of capture processes. For a wide range of photon energies ω , the calculation of photoabsorption cross sections can be restricted however to the (resonant) single-electron photoionization of atoms and matter.
- Photoabsorption: Sometimes, this term is used more restrictive to processes for which the photon energy is completely transferred to an atom or molecule.

Photoabsorption and line-shape function:

- Absorption coefficient $\alpha(\omega)$: For a beam of light that propagates in x -direction, the absorption coefficient is phenomenologically defined in terms of changes of the spectral intensity $I(\omega)$, cf. Hilborn (2002)

$$\frac{1}{I(\omega)} \frac{dI(\omega)}{dx} = -\alpha(\omega).$$

The spectral intensity $I(\omega)$ is spectroscopically a time-averaged quantity over several or many optical cycles.

- Line-shape function $g(\omega)$: In most practical applications, the frequency-dependence of the absorption and emission processes (absorption coefficient) is important but often approximated by means of a normalized line-shape function $g(\omega)$ with $\int_{-\infty}^{\infty} d\omega g(\omega) = 1$, and where negative frequencies have no special physical meaning. Here, the use of $-\infty$ as the lower limit in the normalization integral greatly simplifies the normalization calculation. — For atoms in motion or in collision, the line-shape function $g(\omega)$ describes the appropriate

8. Atomic processes

ensemble-averaged line shape. The line-shape function $g(\omega)$ has the dimensions of 1/angular frequency and, hence, the explicit functional form of $g(\omega)$ and $\tilde{g}(\lambda)$ is not equivalent.

- **Absorption cross section $\sigma^{(\text{photoabsorption})}(\omega)$:** If we assume $\alpha(\omega)$ to be proportional to the number N_o of atoms per unit volume in the lower level $(\beta_o \mathbb{J}_o)$, which the beam intercepts, the absorption cross section is given by:

$$\alpha(\omega) = N_o \sigma^{(\text{photoabsorption})}(\omega).$$

- **Relation between absorption cross section and Einstein's A and B coefficients:** (Hilborn 2002)

$$\begin{aligned} \sigma^{(\text{photoabsorption})}(\omega; i \rightarrow f) &= \frac{g_f}{4 g_i} \lambda_{fi}^2 g(\omega) A_{fi}, & \sigma_o^{(\text{photoabsorption, total})}(\omega) &= \frac{g_f}{4 g_i} \lambda_{fi}^2 A_{fi} \\ \sigma^{(\text{photoabsorption})}(\omega; i \rightarrow f) &= \frac{\hbar \omega}{c} B_{if}(\omega) g(\omega), & \sigma_o^{(\text{photoabsorption, total})} &= \frac{\hbar \omega_{fi}}{c} B_{if}(\omega). \end{aligned}$$

- Relation between line strength and Einstein A coefficient for a spontaneous $i \rightarrow f$ emission:

$$S_{if} = \frac{3 \epsilon_o h c^3}{2 \omega_{if}^3} g_i A_{if}.$$

- **Weighted oscillator strength:** From the principle of detailed balance and in order to avoid confusion about the absorption or emission viewpoint, one often reports the weighted oscillator strength $g f = g_1 f_{12}^{(\text{absorption})} \equiv -g_2 f_{21}^{(\text{emission})}$.

- **Rabi frequency for on-resonance excitations:** For two non-degenerate levels (i, f) and an incident (linearly-polarized) light field at resonance $\omega = \omega_{fi}$, the Rabi frequency can be expressed in terms of the electric field amplitude \mathcal{E} and the transition dipole moment μ_{fi} by

$$\Omega_R = \frac{\mu_{fi} \mathcal{E}}{\hbar}, \quad \mu_{fi} = \langle \alpha_f \mathbb{J}_f, M = 0 | \mathbb{O}^{(\mathbb{M}, \text{absorption})} | \alpha_i \mathbb{J}_i, M = 0 \rangle$$

For degenerate upper and lower levels, there are generally several Rabi frequencies for each combination $\langle \alpha_f \mathbb{J}_f M_f | \mathbb{O}^{(\mathbb{M}, \text{absorption})} | \alpha_i \mathbb{J}_i M_i \rangle$, and this gives usually rise to a rather complicated dynamical behaviour (Hilborn 2002).

8.1.q. Hyperfine-induced transitions (Hfs)

Process, notation & application:

- Hyperfine-induced transition of an atom or ion: $A^{q+*} \longrightarrow A^{q+,(*)} + \hbar\omega$
- Quantum notations used in the formulas below: $|\alpha_i J_i\rangle \longrightarrow |\alpha_f J_f\rangle + \hbar\omega (\mathbb{M})$

8.2. In JAC partly-implemented processes

8.2.a. Multi-photon & multi-color ionization (MultiPhotonIonization)

Process, notation & application:

- Multi-photon ionization: of an atom or ion $A + n \hbar\omega \rightarrow A^{(*)} + e_p^-$
- Quantum notations used in the formulas below: $|\alpha_i \mathbb{J}_i\rangle + \hbar\omega_1(\mathbb{M}_1) + \hbar\omega_2(\mathbb{M}_2) + \dots + \hbar\omega_n(\mathbb{M}_n) \rightarrow |\alpha_f \mathbb{J}_f\rangle + |\varepsilon \kappa\rangle$
- If the photon energy is smaller than the ionization threshold of the atom, it can still be ionized due to its simultaneous interaction with several photons. However, the probability generally decreases rapidly with the number of photons N , that are required to overcome the ionization threshold.
- Multi-photon ionization is studied mainly by means of intense, pulsed lasers. The ionization probability is for moderate intensities proportional to the N -th power of the intensity, I^N , while this power law breaks down at high intensities due to the ac-Stark effect.
- In first strong-field laser experiments, a rather large probability was found for a multiple ionization of atoms, relative to single-ionization probability, and gave rise to various speculation about *collective modes* in the electronic motion of atoms and ions.

Two-photon ionization with monochromatic light:

- Quantum notations used in the formulas below: $|\alpha_i \mathbb{J}_i\rangle + \hbar\omega(\mathbb{M}_1) + \hbar\omega(\mathbb{M}_2) \rightarrow |\alpha_f \mathbb{J}_f\rangle + |\varepsilon \kappa\rangle$; equally-polarized photons
- Final-state density matrix of the ‘photo-ion + photo-electron’: For the two-photon ionization with monochromatic and equally-polarized photons (typically from the same beam), the photoion is found in the final level $(\alpha_f \mathbb{J}_f)$, while the *free* photoelectron is emitted with asymptotic linear momentum \mathbf{p} and spin projection m_s . In a basis of well-defined angular momenta $\mathbb{J}_i, \mathbb{J}_f$, the initial-state density

matrix is $\langle \alpha_i \mathbb{J}_i M_i | \rho_i | \alpha_i \mathbb{J}_i M'_i \rangle$, and the final-state density matrix can be written as:

$$\begin{aligned} \langle \alpha_f \mathbb{J}_f M_f, \mathbf{p} m_s | \rho_f | \alpha_f \mathbb{J}_f M'_f, \mathbf{p}, m'_s \rangle &= \sum_{\lambda_1 \lambda'_1 \lambda_2 \lambda'_2} \langle \mathbf{k} \lambda_1 | \rho_\gamma | \mathbf{k} \lambda'_1 \rangle \langle \mathbf{k} \lambda_2 | \rho_\gamma | \mathbf{k} \lambda'_2 \rangle \langle \alpha_i \mathbb{J}_i M_i | \rho_i | \alpha_i \mathbb{J}_i M'_i \rangle \\ &\times \sum_{\nu} \frac{\left\langle \alpha_f \mathbb{J}_f M_f, \mathbf{p} m_s \left| \sum_j \alpha_j \mathbf{u}_{\lambda_2 j} e^{i \mathbf{k} \cdot \mathbf{r}_j} \right| \alpha_\nu \mathbb{J}_\nu M_\nu \right\rangle \left\langle \alpha_\nu \mathbb{J}_\nu M_\nu \left| \sum_n \alpha_n \mathbf{u}_{\lambda_1 n} e^{i \mathbf{k} \cdot \mathbf{r}_n} \right| \alpha_i J_i M_i \right\rangle}{E_{\alpha_i \mathbb{J}_i} + \omega - E_{\alpha_\nu \mathbb{J}_\nu}} \\ &\times \sum_{\nu} \frac{\left\langle \alpha_f J_f M'_f, \mathbf{p} m'_s \left| \sum_j : \alpha_n \mathbf{u}_{\lambda'_2 j} e^{i \mathbf{k} \cdot \mathbf{r}_j} \right| \alpha'_\nu \mathbb{J}'_\nu M'_\nu \right\rangle \left\langle \alpha'_\nu \mathbb{J}'_\nu M'_\nu \left| \sum_n \alpha_n \mathbf{u}_{\lambda'_1 n} e^{i \mathbf{k} \cdot \mathbf{r}_n} \right| \alpha_i J_i M'_i \right\rangle}{E_{\alpha_i \mathbb{J}_i} + \omega - E_{\alpha'_\nu \mathbb{J}'_\nu}}. \end{aligned}$$

- Total two-photon ionization cross sections for initially unpolarized atoms For initially unpolarized atoms and equally-polarized plane-wave photons with wave vector $\mathbf{k} \parallel \mathbf{e}_z$ and Stokes parameters P_1, P_2, P_3 , the total two-photon ionization cross sections for the transition $|\alpha_i J_i\rangle \rightarrow |\alpha_f J_f\rangle$ is given by:

$$\begin{aligned} \sigma(\alpha_i J_i \rightarrow \alpha_f J_f) &= \frac{32\pi^5 \alpha^2}{\omega^2 [J_i]} \sum_{M_i} \sum_{\lambda_1 \lambda'_1 \lambda_2 \lambda'_2} \langle \mathbf{k} \lambda_1 | \rho_\gamma | \mathbf{k} \lambda'_1 \rangle \langle \mathbf{k} \lambda_2 | \rho_\gamma | \mathbf{k} \lambda'_2 \rangle \sum_{J_t M_t \kappa} \mathcal{M}_{\kappa \mathbb{J}_t M_t}^{\lambda_1 \lambda_2} \mathcal{M}_{\kappa \mathbb{J}_t M_t}^{\lambda'_1 \lambda'_2 *} \\ \mathcal{M}_{\kappa \mathbb{J} M}^{\lambda_1 \lambda_2} &= \sum_{\mathbb{M}_1 \mathbb{M}_2} \sum_{\mathbb{J}_\nu M_\nu} i^{L_1+L_2} \frac{[L_1, L_2]^{1/2}}{[J_\nu, J]^{1/2}} (i \lambda_1)^{p_1} (i \lambda_2)^{p_2} \langle J_i M_i, L_1 \lambda_1 | J_\nu M_\nu \rangle \langle J_\nu M_\nu, L_2 \lambda_2 | J M \rangle \\ &\times \frac{\langle (\alpha_f \mathbb{J}_f, \varepsilon \kappa) \mathbb{J} \parallel \mathbb{O}^{(\mathbb{M}_1, \text{photoionization})} \parallel \alpha_\nu J_\nu \rangle \langle \alpha_\nu \mathbb{J}_\nu \parallel \mathbb{O}^{(\mathbb{M}_2, \text{absorption})} \parallel \alpha_i \mathbb{J}_i \rangle}{E_{\alpha_i \mathbb{J}_i} + \omega - E_{\alpha_\nu \mathbb{J}_\nu}}. \end{aligned}$$

- Total two-photon ionization cross sections for initially unpolarized atoms and unpolarized light: For initially unpolarized atoms and unpolarized plane-wave photons with wave vector $\mathbf{k} \parallel \mathbf{e}_z$, the total two-photon ionization cross sections for the transition $|\alpha_i J_i\rangle \rightarrow |\alpha_f J_f\rangle$ is given by:

$$\sigma(\alpha_i J_i \rightarrow \alpha_f J_f) = \dots$$

8. Atomic processes

- **Nonresonant two-photon (one-electron) ionization:** The nonresonant two-photon ionization is one of the most simplest nonlinear processes in light-matter interactions. While earlier experiments with optical laser were restricted to the ionization of valence-shell electrons, x-ray FEL nowadays allow to study this process also for inner-shell ionization of atoms and molecules. The two-photon K -shell ionization of atoms can be recorded quite easily by the subsequent K -shell fluorescence, and as shown experimentally for neutral Ge and Zr.
- **Atomic ionization by elliptically-polarized pulses:** In contrast to the ionization by purely linearly- or circularly-polarized light, the use of elliptically-polarized pulses enables one to extract the phases and amplitudes of the outgoing partial waves and, hence, information of the scattering process. Recently, Hofbrucker *et al.* (2019) predicted that a maximum elliptical dichroism can be achieved in two-photon ionization for an appropriate choice of radiation wavelength.

Two-color ionization:

➤

Electron vortices from multi-photon ionization:

- **Electron vortices:** Free-electron wave packets with vortex structures have been generated in the photoionization of atoms by (two) time-delayed and counter-rotating circularly-polarized (femtosecond) laser pulses. These vortices typically arise from the interference of two (time-delayed) wave packets with different helicity λ . The creation of such vortices was theoretically predicted and demonstrated experimentally (Pengel *et al.*, 2017), including (so-called) *multi-arm* electron vortices as well as the manipulation of electron vortices by resonance-enhanced multi-photon ionization (REMPI) of atoms.
- **Multi-photon ionization with two-color fields:** Various $(\omega, 2\omega)$ fields have been employed experimentally in order to observe and control the photoelectron angular distributions at atomic time scales. Often, this control is based on the interference of m - and n -photon pathways. For these experiments, two-color fields with either low-order commensurable frequencies or with adjustable frequency ratios are utilized.

Two-color multi-photon ionization:

- **Circular dichroism in the biharmonic $(m\omega, n\omega)$ ionization of atoms:** Volotka *et al.* (2021) studied the circular dichroism in photoelectron angular distributions for the (quite general) $(m\omega, n\omega)$ ionization of atoms. They showed that the maximum circular dichroism can always be achieved all atoms and for any (fundamental) photon energy ω by just controlling the relative flux and phase difference of the two components of the radiation field. A simple analytical description of the circular dichroism has been given in this work along with some ‘experimental guidelines’ that enable full control over the circular dichroism.

- **Biharmonic ($\omega, 2\omega$) photoionization of atomic inner-shell electrons:** Hofbrucker *et al.* (2021) studied the $1s$ photoionization of neon by means of an elliptically polarized biharmonic ($\omega, 2\omega$) field, in which one- and two-photon ionization processes occur simultaneously. In addition to the dichroism due to the two-photon ionization alone, further contributions to the elliptical dichroism arise from the interference between the one- and two-photon ionization pathways.
- **Biharmonic ($\omega, 2\omega$) photoionization of atomic inner-shell electrons:** The biharmonic ($\omega, 2\omega$) photoionization opens up new perspectives for studying nonlinear light-atom interactions at intensities in the transition regime from weak to strong-field physics (Fritzsche and Hofbrucker, 2022). In particular, the control of the frequency and polarization of biharmonic beams enables one to carve the photoelectron angular distribution and to enhance the resolution of ionization measurements by the (simultaneous) absorption of photons. Apart from the quite obvious polarization dependence of the photoelectron angular distributions, these distributions are sensitive also to the (relative) intensity, the phase difference and the temporal structure of the incoming beam components, both at resonant and nonresonant frequencies.
- **Biharmonic (photo-) ionization:** In atomic physics, the term **biharmonic (photo-) ionization** is often used in order to refer to the (single-electron) photoionization of atoms by biharmonic ($m\omega, n\omega$) fields. In practice, however, one often considers the biharmonic ($\omega, 2\omega$) ionization that makes use of the fundamental frequency ω and its second harmonic. For an atom in its initial state $|\alpha_i \mathbb{J}_i M_i\rangle$, the (simultaneous) absorption of either *two* photons of frequency ω or *one* photon with frequency 2ω then leads to photoions in the final states $|\alpha_f \mathbb{J}_f M_f\rangle$ and free electrons $|\mathbf{p}_e m_e\rangle$,

$$|\alpha_i \mathbb{J}_i M_i\rangle + \left\{ \begin{array}{l} 2 \cdot (\hbar\omega) \\ 1 \cdot (2\hbar\omega) \end{array} \right\} \longrightarrow |\alpha_f \mathbb{J}_f M_f\rangle + |\mathbf{p} m\rangle .$$

8.2.b. Coulomb excitation (CoulombExcitation)

Process, notation & application:

- Coulomb excitation of an atom or ion by fast, heavy ions: $A + Z_p \rightarrow A^* + Z_p$ (i.e. the projectile remains unaffected)
- Quantum notations used in the formulas below: $|\alpha_i \mathbb{J}_i\rangle + Z_p(\beta_p) \rightarrow |\alpha_f \mathbb{J}_f\rangle, \quad \beta_p = \frac{v_p}{c}$
- Using JAC: Perform an `Atomic.Computation(..., processSettings=CoulombExcitation.Settings(..), ..)` or call directly functions from the module `CoulombExcitation`.

8. Atomic processes

- In JAC, the partial and total Coulomb excitation cross sections are calculated and tabulated by default for all selected pairs of initial and final levels.
- Basic assumptions: In Coulomb excitation processes, one often assumes that just a single electron from a (fast-moving) projectile ion with relative velocity $\beta_p = v_p/c$ with regard to the target is excited by a target nucleus at rest. — The Coulomb excitation or ionization of the projectile (ion) will be affected, in addition, also by the target electrons (or, *vice versa*, the projectile electrons) but such rather small effects are often not considered in detail.
- Projectile *versus* target excitation: Of course, an analogue process occurs also when we consider the excitation of the target that may occur due to a fast-moving (bare) projectile ion, and in which case the role of the projectile and target need simply to be interchanged in all formulas below.
- Semi-classical approximation: In this approximation, the projectile moves with impact parameter b and with fixed velocity $\beta_p = v_p/c$, relative to the speed of light c , along a straight-line trajectory.
- Symmetry-eikonal approximation (SAE): This approximation goes beyond the semi-classical one and makes use of the initial and final (stationary) states in the form:

$$\psi_i(\mathbf{r}, t) = \psi_i(\mathbf{r}) \exp\left(-i \frac{E_i}{\hbar} t\right) \quad \Rightarrow \quad \psi_i(\mathbf{r}, t) = \psi_i(\mathbf{r}) (v_p r' + \mathbf{v}_p \cdot \mathbf{r}') \exp\left(-i \frac{E_i}{\hbar} t\right)$$

$$\psi_f(\mathbf{r}, t) = \psi_f(\mathbf{r}) \exp\left(-i \frac{E_f}{\hbar} t\right) \quad \Rightarrow \quad \psi_f(\mathbf{r}, t) = \psi_f(\mathbf{r}) (v_p r' - \mathbf{v}_p \cdot \mathbf{r}') \exp\left(-i \frac{E_f}{\hbar} t\right).$$

- Alignment of the excited ions: The Coulomb excitation of few-electron ions in fast ion-atom collisions leads to the formation of excited ionic states. In typical ion-atom collision experiments, a *preferred* direction is hereby defined for the overall systems, both at storage rings and the EBIT, and this typically results in an *alignment* of the excited ions along this distinct direction.
- Impact-parameter dependent probability $P(b)$: The first step in calculating energy- and angle-differential as well as total Coulomb excitation cross sections usually refers to determining the impact-parameter dependence of the excitation probability $P(b)$. The weighted K -shell Coulomb excitation probability $2\pi b P(b)$ is known to have a maximum in the vicinity of the K -shell radius. This is quite similar as for the Coulomb ionization probabilities.

SCA Coulomb excitation amplitude of few-electron projectile ions in position space:

- **Semi-classical approximation (SCA):** In this list, all formula refer to the projectile excitation and the semi-classical approximation for the treatment of the ionic trajectories.
- **Coulomb (excitation) amplitude for the excitation of a (single) projectile electron:** If a one-electron projectile moves at a trajectory with impact parameter b , the amplitude for an excitation from level $i \rightarrow f$ is given by Eichler & Meyerhof (1995, Eq. 6.2)

$$\begin{aligned} \mathcal{M}^{(\text{Coulex: SCA})}(b; i \rightarrow f) &= i \frac{\gamma Z_t e^2}{\hbar} \int dt \exp\left(\frac{i}{\hbar} (E_f - E_i)t\right) \int d^3r \psi_f^\dagger(\mathbf{r}) \frac{(1 - \beta_p \alpha_z)}{r'(t)} \psi_i(\mathbf{r}), \\ r'(t) &= \sqrt{(x - b)^2 + y^2 + \gamma^2(z - v t)^2}, & \beta_p &= \frac{v_p}{c}, \end{aligned}$$

where \mathbf{r} is the coordinate of the projectile electron, $r'(t)$ its (time-dependent) distance from the target nucleus, and where $\psi_f(\mathbf{r})$ and $\psi_i(\mathbf{r})$ denote the final- and initial-state eigenfunctions of the projectile electron with energies E_f and E_i .

- **Coulomb (excitation) amplitude for the excitation of a many-electron projectile (ion):** For the Coulomb excitation of a many-electron projectile from sublevel $|\alpha_i \mathbb{J}_i M_i\rangle \rightarrow |\alpha_f \mathbb{J}_f M_f\rangle$, the excitation amplitude for given impact parameter b can then be written in first-order perturbation theory and natural units ($\hbar = m_e = c = 1$) as:

$$\begin{aligned} \mathcal{M}^{(\text{Coulex: SCA})}(b; i \rightarrow f) &= i \gamma \alpha Z_t \int dt e^{i(E_f - E_i)t} \left\langle \alpha_f \mathbb{J}_f M_f \left| \sum_{k=1}^N \frac{1 - \beta_p \alpha_{k,z}}{r'_k(t)} \right| \alpha_i \mathbb{J}_i M_i \right\rangle \\ &= 2 v_p \left\langle \alpha_f \mathbb{J}_f M_f \left| \sum_{k=1}^N (1 - \beta_p \alpha_{k,z}) e^{i q_0 z_k} K_0 \left(\frac{q_0}{\gamma} \sqrt{(x_k - b)^2 + y_k^2} \right) \right| \alpha_i \mathbb{J}_i M_i \right\rangle \end{aligned}$$

- **Coulomb (excitation) cross section:** From this transition amplitude, the cross section for an excitation of the projectile from (sub-) level $|\alpha_i \mathbb{J}_i\rangle \rightarrow |\alpha_f \mathbb{J}_f M_f\rangle$ can be obtained by integrating over all the impact parameters b and by taking the average over the initial magnetic sublevels M_i .
- In JAC, we do not use the Coulomb excitation amplitude in position space but make use of a representation of this amplitude in momentum space instead, see below.

SCA Coulomb excitation amplitude of few-electron projectile ions in momentum space:

- **Semi-classical approximation (SCA):** In this list, all formula refer to the projectile excitation and the semi-classical approximation for the treatment of the ionic trajectories.
- **Coulomb (excitation) amplitude for the excitation of a (single) projectile electron:** To evaluate the Coulomb excitation cross sections for one- and many-electron atoms, it is often more convenient to work in momentum space and to express all properties in terms of the Fourier transform of the Coulomb excitation amplitude in position space. If we make use of the momentum transfer $\mathbf{q} = (\mathbf{q}_b, q_z)$, the time-integration in this Coulomb (excitation) amplitude can be carried out explicitly (Eichler & Meyerhof 1995, Eq. 6.4)

$$\begin{aligned}\mathcal{M}^{(\text{Coulex: SCA})}(b; i \rightarrow f) &= \frac{i \nu_p}{\pi} \int \frac{d^2 q_b}{q_b^2 + (1 - \beta^2) q_0^2} e^{-i \mathbf{q}_0 \cdot \mathbf{b}} \mathcal{K}^{(\text{Coulex: SCA})}(\mathbf{q}; i \rightarrow f) \\ \mathcal{K}^{(\text{Coulex: SCA})}(\mathbf{q}; i \rightarrow f) &= \langle \psi_f(\mathbf{r}) | (1 - \beta \alpha_z) e^{i \mathbf{q} \cdot \mathbf{r}} | \psi_i(\mathbf{r}) \rangle.\end{aligned}$$

This formula removes the complicated time dependence in $r'(t)$ and replaces it instead by an explicit wave number (momentum transfer) dependence. — In momentum space, indeed, most Coulomb excitation cross sections can be expressed directly in terms of the momentum-space Coulomb excitation amplitude $\mathcal{K}^{(\text{Coulex: SCA})}(\mathbf{q}; i \rightarrow f)$.

- **Coulomb (excitation) amplitude for the excitation of a (single) projectile electron:** Note, that in momentum space, the (momentum-space) Coulomb excitation amplitude $\mathcal{K}^{(\text{Coulex: SCA})}(\mathbf{q}; i \rightarrow f)$ does no longer depend on the impact parameter b but now simply contains an integration over the momentum transfer \mathbf{q} , and which starts from the minimum momentum transfer for the excitation of the initial ion from level $i \rightarrow f$: $q_0 = (E_f - E_i) / v_p$.
- **(Momentum-space) Coulomb excitation amplitude for many-electron projectiles:** This amplitude can be further simplified by using the Wigner-Eckert theorem (Surzhykov and Fritzsche, 2008)

$$\begin{aligned}
\mathcal{K}^{(\text{Coulex})}(\mathbf{q}; i \rightarrow f) &= \left\langle \alpha_f \mathbb{J}_f M_f \left| \sum_k^N [1 - \beta \alpha_z(k)] e^{i \mathbf{q} \cdot \mathbf{r}_k} \right| \alpha_i \mathbb{J}_i M_i \right\rangle \\
&= \sum_{LM} i^L Y_{LM}^*(\arccos(q_0/q), 0) \left\langle \alpha_f \mathbb{J}_f M_f \left| \sum_{k=1}^N [1 - \beta_p \hat{\alpha}_z(k)] j_L(q r_k) Y_{LM}(\vartheta_k, \varphi_k) \right| \alpha_i \mathbb{J}_i M_i \right\rangle, \\
&= \sum_t \frac{1}{\sqrt{2J_f + 1}} \langle J_i M_i, t(M_f - M_i) | J_f M_f \rangle \sum_L i^L Y_{L, M_f - M_i}^*(\arccos(q_0/q), 0) \left\langle \alpha_f \mathbb{J}_f \left\| H_{tL}^{(\text{Coulex})}(q) \right\| \alpha_i \mathbb{J}_i \right\rangle \\
&= \sum_t \frac{1}{\sqrt{2J_f + 1}} \langle J_i M_i, t(M_f - M_i) | J_f M_f \rangle \sum_L i^L Y_{L, M_f - M_i}^*(\arccos(q_0/q), 0) \\
&\quad \times (\delta_{tL} \langle \alpha_f \mathbb{J}_f \left\| \mathbb{K}^{(L, \text{Coulex}, jY)} \right\| \alpha_i \mathbb{J}_i \rangle - \beta_p \langle LM, 10 | tM \rangle \langle \alpha_f \mathbb{J}_f \left\| \mathbb{K}^{(t, \text{Coulex}, jT)} \right\| \alpha_i \mathbb{J}_i \rangle)
\end{aligned}$$

- In JAC, these (momentum-space) Coulomb excitation amplitudes $\mathcal{K}^{(\text{Coulex})}(\mathbf{q}; i \rightarrow f)$ are implemented explicitly and the integration over q is typically performed by a Gauß-Legendre integration.

SEA Coulomb excitation amplitude of few-electron projectile ions in momentum space:

- **Symmetric-eikonal approximation (SEA):** In this list, all formula refer to the projectile excitation and the symmetric-eikonal approximation for the treatment of the ionic trajectories.
- **Symmetric-eikonal approximation (SAE):** This approximation goes beyond the semi-classical one and makes use of the initial and final (stationary) states in the form:

$$\begin{aligned}
\psi_i(\mathbf{r}, t) &= \psi_i(\mathbf{r}) \exp\left(-i \frac{E_i}{\hbar} t\right) & \Rightarrow & & \psi_i(\mathbf{r}, t) &= \psi_i(\mathbf{r}) (v_p r' + \mathbf{v}_p \cdot \mathbf{r}') \exp\left(-i \frac{E_i}{\hbar} t\right) \\
\psi_f(\mathbf{r}, t) &= \psi_f(\mathbf{r}) \exp\left(-i \frac{E_f}{\hbar} t\right) & \Rightarrow & & \psi_f(\mathbf{r}, t) &= \psi_f(\mathbf{r}) (v_p r' - \mathbf{v}_p \cdot \mathbf{r}') \exp\left(-i \frac{E_f}{\hbar} t\right).
\end{aligned}$$

8. Atomic processes

➤ **Solutions of the Hamiltonian in the symmetric-eikonal approximation (SEA):** With $\mathbf{s}_\perp \equiv \mathbf{r}'_\perp = (x - b, y)$ and $s_z \equiv r'_z = \gamma(z - v_p t)$, the eigenfunctions $\psi(\mathbf{r}, t)$ fullfill the equation

$$\left(\mathbb{H} - i \frac{\partial}{\partial t} \right) \psi_i(\mathbf{r}, t) = - \frac{Z_t e^2}{\beta_p} (v_p r' + \mathbf{v}_p \cdot \mathbf{r}')^{-i v_p} \left(\frac{\mathbf{s}_\perp \cdot \boldsymbol{\alpha}_\perp}{s_\perp + s_z} + \frac{\alpha_z}{\gamma} \right) \psi_i(\mathbf{r}) \exp \left(-i \frac{E_i}{\hbar} t \right).$$

➤ **SEA interaction potential:** In the SEA, the interaction potential $\mathbf{V}(\mathbf{s}_\perp) = (\mathbf{V}_\perp, V_z)$ is given with $\omega_{fi} = E_f - E_i$ by

$$\mathbf{V}_\perp(\mathbf{s}_\perp) = - \frac{i}{\gamma} K_1 \left(\frac{\omega_{fi}}{\gamma v} s_\perp \right) \hat{\mathbf{s}}_\perp, \quad V_z(s_\perp) = \frac{1}{\gamma^2} K_0 \left(\frac{\omega_{fi}}{\gamma v} s_\perp \right).$$

➤ **Coulomb (excitation) amplitude for the excitation of a (single) projectile electron:**

$$\begin{aligned} \mathcal{M}^{(\text{Coulex: SEA})}(b; i \rightarrow f) &= -i \int dt \int d^3r \psi_f^+(\mathbf{r}, t) \left(\mathbb{h} - i \frac{\partial}{\partial t} \right) \psi_i(\mathbf{r}, t) \\ &= \frac{2i v_p}{\beta_p} \left\langle \psi_f \left| \exp \left(iz \frac{\omega_{fi}}{v_p} \right) s_\perp^{-2i v_p} \boldsymbol{\alpha} \cdot \mathbf{V}(\mathbf{s}_\perp) \right| \psi_i \right\rangle. \end{aligned}$$

➤ **Coulomb (excitation) amplitude for the excitation of many-electron projectiles:**

$$\mathcal{M}^{(\text{Coulex: SEA})}(b; i \rightarrow f) = \frac{2i v_p}{\beta_p} \left\langle \alpha_f \mathbb{J}_f M_f \left| \sum_k^N \exp(i q_0 z_k) s_{k,\perp}^{-2i v_p} \boldsymbol{\alpha}_k \cdot \mathbf{V}(\mathbf{s}_{k,\perp}) \right| \alpha_i \mathbb{J}_i M_i \right\rangle, \quad s_k = (b - x_k, y_k, \gamma(vt - z_k)),$$

and where $s_k, \boldsymbol{\alpha}_k$ refer to the k -th electron in the rest frame of the target. Obviously, the calculation of these excitation amplitudes requires the control of the corresponding single-electron amplitudes, which itself is a rather hard task.

S-matrix for the Coulomb excitation of projectile ions in momentum space:

➤ **S-matrix description:** In the S-matrix (or momentum-space) description of heavy-ion collisions, the transition amplitude can be obtained by performing the (2-dimensional) Fourier transform of the $\mathcal{M}^{(\text{Coulex: SCA})}(b; i \rightarrow f)$, which is much easier to evaluate. Moreover, the S-matrix contains more information on the collision, particularly if the scattered projectile is not contained in the transition amplitude in b-space.

- **SCA Coulomb (excitation) amplitude for the excitation of single-electron projectiles:** If we introduce $\omega_{fi} = E_f - E_i$ and the momentum transfers $\mathbf{q} = (\mathbf{q}_b, \omega_{fi}/v)$ and $\mathbf{q}' = (\mathbf{q}_b, \omega_{fi}/\gamma v) = (\mathbf{q}_b, q_o/\gamma)$, the SCA Coulomb (excitation) amplitude can be expressed as

$$\begin{aligned}\mathcal{S}^{(\text{Coulex: SCA})}(\mathbf{q}_b; i \rightarrow f) &= i \gamma \frac{Z_t e^2}{v 2\pi} \int d^3r \psi_f^+(\mathbf{r}) (1 - \beta_p \alpha_z) e^{i\mathbf{q} \cdot \mathbf{r}} \psi_i(\mathbf{r}) \frac{1}{\gamma} \int d(vt - z) \gamma \int d(\mathbf{b} - \mathbf{r}_\perp) \exp(i\mathbf{q}' \cdot \mathbf{r}') \frac{1}{r'} \\ &= i \frac{Z_t e^2}{v 2\pi} \int d^3r \psi_f^+(\mathbf{r}) (1 - \beta_p \alpha_z) \exp(i\mathbf{q} \cdot \mathbf{r}) \psi_f i(\mathbf{r}) \int d^3r' \frac{\exp(i\mathbf{q}' \cdot \mathbf{r}')}{r'} \\ &= 2i v_p \int d^2r \psi_f^+(\mathbf{r}) (1 - \beta_p \alpha_z) \frac{\exp(i\mathbf{q} \cdot \mathbf{r})}{q_b^2 + q_o^2/\gamma^2} \psi_f i(\mathbf{r}) \\ &= \frac{2i v_p}{q_b^2 + q_o^2/\gamma^2} \langle \psi_f | (1 - \beta_p \alpha_z) \exp(i\mathbf{q} \cdot \mathbf{r}) | \psi_i \rangle.\end{aligned}$$

Here, the momentum vectors \mathbf{q} and \mathbf{q}' refer to the same momentum transfer but expressed in the target and projectile frame in the present case for the excitation of the projectile ion.

- **SCA Coulomb (excitation) amplitude for the excitation of many-electron projectiles:** With the same momentum vectors from above, the SCA Coulomb (excitation) amplitude can be expressed as

$$\mathcal{S}^{(\text{Coulex: SCA})}(\mathbf{q}_b; i \rightarrow f) = \frac{2i v_p}{q_b^2 + q_o^2/\gamma^2} \left\langle \alpha_f \mathbb{J}_f M_f \left| \sum_k^N (1 - \beta_p \alpha_{k,z}) \exp(i\mathbf{q} \cdot \mathbf{r}_k) \right| \alpha_i \mathbb{J}_i M_i \right\rangle$$

- ... (4-vector) L^μ :

$$\begin{aligned}L^0(\mathbf{q}) &= \frac{2i v_p}{q'^2}, & \mathbf{L}(\mathbf{q}) &= \frac{2i v_p}{q'^2} (0, 0, \beta_p) && \text{semiclassical (first - Born) approximation} \\ L^0(\mathbf{q}) &= 0, & \mathbf{L}(\mathbf{q}) &= -\frac{2i v_p}{q'^2} \left(\frac{q'}{2}\right)^{2i v_p} \boldsymbol{\Omega} && \text{symmetric eikonal approximation}\end{aligned}$$

and where $\boldsymbol{\Omega}$ refers to the vector.

8. Atomic processes

➤ ... vector $\Omega = (\Omega_{\perp}, \Omega_z)$: With the same definition of the momentum transfer $\mathbf{q} = (\mathbf{q}_b, \omega_{fi}/v)$ in the frame and $q' = \sqrt(q_b^2 + q_0^2/\gamma^2)$ from above, one can define the vector $\Omega = (\Omega_{\perp}, \Omega_z)$ as

$$\Omega_{\perp} = \mathbf{q}_b \frac{1 - i v_p}{\beta_p q_o} \Gamma^2 (1 - i v_p) {}_2F_1 \left(1 - i v_p, i v_p; 2; \frac{q_b^2}{q'^2} \right)$$

$$\Omega_z = \frac{1}{\gamma^2 \beta_p} \Gamma^2 (1 - i v_p) {}_2F_1 \left(1 - i v_p, i v_p; 1; \frac{q_b^2}{q'^2} \right)$$

➤ SEA Coulomb (excitation) amplitude for the excitation of single-electron projectiles: This amplitude can be expressed in terms of the (4-vector) as

$$\begin{aligned} \mathcal{S}^{(\text{Coulex: SEA})} (\mathbf{q}_b; i \rightarrow f) &= \frac{2i v_p}{q'^2} \left(\frac{q'}{2} \right)^{2i v_p} \boldsymbol{\Omega} \cdot \langle \psi_f | \exp(i \mathbf{q} \cdot \mathbf{r}) \boldsymbol{\alpha} | \psi_i \rangle \\ &= L^\mu(\mathbf{q}) J_\mu(\mathbf{q}) = L^0(\mathbf{q}) J_0(\mathbf{q}) - \mathbf{L}(\mathbf{q}) \cdot \mathbf{J}(\mathbf{q}). \end{aligned}$$

➤ SEA Coulomb (excitation) amplitude for the excitation of many-electron projectiles: The formula for hydrogenic projectiles can be readily expanded for many-electron projectile and reads as

$$\mathcal{S}^{(\text{Coulex: SEA})} (\mathbf{q}_b; i \rightarrow f) = \frac{2i v_p}{q'^2} \left(\frac{q'}{2} \right)^{2i v_p} \boldsymbol{\Omega} \cdot \left\langle \alpha_f \mathbb{J}_f M_f \left| \sum_k^N \exp(i \mathbf{q} \cdot \mathbf{r}_k) \boldsymbol{\alpha}_k \right| \alpha_i \mathbb{J}_i M_i \right\rangle$$

➤ Covariant atomic form factor: The covariant (4-vector) atomic form factor $J^{(\text{covariant: } \mu)}(q; i \rightarrow f)$, $\mu = 0..3$ is defined as (3-dimensional) Fourier transform of the (4-vector) transition current (Najjari, 2022)

$$J^{(\text{covariant: } \mu)}(q; i \rightarrow f) = \int d^3 r e^{i \mathbf{q} \cdot \mathbf{r}} \psi_f^+(\mathbf{r}) \gamma_0 \gamma^\mu \psi_i(\mathbf{r})$$

$$J^0(\mathbf{q}; i \rightarrow f) = J_0(\mathbf{q}; i \rightarrow f) = \langle \psi_f | \exp(i \mathbf{q} \cdot \mathbf{r}) | \psi_i \rangle,$$

$$\mathbf{J}(\mathbf{q}; i \rightarrow f) = \langle \psi_f | \exp(i \mathbf{q} \cdot \mathbf{r}) \boldsymbol{\alpha} | \psi_i \rangle$$

Coulomb excitation operators and interaction strength:

- This interaction strength still need to be worked out consistently.
- Coulomb excitation (interaction) strength: The (full) Coulomb excitation amplitude in momentum space above combines two kinds of reduced (many-electron) matrix elements due to the two interaction operators: $\sum_{k=1}^N j_L(q r_k) Y_L(\vartheta_k, \varphi_k)$ of rank L as well as $\sum_{k=1}^N j_L(q r_k) \hat{\alpha}(k) \cdot \mathbf{T}_{tL}(\vartheta_k, \varphi_k)$ of rank t , respectively. These two reduced matrix elements are the actual building blocks that are needed in order to represent and to explore the properties of the target or projectile excitation process.
- Coulomb excitation (interaction) strength: The building blocks for the computation of the Coulomb excitation and ionization amplitudes are given by the reduced matrix elements

$$\langle \alpha_f \mathbb{J}_f \parallel \mathbb{K}^{(L, \text{Coulex}, jY)} \parallel \alpha_i \mathbb{J}_i \rangle = \left\langle \alpha_f \mathbb{J}_f \left| \sum_{k=1}^N j_L(q r_k) Y_L(\vartheta_k, \varphi_k) \right| \alpha_i \mathbb{J}_i \right\rangle$$

$$\langle \alpha_f \mathbb{J}_f \parallel \mathbb{K}^{(t, \text{Coulex}, jT)} \parallel \alpha_i \mathbb{J}_i \rangle = \left\langle \alpha_f \mathbb{J}_f \left| \sum_{k=1}^N j_L(q r_k) \hat{\alpha}(k) \cdot \mathbf{T}_{tL}(\vartheta_k, \varphi_k) \right| \alpha_i \mathbb{J}_i \right\rangle$$

Energie-differential, partial and total Coulomb excitation cross sections:

- Partial Coulomb excitation cross section: If the Fourier transformation is performed in order to go from the position to momentum coordinates, the integrals over the time t and the impact parameter b can be evaluated *analytically*. Then, the partial (excitation) cross section for the Coulomb excitation from (sub-) levels $|\alpha_i \mathbb{J}_i\rangle \rightarrow |\alpha_f \mathbb{J}_f M_f\rangle$ can be written as (Surzhykov and Fritzsche, 2008)

$$\begin{aligned} \sigma^{(\text{Coulex})} (\alpha_i \mathbb{J}_i \rightarrow \alpha_f \mathbb{J}_f M_f) &= \frac{2\pi}{2J_i + 1} \sum_{M_i} \int_0^\infty db b \left| \mathcal{M}^{(\text{Coulex})} (b; i \rightarrow f) \right|^2 \\ &= 2\pi \left(\frac{8\pi Z_t \alpha}{\beta_p} \right)^2 \frac{1}{2J_i + 1} \sum_{M_i} \int_{q_0}^\infty dq \frac{q}{(q^2 - q_0^2 \beta_p^2)^2} \left| \mathcal{K}_{fi}^{(\text{Coulex})} (\mathbf{q}; i \rightarrow f) \right|^2. \end{aligned}$$

Alignment of Coulomb-excited ions:

- Alignment of Coulomb-excited ions in level $(\alpha_f \mathbb{J}_f)$: For a well-defined ion-atom collision axis, a Coulomb-excited ion in level $(\alpha_f \mathbb{J}_f)$ is generally aligned. Of course, this alignment depends on the partial Coulomb cross sections $\sigma(\alpha_f \mathbb{J}_f M_f)$ and can be described in terms of one (or several) parameters $\mathcal{A}_k(\alpha_f \mathbb{J}_f)$:

$$\mathcal{A}_k(\alpha_i \mathbb{J}_i \rightarrow \alpha_f \mathbb{J}_f) = \frac{\sqrt{2J_f + 1}}{\sigma(\alpha_i \mathbb{J}_i \rightarrow \alpha_f \mathbb{J}_f)} \sum_{M_f} (-1)^{J_f - M_f} \langle J_f M_f; J_f, -M_f | k 0 \rangle \sigma(\alpha_i \mathbb{J}_i \rightarrow \alpha_f \mathbb{J}_f M_f),$$

8.2.c. Photoionization & fluorescence (PhotoIonizationFluor)

Process, notation & application:

- Photoionization of an atom or ion with subsequent fluorescence emission: $A + \hbar\omega \rightarrow A^* + e_p^- \rightarrow A^{(*)} + e_p^- + \hbar\omega'$
- Quantum notations used in the formulas below: $|\alpha_i \mathbb{J}_i\rangle + \hbar\omega \rightarrow |\alpha_e \mathbb{J}_e\rangle + |\varepsilon\kappa\rangle \rightarrow |\alpha_f \mathbb{J}_f\rangle + |\varepsilon\kappa\rangle + \hbar\omega_f(\mathbb{M})$
- Apart from astrophysical interest, emphasis on the photoionization of inner-shell electrons from multiple and highly charged ions and its subsequent photon emission arises also from the diagnostics of various *laboratory* plasmas.

Density operator of the fluorescence photon $\hbar\omega_f(\mathbb{M})$:

- After the inner-shell photoionization, the photoion appears to be in an excited level $(\alpha_e \mathbb{J}_e)$ that decays subsequently to some energetically lower level $(\alpha_f \mathbb{J}_f)$ by the emission of a characteristic photon.
- **Characteristic photon density matrix in the helicity representation:** For this characteristic photon, the density matrix can be expressed in the form $\langle \mathbf{k}_0 \lambda | \rho_\gamma | \mathbf{k}_0 \lambda' \rangle$, in which $\mathbf{k}_0 \equiv (\vartheta_0, \varphi_0)$ denotes the wave vector along the propagation direction of the fluorescence photon and $\lambda = \pm 1$ its helicity. Note that the helicity representation of this density matrix also describes the photon polarization.

Stokes parameter of the fluorescence photon $\hbar\omega_f(\mathbb{M})$:

- The density matrix of the fluorescence photon $\hbar\omega_f(\mathbb{M})$ is usually parametrized in terms of the so-called Stokes parameters (Blum 1981; Balashov *et al.*, 2001)

$$\langle \mathbf{k}_0 \lambda | \rho_{\omega_f} | \mathbf{k}_0 \lambda' \rangle \equiv c_{\lambda, \lambda'} = \frac{1}{2} \begin{pmatrix} 1 + P_3 & -P_1 + iP_2 \\ -P_1 - iP_2 & 1 - P_3 \end{pmatrix},$$

and which are utilized to characterize both the degree of linear (P_1 and P_2) and circular (P_3) polarization of the light.

- Apart from the population of the excited sublevels $|\alpha_e \mathbb{J}_e M_e\rangle$ and the angle ϑ of the emitted photon, the degree of linear polarization of the characteristic x-ray radiation also depends on the total angular momenta of the excited level ($\alpha_e \mathbb{J}_e$) and the final level ($\alpha_f \mathbb{J}_f$) of the characteristic transition as well as on its *multipolarity*.

8.2.d. Photoionization & autoionization (PhotoIonizationAutoIon)

Process, notation & application:

- Photo ionization of an atom or ion with subsequent autoionization: $A + \hbar\omega \rightarrow A^{+,*} + e_p^- \rightarrow A^{(*)} + e_p^- + e_a^-$
- Quantum notations used in the formulas below: $|\alpha_i \mathbb{J}_i\rangle + \hbar\omega(\mathbb{M}) \rightarrow |\alpha_r \mathbb{J}_r\rangle + |\varepsilon_p \kappa_p\rangle \rightarrow |\alpha_f \mathbb{J}_f\rangle + |\varepsilon_p \kappa_p\rangle + |\varepsilon_a \kappa_a\rangle$

Photo-Auger electron coincidence spectrometry:

- Photo-Auger electron coincidence spectrometry has been found a versatile tool for studying the structure and dynamics of atoms, molecules and solids. In atomic physics, for example, it has been utilized to realize a so-called complete experiment in the photoionization of atoms as well as for exploring small effects of coherence and post-collision interactions in photo-induced Auger processes.
- For a full analysis of the photoionization and subsequent autoionization process, both electrons should be detected in coincidence by measuring the energy and angular distributions, i.e. the photo-Auger electron correlation function.
- The photoionization and subsequent autoionization process differs from the direct double photoionization due to the formation of a (well-defined) intermediate ionic state and, thus, the emission of the two electrons can usually be considered within a two-step model.

8. Atomic processes

- Investigations of the magnetic circular dichroism in the photoemission from solids have been found useful for studying the magnetic properties of solids.

Photo-Auger electron correlation function:

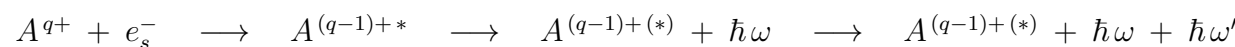
- Sequential ionization of polarized targets: There are three relevant directions that need to be distinguished in the sequential ionization of polarized targets: the direction of the photoelectron $\mathbf{n}_p = (\vartheta_p, \varphi_p)$, those of the Auger electron $\mathbf{n}_a = (\vartheta_a, \varphi_a)$ and the direction of the target polarization $\mathbf{n}_t = (\vartheta_t, \varphi_t)$. Because of these three relevant but independent directions, the (triple-differential) cross sections can be expanded in terms of tripolar spherical harmonics

$$\{\mathbb{Y}_{k_0}(\mathbf{n}_t) \otimes \{\mathbb{Y}_{k_1}(\mathbf{n}_p) \otimes \mathbb{Y}_{k_2}(\mathbf{n}_a)\}_k\}_{k'q'} = \langle \dots | \dots \rangle \langle \dots | \dots \rangle Y_{k_0 q_0}(\vartheta_t, \varphi_t) Y_{k_1 q_1}(\vartheta_p, \varphi_p) Y_{k_2 q_2}(\vartheta_a, \varphi_a)$$

8.2.e. Dielectronic recombination & fluorescence (DielectronicFluores)

Process, notation & application:

- Dielectronic recombination of an atom or ion with subsequent fluorescence:



- Quantum notations used in the formulas below: $|\alpha_i J_i\rangle + |\varepsilon_s \kappa_s\rangle \longrightarrow |\alpha_r J_r\rangle \longrightarrow |\alpha_d J_d\rangle + \hbar\omega_d(M_d) \longrightarrow |\alpha_f J_f\rangle + \hbar\omega_d(M) + \hbar\omega_f(M_f)$

8.2.f. Electron-impact excitation & autoionization (ImpactExcitationAutoIon)

Process, notation & application:

- Electron-impact excitation with subsequent autoionization of an atom or ion: $A + e_s^- \longrightarrow A^* + e_s^{-'} \longrightarrow A^{+(*)} + e_s^{-'} + e_a^-$

- Quantum notations used in the formulas below: $|\alpha_i \mathbb{J}_i\rangle + |\varepsilon_i \kappa_i\rangle \rightarrow |\alpha_r \mathbb{J}_r\rangle + |\varepsilon_r \kappa_r\rangle \rightarrow |\alpha_f \mathbb{J}_f\rangle + |\varepsilon_r \kappa_r\rangle + |\varepsilon_a \kappa_a\rangle$
- Electron-impact excitation with subsequent autoionization occurs frequently in plasma and has been utilized to study the autoionization of atoms and ions.

8.2.g. Multi-photon double ionization (MultiPhotonDoubleIon)

Process, notation & application:

- Multi-photon double ionization: of an atom or ion: $A + n \hbar\omega \rightarrow A^{(*)} + e_{p_1}^- + e_{p_1}^-$
- Quantum notations used in the formulas below: $|\alpha_i \mathbb{J}_i\rangle + \hbar\omega_1(\mathbb{M}_1) + \hbar\omega_2(\mathbb{M}_2) + \dots + \hbar\omega_n(\mathbb{M}_n) \rightarrow |\alpha_f \mathbb{J}_f\rangle + |\varepsilon_1 \kappa_1\rangle + |\varepsilon_2 \kappa_2\rangle$
- The energy of several photons together can also lead to the emission of two electrons: This emission can occur either sequential, direct (non-sequential) or via some given resonances of the atom.
- In this section, we only consider the direct (non-sequential) multi-photon double ionization in which the energy of all photons is continuously shared by the two emitted electrons: $n \hbar\omega = E_f - E_i + \varepsilon_1 + \varepsilon_2$.

8.2.h. Multiple photoionization or photodetachment

Process, notation & application:

- Multiple photoionization or photodetachment: of an atom or ion: $A + \hbar\omega \rightarrow A^{q+} + e_1^- + e_2^- + \dots$

8.2.i. Internal conversion (InternalConversion)

Process, notation & application:

- Internal conversion of an atom or ion: $A^{q+} + \text{nucleus}^* \rightarrow A^{(q+1)+*} + e_c^-$

8. Atomic processes

- Quantum notations used in the formulas below: $|\alpha_i J_i\rangle + \text{nucleus}^*(\{\mathbb{M}\}, \mathcal{E}) \rightarrow |\alpha_f J_f\rangle + e_c^-(\mathbf{p}, m_s)$ or
 $|\alpha_i J_i\rangle + \text{nucleus}^*(\{\mathbb{M}\}, \mathcal{E}) \rightarrow |\alpha_f J_f\rangle + |\varepsilon \kappa\rangle, \quad \varepsilon = \mathcal{E} - (E_i - E_f)$
- Here, the excited nucleus decays under the release of the energy \mathcal{E} by (several) multipoles $\{\mathbb{M}\}$ and , leading to an emitted electron with well-defined kinetic energy ε .
- Internal conversion: formally refers to the decay an excited nucleus to its ground or some lower-lying level, and where the excitation energy is given to a (bound) electron, leading to an ionization of the atom or ion. In general, the internal (energy) conversion competes with the gamma-ray emission as well as the formation of a electron-positron pair for nuclear excitation energies above 1.022 MeV.
- Often, the continuum wave of the outgoing electron has been calculated in the (final-state) atomic potential with a vacancy in the inner shell. Sometimes, however, this hole has been disregarded, leading to differences in the internal conversion coefficients as large as $\sim 15\%$ for low kinetic energies $\varepsilon \sim 1$ keV and $L = 5$ transitions.

Nuclear decay by internal conversion:

- The internal conversion is more than a simple photoionization process, in which an emitted γ photon leads to the emission of electrons, but refers to an alternative de-excitation of excited nuclei.
- Electron conversion coefficient: In the internal conversion process, an atomic electron is ejected from one of the atomic shells. The electron conversion coefficient is defined as the probability ratio for emitting an atomic electrons from shell x to the emission of a γ -ray, $a_x = P_x / P_\gamma$.
- The kinetic energy of the emitted electron $\varepsilon = \Delta E_{\text{nuc}} - E_b$ can be deduced from the nuclear transition energy, the binding energy of the atomic electron and the recoil energy of the emitting atom, which is typically very small. Transitions involving conversion electrons are only possible if $\varepsilon > 0$.
- The internal conversion process (ICP) has been found a versatile tool for studying nuclear structure. In particular, the measurement and analysis of conversion electron spectra reveal possible transitions between nuclear levels. From the comparison of these spectra with calculated internal conversion coefficients, it is often possible to assign a unique multipolarity to the nuclear gamma radiation and, hence, a total angular momentum and parity to the excited nuclear states.
- The internal conversion coefficients can provide detailed information about the atomic nucleus if theoretical and experimental values are compared for transitions of different multipolarity and mixing ratios. A detailed knowledge of these coefficients is needed, for instance, for deriving absolute transition rates and for the normalization of decay schemes, for Mössbauer spectroscopy, for nuclear reaction computations as well as for the calculation of the decay heat of the fuell cells of nuclear reactors.

- The internal conversion process is largely independent of the nuclear structure, although a non-zero probability requires a finite nuclear size and a finite probability of the electron to be found inside of the nucleus. For highly suppressed transitions, this finite-size effect can become quite significant. For these transitions, Pauli developed formulae to correct the theoretical conversion coefficient for both, the electric and magnetic multipolarities.

General theory:

- The internal conversion can be described as QED process by the retarded interaction of charges.
- In particular, the internal conversion is a second-order quantum-electrodynamical process in which a virtual photon is exchanged between the nucleus (proton) and an electron.
- **Internal conversion amplitude:** The (single-electron) matrix element of the conversion transition can be written in terms of the Hamiltonian (Listengarten 1961; Band *et al.*, 2002)

$$\langle f | h^{(\text{conversion})} | i \rangle = -e \int d^3\mathbf{r} \psi_f^*(\mathbf{r}) [\Phi(\mathbf{r}) + \boldsymbol{\alpha} \cdot \mathbf{A}(\mathbf{r})] \psi_i(\mathbf{r}),$$

where $\Phi(\mathbf{r})$ and $\mathbf{A}(\mathbf{r})$ are the time-independent parts of the scalar and vector potentials of the electro-magnetic field that arise due to the **nuclear transition charges and currents**, and by including the retardation of these interactions.

- The retarded potentials in the internal conversion amplitude above are

$$\Phi(\mathbf{r}, t) = e^{-i\omega t} \Phi(\mathbf{r}), \quad \Phi(\mathbf{r}) = \int d^3\mathbf{R} \frac{\rho(\mathbf{R})}{|\mathbf{r} - \mathbf{R}|} e^{ik|\mathbf{R} - \mathbf{r}|} = \sum_{LQ} \Phi_{LQ}(\mathbf{r})$$

$$\mathbf{A}(\mathbf{r}, t) = e^{-i\omega t} \mathbf{A}(\mathbf{r}), \quad \mathbf{A}(\mathbf{r}) = \frac{1}{c} \int d^3\mathbf{R} \frac{\mathbf{J}(\mathbf{r})}{|\mathbf{R} - \mathbf{r}|} e^{ik|\mathbf{R} - \mathbf{r}|} = \sum_{LQ} \mathbf{A}_{LQ}(\mathbf{r})$$

with the wavenumber $k = \omega/c = \mathcal{E}/\hbar c$, and where $\mathbf{r} = (r, \vartheta, \varphi)$ and \mathbf{R} are the coordinates of the electron and nucleus (proton), respectively.

- Here, we shall not go into further details for the representation of these potentials but just note that these interaction potentials can be written as a sum over multipole contributions as well as in terms of the nuclear charge density $\rho(\mathbf{R})$ and current density $\mathbf{J}(\mathbf{r})$ of the bound electrons, respectively.

Internal conversion coefficients:

- **Internal conversion coefficient:** The internal conversion coefficient is defined as the ratio of the number of electrons N_e ejected from the atomic shell ($n\ell$) to the number of gamma quanta N_γ leaving the atom during the same time:

$$\alpha^{(\text{conversion})}(n\ell) = \frac{N_e}{N_\gamma}, \quad \alpha^{(\text{conversion})}(\alpha_i J_i) = \sum_f \alpha^{(\text{conversion})}(n\ell)$$

The total internal conversion coefficient of a given (initial) level $\alpha^{(\text{conversion})}(n\ell)$ of the nucleus is the sum of partial conversion coefficient associated with all possible ionization channels (lines) of the atom or ion.

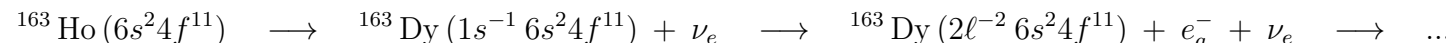
- Internal conversion coefficients have been tabulated in a larger number of tables and compilations; in these tabulations, the screening of the nuclear electric field by the atomic electrons was often treated in the framework of either some statistical Thomas-Fermi-Dirac or Dirac-Fock-Slater models.
- For different x_α pre-factors in the Dirac-Fock-Slater (type) potentials, the differences in the calculated conversion coefficients are typically small $\sim 1\%$ for K -shell electrons but may increase to $\sim 70\%$ for outer electrons or even larger for low kinetic energies of the conversion electron (≤ 1 keV). The question of whether the electronic hole should be taken into account into the atomic potential has been explored previously but seem to have a minor role only.
- A new internal conversion coefficient database BRICC has been developed that includes various tabulations of internal electron conversion (IECC), internal electron-positron pair conversion coefficients (IPCC) as well as the *electronic* factors $\Omega(E0)$.
- Theoretical conversion coefficients $\alpha^{(\text{internal-conversion})}$ are associated with two kinds of uncertainties: (i) due to the physics model that is used in the computations and (ii) due to the spline interpolation that is frequently used in order to generate the tabulations. The physics model is typical based on assumptions about the atomic nucleus and the electron density.

8.2.j. Nuclear electron capture and β^\pm decay

Process, notation & application:

- Electron capture of an atom or ion by nuclear decay: $A(Z+1) + e^- \longrightarrow A(Z) + \nu_e$

- Quantum notations used in the formulas below: $E_\nu = Q^+ - E_f - E_b > 0$
- Here, the nucleus decays by capturing an atomic electron (often from the K-shell), and under the emission of an electron neutrino. Here, Q^+ is the energy difference due to the rest masses of the parent and daughter nucleus, E_f the energy of the final nuclear state of the daughter nucleus and E_b the binding energy of the captured electron. The release energy E_ν will be shared between the emitted neutrino and, possible, some bremsstrahlungs photon or the shake-up/shake-off of a valence electron.
- For allowed nuclear transitions, nearly all vacancies occur in the ns shells of the atoms or ions, i.e. in the K, L₁, M₁, ... shells.
- **Measurement of the electron neutrino mass:** The mass of the electron neutrino can be determined by studying the electron capture of ¹⁶³Ho and, in particular, the energy-differential electron capture rate as function of the energy-sharing between the neutrino and the inner-shell excited atom. However, there are many resonances in the energy-differential electron capture rate owing to the autoionization of the generated hole states in the daughter ion, and which are caused by inter-electronic interactions. These resonances are generally superposition of Lorentzian, Mahan- and Fano-like line-shapes.
- **Electron capture (EC) spectrum of ¹⁶³Ho:** ¹⁶³Ho are known to decay by electron capture to the inner-shell ionized ¹⁶³Dy atom



The recoil energy of the daughter atom exhibits an interesting structure due to subsequent decay via many different Auger channels. The endpoint of this spectrum is determined by the energy difference of the holmium and dysprosium ground-state energies minus the rest mass of the created neutrino. Obviously, a very high statistics and high resolution is required in order to determine the energy spectrum of the emitted ¹⁶³Dy atoms (Brass and Haferkort, 2020).

Nuclear electron capture:

- **Nuclear electron capture:** Micro calorimeters allow to record high-resolution spectra from large arrays of detectors. In all calorimetric experiments, however, the details of the inner-shell decay (whether by radiation or electron ejection) remains indifferent since all energy is simply converted to heat, apart from the those of the neutrino.
- **Determination of nuclear Q values:** The nuclear Q values is central for the observed electron and positron spectra in β^\pm decays. The Q values is often deduced from the β spectrum itself by means of (so-called) Kurie plots. However, if the shape of the spectrum is not known from theory or prior measurements, the extracted Q value can significantly differ from the *true* value. Nowadays, high-precision Penning-trap mass spectrometry provides a direct and rather independent way for determining the Q values of nuclear reactions by just measuring the mass difference between the parent and daughter nuclides (Filianin *et al.*, 2021).

Neutrino mass and oscillations:

- **Electron neutrino mass:** A finite neutrino mass implies physics beyond the standard model of particle physics. Therefore, much recent interest has been devoted to determine this neutrino mass on an absolute scale, unlike to the observed neutrino flavor oscillations. Despite a good deal of effort, however, the measurement of the neutrino mass remains difficult as the masses are (likely) very small and the neutrinos interact very weakly with other matter.
- **Electron neutrino mass:** Two nuclides are nowadays in the focus of electron neutrino mass measurement, namely ^{163}Ho and ^3H . For (nearly) massless neutrinos, planned measurements relies on a precise knowledge of the expected spectral shape for the case of massless neutrinos.
- **Neutrino mass:** The discovery of neutrino oscillations from solar, reactor and atmospheric neutrinos have confirmed neutrinos as massive particles, in contrast to the standard model that predict their mass to be zero. Until the present, however, little is known about the absolute mass of neutrinos nor about the mechanism of how this mass is acquired. **The neutrino mass is often taken as a sign for new physics at high mass scales.**
- **Neutrino oscillations:** The observed oscillation of neutrinos of different kind can only provide the differences between the (squares of) masses and constrain their *averaged* mass to at least 0.02 eV. On the other hand, laboratory measurements of the β spectrum of tritium give rise to an upper limit of the neutrino mass of less or ~ 1 eV. Various (more sensitive) laboratory measurements are carried out to further constrain this upper limit, and which help constrain cosmological parameters in the future, such as equation of state of dark energy

8.3. Further processes, not yet considered in JAC

8.3.a. Coulomb ionization (CoulombIonization)

Process, notation & application:

- Coulomb ionization by fast, heavy ions: $A^{(q+1)+} + Z_p \rightarrow A^{(q+1)+(*)} + e^- + Z'_p$
- Quantum notations used in the formulas below: $|\alpha_i J_i\rangle + Z_p(\dots) \rightarrow |\alpha_f J_f\rangle + e^-$
- The Coulomb ionization of projectile ions by target atoms leads to a different charge state of the ions and often determines their lifetime in storage rings.
- If one of the projectile electrons is ionized, the ion is lost from the ring since it will be misbent by subsequent steering magnets.

Perturbative calculation of ionization cross sections:

- Semi-relativistic treatment of the Coulomb ionization: In their semi-relativistic treatment, Anholt and Becker (1987) distinguish three contributions to the ionization cross sections due to Coulomb ionization, transverse ionization, and the ionization due to the spin-flip of the ionized electron. These three contributions have different asymptotic behaviour in ultra-relativistic collisions. — In this approach, the Coulomb ionization cross section is the same as in the plane-wave Born approximation for nonrelativistic projectiles.
- The Coulomb part is dominant at nonrelativistic energies, while the transverse part mainly arise from the magnetic interactions at large impact parameters.
- The cross section for the (projectile) ionization of a $1s$ electron increases as $\ln \gamma$ due to the transverse interaction for high projectile energies and if the target screening is neglected. This transverse interaction is however screened and reduced if the charge of the projectile is smaller than those of the target, $Z_p < Z_t$.
- For fast collisions and for impact parameters b comparable with, or larger than the ionic K -shell radius, the perturbation of the target atom by the projectile can be treated in first-order time-dependent perturbation theory, even for high- Z projectiles.
- Perturbation theory breaks generally down for high- Z projectiles (or high- Z targets). For these high- Z projectiles, an approximate scaling rule for the ionization probability at high relativistic energies ($\gamma > 5$) and fixed impact parameters has been established by numerical calculations. For $b = 0$, for example, the ionization probability $P(b = 0) = 1.8 \times 10^{-4} Z_p^2$ is independent of the target charge within about $\pm 10\%$ up to the heaviest elements.

8.3.b. Bremsstrahlung (BremsStrahlung)

Process, notation & application:

- Bremsstrahlung emitted by an electron in the field of an atom or ions $A^{q+} + e_i^- \rightarrow A^{(q)+*} + e_f^- + \hbar\omega$
- Quantum notations used in the formulas below: $|\alpha_i J_i\rangle + |\varepsilon_i \kappa_i\rangle \rightarrow |\alpha_f J_f\rangle + |\varepsilon_f \kappa_f\rangle + \hbar\omega(\mathbb{M})$
- Bremsstrahlung arises generally if a charged particle is decelerated or deflected by another charged particle, often an electron or nucleus, and if parts of its kinetic energy is converted into radiation.
- More generally speaking, bremsstrahlung or braking radiation refers to any radiation that arises due to the **deceleration of charged particle, including synchrotron radiation from relativistic particles or cyclotron radiation from non-relativistic particles**.
- In atomic physics, bremsstrahlung often refers to the radiation from electrons that are slowed down in matter.
- **Atomic bremsstrahlung:** This term sometimes refers also to the polarized radiation that arise from the Coulomb field of the incident charged particle.
- Bremsstrahlung has a continuous spectrum and a peak intensity that shifts toward higher frequencies with an increasing energy transfer from the decelerated particles.

8.3.c. Inverse bremsstrahlung

Process, notation & application:

- Inverse bremsstrahlung of a charged particle in the field of an atom or ions $\hbar\omega + A^{q+} + e_i^- \rightarrow A^{(q)+} + e_f^-$
- Quantum notations used in the formulas below: $\hbar\omega(\mathbb{M}) + |\alpha_i J_i\rangle + |\varepsilon_i \kappa_i\rangle \rightarrow |\alpha_f J_f\rangle + |\varepsilon_f \kappa_f\rangle$
- In the inverse bremsstrahlung process, a free electron gains kinetic energy due to the absorption of a photon.

8.3.d. Radiative recombination & fluorescence

Process, notation & application:

- Radiative recombination & fluorescence of an ion: $A^{q+} + e_s^- \rightarrow A^{(q-1)+,*} + \hbar\omega_r \rightarrow A^{(q-1)+} + \hbar\omega_r + \hbar\omega_f$
- Quantum notations used in the formulas below: $|\alpha_i J_i\rangle + |\varepsilon_i \kappa_i\rangle \rightarrow |\alpha_r J_r\rangle + \hbar\omega_r(\mathbb{M}_r) \rightarrow |\alpha_f J_f\rangle + \hbar\omega_r(\mathbb{M}_r) + \hbar\omega_f(\mathbb{M}_f)$
- In the photorecombination & fluorescence process, also known radiative recombination (RR) or radiative electron capture (REC), an electron is captured by the ion into an excited state that subsequently decay under fluorescence emission.

8.3.e. Resonant two-color (two-photon, single-electron) ionization

Process, notation & application:

- Resonant two-color (two-photon, single-electron) ionization of an ion: $A + \hbar\omega + \hbar\omega' \rightarrow A^* + \hbar\omega' \rightarrow A^{+*} + e_p^-$
- Quantum notations used in the formulas below: $|\alpha_i J_i\rangle + \hbar\omega(\mathbb{M}) + \hbar\omega'(\mathbb{M}') \rightarrow |\alpha_r J_r\rangle + \hbar\omega'(\mathbb{M}') \rightarrow |\alpha_f J_f\rangle + |\varepsilon \kappa\rangle$
- In the resonant two-color photoionization, an atom or ion is resonantly excited by one photon and subsequently ionized by a second photon of the same or some different frequency.

8.3.f. Interference of multi-photon ionization channels (MultiPhotonInterference)

Process, notation & application:

- Interference of *non-resonant* one-photon (2ω) and *resonant* two-photon (ω) ionization of an atom or ion:

$$A + \begin{bmatrix} \hbar(2\omega) \\ \hbar\omega + \hbar\omega \end{bmatrix} \rightarrow A^+ (*) + e_p^-$$

➤ Quantum notations used in the formulas below:

$$|\alpha_i J_i\rangle + \begin{bmatrix} \hbar(2\omega) \\ \hbar\omega + \hbar\omega \end{bmatrix} \longrightarrow |\alpha_i J_i\rangle + |\varepsilon\kappa\rangle$$

- The two-pathway quantum interference has been explored in order to better understand the [quantum control of atoms and ions](#).
- Such quantum control studies were initially stimulated by the small fraction of the second harmonic that typically arise at XFEL and that cannot so easily be filtered out, though it may strongly influence the experimental from two-photon ionization experiments. Despite of the rather small intensity of the second harmonic, the ionization by photons with frequency 2ω (second harmonic, first-order process) can readily compete with, or even dominate, the two-photon ionization by photons with frequency ω .

Interference of non-res. one-photon (2ω) and resonant two-photon (ω) ionization:

- [Experimental signals](#): For a linearly-polarized bichromatic beam, the interference due to different quantum paths manifests itself in an asymmetry of the photoelectron angular distributions (PAD) with respect to the plane that is perpendicular to the electric field of the incident radiation; cf. Grum-Grzhimailo *et al.*(2015).
- [Photoelectron angular distribution \(PAD\)](#): In the dipole approximation and for an isotropic target, this angular distribution must be axially symmetric with regard to the polarization direction

$$\frac{dW}{d\Omega} = \frac{W_o}{4\pi} \left[1 + \sum_{k=1}^K \beta_k P_k(\cos \vartheta) \right]$$

where ϑ is the angle of the photoelectron with regard to the polarization direction (**E**-field) and β_k the corresponding anisotropy parameters, which can be expressed in terms of the photoionization amplitudes.

- For the interference of one-photon and two-photon ionization paths, all terms with $k = 1, 2, 3, 4$ must be taken into account in the PAD above. The odd polynomials arises from the photoelectron partial waves with opposite parities due to the interaction of the atom with the fundamental and second harmonic of the radiation.
- The quantum interference of absorption amplitudes with an even and odd number of photons, such as $(\omega + 2\omega)$ photoionization, does not modify the total yield but only affect the angle-resolved observations. The interference between an even or odd number of photons lead to photoelectron partial waves with opposite parities.
- [Interference in photoionization](#): Many photoionization experiments have been performed in order to better understand the [concept of quantum-mechanical interference](#). Interference in photoionization occurs since the phase of the incident photons is eventually imprinted upon

the wave of the emitted electron. Apart from cross sections, this phase imprint enables one to extract the phases from the measurements, and which could not be derived for classical particles.

- **Interference in photoionization:** Using a seeded free-electron laser, first coherent optical experiments have been performed also at short wavelengths; in these experiments, high xuv harmonics have been utilized to coherently control the outcome of experiments by controlling the electron beam in the accelerator. Such a control requires to precisely know both, the amplitude and phase of each harmonic.
- **Time-dependent electric field in two-color experiments:** In two-color experiments, the field is often approximated by (DiFraia *et al.*, 2019)

$$\mathcal{E}(t) = \sqrt{I_\omega(t)} \cos \omega t + \sqrt{I_{2\omega}(t)} \cos(2\omega t - \phi), \quad \mathbf{\mathcal{E}}(t) = \mathcal{E}(t) \mathbf{e}_z,$$

and where $I_\omega(t)$, $I_{2\omega}(t)$ are the envelopes of the two pulses and ϕ the relative phase between the $\omega - 2\omega$ pulses. In this definition, the larger ϕ as more the 2ω pulse is delayed.

8.3.g. Two-color multi-photon interference ionization (TwoColorInterferenceIon)

Process, notation & application:

- Two-color multi-photon interference ionization of an ion: $A + m\hbar\omega + n\hbar\omega' \rightarrow A^{+*} + e_p^-$
- Quantum notations used in the formulas below: $|\alpha_i J_i\rangle + m\hbar\omega(\mathbb{M}) + n\hbar\omega'(\mathbb{M}') \rightarrow |\alpha_f J_f\rangle + |\varepsilon\kappa\rangle$
- In the two-color multi-photon interference ionization, an atom or ion emits an electron whose angular distribution is affected by the interference of different ionization pathes.

8.3.h. Two-photon above-threshold ionization (ATI) (TwoColorInterferenceIon)

Process, notation & application:

- Two-photon above-threshold ionization of an ion:

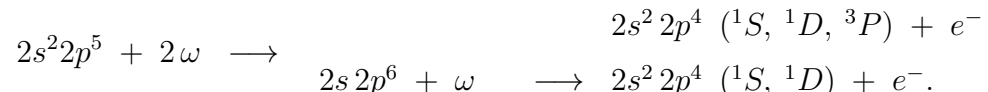
8. Atomic processes

- Quantum notations used in the formulas below:
- Petrov *et al.* (2019) considered the two-photon $3p$ ionization of argon: $\text{Ar } 3p^6 + 2\gamma \longrightarrow 3p^5 \varepsilon \kappa$ with $\varepsilon > \hbar\omega$.

8.3.i. Photon-stimulated Auger decay (PSAD)

Process, notation & application:

- Photon-stimulated Auger decay of an ion:
- Quantum notations used in the formulas below:
- Photon-stimulated Auger decay (PSAD): Multi-photon stimulated Auger decay is a non-linear process that was observed for the $3s$ ionization of argon and for a few other sub-valence shell ionized noble gases that normally decay by fluorescence emission. If an ion absorbs one or more additional photons from a strong field, it may decay also to a $3p^{-2}$ doubly ionized level. PSAD can be utilized to coherently create singly and doubly ionized atoms in two-color experiments. In neon, for example, the following photon-stimulated Auger processes may occur and interfere in a sufficiently strong field:



If the two light pulses with frequencies ω and 2ω are phase coherent, the two paths above to the ${}^1S, {}^1D$ final levels can interfere but no interference occurs for 3P (Iablonskyi *et al.*, 2017).

8.3.j. Positron-annihilation-induced autoionization

Process, notation & application:

- Positron-annihilation-induced autoionization of an ion: ...
- Quantum notations used in the formulas below:

- **Positron-annihilation-induced Auger electron spectroscopy (PAES):** This positron-induced autoionization help explore surface structures and the observation of segregation processes. The time-dependent PAES has been utilized as a novel technique for the selective investigation of, e.g. heterogeneous catalysis, corrosion, or surface alloying.
- Mayer *et al.* (2010) applied the time-resolved PAES for the first time in order to determine the time constant for segregation as well as the final segregated configuration at the surface. For Cu-Pd alloys, for example, the amount of Cu atoms and their exact position was found to strongly affect the mechanical stability and the catalytic properties of Pd membranes. These authors also investigated the stability and dynamics of thin Cu layers on the surface of poly-crystalline Pd. When compared with the electron-induced Auger electron spectroscopy, the PAES appears intrinsically to be sensitive to the topmost atomic layer of a sample. These experiments were performed by means of the high intensity neutron-induced positron source Munich (NEPOMUC) which delivers about 10^9 monoenergetic positrons per second.
- **Positron affinity:** PAES is a highly selective technique for selecting specific atoms at surfaces because of the quite different positron affinities of the surface atoms. If more than a single element is present at some surface, the positrons are attracted to and annihilated with those atoms that have a higher relative positron affinity. Because of the high positron affinities of Pd, the positron will likely annihilate with electrons from Pd atoms in a Cu-Pd alloy, if such atoms are within the diffusion length of the positron at the surface.

8.3.k. Resonant excitation with sequential double autoionization (RESDA):

Process, notation & application:

- Resonant excitation with sequential double autoionization (RESDA) of an ion: ...
$$A^{q+} + e_s^- \longrightarrow A^{(q-1)+,*} \longrightarrow A^{q+,*} + e_{a_1}^- \longrightarrow A^{(q+1)+} + e_{a_1}^- + e_{a_2}^-$$
- Quantum notations used in the formulas below: $|\alpha_i \mathbb{J}_i\rangle + |\varepsilon_i \kappa_i\rangle \longrightarrow |\alpha_m \mathbb{J}_m\rangle \longrightarrow |\alpha_n \mathbb{J}_n\rangle + |\varepsilon_1 \kappa_1\rangle \longrightarrow |\alpha_f \mathbb{J}_f\rangle + |\varepsilon_1 \kappa_1\rangle + |\varepsilon_2 \kappa_2\rangle$
- Lithium-like ions are perhaps the simplest ions in whicha RESDA can occur. This process can be observed by measuring the ratio of the numbers of trapped ions of two neighbouring charge states as a function of electron energy within an electron beam ion trap.

8.3.I. Resonant excitation with direct double autoionization (REDDA):

Process, notation & application:

- Resonant excitation with direct double autoionization (REDDA): of an ion: ...



- Quantum notations used in the formulas below: $|\alpha_i J_i\rangle + |\varepsilon_i \kappa_i\rangle \longrightarrow |\alpha_m J_m\rangle \longrightarrow |\alpha_f J_f\rangle + |\varepsilon_1 \kappa_1\rangle + |\varepsilon_2 \kappa_2\rangle$

- In the REDDA process, an electron is resonantly captured into a (doubly) excited level that subsequently decays by the simultaneous emission of two electrons, a so-called double autoionization, and where the two electrons share the overall excess energy.

8.3.m. Radiative double electron capture

Process, notation & application:

- Radiative double electron capture (RDEC) of an ion: $A^{q+*} + e_1^- + e_2^- \rightarrow A^{(q-2)+} + \hbar\omega$
- Quantum notations used in the formulas below: $|\alpha_i J_i\rangle + |\varepsilon_1 \kappa_1\rangle + |\varepsilon_2 \kappa_2\rangle \rightarrow |\alpha_f J_f\rangle + \hbar\omega(\mathbb{M})$
- The radiative double electron capture (RDEC) is the time-reversed process of the single-electron direct double photoionization; it includes the transfer of two target electrons into a bound state of the projectile under the simultaneous emission of a single photon. Indeed, RDEC can be considered as the simplest and (almost) background-free tool for studying electron-electron correlations in high- Z ions.
- **Experimental evidence:** Simon *et al.* (2010) have presented experimental evidence of radiative double electron capture in the collision of 38 MeV O⁸⁺ with a carbon foil. When compared to theoretical cross sections, the experiments suggest a 5 times larger cross sections. This discrepancy may arise from the fact that no capture into excited states were included into the computations and that the electrons were considered as quasi-free in all computations.
- The (non-resonant) radiative electron capture is known to be dominant for fast collisions of heavy ions with light target atoms and shows a rather weak dependence on the inter-electron interaction between the projectile and target ions. **The RDEC is a single-step process where the energy of two correlated captured electrons are converted into the energy and momentum of one emitted photon** (Chernovskaya *et al.*, 2011).
- The RDEC can be described as the inverse process to double photoionization. Indeed, RDEC can be seen as a prominent tool for investigating the role of interelectronic interactions in the process of ion-atom collisions.
- **Radiative double-electron capture:** This is the time-revered process to the double photo ionization and has been experimentally explored for initially bare oxygen and uranium ions.

8.3.n. Generalized oscillator strengths (GOS)

Process, notation & application:

- Inelastic scattering of high-energetic photons or electrons The generalized oscillator strengths has been utilized to describe the inelastic scattering of high-energetic photons or fast electrons at atoms. This inelastic scattering has been discussed quite early by Bethe (1931) but has received less attention afterwards.

8. Atomic processes

- Inelastic scattering of a fast electron by an atom or ion: $A^{q+} + e_s^- \rightarrow A^{r+} + e_s^-'$ with $r \geq q$.
- The notion of GOS has been introduced if only the effective scattering cross section (strength) is of interest and if all the other released electrons are neglected from the theoretical treatment.

GOS expressions:

- **Fast electron impact:** The GOS for an excitation of the atom by fast electrons has been expressed as (Zhu *et al.*, 2006)

$$f(E, K) = \frac{E}{2} \frac{p_i}{p_f} K^2 \frac{d\sigma}{d\Omega} = \frac{2E}{K^2} |\langle \alpha_f \mathbb{J}_f M_f | T_1(\mathbf{K}) | \alpha_i \mathbb{J}_i M_i \rangle|^2,$$

where E is the excitation energy, K the momentum transfer, p_i, p_f the incident and scattered electron momenta, while $\frac{d\sigma}{d\Omega}$ refers to the differential scattering cross section of the incident electron.

8.3.o. Nuclear excitations due to electronic transitions and capture

Nuclear excitation by two-photon decay (NETP):

- **NETP:** Nuclear excitation due to the coupling of the nucleus to the two-photon decay of excited atomic states.
- **NETP:** Volotka *et al.* (2016) proposed a new mechanism of nuclear excitation via two-photon electron transitions (NETP) and performed detailed calculations especially for the E1E1 $1s2s \ ^1S_0 \rightarrow 1s^2 \ ^1S_0$ two-photon decay of helium-like $^{225}\text{Ac}^{87+}$ ions with a resonant excitation of the $3/2^+$ nuclear (isomeric) level with energy 40.09 (5) keV. For this two-photon decay, the NETP probability is $P^{(\text{NETP})} = 3.5 \cdot 10^{-9}$, when compared with the standard E1E1 decay, and this probability is comparable with other mechanisms, such as NEET or NEEC.
- **NETP scheme:** Scheme of the nuclear excitation due to the coupling of the nucleus to the two-photon decay (NETP) of excited atomic states; cf. Figure 8.2. A key advantage of the NETP process is that, in contrast to the NEET and NEEC, such resonant nuclear excitations may happen for all nuclear levels with an access energy smaller than the total transition energy.
- **NETP for the E1E1 $1s2s \ ^1S_0 \rightarrow 1s^2 \ ^1S_0$ two-photon decay of helium-like $^{225}\text{Ac}^{87+}$ ions:** For $^{225}\text{Ac}^{87+}$ ions, Volotka *et al.* (2016) determined a rate $W^{(\text{NETP})} = 0.21 \cdot 10^5 \text{ s}^{-1}$ and a (relative) probability $P^{(\text{NETP})} = W^{(\text{NETP})}/W^{(2\text{E}1)} \approx 3.5 \cdot 10^{-9}$. This probability is comparable with typical probabilities $P^{(\text{NEET})} \propto 10^{-7} \dots 10^{-12}$.

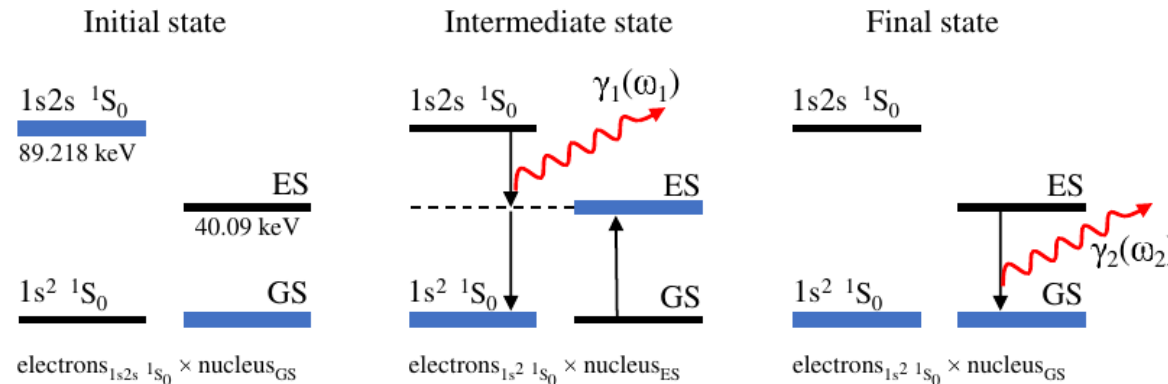


Figure 8.2.: NETP mechanism for a helium-like $^{225}\text{Ac}^{87+}$ ion. The initial state (left panel), which is characterized by the $1s2s \ ^1S_0$ electronic state and the nuclear ground level, decays into the final state (right panel), where both the electrons and nucleus are in their ground states $1s^2 \ ^1S_0$. This second-order process occurs via the intermediate cascade state (middle panel) with the nucleus being in an excited state. Here, the electron-decay photon γ_1 and the nuclear-fluorescence photons γ_2 are depicted by wavy lines with arrows; taken from Volotka *et al.* (2016).

- **NETP for the E1E1 $1s2s \ ^1S_0 \rightarrow 1s^2 \ ^1S_0$ two-photon decay of helium-like $^{225}\text{Ac}^{87+}$ ions:** To observe a NETP deexcitation, the resolution of the x-ray detection must be high enough to discriminate the decay with regard to the dominant 2E1 decay channel. For typical x-ray detectors with resolutions of, say, 1 eV, 10 eV, 100 eV, the partial NETP probability becomes $1 \cdot 10^{-4}$, $1 \cdot 10^{-5}$, $1 \cdot 10^{-6}$, and makes the observation of this decay channel rather a challenge.

Nuclear excitation by electronic transition (NEET):

- **NEET:** Nuclear excitation by electronic transition, i.e. due to the coupling of the nucleus to the – real or virtually – single-excited electronic states.
- **NEET:** The NEET process has been verified experimentally for ^{197}Au , ^{189}Os and ^{193}Ir atoms.

Nuclear excitation by electron capture (NEEC):

- **NEEC:** Nuclear excitation by electron capture as mediated by the coupling of the nucleus to doubly excited electronic resonances.

8. Atomic processes

- **NEEC:** In NEEC, the energy from a captured electron is directly transferred to a nuclear internal excitation, and from which it is released by nuclear deexcitation, i.e. by photon emission or due to internal conversion.

8.3.p. Electron-impact multiple ionization

Process, notation & application:

- Electron-impact multiple ionization of an atom or ion: $e_s^- + A \rightarrow A^* + e_s^{-'} + e_a^- + e_b^- + \dots$
- Quantum notations used in the formulas below: $|\alpha_i J_i\rangle + |\varepsilon_i \kappa_i\rangle \rightarrow |\alpha_f J_f\rangle + |\varepsilon_f \kappa_f\rangle + |\varepsilon_a \kappa_a\rangle + |\varepsilon_b \kappa_b\rangle + \dots$
where $|\varepsilon_a \kappa_a\rangle$, $|\varepsilon_b \kappa_b\rangle$, ... refer to the initially bound *atomic* electrons.
- To describe the **multiple ionization in electron-impact processes**, one needs to consider the (electron-impact) excitation, ionization as well as several resonant excitation processes. This is usually done in the **isolated resonance approximation**, in which all the processes are treated independently. The multiple ionization is then obtained from a proper summation over individual decay pathways and branching ratios.
- **Charge state distribution (CSD) in plasma:** Electron-impact double and multiple ionization plays a central role upon the charge state distribution of a plasma if the electron temperature changes rapidly either in time or space.
- For a plasma in a **collisional-ionization equilibrium**, the CSD is determined by the balance between electron-ion recombination and electron-impact – single and multiple – ionization. Therefore, accurate electron-impact excitation and ionization cross sections are important for plasma diagnostics over a wide range of plasma (electron) temperatures, electron densities and elemental abundancies.

8.3.q. Three-body recombination

Process, notation & application:

- Three-body recombination of an ion: $A^{q+} + e_i^- + e_c^- \rightarrow A^{(q-1)+} + e_f^-$
- Quantum notations used in the formulas below: $|\alpha_i J_i\rangle + |\varepsilon_i \kappa_i\rangle + |\varepsilon_c \kappa_c\rangle \rightarrow |\alpha_f J_f\rangle + |\varepsilon_f \kappa_f\rangle$
- The three-body recombination of an ion is the inverse process of the electron-impact ionization.

- The three-body recombination combination of an electron results in the capture of an electron by an positive ion due to energy and momentum transfer of the (captured) free electron to another free electron in the neighborhood of the atom or ion.
- **Three-body recombination:** For low-temperature afterglow and recombination-laser plasmas, the three-body collisional recombination to higher levels and deexcitation between higher levels are often dominant.

8.3.r. Elastic scattering of electrons and ions

Process, notation & application:

- Elastic scattering of electrons and positrons by atoms and ions of an ion: $A^{q+} + e_i^- \rightarrow A^{q+} + e_f^-$
- Quantum notations used in the formulas below: $|\alpha_i \mathbb{J}_i\rangle + |\varepsilon_i \kappa_i\rangle \rightarrow |\alpha_f \mathbb{J}_f\rangle + |\varepsilon_f \kappa_f\rangle^+$
- Potential scattering of relativistic electrons and positrons: The scattering of relativistic electrons or positrons by a – real or complex – central-field $V(r)$ is completely described by the direct scattering amplitude $f(\vartheta)$ and the spin-flip scattering amplitude $g(\vartheta)$, which are both complex functions of the polar scattering angle ϑ .
- These scattering amplitudes are derived from the asymptotic behaviour for $r \rightarrow \infty$ of the distorted plane-wave solutions of the Dirac equation plus an outgoing spherical wave.
- **Elastic collisions:** While elastic collisions do generally not lead to an (electronic) excitation of the target atom, they may cause sizeable deflections of the projectile and, hence, change the trajectories of (fast) particles moving in a medium. Moreover, each collision also comprises an energy transfer from the projectile to the target atom that is seen in the recoil and that leads to (so-called) nuclear contribution to the stopping power.
- **Scattering amplitude of elastic collisions:** Quantum mechanically, the scattering amplitude is usually expressed as by means of a partial-wave expansion of the (wave function of the) scattered particle. In this expansion, the coefficients of the partial wave are determined by the phase shifts as the overall contribution of the scattering potential to the asymptotic behavior of (spherical) waves with well-defined angular momentum.
- **Scattering amplitude of elastic collisions:** Because of the (very) short de Broglie wave length of heavy projectiles and the slow convergence of the partial-wave series, this method cannot be applied for heavier particles, such as muons or ions. The Broglie wave length affects directly the stability of the radial wave equation (Salvat *et al.*, 2022).

Static scattering potentials:

- **Static-field approximation:** This approximation only includes the (electro-) static potential *plus* approximate local exchange potential for the interaction between the incoming or outgoing electron and the (target) ion. For electrons with kinetic energies $E_{\text{kin}} \lesssim 10$ keV, moreover, one often includes optionally a semi-empirical correlation-polarization potential in order to account for the dynamically induced polarization of the target.
- **Local exchange potential:** For electron scattering processes, three simple analytical approximations for a local exchange potential refer to the Thomas-Fermi, Furness-McCarthy as well as the Riley-Truhlar potential (Salvat *et al.*, 2005).
- **Absorption potential:** For the calculation of elastic scattering cross sections, it is sometimes helpful to optionally include an imaginary (absorptive) part into the static potential in order to account for the coupling with inelastic channels.
- **Exchange potential:** For in- and/or outgoing electrons, a possible exchange with a bound electron need to be taken into account as it occurs naturally if all electrons are treated together by an (antisymmetrize) Slater determinant. In general, however, these exchange terms in the Dirac-Hartree-Fock equations are difficult to deal with and are often approximated in some suitable form.

Scattering amplitudes and cross sections:

- **Partial-wave expansion of the scattering amplitudes:** For a projectile with wave number $k = \hbar/p$ and kinetic energy E , the direct and spin-flip scattering amplitudes are given by

$$\begin{aligned} f(\vartheta) &= \frac{1}{2ik} \sum_{\ell=0}^{\infty} \{ (\ell+1) [\exp(2i\delta_{\kappa=-\ell-1}) - 1] + \ell [\exp(2i\delta_{\kappa=\ell}) - 1] \} P_{\ell}(\cos \vartheta) \\ g(\vartheta) &= \frac{1}{2ik} \sum_{\ell=0}^{\infty} [\exp(2i\delta_{\kappa=\ell}) - \exp(2i\delta_{\kappa=-\ell-1})] P_{\ell}^1(\cos \vartheta), \end{aligned} \quad (c\hbar k)^2 = E(E + 2mc^2),$$

and where $P_{\ell}^1(x)$ is an associated Legendre function. The scattering amplitudes above apply for both, electrons and positrons if the sign of their charges is taken into account, and which turns an attractive potential into a repulsive potential and *vice versa*.

- Analogue to non-relativistic theory, **attractive potentials are generally associated with positive phase shifts and repulsive potentials with negative phase shifts.**

- Elastic differential and total CS: (Salvat *et al.*, 2005)

$$\frac{d\sigma^{(\text{elastic})}}{d\Omega} = |f(\vartheta)|^2 + |g(\vartheta)|^2, \quad \sigma^{(\text{elastic})} = \int d\Omega \frac{d\sigma^{(\text{elastic})}}{d\Omega} = 2\pi \int_0^\pi d\vartheta \sin \vartheta \frac{d\sigma^{(\text{elastic})}}{d\Omega}.$$

Spin-polarization of elastically scattered electrons:

- Sherman function: This function describes the degree of spin polarization of electrons or positrons as function of the scattering angle ϑ for an initially unpolarized beam

$$S(\vartheta) \equiv i \frac{f(\vartheta) g^*(\vartheta) - f^*(\vartheta) g(\vartheta)}{|f(\vartheta)|^2 + |g(\vartheta)|^2}.$$

Applications of elastic scattering:

- Application of differential elastic cross sections $\frac{d\sigma^{(\text{elastic})}}{d\Omega}$: Accurate differential cross sections (DCS) for the elastic scattering of electrons and positrons by atoms and molecules are required in surface science, electron microscopy, electron-probe microanalysis, the design of radiation detectors, radiation protection, radiation-therapy planning and at several places elsewhere (Salvat *et al.*, 2005). Moreover, DCS for the elastic scattering by positive ions are needed also in order to describe the electron transport in plasmas.

8.3.s. Negative-continuum dielectronic recombination

Process, notation & application:

- Negative-continuum dielectronic recombination of an ion: $A^{q+} + e_s^- \rightarrow A^{(q-2)+*} + e^+$
- Quantum notations used in the formulas below: $|\alpha_i \mathbb{J}_i\rangle + |\varepsilon_i \kappa_i\rangle \rightarrow |\alpha_f \mathbb{J}_f\rangle + |\varepsilon_f \kappa_f\rangle^+$

8. Atomic processes

- The capture of an electron by a bare heavy nucleus may occur non-resonantly via the creation of a free-positron-bound-electron pair. This process is referred to as **negative-continuum dielectronic recombination** since it leads to the capture of (two) electrons into a bound state while a positron is released.

8.3.t. Inter-Coulombic capture and decay

Inter-Coulombic capture:

- Interatomic Coulombic electron capture (ICEC): ICEC describes the capture of a free electron by an ion, atom or molecule due to the assistance of neighbouring systems that carry away the excess energy of the electron attachment. Sisourat *et al.* (2018) propose an analytical formula for this ICEC mechanism for large distances of these neighbors. However, such an asymptotic analysis cannot *replace* a more complete quantum treatment. Up to the present, this ICEC mechanism has not been approved experimentally.

Inter-Coulombic decay:

➤

8.4. More processes, not yet considered in JAC

8.4.a. Nonradiative electron capture (NRC)

Process, notation & application:

- Non-radiative electron capture of an ion: ... $A^{q+} + e^- + Z_t \longrightarrow A^{(q-1)+, (*)} + Z'_t$
- Quantum notations used in the formulas below: $|\alpha_i \mathbb{J}_i\rangle + |\varepsilon_f \kappa_f\rangle \longrightarrow |\alpha_f \mathbb{J}_f\rangle$
- The nonradiative electron capture of a quasi-free electron by a projectile ion mainly occurs if the electron and ion velocities match to each other.
- The nonradiative capture is often described within the eikonal approximation, which enables one to estimate the capture from any filled shell of the target to any shell of the projectile.
- In high-Z targets, the nonradiative electron capture into excited states of the projectile is dominant, as predicted by the eikonal calculations and confirmed by measurements.

Nonrelativistic capture cross sections:

- In the nonrelativistic theory, the (nonradiative electron capture) cross section of a stationary bare nucleus to capture an electron with energy $E = \frac{m}{2} v^2$ is given by (Spitzer, 1956)

$$\sigma^{(\text{NRC, non-rel})}(E) = A \sum_{n=1}^{\infty} \frac{\varepsilon_g}{\hbar \omega_n E n^3} g_n,$$

where $A = 32\pi/\sqrt{27}\hbar e^2/(m^2 c^3) \approx 2.11 \times 10^{-22} \text{ cm}^2$, ε_g is the ground-state binding energy of the hydrogenic projectile and $\hbar \omega_n = E - \varepsilon_n$ the emitted photon energy for capture into level n . The factor $g_n \approx 1$ is a correction factor which is typically not specified in detail for most computations.

- For $g_n = 1$, this cross section can be written

$$\sigma^{(\text{NRC, non-rel})}(E) = A \left(\frac{\varepsilon_g}{E} \right) \sum_{n=1}^{\infty} \frac{1}{n(n^2 + \frac{\varepsilon_g}{E})} = \frac{A\varepsilon_g}{2E} \left\{ \psi \left(1 + i\sqrt{\frac{\varepsilon_g}{E}} \right) + \psi \left(1 - i\sqrt{\frac{\varepsilon_g}{E}} \right) + 2\gamma_E \right\}$$

where $\psi(z) = \frac{1}{\Gamma(z)} \frac{d}{dz} \Gamma(z)$ is the digamma function and $\gamma_E \approx 0.57772$ is Euler's constant.

8. Atomic processes

➤ Using the asymptotic form of $\psi(z)$, the cross sections can then be approximated as

$$\sigma^{(\text{NRC, non-rel})}(E) = A \left(\frac{\varepsilon_g}{E} \right) \left[\gamma_E + \ln \sqrt{\frac{\varepsilon_g}{E}} \right].$$

Velocity distributions:

- Two velocity distributions have been frequently applied to study nonradiative electron capture processes at proton and heavy-ion storage rings.
- Maxwell distribution: $f(E) = \frac{1}{(2\pi kT/m)^{3/2}} \exp\left(-\frac{E}{kT}\right).$
- 'Flattened' Maxwell distribution: $f(E) = \frac{1}{(2\pi kT/m)} \exp\left(-\frac{E}{kT}\right) \delta(v_{\text{ex}})$
which is obtained by suppressing one of the components of velocity.
- Nonradiative electron-capture rates: By using the asymptotic form of the digamma function in the nonradiative electron capture cross section above but different velocities distributions for the electrons to capture, various approximations for the capture rates can be derived. From the capture cross section $\sigma^{(\text{NRC, non-rel})}(E)$, the averaged coefficient α_r can be evaluated analytically for different velocity distributions

$$\alpha_r^{(\text{NRC, non-rel})} (\text{Maxwell}) = \frac{\sqrt{2} A \varepsilon_g}{\sqrt{m \beta, kT}} \frac{2}{\sqrt{\pi}} \left\{ \gamma_1 + \frac{\gamma_E}{2} + \Gamma\left(\frac{4}{3}\right) \gamma_2 \left(\frac{kT}{\varepsilon_1}\right)^{1/3} + \ln \sqrt{\frac{\varepsilon_1}{kT}} \right\}$$

$$\alpha_r^{(\text{NRC, non-rel})} (\text{flattened}) = \frac{\sqrt{2} A \varepsilon_g}{\sqrt{m kT}} \sqrt{\pi} \left\{ \gamma_1 + \frac{\gamma_E}{2} + \Gamma\left(\frac{5}{6}\right) \frac{\gamma_2}{\sqrt{\pi}} \left(\frac{kT}{\varepsilon_g}\right)^{1/3} + \ln \left(2\sqrt{\frac{\varepsilon_1}{kT}}\right) \right\}.$$

Semi-relativistic capture cross sections:

- Cross section calculations for nonradiative electron capture in relativistic heavy-ion collisions are often based on an eikonal approximation. Anholt (1985) adapted some prior form of the asymmetric eikonal theory in order to calculate total nonradiative electron capture cross sections from any filled target shell to any projectile shell by just scaling the nuclear charges Z_t and Z_p by the principal quantum numbers n_t and n_p . In general, this approximation was found to become better for high-energetic ions and can be applied confidently also for ultra-relativistic collisions.

8.4.b. Vacuum-electron capture

Process, notation & application:

- Vacuum electron capture of an ion: ... $A^{q+} + Z_t + e^- + e^+ \rightarrow A^{(q-1)+, (*)} + Z'_t + e^+$
- Quantum notations used in the formulas below: $|\alpha_i \mathbb{J}_i\rangle + |\varepsilon_- \kappa_-\rangle + |\varepsilon_+ \kappa_+\rangle \rightarrow |\alpha_f \mathbb{J}_f\rangle + |\varepsilon_+ \kappa_+\rangle$
- The vacuum electron capture process refers to the capture of an electron by fast projectiles due to the creation of an electron-positron pair and under the emission of the positron.
- In the vacuum electron capture, the target is considered to act as a perturbing potential that helps create an electron-positron pair in the field of the projectile nucleus. While the electron is captured in one of the bound states (predominantly into $1s$), the positron is emitted.
- The creation of an electron-positron pair from the vacuum is similar to the Coulomb ionization process of the projectile ion, except that the relative momentum of the ion is imparted into the vacuum instead of exciting an electron into a higher state of the projectile.

Semi-relativistic capture cross sections:

- Due to the high value of momentum transfer, which is needed to excite an electron-positron pair from the vacuum, **vacuum-electron capture takes place predominantly at small impact parameters**, where the screening of the target nucleus by the target electrons is unimportant.
- **Vacuum-capture cross sections** The vacuum-capture process involves a momentum transfer from the target nucleus to the vacuum followed by an electron capture into the projectile K-shell. Therefore, the vacuum capture cross section is $\sim Z_t^2$, similar to most momentum transfer processes like excitation and ionization, and also $\sim Z_p^5$ as typical for projectile electron capture processes. For large γ , the cross sections increases as $\ln \gamma$ because they vanish for $v \ll c$ unlike for projectile ionization.

8. Atomic processes

- Anholt and Becker (1987, table I) provide (reduced) vacuum capture cross sections for any combination of target-projectile and for $\gamma \geq 10$. For these large values of γ , the cross section is approximately

$$\sigma^{(\text{VAC})} = Z_p^5 Z_t^2 a \ln\left(\frac{\gamma}{\gamma_0}\right) \quad (\gamma > \gamma_0)$$

where $a(Z_p)$ is a slowly varying function between 0.4 and 2.7 and γ_0 is an offset. As the capture into higher shells than the K-shell varies as n^{-3} , the cross section for $1s$ has been multiplied by 1.2 by Anholt and Becker to provide an estimate for the total capture. For $\gamma > 10$, these cross sections are expected to be accurate within approximately 20 %.

- The capture of an electron into the $1s$ shell of the projectile under the simultaneous emission of a positron has been calculated by Becker *et al.* (1987) and by Bertulani and Bauer (unpublished).

8.4.c. Positron-bound-electron pair annihilation with single-photon emission (PairAnnihilation1Photon)

Process, notation & application:

- Positron-bound-electron pair annihilation with single-photon emission from an atom or ion: $A^{q+} + e^+ \rightarrow A^{(q+1)+*} + \hbar\omega$
- Quantum notations used in the formulas below: $|\alpha_i J_i\rangle + |\varepsilon \kappa\rangle^+ \rightarrow |\alpha_f J_f\rangle + \hbar\omega(M)$
- A positron can annihilate with a bound electron from an atom or ion under the emission of one, two or more photons. Here, we consider the emission of a single photons which is possible only due to the presence of the atom.

8.4.d. Positron-bound-electron pair annihilation with two-photon emission (PairAnnihilation2Photon)

Process, notation & application:

- Positron-bound-electron pair annihilation with two-photon emission from an atom or ion: $A^{q+} + e^+ \rightarrow A^{(q+1)+*} + \hbar\omega_1 + \hbar\omega_2$
- Quantum notations used in the formulas below: $|\alpha_i J_i\rangle + |\varepsilon \kappa\rangle^+ \rightarrow |\alpha_f J_f\rangle + \hbar\omega_1(M_1) + \hbar\omega_2(M_2)$

- A positron can annihilate with a bound electron from an atom or ion under the emission of one, two or more photons. Here, we consider the emission of two photons.
- **Positron-emission tomography:** A detailed understanding of the angular distribution of photon pairs from the (e^- , e^+) annihilation determines the spatial resolution of tomography and the defect analysis of tissue and materials. A good quantitative understanding of this emission is relevant also for upcoming positron facilities, e.g. at the Lawrence Livermore National Laboratory.

Cross section for positron-bound-electron annihilation:

- **Differential cross section for positron-bound-electron annihilation:** The differential cross section for the annihilation of a positron with energy ε_i and velocity v_i by a bound electron with energy ε_a via the simultaneous emission of a photon pair is given (in relativistic units) by (Zaytsev *et al.*, 2019)

$$\frac{d^2 \sigma}{d \mathbf{k}_1 d \mathbf{k}_2} = 4 \alpha^2 \frac{(2\pi)^6}{v_i} |\mathcal{M}|^2 \delta(\varepsilon_a + \varepsilon_i - \omega_1 - \omega_2)$$

$$\mathcal{M} = - \sum_n \left(\frac{\langle (-p_i \mu_i) | \boldsymbol{\alpha} \cdot \mathbf{A}_{\mathbf{k}_2 \lambda_2}^* | n \rangle \langle n | \boldsymbol{\alpha} \cdot \mathbf{A}_{\mathbf{k}_1 \lambda_1}^* | a \rangle}{\varepsilon_a - \omega_1 - \varepsilon_n (1 - i 0)} + \frac{\langle (-p_i \mu_i) | \boldsymbol{\alpha} \cdot \mathbf{A}_{\mathbf{k}_1 \lambda_1}^* | n \rangle \langle n | \boldsymbol{\alpha} \cdot \mathbf{A}_{\mathbf{k}_2 \lambda_2}^* | a \rangle}{\varepsilon_a - \omega_2 - \varepsilon_n (1 - i 0)} \right)$$

Here, \sum_n implies the summation over the complete spectrum of the single electron, including the summation over the positive and negative parts of the continuum. μ_i is the helicity of the incident positron. Both, the double-differential cross section and the amplitude follow standard lines from the QED formalism.

- **Differential cross section for positron-bound-electron annihilation:** In practice, one typically needs to consider only the **double differential angular cross section**

$$\frac{d^2 \sigma}{d \Omega_1 d \Omega_2} = \int d\omega_1 d\omega_2 \omega_1^2 \omega_2^2 \frac{d^2 \sigma}{d \mathbf{k}_1 d \mathbf{k}_2},$$

and which needs to be further averaged over the angular momentum and spin projections of the bound electron and positron as well as (to be summed over) the polarization of the emitted photons.

:

➤

8.4.e. Positron-bound-electron pair production by a photon (PairProduction)

Process, notation & application:

- Positron-bound-electron pair production by a (single) photon of an atom or ion: $A^{q+} + \hbar\omega \rightarrow A^{(q-1)+*} + e^+$
- Quantum notations used in the formulas below: $|\alpha_i J_i\rangle + \hbar\omega(M) \rightarrow |\alpha_f J_f\rangle + |\varepsilon \kappa\rangle^+$
- At high photon energies, the electron-photon interaction can lead to the creation of an electron-positron from which the electron is eventually bound by a multiply or highly-charged ion.

8.4.f. Pair production in intense laser fields

Process, notation & application:

- Classical *versus* quantum electrodynamics: If quantum (field) theory is assumed to be *fundamental*, Maxwell's classical theory should be retained from QED in the limit $\hbar \rightarrow 0$. Indeed, various QED terms are suppressed parametrically with \hbar and were worked out in the 1930s by Heisenberg and Euler. These authors considered the effective self-interaction of a slowly varying electromagnetic field due to vacuum fluctuations of the electrons-positron field and derived non-linear coupling terms from this interaction. These coupling terms 'violate' the superposition principle of Maxwell's theory but are suppressed with inverse powers of the electron mass; cf. Karbstein and Mosman (2020).
- Critical fields of the quantum vacuum: In QED, the (self-) interaction of macroscopic electromagnetic fields scales inversely with powers of the critical electric and/or magnetic fields

$$\mathcal{E}^{(\text{critical})} = \frac{m^2 c^3}{e \hbar} \approx 1.3 \times 10^{18} \text{ V m}^{-1} \quad \text{critical electric field}$$

$$\mathcal{B}^{(\text{critical})} = \frac{\mathcal{E}^{(\text{critical})}}{c} \approx 4 \times 10^{19} \text{ T} \quad \text{critical magnetic field.}$$

So far, the strongest macroscopic fields in the laboratory at the peak intensity of high-intensity lasers amount to $\mathcal{E} \simeq \mathcal{O}(10^{14})$ V/m and $\mathcal{B} \simeq \mathcal{O}(10^6)$ T. Although these fields are clearly (very) weak, when compared to $\mathcal{E}^{(\text{critical})}$, $\mathcal{B}^{(\text{critical})}$, they might be sufficient to detect QED signatures of the quantum vacuum for the first time.

- **Locally constant-field approximation (LCFA):** The effective interaction of two (strong) laser fields is often based on the one-loop Heisenberg-Euler effective Lagrangian and treated within the LCFA. Such an approximation appears justified for weakly-varying electromagnetic fields with photon energies $\hbar\omega \ll mc^2$.
- **Photon-photon scattering:** Photon-photon scattering processes have generally (very) small cross sections and, up to the present, only an upper bound for these cross sections has been determined experimentally. Although some evidence for photon splitting has been seen at high photon energies, accurate measurements were found difficult due to the competition of other processes (Koga and Hayakawa, 2017). Photon merging has not (yet) been observed, despite of various proposals based on petawatt lasers and protons.

Signatures from the quantum vacuum in intense laser fields:

- **Quantum vacuum:** In strong contrast to the classical view, the quantum vacuum has a non-trivial structure. It refers to a complex state of matter, whose properties is determined by (so-called) quantum fluctuations. These fluctuations can be stimulated by different experimental means, including (strong) static or dynamic fields. In quantum field theory, for example, strong laser fields directly couple to the particle fields (via pair creation) and may give rise to ‘experimental signatures’ of the quantum vacuum. In the standard model, the leading contributions of the quantum-vacuum state to observations arise from the (effective) coupling of – either real or virtual – electromagnetic fields to the electron-positron pairs in the vacuum (Karbstein *et al.*, 2019).
- **Quantum vacuum:** In relativistic quantum field theory, a proper microscopic treatment of the light-matter interactions is by far non-trivial since quantum vacuum fluctuations effectively lead to various non-linear couplings among the electromagnetic fields. **For sufficient weak fields, when compared to the critical fields below, all leading signatures of the quantum vacuum arise from an effective four-photon coupling mediated by an electron-positron loop.**
- **Signatures from the quantum vacuum:** QED predicts various signatures due to non-linear photon-photon interactions or, more generally, due to coupling of the electromagnetic to the quantum matter fields. **Until the present, however, none of these signatures have been directly observed for macroscopically controlled fields** because of the strong suppression of these interactions. Indeed, these signatures from the (non-linearity of the) QED quantum vacuum are elusive in all experiments and have not been verified by observations with macroscopic fields so far (Karbstein *et al.*, 2019).
- **Vacuum birefringences:** To observe the birefringence of x-ray photons, a linearly-polarized probe photon beam could be sent through a strong-field (region) in order to observe scattered photons with perpendicular polarization. Obviously, however, the great majority of the incident x-ray photons will simply pass the strong-field region unaltered.

Effective interaction of the quantum vacuum with a macroscopic field:

- **One-loop Heisenberg-Euler (HE) Lagrangian:** In the Heaviside-Lorentz systems and by using natural units, the leading term of the Heisenberg-Euler Lagrangian is given by (Karbstein *et al.*, 2019)

$$\mathcal{L}^{(\text{HE: 1-loop})} \simeq \frac{m^4}{8\pi^2 45} \left(\frac{e}{m^2} \right)^4 [(\mathbf{B}^2 - \mathbf{E}^2)^2 + 7(\mathbf{B} \cdot \mathbf{E})^2].$$

This one-loop approach to the full photon-photon interaction is valid for $\mathcal{E} \ll \mathcal{E}^{(\text{critical})}$ and $\mathcal{B} \ll \mathcal{B}^{(\text{critical})}$ and should allow reliable predictions of **optical QED signatures from the quantum vacuum** at present-day laser facilities at the 1 %-level (Karbstein *et al.*, 2019).

- **Polarization and magnetization of the quantum vacuum:** Making use of the Heisenberg-Euler (HE) Lagrangian, the polarization \mathbf{P} and magnetization \mathbf{M} contributions to the electromagnetic field are defined as

$$\mathbf{P} = \frac{\partial \mathcal{L}^{(\text{HE: 1-loop})}}{\partial \mathbf{E}}, \quad \mathbf{M} = - \frac{\partial \mathcal{L}^{(\text{HE: 1-loop})}}{\partial \mathbf{B}}$$

- **Current density:** The 4-current density, that gives rise to a signature, is given by:

$$j_\mu(x) = 2 \frac{\partial^\alpha \mathcal{L}^{(\text{HE: 1-loop})}}{\partial F^{\alpha\mu}}.$$

8.4.g. Thomson scattering

Process, notation & application:

- **Thomson scattering** generally refers to the elastic scattering of photons by charged particles (electrons, nuclei, etc.). This elastic scattering is one of the most fundamental interaction processes in electrodynamics that frequently occurs in different laboratory and astrophysical sources of high-energy x-rays. While the *linear* Thomson scattering has been explored for many decades, the *nonlinear* Thomson scattering regime became accessible only recently due the development of high-intensity laser with sufficiently high electromagnetic field strengths.

- **Thomson scattering:** generally refers to the scattering of electromagnetic radiation by electrons in matter, and if described within a non-relativistic (or weakly-relativistic) regime (Crowley and Gregori, 2014). Beyond rather only a *qualitative* discussion, quite different contributions to this scattering must be distinguished explicitly. However, two well-known features of Thomson scattering are: (i) its sensitivity to correlation contributions among the electrons and (ii) that the polarization of the scattered radiation is mainly determined by the polarization of the incident radiation and the scattering angle. This second property arises from the weak coupling of the spatial and spin degrees of freedom within the nonrelativistic theory.
- **Role of normalized vector potential a_o :** In the (low-field) linear Thomson scattering regime ($a_o \ll 1$), the electrons oscillate non-relativistically along the field and scatter the light in the dipole-radiation pattern at the (same) frequency of the incident field. Modern, high-intensity lasers now support field strength upto $a_o \gtrsim 10 \gg 1$ in the nonlinear regime, in which the contribution of the electric and magnetic field to the (Lorentz) force become comparable.
- **Thomson scattering at fast electron beams:** Already in classical electrodynamics, Thomson scattering of short (laser) pulses at charged particles (electrons) gives rise to well-defined and readily tunable (monochromatic) x-ray beams. Hereby, the quasi-monochromatic scattering is closely related to the short wiggling period of the electrons in the incident laser pulses and, hence, to the pulse length itself. For a near head-on collision of a laser pulse with frequency ω with an relativistic electron bunch, the backscattered photons have the frequency

$$\omega' = \omega \frac{2(1 + \beta \cos \vartheta) \gamma^2}{1 + a_o^2/2 + \gamma^2 \vartheta_o^2} \approx \omega \frac{4 \gamma^2}{1 + a_o^2/2 + \gamma^2 \vartheta_o^2}$$

Here, a_o is the (frequency-) normalized vector potential, ϑ the interaction angle and ϑ_o the observation angle, both taken w.r.t. the velocity of the electron beam (quantization axis). As seen from this formula, the scattered radiation is monochromatic for well-collimated and monoenergetic electrons and laser beams, a (normalized) field strength $a_o \ll 1$ and a small observation area (for instance, purely back-scattered light).

- **Relativistic quiver motion of electrons in intense fields:** In the relativistic regime, the electrons follow a [figure-8 motion that is analogue to the electromagnetic wiggler motion at synchrotrons](#). This quiver motion of the electron also leads to a [red-shift of the scattered photon \(spectrum\)](#) as predicted by classical electrodynamics for an incident field of frequency ω , $\omega' = \omega (1 + a_o^2/2)$, as well as to elliptically-scattered multipole-radiation pattern. In most experiments, this red-shift is more than compensated by the (double) Doppler up-shift $\omega'' \approx 4\gamma\omega'^2$, where γ refers to the relativistic Lorentz factor of the electrons.
- **Number of back-scattered photons per pulse-collision:** For an head-on collision of an electron bunch with N_e electrons and (intense) laser

8. Atomic processes

pulse of N_c cycles, the number of back-scattered photons is approximately given by (Khrennikov *et al.*, 2015)

$$N' = \frac{\pi \alpha N_c N_e a_o^2}{3 \langle n \rangle} \left[\frac{1 - \beta}{1 + \beta} + \frac{a_o^2 (1 - \beta)}{4 \gamma^2 (1 + \beta)^2} \right],$$

and where $\langle n \rangle$ is the averaged number of scattered photons per electron (harmonic number); this number strongly depends on the intensity of the incident laser pulse.

- **Expansion opacity:** In expanding (or contracting) objects, the absorption of spectral lines can be more efficient than in static environments (Karp *et al.*, 1977). In these objects, the frequency of the propagating photons are continuously red-shifted (Doppler shifted) relative to the rest frame of the expanding gas due to the velocity gradient in the medium. Any given photon therefore appears more and more red-shifted as it travels through the medium, and gives rise to an effective increase of the opacity of the gas. This is quite analogue to the red-shift of photons in the expanding Universe. The changes of the opacity due to the expansion (contraction) of the medium can be accounted for by the **expansion opacity**, which is a function of the temperature, density and the velocity gradient of the plasma. In short, each photon has an increased probability of interacting with a given line by passing through the medium.
- **Red-shifted photons in expanding objects:** In optically thick supernova shells, the red-shift of photons has been found important for both, the increase of the total opacity and as well as for maintaining the radiation in an thermal equilibrium (Karp *et al.*, 1977). The increase of the opacity can range from $\lesssim 1\%$ to more than an order of magnitude. The detailed size of the opacity depends of course on the temperature, density, and velocity gradient.
- **Thomson scattering process:** The process can be described (to a large extent) either in classical ED or quantum ED, and often with very similar resultss. Prunty (2014) provides a pedagogical eleborate and very careful treatment of the Thomson scattering from the viewpoint of classical ED. The quantum description then leads in a natural way also to the **Compton effect**, which is considered to be negligible at classical (non-relativistic) wavelength of the incident light. In classical ED, moreover, the Thomson scattering process is first of all an *incoherent* process due to the elastic scattering light of light from different charges.
- **Thomson scattering of light in high-temperature plasmas:** Thomson scattering of light frequently occurs in high-temperature plasmas as generated by modern experiments. In such high-temperature plasmas, the strength of the scattered signal provides information on the electron density, while the width of the scattered spectrum provides information on the plasma temperature. In high-temperature plasmas, the electrons move with a substantial fraction of the speed of light and, hence, the scattering of light has to be treated *relativistically*. Both the relativistic theory and computations are then lengthy but may give rise to subtle differences.
- **Applications of Thomson scattering:** This process can be utilized for the diagnostics of high-temperature plasmas in magnetic fusion and for high-density plasmas in inertial confinement fusion. It also help develop a **new class of accelerator-driven x-ray** (so-called Thomson or Compton) sources that are suitable for nuclear-physics studies and highly-charged ions.

- **Application of Thomson scattering:** This scattering process is a powerful and *non-perturbing* diagnostic technique in plasma physics research that provides information on the electron (or ion) density and the electron (or ion) velocity distribution (and hence, temperature). Usually, a high-intensity monochromatic light beam (from a high-power Q-switched laser beam) passes through a plasma and enforces the (quasi-) free electrons near to the laser focus to oscillate at the incident laser frequency. This oscillation then causes the electrons to emit dipole radiation that can be recorded and analysed. In these recorded spectra, the Doppler-shifted laser frequencies, if integrated over all scattered wavelength, is proportional to the electron density and the width of the Doppler-broadened provides information on the electron temperature. Indeed, the Thomson scattering diagnostic has been found as an important diagnostic tool since it provides a direct handle on the evolution of the plasma. However, because of the intrinsic small scattering cross-section, Thomson scattering diagnostics has become feasible with the development of short-pulse, high-power plasma.

Nonlinear Thomson scattering:

- **High-order multiphoton Thomson scattering:** A high-intensity laser field enables the electron to scatter simultaneously multiple photons into a single high-energy photon with (harmonic) frequency $\omega' = n \omega$. Here, n refers to both, the order of the (non-linear) interaction and to the number of incident photons scattered per electron.

8.5. Other topics related to atomic processes

8.5.a. Atomic databases from the literature

CHIANTI: A database for emission lines:

- CHIANTI is a database of assessed atomic parameters and transition rates that are required and utilized for the simulation of line and continuum emission spectra from optically thin and collisionally-dominated plasma.
- CHIANTI was first released in 1996 and, since then, several new up-dates have been made available in order to expand the database and improve the quality of the data. Emphasis in developing this database has been given especially to the line identification and improvement of the reference wavelengths.
- For several ions, the wavelengths and identifications from CHIANTI are different from and considered to be more accurate than those of the NIST database. Therefore, CHIANTI is now often applied as a reference atomic database for ions and has been included into several other atomic codes and packages.
- In its last version (Del Zanna *et al.*, 2015), the CHIANTI database includes a large amount of new data which improve simulations for the soft x-ray, extreme UV (EUV) as well as UV spectral regions. These regions are currently covered by several space missions.

DREAM: A database for lanthanide spectra:

- **DREAM database** The Mons group (Biemont and coworkers) have calculated various neutral and near-neutral lanthanide spectra; these data are kept within the DREAM database. In these computations, they employed the least-squares fitting procedure in the Cowan code (Cowan 1981) together with a core-polarization potential in order to obtain spectroscopic quality radiative rates.

NIST-ESTAR:

- The ESTAR database provides (electron) stopping powers and ranges for incident electrons with energies between 10 keV and 1 GeV, and as derived from the so-called ICRU Report (Amako *et al.*, 2005). In particular, the associated ESTAR web-interface computes stopping power, density effect parameters, range, and radiation yield tables for electrons in various materials.
- **Collision stopping powers:** In the ESTAR database, such stopping powers have been calculated with Bethe's theory and by applying Sternheimer's correction due to density effects of the materials.

- **Radiative stopping powers:** Radiative stopping powers are evaluated in the ESTAR database by means of theoretical Bremsstrahlung cross sections. While reasonably accurate numerical stopping powers were calculated just below 2 MeV, an approximate high-energy formula has been applied above 50 MeV.
- The user can select a material and (a range of) energies [in MeV] between 0.001 MeV to 10000 MeV.

NIST-PSTAR:

- The PSTAR and ASTAR databases provide (proton) stopping powers and ranges for incident protons with energies between 1 keV – 10 GeV; they were derived from the so-called ICRU Report 49.
- The user can (again) select a material and (a range of) energies [in MeV] between 0.001 MeV to 10000 MeV.

NIST-XCOM:

- The XCOM database provides photon scattering data and attenuation coefficients between 1 keV and 100 GeV for all the elements of the periodic table. It also lists total cross sections, attenuation coefficients and partial interaction coefficients for selected processes, such as Compton and Rayleigh scattering, photoelectric absorption as well as pair production (Amako *et al.*, 2005).

8.5.b. Codes from astro and plasma physics that require atomic data input

AtomDB:

- **ATOMDB** is an atomic database and program environment for X-ray plasma spectral modeling. Its current version is primarily used for modeling the x-ray emission from collisional plasmas of hot electrons in collision with astrophysically abundant elements and ions. ATOMDB has been found useful also to model the absorption by elements and ions or even photoionized plasmas, if x-ray photons (often from a simple power-law source) interact with elements and ions and lead to quite complex spectra.
- ATOMDB calculates the x-ray/UV spectrum of a hot, collisionally-dominated optically-thin plasma, based on knowledge of the atomic transition rates and energies of the involved ions. This code also help analyse the interplay between the different rates. The line and continuum results of ATOMDB (<http://www.atomdb.org>) apply to an **optically-thin thermal plasma with astronomical abundances**; cf. Anders and Grevesse (1989).

8. Atomic processes

- ATOMDB aims for to incorporate all relevant data, generated both from theoretical models and experiment, and to evaluate these data quite critically. Each revision of the critically evaluated database is given a version number to aid reference.
- ATOMDB provides improved spectral modeling capability by making use of additional emission lines as well as of accurate wavelengths for most strong x-ray transitions. These improvements refer to the x-ray grating data analysis and to improve the knowledge about spectra at moderate (CCD) resolution.

CLOUDY:

- **CLOUDY** is an open-source, spectral synthesis code in order simulate interstellar matter under a broad range of conditions. In particular, it simulates astronomical clouds and their spectra.
- Astrophysical (spectral) observation can be used to directly measure the temperature, density, pressure or composition of a cloud of gas or a star, using a telescope and a spectrometer. Since the spectra are formed in highly non-equilibrium gas and dust, numerical simulations are generally required in order simulate the spectra.
- CLOUDY is a code that computes the ionization, chemistry, radiation transport, and dynamics simultaneously and self consistently, based on a good deal of atomic and molecular data.

FLYCHK and GALAXY:

- FLYCHK uses a hydrogenic approximation in order to calculate energy levels and level populations in plasma. However, the results of GALAXY and FLYCHK largely deviate from measured ones.
- FLYCHK is based on the K-shell spectroscopy code FLY and has bee developed in order to study hot dense plasmas. Its ease of use for the simulation of synthetic spectral has made the code attractive to both experimentalists and modelers. The goal of FLYCHK is to provide a simple and general capability for a wider range of plasmas. In practice, unfortunately, benchmark experiments or calculations are quite scarce and the limitations and validity ranges of FLYCHK are not well known.
- GALAXY employs an average-of-configuration approximation for the electronic states as well as screened hydrogenic wave functions for both, the collisional and radiative processes. This code also employes Hartree-Dirac-Slater or Kramers cross-sections for photoionization.

LTE:

- **LTE code:** This code applies the Boltzmann and Saha equations in order to obtain the ionization and excitation state of each element. It assumes a local thermodynamic equilibrium and that all scattering processes are negligible.

- The LTE code often applies atomic data from NIST to determine the relative strengths of the lines.

MOOG:

- **MOOG code:** This code generates synthetic absorption spectra of photospheres in cool stars by assuming a local thermodynamic equilibrium. It requires an (externally given) model atmosphere in order to derive the temperature, gas pressure and electron density at different layers of the surface gas. The code also requires an atomic line list that comprises all data about the absorption transitions (at rest), oscillator strength as well as excitation (ionization) energies of the lower levels for the element or ion of interest.
- In the MOOG code, the strengths of the observed absorption features are obtained by solving the radiative transfer equations with a plane-like parallel treatment of the atmosphere, and where the velocity distribution of the ions is assumed to be Maxwellian. Moreover, the excitation and ionization processes of the ions in selective charge states are described by the Boltzmann and Saha equations.
- The MOOG code has often been applied with Kurucz' model atmosphere and with data from the NIST data base.
- **MOOG:** This code help perform a variety of LTE line analysis and spectrum synthesis tasks. In particular, MOOG assists to determine the chemical composition of a star. The implementation of MOOG hereby follows an earlier formulation of the line analysis by Edmonds, Jr. (1969, JQSRT).

RCF:

- **Radiative-Collisional code based on FAC, RCF:** This code has been used to simulate steady-state plasmas under non-local thermodynamic equilibrium condition, and especially for photoionization-dominated plasmas. RCF takes almost all of the radiative and collisional atomic processes into account by rate equations in order to interpret the plasmas systematically. The Flexible Atomic Code (FAC) supplies all the atomic data that are needed for RCF in order to ensures completeness and consistency of the atomic data.
- **RCF** is a steady-state, collisional-radiative, optically thin model. Its rate-equation

$$\frac{dN_{i,j}}{dt} = \text{populating processes} - \text{depopulating processes} = 0$$

where $N_{i,j}$ is the density of the j-th level in the i-th charge state. RCF includes ionization and recombination between neighboring charge states as well as the excitation and de-excitation within the same charge state.

TARDIS:

- **TARDIS code:** This is an open-source Monte Carlo radiative-transfer spectral synthesis code for 1D models of supernova ejecta. It has been designed for rapid spectral modelling of supernovae, cf. <https://tardis-sn.github.io/tardis/>
- **Radiative transfer** generally describes how the properties of the electromagnetic radiation field change as it passes through an ambient material. Because of the many and complex interactions of the photons with the matter (clouds), radiative transfer need to be studies numerically. Although different numerical techniques are available, Monte Carlo techniques have become a successful and elegant tool particularly for radiative transfer problems in supernovae.
- **Monte-Carlo Radiative Transfer** methods are probabilistic techniques that follows the interaction of individual photons in propagating through an ambient material. In particular, a quite large number of representative ‘machine photons’ are solved in a stochastic process.

XSTAR:

- **XSTAR (Mendoza *et al.*, 2021):** This code derives the emission spectra of a photoionized gas for given astrophysical conditions and for a (given) set of atomic data. It assumes an ionizing radiation source of predefined strength, which is surrounded by a spherical gas shell and which absorbs and modifies the radiation to finally emit an EUV and x-ray spectrum.
- XSTAR is a command-driven, interactive, computer program for calculating the physical conditions and emission spectra of photoionized gases; cf. <http://ascl.net/9910.008>. It may be applied in a wide variety of astrophysical contexts. In particular, XSTAR computes the re-radiated light when the gas of a star absorbs energy.
- **Features of the XSTAR code:** This code computes the ionization balance, level population and temperature of the gas shell and, hence, help draw conclusions about the mean opacities of the gas shell as well as the line spectrum of radiation.
- **Applications of XSTAR:** An recent update of this software was made for modeling the x-ray spectra of XRISM and ATHENA which will be launched in forthcoming years. Further work is needed to understand of whether the completeness and accuracy of the given atomic data is good enough in order to support the high resolution and microcalorimeter-based spectrometers aboard on these new x-ray space telescopes.
- **Atomic data for the XSTAR modeling code:** Palmeri *et al.* (2008) provide a set of atomic data to improve the data base and to support the computation of photoabsorption cross sections and for which radiative and Auger processes are key contributions. This work also includes a number of tables suitable for comparing radiative and Auger energies, lifetimes, etc. from current calcuations of JAC with previous computations and experiment.

Further codes:

- In PHICRE, the energy levels and spontaneous decay rates are taken from the NIST database, and other rate coefficients are calculated by widely used formulas.
- **CRMODEL code:** This code by Hartgers *et al.* (2001) support a variety of plasmas that consist out of just a single atomic species but with any (finite) number of excited states between the ground level and the ionization threshold of the ion. The code assumes however that the density of all excited states remains small when compared to the ground-state density. The flexibility of this code makes it useful to investigate the effects of different cross section expressions.
- **STiC:** de la Cruz Rodríguez *et al.*(2019) present and discuss the STockholm inversion COde (STiC) that enables one to model the spectral lines from different atoms simultaneously. It is based on partial redistribution effects (PRD) of scattered photons in angle and frequency as well as a so-called Levenberg-Marquardt algorithm. Until the present, however, it remains pretty unclear to which extent such a code might benefit from a good set of atomic data.
- **NESSY:** The NLTE Spectral SYnthesis code (NESSY) code supports the computation of synthetic spectra for various solar regions, such as quiet and magnetically-dominated regions and domains of magnetically-driven variability. NESSY has been built upon the COde for Solar Irradiance (COSI) and can now be utilized for modeling of the entire — UV-, visible-, IR and radio — spectra of solar and stellar regions; moreover, this code is considered to be substantially faster than COSI and allows for reliable calculation of the entire solar spectrum (Tagirov *et al.*, 2017).
- **SNEC code:** The SuperNova Explosion Code (SNEC) is a spherically symmetric 1D Lagrangian radiation–hydrodynamics code that has been applied to simulate core-collapse supernova explosions and to generate synthetic color light curves (Wu *et al.*, 2022). The SNEC code makes use of an equation of state based on different contributions from ions, electrons and radiation. In these simulations, the ion balance is based on the Saha equations.

8.5.c. Electro-magnetic transients & light curves from astrophysical matter clouds

Observation from astrophysical matter clouds:

- **Light curves from stars & temperature:** The light observed from a star typically originates from its atmosphere, i.e. a gas layer that surrounds some (more or less) opaque interior. In equilibrium, the photons from this atmosphere carry away (i) the gravitational energy

8. Atomic processes

that is released by the collapse of the matter cloud; (ii) the energy released from the thermonuclear reaction within the core of the star as well as (iii) the released cooling energy of, for instance, white dwarfs, once the thermonuclear reactions has stopped (Pettini 2018).

- **δ Cephei stars:** The so-called β -Cephei stars are hot blue-white stars of spectral class B. These stars have masses of $8 \dots 20 M_{\odot}$ and their magnitude ranges from +3.16 to +3.27. These stars pulsate through the (so-called) κ mechanism that is related to the M-shell transitions of these elements. The Cepheid stars are known to be used in order to estimate stellar distances. These distances are now better understood after the opacities were revised by about a factor two for various species of atomic number $Z > 2$, and as confirmed also by recent measurements of absorption coefficients. The opacities of the iron group elements (Cr, Fe, Ni and Cu) for $T \approx 2 - 3 \times 10^5$ K and $\rho = 10^{-7} \dots 10^{-6}$ g/cm³ have been found important for analyzing these stars.
- **Local Thermodynamic Equilibrium (LTE):** Despite the complexity of (and complications with) astrophysical plasma, one makes often use of the LTE approximation as long as the mean free path of the photons and particles is small compared to the scale over which the temperature changes significantly. This applies for instance to many stellar interiors because of the high density and temperature and, hence, quite small mean distances between collisions.

Temperature of stars in astrophysical matter clouds:

- **Temperature of stars:** The temperature can be defined in various different ways, namely as (Pettini 2018):
 1. **Effective temperature:** as defined in terms of the luminosity of the star and its radius;
 2. **Excitation temperature:** as given by the relative population of different excited levels of an atom or ion in the plasma, and by using Boltzmann's equation;
 3. **Ionization temperature:** as defined by the relative population of different ionisation stages of an atom, and by using Saha's equation;
 4. **Kinetic temperature:** as defined by the Maxwell-Boltzmann distribution:

$$n_v dv = n \left(\frac{m}{2\pi kT} \right)^{3/2} e^{-mv^2/2kT} 4\pi v^2 dv$$

with the number density n_v (number of particles per unit volume) of particles with speeds between $v \dots v + dv$ and the total number density n of all particles with the given mass m ;

- 5. **Color temperature:** as the temperature of the blackbody whose spectral energy distribution resembles most closely that of the given star.

Photoionized, steady-state plasma:

- **Calculation of ion distributions:** The standard method for calculating the ion distribution in a non-LTE system is to solve the rate equations for all the important ionic states and by including different excitation and ionization channels due to the incident radiation. From the solutions of these rate equations, a time history of the electron temperature and density as well as the time evolution of the different charge states in the plasma can be evaluated. The **steady-state solution** is then obtained by following the time evolution until the populations do no longer change with time.
- **Calculation of ion distributions:** In non-LTE plasma, a major simplification in the calculation of ion distributions is achieved if only the shell populations is taken into account within the **average-atom model**. In this model, the shell distribution is averaged over the distribution of the ionic states. Indeed, this approach reduces the number of differential equations significantly, when compared to a detailed treatment of all charge states, although the shell occupancies are non-integers in the average-atom model.
- **Calculation of ion distributions:** The photoexcitation and photoionization as well as their inverse rates are often approximated by Kramers' (1923) simple expressions, convolved with the intensity of the ambient radiation field.

Need of astrophysical opacities:

- **Applications of opacity calculations:** Three typical example applications for opacity calculations are: (i) The iron opacities at conditions of the solar convection zone, (ii) nickel opacities for modeling various stellar envelopes, and (iii) the samarium opacities for the modeling of light curves as produced by neutron star mergers.
- **Frequency-dependent opacity:** In recent work, the frequency-dependent LTE opacity of iron has been studied for the conditions of the solar convection zone. These studies revealed rather large (30–400%) differences between experiment and theory for the monochromatic opacity of an neon-like iron plasma (or nearby charge states). Until the present, the source of this not yet fully understood and remains an active area of research.

Gravitational-wave astronomy:

- **Discovery of gravitational waves (GW):** The discovery of GW from the inspiral and coalescence of binary black holes (BH) and/or neutron stars (NS) by the Laser Interferometer Gravitational Wave Observatory (LIGO) has opened a new window on the cosmos.

8. Atomic processes

- **Discovery of gravitational waves (GW):** The discovery of electromagnetic signals in coincidence with a chirp at the gravitational-wave detectors leads to a better location and a much richer picture about the initially merger process. This may allow to extract directly information on the formation of the binary channels, the age of the stellar population as well as the dynamics of binary mergers.
- **Merger of black-hole binaries:** In general, the merger of BH binaries is not expected to produce luminous electro-magnetic emission because there is not enough baryonic matter in these systems.
- **Gravitational-wave (GW) astronomy:** The direct detection of GW opened a new era of (GW) astronomy. To further understand the astrophysical nature of GW sources, the **identification of their electromagnetic (EM) counterparts is crucial, since the GW detectors are generally not accurate enough to pin down the position of these GW sources.**
- **Sources of gravitational waves (GW):** Despite of a rather large number of expected BH-BH mergers during the next few years, a better synthesis and analysis of gravitational wave and the associated electro-magnetic signals will probably come from NS-NS or BH-NS mergers, i.e. if neutron stars are involved.
- **Sources of gravitational waves (GW):** While most detected GW sources are nowadays believed to arise from black-hole binaries, neutron star mergers are another major source of gravitational waves. **For these NS mergers, an electro-magnetic signal is expected to arise in two forms: gamma-ray bursts (GRB) or from kilonovae (Metzger *et al.*, 2010).** The GRB are expected to be short-lived with a jet-type signal, while the kilonovae are predicted to generate relatively isotropic signals.
- **Sources of gravitational waves:** In practice, it is not easy to precisely locate the sky position of GW sources since it needs to be determined by triangulation, i.e. from the arrival times of the GW signals at different detectors. At present, the uncertainties in this triangulation are quite large, although these uncertainties will be reduced to $\approx 10 - 100 \text{ deg}^2$, once Virgo in Italy and, eventually, KAGRA in Japan and LIGO-India will join the network (Metzger 2017). Initially, these uncertainties were $\approx 850 \text{ deg}^2$ for GW15091 and with a later improvement to $\approx 250 \text{ deg}^2$.
- **Sources of gravitational waves:** Even an localisation of the GW signals within $10 - 100 \text{ deg}^2$ greatly exceeds the fields of view of most radio, optical and x-ray telescopes, and in particular the field of view of those telescopes that are sensitive enough to detect the electro-magnetic counterparts of NS-NS and BH-NS mergers.
- **γ -ray bursts (GRB):** Although short GRB are (very) bright and high-energetic events, only a subset of these bursts will be observed on Earth since the most intense emission from a given merger will typically not intersect the line of sight from the Earth.
- **γ -ray bursts (GRB):** Short GRB are commonly believed to be powered by the accretion of a massive remnant disk, following some BH and/or NS mergers. These GRB are typically expected to occur already within seconds of the GW chirp, providing an unambiguous temporal signature to the GW signal. Although such short GRB are likely the cleanest electro-magnetic counterparts to the GW signals,

their measured rate will remain low within the Advanced LIGO detection volume. This rate is probably less than one observable event per year if the GW signal arises from NS-NS mergers since the γ -ray emission is beamed into a narrow solid angle not seen from Earth (Metzger 2017).

- **Electro-magnetic counterparts of GW:** NS-NS and BH-NS mergers are also predicted to be accompanied by a more isotropic counterpart, commonly known as kilonovae. These kilonovae provide both a robust electro-magnetic counterpart to the GW chirp, and which is expected to accompany a good fraction of BH-NS mergers and essentially all NS-NS mergers (Metzger 2017).
- **Sources of gravitational waves:** The single NS-NS merger event (GW170817, GRB170817A, AT2017gfo) made a big qualitative step for gravitational-wave astronomy since it showed that these mergers can be observed and are directly linked to gravitational waves, gamma-ray bursts, kilonovae as well as the generation of heavy elements (nucleosynthesis).
- **Role of opacity for light curves:** The electromagnetic signal from kilonova arises from the radioactive decay of (freshly) synthesized nuclei. However, the luminosity, color and spectral distribution of the observed signals strongly depend on the (atomic) opacities of the produced elements, involved in the plasma. For the electromagnetic signal from neutron-star mergers, in particular, the opacities of the lanthanide and actinide elements have attracted recent interest owing to their large density of bound-bound transitions.
- **Role of neutrinos for neutron-star mergers:** The absorption of neutrinos can make the ejected material from neutron-star mergers less neutron-rich and can increase the so-called **electron fraction Y_e** , e.g. the number of protons per nucleon.
- **Simulation of neutron-star mergers:** While different (relativistic) simulations of NS mergers have predicted a wide ranges of electron fractions $Y_e = 0.05, \dots, 0.45$, although a detailed understanding of the electron distribution depends on the nuclear equations of state as well as the masses and mass ratio of the neutron stars. For the sake of simplicity, a flat mass distribution and an electron fraction $Y_e = 0.1, \dots, 0.4$ are assumed to represent dynamical ejecta.
- **Spectra from AT2017gfo:** A series of spectra have been observed from this merger has enabled one to analyze the evolution of the kilonova's primary electromagnetic output from 1.5 days until 10 days after the event (Watson *et al.*, 2019). It is expected from rather simple estimates that a large number of moderate-to-weak lanthanide lines with unknown oscillator strengths dominate the observed spectra. For a spherically expanding ejecta, the line broadening should be then comparable to the expansion velocity of the gas. However, a more detailed analysis will require also additional knowledge about the geometry of the gas cloud and the wavelength-dependent opacities over a wide range of elements.
- **GW170817 and AT2017gfo event:** The electromagnetic event AT2017gfo was observed in August 2017 following the detection of gravitational waves from a neutron star merger by the LIGO-Virgo experiment (GW170817). This electromagnetic signal exhibits a number of unique characteristics that differ from other transient observation with regard to its unusually high optical brightness in the days following the explosion as well as a long-lived infrared emission, which lasted nearly two weeks.

8. Atomic processes

- **Sources of gravitational waves:** The discovery of a kilonova in coincidence with a gravitational-wave signal from a binary neutron-star merger *and* with a short burst of γ -rays provides **striking evidence for the main theoretical picture of neutron-star mergers**. In particular, these detections confirm that binary neutron-star mergers produce kilonovae with emission properties in reasonable agreement with theoretical predictions.
- **Orbit of compact binary systems:** The orbit of compact systems, such as NS-NS and NS-BH, decreases steadily due to the emission of gravitational waves.

Modeling of kilonovae:

- **Modeling of kilonovae:** Until the present, local thermodynamic equilibrium (LTE) conditions are typically assumed for modeling kilonovae. In practice, however, such a LTE seem to be oversimplified in view of the internal dynamics and the transient nature of all merger events. For any reliable non-equilibrium modeling, a large number of atomic data is needed that cannot so easily (if at all) be calculated for medium and heavy elements, including those of practical interest.
- **Kilonova emission:** Although kilonovae seem first of all to arise from the merger of compact NS-NS systems, other observations indicate a rather large variability between different kilonova events that is not yet fully understood. Kilonovae are assumed to be powered by the radioactive decay of r-process elements that are synthesized in the ejecta. Therefore, the variability between different kilonova events may arise from either viewing angle or other differences in the composition of the NS-NS and NS-BH compact systems. Eventually, the kilonova emission is generated by the expanding cloud of radioactive ejecta, similar as for Type Ia (thermo-nuclear) supernovae. Indeed, quite similar arguments as for supernovae have been used in order estimate the emitted light curves from kilonovae. For different matter compositions, opacities between $1..50 \text{ cm}^2/g$ are typically expected.
- **Light curves from kilonovae:** The light curves of several kilonovae emissions show broad features that have been modeled by means of simple, single-zone (semi-analytical) models. In these models, effective grey opacities and heating rates are usually applied.

Element identification from light curves:

- **Element identification from light curves:** Difficulties with the identification of *r*-process elements arise from the large expansion velocities, the large number and incomplete knowledge of atomic lines for open-shell atoms as well as a severe line blending.
- **Element identification from light curves:** Until the present, only strontium (Sr) has been identified tentatively from kilonovae light curves, although nuclear network calculations also suggest similar features in the light curve for the elements platinum (Pt) and gold (Au). Overall the modeling of these spectra depend on (too) many parameters that are all rather weakly understood.

- **Light emission from neutron star mergers:** Watson *et al.* (2019) have analysed the light curves from GW170817 under the assumption that the ejecta can be modeled as a single-temperature blackbody and by including a selected number of atomic lines. These lines are responsible for the structure in the light curves during the ~ 1 to 5 days after the event. From their analysis, they concluded that some central part of the spectrum is consistent with the P Cygni profile as it is produced by Sr II doublet lines at 4078, 4215 Å and a triplet at 10327, 10037, 10915 Å. The reasoning of the paper by Watson *et al.* (2019) remains however unclear from an atomic physics viewpoint.

Neutron-star merger:

- **Neutron star merger:** In 2017, the LIGO/Virgo collaboration detected the first gravitational-wave signal due to the merger of a neutron-star binary system. Less than two seconds after this signal, several telescopes detected first a short gamma-ray burst and later a rather long optical ‘afterglow’. This afterglow is likely powered by the radioactive decay of the (very) neutron-rich material that is created and ejected during the merger: **The observed light curves from such a (radioactive) decay and afterglow is known also as kilonova.**
- **Opacities for ejecta from neutron-star mergers:** At the near-IR/optical frequencies, the dominant source of opacity arises from the many bound-bound transitions between the low-lying levels of the atoms and ions. **For this continuum of lines, the opacity is determined by the strength and wavelength density of all lines,** and which depend sensitively on the composition of the ejecta.
- **Opacities for ejecta from neutron-star mergers:** The opacity of the ejecta from NS mergers can significantly rise if they just contain a modest fraction of elements with a partially-filled *f*-shell, such as the elements from the lanthanide and actinide groups.
- **Plasma of neutron-star mergers:** Because of the rather cold (~ 1 eV) conditions in the plasma of a neutron-star merger, it is typically sufficient to include a small number of low-lying configurations for each ion stage in order to obtain a **converged set of fine-structure level populations, making use of a local-temperature equilibrium Saha-Boltzmann statistics.** Fontes *et al.* (2015) used such a small number of configurations and generated about 10^5 levels and 3.3×10^8 lines.
- **Plasma of neutron-star mergers:** Results from a multi-dimensional ray-trace merger calculation for neutron-star ejecta suggest that the radioactively-powered heavy materials are more difficult to observe in the r-process, than it was previously believed (Fontes *et al.*, 2017).
- **Opacities of ejecta from neutron-star mergers:** At rather low plasma temperatures $T \lesssim 103$ K of the neutron-star ejecta, a further uncertainty arise from a improved treatment of the (initially) gaseous to a solid-state phase. Until the present, **it remains unclear whether such r-process dust then increases or decreases the optical/UV opacity** as this will depend how the dust condenses and how quickly it grows in size.
- **Light emission from neutron-star mergers:** The light emission from the ejecta of neutron star mergers strongly depends on the ejecta material. Therefore, Tanaka *et al.* (2018) performed limited atomic structure calculations for the r-process elements: Se ($Z = 34$), Ru

8. Atomic processes

($Z = 44$), Te ($Z = 52$), Ba ($Z = 56$), Nd ($Z = 60$) and Er ($Z = 68$). These computations confirmed, in particular, that the bound-bound (expansion) opacities of the two lanthanides Nd and Er with an open f -shell are significantly larger than those of the mid- Z elements over a rather wide range of wavelengths. These authors focused especially on neutral atoms as well as on singly- and doubly-ionized ions which are expected to be most common at $t = 1$ day after the merger.

- **Opacities for neutron-star mergers:** Because of the lack of atomic data for the r-process elements, one has often just applied the opacities of iron in order to simulate neutron-star mergers. However, in order to predict the emission properties of kilonova, (more) systematic atomic data for r-process elements are highly desirable.
- **Neutron capture processes:** For all elements heavier than iron, their production mechanisms have been explored for several decades already. This mechanism includes various slow and rapid neutron capture processes, known as s- and r-processes, in dependence of the neutron density in the given astrophysical environment. While the s-process is known to occur especially in the asymptotic giant branch (AGB) stars, the astrophysical sites of the r-process are less explored. There is some evidence that the r-process occurs after (gravitational) merger events.
- **Neutron stars:** These stars have been postulated already short after the discovery of the neutron as the **ultimate fate of massive stars which end in a supernova**. The existence of neutron stars was later shown in the 1960s following the observation of the first pulsars.
- **Distribution of neutron star masses:** Today, the equation of state and the distribution of neutron star masses are believed to be known reasonably well.
- **Material ejected from neutron-star mergers:** The material that is ejected during or immediately after the merger of two neutron stars may produce considerable amounts of heavy elements through the r -process. The subsequent radioactive decay of these (neutron-rich) nuclei can power transient electromagnetic emission similar to, but significantly dimmer than, an ordinary supernova (Kasen *et al.*, 2013). One goal of future observations of the electro-magnetic transients in gravitational-wave astronomy is to better understand the r -process and, hence, the astrophysical sources of gravitational waves.
- **Material ejected from neutron-star mergers:** A key in studying the matter outside of the remnant of the neutron-star merger is the release of neutron rich-matter and the cascade of nuclear reactions. These nuclear reaction gives then rise to **kilonova which can be observed on the time scale of hours, days and even months due to the radioactive decay of freshly synthesized, neutron-rich elements in the ejected matter**.
- **Mass of ejecta from neutron-star mergers:** This mass is predicted to be rather high and to reach from $10^{-3} \dots 10^{-2} M_{\odot}$ for the overall r-process matter.
- **Light curves from neutron-star mergers:** Since very little is known about the optical properties of the heavy r -process elements, most previous light-curve models have adopted the opacities from the iron group elements. Barnes and Kasen (2013) considered first the

opacities of lanthanides and concluded, that the opacity of the ejecta material from neutron-star mergers might be larger by several orders of magnitude. In further detail, Barnes and Kasen included these opacities into time-dependent, multi-wavelength radiative transport calculations in order to predict the broadband light curves for a range of masses and velocities of the ejecta.

- **Light curves from neutron-star mergers:** In neutron-star mergers, the light curves usually decline rapidly in the *optical* region, while they evolve more slowly in the *near-infrared* (NIR) region. Moreover, a high expansion velocity is expected if featureless spectra are observed.
- **Neutron star merger:** These mergers may give rise to both, short-duration gamma-ray bursts as well as the production of *r*-process elements in the universe.
- **Light curves from neutron-star mergers:** One current question about neutron-star merger is of whether the emitted electro-magnetic radiation can be observed in the optical or infrared bands. In order to model the light curves and spectra produced by NS merger, it appears necessary to calculate the radiative opacities from heavy elements, such as the lanthanides. These elements are expected to be present due to the capture of rapid neutrons during the r-process.
- **Simulation of neutron-star mergers:** Metzger (2017) introduces a [vanilla model of lanthanide-rich ejecta](#) that is heated by radioactivity in a week-long transient state of the ejecta from the merger process. This transient matter state may lead to the emission of optical (blue) light due to basically Lanthanide-free components of the ejecta or, possibly, to an early UV-bright [precursor that is powered by the decay of free neutrons in the outermost layers of the ejecta](#) (Metzger 2017).
- **Numerical simulations of neutron-star mergers:** Such simulations are often considered as a cornerstone for understanding the multi-messenger signatures and nucleosynthesis in the ejecta of neutron-star mergers.
- **Binary neutron-star mergers:** These binary neutron-star mergers are excellent examples of multi-physics problems that combine knowledge and data from strong-field gravity, strongly interacting matter, relativistic (magneto-) hydrodynamics and neutrino transport (Arcavi *et al.*, 2018).
- **Nuclear reactions in neutron-star mergers:** The high neutron densities in ejected NS mergers permit a violent r-process, leading to a fission cycle that produces very heavy nuclei in regions far from (nuclear) stability.
- **Spectrum of AT2017gfo:** A few days after the merger, the emission and absorption features in the spectrum of AT2017gfo indicated many lines that are compatible with the (forest of) lines from the lanthanides and actinides. Apart from a qualitative of this line forest, however, a detailed identification of isotopes with mass number $A \sim 100$ has been found not simple.

r-process:

8. Atomic processes

- **Rapid neutron-capture in elements beyond iron:** Burbidge *et al.* (1957) and Cameron (1957) realized already more than 60 years ago that approximately half of the elements heavier than iron are synthesized via the **capture of neutrons by light seed nuclei**, such as iron, in a dense neutron-rich environment, in which the time scale for neutron capture is shorter than the lifetimes for β -decay.
- **Opacities of *r*-process elements:** Barnes and Kasen (2013) showed that more realistic opacities of the *r*-process material may have a dramatic effect upon the predicted **light curves of a kilonovae**. In these simulations, they applied improved estimates of the radiative opacities of heavy elements as derived from *ab-initio* atomic-structure computations. The enhanced opacities of the lanthanides strongly affect the radio-active powered light curves from the ejecta of the neutron-star merger.
- **Production of heavy elements:** In all suggested scenarios, the *r*-process nuclei are produced within two steps. (i) An initial explosion burns at high temperatures until the electrons and ions freeze-out during expansion of the ejecta, although still with a high neutron-to-seed ratio. This initial expansion is followed by (ii) the rapid capture of neutrons by the seed nuclei, leading eventually to heavy nuclei.
- **Production of heavy elements:** Despite of intense research, little is known so far about the neutron-rich and in the *r*-process produced heavy elements. Indeed, the nuclei beyond the iron group elements (with mass numbers $A \sim 90..100$) need to be formed via successive neutron capture, because all other nuclear reactions with charged particles exhibit a high Coulomb barrier.
- **Rapid neutron-capture:** The *r*-process always occurs along a nuclear path which resides quite far on the neutron-rich side of the valley of stable isotopes. Despite some seminal works on the *r*-process, however, the astrophysical environments, that are particularly suitable to this process, are not yet well understood. Indeed, a better understanding of the *r*-process environments is one of the great challenges in nuclear astrophysics.
- ***r*-process *versus* supernovae:** The rapid neutron capture or (so-called) *r*-process is considered to be responsible for about half of the elements heavier than iron, although this process was previously attributed also to core-collapse supernovae. However, recent studies of the *r*-process have disfavored supernovae because their conditions are not suitable to produce the heavy elements near to the *platinum peak* around $A \propto 195$. Instead, neutron-star mergers have received a lot of recent interest as a major *r*-process production site (Tanvir *et al.*, 2017).
- **Astrophysical environments for the *r*-process:** A question in contemporary astrophysics is whether the mergers of neutron stars give rise to a robust *r*-process environment that lead to heavy neutron-rich isotopes with mass $A \geq 130$, and whether the generated proportions are similar to solar abundances (Thielemann *et al.*, 2017). In the neutron-rich ejecta from neutron star (NS-NS) and BH-NS binaries, in particular, the *r*-process is expected to proceed rapidly, leading to many heavy elements like gold, platinum and many others.
- **Astrophysical environments for the *r*-process:** Various astrophysical sites have been suggested for the *r*-process of the nucleosynthesis. Apart from regular supernovas, the *r*-process has been associated especially with neutrino-induced processes in the outer shells of massive

stars, the ejecta from compact binary mergers as well as from so-called magneto-hydrodynamic (MHD) jet supernovae which exhibit high magnetic fields and neutron-rich jet ejecta along the poles.

- **Astrophysical environments for the r-process:** In astrophysical environments, the theory of the r-process was worked out 60 years ago and made it clear that an enormous neutron flux is required in order to explain the observed abundances of the elements. Because of this enormous flux, the details and necessary conditions of the r-process is still under debate in astrophysics. New interest in this topic arose from the neutron-star mergers as a very probable r-process site, and the discovery of freshly synthesized r-process elements will stimulate this discussion.
- **Astrophysical environments for the r-process:** The observation of the solar abundance of elements suggest just two (rather extreme) environments for neutron capture in nature: Either by the slow *s*-process production of β -stable isotopes or by the fast *r*-process for isotopes far from the stability (Freiburghaus *et al.*, 1999). Here, three interesting questions about the *r*-process refer to: (i) How frequently merge two neutron stars or a neutron star with a black hole ? (ii) How much mass is typically ejected per event ? (iii) How much of these ejected material contributes indeed to the *r*-process ?
- **Heavy-element production:** Today, most heavy elements are assumed to be synthesized in neutron star mergers. The radioactive decay of the freshly synthesized elements heats the ejecta and gives eventually rise to the observed ultraviolet, optical and near-infrared light curves that are known for kilonova.

Kilonovae:

- **Simulation of kilonovae:** Although these simulations help explain some of the observed spectral features, they are still in their infancy and suffer from rather incomplete atomic data of the r-process elements. In particular, atomic data are available only for small number of r-process elements and with an expect accuracy $\lesssim 30\%$, although a more detailed comparison is difficult as well as because of insufficient measurements.
- **Modelling of kilonovae:** The recent progress with **opacity computations moved the predicted peak emission towards longer wavelengths**; the currently best estimates refer to the near-infrared band, and this shift need to be taken into account in the modelling of kilonovae.
- **Model for early kilonovae:** Various models have been suggested in the literature to describe the early emission of kilonovae, including the radioactive decay of heavy elements as in the later phase, the β -decay of the free neutrons or the interaction of the relativistic jet from the merger with the surrounding ejecta. Many of these models appear however rather speculative with limited insight into the complexity of the underlying physics. A better understanding of the early emission from kilonovae will help reveal the abundance of elements in the outer ejecta, since only the photons from the outer layer can escape at an early time.
- **Kilonovae:** Kilonovae are day to week-long thermal, supernova-like transients which are powered by the radioactive decay of heavy, neutron-rich elements synthesized in the expanding ejecta of NS-NS or NS-BH mergers. The radioactive decay of such unstable neutron-rich nuclei powers a rapid evolution of a supernova-like transition of stellar matter that is **known as kilonova or macronova** in the literature. These kilonovae can be understood also as **roughly isotropic electromagnetic counterpart to the GW signal** and, thus, provide a unique and direct probe of such r-process sites (Metzger 2017).
- **Kilonovae** refer to optical transients that are powered by the radioactive decay of material ejected in the neutron-star merger. Simulations suggest an ejected mass of $10^{-4} \dots 10^{-1} M_{\odot}$ due to a tidal stripping during the merger process itself or by a subsequent disk wind in course of the evolution of a post-merger remnant.
- **Kilonovae versus γ -ray burst:** Kilonovae are powered by the radioactive decay of it excited nuclear matter. These kilonovae will emit more isotropically (when compared to the aggregation disk of the merger event) and will peak later than short-GRB afterglows. Kilonovae are the best candidates for the electromagnetic counterparts of the GW detection.
- **Photon emission from kilonovae:** A detailed understanding of the photon emission from kilonovae require (detailed) information and simulations on the composition, velocity structure and the opacity of the ejecta as well as on the transport of radiation through the ejecta. The kilonova emission from NS mergers is centered around the optical/IR bands since this is the first spectral window through which the expanding ejecta from NS-NS mergers becomes transparent.

- **Key observables of kilonovae:** Three main ingredients need to be understood in order to quantify the key observables of a kilonovae, namely its peak time scale, the luminosity and the effective temperature. In more details, these ingredients are: (i) The mass and velocity of the ejecta from NS-NS or BH-NS mergers; (ii) the opacity κ of the expanding neutron-rich matter; and (iii) the variety of sources which contribute to the heat of the ejecta $Q(t)$. These ingredients are important especially on the time scale of $t^{(\text{peak})}$, when the ejecta is first becoming transparent.
- **Kilonovae:** This term refers to an optical/infrared transient that has been observed a few days after the merger of two neutron stars. These transient spectra may allow to observe spectral signatures of newly created neutron-capture elements. For example, Watson *et al.* (2019) reported the identification of the neutron-capture element strontium from a detailed re-analysis of the observed transient spectra. The identification may prove that neutron stars are made of neutron-rich matter, although the discussion by Watson *et al.* seem not so stringent.

White-dwarf modeling::

- **Opacity of white-dwarfs:** The opacity of white-dwarfs is needed for modeling their cooling process of the accretion of matter. For white-dwarfs, partially to fully ionized and moderately coupled plasmas need to be modeled.

Source of γ -ray emissions:

- **Multi-photon Compton scattering:** Multi-photon Compton scattering has been studied experimentally at the Stanford Linear Accelerator Center (SLAC) (Bula *et al.*, 1996) as a possible source of gamma rays that are emitted from various astrophysical objects. From classical electrodynamics, it is well known that accelerated, charged particles emit em radiation which, in turn, affects their own dynamics through recoil. In astrophysical models, the particle dynamics and emitted radiation must be coupled self-consistently to each other. This coupling is also called **radiation reaction** and is typically neglected in all nonrelativistic plasmas. This coupling is very closely related also to the electron self-interaction problem in both, the classical and quantum electrodynamics (ED). In classical ED, the Dirac-Lorentz equation (Dirac 1938) describes the covariant dynamics of a point charge including the radiative corrections due to the recoil momentum of the photon field. This radiative correction can be interpreted also as **reaction force due to the self-interaction of a charged particle with its own em field**.

8.5.d. Absorption and emission spectra of distinct astrophysical objects

Infra-red emission spectra from astrophysical missions:

- **Radiation from astrophysical objects:** Almost all information about astrophysical objects is obtained from their emitted radiation over the whole electro-magnetic spectrum. Further information from gravitational waves, charged particles or neutrinos is restricted to particular sources and overall of quite different relevance.
- **Astrophysical observation of infra-red spectra:** Various astrophysical missions and spectrographs, such as GIANO, CRIRES or SOFIA have moved the observations into the infra-red region. These observations made visible a large number of new objects because of the higher transmission of infra-red radiation through dust clouds. In the infra-red spectra, many of the observed lines hereby arise from either forbidden transitions within the ground-state configuration or from Rydberg series of rather highly-excited atoms and ions.
- **Fe II spectrum in astrophysics:** The lines from singly-ionized iron (Fe II) have been found in the spectra of different astrophysical sources, including active galactic nuclei (AGN) and solar or late-type-star atmospheres. A detailed analysis of the spectrum Fe II may affect also the prediction of cosmological supernova light curves or the afterglow from gamma-ray bursts (GRB); cf. Bautista *et al.* (2015).
- **Spectral modeling of singly-charged ions:** In astrophysics, the modeling of EUV and x-ray spectra also requires a detailed treatment of the electron-impact excitation of metastable levels, along with their spontaneous decay through dipole-forbidden transitions. In practice, however, accurate electron-impact collision strengths and Einstein A-values are still a challenge for present-day theory, if such data are required for open-shell atoms and ions, and despite of all the effort during the last decades.

EUV emission spectra from astrophysical missions:

- **High-quality EUV spectra:** The Solar EUV Rocket Telescope and Spectrograph (SERTS, 1992) and the Extreme Ultraviolet Explorer (EUVE, 1990) spectrometers provided high-quality EUV spectra and helped improve the diagnostics of high-temperature plasmas in astrophysical objects.
- **High-quality EUV spectra:** The ability to resolve a large number of individual emission lines and to measure the accurate intensities over a wide wavelength range have enabled one to analyze the temperatures, densities and abundances of elements in a variety of astrophysical sources (Brickhouse *et al.*, 1995).
- **High-quality EUV spectra:** The fine structure of (line) multiplets nowadays allow to solve the full rate equations for several atoms in the plasma, including collisions among all levels and cascades. This enables one to calculate also the **emissivities of weak lines that were previously omitted from the investigation**.

- **SERTS catalog:** The SERTS catalog provides for an average solar active region about 270 emission lines between 170 to 450 Å from which about 90 lines from Fe IX to Fe XVII are identified. These lines cover a temperature range between $4 \cdot 10^5$ to $6 \cdot 10^6$ K. Indeed, these observations combine an excellent spectral and spatial resolution with a good calibration of most lines between 235 ... 450 Å. In these spectra, each charge state of iron contains at least four lines, making it possible to determine the relative line intensities for each model atom.
- **Absorption spectra of Fe II:** Absorption and emission lines of Fe II are prominent in the infrared, optical and ultra-violet spectra of many astrophysical sources. These lines have therefore been used for the quantitative analysis of many observations. For example, they have been detected in active galactic nuclei (AGN), gaseous nebulae, supernovae remnants as well as from interstellar media. For the symbiotic star AG Pegas, Eriksson, Johansson and Wahlgren (2006) assigned 346 out of more than 600 observed lines to Fe II. For an accurate analysis, however, reliable atomic structure calculations and data are needed over a good range of configurations and lines (Smyth *et al.*, 2019). Large discrepancies for these Fe II have been found especially for the effective collision strengths, and which differ by up to a factor 3 between different computations. These data are also said to be relevant for the quantitative analysis of the spectra of PHL 1811 (Smyth *et al.*, 2019).

x-ray emission spectra from astrophysical missions:

- **X-ray emission from astrophysical objects:** From the analysis of line intensities in exotic dense-plasma environments, several key properties of astrophysical objects may be derived that are not attainable through other observational windows.
- **x-ray spectra from Chandra and XMM-Newton:** In x-ray astronomy, the satellites Chandra and XMM-Newton provided (x-ray) spectra from many different astronomical objects, including *K*-shell transitions of carbon, nitrogen, oxygen, neon, silicon and sulphur as well as *K*-shell transitions from the iron-group elements with wavelength between 5–45 Å. These spectra help understand extreme astrophysical environments in active galactic nuclei, x-ray binary systems, Wolf-Rayet Stars as well as from interstellar media (ISM; Sant'Anna *et al.*, 2011). A detailed analysis of spectra from XMM-Newton enables one to characterize the ISM if the absorption cross sections near to *K*-edge are known.
- **High-resolution x-ray observations from XMM-NEWTON:** Sako *et al.* (2001) present first results from high-resolution x-ray observation of IRAS 13349+2438 with the XMM-NEWTON observatory. The observed spectrum was obtained with the Reflection Grating Spectrometer (RGS) and shows a wealth of discrete spectral features, including the (first) astrophysical detection of an unresolved transition array (UTA) due to the $2p - 3d$ inner-shell excitations of *M*-shell iron ions. These spectral features could have been easily misidentified, for instance, as an O VII edge, when observed with only moderate resolution spectrometers.

8. Atomic processes

- **High-resolution x-ray observations from XMM-Newton:** Other prominent features in the spectra of Sako *et al.* (2001) were the K -shell absorption lines of hydrogen- and helium-like carbon, nitrogen, oxygen and neon as well as the L -shell lines of Fe XVII-XX.
- **Diffusion approximation for the radiative flux in a plasma:** In optically thick layers, the diffusion approximation is justified in which the variation of the radiation flux \mathbf{F} in the plasma is related to the (radiative) luminosity L_r by

$$\delta \operatorname{div} \mathbf{F} = \frac{1}{4\pi r^2} \frac{d\delta L_r}{dL_r}, \quad \frac{d\delta L_r}{dL_r} = \frac{dr}{d\ln T} - \frac{d\kappa^{(\text{Rosseland})}}{\kappa^{(\text{Rosseland})}} + A \left(\frac{\delta T}{T} + \frac{\delta r}{r} \right)$$

In this expression, the first term describes the **radiative dissipation that stabilizes the star**. Moreover, the term $\delta T/T$ is also known as γ mechanism and describes the direct influence of the temperature variation on the luminosity (this is typically small), $\kappa^{(\text{Rosseland})}$ is the Rosseland mean opacity, A a constant and the last term contributes to the instability because the radiating area is reduced in case of the compression.

- **Diffusion theory:** In optically thick objects, diffusion theory typically allows to predict the rate of radiation transport with the Rosseland mean opacity as the central quantity. This Rosseland mean opacity can be calculated by averaging the photon mean free path over the temperature derivative of the Planck function.
- **Accretion disks of compact astrophysical objects:** The inner regions of the accretion disks of compact objects, in which absorption and emission of high-energy photons occur, are expected to have plasma densities $10^{15} \dots 10^{22} \text{ cm}^{-3}$. These (modified) x-ray emission spectra are observed with current space telescopes, such as NuSTAR, CHANDRA, and XMM-NEWTON.
- **K_α emission from highly-charged Fe ion:** The K_α emission from highly-charged Fe ions have been studied in astrophysics and astronomy because of their rather high abundance, large rates and the low intergalactic absorption. The K_α lines of iron therefore constitute prominent features to many astrophysical x-ray spectra; they have often been applied for studying x-ray binaries and active galactic nuclei. These lines were considered also for studying gravitational lenses or the polarization of light from interstellar media.

Emission spectra from the solar photo- and chromosphere & comets:

- **x-ray emission from comets:** The discovery of x-ray emission from the comet **Hyakutake** was initially found surprising since comets are known to be quite cold (Cravens, 2002). First observations of such x-ray emissions were made with the x-ray satellite ROSAT; they clearly indicated that x-rays are produced by almost all comets due to charge-exchange collisions of highly-charged ions from the solar wind with neutral atoms from the comets. Meanwhile, x-rays were observed from several 10 comets with emphasis upon their total luminosity, spatial morphology, temporal variation as well as their energy spectrum. Since these spectra include multiple emission lines, they are related to various electron capture processes and to K_α emissions.

- **Composition of the solar wind:** Apart from (mainly) protons and electrons, the solar wind also contains minor fractions of O^{7+} , O^{6+} , C^{6+} , C^{5+} , N^{6+} , Ne^{8+} , Si^{9+} and Fe^{12+} ions. In collision with (nearly-) neutral atoms and molecules, these ions will capture electrons into some excited shell and emit x-rays.
- **x-ray emission from comets:** In collision with comets, the ions from the solar wind will mainly recombine. A better understanding of the underlying charge-transfer processes require a suitable magnetic & hydrodynamic model, a better knowledge about the solar wind as well as reliable charge-transfer cross sections from either laboratory measurements and/or atomic theory. The energy of the x-ray emission from comets is therefore stored as potential energy in the multiply-charged ions and arise directly from the sun.

Generation of synthetic spectra:

- **Synthetic stellar spectra:** The generation and comparison with synthetic spectra is a primary instrument in order to understand the atmospheres of stars. Different elements in the stellar plasma occur in millions of spectral lines, and from which the plasma decomposition and properties need to be derived. Apart from using a local-thermodynamical equilibrium (LTE), non-LTE (NLTE) approaches have become relevant to gain a better understanding. However, these NLTE approaches are computationally (much) more demanding. In a NLTE plasma, the population of energy levels and the intensity of the radiation affect each other and need to be solved *simultaneously*, for instance by using radiative transfer equation (Tagirov *et al.*, 2017).
- **Plasma parameters and ion abundances:** Different theoretical (spectral) models are needed in astro and plasma physics in order to determine the electron temperature, (electron) density distribution as well as the abundances of ions and elements in different environments. In astrophysics, simulation codes usually differ in the number of (astrophysically relevant) elements as well as in the number (and quality) of the emission lines. A comparison of different simulations shows that the use of (most) recent atomic data and a proper treatment of the continuum processes is very crucial.
- **Oxygen abundance:** Since oxygen is the third most abundant element in the Universe, its $1s-2p$ resonance line has been frequently observed in a large number of astrophysical sources. Apart from extracting the relative abundance of oxygen, the Doppler shift of this resonance line enables one to determine the radial velocity.
- **Comparison of line strength for Nd II and Nd III:** cf. Figure 8.3.

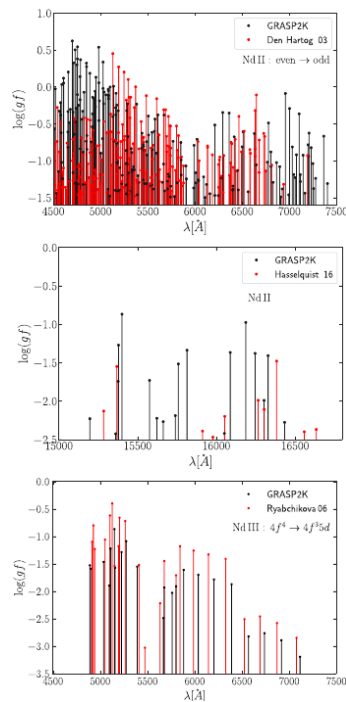


Figure 8.3.: Comparison of line strengths of Nd II and Nd III computed by using GRASP2K with the experimental results and the APOGEE line list for Nd II and Nd III line list based on the stellar spectrum of a strongly magnetic Ap star; from Hotokezaka *et al.* (2000).

8.5.e. Supernovae and kilonovae observations

Energy transport in plasma:

- **Supernovae heating:** Previous observations of supernovae, such as SN 1987A, have brought evidence that Type II and Ib supernovae are powered by the radioactive decay of ^{56}Ni which decays with a lifetime of 8.8 days to ^{56}Co , and further with a lifetime of 111.26 days to ^{56}Fe . Indeed, this decay chain has been seen for a long time as the standard model for most Type Ia supernovae. This chain predicts that the emissions from ^{56}Co becomes relevant after about one months and that the radioactive decay results in $\sim 1 \text{ MeV}$ γ -rays that are Compton scattered off free and bound electrons from the medium. This Compton scattering also results in high-energy electrons with energies of $\sim 0.01 - 1 \text{ MeV}$.

- **Supernovae heating:** The energetic electrons in supernovae, heated up by Compton scattering of γ -rays, heat themselves other free thermal electrons, make electron-impact excitation and ionization and, thus, give rise to whole cascades of electrons with different energies. Moreover, electron-impact ionization leads to a large number of secondary electrons. Indeed, high-energy electrons can deposit their energy only into heating, excitation, and ionization, while passing through an ambient medium.

8.5.f. Radiation transport in astrophysical and hydrodynamical environments

Energy transport in plasma:

- **Role of radiation and neutrino transport:** Radiation transport plays a key role for the dynamics of many astrophysical processes; for instance, the radiation feedback from stars and black holes plays an essential role for the rate of gas accretion in the formation of stars within galaxies. The **star formation rate determines the observable properties from galaxies**, such as stellar luminosity, color, and age.
- **Energy transport in plasma:** Energy transport simulations in plasma is a very complex or even formidable task for various reasons:
 - (1) There occurs a large number of processes at the atomic scale, including, e.g., emission, absorption, scattering;
 - (2) the vast majority of astrophysical scenarios are intrinsically three-dimensional (Reed *et al.*, 2018).
- **Energy transport in plasma:** In many astrophysical environments, the energy transport by radiation or relativistic particles is ubiquitous and need to be modelled by hydrodynamical simulations. Examples of such environments range from the formation of planets to the evolution of cosmic structures, and up to core collapse supernova or gamma-ray bursts.
- **Energy transport in plasma:** Often, the energy transport simulations in plasma are limited by the (approximate) treatment of the radiation transport and the relativistic particles. These limitations also hinder our understanding of the complex astrophysical Universe as well as the star and galaxy formation. Many requirements for an improved understanding arise similarly at short time scales and for large astrophysical environments.
- **Radiation and neutrino transport (RT/NT) codes:** Most of the presently available codes apply very approximate algorithms and can be utilized only for a limited range of parameters and conditions, e.g. a single radiative source with an optically thin diffuse gas. This limitation is quite in contrast to the typically large dynamical structures in astrophysics and, hence, to the large effective range of the optical depth that occur in such environments.
- **Radiative transfer (RT):** RT generally combines concepts from atomic physics, kinetic theory, special relativity, optical physics as well as a good deal of quantum mechanics. It provides the framework to model the emitted radiation field in response to its interaction with

8. Atomic processes

the evolving (dynamical) medium. In practise, complex numerical schemes need to be developed in multiple dimensions to model the propagation of light through the medium, and especially if quantum scattering processes play a role.

- **Radiative transfer (RT):** Radiation transfer computations play a crucial role in astrophysics as they provide the necessary link between the properties and dynamics of the object, the underlying atomic and molecular physics processes and the emitted (observed) radiation. In modern astrophysics, the quality of observational data and the dynamical modeling has enormously advanced the radiation transfer simulations. More often than not, the radiation transfer is modeled by Monte-Carlo techniques to obey the large number of geometries and processes for generating and manipulating photons. All these Monte-Carlo radiation transfer (MCRT) methods have to deal however with the typical Monte Carlo noise. While different methods exist to suppress this noise, they all have pros and cons and come with a price for different applications.
- **Radiative transfer (RT):** In RT, particles move, get scattered or absorbed during the simulations. For a given test particle, the decision about its next step in the propagation is often taken stochastically. This random propagation must model when, where and how the particle interacts. If the sample size is sufficiently large, an accurate representation of the transfer process and the evolution of the radiation field is possible.
- **Monte-Carlo *versus* deterministic RT methods:** MCRT methods have the advantage over the traditional, deterministic solution of the RT that scattering processes can be incorporated more easily.
- **Radiative transfer equations:** In RT, the radiation field is often treated by means of a position and time-dependent intensity field $I(\mathbf{r}, t; \mathbf{n}, \omega)$ that propagates with velocity c into the direction \mathbf{n} . This intensity field fulfills the transfer equation (Noebauer and Sim, 2019)

$$\left(\frac{1}{c} \frac{\partial}{\partial t} + \boldsymbol{\nabla} \cdot \mathbf{n} \right) I(\mathbf{r}, t; \mathbf{n}, \omega) = \eta(\mathbf{r}, t; \mathbf{n}, \omega) - \kappa(\mathbf{r}, t; \mathbf{n}, \omega) I(\mathbf{r}, t; \mathbf{n}, \omega)$$

$$dE(\mathbf{r}, t; \mathbf{n}, \omega) = I(\mathbf{r}, t; \mathbf{n}, \omega) d\omega dt d\Omega d\mathbf{a} \cdot \mathbf{n},$$

and where $dE(\mathbf{r}, t; \mathbf{n}, \omega)$ is the energy in the frequency interval $[\omega, \omega + d\omega]$ that propagates through the surface element $d\mathbf{a}$ in time dt into the solid angle $d\Omega$ around the direction \mathbf{n} . The radiative transfer equations therefore describe the change of the intensity field in terms of the in- and outflows (left hand side) and relates these changes to the interaction with the ambient medium. This interaction contains the emissivity $\eta(\mathbf{r}, t; \mathbf{n}, \omega)$ and the opaqueness $\kappa(\mathbf{r}, t; \mathbf{n}, \omega) I(\mathbf{r}, t; \mathbf{n}, \omega)$ of a medium as two material functions.

- **DIAPHANE library:** This library provides various radiation and neutrino transport (RT/NT) routines for a wide range of astrophysics simulations (Reed *et al.*, 2018). These routines can be utilized directly in simulations, although it remains rather unclear from this write-up

which hierarchy of models apply and how they need to be adapted for certain physical environments. In this library, the mean opacity $\kappa(\rho, T)$ is simply interpolated from a table of Rosseland mean opacities.

8.5.g. Plasma light sources for nanolithography

EUV light sources:

- **EUV light sources at 13.5-nm wavelength:** In order to generate extreme ultraviolet (EUV) light at 13.5-nm wavelength by laser-produced plasmas, the emission of multiply-charged tin ions have been found promising for nanolithographic applications. For these ions, the EUV light is generated by thousands of transitions that form so-called unresolved transition arrays (UTA), and with rather little dependence on the particular charge state of the tin ions (Winderberger *et al.*, 2016).
- **EUV light sources from multiply-charged tin ions:** For multiply charged tin ions with a [Kr] $4d^m$, $m = 6 \dots 0$ configuration, the upper configurations for an EUV emission are [Kr] $(4p^6 4d^{m-1} 4f + 4p^6 4d^{m-1} 5p + 4p^5 4d^{m+1})$ (Winderberger *et al.*, 2016).
- **Intense soft x-ray radiation sources:** Intense radiation sources in the EUV and soft x-ray region are needed in many research and industrial branches, including high-resolution imaging of biological samples, material science or the production of integrated circuits (IC). A current goal in the semiconductor industry is the printing of sub-10 nm feature sizes on IC.
- **Extreme ultraviolet lithography (EUVL):** The EUVL aims for printing features at the nm-scale upon IC at industrial standards. In the present industrial settings, the EUV light is generated in a laser-produced plasma (LPP) with moderate electron temperatures and densities ($T_e \approx 20\text{--}40$ eV, $n_e \approx 10^{18} - 10^{19}$ cm $^{-3}$) by irradiating tin microdroplets with CO₂ laser light ($\lambda = 10.6$ μm). Such a tin plasma then contains a rather large population of Sn⁸⁺ – Sn¹⁴⁺ ions, and which lead to the emission of intense, narrow-band and peaked radiation near 13.5 nm (Sheil *et al.*, 2021). Indeed, the emission band near 13.5 nm is attributed mainly to transition arrays from the $4p^6 4d^m - (4p^5 4d^{m+1} + 4p^6 4d^{m-1} 4f)$, $m = 6 \dots 0$ configurations of Sn⁸⁺ – Sn¹⁴⁺ ions.
- **Magnetized plasma:** The observed radiation spectrum from a (dense) astrophysical magnetized plasma appears to be quite different from the black-body spectrum and typically leads to an anisotropic angular distribution of the emitted photons. However, the detailed x-ray emission from such plasma depends on its chemical decomposition. Different effects have been investigated in order to explore how the magnetic field affect different test particle in magnetized plasma.

8.5.h. Laser-induced fluorescence spectroscopy (LIFS) in flames

Laser-induced fluorescence & applications:

- **Laser-induced fluorescence** describes the spontaneous emission from atoms or molecules following the prior excitation by laser irradiation. In multi-level atoms or molecules, the laser is usually tuned to one of the absorbing transitions. From the so-excited level, the atoms then decay either to some lower lying state or are re-populated by collisions to adjacent states. In LIFS, therefore, a fluorescence spectrum is observed that contains individual transition of the excited level as well as from levels nearby (Daily 1997).
- **Laser-induced fluorescence signal:** The laser-induced fluorescence signal after laser excitation can be exploited in various ways: (i) The observed spectrum provides a measure for the population of the initially excited states; (ii) it allows to extract the total number density of different species in the probe, if a clear relationship can be established between the number density of all involved quantum states; (iii) the observed spectrum (may) help deduce the ground-state distribution function and, hence, the temperature of the probe. Moreover, (iv) the pressure, temperature and velocity may be deduced from the observed line shapes under suitable circumstances.
- **Application of LIFS:** LIFS has been utilized for studying combustion processes, to measure species concentration, temperature, pressure and velocity in flames. Indeed, LIFS contributes today significantly to many experimental combustion studies.

Combustion processes:

- **Combustion:** Combustion is the primary propulsion technology and is very frequently applied for the generation of electricity, the heating of buildings and at many places elsewhere. Combustion is applied also for the synthesis of new materials and for chemical processing (Daily 1997). In nature, combustion is a frequent source when natural areas are changed by fire.
- **Combustion systems:** Flames and combustion systems vary widely in their size, fuel type and purpose. They range from small mm-to-cm systems, such as furnace and stove pilot flames, gas stove burners or small laboratory burners to medium-size motors and heating systems, and up to pulverized coal fire boilers, marine diesels and forest fires, each with length scales on the order of several meters (Daily 1997).
- **Performance evaluation of combustion processes:** Combustion processes are often analyzed with regard to their energy conversion efficiency, material synthesis yield, material purity and/or pollutant emissions. This analysis is often made by measuring the exhaust and without that the combustion zone is affected directly.

8.5.i. Synthetic spectra for laser-induced breakdown spectroscopy (LIBS)

Laser-induced breakdown spectroscopy:

- **Laser-induced breakdown spectroscopy (LIBS)** has been found a versatile analytical tool with various applications. In this technique, a high-power laser beam is typically focused upon the surface of a sample that need to be analyzed. If the laser power exceeds a certain threshold, an optical breakdown occurs due to the formation of a laser-induced plasma. In practice, **the breakdown threshold depends on the wavelength and duration of the laser pulses as well as on the analyzed media.**
- **LIBS for nanosecond laser ablation:** For a nanosecond laser ablation, for example, the threshold varies from $1.9 \cdot 10^8 \text{ W cm}^{-2}$ for copper up to $10^{10} \dots 10^{11} \text{ W cm}^{-2}$ for aqueous solutions (Yaroshchyk *et al.* 2006).

Simulation of LIBS spectra:

- **Synthesized LIBS spectra:** Ciucci *et al.* (1999) first estimated theoretically with limited accuracy the composition of a laser-induced plasma by using computational tools instead of the (standard) calibration. Their computation were based on the assumption that the plasma and sample compositions are the same and that the plasma is optically thin and in local thermal equilibrium (LTE) during the observation.
- **Synthesized LIBS spectra:** Yaroshchyk *et al.* (2006) describe some software for synthesizing laser-induced breakdown spectroscopy emission spectra and to predict sample compositions by using a proposed **calibration-free algorithm**. This code applies a database of atomic emission lines in order to create a theoretical emission spectrum for selected elements using defined plasma parameters.
- **Synthesized LIBS spectra:** The code by Yaroshchyk *et al.* (2006) is also based on the assumption of a LTE and a well-defined plasma temperature and electron density; it takes a number of characteristics atomic emission lines as input to create a synthesized theoretical emission spectrum of selected elements which are compared to the spectra of four separate compact spectrometers covering the spectral region 185–950 nm.
- **Synthesized LIBS spectra:** Until the present, all heavy elements are typically represented in LIBS plasmas only by their neutral atoms as well as their singly- and doubly-charged ions, that emit radiation at characteristic wavelengths. From the intensity of the individual wavelength, the composition of the samples are then estimated both, qualitatively and quantitatively.

8.5.j. Laser-produced plasma

Remarks and properties of laser-produced plasma (LPP):

- Laser-produced plasmas (LPP) have attracted recent interest because of their use in developing laboratory ion sources and pulsed light sources at short wavelengths.
- In LPP, hot electrons can subsequently ionize the much cooler atoms, forming an x-ray-emitting, high-temperature plasma spark at the surface of the solid (Murnane *et al.*, 1991).
- The emitted x-rays from LPP are generally incoherent but have a high brightness because of the small size, short lifetime and the high temperature of the radiating plasma.
- The deposition of laser energy at high densities is crucial for the production of short x-ray pulses. If the LPP is produced by short pulses, the electron heating and the rise time of the emitted x-ray pulse will be comparable to the duration of the laser pulse.
- Properties of LPP: To determine the properties of LPP, such as temperature, density or its radiation emission, one needs a proper model for the coupling of the laser light with the heavy element (solid-state) target.
- Scaling laws for LPP: Scaling laws predict that brighter and more efficient x-ray sources will be obtained if (more) intense laser pulses are employed. These sources can then be used for time-resolved x-ray scattering studies and for the development of x-ray lasers.
- Scaling laws for LPP: Simple arguments can be used to derive scaling laws predict the response of the LPP if the laser parameters are varied. If any hydrodynamic expansion is neglected during the interaction with the laser pulse, we can equate the incident heating flux to the cooling flux that occurs due to classical thermal conduction.

Applications of LPP:

- EUV lithography: LPP will find applications in extreme ultraviolet (EUV) lithography, EUV metrology as well as in the modification of surfaces.
- Water window: LPP sources have been developed for x-rays in the water window, though with limited conversion efficiency and/or brightness so far. These plasmas can be used for novel microscope designs as well as for cell tomography.
- Source of x-rays and multiply-charged ions: LPP have been proposed as source of both, x-rays and multiply-charged ions. Whereas x-ray sources aim for a high radiation loss from the plasma due to the generation of highly stripped atoms, high charge states of ions are mainly produced by a high plasma temperature and a low radiation level (loss).

8. Atomic processes

- **Time-resolved x-ray scattering:** Fast x-ray sources from LPP can be applied to investigate the time-resolved x-ray scattering from rapidly evolving materials (for example, the diffraction from materials with rapid phase transitions), time-resolved photoemission, or the flash-lamp pumping of x-ray lasers.

Ultrafast x-ray pulses from LPP:

- A high-temperature plasma is created when an intense laser pulse is focused onto the surface of a solid (Murnane *et al.*, 1991). From such a plasma, an **ultrafast pulse of x-ray radiation is emitted when the laser pulse duration is less than about a picosecond**.
- X-ray pulses with a duration of a picosecond or less have been observed, more than an order of magnitude shorter than those produced by any other x-ray source.
- A direct comparison of fast x-ray pulses from LPP with other x-ray sources is difficult; in general, however, LPP yield x-rays with much higher peak power but lower average power than synchrotrons and other high-average power sources such as rotating anode tubes.
- Short x-ray pulses are expected if the plasma can cool rapidly. Deposition of laser energy at solid density allows such a rapid cooling because (i) the associated high thermal gradient allows rapid conduction of electron energy into the bulk of the solid beyond the optical skin depth; (ii) the associated high pressure gradient allows rapid cooling by expansion into the vacuum in front of the surface; and (iii) nonequilibrium conditions in the underionized plasma allow hot electrons to cool rapidly by inelastic collisions with atoms and ions (Murnane *et al.*, 1991).

Ionization models for LPP:

- **Collisional-radiative (CR) ionization model:** A CR model can be applied to LPP with temperatures above a few tens of eV. At these temperatures, the average ionization stage A^{q+} of a given element is dominated by the electron plasma temperature due to electron and photon-impact excitation and ionization processes.
- **Collisional *versus* radiative processes:** Indeed, **two main types of excitation and ionization processes occur in LPP:** collisional and radiative processes, and where the corresponding de-excitation and recombination simply refer to the time-reversed processes. The ionization-recombination equations for both processes are:



- **Ionization-recombination equations:** In the set of ionization-recombination equations, one often only considers collisions with (free) electrons since these collisions are much more efficient than those with heavier particles. Obviously, however, these equations neglect autoionization and its (inverse) dielectronic recombination.
- **Local thermodynamic equilibrium (LTE):** For many laboratory plasmas, a local thermodynamic equilibrium (LTE) can be assumed, in which the collisional excitation and ionization processes are just balanced by their inverse processes, namely the collisional decay and recombination. These plasma are very different from **corona (models)** for which no detailed balance applies since the collisional excitation and ionization lead predominantly to spontaneous line emission and radiation loss.

Deflagration models for LPP:

- **Deflagratio** refers to an explosion, in which the speed of burning is lower than the speed of sound in the surroundings. In other words, a deflagration is a fire in which a flame travels rapidly through a gas, but at subsonic speed.
- **Radiative deflagration model:** T model describes the rapid interaction of the incident laser radiation with a very thin layer near to the target surface. In this layer, the electron density reaches a cut-off density $n^{(\text{cut-off})} = 10^{21} / \lambda^2 [\mu\text{m}]$. This rapid interaction also leads to a (very) **hot plasma that expands into the vacuum** and which, *vice versa*, results in a shock wave into the solid owing to momentum conservation.
- **Hot plasma:** The properties of the hot plasma in the (thin) interaction layer can be determined mainly from the power density in the focal zone and the wavelength of the incident radiation.

Laser-produced plasmas for laboratory astrophysics:

- **Laser-produced plasma:** Laser-produced plasmas have been successfully generated to simulate astrophysical plasmas in the laboratory for more than a decade. Indeed, researchers can nowadays create, control and characterize plasmas in the laboratory that replicate important features of different astrophysical objects. At present, high-intensity, femtosecond laser systems are available with peak powers between terawatt to petawatt. Often, they are used together with synchronized and laser-accelerated electron bunches with subpicosecond duration and terahertz bandwidths; cf. 8.5.k.
- **Application of laser-produced plasma:** These plasmas can be utilized to explore selected phenomena from supernovae, stellar evolutions, the solar corona, cosmic rays, planetary and celestial matter, or interstellar plasmas (Hartemann *et al.*, 2000). Together with a proper scaling, moreover, these plasmas can model a wide range of temperatures and densities that arise in astrophysical environments. Laboratory-based experiments help interpret astrophysical data by focusing up on the most relevant (physical) processes, and often without the need to reproduce the exact conditions.

8. Atomic processes

➤ **Laser-electron interactions in intense light beams:** The laser-electron interaction changes the (relativistic) intensity of a laser pulse drastically when it passes through matter. This can be understood already from the high transverse momenta of the electrons in the generated plasma wave. In some more details, three laser-electron interaction processes are particular relevant: (1) a relativistic ponderomotive scattering for the collinear propagation of the laser and electrons; (2) the intense Compton backscattering in head-on collisions; and (3) the nonlinear Kapitza-Dirac scattering in standing laser waves.

8.5.k. Laser wake-field acceleration (LWFA) of particles

Laser wake-field acceleration (LWFA):

- **Laser-wakefield acceleration (LWFA) of electrons:** In a laser-produced plasma, a wakefield acceleration of electrons can be used to generate stable, tunable and nearly monoenergetic electron bunches at the MeV-GeV energy scale and with some (tens of) pC charge. These bunches have a quite short duration (\sim fs), small transverse bunch size (\sim μm) and low divergence (\sim mrad); they are comparable with bunches at conventional state-of-the-art linear accelerators (Khrennikov *et al.*, 2015).
- **Application of LWFA bunches of electrons:** The unique properties of such laser-accelerated electron bunches make them very promising for developing cheap and compact x-ray sources with high peak brilliance. Indeed, these sources might fill the gap in price and performance between standard laboratory x-ray tubes and large-scale synchrotrons, with an inherent synchronization to both, the laser and electron beam. These novel x-ray sources can be applied also in other research areas, such as clinical imaging, material research, few-fs time-resolved x-ray emission spectroscopy and ultrafast pump-probe studies of structural dynamics (Khrennikov *et al.*, 2015).
- **Laser-wakefield acceleration (LWFA) of electrons:** When an intense laser pulse ($a_o > 1$) passes through an underdense plasma, it generates a plasma wave by first repelling electrons from the region of high intensity due to the ponderomotive force of the light field. The phase of this plasma wave is hereby equal to the group velocity of the laser field, and both close to the (vacuum) speed of light. The plasma wave then results in a fast-moving longitudinal electric field that accelerates the electrons that remain (trapped) in the high-intensity region. The energy spread of the accelerated electrons can be further reduced, if a shock-front injection of electrons is employed (Khrennikov *et al.*, 2015). Such a shock-front can be created by placing some proper nozzle into the plasma-forming gas stream.
- **Jovian radiation belts:** These Jovian radiation belts refer to specially shaped magnetic fields around the planets which are able to trap electrons. Since Jupiter is surrounded by a powerful magnetic field, electrons in its Jovian belts can be accelerated to energies that are about ten times larger than the electrons in the (equivalent) radiation belts of the Earth. In the inner belt of Jupiter, electrons with energy up to 100 MeV have been observed and should exhibit an exponential decay according to the (so-called) Jovian Specification Environment model (Budriga and Ticos, 2020). Such broad radiation spectra cannot be obtained by conventional accelerators, and where the accelerated electrons beams more often than not are mono-energetic. However, such beams might be obtained by laser particle acceleration in underdense plasmas with PW class lasers.

8.5.l. Fusion research

Hot fusion plasma:

- **Tungsten as key element for fusion research:** Tungsten (W, $Z = 74$) has found much attention for building magnetic fusion devices, such as ITER (Cadarache, France) or WendelsteinX (Greifswald, Germany), and elsewhere. It is often considered as primary facing material within the vacuum vessel due to its low sputtering rate, high-temperature characteristics and low tritium absorption. Apart from this ability to withstand intense energy loads, however, tungsten is a high- Z element that may contaminate the plasma and may then lead to large radiative power loss. Many theoretical case studies have therefore been performed to understand, predict and control the behaviour of tungsten in quite many charge states. Owing to the ionization dynamics of multiply-charged ions, only a few charged states typically dominate the overall ion dynamics.
- **Spectroscopy of tungsten:** In most spectroscopic studies of tungsten plasma, the dominant line emissions arise from ions with either a closed-shell structure (for instance, Pd-like) or from configurations with a single electron outside a closed (sub-) shell (for instance, Ag-like). These line spectra are quite *sparse* and do not suffer from a spread over a large (huge) number of fine-structure transitions.
- **Tungsten as fusion-wall material:** Tungsten is currently chosen as wall and divertor material in magnetic fusion devices owing to its high melting temperature, resistivity to chemical erosion and low sputtering rate. For instance, it has been used near the outer strike point in the JET divertors. To understand the sputtering quantitatively, the electron-impact ionization (cross sections) of low charge states of tungsten need to be calculated. However, this wall material also contributes to the radiation loss, and which often restricts the ignition of a thermonuclear reaction.

8.5.m. Mass attenuation coefficients

Attenuation coefficients:

- **photon mass-attenuation coefficient μ/ρ :** The photon mass-attenuation coefficient is calculated from the density ρ of the target material and the thickness d of the material in the direction of the incident photons as

$$\frac{\mu}{\rho} = - \frac{1}{\rho d} \ln \left(\frac{N}{N_o} \right),$$

and where N_o , N are the numbers of incident and transversing photons, respectively.

8.5.n. Associated and Penning ionization in low-energy atom-atom collisions

Penning *versus* associative ionization:

- **Chemi-ionization:** general refers to all scattering processes of (neutral) reagents that lead to the ionization of one or more reaction partners. Two well known chemi-ionization processes are the Penning and associative ionization which lead to the emission of one electron. Such collisions have been observed especially for electronically excited noble gases, such as helium and neon, with different partner and practically allow barrierless reactions. Using level selected beams and high resolution, the associative-to-Penning branching ratio has been measured also experimentally.
- **Penning *versus* associative ionization:** If two atoms A and B collide with each other and if one of them (here B) is initially in a metastable state, Penning and associative ionization refers to:



While, in Penning ionization, the excited (metastable) atom returns back to its ground state, an ionic dimer $(AB)^+$ is formed in the associative ionization. Therefore, both ionization processes can eventually lead to the same molecular (scattering) channel if the dimer further decays as: $(AB)^+ \rightarrow A^+ + B$.

- **Penning ionization of metastable helium & lithium:** A well-known Penning ionization reaction is



and for which associative ionization is known to be negligible owing to the (very) weakly-bound dimer HeLi^+ .

8.5.o. X-ray absorption of solid-state materials

Near-edge spectroscopy of solid-state samples:

- **Chemical sensitivity:** In the near-edge region of materials and samples, one is very sensitive to the surroundings of the absorbing atom. This makes absorption spectroscopies a very useful tool to investigate the geometric and electronic structure of the samples.

8. Atomic processes

- **X-ray near-edge absorption (XANES):** XANES as well as other related spectroscopies, such as the resonant x-ray scattering spectroscopy (RXS) and x-ray magnetic circular dichroism (XMCD), are powerful spectroscopic techniques for probing the electronic structure around the absorbing atom in a fluid or solid-state probe sequences (Bunau and Joly, 2009).
- **X-ray absorption spectroscopy (XAS):** This technique is widely used at synchrotron radiation facilities for determining the local geometric and/or electronic structure of matter, such as gases, solutions, or solids.
- **X-ray absorption spectroscopy (XAS):** The absorption of x-ray photons result in a core-excited initial state with a well-defined symmetry, and which determines due to selection rules also the final states in the continuum following the relaxation of the core holes. While the most intense features arise of course from electric-dipole allowed transitions, mixtures of multipole components may also occur. The most intense features at a K -edge are typically due to the $1s \rightarrow np$ core excitations, and at the L_3 -edge those due to $2p \rightarrow nd$ excitations.
- **X-ray absorption spectroscopy (XAS):** X-ray absorption spectroscopy (XAS) has been found a powerful method to derive information about the electronic and geometrical structure near to a well-defined absorbing atom. XAS can be employed for quite different target materials, from fluids to condensed matter, to materials, and up to biological samples. In particular, the low energy part of the XAS spectrum often appears reach of information about the symmetry of the unit cells, the oxidation state of selected components or the interatomic distances and angles.
- **In x-ray absorption spectroscopy, codes are needed and greatly appreciated that help reproduce the near-edge structure within a reasonable calculation time.**
- **Classification of codes for x-ray absorption spectroscopy:** These codes can be classified into two major categories:
 - i) multi-electronic but monoatomic codes which are based on some multiplet theory and which give rise to a proper parametrized description of the localized electronic state. In these codes, however, the delocalized states are often not described correctly.
 - ii) multi-atomic but mono-electronic codes which provide correct description of the extended states but fail to account for the highly correlated state that interact with the core hole. This applies, for example, for the calculation of the L2 and L3 edges of the $3d$ elements.
- **Multi-atomic and multi-electronic absorption calculations:** There have been various attempts in the literature to perform multi-atomic and multi-electronic x-ray absorption calculations based on either the time-dependent density functional theory, the Bethe-Salpeter equation or on other multi-channel methods. However, most of these approaches are still in their early phase and will require much further work.
- **X-ray absorption spectroscopy (XAS):** XAS forms a complementary method to (standard) x-ray diffraction as one of the most fundamental technique in biochemistry and materials science in order to explore the local structure and oxidation states in catalysts and other chemical complexes. For example, XAS helped study the electronic structure of many metal complexes.

Nonlinear optical properties of mesoscopic composite materials:

➤ Free atoms *versus* bulk materials: Apparently, the optical and spectral properties of bulk material, such as of metals or semiconductors, are usually quite different from those of the constituent atoms. Indeed, most of these properties are determined by the extended (non-localized) electronic states and must then be characterized by the electron mean free path, the electron/hole Bohr radii, or the de-Broglie wavelength of the electrons in the bulk. Non-linear interaction processes of materials with light can drastically modify the behaviour of materials, for instance, by opening additional optical channels and quantum interferences. Different non-linear interaction mechanisms can be analyzed by means of saturation spectroscopy, two-photon spectroscopy, photon echo and other techniques (Flytzanis, 2005).

8.5.p. X-ray magnetic circular dichroism (XMCD)

XMCD spectroscopy:

- **X-ray magnetic circular dichroism (XMCD):** XMCD has been found a powerful method to analyze the electronic and magnetic structure of nanoparticles, molecular materials, single molecule magnets, organometallic complexes and several other materials. This spectroscopy for studying magnetic materials emerged in the 1990s, and since then various (> 50) state-of-the-art beamlines for XMCD have been built-up around the world.
- **X-ray magnetic circular dichroism (XMCD):** In XMCD, the scattered photon spectra are obtained by taking the difference of two XAS spectra as well as by flipping the circular polarization of the incident radiation from parallel to antiparallel w.r.t. to the external magnetic field. The XMCD are mainly determined by the asymmetric excitation of a core electron into the unoccupied states of the conduction band. This is in contrast to XAS itself where the coupling of the valence electrons plays a prominent role (as well).
- **Optical selection rules in XMCD:** The interaction of the core electrons with light of different helicity gives rise to (so-called) **optical selection rules because electric-dipole transitions from the ground state are possible only to a limited subset of final states** (van der Laan and Figueroa, 2014). These selection rules make the XAS spectra very sensitive to crystal fields, the spin-orbit interaction as well as the particular spin configurations of the valence states, up to studies on the Jahn-Teller effect.
- **Spin versus orbital part of the magnetic moment:** Since the light interacts first of all only with the orbital but not the spin part of the electronic wave function, XMCD help distinguish also between the spin and orbital part of the magnetic moment. **Various sum rules exist that relate integrated intensities over certain parts of the XAS spectrum to the spin and orbital moments of the excited inner-shell electrons.** The discovery and application of these sum rules made the XMCD spectroscopy a powerful tool to provide element-specific local moments. time scale.

8.5.q. Coherent x-ray scattering at high intensities

Novel x-ray radiation sources:

- **Linac Coherent Light Source (LCLS):** In 2009, the Linac Coherent Light Source (LCLS) at the SLAC National Accelerator Laboratory was the first x-ray FEL in operation with photon energies up to 8.3 keV, up to 2×10^{12} photons per pulse, and with a pulse length of just a few femtoseconds.
- **Current x-ray FEL:** Nowadays, further x-ray FEL include the SPring-8 Compact SASE Source (SCSS, Japan) and the European x-ray FEL (XFEL) at DESY. The XFEL can deliver photon energy up to 14 keV and has a 50–500 times higher average brightness than the (early) LCLS.
- **X-ray free-electron lasers (XFEL):** XFEL belong today to the most brilliant x-ray sources with up to 10^{14} photons per pulse and for pulse durations of (sub-) femtoseconds. These short x-ray pulses facilitate not only the time resolution of ultrafast electron processes at the atomic scale but also enable one to study short-living resonances and transition states.
- **XFEL radiation:** The Linac Coherent Light Source (LCLS) in the USA and the X-ray Free-Electron Laser projects in Germany and Japan provide beams with up to 10 keV photon energies and a flux that is order(s) of magnitude larger than those from other traditional sources.
- **XFEL pulses:** Pulses from modern x-ray FEL facilities exhibit high photon fluxes ($\sim 10^{12}$ per pulse), short pulse durations (2–50 fs), and peak powers in the keV regime. In particular, the rather high intensity of these pulses allow the observation of non-linear processes, such as double-core hole formation, two-photon absorption, amplified spontaneous x-ray emission, plasma creation, x-ray-optical wave mixing, x-ray second harmonic generation and anomalous x-ray Compton scattering.
- **XFEL operation modes:** The currently existing x-ray FEL are usually operated either in the self-amplified spontaneous emission (SASE) or the high-gain-harmonic-generation (HGHG) regime. So far, the HGHG regime has been utilized only with soft x-rays down to about 4 nm wavelength, but were then found to result in a better temporal coherence and wavelength stability. SASE machines have been operated also at harder x-rays down to 1 Å as their fundamental wavelengths.
- **Stimulated x-ray emission:** is a nonlinear process, in which an increased peak intensity results in a multiple increase of the signal, and which can be applied to analyze yet unexplored excited states of atoms and molecules.
- **Stimulated x-ray emission:** Stimulated x-ray emission has been observed in dense gases, liquids as well as solids in various attempts to develop a stimulated x-ray Raman scattering (SXRS). This stimulated scattering is often taken as basic building block of nonlinear x-ray spectroscopy. However, direct measurements of SXRS are often hampered by a large background that arises from the primary photons and

8. Atomic processes

that contribute photon momenta comparable to the scattered photons. Eichmann *et al.* (2020) introduced so-called photon-recoil imaging in which the momentum transfer from the photons to the atoms are monitored by the deflection of their path in a supersonic beam.

Single-shot imaging:

- **Probe-before-destroy principle:** Intense and ultrashort x-ray pulses are required for single-particle imaging as well as for x-ray spectroscopy and femtosecond crystallography in order to *probe* the target before it is destroyed. However, such intense pulses cause also a number of nonlinear processes.
- **Single-shot imaging:** One central goal and application of the European XFEL is **single-shot imaging of individual macromolecules by means of coherent x-ray scattering**. Such an imaging should help determine the atomically resolved structure of non-crystallized nanoparticles and biomolecules. Single-shot imaging might become possible for a sufficiently high-fluence and well-focused FEL pulse that generate a large-enough number of scattered photons from each (single-molecule) sample.
- **Radiation damage:** One of the key problems in single-shot imaging is the radiation damage in course of the irradiation of the sample. Typically, a much higher flux is required than the **conventional radiation damage limit of about 200 photons/Å²** (for bio- and nanomaterials), and this may seriously degrade the scattering pattern and the possibility of determining the atomic positions within the target molecule (Son *et al.*, 2011). Single-shot imaging will therefore require a sufficiently short duration of the intense x-ray pulse of less than 10 fs in order to keep the atomic position effectively frozen during the irradiation by the pulse.
- **Single-shot imaging:** Even if the atomic positions are nearly frozen, the single-shot imaging will be affected also by dynamical changes in the electron density of the target. This makes it necessary to understand the detailed ionization and relaxation dynamics in individual parts of the molecules under ultrashort and ultraintense x-ray pulses (Son *et al.*, 2011). This electron-density dynamics can be simulated by means of time-dependent rate equations in order to explore the formation and relaxation of the inner-shell vacancies.

Ionization dynamics in short light pulses:

- **Rate equations for configuration-averaged population dynamics:** The transitions among all possible electronic configurations c of a given atom are described by a set of coupled rate equations of the form,

$$\frac{d P_c(t)}{dt} = \sum_{c' \neq c} (A_{c' \rightarrow c} P_{c'}(t) - A_{c \rightarrow c'} P_c(t))$$

where P_c is the (relative) population of the c -th configuration, $\Gamma_{c' \rightarrow c}$ is the rate for generating the configuration c from c' and $A_{c \rightarrow c'}$ the rate for all decay transitions from configuration c to other configurations c' . In a simplified dynamical model, A can be either a

(configuration-averaged) time-independent Auger or fluorescence rate, or a time-dependent photoionization rate. For the photon flux $J(t)$ of the x-ray pulse at some given time t , the photoionization rate is given by $\sigma_p J(t)$ with .

- **Anlge-differential cross section for coherent x-ray scattering:** For unpolarized and linearly-polarized x-rays, the anlge-differential cross section for coherent scattering is given by (Son *et al.*, 2011)

$$\frac{d\sigma^{(\text{unpolarized})}}{d\Omega} = \alpha^4 |f^{(0)}(Q)|^2 \frac{1 + \cos^2 \vartheta}{2}, \quad \frac{d\sigma^{(\text{lin-polarized})}}{d\Omega} = \alpha^4 |f^{(0)}(Q)|^2 (1 - \cos^2 \varphi \sin^2 \vartheta),$$

where φ is the azimuthal angle of the scattered photon momentum with respect to the polarization axes in the plane perpendicular to the x-ray propagation. This angle-differential cross section gives well-defined distributions of the scattered x-ray emission if one restricts the model to fixed electronic configurations. From measurement of the x-ray distribution, *vice versa*, one can retrieve information about the electronic density.

- **Configuration-averaged anlge-differential cross section for coherent x-ray scattering:** If an atomic cloud is exposed to an ultraintense x-ray pulse, the atomic electron density is dynamically modified. This may require to introduce a suitably averaged, time-dependent differential scattering cross section,

$$\frac{d\sigma^{(\text{averaged})}}{d\Omega}(t) = \sum_c^{\text{all configs}} P_c(t) \frac{d\sigma^{(c)}}{d\Omega}$$

where $P_c(t)$ is the population of the c -th configuration as obtained from the rate equations above. The differential scattering cross section for the c -th configuration is evaluated from the form factor for the charge density $\rho(r)$ of the c -configuration.

8.5.r. X-ray quantum optics

Phenomena in x-ray quantum optics:

- **X-ray quantum optics** has rapidly evolved during the last years owing to the development of novel x-ray light sources and x-ray optics. In particular, the resonant interaction of x-ray photons with nuclear transitions has attracted recent interest.
- **Phenomena from quantum optics:** A few important phenomena from x-ray quantum optics include: i) x-ray parametric down conversion; ii) nuclear γ -ray superradiance, and several others. Indeed, various concepts from conventional (visible or nearly-visible) quantum optics have been suggested also at higher photon energies. These concepts include photon correlations and entanglement, squeezing, and others.

8. Atomic processes

- **Optical *versus* x-ray quantum optics:** There are important differences between the interaction of x-rays and optical photons due to the inner-shell atomic excitations, the occurrence of nuclear resonances, or quite large energy shifts in Compton scattering when the photon energies approach the electron rest mass.
- **Advantages of x-ray photons:** Hard x-ray photons with an energy of ~ 10 keV are easy to detect, can be focused to small spot sizes and can penetrate quite deeply into materials. They may also lead to fast information processing owing to their higher frequencies.

8.5.s. Gamma-factory project

Gamma-factory:

- **Forthcoming CERN research program:** The long-term planning at CERN requires to discuss also applications outside of the original high-energy community. A multipurpose Gamma Factory has therefore been suggested as a novel (Compton backscattered) light source, based on existing accelerator infrastructures.
- **Design parameters of the planned Gamma factory:** For sufficiently strong lasers and ions beams, the gamma factory might push the intensity limit several orders of magnitude with an estimated photon flux of 10^{17} photons/s at the gamma-ray photon energies $1 < E^{(\text{photon})} < 400$ MeV. These photon energies are out of reach for the FEL-based light sources. The energy-tuned, quasi-monochromatic gamma beams, together with the gamma-beam-driven, high intensity secondary beams of polarized positrons, polarized muons, neutrons and radioactive ions would constitute the basic research tools of the proposed Gamma Factory.
- **Elastic light scattering by relativistic ions:** The elastic scattering of light by fast ultra-relativistic ions (beams) gives rise in the laboratory frame to well-collimated beams of scattered γ -ray photons owing to the Lorentz transformation; this up-conversion of the photon energy is the central idea behind the suggested Gamma Factory at CERN. To increase the intensity (scattering cross section), the incident photons need to be properly adjusted to the energies of the ions. Moreover, the polarization of the γ -ray photons sensitively depends on the angular distribution and polarization of the outgoing (secondary) photons in the laboratory frame. Volotka *et al.* (2021) applied the density-matrix theory, together with the irreducible polarization tensors, in order to investigate the angular distribution and polarization of the photons that are resonantly scattered by ultra-relativistic ions. Emphasis was especially placed on the question how the polarization of incident light and/or ions affect the angular and polarization properties of the scattered light.
- **γ -ray photons with tailored polarization properties:** Polarized γ -ray photons are desired for the creation of polarized muons and pions, the search for atomic parity non-conservation as well as for nuclear physics spectroscopy.
- **Compton backscattered light from ions:** Head-on collisions of light with fast ions leads predominantly to the Compton (back-) scattering of photon that are *twice* Doppler-shifted (in the absorption and re-emission process) and which are concentrated in a quite narrow cone around the propagation direction of the ions

$$\omega'' = \gamma \omega' (1 + \cos \vartheta') = \frac{4 \gamma^2 \omega}{1 + (\gamma \vartheta_o)^2}.$$

Here ϑ_o is the observation angle for recording the photons with regard to the ion beam axis. These backscattered photon energies can therefore take values up to 10 MeV for initially optical light and the $\gamma \lesssim 2000$ parameters from above. When compared with synchrotrons,

the generated laser frequency ω'' can hereby be tuned by either the incident laser frequency *or* the γ -factor of the ion beam.

8.5.t. Spin-waves and spin-wave engineering (magnomics)

Magnons:

- **Magnons** generally refer to quantized (magnetic) excitations in an ordered ensemble of magnetic moments; these magnetic excitations are closely related to the **spin waves** in a classical ensemble of magnetic moments. For example, (metastable) magnons have been studied in geometrically frustrated magnets where they occur as persistent magnetic excitations even at very low temperatures.
- **Spectra of magnons:** High-resolution spectroscopic techniques are typically required in order to measure the spectrum of such magnons, for instance, by the scattering of light. In the optical regime, Brillouin light scattering enables one to probe magnons with high energy resolution, while a high spatial resolution can be obtained by resonant inelastic x-ray or neutron scattering (Roehlsberger, 2014). In particular, inelastic neutron scattering on magnons has been applied for several decades, while the x-ray scattering on single magnons has been achieved only recently. In all these measurements, however, the energy resolution of such magnon spectra was limited by the energy resolution of the incident particles and/or the analyzers.
- **Spin waves:** Spin waves describe the classically-collective motion of a large number of (atomic) magnetic moments in a given sample; they are usually represented by a (local) magnetization vector $\mathbf{m} = \mathbf{m}(t)$ that precesses with some angular frequency Ω around the direction of the *effective* magnetic field $\mathcal{B}^{(\text{eff})}$, forming the surface of cone.

8.5.u. Hollow atom and ion formation

Hollow atoms and ions:

- **Hollow atoms:** The removal of all electrons from an inner atomic shell was first observed and studied in the 1970s for the double K-shell nuclear electron capture and for the photo-double ionization. Such double K-shell vacancy states can be produced also by (single-photon) excitation and generally result in (fast) satellites and hypersatellites. Often, the broad K-lines in the observed x-ray spectra are composed out of an array of such (hyper-) satellite lines.
- **Hollow atoms:** If the hollow atoms are formed by collision of naked ions with surfaces, the $K - L$ satellite lines shows a distribution that depends on the rate, with which the L-shell is filled and which becomes broader, if the L-shell is filled quickly.
- **Hollow atoms:** Briand *et al.* (1990) studied the capture of electrons by slow Ar^{17+} ions in soft collisions with a metallic surface. In such collisions, highly-charged ions capture may capture a large number of electrons from the target surface within a very short time.
- **Hollow atoms:** The interaction between HCl and matter has often been described by two separate steps: (i) The initial electron capture (mechanism), and (ii) the subsequent relaxation of the excited projectile.
- **Classical over-the-barrier (COB) model:** In the COB model, the first resonance charge transfer from a flat surface arises approximately at the distance d_c into the shell n_c

$$d_c = \frac{2q}{W}, \quad n_c = \frac{q}{2W} \left(1 + \frac{q - 1/2}{\sqrt{8q}}\right)^{-1/2}$$

where q is the charge of the ion, W is the work function of the target. The COB model also provides estimates about the interaction time t_I for a HCl above of the target surface. This interaction time is determined by the image acceleration and the neutralization dynamics of the ions.

8.5.v. Decay of medical radioactive isotopes

Radioactive isotopes used in clinical therapy:

- **Linear energy transfer (LET):** Most radioactive isotopes, that are used in clinical therapy, emit β particles as ionizing radiation. The biological effect of this radiation is often characterized by the so-called linear energy transfer (LET) and measured in units of [keV/ μm] for the deposited energy along the particle track.
- **LET versus kinetic energies:** The electrons and positrons emitted in the nuclear β decay or in internal conversion processes often have kinetic energies from tens of keV to several MeV, while their LET ~ 0.2 [keV/ μm] is much lower than for α emitters.
- **α -emitters:** A new class of radioactive nuclides refer to the α emitters ^{149}Tb , ^{213}Bi , ^{211}Po , ^{211}A , ^{223}Ra , ^{225}Ac , ^{227}Ac , ^{226}Th and ^{230}U , which have been considered for therapy.
- **α -emitters:** The LET for most therapeutic α emitters ranges from 25 to 230 [keV/ μm].
- **LET of Auger electrons:** Auger electrons with relatively low energies can have a much higher LET due to their short range (nm to μm). For electron energies below 1 keV, for example, the LET peaks at around 26 [keV/ μm]. Auger electrons have a much shorter range in materials, when compared to the emission of α and β particles, and this makes them ideal tools for targeted radiation therapy.

8.5.w. Universal shape function for charged-particle impact ionization

Universal shape functions:

- **Universal shape function for charged-particle impact ionization cross sections:** A universal shape function can be formulated for the cross sections of single and multiple impact ionization by charged particles. If we refer to the position and the height of the cross section maximum by E_M and σ_M , and if E refers to the *excess* energy of the particle impact, this parametrization is given by (Pattard, 2002)

$$\sigma(E) = \sigma_M x^\alpha \left(\frac{\alpha + 1}{\alpha x + 1} \right)^{\alpha + 1}, \quad x = E/E_M.$$

Here, α is the **Wannier exponent that is characteristic for the given process**, and which follows from Wannier theory. Note that the *excess* energy E is not the projectile (kinetic) energy but the energy that is left to all collision partners after ionization.

- **Universal shape function for charged-particle impact ionization cross sections:** The parametrization above describes indeed the particle-impact ionization cross sections quite well **as long as no excitation-autoionization processes occur at these impact energies.** Apart from the position and height of the *cross section maximum*, the formula is free of further parameters and can be readily applied for fittings (Pattard, 2002).
- **Universal shape function for charged-particle impact ionization cross sections:** The reason that the impact ionization by different particles, such as electrons, positrons, protons or even antiprotons, all follow the same parametrization is given by the **inclusion of the correct power law behaviour** (which is of course different for the different projectiles) near to the ionization threshold. The derivation and use of such threshold laws has been found useful also for parametrizing few-body Coulomb break-up processes.
- **Universal shape function for single-photon multiple-ionization cross sections:** The shape function by Pattard (2002) provides an excellent parametrization of photoionization cross sections if *all* electrons are ionized simultaneously, e.g. for helium. It help parametrize multiple-ionization cross sections whose *ab-initio* calculations is highly non-triveal, especially if three or more electrons are involved. — For photon impact, a universal shape function can only be derived for multiple, at least double, (photo-) ionization.
- **Universal shape function for single-photon multiple-ionization cross sections:** For single-photon multiple-ionization, Pattard (2002) suggest the parametrization

$$\sigma(E) = \sigma_M x^\alpha \left(\frac{\alpha + 7/2}{\alpha x + 7/2} \right)^{\alpha + 7/2}, \quad x = E/E_M,$$

and which obeys the correct limits at low and high photon energies. This is in contrast to the parametrization for charged-particle impact, for which the $\ln E/E$ was neglected for the sake of simplicity.

- **Cross sections at high energies:** From hydrogenic atoms, it is known that photoionization cross sections are proportional to $e^{-7/2}$, while particle-impact cross sections typically follow a E^{-1} or $\ln E/E$ behaviour.

8.5.x. Configuration-averaged energies and cross sections

Configuration averages:

- Configuration-averaged energies: For various applications, it is desirable to use and readily access configuration-averaged energies, rates and cross sections.
- Configuration-averaged energies: Cowan (1981) provides a non-relativistic expression for the configuration-averaged energy as it often occurs in the computation of radiative and collisional rates (Peyrusse, 1999)

$$E_c = \sum_a N_a \langle a \rangle + \sum_{ab} N_a (N_b - \delta_{ab}) \langle a, b \rangle$$

$$\langle a \rangle = \varepsilon_a + \left\langle a \left| -V^{(\text{SCF})}(r) - \frac{2Z}{r} \right| a \right\rangle, \quad \langle a, b \rangle = \frac{1}{2} \frac{g_a}{g_a - \delta_{ab}} \left[R^{(0)}(ab, ab) - \frac{1}{2} \sum_k \begin{pmatrix} \ell_a & k & \ell_b \\ 0 & 0 & 0 \end{pmatrix}^2 R^{(k)}(ab, ba) \right].$$

Here, $g_a = 2(2\ell_a + 1)$ is the degeneracy of subshell a , $V^{(\text{SCF})}(r)$ is the self-consistent atomic potential and $R^{(k)}(ab, cd)$ is the non-relativistic Slater integral.

9. Atomic cascades

Glossary:

- **Absorption cross sections:** The absorption cross section of an atomic cloud is (mainly) determined by contributions from photoionization and the photoexcitation with subsequent autoionization. In JAC, estimates of the absorption cross sections are therefore obtained from a cascade simulation that includes data from an `PhotonIonizationScheme` and `PhotonExcitationScheme` for the photon energies of interest.
- **Cascade approach:** Since atomic cascades may require a large or even huge computational effort, different *approaches* of increasing complexity are distinguished in order to establish a hierarchy of approximations. These approaches differ by the generation and use of the required orbitals, the use of configuration-averaged energies as well as the treatment of electronic correlations (configuration mixing) in the representation of the ASF. In JAC, the (abstract data) `struct Cascade.AbstractCascadeApproach` has been introduced to distinguish and deal with the different approaches.
- **Cascade block:** A group of electron configurations that is described by a common SCF field and Hamiltonian matrix and, hence, accounts for all or parts of the configuration mixing within this group of levels.
- **Cascade:** A cascade typically includes ions of an element in three or more charge states that are connected to each other by different atomic processes, such as photoionization, Auger emission or radiative transitions. A quantum modelling of a cascade requires to follow all possible *pathways* that the ions leads eventually into some stable ground state. In JAC, we distinguish between different *cascade schemes* (photoionization or photoexcitation cascades, decay cascades, electron-capture cascades) and *cascade approaches* to account for different computational models in dealing with the pathways.
- **Cascade computation:** Formally, each cascade computation is splitted into several steps which are treated independently:
 - (i) A list of electron configurations is generated as they may occur during the (photo-) excitation, ionizatiton, electron-capture or decay of levels from one or several initial configurations.
 - (ii) From these configurations, a list of *cascade blocks* (groups of configurations) is then formed and a common SCF field and Hamiltonian matrix calculated for each of these blocks.
 - (iii) For each pair of such cascade blocks, all fine-structure transitions are calculated for the selected excitation, electron-capture or decay processes.
 - (iv) A (common) list of radiative lines, Auger

9. Atomic cascades

lines, etc. is compiled and (usually) written to disk; this *line lists* later form the basis for all subsequent cascade simulations to be considered for the atoms or ions.

- **Cascade scheme:** Since the ‘basic physics’ of an atomic cascade can be very different as well, a number of cascade *schemes* are distinguish internally by introducing the (abstract data) struct `Cascade.AbstractCascadeScheme`. At present, JAC supports the computation of decay cascades (`StepwiseDecayScheme`), photoionizing cascades (`PhotonIonizationScheme`), photoexciting cascades (`PhotonExcitationScheme`) and electron-capture (`ElectronCaptureScheme`), respectively.
- **Cascade simulation:** A cascade simulation makes use of a pre-calculated list of (many-electron) amplitudes, rates and/or cross sections in order to derive different ion, photon and/or electron distributions and spectra, and which can be compared directly to experiment. In JAC, cascade computations and cascade simulations are always handled independently.
- **Distribution:** Experimentally, different ion distributions or photon and electron spectra are measured and need to be compared with simulated data. JAC attempts to model such distributions following the prior excitation, ionization or electron capture of atoms.
- **DR plasma rate coefficients:** The computation of these coefficients require large effort to generate the electron-capture rates into doubly-excited configurations as well as their radiative stabilization. In Jac, estimates of the DR plasma rate coefficients are therefore obtained from cascade simulations that include date from an `ElectronCaptureScheme` as well as a (radiative) `StepwiseDecayScheme`.
- **Electron configuration:** Describes the occupation of shells within the atomic shell model, for instance, $1s^2 2s^2 2p^6 3s^2$. In JAC, closed-shell configurations can be abbreviated by using the noble gases or selected (closed-shell) atoms with a closed ground-state configuration.
- **Graphical representation of a cascade:** The level energies of the different ionization stages of an atom can be arranged as *columns* of either a table or graph; for large cascades, the total table/graph can then be readily ‘reduced’ to a selected energy interval and/or a range of ionization stages. Typically, such a list/graph can provide the user with a very first overview about the cascade. It als enables one to ‘zoom’ into details of the cascade or may form the basis for more sophisticated graphs which, for instance, allow access to lifetimes or *transition data* for pairs of fine-structure levels.
- **Line:** A (transition) line refers to an atomic fine-structure transition that is characterized in terms of a well-defined initial and final levels; these lines frequently occur in the computation of atomic properties, such as cross sections or rates, angular distribution parameters and others. Typically, a line contains various channels (sublines), for instance, due to occurrence of multipoles or of partial waves in the decomposition of the many-electron levels and/or matrix elements.
- **Pathway:** In contrast to an (atomic fine-structure) line, that is characterized by an initial- and a final-level (from the corresponding multiplets), a pathway describe a sequence of three or more levels, and which are often connected via different atomic processes. These levels are usually referred to as initial, (one or several) intermediate as well as the final level of the pathway. Pathways occur naturally in

dielectronic recombination of ions, in various excitation-ionization or excitation-autoionization processes and in photoionization and decay cascades.

- **Shake configuration:** An electron-configuration that does directly occur in an atomic cascade due to photon or electron emission but which may appear by taking *one* or more additional (de-) excitations of electrons into account. These shake configurations can often be considered also as configurations that occur due to (auto- or photo-) *ionization-with-excitation* processes.

Role of atomic cascades:

- **Atomic cascades:** are ubiquitous in nature and have been explored within very different scenarios, from precision measurements to the modeling of astrophysical spectra, and up to the radiation damage in biological matter. Up to the present, however, their quantitative analysis often fails because of complexity. Apart from utilizing the rotational symmetry of atoms and a proper distinction of different physical schemes, a hierarchy of useful approaches is hereby needed in order to keep cascade computations feasible. In JAC, we suggest a classification of atomic cascades that clearly distinguishes between physical scenarios (schemes) and a hierarchy of computational approaches in order to deal with complex shell structures of the atoms and ions.
- **Atomic cascades:** Numerous investigations in physics, astronomy and elsewhere are (strongly) affected by atomic cascades. Examples range from the spectroscopy of few-electron ions to the study of inner-shell phenomena, the diagnostics of plasmas, the interpretation of astrophysical spectra and up to the chemical evolution of the universe. In astrophysics, for example, a current goal refers to a detailed understanding of light curves that help resolve the chemical evolution of the early universe.
- **Atomic cascades:** can exhibit an enormous complexity in practice, even if only the dominant decay paths are considered. This complexity arises first of all from the (often) huge number of decay paths, whose relative importance has been found difficult to estimate in advance.
- **Observations from atomic cascades:** Atoms or ions with inner-shell holes usually emit (Auger) electrons and/or photons of different energy, and which can be observed as — electron or light — spectra by different spectroscopic and detector set-ups. In astrophysics, for instance, much of the information about distant stars and many other astrophysical objects originate from the photon emission of particular atoms or molecules at well-defined wavelength, and which then (may) help reveal the chemical composition of these objects. In practice, however, very rich line spectra have been found in different frequency regions and need to be understood in good detail for analyzing astrophysical observations.

9.1. Cascade computations and cascade simulations

Atomic cascades often require an **enormous computational effort** in order to generate, simulate and interpret all data as required for a given **experiment**. It is therefore both, necessary and desirable, to distinguish between a number of **cascade schemes** to deal with the underlying physics as well as **cascade approaches** to handle a hierarchy of different computational models (approximations). Here, we shall briefly summarize those features that currently supported by the JAC toolbox and by providing a few technical details.

Cascade computations:

- **Cascade computations:** The user has to make sure that all physical-relevant transition data were generated by some prior cascade computation(s) and that they can be uniquely distinguished by the subsequent cascade simulation. In a cascade computation, no attempt is made internally in order to decide, that all relevant data are computed *nor* that all computed data are relevant for the requested simulations. The proper choice and control of these cascade computations therefore require physical insights by the user that goes well beyond of what is done automatically in the present implementation.
- **Complexity of atomic cascades:** Atomic cascades may require a (very) large computational effort in order to generate, simulate and interpret all data as needed for modeling a given experiment. Any cascade computation hereby starts from setting up the cascade *tree*, i.e. the list of configurations, their arrangement into blocks as well as the selection of all relevant steps of the cascade due to the user-allowed (decay) processes. In most cases, these lists of configurations are generated automatically and (may) serve as starting point in order to *group* configurations into the cascade blocks.
- **Cascade computations:** While the cascade computations just generate all the necessary and often rather expensive (many-electron) transition amplitudes and rates, the cascade simulations make use of these data in order to derive ion, photon or electron distributions, rate coefficients or any other information. These cascade simulations are typically much faster than the prior computations, and often quite similar simulations are performed repeatedly for different initial level occupations, energy ranges, or even for different spectra, based on the same data. These simulations need to be *guided*, or sometimes the code even extended, by the user in order to extract the relevant information.
- **Atomic cascades:** While a good number of atomic structure codes exist to model the low-lying levels, recent progress in experimental and experimental techniques support studies on the properties of highly excited levels, such as level densities and x-ray spectra. For these studies, a large number of eigenstates are required by diagonalizing a properly constructed Hamiltonian matrix.

Cascade schemes:

- **Abstract type:** The abstract type `Cascade.AbstractCascadeScheme` defines internally an abstract (data) type to distinguish different excitation, ionization and decay schemes of an atomic cascade. Currently (partly) supported sub-types are `StepwiseDecayScheme`, `PhotonIonizationScheme`, `ElectronCaptureScheme`, `ElectronExcitationScheme`.
- **Decay cascade:** Such a cascade starts from either a few excited (electron) configurations or a given set of initial levels. These (inner-shell) excited levels can then decay by different user-selected atomic processes, such as autoionization, photon emission and others, until a given number of electrons is released and/or the ions cannot further decay to lower levels.
- **Photoionization step:** A photoionization step just models the first (photo-) ionizing part of a cascade. It usually starts from the ground configuration of the atom and automatically includes all those configurations with one electron less that can be reached for the given photon energy. These computation return a (line) list of photoionization amplitudes which, in a cascade simulation, can be combined with data from a subsequent decay cascade.
- **Photoexcitation step:** A photoexcitation step just models the first (photo-) exciting part of a cascade. It usually starts from the ground configuration of the atom and automatically includes all those excited configurations that can be reached by photons from a given energy range. These computation return a (line) list of photoexcitation amplitudes which, in a cascade simulation, can be combined with data from a subsequent decay cascade.
- **Electron-capture step:** A electron-capture step just models the electron-capture part of a cascade. It usually starts from the ground configuration of the atom and automatically includes all those doubly-excited configurations with one electron more that can be reached by the capture of an electron from a given energy range. These computation return a (line) list of electron-capture amplitudes which, in a cascade simulation, can be combined with data from a subsequent (radiative) decay cascade to model the stabilization.

Cascade approaches (computations):

- **Abstract type:** The abstract type `Cascade.AbstractCascadeApproach` defines internally an abstract (singleton data) type to distinguish between various computational approaches/models that can applied to generate and evaluate a cascade. Currently (partly) supported sub-types are `AverageSCA`, `SCA`.
- Here, we briefly summarize these (pre-defined) approaches which can be further controlled by choosing proper parameters for the given cascade computation.
 - i) **Average singe-configuration approach (AverageSCA):** In this approach, just **one common set of orbitals from the initial set of levels is applied for all subsequent ionization stages**. Moreover, all electron configurations in the cascade are treated as a set of single-CSF levels, i.e. without any configuration mixing. Further restrictions of this approach include: Only E1 dipole transitions are applied in all radiative

9. Atomic cascades

decay steps; only the Coulomb interaction is taken into account; each decay step, a (single) set of continuum orbitals is used with energies as obtained from the configuration-average from the initial- and final-state levels of the corresponding configuration blocks, or even simpler from previously generated configuration blocks.

- The AverageSCA approach is likely the simplest way to describe a decay cascade as a sequence of atomic (fine-structure) levels that contribute to the (de-) excitation of inner-shell excited atoms. This simple approach should be realistic in practice for (almost) all atoms and ions from the periodic table. However, much further work is needed to understand how well this approach describes the underlying physics of particular photoexcitation, photoionization, electron-capture or autoionizing cascades.
 - ii) **Single-configuration approach (SCA):** This approach applies a **common set of orbitals for each individual electron configuration (cascade block)** in the given cascade. This includes the configuration mixing among all levels from the same configuration. Some further restrictions of this approach include: Again, only E1 dipole transitions are applied in all radiative decay steps; only the Coulomb interaction is taken into account for the configuration mixing or electron cature; all continuum orbitals are generated without *exchange* with the bound electrons but for the correct fine-structure transition energies in this approach.
 - iii) **Multiple-configuration approach (UserMCA):** In this approach, we intent to support further configuration mixing (electron-electron correlations) between user-selected (and close-in-energy lying) configurations. Here, the user need to *group* different configurations together due to physical insight into the cascade process. Some further restrictions of this approach include:
- For each of these three (cascade) approaches above, the mean computational effort is expected to increase by (at least) one order of magnitude, perhaps also by several orders in going from one to the nexxt step of sophistication.
 - Although the overall computational effort is quite difficult to estimate and formalize in advance for general atomic systems, **the different cascade approaches of the JAC toolbox should be clearly discernible from each other, and the 'cost' of any simpler approach (than some currently selected cascade approach) should be typically negligible**. In general, however, by far not all of these envisaged approaches will be feasible for all requested (or desired) cascade computation.
 - **Cascade approaches** For the given hierarchy of cascade approaches, the mean computational effort is expected to increase by (at least) one or even several orders of magnitudes in going from one approach to the next sophisticated one. These cascade approaches should therefore be clearly discernible from each other, although likely not all of them will be feasible for most atoms and ions. On the other hand, the "cost" of any *simpler* approach will be negligible, when compared to the *best* cascade model that remains feasible in its computations. A refinement of this hierarchy is possible by choosing different physical parameters, e.g. by considering more processes, other multipoles or simply by a better treatment of the continuum for each individual approach.

Implementation of cascade computations:

- **List of electron configurations:** An automatically generated list of electron configurations forms the basic *framework* of all the (implemented) cascade approaches; such a list is also the starting point in order to *group* configurations into the cascade blocks.
- **List of electron configurations:** It is quite *easily possible to remove* electron configurations from the automatically generated list of configurations, either 'by hand' in order to reduce the size of a given cascade computation by physical insight and/or by practical needs; here, further information about the actual size of a given computation should always be made available *before* this 'removal' is made explicit.
- **Line list:** A cascade computation always returns one (or a few) line lists which comprises all lines of the same type, such as `PhotoExcitation.Line`, `PhotoEmission.Line`, `AutoIonization.Line`, `ElectronCapture.Line`, etc. These lines may occur in any order with regard to their transition energies, level specification, or even the charge state of the ions. *These line lists are the expensive parts of any cascade computation and, hence, are stored on disk; they form the input for all subsequent cascade simulations.*
- Since we always have a quite simple access to a list of all levels of the cascade (with more or less full physical specification of each level with regard to its coupling and quantum numbers), it would/should not be difficult to 'add' (or 'replace' some further) rates or transition amplitudes. Such an explicit setting would enable one to incorporate additional 'decay steps' into the cascade, such as double Auger, two-photon decay, etc., and even if the corresponding decay processes are not (yet) supported by the standard scheme of JAC.
- **Initial levels:** A short table is printed for all initial levels, and to which all configurations/levels from the subsequent steps of the cascades are already related.
- **Cascade blocks:** To enable the user to analyze and 'reconstruct' the computations, the program prints the list of generated cascade blocks as well as their size, i.e. the number of CSF, as well as the range of fine-structure energies of each block.
- **Cascade steps:** The requested atomic processes, such as photoexcitation, photoionization, photoemission or electron-capture, is considered for all pairs of cascades blocks; these pairs then define the (so-called) *cascade steps*. Since these steps may consider quite large fine-structure array for both, the initial- and final-state arrays of the given block, the size of the particular output depend on the complexity of the computation. *For each of these steps, moreover, JAC reports the number of lines that are appended to some line list as well as the total number of such line in the list.*
- **Cascade data:** In JAC, the output of different cascade computations is distinguished by the (abstract data) `struct Cascade.AbstractCascadeData` with the presently supported sub-types: `DecayData`, `PhotoIonData`, `PhotoExcData`, `ElectronCaptureData`; cf. below for further details.
- **File storage on disk:** The obtained *line list* are printed to disk eventually by means of the JLD package (and format). JAC tells the user the filename of the given computation, and which are needed as input for all subsequent cascade simulations with the pre-generated line lists.

9. Atomic cascades

- If the fine-structure splitting of two or more intermediate levels in an Auger cascade is small or comparable to the natural line widths of these levels, the angular emission of the subsequently emitted Auger electrons can be described no longer by some incoherent summation over the individual decay paths from the first and second steps of the cascade. For such small level splittings, the **coherence transfer** through all major and nearly degenerate decay channels need to be taken into account by combining, for instance, the many-electron Auger amplitudes from above with the density matrix formalism. This coherence transfer is however not yet considered in JAC.

Cascade simulations:

- **Cascade computations** *versus* **cascade simulations**: While a cascade computation just generates all the necessary and often expensive (many-electron) transition amplitudes and rates, a cascade computation applies the results from one or several such computations in order to obtain the desired ion, photon or electron distributions, or rate coefficients. These cascade simulations are typically much faster than the corresponding cascade computations, and the existing features can be readily extended due to the needs of the users. However, it remains the task of the user to make sure that all physical-relevant transition data were generated by some prior cascade computation and that they can be uniquely distinguished by the subsequent cascade simulation. Because of the complexity of (most) cascades, special care has to be taken by the user to ensure *consistency* of all generated data. To ensure this consistency, JAC can provide only very limited support.
- **Cascade simulations**: typically require to follow (in time) the *flux* of quantum probability, by starting from some initial level population. The detailed re-population of levels in course of the cascade determines the distribution of the emitted electrons and photons, the final charge states as well as many other observables. Different methods can be applied to propagate the quantum probability through a cascade.
- **Cascade simulations**: In the JAC toolbox, the (occupation) probabilities of the atomic levels are propagated from level to level until no further changes *do* occur in the level population. Alternative methods refer to the use of rate equations or Monte-Carlo techniques by randomly generating pathways and by utilizing the corresponding transition amplitudes.
- **Cascade simulations**: Insight into the set-up of an experiment, its geometry, detectors as well as into possible limitations of the set-up is typically required in order to extract the relevant information from a cascade and to compare them with given measurements. More general, perhaps, cascade simulations aim to utilize the transition amplitudes from the previous computations and to combine them according to some particular experiment or measurement. Therefore, the transition data (amplitudes and rates) from the *same* cascade computation can give rise to very different spectra and distributions.
- **Simulation methods**: Various methods can be applied to *simulate* the propagation of the (quantum) probability distribution through an atomic cascade. In JAC, these methods are distinguished by means of the (abstract singleton data) **struct** `Cascade.AbstractSimulationMethod` which, at present, supports the sub-types `ProbPropagation` in order to stepwise propagate the (occupation) probabilities of the atomic levels until no further changes *do* occur. Other possible methods refer to Monte-Carlo methods

(MonteCarlo) to simulate large cascades by the random selection and analysis of pathways or by means of rate equations (RateEquations). However, the latter two methods are not (yet) supported at present.

- **Simulation properties:** In JAC, different properties (distributions) of a cascade can be simulated; they are internally distinguished by means of the (abstract data) struct `Cascade.AbstractSimulationProperty` with the presently supported sub-types: `IonDistribution`, `FinalLevelDistribution`, `DecayPathes`, `ElectronIntensities`, `PhotonIntensities`, `AbsorptionCrossSection` or `DrRateCoefficient`; cf. below for further details.
- **Ion distribution:** Determine the distribution of the ionic charge states after the (decay) cascade of some initially excited atomic levels; cf. `Cascade.IonDistribution`.
- **Final-level distribution:** Determine the final-level distribution of one or several ionic charge states after the (decay) cascade of some initially excited atomic levels; cf. `Cascade.FinalLevelDistribution`.
- **Photon spectra:** Determine the photon (-line) intensities of a cascade as function of energy; cf. `Cascade.PhotonIntensities`.
- **Electron spectra:** Determine the electron (-line) intensities of a cascade as function of energy; cf. `Cascade.ElectronIntensities`.
- **Absorption cross sections:** Determine the total absorption cross section of atoms or ions in a given ground-state configuration as function of photon energy; cf. `Cascade.AbsorptionCrossSection`.
- **DR plasma rate coefficients:** Determine the DR plasma rate coefficients for one or several electron temperatures; cf. `Cascade.DrRateCoefficient`.

Selected cascade computations using Jac:

- **Multiple photoionization of Fe²⁺ ions:** Schippers *et al.* (2020) report relative cross section measurements for single and up to five-fold photoionization of (initially) Fe²⁺ ions, following the photoexcitation and ionization with 690–920 eV photons. This photon range contains the 2p and 2s ionization thresholds. Good agreement were found between the experimental and calculated cross sections, if the simulated spectra were shifted in energy by up to 2.5 eV and if suitable assumptions were made about the initial experimental population of the levels of the Fe²⁺ ([Ar] 3d⁶) ground configuration. While the experimental (threshold) energies are essential for understanding the astronomical observations, the theoretical data can be utilized to generate the required photoabsorption cross-section data for cold ions, and for which the experimental data are not appropriate because of the initial level population.

9.2. In JAC implemented cascade schemes

9.2.a. Decay cascades

Remarks on implementation:

- **Decay cascade:** Such a cascade starts from either a few excited (electron) configurations or a given set of initial levels. These (inner-shell) excited levels can then decay by different user-selected atomic processes, such as autoionization, photon emission and others, until a given number of electrons is released and/or the ions cannot further decay to lower levels.
- **Using JAC:** Perform an `Cascade.Computation(..., approach=Cascade.AverageSCA(), scheme=Cascade.StepwiseDecayScheme([Auger(), Radiative(), ...], ...), initialConfigs=[Configuration(..), ...])`.
- In JAC, a step-wise decay cascade is specified by `scheme=Cascade.StepwiseDecayScheme([process1, process2, ...], nmax, nshake, ...)`, where $process_i$ refers to one of the allowed decay processes of JAC, n_{max} is the (maximum) number of electrons in which the initial- and final-state configurations can differ from each other and n_{shake} the maximum number of electron displacements due to shake-up or shake-down processes in any individual step of cascade (not yet supported).
- **Output data:** The final results of a decay-cascade computation is provided by an instance of the (data) `Cascade.DecayData <: Cascade.AbstractData` that defines a container for a lists of radiative and/or Auger lines.

9.2.b. Photoionization step of a cascade

Remarks on implementation:

- **Photoionization step of a cascade:** A photoionization step just models the first (photo-) ionizing part of a cascade. It usually starts from the ground configuration of the atom or ion and automatically includes all those configurations with one electron less, which can be reached for the given photon energy. These computation return a (line) list of photoionization amplitudes which, in a cascade simulation, can be combined with data from a subsequent decay cascade.
- **Using JAC:** Perform an `Cascade.Computation(..., approach=Cascade.AverageSCA(), scheme=Cascade.PhotonIonizationScheme([Photo()]), ...), initialConfigs=[Configuration(..), ...])`.

- In JAC, a photoionization step is specified by `scheme=Cascade.PhotonIonizationScheme([Photo()], nmax, [e1, e2])`, where `Photo()` refers to the photoionization process, `nmax` is the (maximum) number of photoelectrons, i.e. the number of electrons in which the initial- and final-state configurations can differ from each other and `ei` refers to a list of incident photon energies. At present, only single photoionization (`nmax=1`) is supported by JAC.
- If, as usual, the photoionization leads to a subsequent photon and/or Auger electron emission, a *decay-cascade* computation has to be performed independently, and the data (from these two or more cascade computations) later combined within the cascade simulations.
- **Output data:** The final results of a photoionization step is provided by an instance of the (data) `Cascade.PhotoIonData <: Cascade.AbstractData` that defines a container for a lists of photon energies and associated photoionization lines.

9.2.c. Photoexcitation step of a cascade

Remarks on implementation:

- **Photoexcitation step of a cascade:** A photoexcitation step just models the first (photo-) exciting part of a cascade. It usually starts from the ground configuration of the atom or ion and automatically includes all those excited configurations that can be reached for the given photon energies. These computation return a (line) list of photoexcitation amplitudes which, in a cascade simulation, can be combined with data from a subsequent decay cascade.
- **Using JAC:** Perform an `Cascade.Computation(.., approach=Cascade.AverageSCA(), scheme=Cascade.PhotonExcitationScheme([PhotoExc()], ...), initialConfigs=[Configuration(..), ...])`.
- In JAC, a photo-exciting cascade is specified by `scheme=Cascade.PhotonExcitationScheme([PhotoExc()], minPhotonEnergy, maxPhotonEnergy, NoExcitation, ...)`, where `minPhotonEnergy`, `maxPhotonEnergy` determines the range of photon energies, and hence excited configurations, that need to be considered. `NoExcitations` refer to the (maximum) number of electron replacements with regard to the initial configurations/multiplets.
- If, as usual, the photoexcitation leads to a subsequent photon or Auger electron emission, a *decay-cascade* computation has to be performed independently, and the data (from these two or more cascade computations) later combined within the cascade simulations.
- **Output data:** The final results of a photoexcitation computation is provided by an instance of the (data) `Cascade.PhotoExcData <: Cascade.AbstractData` that defines a container for a lists of photon energies and associated photoexcitation lines.

9.2.d. Hollow-ion cascades

Remarks on implementation:

➤ **Photon emission from hollow ions:** Photon spectra from multiply charged ions are ubiquitous in nature and arise at quite different frequency regions because the emission of photons *is* an important deexcitation mechanism in the stabilization of atoms and ions towards their ground level. Such photon spectra also occur after photoexcitation and particle impact (by electrons, positrons, protons, etc.), or the capture of electrons. For the placement of electrons into shells with medium and high principal quantum n , their stepwise decay towards the ground level typically results in an “emission spectrum” that is characteristic for the initial distribution of the electrons among the occupied subshells.

9.2.e. Radiative recombination cascade

Remarks on implementation:

➤

9.2.f. Dielectronic recombination cascade

Remarks on implementation:

➤

9.2.g. Electron-capture step of a cascade

Remarks on implementation:

- **Electron-capture step of a cascade:** A photoexcitation step just models the electron-capture part of a cascade. It usually starts from the ground configuration of the atom or ion and automatically includes all those excited configurations that can be reached for the given photon energies. These computation return a (line) list of electron-capture amplitudes which, in a cascade simulation, can be combined with data from a subsequent decay cascade.
- **Using JAC:** Perform an `Cascade.Computation(..., approach=Cascade.AverageSCA(), scheme=Cascade.ElectronCaptureScheme([Capture()], ...), initialConfigs=[Configuration(..), ...])`.
- In JAC, an electron-capture cascade is specified by `scheme=Cascade.ElectronCaptureScheme([Capture()], ...)`, where ... determines the range of photon energies, and hence excited configurations, that need to be considered. `NoExcitations` refer to the (maximum) number of electron replacements with regard to the initial configurations/multiplets.
- If, as usual, the electron capture leads to doubly-excited configurations and the radiative stabilization, a (radiative) *decay-cascade* computation has to be performed independently, and the data (from these two or more cascade computations) later combined within the cascade simulations.
- **Output data:** The final results of an electron-capture computation is provided by an instance of the (data) `Cascade.ElectronCaptureData <: Cascade.AbstractData` that defines a container for a lists of capture electron energies and associated capture lines.

9.2.h. Ion impact step of a cascade

Remarks on implementation:

- **Electron-impact excitation cascade:** It is planned to extend JAC towards electron-impact processes, and which would allow to implement some similar procedure as for photoionization cascades. However, this has not yet been done.

9.3. In JAC implemented cascade approaches

9.3.a. Average single-configuration approach (AverageSCA), based on a common set of orbitals (Cascade)

Cascade, notations & application:

- **AverageSCA approach:** This approach simply applies a **common set of orbitals** (from the initial ground- or hole-state configuration of the atom or ion) for all subsequent steps of the cascade. Moreover, each single configuration, that occurs in the decay of the initially excited levels, forms an independent multiplet (cascade block), and each CSF of this configuration also an approximate atomic state; i.e. all further configuration interactions are omitted in this simple approach. This **single-CSF representation of all atomic levels** is assumed to be rather equivalent to using *configuration-averaged rates and cross sections*, although this equivalence is far from being obvious for complex configurations.
- **General restrictions:** (a) Only electric-dipole (E1) transitions are included for all radiative decays; (b) only the Coulomb interaction is taken into account in the configuration mixing and autoionization; (c) continuum orbitals are always generated at an configuration-averaged transition energy and only for partial waves with $|\kappa| \leq 4$.

Computational steps of the AverageSCA and SCA approaches:

- The following steps are carried out separately in both of these two approaches:

 - 1) **Determination of all cascade blocks:** Determine all single configurations that may energetically occur due to photoexcitation, photoionization, photoemission and autoionization processes from the initially chosen configurations/levels, and until a given maximum number of electrons are released from the atom or ion. These electron configurations then form a list of (so-called) **cascade blocks**, from which the decay cascade is built by just calculating all possible decay lines of the user-selected atomic processes for each pair of blocks.
 - 2) **Radial orbitals:** Bound radial orbitals are calculated only for the first (and uppermost) block in the cascade, i.e. the initial hole configuration with the energetically highest-lying energy levels. These bound orbitals are utilized to make the **basis::Basis** of all other blocks explicit together with the geometric specification of all CSF.
 - 3) **Level representation:** An individual level multiplet is calculated for each single non-relativistic electron configuration (cascade block) but without any CI, i.e. without all configuration mixing. Therefore, the levels in all cascade blocks are given by a single CSF, and no explicit diagonalization of the Hamiltonian matrix is required in this approach; the energies of these levels just coincide with the diagonal matrix elements $\langle \gamma J | H^{(\text{Dirac-Coulomb})} | \gamma J \rangle$.

- 4) **Decay processes & cascade steps:** The user-requested radiative and non-radiative excitation and decay processes are considered for all pairs of cascade blocks (configurations). For each of these pairs, standard atomic computations are performed by using the submodules `AutoIonization`, `PhotoExcitation`, `PhotoEmission`, `PhotoIonization`, etc. For a user-selected atomic – excitation or decay – process, this step gives rise to a number (array) of `lines`, if this process can connect this pair of cascade blocks. However, by far not all details of these line computations are printed to screen.
- 5) **Excitation, ionization or decay lines:** All these decay line data are comprised into a few common lists `linesR` (radiative lines), `linesA` (Auger lines), `linesP` (photoionization lines), `linesE` (photoexcitation lines), `linesC` (capture lines), ... and which are finally returned by an instance of `Cascade.Data`.

9.3.b. Single-configuration approach (SCA) with individual sets of orbitals (Cascade)

Cascade, notations & application:

- **SCA approach:** This approach applies an **individual set of orbitals for all blocks of the cascade**, while each electron configuration in the decay tree still forms an independent cascade block, i.e. level multiplet. For each of these blocks, an independent SCF is generated and the configuration mixing included by diagonalizing the Hamiltonian matrix of this configuration. **The single-configuration approach (SCA) is expected to already provide a quite reasonable description of all strong decay pathes.**
- **General restrictions:** (a) Multipoles of the radiative transitions can be defined by the given `Settings` of the cascade computation; (b) continuum orbitals are generated in a slightly simplified Dirac-Fock-Slater potential of the corresponding (final-level) configuration but for energies that are specific to the individual fine-structure transitions; (c) no orbital relaxation is incorporated into the amplitudes apart from those due to the separate orbital representation (SCF) of the initial and final levels.
- See subsection 9.3.a for the individual steps of the cascade computation.

9.4. In JAC partly-implemented cascade approaches

9.4.a. User-grouped multi-configuration approach (**UserMCA**; Cascade)

Cascade, notations & application:

- **UserMCA approach:** This approach also applies an **individual set of orbitals for each block of the cascade which, in addition, can be compiled by the user**. To facilitate the compilation of these cascade blocks, the program first provides a list of (electron) configurations that can be either combined interactively or by some explicitly provided (code). For each of these user-specified cascade blocks, an independent SCF is generated and the full configuration mixing included by diagonalizing the corresponding Hamiltonian matrix. In comparison to the SCA above, **the UserMCA enables one to include further physical insight about strong configuration mixing into the computation of the cascade**.
- **General restrictions:** (a) Multipoles of the radiative transitions can be defined by the given **Settings** of the cascade computation; (b) continuum orbitals are generated in a slightly simplified Dirac-Fock-Slater potential of the corresponding (final-level) configuration but for energies that are specific to the individual fine-structure transitions; (c) no orbital relaxation is incorporated into the amplitudes apart from those due to the separate orbital representation (SCF) of the initial and final levels.
- In this approach, the user can *group* various (electron) configurations together in order to better account for electron-electron correlations (configuration mixing). The set-up of these groups will be supported in JAC by an automatically generated list of electron configurations and by simple tools to compile them together into **cascade blocks** using some list indices.
- For each stage of ionization, the arrangement of electron configurations into a *group* is typically based on either the mean energy, a maximum size (No. of CSF) of individual groups, or upon prior knowledge about strongly-interacting configurations. **This UserMCA approach often requires manual work and, thus, is also prone for making errors.**
- A full (average-level) MCDF approach of all atomic levels can be considered as well within this approximation, if all configurations of each ionization stage are simply grouped together; in practice, however, such a computation is likely unfeasible and of little practical interest.
- Analogue to the SCA approaches, the energies, amplitudes, etc. are calculated for all pairs of levels within a given cascade block (configuration group) or from two such blocks. As before, all line data are comprised into a number of line lists and are returned by a **CascadeData** structure, and before these data can be utilized in simulations of the cascade.

9.4.b. Multi-configuration approach with shake transitions (**ShakedMCA**; Cascade)

Cascade, notations & application:

- **ShakedMCA approach:** Like the UserMCA, this approach also applies an **individual set of orbitals for each block of the cascade**. However, these cascade blocks may include not only those electron configurations that obviously occur in the cascade due to the emission of photons and electrons but also configurations with a *replacement of additional electrons*, and which correspond to additional shake-up or shake-down transitions. The generation of these additional configurations are done via a *maximal number of electron replacements* (input parameters) that are considered in addition to the standard decay configurations.
- **General restrictions:** (a) Multipoles of the radiative transitions can be defined by the given **Settings** of the cascade computation; (b) the use of the Breit interaction in the autoionization and electron capture can also be defined by **Settings**; (c) the continuum orbitals are generated in a slightly simplified Dirac-Fock-Slater potential of the corresponding (final-level) configuration but for energies that are specific to the individual fine-structure transitions; (d) no orbital relaxation is incorporated into the amplitudes apart from those due to the separate orbital representation (SCF) of the initial and final levels.
- These **shake configurations** can be treated as individual groups of configurations or can be grouped together with other configurations of the decay cascade.
- Analogue to the UserMCA approach, the program first provides a list of automatically generated (electron) configurations that can be either combined interactively or by some explicitly provided code. For each of these user-specified cascade blocks, again, an independent SCF is generated and all configuration mixing included by diagonalizing the corresponding Hamiltonian matrix.
- Although the UserMCA and ShakedMCA are quite similar in spirit, the incorporation of shake-up or shake-down configurations typically enlarges the effort enormously and need to be handled with great care. **The ShakedMCA enables one to include further physical insight about strong shake processes and configuration mixing into the computation of the cascade.**

9.5. In JAC implemented cascade simulations

Concept and control of cascade simulations:

- **Concept:** While the ‘physics’ of cascade is often dominated by a few atomic processes, such as photoionization, (spontaneous) photon emission or autoionization, the experimentally observed spectra and distribution depend on the particular set-up and geometry of detectors, spectrographs, etc. Here, the **cascades simulation** may help to flexibly adapt JAC to the particular needs of an experiment. Only a few *standard* simulations (properties) are pre-defined and can be further controlled by some proper settings.
- **Simulation properties:** In JAC, different properties (distributions) of a cascade can be simulated; they are internally distinguished by means of the (abstract data) struct `Cascade.AbstractSimulationProperty` with the presently supported sub-types: `IonDistribution`, `FinalLevelDistribution`, `DecayPathes`, `ElectronIntensities`, `PhotonIntensities`; cf. below for further details.
- **Settings (`Cascade.SimulationSettings`):** All cascade simulation can be further controlled by the setting which allow to specify:
 - `minElectronEnergy ::Float64` ... Minimum electron energy for the simulation of electron spectra.
 - `maxElectronEnergy ::Float64` ... Maximum electron energy for the simulation of electron spectra.
 - `minPhotonEnergy ::Float64` ... Minimum photon energy for the simulation of photon spectra.
 - `maxPhotonEnergy ::Float64` ... Maximum photon energy for the simulation of electron spectra.
 - `initialPhotonEnergy ::Float64` ... Photon energy for which photoionization data are considered.
 - `initialOccupations ::Array{Tuple{Int64,Float64,1}}` ... List of one or several (tupels of) levels in the overall cascade tree together with their relative population.
- **Simulation data:** All simulations are based on data from prior cascade computations, and which are provided by a list of dictionaries, `computationData::Array{Dict{String,Any},1}`.

9.5.a. Ion distributions (Cascade)

Remarks on implementation:

- **Ion distribution:** Determine the distribution of the ionic charge states after the (decay) cascade of some initially excited atomic levels; cf. `Cascade.IonDistribution`.

- Using JAC: Perform an `Cascade.Simulation(..., properties=Cascade.AbstractSimulationProperty[Cascade.IonDistribution()], settings=Cascade.SimulationSettings(...), computationData=data)`.

9.5.b. Final-level distributions (Cascade)

Remarks on implementation:

- **Final-level distribution:** Determine the final-level distribution of one or several ionic charge states after the (decay) cascade of some initially excited atomic levels; cf. `Cascade.FinalLevelDistribution`.
- Using JAC: Perform an `Cascade.Simulation(..., properties=Cascade.AbstractSimulationProperty[Cascade.FinalLevelDistribution()], settings=Cascade.SimulationSettings(...), computationData=data)`.

9.5.c. Photon intensity spectra (Cascade)

Remarks on implementation:

- **Photon spectra:** Determine the photon (-line) intensities of a cascade as function of energy; cf. `Cascade.PhotonIntensities`.
- Using JAC: Perform an `Cascade.Simulation(..., properties=Cascade.AbstractSimulationProperty[Cascade.PhotonIntensities()], settings=Cascade.SimulationSettings(...), computationData=data)`.

9.5.d. Electron-ion coincidence spectroscopy (Cascade)

Remarks on implementation:

- **Electron-ion coincidence spectra:** Determine the; cf. `Cascade.PhotonIntensities`.
- **Resonant $4d \rightarrow nf$ Auger decay of Xe^{5+} ions:** Bizau *et al.* (2016) measured the resonant $4d \rightarrow nf$ ($n = 4, 5$) Auger decay of Xe^{6+} photoion by coincidence of the Auger electrons and the Xe^{6+} ion. Such coincidence measurements allow to distinguish between different decay paths and their branching ratios of the total photoionization cross section.

9.6. In JAC partly-implemented cascade simulations

9.6.a. Absorption cross sections (Cascade)

Remarks on implementation:

- **Absorption cross sections:** Determine the continuous and resonance parts of the absorption cross sections; cf. `Cascade.AbsorptionCrossSections`.
- Using JAC: Perform an `Cascade.Simulation(..., properties=Cascade.AbstractSimulationProperty[Cascade.AbsorptionCrossSections()], settings=Cascade.SimulationSettings(...), computationData=data)`.

9.6.b. DR plasma rate coefficient (Cascade)

Remarks on implementation:

- **DR plasma rate coefficient:** Simulate the DR plasma rate coefficients as function of the plasma parameter and for one selected (ground) state of the initial ion; cf. `Cascade.DrPlasmaCoefficients`.
- Using JAC: Perform an `Cascade.Simulation(..., properties=Cascade.AbstractSimulationProperty[Cascade.DrPlasmaCoefficients()], settings=Cascade.SimulationSettings(...), computationData=data)`.

9.6.c. Electron intensity spectra (Cascade)

Remarks on implementation:

- **Electron spectra:** Determine the electron (-line) intensities of a cascade as function of energy; cf. `Cascade.ElectronIntensities`.
- Using JAC: Perform an `Cascade.Simulation(..., properties=Cascade.AbstractSimulationProperty[Cascade.ElectronIntensities()], settings=Cascade.SimulationSettings(...), computationData=data)`.

10. Collision- and field-induced atomic responses

10.1. Interaction with external particles and fields. Notations

10.1.a. Atoms interacting with external particles

Ion-atom collisions:

- **Coupled-channel calculations:** In particular, coupled-channel calculations within an independent-electron model has been found capable to predict the single-electron capture in slow collisions with helium.
- **Application of ion-atom collision data:** A detailed understanding of the ionization and charge-exchange phenomena in ion-atom collisions is essential for different fields of physics, such as astrophysics, plasma physics or hadron therapy
- **First Born approximation (FBA):** This approximation has often been applied to high-energy ion-atom collisions for which the coupling between different excitation or ionization channels is expected to be negligible. There exist several versions of the FBA approximation to calculate, for instance, electron-capture cross sections in the p-He collisions. For example, a FBA with corrected boundary conditions were developed and utilized at intermediate-to-high energies collision energies, usually based in some independent-particle model. However, the FBA and other perturbative approaches become unreliable whenever the speed of the projectiles is comparable or smaller than the velocity of the target (valence) electrons. For such collisions, a **semi-classical close-coupling approach** is a useful alternative, although these approaches are expensive and often appear quite sensitive to the choice of basis functions as well as to a proper *completeness* of the basis.

10.1.b. Atoms in time-harmonic (Floquet) fields

Floquet formalism:

- **Floquet formalism:** Many physical systems are time-periodic to a good approximation. For these systems, the (time) evolution can be solved either directly by numerical integration of the (time-dependent) SE or by making use of the **Floquet ansatz** to separate out parts of the (time-dependent) Hamiltonian.
- **Floquet formalism:** For a periodic evolution, any time-dependent problem can be transformed also quite easily into a time-independent problem by applying the Floquet formalism. Such a transformation may simplify the solution considerably since time-independent problems can often be solved more efficiently.

10.1.c. Atoms in intense radiation fields

Electron dynamics & processes in intense radiation fields:

- **Simple man's model:** This **three-step model for the electron dynamics in intense radiation fields** provides an intuitive basis for both, the (analytical) strong-field approximation (SFA) as well as for interpretations of the (numerical) solutions of the time-dependent Schrödinger equation. In particular, this model help explain different strong-field phenomena, such as high-harmonic generation (HHG), above-threshold ionization (ATI), the non-sequential multi-electron ionization (NSMI), and several others.
- **Keldysh parameter γ :** The ionization regimes of strong-field processes are often classified by means of the Keldysh parameter

$$\gamma = \sqrt{\frac{I_p}{2U_p}} = \frac{\omega\sqrt{2I_p}}{\mathcal{E}_o} \approx \frac{\omega}{\mathcal{E}_o}, \quad U_p = \frac{e^2 \mathcal{E}_o^2}{4m_e \omega_o^2} = \frac{I_o^2 e^2 \lambda_o^2}{8\pi^2 m_e \epsilon_o c^3} = 9.337 \cdot 10^{-20} I_o \lambda_o^2 \frac{\text{eV}}{\text{W cm}^{-2} \text{nm}^2}.$$

Here, \mathcal{E}_o is the electric-field amplitude, m_e the mass of the electron, and ω_o , λ_o , I_o refer to the central frequency, wavelength and, respectively, the intensity of the incident laser radiation. As usual, moreover, ϵ_o is the vacuum permittivity and c the speed of light.

- **Ionization regimes:** Different operational conditions for strong-field ionization processes are often distinguished in the literature due to the photon energy ω , ionization potential I_p of the atomic targets as well as the ponderomotive energy of the laser field U_p . This table has been adapted from Amini *et al.* (2019).

| Ionization regime | Conditions |
|----------------------------------|-----------------------------|
| Single-photon ionization (SPI) | $\hbar\omega > I_p \gg U_p$ |
| Multi-photon ionization (MPI) | $I_p > \hbar\omega \gg U_p$ |
| Above-threshold ionization (ATI) | $I_p > U_p > \hbar\omega$ |
| Tunnel ionization (TI) | $U_p > I_p > \hbar\omega$ |

- **Above-threshold ionization (ATI)** is a natural extension of multi-photon ionization but where one or several photons *more* are absorbed of which are needed in order to surpass the ionization potential I_p of the atom. In general, ATI processes are often governed by the coexistence of perturbative and non-perturbative distortions of the electron dynamics.

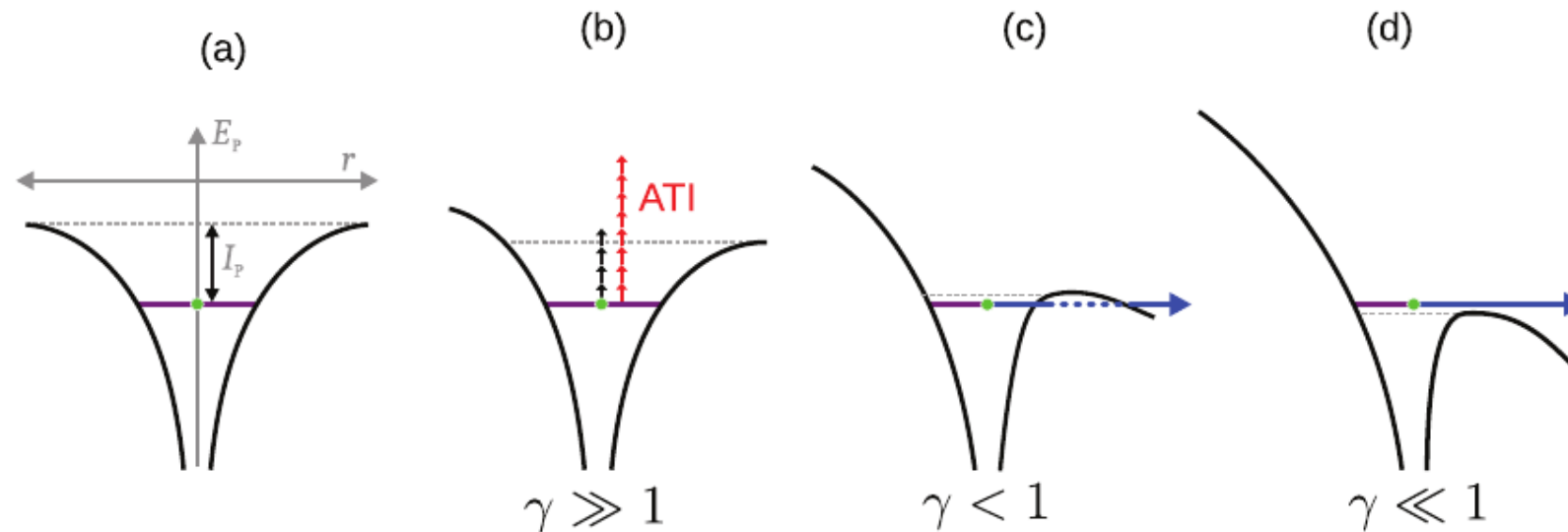


Figure 10.1.: Atomic potential in the presence of an intense laser field: (a) without the laser; (b) ATI absorbs more photons than required for the release of an electron; (c) tunnel ionization, and (d) over-the-barrier ionization. Taken from Amini *et al.* (2019, Fig. 1).

- **High-order ATI (HATI):** In the high-energy region of the photoelectron spectrum at $2 U_p \leq \varepsilon_p \leq 10 U_p$, the electron dynamics is strongly governed by recollisions and the interplay between elastic and inelastic scattering processes.

10. Collision- and field-induced atomic responses

- **Frustrated tunnel ionization:** Frustrated tunnel ionization is one of the dominant channels in strong-field ionization that results in the excitation of atoms. Theory predicts that the excitation efficiency increases with the pulse duration and decreases when going to a few-cycle regime.
- **Tunnel ionization:** Modern short-pulse laser fields can be as intense as the internal atomic fields and, hence, allow ionization of the atom or ions, since the electron just tunnels through the potential barrier.
- **Semi-classical models to strong-field ionization:** In the frequently-applied semi-classical models, an electron first tunnels (nonperturbatively) through the tilted Coulomb potential barrier, and before it can follow a classical trajectory within the field. These models make widely use of the (so-called) **adiabatic tunneling condition**, in which the laser frequency is assumed to be much smaller than the frequency of the bound electron. In practice, however, this approximation has been questioned in the literature since the tunneling (process) is time-dependent. Moreover, these model lost their predictive power for more advanced experiments because its free parameters can always be adapted to some given experiment and does not provide useful predictions.
- **Strong-field ionization of atoms and molecules:** For intense, optical laser fields, the ionization probability depends nonlinear on the field strength and is thus limited for each ionization step to a rather narrow intensity and time interval. In intense laser pulses, therefore, there is virtually no ionization, neither at low intensity (owing to the negligible ionization rate) nor at high intensity (since all ions of the considered charge state are already ionized).
- **Ponderomotive energy:** The ponderomotive energy U_p refers to the time-averaged kinetic energy of a free electron in a laser field.

Rescattering in strong laser fields:

- **Rescattering in strong laser fields:** The rescattering of a photoelectron at its parent ion is a crucial process for describing the multi-electron dynamics in strong light fields. In semi-classical theory, a laser-driven rescattering of the photoelectron leads to the well-known “ $3.2 U_p$ ” rule for the maximum energy of the recurring electron, and where the ponderomotive potential U_p denotes the quiver energy, i.e. the mean kinetic energy of a free electron in the laser field.
- **Rescattering in strong laser fields:** The scattering of the photoelectron at its parent ion gives rise to the high-energy plateau in the above-threshold ionization (ATI), to the inner-shell excitation of the parent ion, the generation of high harmonics as well as to attosecond pulses in the soft x-ray region.
- **Re-scattering in SFA:** In the strong-field approximation, the **re-scattering of electrons can be taken into account via a Born-like rescattering matrix element**, and which clearly improves the agreement with experiment for high photoelectron momenta and emission angles, for which the direct SFA matrix element alone results in quite small probabilities. Indeed, the low-energy structures in the photoelectron spectra

mainly arise from soft (multiple) laser-driven recollisions and are encoded in the rescattering SFA matrix element. In the SFA, no particular features arise around $2 U_p$, although the re-scattering SFA matrix element is known to become dominant between $2..4 U_p$. The re-scattering contributions are relevant up to the re-scattering cutoff around $10 U_p$, from where on the photoelectron yield ceases quickly with increasing energy (Keil *et al.*, 2016). If, in addition, the Coulomb potential is taken into account, the probability for direct and rescattering ionization can become comparable even between $0..2 U_p$.

- **Over-barrier-ionization (OBI) field:** The electron field for a (classical) over-the-barrier ionization is classically given by: $\mathcal{E}^{(\text{OBI})} = i_p^2/(4 e^3 Z)$.

Strong-field spectroscopy:

- **Laser-induced electron diffraction (LIED)** refers to a spectroscopic technique in which structural information about the atomic target is derived by measuring the doubly-differential elastic scattering cross-sections in the re-collision of electrons with the target atoms. Obviously, however, a very detailed theoretical understanding of the ATI and HHG processes is hereby needed in order to extract useful information from (time-resolved) LIED and HHG spectrum. In the simple man's model, contributions to the LIED spectrum arise especially from highly-energetic returning electrons with $2 U_p \leq \varepsilon_p \leq 10 U_p$ that collide elastically with their parent ion and that lead to a very characteristic momentum transfer and momentum distributions of the released electrons.
- **Above-threshold ionization (ATI) spectroscopy:** Since both, the bound-free and the rescattering continuum-continuum transitions are CEP sensitive, the ATI photoelectron distribution can be utilized also in order to extract information about the electronic structure of the target atoms.
- **Subcycle tracing of ionization enabled by infrared (STIER) pulses:** STIER pulses refers to a streak camera that temporally resolves strong-field ionization caused by a linearly-polarized few-cycle pulse. STIER provides insight into the sub-cycle dynamics of strong-field ionization. STIER samples the photoelectrons produced by a few-cycle laser pulse in the near-visible spectral range, for example at 735 nm (Kübel *et al.*, 2017).
- **STIER:** This method enables one to separate the electron wave packets generated at different half-cycle maxima of the visible pulse. The best separation occurs, when the visible pulse is centered around a field maximum of the IR pulse, i.e. when the signal in the STIER trace is centered around $p_z = 0$. In this case, the observed momentum distribution directly reflects the ionization dynamics during a single half-cycle.
- **Stimulated Raman adiabatic passage (STIRAP) in the x-ray regime:** The STIRAP technique has been utilized to engineer molecules and quantum matter. While it was first explored in the optical region, it can be expanded to the x-ray regime by combining x-ray lasers and

10. Collision- and field-induced atomic responses

x-ray spectroscopy. In this regime, the light interacts non-linearly with the core electrons at the atomic length and time scales of inner-shell electrons.

Nonsequential double ionization (NSDI):

- Non-sequential double ionization (NSDI): NSDI of atoms is often discussed as a pure and classic prototype for the multi-electron dynamics in strong fields. NSDI was first reported in the 1980s for rare gas atoms and has been explained (at least qualitatively) within the single-active electron approximation, where both electrons are assumed to be ionized sequentially, though not independent of each other and by accounting for some explicit correlation mechanism.
- Non-sequential double ionization (NSDI): The observed momentum spectra from doubly and multiply charged ions clearly indicate that the emission of the second, third, etc. electron is usually triggered by the laser-driven recollision of the first electron with its parent ion. In kinematically complete experiments, the correlated two-electron momentum distributions has been explored for different laser parameters.
- NSDI mechanisms: Different mechanisms can be distinguished in the NSDI: (i) the well-known $(e, 2e)$ -mechanism due to a direct electron-impact ionization of a second electron by the re-colliding first electron; (ii) recollision-induced excitation with subsequent ionization (RESI), in which the re-colliding electron makes an electron-impact excitation of the second electron, and which is subsequently field-ionized. RESI is sometimes expected to contribute with a delayed emission of the second electron with regard to the recollision itself.

10.1.d. Atoms in few-cycle pulses

Few-cycle intense laser pulses:

- Intense laser pulses: Nowadays, few-cycle femtosecond laser pulses can be routinely produced **both, in the visible as well as mid-infrared regimes**. If these few-cycle pulses are focused properly, **ultra-intense electric fields can be generated with peak-field strengths which are comparable to the (static field) in the atom**.
- Carrier-envelope phase (CEP): Light pulses with a well-defined absolute or **carrier-envelope phase (CEP)** are crucial for extracting information about the electron dynamics in strong-field physics. A good control of the CEP is particularly important if the HH are generated by pulses with just one or a few optical cycles, since the CEP phase then directly determines the relevant electron trajectories and whether a single or multiple attosecond bursts of radiation is emitted.

- **Double ionization of Ar by near-single-cycle laser pulses:** Bergues *et al.* (2012) report the double ionization of Ar by near-single-cycle laser pulses. In particular, they measured the two-electron momentum spectra that substantially differ from prior spectra, based on multi-cycle pulses. These spectra have been interpreted as strong-field NSDI of argon atoms with a cross-shaped structure. From the CEP-resolved spectra, moreover, these authors were able to identify the correlated emission of two electrons at sub-femtosecond timescales.

Attosecond pulse trains & spectroscopy:

- **Attosecond pulse trains:** The high-harmonic process can be applied to generate attosecond pulses with excellent coherence in the extreme ultraviolet or even in the soft x-ray regime; here, an unprecedent time structure of these trains can arise quite readily since the ionization of the electrons occurs just close to the maxima of the electric field and, hence, the electrons always return *in time*, namely, when the laser field is just zero.
- **Attosecond pulse trains:** Such pulse trains are generated by means of multi-cycle femto-second laser pulse, while a single broadbanded attosecond pulse can be produced from a single-cycle continuous broadband spectrum.
- **Circularly-polarized attosecond pulse trains (APT):** Because of the spatial separation of the left- and right-circularly polarized harmonics at the detector, twisted APT with well-defined circular polarization can be generated. For example, one obtains a right-circularly polarized APT for low angles of divergence $\beta \approx 1$ mrad, and right-circularly polarized APT for $\beta \approx 2$ mrad.
- **Attosecond pulses:** The generation of structured high-frequency pulses with well-defined torus-knot angular momentum also results in bright xuv radiation with customized polarization and OAM. These pulses may enable one to explore the spin-orbit coupling at the nanoscale or to study subtle changes in the photoionization dynamics of single atoms or molecules.
- **Attosecond pulses:** Attosecond pulses from laser-driven XUV sources support a high temoral resolution but are typically available only for photon energies below 50 eV. This limitation has excluded so far XUV-pump/XUV-probe investigation of inner-shell processes. This limitation can be partly surpassed by making use of two-photon absorption processes. Bergues *et al.* (2018) report measurements on xenon with excitation energies of 93 eV and 115 eV, which has opened the door for attosecond real-time observation of nonlinear electron dynamics deep inside atoms.
- **Attosecond pulse measurements:** Attosecond pulses help resolve the electronic motion in atoms, molecules and solid-state matter and have lead to number of novel spectroscopic techniques, such a attosecond streaking or ...
- **Photoelectron momentum distributions in attosecond pulses:** In any (attosecond) light pulse, the asymptotic momentum of the photo-electron depends of course on the em fields (vector potential) of the streaking pulse and how the electron propagates in the continuum. A particular streaking trace can be obtained by detecting the asymptotic momentum (for a given direction in the PMD) as a function

10. Collision- and field-induced atomic responses

of the time delay between the ionizing and streaking pulses. A (so-called) **temporal shift (streaking time delay)** can be assigned to each streaking trace when compared to the oscillation of the incident vector potential. This streaking time delay is often expressed as sum of the Wigner-Smith time delay and a laser-Coulomb (coupling) delay (Goldsmith *et al.*, 2017)

$$\Delta t^{(\text{streaking})} = \Delta t^{(\text{Wigner-Smith})} + \Delta t^{(\text{laser-Coulomb delay})}.$$

While the Wigner-Smith time delay is related to the short-range potential of the residual photoion, the laser-Coulomb (coupling) delay follows from the long-range part of the Coulomb potential. Predictions for this time delay have been performed both, numerically and analytically.

- **Attosecond spectroscopy:** Predictions on the outcome of attosecond experiments depend sensitively on how well the under-the-barrier dynamics of the electron can be described just at the onset of tunneling ionization. Experimentally, this requires good control of the incident laser pulse with high time and/or energy resolution.
- **Application of attosecond pulses:** The recent progress in developing ultrashort optical light sources with quite high intensity has lead to new applications, such as attosecond science, the extreme ultraviolet (XUV) nonlinear optics or molecular imaging. These developments may enable one to measure or even control the electronic motion in atoms, molecules and solids.
- **Attosecond XUV-pump & attosecond-XUV-probe experiments:** Such attosecond XUV pump-probe experiments have not (yet) been implemented and are technically rather difficult to perform. However, theoretical studies suggest that such experiments can make visible the correlated electron dynamics, for instance, by recording the corresponding momentum distribution of two subsequently emitted electrons.
- **Attosecond spectroscopy:** The recollision of electrons with their target atoms has been found a key for understanding the electron dynamics in atoms and molecules. However, such a re-collision is suppressed in an intense circularly-polarized field, including HHG and nonsequential double ionization. In circularly-polarized fields, instead, the sequential double ionization provides information on interelectronic correlations and has been explored by angular streaking in the femtosecond regime. In this regime, the ionization time is mapped upon the ejection angle of the emitted electrons (Winney *et al.*, 2017).
- **Attoclock experiments:** These experiments have mainly explored the adiabatic tunnel ionization of atoms in elliptically-polarized few-cycle pulses and have shown that the angular distribution in the (azimuthal) polarization plane, i.e perpendicular to the laser propagation, shows a shift with regard to the direction of the (strongest) electric field in the laser pulse. This shift in the azimuthal angle φ has (partially) be attributed to a time delay of the ionization due to the tunneling of the electron through the barrier that is formed by the potential of the atomic core and the adiabatically changing electric field of the laser. Until the present, however, **there is no clear evidence that such a ‘tunneling time’ has any physical relevance.**

Attosecond streaking spectroscopy:

- **Attosecond streaking spectroscopy:** This spectroscopy permits the observation of single-electron dynamics with an attosecond time resolution because a (strong) few-cycle infrared laser field is utilized as a clock.

10.1.e. Atoms forming local plasma

None.

10.2. In JAC considered ion-atom collisional responses

10.2.a. Semi-classical ion-atom collisions [theoretical background]

Semi-classical approximation for ion-atom collisions:

- **Semi-classical approximation (SCA) for ion-atom collisions:** In the semi-classical approximation, the target is often assumed to be fixed (for instance, at the origin of the coordinates), while the projectile moves with constant speed v_p along a straight line with impact parameter b : $\mathbf{R}(t) = (b, 0, v_p t)$.
- **Goals of the SCA:** The goal is to solve an **effective single-electron TDSE** for initially occupied target electrons; in general, the *key* in using the SCA is to find a proper potential to be included into the single-electron TDSE.

$$i \frac{\partial \phi_k(\mathbf{r}, t)}{\partial t} = h(t) \phi_k(\mathbf{r}, t), \quad k = 1, \dots, N.$$

- **Charge-exchange in ion-atom collisions:** The charge-exchange or (charge-) transfer between bare projectiles and multi-electron atoms has mainly been studied experimentally during the past decades. In most early measurements, however, the capture into specific shells of the target could not be resolved and only estimates of the total capture cross sections could be made. For low collision energies, the charge transfer is dominated by the capture of electrons from the outermost target shells, while at higher collision energies more and more inner-shell electrons get involved. At the intermediate and practically most interesting collision energies, therefore, the interplay (interferences) due to the capture of both, inner-and outer-shell electrons, need to be taken into account and may considerably change the curvature of the total cross sections. This is in contrast to ion-hydrogen collisions for which the charge-transfer cross section usually vary monotonically at all energies (Belkic, 1988)).

Applications of ion-atom collisions:

- **Proton-atom collisions & ionization:** Chuluunbaatar *et al.* (2019) presents fully differential single-ionization cross sections for the impact of 1 MeV protons on helium. Both, ultra-high resolved experimental and theoretical cross sections in Born approximation are provided and agree reasonably well within the *kinematic* regime close to the (so-called) Bethe ridge. Further away from this region, however, the binary peak is clearly shifted with regard to the observations.

- **Measurement of ion-atom collision cross sections:** The cold-target recoil ion momentum spectroscopy (COLTRIMS) has been found a versatile tool for measuring and analyzing ion-atom ionization processes since it help determine the three-dimensional angular distribution of electrons at given values of energy and momentum transfer. Moreover, COLTRIMS has reached an unprecedented precision.
- **Application of ion-atom collisions:** Studies of ion-impact ionization processes are of fundamental and applied interest in order to understand, for instance, the penetration of swift ions through matter. Moreover, ion-atom collisions find their application in radiation material science and ion therapy.
- **Measurement of ion-atom collision cross sectionss:** In COLTRIMS measurement, the following fully-differential cross sections (FDCS) have been recorded for proton-helium collisions with regard to the energy E_e and solid angle Ω_e of the electron as well as the solid angles of the scattered proton Ω_p :

$$\text{FDCS} := \frac{d^5 \sigma}{dE_e d\Omega_e d\Omega_p} = \frac{k_e m_p^2}{(2\pi)^5} |T_{if}|^2; \quad \text{FDCS} := \frac{d^5 \sigma}{dE_e d\vartheta_e d\varphi_e dq d\varphi_q} = |\sin \vartheta_e| \frac{k_e q}{(2\pi)^5 v_p^2} |T_{fi}|^2,$$

and where (ϑ_e, φ_e) are the angles of the emitted electrons with regard to the axis of the incident proton beam and φ_q the azimuthal angle of the momentum transfer.

- **Fully-differential cross sections:** The upper form of the FDCS is used especially for studying the binary and recoil peaks in the electron angular distribution and how these peaks are shifted with regard to those from a simple Born approximation. In contrast, the second form can hardly be compared with experiment but has been applied in order to analyze various kinks in the cross sections as well as the asymmetry of the FDCS in forward and backward directions.
- **Kinematic region for ion-atom collisions:** For proton-helium collisions, most previous computations were done so far for the kinematic regime of small momentum transfer (0.75 a.u.) and low ejected-electron energy (6 eV).

Single-electron capture and subsequent x-ray emission in ion-atom collisions:

- Leung *et al.* (2015) studied the x-ray spectra following the single-electron capture in collisions of 4.54 keV/amu bare Ne¹⁰⁺ ions with helium, neon and argon gas targets. In this work, the single-particle capture probabilities were calculated by using the two-center basis generator method, based on independent electrons. Moreover, the response of the target on the capture cross sections and x-ray spectra was modeled by means of an time-dependent screening potential.
- Using COLTRIMS techniques, a triple-coincidence measurement on 4.54 keV/amu Ne¹⁰⁺ ion collisions with helium, neon and argon gas targets were carried out by Ali *et al.* (2010) who obtained (relative) shell-selective capture cross sections and x-ray spectra. In these

10. Collision- and field-induced atomic responses

measurements, the x-ray spectra from single-electron capture were separated from those from a multiple-electron capture due to coincidences with hydrogenic Ne^{9+} ions.

- Several groups have studied charge-exchange collisions in the laboratory in order to measure capture cross sections and the subsequent x-ray emission. For example, the Lyman-*alpha* emission was recorded for $\text{C}^{6+}\text{-Kr}$ and $\text{O}^{8+}\text{-Kr}$ collisions at low and intermediate collision energies. In these studies, emphasis was placed especially to estimate reliable single-electron capture cross sections.
- **Classical overbarrier model (OBM):** This model suggests that hydrogen and krypton should have (very) similar shell-selective capture cross sections because of the similar ionization potentials of 13.6 eV and 14.0 eV, respectively. However, a comparison of experimental data shows a rather different subshell selectivity, i.e. with regard to the electron capture rate into $(n\ell)$ subshells.
- To model the single-electron capture cross sections from a krypton target, an effective ground-state potential was obtained from the optimized-potential method by Talman and coworkers which includes the electron-nucleus interaction as well as terms due to screening and exchange (Leung *et al.*, 2018)).

10.3. In JAC considered high harmonic (HH) responses

10.3.a. High-harmonic generation HHG [phenomenology]

Basics of HHG:

- **HHG:** High-order harmonic generation is a non-linear (optical) up-conversion process for which the conservation of energy, linear momentum as well as spin and orbital angular momentum of individual harmonics can often be expressed by means of simple selection rules. This non-linear process is mediated by a laser-driven recollision mechanism of electrons, and which may lead to high harmonics with photon energies hundreds or even thousands times larger than the driving laser frequency.
- **HHG:** In HHG, an electron wavepacket in an atomic, molecular or material system is liberated and accelerated by an intense laser field. The oscillations of the laser field then drives back (parts of) the electron wave packet to its parent ion, and where the acquired kinetic energy is released in terms of a high-order harmonics. The energies of these harmonics can span deep into the EUV and soft x-ray spectral regions (Dorney *et al.*, 2018).
- **High-harmonic generation:** When an *intense* laser ($I \sim 10^{14} \text{ W cm}^{-2}$) irradiates an (atomic) gas target, coherent radiation at multiples of the fundamental laser frequency is emitted. This process is called **high-harmonic generation (HHG)**.
- **Regions of the high-harmonic spectrum:** For a given ponderomotive potential $U_p = I/4\omega_o^2$ (in atomic units), the harmonic spectrum can often be decomposed into two regions: (i) the plateau of harmonics with photon energies below $3.17 U_p + I_p$ and with rather constant yields as well as (ii) the harmonics of higher energy but with rapidly decreasing yield. Hereby, the (so-called) **harmonic cut-off energy** increases linearly with the peak intensity I and decreases quadratically with the incident laser frequency ω_o .
- **HHG versus multi-photon emission:** In comparison to HHG, most multi-photon emission and ionization processes have a rather limited complexity and can be described perturbatively.
- **Maximum harmonic order:** In a classical model, the electron can gain in a field with ponderomotive potential $U_p = I/4\omega^2 = \mathcal{E}_o^2/4\omega^2$ a maximum of $3.17 U_p$ kinetic energy and, hence, the (so-called) **cut-off energy for the harmonics is $3.17 U_p + I_p$** . In the saddle-point approximation, in contrast, one finds solutions where the electron returns with a kinetic energy $\gtrsim 4 U_p$ and which correspond to orbits with no *classical* counterpart.
- **Plateau auf HH:** If the high harmonics arise from the excitation with low-frequency lasers, the (HH) spectrum exhibits a characteristic behaviour, namely, a rapid decrease of the yield for the first few harmonics, and which is followed then by a **plateau and a rather abrupt cut-off**.

10. Collision- and field-induced atomic responses

- **HHG** is known as a unique source of coherent and collimated xuv femto- and attosecond pulses. However, the efficiency of HHG is notoriously low, although it might be (moderately) enhanced if the resonances of the atomic or molecular targets are properly exploited. Indeed, the *free* one-dimensional motion of the electrons in the laser field is very essential for HHG as seen from the rapid decrease of the harmonic yield for an incident elliptical laser.
- **Efficiency of HHG:** Great efforts have been undertaken in order to increase the efficiency and photon flux in HHG. This efficiency is strongly influenced also by collective effects, such as the propagation and phase matching of the HH emitted from individual atomic targets, and where the maximum efficiency is affected by the absorption of the harmonics in the surrounding gas.
- **Conversion efficiency of HHG:** The conversion efficiency of HHG from the infrared to the XUV regime decreases rapidly owing to an enhanced ionization of the target (atoms) and an increasing phase-matching sensitivity.
- **Gas-phase HH generation:** Gas-phase HH are generated when a (gas-jet) of atoms or molecules are irradiated by strong laser pulses. The emitted harmonics from such a jet are *coherent* and may easily reach the soft x-ray regime. HHG is now frequently applied in various ultrafast-science experiments. HHG can be utilized to generate single attosecond pulses and attosecond pulse train, and which open the door to time-resolved studies of the electron dynamics at the attosecond scale.
- **HHG conversion efficiency:** The typical macroscopic conversion efficiency of the high-order harmonic (HH) process is about 10^{-4} at 30 eV and decreases rapidly down to 10^{-9} at 300 eV. For near- to mid-infrared laser pulses, moreover, the conversion efficiency of HHG decreases exponentially with (increasing) wavelengths, and has been demonstrated experimentally and theoretically. The largest conversion efficiency is achieved if the (macroscopic) contributions of absorption, laser focusing and phase matching is optimized simultaneously.
- **Absorption-limited conversion efficiency of HHG:** Constant *et al.* (1999) found that the maximum conversion efficiency of HHG is ultimately limited by reabsorption of the generated HH photons within the (generating atomic) medium itself. In particular, this so-called **absorption-limited conversion efficiency** is proportional to the absorption cross section $\sigma(q\omega)$ at the frequency $q\omega$ of the q -th harmonic. Therefore, the efficiency can be enhanced only if the emission cross section can be enhanced independent of the absorption.
- **HHG:** High-order harmonics, i.e. highly-energetic photons at multiples of the (fundamental) laser frequency, can be produced by focusing either a high-frequency (excimer) laser or some low-frequency laser (Nd:glass, Ti:sapphire) into an atomic gas.
- **HH spectra:** The properties of high-harmonic spectra have been intensively explored with regard to the energy, linear momentum as well as the orbital and spin angular momenta of the individual harmonics.
- **Role of the atomic target for HHG:** For atoms, only the valence electrons (orbital) are considered to be relevant for HHG and, hence, a direct link between HHG and valence-shell photoionization might exists and might be observed in the spectra. For example, the HHG spectrum is known to show a lower intensity at the Cooper minimum in the photoionization cross section of argon atoms. Such a correspondence

between the HHG and photoionization exist also for resonances in the photoionization cross sections and might help enhance the low efficiency of the HHG process. For the resonances in the photoionization cross sections, indeed, a large number of case studies exist in the literature and helped establish relations to the autoionization or to the shape and giant resonances of atoms.

- **HHG with linear *versus* circularly-polarized beams:** All harmonics that are generated by means of linearly-polarized beams are generally also linearly polarized, while HHG with (single) circularly-polarized beams is strongly suppressed, since the classical trajectories of the electrons will not come back so easily to the parent ion (Lorentz force) and since the (same) helicity of several photons *cannot* be add up to a well-defined helicity of the HH.
- **HHG with bicircularly-polarized beams:** HHG becomes possible for superposition of a circularly-polarized beam with its counter rotating second (or higher) harmonic. For such a superposition of two counter-rotating fields, the electric field of a bicircular field exhibits a Lissajous (-type) figure, and this obviously help return the electron back to the parent ion; cf. Figure 10.2
- **High-gain harmonic-generation at free-electron lasers:** Such a high-gain HHG@FEL has been demonstrated experimentally by means of laser-seeding in order to produce amplified, longitudinally coherent and Fourier transform-limited output at a certain harmonic of the seed laser. For example, a seed carbon dioxide laser with 10.6 micrometers help produce saturated and amplified second-harmonic wavelength at 5.3 micrometers. These experiments helped verify the technique and paved the way for its application in the vacuum ultraviolet region of the spectrum, and perhaps to even provide intense and highly-coherent hard x-rays in the future.
- **High-gain harmonic-generation at free-electron laser:** Single-pass FEL bunches provide the intensity and spatial coherence of SASE but with high temporal coherence. In the HHG@FEL, a seed laser imposes a small energy modulation of the electron beam while passing through a short undulator (the modulator). This energy modulation is then converted into a coherent spatial density modulation as the electron beam traverses a dispersion magnet (a three-dipole chicane). If a second undulator (the radiator) is tuned to a higher harmonic of the seed frequency ω , a microbunched electron beam emits coherent radiation at the harmonic frequency $n\omega$. These HH have a single phase that is determined by the seed laser and spectral bandwidth that is limited by the Fourier transform. **The HHG@FEL may result in a high degree of stability and control of the central wavelength, bandwidth, energy, and duration of the output pulse.**
- **High-harmonic spectroscopy (HHS):** The term HHS has been used in the literature in order to refer to measurements on the electron dynamics at its natural timescale, such as the analysis of electron-ion recollisions, delay times in photoionization or charge migration (Fareed *et al.*, 2018).
- **Behavoir of harmonic spectra:** High harmonics have been generated with frequencies several hundred times the fundamental frequency by irradiating atoms and molecules by intense laser light and under suitable conditions. The harmonic spectrum is typically characterized by a fast decrease in the low-energy region, a plateau at medium and high frequencies, and followed by a sharp cutoff. Studies have shown also a moderate minimum within the plateau region that is associated with the electronic structure of the target atoms or molecules.

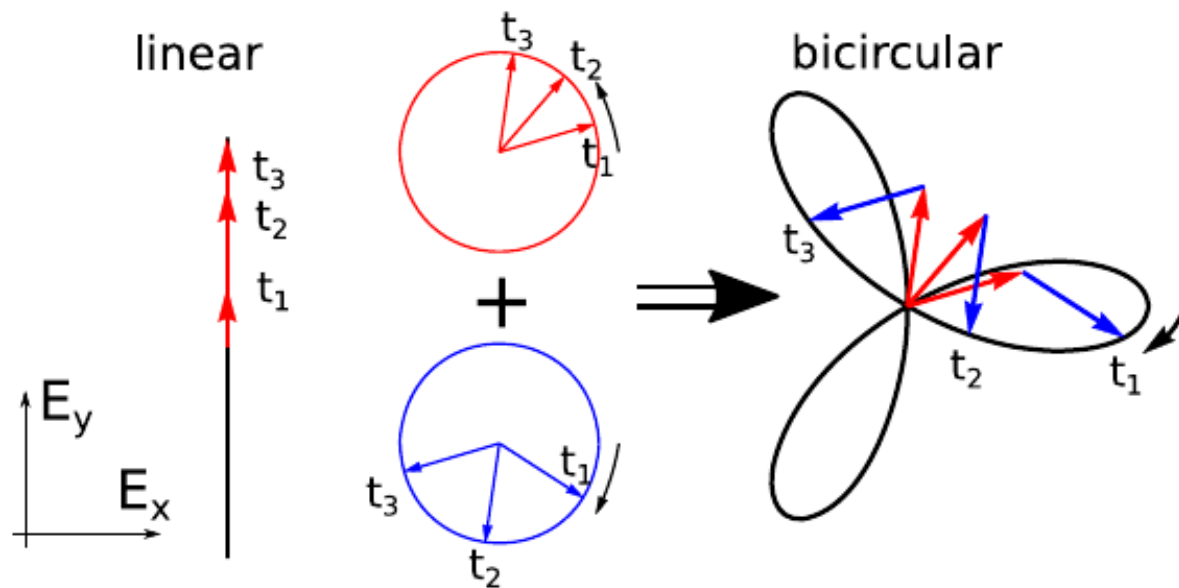


Figure 10.2.: Parametric plots of the electric field vectors at different times t_1, t_2, \dots . (Left) The electric field vector in a linearly-polarized beam just oscillates in one dimension. The red arrows indicate the electric field vectors at three different times. (Middle) Circularly-polarized field (red) and its counter-rotating second harmonic (blue). The arrows indicate the electric field vectors at the same times as for the linearly-polarized field. (Right) Bicircular field as a superposition of a circularly-polarized beam and its counter-rotating second harmonic, which gives rise to a Lissajous figure for the electric field. From Paufler *et al.* (2019, Fig. 5)

- **HHG with a xenon target:** A giant resonance structure in the harmonic spectrum has been reported for an xenon target if irradiated by mid-infrared laser pulses. In particular, a sudden increase in the harmonic yield arises around 100 eV that is related to the giant $4d$ resonance in the photoionization cross sections and that arises from the large $4d - 4f$ oscillator strength. This is often called a collective pheomonon, although neither a truly collective theory exists nor is it needed in order to understand the increase in the photoionization cross sections.
- **High-harmonic generation (HHG):** HHG has been shown with gas jets, laser-ablated plumes and a number of other targets.
- **FERMI FEL:** FERMI is located at the Elettra laboratory in Trieste; it covers the VUV to soft x-ray photon energy range with two FEL that are both based on High-Gain Harmonic Generation (HGHG) seeded mode.

- **Rates for HHG:** Explicit formulas for the HHG rate within the three-step model are provided, for instance, by the Lewenstein model and include a *factor* from the field-free photorecombination cross section (third step). While the derivation of these formulas are made in the single active-electron approximation, the proportionality of the HHG rate to the field-free photorecombination cross section already indicates quite **strong multi-electron effects upon the HHG rate for most atoms, since the photorecombination cross section are know to be sensitive to the description of the many-electron wave functions.** Although the role of such electron correlations upon the HHG spectra has been discussed *qualitatively* in the literature, not many detailed computations have been carried out so far.
- **Resonant electron capture in HHG:** If the relative phase of different capture processes is neglected, the dielectronic resonance strength $S(i \rightarrow d \rightarrow f) \propto \frac{2\pi^2 \hbar}{k_i^2} A_r$ determines entirely the behaviour of the resonance. For low- and medium-Z elements, therefore, no significant enhancement in the HHG spectrum is expected even if the capture (Auger) rate for the formation of the doubly-excited states is quite large.
- **Microscopic and macroscopic view of HHG:** Any theoretical modelling of HH spectra in a gaseous medium must combine a microscopic *and* macroscopic analysis of the generation and superposition of the emerging high-frequency radiation field. In the microscopic model, the harmonic spectrum of the individual atoms is obtained from the (approximate) solution of the Schrödinger equation, and these single-atom spectra need then to be superposed from a macroscopic viewpoint due to the target and intensity distribution within the focus area of the laser. Of course, this superposition generally leads to a loss of coherence and to a broadening of the HH.
- **Harmonic emission rates of single-active electron atoms:** If the laser field is not too strong, the harmonic emission rates can be estimated from perturbation theory. For a strong laser pulse, in contrast, one needs either to resort to the direct numerical solution of the time-dependent Schrödinger equation (TDSE) or to the strong-field approximation (SFA). While a direct solution of the TDSE is often possible only for some (1D or 3D) *model atom*, the SFA combines a rigorous theoretical treatment (of parts of the electronic motion in the TDSE) with various semi-empirical arguments about the generation and the potentials, as seen by the *free* electrons. Such a quantum-mechanical description of harmonic generation was originally formulated by Lewenstein *et al.* (1994). Both approaches give rise to very similar results for the (so-called) *cut-off* frequency $\omega^{(\text{cut off})} \approx I_p + 3.2 U_p$ of the harmonic spectrum in terms of the ionization potential I_p and the ponderomotive energy $U_p = \mathcal{E}_o^2/(4\omega^2)$, i.e. the mean kinetic energy of an electron in the laser field.
- **Cutoff in HHG:** Using the semi-empirical three-step model, the high-harmonic cutoff has been estimated $E^{(\text{cutoff})}[\text{eV}] = I_p + 3.17 U_p = I_p + 2.96 \cdot 10^{-13} I \text{ W/cm}^2 (\lambda [\mu\text{m}])^2$, and where I_p , U_p , I , λ refer to the ionization potential, the ponderomotive energy, laser intensity and the laser wavelength, respectively.
- **Blueshift and reduction of the laser intensity in HHG:** In experiments with increasing laser intensities or gas densities (or length), the driving laser field can be remarkably re-shaped during its propagation through the atomic cloud, and this then leads to a **blueshift and an intensity reduction of the laser pulse.** For similar reasons also, the recorded high-order harmonic spectra crucially depends on the frequencies and phase matching that may or may not arise during the propagation of the pulse.

HHG from solid-state targets:

- **HHG with solid targets:** High-harmonic spectra from solid targets generally display a quite different behaviour, when compared with gaseous targets. In particular, **the cut-off energy does not increases linearly with the peak intensity but more with the peak electric-field amplitude \mathcal{E}_0 of the driving laser field.** In solids, moreover, one sometimes distinguishes between intra-and interband excitations due to the laser frequency, but where these terms are usually not well defined nor explained.
- **HHG from laser-ablated plumes:** Since laser-ablated plumes can serve for HHG as a nonlinear medium, laser ablation is a technique to generate high harmonics from many solid-state materials. This technique helped widen the choice of atoms and molecules for which the (attosecond) electron dynamics can be studied through high-harmonic spectroscopy. These solid-state targets also provide other resonances, including (giant) autoionizing resonances, and which are known to affect the high-harmonic spectra in the vicinity of these resonances. Emphasis has been placed recently for studying the impact of such giant resonances upon the ultrafast ionization dynamics of transition metal atoms.
- **Multi-electron contributions to HHG:** Little is known so far how inter-electronic contributions affect the high-harmonic spectra, although rather intense harmonics have been demonstrated for a xenon gas jet near the $4d$ autoionization resonance at 100 eV. In these earlier studies, semi-empirical arguments were sufficient in order to explain the HH spectrum due to the Coulomb interaction between the $4d$ electrons and the tunnel-ionized $5p$ in atomic xenon.

Phase matching of HHG spectra:

- **Phase matching of HHG:** Usually, rather dense atomic targets of $\sim 10^{17}$ atoms/cm $^{-3}$ are needed in order to generate high-order harmonics. Apart from the microscopic interaction of individual atoms, however, one has also to consider also the macroscopic target distribution in order to analyze the superposition of all individual responses.
- **Phase matching of HHG:** Any theoretical treatment of HHG must incorporate both, the microscopic response of the atoms to the local em field as well as the macroscopic propagation of the field through the (extended) gas cloud. Such a complete treatment formally requires the self-consistent solution of Maxwell's equations in three dimensions and coupled to the time-dependent Schrödinger equations (TDSE) for the atoms, a truly prohibitive task. In practice, even the solution of the TDSE for the response of the atoms is usually replaced by a separation of the electron excitation into the ionization (low-frequency part) and the high-harmonic radiation that is emitted during the oscillation of the electrons with regard to their parent ions (high-energy part). Moreover, this high-energy part is often treated semi-classically and by neglecting the potential of the ionic core upon the oscillations. Such a classical model then enables one to simulate experimental gas lengths and studies on control strategies, based on the trajectories of electrons after ionization (Berman *et al.*, 2018).

- **Phase matching of HHG sources:** Since HHG requires the (collective) superposition from many individual emitters, the phase matching of the driving laser and the emitted harmonics in the gas medium is crucial. In practice, this phase matching is known to depend on a multitude of parameters, such as gas pressure, interaction length, focus position with respect to the gas target, laser intensity as well as a few others.
- **Phase matching of HHG:** A (phase matching) analysis of the HH spectrum may help improve the conversion efficiency and provides information about the cutoff of the harmonics. It also aims to find conditions so that the radiation from most atoms to a given harmonic add up constructively at the detector.
- **Size of atomic targets for HHG:** For the HHG with Gaussian beams, a sufficient intensity often occurs only within a thin cylinder of $\simeq 7$ mm length and a radius of $\simeq 730 \mu\text{m}$, and with about 1000 atoms within this tiny volume. Even for such a rather small volume, however, the radiation emitted from different atoms is not in phase. **Phase-matching aims to find areas in the interaction regions, for which an intense signal with good phase is obtained at the detector.**
- **Phase of the emitted radiation:** For target atoms at different positions, two contributions crucially determine the phase of the q -th harmonic, namely, (i) **the dipole phase owing to the response of a single atom to the local intensity** of the beam as well as (ii) **the intrinsic beam phase** as it naturally arise from focusing the laser beam.
- **Phase matching on axis:** For Gaussian beams, this just refers to a simplified 1-dimensional model, and which can be adapted also to Laguerre-Gaussian beams.

High-harmonic generation (HHG) with twisted light beams:

- **High harmonics with well-defined OAM:** Circularly-polarized HH with well-defined OAM can be generated with bicircular LG beams. Moreover, these HH may form also **circularly-polarized (twisted) attosecond pulse trains** if the intensity ratio of the bicircular driving fields has been tailored properly.
- **Microscopic & macroscopic interplay of HHG with twisted beams:** For driving beams with helical phase fronts, in particular, both the (microscopic) interaction of the individual target atoms as well as the (macroscopic) superposition of the emitted radiation in the far-field plays a crucial role for the generation and detection of HH. The interplay of these two components to the recorded spectra determines eventually the OAM as well as divergence of the emitted high harmonics.
- **HHG with OAM:** The OAM of the HH can be controlled, or even explicitly *selected*, by tuning the polarization, intensity (ratio) and OAM of the driving laser fields.

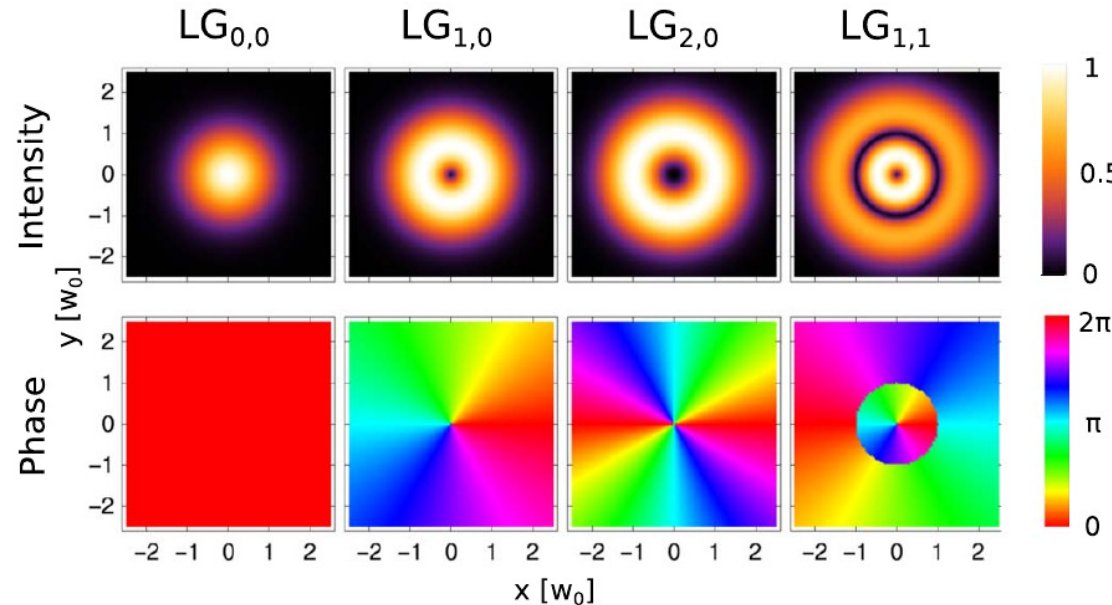


Figure 10.3.: Intensity (upper panel) and phase profiles (lower panel) of different LG beams at the focal plane ($z = 0$). Left column: A Gaussian beam has its intensity maximum at the beam axis and a constant phase profile because of its *zero* OAM. Middle columns: $\text{LG}_{\ell,p}$ beams with angular momentum ℓ , in contrast, have zero intensity at the beam axis and a $2\pi \ell$ phase change in going once around the beam axis. Right column: $\text{LG}_{\ell,p}$ beams with $p > 0$ exhibit $p + 1$ rings in the intensity profile and a corresponding phase profile with a p -dependent phase and a phase change $2\pi \ell$. From Paufler *et al.* (2019, Fig. 1).

➤ **Selection rules for the q -th harmonic:** For an (incident) linearly-polarized twisted light beam with frequency ω and orbital angular momentum ℓ , the q -th harmonic obeys the selection rules:

$$\text{HHG @ } \text{LG}_{\ell,p}^{\omega \leftrightarrow} \longrightarrow \begin{cases} \omega_q = q \cdot \omega \\ \ell_q = q \cdot \ell \\ \text{linearly-polarized} \end{cases} .$$

➤ **Selection rules for the q -th harmonic:** For (a co-linear superposition of) two bicircular light beams with frequencies ($\omega, 2\omega$) and orbital

angular momenta (ℓ_1, ℓ_2) , both the SAM and OAM are conserved simultaneously, and the q -th harmonic obeys the selections rules:

$$\text{HHG @ } \text{LG}_{\ell_1,0}^{\omega\circlearrowleft} \oplus \text{LG}_{\ell_2,0}^{2\omega\circlearrowleft} \longrightarrow \begin{cases} \omega_q = q\omega = m\omega + n2\omega \\ \ell_q = m\ell_1 + n\ell_2 \\ m - n = \pm 1 \end{cases}.$$

For this particular HHG scheme with bicircular $(\omega, 2\omega)$ beams, every *third* harmonic is suppressed, while the other two contributing harmonics exhibit alternating helicities due to $m = n \pm 1$. This can be seen also from the photon-coupling diagram for each harmonic and, hence, the OAM of the generated harmonics can be tailored explicitly for a proper combination ℓ_1, ℓ_2 of the bicircular beam, cf. Fig. ???. In addition, it is possible that all generated harmonics carry the same modulus of OAM if the incident beams have the OAM $\ell_1 = -\ell_2$.

More caption for Figure ??: Different arrows from the left-upper corner here represent the absorption and emission of photons from different beams. (a) Superposition of two linearly-polarized LG beams with the same photon energy but different OAM. This scheme gives rise to **multiple couplings for the generation of each harmonic order and, hence, each harmonic may carry different values of OAM**. (b) Non-collinear superposition of a strong Gaussian beam with a weaker LG beam gives rise to the spatially separated xuv-vortices with a well defined OAM. (c) Non-collinear superposition of a strong Gaussian with its second harmonic. Similar to (b), we get spatially separated xuv-vortices, each with well-defined that carry a well-defined OAM as well. (Right) Photon-coupling diagrams of HHG with with bicircular twisted beams. (a) Superposition of two LG beams with the same OAM. For each harmonic order, **there is only one possible diagram which gives rise to xuv vortices with well-defined OAM**. Each of these harmonic is circularly-polarized. (b) Superpositions of two LG beams with opposite OAM. Since the number of photons absorbed from the ω -beam always differs by one from the number of photons absorbed from the 2ω beam, the modulus of the OAM of each xuv vortex is $|\ell| = 1$.

- **HHG with two-color, counter-rotating LG beams:** Paufler *et al.* (2018) reports a method that help generate extreme ultraviolet vortices from the high-order harmonic generation with two-color counter-rotating Laguerre-Gaussian (LG) beams. High harmonics with all possible values of OAM can be generated if the two incoming LG modes are properly chosen. It is shown that **HHG with two-color counter-rotating LG modes result in circularly-polarized XUV vortices with still well-defined OAM**, and for which the formation rules for bi-circular fields can be readily extended to account for frequency (ratio) and the OAM values of the bichromatic field.
- **Formation rules for HHG:** To generate the q -th harmonic with well-defined energy $\hbar\omega_q = q\hbar\omega$ and OAM, one has first to determine the number of photons that need to be absorbed from each beam

$$m = \frac{q \pm 2}{3}, \quad n = \frac{q \mp 1}{3}, \quad m, n, q \in \mathbb{N},$$

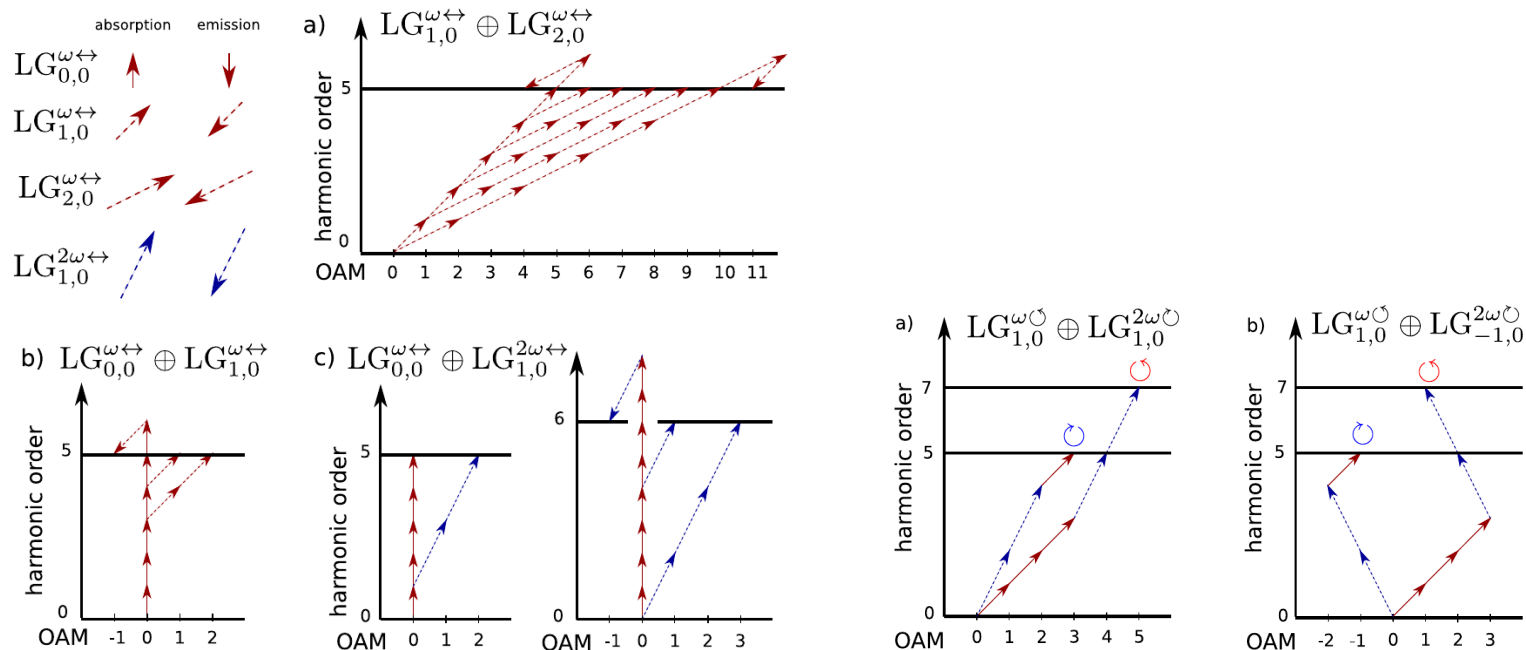


Figure 10.4.: Photon-coupling diagrams in HHG. (Left) Three different scenarios of HHG with superpositions of two linearly-polarized (Laguerre-) Gaussian beams are shown and can be utilized in order to control and manipulate the OAM of the generated harmonics. ...

and which implies that every third harmonic (if q is a multiple of 3) is clearly suppressed. In order to determine the OAM of the incident beams, the linear Diophantine equations

$$\ell_q = m \ell_1 + n \ell_2, \quad m - n = \pm 1, \quad \Rightarrow \quad \begin{cases} \ell_1 = a n \\ \ell_2 = -a n \end{cases} \quad a \in \mathbb{Z},$$

and which have a solution for all non-suppressed harmonics. Note that the (projection of the) OAM values ℓ_1, ℓ_2 can hereby be also negative; c. Table 10.5.

High-harmonic generation (HHG) with linearly-polarized LG beams:

| Frequencies | Harmonic order | OAM | m | n | SAM | ℓ_1 | ℓ_2 |
|---------------------|---|--------------|-----------------------|-----------------------|--------------|---------------------|---------------------|
| $\omega + 2\omega$ | $q = m + 2n$ | ℓ_{H_q} | $\frac{q \pm 2}{3}$ | $\frac{q \mp 1}{3}$ | $m - n = 1$ | $\ell_{H_q} + a n$ | $-\ell_{H_q} - a m$ |
| | $q = 1, 2, 4, 5, \dots$ | | | | $m - n = -1$ | $-\ell_{H_q} + a n$ | $\ell_{H_q} - a m$ |
| $\omega + 3\omega$ | $q = m + 3n$ | ℓ_{H_q} | $\frac{q \pm 3}{4}$ | $\frac{q \mp 1}{4}$ | $m - n = 1$ | $\ell_{H_q} + a n$ | $-\ell_{H_q} - a m$ |
| | $q = 1, 3, 5, 7, \dots$ | | | | $m - n = -1$ | $-\ell_{H_q} + a n$ | $\ell_{H_q} - a m$ |
| $r\omega + s\omega$ | $q = rm + sn$ | ℓ_{H_q} | $\frac{q \pm s}{r+s}$ | $\frac{q \mp r}{r+s}$ | $m - n = 1$ | $\ell_{H_q} + a n$ | $-\ell_{H_q} - a m$ |
| | $q = r, s, 2r + s, 2s + r, 3r + 2s, 3s + 2r, \dots$ | | | | $m - n = -1$ | $-\ell_{H_q} + a n$ | $\ell_{H_q} - a m$ |

Figure 10.5.: Parameters of the incident bi-circular LG beams that enable one to generate high-order harmonics with well-defined OAM. Apart from the frequency ratio of the counter-rotating beams (first column), the harmonic order and the OAM of the emitted harmonic (second and third column) are shown. m and n in the fourth and fifth columns are the number of photons from the first and second incident beams which lead to the q -th harmonic. The column labeled with SAM gives the SAM of the q -th harmonic if the first beam has SAM $\ell_1 = 1$ and the second beam SAM of $\ell_2 = -1$, respectively. The last two columns can be used to determine the required OAM of the incident beams in order to generate the q -th harmonic with an OAM of ℓ_q ; taken from Paufler *et al.* (2018).

➤ **HHG with two (non-) colinear but linearly-polarized LG beams:** The OAM of the generated harmonics can be controlled by using superpositions (so-called mode mixing) of two or more twisted beams; cf. Figure ??.

(1) For two co-linear and linearly-polarized LG beams with the same frequency but different OAM, let us simply write

$$\text{HHG @ } \text{LG}_{1,0}^{\omega \leftrightarrow} \oplus \text{LG}_{2,0}^{\omega \leftrightarrow} \Rightarrow .$$

For such mixed beams, different photon pathes contribute to the q -th harmonic; cf. the photocoupling diagrams in Fig. ???. Obviously, however, if the electron absorbs n photons from the first beam, it must emit $q - n$ from the second beam (and where $n > q$ is also possible, though much less likely). Quite generally, the HHG probability decreases with the (total) number of photons that are involved in the process, and with a rather sharp cut-off criterion.

10. Collision- and field-induced atomic responses

- (2) For two non-colinear but linearly-polarized LG beams with the same frequency and different OAM, we write instead

$$\text{HHG} @ \text{ LG}_{0,0}^{\omega \leftrightarrow} \oplus \text{LG}_{1,0}^{\omega \leftrightarrow}, \angle.$$

For such a superposition, the high harmonics will not have a well-defined OAM here but their wave vectors still need to fullfil $\mathbf{k}_q = n_1 \mathbf{k}_1 + n_2 \mathbf{k}_2$, $n_1 + n_2 = q$. Therefore, the harmonics generated by different pairs of photon numbers (n_1, n_2) will eventually be spatially separated at the detector.

- (3) For two non-colinear but linearly-polarized LG beams with different frequencies and different OAM, we write

$$\text{HHG} @ \text{ LG}_{0,0}^{\omega \leftrightarrow} \oplus \text{LG}_{1,0}^{2\omega \leftrightarrow}, \angle.$$

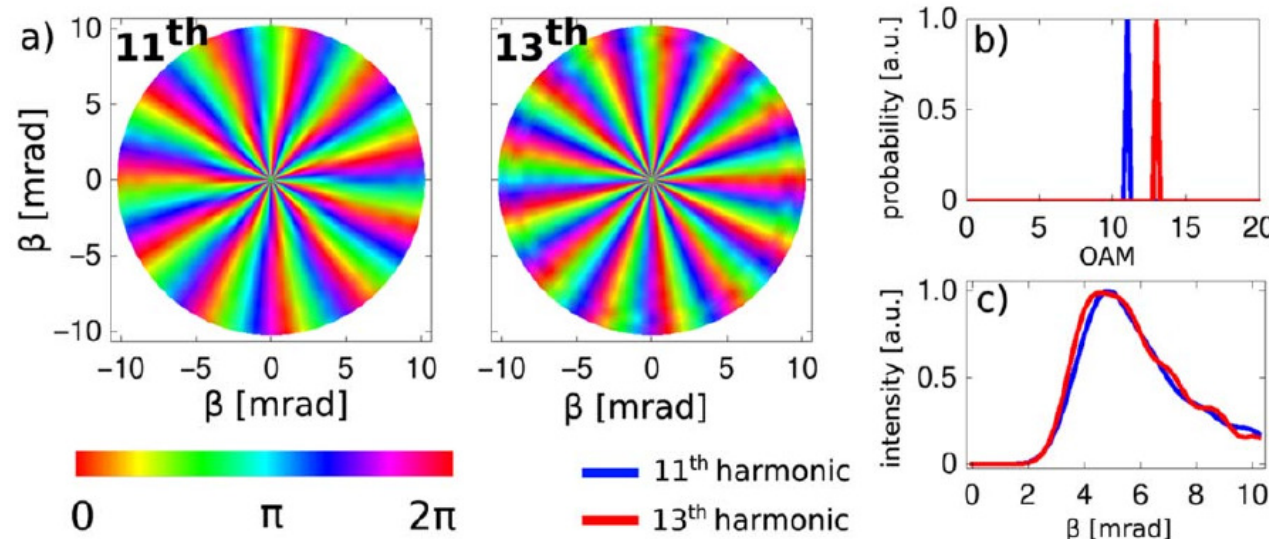


Figure 10.6.: Phase profile and spectrum of HH, generated with a linearly-polarized LG beam: (a) Phase profiles of the 11th and 13th harmonic at the detector, and where the OAM (number of phase canges of π) is equal to the harmonic order. (b) OAM of the 11th (blue) and 13th (red) harmonic as obtained by a Fourier transform along the azimuthal coordinate. (c) Intensity distributions of the 11th (blue) and 13th (red) harmonic in the far-field. From Paufler *et al.* (2019, Fig. 3).

10.3. In JAC considered high harmonic (HH) responses

10.3.b. High-harmonic generation in the strong-field approximation [theoretical background]

High-harmonic theory:

- **Modelling of HHG:** Various methods have been applied to model the HH spectra for incident laser fields with different polarization. Apart from solving the time-dependent Schrödinger equation (TDSE) for the active electron or even in some *reduced* dimension, semi-empirical quantum orbits, strong-field theory (Lewenstein model), factorization methods as well as the *quantitative* rescattering (QRS) method were used with different success. In addition, the HHG by vortex beams and noncollinear two-color laser field have attracted recent attention.
- **Lewenstein's model for HHG:** This model describes the interaction of a single (-electron) atom with a plane-wave laser within the **dipole approximation** (homogeneous electric field). In this approximation, the time-dependent SE can be solved analytically if the following three assumptions are made: (i) only the ground state and the continuum states of the electron contribute to the overall time-evolution of the state of the atom; (ii) the electron always moves as *free* particle within the continuum, independent of the remaining potential $V(r)$ of the parent ion; and (iii) the time evolution of the electronic state does not lead to a depletion of the ground state.
- **Lewenstein's model for HHG with twisted beams:** This model, and especially the dipole approximation, is still justified to describe the HHG with twisted light beams, if the **azimuthal phase dependence due to the OAM ℓ is properly taken into account**. In particular, the dipole approximation remains valid here in the optical and infra-red regions since the released electron in the HHG process typically just travels 1-2 nm away from its target atom and, hence, does not feel (much of) the spatial structure of the twisted light field.
- **Lewenstein's model of HHG** is therefore expected to be valid for low-frequency and rather intense lasers, i.e. the basic assumptions of SFA. The long-wavelength limit for λ_o (when compared with the Bohr radius $a_o = 5.29 \cdot 10^{-11}$ m) ensures a spatially homogeneous electric field over the extent of the atom (**dipole approximation**),

$$\mathbf{E}(t) = \mathcal{E}_o f(t) \sin(\omega_o t + \phi_o) \mathbf{e}_z.$$

- **HHG power spectrum:** From the time-dependent dipole amplitude $d(t)$, the HHG power spectrum is obtained as the time-integrated Fourier transform

$$d(\omega, \omega^{(\text{laser})}) = \frac{i}{\omega T} \int_{-T}^T dt e^{-i\omega t} d(t), \quad \mathcal{P}(\omega, \omega^{(\text{laser})}) = |d(\omega, \omega^{(\text{laser})})|^2.$$

- **HHG at relativistic intensities:** At these intensities, the Lorentz deflection becomes so large that no recombination occurs and the HHG plateau terminates earlier than at lower intensities.

High-harmonic amplitudes in the near- and far-field:

- **Far-field HH spectra from twisted beams:** To predict (and explain) the HH spectra in the far-field at the detector, one needs to sum over all the single-atom responses due to the interaction of these atomic centers with the twisted beam. Obviously, this summation affects the overall phase and intensity profile as well as the OAM of the observed HH radiation in the far-field.
- **Fraunhofer diffraction formula:** This formula can be applied in order to calculate the phase and intensity profile of the far-field for the different orders of the HH. To make use of this formula, the contributions of the individual target atoms to the HH amplitude need to be model properly, for instance by assuming a thin layer of (target) atoms, and which might be displaced with regard to the focus plane.
- **Complex amplitude of q -th harmonic:** Using Fraunhofer's diffraction formula, the spatically-dependent (complex) light field, averaged over time, can be written in terms of the wavelength $\lambda_q = \lambda/q$ and the (complex) near-field amplitude $A_q^{(\text{near-field})}(\rho', \varphi', z')$ of the q -th harmonic

$$A_q^{(\text{far-field})}(\beta, \varphi) = \int_0^\infty d\rho' \rho' \int_0^{2\pi} d\varphi A_q^{(\text{near-field})}(\rho', \varphi', z') \exp\left(-\frac{2\pi i}{\lambda_q} q' \tan \beta \cos(\varphi - \varphi')\right),$$

and where β refers to the polar angle (angle of divergence) with regard to the incident beam.

- **Near-field amplitude of the q -th harmonic & for an incident twisted beam:** In Lewenstein's model, the near-field amplitude of the q -th harmonic can be expressed as $A_q^{(\text{near-field})}(\rho', \varphi') = f(\rho') e^{i\ell_q \varphi'}$, and where $f(\rho')$ includes all the radial dependence.
- **Complex amplitude of q -th harmonic:** For this simple expression of the near-field amplitude from Lewenstein's model, the integration over the azimuthal angle φ' in the complex far-field amplitude above can be carried out analytically

$$A_q^{(\text{far-field})}(\beta, \varphi) = 2\pi i^{\ell_q} e^{i\ell_q \varphi} \int_0^\infty d\rho' \rho' J_{\ell_q}\left(\frac{2\pi}{\lambda_q} \beta \rho'\right).$$

Here, $J_k(x)$ refers to a Bessel function of the first kind. The polar angle β_{\max} , for which the (modulus of the) far-field amplitude reaches its maximum, is a simple measure for the divergence of each harmonic order. Apparently, this divergence increases with the OAM $\ell_q \propto q \cdot \ell$ but decreases with the harmonic order q . Therefore, **all harmonics are emitted with quite similar divergence**.

Phase of target atoms to the far-field amplitude:

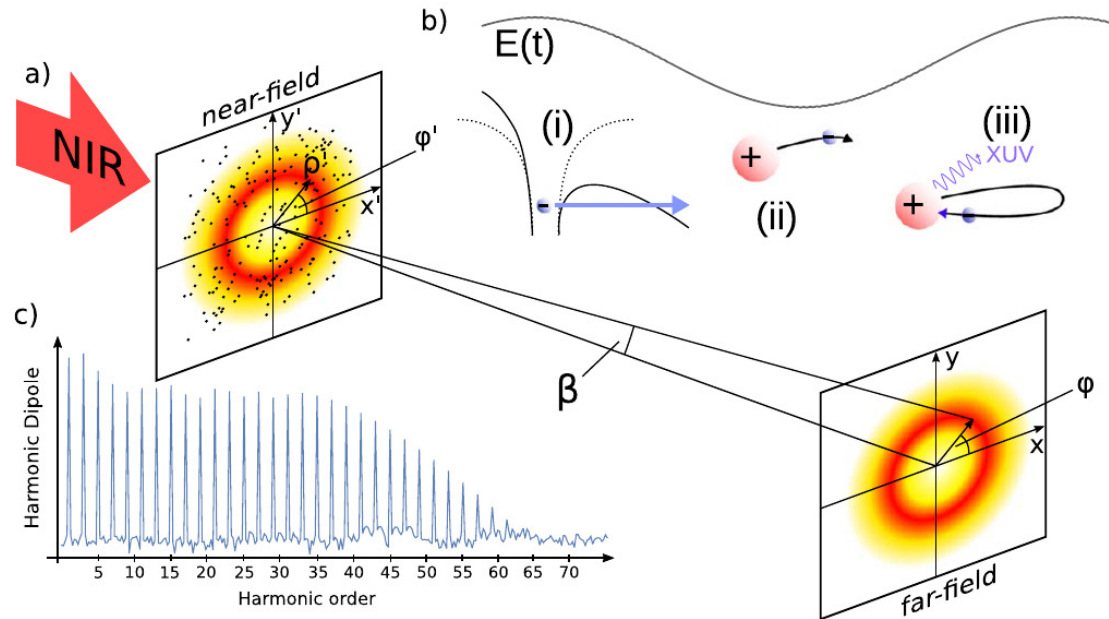


Figure 10.7.: HHG in the near- and far-field. (a) Superposition of the far-field due to locally generated HH in the near field and as described by the Fraunhofer diffraction formula. (b) Illustration of the simple man's three step model: (i) release of the electron by tunnel ionization, (ii) propagation and acceleration of the free electron in the strong laser field and (iii) recombination of the electron with the parent ion under the emission of a high-energetic photon at multiple laser frequency. (c) Typical high-harmonic spectrum as generated with a linearly-polarized laser field, and where only odd harmonic orders contribute to the spectrum. From Paufler *et al.* (2019, Fig. 2).

➤ **Effective dipole phase:** Different terms contribute to the effective dipole phase of an atomic target atom:

- (i) The **focal phase** arises from the phase-front ratio $R(z) = z(1 + z_r^2/z^2)$ due to the non-zero Rayleigh range $z_r = k W_o^2/2$ and the finite beam waist W_o . For LG beams, the focal phase is $k r^2 / 2 R(z)$ and, hence, independent of the OAM of the beam.
- (ii) The **intrinsic phase** owing to the Gouy phase as well as the OAM of the beam.

➤ **Coherence length of HHG:** This length characterizes the (changes in the) total phase of the HH amplitude and is simply given by:

$$L_q^{(\text{coherence-length})}(r, z) = \frac{\pi}{|\nabla \phi_q(r, z)|}.$$

This expression shows immediately that a zero phase-mismatch results in perfectly matched harmonics $L_q^{(\text{coherence-length})} \rightarrow \infty$. In practice, a coherence length ~ 1 mm already refers to quite good experimental conditions.

Phase matching in HHG with twisted light:

- **Phase matching on maximum:** For an incident Gaussian beam, HH are dominantly emitted *along* the (beam) axis since these harmonics mainly arise near to the intensity maxima in the cross section perpendicular to the direction of the beam. In the phase-matching analysis, it is therefore often sufficient to consider the target distribution just *on axis*, a simplification known as **phase matching on axis**. A similar simplification can be made also for LG beams if this ‘fictitious axis’ is either shifted to the first intensity maximum of the beam or if one just considers the target distribution along the ‘ring’ as defined by the first intensity maximum. We here refer to this approximation as **phase matching on maximum**.
- **Intensity maximum of LG beams:** For an $\text{LG}_{\ell,0}$ beam, the first intensity maximum can be written in terms of the beam waist W_o and the Rayleigh length z_r ; it is given by the radius

$$r_{\ell}^{(\max)}(z) = \sqrt{\frac{|\ell|}{2}} W(z) = \sqrt{\frac{|\ell|}{2}} W_o \sqrt{1 + \frac{z^2}{z_r^2}}.$$

10.3.c. High harmonic spectra from localized target clouds [partly-implemented in Jac]

Use & notations:

- Using JAC: Perform an `HighHarmonic.Computation(..., observable=[UniColorSpectrum, BiColorSpectrum, ...], configs=[..], hhgSettings=HighHarmonics.Settings(..), ..)` or call directly functions from the module `HighHarmonic`.

10.3.d. Phase matching in high-harmonic generation from extended target clouds [partly-implemented]

Use & notations:

10. Collision- and field-induced atomic responses

➤ Using JAC: Perform an `HighHarmonic.Computation(..., observable=[UniColorSpectrum, BiColorSpectrum, ...], configs=[..], hhgSettings=HighHarmonics.Settings(..), ..)` or call directly functions from the module `HighHarmonic`.

10.3.e. Far-field phase distributions [not yet implemented]

None.

10.3.f. Far-field intensity distributions [not yet implemented]

None.

10.4. In JAC considered above-threshold ionization (ATI) processes

10.4.a. ATI in the strong-field approximation [phenomenology]

Above-threshold ionization (ATI):

- Above-Threshold Ionization refers to the absorption by an atomic electron of more photons than are required for ionization. ATI was discovered in 1979 and is a rather universal phenomenon. This process occurs in light pulses that are short and strong enough to eliminate the influence of collisions.
- **ATI in strong fields:** In this multi-photon ionization regime (with Keldysh parameter $\gamma > 1$), the atom absorbs more photons than required for the release of one of its bound electrons. This multi-photon absorption leads to the characteristic above-threshold ionization (ATI) peaks in the photoelectron spectra that are separated by the energy of the laser photons. Moreover, the overall spectrum is shifted by the ponderomotive potential with regard to a perturbative treatment of the binding and photon energies.
- **ATI by plane-wave pulses:** During the past decades, the ATI of atoms by plane-wave femtosecond pulses has been studied extensively, both by experiment and theory. These studies showed that the shape and symmetry of the photoelectron momentum distributions depend quite sensitively on the duration and carrier envelope phase of the ionizing pulse. Apart from simple monochromatic plane-wave pulses, bi-circular pulse have been investigated as well.
- **Photon *versus* momentum transfer in ATI experiments:** In the ATI of atoms and molecules, the absorption of energy ΔE from the laser field goes along with a transfer of linear momentum of $\Delta p_z = \Delta E/c$ along the propagation direction. This momentum is absorbed by the total system ‘photoion + photoelectron’ and can be shared in different ways. This momentum transfer is neglected in the electric-dipole approximation to the light-matter interaction.
- **Photoelectron holography:** The photoelectron holography refers to the interference between the direct and forward scattered electrons. This interference is visible especially at intermediate energies of the photoelectron below the classical cutoff near $2U_p = 2\mathcal{E}_o^2(4\omega^2)$. Energies larger than $2U_p$ can be obtained only by elastically re-scattered electrons due to their subsequent acceleration in the laser field. In this high-order ATI (HATI) process, photoelectron energies up to about $10U_p$ can be reached.
- **Recollision dynamics of HATI photoelectrons:** For a re-collision, the electron has to return close to the parent ion and to interact with the parent ion. Therefore, differences in the non-dipole shifts of HATI photoelectrons are influenced also by the electron-electron interaction with the ionic core and might be sensitive to details of the re-collision process.

- **Strong-field ionization in elliptically-polarized fields:** In an elliptically-polarized field, the ionization takes mainly place at times t_o , when the electric field is directed along the major axis of the polarization ellipse. The electrons, ionized at t_o , acquire a drift momentum $p = e A(t_o)$ since the photoelectron momentum distribution follows the vector potential $A(t)$ at the instant of ionization and, hence, also characterizes the intensity at this time (Wustelt *et al.*, 2015). The uncertainty, which is introduced by the approximation $p = e A(t_o)$, is considered to be small for small Keldysh parameters, i.e. in the tunneling regime.
- **Saturation intensity for ions with given charge state in strong-field ionization:** The over-the-barrier ionization (OBI) provides a simple estimate for the saturation intensity of ions with given charge state, i.e. by using the intensity for which the Coulomb barrier is lowered below the ground state energy. Another estimate for the saturation intensity is based on the ADK tunneling rate. Both estimates have their problems; the OBI model is still under critical debate, whereas the ADK rate is generally not valid at saturation intensities of femto-second pulses.

10.4.b. ATI in the strong-field approximation [theoretical background]

....

- **Strong-field approximation *versus* time-dependent SE:** Quite different photoelectron spectra were obtained from these (two) methods for low photoelectron energies as well as for the photoelectrons around twice the ponderomotive energy, where re-scattering processes are known to become relevant. In this *transition* regime from the direct-to-rescattering ionization, simple SFA models can underrate the ionization probability by several orders of magnitude.
- **ADK ionization rate of atoms in strong fields:** While the time-dependent Schrödinger equation within the single-active electron (SAE) model has been applied to calculate ionization rates, simple analytical expression for the tunnelling ionization are available as well. For example, the Ammosov-Delone-Krainov (ADK) theory applies the WKB approximation in order to obtain an ionization rate in a static electric field \mathcal{E}_o . The ADK rate is valid for photon energies $\hbar\omega \ll I_p$ and for level energies well below (the top of) the effective one-dimensional potential barrier in the static field \mathcal{E}_o .
- **Atomic ionization in optical fields:** is caused mainly by the electric-dipole interaction of the (atomic) electrons with the light field. Therefore, the angular distributions of emitted photoelectrons is generally governed by the direction and symmetries of the electric field. For the photoionization of an unpolarized target by linearly- or circularly-polarized light, the symmetry of the final electronic state is — within the dipole approximation — the same as the symmetry of the ionizing field in terms of its Stokes parameters.

- **Two-color ATI of atoms:** Seipt *et al.* (2016) investigated the two-color above-threshold ionization (ATI) of atoms and ions for a vortex (XUV) Bessel beam and a strong near-infrared (NIR) light field. While the photoionization is caused by the photons from the weak but XUV vortex Bessel beam, the photoelectron energy spectrum and angular distribution are affected by the plane-wave NIR field. This also applies to the sideband in the photoelectron spectrum.
- **Dichroism in two-color ATI of atoms:** In typical two-color ATI experiments, seven kinds of different dichroism signals occur for (XUV) vortex Bessel beams due to the various combinations of the orbital and spin angular momenta of the two light fields. This is analog to the well-known circular dichroism in the two-color ATI of atoms with plane-wave pulses. For macroscopically extended targets, however, three of these seven dichroism signals are close to *zero*, while the other four just coincide with the standard circular dichroism, similar as expected for localized targets but for Bessel beams with a small opening angle (Seipt *et al.*, 2016).

10.5. In JAC considered non-sequential double ionization (NSDI) processes

10.5.a. NSDI in the strong-field approximation [phenomenology]

Non-sequential double ionization (NSDI):

- Non-sequential double ionization (NSDI): This (non-linear) strong-field process has been studied for more than 30 years but still attracts good attention for its sensitivity with regard to (a proper many-electron description of) the correlated motion of the two emitted electrons. The *observed (and characteristic) knee structure* provides clear evidence for NSDI since the double-ionization yield strongly increases at the 'knee' by one or several orders of magnitude. Indeed, this increase is much larger than predicted for a subsequent emission of two electrons from the same atom.
- Rescattering picture of NSDI: In the *rescattering picture of strong-field physics*, NSDI is simply attributed to the inelastic scattering of the returning electron in the (static) potential of the parent ion. Already this quite simplified picture requires however to take different ionization mechanisms into account: the recollision direct ionization (RDI) and the recollision excitation with subsequent ionization (RESI); cf. Chen *et al.* (2020).
- NSDI: This (non-linear) process depends crucially on the laser intensity as seen, for instance, from recoil-ion momentum measurements. In these measurements, a single peak in the momentum distribution becomes a double-hump structure as the intensity increases near to or beyond the threshold intensity. Moreover, the electron-electron (momentum) correlation function then displays a clear transition from an (angle-) correlated into an anti-correlated emission if the laser intensity decreases below of the threshold intensity. In particular, prominent finger-like structures in the PEMD have been observed at the relatively low intensity of the laser field. These features show the correlated many-electron features of NSDI.
- NSDI: The NSDI process is known to exhibit strong correlations due to electron-electron interactions. A 'knee' structure in the double ionization yield as function of laser intensity has first been observed 1983 by l'Huillier and coworkers and, since then, was approved in many experiments. It was shown that this structure cannot be explained in a single-active-electron model, such as the ADK theory.

10.5.b. NSDI in the strong-field approximation [theoretical background]

...:

- **Theoretical models for NSDI:** The NSDI process has been explored by various models, including a semi-classical quasi-static model, the quantitative rescattering (QRS) model or the explicit solution of some (simplified) time-dependent Schrödinger equation. All these models confirmed, or at least indicate, that the finger-like structures in the PEMD at low laser intensity arises from the Coulomb interaction among the emitted electrons. However, different mechanisms are emphasized in most of these models, such as the *shake-off* of the second electron by the nonadiabatic change of the atomic potential if the first electron is released, some $(e, 2e)$ collision due to the ionized electron if driven back by the laser, or other mechanisms. Today, the role of laser-induced recollisional excitation and ionization model as the major mechanism is widely accepted, and the number of (sub-) mechanisms has been further refined for the NSDI (Chen *et al.*, 2020): (1) The interaction of the laser field with both electrons; (2) Coulomb interaction of the residual photoion and the two electrons; (3) the interaction among the electrons. Obviously, all these interactions can be easily read-off the (many-electron) Hamiltonian and should be treated on similar footings, if possible.
- **Quantitative rescattering (QRS) model for NSDI:** The QRS model was originally developed for high-order above-threshold ionization (HATI) as well as HHG but has been further improved over the years. This model nowadays incorporates different mechanisms, such as the lowering of the threshold potential due to the electric field at the time of recollision. This model is based on the S-matrix theory and strong-field approximation, and it has been applied to simulate the total double ionization yield, the cross section ratio for double-to-single ionization as well as correlated two-electron momentum distributions. In practice, the QRS model is conceptual much simpler than the explicit solution of the time-dependent Schrödinger equation or even the time-dependent Newton equations of the two electrons. The QRS model basically *factorizes* the electron dynamics of the two electrons into a returning wave packet for the initially ionized electron as well as the differential cross sections for its inelastic scattering with a second electron in the potential of the parent ion (Chen *et al.*, 2019).

10.6. In JAC considered collisional-radiative (CR) models

10.6.a. Simple CR models [phenomenology]

Role and applications of CR models:

- Collisional-radiative (CR) models: These zero-dimensional plasma models are typically applied in order to compute atomic charge-state distributions for – (ionic) mixtures of – one or several elements, and in particular as function of particle densities and temperatures.
- Different CR models have been found useful for the interpretation of experimental observations, for instance in order to derive the electron density and temperature in plasma. In addition, CR models can be applied to determine effective ionization and recombination rates as well as the effective emissivity of plasma as function of its electron temperature and density.
- Atomic level population densities: CR models help determine atomic level population densities of atoms in different plasma environments. Calculations are typically based on the CR recombination and ionization rate coefficients, radiative energy losses as well as on various individual rate coefficients.
- Classification of CR models: Different CR models can be distinguished due to the – analytical or numerical – treatment of the rate coefficients as well as due to the number and type of processes, for which such (effective) rate coefficients are taken into account.
- Effectice rates: CR models can be applied to calculate the effective emissivity or the effective ionization and recombination rates as function of electron temperature and density. In particular, these rates can later be utilized in plasma transport model in order to determine local ionization, recombination and radiation effects.

Frequent assumptions of CR models:

- Collisional radiative models are sometimes called also zero-dimensional plasma models. In these models, one often assumes that the radiative absorption and emission as well as electron-collision processes dominate the plasma and that all other (ion-atom, three-atom, ...) processes are negligible.
- In most CR models, the plasmas just consist out of a single atomic species but with various excited states in between the ground state of some charge state A^{q+} of the ion and the ground state of the next higher charge state $A^{(q+1)+}$. A further typical restriction of such models is that the density of the excited states is assumed to be small, when compared to the (two) ground state densities.

10.6.b. CR models [theoretical background]

Time-evolution of level densities:

- Level densities $n(p)$: CR models are typically built on the level densities $n(p)$, $p = p_1, p_2, \dots, p_N$ of a series of levels whose temporal and spatial distribution is related to each other by the diffusion equation

$$\left(\frac{\partial n(p)}{\partial t} \right)_{\text{CR}} = \frac{\partial n(p)}{\partial t} + \nabla \cdot (n(p) \boldsymbol{\omega}(p)).$$

- Dominance of radiative and collisional (de-) excitation processes: If changes in the level density are dominated by radiative and collisional (de-) excitation processes, most CR models simply assume

$$\left(\frac{\partial n(p)}{\partial t} \right)_{\text{CR}} = 0 = P(p) - n(p) D(p)$$

and just solve a (single) matrix equation. Here, $P(p)$ is the collisional and radiative production rate, and $D(p)$ the (so-called) *destructive factor*. The two functions $P(p)$, $D(p)$ can be written in terms of different rate coefficients for electron-impact excitation, ionization as well as for radiative and three-body recombination.

10.7. Atomic responses not yet considered in JAC

10.7.a. Floquet theory [theoretical background]

Time-dependent SE and master equations:

- Quasi-energy spectrum in a time-harmonic (ac) electric field: For a monochromatic (time-harmonic) external field, the Schrödinger equation is formally solved by the Floquet's theorem on linear homogenous differential equations with periodic coefficients:

$$\psi(\mathbf{r}, t) = \exp(-i E_o t) \phi(\mathbf{r}, t), \quad \phi(\mathbf{r}, t) = \phi\left(\mathbf{r}, t + \frac{2\pi}{\omega}\right)$$

$$\psi(\mathbf{r}, t) = \exp(-i E_o t) \sum_{k=-\infty}^{k=\infty} c_k(\mathbf{r}) \exp(-i k \omega t).$$

In a monochromatic external field, therefore, the total wave function $\psi(\mathbf{r}, t)$ is a superposition of *stationary* quasi-energy states with energies $E_o \pm k\omega$, and where E_o is referred to a quasi-energy. In physical settings, the number of quasi-energies is equal to the number of (unperturbed) level energies, while the (sideband) energies $E_o \pm k\omega$ are known also as *spectrum of quasi-harmonics*. In atoms, the formation of a quasi-harmonic spectra (sidebands) can be observed especially, if the laser frequency is small but sufficiently intense, when compared to the (atomic) excitation energies to neighbouring levels.

- Time-dependent single-electron Schrödinger equation: In quasi-harmonic light fields (and elsewhere), the single-electron SE can be written as

$$i \hbar \frac{\partial}{\partial t} \Psi(\mathbf{r}, t) = H(\mathbf{r}, t) \Psi(\mathbf{r}, t) = \left(\frac{1}{2m} [-i\hbar \nabla + e \mathbf{A}(t)]^2 + V^{(\text{atom})} \right) \Psi(\mathbf{r}, t),$$

$$i \hbar \frac{\partial}{\partial t} \Psi(\mathbf{r}, t) = \left(\frac{\hbar^2}{2m} \nabla^2 - \frac{i e \hbar}{m} \mathbf{A}(t) \cdot \nabla + V^{(\text{atom})} \right) \Psi(\mathbf{r}, t) \quad \dots \text{velocity gauge}$$

$$i \hbar \frac{\partial}{\partial t} \Psi(\mathbf{r}, t) = \left(\frac{\hbar^2}{2m} \nabla^2 + e \mathbf{E}(t) \cdot \mathbf{r} + V^{(\text{atom})} \right) \Psi(\mathbf{r}, t) \quad \dots \text{length gauge},$$

and where the atomic potential $V^{(\text{atom})}$ is often modeled by a Yukawa and a long-range Coulombic potential.

- Relation between the wave functions (solutions) in length and velocity gauge:

$$\exp \left[-i \frac{e^2}{2m\hbar} \int dt \mathbf{A}^2(t) \right] \Psi^{(\text{velocity})}(\mathbf{r}, t) = \exp \left[-i \frac{e}{\hbar} \mathbf{A}(t) \cdot \mathbf{r} \right] \Psi^{(\text{length})}(\mathbf{r}, t) \equiv \Psi(\mathbf{r}, t).$$

Floquet ansatz:

- **Floquet ansatz:** With this ansatz, the time-dependent SE in a stationary incident field can be simplified to a set of time-independent coupled differential equations. This set of equations need to be solved by imposing (so-called) Siegert boundary conditions on the wave function and by expanding it, for instance, upon a complex basis set.
- **Generalized Floquet ansatz:** For the interaction with two laser fields with frequencies ω_1, ω_2 , the Floquet ansatz can be written

$$\Psi^{(\text{velocity, length})}(\mathbf{r}, t) = e^{-iEt/\hbar} \sum_{N_1 N_2} e^{-i(N_1 \omega_1 + N_2 \omega_2)} F_{N_1 N_2}(\mathbf{r}).$$

In this ansatz, the Floquet components $F_{N_1 N_2}(\mathbf{r}) \equiv F_{N_1 N_2}^{(\text{velocity, length})}$ and energies $E \equiv E^{(\text{velocity, length})}$ satisfy a system of time-independent equations that are equivalent to the time-dependent Schrödinger equation, cf. Potvliege (1998).

- **Floquet ansatz for the wave function:**

$$\psi(t) = \exp(-iEt) \sum_{n=-\infty}^{\infty} \exp(-in\omega t) \psi_n, \quad E = \Re(E) - i\Gamma/2,$$

where the functions ψ_n are often called the harmonic components, while E is the complex quasi-energy of the Siegert state $\psi(t)$ and Γ the total ionization rate of this state.

Applications of Floquet theory to HHG:

- Induced electric-dipole moment: The induced electric-dipole moment from the theory of high harmonics can be expressed within the Floquet theory in the form (Gebarowski *et al.* 1997)

$$\mathbf{D}(t) = \exp(-\Gamma t) \left[\mathbf{D}_o + 2 \sum_{q=1}^{\infty} \Re[\mathbf{D}_q \exp(-iq\omega t)] \right], \quad \mathbf{D}_q = \sum_{n=-\infty}^{\infty} -\langle \psi_{n-q} | \mathbf{R}_N | \psi_n \rangle.$$

- Emission rate for photons with frequency $\omega_q = q\omega$ and polarization λ : The rate for emission of photons into a given solid angle $d\Omega$ is then obtained by summing over all polarizations of the emitted radiation

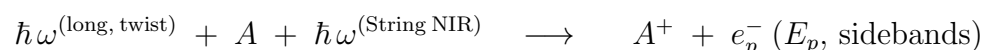
$$\frac{dR(\omega_H, \lambda)}{d\Omega} = \frac{\omega_H^3}{2\pi c^3} |\lambda^* \cdot \mathbf{d}_q|^2,$$

and the total emission rate by integrating over all directions.

10.7.b. Two-color sideband formation in atomic photoionization [theoretical background]

Processes & notations:

- Photoionization by a long twisted pulse and a long NIR pulse:



- In this strong-field ionization process, the photoelectron moves after its ionization in a Volkov state with the NIR field, and this gives rise to well-defined sidebands in the photoionization probability $W(E_p; m, \Lambda_X, \Lambda_L)$.

10.7.c. Phase control of atomic photoionization in multi-color fields [theoretical background]

Processes & notations:

- **Coherent-control schemes:** While various quantum coherent-control schemes have been developed and utilized already within the optical and IR regions, their use at high frequencies has been hampered by the lack of sufficient coherent xuv sources. An important step ahead was made by seeded FEL beams, for instance at FERMI, which provide high longitudinal coherence. This coherence of the light beams enables one to observe interference of two- and one-photon pathways in the photoelectron angular distributions following the xuv irradiation.
- **Application of phase control:** The phase control of photoprocesses has attracted much recent interest and has found promising applications, such as the control of chemical reactions, the study of biological changes, ultrafast and nonlinear optics as well as four-dimensional (4D) ultrafast electron microscopy.
- **Differential ionization probability:** In second-order perturbation theory, the angle-differential ionization probability for the emission of a photoelectron and for a transition $i \rightarrow f$ of the photoion can be expressed as

$$\frac{dW}{d\Omega} = \frac{1}{2J_i + 1} \sum_{M_i, M_f \mu} \left| \eta U_{M_i, M_f \mu}^{(1, 2\omega)} + U_{M_i, M_f \mu}^{(2, \omega)} \right|^2$$

where $U_{M_i, M_f \mu}^{(1, 2\omega)}$ is the first-order amplitude for ionization by the second harmonic and $U_{M_i, M_f \mu}^{(2, \omega)}$ the second-order amplitude for two-photon ionization by the fundamental frequency. Here, the magnetic quantum numbers refer to the initial atomic state state $|J_i M_i\rangle$, the residual ion $|J_i M_i\rangle$ as well as the photoelectron $|\mathbf{p} \mu\rangle$.

- **Electric dipole approximation:**

$$U_{M_i, M_f \mu}^{(1, 2\omega)} = -i \langle \alpha_f J_f M_f, \mathbf{p} \mu^{(-)} | e \mathbb{D} | \alpha_i J_i M_i \rangle T^{(1)}$$

$$U_{M_i, M_f \mu}^{(2, \omega)} = \sum_{\nu} \int \langle \alpha_f J_f M_f, \mathbf{p} \mu^{(-)} | e \mathbb{D} | \alpha_{\nu} J_{\nu} M_{\nu} \rangle \langle \alpha_{\nu} J_{\nu} M_{\nu} | e \mathbb{D} | \alpha_i J_i M_i \rangle T_{E_{\nu}}^{(2)}.$$

Here α_{ν} specifies the quantum numbers of the intermediate states ν , while $\sum_{\nu} \int$ denotes the infinite summation over all discrete and continuum states. The minus sign in the outgoing electron wave indicates the proper asymptotic form of the continuum wave function, E_{ν} is the energy of the intermediate virtual atomic state. The time-dependent $T^{(1)}$ and $T_{E_{\nu}}^{(2)}$ were described elsewhere in the literature (Gryzlova *et al.*, 2018).

10. Collision- and field-induced atomic responses

- **Asymmetric ionization yield in strong-field ionization:** An asymmetric ionization yield has been found for counter-rotating and co-rotating, circularly-polarized laser pulses and in both, the tunneling and multi-photon regime

10.7.d. Amplified spontaneous emission (ASE) & superfluorescence (SF)

Motivation:

- **Nonlinear optical light-matter interactions:** In the optical regime, the two nonlinear phenomena **Amplified spontaneous emission (ASE)** and **superfluorescence (SF)** have been studied, both experimentally and theoretically. In these processes, a short and intense light pulse partly creates a population inversion of some excited level(s), and which may then decay either by fluorescence or stimulated emission. In an ASE spectrum, the number of emitted photons increases exponentially with the density of the excited-state(s), while the duration of light emitted also increases. In superfluorescence spectra, in constast, the number of emitted photons just depends linearly on the density of the excited-state(s), and the emitted fluorescence occurs slightly delayed with regard to the incident light and *reduced* in duration.
- **Nonlinear optical light-matter interactions:** In optical experiments, both phenomena (ASE and SF) have been explored and distinguished by counting the total photon yield and/or by measuring the time-dependence of the emitted radiation as function of the intensity of the incident pulse. Theoretically, most computations are based on (so-called) time-dependent Maxwell-Bloch equations, in which the spontaneous emission is described by some stochastic noise. In practice, this model is not able to obtain the exponential increase of the emission intensity in ASE but just gives rise to a delayed peak in the temporal profile of the emitted field, and with regard to the incident field.

10.7.e. Two-color streaking in atomic photoionization

Motivation:

- **Attosecond streaking with twisted X waves:** Böning *et al.* (2017) analyzed the photoionization of atoms by attosecond *X* waves within a strong and linearly-polarized, near infrared (NIR) laser pulse. Since the *X* waves carry an OAM and have a spatially-varying temporal profile, the ionization process and especially the streaking of photoelectrons is modified for both, localized and macroscopically extended targets.

- **Attosecond streak camera:** Such a ‘camera’ applies photoionization of atoms by an attosecond pulse in the presence of a moderately strong near infrared (NIR) pulse. While the temporal structure of the attosecond pulse is imprinted upon the photoelectron wave packet, the NIR pulse then streaks the photoelectrons away from the ion and acts as an ultrafast phase modulator on this wave packet (Böning *et al.*, 2017). A change in the relative phase of the NIR field and X-wave pulse then affects the energy distribution and enables one to extract both, the attosecond pulse duration as well as the chirp from the photoelectron spectra.

10.8. Theoretical background to atomic responses considered above

Theoretical methods:

- **Time-dependent CI singles (TDCIS):** This one-electron formulation for describing strong-field ionization is guided mainly by the first step in all strong-field processes, in which an electron is pulled away from the parent ion by the laser field. The use of the single-active electron (SAE) approximation has been shown to be sufficient to predict the single-ionization production, the cutoff in the HHG spectrum as well as the ATI photoelectron spectra in different atoms.
- **TDCIS:** This is an approximate one-electron approach that goes beyond the SAE treatment. In this *ab-initio* electronic-structure method, the time-dependent wave function is restricted to spin-singlets which conserve single-particle excitations from the ground-state determinant.

10.8.a. Strong-field approximation (SFA) [background]

Elements of SFA:

- **Strong-field approximation (SFA):** This approximation assumes a Keldysh parameter $\gamma < 1$ and, hence, is expected to be valid especially for intense, low-frequency laser fields. For such fields, the electron dynamics of the electron in the continuum is distorted only weakly by the (Coulomb) field of the residual ion, and this influence of the atom is then described perturbatively. With these assumptions in mind, the *standard* SFA can be summarized as follows (Amini *et al.*, 2019):
 1. The strong laser field couples only to the atom in its ground state or to one (active) electron in the continuum, and only this *active* electron has a spatial structure and is included into the dynamics.
 2. An approximate time-dependent amplitude $a(t)$ of the active electron in the ground-state of the atom is considered to be known.
 3. The *continuum* is formed by all solutions of the Schrödinger equation (with the atomic single-electron Hamiltonian $H^{(\text{atom})}$) with well-defined (kinetic) momentum \mathbf{p} : $H^{(\text{atom})} |\mathbf{p}\rangle = \frac{\mathbf{p}^2}{2m} |\mathbf{p}\rangle$. In the evaluation of the continuum-continuum matrix elements, however, the interaction with the atomic potential is treated only perturbatively.
- **Representation of the time-dependent wave function:** In the SFA, the wave function of the active electron is given by

$$|\psi(t)\rangle = e^{i I_p t/\hbar} \left(a(t) |0\rangle + \int d^3\mathbf{p} b(\mathbf{p}, t) |\mathbf{p}\rangle \right)$$

where $|0\rangle$ is the ground (product) state of the active electron in the atomic potential, and I_p its binding energy. While the amplitude $a(t)$ is assumed to be known, the quantum (transition) amplitude $b(\mathbf{p}, t)$ of (quasi-) free electrons with well-defined \mathbf{p} need to be determined as solution of the (single-electron) TDSE. This quantum amplitude depend not only on the *kinetic* momentum \mathbf{p} of the outgoing electron but also on the laser pulse and, parametrically, on the potential of the residual ion.

- **Approximate time-dependent amplitude $a(t)$ of the active electron in the atomic ground level:** There are various methods to find an approximate time-dependent amplitude $a(t)$ for an atom in the light field, either from the single-electron TDSE or by using some cheaper method, such as phase-space averaging or the truncated Wigner approximation (Berman *et al.*, 2018). Moreover, for very short pulses *or* long-but-weak pulses, one may simply assume $a(t) \simeq 1$, i.e. that the depletion of the ground level is negligible.
- **Electric-dipole matrix elements in the SFA:** To evaluate the interaction of the active electron with the laser field, one needs to know the dipole-interaction matrix elements between the continuum states $\langle \mathbf{p} | \mathbf{d} | \mathbf{p}' \rangle$ and from the atomic ground state to the continuum $\langle \mathbf{p} | \mathbf{d} | 0 \rangle$, respectively. In the nonrelativistic theory, these matrix elements can be written as (Amini *et al.*, 2019)

$$\langle \mathbf{p} | \mathbf{d} | \mathbf{p}' \rangle = e \langle \mathbf{p} | \mathbf{r} | \mathbf{p}' \rangle = i e \nabla_{\mathbf{p}} \delta(\mathbf{p} - \mathbf{p}') + \hbar \mathbf{g}(\mathbf{p}, \mathbf{p}'), \quad \langle \mathbf{p} | \mathbf{d} | 0 \rangle = e \langle \mathbf{p} | \mathbf{r} | 0 \rangle = \mathbf{d}(\mathbf{p}).$$

Note that, if $\mathbf{g}(\mathbf{p}, \mathbf{p}')$ is neglected, the dipole matrix elements $\langle \mathbf{p} | \mathbf{r} | \mathbf{p}' \rangle = i e \nabla_{\mathbf{p}} \delta(\mathbf{p} - \mathbf{p}')$ are here the same as for plane-waves (*free* electrons without the atomic potential) or Volkov states (electrons in a plane-wave laser field).

- **Solution of the SFA equations:** Using the SFA ansatz of the time-dependent wave function in the (time-dependent) Schrödinger equation and by using the length gauge for the coupling of the laser field, the time-derivatives of the quantum amplitudes are given by (Amini *et al.*, 2019)

$$\dot{a}(t) = \frac{i}{\hbar} \int d^3 \mathbf{p} \mathbf{E}(t) \cdot \mathbf{d}^*(\mathbf{p}) b(\mathbf{p}, t)$$

$$\dot{b}(\mathbf{p}, t) = -\frac{i}{\hbar} \left(\frac{\mathbf{p}^2}{2m} + I_p \right) b(\mathbf{p}, t) + \frac{i}{\hbar} \mathbf{E}(t) \cdot \mathbf{d}(\mathbf{p}) a(t) - e \mathbf{E}(t) \cdot \nabla_{\mathbf{p}} b(\mathbf{p}, t) + i \mathbf{E}(t) \cdot \int d^3 \mathbf{p}' b(\mathbf{p}', t) \mathbf{g}(\mathbf{p}, \mathbf{p}').$$

For $\dot{b}(\mathbf{p}, t)$, the first term on the rhs represents the time-evolution of a (*quasi-*) *free* electron in the potential of the residual ion and without the oscillating laser field. Moreover, the second term describes the coupling due to the laser field of these (*quasi-*) *free* electrons to the ground state, the third term its coupling due to the laser to other (*quasi-*) *free*-electron states, while the last term the modification in the continuum-continuum coupling due to the re-scattering of the electron by the atomic potential. Obviously, the time-derivative $\dot{b}(\mathbf{p}, t)$ is

10. Collision- and field-induced atomic responses

described by an integro-differential equation that need to be solved iteratively. This iterative procedure gives rise to the – usual separation of – a **direct-ionization amplitude** $b_0(\mathbf{p}, t)$ and a **re-scattering amplitude** $b_1(\mathbf{p}, t)$.

- **Direct-ionization amplitude** $b_0(\mathbf{p}, t)$: This amplitude is obtained by simply omitting the 4-th term for $\dot{b}(\mathbf{p}, t)$, and which is then the solution of a first-order inhomogeneous differential equation. This equation can be formally integrated (Amini *et al.*, 2019)

$$\begin{aligned}\dot{b}_0(\mathbf{p}, t) &= -\frac{i}{\hbar} \left(\frac{\mathbf{p}^2}{2m} + I_p \right) b_0(\mathbf{p}, t) + \frac{i}{\hbar} \mathbf{E}(t) \cdot \mathbf{d}(\mathbf{p}) a(t) - e \mathbf{E}(t) \cdot \nabla_{\mathbf{p}} b_0(\mathbf{p}, t) \\ b_0(\mathbf{p}, t) &= \frac{i}{\hbar} \int_0^t d\tau \mathbf{E}(\tau) \cdot \mathbf{d}(\mathbf{p} + e \mathbf{A}(t) - e \mathbf{A}(\tau)) \exp \left(-\frac{i}{\hbar} \int_\tau^t d\tau' \left[\frac{(\mathbf{p} + e \mathbf{A}(t) - e \mathbf{A}(\tau'))^2}{2m} + I_p \right] \right) a(\tau)\end{aligned}$$

This formal solution is written for the case that the electron appears in the continuum at time τ with kinetic momentum $\mathbf{p}(\tau) = \mathbf{p} + e \mathbf{A}(t) - e \mathbf{A}(\tau)$, and where \mathbf{p} is the final kinetic momentum at the detector and $\mathbf{A}(t) = \int_0^t d\tau \mathbf{E}(\tau)$ the vector potential of the electro-magnetic field.

- **Applications of SFA**: This theory help explain multi-photon ionization (MPI), above-threshold ionization (ATI), tunnel ionization (TI) as well as over-the-barrier (OTB) ionization. In the strong-field regime, the forces of the laser field are comparable to those of the Coulomb force between the nucleus and electrons so that neither one can be described (only) perturbatively. Such a distortion of the Coulomb potential often also leads to a lowering of the ionization barrier.

- **Angular-dependent PEMD**: The angular-dependent PEMD of an electron with asymptotic momentum is

$$\frac{d^3 \mathcal{P}^{(\text{SFA})}}{dp_x dp_y dp_z} = |\{\text{SFA}\}(\mathbf{p})|^2.$$

For a linearly- or circularly-polarized laser field, the angular-dependent PEMD has cylindrical symmetry and, hence, a 2-dimensional PEMD can be defined by

$$\frac{d^2 \mathcal{P}^{(\text{SFA})}}{dp_\perp dp_z} = 2\pi p \sin \vartheta_p |\{\text{SFA}\}(\mathbf{p})|^2, \quad p_\perp = \sqrt{p_x^2 + p_y^2},$$

and where ϑ_p is the angle between the polarization axis $\mathbf{E} \parallel \mathbf{e}_z$ and the direction of the emitted photoelectron (linear polarization) or the polar angle between the photoelectron and the propagation axis of the laser $\mathbf{k} \parallel \mathbf{e}_z$ (circular polarization), respectively. In both cases, the integration over the azimuthal angle φ_p can be carried out explicitly.

- **Energy-dependent PEMD:** The energy-dependent distribution is obtained from the SFA amplitude by

$$\frac{d \mathcal{P}^{(\text{SFA})}}{d E} = 2\pi \sqrt{2E} \int_{-1}^1 d(\cos \vartheta_p) |\{\}^{(\text{SFA})}(\mathbf{p})|^2.$$

- **Simplest form of SFA:** In its simplest form, the SFA neglects the interaction of the photoelectron with the parent ion as well as the modification (dressing) of the atomic bound state by the laser. Still, most features of ATI spectra can be reproduced qualitatively by this simple form.
- **Dipole approximation of SFA:** Most SFA based photoionization studies neglect all non-dipole contributions from in the atom-laser interaction. This is justified for plane-wave laser fields, for which relativistic and magnetic effects often do not play any significant role, but may become questionable for structured light fields.
- **SFA in partial-wave representation:** Böning and Fritzsche (2020) reformulated the (standard) SFA in terms of partial waves and spherical tensor operators. Such a reformulation facilitates the implementation and the comparison of quite different treatments of the active (photo)electron and laser pulses. It helps adopt also the SFA to new experimental setups and to studies of non-dipole contributions to strong-field ionization processes. This reformulation easily supports modifications on the target potentials, the representation of the initial bound state and the (Volkov) continuum as well as in the description of the driving laser pulses. A series of detailed computations have been carried out in order to confirm the validity of the reformulation and to show how the representations of the bound and continuum states affect the predicted above-threshold ionization spectra and related observables.
- **SFA in partial-wave representation:** In general, the partial-wave representation help separate the directional dependence of the amplitude from the physical interaction. It will also pave the way to extend the strong-field theory toward studies of non-dipole contributions in light-atom interactions, the treatment of initially excited levels, the rescattering of the electrons at the target, and/or many-particle correlations in strong-field ionization processes.
- **Properties of laser pulses:** Today, the temporal shape and duration of ultrashort laser pulses can be controlled quite easily to study their non-linear interaction with matter. Despite of large experimental progress, the standard SFA is often still used to explain strong-field ionization processes by rather an over-simplified treatment of the (atomic) targets and electronic motion in excitation and ionization processes.
- **Limitations of standard SFA:** Limitations concern (i) the incorporation of realistic atomic potentials for the initially bound and finally emitted electron; (ii) the use of Volkov continuum states without the field of the ions; (iii) the assumption of initially hydrogenic $1s$ orbitals, though with scaled nuclear charge. All these simplifications omit large parts of the electronic structure and dynamics. Recent studies have therefore incorporated either the Coulomb potential of the photoion into the shape of the continuum states *or* the use of realistic ionic

10. Collision- and field-induced atomic responses

potentials. In HHG computations, moreover, the coupling of the ground and continuum states to other bound states has been explored to some extent.

Transition amplitudes in SFA:

- **Probability to detect electrons with asymptotic momentum \mathbf{p} :** In the SFA, the probability to detect a photoelectron with (asymptotic) energy ε_p is given in terms of the transition amplitude $\mathcal{T}^{(\text{SFA})}(\mathbf{p})$ and momentum $\mathbf{p} = (p, \vartheta_p, \varphi_p) = (\sqrt{2\varepsilon_p}, \vartheta_p, \varphi_p)$ by

$$\mathcal{P}^{(\text{SFA})}(\mathbf{p}) = \frac{d^3 \mathcal{P}^{(\text{SFA: density})}(\mathbf{p})}{d\Omega_{\mathbf{p}} d\varepsilon_p} = p |\mathcal{T}^{(\text{SFA})}(\mathbf{p})|^2.$$

This simple relation follows from the **transformation of the (triple-) differential probability density** for the emission of an electron in momentum space to a differentially-mixed representation in energy and the angular variables in momentum space; this transformation is then readily obtained by using $d^3 \mathbf{p} = p^2 d\Omega_{\mathbf{p}}$ and the non-relativistic energy-momentum relation ($d\varepsilon_p = p dp$):

$$\mathcal{P}^{(\text{total SFA})} = \int d^3 \mathbf{p} |\mathcal{T}^{(\text{SFA})}(\mathbf{p})|^2 = \int d\Omega_{\mathbf{p}} d\varepsilon_p |\mathcal{T}^{(\text{SFA})}(\mathbf{p})|^2 \frac{d^3 \mathbf{p}}{d\Omega_{\mathbf{p}} d\varepsilon_p} = \int d\Omega_{\mathbf{p}} d\varepsilon_p p |\mathcal{T}^{(\text{SFA})}(\mathbf{p})|^2.$$

- **Transition amplitude $\mathcal{T}^{(\text{SFA})}(\mathbf{p})$:** In the SFA, the interaction of the photoelectron with the residual ion is assumed to be weak and, hence, treated perturbatively. With this assumption in mind, the total transition amplitude $\mathcal{T}^{(\text{SFA})}(\mathbf{p})$ can be expressed approximately as sum of a (so-called) **direct** and — one or several — **rescattering amplitudes** as

$$\mathcal{T}^{(\text{SFA})}(\mathbf{p}) = \mathcal{T}^{(\text{SFA: direct})}(\mathbf{p}) + \mathcal{T}^{(\text{SFA: rescattering})}(\mathbf{p}) + \dots$$

$$\mathcal{T}^{(\text{SFA: direct})}(\mathbf{p}) = -i \int_{-\infty}^{\infty} d\tau \langle \chi_{\mathbf{p}}^{(\text{Volkov})}(\tau) | \mathbb{H}^{(\text{laser})}(\tau) | \Psi_i(\tau) \rangle$$

$$\mathcal{T}^{(\text{SFA: rescattering})}(\mathbf{p}) = (-i)^2 \int_{-\infty}^{\infty} d\tau \int_{\tau}^{\infty} d\tau' \langle \chi_{\mathbf{p}}^{(\text{Volkov})}(\tau') | \mathbb{V}^{(\text{atom})} \mathbb{U}^{(\text{laser})}(\tau', \tau) \mathbb{H}^{(\text{laser})}(\tau) | \Psi_i(\tau) \rangle.$$

Here $\Psi_i(t)$ refers to the (time-dependent) atomic ground state and $|\chi_{\mathbf{p}}^{(\text{Volkov})}(t)\rangle$ to a Volkov state of the 'atom + photoelectron', in which the outgoing electron moves in the field of the laser (and, perhaps, in the potential of the ionic core). Moreover, $\mathbb{V}^{(\text{atom})}$ is the atomic

potential of the ionic core, $\mathbb{U}^{(\text{laser})}(t', t) \equiv \mathbb{U}^{(\text{electron-field interaction})}(t', t)$ the time evolution operator of the atom due to the interaction with the (intense) laser field and $\mathbb{H}^{(\text{laser})} \equiv \mathbb{H}^{(\text{electron-field interaction})}$ the associated interaction Hamiltonian of the (atomic) electrons with the laser field. In the first line, the dots indicate that second- and higher-order (in the atomic potential $\mathbb{V}^{(\text{atom})}$) re-scattering terms will generally also contribute to the total transition amplitude, although such higher-order terms have rarely been considered in the literature.

- **Initial atomic state:** For a many-electron atom, the initial (ground) state is simply given by a state (level) with well-defined angular momentum:

$$|\Psi_i(t)\rangle = e^{-iE_i t} |\psi_i\rangle = e^{-iE_i t} |\alpha_i J_i M_i\rangle .$$

- **Initial (non-relativistic) hydrogenic state:**

$$|\Psi_i(t)\rangle = e^{-i\varepsilon_i t} |n\ell m\rangle = e^{-i\varepsilon_i t} \frac{P_{n\ell}(r)}{r} Y_{\ell m}(\vartheta, \varphi) \implies |\Psi_i(t)\rangle = e^{-i\varepsilon_i t} \sum_{m_\ell, m_s} |n\ell jm\rangle \langle jm| \ell m_\ell, 1/2 m_s\rangle .$$

The expression on the rhs here indicates that most atomic bound states are most readily classified as above by their total angular momentum J_i , M_i and parity P_i : $|\alpha_i J_i M_i\rangle \equiv |\alpha_i J_i^{P_i} M_i\rangle$, and where α_i refers to all additional quantum numbers that are needed for a unique specification of the state.

- **Electron-field interaction Hamiltonian $\mathbb{H}^{(\text{laser})}$ in Coulomb gauge:** The interaction operator for a single or many-electron atom reads (with $\mathbf{d} = -e\mathbf{r}$) as

$$\mathbb{H}^{(\text{laser})} = \begin{cases} -\mathbf{d} \cdot \mathbf{E}(\mathbf{r}) & \implies -\mathbb{D} \cdot \mathbf{E}(\mathbf{r}) & \text{length gauge} \\ \mathbf{A}(t) \cdot \mathbf{p} + \frac{\mathbf{A}^2}{2} & \implies \mathbf{A}(t) \cdot \left(\sum_j^N \mathbf{p}_j \right) + \frac{\mathbf{A}^2}{2} & \text{velocity gauge.} \end{cases}$$

In the treatment of the electron-field interaction, the Coulomb gauge $\nabla \cdot \mathbf{A}(\mathbf{r}, t) = 0$ is usually adopted for the vector potential $\mathbf{A}(\mathbf{r}, t)$; this is trivial for a purely time-dependent field $\mathbf{A}(t)$ but crucial for a general $\mathbf{A}(\mathbf{r}, t)$ to get ride of a term $\mathbf{p} \cdot \mathbf{A}(\mathbf{r}, t)$ in $\mathbb{H}^{(\text{laser})}$.

- **Volkov state:** A Volkov state generally describes a scattering state of '(one quasi-) free photoelectron, in which the free electron moves in the laser field and, perhaps, some ionic potential. However, since these solutions to the Schrödinger equation are not known for general atomic (ionic) potentials, approximate solutions for a (quasi-) free electron in an intense field are typically applied in order to evaluate

10. Collision- and field-induced atomic responses

the SFA transition amplitudes above. In our notation, the Volkov states are therefore formally defined as solutions of the (full singleton) Hamiltonian but for some — more or less approximate — atomic potential:

$$\mathbb{H} = \frac{\mathbf{p}^2}{2} + \mathbb{V}^{(\text{atom})} + \mathbb{H}^{(\text{laser})}.$$

Obviously, these approximate (quasi-free) Volkov solutions also depend on the vector potential $\mathbf{A}(t)$ and, hence, the gauge for the coupling of the radiation field to the electronic motion.

- **Spherical-Volkov states:** If one assumes that the quasi-free electron only feels the laser field, the Volkov state of the photoelectron with kinetic (asymptotic) momentum \mathbf{p} can be written as

$$|\chi_{\mathbf{p}}^{(\text{Volkov})}(t; \mathbf{A})\rangle = \begin{cases} \frac{1}{(2\pi)^{3/2}} e^{-iS^{(\text{Volkov})}(t)} e^{i(\mathbf{p} + \mathbf{A}(t)) \cdot \mathbf{r}} & \text{length gauge} \\ \frac{1}{(2\pi)^{3/2}} e^{-iS^{(\text{Volkov})}(t)} e^{i\mathbf{p} \cdot \mathbf{r}} & \text{velocity gauge} \end{cases}$$

$$S^{(\text{Volkov})}(t; \mathbf{A}) \equiv S^{(\text{Volkov})}(t) = \frac{1}{2} \int^t d\tau (\mathbf{p} + \mathbf{A}(\tau))^2.$$

In velocity gauge, in particular, the (spherical) partial-wave expansion of the plane-wave $e^{i\mathbf{p} \cdot \mathbf{r}}$ or some related (quasi-) free-electron wave can be used quite easily. For the partial-wave expansion of the plane-wave $e^{i\mathbf{p} \cdot \mathbf{r}}$, we shall below denote the corresponding Volkov state sometimes also by $|\chi_{\mathbf{p}}^{(\text{Volkov})}(t; \mathbf{A})\rangle^{(\text{spherical, } V \equiv 0)}$ for the sake of simple comparison.

- **Coulomb-Volkov states:** If one assumes that the electron feels the laser *and* a Coulomb field from the residual ion, the Volkov state of a photoelectron with (asymptotic) kinetic momentum \mathbf{p} can be written in terms of outgoing Coulomb waves $|\phi_{\mathbf{p}}\rangle$ as

$$|\chi_{\mathbf{p}}^{(\text{Coulomb-Volkov})}(t; \mathbf{A})\rangle = e^{-iS^{(\text{Volkov})}(t)} |\phi_{\mathbf{p}}\rangle = e^{-iS^{(\text{Volkov})}(t)} \frac{1}{(2\pi)^{3/2}} e^{\pi\eta_p/2} \Gamma(1 + i\eta_p) e^{i\mathbf{p} \cdot \mathbf{r}} {}_1F_1(-i\eta_p; 1; -i(pr + \mathbf{p} \cdot \mathbf{r}))$$

$$|\phi_{\mathbf{p}}\rangle = 4\pi \sum_{\ell_p=0}^{\infty} \sum_{m_p=-\ell_p}^{\ell_p} i^{\ell_p} \frac{w_{\ell_p}(\eta_p, pr)}{r} Y_{\ell_p, m_p}^*(\vartheta_p, \varphi_p) Y_{\ell_p, m_p}(\vartheta, \varphi)$$

with $\eta_p = Z/p$, the gamma function $\Gamma(x)$ and the confluent hypergeometric function ${}_1F_1(\dots)$. Here, the second line represents the partial-wave expansion of a (pure) Coulomb wave with well-defined asymptotic momentum \mathbf{p} .

- Partial-wave expansions for a (quasi-) free electron with well-defined asymptotic momentum \mathbf{p} : A (quasi-) free-electron wave with well-defined (asymptotic, i.e. far away from the center of the potential) momentum propagates in its asymptotic region like a plane wave with given kinetic momentum $|\mathbf{p}; r \rightarrow \infty\rangle \propto e^{i\mathbf{p}\cdot\mathbf{r}}$. For any short-range central-field potential $V = V(r)$ with Coulombic tail, and if normalized to one electron per unit volume, such a (distorted) free-electron wave can be expressed analogue to the well-known [partial-wave expansion of a plane-wave](#)

$$|\mathbf{p}\rangle^{(\text{spherical})} = \sqrt{\frac{2}{\pi}} \sum_{\ell_p=0}^{\infty} \sum_{m_p=-\ell_p}^{\ell_p} Y_{\ell_p, m_p}^*(\vartheta_p, \varphi_p) |\varepsilon_p \ell_p m_p\rangle^{(\text{spherical})}, \quad |\varepsilon_p \ell_p m_p\rangle^{(\text{spherical})} = i^{\ell_p} j_{\ell_p}(pr) Y_{\ell_p, m_p}(\vartheta, \varphi)$$

$$|\mathbf{p}\rangle = \sqrt{\frac{2}{\pi}} \sum_{\ell_p=0}^{\infty} \sum_{m_p=-\ell_p}^{\ell_p} Y_{\ell_p, m_p}^*(\vartheta_p, \varphi_p) |\varepsilon_p \ell_p m_p\rangle, \quad |\varepsilon_p \ell_p m_p\rangle = i^{\ell_p} \frac{P_{\varepsilon_p \ell_p}(r)}{r} Y_{\ell_p, m_p}(\vartheta, \varphi).$$

if the partial waves $|\varepsilon_p \ell_p m_p\rangle$ just refer to solutions of the Schrödinger equation in the given potential:

$$|\varepsilon_p \ell_p m_p\rangle = |\varepsilon_p \ell_p m_p\rangle^{(\text{spherical, } V \equiv 0)} \implies \begin{aligned} &|\varepsilon_p \ell_p m_p\rangle^{(\text{Coulomb})} \\ &|\varepsilon_p \ell_p m_p\rangle^{(\text{distorted})} \end{aligned}.$$

Here, *distorted* refers to any [distorted Coulomb potential](#), i.e. a short-range central-field potential with a Coulombic tail. Of course, the same expansions still apply if we consider electron waves with given spin projections:

$$|\mathbf{p} m'_s\rangle \longrightarrow |\varepsilon_p \ell_p m_p\rangle |m'_s\rangle = |\varepsilon_p \ell_p m_p m'_s\rangle.$$

- Partial-wave expansions for a (quasi-) free electron with well-defined asymptotic momentum $\mathbf{p} + \mathbf{A}(t)$: The same expansion as above can be used to describe a (quasi-) free-electron wave with well-defined asymptotic (canonical) momentum $\mathbf{p} + \mathbf{A}(t)$ if the correct energy

10. Collision- and field-induced atomic responses

$\varepsilon = (\mathbf{p} + \mathbf{A}(t))^2/2$ is used for the associated partial waves $|\varepsilon_{p+A(t)}\ell_p m_p\rangle^{(\text{spherical})}$

$$e^{i(\mathbf{p} + \mathbf{A}(t)) \cdot \mathbf{r}} = 4\pi \sum_{\ell_p=0}^{\infty} \sum_{m_p=-\ell_p}^{\ell_p} i^{\ell_p} j_{\ell_p}((p + A(t))r) Y_{\ell_p, m_p}(\vartheta, \varphi)$$

$$|\mathbf{p} + \mathbf{A}(t)\rangle^{(\text{spherical})} = \sqrt{\frac{2}{\pi}} \sum_{\ell_p=0}^{\infty} \sum_{m_p=-\ell_p}^{\ell_p} Y_{\ell_p, m_p}^*(\vartheta_p, \varphi_p) |\varepsilon_{p+A(t)}\ell_p m_p\rangle^{(\text{spherical})}$$

➤ Partial-wave expansion for a free electron with well-defined asymptotic momentum \mathbf{p} in a coupled basis: An analogue expansion can be written in terms of the coupled basis by using

$$|\mathbf{p} m'_s\rangle = \sqrt{\frac{2}{\pi}} \sum_{\ell_p=0}^{\infty} \sum_{m_p=-\ell_p}^{\ell_p} \sum_{j_p} Y_{\ell_p m_p}^*(\vartheta_p, \varphi_p) \langle \ell_p m_p, 1/2 m'_s | j_p, m_p + m'_s \rangle |\varepsilon_p \ell_p j_p, m_p + m'_s\rangle.$$

➤ Partial-wave expansion for free-electron Volkov states in velocity gauge: In velocity gauge, the time-dependent Coulomb-Volkov and distorted-Volkov states can still be written analogue to the spherical-Volkov states from above, if the corresponding partial-wave expansions are applied:

$$|\chi_{\mathbf{p}}^{(\text{spherical-Volkov})}(t; \mathbf{A})\rangle = \sqrt{\frac{2}{\pi}} e^{-i S^{(\text{Volkov})}(t; \mathbf{A})} \sum_{\ell_p=0}^{\infty} \sum_{m_p=-\ell_p}^{\ell_p} Y_{\ell_p, m_p}^*(\vartheta_p, \varphi_p) |\varepsilon_p \ell_p m_p\rangle^{(\text{spherical})}$$

$$|\chi_{\mathbf{p}}^{(\text{spherical-Volkov})}(t; \mathbf{A})\rangle \implies \begin{cases} |\chi_{\mathbf{p}}^{(\text{Coulomb-Volkov})}(t; \mathbf{A})\rangle & \text{for } |\varepsilon_p \ell_p m_p\rangle^{(\text{spherical})} \implies |\varepsilon_p \ell_p m_p\rangle^{(\text{Coulomb})} \\ |\chi_{\mathbf{p}}^{(\text{distorted-Volkov})}(t; \mathbf{A})\rangle & |\varepsilon_p \ell_p m_p\rangle^{(\text{spherical})} \implies |\varepsilon_p \ell_p m_p\rangle^{(\text{distorted})} \end{cases}.$$

An analogue expansion also applies if the spherical Volkov states $|\chi_{\mathbf{p}}^{(\text{spherical-Volkov})}(t), m'_s\rangle$ include a well-defined spin-projection and, even if the rhs of the partial-wave expansion is written in a *coupled* basis of well-defined total angular momenta j : $|\varepsilon_p \ell_p m_p m_s\rangle \rightarrow |\varepsilon_p \ell_p j_p m'_p\rangle$.

To understand this rather straight generalization, we may argue here that the laser field gives rise to a time-dependent Volkov phase, while

it does not affect the spatial structure of the outgoing plane-wave electron. Therefore, the spherical Volkov states just become simple plane waves (and, analogue, for the Coulomb-Volkov and distorted-Volkov states, etc.) if the laser field is turned off ($|\mathbf{A}(t)| \rightarrow 0$). Following these arguments, the proper time dependence just arises by multiplying the (asymptotic) continuum states with the factor $e^{-iS^{(\text{Volkov})}(t; \mathbf{A})}$, and the same arguments still hold if the electron wave includes a well-defined spin-projection or is described within the *coupled* basis $\{|\varepsilon_p \ell_p j_p m'_p\rangle\}$. The same argument still holds for the many-electron atom if one assumes that the photoelectron moves in the (static) potential of the final ion.

- Partial-wave expansion for free-electron Volkov states in velocity gauge and within a coupled basis: A straightforward use of the partial-wave expansion from above gives rise to the corresponding expansion of the free-electron Volkov states as

$$|\chi_{\mathbf{p}}^{(\text{spherical-Volkov})}(t; \mathbf{A}), m'_s\rangle = \sqrt{\frac{2}{\pi}} e^{-iS^{(\text{Volkov})}(t; \mathbf{A})} \sum_{\ell_p=0}^{\infty} \sum_{m_p=-\ell_p}^{\ell_p} \sum_{j_p \geq 1/2} Y_{\ell_p m_p}^*(\vartheta_p, \varphi_p) \langle \ell_p m_p, 1/2 m'_s | j_p, m_p + m'_s \rangle |\varepsilon_p \ell_p j_p, m_p + m'_s\rangle^{(\text{spherical})}.$$

- Partial-wave expansion for (quasi-) free electron Volkov states in length gauge: In length gauge, the Volkov states $|\chi_{\mathbf{p}}^{(\text{Volkov})}(t; \mathbf{A})\rangle$ states cannot be so easily expanded since the kinetic momentum \mathbf{p} in the exponential has then to be replaced by the canonical momentum $\mathbf{p} + \mathbf{A}(t)$. Until the present, therefore, we here restrict the further treatment to the SFA in velocity gauge. However, the length gauge should be re-considered since this gauge often yields more reliable results for the photoelectron momentum distributions in the SFA, and this has been confirmed especially if the initial state is not spherical-symmetric. An expansion of the free-electron Volkov states in length gauge was performed by Milosevic and Becker (2019; appendix); in this treatment, a $j_\ell(A(t)r)$ -term occurs from the expansion of $e^{-i\mathbf{A}(t)\cdot\mathbf{r}}$, although this need to be explored in further detail.
- Partial-wave expansion for free-electron Volkov states in length gauge: In length gauge, the time-dependent Volkov states can be written in terms of the partial-wave expansion from above:

$$|\chi_{\mathbf{p}+\mathbf{A}}^{(\text{spherical-Volkov})}(t; \mathbf{A})\rangle = \sqrt{\frac{2}{\pi}} e^{-iS^{(\text{Volkov: length})}(t; \mathbf{A})} \sum_{\ell_p=0}^{\infty} \sum_{m_p=-\ell_p}^{\ell_p} Y_{\ell_p m_p}^*(\vartheta_p, \varphi_p) |\varepsilon_{p+A(t)} \ell_p m_p\rangle^{(\text{spherical})}$$

- Spherical unit vectors: To make use of the rotational symmetry of atoms and ions, all operators are typically expressed as spherical tensors, and by using a basis of (spherical) unit vectors. In this framework, one typically needs to distinguish between the covariant spherical basis

10. Collision- and field-induced atomic responses

$\{\mathbf{e}_+, \mathbf{e}_-, \mathbf{e}_0\}$ and the contravariant spherical basis $\{\mathbf{e}^+, \mathbf{e}^-, \mathbf{e}^0\}$:

$$\mathbf{e}_\pm = \frac{1}{\sqrt{2}} (\mathbf{e}_x \pm i \mathbf{e}_y), \quad \mathbf{e}_0 = \mathbf{e}_z = \mathbf{e}^0, \quad \mathbf{e}^\pm = \frac{1}{\sqrt{2}} (\mathbf{e}_x \mp i \mathbf{e}_y).$$

This distinction between the covariant and contravariant spherical basis is necessary since only (unit) vectors from the co- and contravariant basis are still pairwise orthonormal, $\mathbf{e}_q \cdot \mathbf{e}^s = \mathbf{e}^q \cdot \mathbf{e}_s = \delta_{qs}$ but, for instance, $\mathbf{e}_+ \cdot \mathbf{e}_+ \neq 1$.

- Spherical decomposition of a vector in the covariant spherical basis: A (cartesian) vector $\mathbf{v} = (v_x, v_y, v_z) = v_x \mathbf{e}_x + v_y \mathbf{e}_y + v_z \mathbf{e}_z$ is usually expressed in the covariant spherical basis by:

$$\mathbf{v} = v_+ \mathbf{e}_+ + v_0 \mathbf{e}_0 + v_- \mathbf{e}_-, \quad v_+ = \mathbf{e}^+ \cdot \mathbf{v} = \frac{1}{\sqrt{2}} (v_x - i v_y), \quad v_- = \frac{1}{\sqrt{2}} (v_x + i v_y), \quad v_0 = v_z.$$

- Polarized light in the spherical basis: The (complex) polarization vector \mathbf{u} for circularly- and linearly-polarized light can of course be expressed also in the spherical basis. If we associate left-circularly polarized light with $\lambda = +1$ (mathematical positive) and right-circularly polarized light with $\lambda = -1$, their (unit) polarization vectors are simply given by

$$\mathbf{u}^{(\text{circular})} = \frac{1}{\sqrt{2}} (\mathbf{e}_x + i \lambda \mathbf{e}_y) = \sum_{q=\pm 1, 0} u_q \mathbf{e}_q$$

$$\mathbf{u}^{(\text{left-circular})} = \frac{1}{\sqrt{2}} (\mathbf{e}_x + i \mathbf{e}_y); \quad u_+ = 1, \quad u_- = u_o = 0$$

$$\mathbf{u}^{(\text{right-circular})} = \frac{1}{\sqrt{2}} (\mathbf{e}_x - i \mathbf{e}_y); \quad u_- = 1, \quad u_+ = u_o = 0.$$

For linearly-polarized light, $\mathbf{u}^{(\text{linear})}$, one similarly finds

$$\mathbf{u}^{(\text{linear})} = \mathbf{e}_x : \quad u_+ = u_- = \frac{1}{\sqrt{2}}, \quad u_0 = 0$$

$$\mathbf{u}^{(\text{linear})} = \mathbf{e}_y : \quad u_+ = -u_- = -\frac{i}{\sqrt{2}}, \quad u_0 = 0.$$

- **Relation between the complex- and real-valued vector potential:** In the framework of spherical tensors, a complex-valued vector potential is usually applied for a monochromatic wave with well-defined amplitude A_o , frequency ω , carrier-envelope phase $\phi^{(\text{cep})}$ and (unit) polarization vector \mathbf{u} , $\mathbf{A}_c(t) = A_o \mathbf{u} e^{-i(\omega t + \phi^{(\text{cep})})}$. Of course, the electron-field interaction with the laser depends only on the real part of this complex potential

$$\mathbf{A}(t) = \Re\{\mathbf{A}_c(t)\} = \frac{1}{2} (\mathbf{A}_c(t) + \mathbf{A}_c^*(t)).$$

Below, the – physical part of – $\mathbf{A}(t)$ always occurs in the evaluation of the Volkov phases and related quantities, while the complex-valued form is required to make proper use of the spherical-tensor formalism.

- **Electron-field interaction Hamiltonian $\mathbb{H}^{(\text{laser})}(t)$ in velocity gauge:** With the simple relation above, the electron-field interaction Hamiltonian in (Coulomb +) velocity gauge can be re-written in terms of the complex-valued vector potential as

$$\begin{aligned} \mathbb{H}^{(\text{laser})}(t) &= \mathbf{A}(t) \cdot \mathbf{p} + \frac{1}{2} \mathbf{A}^2(t) = \frac{1}{2} \mathbf{A}_c(t) \cdot \mathbf{p} + \frac{1}{2} \mathbf{A}_c^*(t) \cdot \mathbf{p} + \frac{1}{8} (\mathbf{A}_c(t) + \mathbf{A}_c^*(t))^2 \\ &= -\frac{i}{2} \mathbf{A}_c(t) \cdot \boldsymbol{\nabla} - \frac{i}{2} \mathbf{A}_c^*(t) \cdot \boldsymbol{\nabla} + \frac{1}{8} (\mathbf{A}_c(t) + \mathbf{A}_c^*(t))^2. \end{aligned}$$

- **Electron-field interaction Hamiltonian $\mathbb{H}^{(\text{laser})}(t)$ in length gauge:** With the simple relation above, the electron-field interaction Hamiltonian in length gauge can be re-written in terms of the complex-valued electric field as

$$\mathbb{H}^{(\text{laser})}(t) = \mathcal{E} \cdot \mathbf{r} = \frac{\mathcal{E}_c + \mathcal{E}_c^*}{2} \cdot \mathbf{r}.$$

- **Spherical decomposition of the electron-field interaction:** The interaction of an electron (with momentum \mathbf{p}) with the complex-valued vector potential $\mathbf{A}_c(t) = A_o \mathbf{u} e^{-i(\omega t + \phi^{(\text{cep})})}$ leads obviously to scalar products, such as $\mathbf{u} \cdot \mathbf{p}$ and $\mathbf{u}^* \cdot \mathbf{p}$. These scalar products need to be expressed in a spherical basis ($\mathbf{e}^q = \mathbf{e}_q^*$, $\mathbf{e}_q^* \cdot \mathbf{e}_s = \mathbf{e}^q \cdot \mathbf{e}_s = \delta_{qs}$)

$$\mathbf{u} \cdot \mathbf{p} = \sum_{q,s=0,\pm 1} u_q p_s \mathbf{e}_q \cdot \mathbf{e}_s = \sum_{q,s=0,\pm 1} (-1)^q u_q p_s \mathbf{e}_{-q}^* \cdot \mathbf{e}_s = \sum_{q=0,\pm 1} (-1)^q u_q p_{-q}$$

$$\mathbf{u}^* \cdot \mathbf{p} = \sum_{q,s=0,\pm 1} u_q^* p_s \mathbf{e}_q^* \cdot \mathbf{e}_s = \sum_{q=0,\pm 1} u_q^* p_q.$$

10. Collision- and field-induced atomic responses

These decompositions of the scalar products are necessary in order to make use of the Wigner-Eckardt theorem and to apply the (standard) **reduced matrix elements of the momentum operator** in the partial-wave decomposition of the electron waves and its interaction with the laser field.

- **Complex-value electric field of a \sin^2 plane-wave pulse:** For a \sin^2 plane-wave pulse and in dipole approximation, the electric field $\mathbf{E}(t) = \Re\{\mathcal{E}_c(t)\} = \frac{1}{2}(\mathcal{E}_c(t) + \mathcal{E}_c^*(t))$ can be written in terms of a complex-value field as:

$$\begin{aligned}\mathcal{E}_c(t) &= -\frac{\partial \mathbf{A}_c}{\partial t} = \frac{A_o \omega}{2} \mathbf{u} e^{-i(\omega t + \phi_{cep})} \sin\left(\frac{\omega t}{2n_p}\right) \left[\frac{i}{n_p} \cos\left(\frac{\omega t}{2n_p}\right) + \sin\left(\frac{\omega t}{2n_p}\right) \right] \\ \mathcal{E}_c^*(t) &= -\frac{\partial \mathbf{A}_c^*}{\partial t} = \frac{A_o \omega}{2} \mathbf{u}^* e^{i(\omega t + \phi_{cep})} \sin\left(\frac{\omega t}{2n_p}\right) \left[\frac{-i}{n_p} \cos\left(\frac{\omega t}{2n_p}\right) + \sin\left(\frac{\omega t}{2n_p}\right) \right]\end{aligned}$$

- **Reduced matrix elements of the $\mathbf{u} \cdot \mathbf{p}$ interaction with an external field in velocity gauge:** In the product basis of spin-orbitals $\{|nlm_\ell m_s\rangle\}$, the electron-field interaction can be traced back to the following matrix elements, and can be further *reduced by means of the Wigner-Eckardt theorem*:

$$\begin{aligned}\langle \varepsilon_p \ell_p m_p | \mathbf{u} \cdot \mathbf{p} | n \ell m \rangle &= \sum_{q=0,\pm 1} (-1)^q u_q \langle \varepsilon_p \ell_p m_p | p_{-q} | n \ell m \rangle = \sum_{q=0,\pm 1} (-1)^q u_q \langle \ell m, 1(-q) | \ell_p m_p \rangle \langle \varepsilon_p \ell_p \| \mathbf{p} \| n \ell \rangle \\ \langle \varepsilon_p \ell_p m_p | \mathbf{u}^* \cdot \mathbf{p} | n \ell m \rangle &= \sum_{q=0,\pm 1} u_q^* \langle \varepsilon_p \ell_p m_p | p_q | n \ell m \rangle = \sum_{q=0,\pm 1} u_q^* \langle \ell m, 1q | \ell_p m_p \rangle \langle \varepsilon_p \ell_p \| \mathbf{p} \| n \ell \rangle.\end{aligned}$$

Rather analogue, these matrix elements read in the (coupled) basis of spin-orbital basis $\{|nljm\rangle\}$ as:

$$\begin{aligned}\langle \varepsilon_p \ell_p j_p m_p | \mathbf{u} \cdot \mathbf{p} | n \ell j m \rangle &= \sum_{q=0,\pm 1} (-1)^q u_q \langle \varepsilon_p \ell_p j_p m_p | p_{-q} | n \ell j m \rangle = \sum_{q=0,\pm 1} (-1)^q u_q \langle jm, 1(-q) | j_p m_p \rangle \langle \varepsilon_p \ell_p j_p \| \mathbf{p} \| n \ell j \rangle \\ \langle \varepsilon_p \ell_p j_p m_p | \mathbf{u}^* \cdot \mathbf{p} | n \ell j m \rangle &= \sum_{q=0,\pm 1} u_q^* \langle \varepsilon_p \ell_p j_p m_p | p_q | n \ell j m \rangle = \sum_{q=0,\pm 1} u_q^* \langle jm, 1q | j_p m_p \rangle \langle \varepsilon_p \ell_p j_p \| \mathbf{p} \| n \ell j \rangle\end{aligned}$$

$$\begin{aligned}
 \langle \varepsilon_p \ell_p j_p \| \mathbf{p} \| n\ell j \rangle &= \frac{\langle \varepsilon_p \ell_p \| \mathbf{p} \| n\ell \rangle}{\langle jm_j, 1(-q) | j_p m_p \rangle} \left[\sum_{m_\ell m_s, m'_p} \langle \ell_p m'_p, 1/2m_s | j_p m_p \rangle \langle \ell m_\ell, 1/2m_s | jm_j \rangle \langle \ell m_\ell, 1(-q) | \ell_p m'_p \rangle \right] \\
 &= (-1)^{\ell_p + 2j_p - j + 3/2} [j_p] \begin{Bmatrix} \ell_p & 1/2 & j_p \\ j & 1 & \ell \end{Bmatrix} \langle \varepsilon_p \ell_p \| \mathbf{p} \| n\ell \rangle
 \end{aligned}$$

➤ Reduced matrix elements of the momentum operator $\langle \varepsilon_p \ell_p \| \mathbf{p} \| n\ell \rangle$: The reduced matrix element of the momentum operator occurs at various places in atomic structure theory and can be written in terms of the reduced matrix elements of the $\mathbf{C}^{(1)}$ tensors and some radial integrals as

$$\begin{aligned}
 \mathbf{p} &= -i \nabla = -i \left[\mathbf{C}^{(1)} \frac{\partial}{\partial r} - \frac{\sqrt{2}}{r} (\mathbf{C}^{(1)} \otimes \mathbf{L}^{(1)})^{(1)} \right] \\
 \langle \ell_p \| \mathbf{p} \| \ell \rangle &= -i \langle \ell_p \| \mathbf{C}^{(1)} \| \ell \rangle \left[\frac{\partial}{\partial r} - \frac{(\ell_p - \ell)(\ell_p + \ell + 1) - 2}{2r} \right], \quad \langle \ell_p \| \mathbf{C}^{(1)} \| \ell \rangle = (-1)^{\ell_p} [\ell_p, \ell]^{1/2} \begin{pmatrix} \ell_p & 1 & \ell \\ 0 & 0 & 0 \end{pmatrix}
 \end{aligned}$$

$$\begin{aligned}
 \langle \varepsilon_p \ell_p \| \mathbf{p} \| n\ell \rangle &= (-i)^{\ell_p} \int dr r^2 \frac{P_{\varepsilon_p \ell_p}(r)}{r} \langle \ell_p \| \mathbf{p} \| \ell \rangle \frac{P_{n\ell}(r)}{r} \\
 &= (-i)^{\ell_p+1} \langle \ell_p \| \mathbf{C}^{(1)} \| \ell \rangle \int dr r^2 \frac{P_{\varepsilon_p \ell_p}(r)}{r} \left[\frac{\partial}{\partial r} - \frac{(\ell_p - \ell)(\ell_p + \ell + 1) - 2}{2r} \right] \frac{P_{n\ell}(r)}{r} \\
 &= (-i)^{\ell_p+1} \langle \ell_p \| \mathbf{C}^{(1)} \| \ell \rangle \int dr P_{\varepsilon_p \ell_p}(r) \left[\frac{\partial P_{n\ell}}{\partial r} - \frac{(\ell_p - \ell)(\ell_p + \ell + 1)}{2r} P_{n\ell} \right].
 \end{aligned}$$

10. Collision- and field-induced atomic responses

➤ Reduced matrix elements of the momentum operator $\langle \varepsilon_p \ell_p j_p \| \mathbf{p} \| n\ell j \rangle$:

$$\begin{aligned}\langle \varepsilon_p \ell_p j_p m_p | \mathbf{p} | n\ell j m \rangle &= \langle jm, 1q | j_p m_p \rangle \langle \varepsilon_p \ell_p j_p \| \mathbf{p} \| n\ell j \rangle \\ &= \sum_{m_\ell m_s, m'_p m'_s} \langle \ell_p m'_p, 1/2m'_s | j_p m_p \rangle \langle \ell m_\ell, 1/2m_s | jm \rangle \langle \varepsilon_p \ell_p m'_p m'_s \| \mathbf{p} \| n\ell m_\ell m_s \rangle \\ &= \sum_{m_\ell, m'_p m'_s} \langle \ell_p m'_p, 1/2m'_s | j_p m_p \rangle \langle \ell m_\ell, 1/2m'_s | jm \rangle \langle \ell m_\ell, 1q | \ell_p m'_p \rangle \langle \varepsilon_p \ell_p \| \mathbf{p} \| n\ell \rangle \\ \langle \varepsilon_p \ell_p j_p \| \mathbf{p} \| n\ell j \rangle &= \end{aligned}$$

➤ Reduced matrix elements of the $\mathbf{u} \cdot \mathbf{r}$ interaction with an external field in length gauge: In the product basis of spin-orbitals $\{|n\ell m_\ell m_s\rangle\}$, the electron-field interaction can be traced back to the following matrix elements, and can be further *reduced* by means of the Wigner-Eckardt theorem:

$$\langle \varepsilon_p \ell_p m_p | \mathbf{u} \cdot \mathbf{r} | n\ell m \rangle = \sum_{q=0,\pm 1} (-1)^q u_q \langle \varepsilon_p \ell_p m_p | p_{-q} | n\ell m \rangle = \sum_{q=0,\pm 1} (-1)^q u_q \langle \ell m, 1(-q) | \ell_p m_p \rangle \langle \varepsilon_p \ell_p \| \mathbf{r} \| n\ell \rangle$$

$$\langle \varepsilon_p \ell_p m_p | \mathbf{u}^* \cdot \mathbf{r} | n\ell m \rangle = \sum_{q=0,\pm 1} u_q^* \langle \varepsilon_p \ell_p m_p | p_q | n\ell m \rangle = \sum_{q=0,\pm 1} u_q^* \langle \ell m, 1q | \ell_p m_p \rangle \langle \varepsilon_p \ell_p \| \mathbf{r} \| n\ell \rangle .$$

$$\langle \varepsilon_p \ell_p \| \mathbf{r} \| n\ell \rangle = \langle \ell_p \| \mathbf{C}^{(1)} \| \ell \rangle \int_0^\infty dr P_{\varepsilon_p \ell_p}(r) r P_{n\ell}(r)$$

➤ Overlap integral $\langle \varepsilon_p \ell_p m_p | n\ell m \rangle$: If the radial orbitals $P_{\varepsilon_p \ell_p}(r)$, $P_{n\ell}(r)$ are taken to be *real*, the overlap integral becomes

$$\langle \varepsilon_p \ell_p m_p | n\ell m \rangle = \delta_{\ell_p \ell} \delta_{m_p m} (-i)^{\ell_p} \int dr P_{\varepsilon_p \ell_p}(r) P_{n\ell}(r) .$$

➤ Partial-wave decomposition of the direct transition amplitude $\mathcal{T}^{(\text{SFA:direct})}(\mathbf{p})$ for an infinite plane-wave pulse in velocity gauge: Making use of the partial-wave representation of the (free-electron) Volkov states, this *direct transition amplitude* reads for an infinite plane-wave

pulse $\mathbf{A}_c = A_o \mathbf{u} e^{-i(\omega t + \phi^{(cep)})}$ and for circularly-polarized light ($\lambda = \pm 1$) as:

$$\begin{aligned}
 & \mathcal{T}^{(\text{SFA: direct})}(\mathbf{p}) \\
 &= -i \int_{-\infty}^{\infty} d\tau \langle \chi_{\mathbf{p}}^{(\text{Volkov})}(\tau; \mathbf{A}) | \mathbb{H}^{(\text{laser})}(\tau) | \Psi_i(\tau) \rangle \\
 &= -i \sqrt{\frac{2}{\pi}} \int_{-\infty}^{\infty} d\tau e^{i S^{(\text{Volkov})}(\tau; \mathbf{A})} e^{-i \varepsilon_i \tau} \sum_{\ell_p=0}^{\infty} \sum_{m_p=-\ell_p}^{\ell_p} \\
 &\quad \times \left[A_0 e^{-i(\omega t + \phi^{(cep)})} Y_{\ell_p, m_p}(\vartheta_p, \varphi_p) \sum_{q=0, \pm 1} (-1)^q u_q \langle \ell m, 1(-q) | \ell_p m_p \rangle \langle \varepsilon_p \ell_p \| \mathbf{p} \| n \ell \rangle \right. \\
 &\quad \left. + A_0 e^{i(\omega t + \phi^{(cep)})} Y_{\ell_p, m_p}(\vartheta_p, \varphi_p) \sum_{q=0, \pm 1} u_q^* \langle \ell m, 1q | \ell_p m_p \rangle \langle \varepsilon_p \ell_p \| \mathbf{p} \| n \ell \rangle \right] + \frac{\mathbf{A}^2(\tau)}{2} \sum_{\ell_p=0}^{\infty} \sum_{m_p=-\ell_p}^{\ell_p} \langle \varepsilon_p \ell_p m_p | n \ell m \rangle \\
 &= -i \sqrt{\frac{2}{\pi}} \int_{-\infty}^{\infty} d\tau e^{i S^{(\text{Volkov})}(\tau; \mathbf{A})} e^{-i \varepsilon_i \tau} \\
 &\quad \times \left[A_0 e^{-i(\omega t + \phi^{(cep)})} \sum_{\ell_p=0}^{\infty} \sum_{q=0, \pm 1} Y_{\ell_p, m+q}(\vartheta_p, \varphi_p) (-1)^q u_q \langle \ell m, 1(-q) | \ell_p, m-q \rangle \langle \varepsilon_p \ell_p \| \mathbf{p} \| n \ell \rangle \right. \\
 &\quad \left. + A_0 e^{i(\omega t + \phi^{(cep)})} \sum_{\ell_p=0}^{\infty} \sum_{q=0, \pm 1} Y_{\ell_p, m+q}(\vartheta_p, \varphi_p) u_q \langle \ell m, 1q | \ell_p, m+q \rangle \langle \varepsilon_p \ell_p \| \mathbf{p} \| n \ell \rangle \right] + \frac{\mathbf{A}^2(\tau)}{2} \langle \varepsilon_p \ell m | n \ell m \rangle .
 \end{aligned}$$

For a circularly-polarized beams, we can use either the real or complex-valued vector potential in the quadratic term since $\mathbf{A}^2(t) = A_o^2 f^2(t) (\cos^2(\dots) + \lambda^2 \sin^2(\dots)) = A_o^2 f^2(t)$.

In the [electric-dipole approximation](#), moreover, the term in the last line vanishes if $|\varepsilon_p \ell_p m_p\rangle$ and $|n \ell m\rangle$ are eigenfunctions of the same

10. Collision- and field-induced atomic responses

(atomic) Hamiltonian, $\langle \varepsilon_p \ell_p m_p | n\ell m \rangle = \delta_{\ell_p, \ell} \delta_{m_p, m} (-i)^{\ell_p} \int dr P_{\varepsilon_p \ell_p}(r) P_{n\ell} = 0$ and, hence, the $\mathbf{A}^2(t)$ term from the electron-field interaction operator $\mathbb{H}^{(\text{laser})}$ does not contribute in this particular case. This applies, for instance, if a Coulomb or distorted central-field potential *and* the corresponding (free-electron) Coulomb-Volkov or, respectively, distorted-Volkov state are utilized together in the computations.

In the direct amplitude $\mathcal{T}^{(\text{SFA:direct})}(\mathbf{p})$ above, moreover, a simple factor $\langle m'_s | m_s \rangle = \delta_{m'_s, m_s}$ occurs in addition to the given expressions if the spin-projection of the electron is taken into account in the representation of the initial state and the final (Volkov) wave of the outgoing electron; this simple factorization just shows that the electron-field interaction does not depend on the spin (projection) of the electron and, hence, leaves the spin-projection unaffected.

- **Partial-wave decomposition of the direct transition amplitude $\mathcal{T}^{(\text{SFA:direct})}(\mathbf{p})$ for a finite and circularly-polarized pulse:** For a finite pulse with envelope $f^{(\text{env})} \equiv f^{(\text{envelope})}(t)$ and vector potential $\mathbf{A} = A_o e^{-i(\omega t + \phi^{(\text{cep})})} \mathbf{u} f^{(\text{env})}(t)$, the direct transition amplitudes reads as

$$\begin{aligned} \mathcal{T}^{(\text{SFA:direct})}(\mathbf{p}) &= -i \int_{-\infty}^{\infty} d\tau \left\langle \chi_{\mathbf{p}}^{(\text{Volkov})}(\tau; \mathbf{A}) \middle| \mathbb{H}^{(\text{laser})}(\tau) \right| \Psi_i(\tau) \rangle \\ &= -i \sqrt{\frac{2}{\pi}} \mathcal{F}^{(\text{Volkov})}[-; \omega; f^{(\text{env})}; \mathbf{A}] \left(\sum_{\ell_p=0}^{\infty} \sum_{q=0, \pm 1} Y_{\ell_p, m_p}(\vartheta_p, \varphi_p) (-1)^q u_q \langle \ell m, 1(-q) | \ell_p, m - q \rangle \langle \varepsilon_p \ell_p \| \mathbf{p} \| n\ell \rangle \right) \\ &\quad -i \sqrt{\frac{2}{\pi}} \mathcal{F}^{(\text{Volkov})}[+; \omega; f^{(\text{env})}; \mathbf{A}] \left(\sum_{\ell_p=0}^{\infty} \sum_{q=0, \pm 1} Y_{\ell_p, m_p}(\vartheta_p, \varphi_p) u_q^* \langle \ell m, 1q | \ell_p, m + q \rangle \langle \varepsilon_p \ell_p \| \mathbf{p} \| n\ell \rangle \right) \\ &\quad -i \frac{1}{\sqrt{2\pi}} \mathcal{F}^{(\text{quad, Volkov})}[f^{(\text{env})}; \mathbf{A}] \langle \varepsilon_p \ell m | n\ell m \rangle \\ \mathcal{F}^{(\text{Volkov})}[\pm; \omega; f^{(\text{env})}; \mathbf{A}] &= A_o e^{\pm i\phi^{(\text{cep})}} \int_{-\infty}^{\infty} d\tau f^{(\text{envelope})}(\tau) e^{-i(\varepsilon \mp \omega)\tau + iS^{(\text{Volkov})}(\tau; \mathbf{A})} \\ \mathcal{F}^{(\text{quad, Volkov})}[f^{(\text{env})}; \mathbf{A}] &= \int_{-\infty}^{\infty} d\tau \mathbf{A}^2(\tau) e^{-i\varepsilon_i \tau + iS^{(\text{Volkov})}(\tau; \mathbf{A})} \end{aligned}$$

Here, we have introduced the two **pulse-envelope integrals** $\mathcal{F}^{(\text{Volkov})}[\pm; \omega; f^{(\text{env})}; \mathbf{A}]$ and $\mathcal{F}^{(\text{quad, Volkov})}[f^{(\text{env})}; \mathbf{A}]$ in order to separate the contribution of the time-dependent laser pulse with its frequency, envelope, carrier-envelope phase and polarization from the (effective)

electron-field interaction to the transition amplitudes. These pulse-envelope integrals refer to standard integrals as they frequently appear in SFA computations. For a time-harmonic pulse of infinite duration $f^{(\text{envelope})}(t) = 1$, these pulse-shape integrals can be evaluated analytically, especially for circularly-polarized laser pulses. For other pulses, these integrals are often solved numerically, while the Volkov phase $S^{(\text{Volkov})}(t; \mathbf{A})$ may still be evaluated analytically.

- **Partial-wave decomposition of the direct transition amplitude** $\mathcal{T}^{(\text{SFA:direct})}(\mathbf{p})$ **for a finite and circularly-polarized pulse in the coupled basis:** For a finite pulse with envelope $f^{(\text{env})} \equiv f^{(\text{envelope})}(t)$ and vector potential $\mathbf{A} = A_o e^{-i(\omega t + \phi^{(\text{cep})})} \mathbf{u} f^{(\text{env})}(t)$, the direct transition amplitudes reads for states of well-defined total angular momentum j, m as

$$\begin{aligned} \mathcal{T}^{(\text{SFA:direct})}(\mathbf{p}) &= -i \int_{-\infty}^{\infty} d\tau \left\langle \chi_{\mathbf{p}}^{(\text{Volkov})}(\tau; \mathbf{A}), m'_s \right| \mathbb{H}^{(\text{laser})}(\tau) \left| n\ell jm \right\rangle \\ &= -i \sqrt{\frac{2}{\pi}} \mathcal{F}^{(\text{Volkov})}[-; \omega; f^{(\text{env})}; \mathbf{A}] \left(\sum_{\ell_p=0}^{\infty} \sum_{j_p \geq 1/2}^{\infty} \sum_{q=0,\pm 1} Y_{\ell_p, m_j - m'_s - q}(\vartheta_p, \varphi_p) (-1)^q u_q \langle jm_j, 1(-q) | j_p, m_j - q \rangle \right. \\ &\quad \times \left. \langle \ell_p, m_j - m'_s - q, 1/2m'_s | j_p, m_j - q \rangle \langle \varepsilon_p \ell_p j_p \| \mathbf{p} \| n\ell j \rangle \right) \\ &\quad -i \sqrt{\frac{2}{\pi}} \mathcal{F}^{(\text{Volkov})}[+; \omega; f^{(\text{env})}; \mathbf{A}] \left(\sum_{\ell_p=0}^{\infty} \sum_{j_p \geq 1/2}^{\infty} \sum_{q=0,\pm 1} Y_{\ell_p, m_p}(\vartheta_p, \varphi_p) u_q^* \langle jm_j, 1q | j_p, m_j - q \rangle \right. \\ &\quad \times \left. \langle \ell_p, m_j - m'_s - q, 1/2m'_s | j_p, m_j - q \rangle \langle \varepsilon_p \ell_p j_p \| \mathbf{p} \| n\ell j \rangle \right) \\ &\quad -i \frac{1}{\sqrt{2\pi}} \mathcal{F}^{(\text{quad, Volkov})}[f^{(\text{env})}; \mathbf{A}] \langle \varepsilon_p \ell_p j_p \| \mathbf{p} \| n\ell j \rangle \end{aligned}$$

Of course, the summation over ℓ_p and j_p is not independent of each other due to the Clebsch-Gordan coefficients. Within the non-relativistic theory, the reduced matrix elements $\langle \varepsilon_p \ell_p j_p \| \mathbf{p} \| n\ell j \rangle \equiv \langle \varepsilon_p \kappa_p \| \mathbf{p} \| n\kappa \rangle$ can be expressed again in terms of the matrix elements $\langle \varepsilon_p \ell_p \| \mathbf{p} \| n\ell \rangle$, while a proper expression need to be found in the relativistic case.

- **Partial-wave decomposition of the direct transition amplitude** $\mathcal{T}^{(\text{SFA:direct})}(\mathbf{p})$ **for an infinite plane-wave pulse in length gauge:** Making use of the partial-wave representation of the (free-electron) Volkov states, this **direct transition amplitude reads for an infinite plane-wave**

pulse

$$\begin{aligned}
 & \mathcal{T}^{(\text{SFA: direct})}(\mathbf{p}) \\
 &= -i \int_{-\infty}^{\infty} d\tau \langle \chi_{\mathbf{p}}^{(\text{Volkov: length})}(\tau; \mathbf{A}) | \mathbb{H}^{(\text{laser: length})}(\tau) | \Psi_i(\tau) \rangle \\
 &= \dots \quad -i \sqrt{\frac{2}{\pi}} \int_{-\infty}^{\infty} d\tau e^{i S^{(\text{Volkov})}(\tau; \mathbf{A})} e^{-i \varepsilon_i \tau} \sum_{\ell_p=0}^{\infty} \sum_{m_p=-\ell_p}^{\ell_p} \\
 &\quad \times \left[A_0 e^{-i(\omega t + \phi^{(\text{cep})})} Y_{\ell_p, m_p}(\vartheta_p, \varphi_p) \sum_{q=0, \pm 1} (-1)^q u_q \langle \ell m, 1(-q) | \ell_p m_p \rangle \langle \varepsilon_p \ell_p \| \mathbf{p} \| n \ell \rangle \right. \\
 &\quad \left. + A_0 e^{i(\omega t + \phi^{(\text{cep})})} Y_{\ell_p, m_p}(\vartheta_p, \varphi_p) \sum_{q=0, \pm 1} u_q^* \langle \ell m, 1q | \ell_p m_p \rangle \langle \varepsilon_p \ell_p \| \mathbf{p} \| n \ell \rangle \right] + \frac{\mathbf{A}^2(\tau)}{2} \sum_{\ell_p=0}^{\infty} \sum_{m_p=-\ell_p}^{\ell_p} \langle \varepsilon_p \ell_p m_p | n \ell m \rangle \\
 &= -i \sqrt{\frac{2}{\pi}} \int_{-\infty}^{\infty} d\tau e^{i S^{(\text{Volkov})}(\tau; \mathbf{A})} e^{-i \varepsilon_i \tau} \\
 &\quad \times \left[A_0 e^{-i(\omega t + \phi^{(\text{cep})})} \sum_{\ell_p=0}^{\infty} \sum_{q=0, \pm 1} Y_{\ell_p, m+q}(\vartheta_p, \varphi_p) (-1)^q u_q \langle \ell m, 1(-q) | \ell_p, m-q \rangle \langle \varepsilon_p \ell_p \| \mathbf{p} \| n \ell \rangle \right. \\
 &\quad \left. + A_0 e^{i(\omega t + \phi^{(\text{cep})})} \sum_{\ell_p=0}^{\infty} \sum_{q=0, \pm 1} Y_{\ell_p, m+q}(\vartheta_p, \varphi_p) u_q \langle \ell m, 1q | \ell_p, m+q \rangle \langle \varepsilon_p \ell_p \| \mathbf{p} \| n \ell \rangle \right] + \frac{\mathbf{A}^2(\tau)}{2} \langle \varepsilon_p \ell m | n \ell m \rangle .
 \end{aligned}$$

➤ In JAC, the pulse-envelope integrals $\mathcal{F}^{(\text{Volkov})}[\pm; \omega; f^{(\text{env})}; \mathbf{A}]$ and $\mathcal{F}^{(\text{quad, Volkov})}[f^{(\text{env})}; \mathbf{A}]$ are implemented for a number of frequently

applied pulse envelopes; their use is simply controlled by a (singleton) variable `envelope::AbstractEnvelope` which may take the values `InfiniteEnvelope()`, `RectangularEnvelope()`, `SinSquaredEnvelope()`, `GaussianEnvelope()`.

Further discussion and publications:

- How can we calculate $\langle \varepsilon_p \ell_p j_p \| \mathbf{p} \| n \ell j \rangle$ within a relativistic framework ??
- How does the figures from the last MS 'change' if, for neon or argon, we consider:
 1. hydrogenic $2p$ with adapted effective charge;
 2. realistic $2p$ due to Bunge (1993);
 3. relativistic $2p_{1/2,3/2}$ electrons from JAC is taken into account, including perhaps 2 gauges.
- Which of these figures could be readily repeated in JAC ?? Which of them should be sensitive w.r.t. the electronic structure of the bound electrons.
- Compare relativistic computations for $2s$ of lithium with full $1s^2 2s$ computations, including the angular machinery. These computations should be equivalent ... but would prove the many-electron implementation.

Envelopes and Volkov phases of common laser pulses:

- Pulse envelope $f^{(\text{env})}(t)$ and carrier-envelope phase $\phi^{(\text{cep})}$: A laser pulse is commonly parametrized by its frequency, (real-valued) pulse envelope $f^{(\text{env})}(t)$, the carrier-envelope phase $\phi^{(\text{cep})}$, the (real-valued) amplitude A_o as well as the (complex-valued and unit) polarization vector \mathbf{u} ; these pulses are then formally applied in terms of the — complex or real-valued — vector potential. For circularly-polarized light, this vector potential can be written as

$$\mathbf{A}_c(t) = A_o f(t) \mathbf{u} e^{-i(\omega t + \phi^{(\text{cep})})}$$

$$\mathbf{A}(t) = \Re[\mathbf{A}_c(t)] = \frac{A_o}{\sqrt{2}} f(t) [\cos(\omega t + \phi^{(\text{cep})}) \mathbf{e}_x + \lambda \sin(\omega t + \phi^{(\text{cep})}) \mathbf{e}_y].$$

Similar formulas apply for linearly-polarized light with $\lambda = 0$ and $A_o \rightarrow \sqrt{2} A_o$; however, linearly-polarized light is less relevant if only the *direct* and no *rescattering* amplitudes are considered. Unpolarized light is usually not considered by the strong-field community but could be treated by taking a proper superposition of circularly-polarized light.

10. Collision- and field-induced atomic responses

➤ Volkov phase for circularly-polarized pulses with $\lambda = \pm 1$: For a (in)finite pulse with well-defined carrier-envelope phase and for photoelectrons with asymptotic momentum $\mathbf{p} = (p, \vartheta_p, \varphi) = (\sqrt{2\varepsilon_p}, \vartheta_p, \varphi_p)$ in spherical coordinates the Volkov phase can be written as:

$$\begin{aligned} S^{(\text{Volkov})}(t; \mathbf{A}) &= \frac{1}{2} \int^t d\tau (\mathbf{p} + \mathbf{A}(\tau))^2 = \frac{1}{2} \int^t d\tau (\mathbf{p}^2 + 2\mathbf{A}(\tau) \cdot \mathbf{p} + \mathbf{A}^2(\tau)) \\ &= \underbrace{\frac{p^2}{2} t}_{\varepsilon_p} + \frac{A_o}{\sqrt{2}} \int^t d\tau f(\tau) [p_x \cos(\omega\tau + \phi^{(\text{cep})}) + \lambda p_y \sin(\omega\tau + \phi^{(\text{cep})})] + \frac{A_o^2}{4} \int^t d\tau f^2(\tau) \\ &= \varepsilon_p t + \frac{A_o p \sin \vartheta_p}{\sqrt{2}} \int^t d\tau f(\tau) \cos(\omega\tau + \phi^{(\text{cep})} - \lambda \varphi_p) + \frac{A_o^2}{4} \int^t d\tau f^2(\tau). \end{aligned}$$

In the last line, use is made of the addition theorem of the cosine and the allowed values of the helicity $\lambda = \pm 1$.

➤ Volkov phase for linearly-polarized pulses: For a (in)finite pulse

$$S^{(\text{Volkov})}(t; \mathbf{A}) =$$

➤ Pulse envelope (time) integrals: From the decomposition of the *direct* SFA amplitude $\mathcal{T}^{(\text{SFA: direct})}(\mathbf{p})$, we find that the influence of the (time-dependent) laser pulse can be *factorized* from the contributions of the effective atom-field interaction and captured in terms of the (so-called) pulse envelope (time) integrals

$$\begin{aligned} \mathcal{F}^{(\text{Volkov})} [\pm; \omega; f^{(\text{env})}; \mathbf{A}] &= A_o e^{\pm i \phi^{(\text{cep})}} \int_{-\infty}^{\infty} d\tau f^{(\text{envelope})}(\tau) e^{-i(\varepsilon \mp \omega)\tau + i S^{(\text{Volkov})}(\tau; \mathbf{A})} \\ \mathcal{F}^{(\text{quad, Volkov})}[f^{(\text{env})}; \mathbf{A}] &= \int_{-\infty}^{\infty} d\tau \mathbf{A}^2(\tau) e^{-i\varepsilon_i \tau + i S^{(\text{Volkov})}(\tau; \mathbf{A})} \end{aligned}$$

Infinite pulse (continuous beam):

➤ Pulse envelope: $f^{(\text{env})} \equiv 1$

➤ Volkov phase for a circularly-polarized pulse: From the general expression above, the Volkov phase simplifies to:

$$S^{(\text{Volkov})}(t; \mathbf{A}) = \underbrace{\varepsilon_p t + \frac{A_o p \sin \vartheta_p}{\sqrt{2}\omega}}_a \sin(\omega t + \phi^{(\text{cep})} - \lambda \varphi_p) + \underbrace{\frac{A_o^2}{4}}_{U_p} t$$

$$e^{i S^{(\text{Volkov})}(t; \mathbf{A})} = e^{i(\varepsilon_p + U_p)t} e^{i a \sin(\omega t + \phi^{(\text{cep})} - \lambda \varphi_p)} = e^{i(\varepsilon_p + U_p)t} \sum_{s=-\infty}^{\infty} J_s(a) e^{is\omega t} e^{is(\phi^{(\text{cep})} - \lambda \varphi_p)},$$

where $U_p = A_o^2/4$ is the **ponderomotive energy**, i.e. the cycle-averaged kinetic energy of a classical electron moving in the oscillating electric field of the laser pulse. Moreover, the constant a is just used as short-hand notation in the expressions below.

➤ Pulse envelope (time) integrals for a circularly-polarized pulse: These integrals can be simplified with the identity $\int dx e^{ixy} = 2\pi \delta(y)$ to

$$\begin{aligned} \mathcal{F}^{(\text{Volkov})} [\pm; \omega; f^{(\text{infinite})}; \mathbf{A}] &= A_o e^{\pm i \phi^{(\text{cep})}} \int_{-\infty}^{\infty} d\tau e^{-i(\varepsilon_i \mp \omega)\tau + i S^{(\text{Volkov})}(\tau)} \\ &= A_o e^{\pm i \phi^{(\text{cep})}} \sum_{s=-\infty}^{\infty} J_s(a) e^{is(\phi^{(\text{cep})} - \lambda \varphi_p)} \int_{-\infty}^{\infty} d\tau e^{i[(s \pm 1)\omega + \varepsilon_p - \varepsilon_i + U_p]\tau} \\ &= 2\pi A_o e^{\pm i \phi^{(\text{cep})}} \sum_{s=-\infty}^{\infty} J_s(a) e^{is(\phi^{(\text{cep})} - \lambda \varphi_p)} \delta((s \pm 1)\omega + \varepsilon_p - \varepsilon_i + U_p) \end{aligned}$$

$$\begin{aligned} \mathcal{F}^{(\text{quad, Volkov})}[f^{(\text{infinite})}; \mathbf{A}] &= \int_{-\infty}^{\infty} d\tau \mathbf{A}^2(\tau) e^{-i\varepsilon_i\tau + i S^{(\text{Volkov})}(\tau)} = \frac{A_o^2}{2} \sum_{s=-\infty}^{\infty} J_s(a) e^{is(\phi^{(\text{cep})} - \lambda \varphi_p)} \int_{-\infty}^{\infty} d\tau e^{i[s\omega + \varepsilon_p - \varepsilon_i + U_p]\tau} \\ &= 4\pi U_p \sum_{s=-\infty}^{\infty} J_s(a) e^{is(\phi^{(\text{cep})} - \lambda \varphi_p)} \delta(s\omega + \varepsilon_p - \varepsilon_i + U_p) \end{aligned}$$

Rectangular pulse:

➤ Pulse envelope: For a pulse of n_p optical cycles (integer), the pulse envelope and duration are given by

$$f(t) = \begin{cases} 1 & 0 \leq t \leq T_p, \\ 0 & \text{otherwise} \end{cases}, \quad T_p = n_p \frac{2\pi}{\omega}.$$

➤ Volkov phase for a circularly-polarized pulse: For such a rectangular pulse envelope, the Volkov phase needs to be evaluated piecewise in *three* separate regions

$$S^{(\text{Volkov})}(t \leq 0) = \varepsilon_p t$$

$$\begin{aligned} S^{(\text{Volkov})}(0 \leq t \leq T_p; \mathbf{A}) &= \varepsilon_p t + \frac{A_o p \sin \vartheta_p}{\sqrt{2}} \int_0^t d\tau \cos(\omega \tau + \phi^{(\text{cep})} - \lambda \varphi_p) + \frac{A_o^2}{4} \int_0^t d\tau \\ &= \varepsilon_p t + \underbrace{\frac{A_o p \sin \vartheta_p}{\sqrt{2} \omega}_a} [\sin(\omega t + \phi^{(\text{cep})} - \lambda \varphi_p) - \sin(\phi^{(\text{cep})} - \lambda \varphi_p)] + U_p t \end{aligned}$$

$$\begin{aligned} S^{(\text{Volkov})}(t > T_p; \mathbf{A}) &= \varepsilon_p t + \frac{A_o p \sin \vartheta_p}{\sqrt{2}} \int_0^{T_p} d\tau \cos(\omega \tau + \phi^{(\text{cep})} - \lambda \varphi_p) + \frac{A_o^2}{4} \int_0^{T_p} d\tau \\ &= \varepsilon_p t + \underbrace{\frac{A_o p \sin \vartheta_p}{\sqrt{2} \omega}_a} [\sin(\omega T_p + \phi^{(\text{cep})} - \lambda \varphi_p) - \sin(\phi^{(\text{cep})} - \lambda \varphi_p)] + U_p T_p \end{aligned}$$

➤ Pulse envelope (time) integrals for a circularly-polarized pulse: For this Volkov phase, the pulse-envelope integrals can be solved analytically

$$\text{with } a = \frac{A_o p \sin \vartheta_p}{\sqrt{2} \omega}$$

$$\mathcal{F}^{(\text{Volkov})} [\pm; \omega; f^{(\text{rectangular})}; \mathbf{A}]$$

$$\begin{aligned} &= A_o e^{\pm i \phi^{(\text{cep})}} \int_{-\infty}^{\infty} d\tau f^{(\text{rectangular})}(\tau) e^{-i(\varepsilon_i \mp \omega)\tau + i S^{(\text{Volkov})}(\tau; \mathbf{A})} \\ &= A_o e^{\pm i \phi^{(\text{cep})}} \int_0^{T_p} d\tau e^{-i(\varepsilon_i \mp \omega)\tau + i S^{(\text{Volkov})}(\tau; \mathbf{A})} = A_o e^{\pm i \phi^{(\text{cep})}} e^{-i a \sin(\phi^{(\text{cep})} - \lambda \varphi_p)} \int_0^{T_p} d\tau e^{-i(\varepsilon_i \mp \omega - \varepsilon_p - U_p)\tau + ia \sin(\omega \tau + \phi^{(\text{cep})} - \lambda \varphi_p)} \\ &= e^{-i a \sin(\phi^{(\text{cep})} - \lambda \varphi_p)} \sum_{s=-\infty}^{\infty} J_s(a) e^{is(\phi^{(\text{cep})} - \lambda \varphi_p)} \int_0^{T_p} d\tau e^{i[(s \pm 1)\omega + \varepsilon_p - \varepsilon_i + U_p]\tau} \\ &= -i e^{-i a \sin(\phi^{(\text{cep})} - \lambda \varphi_p)} \sum_{s=-\infty}^{\infty} \frac{J_s(a) e^{is(\phi^{(\text{cep})} - \lambda \varphi_p)}}{(s \pm 1)\omega + \varepsilon_p - \varepsilon_i + U_p} (e^{i[(s \pm 1)\omega + \varepsilon_p - \varepsilon_i + U_p]T_p} - 1) \end{aligned}$$

$$\mathcal{F}^{(\text{quad, Volkov})} [f^{(\text{rectangular})}; \mathbf{A}]$$

$$\begin{aligned} &= \int_{-\infty}^{\infty} d\tau \mathbf{A}^2(\tau) e^{-i\varepsilon_i\tau + i S^{(\text{Volkov})}(\tau; \mathbf{A})} = \frac{A_o^2}{2} \int_0^{T_p} d\tau e^{-i\varepsilon_i\tau + i S^{(\text{Volkov})}(\tau; \mathbf{A})} \\ &= \frac{A_o^2}{2} e^{-i a \sin(\phi^{(\text{cep})} - \lambda \varphi_p)} \int_0^{T_p} d\tau e^{-i(\varepsilon_i - \varepsilon_p - U_p)\tau + ia \sin(\omega \tau + \phi^{(\text{cep})} - \lambda \varphi_p)} \\ &= \frac{A_o^2}{2} e^{-i a \sin(\phi^{(\text{cep})} - \lambda \varphi_p)} \sum_{s=-\infty}^{\infty} J_s(a) e^{is(\phi^{(\text{cep})} - \lambda \varphi_p)} \int_0^{T_p} d\tau e^{i(s\omega + \varepsilon_p - \varepsilon_i + U_p)\tau} \\ &= 2U_p e^{-i a \sin(\phi^{(\text{cep})} - \lambda \varphi_p)} \sum_{s=-\infty}^{\infty} \frac{J_s(a) e^{is(\phi^{(\text{cep})} - \lambda \varphi_p)}}{s\omega + \varepsilon_p - \varepsilon_i + U_p} (e^{i(s\omega + \varepsilon_p - \varepsilon_i + U_p)T_p} - 1) \end{aligned}$$

sin² pulse:

➤ Pulse envelope: For a pulse of n_p optical cycles (integer), the pulse envelope and duration are given by

$$f(t) = \begin{cases} \sin^2\left(\frac{\omega}{2n_p} t\right) & 0 \leq t \leq T_p, \\ 0 & \text{otherwise} \end{cases}, \quad T_p = n_p \frac{2\pi}{\omega}.$$

➤ Volkov phase for a circularly-polarized pulse: For such a sin² pulse envelope, the Volkov phase need again to be evaluated piecewise in *three* separate regions

$$S^{(\text{Volkov})}(t \leq 0) = \varepsilon_p t$$

$$S^{(\text{Volkov})}(0 \leq t \leq T_p; \mathbf{A}) = \varepsilon_p t + \frac{A_o p \sin \vartheta_p}{\sqrt{2}} \int_0^t d\tau \sin^2\left(\frac{\omega}{2n_p} \tau\right) \cos(\omega \tau + \phi^{(\text{cep})} - \lambda \varphi_p) + \frac{A_o^2}{4} \int_0^t d\tau \sin^4\left(\frac{\omega}{2n_p} \tau\right)$$

$$= \varepsilon_p t + \frac{3}{8} U_p t - \frac{U_p n_p}{2\omega} \sin\left(\frac{\omega}{n_p} t\right) + \frac{U_p n_p}{16\omega} \sin\left(\frac{2\omega}{n_p} t\right)$$

$$+ a \sum_{k=-1}^1 \frac{c_k}{1 + \frac{k}{n_p}} \left[\sin\left(\omega \left(1 + \frac{k}{n_p}\right) t + \phi^{(\text{cep})} - \lambda \varphi_p\right) - \sin(\phi^{(\text{cep})} - \lambda \varphi_p) \right]$$

$$S^{(\text{Volkov})}(t > T_p; \mathbf{A}) = \varepsilon_p t + \frac{A_o p \sin \vartheta_p}{\sqrt{2}} \int_0^{T_p} d\tau \sin^2\left(\frac{\omega}{2n_p} \tau\right) \cos(\omega \tau + \phi^{(\text{cep})} - \lambda \varphi_p) + \frac{A_o^2}{4} \int_0^{T_p} d\tau \sin^4\left(\frac{\omega}{2n_p} \tau\right)$$

$$= \varepsilon_p t + \frac{3}{8} U_p T_p - \frac{U_p n_p}{2\omega} \sin\left(\frac{\omega}{n_p} T_p\right) + \frac{U_p n_p}{16\omega} \sin\left(2\frac{\omega}{n_p} T_p\right)$$

$$+ a \sum_{k=-1}^1 \frac{c_k}{1 + \frac{k}{n_p}} \left[\sin\left(\omega \left(1 + \frac{k}{n_p}\right) T_p + \phi^{(\text{cep})} - \lambda \varphi_p\right) - \sin(\phi^{(\text{cep})} - \lambda \varphi_p) \right].$$

- Pulse envelope (time) integrals for a circularly-polarized pulse: These integrals could be solved analytically by applying the Jacobi-Anger expansion to all factors of the form $\exp(-i z \sin \theta)$. This leads to five infinite summations and is therefore not so practical for numerical computations since each summation should include about 5 to 10 terms for reasonable convergence. Instead, the integrals can be simpler solved numerically by using the analytical expression for the Volkov phase from above.

Gaussian pulse:

- Pulse envelope: For a Gaussian envelope with FWHM T_p , which is taken also as pulse duration, the pulse envelope is given by

$$f(t) = \exp\left(-4 \ln(2) \left(\frac{t}{T_p}\right)^2\right).$$

- Volkov phase for a circularly-polarized pulse: With the error function $\text{erf}(x) = \frac{2}{\sqrt{\pi}} \int_0^x e^{-y^2} dy$ and the abbreviation $\xi = \phi^{(\text{cep})} - \lambda \varphi_p$, the Volkov phase of a Gaussian envelope can be written as

$$\begin{aligned} S^{(\text{Volkov})}(t; \mathbf{A}) &= \varepsilon_p t + \frac{A_o p \sin \vartheta_p}{\sqrt{2}} \int^t d\tau f(\tau) \cos(\omega\tau + \phi^{(\text{cep})} - \lambda \varphi_p) + \frac{A_o^2}{4} \int^t d\tau f^2(\tau) \\ &= \varepsilon_p t + \frac{A_o p \sin \vartheta_p}{\sqrt{2}} \int^t d\tau \exp\left(-4 \ln(2) \left(\frac{t}{T_p}\right)^2\right) \cos(\omega\tau + \phi^{(\text{cep})} - \lambda \varphi_p) + U_p \int^t d\tau \exp\left(-8 \ln(2) \left(\frac{t}{T_p}\right)^2\right) \\ &= \varepsilon_p t + U_p \sqrt{\frac{\pi}{\ln(4)}} \frac{T_p}{4} \operatorname{erf}\left(2\sqrt{\ln(4)} \frac{t}{T_p}\right) \\ &\quad + \frac{A_o p \sin \vartheta_p T_p}{\sqrt{2}} \frac{1}{8} \sqrt{\frac{\pi}{\ln(2)}} e^{-\frac{\omega^2 T_p^2}{\ln(65536)}} \left[e^{-i\xi} \operatorname{erf}\left(\frac{i T_p^2 \omega + 8 \ln(2) t}{4 T_p \sqrt{\ln(2)}}\right) - e^{i\xi} \operatorname{erf}\left(\frac{i T_p^2 \omega - 8 \ln(2) t}{4 T_p \sqrt{\ln(2)}}\right) \right] \end{aligned}$$

- Pulse envelope (time) integrals for a circularly-polarized pulse: As for a \sin^2 pulse, the pulse-envelope integrals are better solved numerically by using the analytical expression for the Volkov phase from above. If the trigonometric and error functions are available, such a 1-dimensional integration should be quite easy.

Vector potentials and fields in dipole approximation:

- Electric field: For a linearly-polarized laser field, the electric field is often taken as:

$$\mathbf{E}(t) = \mathbf{E}_o \cos(\omega t) \mathbf{e}_x, \quad \mathbf{A}(t) = -\frac{\mathbf{E}_o}{\omega} \sin(\omega t) \mathbf{e}_x.$$

- Vector potential: $\mathbf{E}(t) = \frac{\partial \mathbf{A}(t)}{\partial t}$.

Time-dependent dipole amplitudes:

- Continuum orbital of free electrons with asymptotic momentum \mathbf{p} , $|\mathbf{p}\rangle = e^{-i\mathbf{p}\cdot\mathbf{r}}$: Free electrons are described by (continuum solutions of the) Hamiltonian

$$H_o |\mathbf{p}\rangle = \frac{p^2}{2} |\mathbf{p}\rangle.$$

- Time-dependent dipole amplitude: If the electron is initially in the bound-state $|\phi_o\rangle$ of the atom, the time-dependent dipole amplitude is given by

$$\mathbf{d}(\mathbf{p}) = \langle \mathbf{p} | \mathbf{r} | \phi_o \rangle.$$

- Time-dependent dipole amplitude for non-relativistic hydrogenic $1s$ orbitals: If the bound electron is initially in the $1s$ orbital, the dipole amplitude is given by

$$\mathbf{d}(\mathbf{p}) = -i 2^{7/2} \alpha^{5/4} \frac{\mathbf{p}}{\pi (p^2 + \alpha)^3}.$$

Approximations to the Volkov phase:

- Kinetic *versus* canonical momentum of a particle in an em field: The (dressed) kinetic momentum $\pi(\mathbf{p}, t) = \mathbf{p} + \mathbf{A}(\mathbf{r}, t)$ of a particle with charge e differs from its canonical momentum \mathbf{p} by the (coupling of the local) vector potential and, hence, the dressing of the em field. Often, one considers the motion of electrons in either a linearly- or circularly-polarized field.
- Volkov phase: The classically accumulated action of the electron, if it propagates in a laser field, reflects the dressing of the particle by the field; in the SFA, this action appears in the (so-called) Volkov phase

$$S(\mathbf{p}, t, t') = \int_{t'}^t dt'' \frac{[\mathbf{p} + \mathbf{A}(\mathbf{r}, t'')]^2}{2} + I_p$$

- Saddle point of the time-dependent momemtum: The saddle point fulfills the equation $\nabla_{\mathbf{p}} S(\mathbf{p}, t, t') = 0$

$$\mathbf{p}^{(\text{saddlepoint})} = -\frac{1}{t - t'} \int_{t'}^t d\tau \mathbf{A}(\tau).$$

- Saddle-point approximation to the Volkov phase: This approximation leads for the q -th harmonic to three equations for the canonical momentum \mathbf{p}_s at the saddle point

$$\mathbf{p}_s(t, t') = \frac{1}{t - t'} \int_{t'}^t dt'' \mathbf{A}(t''), \quad \frac{[\mathbf{p} + \mathbf{A}(t')]^2}{2} = -I_p, \quad \frac{[\mathbf{p} + \mathbf{A}(t)]^2}{2} = q\omega - I_p.$$

The last two relations simply reflect the **conservation of energy**, namely, for the *release* of the electron into the continuum at the *ionization* time t' and for its recombination with the parent ion at the (*recombination*) time t . Both of these times are generally complex because $I_p > 0$.

Time-dependent dipole moment $\mathbf{D}(t)$:

- Time-dependent dipole moment:

$$\mathbf{D}(t) = \int_{-\infty}^t dt' \int d^3\mathbf{p} \, \mathbf{d}^*(\mathbf{p} + \mathbf{A}(t)) \, \mathbf{E}(t') \, \mathbf{d}(\mathbf{p} + \mathbf{A}(t')) e^{-i S(\mathbf{p}, t, t')} + \text{c.c.}$$

- Time-dependent dipole moment in saddle-point approximation: In the saddle-point approximation, the dipole moment with $\mathbf{p}^{(\text{sp})} \equiv \mathbf{p}^{(\text{saddle-point})}$ to:

$$\mathbf{D}^{(\text{saddle-point approx})}(t) = \int_{-\infty}^t dt' \left(\frac{2\pi i}{(t - t' - i\epsilon)} \right) \mathbf{d}^*(\mathbf{p}^{(\text{sp})} + \mathbf{A}(t)) \, \mathbf{E}(t') \, \mathbf{d}(\mathbf{p}^{(\text{sp})} + \mathbf{A}(t')) e^{-i S(\mathbf{p}^{(\text{sp})}, t, t')} + \text{c.c.},$$

and where ϵ is ...

Frequency-dependent power spectrum $\mathbf{D}(q\omega)$:

- Frequency-dependent dipole moment in saddle-point approximation: For the q -th order of the high-harmonic, the dipole moment in saddle-point approximation is given with $\mathbf{p}^{(\text{sp})} \equiv \mathbf{p}^{(\text{saddle-point})}$ by

$$\mathbf{D}^{(\text{saddle-point approx})}(q\omega) = i \int_{-\infty}^{\infty} dt \int_{-\infty}^t dt' \left(\frac{2\pi i}{(t - t' - i\epsilon)} \right) \mathbf{d}^*(\mathbf{p}^{(\text{sp})} + \mathbf{A}(t)) \, \mathbf{E}(t') \, \mathbf{d}(\mathbf{p}^{(\text{sp})} + \mathbf{A}(t')) e^{iq\omega t - i S(\mathbf{p}^{(\text{sp})}, t, t')} + \text{c.c.}$$

- Frequency-dependent dipole moment in saddle-point approximation: In this approximation, the frequency-dependent dipole moment of the q -th harmonic can be expressed as a sum of products [field \times dipole amplitude], and which just need to be evaluated at the saddle points:

$$\mathbf{D}(q\omega) = i \sum_s \frac{2\pi}{\sqrt{\det(S'')}} \left(\frac{2\pi}{t_s - t'_s} \right) \mathbf{d}^*(\mathbf{p}_s + \mathbf{A}(t_s)) \, \mathbf{E}(t'_s) \, \mathbf{d}^*(\mathbf{p}_s + \mathbf{A}(t'_s)) \exp[-i S(\mathbf{p}_s, t_s, t'_s) + iq\omega t_s].$$

Here $S'' = \frac{\partial S(\mathbf{p}, t, t')}{\partial t \partial t'}|_{(\mathbf{p}_s, t_s, t'_s)}$ denotes the Hessian matrix of the action at the saddle point. The saddle-point approximation is closely related to the classically allowed trajectories of a free electron in a strong laser field.

- Power spectrum of high harmonics, $\mathbf{D}(q\omega)$: The (so-called) power spectrum of the emitted harmonic radiation is obtained from the Fourier transform of the dipole acceleration $\frac{\partial^2 \mathbf{D}(t)}{\partial t}$.

Semi-classical trajectories of electrons in Lewenstein's model:

- Harmonics of well-defined order: In practice, only a very small fraction of the released electrons find their way back to the parent ion and will recombine eventually. Obviously, the harmonic order is determined by the (dressed) kinetic momentum $\mathbf{p} + \mathbf{A}(t)$ at the recombination time.
- Long and short trajectories: There are exactly two trajectories per half cycle which return the electron, and with the same energy, to the parent ion. Both trajectories will therefore contribute to the same harmonic order, though they are often referred to as *long* and *short* trajectories because of the different travel time of the electron along these trajectories.
- Dipole phase of the short and long trajectories: For the harmonics at the plateau, the dipole phases of the short and long trajectories clearly differ from each other because of the different travel times along these orbits, while the phases approach each other towards the cut-off [cf. Paufler *et al.* (2019), Fig. 1]. Moreover, the dipole phase generally depends linear on the intensity of the incident beam.

10.8.b. Rotating-frame approximation [background]

Rotating-frame:

- Rotating-frame: The time-dependent Schrödinger equation of an (atomic) electron in a short-range potential and an external circularly-polarized electro-magnetic field can be transformed into a time-independent equation, if we make use of coordinates that rotate with the frequency of the external field around its propagation direction (z -axis). In this rotating framework, the Hamiltonian in atomic units reads as

$$\mathbb{H} = -\frac{\Delta}{2} + V(\mathbf{r}) - \omega l_z + \mathcal{E}x,$$

where $V(\mathbf{r})$ is a short-range potential, l_z the projection of the orbital angular momentum and ω the frequency of the laser field. The rotating-frame coordinates can be utilized to find an equation for the (complex-value) energy of an electron in a circularly-polarized field. Moreover, such a frame leads to the (so-called) *rotation-frame approximation*, in which the slow-varying and fast-oscillating terms in the

Schrödinger equation are separated from each other, and where the fast-oscillating terms are just treated *effectively* in some time-averaged mode.

10.8.c. Kramers-Henneberger frame [background]

Kramers-Henneberger framework:

- **Kramers-Henneberger framework:** In this framework, the electron in a (strong external) oscillating field remains *at rest*, i.e. the coordinates follow the motion of the electron. The transformation of the wave function and Schrödinger equation from the laboratory to the Kramers-Henneberger coordinates then requires a time-dependent unitary transformation which is given for a monochromatic and linearly-polarized field by

$$\psi^{(\text{KH})} = \exp\left(i \frac{\mathbf{r} \cdot \mathcal{E}}{\omega} \sin \omega t\right) \psi^{(\text{Schroedinger})}, \quad i \frac{\partial \psi^{(\text{KH})}}{\partial t} = -\frac{\Delta}{2} \psi^{(\text{KH})} + V\left(\mathbf{r} + \frac{\mathcal{E}}{\omega^2} \cos \omega t\right) \psi^{(\text{Schroedinger})}.$$

While this transformation is formally exact, it is useful especially in the **high-frequency limit**, in which the electron-laser interaction is much larger than the (unperturbed) binding energy of the electron. In this limit, the time-dependent Schrödinger equation can be reduced to a time-independent equation with a potential

$$V^{(\text{KH})}(\mathbf{r}) = \frac{1}{2\pi} \int_0^{2\pi} d(\omega t) V\left(\mathbf{r} + \frac{\mathcal{E}}{\omega^2} \cos \omega t\right),$$

that is just the *zero-time* Fourier component of the orginal potential above. In this high-frequency limit, the (1D) electronic wave functions just describe **two probability clouds which are separated by $2a = \mathcal{E}/\omega$** , i.e. twice the amplitude of the oscillating electron is the field. This separation of the probability density is known also as *dichotomy*.

10.8.d. Guo-Aberg-Crasemann (GAC) theory [background]

Differential GAC ionization cross sections:

- Lowest-order perturbation theory typically fails to explain the shape of the envelope of the individual ATI photoelectron peaks. Perturbation theory also fails to predict the dependence of the strength of the ATI peaks on the intensity of the laser light, if the laser intensity exceeds 1 TW cm^{-1} .
- **Differential transition-rate formula:** Within the GAC theory, the lowest-order transition matrix element can be utilized together with the (integer) constraint $z = m - n$, in order to obtain a **differential transition-rate formula for the ionization of electron that have absorbed $q = l|m$ photons** (Guo *et al.*, 1989)

$$\frac{d\omega}{d\Omega} = \frac{(2m^3\omega^5)^{1/2}}{4\pi^2} |\Phi_i(\mathbf{p} - q\mathbf{k})|^2 q^2 \left(q - \frac{E_b}{\omega}\right)^{1/2} |\mathcal{J}_{q+z}|^2 |\mathcal{J}_z|^2,$$

where $\Phi_i(\mathbf{p} - q\mathbf{k})$ is the Fourier transform of the initial-state wave function with binding energy E_b . The angular and polarization dependences of this differential transition-rate formula are determined by $\mathbf{p} - q\mathbf{k}$ in Φ_i as well as by the arguments of the two **elliptically polarized Bessel functions** \mathcal{J}_t .

- In the nonrelativistic limit and for a large photon-number, the final state can be reduced to a single but modified Volkov state, if the ponderomotive energy is an integer multiple of the photon energy. Therefore, the scattering amplitude strictly exists only in the integer case, where it becomes a product of the original KFR amplitude and the overlap between the final plane-wave state and the Volkov state, and vanishes otherwise.

10.8.e. Twisted light beams [background]

11. Time-evolution of many-electron atomic state functions and density matrices

11.1. Time-dependent approximations of many-electron states

Time-dependent methods:

- **Time-dependent theory:** The response of multi-electron atoms to strong laser fields with intensity $\sim 10^{14}$ W/cm² can be typically described only by explicitly time-dependent approaches. For short and intense light pulses, for example, the ionization rate is known to change rapidly during the pulse, and this makes the use of just a monochromatic field incorrect in the theoretical description. For laser intensities $\gtrsim 10^{16}$ W/cm², moreover, the electric field becomes even stronger than the inter-atomic fields, leading to a breakdown of perturbation theory. Then, the time-dependent Schrödinger equation need to be integrated explicitly in order to properly deal with the shape and intensity of the light pulses, although the *limits* of perturbation theory are not yet well understood in this time and intensity domain.
- **Light sources for studying electron dynamics in atoms:** New light sources and technologies facilitate nowadays various experiments with intense attosecond extreme-ultraviolet (XUV) pulses in order to resolve in time the ejection of electrons from the atomic target.
- **New coherent light sources:** Recently developed light sources include attosecond lasers, high-order-harmonic generation (HHG) sources or free-electron lasers. These novel light will pave the way for studying the interaction of matter with intense femtosecond or even sub-femtosecond radiation pulses in the visible and XUV regime.
- **New light sources:** Recent advances in the generation of ultra-short and extreme ultraviolet (XUV) pulses at free-electron lasers (FEL), attosecond high harmonic pulses or few-cycle optical laser pulses have paved the way for imaging and controlling the electronic and nuclear dynamics in molecules, and with many exciting applications in physics, chemistry and elsewhere. In particular, table-top HHG sources of femtosecond and sub-femtosecond XUV pulses enable one to observe the dynamics at the attosecond time scale.

11. Time-evolution of many-electron atomic state functions and density matrices

- **X-ray free-electron lasers (XFEL):** Various XFEL's worldwide have recently extended the range of nonlinear processes due to intense ionizing radiation ($> 10^{15}$ PW/cm²).
- **FEL versus synchrotron sources:** Although both are based on accelerator technology, FEL (may) emit *coherently* because of its multi-electron coherence, while synchrotron radiation is always emitted incoherently due to its independently radiating electrons. Therefore, FEL are able to combine the intensity and coherence of an (optical) laser with the broad spectral coverage of synchrotrons.
- **Femto-second pulses at FEL:** Free-electron lasers nowadays produce femto-second pulses at EUV to x-ray frequencies.
- **Third-generation synchrotrons:** Modern synchrotron facilities support ionization studies of atoms and molecules across a wide energy range, using quite stationary conditions, and with much higher resolution than ever before. Moreover, these spectroscopic studies are often combined with synchronized laser pulses.
- The development of sub-femtosecond radiation pulses enables one to explore the electron dynamics in atoms *or* the (combined) electron and nuclei dynamics in molecules with a high degree of temporal and spatial resolution.
- **Femto-slicing:** Ultra-short x-ray pulses are nowadays an indispensable tool for visualizing ultra-fast processes in molecules, liquids and solids. Such ultra-short pulses can be generated by femto-slicing, i.e. if the relativistic electrons in an undulator are accompanied by some ultra-short and co-propagating laser pulse. This technique enforces x-ray pulses with just 100 fs duration and at a time-scale that is comparable to atomic ordering phenomena in solids.
- **Femto-slicing:** This technique was first proposed by Zholents and Zoloterev in 1996 in order to generate ultra-short x-ray pulses at synchrotron facilities, and it was later demonstrated experimentally at the Advanced Light Source (ALS) in Berkeley. A first undulator-based femto-slicing source was completed at BESSY II in Berlin in 2004. This technique has been further advanced during recent years in high-flux beamline and by using novel Zone Plate Monochromator (ZPM).
- **Short-pulse, short-wavelength radiation:** There are several approaches known for achieving ultra-short and high-energetic photon pulses:
 - The conversion of fs laser pulses to higher photon energy by (i) HHG, (ii) by plasma generation with intense laser pulses, and which then emits x-rays, or (iii) by relativistic Thomson scattering.
 - The time structure of electron bunches can be changed in a storage ring, for instance, if the (so-called) momentum-compaction factor is changed or if the laser-induced energy modulation is modified (**femto-slicing**), or by further compression of electron bunches in linear accelerators and especially at free-electron laser (FEL). In this regime, however, only laser-based techniques (femto-slicing and seeded FELs) facilitate a natural synchronization between the laser and the x-ray pulses for pump-probe experiments.
- **Need for new time-dependent theoretical models:** To support modern experiments with intense attosecond pulses, new time-dependent models and methods need to be developed beyond the current standard schemes, such as the single-active-electron approximation.

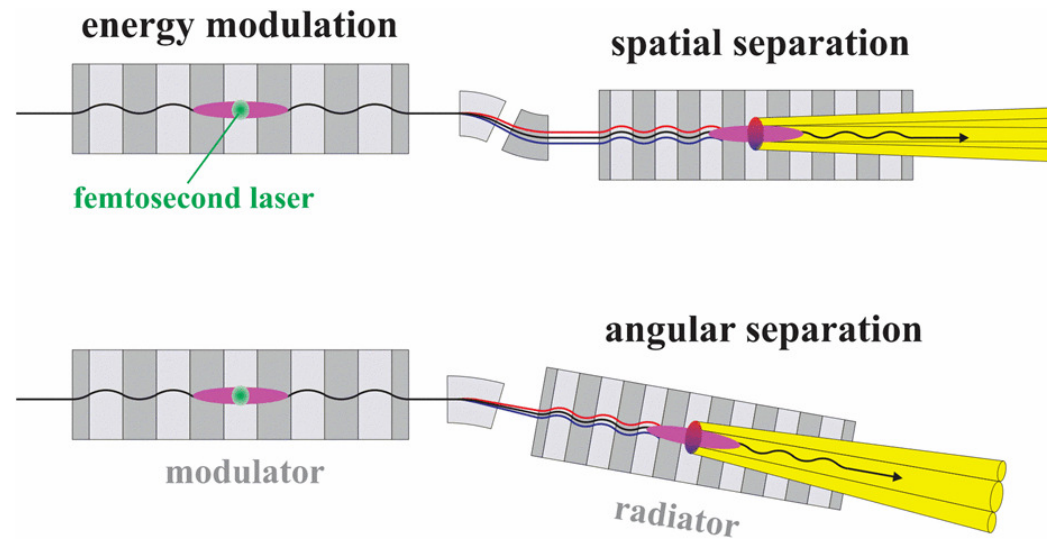


Figure 11.1.: Generation of short x-ray pulses by laser-induced energy modulation of electrons and subsequent spatial (top) and angular (bottom) separation.
From Ref. DOI: 10.1109/PAC.2005.1590500.

- **Time-dependent Hartree-Fock (TDHF) method:** In this method, the time evolution of the electronic orbitals is accounted for during the interaction with an external field or collision partner by following the (time-dependent) mean field of the total electron density in the given potential. This method therefore properly treats the nuclear interaction and the *mean field* of the electrons but averages over all electronic correlations. In practice, such a mean-field approximation significantly reduces the dimension of the N -particle quantum system from $3N$ spatial coordinates to just three coordinates for the *mean* density. **The TDHF method is an initial value problem that typically starts from the wave function of the static ground state of the system.**
- **Time-dependent RAS method with space partition:** In this method, the wave functions are expanded in terms of Slater determinants with explicitly time-dependent CI coefficients. The Slater determinants are usually based on two type of time-independent orbitals: (i) Orbitals that are just defined in an inner region close to the atomic nucleus and (ii) orbitals in an outer region with zero-contribution to the inner region (Miyagi and Madsen, 2017).
- **Space partition methods:** A partitioning of space has been widely utilized for describing atom-electron collisions since the very first advent of the R-matrix theory. In all these models, a configuration-interaction (CI) expansion of the many-electron wave function is typically made in some inner region in order to deal with electronic correlations. In the outer region, in contrast, the electrons are supposed to move

11. Time-evolution of many-electron atomic state functions and density matrices

independently of each other in just a long-range effective potential, and without that further exchange and correlation contributions are taken into account. This piecewise definition of the wave function then requires to make sure that it remains continuously differentiable across the surface between the two regions.

- **Time-dependent MCHF (TD-MCHF) method:** This method is presently seen as the most accurate and widely used technique in order to describe the many-electron dynamics in explicitly time-dependent potentials, such as the laser-induced dynamics of N -electron atoms. When compared to the space-partition methods, the TD-MCHF method has the great advantage that, for a sufficiently large (radial) domain of the orbitals, all single- and multi-electron interactions (continua) can be taken into account, at least in principle.
- **Time-dependent complete-active-space SCF (TD-CASSCF) method:** Sato *et al.* (2016) describes a (non-relativistic) numerical implementation of the time-dependent complete-active-space self-consistent-field (TD-CASSCF) method, if the atoms are driven by a strong linearly-polarized laser pulse. This method is based on a gauge-invariant frozen-core approximation and a split-operator techniques in order to ensure a stable propagation of stiff spatial derivative operators. In this work, the method is applied to high-harmonic generation in helium, beryllium and neon to better understand the role of electron correlations. Despite of all the technical details in this paper, no attempt has been made to compare the results with (any kind of) experiment.
- **TDSE:** While the TDSE provides the rigorous (theoretical) framework for studying the electron dynamics in atoms and molecules, its explicit solution will remain rather unfeasible for systems with more than two (active) electrons.
- **TD-CASSCF:** As mainly known from quantum chemistry, the use of complete or restricted active-space methods often starts from a *prior* decomposition of a (finite) orbital space into *core* and *active* orbital subspaces. Hereby, the core electrons form a closed-shell wave function that is treated like in the (much) simpler time-dependent Hartree-Fock (TDHF) method. **Correlations are thus included only for the active electrons and within the initially-specified active space.** While all orbitals are varied in time, the orbital space is effectively splitted into time-independent frozen-core and time-dependent dynamical-core orbitals, and which reduces the dimension of the CI matrices significantly. The TD-CASSCF method is based on the assumption that the core electrons do not feel the intense long-wavelength field; however, core-polarization contributions may lead to a quick breakdown of this assumption for all angle- and polarization-resolved measurements in strong fields.
- **Time-evolution with separable (atomic) potentials (TESP):** Galstyan *et al.* (2018) describe a new and **computationally inexpensive method for studying the interaction of complex atoms or molecules with intense ultrashort laser pulses within the single active electron approximation.** With this method, they have analyzed the photoionization of water molecules from the highest occupied molecular orbital and calculated, in particular, the ionisation yield for different orientations of the molecule with regard to the polarization of the incident pulse.

- **TESP method:** This method is an approximation since the exact solution would require to incorporate an infinite number of separable potentials in the representation of the kernel. This method is therefore especially useful for pulses with high frequency where only the lowest (few) levels play a crucial role for the ionization of the system.
- **Central idea of the TESP method:** The main idea of this method is to work in **momentum space and to replace the kernel of the Coulomb potential by a sum of N symmetric separable potentials which each support just a single bound state of the system**. The use of separable potentials enables one to reduce the N -dimensional time-dependent Schrödinger equation (TDSE) to a system of N one-dimensional Volterra integral equations which only depend on time. This method is known also by Separable Potentials for Atoms and Molecules (SPAM).
- **Weaknesses of the TESP method:** The separable potential is not necessarily unique and does usually not represent the correct asymptotic behaviour of the potential. Moreover, the method is not gauge invariant and the question about proper gauges will need to be explored in further detail.
- **Time-resolved electron dynamics:** Various experimental techniques have been developed in order to perform time-resolved studies of the electron dynamics in atoms and molecules, such as **re-collision imaging, attosecond streaking or time-resolved photoionization studies**. Until the present, however, most of these observations have been simulated only in effective single-electron models, and with little care about the many-electron dynamics in realistic systems. For an accurate interpretation of such experiments, however, either the time-dependent (many-electron) Schrödinger equation need to be solved or, at least, many-electron correlation contributions has to be taken into account. Moreover, since perturbation theory is not appropriate in the strong-field regime, either a direct numerical integration of the TDSE or further advances of the strong-field theory are required.
- **Time-dependent complete-active-space self-consistent-field (TD-CASSCF) method:** Sato and Ishikawa (2013) have worked out this method for describing the multi-electron dynamics in intense laser fields. In practice, they distinguished between different orbital spaces that can be summarized as follows
 - (1) a frozen core for all tightly bound electrons that do not respond at all to the laser field;
 - (2) a dynamic core whose electrons remain bound but respond to the field due to their correlated motion, and
 - (3) active electrons that are ionized by the field.

Time-evolution of ASF:

- A reliable description of the time-dependent (TD) many-electron dynamics has attracted recent interest in order to theoretically support a real-time analysis and control of the ultrafast electronic and nuclear dynamics of atoms and molecules in intense laser pulses.

11. Time-evolution of many-electron atomic state functions and density matrices

- A computational and conceptual simple approach to the many-electron dynamics is the TD configuration-interaction singles (TD-CIS) method in which only singly excited configurations, relative to the Hartree-Fock ground state, are taken into account in the configuration interaction expansion.
- Miyagi and Madsen (2013) make use of the TD-CIS method by performing an optimization of the orbitals as well as the expansion coefficients at each time step in the evolution. This separate optimization makes it possible to construct a reasonable accurate wave function with just a relatively small number of electronic configurations. For the optimization, Miyagi and Madsen (2013) utilized the Dirac-Frenkel-McLachlan TD variational principle.

11.2. Time-dependent statistical tensors

Motivation:

- In physics, Liouville's theorem is known from classical statistical and Hamiltonian mechanics, and it asserts that the phase-space distribution function is constant along the trajectory of the system.
- Similarly, the quantum-mechanical analog of Liouville equation describes the time evolution of a mixed state. The quantum form can be obtained by the standard replacements of classical variables with quantum operators and Poisson brackets with commutators.
- The Liouville equation for the atomic density matrix ρ reads

$$\frac{\partial \rho}{\partial t} = -\frac{i}{\hbar} [\mathbb{H}, \rho] - \Gamma \rho, \quad \mathbb{H} = \mathbb{H}^{(\text{atom})} + \mathbb{H}^{(e-\gamma)}$$

where the first term in the Hamiltonian describes the (inner-) atomic and the atom-photon interactions, and the second term the relaxation matrix Γ . This relaxation matrix accounts for the atomic spontaneous decay due to either radiative or nonradiative (Auger) processes of the atom.

11.3. Time-integration of statistical tensors

Motivation:

- Various methods can be applied to solve the coupled first-order odg's for the time-evolution of the statistical tensors. Apart from those methods which solve the equations with given accuracy (but typically require the evaluation of the rhs at any given time t), we are mainly interested in *shooting* or *predictor-corrector* methods which makes only use of previous solutions of ρ and $d\rho/dt = f$ on a equidistant time grid.

Numerical methods:

- If we use a step-size h and define $\rho(t_j) = \rho_j$, $\frac{d\rho}{dt}(t_j) = f_j$, the following integration formulas can be applied.
- Euler's methods:

$$\rho_{j+1} = \rho_j + h f_j$$

- Adams-Bashford methods:

$$\rho_{j+1} = \rho_j + h \left[\frac{3}{2} f_j - \frac{1}{2} f_{j-1} \right]$$

$$\rho_{j+1} = \rho_j + h \left[\frac{23}{12} f_j - \frac{16}{12} f_{j-1} + \frac{5}{12} f_{j-2} \right]$$

$$\rho_{j+1} = \rho_j + h \left[\frac{55}{24} f_j - \frac{59}{24} f_{j-1} + \frac{37}{24} f_{j-2} - \frac{9}{24} f_{j-3} \right]$$

11.4. Time evolution of statistical tensors. Formalism

11.4.a. Liouville equation for the atomic density matrix

Vector potential and state multipoles:

- In the electron-photon interaction, the vector potential of the electromagnetic field is typically chosen to fulfill $\text{div} \mathbf{A}(\mathbf{r}_i, t) = 0$.
- When the electron-photon interaction Hamiltonian $\mathbb{H}^{(e-\gamma)}$ is applied upon the density operator ρ , we shall consider only processes with one photon.
- Moreover, we assume a vector potential for a monochromatic field with frequency ω and wave vector $\mathbf{k} = (\vartheta_k, \varphi_k)$ ($|\mathbf{k}| = \frac{\omega}{c}$) with regard to the coordinates in the laboratory system.
- **Envelope of the vector potential:** For a pulse with (real) envelope $f(t)$, the vector potential then includes two terms

$$\mathbf{A}(\mathbf{r}, t) = \mathbf{A}(\mathbf{r}) f(t) e^{-i\omega t} + \mathbf{A}^*(\mathbf{r}) f^*(t) e^{i\omega t}.$$

Liouville equation in the representation of well-defined angular momenta:

- **Liouville equation:** In an atomic basis with well-defined total angular momenta and parity, the Liouville equation can be re-written as

$$\begin{aligned} \frac{\partial}{\partial t} \langle \alpha J_\alpha M_\alpha | \rho | \beta J_\beta M_\beta \rangle &= -\frac{i}{\hbar} (E_\alpha - E_\beta) \langle \alpha J_\alpha M_\alpha | \rho | \beta J_\beta M_\beta \rangle \\ &\quad - \frac{i}{\hbar} \sum_{\nu J_\nu M_\nu} (\langle \alpha J_\alpha M_\alpha | \mathbb{H}^{(e-\gamma)} | \nu J_\nu M_\nu \rangle \langle \nu J_\nu M_\nu | \rho | \beta J_\beta M_\beta \rangle - \langle \alpha J_\alpha M_\alpha | \rho | \nu J_\nu M_\nu \rangle \langle \nu J_\nu M_\nu | \mathbb{H}^{(e-\gamma)} | \beta J_\beta M_\beta \rangle) \\ &\quad - \sum_{\gamma J_\gamma M_\gamma} \langle \alpha J_\alpha M_\alpha | \Gamma | \gamma J_\gamma M_\gamma \rangle \langle \gamma J_\gamma M_\gamma | \rho | \beta J_\beta M_\beta \rangle \end{aligned}$$

11.4.b. Time-dependent statistical tensors of atomic lines

Time-dependent statistical tensors:

➤ **Statistical tensors:** With the substitutions of the statistical tensors from above and the notations $[ab...c] \equiv (2a+1)(2b+1)...(2c+1)$, the Liouville equation can be written as Grum-Grzhimailo, 2012)

$$\begin{aligned}
i\hbar\dot{\tilde{\rho}}_{kq}(\alpha J_\alpha, \beta J_\beta) &= -2\pi \sqrt{\frac{\hbar}{ck}} \sum_{\nu J_\nu KQ} \\
&\left[f(t) e^{-i(\omega-\omega_{\alpha\nu})t} \sum_{LM\lambda} g_\lambda(-1)^{J_\alpha+J_\beta+K+L} [LK]^{1/2} \langle KQ, LM | kq \rangle \left\{ \begin{array}{ccc} J_\alpha & J_\beta & k \\ K & L & J_\nu \end{array} \right\} D_{M\lambda}^L(\varphi_k, \vartheta_k, 0) \left(\langle \alpha J_\alpha \parallel T_L^{(m)} \parallel \nu J_\nu \rangle + i\lambda \langle \alpha J_\alpha \parallel T_L^{(e)} \parallel \nu J_\nu \rangle \right) \tilde{\rho}_{KQ}(\nu J_\nu, \beta J_\beta) \right. \\
&- f^*(t) e^{i(\omega-\omega_{\nu\alpha})t} \sum_{LM\lambda} g_\lambda^*(-1)^{J_\beta+k+J_\nu+L} [Lk]^{1/2} \langle kq, LM | KQ \rangle \left\{ \begin{array}{ccc} J_\alpha & J_\beta & k \\ K & L & J_\nu \end{array} \right\} D_{M\lambda}^{L*}(\varphi_k, \vartheta_k, 0) \left(\langle \nu J_\nu \parallel T_L^{(m)} \parallel \alpha J_\alpha \rangle - i\lambda \langle \nu J_\nu \parallel T_L^{(e)} \parallel \alpha J_\alpha \rangle \right) \tilde{\rho}_{KQ}(\nu J_\nu, \beta J_\beta) \\
&+ f(t) e^{-i(\omega-\omega_{\nu\beta})t} \sum_{LM\lambda} g_\lambda(-1)^{J_\alpha+J_\beta+K} [LK]^{1/2} \langle KQ, LM | kq \rangle \left\{ \begin{array}{ccc} J_\alpha & J_beta & k \\ L & K & J_\nu \end{array} \right\} D_{M\lambda}^L(\varphi_k, \vartheta_k, 0) \left(\langle \nu J_\nu \parallel T_L^{(m)} \parallel \beta J_\beta \rangle + i\lambda \langle \nu J_\nu \parallel T_L^{(e)} \parallel \beta J_\beta \rangle \right) \tilde{\rho}_{KQ}(\alpha J_\alpha, \nu J_\nu) \\
&- f^*(t) e^{i(\omega-\omega_{\beta\nu})t} \sum_{LM\lambda} g_\lambda^*(-1)^{J_\alpha+K+J_\nu} [Lk]^{1/2} \langle kq, LM | KQ \rangle \left\{ \begin{array}{ccc} J_\alpha & J_\beta & k \\ L & K & J_\nu \end{array} \right\} D_{M\lambda}^{L*}(\varphi_k, \vartheta_k, 0) \left(\langle \beta J_\beta \parallel T_L^{(m)} \parallel \nu J_\nu \rangle - i\lambda \langle \beta J_\beta \parallel T_L^{(e)} \parallel \nu J_\nu \rangle \right) \tilde{\rho}_{KQ}(\alpha J_\alpha, \nu J_\nu) \\
&\left. - i\hbar \sum_{\gamma J_\gamma} G_{kq}^{KQ}(\alpha J_\alpha, \beta J_\beta, \gamma J_\gamma) e^{i\omega_{\alpha\gamma}t} \tilde{\rho}_{KQ}(\gamma J_\gamma, \beta J_\beta) \right]
\end{aligned}$$

11.5. Observables to be derived from time-dependent statistical tensors

Motivation:

- If we solve the set of time-dependent (Liouville) equations for the state multipoles, we can obtain the atomic statistical tensors for
- (a) discrete atomic states $\rho_{kq}(\alpha \mathbb{J}_\alpha; \beta \mathbb{J}_\beta)$
 - (b) for atomic states with one electron in continuum $\rho_{kq}(\alpha_f \mathbb{J}_f, \varepsilon \kappa : \alpha \mathbb{J}_\alpha, \alpha'_f \mathbb{J}'_f, \varepsilon' \kappa' : \alpha \mathbb{J}_\alpha)$,
 - (c) *nondiagonal* elements $\rho_{kq}(\alpha_f \mathbb{J}_f, \varepsilon \kappa : \alpha \mathbb{J}_\alpha, \beta \mathbb{J}_\beta)$ and $\rho_{kq}(\alpha_f \mathbb{J}_f, \varepsilon \kappa : \alpha \mathbb{J}_\alpha, \alpha'_f \mathbb{J}'_f, \varepsilon' \kappa' : \beta \mathbb{J}_\beta)$.

12. Atomic descriptors

Machine learning. Basic concepts, goals & notations:

- Machine learning (ML): Methods in ML basically apply **statistical algorithms** whose performance improve with training, similar as in daily life. ML approaches are therefore able to learn the rules that underlie a given dataset. These approaches access some available portion of data and **build automatically a model to make predictions for so-far unknown systems**.
- Machine learning (ML) in quantum chemistry and material science: ML methods **circumvent the task of solving the SE explicitly by using instead the data from a finite subset of well-known solutions in order to estimate solutions for (yet) unknown systems and materials**. Since, more generally, many research fields require a frequent solution of the SE, ML methods may enable one to explore quantum behavior in much larger spaces, such as the (so-called) **chemical compound space in material science**.
- Goals of machine learning: The goal of ML is to automatically derive a function (or relation) that, for a specific set of input data, is able to predict the desired output values to an acceptable degree of fidelity.
- Machine learning algorithms: These algorithms generally establish a nonlinear map between input data (descriptors) and the specific property that need to be predicted; their **efficiency mainly depend on how well the input data are represented by the various descriptors**.
- Artificial-intelligence methods: The emergence of contemporary artificial-intelligence methods has substantially altered and enhanced the role of computers in science and engineering during the past years (Butler *et al.*, 2018).
- Fourth paradigm of science: The combination of artificial-intelligence methods with large data sets has been termed in the public discussion as **fourth paradigm of science or fourth industrial revolution**. This new paradigm includes in particular a rapidly increasing number of applications in chemistry and material science. This paradigm is also quite different from most traditional computations, where computers simply acts as ‘calculator’ and just employ some hard-coded algorithm as provided by some human expert (Butler *et al.*, 2018).
- Inverse design: This new paradigm in designing molecules and materials start from the functionality and then searches for some (ideal) molecular structure, for which this functionality is realized. In contrast to quantum-chemical methods, here the **input is the desired property, while the output is a corresponding (geometrical) structure and composition of the molecule**. Typically, however, a give function does not

12. Atomic descriptors

map uniquely to just *one* molecular structure but to a distribution of *probable or nearby* geometrical structures (Sanchez-Lengeling and Aspuru-Guzik, 2018).

- **Deep learning algorithms** aim for generating data distributions by training with large data sets. The **loss function** is hereby a measure how the empirically observed and the generated distribution differ from each other.
- **High-throughput calculations** of atomic level representations (state vectors) and processes is usually highly time-consuming. This suggests to make use of ML approaches in order to predict atomic data as they are needed, for instance, in astro and plasma physics. Once a ML model has been trained on an atomic (training) set, ML based computations are expected to be very fast.
- **High-throughput virtual screening (HTVS):** This simulation method has its roots in the pharmaceutical industry for drug discovery in order to screen a (very) large number of synthesized or potentially useful molecules. While HTVS appears in spirit quite similar to inverse material design, it differs in philosophy since HTVS also includes automation and time-critical performance with the goal to identify ‘promising candidates’, and which are later further processed by more expensive methods.

Feature selection and engineering in atomic physics:

- **Feature engineering:** Like in (human) learning, a machine-learning algorithm might learn more effectively by using one *particular* format rather than other formats (Butler *et al.*, 2018). Therefore, the raw input data need to be converted into a more suitable form for a given algorithm, a process that is known as **featurization** or **feature engineering**. In practice, however, it is by far not obvious which particular descriptor will eventually give rise to the best performance of an machine-learning algorithm, and special intuition and experience are typically required for each particular field of application.
- **Feature engineering:** The selection and transformation of (given) input data into proper descriptors is a highly non-trivial task and requires special insight into a particular research field. In practice, this transformation has to be based more on intuition than a systematic treatment, since descriptors need to be computed frequently and easily.
- **Role of descriptors:** Machine learning typically starts with a rather silent and unspectacular task, namely the **choice of proper descriptors**, i.e. the choice of useful parameters that connects available data sets with some learning method. If the choice of descriptors is inappropriate, it remains usually unclear of what can be learned from the (given) descriptor-property relations.
- **Descriptors** or (so-called) features generally define (vector) variables owing to some particular parametrization of data, suitable for ML. In this parametrization, **domain knowledge is very important in order to obtain a *best* set of descriptors**. Moreover, these descriptors should be independent of each other. Different ML methods help identifying more (and less) relevant descriptors, although some ambiguity in choosing these descriptors usually remains.

- **Atomic descriptors:** The definition of proper (atomic) descriptors is central for building models for machine learning and for predicting the physical properties and behaviour of atomic systems. These descriptors are also known also as **feature transformations** in the literature.
- **Descriptors for atomic (or molecular) states:** In electronic structure theory, the (electronic) state of an atom or molecule need to be transformed into a (more or less) **simple vector representation, called descriptor**. A set of such descriptors are then utilized as input for training a machine learning model on one or a few selected properties, and as associated with one or several atomic states.
- **Atomic descriptors:** A fast ML scan are often faster by a few (2-3) orders of magnitude, when compared with full quantum-mechanical computations, and may be applied as a preliminary step before detailed computations are made for selected structures and processes.
- **Data parallelism:** Since the descriptors of a *given* atomic system are usually independent from those of other systems, the computation of descriptors can easily be parallelized. Any useful implementation of such feature transformations should therefore **consider a parallel descriptor creation for multiple samples**.
- **Property-labelled atomic fragments:** Since not all atomic properties can likely be derived from a single set of descriptors, it is desirable to construct so-called property-labelled atomic fragments in order to simplify the feature selection process.
- **Property-Labelled Atomic Fragments (PLAF):** Following ideas from material science, it might be desirable to represent atomic (many-electron) states by graphs and to associate fragment descriptors to certain parts of these graphs. However, not much work has been done in this direction so far.
- **Fragment descriptors:** For each atomic property $q(r)$, such as electron densities, density convolutions, etc., one may also consider the minimum [$\min(q)$], maximum [$\max(q)$], total sum [$\sum q$], average [$\text{avg}(q)$] as well as the standard deviation [$\text{std}(q)$] of property q as potential descriptors in order to encode an atomic level or the underlying electron configuration.
- **Primary features of an atom or ion:**
 - ionization potential (IP) and electro-negativity (EA);
 - energies of the highest-occupied and lowest-unoccupied shell;
 - radii of maximum charge distribution of all individual shells, calculated in a rather simplified shell model.

12.1. In JAC implemented atomic descriptors

None.

12.2. In JAC partly-implemented atomic descriptors

12.2.a. Descriptors for electronic densities (Descriptor)

Feature transformations:

- A feature transformation of the electron density is often applied in material science and will likely help also to characterize atomic (shell) structures and levels.

Use & notations:

- Using JAC: Perform an `Atomic.Descriptor(feature::AbstractFeature, ..., Descriptor.Settings(..))` or call directly functions from the module `Descriptor`.
- In JAC, we shall provide a list of features to which an approximate electron density can be transformed to.

4D surfaces of spatial densities:

- Use of a 4-dimensional unit sphere: Bartok *et al.* (2010) projected the electron densities of all atoms (in some given unit cell) upon the surface of a four-dimensional unit sphere. This can be achieved by a very similar transformation as applied for constructing the Riemann sphere

$$(\varphi, \vartheta, \vartheta_o) = [\tan^{-1}(y/x), \cos^{-1}(z/|\mathbf{r}|), |\mathbf{r}|/r_o], \quad r_o > r_{\text{cut}}/\pi$$

- The use of this transformation has the advantage that all the information from the 3D spherical region inside the cutoff is now encoded by three angles of the 4D surface, and including the radial dependence of the (electron) density.

- 4D spherical harmonics $U_{mm'}^{(j)}$: For such a four-dimensional unit sphere, the 4D spherical harmonics $U_{mm'}^{(j)}$, also known as the **Wigner matrices**, provide a natural complete basis for the interior of the 3D sphere and without the need for radial basis functions. An approximate projection of the atomic density upon the 4D sphere is then obtained by just using a subset of expansion coefficients $c_{mm'}^{(j)} = \langle U_{mm'}^{(j)} | \rho \rangle$.

Bispectra of electronic densities:

- Bispectrum of an atomic density: A descriptor of the electron density can be formed also by means of the bispectrum of the projection coefficients $(c_{mm'}^{(j)})$ of some atomic or shell density upon a 4D sphere as well as the standard Clebsch-Gordan coefficients

$$B_{j_1,j_2,j} = \sum_{m_1,m'_1=-j_1}^{j_1} \sum_{m_2,m'_2=-j_2}^{j_2} \sum_{m,m=-j}^j (c_{m'm}^{(j)})^* \langle j_1 m_1, j_2 m_2 | jm \rangle \langle j_1 m'_1, j_2 m'_2 | jm' \rangle c_{m'_1 m_1}^{(j_1)} c_{m'_2 m_2}^{(j_2)}.$$

- Bispectrum of an atomic density: The elements of the three-index array $\mathbf{b} = (B_{j_1,j_2,j})$ from above are invariant with respect to rotations of the 4D space, and hence also to rotations of the 3D space. In practice, one can easily limit the spatial resolution in describing the atomic density by truncating the summation to $j, j_1, j_2 \leq J_{\max}$.

Partial radial distribution functions (PRDF):

- Partial radial distribution function (PRDF): These functions have been widely applied in the analysis of x-ray powder diffraction patterns in crystallography as well as for text mining in computer science. In physics, the PRDF representation may encode the distribution of pairwise distances d_{ab} between two (given) atoms or atomic levels of type a and b .
- PRDF: In molecular physics and material science, the PRDF can be seen as the density of atom-type b in a shell of radius r that is centered around atom a . If averaged over all atoms of a given type, the discrete PRDF representation is given by (Schütt *et al.*, 2014)

$$g_{ab}(r) = \frac{1}{N_a V_r} \sum_{i=1}^{N_a} \sum_{j=1}^{N_b} \Theta(d_{a_i b_j} - r) \Theta(r + dr - d_{a_i b_j}),$$

where N_a, N_b are the (total) number of atoms of type a, b , and V_r is the volume of the sphere. In solid-state physics, one usually considers the atoms in the unit cell. The PRDF representation has the advantage that it is not fixed to a certain number of atoms in the unit cell of the training materials and, hence, can be used also in order to predict the properties of other (related) systems.

12.2.b. Descriptors for pairs of atomic levels

Feature transformations:

- Descriptors for a single atomic level might include: various radii, one-electron binding energies, bispectrum of atomic density; effective atomic charges for shells/subshells.
- Descriptors for pairs of atomic levels: overlap integrals of valence electrons.
- **Shell-coupling labeled atomic fragments:** It still need to be worked out how the coupling information of atomic levels can be transformed into useful features.
- **Cocatenation of descriptors:** All fragment-based atomic descriptors can be concatenated quite easily in order to represent a particular level uniquely. From this concatenated vector descriptor, one then has to **filter out low-variance as well as highly-correlated features in order to ensure a stable learning process.**

12.3. Methods of machine learning

Machine learning. A short overview:

- **Machine learning (ML):** Frankly speaking, ML methods can be understood as a collection of computational methods which make use of data to predict yet unknown, though helpful new information. **ML is closely related to data mining** which applies machine learning and other methods to unveil information that is already within the data but did not (yet) become apparent so far.
- **Machine learning (ML):** The widespread use of ML methods in engineering sciences, social sciences, financial sciences, statistics, marketing, etc., has lead to many new methods and techniques which are independent of the research field they were developed originally.
- **Machine learning** includes several generic tasks, rather independent of the particular application: (i) Modelling of existing data by means of probability distributions; (ii) clustering and classification of data; (iii) regression analysis; and (iv) feature reduction. Different – formal and numerical – techniques have been developed and applied in order to deal with each of these tasks.
- **Mathematics behind ML methods:** These methods usually return a statistics-based model for some given data set, and which is then utilized in order to interpolate between the known data. A high accuracy in fitting the available data (low bias) often results in a rather high variance *between* these data points. Therefore, the accuracy of the fitting need to be tested by some cross-validation with test data or with experiment.

- **Branches of machine learning:** Three branches (classes) of ML methods are often distinguished: (i) Supervised learning; (ii) unsupervised learning as well as (iii) reinforcement learning (RL).
- **Supervised learning:** This approach is the **most mature and powerful learning approach** and, hence, has been applied in a large number of machine-learning studies in the physical and natural sciences, such as in the mapping of chemical compositions to some property of interest, picture recognition and elsewhere.
- **Supervised learning** aims for learning some conditional distribution $P(\mathbf{y}|\mathbf{x})$, and by assigning labels \mathbf{y} to the classification data \mathbf{x} based on training data from the distribution $P(\mathbf{y}, \mathbf{x})$. For example, supervised learning may aim to ‘learn’ a function $y = f(x)$ from a given data set.
- **Unsupervised learning** aims to identify certain structures within a given distribution $P(\mathbf{x})$, such as some clustering of data.
- **Reinforcement learning** tries to learn some correct behavior due to (so-called) reinforcement signals-rewards or punishments. The agent’s goal is to obtain rewards with a high probability (Dunjko *et al.*, 2016).
- **Generative models for machine learning:** While there are various ways for building generative models, the main three approaches are: (i) variational autoencoders (VAEs); (ii) reinforcement learning (RL); and (iii) generative adversarial networks (GAN).
- **Quantum machine learning:** Analogue to quantum computing, this field aims to devise and implement explicit quantum algorithms (software) for machine learning that are faster than any known algorithms on some classical computers. Although a number of quantum algorithms are meanwhile well established, there are still many hardware and software challenges to be solved (Biamonte *et al.*, 2016). The use of quantum instead of classical algorithms is also known as **quantum speedup**. Quantum software makes in particular use of quantum algorithms to process information.
- **Quantum machine learning:** This field aims to develop new ideas how machine learning can be applied to quantum information theory in order exploit quantum superposition more efficiently. In particular, machine learning can be applied for analyzing the separability of quantum states or to classify phases in condensed matter physics. This is quite in contrast to quantum-state tomography which becomes rapidly intractable as the size of the system increases.
- **Statistical regression techniques:** In the last few years, various statistical regression techniques have been applied in order to approximate effectively the properties of systems, for which a rather small number of accurate and demanding reference calculations can be performed. To make use of these regression techniques, atomic-scale representations (descriptors) need to be developed to encode the **fundamental symmetries and properties of a class of systems**. Well-selected descriptors can hereby substantially improve the performance of the regression; good descriptors may also offer insights into the chemistry of the system. For instance, Willat *et al.* (2018) report a data-driven analysis of the *similarity* between pairs of elements that resembles the periodic table of the elements.

12.3.a. Supervised learning methods

Concepts & notations:

- **Supervised learning models:** These models can be used to predict output values from either a discrete set (e.g. classification of materials) or a continuous set of date (e.g. polarizability). To make predictions from a discrete set requires classification, while regression is needed to forecast continuous data.
- **Kernel-based learning methods:** These methods are based on the mapping of (atomic or molecular) data upon a high-dimensional feature space. This mapping is made implicitly by using a **kernel function**, e.g., a Gaussian kernel $k(x, y) = \exp(-x - y/\sigma^2)$ or some Laplacian kernel $k(x, y) = \exp(-x - y/\sigma)$. Here, the kernel can be interpreted as a **measure to characterize the similarity between the given and predicted data**. The predicted property is then computed as a linear combination of kernel functions that depend on the material of interest and the training materials (Schütt *et al.*, 2014).

Advantages & limitations:

- Since the regression coefficients $\{c_i\}$ arise from a nonlinear model, i.e. due to a nonlinear transformation of the training data, such a kernel-based ML model is specific to some selected property and cannot be applied to any other properties or regions of compound space.

Kernel ridge regression (KRR) method:

- **Regression model based on the Coulomb matrix:** Rupp *et al.* (2012) apply a ML model, in which the energy of a molecule is expressed as a sum over weighted Gaussians

$$E^{(\text{estimate})}(\mathbf{M}) = \sum_i^N c_i \exp \left[-\frac{d(\mathbf{M}, \mathbf{M}_i)^2}{2\sigma^2} \right]$$

where i runs over all molecules $\{\mathbf{M}_i\}$ from the training set. The training on the available reference data $\{\mathbf{M}_i, E_i^{(\text{reference})}\}$ then results in a set of regression coefficients $\{c_i\}$ as well as the length-scale parameter σ . In such a regression model, each molecule i from the training set contributes not only by its distance but also due to its regression coefficient c_i .

- **Kernel ridge regression:** In this regularized model, the norm of regression coefficients $\{c_i\}$ is restricted to ensure the transferability of some model towards some unexplored species. For a given length-scale parameter σ and regularization parameter λ , the regression coefficients

are obtained by determining the minimum of the function (Rupp *et al.*, 2012)

$$\min_{\{c_i\}} \sum_i \left(E^{(\text{estimate})}(\mathbf{M}_i) - E_i^{(\text{reference})} \right)^2 + \lambda \sum_i c_i^2 \implies \mathbf{c} = \frac{\mathbf{E}^{(\text{reference})}}{(\mathbf{K} + \lambda \mathbf{I})}, \quad K_{ij} = \exp \left[-\frac{d(\mathbf{M}_i, \mathbf{M}_j)}{2\sigma} \right].$$

\mathbf{K} is called the Kernel matrix of all training molecules, while \mathbf{I} here denotes the identity matrix.

- **Locality of the kernel ridge regression:** The locality of this model is measured by the length scale σ ; this parameter determines a range outside of which any training molecule \mathbf{M}_i only contributes with (a rather) negligible weight to the selected property. Usually, the length scale σ is determined by some ML method and becomes smaller as the size of the training set increases, i.e. a model is said to become more *local* as more training data are available.

12.3.b. Neural network (NN) methods

Concepts & notations:

- **Deep neural network (DNN) model:** In these models, atomic or molecular representations are transformed first by a linear and later nonlinear function across several stages (layers) of the network. For a given task and associated loss function, the parameters for each layer (weights) are then optimized via the **backpropagation algorithm**.
- **Deep learning:** Since the DNN architecture transforms the original data into some other representation, more suitable for tasks like classification or generation, deep learning is often characterized as **representation learning**.
- **Deep neural network (DNN):** A DNN refers to multiple layers of neurons; each layer receives its input from the neuron activation of the previous layer, performs a simple transformation (computation), and transmits the (non-linear) activation to the next layer. In a DNN, therefore, all neurons of a given network implement altogether a nonlinear mapping of input (activation) data upon output data. A DNN learns from given test data by adapting the weights of each neuron due to **backpropagation techniques**.
- **Generative adversarial network:** This network consists of two parts: **The generator produces data similar to a true data set, while the discriminator tries to distinguish between true and fake data.** The generator and discriminator hereby learn like in an adversarial game. For a proper set-up of the network, the game may converge to the point where the generated data shows *true* statistics, and the discriminator can no longer distinguish between the true and generated data (Lloyd and Weedbrook, 2020).

12.3.c. autoencoder methods

Concepts & notations:

- **Autoencoder (AE) model:** Such model includes two steps, namely, the encoding of descriptors into some lower-dimensional (latent) space, and the mapping of the latent vector back to the original representation. These AE models often work better if the latent vector are generated by means of probability distribution so that a (single) descriptor is no longer represented as single point but rather as **probability distribution in the latent space**.
- In AE models, systems and properties are represented as continuous and differentiable vectors from some probabilistic manifold (Sanchez-Lengeling and Aspuru-Guzik, 2018).
- **Latent vector spaces:** These are continuous vector space and, hence, enable one to apply direct gradient-based optimization procedures. Nevertheless, the manifold of (atomic or molecular) data may lead to many local minima, so that other optimization approaches are also necessary.
- **Multilevel variational AE:** These AE refer to structured architectures and are presently promising research directions in ML, including so-called **reinforcement learning (RL) methods**.

12.3.d. Other methods

Concepts & notations:

- **Active learning approaches** attempt to provides guidance to optimize a particular property for some large and unexplored class of systems. So far, however, very little is known how some available or possible experimental set-ups should be sampled in order to obtain optimal output. Here, **active learning techniques aim to predict optimal future experiments** that enable one to better understand a given problem. In particular, such active machine-learning approaches may help directly select future experiments, a feature that has been discussed, for instance, in crystallography.

12.4. Feature transformations & applications of machine learning

12.4.a. Feature transformation and engineering

Requirements & notations:

- The recent boom in ML applications in molecular physics and material science has led to a plethora of (atomistic) descriptors that are — more or less — suitable for ML algorithms. However, a proper software implementation of these descriptors is either not accessible so easily for the users or is widely scattered across different programs and libraries.
- Least absolute shrinkage and selection operator (**LASSO**): In the selection of proper features, it is usually desirable to determine a small set of parameters that is able to keep all relevant information about the given data.
- Feature selection: This term comprises a rather widespread set of techniques that are used in statistical analysis in different fields, and the least absolute shrinkage and selection operator (**LASSO**) is just one of them.
- Feature selection: To reduce the size of the feature space, one often defines rules for linear and non-linear combinations of the primary features. This then usually gives rise to a very large number of candidate descriptors.
- Transferability of machine learning: Transferability describes the potential and/or the known features of a trained algorithm that are applicable also for related tasks. The transferability of neural networks has been explored in molecular structure theory by predicting the CCSD and MP2 correlation energies for different molecules and geometries, although without any clear conclusions about the quality of general predictions.

Properties of good descriptors:

- In material science, the properties of good (molecular) descriptors have been summarized at various places in the literature; cf. Himanen *et al.* (2019). In particular, such descriptors should be:
 - (a) **invariant with regard to a spatial translation** of the coordinate system;
 - (b) **invariant with regard to a rotation** of coordinates;
 - (c) **unique**, i.e. there should be a single way to construct a descriptor from the (atomic) structure and occupation of the unit cell, and the descriptor itself just refers to a single property of the material;
 - (d) **continuous**, i.e. small changes in the atomistic structure of the unit cell should translate into small changes in the descriptor;

12. Atomic descriptors

- (e) computationally cheap since the computation of descriptor should be significantly faster than any direct computation of the property of interest.
- **Properties of useful descriptors:** The following properties are considered to be important if not even necessary (Ghiringhelli *et al.*, 2015) but are very similar to the criteria above:
- (a) A vector descriptor \mathbf{d}_i should uniquely characterizes the system or process of interest.
 - (b) Different (similar) systems or processes should be characterized by different (similar) vector descriptors.
 - (c) The computation of the vector descriptor should be (much) cheaper than the property of interest.
 - (d) The vector dimension Ω of the descriptor should be as low as possible (for a certain request of accuracy).

12.4.b. Applications in molecular physics

Special concepts & notations of ML in molecular physics:

- **Machine learning for the electronic structure of molecules:** A deep learning approach has been realized and demonstrated to predict molecular orbital energies for molecules up to the size of salicylic acid, usually based on DFT data. Moreover, ANN have also been trained to predict the (spin-state) splitting of transition-metal complexes. Machine learning methods have been used to predict dissociation energies for different molecular geometries or to construct empirical potential energy surfaces for molecular dynamics. The correlation energy, predicted by machine learning, have been generated for a large set of organic molecules.
- **Molecular graphs:** Molecular systems can be quite readily described by graphs in which vertices represent the atoms and edges the chemical bonds. In such a representation, fragment descriptors characterize subgraphs of the full 3D molecular network. From this perspective, different materials can be considered as coloured graphs, where different colors represent different atoms and interatomic interactions. Such a graphical perspective also enables one to represent the individual parts of a molecular graph by linear combinations of fragment descriptors and, hence, to simplify the computation, storage and interpretation of the different descriptors.
- **Molecular graphs:** Following semi-empirical rules from bond theory, every molecule can be easily expressed as an undirected graph where each atom is a node and the bonds are the edges. In these graphs, all hydrogen atoms are usually treated implicitly in order to keep the size of the graphs moderate.
- **Molecular graphs:** SMILES strings form an established standard for molecular graphs; these strings follow the typical text encoding of the standard chemical notation (e.g., H₂O or C₂H₅OH). Other and more advanced representation use weighted graphs with various vector

features in order to assign bonding type, aromaticity, charge, and distance to the edges and nodes of the graph (Sanchez-Lengeling and Aspuru-Guzik, 2018).

- **Molecular graphs:** Since there is generally no unique translation between the molecular structure and some corresponding graph, the use of different such ‘translations’ can either appear to be advantageous (e.g., for further data augmentation) or disadvantageous, if different graphs cause noise in the ML process.
- **Chemical space project:** The chemical space formally comprises the set of all possible molecular and solid-state compounds which, obviously, still contains huge unexplored regions. For pharmacologically relevant small molecules, the number of structures is estimated to be on the order of 10^{60} (Sanchez-Lengeling and Aspuru-Guzik, 2018). In the chemical space project, a total of 166.4×10^9 billion molecules with at most 17 heavy atoms have been (formally) summarized.
- **Compound space in quantum chemistry:** ML models are often based on measuring distances in compound space in order to extract useful information about the stoichiometry and the configurational variation of different molecules. This requires of course a **measure measure of molecular (dis)similarity** that should be invariant with regard to translations, rotations and the particular ordering of atoms.
- **Gaussian approximate potentials (GAP):** Even for rather small systems, the GAP model for molecular potential energy surface is orders of magnitude faster than standard plane-wave DFT codes, although significantly more expensive and accurate than simple analytical potentials (Bartok *et al.*, 2010).

Machine learning for configuration interaction (MLCI):

- **Machine learning for configuration interaction (MLCI) calculations:** Coe (2019) report about an ANN to choose on fly important configurations to successively enlarge the CI space. Such a network was shown to (significantly) reduce the number of iterations until convergence was found for molecules of moderate size. Therefore, such a network requires less time than other methods for choosing configurations.
- **Machine learning for configuration interaction (MLCI) calculations:** Selected CI approaches attempt to construct well-condensed (compact) wave functions that still capture all important contributions (with regard to full CI). Such selected CI approaches have become increasingly popular during recent years. They make use of the (well-known) observation that the majority of the CI mixing coefficients are usually negligible but that important admixtures are difficult to recognize in advance. Here, neural networks might help to select important classes of virtual excitations. The so-called heat-bath CI designates a special way of choose configurations and has been applied to calculate potential energy curves for C₂ or the geometry of chromium dimer.
- **Machine learning for configuration interaction (MLCI) calculations:** Coe (2018) proposed the machine learning configuration interaction (MLCI) method, in which an artificial neural network (ANN) is trained on-the-fly in order to predict the *important* configurations for

12. Atomic descriptors

an iterative selected configuration interaction procedure. The results of this selection are then compared with other methods: first-order coupling, random selection or Monte Carlo configuration interaction. This method aims for improving the accuracy and for accelerating the convergence of iterative selected configuration interaction calculations.

Molecular descriptors:

- **Molecular descriptor:** A better representation of data requires less computational resources in order to *learn* the underlying patterns. For example, a representation that can span all of chemical space would need to capture all the symmetries of the Schrödinger equation, such as the permutational, rotational, reflectional as well as translational invariance for particles of the same type.
- **Molecular descriptor:** The Coulomb matrix and other descriptors often refer in counting atoms to their nuclear charge, although other criteria, such as the electron configuration or number of valence electrons could be used as well.
- **Molecular descriptor:** The finding of good molecular representations is presently an open research area. While there are various representations available, **no single representation seems to work for all properties of interest.** More general, those representations that encode the relevant physics will result in a better learning process.
- **Types of molecular descriptors:** Three such types are often distinguished, namely, discrete (e.g., text), continuous (e.g., vectors and tensors) or weighted graphs. Although each graphs can be re-expressed also as sparse matrices, graphs are quite different of how they are processed within the models of machine learning (Sanchez-Lengeling and Aspuru-Guzik, 2018).
- **Mulliken electro-negativity of an atom:** $E^{(MN)} = -(IP + EA)/2$; it is simply formed from the ionization potential (IP) and the electro-negativity (EA) of the atom or ion.
- **Coulomb matrix:** This matrix representation encodes the Coulombic forces between the nuclear charges of each atom.
- **Coulomb matrix:** This molecular descriptor has not always been found useful in ML and this applies, in particular, to periodic solids.
- **Coulomb matrix:** For single molecules with nuclear charges $\{Z_i\}$ and positions $\{\mathbf{r}_i\}$ of all atoms, the Coulomb matrix has been found a good (molecular) descriptor

$$C_{ij}^{(\text{molecule})} = \begin{cases} 0.5 Z_i^{2.4} & \text{for } i = j \\ \frac{Z_i Z_j}{|\mathbf{r}_i - \mathbf{r}_j|} & \text{for } i \neq j. \end{cases}$$

The Coulomb matrix is invariant under rotation and translation but cannot be applied so easily to infinite periodic crystals.

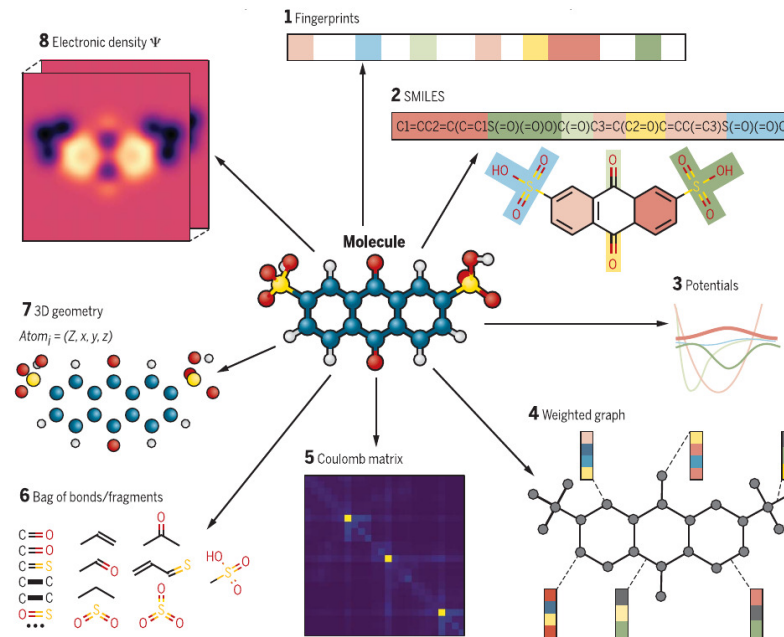


Figure 12.1.: Different types of molecular descriptors that can be applied to some molecule: (1) A fingerprint vector that quantifies the presence or absence of certain molecular environments; (2) SMILES for simple text encoding of the chemical species; (3) various potential energy functions that model the interactions and symmetries of the molecule; (4) a graph with atoms and bond weights; (5) Coulomb matrix; (6) a bag of bonds and fragments; (7) 3D geometry with associated atomic charges; and (8) encoding of the electronic density; taken from: Sanchez-Lengeling and Aspuru-Guzik (2018).

➤ **Galvez matrix of molecular graphs:** The construction of descriptors can be inspired also by (so-called) topological charge indices or Kier-Hall electro-topological state indices. In this construction scheme, a **Galvez matrix** $M = A \cdot D$ is formed by multiplying the adjacency matrix A of the graph by the reciprocal square distance matrix ($D_{ij} = (1/r_{ij}^2)$). Obviously, this is a $n \times n$ quadratic matrix with n being the number of atoms in the unit cell. From the Galvez matrix, various descriptors of some reference property \mathbf{q} can be calculated by

12. Atomic descriptors

(Isayev *et al.*, 2017):

$$T = \sum_{i=1}^{n-1} \sum_{j=i+1}^n |q_i - q_j| M_{ij}, \quad T_{\text{bond}} = \sum_{i,j \in \text{bonds}} |q_i - q_j| M_{ij}.$$

- Feature matrix ($X_{ij,n} = g_{ab}(r_n)$): Matrix of the PRDF of all pairs of atoms (a, b) , evaluated for some cut-off radius r_n . The distance of two molecules or crystals is then defined by the Frobenius norm between these matrices; these distances can be directly used also for some of the kernels of ML methods. The feature matrix is a global descriptor for the similarity of molecules, which is invariant under translation, rotation, and the particular choice of the unit cell (Schütt *et al.*, 2014).

Applications:

- Potential energy surface (PES): ML approaches has been used to predict the Born-Oppenheimer potential energy surface (PES) for a set of atoms without explicit molecular computations. For example, Bartok *et al.* (2010) modeled the bulk phases of carbon, silicon, germanium, iron and gallium nitride, based on a unified framework in forming atomistic descriptors. These authors also developed a framework for automatically generating finite range interatomic potential models from quantum-mechanically calculated atomic forces and energies.

12.4.c. Applications in solid-state physics and material science

Special concepts & notations of ML in material science:

- Machine learning in material science: ML methods will likely augment or even supplant in the (near) future the time consuming and often intuition-based, trial-and-error experimentation for the design and discovery of new materials.
- Machine learning in material science: Methods in ML may help optimize several properties simultaneously with the best trade-off, for example, by maximizing one property, while keeping another property bound near to some required value. In a Pareto plot with axis due to these properties, this means to identify the boundary for one given property, which the materials cannot cross without deteriorating the value of some other properties.

- **Machine learning in crystallography:** Computationally efficient ML models have been applied during recent year in order to predict molecular properties of many crystals with similar accuracy as obtained from DFT. These models are especially useful to systematically screen millions of crystals with only milliseconds per single prediction (Faber *et al.*, 2016).
- **Material Genome Initiative (MGI):** In 2011, Obama announced this initiative to maintain the US manufacturing competitiveness by halving the time it takes to discover new materials. Since then, this initiative has been supported and sustained by various US agencies. **New materials are sought in order to reduce the costs and environmental friendliness**, with special focus upon Kevlar and Li-based batteries and their potential replacements.
- **Inverse material design:** Since it appears intractable to explore the huge space of (different classes of) materials, neither computationally nor experimentally, the **inverse design aims to discover tailored materials by starting directly from some desired functionality** and to combine available databases with methods from machine learning.
- **Inverse material design:** Various approaches to inverse material design has been proposed and benefitted from recent developments in machine learning. In particular, **deep generative models** have been applied to numerous classes of materials including the rational design of prospective drugs, synthetic routes to organic compounds as well as a further optimization of photovoltaics and redox flow batteries (Sanchez-Lengeling and Aspuru-Guzik, 2018).
- **Structure maps:** Originally, these maps refer to simple scatter plots that display two physical properties *versus* each other for a number of compounds or materials, such as ionization potentials, valences, ionic radii, etc. These structure plots have been frequently used in material science in order to identify class of systems whose physical properties come already close to some desired behaviour. In particular, the Periodic Table is a particular structure map that establishes trends in the chemical properties of all atoms, if one moves along its rows or columns.
- **Structure maps:** Various well-known structure maps in chemistry and material science are based on symmetric combinations, e.g., sums or differences, of ionic radii which are computed by means of pseudopotential. Since the use of coordinates do not require extra computation nor measurements, they can be easily applied in structure maps for clustering physical properties other than crystal structure or melting temperatures, etc.
- **Structure maps:** ML methods can extent traditional structure maps towards three or more dimensions and, hence, remove the subjectivity or ambiguity in the decisions of where to draw the boundaries for clusters and to replace simple boundaries by more sophisticated and flexible manifolds (Gubernatis and Lookman, 2018).
- **Ashby plot:** Historically, an Ashby plot displayed the Young's modulus *versus* the density of some material in order to show overlays of metals, polymers, ceramics, foams, etc. This structure map has been applied in material engineering in order to select the most appropriate material for a particular application.

12. Atomic descriptors

- **Molecular fragments:** This concept from molecular physics has been adopted in material science during the last years to design crystalline materials and has helped improve the molecular nomenclature and representation.
- **Property-Labelled Material Fragments (PLMF):** Fragments or (vector) descriptors that are just associated with a certain parts of a molecular or material graph.

Descriptors for solid-state physics and material science:

- **Descriptors for material science:** Coulomb matrix, Ewald sum matrix, sine matrix, Many-body Tensor Representation (MBTR), Atom-centered Symmetry Functions (ACSF) and Smooth Overlap of Atomic Positions (SOAP); cf. Himanen *et al.* (2019).
- **Smooth overlap of atomic positions (SOAP):** The SOAP formalism provides an elegant framework in order to construct a rotationally-invariant representation (descriptors) of the atomic density that can be used for machine-learning purposes. While the formalism itself provides a complete representation of structural correlations of a given order within an atomic environment, the quality and the computational cost of the regression scheme can be further improved by modifying the representation and by including chemical intuition (Willat *et al.*, 2018). For example, the use of multiple kernels due to different interatomic distances was found to lead to an improve machine learning behaviour.
- **Descriptors for material science:** To encode the atomistic structure of some molecule or material, the descriptor either depicts a local atomic environment or the structure as a whole. Global descriptors encode information about the whole atomistic structure, such as the size, temperature variation, etc.
- **Voronoi cells:** A Voronoi tessellation is a partitioning of space into regions based on some predefined subset of points, called seeds, sites, or generators. For each of these seeds, there is a region consisting of all points closer to that seed than to any other one; these regions are called Voronoi cells. The Voronoi cells of a crystal coincide with the so-called Wigner-Seitz cells of each atom, if the atomic sites are taken as seeds. **The tessellation of a crystall is unique and insensitive to the particular choice of unit cell.**

Applications:

- **Formation energy of elpasolites:** Faber *et al.* (2016) introduced a newly developed ML model to investigate and predict the formation energies of all $\sim 2 \times 10^6$ elpasolites that can be (formally) constructed from all main-group elements up to Bi. These predictions helped identify a new elemental order of descending elpasolite formation energy, including crystals with quite peculiar atomic charges.
- **Formation enthalpy of binary compounds:** Curtarolo *et al.* (2003) built a ML model for predicting the formation enthalpy of binary compounds, and which was based on the formation enthalpies of the same elements but in other chemical and solid-state structures.

- High-throughput density functional theory (HT-DFT) calculations: In materials science, large data bases have been generated by HT-DFT calculations and in a few cases by high throughput experiments.

12.4.d. Other applications

ML in text mining:

- Text mining: Because of the rapid increase of information, available to researchers via the web and scientific literature, navigation has become more and more difficult. Here, text mining became a popular approach to identifying and extracting information from unstructured text sources.
- Text mining aims for extracting facts and relationships in a structured form in order to create specialized databases, to transfer knowledge between domains or, more generally, to support decision-making (Butler *et al.*, 2018).

13. Semiempirical estimates

13.1. In JAC implemented estimates for atomic properties and data

13.1.a. Data from the periodic table of elements (PeriodicTable)

Symbols, atomic mass and ionization potentials:

- In JAC, the (mean) atomic masses of all elements are obtained from a call of `[PeriodicTable.]get(Z::Int64)` or `[PeriodicTable.]get(sy::Symbol)`, if `sy` refers to a valid element symbol.
- In JAC, the first ionization potential of a given element with nuclear charge `Z` or symbol `Sy` is obtained from a call of `[PeriodicTable.]get("", Z::Int64)` or ...
- Atomic mass:

13.1.b. Isotope data (PeriodicTable)

:

- Detailed isotope data are required, for instance, to calculate hyperfine A , B parameters, isotope-shift parameters, and at various places elsewhere.
- The isotope data need to be specified for the nuclear model `nm::Nuclear.Model`, if such properties are to be calculated.
- In JAC, a few selected isotope-specific data can be obtained by a call to `[PeriodicTable.]getIsotope(" ", ..., Z::Int64)`. However, no attempt is made to provide data for all isotopes and elements; instead we encourage the user to add further data as the need arises in specific applications.

13. Semiempirical estimates

13.1.c. Binding energies of inner- and valance-shell electrons (PeriodicTable)

Binding energies:

- In JAC, an estimate for the binding energy of an $n\ell$ -electron in the neutral atom can be obtained from [PeriodicTable.]get("ionization potential: inner-shell", shell::Shell, Z::Int64).

13.1.d. Atomic radii, susceptibilities and polarizibilities (PeriodicTable)

Atomic polarizibilities:

- In JAC, ... can be obtained from [PeriodicTable.]get().
- Further details

Atomic radii:

- In JAC, ... can be obtained from [PeriodicTable.]get().
- **Atomic radii:** The concept of atomic and ionic radii has been found helpful for understanding, explaining or even predicting various physico-chemical properties of atoms, ions and molecules. However, this is quite different to the use of such radii in crystal chemistry where they are used in order to estimate and to explain the binding lengthes in crystal lattices.
- **Atomic radii:** Ghosh (2002) applied computed theoretical radii in order to estimate a number of size-dependent physical properties of isolated atoms: (1) the diamagnetic part of the magnetic susceptibility $\chi^{(\text{diamagnetic})}$ for all elements up to xenon, (2) the atomic polarizability α and (3) the global hardness η for all elements of the periodic table.

13.2. In JAC partly-implemented estimates for atomic properties and data

13.2.a. Weak-field ionization of effective one-electron atoms

Property & notations:

- Field ionization: by a quasi-static external field: $A^{(*)} + F \mathbf{e}_z \longrightarrow A^+ * e^- .$
- Formal quantum notation: $|\alpha J\rangle \longrightarrow \dots$
- Not yet implemented.
- In JAC, all estimates on the field-ionization rates of atoms are always based on a non-relativistic, single-electron approach. No attempt has (yet) been made to generalize this approximation towards real many-electron atoms and ions with their fine-structure.

Motivation:

- Ionization of atoms by an external electric field is a fundamental atomic process that plays an important role, for instance, in the formation of charge-state distributions in (dilute) plasma under strong fields.
- **Vice versa:** The observations of temporal variations in the line intensities of ions, that are produced by field ionization, can help determine spectroscopically the macroscopic-field distribution in plasma.
- Since the field-ionization probability grows (very) rapidly with the electric field strength F , the field strength can be derived from accurate measurements of the ionization probabilities.

Further information:

- Ionization probabilities are often calculated within the WKB approximation, i.e. in the weak-field limit. In general, field ionization probability depends critically on the projection of the total orbital angular momentum upon the direction of the field.

13. Semiempirical estimates

- In most field-ionization probability computations, a quasi-static and homogeneous electric field is assumed as it occurs, for example, for macroscopic-scale fields in plasma. This assumption is in contrast to many local fields that may occur at the atomic scale.
- For the case of a single electron with binding energy E in the valence shell ($n \ell$) and outside of closed shells otherwise, the quasi-classical escape rate is given by (Fisher *et al.*, 1998)

$$\Gamma(E, \ell, m) = B_{n\ell}^2 \frac{(2\ell+1)(\ell+m)!}{2^{m+1} k^m m! (\ell-m)!} \left(\frac{2k^2}{F}\right)^{2Z/k - m - 1} \exp\left(-\frac{2k^3}{3F}\right)$$

where Z is the charge of the parent ion as seen by the electron are large r , $k = \sqrt{2|E|}$ is the modulus of the (electron's) wave vector and $B_{n\ell}$ is the amplitude that characterizes the outgoing electron wave.

13.2.b. Tunnel ionization rates

Tunnel ionization rates:

- **ADK rate for tunnel ionization:** The first step in the strong-field photoionization by a linearly-polarized laser field (with $\gamma < 1$) is often modeled by means of the Ammosov-Delone-Kainov (ADK) rate for the tunnel ionization of an atom in an oscillating electric field. This rate is given by (Chen *et al.*, 2019)

$$W^{(\text{ADK})}(|\mathcal{E}(t)|) = |c_{n^*\ell^*}|^2 f(\ell, m) I_p \left(\frac{2\kappa}{|\mathcal{E}(t)|}\right)^{2n^* - |m| - 1} \exp\left(-\frac{2\kappa}{3|\mathcal{E}(t)|}\right), \quad n^* = \frac{Z^{(\text{ion})}}{\sqrt{2I_p}}, \quad \ell^* = n^* - 1$$

$$|c_{n^*\ell^*}|^2 = \frac{2^{2n^*}}{n^* \Gamma(n^* + \ell^* + 1) \Gamma(n^* - \ell^*)}, \quad f(\ell, m) = \frac{(2\ell+1)(\ell+|m|)!}{2^{|m|} |m|! (\ell-|m|)!}, \quad \kappa = (2I_p)^{3/2}.$$

In this notation, (n^*, ℓ^*) are effective quantum numbers, while (ℓ, m) are the orbital and magnetic quantum numbers of the (single-active) valence electron, and $Z^{(\text{ion})}$ is the charge of the residual ion.

- **ADK rate for tunnel ionization:** Tong and Lin (2005) found that the ADK rates significantly overestimate the (static) ionization rate if calculated numerically in an barrier-suppressing electric field. In the near- and over-the-barrier regimes, these authors suggested instead

the modified ADK rate

$$W^{(\text{modified ADK})}(|\mathcal{E}(t)|) = W^{(\text{ADK})}(|\mathcal{E}(t)|) \exp\left(-\mu \frac{[Z^{(\text{ion})}]^2}{I_p} \frac{|\mathcal{E}(t)|}{\kappa}\right), \quad 6 < \mu < 10 \quad \dots \text{fitting parameter.}$$

For a few atoms and ions, the fitting parameters μ is given by Tong and Lin (2005).

- **PPT rate for tunnel ionization:** The ADK rate for tunnel ionization is the limit of an extremely strong laser field ($\gamma \rightarrow 0$) of a more general model by Perelomov, Popov, and Terent'ev (PPT) from (1967) which was originally derived for arbitrary values of the Keldysh parameter γ . In this PPT model, the ionization rate is given by

$$\begin{aligned} W^{(\text{PPT})}(|\mathcal{E}(t)|, \omega) &= |c_{n^*\ell^*}|^2 f(\ell, m) I_p \left(\frac{2\kappa}{|\mathcal{E}(t)|} \right)^{2n^* - |m| - 1} (1 + \gamma^2)^{|m|/2 + 3/4} A_m(\omega, \gamma) \exp\left(-\frac{2\kappa}{3|\mathcal{E}(t)|} g(\gamma)\right) \\ g(\gamma) &= \frac{3}{2\gamma} \left[\left(1 + \frac{1}{2\gamma^2}\right) \sinh^{-1} \gamma - \frac{\sqrt{1 + \gamma^2}}{2\gamma} \right], \quad A_m(\omega, \gamma) \dots \text{see literature,} \end{aligned}$$

while all other entities are the same as in the ADK rate above.

- **Total ionization probability from tunnel ionization rate:** For a given laser pulse $\mathcal{E}(t)$, the total ionization probability is given by

$$\mathcal{P}^{(\text{tunnel rate})} = 1 - \exp\left(\int_{-\infty}^{\infty} dt W^{(\text{tunnel rate})}(|\mathcal{E}(t)|, \dots)\right),$$

and where $W^{(\text{tunnel rate})}$ refers to one of the tunnel ionization rates from above.

- **Tunnel ionization rate in quasi-static approximation:** In the quasi-static approximation, the tunnel ionization rate for a valence electron in shell $(n\ell)$ is given by (Yudin and Ivanov, 2001)

$$\begin{aligned} \Gamma^{(\text{tunneling})} &= A_{n^*,\ell^*} B_{\ell,|m|} I_p \left(\frac{2(2I_p)^{3/2}}{\mathcal{E} f(t) |\cos \phi(t)|} \right)^{2n^* - |m| - 1} \exp\left(-\frac{2(2I_p)^{3/2}}{3\mathcal{E} f(t) |\cos \phi(t)|}\right), \quad \phi(t) = \omega t - \phi_o \\ A_{n^*,\ell^*} &= \frac{2^{2n^*}}{n^* \Gamma(n^* + \ell^* + 1) \Gamma(n^* - \ell^*)}, \quad B_{\ell,|m|} = \frac{(2\ell + 1) (\ell + |m|)!}{2^{|m|} |m|! (\ell - |m|)!}, \quad n^* = Z/\sqrt{2I_p}, \end{aligned}$$

13. Semiempirical estimates

and where $\phi(t)$ is the instantaneous phase of the linearly-polarized laser field. The coefficient A_{n^*,ℓ^*} arises from the radial part of the wave function at $r \gg 1/\sqrt{2I_p}$, while the coefficient $B_{\ell,|m|}$ arises from the angular part of the wave function.

13.2.c. Electron-impact ionization. Cross sections

Process, notation & application:

- Electron-impact ionization (EII) of an atom or ion: $e_s^- + A^{q+} \rightarrow A^{(q+1)+*} + e_s^-' + e^-$
- Quantum numbers and notations used in the formulas below: $|\alpha_i J_i\rangle + |\varepsilon_i \kappa_i\rangle \rightarrow |\alpha_f J_f\rangle + |\varepsilon_f \kappa_f\rangle + |\varepsilon_c \kappa_c\rangle$ where we use $\varepsilon \equiv \varepsilon_i$ below to denote the energy of the incoming electron and where $|\varepsilon_c \kappa_c\rangle$ refers to the initially bound and eventually ionized *atomic* electron.
- The electron-impact ionization process is important in all (high-temperature) plasma, both in astro and plasma physics, and at several places elsewhere. It is the inverse process to the three-body recombination, $A + e_i^- \leftrightarrow A^+ + e_f^- + e_c^-$.
- We refer to the three *free* electrons in this EII process as incident, (final-) scattered and (additionally released) continuum electron, and with the corresponding indices above.
- **Electron-impact ionization (EII) cross sections:** In the distorted-wave approximation, the differential (in energy) EII cross sections can be obtained from the formulas of the electron-impact excitation (EIE) cross section, if the excited bound electron is replaced by another continuum electron. Unfortunately, such a simple replacement increases the number of ionization channels considerably, since now two *free* electrons need formally to be coupled to the final state of the residual ion and because an additional summation occurs over all (total) angular momenta of the scattering states due to the coupling sequence of the two free electrons. Here, a concise notation for all incoming and outgoing electron waves is crucial to adopt the EII process to different physical scenarios. Until the present, most derivation have been made with very specific assumptions in mind about the behavior of the EII cross sections, and often by using rather intransparent notations.
- **Differential versus partial versus total cross sections:** While partial cross sections always refer to the EII of an electron from the particular shell $(n\ell)^q$ of atoms in a given electron configuration, the total EII cross sections refer to the sum of the partial cross sections over all shells. No fine-structure resolved EII cross sections are typically distinguished within the empirical treatment. Although both, partial-differential and total-differential cross sections can be readily distinguished within JAC, no differential cross sections are implemented and supported so far.

- **Quantum *versus* empirical EII cross sections:** Owing to the complexity of quantum EII cross sections, we first implement and support only a few (semi-) empirical approximations to the EII cross sections that are mainly based on the work by Kim and coworkers (2000, 2001).
- Four approximations are presently supported by JAC: `BEBapproximation`, `RelativisticBEBapproximation`, `BEDapproximation`, `RelativisticBEDapproximation`.
- Using JAC: Perform an `Empirical.Computation(...)` or call directly functions from the module `ImpactIonization`.

Semi-empirical cross sections:

- **Lotz formula:** For atoms and ions in their ground configuration, Lotz (1967) first modeled the partial EII cross sections for ionizing an $(n\ell)$ -shell electron with binding energy $\varepsilon_{n\ell}$ by

$$\sigma^{(\text{EII})}(\varepsilon) = a q \frac{\ln(\varepsilon/I_p)}{\varepsilon/I_p} [1 - b \exp(-c(\varepsilon/I_p - 1))],$$

and where a [$10^{-14}\text{cm}^2 \text{ eV}^2$] and b, c [dimensionless] are individual fitting coefficients for each element and charge state. If the proper binding energies and fit coefficients are applied, many experimental results can be approximated by this formula within 10 % for a good range of energies. Table 13.1 displays a few such coefficients for selected atoms and ions.

- **Modified Lotz formula by Bernshtam *et al.* (2000):** Bernshtam and coworkers analyzed a good number of published data and proposed for the partial EII cross section of positive ions the empirical formula

$$\sigma^{(\text{EII})}(\varepsilon) = C_\ell \left(\frac{R}{I_p} \right)^{2-\delta_\ell} q b \frac{\ln(\varepsilon/I_p)}{\varepsilon/I_p}.$$

In this expression, the branching ratio b denotes the probability. The coefficients C_ℓ [cm^2] and δ_ℓ depend on the orbital quantum number ℓ and are determined by a fit of published EII cross sections. These coefficients are available for $\ell = 0, 1$, and 2 only due to missing EII cross sections for $\ell > 2$, cf. Table 13.2.

- **Partial and total electron-impact ionization cross sections:** Within the binary-encounter-Bethe (BEB) and binary-encounter-dipole (BED) approximations, Kim *et al.* (2000) discuss and compile useful formulas for (semi-empirical) partial EII cross sections for an electron in the shell $(n\ell)^q$, with occupation q . They also extend these two approximations to relativistic impact energies of the incident electron. In general, the relativistic contributions can double the total EII cross section of H and He at incident electron energies $\varepsilon \equiv \varepsilon_i \approx 300$ keV and will become dominant at even higher energies. Kim *et al.* (2000) also suggest modifications to the partial BEB and BED cross sections that can be applied for multiply-charged ions and for inner-shell electrons of neutral atoms and molecules.

13. Semiempirical estimates

Table 1. Relevant data for all experimentally well known electron-impact ionization cross-sections for single ionization from the ground state. Constants a , b , and c are used in formula (7) [sodium and mercury: formula (4)] to calculate cross-sections¹³, which are marked in Fig. 1 through 4 by small circles. Constant a is given in $10^{-14} \text{ cm}^2 (\text{eV})^2$

| Species | Configuration | Binding energies in eV | | | Constants | | |
|---------|---------------------|------------------------|-------|-------|-----------|------|------|
| | | P_1 | P_2 | P_3 | a | b | c |
| H I | $1s$ | 13.6 | — | — | 4.0 | 0.60 | 0.56 |
| He I | $1s^2$ | 24.6 | — | — | 4.0 | 0.75 | 0.46 |
| He II | $1s$ | 54.4 | — | — | 4.4 | 0.38 | 0.60 |
| Li I | $1s^2 2s$ | 5.39 | 58 | — | 4.0 | 0.70 | 2.4 |
| Li II | $1s^2$ | 75.6 | — | — | 4.0 | 0.48 | 0.60 |
| N I | $2s^2 2p^3$ | 14.5 | 20.3 | — | 3.4 | 0.83 | 0.22 |
| N II | $2s^2 2p^2$ | 29.6 | 36.7 | — | 4.1 | 0.46 | 0.62 |
| O I | $2s^2 2p^4$ | 13.6 | 28.5 | — | 2.8 | 0.74 | 0.24 |
| Ne I | $2s^2 2p^6$ | 21.6 | 48.5 | — | 2.8 | 0.92 | 0.19 |
| Ne II | $2s^2 2p^5$ | 41.1 | 66.4 | — | 3.2 | 0.83 | 0.48 |
| Na I | $3s$ | 5.14 | — | — | 4.0 | 0 | — |
| | $2p^6$ | — | 34 | — | 3.6 | 0.84 | 0.32 |
| Na II | $2s^2 2p^6$ | 47.3 | 80.1 | — | 3.6 | 0.84 | 0.32 |
| A I | $3s^2 3p^6$ | 15.8 | 29.2 | — | 4.0 | 0.62 | 0.40 |
| K I | $3p^6 4s$ | 4.34 | 18.7 | — | 4.0 | 0 | — |
| K II | $3s^2 3p^6$ | 31.7 | 47.9 | — | 3.8 | 0 | — |
| Kr I | $3d^{10} 4s^2 4p^6$ | 14.0 | 27.5 | 93 | 4.0 | 0.71 | 0.76 |
| Rb I | $4p^6 5s$ | 4.18 | 15.3 | — | 4.0 | 0 | — |
| Xe I | $4d^{10} 5s^2 5p^6$ | 12.1 | 23.4 | 67 | 4.0 | 0.54 | 0.64 |
| Cs I | $5p^6 6s$ | 3.89 | 12.3 | — | 4.0 | 0 | — |
| Hg I | $6s^2$ | 10.4 | — | — | 4.0 | 0.55 | 4 |
| | $5d^{10}$ | — | 14.8 | — | 4.0 | 0.88 | 0.16 |

Figure 13.1.: Useful fitting coefficients for the Lotz formula; taken from .

- **Binary-encounter-dipole (BED) approximation:** In the non-relativistic formulation, the incident electron energy is often replaced by $\varepsilon \rightarrow \varepsilon + u_{n\ell} + \varepsilon_{n\ell}$, and where $u_{n\ell} = \langle \mathbf{p}_{n\ell}^2 / 2m \rangle$ denotes the kinetic energy of the bound electron in the shell $(n\ell)$ and $\varepsilon_{n\ell}$ the corresponding binding energy. With this modification, the partial, energy-differential BED cross section for the EII of an atomic electron

| l | C_l [cm ²] | δ_l |
|-----|--------------------------|------------|
| s | 1.7794×10^{-16} | 0.0471 |
| p | 2.1597×10^{-16} | 0.0910 |
| d | 1.2131×10^{-16} | 0.3319 |

Figure 13.2.: Coefficients C_l [cm²] and δ_l for the formula by Bernshtam *et al.* (2000); taken from .

in the shell $(n\ell)^q$ is given in [a.u.] by (Kim *et al.*, 2000)

$$\left(\frac{d\sigma}{d\varepsilon_c} \right)^{\text{(EII: partial BED)}} = \frac{\pi a_o^2 q}{\varepsilon_{n\ell}^3 (t + u + 1)} \left\{ \frac{N_i/q - 2}{t + 1} \left(\frac{1}{w + 1} + \frac{1}{t - w} \right) + \left[2 - \frac{N_i}{q} \right] \left[\frac{1}{(w + 1)^2} + \frac{1}{(t - w)^2} \right] + \frac{\ln t}{q(w + 1)} \frac{df}{dw} \right\}$$

$$t = \frac{\varepsilon}{\varepsilon_{n\ell}}, \quad u = \frac{u_{n\ell}}{\varepsilon_{n\ell}}, \quad w = \frac{\varepsilon_c}{\varepsilon_{n\ell}}, \quad N_i = \int_0^\infty dw \frac{df}{dw},$$

and where $\frac{df}{dw}$ is the (so-called) differential dipole oscillator strength. In this expression, the first two terms in the curly brackets with the $\pm (2 - N_i/q)$ arise from the Mott cross section, while the last term with $\frac{df}{dw}$ is the leading dipole term from the Bethe cross section. In this empirical modeling, moreover, corrections due to relativistic incident energies ε must be introduced in the differential ionization cross section (Kim *et al.*, 2000).

- **Differential dipole oscillator strength $\frac{df}{dw}$:** The differential dipole oscillator strengths is related to partial photoionization (PI) cross section for an electron of the given shell and can be expressed as [Gallagher *et al.* (1988), J. Phys. Chem. Ref. Data 17]:

$$\frac{df}{dE} [\text{eV}^{-1}] = \frac{\sigma^{(\text{PI})}(n\ell)}{109.75} [10^{-22} \text{ m}^2], \quad \frac{df}{dE} = \frac{df}{d\varepsilon_c} = \frac{1}{\varepsilon_{n\ell}} \frac{df}{dw}$$

where $\sigma^{(\text{PI})}(n\ell)$ is the photoionization cross section and

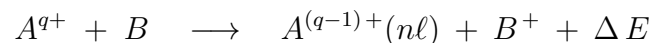
- **Binary-encounter-dipole (BED) approximation:** In the non-relativistic formulation, the partial EII cross section then becomes:

$$\sigma^{(\text{EII: partial BED})} = \frac{\pi a_o^2 q}{\varepsilon_{n\ell}^2 (t + u + 1)} \left[D(t) \ln t + \left(2 - \frac{N_i}{q} \right) \left(1 - \frac{1}{t} - \frac{\ln t}{t + 1} \right) \right], \quad D(t) \equiv \frac{1}{q} \int_0^{(t-1)/2} dw \frac{1}{w + 1} \frac{df(w)}{dw}.$$

13.2.d. Charge-exchange cross sections

Charge-exchange:

- **Charge exchange (CX):** In many astrophysical environments, CX collisions occur when a projectile ion captures an electron from some neutral target atom. If we restrict ourselves to the (dominant) single-electron capture (SEC), process can be summarized as



for the capture into the shell $(n\ell)$, and where ΔE refers to the released kinetic energy in the center-of-mass system.

- ***n*-resolved CX cross sections:** In ion-atom collisions, the charge exchange leads most likely to electrons with principal quantum number n

$$n = \sqrt{\frac{I_H}{I_{\text{target}}}} q^{3/4},$$

where I_{target} is the ionization potential of the target (in units of I_H , the Rydberg unit) and q the charge state of the projectile. This simple scaling tells that electron are mainly captured into shells with $n = 3.5$ for collisions with He and into $n = 4.5$ for collisions of Ne^{8+} with H_2 (Xu *et al.*, 2021).

- **Charge exchange (CX):** Charge exchange or charge transfer is an important process in astrophysics in order to determine the ionization balance and emissivity for a range of terrestrial and astrophysical plasmas. For different environments, the charge transfer proceeds more rapidly than the radiative and dielectronic recombination and, hence, reduces the mean charge state of the ions. It is often also much faster than the electron-impact ionization and photoionization which increase the charge state.
- **CX plasma rate coefficients:** Kingdon (1995) calculates charge transfer rate coefficients for selected reactions between neutral hydrogen and several ions by using the Landau-Zener approximation and for rather a wide range of astrophysically relevant temperatures.
- **Charge exchange (CX) probability in the Landau-Zener approach:** While quantum calculations have been carried out for a few selected collision systems, useful results can be obtained also by using the Landau-Zener approach. In this approach, the probability for a reaction

is given by (Kingdon 1995; Bates and Moiseiwitsch, 1954)

$$p \equiv e^w = \exp \left(\frac{\pi^2 [\Delta V(R_o)]}{h v \left[\frac{d}{dR} (H_{11} - H_{22}) \right]_{R_o}} \right),$$

where $\Delta V(R_o)$ is the separation of the potential at the position of distance R_o of avoided crossing, v the radial component of the relative velocity of the collision partners, and H_{11}, H_{22} the incoming and outgoing diabatic potential curves if no interaction and rearrangement of the active electron would occur. With this reaction probability p , the corresponding reaction cross-section as function of the collision energy E is given by

$$\sigma^{(\text{CX})}(E) = 4\pi R_o^2 p_o (1 + \lambda) \int_1^\infty dx (1 - e^{-wx}) \frac{e^{-wx}}{x^3}, \quad \lambda = \frac{H_\infty - H_{11}(R_o)}{E}$$

where p_o the fraction of initial (molecular) states that also contribute to the final states.

- CX cross sections for the collision of hydrogen with different ions: cf. Figure 13.3.

Multichannel Landau-Zener (MCLZ) approach:

- Multichannel Landau-Zener (MCLZ) approach: The MCLZ approach has been applied to compute total, shell-resolved as well as term-resolved CX cross sections. The MCLZ approach is efficient and provides good estimates. More elaborate methods include the molecular-orbital close-coupling (QMOCC) approximation but which comes for the price of high computational and conceptional efforts.
- Shell distribution of the captured electron: The Landau-Zener approach assumes some basic knowledge of the (sub-) shell distribution of the captured electron; useful distributions include the statistical, the low-energy, the separable and the modified low-energy ℓ -distributions

13. Semiempirical estimates

| Ion | State | 0.2 eV | 0.5 eV | 1.0 eV | 2.0 eV | 5.0 eV | Ion | State | 0.2 eV | 0.5 eV | 1.0 eV | 2.0 eV | 5.0 eV |
|------------------|--|----------|---------|---------|----------|----------|--|--|----------|----------|----------|----------|----------|
| Be ⁺⁴ | 3s ² S | 2.16(0) | 3.66(0) | 6.29(0) | 1.05(1) | 1.75(1) | ⁽² P _{1/2})3d ³ D ^o | ⁽² P _{1/2})3d ³ D ^o | 1.08(-1) | 2.57(-1) | 6.22(-1) | 1.50(0) | 3.85(0) |
| | 3p ² P ^o , 3d ² D | 2.19(0) | 3.71(0) | 6.36(0) | 1.06(1) | 1.75(1) | | 3d ¹ P ^o | 2.21(-1) | 4.33(-1) | 8.57(-1) | 1.66(0) | 3.27(0) |
| B ⁺⁴ | 2p ¹ P ^o | 8.64(-1) | 1.36(0) | 2.17(0) | 3.35(0) | 5.07(0) | ⁽² P _{1/2})4s ¹ P ^o | ⁽² P _{1/2})4s ¹ P ^o | 9.29(-1) | 5.66(-1) | 3.97(-1) | 2.80(-1) | 1.77(-1) |
| F ⁺³ | ⁽¹ D)3s ² D | 9.75(-1) | 1.99(0) | 3.22(0) | 4.61(0) | 6.07(0) | | 4s ³ P ^o | 7.31(0) | 4.49(0) | 3.16(0) | 2.24(0) | 1.43(0) |
| | 3p ² S ^o | 6.33(-1) | 1.20(0) | 1.85(0) | 2.54(0) | 3.19(0) | Ca ⁺³ | 4s ³ P ^o | 3.19(-2) | 1.87(-1) | 6.88(-1) | 2.07(0) | 6.01(0) |
| F ⁺³ | 3p ⁴ D ^o | 2.45(1) | 2.57(1) | 2.57(1) | 2.43(1) | 2.08(1) | | 4s ¹ P ^o | 3.57(-1) | 9.66(-1) | 1.94(0) | 3.36(0) | 5.40(0) |
| | 3p ⁴ P ^o | 3.37(1) | 2.88(1) | 2.51(1) | 2.12(1) | 1.61(1) | Ca ⁺⁴ | 4p ³ S | 3.72(-2) | 2.32(-2) | 1.63(-2) | 1.15(-2) | 7.28(-3) |
| F ⁺³ | 3p ² D ^o | 9.92(0) | 6.65(0) | 4.94(0) | 3.64(0) | 2.41(0) | | 4p ⁴ P ^o | 1.26(-4) | 6.26(-4) | 3.50(-3) | 2.19(-2) | 1.87(-1) |
| | 3p ⁴ S ^o | 4.88(0) | 3.19(0) | 2.33(0) | 1.69(0) | 1.10(0) | 4p ⁴ D ^o | 4p ² P ^o | 3.68(-3) | 1.36(-2) | 5.36(-2) | 2.20(-1) | 1.10(0) |
| F ⁺³ | 3p ² P ^o | 2.44(0) | 1.54(0) | 1.09(0) | 7.77(-1) | 4.95(-1) | | | | | | | |

Figure 13.3.: Cross-sections in 10^{-16} cm^2 ; from Kingdon (1995).

given by

$$W^{(\text{statistical})}(n\ell) = \frac{2\ell + 1}{n^2}, \quad E_i \gtrsim 10 \text{ keV/u}$$

$$W^{(\text{low energy})}(n\ell) = (2\ell + 1) \frac{[(n-1)!]^2}{(n+\ell)! (n-1-\ell)!}, \quad E_i \lesssim 10 \dots 100 \text{ keV/u}$$

$$W^{(\text{modified low energy})}(n\ell) = \ell (\ell + 1) (2\ell + 1) \frac{(n-1)! (n-2)!}{(n+\ell)! (n-1-\ell)!}$$

$$W^{(\text{separable})}(n\ell) = \frac{2\ell + 1}{q} \exp\left(\frac{-\ell(\ell+1)}{q}\right).$$

The modified low-energy distribution gives a *zero* occupation of *s*-states, while the separable distribution depends on the charge *q* of the

incident projectile. However, none of the distribution functions has an explicit dependence on collision energy.

X-ray spectra following charge-exchange (CX):

- **Charge exchange (CX):** CX is an important process for modeling the x-ray spectra from different astrophysical objects. Such CX spectra have been observed, for example, by the Chandra, XMM-Newton, and Suzaku x-ray observatories and will be recorded by forthcoming astrophysical missions. At present, a detailed understanding of the observed x-ray spectra is often hampered, however, by the incompleteness and uncertainty of the available atomic and molecular data for CX (and other processes). Indeed, the CX atomic data are often insufficient in order to approve the completeness and validity of the applied models.
- **Landau-Zener theory for CX:** To estimate total, shell-resolved or even term-resolved CX cross sections, the Landau-Zener theory has been applied for many different ion-target charge-exchange collisions. When combined with a proper cascade model for the subsequent x-ray emission, these estimates facilitate the generation of synthetic x-ray spectra.
- **Charge exchange (CX):** The CX process has been found essential for the x-ray emission from quite different astrophysical environments, such as comets, supernova remnants, heliosphere, astrospheres of stars and, more general, highly ionized regions of interstellar medium (Mullen *et al.*, 2016).

13.3. Further estimates on atomic properties, not yet considered in JAC

13.3.a. Electron and positron stopping powers (StoppingPower)

Property & notations:

- Stopping power: due to the penetration of electrons and positrons through matter: $A^{(*)} \dots$.

Motivation:

- Stopping powers of matter for electrons are important for many applications involving energy deposition. In radiation physics, chemistry, biology and medicine, it is important to have simple but accurate estimates about the stopping power of energetic electrons in various media for (Gümüs, 2005).
- Until the present, no simple and practical model exists for the stopping power of electrons with energies below 10 keV.

Approximate stopping power formulas:

- The stopping power of materials arise from two types of processes, namely collisional and radiative processes. The collisions of the incident particles with the target material is most important and mainly arises from collisions between the incident particles and the atomic electrons.

$$\frac{dE}{dx} = \left(\frac{dE}{dx} \right)^{\text{(collision)}} + \left(\frac{dE}{dx} \right)^{\text{(radiative)}}$$

- For incoming electrons, a modified collisional stopping power formula for incoming electrons can be written as given by Sugiyama (1985) or Rohrlich and Carlson (1954)
- Full Bethe-Bloch formula:

$$-\frac{dE}{dx} = \left(\frac{e^2}{4\pi\epsilon_0} \right) \frac{4\pi z^2 N_A Z \rho}{mc^2 \beta^2 A} \left[\ln \left(\frac{2mc^2 \beta^2}{I} \right) - \ln(1 - \beta^2) - \beta^2 \right]$$

- **Energy loss of fast electrons by Coulomb scattering:** The energy loss of fast electrons by Coulomb scattering with thermal electrons has been modeled by Kozma and Fransson (1992) as

$$L^{(e^- : \text{Coulomb})}(E) = - \left(\frac{dE}{dx} \right)^{(e^- : \text{Coulomb})} = n_e \frac{2\pi e^4}{E} \ln \left(\frac{2E}{\xi} \right), \quad E > 14 \text{ eV}$$

$$L^{(e^- : \text{Coulomb})}(E) = - \left(\frac{dE}{dx} \right)^{(e^- : \text{Coulomb})} = n_e \frac{2\pi e^4}{E} \ln \left(\frac{m v^3}{\gamma e^2 \omega_p} \right), \quad kT \ll E < 14 \text{ eV}$$

$$\xi = \hbar \omega_p = \hbar \sqrt{\frac{4\pi n_e e^2}{m}},$$

where γ is the Euler constant, and where the logarithms are the only places at which the total density enters the energy loss. This makes the energy loss of electrons rather insensitive to the value of the total electron density.

- **Stopping power for electrons:** The stopping power for relativistic electrons with mass m_o and kinetic energy T and total energy E is given by the Bethe formula

$$L(E)^{(\text{e: relativistic})} \approx \frac{4\pi Z e^4}{m v^2} \left[\ln \left(\frac{\sqrt{m v^2 T}}{\sqrt{2} \langle I_p \rangle \sqrt{1 - \beta^2}} \right) - \left(\sqrt{1 - \beta^2} - \frac{1 - \beta^2}{2} \right) \ln 2 + \frac{1 - \beta^2}{2} + \frac{1}{16} (1 - \sqrt{1 - \beta^2})^2 \right],$$

where Z is the charge of the target ion, $\langle I_p \rangle$ is the mean ionization energy of the stopping material whose values can be taken from the ESTAR data base.

13.3.b. Stopping power of multiply-charged ions

Motivation:

- **Stopping power of multiply-charged ions:** The energy loss and the range of penetration of multiply-charged ions in matter is relevant for different fields, from radiation damage and dosimetry to radiation chemistry and biology, to nuclear and health physics, and at several places in science and technology (Ziegler and Manoyan, 1988).

13. Semiempirical estimates

- **Stopping power of multiply-charged ions:** The stopping power pf medium and heavy ions generally depends on the charge and velocity of the incident ions. In particular, the velocity need to be compared with the (so-called) Bohr velocity $v^{(\text{Bohr})} \approx 25 \text{ keV/amu}$, i.e. the velocity of electrons in the conduction band of a solid. While ions with $v < v^{(\text{Bohr})}$ undergo adiabatic collisions with the target electrons and, hence, experience only a small stopping power in the material, the stopping power increases for ions with nuclear charge Z with the velocity for $v > v^{(\text{Bohr})}$ until a peak occurs at about $v^{(\text{peak})} \approx 3v^{(\text{Bohr})}Z^{2/3}$. For velocities $v > v^{(\text{peak})}$, the interaction of the ions with the target electrons become less relevant owing to the shorter effective interation time and, thus, the stopping power decreases with increasing velocity of the ions (Ziegler and Manoyan, 1988).
- **SRIM code:** This code estimates stopping powers and ranges for different ions and target materials. Since an earlier version from 1985, a few major upgrades have been published about every six years, and with good number of citations (~ 700) every year. In the SRIM-2010 version, a number of major improvements have been made (Ziegler *et al.*, 2010): (1) Further experimental stopping powers were added to the database and now contains a total of about 28,000 stopping powers; (2) improved corrections were made for the stopping power of ions in various compounds; (3) a number of additional computations of stopping powers have been carried out for heavy ions and now lead to more accurate predictions; (4) the development of a self-contained SRIM module for the stopping powers and range values of ions that can be invoked by other software tools; (5) incorporation of interatomic potentials for selective ion-atom collisions.

Empirical rules:

- **Stopping power of ions in different target materials:** Apart from the charge and velocity of the incident ions, the stopping power also depends on the target materials. For a hydrocarbon target gas, the stopping power can be derived approximately from the stopping powers of pure carbon and hydrogen targets by following **Bragg's empirical rule**. A number of earlier works discussed the possibility of finding the stopping power for other targets by using the results of hydrocarbon target gases.
- **Empirical Bragg rule for stopping powers:** This rule tells that the stopping power of a compound target can be estimated by using a linear combination of the stopping powers of the individual elements. While this rule has been found reasonably accurate within about 20 %, all further improvements of this rule failed since the stopping power depend of course also on the detailed electronic structure and the excitation energies in the target.
- **Sigmund's theory of stopping power (1982):** This theory allows for rather arbitrary electronic configurations of the target, and it also takes the detailed internal motion of the electrons into account. This theory has been applied by Sabin and coworkers to evaluate stopping powers for both, individual elements and for the stopping of protons in hydrocarbons. This theory often predicts stopping powers which agree with experiment by a few percent.

- **Brandt-Kitagawa rules:** Ziegler and Manoyan (1988) apply the (so-called) Brandt-Kitagawa rules in order to apply the known stopping powers *one* ion to other ions. In practice, these rules scale the proton stopping powers to those of other ions at the same velocity by making a few simple assumptions: (i) The heavy ions will loose all electrons that are slower than the velocity of the incident ion relative to the target material; (ii) the size of the ions shrinks due to the electron loss to the size of hydrogenic ions of charge $Z^{(\text{eff})}$. – However, the presentation and notation by Ziegler and Manoyan (1988) is quite cumbersome, although the parametrizations look overall rather simple. Moreover, all the write-ups by Ziegler (1988) and by Ziegler and coworkers (1999, 2010) are rather sophisticated and do not make use of standard atomic notations.
- **Stopping power at high ion velocities:** Two assumptions are often made for light ions with incident velocities much higher than those of the projectile electrons: (i) All electrons are stripped off the ions; (ii) even light and medium-heavy ions are much heavier than the target electrons. These assumptions apply for light ions with incident energies between 1 MeV/u and 10 GeV/u.

Empirical theories:

- **Bohr's model for the stopping power of ions in matter:** Following Bohr, the energy loss of ions, passing through matter, can be divided into two contributions: (i) a nuclear contribution due to the (positive) charge of the ions in the material and (ii) due to the (quasi-) free electrons of the material, and which is often dominant. Bohr's considerations are mainly based on the relative masses and the abundances of the target electrons and ionic cores. For incident ions with nuclear charge Z and valence electron with orbital frequency ω , a simple model gives rise to the energy loss that can be extended towards relativistic energies ($\gamma = 1/\sqrt{1 - v^2/c^2}$) (Ziegler 1999)

$$\frac{dE}{dx}^{(\text{non-relativistic})} = 4\pi Z^{(\text{target})} \frac{Z^2 e^4}{m v^2} \ln\left(\frac{m v^3}{Z e \omega}\right) \implies \frac{dE}{dx}^{(\text{relativistic})} = 4\pi Z^{(\text{target})} \frac{Z^2 e^4}{m v^2} \ln\left(\frac{\gamma^2 m v^3}{Z e \omega}\right)$$

13.3.c. Stark broadening of spectral lines in plasma

Motivation:

- **Plasma-induced Stark broadening of lines:** For isolated lines and at sufficiently low densities, the Stark broadened line shape is still Lorentzian since only the free electrons are strong perturbers. Then, the modeling of the full-width-at-half-maximum of the lines is reduced

13. Semiempirical estimates

to incorporate the elastic and inelastic scattering of electrons from the lower and upper states to a given transition. The line shape of plasma lines become however (much) more complex, if the dynamics of the ions can no longer be ignored. Such an ion dynamics requires to combine molecular dynamics simulations for ion microfield distribution with the standard line-shape theory (Gu and Beiersdorfer, 2020).

- **Stark broadening of spectral lines:** This broadening has been found very important in (so-called) DA and DB white dwarf atmospheres.
- **Stark broadening of radiative transitions:** For hydrogen-like ions, the Stark broadening of radiative transitions from or between high- n levels appears to be quite complex and computationally cumbersome. This complexity arises first of all from the large number of levels nearby. To facilitate estimates for the line shapes of these transitions, Stambulchik and Maron (2008) suggest a simple analytical method. The Stark broadening of transitions involving Rydberg states has been utilized for the diagnostics of laboratory and space plasmas, such as for density measurements in tokamak, pinch and laser-produced plasmas, flames, or for the solar and stellar atmospheres.
- Apart from white dwarfs, Stark broadening of spectra is also an important pressure-broadening mechanism for various types of other stars.
- Various semi-empirical calculations of the Stark widths and shifts have been performed in the impact approximation by using Griem's (1968) formula.
- For selected lines, it was shown that Stark broadening can change the observed widths by 10-45 %.

Semi-empirical approximations:

- **Lorentzian profile of isolated lines:** For isolated lines $|\alpha_i J_i\rangle \rightarrow |\alpha_f J_f\rangle$ with level energies E_i and E_f , the line profile is often assumed to be Lorentzian, shifted by the energy d and with the (total) line widths Γ due to the (plasma) Stark broadening.

$$F(\omega) = \frac{(\Gamma/2\pi)}{(\omega - \omega_{if} - d)^2 + (\Gamma/2)^2}, \quad \omega_{if} = \frac{E_i - E_f}{\hbar}.$$

where

- **Energy shift and (total) widths of the Stark-broadened line:** Both, the energy shift d as well as the (total) widths Γ can be expressed in terms of the velocity distribution $f(v)$ of the electrons in the plasma, its density $N^{(\text{elec})}$, the impact parameter b of the incident electrons as well as the elastic and inelastic (electron-impact excitation) cross sections for **excitations of the initial and final levels to neighboured levels**.

$$\Gamma = N^{(\text{elec})} \int dv v f(v) (\sigma^{(\text{elastic})} + \sigma^{(\text{inelastic})}); \quad d = N^{(\text{elec})} \int dv v f(v) \int_{R_1}^{R_{\text{Debye}}} db 2\pi b \sin(\phi_p)$$

and where ϕ_p is a plasma-specific phase shift. Further details on the Stark broadening of spectral lines are given by Dimitrijevich and Sahel-Brechot (1996).

- In 1968, Griem suggested simple semiempirical formulas for the Stark line shift and widths in impact approximation which is based on some original formular by Baranger (1958) as well as an effective Gaunt factor by Seaton (1962) and Regemorter (1962). With these formulas, the Stark linewidths and Stark line shifts can be obtained by:

$$\frac{\Gamma}{[a.u.]} = 8 \left(\frac{\pi}{3} \right)^{3/2} \frac{\hbar}{m a_o} N_e \left(\frac{E_H}{kT} \right)^{1/2} \left[\sum_{i'} |\langle i' | r | i \rangle|^2 g_{se} \left(\frac{E}{\Delta E_{i'i}} \right) + \sum_{f'} |\langle f' | r | f \rangle|^2 g_{se} \left(\frac{E}{\Delta E_{f'f}} \right) \right]$$

$$\frac{d}{[a.u.]} = -8 \left(\frac{\pi}{3} \right)^{3/2} \frac{\hbar}{m a_o} N_e \left(\frac{E_H}{kT} \right)^{1/2} \left[\sum_{i'} \left(\frac{\Delta E_{i'i}}{|\Delta E_{i'i}|} \right) |\langle i' | r | i \rangle|^2 g_{sh} \left(\frac{E}{\Delta E_{i'i}} \right) + \sum_{f'} \left(\frac{\Delta E_{f'f}}{|\Delta E_{f'f}|} \right) |\langle f' | r | f \rangle|^2 g_{sh} \left(\frac{E}{\Delta E_{f'f}} \right) \right]$$

In these formulae, E_H is the hydrogen ionization energy, N_e is the free-electron density of the perturber levels, T is the electron temperature, $E = 3/2 kT$ the mean energy of the perturbing electron and g_{se} , g_{sh} are the effective Gaunt factors which are calculated and tabulated by Griem. These Gaunt factors are slowly varying functions of $x_{j'j}$ where $x_{j'j} = E/\Delta E_{j'j}$ is the energy difference between a perturbing level j' and the perturbed initial/upper (final/lower) level j .

- The atomic matrix elements need often to be obtained from *ab-initio* Hartree-Dirac-Fock computations, and the summation over the levels is obtained by making use of the table by Moore (1958).

13.3.d. Atomic electron-momentum densities

Definition & notations:

- For a given atomic level (αJ) , the (radial electron) momentum density $I(p; \alpha J)$ and the one-electron momentum density $\Pi_{n\kappa}(p; \alpha J)$ and is given by (Koga and Thakkar, 1996)

$$I(p; \alpha J) = 4\pi p^2 \Pi(p; \alpha J), \quad \Pi(p; \alpha J) = \frac{1}{4\pi p^2} \sum_{i=1}^N \langle \psi_\alpha | \delta(p - p_i) | \psi_\alpha \rangle.$$

- The radial one-electron momentum density I is used to calculate the corresponding **moments of the momentum density**

$$\langle p^k \rangle = \int_0^\infty dp p^k I(p; \alpha J), \quad -2 \leq k \leq 4$$

- These moments are often applied in:

- density functional theory: since $\langle p \rangle / \pi$ is close to the Dirac-Slater exchange energy;
- x-ray crystallography: since $\langle p^3 \rangle$ is roughly proportional to the initial value of the so-called Patterson function
- Compton profiles: since $J(q) = \frac{1}{2} \int_{|q|}^\infty dp p^{-1} I(p)$ is twice the peak height of the isotropic Compton profile.

14. Beams of light and particles

Structured beams of light and particles:

- **Vortex beams of particles:** Following the basic concepts of wave mechanics, vortex beams have been generated with electrons and neutrons, and have been proposed for atoms as well. Such beams may help manipulate matter on small length scales. In contrast to light beams, which are known to follow Maxwell's relativistic wave equation, particle beams can be described either by the (non-relativistic) Schrödinger equation or by relativistic wave equation.
- **Nonrelativistic *versus* relativistic description of vortex beams:** A proper description of particle vortex beams depend not only on the energy of the particles but also on the role of spin-orbit interactions. In magnetic fields, for instance, there strong interaction of the spin with the external field suggest to apply Dirac's equation, in which the spin is taken into account right from the beginning.
- **Structure light and particle fields:** has been generated, detected and applied experimentally for more than 25 years. Today, structured light fields with orbital angular momentum (OAM), nondiffraction and self-healing properties can readily be created. This includes also beams of neutron and electrons with well-defined OAM as well as lattices of optical OAM beams. In so-called spin-orbit beams, the orbital degree of freedom is coupled to either the polarization of light or the spin for electrons and neutrons.
- **Light fields with OAM:** Following the pioneering work by Allen and co-workers in the 1990's, the interest on light fields with OAM and how they interact with matter has steadily grown through recent years and now represents a very active field of research.

14.1. Helmholtz wave equation

Propagation of light in free space:

14. Beams of light and particles

- **Helmholtz wave equation:** If we consider the propagation of light in free space, the Maxwell equations simplify and the spatial structure of their solution satisfy the well-known **Helmholtz wave equation**, an elliptic partial differential equation

$$\nabla^2 u(\mathbf{r}) + k^2 u(\mathbf{r}) = 0.$$

This equation readily follows from the (full) time-dependent wave equations due to the **separation of variables**.

- **Time-harmonic solutions of wave equation:** The solution in time is a linear combination of sine and cosine functions with angular frequency ω , while the form of the spatial solution of the Helmholtz equation crucially depends on the given boundary conditions.
- **Harmonic solutions of the Helmholtz equation:**

$$u(\mathbf{r}) = C_1 e^{i\mathbf{k}\cdot\mathbf{r}} + C_2 e^{-i\mathbf{k}\cdot\mathbf{r}}, \quad k = |\mathbf{k}| = \frac{\omega}{c}.$$

- **Vector potential of optical beams:** There are various solutions of the Helmholtz equation known in order to represent the vector potential of optical beams of different kind and spatial structure. These solutions (expressions) generally represent different spatial structures and phases. Below, several of these solution are provided for different beams in terms of the (scalar) amplitudes $u(\mathbf{r})$ of the corresponding light fields.
- **Synonym notions of vortex beams:** helically-phased light beams; optical vortex beams with a field dependence $e^{im\varphi}$,
- **Scalar Helmholtz equation:** Typical paraxial and time-harmonic beam solutions with wave number $k = 2\pi/\lambda$ obey the scalar equation:

$$(\Delta + k^2)\mathcal{E} = 0, \quad \mathcal{E} = u(x, y, z) \exp[i(kz - \omega t)] = u(\rho, \varphi, z) \exp[i(kz - \omega t)].$$

Solutions to this scalar Helmholtz equation are know in cartesian, cylindrical as well as other coordinates.

- **Slowly varying envelop approximation:** In this approximations, one assumes in addition to the scalar Helmholtz equation:

$$\frac{\partial^2 u}{\partial z^2} \ll k^2 u, \quad \frac{\partial^2 u}{\partial z^2} \ll k \frac{\partial u}{\partial z}.$$

Paraxial approximation to the Helmholtz equation:

- **Paraxial approximation:** The Helmholtz equation still represents a rather complicated partial differential equation; in optics, one often has well-defined paraboloidal waves or Gaussian beams, in which the field change along the propagation direction is small when compared to changes perpendicular to the beam axis; $\frac{\partial u}{\partial z} \ll \frac{\partial u}{\partial x}, \frac{\partial u}{\partial y}$.
- For these *paraxial* conditions, the **Helmholtz equation** simplifies to

$$\nabla_{\perp}^2 u(\mathbf{r}) + 2ik \frac{\partial u}{\partial z}(\mathbf{r}) = 0.$$

- **Paraxial approximation:** This approximation assumes that the transverse profile changes only rather slowly along the propagation (z -) direction. This assumption means that the electric and magnetic fields have no longitudinal components in lowest order of the ratio λ/w . The paraxial approximation is often valid if the beam is not tightly focused.
- **Conditions for the paraxial approximation:** The paraxial conditions, that need to be fulfilled by the amplitude function $u(\mathbf{r})$, are often written in the form:

$$\left| \frac{\partial u}{\partial z} \right| \ll |k u| \quad \text{and} \quad \left| \frac{\partial^2 u}{\partial z^2} \right| \ll |k^2 u|.$$

- **Paraxial approximation:** This approximation is obtained if the ansatz $\tilde{u}(\mathbf{r}) = u(\mathbf{r}) e^{ikz}$ is used in the Helmholtz equation and if the term $\sim \frac{\partial^2 u}{\partial z^2}$ is neglected when compared with $\sim \frac{\partial \tilde{u}}{\partial z}$.

14.2. Symmetries of light beams

14.2.a. Orbital and spin angular momentum

Angular momentum (AM) of photons:

- **Angular momentum of photons:** Following Maxwell's theory, the angular momentum quantum numbers of the photon are integers [in units of the Planck constant \hbar] for all (usual) three-dimensional field configurations. However, photons can also have some half-integer total angular momentum, if the light field propagates in reduced dimensions. Such an half-integer quantization of the total angular momentum is known also from the quantum Hall effect and can be detected by means of (so-called) **noise measurements**. For similar reasons, new forms of quantization may arise for photons in a beam, and as known also for electrons in reduced dimensions.
- **Photon propagation in 3 dimensions:** The free (3-dimensional) propagation of photons follows Maxwell's equations and, hence, only the total angular momentum $\mathbf{j} = \mathbf{l} + \mathbf{s}$ and its projection upon the quantization axis $j_z = l_z + s_z$ is conserved because of the rotational invariance of the Maxwell equations.
- **Measurement of the photon's AM:** The angular momenta of photons can be measured by means of a Mach-Zehnder interferometers. Such an interferometer can be applied quite independent of whether the AM is of type spin, orbital or total angular momentum. It is only important that the eigenstates of the light field, associated with some given AM operator, picks up a proper phase factor by passing through the interferometer. This interferometric technique can be generalized also for half-integer and even rational eigenvalues of the AM operator if proper wave plates and prism are applied, such that the spatial and spin components of the light field rotates properly (Ballantine *et al.*, 2016). For example, a half-wave plate reverses the sign of the spin quantum number $\lambda = \pm 1$ but does not affect the orbital angular momentum and, hence, results in a torque of $2\hbar\lambda$ per photon. In contrast, an ideal polarization-preserving Dove prism leads to an inversion of orbital angular momentum and results in a torque of $2\hbar\ell$ per photon (Ballantine *et al.*, 2016).
- **Applications of the AM of photons:** The angular momentum of photons may cause various optomechanical effects in optical trapping as well as support the manipulation of — microscopic and mesoscopic — particles. This angular momentum can be utilized also to remotely detect rotations of light in astronomy at radio-frequencies. In QIP, the angular momentum of light is applied in order to create high-dimensional entanglement, quantum dense coding or for the identification of different objects.
- **Complex Jones vector $\mathcal{E}(t)$:** For a paraxial beam, the two-component complex (Jones) vector field $\mathcal{E}(t)$ generally comprises the amplitudes of both polarizations of the electric field in the plane perpendicular to the beam axis. If polar coordinates (ρ, φ) and a helicity basis is used in this plane, the angular momentum (AM) operators can generate only rotations of the field around the beam axis. For a paraxial beam, this AM operator includes the 3×3 Pauli matrix $s_z = \hbar\sigma_z$, that rotates the polarization direction homogeneously across the

beam. Moreover, the projection of the orbital angular momentum $l_z = -i\hbar \frac{d}{d\varphi}$ rotates the spatial beam profile but leaves the polarization unchanged. Obviously, both of these rotations keep the light field (\mathcal{E} -field) transverse to the beam propagation so that the projections of the spin and orbital angular momenta are conserved independently.

- **OAM versus SAM:** In an optical wave, the spin and orbital angular momentum are conserved, though in general not independently. The conservation of these angular momenta help control light-matter interactions or to elucidate the structure and dynamics of complex systems. It also facilitate the generation of circularly-polarized vortices with tailored orbital angular momentum as well as of harmonic vortices with well-defined OAM and circular polarization

Beams with well-defined OAM:

- **Photons from twisted (OAM) beams:** For a beam with well-defined (projection of the) orbital angular momentum, the relevant quantum numbers are the eigenvalues [in units of \hbar] of the spin and orbital angular momentum operators, l_z and s_z , respectively. While the spin quantum number $\lambda = \pm 1$ characterizes the circular polarization of the beam, the orbital quantum number $\ell = 0, \pm 1, \pm 2, \dots$ typically characterizes the phase $e^{i\ell\varphi}$ of the spatial part of the light field. For paraxial beams, then, the conservation of the (projection of the) total angular momentum, $j_z = l_z + s_z$ still ensures integer eigenvalues (Ballantine *et al.*, 2016).
- The conservation of the total angular momentum $j_z = l_z + s_z$ follows from the rotational symmetry of the Maxwell equations. Since this symmetry is no longer fulfilled for a light beam with a given propagation direction, only the angular momentum (operator) as associated with the propagation of photons in the 2-dimensional cross section of the beam will be conserved owing to the Noether theorem. This angular momentum operator then just generates rotations of the beam around the propagation direction. Moreover, this *restricted* symmetry leads to a new form of total angular momentum with either half-integer or even rational eigenvalues. This quantization of the light field of optical beams can be verified also experimentally by analyzing the noise in the total angular momentum current (Ballantine *et al.*, 2016).
- **Photons from twisted (OAM) beams:** The total angular momentum operator j_z generates simultaneous rotations of the polarization and the spatial part of the light field, although generally through different angles. However, this projection of the total angular momentum is only conserved, e.g. a good quantum number, if the field can be (completely) expanded into eigenfunctions of j_z and if these eigenfunctions are, up to a phase factor, invariant under the associated rotations. For a monochromatic beam, the solutions must then fulfill the eigenvalue equations

$$(l_z + \gamma s_z) \mathcal{E} = j_z^{(\gamma)} \mathcal{E}, \quad \mathcal{E} = c_1 e^{i\ell_1 \varphi} \mathbf{e}_1 + c_{-1} e^{i\ell_2 \varphi} \mathbf{e}_{-1}$$

where \mathbf{e}_1 \mathbf{e}_{-1} are the polarization (unit) vectors in the helicity basis. Moreover, the radial dependence of these eigenmodes is *irrelevant* and omitted from the notation. Since the \mathcal{E} should be unchanged by a complete rotation $(2n\pi)$, both ℓ_1, ℓ_2 must be integer. Since all

14. Beams of light and particles

modes are simply superpositions of two states with definite spin and orbital angular momenta, the gyroscopic factor γ and the eigenvalue of the total angular momentum operators are given by

$$\gamma = \frac{\ell_2 - \ell_1}{2}, \quad j^{(\gamma)} = \frac{\ell_2 + \ell_1}{2}$$

- **SAM versus OAM of twisted light:** For twisted light beams, the relative orientation of the OAM and SAM of the photons becomes important. If, in particular, OAM and SAM are antiparallel to each other, a rather strong longitudinal field component usually arise and makes the light-matter interaction different for beams with parallel or antiparallel momenta (Quinteiro *et al.*, 2017). Laguerre-Gaussian (LG) beams are known to have a non-negligible longitudinal component when spin and orbital angular momenta are opposite to each other. This can be seen from a *transverse* cut of the electric field for parallel or antiparallel OAM and SAM.

14.2.b. Torus-knot angular momentum

Coordinated rotations (CR) of light fields:

- **Coordinated rotations (CR) of light fields:** These rotations describe symmetry transformations in which the spatial component of the light field is rotated by some azimuthal angle ϕ_o around the beam axis (z axis), while the electric-field vector (polarization) is rotated by the angle $\gamma \phi_o$. Here γ is generally referred to as **gyroscopic factor** or **coordination parameter**.
- **Coordinated rotations (CR) of light fields:** These symmetry operations are generated by the linear combination of the OAM and SAM projection operators, $j_z^{(\gamma)} = l_z + \gamma s_z$, and whose (eigen-) values are independently conserved only within the paraxial regime. For paraxial beams, therefore, not only the eigenvalues ℓ and λ are good quantum numbers but also the **torus-knot angular momentum** $j^{(\gamma)}$, although these values need no longer to be integer. The coordinated rotations are sometimes said to induce Möbius-stripe topologies.
- **Gyroscopic factor:** For monochromatic light, the gyroscopic factor γ can take only integer or half-integer values and can be mathematically related to the topology of a Möbius strip. For bichromatic fields, in contrast, the gyroscopic factor γ can take all rational values, at least in principle.
- **Monochromatic bicircular fields:** For monochromatic light, the gyroscopic factor γ for a coordinated rotation of the light field must be either integer or a half-integer, since the polarization ellipse of the overall beam coincides with itself only for a rotation of $n\pi$ after each half-cycle, $\gamma \propto n/2$. However, this restriction does not apply to general electromagnetic fields. For bicircular fields, of course, only

bichromatic superpositions need to be considered in order to analyze all the possible coordinated rotations for counter-rotating bicircular fields.

- **Symmetries of the electric-field:** Even for a monochromatic beam, the real-valued electric field $\mathcal{E}(\mathbf{r}, t) = \Re(\mathcal{E}^{(\text{complex})} e^{-i\omega t})$ is generally not an eigenstate of the torus-known angular momentum operator (symmetry operator). A well-defined TKAM can only be assigned if the optical field fulfills the combined symmetry and time-translation operation of a coordinated rotation (Pisanty *et al.*, 2019)

$$R(\gamma\alpha) \mathcal{E}(R^{-1}(\alpha)\mathbf{r}, t) = \mathcal{E}(\mathbf{r}, t + \tau\alpha),$$

and where τ [time] is a constant and $R(\alpha)$ a 2×2 rotation matrix for a rotation by the angle α of the coordinates perpendicular to the beam axis.

Beams with well-defined torus-knot angular momentum:

- **Beams with well-defined torus-knot angular momentum:** Pisanty *et al.* (2019) showed that the eigenvalues $j^{(\gamma)}$ of the torus-knot angular momentum, known also as the **torus-knot topological charge**, are conserved for beams with a properly defined gyroscopic factor $\gamma \in \mathbb{Q}$. This topological can help classify the high-harmonics as generated from such bichromatic and bicircular beams. Since TKAM beams are invariant under coordinated rotations for the associated coordination factor $\gamma \in \mathbb{Q}$, the non-linear HHG process will preserve also the torus-knot topological charge, in addition to the conserved charges of the OAM and SAM.
- **Beams with well-defined TKAM:** These beams are not only invariant under coordinated rotations but also associated with a *combined* angular momentum operator $j_z^{(\gamma)} = l_z + \gamma s_z$ of the (projections of the) orbital l_z and spin s_z angular momentum operators with regard to the beam axis. In the paraxial approximation, both the OAM and SAM (projections) are conserved and can be measured independently.
- **Symmetry classification of torus knots & Lissajous figures:** These knots can be characterized by two indices, namely the **symmetry order m of the (polarization) Lissajous figure** itself as well as the **spatial rotation number n** , how often this Lissajous figure rotates if one goes once around the beam axis within the cross section of the beam. For each symmetry order m , the spatial rotation number n characterizes the spatial topology of the optical field (beam).
- **Construction of the torus:** From the Ferris-wheel diagram, the topology of a torus can be immediately read off if one follows the tips of the trefoil and fold this together after going once around the beam axis. This twists the m tips of the tre-foil n times around and can be understood as m lines (symmetry order) on a torus that crosses its – inner – equatorial plane at n **torus** knots (spatial rotations). A similar analysis can be made for the eigenvalues of the torus-known angular momentum operator.

14. Beams of light and particles

- **Torus-knot angular momentum:** Because of the algebraic identification of beam topology and the operator for a coordinates rotation, we can refer to the subgroup generator $j^{(\gamma)}$ as the torus-knot angular momentum (TKAM). The name of this (formal) angular momentum is derived from the close relation of the generated coordinated rotation and the topology of the torus.
- **Concept of torus knot:** This concept appears in different optical situations, for instance, for generating special optical vortices (or so-called C-lines) and field lines. However, neither the torus nor the knots with its equatorial plane does exist as real-space 3D object for a given beams, although this concept help characterize the topology of beams with regard to their properties such a as paraxial, the possible Lissajous-type figures and others.

$\omega - 2\omega$ bichromatic bicircular beams:

- **$\omega - 2\omega$ bichromatic bicircular fields:** These bichromatic fields with counter-rotating right- (\circlearrowleft) and left-handed circular (\circlearrowright) polarizations can be characterized by their *two* (well-defined) orbital angular momenta, ℓ_1 and ℓ_2 , or by just *one* torus-knot angular momentum $j^{(\gamma)} = j^{(\gamma)}(\ell_1, \ell_2)$. Indeed, the particular combination of (ℓ_1, ℓ_2) OAM uniquely determines the allowed gyroscopic factor γ for which the overall bicircular beam is invariant with regard to a coordinated rotation of the spatial and spin-components of the light beam.
- **TKAM charges of bichromatic beams:** For a bichromatic beam, the two (monochromatic) driving fields must have different TKAM charges in order to fullfill the overall dynamic symmetry of a coordinated rotation as the local phases of the light field depend on the frequencies.
- **$\omega - 2\omega$ bichromatic bicircular fields:** The two frequency components of a $\omega - 2\omega$ bichromatic and bicircular beam with well-defined OAM have the TKAM quantum numbers $j_1^{(\gamma)} = \ell_1 + \gamma$ and $j_2^{(\gamma)} = \ell_2 - \gamma$. For the q -t harmonic, this gives rise to the TKAM value $j_q^{(\gamma)} = q j_1^{(\gamma)}$, i.e. in a **linear increase of the TKAM with the order q of the harmonic**. Of course, the orbital angular momenta ℓ_q can be obtained directly from the torus-knot angular momentum $j_q^{(\gamma)}$, and if the assigned (right- and left-handed) polarization of the $\omega - 2\omega$ incident beam, e.g. $\text{LG}_{\ell_1, p_1}^{\omega \circlearrowleft} \oplus \text{LG}_{\ell_2, p_2}^{2\omega \circlearrowright}$, is taken into account.
- **$\omega - 2\omega$ bichromatic bicircular fields with $\ell_1 = \ell_2 = 1$:** For $\text{LG}_{\ell_1, p_1}^{\omega \circlearrowleft} \oplus \text{LG}_{\ell_2, p_2}^{2\omega \circlearrowright}$ bicircular beam, one finds: $j_1^{(\gamma)} = 2/3$, $j_q^{(\gamma)} = 2/3q$.
- **$\omega - 2\omega$ bichromatic bicircular fields:** Counter-rotating circularly polarized beams at different frequencies help construct beams of light that are **invariant under coordinated rotations** for quite arbitrary rational gyroscopic factors γ . This additional freedom of bichromatic field for choosing a well-defined TKAM arise from the higher internal symmetry of these bichromatic superpositions. It was shown that these beams can be classified by means of the topology of a torus knot and, more specifically, by the eigenvalues $j^{(\gamma)}$ of a (so-called) torus-knot angular momentum (operator) $j_z^{(\gamma)} = l_z + \gamma s_z$.
- **$\omega - 2\omega$ bichromatic bicircular fields:** These beams forms so-called **bicircular trefoil-shaped Lissajous figures**.

- **$\omega - 2\omega$ Bichromatic bicircular fields:** The tre-foil polarization figure of these beams rotates smoothly when one goes once around the beam axis (in the plane perpendicular to it). This can be read off immediately from a so-called **Ferris-wheel diagram** which display the Lissajous figure at different angles φ in the cross section of the beam. From such figures, it can be seen also that the internal rotation of the Lissajous figure induces a Möbius-strip topology to the polarization.
- **$\omega - 2\omega$ bichromatic bicircular fields:** The concept of monochromatic bicircular fields can be generalized towards bichromatic bicircular fields which posess a high symmetry order m in their (polarization) Lissajous figures. For a $\omega - 2\omega$ bichromatic bicircular beam with a right-circularly polarized beam component at fundamental frequency ω and a left-circularly polarized second harmonic, for example, the fundamental component rotates counterclockwise by 120° , while the 2ω component rotates clockwise by 240° . Therefore the polarization (electric-field vector) at all spatial points in the beam is symmetric with regard to a rotation by $2\pi/3 = 120^\circ$.
- **$r\omega - s\omega$ bichromatic bicircular fields:** A $r\omega - s\omega$, bichromatic beam with coprime numbers r, s generally has a $(r+s)$ -fold symmetric Lissajous figure.
- **$r\omega - s\omega$ bichromatic bicircular fields:** For such a bichromatic beam with orbital angular momenta ℓ_r and ℓ_s of the right- and left-circularly polarized field components, the winded tips still confine to the surface of a torus, from which the two characteristic symmetry numbers can be read off: (1) the symmetry number $m = r + s$ as number of points that appear with fixed angle φ_o in the cross each cross section of the torus and that is equal to the lobes of the Lissajous figure; (2) a signed (spatial) number $n = r\ell_r - s\ell_s$ for the spatial symmetry. While $|n|$ denotes the number of crossings in the – inner – equatorial plane of the torus, the characerizes the phase changes of the right- and left-circularly polarized beam components.

14.2.c. Chirality of beams

Optical chirality:

- **Optical chirality (OC):** OC has been introduced as measure of the local and instantaneous density of chirality of electromagnetic waves. This concept has been found useful to define **superchiral fields** than exhibit a larger OC and found for circularly-polarized fields. These superchiral fields show particularly strong interactions with chiral molecules. For instance, HHG in chiral media also appears to be sensitive to the optical chirality.
- **Optical chirality (OC):** The OC of an light field is defined in SI units as (Neufeld and Cohen, 2018)

$$C = \frac{\epsilon_o}{2} \boldsymbol{\mathcal{E}} \cdot \boldsymbol{\nabla} \times \boldsymbol{\mathcal{E}} + \frac{1}{2\mu_o} \boldsymbol{\mathcal{B}} \cdot \boldsymbol{\nabla} \times \boldsymbol{\mathcal{B}} .$$

14. Beams of light and particles

➤ **Optical chirality for a circularly-polarized, transversal and paraxial beam:** The OC for such a beam is obtained by omitting the z -component and the transverse derivatives (Neufeld and Cohen, 2018)

$$\begin{aligned}
 C^{(\text{SAM})} &= \frac{\epsilon_o}{2} (\mathcal{E}_y \partial_z \mathcal{E}_x - \mathcal{E}_x \partial_z \mathcal{E}_y) + \frac{1}{2\mu_o} (\mathcal{B}_y \partial_z \mathcal{B}_x - \mathcal{B}_x \partial_z \mathcal{B}_y) \\
 &\approx \frac{\epsilon_o}{2c_o} (\mathcal{E}_y \partial_t \mathcal{E}_x - \mathcal{E}_x \partial_t \mathcal{E}_y) + \frac{1}{2\mu_o c_o} (\mathcal{B}_y \partial_t \mathcal{B}_x - \mathcal{B}_x \partial_t \mathcal{B}_y) \quad \text{for a slowly varying envelope.} \\
 &= \frac{\epsilon_o}{2c_o} \mathcal{E}^2 \partial_t \phi(t) + \frac{1}{2\mu_o c_o} \mathcal{B}^2 \partial_t \left(\phi(t) + \frac{\pi}{2} \right), \quad \phi(t) = \tan^{-1}(\mathcal{E}_y(t)/\mathcal{E}_x(t))
 \end{aligned}$$

where, in the last line, $\phi(t)$ is the angle of the electric field \mathbf{E} with regard to the x -axis, while the magnetic field vector is rotated by $\pi/2$.

14.3. Light beams

Light beams:

- **Characterization and properties of beams:** In studying light-matter interactions, **light beams** play a major practical role and, hence, their characterization and properties are very important in order to understand the details of the interaction.
- **Beams from applications:** Light beams are usually formed when the em field from a given source is projected by filters and blends into a beam. In some lighting devices, lamps or parabolic reflector are used to produce an artificially light beam with a more or less large divergence (for example, car headlights, spotlights, ect.).
- **Experimental beam parameters:** The geometry and behavior of a Gaussian beam are governed by a set of beam parameters which are defined slightly different for different kinds of beams but which are often used to characterize the beams. These beam parameters include:
 - **Beam width:** There are over five definitions of beam width.
 - **Beam quality:** Quantified by the beam quality parameter, M₂.
 - **Beam divergence:** This is a measure of how the beam spreads with distance with regard to the focus plane.
 - **Beam profile:** A beam profile is the 2D intensity plot of a beam at a given location along the beam path. A Gaussian or flat-top profile is often desired for many applications. The beam profile indicates nuisance due to high-order spatial modes in a laser cavity as well as hot spots in the beam.
 - **Beam astigmatism:** A beam is called **astigmatic** when the vertical and horizontal focus of the beam is placed at different locations along the beam path.
 - **Beam wander or jitter:** The amount by which the centroid or peak value of the beam profile moves with time.

Twisted (vortex) light beams:

- Charles Darwin (1932; 1887-1962) was one of the first who worked on **light with a spatial structure of the phase**.
- For circularly-polarized plane-wave light, the photons carry a projection of the angular momentum $\Delta L_z = \pm \hbar$ upon the propagation direction.
- **Polarization state of a light beam:** In 1892, Poincare showed that the state of polarization of a light beam can be described as a point on the surface of a unit sphere now known as the Poincare sphere.

14.3.a. Gaussian beams

Characterization and use:

- **Gaussian beam:** In optics, a Gaussian beam is a beam of electromagnetic radiation whose transverse electric field amplitude and, hence, its intensity distributions are approximately described by some Gaussian distribution.
- Both, planes waves and Gaussian beams are solutions of the Maxwell equation and the homogenous wave equation they both generally possess a **polarization** but can be readily described in terms of complex amplitudes.
- **Complex-valued electric field amplitude $u(\mathbf{r})$:** In a Gaussian beam, the electric field amplitude

$$u(\rho, z) = u_0 \frac{w_0}{w(z)} \exp\left(\frac{-\rho^2}{w^2(z)}\right) \exp\left(-ikz - ik\frac{\rho^2}{2R(z)} + i\zeta(z)\right)$$

obeys the paraxial Helmholtz equation. This amplitude is sufficient in order to describe the properties of the beam since the electric field and magnetic field propagate together and obey the same wave equation.

- **Characteristic parameters:** In the definition of the electric-field amplitude above, we have
 - ρ ... radial distance from the center axis of the beam;
 - z ... the axial distance from the beam's narrowest point (the **beam waist**),
 - $k = \frac{2\pi}{\lambda}$... the wave number (in radians per meter), $E_0 = |E(0, 0)|$
 - $w_0 = w(0)$... the waist size,
 - $w(z)$... the radius at which the field amplitude drop to $1/e$ and, hence, the intensity to $1/e^2$ at axis with regard to $w_0 = w(0)$,
 - $R(z)$... the radius of curvature of the beam's wavefronts,
 - $\zeta(z)$... the Gouy phase shift, an extra contribution to the phase that is seen in Gaussian beams.
- **Gaussian beam (GB):** The GB satisfy the free-space paraxial wave equation and are given by

$$\text{GB}(\mathbf{r}) = \frac{w_o}{w(z)} \exp\left[\frac{-r^2}{w^2(z)} + i\frac{k r^2}{2 R(z)} - i\psi(z)\right],$$

with the z -dependent beam waist $w^2(z) = w_o^2 \left(1 + \frac{z^2}{z_R^2}\right)$, the Rayleigh range $z_R = k w_o^2 / 2$, the radius of the phase-front curvature $R(z) = z + \frac{z_R^2}{z}$ and the Gouy shift $\psi(z) = \arctan(z/z_R)$. These GB can be utilized also to construct an ansatz for the free-space paraxial wave equation in elliptical coordinates.

- In fact, many lasers emit beams with roughly a Gaussian profile; these beams are often called the TEM₀₀ fundamental modes of the laser's optical resonator. **Gaussian beams form a widespread model in laser physics.**

14.3.b. Vortex beams. Characterization and properties

General remarks:

- The recent years have seen a tremendous effort in generating and manipulating vortex beams together with a good number of new or promising applications, including the capture, manipulation and transport of nanoscopic particles (optical tweezer), high-resolution microscopy or for data transmission.

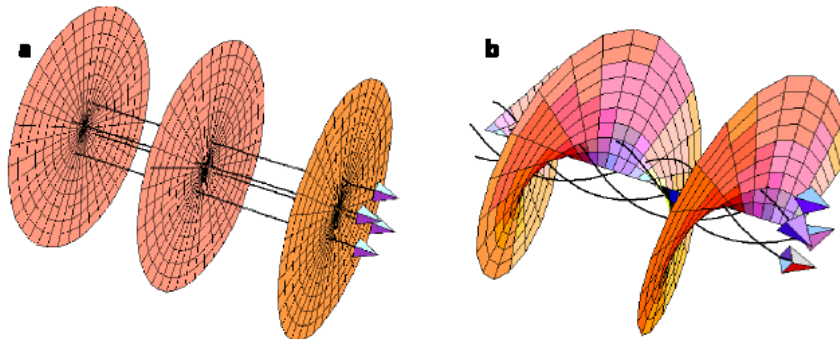


Figure 14.1.: Laser beams usually have planar wavefronts with wavevectors parallel to the beam axis. Beams with helical wavefronts have wavevectors which spiral around the beam axis and give rise to an orbital angular momentum; from Padgett and Allen (2000).

- Twisted photons carry both, spin angular momentum (SAM) as well as orbital angular momentum (OAM) along their propagation direction.
- **Topological charge** The z -projection of the OAM, m , is often called the topological charge or the **winding number of the beam**. This charge describes the number of the 2π windings of the helical phase around the vortex in one wavelength.
- **Synonym notions of vortex beams:** helically phased light beams; optical vortices with a field dependence $e^{im\varphi}$.

14. Beams of light and particles

- Optical vortex beams are well-known and have been routinely used for the last 20 years; a first demonstration dates back to Durnin *et al.* (1987).
- For optical vortices, charge values of $m \leq 5000$ have been realized (Shen *et al.*, 2013).
- Reviews on optical vortex beams are given by Allen *et al.* (1999); Franke-Arnold *et al.* (2008), Zhan (2009) and Yao and Padgett (2011).

Characterization of vortex beams:

- A vortex state of light carries a well-defined projection of the orbital angular momentum (OAM) with respect to the beam axis.
- **Wave functions:** $\sim e^{im\varphi}$ are eigenfunctions of $\ell_z = \frac{\partial}{\partial\varphi}$.
- **Photon field:** For a quantized radiation field, each particle also carries a projection $m\hbar$ of the OAM, that is part of the total angular momentum. In general, the spin and orbital angular momentum cannot be separated.
- In the paraxial approximation, the spin and OAM longitudinal components of the vortex state can be separated from each other. Beyond the paraxial limit, however, the spin-orbit interaction does not allow a simple separation of the spin and orbital angular momentum.
- **Intensity profile of structured light:** For twisted light (beams), the intensity profile not uniform but is often described by concentric (and alternating) dark and bright rings. Apart from the intensity, such complex profiles also occur for the (direction of the) energy flow within the beam, including some backward-directed energy flow in certain restricted regions of a beam.
- **Control of energy flows in structured light fields:** Information about the energy flow in structured light fields are essential for different applications, such as the optical micromanipulation or the development of novel quantum information protocols.
- **Measurement of the energy flow in structured light fields:** Methods for measuring the energy flow are often based on either (i) the mechanical action of the optical field upon the probe microparticles or (ii) observations of the intensity profile of the free-space propagating beams. Alternatively, this flow can be visualized by the distribution of the emitted photoelectrons.
- **Analysis of OAM beams:** For a given light field, the contributions of different OAM modes can be obtained from a Fourier-Bessel decomposition of the field (Mock *et al.*, 2020)

$$E_r(r, \varphi, z_o) = \sum_{\ell} d_{\ell} J_{\ell}(kr) e^{i\ell\varphi}, \quad d_{\ell} = \int_0^{2\pi} d\varphi \int_0^{\infty} dr r E_r(r, \varphi, z_o) J_{\ell}(kr) e^{i\ell\varphi}.$$

From this decomposition, the normalized power of each mode is obtained by $P_{\ell} = |d_{\ell}|^2 / \sum_{\ell'} |d_{\ell'}|^2$ and can be readily displayed for discussion and analysis.

Properties of vortex beams:

- For all points in the beam, the ratio between the azimuthal and z -components of the momentum is found to be ℓ/kr .
- The linear momentum of each photon is given by $\hbar k$; since the azimuthal component of the wavevector is m/r and is independent of the wavelength, the orbital angular momentum per photon is

$$p = \hbar k \quad \rightarrow \quad p_\varphi = \hbar k \phi \quad \rightarrow \quad \ell = r \times p_\varphi = r \times \frac{\phi}{r} = m\hbar$$

- However, OAM \neq SAM, despite the rather similar illustrations in the literature; in particular, there exist also vortex states for spin-less waves, such as acoustic vortex waves.

14.3.c. Vortex beams. Generation & manipulation

Generation of vortex beams with different photon energies:

- For intense, short-wavelength FEL radiation, optical methods can often not be applied due to strong limitations and difficulties in the fabrications of optical surfaces (Terhalle *et al.* 2011, Peele *et al.* 2002).
- **Twisted EUV beams:** Ribic and coworkers (2014) proposed an efficient scheme in order to generate intense coherent and twisted OAM beams in the EUV region. These beams can be realized by means of a seeded FEL, i.e. by using a (seeding) laser pulse with a transverse, staircaselike phase. For this phase pattern, in particular, the diffraction and mode selection drive the radiation profile towards a dominant OAM mode at saturation.
- **Twisted x-ray beams:** Hemsing and coworkers proposed two clever approaches for generating FEL vortex beams within the x-ray region:
 - (i) By using the interaction of an electron beam with a seeded laser within a helical undulator (Hemsing *et al.*, 2011);
 - (ii) by using a so-called echo-enabled harmonic generation (EEHG) scheme, in which two seed lasers and two magnetic chicanes are utilized in order to produce harmonic microbunches of an electron beam with a corkscrew distribution.

Generation of vortex beams by pitch-fork holograms:

- The superposition of a regular phase profile with some proper grating already results in a fork hologram that help generate vortex beams.
- Fork-like or pitch-fork holograms are known to diffract the light and to generate beams with OAM. Such holograms can be generated also dynamically by using a spatial light modulator and readily controlled by a computer.
- A pitchfork hologram is obtained adding a twisting and an oblique phase. The width of six 2π phase ramps is highlighted.

Generation of vortex beams by spiral phase plates:

- A (plane-wave) light beam can acquire a non-zero OAM by crossing a spiral phase plate with an inhomogeneous thickness.
- **Spiral phase plates (SPP):** Such a SPP is a transparent dielectric plate with a thickness that varies as a smooth ramp; this variation in the thickness adds a phase shift to an incident field that increases linear with the azimuthal angle φ .
- **Light field:** If a SPP is placed into the waist of a Laguerre-Gaussian beam with well-defined quantum numbers, u_{lp}^{LG} , the complex light amplitude just behind the plate can be described by means of a phase-plate operator $S(m_s, \alpha)$

$$\langle r, \varphi | S(m_s, \alpha = 0) | l, p \rangle = u_{lp}^{\text{LG}}(r, \varphi) e^{im_s \varphi},$$

and where m_s is the phase shift per unit angle of the given SPP.

- SPP help explore high-dimensional entanglement with just two detector, while 6 detectors are required by other popular methods in order to prove the entanglement of the OAM degree of freedom for two entangled photons (Oemrawsingh *et al.*, 2004).
- The figure below shows the transformation of a TEM_{00} mode into a helical beam.

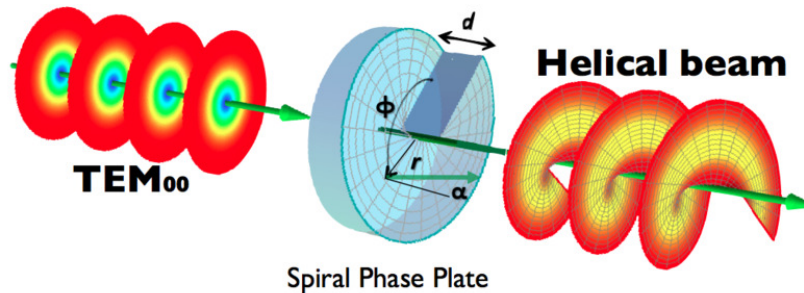


Figure 14.2.: Experimental scheme for generating light orbital angular momentum with spiral phase plates. Taken from Beijersbergen *et al.* (1994).

Generation of vortex beams by q-plates:

- **q-plate:** A (so-called) q-plate is a device that is realized by means of liquid crystals, polymers or sub-wavelength gratings; this device exploits a change of sign if the polarization of the incoming light is modified.

Generation of vortex beams by spatial light modulators:

- A spatial light modulator (SLM) is an object that imposes some form of spatially varying modulation on a beam of light. A simple example is an overhead projector transparency. Usually when the phrase SLM is used, it means that the transparency can be controlled by a computer. In the 1980s, large SLMs were placed on overhead projectors to project computer monitor contents to the screen. Since then more modern projectors have been developed where the SLM is built inside the projector. These are commonly used in meetings of all kinds for presentations.

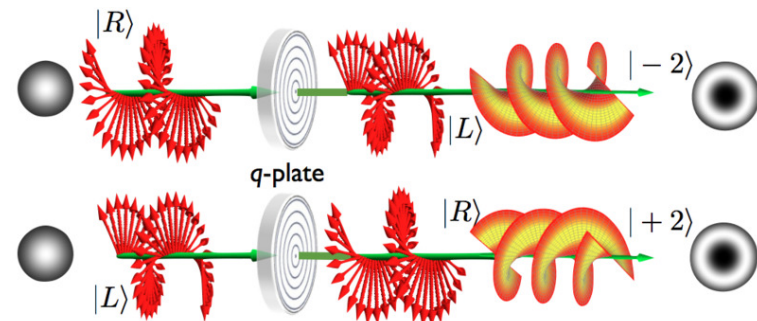


Figure 14.3.: The *q*-plate effect for left and right-hand circular polarizations.

Generation of vortex beams by cylindrical mode converters:

- A Hermite-Gaussian beam can be converted into a Laguerre-Gaussian beam with well-defined OAM by using an **astigmatic** system with two well-aligned cylindrical lenses. In this scheme, these lenses are placed at some specific distance in order to introduce a well-defined relative phase between the horizontal and the vertical Hermite-Gaussian beams.

Generation of vortex beams by helical undulators:

- X-ray vortex beams with photon energies $\hbar\omega \approx 100$ eV have been generated in a helical undulator by Bahrdt *et al.* (2013) and Hemsing *et al.* (2013).
- Another interesting approach has been suggested by Ribic and coworkers (2014). These authors proposed to modify the phase mask and to manipulate directly the seeding laser in order to change the transverse properties of the FEL light.

Optical elements:

- **Dove prism:** This is a (type of) reflective prism that can be used to invert a given image. These prisms are often shaped from a truncated right-angle prism.
- If a beam enters the prism at one of the sloped faces and parallel to the longitudinal axis, it undergoes total internal reflection at the inside of the longest (bottom) face, and then leaves the prism at the opposite sloped face. Therefore, any image that passes through the prism is flipped (mirrored) and also inverted but not laterally transposed.

- **Hologram:** A hologram usually refers to a three-dimensional image of an object that is created by holography, i.e. an optical technique for recording and reconstructing the amplitude and phase distributions of a coherent wave. Holography is often used to produce three-dimensional images or holograms.
- **Half-wave plate:** A wave plate, sometimes known as a retarder, designates an optical device that alters the polarization state of a light wave. While a half-wave plate shifts the polarization direction of linearly polarized light, a quarter-wave plate converts linearly-polarized light into circularly-polarized light and vice versa. Quarter-wave plate can be used also in order to produce elliptically-polarized light.
- ***q*-plate:** The *q*-plates often refer to a slab of patterned liquid crystals that couple the spin and OAM of a beam. In the circular polarization basis, the *unitary* action of a *q*-plate can be described by

$$U^{(\text{q-plate})} \cdot \begin{bmatrix} \mathbf{e}_L \\ \mathbf{e}_R \end{bmatrix} = \cos\left(\frac{\delta}{2}\right) \begin{bmatrix} \mathbf{e}_L \\ \mathbf{e}_R \end{bmatrix} + i \sin\left(\frac{\delta}{2}\right) \begin{bmatrix} \mathbf{e}_R e^{+2i(q\varphi + \alpha_o)} \\ \mathbf{e}_L e^{-2i(q\varphi + \alpha_o)} \end{bmatrix}$$

In this transformation, q denotes the (half-integer) topological charge of the liquid crystal pattern, α_o the azimuthal orientation of the liquid crystal element in the laboratory frame ($\varphi = 0$ corresponds to the x -axis) and δ refers to the optical retardation of the *q*-plate (Bouchard *et al.*, 2016).

- **Tailored light fields:** Interactions that mix the spatial and spin degrees of freedom have become an powerful tool in order to tailor the amplitude and phase of light beams. Such interactions are often mediated by photonic elements that modify the spatial profile of the beam and which are often based on quite a sophisticated fabrication.
- **Spiral phase plate:** A spiral phase plate provides a refracting or reflecting surfaces that is shaped into one turn of a helicoid and that exhibits a well-defined phase step. Such phase plates generally create screw-dislocated waves.
- **Spatial light modulators (SLM):** A SLM is an optical device that supports the spatio-temporal modulation of the phase, polarization as well as the amplitude of optical fields. These devices are often based on liquid crystals owing to their high sensitivity to external fields and their large birefringence (Ghadimi and Brasselet, 2018). Based on liquid crystals, such electrically controlled SLM have been frequently applied to manipulate and control stuctured light fields.
- **Manipulation of vortex beams:** The wave fronts of vortex beams can be shaped directly by spiral phase plates and spin-to-orbital angular momentum convertors. They can also be manipulated by diffraction techniques, such as computer-generated holograms, fork grating and spiral zone plates. Further techniques make use of photon sieves and Vogel spiral arrays (Yang *et al.*, 2017).

Mach-Zehnder interferometers:

14. Beams of light and particles

- These interferometers make use of two separate beam splitters in order to split and recombine an input beam but from which the beam can emerge and detected at two outputs. The optical path lengths in the two arms of the interferometer may be nearly identical or may be different in order to introduce an extra delay path.
- If a beam is sent through the interferometer, the optical powers at the two outputs depends on in practice sensitively on the the precise difference in optical arm lengths as well as on the wavelength of the light.
- The Mach-Zehnder interferometer was first developed by Ludwig Mach and Ludwig Zehnder.

Theoretical manipulation of OAM beams:

- (Coupling) Operator for the coupling of the OAM and polarization state of a beam: If $e^{\pm i\ell\varphi}$ refers to the raising and lowering OAM operators and $\sigma_{\pm} = (\sigma_x + \sigma_y)/2$ to the corresponding Pauli operators, the coupling operator can be written as

$$U = \exp \left\{ i \left(\frac{\pi r}{2r_c} \right) [\cos \varphi \sigma_x + \sin \varphi \sigma_y] \right\} = \cos \left(\frac{\pi r}{2r_c} \right) \mathbb{1} + i \sin \left(\frac{\pi r}{2r_c} \right) (l_+ \sigma_- + l_- \sigma_+).$$

Here, the length r_c is defined as the smallest radial distance at which the polarization (degree-of-freedom) undergoes a π rotation within the plane of the lattice.

14.3.d. Hermite-Gaussian beams

Characterization and use:

- Hermite-Gaussian modes HG_{mn} : have a rectangular symmetry and are described by means of two mode indices m and n ; these mode indices give the number of nodes in the x and y directions respectively.
- Hermite-Gaussian modes: These modes are a convenient description for the output of lasers whose cavity design is not radially symmetric but asymmetric in horizontal and vertical directions.
- Hermite-Gauss modes: The Hermite-Gauss modes $HG_{mn}(x, y, z)$ are found as solutions of the scalar Helmholtz equation by the separation

of the x and y coordinates and by using the slowly varying envelop approximation. These modes can ben written as

$$u(x, y, z) \equiv \text{HG}_{mn}(x, y, z) = \mathcal{E}_o H_m \left(\frac{\sqrt{2} x}{w(z)} \right) H_n \left(\frac{\sqrt{2} y}{w(z)} \right) \frac{w_o}{w(z)} \exp[-i\phi_{mn}(z)] \exp \left[i \frac{k \rho^2}{2q(z)} \right],$$

$$q(z) = z - iz_o = z - i \frac{\pi w_o^2}{\lambda}, \quad z_o = \frac{\pi w_o^2}{\lambda}, \quad \phi_{mn}(z) = (m+n+1) \tan^{-1} \left(\frac{z}{z_o} \right),$$

where $H_m(x)$ denote the Hermite polynomials, $w(z)$ is the beam size a function of the propagation direction and $w_o = w(0)$ the beam size at the (beam) waist. Moreover, $q(z)$ is the (so-called) Rayleigh range and $\phi_{mn}(z)$ the Gouy phase shift.

➤ **Gauss modes:** For $m = n = 0$, the modes $\text{HG}_{mn}(x, y, z)$ simplify to

$$\text{HG}_{00}(x, y, z) = u(\rho, z) = \mathcal{E}_o \frac{w_o}{w(z)} \exp[-i\phi(z)] \exp \left[i \frac{k \rho^2}{2q(z)} \right], \quad \phi(z) = \tan^{-1} \left(\frac{z}{z_o} \right).$$

➤ **Hermite-Gaussian (LG) modes:** The normalized HG modes are written in terms of the quantum numbers n_x and n_y and are given by

$$\text{HG}_{n_x, n_y}(x, y, z) = \frac{\mathcal{N}}{w(z)} H_{n_x} \left(\frac{\sqrt{2} x}{w(z)} \right) H_{n_y} \left(\frac{\sqrt{2} y}{w(z)} \right) \exp \left[-\frac{r^2}{w^2(z)} \right] \exp \left[i \left(kz + \frac{k r^2}{2R(z)} - (n_x + n_y + 1) \psi(z) \right) \right]$$

$$\mathcal{N} = \left[\frac{1}{2^{n_x+n_y-1} \pi n_x! n_y!} \right]^{1/2}$$

and where $H_n(x)$ are the n th-order Hermite polynomials.

14.3.e. Laguere-Gaussian beams

Characterization and use:

➤ The Laguerre-Gaussian (LG) beams carry an intrinsic OAM like the intrinsic SAM for beams with a circular polarization (Allen *et al.* 1992, 2003). This appeared originally rather surprising as the OAM of LG beams arise from the helical phase distribution about the beam axis, and which coincides also with a phase singularity (Nye and Berry, 1974).

14. Beams of light and particles

- **Laguerre-Gaussian modes** $u_{\ell p}^{\text{LG}}$: For a Laguerre-Gaussian beam with well-defined magnetic and radial quantum numbers (m, p) , the complex amplitude of the light field in the waist of the beam is defined as in the polar representation

$$u_{\ell p}^{\text{LG}}(r, \varphi) = \langle r, \varphi | m, p \rangle = R_{mp}(r) \Phi_m(\varphi) \quad \text{with} \quad \Phi_m(\varphi) = \frac{e^{im\varphi}}{\sqrt{2\pi}}$$

- **Laguerre-Gaussian modes** $u_{\ell p}^{\text{LG}}$: If the problem is cylindrically symmetric, these modes are the natural solution of the paraxial wave equation. They are often written in cylindrical coordinates by using Laguerre polynomials.

- **Laguerre-Gauss modes:** The Laguerre-Gauss modes $\text{LG}_{mn}(\rho, \varphi, z)$ are found as solutions of the scalar Helmholtz equation by the separation of the ρ and ϕ coordinates and **by using the slowly varying envelop approximation**. These modes can ben written as

$$u(x, y, z) \equiv \text{LG}_{p\ell}(\rho, \varphi, z) = \mathcal{E}_o \left(\frac{\sqrt{2} \rho}{w(z)} \right)^\ell L_p^\ell \left(\frac{2 \rho^2}{w^2(z)} \right) \frac{w_o}{w(z)} \exp[-i \phi_{p\ell}(z)] \exp \left[i \frac{k \rho^2}{2 q(z)} \right] \exp(i \ell \varphi),$$

$$q(z) = z - i z_o = z - i \frac{\pi w_o^2}{\lambda}, \quad z_o = \frac{\pi w_o^2}{\lambda}, \quad \phi_{p\ell}(z) = (2p + \ell + 1) \tan^{-1} \left(\frac{z}{z_o} \right),$$

and where $L_p^\ell(x)$ is the associated Laguerre-polynomial. For $p = \ell = 0$, the Laguerre-Gauss modes $\text{LG}_{p\ell}(\rho, \varphi, z)$ also simplify to the fundamental Gauss mode, while they have a particular phase factor $i \ell \varphi$ otherwise.

- **Laguerre-Gaussian (LG) modes:** The normalized — even and odd — LG modes are typically written in terms of the radial number n and the OAM or winding number ℓ as

$$\begin{aligned} \text{LG}_{n,\ell}^{(\text{even, odd})}(r, \varphi, z) &= \frac{\mathcal{N}}{w(z)} \begin{pmatrix} \cos \ell \varphi \\ \sin \ell \varphi \end{pmatrix} \left[\frac{\sqrt{2} r}{w(z)} \right]^\ell L_{n,\ell} \left(\frac{2 r^2}{w^2(z)} \right) \exp \left[-\frac{r^2}{w^2(z)} \right] \exp \left[i \left(kz + \frac{k r^2}{2 R(z)} - (2n + \ell + 1) \psi(z) \right) \right] \\ \mathcal{N} &= \left[\frac{4 n!}{(1 + \delta_{0,\ell}) \pi (n + \ell)!} \right]^{1/2} \end{aligned}$$

and where $L_{n,\ell}(x)$ are the generalized Laguerre polynomials.

- **Cylindrically-polarized LG beams:** Cylindrically-polarized LG beams can be constructed as linear combination of two circularly polarized LG modes, and which gives rise to non-separable spatial and polarization modes. For this reason also, the the polarization state of

cylindrically-polarized LG beams is spatially inhomogeneous over the cross section of the beam. More general, such linear combinations of two LG modes are known as vector beams in the literature and form a vector solution for the paraxial wave equation.

Product of two LG beams:

- **Product of two LG beams:** The product of two LG beams can be written again as sum of LG beams with certain geometrical coefficients (Kotlyar *et al.*, 2022). In particular, the product of two identical LG beams gives rise to a (so-called) ‘squared’ LG beam $(LG)^2$. For the product of two LG beams with orbital quantum numbers $\ell_1 - \ell_2$ and $\ell_1 + \ell_2$, explicit expressions for the complex coefficients were derived.

14.3.f. Ince-Gaussian beams

Characterization and use:

- **Ince-Gaussian (IG) beams:** IG beams represent the exact, complete and orthogonal solutions of the PWE in elliptical coordinates. Their transverse field distribution possesses an inherent elliptical symmetry. These spatially structured IG beams are universal as they include both, the Laguerre-Gaussian beams for $\epsilon \rightarrow \infty$ and the Hermite-Gaussian beams for $\epsilon \rightarrow 0$. Therefore, by just changing the ellipticity ϵ one is able to explore a whole family of beams, from LG to IG and up to the HG beams.
- **Elliptical coordinates used for the IG beams:** In the transverse plane $z = 0$, the elliptical coordinates are defined in terms of the ellipticity ϵ and the beam waist w_o at the origin as

$$x = w_o \sqrt{\frac{\epsilon}{2}} \cosh \xi \cos \eta, \quad y = w_o \sqrt{\frac{\epsilon}{2}} \sinh \xi \cos \eta, \quad \xi \in [0, \infty), \quad \eta \in [0, 2\pi].$$

For a given beam waist w_o , each choice of ϵ specifies a different set of coordinates and a different set of IG beams (solutions). The elliptical coordinates (ξ, η) also include the Cartesian coordinates for $\epsilon \rightarrow 0$ and the cylindrical coordinates for $\epsilon \rightarrow 0$.

- **Even and odd Ince polynomials:** For the (so-called) *periodic* differential equation, there exists two independent solutions that are known

14. Beams of light and particles

as the even and odd Ince polynomials of order p and degree m

$$\text{even : } C_p^m(\eta, \epsilon), \quad 0 \leq m \leq p, \quad (-1)^{p-m} = 1$$

$$\text{odd : } S_p^m(\eta, \epsilon), \quad 1 \leq m \leq p, \quad (-1)^{p-m} = 1,$$

and where the (quantum) number m refers to the number of hyperbolic nodal lines in the (perpendicular) intensity distribution of the beam, and $(p - m)/2$ to the number of elliptical lines, though without counting the line at $\xi = 0$.

➤ **Intensity profiles of odd and even IG beams:** in the transverse plane at $z = 0$ and for an ellipticity $\epsilon = 2$; cf. Figure 14.4

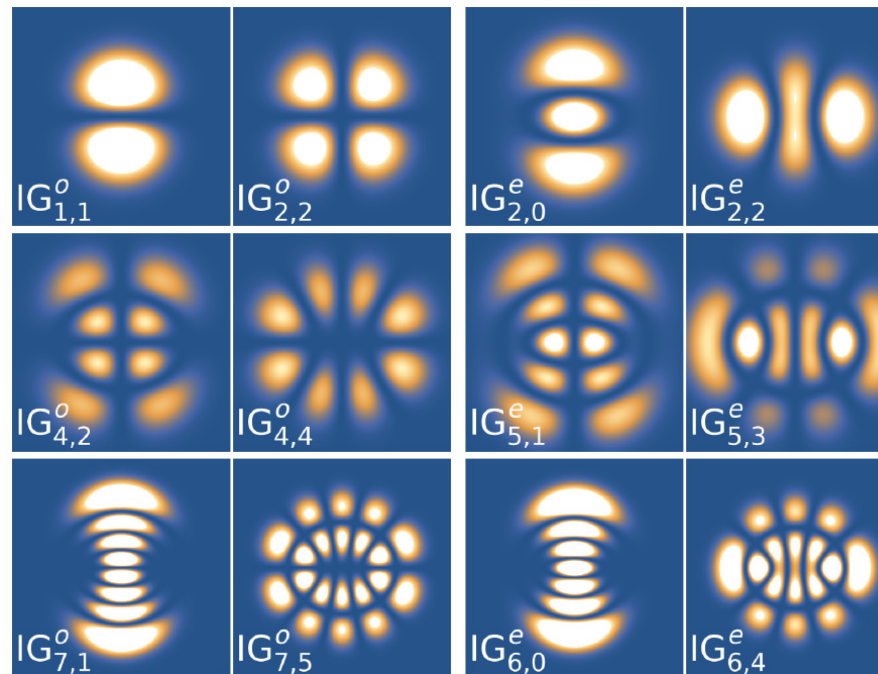


Figure 14.4.: Intensity profiles of odd and even IG beams in the transverse plane at $z = 0$ and for an ellipticity $\epsilon = 2$. The number of hyperbolic and elliptic nodal lines correspond to m and $(p - m)/2$, respectively, and without counting the interfocal nodal line at $\xi = 0$ for the odd mode; from Baghdasaryan and Fritzsche (2020).

- Even and odd Ince-Gaussian (IG) modes: The even and odd Ince-Gaussian beams can be expressed in terms of the corresponding Ince polynomials

$$\text{IG}_{p,m}^{(\text{even})}(\mathbf{r}; \epsilon) = \frac{C w_o}{w(z)} C_p^m(i\xi, \epsilon) C_p^m(\eta, \epsilon) \exp\left[-\frac{r^2}{w^2(z)}\right] \exp\left[i k z + \frac{i k r^2}{2 R(z)} - (p+1) \psi(z)\right]$$

$$\text{IG}_{p,m}^{(\text{odd})}(\mathbf{r}; \epsilon) = \frac{S w_o}{w(z)} S_p^m(i\xi, \epsilon) S_p^m(\eta, \epsilon) \exp\left[-\frac{r^2}{w^2(z)}\right] \exp\left[i k z + \frac{i k r^2}{2 R(z)} - (p+1) \psi(z)\right]$$

and where C and S are two normalization constants. As seen from this representation, the transverse distribution of the IG beams at the plane $z = 0$ is fully determined by the (quantum) numbers p and m , the ellipticity ϵ as well as the beam waist w_o .

14.3.g. Bessel-Gauss beams

Characterization and use:

- Bessel-Gauss modes: The Bessel-Gauss modes $\text{BG}_{mn}(\rho, \varphi, z)$ are solutions of the scalar Helmholtz equation and **by using the slowly varying envelop approximation**. These Bessel-Gauss modes are independent of φ and can be written as

$$u(x, y, z) \equiv \text{BG}_\beta(\rho, z) = \mathcal{E} \frac{w_o}{w(z)} \exp[-i\phi(z)] \exp\left[i \frac{k \rho^2}{2 q(z)}\right] J_0\left(\frac{\beta \rho}{1 + i z/z_o}\right) \exp\left(-\frac{\beta^2 z/(2k)}{1 + i z/z_o}\right)$$

$$q(z) = z - i z_o = z - i \frac{\pi w_o^2}{\lambda}, \quad z_o = \frac{\pi w_o^2}{\lambda},$$

and where $J_0(x)$ is the Bessel function of first kind, $\phi(z)$ the Gouy phase and β is a constant scale parameter. These modes reduce to the fundamental Gauss mode for $\beta \rightarrow 0$.

- Azimuthally-polarized vector Bessel-Gauss modes: The (separation) ansatz $\mathbf{E}(\rho, z) = u(\rho, z) \exp[i(kz - \omega t)] \mathbf{e}_\varphi$ together with the slowly varying envelop approximation gives rise to the generating ODE and the corresponding azimuthally-polarized vector Bessel-Gauss modes (Zhan, 2009):

$$\frac{1}{\rho} \frac{\partial}{\partial \rho} \left(\rho \frac{\partial u}{\partial \rho} \right) - \frac{u}{\rho^2} + 2ik \frac{\partial u}{\partial z} = 0 \quad \Rightarrow \quad u(\rho, z) = \mathcal{E}_o J_1\left(\frac{\beta \rho}{1 + i z/z_o}\right) \exp\left(-i \frac{\beta^2 z/(2k)}{1 + i z/z_o}\right) \text{HG}_{00}(\rho, z),$$

14. Beams of light and particles

and where β is a constant scale factor.

14.3.h. Bessel beams

Characterization and use:

- **Bessel beams:** A Bessel beam refers generally to an electromagnetic field whose amplitude is given by a Bessel function of the first kind. 5
- Although these beams are an idealization, true **Bessel beam** are monochromatic and non-diffractive and, hence, do not not diffract and spread out when they propagate. This behaviour is quite in contrast to other typical optical (or sound) waves if they are focused at some spot.
- Bessel beams are known to be self-healing if they are obstructed at some point, i.e. they reform to a Bessel beam again further down the beam axis.
- Pure Bessel modes generally carry a well-defined OAM; in particular, they typically include three components of the topological charge since only the (projection of the) total angular momentum is conserved for these beams. For this reason, the z -projections of the orbital and spin angular momentum are not defined independently.
- **Bessel modes $|\kappa, m\rangle$:** Bessel beams can be written also as a superposition over plane waves with well-defined (fixed) transverse momentum , longitudinal momentum as well as circular polarization

$$\psi(\mathbf{r}) = e^{-i\omega t + ik_z z} |\kappa, m\rangle, \quad |\kappa, m\rangle \propto e^{im\varphi} J_m(\kappa \rho)$$

- **Vector potential:** The vector potential of the Bessel beams is often written as Fourierintegral over Bessel states of different projections of the orbital angular momentum $a_{\kappa m}(\mathbf{k}_\perp)$,

$$\mathbf{A} = e^{-i\omega t} \frac{1}{(2\pi)^2} \int d\mathbf{k}_\perp e^{-i\mathbf{k}\cdot\mathbf{r}} a_{\kappa m}(\mathbf{k}_\perp) \mathbf{e}_{\mathbf{k},\lambda}, \quad a_{\kappa m}(\mathbf{k}_\perp) = \sqrt{\frac{2\pi}{\kappa}} (-i)^m e^{-im\varphi_\mathbf{k}} \delta(k_\perp - \kappa)$$

$$\mathbf{e}_{\mathbf{k},\lambda} = \frac{1}{\sqrt{2}} \begin{pmatrix} \cos \vartheta_k \cos \varphi_k - i\lambda \sin \varphi_k \\ \cos \vartheta_k \sin \varphi_k + i\lambda \cos \varphi_k \\ -\sin \vartheta_k \end{pmatrix} \quad \tan \vartheta_k = \frac{\kappa}{k_z}$$

and where $\mathbf{e}_{\mathbf{k},\lambda}$ are known as polarization (unit) vector and ϑ_k as the opening angle of the Bessel beam.

- **Plane-wave expansion:** Of course, every monochromatic plane-waves can be expanded also in terms of Bessel waves as they are both just two different bases in order to describe wave packets

$$e^{i(\mathbf{k} \cdot \mathbf{r} - \omega t)} = \sum_{m=-\infty}^{\infty} e^{-i\omega t + ik_z z} i^m e^{-im\varphi_k} |\kappa, m\rangle$$

- **Electron-photon interaction operator for Bessel beams:** For (a Bessel beam of) twisted photons, the transition operator reads as:

$$V^{(\text{tw})} = \alpha \mathbf{A}_{\varkappa m_\gamma k_z \lambda}(\mathbf{r}) \mathbf{p}.$$

$$\mathbf{A}_{\varkappa m_\gamma k_z \lambda}(\mathbf{r}) = \int \mathbf{e}_{\mathbf{k}\lambda} e^{i\mathbf{k}\mathbf{r}} a_{\varkappa m_\gamma}(\mathbf{k}_\perp) e^{-i\mathbf{k}_\perp \mathbf{b}} \frac{d^2 k_\perp}{(2\pi)^2}, \quad a_{\varkappa m_\gamma}(\mathbf{k}_\perp) = (-i)^{m_\gamma} e^{im_\gamma \varphi_k} \sqrt{\frac{2\pi}{k_\perp}} \delta(k_\perp - \varkappa).$$

In this expression, the factor $e^{-i\mathbf{k}_\perp \mathbf{b}}$ specifies the position of a target atom within the incident wave-front, and which refers to the complex spatial structure of the Bessel beam.

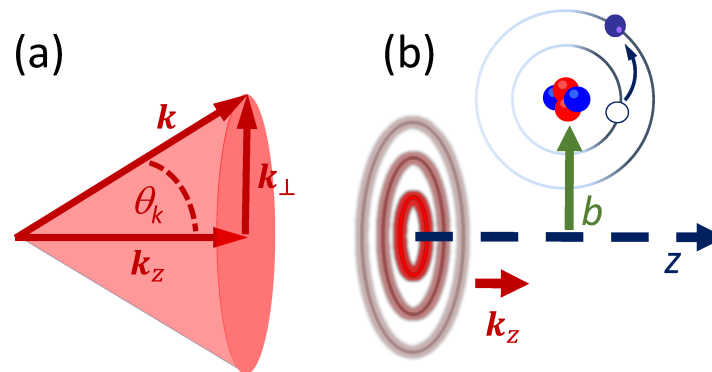


Figure 14.5.: (a) In momentum representation, the twisted light can be seen as a coherent superposition of plane waves. These plane waves with wavevectors \mathbf{k} are all lying on a cone with (polar) opening angle $\vartheta_k = \arctan(|\mathbf{k}_\perp|/k_z)$ and with polarization vectors $\mathbf{e}_{\mathbf{k},\lambda}$ which are perpendicular to \mathbf{k} . (b) For a given atom, the absorption amplitude depends on the position of the atom in a plane perpendicular to the propagation direction. The position of the target atom with regard to the beam axis is specified by the impact parameter (vector) \mathbf{b} (c-05-photobeam-interaction.eps).

14. Beams of light and particles

- **Poynting vector field of Bessel beams:** To display the energy flux in Bessel beams, Surzhykov *et al.* (2016) proposed to measure the photoelectron angular distribution from atoms at different position in the beam profile. Such measurements appear feasible since the angular distribution of photoelectrons, emitted from some *local* atomic target, appears to be sensitive to the (local) direction of the Poynting vector. This proposal has been supported also by detailed computations for the ionization of sodium atoms by nondiffractive Bessel beams.
- **Generation of Bessel beams:** Today, Bessel beams can be generated with quite different photon energies from meV to hundreds of eV, and with projections of the OAM up to $\hbar m_\ell \gtrsim 1000 \hbar$.
- **Magnetic field of a Bessel beam:** Using the vector potential of a non-paraxial Bessel beam with opening angle $\theta_k = \tan^{-1} \kappa/k_z = \tan^{-1} k_{\rho,o}/k_z$, helicity $\lambda = \pm 1$ and the polarization coefficients c_o, c_\pm in cylinder coordinates, the magnetic field can be written as (Surzhykov *et al.*, 2016)

$$\mathbf{B}^{(\text{Bessel})} = \text{rot } \mathbf{A}^{(\text{Bessel})} = \mathbf{e}_z \mathcal{B}_z(\mathbf{r}) + \mathbf{e}_\rho \mathcal{B}_\rho(\mathbf{r}) + \mathbf{e}_\varphi \mathcal{B}_\varphi(\mathbf{r}), \quad \mathbf{r} = (\rho, \varphi, z), \quad \mathbf{k} = (k_\rho, k_\varphi, k_z)$$

$$\mathcal{B}_z(\mathbf{r}) = \omega \sqrt{\frac{\kappa}{2\pi}} e^{ik_z z} e^{im\varphi} J_m(k_\rho \rho) \sin \theta_k, \quad \mathcal{B}_\rho(\mathbf{r}) = i \omega \lambda \sqrt{\frac{\kappa}{2\pi}} e^{ik_z z} e^{im\varphi} [J_{m+1}(k_\rho \rho) c_- + J_{m-1}(k_\rho \rho) c_+]$$

$$\mathcal{B}_\varphi(\mathbf{r}) = \omega \lambda \sqrt{\frac{\kappa}{2\pi}} e^{ik_z z} e^{im\varphi} [J_{m+1}(k_\rho \rho) c_- - J_{m-1}(k_\rho \rho) c_+],$$

where $J_m(x)$ refers to a Bessel function of the first kind. From these expressions, the electric field is simply obtained by $\mathbf{E}^{(\text{Bessel})} = i \lambda \mathbf{B}^{(\text{Bessel})}$, and where the *physical fields* are the real parts of $\mathbf{E}^{(\text{Bessel})}(\mathbf{r})$ and $\mathbf{B}^{(\text{Bessel})}(\mathbf{r})$, respectively.

- **Time-averaged Poynting vector:** With the opening angle $\theta_k = \tan^{-1} \kappa/k_z = \tan^{-1} k_{\rho,o}/k_z$, the time-averaged Poynting vector of a Bessel beam becomes:

$$\mathbf{P}^{(\text{Bessel})} = \frac{1}{2} \Re (\mathbf{E}^{(\text{Bessel})} \times \mathbf{B}^{(\text{Bessel})*}) = \mathbf{e}_z P_z(\mathbf{r}) + \mathbf{e}_\rho P_\rho(\mathbf{r}) + \mathbf{e}_\varphi P_\varphi(\mathbf{r}),$$

$$P_\rho(\mathbf{r}) = 0, \quad P_\varphi(\mathbf{r}) = \frac{\kappa \omega^2}{4\pi} \sin \theta_k J_m(k_\rho \rho) [J_{m+1}(k_\rho \rho) c_- + J_{m-1}(k_\rho \rho) c_+]$$

$$P_z(\mathbf{r}) = \frac{\kappa \omega^2 \lambda}{4\pi} [J_{m+1}^2(k_\rho \rho) c_-^2 - J_{m-1}^2(k_\rho \rho) c_+^2]$$

The Bessel beams are called *non-diffractive* since $P_\rho(\mathbf{r}) = 0$, i.e. there occurs no radial energy flux. Moreover, the (time-averaged) energy flux is azimuthally-symmetric since the other two components, P_φ and P_z , just depend on the transverse coordinate ρ but not on the angle φ .

- **Bessel beams:** These beams are solutions of the wave equation

$$\left(\Delta - \alpha^2 \frac{\partial^2}{\partial t^2} \right) \mathbf{A}_{\varkappa m k_z \lambda}^{(\text{Bessel})}(\mathbf{r}, t) = 0, \quad j_z \mathbf{A}_{\varkappa m k_z \lambda}^{(\text{Bessel})}(\mathbf{r}, t) = m \mathbf{A}_{\varkappa m k_z \lambda}^{(\text{Bessel})}(\mathbf{r}, t) = m \mathbf{A}_{\omega \theta_k m \lambda}^{(\text{Bessel})}(\mathbf{r}, t),$$

and where $j_z = l_z + s_z$ is the projection of the total angular momentum (TAM) operator. The Bessel beams are thus characterized by the energy ω , the opening angle $\theta_k = \tan^{-1} \varkappa/k_z$, the projection of the TAM and the helicity λ . Apart from very small opening angles, the Bessel beams do not have a well-defined OAM.

- **Plane-wave limit of a Bessel beam:** In the limit $\theta_k \rightarrow 0$, the vector potential of a Bessel beam $\mathbf{A}_{\varkappa m k_z \lambda}^{(\text{Bessel})}(\mathbf{r}, t) = \mathbf{A}_{\omega \theta_k m \lambda}^{(\text{Bessel})}(\mathbf{r}, t)$ retains only the term $m_s = \lambda$ in the expansion and, thus, becomes:

$$\begin{aligned} \mathbf{A}_{\varkappa m k_z \lambda}^{(\text{Bessel})}(\mathbf{r}, t) &= e^{-i\omega t} \sum_{m_s=0, \pm 1} \mathbf{e}_{m_s} \mathbf{A}_{\varkappa m_s k_z \lambda}^{(\text{Bessel})} \quad \Rightarrow \quad \mathbf{A}^{(\text{plane})}(\mathbf{r}, t) = \mathbf{e}_\lambda \sqrt{\frac{\varkappa}{2\pi}} (-i)^\lambda c_\lambda J_{m-\lambda}(\varkappa r) e^{i(m-\lambda)\varphi} e^{i(k_z z - \omega t)} \\ s_z \mathbf{A}^{(\text{plane})}(\mathbf{r}, t) &= \lambda \mathbf{A}^{(\text{plane})}(\mathbf{r}, t), \quad l_z \mathbf{A}^{(\text{plane})}(\mathbf{r}, t) = (m - \lambda) \mathbf{A}^{(\text{plane})}(\mathbf{r}, t). \end{aligned}$$

In this limit, obviously, the projections of the spin and orbital angular momentum decouple. Moreover, we then have $\varkappa = k \sin \theta_k \rightarrow 0$ and, thus, $J_{m-\lambda}(\varkappa r) \rightarrow \delta_{m\lambda}$. Therefore, the expression above refers to a standard plane-wave solution and the X wave vector potential reduces to a circularly-polarized plane-wave pulse in the paraxial limit.

- **Vector potential of a Bessel pulse in cartesian coordinates:** Böning *et al.* (2018) made use of the imaginary part of the vector potential of

14. Beams of light and particles

a Bessel pulse with opening angle $\theta_k = \tan^{-1} \kappa/k_z$ and with envelope $f(t)$ to construct a real-valued vector potential in the form:

$$A_x^{(\text{Bessel pulse})}(\mathbf{r}, t) = f(t) \sqrt{\frac{\kappa}{4\pi}} \{ c_- J_{m+1}(\kappa r) \cos[(m+1)\varphi + k_z z - \omega t] + c_+ J_{m-1}(\kappa r) \cos[(m-1)\varphi + k_z z - \omega t] \}$$

$$A_y^{(\text{Bessel pulse})}(\mathbf{r}, t) = f(t) \sqrt{\frac{\kappa}{4\pi}} \{ c_- J_{m+1}(\kappa r) \sin[(m+1)\varphi + k_z z - \omega t] + c_+ J_{m-1}(\kappa r) \sin[(m-1)\varphi + k_z z - \omega t] \}$$

$$A_z^{(\text{Bessel pulse})}(\mathbf{r}, t) = f(t) \sqrt{\frac{\kappa}{2\pi}} c_0 J_m(\kappa r) \sin[m\varphi + k_z z - \omega t].$$

Since the vector potential is real-valued, the same then applies for the corresponding electric and magnetic fields.

- **Vector potential of a Bessel pulse in the plane-wave limit:** In the limit $\theta_k \ll 1$ and $m = \lambda$, the expansion coefficients are $c_j \rightarrow \delta_j \lambda$ and the vector potential becomes (Böning *et al.*, 2018)

$$A_x^{(\text{Bessel: } \theta_k \ll 1)}(\mathbf{r}, t) = \sqrt{\frac{\kappa}{4\pi}} A_o \sin^2 \left(\frac{\omega t}{2n_p} \right) \cos(\omega t - k_z z)$$

$$A_y^{(\text{Bessel } \theta_k \ll 1)}(\mathbf{r}, t) = \sqrt{\frac{\kappa}{4\pi}} A_o \sin^2 \left(\frac{\omega t}{2n_p} \right) \sin(\omega t - k_z z), \quad A_z^{(\text{Bessel } \theta_k \ll 1)}(\mathbf{r}, t) = 0.$$

- **Cycle-averaged Poynting vector of a Bessel pulse:** For a Bessel pulse, the Poynting vector has apart from its z -component also an azimuthal component that depends on the radial coordinate ρ . Nevertheless, one often defines the intensity of a Bessel beam by the (longitudinal) z -component of the Poynting vector in the limit of a long pulse:

$$I_\perp(r) = \frac{A_o^2 \omega^2 \kappa}{4\pi} |c_+^2 J_{m-1}^2(\kappa r) + c_-^2 J_{m+1}^2(\kappa r)|.$$

- **Vector potential of the XUV Bessel beam in cylindrical coordinates:** With the wave-vector dependent polarization vector $\mathbf{u}(\mathbf{k}, \lambda)$, the vector potential of the XUV Bessel beam in cylindrical coordinates can be written as

$$\mathbf{A}^{(\text{Bessel})}(\mathbf{r}) = \sum_{q=-1,0,1} \mathbf{e}_q \frac{\kappa_\perp}{\sqrt{2\pi}} c_q e^{ik_z z} i^{\lambda-q} e^{i(m+\lambda-q)\varphi} J_{m+\lambda-q}(\kappa_\perp r_\perp), \quad c_0 = -\frac{\sin \vartheta_k}{\sqrt{2}}, \quad c_\pm = \frac{\cos \vartheta_k \pm \lambda}{2}.$$

In this expression, \mathbf{e}_q are the standard spherical unit vectors. A Bessel beam therefore consist of three terms with topological charges $m + \lambda$ and $m + \lambda \pm 1$. The relative weight of these terms depends on the opening angle ϑ_k and only the one with the topological charge m remains nonzero for paraxial beams with $\vartheta_k \ll 1$.

14.3.i. Airy beams

Characterization and use:

- **Airy beams:** Similar to Bessel beams, the cross section of an ideal Airy beam has an area of principal intensity and with a series of adjacent, less luminous areas up to infinity. Airy beams can be derived from the Airy integral that was first developed by George Biddell Airy in the 180s in order to explain the optical caustics in a rainbow and elsewhere.
- An Airy beam preserves its shape of intensity during propagation and forms a parabolic curve, quite analogue to the trajectory of a free projectile as seen in a plane perpendicular to the propagation.
- Airy beam are freely accelerating, i.e. they bend to form a parabolic arc as they propagate (Berry and Balazs, 1979; Siviloglou *et al.*, 2007), although the linear momentum remains conserved for these beams since the intensity centroid of an Airy beam forms a straight line.
- Airy beam do also not diffract, i.e. they do not spread out after focussing.

14.3.j. Necklace ring beams

Characterization and use:

- **Necklace ring beams:** These beams refer to optical vector solitons that consist of incoherently coupled self-trapped ‘necklace’ beams; these beams can carry zero, integer or even some fractional angular momentum.
- Necklace ring beams exhibit a self-stabilizing mutual attraction between different beam components and a quasistable propagation for much larger distances than the corresponding scalar vortex solitons

14.3.k. Lattices of OAM beams

Characterization and use:

- **Lattice of OAM beams:** While there is just one fixed axis in space for a single OAM beam, a two-dimensional array of such axes occurs for a beam that carries a lattice of OAM states, and this modifies the light field within each light cell.

14.3.l. Light beams with non-integer OAM

Characterization and use:

- **Beams with non-integer OAM:** These beams refer to structurally propagation invariant light beams carrying non-integer orbital angular momentum (OAM) using Hermite-Laguerre-Gaussian (HLG) modes.

14.3.m. Vector beams

Characterization and use:

- **Vector beams:** The vector beams need to be described in the product space of the optical SAM and OAM subspaces and are characterized by higher-order Stokes parameters.
- **Polarization state of light:** Homogenous polarization states do not depend on the spatial location in the beam profile and include the well-known linear, elliptical, and circular polarization of light. Apart from beams with a homogenous polarization state, beams with a spatially variable light polarization can be generated as well.
- Vector beams exhibit a spatially variant polarization.
- Cylindrical vector beams are axially symmetric solution to the full electromagnetic (vector) wave equation.
- **Generation of vector beams:** These beams can be generated via different active and passive methods.
- **Beams with spatially-dependent polarization:** Beams with a spatially-dependent polarization pattern can be readily generated today by spatial light modulators and other optical elements. Apart from the **radially-symmetric vector beams, lemon- and star-like polarization patterns can be created as well.** The spatial structure of the polarization may help also to control the propagation of beams in non-linear media.
- **Light beams with stable spatial profiles:** In non-linear media, spatial solitons and self-trapped light filaments are formed by a suitable balance of the (usual) linear diffraction and the non-linear, self-focusing contributions which cause a beam to narrow down (Bouchard *et al.*, 2016). For media with a intensity-dependent (non-linear) refraction index, the linear diffraction and self-focusing can be balanced out by a suitable choice (and superposition) of twisted beams. The same affects may also lead to a chain of solitons with particle-like properties.
- **Vector beams:** Vectorial superpositions of beams with OAM tend to propagate much longer quasi-stable in nonlocal media than the underlying scalar vortex beams (Bouchard *et al.*, 2016). This has been proven both, theoretically and experimentally.

14. Beams of light and particles

- **Vector beams:** These beams are constructed as correlated solutions to the [vector paraxial wave equation](#) with a space-dependent polarization profile. These beams include as subclass the [cylindrical vector beams](#) with an axially-symmetric polarization profile with regard to the propagation axis.
- **Antivortices or π -vortices:** Antivortices refer to beams with a [hyperbolic polarization structure](#); these beams may have advantages in engineering tight focusing, optical trapping or beam transformation in nanophotonics (Jimenez-Garcia *et al.*, 2017).
- **Application of radially polarized beams:** Radially-polarized beams can be focused on the sub-diffraction-limited because of their strong longitudinal field components. These beams can help improve material processing and have been applied in Raman spectroscopy, optical tweezers or for observing circular dichroism in nonchiral nanostructures.

Cylindrical vector beams:

- **Cylindrical vector beams:** This class comprises vector beams with radial, azimuthal, and spiral polarization distributions.
- **Cylindrical-symmetric vector beams:** These beams refer to solutions of Maxwell's equations with an axial symmetry in both, the amplitude and phase of the light field, such as radially- and azimuthally-polarized vector beams. These cylindrical-symmetric vector beams have often been applied in free-space.
- **Generation of cylindrical-symmetric vector beams:** Various passive methods have been applied to generate such beams in free space. These methods often start from beams with a spatially homogeneous polarization and apply different devices with spatially variable polarization properties, for example, with an axial birefringence and dichroism (Zhan, 2009).
- **Manipulation of cylindrical-symmetric vector beams:** There are devices available to perform basic manipulations on cylindrical-symmetric vector beams, such as reflection, polarization rotation and retardation, and which maintain the polarization symmetry of the beam. However, special care has to be taken since the polarization symmetry can easily be broken by anisotropic reflection coefficients.
- **Cylindrically-polarized LG beams:** Radial and azimuthal polarizations are two special cases of cylindrically-polarized LG beams if two modes with OAM projection $m = \pm 1$ and helicity $\lambda = \pm 1$ are chosen. For a radially-polarized LG beam, the electric field always points in the radial direction, perpendicular to the beam axis. The vector potential of a radially polarized LG beam is constructed as a linear combination of vector potential of right-circularly polarized and left-circularly polarized LG beams

$$\mathbf{A}_p^{(\text{radial})}(\mathbf{r}) = \frac{-i}{\sqrt{2}} \left[\mathbf{A}_{m_\ell=1, \lambda=-1, p}^{(\text{circ})}(\mathbf{r}) + \mathbf{A}_{m_\ell=-1, \lambda=1, p}^{(\text{circ})}(\mathbf{r}) \right].$$

Similarly, the electric field direction of the azimuthally-polarized LG beams is always perpendicular to the radial direction; its vector potential is given by

$$\mathbf{A}_p^{(\text{azimuthal})}(\mathbf{r}) = \frac{1}{\sqrt{2}} \left[\mathbf{A}_{m_\ell=1, \lambda=-1, p}^{(\text{circ})}(\mathbf{r}) - \mathbf{A}_{m_\ell=-1, \lambda=1, p}^{(\text{circ})}(\mathbf{r}) \right].$$

Poincare vector beams:

- Poincare beams: These are **vector beams with a non-uniform polarization profile and singularities in their polarization distribution**. Poincare beams are often formed by the superposition of two orthogonally-polarized LG modes of different OAM and, hence, carry a net value of OAM (Bouchard *et al.*, 2016).
- Poincare beams: Such beams with a non-uniform polarization profile are obtained, for instance, if the two transverse beams $\mathcal{E}_1, \mathcal{E}_2$ have a *zero* and a *nonzero* OAM. The polarization profile then varies in both, the angular and radial coordinates, and enables one to represent different states on the Bloch sphere.

Generation of vector beams:

- Generation of vector beams: A spatially inhomogeneous polarization profile can be generated by a superposition of **two spatial transverse modes with orthogonal polarization vectors \mathbf{e}_1 and \mathbf{e}_2** :

$$\mathcal{E}(r, \varphi, z) = \mathcal{E}_1(r, \varphi, z) \mathbf{e}_1 + \mathcal{E}_2(r, \varphi, z) \mathbf{e}_2.$$

This applies especially for two transverse LG modes and a circular polarization basis, $\mathbf{e}_1 = \mathbf{e}_L$ and $\mathbf{e}_2 = \mathbf{e}_R$, respectively.

- Generation of vector beams: To generate radial, azimuthal or spiral vector beams, a linearly-polarized Gaussian beam can be sent to a rotated $\delta = \pi/4$ *q*-plate of topological charge $q = 1/2$. Apart from a global phase, the generated beam is then given by $[\text{LG}_{0,-1}(r, \varphi, z) \mathbf{e}_L + \exp(i\beta) \text{LG}_{0,1}(r, \varphi, z) \mathbf{e}_R]/\sqrt{2}$, and where $\beta = 4\alpha_o$ depends on the orientation of the *q*-plate with respect to the polarization of the input beams. The so generated beams then correspond to radial ($\beta = 0$), azimuthal ($\beta = \pi$), and spiral ($\beta = \pm\pi/2$) vector vortex beams.

14.3.n. Traktor beams

Characterization and use:

- **Tractor beam:** These beams refer to optical fields that help attract one object to another from a distance.
- The concept of tractor beams originates from the novel Spacehounds of IPC by E. E. Smith (1931) and by re-coining an earlier ‘attractor beam’, in contrast to other, ‘repulser beams’.
- Tractor beam are defined to use (a negative) nonconservative radiation pressure, that differs from a gradient force, and which is directed towards the source. This generally requires a continuous redirection of momentum flux (Sukhov and Dogariu, 2010, 2011; Chen *et al.* 2011).
- Traktor beams are based on the maximization of forward scattering of light due to interference of different radiation multipoles. It was shown especially that an simultaneous excitation of multipoles is necessary in the particle in order to realize a negative (pulling) optical force.
- **Tractor beams:** These beams exert a *pulling* force on objects due to the (gradient) field of structured light. Tractor beams are often modeled by means of non-diffractive Bessel beams. Such tractor beams have been shown in optics and acoustics.
- **Tractor beams:** Different environments have been explored to *reverse* the light forces, including the interface between two media, plasmonic interfaces or the use of anisotropic materials. In practice, of course, the pulling forces will depend also on the (material) properties of the scattered particle, such as its chirality and structure. Experiments with tractor beams have shown the role these properties for achieving optical micromanipulations.

14.3.o. Polarization radiation

Characterization and use:

- In electrodynamics, one generally distinguishes **two classes of emitted radiation: bremsstrahlung and polarization radiation**. While bremsstrahlung is produced by accelerated charges, polarization radiation can be emitted by a uniformly moving charge, although only in the presence of a medium.
- In dependence on the given medium or target geometry, one distinguishes various forms of polarization radiation: Cherenkov radiation, transition radiation, diffraction radiation as well as Smith-Purcell radiation.

- **Polarization radiation:** Electromagnetic radiation can be emitted not only by accelerated charges but also due to the motion of magnetic moments and higher multipoles. Until the present, however, this (so-called) polarization radiation has never been verified experimentally for any frequency of light.
- The main experimental difficulty for approving this radiation refers to the (very) small current of a magnetic moment that is suppressed by $\sim 10^{-5}$ w.r.t. a corresponding charge current.
- A pure quasi-classical treatment of the polarization radiation is inconsistent since quantum corrections are of the same order for this type of radiation phenomena.

14.3.p. X-waves

Characterization and use:

- **X-waves:** X waves describe non-diffracting pulses, which carry orbital angular momentum and which are formed by a superposition of Bessel beams. This can be mathematically described by a convolution of monochromatic Bessel beams with constant opening angle θ_k and a Gaussian spectral distribution of width $\Delta\omega = 1/T_X$. This gives rise to the vector potential for an X wave in terms of the central frequency ω_o and the pulse duration T_X as

$$\mathbf{A}^{(\text{X-wave})}(\mathbf{r}, t) = \int_0^\infty \frac{d\omega}{\sqrt{2\pi} \Delta\omega} \exp\left[\frac{1}{2} \left(\frac{\omega - \omega_o}{\Delta\omega}\right)^2\right] \mathbf{A}_{\varkappa m k_z \lambda}(\mathbf{r}, t)$$

14.3.q. Optical forces of vortex beams

Optical forces:

- **Radiation pressure & optical forces:** In classical electrodynamics, the **radiation pressure is usually expressed in terms of the linear momentum (density) of light** and, thus, gives rise to optical forces that are aligned with the propagation direction (\mathbf{k} -vector). Because of the spin momentum (polarization), however, optical forces may have a non-vanishing component perpendicular to the \mathbf{k} -vector. A detailed understanding of such optical forces in structured light fields helps to use and control opto-mechanical devices.
- **Radiation pressure:** Both, in classical and quantum mechanics, the momentum of a (light) wave can be measured by its pressure upon an absorbing or scattering detector. In electrodynamics, the canonical momentum density is often expressed in terms of the Poynting vector $\mathbf{P} \propto \mathbf{E} \times \mathbf{B}$, i.e. the cross product of the electric and magnetic field vectors. Only for a homogeneous plane-wave, this cross product is aligned with the wave vector (\mathbf{k} -vector), while a more complex dependence will occur for all non-transverse fields
- **Radiation pressure & light forces:** From Maxwell's theory, one can readily derive the radiation pressure and, thus, a *pushing* force for any (non-gradient) light upon an object. More surprising, perhaps, was the **discovery of pulling forces in the (gradient) field of structured light**. These pulling forces usually arise from an enhanced forward light scattering, and which result in an increased field momentum that is balanced by a backward momentum of the scatterer to conserve the overall momentum. Such pulling forces have been analyzed if classical fields interact with atoms and molecules.
- A positive radiation force is relatively intuitive and occurs in the backscattering or absorption of the forward-directed momentum of a beam; it was first reported already by Nichols and Hull (1903).

Canonical versus spin momentum of light fields:

- **Poynting vector:** In general, the Poynting vector $\mathbf{P} \propto \mathbf{E} \times \mathbf{B}$ is *not* aligned with the (local) wave vector \mathbf{k} for typical structured optical fields, such as interference, optical vortices or near fields. This non-alignment directly affects the optical forces and how light acts upon matter.
- **Momentum of electromagnetic fields:** Following Noether's theorem, the translational symmetry of spacetime gives rise to momentum conservation of the electromagnetic field. If applied to the Langrangian of the em field, Noether's theorem yields the canonical momentum density $\mathbf{P}^{(\text{canonical})}$ and which, in the framework of QFT, generates spatial translations of the field, quite similar as $\mathbf{p} = -\hbar \nabla$ generates a translation of the particle's wavefunction (Antognozzi *et al.*, 2016).

- **Spin momentum of monochromatic optical fields:** Apart from the canonical momentum density (or Poynting vector) $\mathbf{P}^{(\text{canonical})}$, Belinfante (1936) recognized that the local polarization of the field gives rise to a spin-momentum (density) $\mathbf{P}^{(\text{spin})} = 1/2 (\nabla \times \mathbf{S})$ as produced by the spin-angular momentum density \mathbf{S} . While this spin momentum does not transport energy, owing to its solenoidal nature for a monochromatic field, it is determined by the (circular) polarization and inhomogeneity of the field, and this spin momentum is independent of the wave vector.

14.3.r. Application of optical (vortex) beams

Remarks:

- Different applications of optical vortex beams and the angular momentum of light have been envisaged and are currently explored in research laboratories, although no real commercial application are yet known.
- **Fields of applications:** Cold atoms, trapped nanoparticles, micro manipulation and detection of spinning objects, remote measurement of the rotation of mesoscopic particles, entanglement and quantum information, optical data transmission, interaction with matter, microscopy and astrophysics.
- **X-ray magnetic circular dichromism** By using different OAM states in the measurements, the dipole and quadrupole contributions to the circular dichroism signal can be separated from each other.
- **Interaction of beams with materials:** The propagation and changes of the polarization properties of light beams in their interaction with materials are explored in different field of physics, including metrology, data storage, optical communications, materials and bio sciences, or even in astronomy. More often than not, light with a spatially homogeneous (states of) polarization are considered, such as linearly, elliptically or circularly-polarized light.

Optical tweezer:

- **Optical tweezer:** These tweezers usually refer to single-beam gradient force trap that are realized by some highly focused laser beam. These focused beams provide an attractive or repulsive force on nano- or mesoscopic dielectric objects.
- Optical tweezers have been utilized to manipulate the orientation of particles or particle aggregates.
- In optical tweezers, the forces are typically on the order of piconewtons; they depends on the **refractive index** of the object.

Optical phasors:

- Phasor: A complex constant in **complex wave notation** that encapsulates the amplitude; sometimes known also as sinor or complexor.

Applications in quantum information theory:

- The orbital-angular momentum (OAM) of light has recently emerged as a promising candidate for quantum and classical information systems.
- In OAM beams, the spatial degrees of freedom provide a high-dimensional alphabet to quantum information processing which enables one to use qunits instead of qubits.
- **Quantum information encoding,** Higher-dimensional quantum information encoding has been discussed in the literature for possible future applications in quantum cryptography or quantum computations. The discrete, unbounded state-space of OAM promises in particular vastly enhanced data rates as well as an increased tolerance to eavesdropping in quantum communication.

14.4. Electron beams

Electron beams:

- Electron beams are quite frequently applied in physics; such beams may refer, for instance, to some stream of electrons as obtained from a betatron. Electron beams are generally generated either by heat (thermionic emission), bombardment of surfaces with charged atoms or particles (secondary electron emission), or by means of strong electric fields (field emission).
- Electrons may be collimated by holes and slits. Because they are electrically charged, they can also be deflected, focused or accelerated by electric and magnetic fields.

Twisted electron beams:

- Apart from twisted (vortex) solutions of the Dirac equation, a quasi-relativistic wave equation for twisted relativistic electron in arbitrary electric and magnetic fields can be derived by using a Foldy-Wouthuysen transformation.
- The interaction of twisted (vortex) electrons with electric and magnetic fields can be described quite readily, based on Lorentz transformations.

14.4.a. Gaussian electron beams

Characterization and use:

- It has been demonstrated experimentally that a Gaussian-profile model better describes the (equilibrium) electron beam than a beam with a uniform-profile model.

14.4.b. Vortex electron beams

General remarks:

14. Beams of light and particles

- Electron vortex beams were first realized experimentally by Uchida and Tonomura (2010), Verbeeck, Tian and Schattschneider (2010) and McMorran *et al.* (2011). Uchida and Tonomura, in particular, generated an electron vortex beams with (electron) energy $E = 300$ keV, a projection of the OAM with $m \lesssim 100$ and by focusing the electron beam to a spot size of 1.2 \AA .
- Vortex electrons can generally carry a rather large intrinsic projection of the orbital angular momentum (OAM) $m \sim 100$ with respect to their propagation direction. Therefore, the magnetic moment of vortex electrons $\mu \approx m \mu_B$ is similarly large, when compared with the Bohr magneton μ_B due to the spin motion of the electron.
- The magnetic moment of twisted electrons due to their OAM comes in addition to the known magnetic moment due to the spin motion.
- Since Vortex electrons are sensitive to external magnetic fields, they can be utilized to probe atomic magnetism and, thus, open novel opportunities for electron microscopy.
- While vortex photon beams have been created and routinely used for several decades already, the vortex states of electrons and charged particles is a presently emerging field.
- **Relativistic vortex beams of electrons:** Van Kruining *et al.* (2017) analytically solved the Dirac equation for an electron in a homogeneous magnetic field. As in Landau's (non-relativistic) theory, the beam is then confined by the magnetic field and exhibits a set of discrete energy levels (Landau levels), and which are Zeeman shifted relative to each other for the positive and negative spin states. Therefore, only the combined (quantized) contributions of the magnetic field and the Zeeman shifts determines together, which of the levels are affected by spin-orbit interaction and which retain more or less remain unaffected. Explicit solutions of the positive and negative-energy states are provided by van Kruining *et al.* (2017) for four cases (spin > 0 , OAM > 0 ; spin > 0 , OAM < 0 ; etc.), and with further details provided in some Supplemental Material.
- **Electron vortex beams:** Twisted electron beams with large OAM up to $1000 \hbar$ have been generated experimentally.

14.4.c. Generation of vortex electron beams

Generation of vortex electron beams with different energies:

- Indeed, several new ideas were proposed in the literature in order to create electron vortex beams experimentally.

Generation of vortex electron beams by undulators:

- Electrons in a helical modulator: cf. Figure ??

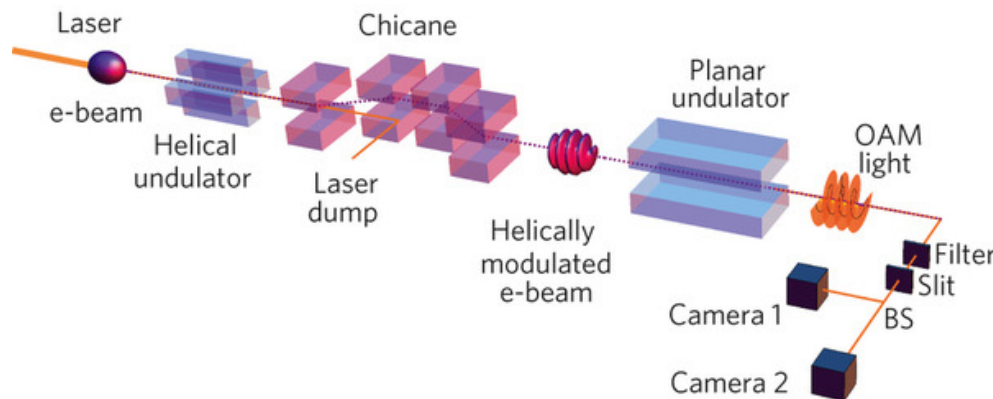


Figure 14.6.: An unmodulated relativistic electron beam interacts with a linearly polarized laser in a helical undulator, which gives the electrons an energy kick that depends on their position in the focused laser beam.

Generation of vortex electron beams by transmission electron microscopes:

- Voloch-Bloch *et al.* (2013) generated Airy electron beams by using a holographic technique within a transmission electron microscope. Both, self-bending and self-healing features were observed in the experiments if the beam was obstructed by a small object during its propagation.

Generation of vortex electron beams by holograms:

- Grillo *et al.* (2014) generated an electron Bessel beam by the diffraction of electrons at a nanoscale phase hologram. This hologram imposed a conical phase structure upon the electron wave-packet. The so obtained beams propagated for 0.6 m without measurable spreading and could reconstruct also its intensity distributions, if these beams where partly obstructed by an obstacle.

14.4.d. Laguerre-Gaussian electron beams

Characterization and use:

- **Landau states:** The (nonrelativistic) Schrödinger equation for an electron in an homogeneous magnetic field $\mathbf{B} \parallel \mathbf{e}_z$ can be solved and leads to the (so-called) Landau Hamiltonian and solutions

$$\begin{aligned}\mathbb{H} &= \frac{1}{2m} \left[-\nabla^2 + ie\mathcal{B} \frac{\partial}{\partial\varphi} + \frac{e^2 \mathcal{B}^2 r^2}{4} - e\boldsymbol{\sigma} \cdot \mathbf{B} \right], & A_\varphi &= \frac{\mathcal{B}r}{2}, & A_r = A_z &= 0 \\ \psi(r, \varphi, z) &= \mathcal{N} \exp(i\ell\varphi) \exp(ip_z z) = \frac{C_{n\ell}}{w_m} \left(\frac{\sqrt{2}r}{w_m} \right)^{|\ell|} L_n^{|\ell|} \left(\frac{2r^2}{w_m^2} \right) \exp\left(-\frac{r^2}{w_m^2}\right) \chi_{\pm 1/2} \exp(i\ell\varphi) \exp(ip_z z) \\ C_{n\ell} &= \sqrt{\frac{2n!}{\pi(n+|\ell|)!}}, & w_m &= \frac{2}{\sqrt{|e|\mathcal{B}}}, & \int dr d\varphi r \psi^* \psi &= 1,\end{aligned}$$

and where $n = 0, 1, \dots$ is the radial quantum number. A distinctive feature of these Landau solutions is their trivial (exponential) dependence on z . For fixed values of p_z , $\psi(r, \varphi, z)$ is also an eigenfunction of $p_z = -i\hbar \frac{\partial}{\partial\varphi}$ with (integer) eigenvalues ℓ .

- **Solutions of the paraxial wave equation:** The twisted states of free photons and electrons are defined by the paraxial wave equation (Zou *et al.*, 2021):

$$\left(\nabla_{\perp}^2 + 2ikz \frac{\partial}{\partial z} \right) \psi(r, \varphi, z) = 0 \quad \nabla_{\perp}^2 = \frac{\partial^2}{\partial r^2} + \frac{1}{r} \frac{\partial}{\partial r} + \frac{1}{r^2} \frac{\partial^2}{\partial \varphi^2}.$$

For electrons, this equation can be obtained from the Dirac equation by applying a Foldy-Wouthuysen (FW) transformation and by assuming

$|\mathbf{p}_\perp| \ll p$. The solutions to the paraxial wave equation reads as

$$\begin{aligned}\psi(r, \varphi, z) &= \mathcal{N} \exp(i\Phi) = \frac{C_{n\ell}}{w(z)} \left(\frac{\sqrt{2}r}{w(z)} \right)^{|\ell|} L_n^{|\ell|} \left(\frac{2r^2}{w^2(z)} \right) \exp \left(-\frac{r^2}{w^2(z)} \right) \chi_{\pm 1/2} \exp \left[i \left(\ell \varphi + \frac{k r^2}{2R(z)} - \Phi_G(z) \right) \right] \chi_{\pm 1/2} \\ C_{n\ell} &= \sqrt{\frac{2n!}{\pi(n+|\ell|)!}}, \quad w(z) = w_o \sqrt{1 + \frac{z^2}{z_R^2}}, \quad R(z) = z + \frac{z_R^2}{2}, \quad z_r = \frac{k w_o^2}{2} \\ \Phi_G(z) &= N \arctan \left(\frac{z}{z_R} \right), \quad N = 2n + |\ell| + 1, \quad \int dr d\varphi r \psi^* \psi = 1,\end{aligned}$$

and where k is the wave number of the beam, w_o the beam waist, $R(z)$ the radius of curvature of the wave front, $\Phi_G(z)$ the Gouy phase, and z_R is the Rayleigh diffraction length. Obviously, these solutions are spinors for electrons (because of $\chi_{\pm 1/2}$) but are no longer eigenfunctions of p_z . Instead, these solutions can be considered as partial waves.

14.4.e. Bessel electron beams

Characterization and use:

- Quasi-Bessel beams can be obtained within a good approximation, while it is not possible to generate an ideal Bessel beam because they are not normalizable in their total intensity,
- Wave function of a Bessel electron: In cylindrical coordinates r, φ, z , the wave function of electrons in a Bessel beam is given by

$$\psi(r, \varphi, z; t) = J_m(\kappa r) e^{im\varphi} e^{-i(\omega t - k_z z)},$$

where $J_m(x)$ is the m -th order Bessel function of the first kind and κ and k_z denote the transverse and longitudinal components of the wave vector, respectively.

- Probability-density distribution of Bessel electron beams: This wave function give rise to a probability-density distribution $\mathcal{P} = \psi\psi^+$ that is independent of z and t :

$$\mathcal{P}(r, \varphi, z; t) = \mathcal{P}(r, \varphi, 0; 0) = [J_m(\kappa r)]^2.$$

- This shows that the probability-density distribution is stationary in the transverse plane and independent of where this plane is taken.
- The energy of the electron $E = \hbar\omega$ defines the de Broglie wave length and the modulus of the wave vector by

$$k^2 = k_r^2 + k_z^2 = \frac{2m\omega}{\hbar} = \left(\frac{2\pi}{\lambda_{dB}}\right)^2.$$

- For Bessel beams with a nonzero m value, the electrons possess a non-uniform helical phase front with m dislocations in the phase, and where the handedness of the phase front is defined by the sign of m .
- Current density of electron Bessel beam: This current density circulates azimuthally in the transverse plane and introduces an (projection of the total) orbital angular momentum of $m\hbar$ per electron.
- An Bessel electron beam with a nonzero m value possess exhibit a shape with multiple rings and with a null probability density at the origin.
- Bessel electron beams can be represented also as a coherent superposition of conical plane waves along a closed ring (circle).

14.4.f. Airy electron beams

Characterization and use:

- Airy electron beams can be generated by diffraction of electrons through a nanoscale hologram, which imprints a cubic phase modulation on wavefunction of the electrons in the transverse plane.

14.4.g. Application of twisted electron beams

Remarks:

- The scattering of twisted electrons can provide insights into the magnetic structure of the target materials.
- Beams with non-zero OAM helped explore the vacuum Faraday effect as well as Larmor and Gouy rotations.
- Bessel electron beams have been used in electron microscopy.
- **Zeeman interaction with electron vortex beams (EVB):** EVB allow to enhance the Zeeman interaction by more than 2 orders of magnitude due to high OAM, and if compared to the SAM $\hbar/2$ of electrons along the propagation direction.
- **Stationary Pauli equation with a non-uniform magnetic field:** In solid-state materials, the magnetic field is usually not constant. Therefore, the motion of an electron need to be described by means of a Pauli equation with a non-uniform magnetic field $\mathbf{B}(\mathbf{r}) = \nabla \times \mathbf{A}$ and a vector potential in Coulomb gauge $\nabla \cdot \mathbf{A} = 0$ (Edström *et al.*, 2016).

14.5. Quantum technologies

Quantum technologies:

- **Quantum revolution:** While quantum mechanics is known for about a century, it has attracted recent interest due to several technological developments. These technological developments, based on quantum systems, have been termed also as **second quantum revolution**. — Which set-up, phenomena and developments have made this revolution more explicit, actually ? For sure, the improved understanding of the fundamental laws of quantum mechanics at the atomic scale laid the foundation not only for many semiconductor device but also for new techniques of imaging.
- **Quantum revolution:** In particular, lasers are a versatile tool to transmit information, to process and control materials, to generate light, image objects of very different size and composition and to perform many metrological tasks. Indeed, lasers provide important tool to control and tailor such quantum systems.
- **Quantum technologies:** Apart from lasers, a diverse toolbox of quantum systems and techniques is available, including high-finesse cavities, optical frequency combs, frequency converters, source of photon (pairs) in heralded states, low-noise stabilization techniques and several others.

14.5.a. Elements from quantum optics

Photon statistics and bunching:

- **Photon bunching:** If the photons from thermal light sources are detected, they are bunched, i.e. the detection of another photon is more likely when a first photon was seen already. For laser light, in contrast, the probability for measuring a second photon from the beam is independent from the elapse time since the first photon has been detection.
- **Photon antibunching:** Antibunching of photons can be observed in the (resonance) fluorescence of single atoms as shown for sodium by Kimble 1977. This antibunching is easily understood by the – necessary time for the – re-excitation of the atom, once a photon has been emitted, and before the next one can be detected in emission.
- **Photon number statistics:** This statistics enables one to readily distinguish between different types of light. Any state of light gives rise to a well-defined photon number (measurement) statistics and can be characterized by its mean photon number and its variance. Whereas a large number of photon states can be generated today on-demand already, the **creation of pure single-photon Fock states on demand are still a challenge for modern optics.**

- **Multi-optical modes:** The total photon number of multiple optical modes is given by the sum of the individual modes, $N = \sum_k n_k$. These multi-optical modes are in a Fock state, if $\langle(\Delta N)^2\rangle = 0$, while the individual modes may still have a non-zero variance. Therefore, different multi-optical modes can share the same (total) Mandel parameter $Q_M = 0$. These states are central to many quantum-optical applications.
- **Photon statistics of SPDC:** In SPCD, the two-mode photon states have $\langle\Delta(n_s - n_i)\rangle = 0$ because of their mutual correlation.
- **Distribution of photon numbers:** Let n be the number of photons in a given quantum state. Classical light shows a super-Poissonian distribution with $\langle(\Delta n)^2\rangle > \langle n \rangle$, whereas non-classical light has a sub-Poissonian distribution with $\langle(\Delta n)^2\rangle < \langle n \rangle$. For example, classical light arises from the thermal radiation of a light bulb with $\langle(\Delta n)^2\rangle > \langle n \rangle + \langle n \rangle^2$, while the Fock states with well-defined photon numbers have $\langle(\Delta n)^2\rangle = 0$. The coherent states of laser have $\langle(\Delta n)^2\rangle = \langle n \rangle$ and form the boundary between classical and non-classical light; cf. Figure ??.
- **Mandel parameter for characterizing the photon statistics:** The Mandel parameter

$$Q_M = \frac{\langle(\Delta n)^2\rangle}{\langle n \rangle} - 1 \quad \begin{cases} > 0 & \text{super - Poissonian (classical)} \\ = 0 & \text{Poissonian (coherent state)} \\ < 0 & \text{sub - Poissonian (non - classical)} \end{cases}$$

provides a simple and useful measure in order to **characterize the classicality of light**. In general, non-classical quantum states exhibit smaller fluctuations in the measured photon number. In SPDC, the generated photon pairs represent Fock states with (exactly) two photons and vanishing variance. These photon pairs are generally distinguishable and are different also from the general SPDC output state.

Fundamental experiments:

- **Hanbury-Brown and Twiss:** The experiment by Hanbury-Brown and Twiss showed that intensity fluctuations can provide information about the coherence and quantum statistics of light. This even applies for single-photon measurements. When compared with a thermal light source, a laser always leads to a reduced intensity fluctuations, independent of its band widths and intensity.
- **Hong-Ou-Mandel experiment:** In 1987, Hong, Ou and Mandel made use of SPDC photon pairs and impinged these pairs on the two input ports of a 50:50 beam splitter. While classical particles would result into 50 % probability at both output ports, they are always measured, though randomly at the two output ports. This result can be understood as interference of the probability amplitudes of photons at a beam splitter and can be utilized for quantum information tasks.

Tools and devices:

- **Atom laser:** In an atom laser, a coherent beam of atoms was generated, similar as with photons by a (standard) laser. For such atom lasers, the lack of bunching was observed, well in contrast to the bunching of thermal atom beams.
- **Polarizing beamsplitter:** A polarizing beamsplitter separates photons with different (linear) polarization from each other. An incoming and circularly-polarized photon always leaves the polarizing beamsplitter with linear polarization, though either horizontally or vertically-polarized. Polarizing beamsplitter can therefore be used as quantum random number generators.

14.5.b. Spontaneous parametric down-conversion (SPDC)

Spontaneous parametric down-conversion (SPDC):

- **Spontaneous parametric down-conversion (SPDC):** In SPDC, a – nonlinear-responding – quadratic crystal is pumped by a laser field in order to convert (high-energy) photons into correlated photon pairs. In particular, SPDC has been found a robust experimental technique to generate entangled states in a two- or high-dimensional basis. An efficient control of the down-converted photon pairs in SPDC plays a crucial role for various tasks in quantum information processing.
- **SPDC with a Gaussian pump beam:** In typical SPDC set-ups, a Gaussian pump beam with the field $\mathcal{E}^{(p)}(\mathbf{q})$ and beam waist w_p is focused upon the center of the non-local crystal of length L . For such a set-up, the mode function can be written as

$$\mathcal{E}^{(p)}(\mathbf{q}) = \frac{w_p}{\sqrt{2\pi}} \exp\left(-\frac{\mathbf{q}^2 w_p^2}{4}\right)$$

$$\Phi(\mathbf{q}, \mathbf{q}') = K \exp\left(-\frac{|\mathbf{q} + \mathbf{q}'|^2 w_p^2}{4}\right) \operatorname{sinc}\left(\frac{\Delta k(\mathbf{q}, \mathbf{q}') L}{2}\right),$$

and where the proportionality (or normalization) constant K depends on both, the power of the pump beam and the properties (coefficients) of the non-linear crystal. The (spatial) transverse width of the Gaussian pump beam determines how strong the photon pair is correlated in the transverse (spatial) degrees of freedom, while the widths Δk from the phase-matching affects the single-photon bandwidth of the generated photon pair. Typically, the spectral widths of the signal and idler photons are much larger than those of the pump field. The

two terms in the mode function above arises from the energy conservation and phase matching condition, and these conditions give usually rise to a non-separable two-photon mode function $\Phi(\mathbf{q}_s, \mathbf{q}_i) \neq \phi_s(\mathbf{q}_s) \phi_i(\mathbf{q}_i)$.

- **Entanglement of SPDC photon pairs:** SPDC is a robust technique for generating entangled photon pairs in a two- or high-dimensional basis. Hereby, the down-converted photons can be entangled in either their time bins, polarization states, the orbital angular momentum (OAM) of the photons or with regard to their radial structure (quantum numbers). In general , the SPDC two-photon state depends on both, the relative set-up of the beam and crystal (axes, e.g. the geometry) as well as the subsequent partial projection and the coupling of the photon state. Often, the entanglement of such photon pairs is *quantified* in terms of the Schmidt number K by making use of a corresponding (Schmidt) decomposition of the two-photon state.
- **Fiber coupling efficiency:** A larger efficiency for coupling the signal or idler photons to fibers can be achieved for well-focused pump beams and rather long crystals. Pair detection rates $> 10^6$ per mW of the pump beam intensity have been realized experimentally.
- **Entanglement of SPDC photon pairs:** The SPDC has been studied with various pump beams, such as paraxial Hermite-Gaussian (HG) beams, Laguerre-Gaussian (LG) beams, the superposition of LG and HG beams, and with several others. While HG beams are known to be solutions of the free-space paraxial wave equation in Cartesian coordinates, the LG beams are solutions to this equation in cylindrical coordinates.
- **SPDC photon pairs:** The SPDC process in non-linear crystals support a high control of the spatial and spectral properties of the emitted photons. It has been the basis for many (quantum-optical) sources of correlated and entangled photons, including even the generation of spatially entangled photons.
- **Spatial *versus* spectral correlations of two-photon states:** The SPDC process generates photon pairs which are *correlated* in their spatial and spectral degrees of freedom. Several quantum optical applications require to control these (so-called) spatial and spectral correlations by means of crystal engineering, control of the pump beam, the projection of the two-photon states upon well-defined modes, or a number of other techniques. In particular, the properties of the nonlinear crystal play a crucial role in controlling these spatial and/or spectral correlations.
- **Spatial *versus* spectral correlations of two-photon states:** Photon pairs with well-defined spatial and spectral (correlation) properties can be obtained with the help of waveguides.
- **Entanglement of photon pairs with well-defined OAM:** Photons with helical phase structure can have a well-defined projection of the orbital angular momentum (OAM). Since there is no formal limit on this OAM projection, entangled photon pairs with high differences in their OAM quantum numbers can be generated. Fickler *et al.* (2012) demonstrated experimentally the generation of such photon pairs and that the OAM entanglement can improve the sensitivity of angular resolution in remote sensing.

14. Beams of light and particles

- **Entanglement of photon pairs with well-defined OAM:** Because of the low efficiency of the down-conversion process for generating photon pairs with high OAM, Fickler *et al.* (2012) first generated polarization-entangled photon pairs with high fidelity, and which are then transformed to the desired OAM subspaces, i.e. subspaces of well-defined orbital angular momentum. This transfer has been realized by means of spatial light modulators and a folded interferometric structure, that is intrinsically phase-stable and has by design equal arm lengths. The spatial light modulators can be programmed to generate photons with well-defined OAM, depending on the path the polarization-entangled photons take.

Phase matching in nonlinear crystals:

- **Nonlinear crystals:** Most often, the SPDC process makes use of second-order nonlinear crystals, such as bismuth borate (BBO), lithium borate (LBO), lithium niobate (LN) as well as potassium titanyl phosphate (KTP).
- **Birefringent phase matching (BPM):** BMP refers to photon pairs where (at least) one of the signal and idler photons is polarized orthogonal to the pump photons. Whereas the signal and idler photons are co-polarized to each other in Type-I BMP, the idler is co-polarized with the pump photon in Type-II BMP. An BPM is usually achieved by a proper rotation of the crystal.
- **Quasi-phase matching (QPM):** QPM can be utilized to generate photon pairs that propagate (together with the pump photon) along a principal axis of the nonlinear crystal. This avoid spatial divergence of the signal and idler photons and, hence, enables are more efficient use of long nonlinear crystals and waveguide structures.

Correlations of two-photon states:

➤

Notations:

- **Beams and associated wave vectors:** In SPDC, a wave vector $\mathbf{k}_j = (k_{j,x}, k_{j,y}, k_{j,z}) = (k_{j,\rho}, k_{j,\varphi}, k_{j,z})$, $j = \{p, s, i\}$ is assigned to each of the pump, signal and idler beam. The pump beam has always the wave vector $\mathbf{k}_p = (0, 0, k_{p,z})$. Without polarization, therefore, each beam is characterized by three independent parameters; these or a well reduced number of parameters should be visible in all derived quantities of the three-wave mixing, such as the two-photon states and mode functions. This is no need (and justification) for introducing *covariant* coordinates/superscripts.
- **Beams and associated wave vectors in paraxial approximation (transverse mixing):** In in paraxial approximation of the signal and idler beams of SPDC, only two-dimensional wave vectors $\mathbf{p}_j = (p_{j,x}, p_{j,y}, \dots) = (p_{j,\rho}, p_{j,\varphi}, \dots)$, $j = \{p, s, i\}$ are needed for each of the pump, signal and idler beam.

- We should first express some central expressions in such a notation, please.
- Two-photon state $|\Psi\rangle$: Spatially-resolved two-photon state = spatially-resolved state of the photon pair; entangled two-photon state; separable two-photon state = two-photon product state; spatially-resolved and entangled two-photon state.
- Frequency-resolved two-photon state = spectral two-photon state;
- polarization-entangled two-photon state; time-binned entangled two-photon state; spatially-entangled two-photon state; frequency-entangled two-photon; macroscopic two-photon state.
- Two-photon mode function $|\Psi\rangle$:

Two-photon state and mode function:

- Energy and momentum conservation in three-wave mixing:
- Energy and momentum conservation in paraxial approximation for the signal and idler beams:
- Wave-vector representation of the two-photon state: If energy and momentum is conserved, the representation of $|\Psi\rangle$ should contain 8 parameters due to the three wave vector components and the frequency of the signal and idler photons.
- Wave-vector representation of the two-photon state in paraxial approximation: In the paraxial approximation, the representation of $|\Psi\rangle$ should depend on 6 parameters due to the two (transverse) wave vector components and the frequency of the signal and idler photons. This representation is given by

$$|\Psi\rangle = \int \int d\mathbf{q}_s d\mathbf{q}_i d\omega_s d\omega_i \Phi(\mathbf{q}_s, \mathbf{q}_i, \omega_s, \omega_i) \dots$$

This representation describes the generation of a two-photon state with well-defined frequencies $\omega_{s,i}$ and (transverse) wave vectors $\mathbf{q}_{s,i}$ from the vacuum state.

- Expansion of a paraxial beam into Laguerre-Gaussian modes: In the paraxial approximation, any field can be decomposed into Laguerre-Gaussian modes with well-defined radial index r , projection of the OAM ℓ and energy ω :

$$|r, \ell, \omega\rangle = \int d\mathbf{q} LG_r^\ell(\mathbf{q}, \omega) a^+(\mathbf{q}, \omega) |o\rangle .$$

and where $LG_r^\ell(\mathbf{q}, \omega)$ refers to .

14. Beams of light and particles

- **OAM representation of the two-photon state in paraxial approximation:** In the paraxial approximation, the OAM representation of the two-photon state is given (in terms of obviously 6 parameters) by

$$|\Psi\rangle = \int \int d\omega_s d\omega_i \sum_{r_i, r_s=0}^{\infty} \sum_{\ell_i, \ell_s=0}^{\infty} C_{r_i, r_s}^{\ell_i, \ell_s} |r_i, \ell_i, \omega_i\rangle |r_s, \ell_s, \omega_s\rangle$$

$$C_{r_i, r_s}^{\ell_i, \ell_s} \equiv \langle r_i, \ell_i, \omega_i; r_s, \ell_s, \omega_s | \Psi \rangle = \int \int d\mathbf{q}_s d\mathbf{q}_i \Phi(\mathbf{q}_s, \mathbf{q}_i, \omega_s, \omega_i) [LG_{r_i}^{\ell_i}(\mathbf{q}_i, \omega_i)]^* [LG_{r_s}^{\ell_s}(\mathbf{q}_s, \omega_s)]^*$$

- **Two-photon mode function in paraxial approximation:** In the paraxial approximation and if the total transverse momentum is conserved independently, the mode function factorizes for a nonlinear crystal of length L along \mathbf{e}_z into

$$\Phi(\mathbf{q}_s, \mathbf{q}_i, \omega_s, \omega_i) = N_o V_p(\mathbf{q}_i + \mathbf{q}_s) S_p(\omega_i + \omega_s) \int_{-L/2}^{+L/2} dL \exp[i(k_{p,z} - k_{i,z} - k_{s,z})]$$

where N_o is a normalization constant, and $V_p(\mathbf{q})$ and $S_p(\omega)$ the (so-called) spatial and spectral (frequency) distribution of the pump beam.

- **Fourier expansion of the two-photon state in terms of Laguerre-Gaussian modes:** If $|\ell, p\rangle$ denotes a Laguerre-Gaussian mode with winding number (QAM) ℓ and radial index p , the two-photon state can be expanded into a product basis as

$$\Psi(\dots) = \sum_{\ell_s p_s, \ell_i p_i} c(\ell_s p_s, \ell_i p_i) |\ell_s, p_s\rangle |\ell_i, p_i\rangle, \quad c(\ell_s p_s, \ell_i p_i) = \int d^3\mathbf{q}_s d^3\mathbf{q}_i \Phi(\mathbf{q}_s, \mathbf{q}_i) \Psi(\dots)$$

where ℓ_s, p_s and ℓ_i, p_i refer to the mode indices of signal and idler photons, respectively. An expansion into other discrete bases can be made and have found applications in microscopy.

- **Conservation of OAM:** In SPDC, the orbital angular momentum is often conserved for a properly chosen crystal and for a collinear geometry of the pump, signal and idler beams. For a Gaussian pump beam with $\ell_p = 0$, we then have $\ell_p = \ell_s + \ell_i = 0$ and, hence, the generation of OAM entangled photon pairs.

- **Fourier coefficients in the OAM representation of the two-photon state for a Laguerre-Gaussian pump beam:** In the paraxial approximation

and if the pump beam is given by the Laguerre-Gaussian mode $\text{LG}_{r_p}^{\ell_p}(\mathbf{q}_p, \omega_p)$, the Fourier coefficients are given by

$$\langle r_i, \ell_i, \omega_i; r_s, \ell_s, \omega_s | r_p, \ell_p, \omega_p \rangle = \dots \delta_{\ell_i + \ell_s, \ell_p} \sum_i^{r_i} \sum_s^{r_s} \sum_p^{r_p} (T(i; r_i, \ell_i))^* (T(s; r_s, \ell_s))^* (T(p; r_p, \ell_p))^* \sum_{\lambda}^{\ell_p} \sum_{\pi}^p \left(\begin{array}{c} \ell_p \\ \lambda \end{array} \right) \dots$$

$$T(j; r_j, \ell_j) = \sqrt{\frac{r_j! (r_j + |\ell_j|)!}{\pi}} \left(\frac{w_j}{\sqrt{2}} \right)^{2j+|\ell_j|+1} \frac{(-1)^{r_j+j} i^{\ell_j}}{(r_j - j)! (|\ell_j| + j)! j!}, \quad j = p, i.s.$$

Useful approximations for expressing the two-photon state:

- **Paraxial approximation:** This approximation separates the longitudinal and transversal components of the wave vector: $\mathbf{k} = \mathbf{q} + k_z(\omega) \mathbf{e}_z$.
- **Fresnel approximation to the frequency-dependence of the k_z component of the wave vector:** For $|\mathbf{q}|/k \ll 1$ and for small values of the frequency shift Ω in $\omega = \omega(0) + \Omega$, the k_z component of the wave vector can be written as

$$k_z = k(\Omega) \sqrt{1 - \frac{|\mathbf{q}|^2}{k^2}} \approx k + \frac{\Omega}{u} + \frac{G \Omega^2}{2} - \frac{|\mathbf{q}|^2}{2k}, \quad u = \frac{1}{\frac{\partial k}{\partial \Omega}}, \quad G = \frac{\partial}{\partial \Omega} \left(\frac{1}{u} \right).$$

$$k_{j,z} = k_j(\Omega_j) \sqrt{1 - \frac{|\mathbf{q}_j|^2}{k_j^2}} \approx k_j + \frac{\Omega_j}{u_j} + \frac{G_j \Omega_j^2}{2} - \frac{|\mathbf{q}_j|^2}{2k_j}, \quad j = p, i.s.$$

Here $u = \frac{1}{\frac{\partial k}{\partial \Omega}}$ is the group velocity of the beam and $G = \frac{\partial}{\partial \Omega} \left(\frac{1}{u} \right)$ the dispersion of the group velocity.

Three-wave mixing in bulk crystals:

- : Adapted from Anwar *et al.* (2021).

14.5.c. Boson sampling

Boson sampling:

14. Beams of light and particles

- **Boson sampling:** Boson sampling is a simple quantum algorithm that has been designed for platforms of linear optics. This algorithm has been promoted with the goal to demonstrate (so-called) quantum supremacy, a rather sophisticated term. The boson sampling algorithm leads to photon statistics that is determined by complicated matrix functions and that readily becomes intractable at classical computers, if a sufficiently large number of identical photons is applied. If these photons are injected into a linear optical network, the associated matrix function can therefore be solved (evaluated) more quickly than by any classical computer. Since boson sampling can be readily implemented with linear optics, the expected supremacy of quantum machines can be demonstrated experimentally, if once a sufficiently large set of identical photons is available.
- **Boson sampling:** The potential demonstration of computational supremacy with near-term experimental capabilities has raised a large number of proposals, more or less suitable with different hardware components.
- **Boson sampling:** The basic concept of boson (photon) sampling can be summarized as follows. In this sampling scheme, n indistinguishable and noninteracting bosons are injected into n input ports of a quantum circuit that linearly and successively couple the bosonic modes. The circuit is assumed to realize a uniform ('Haar') random unitary matrix that transforms the input into the output ports. For such a setup, the probability to detect n photons at the n output ports is equal to the square (of the absolute value) of the permanent as associated with the transfer matrix. Since the computation of the permanent itself scales exponential with the dimension of the permanent, computational supremacy is reached, if the size of the matrix becomes sufficiently large and computationally intractable. Today, most boson samplers use photons that can be operated at room temperature and are robust to decoherence.
- **Promise of boson sampling:** This sampling is considered a strong algorithm to demonstrate the quantum computational advantage over classical computers and, hence, to perform a task that is believed to be intractable otherwise.
- **Quantum supremacy:** A quantum computational advantage, or quantum supremacy, is shown if the quantum speed-up is so large that no classical computer can perform the same task within a reasonable amount of time, and if no further improvement becomes known for the underlying classical algorithm. It has been sometimes suggested that such a quantum computational advantage will result into a long-term competition between faster classical simulations and improved quantum devices (Zhong *et al.*, 2020).
- **Boson sampling:** Boson sampling was first proposed by Aaronson and Arkhipov (2011) as a feasible protocol for achieving a quantum computational advantage. In this and other sampling variants, nonclassical light is injected into and propagated through a linear optical network. The number- and path-entangled output state are then measured by single-photon detectors. Since the dimension of the entangled state grows exponentially with both the number of photons and the possible modes of the network, this renders the storage and computation of the intermediate quantum probability amplitudes unfeasible.
- **Boson sampling:** The photon distribution at the output ports is related to the (so-called) Torontonian, a matrix function close to the Permanent. Classical computations of the Torontonian is known as a computationally hard problem in the complexity class #P-hard.

- Challenges of large-scale Gaussian boson sampling (GBS): Technological challenges include (i) the generation of indistinguishable single-mode squeezed states with proper squeezing parameters and their collection efficiency; (ii) the set-up of large interferometers with full connectivity, phase stability and near-to-unity transmission rate; (iii) a nearly perfect overlap of wave-packets; (iv) phase control of all single-mode squeezed states; (v) the development of high-efficiency detectors to sample the output distribution; (vi) to validate the output sampling of photon distribution and to compare them with supercomputers.

:

- .

14.5.d. Quantum imaging

Quantum imaging schemes:

- Quantum imaging: Many quantum imaging schemes make use of SPDC photon pairs. Most often, however, only one photon of the generated pair interacts with the sample, while the second photon just mediates the interference that arise due to different crystals, from which the photon pairs may originate. In other schemes, still only one photon interacts with the object, though both of the photons need to be detected.
- Quantum images: These images differ from ordinary intensity images by (i) the coincidence of the signal photons with the position of the idler detector, even if the idler has never passed the detection area (mask of aperture) and (ii) the dimensions and the resolution of the quantum image, which depends on the wavelength and spatial properties of the pump beam. For these images, the intensity distribution of the idler alone does not yield any image, but only in coincidence with the signal photon. Quantum imaging is often analyzed by means of light fields with Gaussian photon statistics.

14.5.e. Other technologies

:

- .

⋮

➤ .

14.5.f.

⋮

➤ .

15. Symbolic evaluation of expressions from Racah's algebra

15.1. Racah's algebra in atomic and many-body physics

15.1.a. Advantages of using Racah's algebra

Goals and use of Racah's algebra:

- The theories of angular momentum and spherical tensor operators play a significant role in atomic and nuclear physics, and at several places elsewhere. These two theories lead to algebraic expressions which are usually written in terms of generalized Clebsch-Gordan coefficients and/or Wigner $3n-j$ symbols as well as the Wigner rotation matrices and spherical harmonics. Although the evaluation and simplification of such expressions is in principle a straightforward task, it can become extremely cumbersome, if more complex systems or physical scenarios are considered.
- Indeed, the study of open-shell atoms and nuclei quickly raises the question how the rotational symmetry of (closed) systems, i.e. the conservation of angular momentum, can efficiently be exploited in understanding many-particle systems. After the pioneering work by Wigner in the late thirties, [Racah \(1941, 1942, 1943\)](#) developed a powerful machinery, known as [Racah algebra](#), to deal with such systems, and which is one of the fundamental concepts in the (quantitative) treatment of many-particle systems.
- In many-particle physics, an explicit re-coupling of the angular momenta is often required due to the use and sequence of different coupling schemes. In general, such recoupling transformations are written in terms of [recoupling coefficients](#) that need to be evaluated over and over again.
- [Spin-angular integration of many-particle matrix elements](#) In atomic and nuclear structure theory, the evaluation and spin-angular integration of many-particle matrix elements is typically based on standard quantities like the matrix elements of the unit tensor, the (reduced) coefficients of fractional parentage as well as a number of other reduced matrix elements for different products of creation and annihilation operators. These quantities arise rather frequently in both, configuration interaction approaches and in the derivation of perturbation expansions for many-particle systems by using symmetry-adapted configuration state functions.

15. Symbolic evaluation of expressions from Racah's algebra

- **Theory of angular momentum** In the treatment of quantum many-particle systems, the **theory of angular momentum offers two crucial advantages:** (i) The reduction of complicated many-electron matrix elements to a rather small number of *standard quantities* and (ii) an elegant and very powerful calculus which help simplify and evaluate sophisticated expressions.
- **Racah algebra techniques:** Owing to these advantages, the techniques from the theory of angular momentum, shortly known also as Racah algebra techniques (Racah 1941, 1942, 1943), have been utilized in a large number of applications and in quite different field of many-particle physics (Wigner 1959, Varshalovich *et al.* 1988).
- **Racah expressions:** With the symbolic evaluation of expressions from Racah's algebra, we wish to focus on the algebraic transformation of **(Racah) expressions** such as:

$$\text{Racahexpr} := \sum_{j_1, j_2, l_1, \dots} (-1)^{2j_1-j_2+\dots} j_1^{3/2} [j_2] \dots \begin{pmatrix} & & j_1 \\ & & \cdot \\ & & \cdot \\ & & \cdot \end{pmatrix} \begin{pmatrix} j_1 & j_2 & \cdot \\ \cdot & \cdot & \cdot \\ \cdot & \cdot & \cdot \end{pmatrix} \left\{ \begin{matrix} & j_3 & \cdot \\ j_1 & \cdot & \cdot \\ J & \cdot & j_2 \end{matrix} \right\} \dots$$

$$\times \int d\Omega_1 Y_{\ell_1 m_1}(\Omega_1) Y_{\ell_2 m_2}(\Omega_2) \int d\beta d_{p_3 q_3}^{j_3}(\beta) d_{p_4 q_4}^{j_4}(\beta') \dots$$

Here, the Clebsch-Gordan coefficients need not to shown explicitly in this expression since, apart from an additional phase, they are equivalent to the Wigner $3-j$ symbols. Up to the present, we (must) also drop the rotation matrices and spherical harmonics which are not (yet) supported in JAC. We introduce this notation of **Racahexpr** with the intention for providing an (internal) data type which facilitates automatic manipulations and which is flexible enough to support a wide range of applications.

- **Racah expressions:** Such expressions may generally include any number of Wigner $n-j$ symbols of different kind as well as (various integrals over) the spherical harmonics and Kronecker and triangular deltas. Of course, the complexity of such Racah expressions increases rapidly as more Wigner symbols are involved in the product terms.
- The symbolic evaluation of typical expressions from Racah's algebra is naturally based on the knowledge of a large set of sum rules that may include rules with a (multiple) summations over dummy indices (Varshalovich *et al.* 1988). For complex and lengthy Racah expressions, moreover, the algebraic simplification can often be considerably accelerated if the graphical rules due to Yutsis *et al.* (1962) are taken into account.
- **Sum and orthogonality rules:** To obtain a simplification for complex Racah expressions, a large variety of sum and orthogonality rules have been implemented from the monograph by Varshalovich *et al.* (1988).
- In the past decades, various techniques in simplifying expressions from Racah's algebra have been developed, based either on graphical methods or on the explicit knowledge of special values and sum rules, as they can be found in some standard form in the literature. The direct application of these rules is however often laborious due to a large number of symmetric forms of the Wigner and related symbols.

- **Graphical loop rules:** These loop rules are typically used in order to find out about and to simplify those parts in a recoupling coefficient (or generally in any Racah expression) that belong together. The implementation of graphical rules even allows to easily simplify recoupling coefficients which include several ten angular momenta to an (completely equivalent) sum of products of Wigner 6– j and/or 9– j symbols, multiplied by proper weights.
- **Algebraic simplifications:** The simplification of expressions from Racah's algebra critically depends how easily **all equivalent symmetric forms of these expression are recognized internally**. Obviously, the symmetry of a Racah expression as a whole is closely related to the symmetries of all the Wigner $3n-j$ symbols which are involved in the expression.
- **Classical symmetries of the Wigner symbols:** Apart from the classical symmetries of the Wigner symbols, there is an extended range of symmetries due to Regge (1958); these symmetries are however of minor practical importance.
- Although the mathematical background of angular momentum theory is today quite well understood, the treatment and simplification of typical expansions as they naturally arise by using Racah's algebra, is often very laborious.
- In JAC, we shall facilitate the symbolic evaluation of expressions from Racah's algebra and, in particular, for (complex) expressions for which the known algebraic and graphical methods start to become tedious and prone to making errors.

15.1.b. Frequently applied symbols and functions from Racah's algebra

Table of symbols and functions from the theory of angular momentum:

- The following symbols and functions from the **theories of angular momentum and irreducible tensor operators** occur very frequently in the computation and analysis of atomic and many-body systems

15. Symbolic evaluation of expressions from Racah's algebra

| Symbol | Designation | Calls in JAC |
|---|--|------------------------------|
| $\begin{pmatrix} a & b & c \\ m_a & m_b & m_c \end{pmatrix}$ | Wigner 3- j symbol | <code>Wigner_3j()</code> |
| $\left\{ \begin{matrix} a & b & c \\ d & e & f \end{matrix} \right\}$ | Wigner 6- j symbol | <code>Wigner_6j()</code> |
| $\left\{ \begin{matrix} a & b & c \\ d & e & f \\ g & h & i \end{matrix} \right\}$ | Wigner 9- j symbol | <code>Wigner_9j()</code> |
| $\left\{ \begin{array}{cccc c} a & b & c & d & s \\ e & f & g & h & \\ i & j & k & l & \end{array} \right\}$ | Wigner 12- j symbol of kind $s = 1, 2$ | Not implemented. |
| $\left\{ \begin{matrix} - & a_2 & a_3 & a_4 \\ b_1 & - & b_3 & b_4 \\ c_1 & c_2 & - & c_4 \\ d_1 & d_2 & d_3 & - \end{matrix} \right\}$ | Sharp's symbol (Sharp 1955) | Not implemented. |
| $\langle a m_a, b m_b c m_c \rangle$ | Clebsch–Gordan coefficient | <code>ClebschGordan()</code> |
| $W(abcd; ef)$ | Racah's W coefficient | Not implemented. |

| Symbol | Designation | Calls in JAC |
|--|---|-------------------------|
| $d_{mm'}^j(\beta)$ | Wigner $d_{mm'}^j(\beta)$ rotation matrix | <code>Wigner_d()</code> |
| $D_{mm'}^j(\alpha, \beta, \gamma)$ | Wigner's D -function | Not implemented. |
| $U_{mm'}^j(\omega; \Theta, \Phi)$ | Rotation matrix $U(\omega)$ | Not implemented. |
| $Y_{\ell m}(\vartheta, \varphi)$ | Spherical harmonic | Not implemented. |
| $\{\mathbf{Y}_{l_1}(\vartheta_1, \varphi_1) \otimes \mathbf{Y}_{l_2}(\vartheta_2, \varphi_2)\}_{LM}$ | Bipolar spherical harmonic | Not implemented. |
| $\{\mathbf{Y}_{l_1}(\vartheta_1, \varphi_1) \otimes \{\mathbf{Y}_{l_2}(\vartheta_2, \varphi_2) \otimes \mathbf{Y}_{l_3}(\vartheta_3, \varphi_3)\}_{l_{23}}\}_{LM}$ | Tripolar spherical harmonic | Not implemented. |
| $\mathbf{Y}_{jm}^l(\vartheta, \varphi)$ | Vector spherical harmonic | Not implemented. |
| $\Omega_{jm}^l(\vartheta, \varphi)$ | Spinor spherical harmonic | Not implemented. |
| $Y_{jm}^{ls}(\vartheta, \varphi)$ | Tensor spherical harmonic | Not implemented. |

Brief explanation of symbols and functions:

- **Wigner $3n-j$ symbols ($n = 1, 2$, and 3):** The Wigner $3n-j$ symbols are all related to the (re-) coupling of angular momenta between different coupling schemes. For $n = 1, 2$, and 3 , these symbols form the basic data types in the symbolic evaluation of expressions from Racah's algebra. Indeed, the Wigner $3n-j$ symbols frequently arise in (almost) all applications of the theory of angular momentum.
- **12– j symbols of first and second type. Sharp's symbol:** Wigner $3n-j$ symbols of higher order ($n \geq 4$) are rarely used in applications as their complexity increases rapidly with n and as several *kinds* of these symbols need to be distinguished (Varshalovich *et al.* 1988). In particular, there are two kinds of 12– j symbols, called the *first* and *second* kind or 12– $j(1)$ and 12– $j(2)$ symbols, respectively. These symbols are often written as

$$\left\{ \begin{array}{cccc|c} a_1 & a_2 & a_3 & a_4 \\ b_1 & b_2 & b_3 & b_4 \\ c_1 & c_2 & c_3 & c_4 \end{array} \right| s \right\},$$

15. Symbolic evaluation of expressions from Racah's algebra

where $s = 1, 2$ selects the *kind*. Instead of the $12-j(2)$ symbol of *second kind*, *Sharp's symbol* (Sharp 1955) is sometimes used that exhibits a slightly higher symmetry. For $n \geq 4$, the properties of the $3n-j$ symbols are still a research topic in modern group theory.

- **Clebsch-Gordan coefficients:** The Clebsch-Gordan or vector coupling coefficients appear naturally as Fourier coefficients in the *re-coupling* of angular momenta; they are closely related to the Wigner $3-j$ symbols. In JAC, we make use of the Condon-Shortley phase convention (Condon and Shortley 1935)

$$\langle j_1 m_1, j_2 m_2 | j_3 m_3 \rangle = (-1)^{j_1 - j_2 + m_3} [j_3]^{1/2} \begin{pmatrix} j_1 & j_2 & j_3 \\ m_1 & m_2 & -m_3 \end{pmatrix}.$$

- **Racah's W coefficients:** The Racah W coefficients, $W(abed; cf) = (-1)^{a+b+d+e} \begin{Bmatrix} a & b & c \\ d & e & f \end{Bmatrix}$, are basically equivalent to the Wigner $6-j$ symbols and were mainly applied in the earlier literature on the recoupling of angular momenta. In the JAC program, we only use the Wigner $6-j$ symbols in all symbolic evaluations.
- **Wigner's D-function $D_{mm'}^j(\alpha, \beta, \gamma)$:** The D -functions are often required for the transformation of wave functions, if either the system or the coordinates are rotated

$$|\Psi_{jm'}(\vartheta', \varphi', \sigma')\rangle = \sum_m |\Psi_{jm}(\vartheta, \varphi, \sigma)\rangle D_{mm'}^j(\alpha, \beta, \gamma).$$

Here ϑ, φ and ϑ', φ' are the polar angles in the initial and the rotated system, while $\sigma(\sigma')$ denote the corresponding spin variables. More general, these functions occur in the transformation of any irreducible spherical tensor of rank j . Therefore, the D -functions occur very frequently in the treatment of scattering processes from elementary particles up to molecules and clusters, and by including capture, transfer, and emission processes. The Wigner D -functions also fulfill a large number of symmetry properties (Varshalovich *et al.* 1988) and are expressed most readily in terms of the Euler angles and the (so-called) Wigner rotation matrix $d_{mm'}^j(\beta)$, see below.

- **Rotation matrix $d_{mm'}^j(\beta)$:** This (real) matrix describes the rotation of any spherical tensor by the angle β around a given axis, say, the quantization axis of the system. Several explicit representations of this real function exist in terms of $\sin(\beta/2)$ or $\cos(\beta/2)$, the hypergeometric function, or various other polynomials. In JAC, the rotation matrix $d_{mm'}^j(\beta)$ is one of the basic data structures in the algebraic manipulation of expressions from Racah's algebra.
- **Spherical harmonics:** The spherical harmonics are applied in many fields of physics. In quantum mechanics, they form an important basis for classifying the one- and many-particle states since they are known to be simultaneous eigenfunctions of one component and of the square of the orbital angular momentum operator $-i\mathbf{r} \times \nabla$. In many-particle physics, the properties of these functions (completeness, orthogonality, ...) are frequently utilized to represent and evaluate the spin-angular part of the corresponding matrix elements analytically.

- **Spherical harmonics $Y_{\ell m}(\theta, \phi)$:** These functions form a complete and orthonormal set on the unit sphere, and are therefore widely used in classical and quantum physics. The spherical harmonics frequently appear in the representation of wave functions for a wide range of physical systems, in the evaluation of the corresponding (quantum) matrix elements, and at many places elsewhere. In JAC, these functions are also one of the basic data structures in the algebraic manipulation of expressions from Racah's algebra.

15.1.c. Symmetries of the Wigner $3n-j$ symbols, rotation matrices and spherical harmonics

Symmetries of the Wigner $3n-j$ symbols:

- **Symmetries of the Wigner $3-j$ symbols:** This symbol has the following symmetries with regard to a permutation of columns and with regard to a change of signs in the projections of all angular momenta

$$\begin{pmatrix} j_1 & j_2 & j_3 \\ m_1 & m_2 & m_3 \end{pmatrix} = \begin{pmatrix} j_2 & j_3 & j_1 \\ m_2 & m_3 & m_1 \end{pmatrix} = \begin{pmatrix} j_3 & j_1 & j_2 \\ m_3 & m_1 & m_2 \end{pmatrix} = (-1)^{j_1+j_2+j_3} \begin{pmatrix} j_1 & j_3 & j_2 \\ m_1 & m_3 & m_2 \end{pmatrix}$$

$$= (-1)^{j_1+j_2+j_3} \begin{pmatrix} j_2 & j_1 & j_3 \\ m_2 & m_1 & m_3 \end{pmatrix} = (-1)^{j_1+j_2+j_3} \begin{pmatrix} j_3 & j_2 & j_1 \\ m_3 & m_2 & m_1 \end{pmatrix}$$

$$\begin{pmatrix} j_1 & j_2 & j_3 \\ m_1 & m_2 & m_3 \end{pmatrix} = (-1)^{j_1+j_2+j_3} \begin{pmatrix} j_1 & j_2 & j_3 \\ -m_1 & -m_2 & -m_3 \end{pmatrix}$$

- **Classical symmetries:** When combined, these symmetry relations give rise to 12 formally different $3-j$ symbols with the same absolute value. There are **additional symmetries known due to Regge (1958)** which are most easily explained in terms of Regge symbols (Varshalovich *et al.* 1988).
- A similar distinction between classical symmetries and additional symmetric forms due to Regge can be made also for the $6-j$ symbols.
- **Number of symmetries of the Wigner $3n-j$ symbols:** The table below lists the number of classical symmetries vs. the overall number of symmetric forms known for the Wigner symbols. In order to simplify Racah algebra expressions, it is crucial to exploit these symmetries; they are therefore all incorporated in the program as it is explained below.
- For practical purposes, however, the classical symmetries are much more important and the distinction is therefore kept. In our notation, the **classical symmetries are a subset of the Regge symmetries**.

15. Symbolic evaluation of expressions from Racah's algebra

- Number of classical symmetries of Wigner 3– j symbols vs. the symmetries known due to Regge (1958)

| 3– j symbol | classical symmetries | Regge symmetries (Regge 1958) |
|---------------|-------------------------|----------------------------------|
| 3– j | 12 | 72 |
| 6– j | 24 | 144 |
| 9– j | 72 | — |

Definition and symmetries of the Wigner D –functions and rotation matrices:

- Wigner D –functions $D_{pq}^j(\alpha, \beta, \gamma)$: The Wigner D –functions are defined as the matrix elements of the rotation operator $\hat{R}(\alpha, \beta, \gamma)$ in \mathcal{R}^3 and are often parametrized in terms of the three Euler angles α , β , and γ . In particular, these functions arise not only in the transformation of tensor components under the rotation of the coordinates but also as the eigenfunctions of the spherical top.
- Definition of the $D_{pq}^j(\alpha, \beta, \gamma)$ and $d_{pq}^j(\beta)$ rotation matrices: The Wigner D –function is defined as a product of three functions that each depend on just a single Euler angle and with the so-called Wigner rotation matrix $d_{pq}^j(\beta)$:

$$D_{pq}^j(\alpha, \beta, \gamma) = e^{-ip\alpha} d_{pq}^j(\beta) e^{-iq\gamma}.$$

- Euler angles (α, β, γ) : These angle can be utilized to characterize all possible rotations of a given (coordinate) system if the following range of values are considered:

$$0 \leq \alpha \leq 2\pi, \quad 0 \leq \beta \leq \pi, \quad 0 \leq \gamma \leq 2\pi.$$

- Symmetries of the D_{pq}^j functions and Wigner rotation matrices d_{pq}^j : The Wigner rotation matrix $d_{pq}^j(\beta)$ satisfies the following basic symmetries (Varshalovich *et al.*, 1988, eq. 4.4.1):

$$\begin{aligned} d_{pq}^j(\beta) &= (-1)^{p-q} d_{-p-q}^j(\beta) &= (-1)^{p-q} d_{qp}^j(\beta) &= d_{-q-p}^j(\beta) \\ &= d_{qp}^j(-\beta) &= (-1)^{q-p} d_{qp}^j(\beta) &= (-1)^{-j-p} d_{-p q}^j(\beta - \pi) &= (-1)^{-j-2p-q} d_{p-q}^j(\beta - \pi) \\ &= (-1)^{-2j} d_{pq}^j(\beta + 2\pi) &= (-1)^{-2j} d_{pq}^j(\beta - 2\pi) &= (-1)^{j-q} d_{p-q}^j(\beta + \pi) &= (-1)^{j-2q-p} d_{-p q}^j(\beta + \pi). \end{aligned}$$

The symmetry properties of the Wigner D -function are listed by Varshalovich *et al.* (1988, Eq. 4.2.2) and are taken into account since the D -function are internally handled in terms of the Wigner rotation matrix.

Symmetries of the spherical harmonics:

➤ **Symmetries:** The spherical harmonics satisfy the following basic symmetries:

$$\begin{aligned} Y_{\ell m}(\vartheta, \varphi) &= (-1)^m e^{2im\varphi} Y_{\ell, -m}(\vartheta, \varphi) = (-1)^m Y_{\ell m}(-\vartheta, \varphi) = e^{2im\varphi} Y_{\ell, -m}(-\vartheta, \varphi) = (-1)^m Y_{\ell, -m}(\vartheta, -\varphi) \\ &= e^{2im\varphi} Y_{\ell m}(\vartheta, -\varphi) = Y_{\ell, -m}(-\vartheta, -\varphi) = (-1)^m e^{2im\varphi} Y_{\ell m}(-\vartheta, -\varphi). \end{aligned}$$

15.1.d. Expansions of the Wigner $3n-j$ symbols, rotation matrices and spherical harmonics

Explicit formulas for the computation of the Wigner $3n-j$ symbols:

➤ Δ symbol:

$$\Delta(a, b, c) = \left[\frac{(a+b-c)! (a-b+c)! (-a+b+c)!}{(a+b+c+1)!} \right]^{1/2}.$$

➤ **Wigner $3-j$ symbol:** The numerical value of a Wigner $3-j$ symbol can be calculated by the expression (Racah, 1942) and has a non-zero value only if the arguments of all factorials are non-negative integers

$$\begin{aligned} \begin{pmatrix} j_1 & j_2 & j_3 \\ m_1 & m_2 & m_3 \end{pmatrix} &= \delta_{m_1+m_2+m_3, 0} (-1)^{j_1-j_2-m_3} \Delta(j_1, j_2, j_3) [(j_1-m_1)! (j_1+m_1)! (j_2-m_2)! (j_2+m_2)! (j_3-m_3)! (j_3+m_3)!]^{1/2} \\ &\times \sum_l \left[\frac{(-1)^l}{l! (j_1+j_2-j_3-l)! (j_1-m_1-l)! (j_2+m_2-l)! (j_3-j_2+m_1+l)! (j_3-j_1-m_2+l)!} \right]. \end{aligned}$$

15. Symbolic evaluation of expressions from Racah's algebra

➤ **Wigner 6-j symbol:** Edmonds (1957) displays the following expression for the computation of a Wigner 6-j symbol

$$\begin{aligned} \left\{ \begin{matrix} j_1 & j_2 & j_3 \\ l_1 & l_2 & l_3 \end{matrix} \right\} = & \Delta(j_1, j_2, j_3) \Delta(j_1, l_2, l_3) \Delta(l_1, j_2, l_3) \Delta(l_1, l_2, j_3) \sum_l \left[\frac{(-1)^l (\ell + 1)!}{(l - j_1 - j_2 - j_3)! (l - j_1 - l_2 - l_3)!} \right. \\ & \times \left. \frac{1}{(l - l_1 - j_2 - l_3)! (l - l_1 - l_2 - j_3)! (j_1 + j_2 + l_1 + l_2 - l)! (j_2 + j_3 + l_2 + l_3 - l)! (j_3 + j_1 + l_3 + l_1 - l)!} \right]. \end{aligned}$$

➤ **Wigner 9-j symbol:** The Wigner 9-j symbol with numeric arguments is usually calculated by the known sum rule over three Wigner 6-j symbols and is zero unless the arguments in each row and column satisfy the triangular relation

$$\left\{ \begin{matrix} j_{11} & j_{12} & j_{13} \\ j_{21} & j_{22} & j_{23} \\ j_{31} & j_{32} & j_{33} \end{matrix} \right\} = \sum_j (-1)^{2j} \left\{ \begin{matrix} j_{11} & j_{21} & j_{31} \\ j_{32} & j_{33} & j \end{matrix} \right\} \left\{ \begin{matrix} j_{12} & j_{22} & j_{32} \\ j_{21} & j & j_{23} \end{matrix} \right\} \left\{ \begin{matrix} j_{13} & j_{23} & j_{33} \\ j & j_{11} & j_{12} \end{matrix} \right\}.$$

Explicit formulas and expansions of the Wigner rotation matrices $d_{pq}^j(\beta)$:

➤ Below, we display six explicit expansions of the Wigner rotation matrices in alphabetical order.

➤ **Asymptotic expansion of d_{pq}^j for $j \gg 1$:** There are three asymptotic expansions of Wigner rotation matrices as displayed by Varshalovich *et al.* (1988, Eqs. 4.18.1–4). For $j \gg 1$, for instance, the Wigner rotation matrix can be written as

$$d_{pq}^j(\beta) \approx \xi_{pq} \sqrt{\frac{s!(s+\mu+\nu)!}{(s+\mu)!(s+\nu)!}} \sqrt{\frac{2}{\pi s}} \frac{\cos[(s + \frac{\mu+\nu+1}{2})\beta - \frac{\pi}{4}(2\mu+1)]}{\sqrt{\sin \beta}} + O\left(\frac{1}{J^{\frac{3}{2}}}\right),$$

and where μ , ν , and s are related to p , q , and j as follows

$$\mu = |p - q|, \quad \nu = |p + q|, \quad s = j - \frac{1}{2}(\mu + \nu), \quad \xi_{pq} = \begin{cases} 1 & \text{if } q \geq p, \\ (-1)^{q-p} & \text{if } q < p. \end{cases}$$

➤ **Asymptotic expansion of d_{pq}^j for $J \rightarrow \infty$ and $\beta \rightarrow 0$:** A second expansion for $j\beta < \infty$ is given in terms of the Bessel functions $J_n(x)$ by

$$d_{pq}^j(\beta) \approx J_{p-q}(j\beta)$$

- Asymptotic expansion of d_{pq}^j for small variations of the rotation axis:

$$d_{pq}^j(\beta) \approx \frac{\xi_{pq}}{\mu!} \sqrt{\frac{(s+\mu+\nu)!(s+\mu)!}{s!(s+\nu)!}} \left(\frac{\beta}{2}\right)^{\mu} \left\{ 1 - \frac{2s(s+\mu+\nu+1)+\nu(\mu+1)}{2(\mu+1)} \left(\frac{\beta}{2}\right)^2 + \dots \right\}, \quad \beta \rightarrow 0$$

$$d_{pq}^j(\beta) \approx \frac{(-1)^s \xi_{pq}}{\nu!} \sqrt{\frac{(s+\mu+\nu)!(s+\nu)!}{s!(s+\nu)!}} \left(\frac{\pi-\beta}{2}\right)^{\mu} \left\{ 1 - \frac{2s(s+\mu+\nu+1)+\mu(\nu+1)}{2(\nu+1)} \left(\frac{\pi-\beta}{2}\right)^2 + \dots \right\}, \quad \beta - \pi \rightarrow 0$$

- Clebsch-Gordan series expansion of products of two $d_{pq}^j(\beta)$ with equal arguments: Products of two Wigner rotation matrices with equal angular arguments can be expanded in terms of their uncoupled and coupled representations, i.e. by means of the Clebsch-Gordan coefficient. When expressed in terms of the Wigner 3-j symbols, the product of two Wigner rotation matrices (with equal angular arguments) are given by

$$d_{p_1 q_1}^{j_1}(\beta) d_{p_2 q_2}^{j_2}(\beta) = \sum_{J P Q} (-1)^{-2J+2j_2-p_2-q_2} (2j_2+1) \begin{pmatrix} J & j_2 & j_2 \\ P & p_2 & -p_2 \end{pmatrix} \begin{pmatrix} J & j_2 & j_2 \\ Q & q_2 & -q_2 \end{pmatrix} d_{PQ}^J(\beta)$$

in terms of two Wigner 3-j symbols and one Wigner rotation matrix $d_{PQ}^J(\beta)$. For $\beta = \frac{\pi}{2}$, in particular, the magnetic quantum numbers can be replaced by $j_1 = j_2 = j$, $p_1 = p_2 = p$ and $q_1 = q_2 = q$, and this gives rise to the expansion

$$\left(d_{pq}^j\left(\frac{\pi}{2}\right)\right)^2 = \sum_{J=0,2,4,\dots} (-1)^{J+2j+2p} (2j+1) \frac{(J-1)!!}{J!!} \begin{pmatrix} J & j & j \\ 0 & p & p \end{pmatrix} \begin{pmatrix} J & j & j \\ 0 & q & q \end{pmatrix}.$$

Such expansion relates the Wigner rotation matrices to the Wigner n -j symbols. These two expansions are displayed in Varshalovich *et al.* (1988, Eq. 4.6.1 and Eq. 4.16.9), although expressed in terms of Clebsch-Gordan coefficients.

Expansions of the spherical harmonics:

- Varshalovich *et al.* (1988, section 5.2) shows several explicit formulas for computing the spherical harmonic for $Y_{\ell m}(\vartheta, \varphi)$ with given integers ℓ and m , and where the summation runs over all terms with non-negative factorials.

15. Symbolic evaluation of expressions from Racah's algebra

➤ Expansion of $Y_{\ell m}(\vartheta, \varphi)$ in terms of $\sin \vartheta$: Varshalovich *et al.* (1988, Eq. 5.2.17)

$$Y_{\ell m}(\vartheta, \varphi) = e^{im\varphi} \sqrt{\frac{2\ell + 1}{4\pi (\ell + m)! (\ell - m)!}} \begin{cases} \sum_{s=|m|, |m|+2, \dots}^{\ell} (-1)^{\frac{s+m}{2}} \frac{(\ell+s)!}{(s+m)!! (s-m)!!} \cdot \frac{(\ell+m)!! (\ell-m)!!}{(\ell+s)!! (\ell-s)!!} (\sin \vartheta)^s & \text{if } \ell - m \text{ is even,} \\ \cos \vartheta \sum_{s=|m|, |m|+2, \dots}^{\ell-1} (-1)^{\frac{s+m}{2}} \frac{(\ell+s)!}{(s+m)!! (s-m)!!} \cdot \frac{(\ell+m-1)!! (\ell-m-1)!!}{(\ell+s-1)!! (\ell-s-1)!!} (\sin \vartheta)^s & \text{if } \ell - m \text{ is odd.} \end{cases}$$

➤ Expansion of $Y_{\ell m}(\vartheta, \varphi)$ in terms of $\sin \vartheta$ and $\cos \vartheta$: Cf. Varshalovich *et al.* (1988, Eq. 5.2.19) with a polynomial in $\cos \vartheta$

$$Y_{\ell m}(\vartheta, \varphi) = e^{im\varphi} \sqrt{\frac{2\ell + 1}{4\pi} \frac{(\ell - m)!}{(\ell + m)!}} (\sin \vartheta)^m \sum_{\substack{s \\ \ell + m - s \text{ even}}} (-1)^{\frac{\ell+m-s}{2}} \frac{(\ell + m + s - 1)!!}{(\ell - m - s)!!} \frac{(\cos \vartheta)^s}{s!}$$

15.2. In JAC implemented symbolic evaluations of Racah algebra expressions

15.2.a. Strategies in the symbolic evaluation of expressions from Racah's algebra

Strategies for simplification:

- For the successful simplification of expressions from Racah's algebra, one need often to exploit the orthogonality relations as well as a variety of important sum rules. The literature about Racah's algebra is therefore devoted to a large extent in order to find and to prove proper relations among the Wigner symbols and/or to compile them in some applicable form.
- **Standard presentation of orthogonality and sum rules:** The standard presentation of the different orthogonality and sum rules, as they are displayed below, gives a first impression how complex expressions can be rewritten in a simpler form. In practice, however, these standard forms are often not of great help since one first need to recognize the equivalence of some part of a Racah algebra expression, for instance with one side of a given sum rule, before this special rule can be applied.
- A numerical evaluation of a Racah expression is of course not possible as long as the input angular momentum quantum numbers are specified numerically. On the other hand, the main strength of using the techniques of Racah's algebra techniques is that such expressions can often be simplified considerably by algebraic transformations.
- Understanding the symmetries and properties of Wigner symbols, three different strategies for the simplification can be derived quite easily:
 - (i) **Use of known special values.** This replaces a Wigner $3n-j$ -symbol by a (much) simpler expression that, in particular, does not contain any implicit summation. For this strategy, each Wigner $3n-j$ symbol can be analysed and perhaps replaced independently by some special-value rules.
 - (ii) **Use of orthogonality properties.**
 - (iii) **Use of sum rules.**
 - (iv) **Use of integration rules** These rules can be formally treated quite similar to the sum rules for the Wigner n-j symbols, if we (can) assume that all sums and integrals can be interchanged in such expressions.
- The main obstacle in applying the strategies (ii) and (iii) is that these strategies require a careful analysis of the Racah expression as a whole. Since all orthogonality relations and sum rules include summations over formal quantum numbers, all summation variables not only have to be in the correct position in the Wigner $3n-j$ -symbols, but they must also contribute to a correct phase and weight of the overall expression. Moreover, the same variables may not occur in other Wigner symbols of the Racah expression which are not part of the selected rule.

15. Symbolic evaluation of expressions from Racah's algebra

- These difficulties in the simplification process are further enhanced by the large number of equivalent forms of the total Racah expression due to the symmetries of the Wigner $3n-j$ symbols. Therefore, in order to simplify a Racah expression by a given sum rule, in practice one has to start with a certain part of the expression and then try to identify equivalence with some relation by means of the various symmetries of the $3n-j$ symbols.
- Once the equivalence has been proven, this part of the Racah expression can be replaced by a corresponding simpler term. In this context, **simplification of a Racah expression always means to 'reduce' the number of summation indices and/or the number of Wigner $3n-j$ symbols.**
- **Aim of symbolic transformations:** The aim of these symbolic transformation is to obtain an *optimum* summation formula in the sense of a minimal number of Wigner $6-j$ symbols and/or summation variables.
- **Results of the simplification process:** The results of the simplification process will be provided as Racah expressions and may thus immediately be used for further derivations and calculations within the theory of angular momentum.
- This rather cumbersome procedure of running through all symmetric forms of a Racah expression and of identifying algebraic equivalent parts makes the simplification of such expressions very suitable for symbolic evaluations. An efficient scheme to perform simplifications of Racah expressions by means of the steps (i-iii) is aimed to be realized by the symbolic evaluations of the JAC tools.
- A major difficulty for the simplification of general Racah expressions arise from the large number of symmetric forms of the total expression which is the direct result of the symmetries of the Wigner $3n-j$ symbols. Apart from the so-called classical symmetries of the Wigner $n-j$ symbols, there are additional symmetries known due to Regge for the $3-j$ and $6-j$ symbols; cf. section 15.1.c. These symmetries need to be exploited in order to simplify general Racah algebra expressions. In JAC, we shall keep the distinction between the classical symmetries and those due to Regge since the classical ones are by far more important for all practical purposes; as mentioned above, we consider the classical symmetries to be a subset of the Regge symmetries.
- **Simplification of Racah expressions:** The *simplification* of a (Racah) expression always results again into a Racah expression, though hopefully a simpler and more compact one. The detailed analysis (and replacement) of the algebraic expression behind this simplification is implemented by means of the function `RacahAlgebra.evaluate()`, and which in turn cycles through all implemented rules. Hereby, a *simplification* and replacement of Wigner $3-j$ symbols has a higher preference than the simplification of Wigner $6-j$ symbols, and these again a higher preference than the Wigner $9-j$ symbols. At present, all these rules are just applied *ones*, even if further cycles might result in yet simpler expressions.
- **Using Racah's algebra within JAC:** The full power of Racah's algebra becomes apparent only, if the (re-) coupling of angular momenta is combined with the use and calculus of irreducible tensor operators and statistical tensors. This combination leads to expressions, in which the Wigner $n-j$ symbols occur together with the — summation and integration over — spherical harmonics and/or rotation matrices. In

15.2. In JAC implemented symbolic evaluations of Racah algebra expressions

practice, of course, such a combined treatment also enhances the structure, variety and (possible) complexity of the expressions that need to be considered.

15.3. In JAC partly-implemented symbolic evaluations of Racah algebra expressions

15.3.a. Recursive relations for the Wigner $3n-j$ symbols and rotation matrices

Recursion relations of the Wigner $3-j$ symbols:

- Four recursion relations of the Wigner $3-j$ symbols are listed by Rotenberg *et al.* (1959, Eqs. 1.45–1.48), and where we use $J = j_1 + j_2 + j_3$.
- **Half-integer recursion:** This recursion relation decreases two j -values by $1/2$

$$\begin{aligned} & [(J+1)(J-2j_1)]^{1/2} \begin{pmatrix} j_1 & j_2 & j_3 \\ m_1 & m_2 & m_3 \end{pmatrix} \\ &= [(j_2+m_2)(j_3-m_3)]^{1/2} \begin{pmatrix} j_1 & j_2 - 1/2 & j_3 - 1/2 \\ m_1 & m_2 - 1/2 & m_3 + 1/2 \end{pmatrix} - [(j_2-m_2)(j_3+m_3)]^{1/2} \begin{pmatrix} j_1 & j_2 - 1/2 & j_3 - 1/2 \\ m_1 & m_2 + 1/2 & m_3 - 1/2 \end{pmatrix}. \end{aligned}$$

- Louck's (1958) half-integer recursion:

$$\begin{aligned} (j_2+m_2)^{1/2} (2j_3+1) \begin{pmatrix} j_1 & j_2 & j_3 \\ m_2-m_3 & -m_2 & m_3 \end{pmatrix} &= -[(J-2j_1)(J+1)(j_3+m_3)]^{1/2} \begin{pmatrix} j_1 & j_2 - 1/2 & j_3 - 1/2 \\ m_2-m_3 & -m_2+1/2 & m_3-1/2 \end{pmatrix} \\ &\quad - [(J-2j_3)(J-2j_2+1)(J+1)(j_3-m_3+1)]^{1/2} \begin{pmatrix} j_1 & j_2 - 1/2 & j_3 + 1/2 \\ m_2-m_3 & -m_2+1/2 & m_3-1/2 \end{pmatrix}. \end{aligned}$$

- **Integer recursion:** A decrease of a single j -values by 1 is made with

$$\begin{aligned} & [(J+1)(J-2j_1)(J-2j_2)(J-2j_3+1)]^{1/2} \begin{pmatrix} j_1 & j_2 & j_3 \\ m_1 & m_2 & m_3 \end{pmatrix} \\ &= [(j_2-m_2)(j_2+m_2+1)(j_3+m_3)(j_3+m_3-1)]^{1/2} \begin{pmatrix} j_1 & j_2 & j_3 - 1 \\ m_1 & m_2 + 1 & m_3 - 1 \end{pmatrix} - 2m_2 [(j_3+m_3)(j_3-m_3)]^{1/2} \begin{pmatrix} j_1 & j_2 & j_3 - 1 \\ m_1 & m_2 & m_3 \end{pmatrix} \\ &\quad - [(j_2+m_2)(j_2-m_2+1)(j_3-m_3)(j_3-m_3-1)]^{1/2} \begin{pmatrix} j_1 & j_2 & j_3 - 1 \\ m_1 & m_2 - 1 & m_3 + 1 \end{pmatrix}. \end{aligned}$$

➤ Magnetic recursion: A recursion relation with regard to the magnetic quantum numbers reads:

$$\begin{aligned} & - [(j_3 + m_1 + m_2 + 1)(j_3 - m_1 - m_2)]^{1/2} \begin{pmatrix} j_1 & j_2 & j_3 \\ m_1 & m_2 & -m_3 + 1 \end{pmatrix} \\ & = [(j_1 + m_1 + 1)(j_1 - m_1)]^{1/2} \begin{pmatrix} j_1 & j_2 & j_3 \\ m_1 & m_2 + 1 & -m_3 \end{pmatrix} + [(j_2 + m_2 + 1)(j_2 - m_2)]^{1/2} \begin{pmatrix} j_1 & j_2 & j_3 \\ m_1 + 1 & m_2 & -m_3 \end{pmatrix}. \end{aligned}$$

Recursion relations of the Wigner 6-j symbols:

➤ No explicit recurrence relation has yet been considered for the Wigner 6-j symbols.

Recursion relations of the Wigner 9-j symbols:

➤ A single recursion relation among the Wigner 9-j symbols is shown by Rotenberg *et al.* (1959, Eq. 3.24).

$$\left\{ \begin{matrix} s & s & 1 \\ l_1 & l_2 & L \\ j_1 & j_2 & L \end{matrix} \right\} = \frac{l_1(l_1+1) + j_2(j_2+1) - j_1(j_1+1) - l_2(l_2+1)}{2[s(s+1)(2s+1)L(L+1)(2L+1)]^{1/2}} \left\{ \begin{matrix} s & s & 0 \\ l_1 & l_2 & L \\ j_1 & j_2 & L \end{matrix} \right\}.$$

Recursion relations of the spherical harmonics:

➤ Recursion relations: Cf. Varshalovich *et al.* (1988, Eqs. 5.7.1–2)

$$\begin{aligned} \cos \vartheta Y_{\ell m}(\vartheta, \varphi) &= \sqrt{\frac{(\ell - m + 1)(\ell + m + 1)}{(2\ell + 1)(2\ell + 3)}} Y_{\ell+1,m}(\vartheta, \varphi) + \sqrt{\frac{(\ell - m)(\ell + m)}{(2\ell - 1)(2\ell + 1)}} Y_{\ell-1,m}(\vartheta, \varphi) \\ - 2m \cos \vartheta Y_{\ell m}(\vartheta, \varphi) &= \sqrt{l(l+1) - m(m+1)} e^{-i\varphi} Y_{\ell,m+1}(\vartheta, \varphi) + \sqrt{l(l+1) - m(m-1)} e^{i\varphi} Y_{\ell,m-1}(\vartheta, \varphi). \end{aligned}$$

15.3.b. Special values of the Wigner $3n-j$ symbols and rotation matrices

Special values of the Wigner $3-j$ symbols:

➤ Edmonds (1957, appendix 2) lists the following 20 special values for $3-j$ symbols

$$\begin{pmatrix} j_1 & j_2 & j_3 \\ 0 & 0 & 0 \end{pmatrix} = (-1)^{J/2} \left[\frac{(j_1 + j_2 - j_3)!(j_1 + j_3 - j_2)!(j_2 + j_3 - j_1)!}{(j_1 + j_2 + j_3 + 1)!} \right]^{1/2} \frac{(J/2)!}{(J/2 - j_1)!(J/2 - j_2)!(J/2 - j_3)!}$$

$$\begin{pmatrix} j_1 & j_2 & j_3 \\ 0 & 0 & 0 \end{pmatrix} = \begin{cases} \text{if } J = j_1 + j_2 + j_3 \text{ is even} \\ \text{if } J = j_1 + j_2 + j_3 \text{ is odd} \end{cases}$$

$$\begin{pmatrix} J + 1/2 & J & 1/2 \\ M & -M - 1/2 & 1/2 \end{pmatrix} = (-1)^{J-M-1/2} \left[\frac{J - M + 1/2}{(2J+2)(2J+1)} \right]^{1/2}$$

$$\begin{pmatrix} J + 1 & J & 1 \\ M & -M - 1 & 1 \end{pmatrix} = (-1)^{J-M-1} \left[\frac{(J - M)(J - M + 1)}{(2J+3)(2J+2)(2J+1)} \right]^{1/2}$$

$$\begin{pmatrix} J + 1 & J & 1 \\ M & -M & 0 \end{pmatrix} = (-1)^{J-M-1} \left[\frac{2(J + M + 1)(J - M + 1)}{(2J+3)(2J+2)(2J+1)} \right]^{1/2}$$

$$\begin{pmatrix} J & J & 1 \\ M & -M - 1 & 1 \end{pmatrix} = (-1)^{J-M} \left[\frac{2(J - M)(J + M + 1)}{(2J+2)(2J+1)(2J)} \right]^{1/2}$$

$$\begin{pmatrix} J & J & 1 \\ M & -M & 0 \end{pmatrix} = (-1)^{J-M} \frac{M}{[(2J+1)(J+1)J]^{1/2}}$$

$$\begin{pmatrix} J + 3/2 & J & 3/2 \\ M & -M - 3/2 & 3/2 \end{pmatrix} = (-1)^{J-M+1/2} \left[\frac{(J - M - 1/2)(J - M + 1/2)(J - M + 3/2)}{(2J+4)(2J+3)(2J+2)(2J+1)} \right]^{1/2}$$

$$\begin{pmatrix} J + 3/2 & J & 3/2 \\ M & -M - 1/2 & 1/2 \end{pmatrix} = (-1)^{J-M+1/2} \left[\frac{3(J - M + 1/2)(J - M + 3/2)(J + M + 3/2)}{(2J+4)(2J+3)(2J+2)(2J+1)} \right]^{1/2}$$

$$\begin{pmatrix} J+1/2 & J & 3/2 \\ M & -M-3/2 & 3/2 \end{pmatrix} = (-1)^{J-M-1/2} \left[\frac{3(J-M-1/2)(J-M+1/2)(J+M+3/2)}{(2J+3)(2J+2)(2J+1)(2J)} \right]^{1/2}$$

$$\begin{pmatrix} J+1/2 & J & 3/2 \\ M & -M-1/2 & 1/2 \end{pmatrix} = (-1)^{J-M-1/2} \left[\frac{(J-M+1/2)}{(2J+3)(2J+2)(2J+1)(2J)} \right]^{1/2} (J+3M+3/2)$$

$$\begin{pmatrix} J+2 & J & 2 \\ M & -M-2 & 2 \end{pmatrix} = (-1)^{J-M} \left[\frac{(J-M-1)(J-M)(J-M+1)(J-M+2)}{(2J+5)(2J+4)(2J+3)(2J+2)(2J+1)} \right]^{1/2}$$

$$\begin{pmatrix} J+2 & J & 2 \\ M & -M-1 & 1 \end{pmatrix} = (-1)^{J-M} 2 \left[\frac{(J+M+2)(J-M+2)(J-M+1)(J-M)}{(2J+5)(2J+4)(2J+3)(2J+2)(2J+1)} \right]^{1/2}$$

$$\begin{pmatrix} J+2 & J & 2 \\ M & -M & 0 \end{pmatrix} = (-1)^{J-M} \left[\frac{6(J+M+2)(J+M+1)(J-M+2)(J-M+1)}{(2J+5)(2J+4)(2J+3)(2J+2)(2J+1)} \right]^{1/2}$$

$$\begin{pmatrix} J+1 & J & 2 \\ M & -M-2 & 2 \end{pmatrix} = (-1)^{J-M+1} 2 \left[\frac{(J-M-1)(J-M)(J-M+1)(J+M+2)}{(2J+4)(2J+3)(2J+2)(2J+1)(2J)} \right]^{1/2}$$

$$\begin{pmatrix} J+1 & J & 2 \\ M & -M-1 & 1 \end{pmatrix} = (-1)^{J-M+1} 2 (J+2M+2) \left[\frac{(J-M+1)(J-M)}{(2J+4)(2J+3)(2J+2)(2J+1)(2J)} \right]^{1/2}$$

$$\begin{pmatrix} J+1 & J & 2 \\ M & -M & 0 \end{pmatrix} = (-1)^{J-M+1} 2M \left[\frac{6(J+M+1)(J-M+1)}{(2J+4)(2J+3)(2J+2)(2J+1)(2J)} \right]^{1/2}$$

$$\begin{pmatrix} J & J & 2 \\ M & -M-2 & 2 \end{pmatrix} = (-1)^{J-M} \left[\frac{6(J-M-1)(J-M)(J+M+1)(J+M+2)}{(2J+3)(2J+2)(2J+1)(2J)(2J-1)} \right]^{1/2}$$

$$\begin{pmatrix} J & J & 2 \\ M & -M-1 & 1 \end{pmatrix} = (-1)^{J-M} (1+2M) \left[\frac{6(J+M+1)(J-M)}{(2J+3)(2J+2)(2J+1)(2J)(2J-1)} \right]^{1/2}$$

$$\begin{pmatrix} J & J & 2 \\ M & -M & 0 \end{pmatrix} = (-1)^{J-M} \frac{2 [3M^2 - J(J+1)]}{[(2J+3)(2J+2)(2J+1)(2J)(2J-1)]^{1/2}}$$

Special values of the Wigner 6-j symbols:

➤ Edmonds (1957, appendix 2, table 5) displays the following 19 special values for 6-j symbols; in this list, moreover, we use $s = a + b + c$.

$$\begin{Bmatrix} a & b & c \\ 1 & c-1 & b-1 \end{Bmatrix} = (-1)^s \left[\frac{s(s+1)(s-2a-1)(s-2a)}{(2b-1)2b(2b+1)(2c-1)2c(2c+1)} \right]^{1/2}$$

$$\begin{Bmatrix} a & b & c \\ 1 & c-1 & b \end{Bmatrix} = (-1)^s \left[\frac{2(s+1)(s-2a)(s-2b)(s-2c+1)}{2b(2b+1)(2b+2)(2c-1)2c(2c+1)} \right]^{1/2}$$

$$\begin{Bmatrix} a & b & c \\ 1 & c-1 & b+1 \end{Bmatrix} = (-1)^s \left[\frac{(s-2b-1)(s-2b)(s-2c+1)(s-2c+2)}{(2b+1)(2b+2)(2b+3)(2c-1)2c(2c+1)} \right]^{1/2}$$

$$\begin{Bmatrix} a & b & c \\ 1 & c & b \end{Bmatrix} = (-1)^{s+1} \frac{2[b(b+1) + c(c+1) - a(a+1)]}{[2b(2b+1)(2b+2)2c(2c+1)(2c+2)]^{1/2}}$$

$$\begin{Bmatrix} a & b & c \\ 3/2 & c-3/2 & b-3/2 \end{Bmatrix} = (-1)^s \left[\frac{(s-1)s(s+1)(s-2a-2)(s-2a-1)(s-2a)}{(2b-2)(2b-1)2b(2b+1)(2c-2)(2c-1)2c(2c+1)} \right]^{1/2}$$

$$\begin{Bmatrix} a & b & c \\ 3/2 & c-3/2 & b-1/2 \end{Bmatrix} = (-1)^s \left[\frac{3s(s+1)(s-2a-1)(s-2a)(s-2b)(s-2c+1)}{(2b-1)2b(2b+1)(2b+2)(2c-2)(2c-1)2c(2c+1)} \right]^{1/2}$$

$$\begin{Bmatrix} a & b & c \\ 3/2 & c-3/2 & b+1/2 \end{Bmatrix} = (-1)^s \left[\frac{3(s+1)(s-2a)(s-2b-1)(s-2b)}{2b(2b+1)(2b+2)(2b+3)} \right]^{1/2} \left[\frac{(s-2c+1)(s-2c+2)}{(2c-2)(2c-1)2c(2c+1)} \right]^{1/2}$$

$$\begin{Bmatrix} a & b & c \\ 3/2 & c-3/2 & b+3/2 \end{Bmatrix} = (-1)^s \left[\frac{(s-2b-2)(s-2b-1)(s-2b)}{(2b+1)(2b+2)(2b+3)(2b+4)} \right]^{1/2} \left[\frac{(s-2c+1)(s-2c+2)(s-2c+3)}{(2c-2)(2c-1)2c(2c+1)} \right]^{1/2}$$

$$\begin{Bmatrix} a & b & c \\ 3/2 & c-1/2 & b-1/2 \end{Bmatrix} = (-1)^s \frac{[2(s-2b)(s-2c) - (s+2)(s-2a-1)] [(s+1)(s-2a)]^{1/2}}{[(2b-1)(2b)(2b+1)(2b+2)(2c-1)2c(2c+1)(2c+2)]^{1/2}}$$

$$\begin{aligned}
 \left\{ \begin{matrix} a & b & c \\ 3/2 & c-1/2 & b+1/2 \end{matrix} \right\} &= (-1)^s \frac{[(s-2b-1)(s-2c) - 2(s+2)(s-2a)]}{[2b(2b+1)(2b+2)(2b+3)]^{1/2}} \frac{[(s-2b)(s-2c+1)]^{1/2}}{[2c(2c+1)(2c+2)(2c-1)]^{1/2}} \\
 \left\{ \begin{matrix} a & b & c \\ 2 & c-2 & b-2 \end{matrix} \right\} &= (-1)^s \left[\frac{(s-2)(s-1)s(s+1)(s-2a-3)}{(2b-3)(2b-2)(2b-1)2b(2b+1)} \right]^{1/2} \left[\frac{(s-2a-2)(s-2a-1)(s-2a)}{(2c-3)(2c-2)(2c-1)2c(2c+1)} \right]^{1/2} \\
 \left\{ \begin{matrix} a & b & c \\ 2 & c-2 & b-1 \end{matrix} \right\} &= (-1)^s 2 \left[\frac{(s-1)s(s+1)(s-2a-2)(s-2a-1)}{(2b-2)(2b-1)2b(2b+1)(2b+2)} \right]^{1/2} \left[\frac{(s-2a)(s-2b)(s-2c+1)}{(2c-3)(2c-2)(2c-1)2c(2c+1)} \right]^{1/2} \\
 \left\{ \begin{matrix} a & b & c \\ 2 & c-2 & b \end{matrix} \right\} &= (-1)^s \left[\frac{6s(s+1)(s-2a-1)(s-2b-1)(s-2a)(s-2b)}{(2b-1)2b(2b+1)(2b+2)(2b+3)} \right]^{1/2} \left[\frac{(s-2c+1)(s-2c+2)}{(2c-3)(2c-2)(2c-1)2c(2c+1)} \right]^{1/2} \\
 \left\{ \begin{matrix} a & b & c \\ 2 & c-2 & b+1 \end{matrix} \right\} &= (-1)^s 2 \left[\frac{(s+1)(s-2a)(s-2b-2)(s-2b-1)(s-2b)}{2b(2b+1)(2b+2)(2b+3)(2b+4)} \right]^{1/2} \left[\frac{(s-2c+1)(s-2c+2)(s-2c+3)}{(2c-3)(2c-2)(2c-1)2c(2c+1)} \right]^{1/2} \\
 \left\{ \begin{matrix} a & b & c \\ 2 & c-2 & b+2 \end{matrix} \right\} &= (-1)^s \left[\frac{(s-2b-3)(s-2b-2)(s-2b-1)(s-2b)}{(2b+1)(2b+2)(2b+3)(2b+4)(2b+5)} \right]^{1/2} \left[\frac{(s-2c+1)(s-2c+2)(s-2c+3)(s-2c+4)}{(2c-3)(2c-2)(2c-1)2c(2c+1)} \right]^{1/2} \\
 \left\{ \begin{matrix} a & b & c \\ 2 & c-1 & b-1 \end{matrix} \right\} &= (-1)^s 4 \frac{[(a+b)(a-b+1) - (c-1)(c-b+1)]}{[(2b-2)(2b-1)2b(2b+1)(2b+2)]^{1/2}} \left[\frac{s(s+1)(s-2a-1)(s-2a)}{(2c-2)(2c-1)2c(2c+1)(2c+2)} \right]^{1/2} \\
 \left\{ \begin{matrix} a & b & c \\ 2 & c-1 & b \end{matrix} \right\} &= (-1)^s 2 \frac{[(a+b+1)(a-b) - c^2 + 1]}{[(2b-1)2b(2b+1)(2b+2)(2b+3)]^{1/2}} \left[\frac{6(s+1)(s-2a)(s-2b)(s-2c+1)}{(2c-2)(2c-1)2c(2c+1)(2c+2)} \right]^{1/2} \\
 \left\{ \begin{matrix} a & b & c \\ 2 & c-1 & b+1 \end{matrix} \right\} &= (-1)^s 4 \frac{[(a+b+2)(a-b-1) - (c-1)(b+c+2)]}{[2b(2b+1)(2b+2)(2b+3)(2b+4)]^{1/2}} \left[\frac{(s-2b-1)(s-2b)(s-2c+1)(s-2c+2)}{(2c-2)(2c-1)2c(2c+1)(2c+2)} \right]^{1/2} \\
 \left\{ \begin{matrix} a & b & c \\ 2 & c & b \end{matrix} \right\} &= (-1)^s \frac{2}{[(2b-1)2b(2b+1)(2b+2)(2b+3)]^{1/2}} \frac{[3X(X-1) - 4b(b+1)c(c+1)]}{[(2c-1)2c(2c+1)(2c+2)(2c+3)]^{1/2}}
 \end{aligned}$$

and where we use $s = a + b + c$ and $X = b(b+1) + c(c+1) - a(a+1)$ in the last relation.

Special values of the Wigner 9–j symbols:

- One special value for a Wigner 9–j symbol reads as

$$\begin{Bmatrix} a & b & 0 \\ c & d & 0 \\ e & f & 0 \end{Bmatrix} = \delta_{ab} \delta_{cd} \delta_{ef} \frac{\delta(a, c, e)}{[a, c, e]^{1/2}}.$$

- Another special value for the Wigner 9–j symbols is given by Varshalovich *et al.* (1988, Eq. 10.9.1)

$$\begin{Bmatrix} a & b & c \\ d & e & f \\ g & h & 0 \end{Bmatrix} = \delta_{cf} \delta_{gh} \frac{(-1)^{b+c+e+f}}{[c, g]^{1/2}} \begin{Bmatrix} a & b & c \\ e & d & g \end{Bmatrix}.$$

15.3.c. Orthogonality and sum rules of the Wigner 3n–j symbols

Remarks:

- A rather comprehensive set of sum rules for the Wigner n – j symbols is given by Varshalovich *et al.* (1988, chapter 12). These rules are most easily be ordered by the number of Wigner n – j symbols that contribute to a given rule. For the case of an equal numbers of such symbols, we further classify these rules by the type of the Wigner symbols.
- **Orthogonality relations:** The Wigner n – j symbols fulfill a variety of orthogonality relations. Two such relations are known for the Wigner 3– j symbols as well as one orthogonality relation for each, the Wigner 6– j and 9– j symbols. Because these orthogonalities have formally the same structure like all other sum rules of the Wigner n – j symbols, they are all treated together in the JAC program.

Sum rules with one Wigner 3-j, 6-j or 9-j symbol:

- Sum rules with one 3-j symbol: Varshalovich *et al.* (1988, Eq. 12.1.2) shows one sum rule with one 3-j symbol

$$\sum_m (-1)^{j-m} \begin{pmatrix} j & j & j' \\ m & -m & m' \end{pmatrix} = [j]^{1/2} \delta_{m'0} \delta_{j'0}.$$

- Sum rules with one 6-j symbol: Rotenberg *et al.* (1959, Eqs. 2.9–10) show sum rules with one 6-j symbol. A more general form is given by Varshalovich *et al.* (1988, Eqs. 12.2.3–4)

$$\sum_X [X] \left\{ \begin{matrix} a & b & X \\ a & b & c \end{matrix} \right\} = (-1)^{2c} \delta(a, b, c)$$

$$\sum_X (-1)^{a+b+X} [X] \left\{ \begin{matrix} a & b & X \\ b & a & c \end{matrix} \right\} = [a, b]^{1/2} \delta_{c0}.$$

- Sum rules with one 9-j symbol: Varshalovich *et al.* (1988, Eqs. 12.2.5–6) give two sum rules with one 9-j symbol

$$\sum_X [X] \left\{ \begin{matrix} a & b & e \\ c & d & f \\ e & f & X \end{matrix} \right\} = \frac{\delta_{bc}}{[b]} \delta(a, b, e) \delta(b, d, f)$$

$$\sum_X (-1)^{a+b+c+d-X} [X] \left\{ \begin{matrix} a & b & e \\ c & d & f \\ f & e & X \end{matrix} \right\} = \frac{\delta_{ad}}{[a]} \delta(d, b, e) \delta(a, c, f).$$

Sum rules with two 3-j, 6-j and/or 9-j symbols:

➤ Orthogonality of two 3-j symbols: Two orthogonality relations for 3-j symbols are given by Rotenberg *et al.* (1959, Eqs. 1.13–14) as well as by Varshalovich *et al.* (1988, Eqs. 12.1.3–4)

$$\sum_{j_3 m_3} (2j_3 + 1) \begin{pmatrix} j_1 & j_2 & j_3 \\ m_1 & m_2 & m_3 \end{pmatrix} \begin{pmatrix} j_1 & j_2 & j_3 \\ m'_1 & m'_2 & m_3 \end{pmatrix} = \delta(m_1, m'_1) \delta(m_2, m'_2)$$

$$\sum_{m_1 m_2} \begin{pmatrix} j_1 & j_2 & j_3 \\ m_1 & m_2 & m_3 \end{pmatrix} \begin{pmatrix} j_1 & j_2 & j'_3 \\ m_1 & m_2 & m'_3 \end{pmatrix} = \frac{\delta(j_3, j'_3) \delta(m_3, m'_3)}{(2j_3 + 1)} \delta(j_1, j_2, j_3).$$

➤ Orthogonality of two 6-j symbols: An orthogonality relation for the Wigner 6-j symbols is given by Rotenberg *et al.* (1959, Eq. 2.6) as well as by Varshalovich *et al.* (1988, Eq. 12.2.7)

$$\sum_X [X] \begin{Bmatrix} a & b & X \\ c & d & p \end{Bmatrix} \begin{Bmatrix} c & d & X \\ a & b & q \end{Bmatrix} = \frac{\delta_{pq}}{[p]} \delta(a, d, p) \delta(b, c, p).$$

➤ Sum rules with two 6-j symbols: Rotenberg *et al.* (1959, Eq. 2.7) as well as Varshalovich *et al.* (1988, Eq. 12.2.8) gives a sum rule for two 6-j symbols

$$\sum_X (-1)^{p+q+X} [X] \begin{Bmatrix} a & b & X \\ c & d & p \end{Bmatrix} \begin{Bmatrix} c & d & X \\ b & a & q \end{Bmatrix} = \begin{Bmatrix} c & a & q \\ d & b & p \end{Bmatrix}.$$

➤ Sum rules with two 6-j symbols: Varshalovich *et al.* (1988, Eq. 12.2.15) show a sum rule including a triple summation over a 6-j symbol

$$\sum_{XYZ} [X, Y, Z] \begin{Bmatrix} X & Y & Z \\ a & b & c \end{Bmatrix} \begin{Bmatrix} X & Y & Z \\ a & b & c \end{Bmatrix} = [a, b, c].$$

➤ Sum rules with one 6-j and one 9-j symbol: Varshalovich *et al.* (1988, Eqs. 12.2.9–10) show two sum rules for one 6-j symbol and one

$9-j$ symbol, and with $R = a + b + c + d + e + f + p + q$

$$\sum_X [X] \begin{Bmatrix} a & f & X \\ d & q & e \\ p & c & b \end{Bmatrix} \begin{Bmatrix} a & f & X \\ e & b & s \end{Bmatrix} = (-1)^{2s} \begin{Bmatrix} a & b & s \\ c & d & p \end{Bmatrix} \begin{Bmatrix} c & d & s \\ e & f & q \end{Bmatrix}$$

$$\sum_X (-1)^{R+X} [X] \begin{Bmatrix} a & f & X \\ d & q & e \\ p & c & b \end{Bmatrix} \begin{Bmatrix} a & f & X \\ b & e & s \end{Bmatrix} = (-1)^{2s} \begin{Bmatrix} p & q & s \\ e & a & d \end{Bmatrix} \begin{Bmatrix} p & q & s \\ f & b & c \end{Bmatrix}.$$

Sum rules for three Wigner $3-j$, $6-j$ and/or $9-j$ symbols:

- Sum rules with three $3-j$ symbols: One such rule is given by Rotenberg *et al.* (1959, Eq. 2.20) as well as by Varshalovich *et al.* (1988, Eq. 2.1.6), and with $S = l_1 + l_2 + l_3 + n_1 + n_2 + n_3$

$$\sum_{n_1 n_2 n_3} (-1)^S \begin{pmatrix} j_1 & l_2 & l_3 \\ m_1 & n_2 & -n_3 \end{pmatrix} \begin{pmatrix} l_1 & j_2 & l_3 \\ -n_1 & m_2 & n_3 \end{pmatrix} \begin{pmatrix} l_1 & l_2 & j_3 \\ n_1 & -n_2 & m_3 \end{pmatrix} = \begin{pmatrix} j_1 & j_2 & j_3 \\ m_1 & m_2 & m_3 \end{pmatrix} \begin{Bmatrix} j_1 & j_2 & j_3 \\ l_1 & l_2 & l_3 \end{Bmatrix}.$$

- Sum rules with two $3-j$ symbols and one $6-j$ symbol: One such rule is given by Rotenberg *et al.* (1959, Eq. 2.19) as well as by Varshalovich *et al.* (1988, Eq. 12.1.5)

$$\sum_{l_3 n_3} (-1)^{j_3+l_3+m_1+n_1} [l_3] \begin{Bmatrix} j_1 & j_2 & j_3 \\ l_1 & l_2 & l_3 \end{Bmatrix} \begin{pmatrix} l_1 & j_2 & l_3 \\ n_1 & m_2 & n_3 \end{pmatrix} \begin{pmatrix} j_1 & l_2 & l_3 \\ m_1 & n_2 & -n_3 \end{pmatrix} = \sum_{m_3} \begin{pmatrix} j_1 & j_2 & j_3 \\ m_1 & m_2 & m_3 \end{pmatrix} \begin{pmatrix} l_1 & l_2 & j_3 \\ n_1 & n_2 & -m_3 \end{pmatrix}.$$

- Sum rules with three $6-j$ symbols: There is a sum rule for three $6-j$ symbols from Biedenharn and Elliot; see also Rotenberg *et al.* (1959, Eq. 2.8) or Varshalovich *et al.* (1988, Eq. 12.2.18), and with $R = a + b + c + d + e + f + p + q + r$

$$\sum_X (-1)^{R+X} [X] \begin{Bmatrix} a & b & X \\ c & d & p \end{Bmatrix} \begin{Bmatrix} c & d & X \\ e & f & q \end{Bmatrix} \begin{Bmatrix} e & f & X \\ b & a & r \end{Bmatrix} = \begin{Bmatrix} p & q & r \\ e & a & d \end{Bmatrix} \begin{Bmatrix} p & q & r \\ f & b & c \end{Bmatrix}.$$

15. Symbolic evaluation of expressions from Racah's algebra

- **Sum rules with three $6-j$ symbols:** Another sum rules corresponds to the representation of the $9-j$ symbol in terms of $6-j$ symbols; see Rotenberg *et al.* (1959, Eq. 3.1) and Varshalovich *et al.* (1988, Eq. 12.2.19)

$$\sum_X (-1)^{2X} [X] \begin{Bmatrix} a & b & X \\ c & d & p \end{Bmatrix} \begin{Bmatrix} c & d & X \\ e & f & q \end{Bmatrix} \begin{Bmatrix} e & f & X \\ a & b & r \end{Bmatrix} = \begin{Bmatrix} a & f & r \\ d & q & e \\ p & c & b \end{Bmatrix}.$$

Sum rules with four Wigner $3-j$, $6-j$ and/or $9-j$ symbols:

- **Sum rules with three $3-j$ symbols:** Rotenberg *et al.* (1959, Eq. 2.18) as well as Varshalovich *et al.* (1988, Eq. 12.1.8) display the representation of a $6-j$ symbol in terms of four $3-j$ symbols, and with $S = l_1 + l_2 + l_3 + n_1 + n_2 + n_3$

$$\begin{aligned} \begin{Bmatrix} j_1 & j_2 & j_3 \\ l_1 & l_2 & l_3 \end{Bmatrix} &= \sum_{m_1 m_2 m_3 n_1 n_2 n_3} (-1)^S \begin{pmatrix} j_1 & j_2 & j_3 \\ m_1 & m_2 & m_3 \end{pmatrix} \begin{pmatrix} j_1 & l_2 & l_3 \\ m_1 & n_2 & -n_3 \end{pmatrix} \begin{pmatrix} l_1 & j_2 & l_3 \\ -n_1 & m_2 & n_3 \end{pmatrix} \begin{pmatrix} l_1 & l_2 & j_3 \\ n_1 & -n_2 & m_3 \end{pmatrix} \\ &= \sum_{m_1 m_2 n_1 n_2 n_3} (-1)^S [j_3] \begin{pmatrix} j_1 & j_2 & j_3 \\ m_1 & m_2 & m_3 \end{pmatrix} \begin{pmatrix} j_1 & l_2 & l_3 \\ m_1 & n_2 & -n_3 \end{pmatrix} \begin{pmatrix} l_1 & j_2 & l_3 \\ -n_1 & m_2 & n_3 \end{pmatrix} \begin{pmatrix} l_1 & l_2 & j_3 \\ n_1 & -n_2 & m_3 \end{pmatrix}. \end{aligned}$$

- Another sum rule for four $3-j$ symbols is given by Varshalovich *et al.* (1988, Eq. 12.1.9).

$$\begin{aligned} \sum_{n_r n_p n_q n_s} (-1)^{p-n_p+q-n_q+r-n_r+s-n_s} \begin{pmatrix} p & a & q \\ n_p & n_a & -n_q \end{pmatrix} \begin{pmatrix} q & b & r \\ n_q & n_b & -n_r \end{pmatrix} \begin{pmatrix} r & s & p \\ n_r & n_s & -n_p \end{pmatrix} \begin{pmatrix} s & c & d \\ -n_s & n_c & n_d \end{pmatrix} \\ = \begin{Bmatrix} a & b & s \\ r & p & q \end{Bmatrix} \sum_{n_s} \begin{pmatrix} a & s & b \\ n_a & n_s & n_b \end{pmatrix} \begin{pmatrix} d & s & c \\ n_d & -n_s & n_c \end{pmatrix}. \end{aligned}$$

- A useful relation between $3-j$ and $9-j$ symbols is due to de-Shalit; cf. Rotenberg *et al.* (1959, Eq. 3.21) as well as Varshalovich *et al.* (1988, Eq. 12.1.11)

$$\sum_{MNRs} \begin{pmatrix} a & e & g \\ n_a & M & N \end{pmatrix} \begin{pmatrix} b & f & h \\ n_b & R & S \end{pmatrix} \begin{pmatrix} e & f & c \\ M & R & n_e \end{pmatrix} \begin{pmatrix} g & h & d \\ N & S & n_x \end{pmatrix} = \sum_{XY} [X] \begin{pmatrix} a & b & X \\ n_a & n_b & Y \end{pmatrix} \begin{pmatrix} X & c & d \\ Y & n_e & n_x \end{pmatrix} \begin{Bmatrix} a & b & X \\ e & f & c \\ g & h & d \end{Bmatrix}.$$

Only this (last) sum rule for four Wigner 3– j symbols need to be implemented explicitly because the other two above can be simplified in a two-step evaluation using other sum rules.

Sum rules with five Wigner 3– j , 6– j and/or 9– j symbols:

➤ Sum rules with five 3– j symbols: Varshalovich *et al.* (1988, Eqs. 12.1.12–14) give three sum rules involving products of five 3– j symbols.

$$\begin{aligned} \sum_{n_p n_q n_r n_s n_t n_u n_v} & (-1)^{p-n_p+q-n_q+r-n_r+s-n_s+t-n_t+u-n_u+v-n_v} \begin{pmatrix} r & t & q \\ n_r & n_t & -n_q \end{pmatrix} \begin{pmatrix} q & p & u \\ n_q & n_p & -n_u \end{pmatrix} \begin{pmatrix} u & a & v \\ n_u & n_a & -n_v \end{pmatrix} \begin{pmatrix} v & s & r \\ n_v & n_s & -n_r \end{pmatrix} \begin{pmatrix} s & p & t \\ -n_s & -n_p & -n_t \end{pmatrix} \\ & = (-1)^{2u} \frac{\delta_{uv} \delta_{a0} \delta_{na0}}{[u]^{1/2}} \left\{ \begin{matrix} q & p & u \\ s & r & t \end{matrix} \right\} \\ \sum_{n_p n_q n_r n_s n_t n_u} & (-1)^{p-n_p+q-n_q+r-n_r+s-n_s+t-n_t+u-n_u} \begin{pmatrix} p & a & q \\ n_p & n_a & -n_q \end{pmatrix} \begin{pmatrix} q & r & t \\ n_q & n_r & -n_t \end{pmatrix} \begin{pmatrix} t & s & p \\ n_t & -n_s & -n_p \end{pmatrix} \begin{pmatrix} s & c & u \\ n_s & n_c & -n_u \end{pmatrix} \begin{pmatrix} u & b & r \\ n_u & n_b & -n_r \end{pmatrix} \\ & = \begin{pmatrix} a & b & c \\ n_a & n_b & n_c \end{pmatrix} \left\{ \begin{matrix} a & b & c \\ u & s & r \end{matrix} \right\} \left\{ \begin{matrix} a & p & q \\ t & r & s \end{matrix} \right\} \\ \sum_{n_p n_q n_r n_s n_t n_u} & (-1)^{p-n_p+q-n_q+r-n_r+s-n_s+t-n_t+u-n_u} \begin{pmatrix} p & a & q \\ n_p & n_a & n_q \end{pmatrix} \begin{pmatrix} p & a & q \\ n_p & n_a & n_q \end{pmatrix} \begin{pmatrix} q & t & r \\ -n_q & -n_t & -n_r \end{pmatrix} \begin{pmatrix} r & b & s \\ n_r & n_b & n_s \end{pmatrix} \\ & \times \begin{pmatrix} s & p & u \\ -n_s & -n_p & -n_u \end{pmatrix} \begin{pmatrix} u & c & t \\ n_u & n_c & n_t \end{pmatrix} = (-1)^{r+b+s} \begin{pmatrix} a & b & c \\ -n_a & -n_b & -n_c \end{pmatrix} \left\{ \begin{matrix} a & b & c \\ p & s & u \\ q & r & t \end{matrix} \right\} \end{aligned}$$

Sum rules with six Wigner 3-j, 6-j and/or 9-j symbols:

- **Sum rules with six 3-j symbols:** A sum rule corresponds to the representation of the 9-j symbol in terms of six 3-j symbols; see Rotenberg *et al.* (1959, Eq. 3.1).

$$\left\{ \begin{matrix} a & b & c \\ d & e & f \\ g & h & j \end{matrix} \right\} = \sum_{ABCDEF GHJ} \left(\begin{matrix} a & b & c \\ A & B & C \end{matrix} \right) \left(\begin{matrix} d & e & f \\ D & E & F \end{matrix} \right) \left(\begin{matrix} g & h & j \\ G & H & J \end{matrix} \right) \left(\begin{matrix} a & d & g \\ A & D & G \end{matrix} \right) \left(\begin{matrix} b & e & h \\ B & E & H \end{matrix} \right) \left(\begin{matrix} c & f & j \\ C & F & J \end{matrix} \right).$$

Graphical loop rules for the Wigner 3-j symbols:

- **Loop rules for one Wigner 3-j symbol:** Several loop rules (n -loops) can be implemented separately for algebraic evaluations. A loop for one Wigner 3-j symbol is given by Varshalovich *et al.* (1988, Eq. 12.1.2)

$$\sum_m (-1)^m \left(\begin{matrix} j & j & J \\ m & -m & M \end{matrix} \right) = (-1)^j [j] \delta_{J0} \delta_{M0}.$$

- **Loop rules for two Wigner 3-j symbol:** Varshalovich *et al.* (1988, Eq. 12.1.3) also displays a loop for two Wigner 3-j symbols

$$\sum_{m_1, m_2} \left(\begin{matrix} j_1 & j_2 & j_3 \\ m_1 & m_2 & m_3 \end{matrix} \right) \left(\begin{matrix} j_1 & j_2 & j'_3 \\ m_1 & m_2 & m'_3 \end{matrix} \right) = \frac{1}{2j_3 + 1} \delta_{j_3, j'_3} \delta_{m_3, m'_3} \delta(j_1, j_2, j_3).$$

- **Loop rules for three Wigner 3-j symbol:** Varshalovich *et al.* (1988, Eq. 12.1.6) also displays a loop for three Wigner 3-j symbols.

$$\begin{aligned} \sum_{m_1, m_2, m_3} (-1)^{-m_1-m_2-m_3} & \left(\begin{matrix} j_1 & j_4 & j_2 \\ m_1 & m_4 & -m_2 \end{matrix} \right) \left(\begin{matrix} j_2 & j_5 & j_3 \\ m_2 & m_5 & -m_3 \end{matrix} \right) \left(\begin{matrix} j_3 & j_6 & j_1 \\ m_3 & m_6 & -m_1 \end{matrix} \right) \\ &= (-1)^{-j_1-j_2-j_3+j_4+j_5+j_6} \left(\begin{matrix} j_4 & j_5 & j_6 \\ m_4 & m_5 & m_6 \end{matrix} \right) \left\{ \begin{matrix} j_4 & j_5 & j_6 \\ j_3 & j_1 & j_2 \end{matrix} \right\}. \end{aligned}$$

15.4. Symbolic evaluations of Racah algebra expressions not yet considered in JAC

15.4.a. Orthogonality, completeness and integral representation of the Wigner rotation matrices:

Unitarity and completeness of the rotation matrices:

➤ **Unitarity condition:** This condition for the Wigner rotation matrices can be written either in terms of the Wigner D -function (Varshalovich *et al.*, 1988, Eqs. 4.1.6) or, equivalently, by means of the Wigner rotation matrices

$$\sum_{p=-j}^j d_{pq}^j(\beta) d_{pr}^j(\beta) = \delta_{qr}, \quad \sum_{q=-j}^j d_{pq}^j(\beta) d_{rq}^j(\beta) = \delta_{pr}.$$

➤ **Orthogonality and normalization condition for the rotation matrices:** The orthogonality and normalization condition in terms of $d_{pq}^j(\beta)$ is shown by Varshalovich *et al.* (1988, Eqs. 4.10.6 and 4.11.7)

$$\int_0^{2\pi} d\beta \sin \beta d_{pq}^j(\beta) d_{pq}^k(\beta) = \frac{2}{2j+1} \delta_{jk}$$

$$\int_0^{2\pi} d\alpha e^{-i(p_1-p_2)\alpha} \int_0^{2\pi} d\gamma e^{-i(q_1-q_2)\gamma} \int_0^\pi d\beta \sin \beta d_{p_1 q_1}^{j_1}(\beta) d_{p_2 q_2}^{j_2}(\beta) = \frac{8\pi^2}{2j_2+1} \delta_{j_1 j_2} \delta_{p_1 p_2} \delta_{q_1 q_2}.$$

➤ **Completeness condition of the rotation matrices:** cf. Varshalovich *et al.* (1988, Eq. 4.10.7) with double domain proportional to $16\pi^2$

$$\sum_{j=0, \frac{1}{2}, 1, \dots}^{\infty} \sum_{p=-j}^{+j} \sum_{q=-j}^{+j} (2j+1) e^{+i[(\alpha_1-\alpha_2)p+(\gamma_1-\gamma_2)q]} d_{pq}^j(\beta_1) d_{pq}^j(\beta_2) = 16\pi^2 \delta(\alpha_1 - \alpha_2) \delta(\cos \beta_1 - \cos \beta_2) \delta(\gamma_1 - \gamma_2).$$

Integrals involving Wigner D_{pq}^j functions or rotation matrices d_{pq}^j :

- The Wigner rotation matrices fulfill various integration rules as well as integration with invariant summation rules, and where some of these integrals involve products of more than one Wigner D -function. Whenever possible, we express the Clebsch-Gordan series as a product of two Wigner 3- j symbols. Most of the following integration rules require solid angle integration either over the standard domain

$$\int d\Omega \equiv \int_0^{2\pi} d\alpha \int_0^{2\pi} d\gamma \int_0^\pi d\beta \sin(\beta)$$

or over an extended domain with

$$\int d\Omega \equiv \int_0^{4\pi} d\alpha \int_0^{2\pi} d\gamma \int_0^\pi d\beta \sin(\beta) \quad \text{or} \quad \int d\Omega \equiv \int_0^{2\pi} d\alpha \int_0^{4\pi} d\gamma \int_0^\pi d\beta \sin(\beta).$$

$$0 \leq \alpha \leq 4\pi, \quad 0 \leq \beta \leq \pi, \quad 0 \leq \gamma \leq 2\pi, \quad \text{or} \quad 0 \leq \alpha \leq 2\pi, \quad 0 \leq \beta \leq \pi, \quad 0 \leq \gamma \leq 4\pi,$$

For this redefinition of the domain of integration, the factors $8\pi^2$ must typically be replaced by $16\pi^2$.

- **Integrals with one $D_{pq}^j(\alpha, \beta, \gamma)$:** Varshalovich *et al.* (1988, Eqs. 4.11.1 and 4.11.6) displays the following normalization integral as well as the corresponding special case for $\alpha = \gamma = 0$ and/or $p = q = 0$

$$\int d\Omega D_{pq}^j(\alpha, \beta, \gamma) = \int d\Omega e^{-i(p\alpha+q\gamma)} d_{pq}^j(\beta) = 8\pi^2 \delta_{j0} \delta_{p0} \delta_{q0}, \quad \text{if } j \text{ is integer}$$

$$\int_0^\pi d\beta \sin \beta d_{00}^j(\beta) = 2 \delta_{j0}.$$

15.4.b. Sum rules for spherical harmonics

Products of two and more spherical harmonics:

➤ Sum rules for two spherical harmonics:

$$\sum_{m=-\ell}^{\ell} (-1)^m Y_{\ell m}(\vartheta, \varphi) Y_{\ell, -m}(\vartheta, \varphi) = \sum_{m=-\ell}^{\ell} |Y_{\ell m}(\vartheta, \varphi)|^2 = \frac{2\ell + 1}{4\pi}$$

$$\sum_{l=0}^{\infty} \sum_{m=-\ell}^{\ell} (-1)^m m Y_{\ell, -m}(\vartheta, \varphi) Y_{\ell m}(\vartheta, \varphi) = 0$$

$$\sum_{l=0}^{\infty} \sum_{m=-\ell}^{\ell} (-1)^m m^2 Y_{\ell, -m}(\vartheta, \varphi) Y_{\ell m}(\vartheta, \varphi) = \frac{l(l+1)(2\ell+1)}{8\pi} \sin^2 \vartheta$$

$$\sum_{l=0}^{\infty} \sum_{m=-\ell}^{\ell} (-1)^m Y_{\ell, -m}(\vartheta, \varphi) Y_{\ell m}(\vartheta', \varphi') = \delta(\varphi - \varphi') \delta(\cos \vartheta - \cos \vartheta') = \delta(\varphi - \varphi') \frac{\delta(\vartheta - \vartheta')}{|\sin \vartheta|}.$$

➤ The Clebsch-Gordan expansion of two spherical harmonics: A product of two spherical harmonics with the same angles can be written as shown by Varshalovich *et al.* (1988, Eq. 5.6.9)

$$Y_{\ell_1 m_1}(\vartheta, \varphi) Y_{\ell_2 m_2}(\vartheta, \varphi) = \sum_{L,M} \left[\frac{(2\ell_1 + 1)(2\ell_2 + 1)}{4\pi(2L + 1)} \right]^{1/2} \langle \ell_1 0, \ell_2 0 | L 0 \rangle \langle \ell_1 m_1, \ell_2 m_2 | LM \rangle Y_{LM}(\vartheta, \varphi)$$

➤ The Clebsch-Gordan expansion of n spherical harmonics: Using this relation $n - 1$ times, one can easily derive a more general expression

$$\prod_{i=1}^n Y_{\ell_i m_i}(\vartheta, \varphi) = \sum_{L_n} B_{L_n} Y_{L_n M_n}(\vartheta, \varphi)$$

$$B_{L_n} = \frac{1}{\sqrt{(4\pi)^{n-1}(2L_n + 1)}} \sum_{\substack{L_1, L_2, \dots, L_n \\ M_1, M_2, \dots, M_n}} \prod_{i=1}^n \sqrt{2l_i + 1} \langle L_{i-1} 0, l_i 0 | L_i 0 \rangle \langle L_{i-1} M_{i-1}, l_i m_i | L_i M_i \rangle.$$

15. Symbolic evaluation of expressions from Racah's algebra

- **Irreducible tensor product of two spherical harmonics:** An irreducible tensor product of two spherical harmonics with the same angles can be written as (Varshalovich *et al.* 1988, Eq. 5.6.14)

$$\{Y_{\ell_1}(\vartheta, \varphi) \otimes Y_{\ell_2}(\vartheta, \varphi)\}_{LM} = \left[\frac{(2\ell_1 + 1)(2\ell_2 + 1)}{4\pi(2L + 1)} \right]^{1/2} \langle \ell_1 0, \ell_2 0 | L 0 \rangle Y_{LM}(\vartheta, \varphi)$$

- **Irreducible tensor product of n spherical harmonics:** Using this relation $n - 1$ times, one finds a more general expression (Varshalovich *et al.* 1988, Eq. 5.6.16):

$$\left\{ \cdot \left\{ \{Y_{\ell_1}(\vartheta, \varphi) \otimes Y_{\ell_2}(\vartheta, \varphi)\}_{L_2} \otimes Y_{\ell_3}(\vartheta, \varphi) \right\}_{L_3} \cdot \otimes Y_{\ell_n}(\vartheta, \varphi) \right\}_{L_n M_n} = \frac{1}{\sqrt{(4\pi)^{n-1}(2L_n + 1)}} \prod_{i=1}^n \left[\sqrt{2\ell_i + 1} \langle L_{i-1} 0, \ell_i 0 | L_i 0 \rangle \right] Y_{L_n M_n}(\vartheta, \varphi).$$

- **Multipole expansions by using spherical harmonics:** The spherical harmonics are not only orthonormal to each other but they also form a complete set of functions for the expansion of any function $f(\Theta, \Phi)$ that satisfies the given condition:

$$\int_0^{2\pi} d\Phi \int_0^\pi d\Theta \sin \Theta |f(\Theta, \Phi)|^2 < \infty : \quad f(\Theta, \Phi) = \sum_{l=0}^{\infty} \sum_{m=-\ell}^{\ell} \tilde{f}_{lm} Y_{\ell m}(\Theta, \Phi), \quad \tilde{f}_{lm} \equiv \int_0^{2\pi} d\varphi \int_0^\pi d\vartheta \sin \vartheta Y_{\ell m}^*(\vartheta, \varphi) f(\vartheta, \varphi).$$

15.4.c. Integrals involving spherical harmonics

Integrals involving spherical harmonics:

- **Orthonormality of the spherical harmonics:**

$$\int_0^{2\pi} d\varphi \int_0^\pi d\vartheta \sin \vartheta Y_{\ell m}^*(\vartheta, \varphi) Y_{\ell' m'}(\vartheta, \varphi) = \delta_{\ell \ell'} \delta_{mm'}.$$

➤ Further integrals over 4π : Cf. Varshalovich *et al.* (1988, Eqs. 5.9.1 and 5.9.5):

$$\int_0^{2\pi} d\varphi \int_0^\pi d\vartheta \sin \vartheta Y_{\ell m}(\vartheta, \varphi) = \sqrt{4\pi} \delta_{\ell 0} \delta_{m 0}$$

$$\int_0^{2\pi} d\varphi \int_0^\pi d\vartheta \sin \vartheta Y_{\ell_1 m_1}(\vartheta, \varphi) Y_{\ell_2 m_2}(\vartheta, \varphi) Y_{\ell_3 m_3}(\vartheta, \varphi) = \sqrt{\frac{(2\ell_1 + 1)(2\ell_2 + 1)(2\ell_3 + 1)}{4\pi}} \begin{pmatrix} \ell_1 & \ell_2 & \ell_3 \\ 0 & 0 & 0 \end{pmatrix} \begin{pmatrix} \ell_1 & \ell_2 & \ell_3 \\ m_1 & m_2 & m_3 \end{pmatrix}.$$

Derivatives of spherical harmonics:

➤ Derivatives of spherical harmonics: Cf. Varshalovich *et al.* (1988, Eq. 5.8.5) and with the associated Legendre polynomials $P_l^m(\cos \vartheta)$

$$\frac{d}{dx} \int_{g(x)}^{h(x)} dy f(y) = \frac{dh(x)}{dx} f(h(x)) - \frac{dg(x)}{dx} f(g(x)) \quad \text{chain rule}$$

$$\frac{d}{d\vartheta} Y_{\ell m}(\vartheta, \varphi) = \frac{1}{2} \sqrt{\ell(\ell+1) - m(m+1)} Y_{\ell, m+1}(\vartheta, \varphi) e^{-i\varphi} - \frac{1}{2} \sqrt{\ell(\ell+1) - m(m-1)} Y_{\ell, m-1}(\vartheta, \varphi) e^{i\varphi}.$$

$$\frac{d}{d\varphi} Y_{\ell m}(\vartheta, \varphi) = i m Y_{\ell m}(\vartheta, \varphi).$$

16. References

- 1998
1979 *Can. J. Phys.* **57** 1708
- Åberg T and Howat G** 1982 in *Corpuscles and Radiation in Matter I*, ed Mehlhorn W (in: Encyclopedia of Physics, vol XXXI; Springer, Berlin, p 469)
Theory of the Auger Effect
- Agostinelli S and Geant 4 collaboration** 2003 *Nuc. Instr. Meth.* **A506** 250 *Geant 4 – A simulation toolkit*
- Allen L, Beijersbergen M W, Spreeuw R J C and Woerdman J P** 1992 *Phys. Rev. A* **45** 8185 *Orbital angular momentum of light and the transformation of Laguerre-Gaussian laser modes*
- Allen L, Barnett S M and Padgett M J** 2003 *Optical Angular Momentum* (Institute of Physics Publishing, Bristol)
- Allen L, Padgett M J and Babiker M** 1999 *Progress in Optics* **39** 291 *The orbital angular momentum of light*
- Amini K, Biegert J, Calegari F, Chacon A, Ciappina M F, Dauphin A, Efimov D K, de Morisson Faria C F, Giergiel K, Gniewek P et al.** 2019 *Rep. Prog. Phys.* **82** 116001 *Symphony on strong field approximation*
- Ashkin A, Dziedzic J M, Bjorkholm J E and Chu S** 1986 *Opt. Lett.* **11** 288 *Observation of a single-beam gradient force optical trap for dielectric particles*
- Astapenko V** 2013 *Polarization Bremsstrahlung on Atoms, Plasmas, Nanostructures and Solids* Springer Series on Atomic, Optical and Plasma Physics 72 (Springer-Verlag Berlin Heidelberg, 2013)
- Astropy Collaboration** 2013 *Astronomy & Astrophys.* **558** A33 *Astropy: A community Python package for astronomy*
- Avgoustoglou E, Johnson W R, Plante D R, Sapirstein J, Sheinerman S and Blundell S A** 1992 *Phys. Rev. A* **46** 5478 *Many-body perturbation theory formulas for the energy levels of excited states of closed-shell atoms*
- Avgoustoglou E, Johnson W R, Liu Z W und Sapirstein J** 1995 *Phys. Rev. A* **51** 1196 *Relativistic many-body calculations of [2p⁵3s] excited state energy levels for neon-like ions*
- Badnell N R** 2011 *Comp. Phys. Commun.* **182** 1528 *A Breit-Pauli distorted wave implementation for AUTOSTRUCTURE*
- Badnell N R, Ballance C P, Griffin D C and O'Mullane M** 2012 *Phys. Rev. A* **85** 052716 *Dielectronic recombination of W²⁰⁺ (4d¹⁰4f⁸): Addressing the half-open f shell*
- Baghdasaryan B and Fritzsch S** 2020 *Phys. Rev. A* **102** 052412 *Enhanced entanglement from Ince-Gaussian pump beams in spontaneous parametric down-conversion*

16. References

- Bahrdt J, Holldack K, Kuske P, Müller R, Scheer M and Schmid P** 2013 *Phys. Rev. Lett.* **111** 034801 *First observation of photons carrying orbital angular momentum in undulator radiation*
- Balashov V V, Grum-Grzhimailo A N and Kabachnik N M** 2000 *Polarization and Correlation Phenomena in Atomic Collisions* (Kluwer Academic Plenum Publishers, New York)
- Ballantine K E, Donegan J F and Eastham P R** 2016 *Sci. Adv.* **2** e1501748 *There are many ways to spin a photon: Half-quantization of a total optical angular momentum*
- Band I M, Trzhaskovskaya M B, Nestor Jr N W, Tikkanen P O and Raman S** 2002 *Atom. Data Nucl. Data Tables* **81** 1 *Dirac–Fock internal conversion coefficients*
- Basset M-G, Setzpfandt F, Steinlechner F, Beckert E, Pertsch T and Gräfe M** 2019 *Laser Phot. Rev.* **13** 1900097 *Perspectives for applications of quantum imaging*
- Bazhenov V Y, Vasnetsov M V and Soskin M S** 1990 *JETP Lett.* **52** 429 *Laser-beams with screw dislocations in their wave-fronts*
- Becke A D and Edgecombe K E** 1990 *J. Chem. Phys.* **92** 5397 *A simple measure of electron localization in atomic and molecular systems*
- Beerwerth R, Buhr T, Perry-Sassmannshausen A, Stock S O, Bari S, Holste K, Kilcoyne A L D, Reinwardt S, Ricz S, Savin D W, Schubert K, Martins M, Müller A, Fritzsch S and Schippers S** 2019 *Astrophys. J.* **887** 189 *Near L-edge single and multiple photoionization of triply charged iron*
- Beijersbergen M W, Coerwinkel R P C, Kristensen M and Woerdman J P** 1994 *Opt. Comm.* **12** 321 *Helical-wavefront laser beams produced with a spiral phase plate*
- Belabbas M, Inal M K and Benmouna M** 2021 *Phys. Rev. A* **104** 042818 *Computations of the multipole cross sections for directional excitation of ions by electron impact*
- Belkic D** 1988 *Phys. Rev.* **37** 55 *Electron capture by fast protons from helium, nitrogen, and oxygen: The corrected first Born approximation*
- Belyov K and Derevianko A** 2008 *Comp. Phys. Commun.* **179** 310 *Application of the dual-kinetic-balance sets in the relativistic many-body problem of atomic structure*
- Berengut J C, Dzuba V A, Flambaum V V and Ong A** 2012 *Phys. Rev. A* **86** 022517 *Highly charged ions with E1, M1, and E2 transitions within laser range*
- Bergues B, Kübel M, Johnson N G, Fischer B, Camus N, Betsch K J, Herrwerth O, Senftleben A, Sayler A M, Rathje T, Pfeifer T, Ben-Itzhak I, Jones R R, Paulus G G, Krausz F, Moshammer R, Ullrich J, and Kling M F** 2012 *Nature Commun.* **3** 813 *Attosecond tracing of correlated electron-emission in non-sequential double ionization*
- Bergues B, Rivas D E, Weidman M, Muschet A A, Helml W, Guggenmos A, Pervak V, Kleineberg U, Marcus G, Kienberger R, Charalambidis D, Tzallas P, Schröder H, Krausz F and Veisz L** 2018 *Optica* **5** 237 *Tabletop nonlinear optics in the 100-eV spectral region*
- Bethe H A and Salpeter E E** 1957 *Quantum Mechanics of One- and Two-Electron Systems* (Springer-Verlag, Berlin, Göttingen, Heidelberg)
- Bezanson J, Edelman A, Karpinski S and Shah V B** 2017 *SIAM Review* **59** 65 *Julia: A fresh approach to numerical computing*
- Bezanson J, Chen J, Chung B, Karpinski S, Shah V B, Vitek J and Zoubitzky J** 2018 *Proceedings of the ACM on Programming Languages* **2** 120 *Julia: Dynamism and performance reconciled by design*

- Bissell M L, Carette T, Flanagan K T, Vingerhoets P, Billowes J, Blaum K, Cheal B, Fritzsche S, Godefroid M, Kowalska M et al.** 2016 *Phys. Rev. C* **93** 064318 *Cu charge radii reveal a weak sub-shell effect at $N = 40$*
- Blenski T and Ishikawa K** 1995 *Phys. Rev. E* **51** 1708 *Pressure ionization in the spherical ion-cell model of dense plasmas and a pressure formula in the relativistic Pauli approximation*
- Bliokh K Y, Bliokh Y P, Savelev S and Bliokh F N** 2007 *Phys. Rev. Lett.* **99** 190404 *Semiclassical dynamics of electron wave packet states with phase vortices*
- Bliokh K Y, Dennis M R and Franco Nori** 2011 *Phys. Rev. Lett.* **107** 174802 *Relativistic electron vortex beams: angular momentum and spin-orbit interaction*
- Blumenhagen K-H, Fritzsche S, Gassner T, Gumberidze A, Märtin R, Schell N, Seipt D, Spillmann U, Surzhykov A, Trotsenko S, Weber G** Yerokhin V A and Stöhlker T 2016 *New J. Phys.* **18** 103034 *Polarization transfer in Rayleigh scattering of hard x-rays*
- Böning B, Paufler W and Fritzsche S** 2017 *Phys. Rev. A* **96** 043423 *Attosecond streaking with twisted x waves and intense infrared pulses*
- Böning B, Paufler W and Fritzsche S** 2018 *Phys. Rev. A* **98** 023407 *Above-threshold ionization by few-cycle Bessel pulses carrying orbital angular momentum*
- Böning B and Fritzsche S** 2020 *Phys. Rev. A* **102** 053108 *Partial-wave representation of the strong-field approximation*
- Borgoo A, Scharf O, Gaigalas G and Godefroid M** 2010 *Comp. Phys. Commun.* **181** 426 *Multiconfiguration electron density function for the ATSP2K-package*
- Bouvie P A, Lopez-Rosa A and Dehesa J S** 2012 *Phys. Rev. A* **86** 012507 *Quantifying Dirac hydrogenic effects via complexity measures*
- Boyle J J and Pindzola M S** 1998 *Many-body atomic physics: Lectures on the application of many-body theory to atomic physics* (Cambridge University Press, Cambridge a o)
- Bozinovic N, Yue Y, Ren Y, Tur M, Kristensen P, Huang H, Willner A E, Ramachandran S** 2013 *Science* **340** 1545 *Terabit-scale orbital angular momentum mode division multiplexing in fibers*
- Briand J-P, de Billy L, Charles P, Essabaa S, Briand P, Geller R, Desclaux P, Bliman S and Ristori C** 1990 *Phys. Rev. Lett.* **65** 159 *Production of hollow atoms by the excitation of highly charged ions in interaction with a metallic surface*
- Butler S E, Heil T G and Dalgarno A** 1980 *Astrophys. J.* **241** 442 *Charge transfer of multiply charged ions with hydrogen and helium: quantal calculations*
- Butler K T, Davies D W, Cartwright H, Isayev O and Walsh A** 2018 *Nature* **559** 547 *Machine learning for molecular and materials science*
- Cai X, Wang J, Strain M J, Johnson-Morris B, Zhu J, Sorel M, O'Brien J L, Thompson M G, Yu S** 2012 *Science* **338** 363 *Integrated compact optical vortex beam emitters*
- Canton-Rogan S E, Wills A A, Gorczyca T W, Wiedenhoeft M, Nayandin O, Liu C-N and Berrah N** 2000 *Phys. Rev. Lett.* **85** 3113 *Mirroring doubly excited resonances in argon*
- Chen J, Ng J, Lin Z and Chan C T** 2011 *Nat. Photonics* **5** 531 *Optical pulling force*
- Chen M H** 1986 *Phys. Rev. A* **34** 1073 *Relativistic calculations of dielectronic recombination coefficients for the Ne isoelectronic sequence*

16. References

- Chen Z, Liu F and Wen H** 2019 *Chin. Phys.* **B28** 123401 *Quantitative rescattering theory for nonsequential double ionization*
- Cheng G and Jiaolong Z** 2008 *Phys. Rev. E* **78** 046407 *Spectrally resolved and Rosseland and Planck mean opacities of iron plasmas at temperatures above 100 eV: A systematic study*
- Coe J P** 2018 *J. Chem. Theo. Comp.* **14** 5739 *Machine learning configuration interaction*
- Cowan R D** 1981 *The Theory of Atomic Structure and Spectra* (University of California Press, 1981, 731 pages)
- Crowley B J B and Gregori G** 2014 *High En. Dens Phys.* **13** 55 *Quantum theory of Thomson scattering*
- Crowley B J B and Gregori G** 2013 *New J. Phys.* **15** 015014 *X-ray scattering by many-particle systems*
- Da Pieve F, Fritzsch S, Stefani G and Kabachnik N M** 2007 *J. Phys. B* **40** 329 *Linear magnetic and alignment dichroism in Auger-photoelectron coincidence spectroscopy*
- Darwin C G** 1932 *Proc. R. Soc. Lond. A* **136** 36 *Notes on the theory of radiation*
- Delone N B and Krainov V P** 1992 *Phys. Uspekhi.* **47** 669 *AC Stark shift of atomic energy levels*
- Deprince J, Bautista M A, Fritzsch S, Garcia J A, Kallman T R, Mendoza C, Palmeri P and Quinet P** 2020 *A&A* **643** A57 *Plasma environment effects on K lines of astrophysical interest. IV. IPs, K thresholds, radiative rates, and Auger widths in Fe II–Fe VII*
- Derevianko A, Johnson W R and Cheng K T** 1999 *At. Data Nucl. Data Tables* **73** 153 *Non-dipole effects in photoelectron angular distributions for rare gas atoms*
- Derevianko A, Johnson W R, Safranova M S and Babb J F** 1999 *Phys. Rev. Lett.* **82** 3589 *High-precision calculations of dispersion coefficients, static dipole polarizabilities and atom-wall interaction constants for alkali-metal atoms*
- Drake G W F** 1986 *Phys. Rev. A* **34** 2871 *Spontaneous two-photon decay rates in hydrogenlike and heliumlike ions*
- Dzikowski K D, Oreshkina N S, Skoromnik O D and Keitel C H** 2022 *J. Phys. B* **54** 115002 *Relativistic effective charge model of a multi-electron atom*
- Dzuba V R and Johnson W R** 1998 *Phys. Rev. A* **57** 2459 *Calculation of the energy levels of barium using B splines and a combined configuration-interaction and many-body-perturbation-theory method*
- Dzuba V A and Flambaum V V** 2009 *Phys. Rev. A* **80** 062509 *Calculation of the (T , P)-odd electric dipole moment of thallium and cesium*
- Dzuba V A, Flambaum V V and Ginges J S M** 2000 *Phys. Rev. A* **61** 062509 *Calculation of parity and time invariance violation in the radium atom*
- Dzuba V A, Flambaum V V and Porseye S G** 2009 *Phys. Rev. A* **80** 032120 *Calculation of (P , T)-odd electric dipole moments for the diamagnetic atoms ^{129}Xe , ^{171}Yb , ^{199}Hg , ^{211}Rn , and ^{225}Ra*
- Edmonds A R** 1957 *Angular Momentum in Quantum Mechanics* (Princeton University Press New York)
- Edström A, Lubk A and Rusz J** 2016 *Phys. Rev. Lett.* **116** 127203 *Elastic scattering of electron vortex beams in magnetic matter*
- Eichler J and Meyerhof W** 1995 *Relativistic Atomic Collisions* (Academic Press, San Diego)
- Fano U** 1965 *Phys. Rev.* **140** A67 *Interaction between configurations with several open shells*
- Feiock F D and Johnson W R** 1968 *Phys. Rev. Lett.* **21** 785 *Relativistic evaluation of internal diamagnetic fields for atoms and ions*
- Feiock F D and Johnson W R** 1969 *Phys. Rev.* **187** 39 *Atomic susceptibilities and shielding factors*
- Fickler R, Lapkiewicz R, Plick W N, Krenn M, Schaeff C, Ramelow S and Zeilinger A** 2012 *Science* **338** 5 *Quantum entanglement of high angular*

momenta

- Filianin P, Lyu C, Door M, Blaum K, Huang W J, Haverkort M, Indelicato P, Keitel C H, Kromer K, Lange D, Novikov Y N, Rischka A, Schüssler R X, Schweiger C, Sturm S, Ulmer S, Harman Z and Eliseev S** 2021 *Phys. Rev. Lett.* **127** 072502 *Direct Q-value determination of the β^- decay of ^{187}Re*
- Fisher D, Maron Y and Pitaevskii L P** 1998 *Phys. Rev. A* **58** 2214 *Ionization of many-electron atoms by a quasistatic electric field*
- Flambaum V V and Ginges J S M** 2005 *Phys. Rev. A* **72** 052115 *Radiative potential and calculations of QED radiative corrections to energy levels and electromagnetic amplitudes in many-electron atoms*
- Fontes C J, Zhang H L, Abdallah Jr J, Clark R E H, Kilcrease D P, Colgan J, Cunningham R T, Hakel P, Magee N H and Sherrill M E** 2015 *J. Phys. B* **48** 144014 *The Los Alamos suite of relativistic atomic physics codes*
- Franke-Arnold S, Allen L, Padgett M J** 2008 *Laser and Photonics Reviews* **2** 299 *Advances in optical angular momentum*
- Freiburghaus C, Rosswog S and Thielemann F-K** 1999 *Astrophys. J.* **525** L121 *r-Process in neutron star mergers*
- Fritzsche S** 1997 *Comp. Phys. Commun.* **103** 51 *Maple procedures for the coupling of angular momenta. I. Data structures and numerical evaluation*
- Fritzsche S** 2001 *J. Electron Spectrosc. Relat. Phenom.* **114-116** 1155 *A toolbox for studying the properties of open-shell atoms and ions*
- Fritzsche S** 2002 *Phys. Scr. T100* 37 *Large-scale accurate structure calculations for open-shell atoms and ions*
- Fritzsche S** 2021 *A. & A.* **656** A163 *Dielectronic recombination strengths and plasma rate coefficients of multiply charged ions*
- Fritzsche S** 2022 *Atoms* **10** 7 *Level structure and properties of open f -shell elements*
- Fritzsche S** 2022 *Symmetry* **13** 1558 *Symbolic evaluation of expressions from Racah's algebra*
- Fritzsche S** 2022 *Atoms* **10** 37 *Photon emission from hollow ions near surfaces*
- Fritzsche S, Palmeri P and Schippers S** 2021 *Symmetry* **13** 520 *Atomic cascade computations*
- Fritzsche S and Surzhykov A** 2021 *Molecules* **26** 2660 *Approximate atomic green functions*
- Fritzsche S, Nikkinen J, Huttula S-M, Aksela H, Huttula M and Aksela S** 2007 *Phys. Rev. A* **75** 012501 *Interferences in the $3p^4nl$ satellite emission following the excitation of argon across the $2p_{1/2}^54s$ and $2p_{3/2}^53d$ $J = 1$ resonances*
- Fritzsche S, Fricke B and Sepp W-D** 1992 *Phys. Rev. A* **45** 1465 *Reduced L_1 level-width and Coster-Kronig yields by relaxation and continuum interactions in atomic zinc*
- Froese Fischer C, Godefroid M, Brage T, Jönsson P and Gaigalas G** 2016 *J. Phys. B* **49** 182004 *Advanced multiconfiguration methods for complex atoms: I. Energies and wave functions*
- Furukawa H and Nishihara K** 1992 *Phys. Rev. A* **46** 6596 *Fermi-degeneracy and discrete-ion effects in the spherical-cell model and electron-electron correlation effects in hot dense plasma*
- Gaidamauskas E, Naze C, Rynkun P, Gaigalas G, Jönsson P and Godefroid M** 2011 *J. Phys. B* **44** 175003 *Tensorial form and matrix elements of the relativistic nuclear recoil operator*
- Gaigalas G, Froese Fischer C, Rynkun P and Jönsson P** 2017 *atoms* **5** 6 *JJ2LSJ: Transformation and unique Labeling for energy levels*
- Gaigalas G, Zalandauskas T and Fritzsche S** 2004 *Comp. Phys. Commun.* **157** 239 *Spectroscopic LSJ notation for atomic levels obtained from relativistic*

16. References

calculations

- Gaigalas G, Fritzsche S and Rudzikas Z** 2000 *At. Data Nucl. Data Tables* **76** 235 *Reduced coefficients of fractional parentage and matrix elements of the tensor $W^{(k_q, k_j)}$ in jj-coupling*
- Gaigalas G, Fritzsche S and Grant I P** 2001 *Comput. Phys. Commun.* **139** 263 *Calculation of pure angular coefficients in jj-coupling*
- Galstyan A, Popov Y V, Janssens N, Mota-Furtado F, O'Mahony P F, Decleva P, Quadri N, Chuluunbaatar O and Piraux B** 2018 *Chem. Phys.* **504** 22 *Ionisation of H_2O by a strong ultrashort XUV pulse: A model within the single active electron approximation*
- Gaunt** 1929 *Proc. R. Soc. A* **122** 513 *IV. The triplets of helium*
- Ghiringhelli L M, Vybird J, Levchenko S V, Draxl C and Scheffler M** 2015 *Phys. Rev. Lett.* **114** 105503 *Big data of materials science: Critical role of the descriptor*
- Ginges J S M, Volotka A V and Fritzsche S** 2017 *Phys. Rev. A* **96** 062502 *Ground-state hyperfine splitting for Rb, Cs, Fr, Ba^+ , and Ra^+*
- Ginzburg V L and Tsytovich V N** 1979 *Phys. Rep.* **49** 1 *Transition radiation and transition scattering*
- Glenzer S H and Redmer R** 2009 *Rev. Mod. Phys.* **81** 1625 *X-ray Thomson scattering in high energy density plasmas*
- Goldman S P and Drake G W F** 1992 *Phys. Rev. Lett.* **68** 1683 *Asymptotic Lamb shifts for helium Rydberg states*
- Gordon R G and Kim Y S** 1972 *J. Chem. Phys.* **56** 3122 *Theory for the forces between closed-shell atoms and molecules*
- Grant I P** 1988 *in: Methods in Computational Chemistry* ed Wilson S, vol 2 (Plenum, New York, p 1) *Relativistic effects in atoms and molecules*
- Grant I P and Pyper N C** 1976 *J. Phys. B* **9** 761 *Breit interaction in multiconfiguration relativistic atomic calculations*
- Grant I P and Quiney H M** 1988 *in: Advances in Atomic and Molecular Physics* **23** eds D Bates and B Bederson (Academic, New York, p 37) *Foundation of Relativistic Theory of Atomic and Molecular Structure*
- Griem H** 1974 *Spectral Line Broadening by Plasmas* (Academic Press, New York, London)
- Grier D G** 2003 *Nature* **424** 810 *A revolution in optical manipulation*
- Grillo V, Gazzadi G-C, Mafakheri E, Frabboni S, Karimi E and Boyd R W** 2015 *Phys. Rev. Lett.* **114** 034801 *Holographic generation of highly twisted electron beams*
- Grum-Grzhimailo A N, Gryzlova E V, Staroselskaya E I, Venzke J and Bartschat K** 2015 *Phys. Rev. A* **91** 063418 *Interfering one-photon and two-photon ionization by femtosecond VUV pulses in the region of an intermediate resonance*
- Gu M F** 2008 *Can. J. Phys.* **86** 675 *The flexible atomic code*
- Gu M F and Beiersdorfer P** 2020 *Phys. Rev. A* **101** 032501 *Stark shift and width of x-ray lines from highly charged ions in dense plasmas*
- Guo D-S, Åberg T and Crasemann B** 1989 *Phys. Rev. A* **40** 4997 *Scattering theory of multiphoton ionization in strong fields*
- Guo D-S and Drake G W F** 1992 *Phys. Rev. A* **45** 6622 *Multiphoton ionization in circularly polarized standing waves*
- Haque A K F, Shahjahan M, Uddin M A, Patoary M A R, Basak A K, Saha B C and Malik F B** 2010 *Phys. Scr.* **81** 045301 *Generalized Kolbenstvedt model for electron impact ionization of the K-, L- and M-shell ions*
- Harman Z, Shah C, Martinez A J G et al.** 2019 *Phys. Rev. A* **99** 012506 *Resonance strengths for KLL dielectronic recombination of highly charged mercury ions and improved empirical Z-scaling law*

- Hartemann F V, Troha A L, Baldis H A, Gupta A, Kerman A K, Landahl E C, Luhmann Jr, N C and van Meter J R** 2000 *Astr. Phys. Suppl.* **127** 347 *High-intensity scattering processes of relativistic electrons in vacuum and their relevance to high-energy astrophysics*
- Hartgers A, van Dijk J, Jonkers J, van der Mullen J A M** 2001 *Comp. Phys. Commun.* **135** 199 *CR-Model: A general collisional radiative modeling code*
- He H, Friese M E J, Heckenberg N R and Rubinsztein-Dunlop H** 1995 *Phys. Rev. Lett.* **75** 826 *Direct observation of transfer of angular momentum to absorptive particles from a laser beam with a phase singularity*
- Hemsing E, Marinelli A Rosenzweig J B** 2011 *Phys. Rev. Lett.* **106** 164803 *Generating optical orbital angular momentum in a high-gain free-electron laser at the first harmonic*
- Hemsing E and Marinelli A** 2012 *Phys. Rev. Lett.* **109** 224801 *Echo-enabled x-ray vortex generation*
- Hemsing E, Knyazik A, Dunning M, Xiang D, Marinelli A, Hast D and Rosenzweig J B** 2013 *Nature Phys.* **9** 549 *Coherent optical vortices from relativistic electron beams*
- Hikosaka Y, Lablanquie P, Kaneyasu T, Suzuki I H, Ishikawa M and Odagiri T** 2021 *J. Phys. B* **54** 185002 *Auger cascade initiated by the Coster-Kronig transition from the Kr 3p core-hole states*
- Hofbrucker J, Böning B, Volotka A V and Fritzsche S** 2021 *Phys. Rev. A* **104** 013102 *Elliptical dichroism in biharmonic ionization of atoms*
- Hofbrucker J, Volotka A V and Fritzsche S** 2016 *Phys. Rev. A* **94** 063412 *Relativistic calculations of the nonresonant two-photon ionization of neutral atoms*
- Hubbell J H, Veigle W J, Briggs E A, Brown R T, Cromer D T and Howerton R J** 1992 *J. Phys. Chem. Ref. Data* **4** 471 *Atomic form factors, incoherent scattering functions, and photon scattering cross sections*
- Huntemann N, Sanner C, Lipphardt B, Tamm C and Peik E** 2016 *Phys. Rev. Lett.* **116** 063001 *Single-ion atomic clock with 3×10^{-18} systematic uncertainty*
- Iglesias C A and Rogers F J** 1979 *Astrophys. J.* **464** 943 *Updated OPAL opacities*
- Inal M K, Surzhykov A and Fritzsche S** 2005 *Phys. Rev. A* **72** 042720 *Linear polarization of the $2p^5 3s \rightarrow 2p^6$ lines following the inner-shell photoionization of sodiumlike ions*
- Inhester L, Burmeister C F, Groenhof G and Grubmüller H** 1992 *J. Chem. Phys.* **136** 144304 *Auger spectrum of a water molecule after single and double core ionization*
- Isinger M, Squibb R J, Bustos D, Zhong S, Harth A, Kroon D, Nandi S, Arnold C L, Miranda M, Dahlström J M, Lindroth E et al.** 2017 *Science* 358 893 *Photoionization in the time and frequency domain*
- Ivanov I P and Karlovets D V** 2013 *Phys. Rev. Lett.* **110** 264801 *Detecting transition radiation from a magnetic moment*
- Jaganathan Y, Id Betan R M, Michel N, Nazarewicz W and Ploszajczak M** 2017 *Phys. Rev. C* **96** 054316 *Quantified Gamow shell model interaction for psd-shell nuclei*
- Jahrsetz T, Fritzsche S and Surzhykov A** 2015 *Phys. Rev. A* **89** 042501 *Inelastic Raman scattering of light by hydrogenlike ions*
- Jia C-S, Diao Y-F, LiuX-J, Wang P-Q, Liu J-Y and Zhang G-D** 2012 *J. Chem. Phys.* **137** 014101 *Equivalence of the Wei potential model and Tietz*

16. References

- potential model for diatomic molecules
- Jiao L G, Zan L R, Zhu L, Ma J and Ho Y K** 2019 *Comp. Phys. Commun.* **244** 217 *Accurate computation of screened Coulomb potential integrals in numerical Hartree-Fock programs*
- Johnson E R** 2011 *J. Chem. Phys.* **135** 234109 *Dependence of dispersion coefficients on atomic environment*
- Johnson W R** 1995 *in: Physics with Multiply Charged Ions* ed D Liesen (NATO ASI Series 348, Plenum Press, New York London, p 1 *Correlation and QED for highly-charged ions*)
- Johnson W R** 2007 *Atomic Structure Theory: Lectures on Atomic Physics* (Springer)
- Johnson W R and Feiock F D** 1968 *Phys. Rev.* **168** 22 *Rayleigh scattering and the electromagnetic susceptibility of atoms*
- Johnson W R, Guo D S, Idrees M and Sapirstein J** 1985 *Phys. Rev.* **A32** 2093 *Weak-interaction effects in heavy atomic systems*
- Johnson W R and Nilsen J** 2020 *Phys. Rev.* **E102** 043209 *Average-atom calculations of bound-free and free-free cross sections in dense plasmas*
- Johnson W R, Guet C and Bertsch G F** 1979 *J. Quant. Spectr. Rad. Trans.* **99** 327 *Optical properties of plasmas based on an average-atom model*
- Jönsson P, Gaigalas G, Bieron J, Froese Fischer C and Grant I P** 2013 *Comp. Phys. Commun.* **184** 2197 *New version: Grasp2K relativistic atomic structure package*
- Judd B R** 1963 *Operator Techniques in Atomic Spectroscopy* (McGraw-Hill New York)
- Jung Y-D** 1997 *Phys. Plasma* **4** 21 *Dynamic plasma screening effects on semiclassical inelastic electron-ion collisions in dense plasmas*
- Kabachnik N M** 1981 *J. Phys.* **B14** L337
- Kabachnik N M, Fritzsche S, Grum-Grzhimailo A N, Meyer M and Ueda K** 2007 *Phys. Rep.* **451** 155 *Coherence and correlations in photoinduced Auger and fluorescence cascades in atoms*
- Karp A H, Lasher G, Chan K L and Salpeter E E** 1977 *Astrophys. J.* **214** 161 *The opacity of expanding media: the effect of spectral lines*
- Kasen D, Badnell N R and Barnes J** 2013 *Astrophys. J.* **774** 25 *Opacities and spectra of the r-process ejecta from neutron star mergers*
- Kassimi N E and Thakkar A J** 1994 *Phys. Rev.* **A50** 2948 *Static hyperpolarizability of atomic lithium*
- Kibeedia T, Burrows T W, Trzhaskovskayac M B, Davidsonc P M and Nestorc W** 2008 *Nucl. Instr. Meth.* **A589** 202 *Evaluation of theoretical conversion coefficients using BrIcc*
- Killoran N, Izaac J, Quesada N, Bergholm V, Amy M and Weedbrook C** 2019 *Quantum* **3** 129 *Strawberry Fields: A Software Platform for Photonic Quantum Computing*
- Kim Y-K** 2001 *Phys. Rev.* **A64** 032713 *Scaling of plane-wave Born cross sections for electron-impact excitation of neutral atoms*
- Kim Y K, Santos J P and Parente F** 2000 *Phys. Rev.* **62** 052710 *Extension of the binary-encounter-dipole model to relativistic incident electrons*
- Kim Y S and Gordon R G** 1974 *Phys. Rev.* **B9** 3548 *Theory of binding of ionic crystals: Application to alkali-halide and alkalene-earth-dihalide cryst.*
- Klar H** 1980 *J. Phys.* **B13** 4741
- Kien F L, Schneeweiss P and Rauschenbeutel A** 2013 *Eur. Phys. J.* **D67** 92 *Dynamical polarizability of atoms in arbitrary light fields: General theory and application to cesium*
- Koga T and Thakkar A J** 1996 *J. Phys. B* **29** 2973 *Moments and expansion coefficients of atomic electron momentum densities: numerical Hartree-Fock*

calculations for hydrogen to lawrencium

- Kong L and Valeev E F** 2011 *J. Chem. Phys.* **134** 214109 *A novel interpretation of reduced density matrix and cumulant for electronic structure theories*
- Kosheleva V P, Zaytsev V A, Müller R A, Surzhykov A and Fritzsche S** 2020 *Phys. Rev. A* **102** 063115 *Resonant two-photon ionization of atoms by twisted and plane-wave light*
- Koszorus A, Vormawah L J, Beerwerth R, Bissell M L, Campbell P, Cheal B, Devlin C S, Eronen T, Fritzsche S, Geldhof S et al.** 2021 *Phys. Lett. B* **819** 136439 *Proton-neutron pairing correlations in the self-conjugate nucleus ^{42}Sc*
- Kotlyar V V, Abramochkin E G, Kovalev A A and Savelyeva A A** 2022 *Photonics* **9** 496 *Product of two Laguerre-Gaussian beams*
- Kottmann J S, Anand A and Aspuru-Guzik A** 2021 *Chem. Sci.* **12** 3497 *A feasible approach for automatically differentiable unitary coupled-cluster on quantum computers*
- Kottmann J S, Alperin-Lea S, Tamayo-Mendoza T, Cervera-Lierta A, Lavigne C, Yen T C, Verteletskyi V, Schleich P, Anand A, Degroote M, et al.** 2020 *Quantum Sci. Technol.* **6** 024009 *TEQUILA: A platform for rapid development of quantum algorithms*
- Kozhedub Y S, Andreev O V, Shabaev V M, Tupitsyn I I, Brandau C, Kozhuharov C, Plunien G and Stöhlker T** 2008 *Phys. Rev. A* **77** 032501 *Nuclear deformation effect on the binding energies in heavy ions*
- Kozma C and Fransson C** 1992 *Astrophys. J.* **390** 602 *Gamma-ray deposition and nonthermal excitation in supernovae*
- Krause M O** 1979 *J. Phys. Chem. Ref. Data* **8** 329 *Atomic radiative and radiationless yields for K and L shells*
- Lebedev V S and Beigman I L** 1998 *Physics of Highly Excited Atoms and Ions* (Springer, Berlin, Heidelberg a o)
- Lembessis V E and Babiker M** 2013 *Phys. Rev. Lett.* **110** 083002 *Enhanced quadrupole effects for atoms in optical vortices*
- Lemos G B, Borish V, Cole G D, Ramelow S, Lapkiewicz R and Zeilinger A** 2014 *Nature* **512** 409 *Quantum imaging with undetected photons*
- Leonov A, Ksenzov D, Benediktovich A, Feranchuk I and Pietsch U** 2014 *IUCrJ* **1** 402 *Time dependence of x-ray polarizability of a crystal induced by an intense femtosecond x-ray pulse*
- Leung A C K and Kirchner T** 2015 *Phys. Rev. A* **92** 032712 *Independent-electron analysis of the x-ray spectra from single-electron capture in Ne^{10+} collisions with He, Ne, and Ar atoms*
- Li W, Grumer J, Brage T and Jönsson P** 2020 *Comp. Phys. Commun.* **xxx** xxx *HFSZEEMAN95 – A program for computing weak and intermediate magnetic-field- and hyperfine-induced transition rates*
- Libermann D A** 1979 *Phys. Rev. B* **20** 4981 *Self-consistent field model for condensed matter*
- Li Y T, Wang K, Si R, Godefroid M, Gaigalas G, Chen C Y and Jönsson P** 2023 *Comp. Phys. Commun.* **283**, 108562 *Reducing the computational load – atomic multiconfiguration calculations based on configuration state function generators*
- Lin K, Brennecke S, Ni H C, Chen X, Hartung A, Trabert D, Fehre K, Rist J, Tong X M, Burgdörfer J** 2022 *Phys. Rev. Lett.* **128** 023201 *Magnetic-field effect in high-order above-threshold ionization*
- Lin K, Chen X, Eckart S, Jiang H, Hartung A, Trabert D, Fehre K, Rist J, Schmidt L P H et al.** 2022 *Phys. Rev. Lett.* **128** 113201 *Magnetic-field effect as a tool to investigate electron correlation*

16. References

- Lindgren I and Rosen A** 1974 *Case Studies in Atomic Physics* **5** Relativistic self-consistent-field calculations with application to atomic hyperfine interaction. Part I: Relativistic self-consistent fields
- Lindgren I and Morrison J** 1986 *Atomic Many-Body Theory*, 2nd ed (Springer Berlin)
- Liu F, Chen Z, Morishita T, Bartschat K, Böning B and Fritzsch S** 2021 *Phys. Rev. A* **104** 013105 Single-cycle versus multicycle nonsequential double ionization of argon
- Liu C-N and Starace A F** 1999 *Phys. Rev. A* **59** 1731(R) Mirroring behavior of partial photodetachment and photoionization cross sections in the neighborhood of a resonance
- Liu P F, Liu Y P, Zeng J L and Yuan J M** 2014 *Phys. Rev. A* **89** 042704 Electron-impact excitation and single- and multiple-ionization cross sections of heavy ions: Sn^{13+} as an example
- Liu Z, Lee H, Xiong Y, Sun C and Zhang X** 2007 *Science* **315** 1686 Far-field optical hyper lens magnifying sub-diffraction-limited objects
- Lucy L B** 2002 *A. & A.* **384** 725 Monte Carlo transition probabilities
- Marty O, Cramer M and Plenio M B** 2016 *Phys. Rev. Lett.* **116** 105301 Practical entanglement estimation for spin-system quantum simulators
- Marxer H** 1991 *Phys. Rev. A* **44** 1543 Exact correspondence relationship for the expectation values of r^{-k} for hydrogenlike states
- Marxer H** 1995 *J. Phys. B* **28** 341 Off-diagonal matrix elements $\langle nl | r^k | nl' \rangle$ for hydrogen-like states: an exact correspondence relationship in terms of orthogonal polynomials and the WKB approximation
- Matula O, Hayrapetyan A G, Serbo V G, Surzhykov A and Fritzsch S** 2013 *J. Phys. B* **46** 205002 Atomic ionization of hydrogen-like ions by twisted photons: angular distribution of emitted electrons
- Matula O, Hayrapetyan A G, Serbo V G, Surzhykov A and Fritzsch S** 2014 *New J. Phys.* **16** 053016 Radiative capture of twisted electrons by bare ions
- Mazevet S and Abdallah Jr J** 2006 *J. Phys. B* **39** 3419 Mixed UTA and detailed line treatment for mid-Z opacity and spectral calculations
- Mazziotti D A** 2012 *Phys. Rev. Lett.* **108** 263002 Structure of fermionic density matrices: complete N -representability conditions
- McArdle S, Endo S, Aspuru-Guzik A, Benjamin S C and Yuan X** 1998 *Rev. Mod. Phys.* **92** 442 Quantum computational chemistry
- McClean J R, Sung K J, Kivlichan I D, Cao Y, Dai C, Fried S E, Gidney C, Gimby B, Gokhale P et al.** 2019 *Phys. Rev. A* in print OpenFermion: The electronic structure package for quantum computers
- McGloin D and Dholakia K** 2005 *Contemp. Phys.* **46** 15 Bessel Beams: Diffraction in a New Light
- McMorran B J, Agrawal A, Anderson I M, Herzing A A, Lezec H J, McClelland J J and Unguris J** 2011 *Science* **331** 192 Electron vortex beams with high quanta of orbital angular momentum
- Mendoza C** 2018 *atoms* **6** 28 Computation of Atomic Astrophysical Opacities
- Metzger B D** 2017 *Living Rev. Relativ.* **20** 3 Kilonovae
- Migdalek J and Baylis W E** 1979 *Can. J. Phys.* **57** 1708
- Milione G, Sztul H I, Nolan D A and Alfano R R** 2011 *Phys. Rev. Lett.* **107** 053601 Higher-order Poincare sphere, Stokes parameters and the angular momentum of light

- Minneker B, Klas R, Rothhardt J and Fritzsch S** 2023 *Photonics* **10** 24 *Critical Laser intensity of phase-matched high-order harmonic generation in noble gases*
- Mirhosseini M, Magana-Loaiza O S, Chen C, Rafsanjani S M H and Boyd R W** 2016 *Phys. Rev. Lett.* **116** 130402 *Wigner distribution of twisted photons*
- Mitroy J, Safranova M S and Clark C W** 2010 *J. Phys. B* **43** 202001 *Theory and applications of atomic and ionic polarizabilities*
- Müller A, Lindroth E, Bari S, Borovik Jr A, Hillenbrand P-M, Holste K, Indelicato P, Kilcoyne A L D, Klumpp S, Martins M, Viehaus J, Wilhelm P and Schippers S** 2018 *Phys. Rev. A* **98** 033416 *Photoionization of metastable heliumlike C^{4+} ($1s2s\ ^3S_1$) ions: Precision study of intermediate doubly excited states*
- Müller A, Borovik Jr A, Bari S, Buhr T, Holste K, Martins M, Perry-Sassmannshausen A, Phaneuf R A, Reinwardt S, Ricz S, Schubert K and Schippers S** 2018 *Phys. Rev. Lett.* **120** 133202 *Near-K-edge double and triple detachment of the F^- negative ion: Observation of direct two-electron ejection by a single photon*
- Müller A, Borovik Jr A, Buhr T, Hellhund J, Holste K, Kilcoyne A L D, Klumpp S, Martins M, Ricz S, Viehaus J and Schippers S** 2018 *Phys. Rev. A* **97** 013409 *Near-K-edge single, double, and triple photoionization of C^+ ions*
- Müller A, Borovik Jr. A, Buhr T, Hellhund J, Holste K, Kilcoyne A L D, Klumpp S, Martins M, Ricz S, Viehaus J and Schippers S** 2015 *Phys. Rev. Lett.* **114** 013002 *Observation of a four-electron Auger process in near-K-edge photoionization of singly charged carbon ions*
- Müller A, Martins M, Borovik Jr. A, Buhr T, Perry-Sassmannshausen A, Reinwardt S, Trinter F, Schippers S, Fritzsch S and Kheifets A S** 2021 *Phys. Rev. A* .. *The role of L-shell single and double core-hole production and decay in m-fold ($m = 1, 2, \dots, 6$) photoionization of the Ar^+ ion*
- Napoli C, Bromley T R, Cianciaruso M, Piani M, Johnston N and Adesso G** 2016 *Phys. Rev. Lett.* **116** 150502 *Robustness of coherence: an operational and observable measure of quantum coherence*
- Neville A, Sparrow C, Clifford R, Johnston E, Birchall P M, Montanaro A and Laing A** 2017 *Nat. Phys.* **13** 1153 *Classical boson sampling algorithms with superior performance to near-term experiments*
- Noebauer U M and Sim S A** 2019 *Liv. Rev. Comp. Astrophys.* **5** 1 *Monte Carlo radiative transfer*
- Nye J F and Berry M V** 1974 *Proc. R. Soc. London Ser. A* **336** 165 *Dislocations in wave trains*
- Oemrawsingh S S R, Aiello A, Eliel E R, Nienhuis G and Woerdman J P** 2014 *Phys. Rev. Lett.* **92** 217901 *How to observe high-dimensional two-photon entanglement with only two detectors*
- Ong W and Russek A** 1978 *Phys. Rev. A* **17** 120 *Simple asymptotic wave function for a continuum Dirac electron*
- Pan L, Taylor K T and Clark C W** 1988 *Phys. Rev. Lett.* **61** 2673 *Computation of the ac Stark effect in the ground state of atomic hydrogen*
- Papoulias A, Carlsson B G and Ekman J** 2016 *Phys. Rev. A* **94** 042502 *Effect of realistic nuclear charge distributions on isotope shifts and progress towards the extraction of higher-order nuclear radial moments*
- Parpia F, Froese Fischer C and Grant I P** 1996 *Comput. Phys. Commun.* **94** 249 *GRASP92: A package for large-scale relativistic atomic structure calculations*
- Patil S H and Tang K T** 2000 *Asymptotic Methods in Quantum Mechanics* (pringer, Berlin, Heidelberg a o)

16. References

- Pattard T** 2002 *J. Phys.* **B35** L207 *A shape function for single-photon multiple ionization cross sections*
- Paufler W, Birger Böning B and Fritzsche S** 2019 *J. Opt.* **21** 094001 *High harmonic generation with Laguerre-Gaussian beams*
- Paufler W, Birger Böning B and Fritzsche S** 2019 *Phys. Rev.* **A100** 013422 *Coherence control in high-order harmonic generation with Laguerre-Gaussian beams*
- Paufler W, Böning B and Fritzsche S** 2011 *Phys. Rev.* **A98** 011401(R) *Tailored orbital angular momentum in high-order harmonic generation with bicircular Laguerre-Gaussian beams*
- Paufler W, Böning B and Fritzsche S** 2018 *Phys. Rev. A* **97** 043418 *Strong-field ionization with twisted laser pulses*
- Peelle A G, McMahon P J, Paterson D, Tran C Q, Mancuso A P, Nugent K A, Hayes J P, Harvey E, Lai B and McNulty I** 2002 *Opt. Lett.* **27** 1752 *Observation of an x-ray vortex*
- Perego A, Vescovi D, Fiore A, Chiesa L, Vogl C, Benetti S, Bernuzzi S, Branchesi M, Cappellaro M, Cristallo C et al.** 2022 *Astrophys. J.* **925** 22 *Production of very light elements and strontium in the early ejecta of neutron star mergers*
- Picon A, Mompart J, Vaizquez de Aldana J A, Plaja L, Calvo G F and Roso L** 2007 *Opt. Express* **18** 3660 *Photoionization with orbital angular momentum beams*
- Piron R and Blenski T** 2018 *Contr. Plasma Phys.* **58** 30 *Review and potential applications to white-dwarf stars*
- Pisanty E, Machado G J, Vicuna-Hernandez V, Celi A, Torres J P and Lewenstein M** 2019 *Nat. Phot.* **13** 569 *Knotting fractional-order knots with the polarization state of light*
- Porsev S G, Kozlov M G and Reimers D** 2009 *Phys. Rev.* **A79** 032519 *Transition frequency shifts with fine-structure constant variation for Fe I and isotope-shift calculations in Fe I and Fe II*
- Porsev S G and Derevianko A** 2006 *J. Exp. Theo. Phys.* **102** 195 *High-accuracy calculations of dipole, quadrupole and octupole electric-dynamic polarizabilities and van-der-Waals coefficients C_6 , C_8 and C_{10} for alkaline-earth dimers*
- Porsev S G, Rakhlina Y G and Kozlov M G** 1999 *Phys. Rev.* **A60** 2781 *Electric-dipole amplitudes, lifetimes, and polarizabilities of the low-lying levels of atomic ytterbium*
- Post D E and Kendall R P** 2004 *Int. J. HPC Applications* **18** 399 *Software project management and quality engineering practices for complex, coupled ...*
- Potvliege R M** 1998 *Comput. Phys. Commun.* **114** 42 *STRFLO: A program for time-independent calculations of multiphoton processes in one-electron atomic systems: I. Quasi-energy spectra and angular distributions*
- Poynting J H** 1909 *Proc. R. Soc.* **A82** 560 *The wave motion of a revolving shaft, and a suggestion as to the angular momentum in a beam of circularly polarised light*
- Prunty S L** 2014 *Phys. Scr.* **89** 128001 *A primer on the theory of Thomson scattering for high-temperature fusion plasmas*
- Purohit G, Kato D, Murakami I, Dhakar K C, Gupta S and Sinha P** 2021 *Eur. Phys. J.* **D75** 219 *Electron impact single ionization cross sections of W^+*
- Quinteiro G F, Schmidt-Kaler F and Schmiegelow C T** 2017 *Phys. Rev. Lett.* **119** 253203 *Twisted-light-ion interaction: The role of longitud. fields*

- Radhakrishnan C, Parthasarathy M, Jambulingam S and Byrnes T** 2016 *Phys. Rev. Lett.* **116** 150504 *Distribution of quantum coherence in multi-partite systems*
- Radice D, Perego A, Hotokezaka K, Fromm S A, Bernuzzi S and Roberts L F** 1992 *Astrophys. J.* **869** 130 *Binary neutron star mergers: mass ejection, electromagnetic counterparts, and nucleosynthesis*
- Radtke T, Fritzsch S and Surzhikov A** 2006 *Phys. Rev. A* **74** 032709 *Density-matrix formalism for the photoion-electron entanglement in atomic photoionization*
- Ramakrishna S, Hofbrucker J and Fritzsch S** 2022 *Phys. Rev. A* **105** 033103 *Photoexcitation of atoms by cylindrically polarized Laguerre-Gaussian beams*
- Ribic P R, Guathier D and De Ninno G** 2014 *Phys. Rev. Lett.* **112** 203602 *Generation of coherent extreme-ultraviolet radiation carrying orbital angular momentum*
- Roberts B M, Dzuba V A and Flambaum V V** 2014 *Phys. Rev.* **89** 042509 *Strongly enhanced atomic parity violation due to close levels of opposite parity*
- Rohrlich F and Carlson B C** 1954 *Phys. Rev.* **93** 38 *Positron-electron differences in energy loss and multiple scattering*
- Rose M E** 1957 *Elementary theory of angular momentum* (Dover Publications Inc., New York 1995)
- Rosenberg L and Zhou F** 2016 *Phys. Rev. A* **47** 2146 *Generalized Volkov wave functions: Application to laser-assisted scattering*
- Rothhardt J, Hädrich S, Demmler S, Krebs M, Fritzsch S, Limpert J and Tünnermann A** 2014 *Phys. Rev. Lett.* **112** 233002 *Enhancing the macroscopic yield of narrow-band high-order harmonic generation by Fano resonances*
- Rose S J, van Hoof P M M, Jonauskas V, Keenan F P, Kisielius R, Ramsbottom C, Foord M E, Heeter R F and Springer P T** 1992 *J. Phys.* **37** L337 *Calculation of photoionized plasmas with an average-atom model*
- Rotenberg M, Bivins R, Metropolis N, and Wooten J K jr** 1959 *The 3-j and 6-j symbols* (The Technology Press Cambridge Massachusetts)
- Rozenbaum E B, Glazov D A, Shabaev V M, Sosnova K E and Telnov D A** 2014 *Phys. Rev. A* **89** 012514 *Dual-kinetic-balance approach to the Dirac equation for axially symmetric systems: Application to static and time-dependent fields*
- Rudzikas Z** 1997 *Theoretical Atomic Spectroscopy* (Cambridge University Press, Cambridge)
- Safranova M S, Porsev S G, Sanner C and Ye J** 2018 *Phys. Rev. Lett.* **120** 173001 *Two clock transitions in neutral Yb for the highest sensitivity to variations of the fine-structure constant*
- Saha B and Fritzsch S** 2006 *Phys. Rev. E* **73** 036405 *Be I isoelectronic ions embedded in hot plasma*
- Saha B and Fritzsch S** 2007 *J. Phys. B* **40** 259 *Influence of dense plasma on the low-lying transitions in Be-like ions: relativistic multiconfiguration Dirac-Fock calculation*
- Saha S and Jos J** 2020 *Int. J. Quant. Chem.* **120** 22 *Shannon entropy as a predictor of avoided crossing in confined atoms*
- Salvat F, Jablonski A and Powell C J** 2005 *Comp. Phys. Commun.* **165** 157 *ELSEPA – Dirac partial-wave calculation of elastic scattering of electrons and positrons by atoms, positive ions and molecules*
- Salvat F, Llosa J, Lallena A M and Almansa J** 2022 *Comp. Phys. Commun.* **277** 108368 *ECCPA: Calculation of classical and quantum cross sections*

16. References

- for elastic collisions of charged particles with atoms
- Sanchez-Lengeling B and Aspuru-Guzik A** 2018 *Science* **361** 360 *Inverse molecular design using machine learning: Generative models for matter engineering*
- Sapirstein** 1987 *Phys. Scr.* **36** 801 *Quantum-electrodynamics of many-electron atoms*
- Sasaki S and McNulty I** 2008 *Phys. Rev. Lett.* **100** 124801 *Proposal for generating brilliant x-ray beams carrying orbital angular momentum*
- Sato T and Ishikawa K L** 2013 *Phys. Rev. A* **88** 023402 *Time-dependent complete-active-space self-consistent-field method for multielectron dynamics in intense laser fields*
- Schauß P, Cheneau M, Endres M, Fukuhara T, Hild S, Omran A, Pohl T, Gross C, Kuhr S and Bloch I** 2012 *Nature* **491** 87 *Observation of spatially ordered structures in a two-dimensional Rydberg gas*
- Schippers S** 2018 *J. Quant. Spec. Rad. Transf.* **219** 33 *Analytical expression for the convolution of a Fano line profile with a Gaussian*
- Schippers S, Bartsch T, Brandau C, Müller A, Gwinner G, Wissler G, Beutelspacher M, Grieser M, Wolf A and Phaneuf R A** 2000 *Phys. Rev. A* **62** 022708 *Dielectronic recombination of lithiumlike Ni^{25+} ions: High-resolution rate coefficients and influence of external crossed electric and magnetic fields*
- Schippers S, Martins M, Beerwerth R, Bari S, Holste K, Schubert K, Viefhaus J, Savin D W, Fritzsche S and Müller A** 2017 *Astrophys. J.* **849** 5 *Near L-edge single and multiple photoionization of singly charged iron ions*
- Schippers S, Beerwerth S, Bari S, Buhr T, Holste K, Kilcoyne A L D, Perry-Saßmannshausen A, Phaneuf R A, Reinhardt S, Savin D W, Schubert K, Fritzsche S, Martins M and Müller A** 2020 *Astrophys. J.* ... *Near L-edge single and multiple photoionization of doubly charged iron ions*
- Schollwöck U** 2011 *Ann. Phys.* **326** 96 *The density-matrix renormalization group in the age of matrix product states*
- Scholz-Marggraf H M, Fritzsche S, Serbo V G, Afanasev A and Surzhykov A** 2014 *Phys. Rev. A* **90** 013425 *Absorption of twisted light by hydrogen-like atoms*
- Schütt K T, Glaweh, Brockherde F, Sanna A, Müüller K R and Gross E K U** 2014 *Phys. Rev. B* **89** 205118 *How to represent crystal structures for machine learning: Towards fast prediction of electronic properties*
- Seipt D, Müller R A, Surzhykov A and Fritzsche S** 2016 *Phys. Rev. A* **94** 053420 *Two-color above-threshold ionization of atoms and ions in XUV Bessel beams and intense laser light*
- Shabaev V M, Tupitsyn I I, Yerokhin V A, Plunien G and Soff G** 2004 *Phys. Rev. Lett.* **93** 130405 *Dual kinetic balance approach to basis-set expansions for the Dirac equation*
- Shabaev V M, Tupitsyn I I and Yerokhin V A** 2013 *Phys. Rev. A* **88** 012513 *Model operator approach to the Lamb shift calculations in relativistic many-electron atoms*
- Sharma L, Surzhykov A, Inal M K and Fritzsche S** 2010 *Phys. Rev. A* **81** 023419 *Polarization transfer in the inner-shell photoionization of sodiumlike ions*
- Sharma L, Surzhykov A, Srivastava R and Fritzsche S** 2011 *Phys. Rev. A* **83** 062701 *Electron-impact excitation of singly charged metal ions*

- Sheil J, Versolato O O, Neukirch A J and Colgan J** 2021 *J. Phys. B* **54** 035002 *Multiply-excited states and their contribution to opacity in CO₂ laser-driven tin-plasma conditions*
- Shen Y, Campbell G T, Hage B, Zou H, Buchler B C and Shen P K L et al.** 2013 *J. Opt.* **15** 044005 *Generation and interferometric analysis of high charge optical vortices*
- Simon A, Warczak A, ElKafrawy T and Tanis J A** 2010 *Phys. Rev. Lett.* **104** 123001 *Radiative double electron capture in collisions of O⁸⁺ ions with carbon*
- Skoromnik O D, Feranchuk I D, Leonau A U and Keitel C H** 2017 *J. Phys. B* **50** 245007 *Analytic model of a multi-electron atom*
- Smith D Y** 1987 *Phys. Rev. A* **35** 3381 *Anomalous x-ray scattering: Relativistic effects in x-ray dispersion analysis*
- Stambulchik E and Maron Y** 2008 *J. Phys. B* **41** 095703 *Stark effect of high-*n* hydrogen-like transitions: quasi-contiguous approximation*
- Stone N J** 2005 *Atomic Data and Nuclear Data Tables* **90** 175 *Table of nuclear magnetic dipole and electric quadrupole moments*
- Sukhov S and Dogariu A** 2010 *Opt. Lett.* **35** 3847 *On the concept of “tractor beams”*
- Sukhov S and Dogariu A** 2011 *Phys. Rev. Lett.* **107** 203602 *Negative nonconservative forces: optical “tractor beams” for arbitrary objects*
- Surzhykov A, Radtke T, Indelicato P and Fritzsche S** 2009 *Eur. J. Phys. Spec. Topics* **169** 129 *Photon polarization in the two-photon decay of heavy hydrogen-like ions*
- Surzhykov A, Volotka A, Fratini F, Santos J P, Indelicato P, Plunien G, Stoohlker and Fritzsche S** 2008 *Phys. Rev. A* **81** 042510 *Angular correlations in the two-photon decay of heliumlike heavy ions*
- Surzhykov A, Jentschura U D, Stöhlker T and Fritzsche S** 2006 *Phys. Rev. A* **73** 032716 *Radiative electron capture into high-*Z* few-electron ions: Alignment of the excited ionic states*
- Surzhykov A, Seipt D and Fritzsche S** 2016 *Phys. Rev. A* **94** 033420 *Probing the energy flow in Bessel light beams using atomic photoionization*
- Surzhykov A, Indelicato P, Santos J P, Amaro P and Fritzsche S** 2011 *Phys. Rev. A* **84** 022511 *Two-photon absorption of few-electron heavy ions*
- Tagirov R V, Shapiro A I and Schmutz W** 2017 *A&A* **603** A27 *NESSY: NLTE spectral synthesis code for solar and stellar atmospheres*
- Tanaka M, Kato D, Gaigalas G, Rynkun P, Radziute L, Wanajo S, Sekiguchi Y, Nakamura N, Tanuma H, Murakami I and Sakaue H A** 2018 *Astrophys. J.* **852** 109 *Properties of kilonovae from dynamical and post-merger ejecta of neutron star mergers*
- Tanaka M, Kato D, Gaigalas G and Kawaguchi K** 2020 *Astrophys. J.* ?? xxx *Systematic Opacity Calculations for Kilonovae*
- Tchang-Brillet W L, Wyart J-F, Meftah A and Mammar S A** 2018 *atoms* **6** 52 *Parametric calculations of radiative decay rates for magnetic dipole and electric quadrupole transitions in Tm IV, Yb V, and Er IV*
- Tong X M and Lin C D** 2005 *J. Phys. B* **38** 2593 *Empirical formula for static field ionization rates of ionization of atoms and molecules by lasers in the barrier-suppression regime*
- Torres and Torner (eds)** 2011 *Twisted photons* (Wiley-VCH, Weinheim)
- Torres J P, Alexandrescu A and Torner L** 2003 *Phys. Rev. A* **68** 050503 *Quantum spiral bandwidth of entangled two-photon states*
- Torretti F, Sheil J, Schupp R, Basko M M, Bayraktar M, Meijer R A, Witte S, Ubachs W, Hoekstra R, Versolato O O, Neukirch A J and Colgan J** 2020 *Nature Commun.* **11** 2334 *Prominent radiative contributions from multiply-excited states in laser-produced tin plasma for nanolithography*

16. References

- Trzhaskovskaya M B, Nikulin V K and Clark R E H** 2010 *At. Data Nucl. Data Tables* **96** 1 *Radiative recombination rate coefficients for highly-charged tungsten ions*
- Tupitsyn I I, Shabaev V M, Lopez-Urrutia J R C, Draganic I, Orts R S and Ullrich J** 2003 *Phys. Rev. A* **68** 022511 *Relativistic calculations of isotope shifts in highly charged ions*
- Tupitsyn I I, Kozlov M G, Safranova M S, Shabaev V M and Dzuba V A** 2016 *Phys. Rev. Lett.* **117** 253001 *Quantum electro-dynamical shifts in multivalent heavy ions*
- Uchida M and Tonomura A** 2010 *Nature* **467** 737 *Generation of electron beams carrying orbital angular momentum*
- Vaeck N, Hansen J E, Palmeri P, Quinet P, Zitane N, Godefroid M, Fritzsche S and Kylstra N** 2001 *Phys. Scr. T95* 68 *Hollow atoms: A theoretical challenge*
- van Veenendaal M and McNulty I** 2007 *Phys. Rev. Lett.* **98** 157401 *Prediction of strong dichroism induced by x rays carrying orbital momentum*
- Varshalovich D A, Moskalev A N, Khersonskii V K** 1988 *Quantum Theory of Angular Momentum* (World Scientific Singapore a.o.)
- Verbeeck J, Tian H and Schattschneider P** 2010 *Nature* **467** 301 *Production and application of electron vortex beams*
- Verner D A and Ferland G J** 1996 *Astrophys. J. Suppl. Series* **103** 467 *Atomic data for astrophysics. I. Radiative recombination rates for H-like, He-like, Li-like and Na-like ions over a broad range of temperature*
- Verner D A, Yakovlev D G, Band I M and Trzhaskovskaya M B** 1993 *At. Data Nucl. Data Tables* **55** 233 *Subshell photoionization cross sections and ionization energies of atoms and ions from He to Zn*
- Viehhaus J, Cvejanovic S, Langer B, Lischke T, Prümper J, Rolles D, Golovin A V, Grum-Grzhimailo A N, Kabachnik N M and Becker U** 2004 *Phys. Rev. Lett.* **92** 083001 *Energy and angular distributions of electrons emitted by direct double Auger decay*
- Voloch-Bloch N, Lereah Y, Lilach Y, Gover A and Arie A** 2013 *Nature* **494** 331 *Generation of Electron Airy Beams*
- Volotka A V, Hofbrucker J and Fritzsche S** 2022 *Phys. Rev. A* **104** L031103 *Steering of circular dichroism in biharmonic ionization of atoms*
- Volotka A V, Bilal M, Beerwerth R, Ma X, Stöhlker T and Fritzsche S** 2019 *Phys. Rev. A* **100** 010502(R) *QED radiative corrections to the ${}^2P_{1/2} - {}^2P_{3/2}$ fine structure in fluorinelike ions*
- Volotka A V, Yerokhin V A, Surzhykov A, Stöhlker T and Fritzsche S** 2016 *Phys. Rev. A* **93** 023418 *Many-electron effects on x-ray Rayleigh scattering by highly charged He-like ions*
- Volotka A V, Surzhykov A, Trotsenko S, Plunien G, Stöhlker T and Fritzsche S** 2016 *Phys. Rev. Lett.* **117** 243001 *Nuclear excitation by two-photon electron transition*
- Volotka A V, Surzhykov A and Fritzsche S** 2020 *Phys. Rev. A* **102** 042814 *Rayleigh scattering of linearly polarized light: Scenario of the complete experiment*
- von der Wense, Seiferle B, Stellmer S, Weitenberg J, Kazakov G, Palfy A and Thirolf P G** 2017 *Phys. Rev. Lett.* **119** 132503 *A laser excitation scheme for ${}^{229m}\text{Th}$*
- Vriens L and Smeets A H M** 1980 *Phys. Rev. A* **22** 940 *Cross-section and rate formulas for electron-impact ionization, excitation, deexcitation and total depopulation of excited atoms*

- Walborn S P, Monken C H, Padua S and Souto Ribeiro P H** 2010 *Phys. Reports* **495** 87 *Spatial correlations in parametric down-conversion*
- Wanajo S, Sekiguchi Y, Nishimura N, Kiuchi K, Kyutoku K and Shibata M** 2014 *Astrophys. J.* **789** L39 *Production of all the r-process nuclides in the dynamical ejecta of neutron star mergers*
- Weber F, Düllmann C E, Gadelshin V, Kneip N, Oberstedt S, Raeder S, Runke J, Mokry C, Thörle-Pospiech P, Studer D, Trautmann and Wendt K** 2022 *Atoms* **10** 51 *Probing the atomic structure of californium by resonance ionization spectroscopy*
- Welte S, Hacker B, Daiss S, Ritter S and Rempe G** 2018 *Phys. Rev. X* **8** 011018 *Photon-mediated quantum gate between two neutral atoms in an optical cavity*
- White A G, Mitchell J R, Nairz O and Kwiat P G** 1998 *Phys. Rev. A* **58** 605 *“Interaction-free” imaging*
- Wouters S and Van Neck D** 2014 *Eur. Phys. J.* **68** 272 *The density matrix renormalization group for ab initio quantum chemistry*
- Wu Z W, Tian Z Q, Jiang J, Dong C Z and Fritzsch S** 2020 *Phys. Rev. A* **102** 042813 *Hyperfine-induced effects on angular emission of the magnetic-quadrupole line $1s2p_{3/2}$ $^3P_2 \rightarrow 1s^2$ 1S_0 following electron-impact excitation of Tl^{79+} ions*
- Wu Z Y, Ricigliano G, Kashyap R, Perego A and Radice D** 2022 *Monthly Notes Roy. Astrophys. Soc.* **512** 328 *Radiation hydrodynamics modelling of kilonovae with SNEC*
- Wustelt P, Möller M, Rathje T, Sayler A M, Stöhlker T and Paulus G G** 2015 *Phys. Rev. A* **91** 031401(R) *Momentum-resolved study of the saturation intensity in multiple ionization*
- Xu Y Q, Qu Y-Z, Zhang X-H and Li J-M** 2000 *Phys. Rev. A* **62** 022715 *Theoretical study of dielectronic recombination between electrons and heliumlike carbon ions*
- Xu W, Xu C X, Zhang R T, Zhu X L, Feng W T, Gu L, Liang G Y, Guo D L, Gao Y, Zhao D M, Zhang S F, Su M G and Ma X** 2021 *Astrophys. J. Suppl. Series* **57** 1708 *Measurement of n-resolved state-selective charge exchange in $Ne^{(8,9)+}$ collision with He and H_2*
- Yan W, Fruhling C, Golovin G, Haden D, Luo J, Zhang P, Zhao B-Z, Zhang J, Liu C, Chen M, Chen S, Banerjee S and Umstadter D** 2017 *Nature Phys.* **11** 514 *High-order multiphoton Thomson scattering*
- Yao A M and Padgett M J** 2011 *Adv. Opt. Photon.* **3** 161 *Orbital angular momentum: origins, behavior and applications*
- Yao K, Geng Z, Xiao J, Yang Y, Chen C, Fu Y, Lu D, Hutton R and Zou Y** 2010 *Phys. Rev. A* **81** 022714 *KLL dielectronic recombination resonant strengths of He-like up to O-like xenon ions*
- Yerokhin V A and Surzhykov A** 2011 *Phys. Rev. A* **84** 032703 *Relativistic theory of the double photoionization of heliumlike atoms*
- Ying B, Machalett F, Huth V, Kübel M, Sayler A M, Stöhlker T, Paulus G G and Wustelt P** 2021 *J. Phys. B* **54** 174002 *Experimental study of the laser-induced ionization of heavy metal and metalloid ions: Au^+ and Si^{2+} in intense and sculpted femtosecond laser fields*
- Yip F L, Rescigno T N, McCurdy C W and Martin F** 2013 *Phys. Rev. Lett.* **110** 173001 *Fully differential single-photon double ionization of neon and argon*
- Yudin V Y, Taichenachev A V and Derevianko A** 2014 *Phys. Rev. Lett.* **113** 233003 *Magnetic-dipole transitions in highly charged ions as a basis of ultraprecise optical clocks*
- Yutsis A P, Levinson I B und Vanagas V V** 1962 *Mathematical apparatus of the theory of angular momentum.* Israel Program for Scientific Translation,

16. References

- Jerusalem 1962
- Zaitsevskii A V und Heully J-L** 1992 *J. Phys.* **B25** 603 *Rayleigh-Schrödinger QDPT for hermitian intermediate Hamiltonians by the shift technique*
- Zambrini R and Barnett S** 2006 *Phys. Rev. Lett.* **96** 113901 *Quasi-intrinsic angular momentum and the measurement of its spectrum*
- Zarrabian S, Laidig W D und Bartlett R J** 1990 *Phys. Rev. A* **41** 4711 *Convergence properties of multireference many-body perturbation theory*
- Zatsarinsky O** 2020 <https://github.com/zatsaroi> (unpublished) *A compilation of atomic code for bound-state and R-matrix computations*
- Zaytsev V A, Volotka A V, Yu D, Fritzsche S, Ma X, Hu H and Shabaev V M** 2019 *Phys. Rev. Lett.* **123** 093401 *Ab initio QED treatment of the two-photon annihilation of positrons with bound electrons*
- Zhan Q W** 2009 *Adv. Opt. Photon.* **1** 1 *Cylindrical vector beams: from mathematical concepts to applications*
- Zhang H L, Sampson D H and Mohanty A K** 1989 *Phys. Rev. A* **40** 616 *Fully relativistic and quasirelativistic distorted-wave methods for calculating collision strengths for highly charged ions*
- Zhang J T and Guo D S** 2013 *Phys. Rev. Lett.* **110** 063002 *Spectral minimum and giant enhancement in photoelectron spectra from xenon atoms driven by intense midinfrared laser fields*
- Zhong H-S, Wang H, Deng Y-H, Chen M-C, Peng L-C, Luo Y-H, Qin J, Wu D, Ding X, Hu Y et al.** 2020 *Science* **370** 1460 *Quantum computational advantage using photons*
- Zhong H-S, Deng Y-H, Qin J, Wang H, Chen M C, Peng L C, Luo Y H, Wu D, Gong S Q, Su H, Hu Y, Hu P et al.** 2021 *Phys. Rev. Lett.* **127** 180502 *Phase-programmable gaussian boson sampling using stimulated squeezed light*
- Zhu X-M and Pu Y-K** 2010 *J. Phys.* **D43** 015204 *A simple collisional-radiative model for low-temperature argon discharges with pressure ranging from 1 Pa to atmospheric pressure: kinetics of Paschen 1s and 2p levels*
- Ziegler J F** 1999 *J. Appl. Phys.* **85** 1249 *Stopping of energetic light ions in elemental matter*

Index

α variation, 278
 differential sensitivity, 278
 enhancement, 278
JAC
 implementation, 43
absorption
 bichromatic, two-photon, 443
 monochromatic two-photon, 441
 photo, 463
addition theorem
 Legendre polynomials, 71
affinity
 positron, 492
algorithm
 PEA, 190
alignment
 Coulomb excitation, 478
amplitude
 absorption, 233
 anapole moment, 229
 dipole \mathbb{D} , 223
 emission, 233
 form factor, 226
 Hamiltonian, 130
 magnetic-quadrupole-moment, 231

many-electron, 130
 absorption, 215
 emission, 215
momentum transfer, 226
multipole, 371
multipole transition, 215, 233
parity violation, 232
PNC, 227
raditive, 233
reduced, 130
scalar-pseudo-scalar, 229
Schiff moment, 228
strong-field, a_o , 217
tensor-pseudo-tensor, 230
time-dependent dipole, 652
ansatz
 Floquet, 621
 generalized Floquet, 621
approach
 SAE, 662
 static field, 500
 TDSE, 662
approximation
 resonant-scattering, 210
approximation

hypernetted-chain, 350
isolated resonance, 498
saddle-point, 653
astrophysical mission
 Chandra, 533
 Cires, 532
 Giano, 532
 Sofia, 532
 XMM, 533
atomic
 density operator, 134
 partition function, 320
atomic cascade
 yields, 272
atomic clock, 275, 278
 nuclear, 317
 thorium, 317
 ytterbium, 317
atomic clocks
 optical, 319
 precision, 319
atomic state
 density operator, 95
 function, 95
atomic state function, 155

- Auger
 - anisotropy parameter, 411
 - positron-induced, 492
- autoionization
 - Auger, 408
 - inter-coulombic, 502
 - sequential double, 493
- background
 - cosmic microwave, 304
- beam
 - cylindrical vector, 742
 - light filament, 741
 - Poincare vector, 743
 - spatial soliton, 741
 - vector, 741
- beams
 - Ince-Gaussian, 731
- binary peak, 592
- bremsstrahlung, 487
 - inverse, 488
- Brillouin theorem, 163
- capture
 - inter-coulombic, 502
 - non-radiative, 503
- CAS, 163
- cascade
 - approach, 565
 - implemented, 571, 576
 - simulation, 565
- channel
 - Green function, 157
- charge
 - nuclear distribution, 86
- chirality
 - optical, 717
- CI, 151
- code
 - ARC, 52
 - ATOMDB, 515
 - AUTOSTRUCTURE, 51, 340
 - BSR, 49
 - CRMODEL, 519
 - CATS, 44, 340
 - CLOUDY, 516
 - DIAPHANE, 538
 - ECCPA, 48
 - ELSEPA, 48
 - FAC, 50, 517
 - FLYCHK, 516
 - GALAXY, 516
 - GEANT4, 48
 - GRASP, 45
 - HULLAC, 47
 - LADW, 46
 - LASER, 46, 51
 - LTE, 516
 - MCDFME, 45
 - MOOG, 517
 - MUONIC ATOMIC CASCADE, 44
 - PHICRE, 519
 - PYSCF, 52
 - QEDMOD, 52
 - QUANTICS, 53
 - RATIP, 47
- RCF, 517
- RMATRX, 46
- SRIM, 704
- STRAWBERRY FIELDS, 193
- SUPERSTRUCTURE, 51
- TARDIS, 518
- XSTAR, 518
- TRECX, 50
- Cowan, 375
- coefficient
 - absorption, 463
 - Einstein A, B, 464
 - emission, 463
 - spin-angular, 154
- coefficient of fractional parentage, 110, 112
- coefficient of fractional parentage; completely reduced, 112
- collision strength, 459
- computation
 - atomic amplitudes, 28, 36
 - atomic cascades, 29
 - atomic descriptors, 30
 - atomic processes, 28, 38
 - atomic properties, 28, 37
 - atomic responses, 29
 - CI, 151
 - configuration interaction, 151
 - interactive, 29
 - overview, 36
 - SCF, 151
 - semi-empirical, 30
 - symbolic simplifications, 29
 - time-evolutions, 29

condition

adiabatic tunneling, 586

configuration

electron, 31

configuration interaction, 151

convergent close-coupling, 49

conversion internal, 481

coordinates

elliptical, 731

correlation

methods, 151

strong, static, 151

weak, dynamic, 151

correlation function

electron-ion, 351

CP-violation, 232

crystal

energy

Gordon-Kim, 322

Löwdin, 322

crystal field, 311

d-shell, 163

dark matter, 278

database

ASTAR, 515

CHIANTI, 514

DREAM, 514

ESTAR, 514

PSTAR, 515

VALD, 340

XCOM, 515

TOPbase, 339

decay

double-Auger, 451

inter-coulombic, 502

multi-photon, 440

radiative-Auger, 455

two-photon, 450

density

level population, 618

descriptor

Coulomb matrix, 682

feature matrix, 684

Galvez matrix, 682

latent vector space, 678

material science, 686

molecular, 682

molecular fragment, 685

property-labelled atomic fragments, 670

types of molecular, 682

Voronoi cell, 686

dielectric constant, 297

diffraction

Frauenhofer, 609

Dirac orbital

matrix elements, 68

dispersion coefficient, 305

distance

equilibrium internuclear, 322

distribution

charge state, 498

electron density, 259

radial density, 263

velocity, 504

distribution function

Thomas-Fermi, 106

Doppler shift, 315

EDM, 232

atomic, 142

enhancement factor, 232

effect

static Stark, 284

electron beam

in magnetic field, 750

vortex, 750

electron capture

vacuum, 505

electron density

relaxation, 151

electron distribution

Maxwell-Boltzmann, 270

electron gas, 281, 350

electron rearrangement, 163

electron relaxation, 163

element

tungsten, 347

elements

lanthanides, 348

emission

stimulated x-ray, 553

two-photon, 447

energy

configuration-averaged, 562

Dirac, 59

dissociation, 322

energy density

spectral, 335

- total, 335
- energy shift
 - black-body radiation, 304
- entropy
 - Renyi, 280
 - Shannon information, 280
 - sub-additivity, 264
 - von Neumann, 261, 264
- equation
 - paraxial wave, 752
 - scalar Helmholtz, 710
 - Schrödinger
 - complex eigenvalues, 152
 - Volterra integral, 663
- equation-of-state, 355
- equilibrium
 - hydrostatic, 346
 - radiative, 346
 - statistical, 346
- excitation
 - Coulomb, 469
 - alignment, 478
 - electron-impact, 457
 - & autoionization, 480
 - multi-photon, 440
 - nuclear, 496
 - photo, 378
 - excitation & autoionization, 427
 - fluorescence, 424
- expansion
 - multipole with two vectors $\mathbf{r}, \mathbf{r}' \ll R$, 70
- experiment
 - high-precision, 137
- f-shell, 163
- Fano
 - profile, 310
- FEL
 - HGHG, 553
 - SASE, 553
- field ionization, 691
 - weak electric field, 691
- fine-structure constant
 - variation of, 278, 319
- force
 - optical, 746
- form factor
 - atomic, 253, 274
 - generalized, 274
 - nucleus, 87
 - standard, 253
 - uniform, 87
 - x-ray, 254
- formalism
 - quasi-spin, 110
- formula
 - Bohr, stopping power, 705
 - Kubo-Greenwood, 334
 - Stewart-Pyatt, 265
- free electron
 - partial wave, 69
- Friedel oscillations, 350
- function
 - dielectric, complex, 353
 - electron localization, 281
 - ELF, 281
 - line-shape, 463
- Sherman, 501
- Voigt, 149
- window, experiment, 145
- gamma-ray burst, 525
- gamma-ray bursts (GRB), 532
- GOS, 495
- graph
 - molecular, 680
- Green function
 - approximate, 157
- Greens funtion
 - Coulomb, relativistic, 66
- groadening
 - Stark, 706
- Hamiltonian
 - Dirac-Coulomb, 153, 163
 - Dirac-Coulomb-Breit, 153, 163
 - electric-quadrupole, 283
 - EQM, 283
 - hyperfine, 236
 - Landau, 752
 - magnetic-quadrupole-moment, 231
 - matrix, 153
 - P-odd, T-odd, 229
 - scalar-pseudo-scalar, 229
 - tensor-pseudo-tensor, 230
 - Hamiltonian $\mathbb{H}^{(BBR)}$
 - black-body radiation, 304
 - Hartree-Fock, 163
 - Helmholtz equation, 709
 - paraxial approximation, 710

HHG, 595
 atomic target, 601
 coherence length, 610
 cut-off, 595
 dipole phase, 601
 from solids, 600
 Lewenstein's model, 608
 phase matching, 611
 phase-matching, 600
 power spectrum, 654
 selection rules, 601
 trajectories, 655
 high harmonics
 far-field amplitude, 609
 high-order, 596
 near-field amplitude, 609
 plateau, 595
 high-harmonic generation, 595
 hydrogen
 molecular, 188
 hyperfine
 IJF coupled basis, 238
 induced, 464
 parameter, 234
 hypernetted chain approximation, 350
 hypernetted-chain approximation
 quantal, 349
 integral
 spin-angular, 154
 intensity
 spectral, 335
 interaction

Lennard-Jones, 321
 orbital, 261
 van-der-Waals, 321
 interaction potential
 atom-atom, 322
 cold temperatures, 321
 ion-atom, 322
 interference
 two-pathway, 490
 internal conversion
 coefficient, 484
 electronic amplitude, 483
 ionization
 above-threshold, 585, 613
 associative, 549
 chemi-, 549
 Coulomb, 487
 double
 multi-photon, 481
 electron-impact, 461, 498
 frustrated tunnel, 585
 HATI, 585
 LIED, 587
 multi-photon, 466, 489, 585
 multiple, 498
 non-sequential, 585
 non-sequential double, 616
 Penning, 549
 photo, 386
 autoionization, 479
 fluorescence, 478
 REC, 396
 two-color, 489
 two-photon
 non-resonant, 489
 resonant, 489
 ionizatiton
 over-the-barrier, 587
 isotope-shift
 M, F, 241
 parameter, 241
 Julia
 promises, 39
 K-matrix, 163
 Keldysh parameter, 584
 King plot
 nonlinear, 248
 Lande
 g_F , 252
 g_J , 249, 252
 Legendre polynomials
 addition theorem, 71
 LG beam
 product, 731
 lifetime
 radiative, 233
 light
 free-space propagation, 709
 Helmholtz equation, 709
 light beam, 719
 Airy, 740
 Bessel, 734
 Bessel-Gauss, 733
 characterization, 722

- Gaussian, 719
- generation, 724
- generation of vortex beams, 724
- Hermite-Gaussian, 728
- historical remarks, 719
- Ince-Gauss, 731
- Laguerre-Gauss, 729
- lattices of, 740
- necklace ring, 740
- topological charge, 721
- tractor, 743
- vector, 741
- vortex, 721
 - with non-integer OAM, 740
- light beam application, 747
- light beam generation
 - by cylindrical mode converters, 726
 - by helical undulators, 726
 - by spatial light modulators, 725
 - by spiral phase plates, 724
 - by a q-plate, 725
 - by pitch-fork holograms, 724
- light beam manipulation
 - by Mach-Zehnder interferometers, 727
- light pulse
 - atto-second trains, 589
 - bicircular, 589
 - carrier-envelope phase, 588
 - few-cycle, 588
- light scattering
 - Brillouin, 558
 - Compton, 432
 - Dellbrück, 438
- elastic, 438
- Rayleigh, 432, 437
 - amplitude, 434
 - cross section, 436
 - photon density matrix, 437
 - polarization, 437
- stimulated Compton, 439
- line profile
 - Gaussian, 145
 - Voigt, 145
- line-shape, 463
- machine learning, 669, 674
 - autoencoder, 678
 - descriptor, 670
 - feature selection, 670
 - goals, 669
 - inverse design, 685
 - loss function, 669
 - methods, 669
 - reinforcement, 674
 - structure maps, 685
 - supervised, 674, 676
 - text mining, 687
 - unsupervised, 674
- machine learning method
 - kernel ridge regression, 676
 - kernel-based, 676
- magnon, 558
- many-electron
 - density operator, 95
 - statistical tensor, 95
- Material Genome Initiative, 684
- matrix elements
 - $\mathbb{C}^{(K)}$, 68
- matter
 - equation of state, 350
 - warm-dense, 350
- MCDHF, 163
- mean free path
 - photon, 335
- measure
 - information, 280
 - quantum similarity, 320
- mesh
 - logarithmic, 72
 - logarithmic-linear, 72
 - radial, 72
- method
 - block Lanczos, 195
 - CI
 - heat-bath, 681
 - Floquet, 584
 - for HH computations, 608
 - Hartree-Fock, 281
 - Lanczos, 183, 195
 - R-matrix, 661
 - space partition, 661
 - SPAM, 663
 - TD-CASSCF, 662, 663
 - TDCIS, 626
 - time-dependent Hartree-Fock, 660
 - time-dependent MCHF, 662
 - time-dependent RAS, 661
 - time-dependent Schrödinger equation, 660
- model

- classical over-the-barrier, 559
- average-atom, 351
 - radial potential, 351
- collisional-radiative, 618
- deflagration, 545
- Gordon-Kim, 324
- Lberman, 355
- nuclear, 86
- quantitative rescattering, 617
- simple man's, 584
- three-step, 584
- moment
 - time-dependent dipole, 654
- momentum transfer, 254
- momentum transfer variable, 254
- Multi-configuration Dirac-Fock, 163
- NCDR, 501
- noise measurement, 712
- notations
 - atomic resonance, 34
 - multipole, 33
 - scattering state, 34
 - shell & subshell, 31
- NRC, 503
- nuclear dynamics, 659
- nuclear model
 - uniform, 87
- nuclear moment
 - anapole, 140
- nuclei
 - active galactic (AGN), 532
- nucleus
- central depression, 89
- folding model, 89
- Helm model, 89
- modified Helm model, 89
- opacity
 - Planck mean, 337
 - radiative, 333
 - Rosseland mean, 337
- open-shell, 163
- operator
 - (em) multipole, 223, 224
- optical depth, 335
- optical phasor
 - seelight beam application, 748
- optical tweezer
 - seelight beam application, 747
- orbital
 - natural, 259
- oscillator strength, 233, 372
 - generalized, 274, 495
- oxygen, 535
- pair annihilation
 - positron-bound-electron, 506
- pair correlation function
 - ion-electron, 351
- pair production, 507
 - intense laser, 508
- parity non-conservation, 227
- partition function, 320
- phase
 - Volkov, 653
- photoionization
 - double, 452
 - time-resolved, 392
 - ultra-short pulses, 625
 - Wigner time, 392
- photon
 - mean free path, 335
- photon emission
 - DR, 422
- photorecombination
 - statistical tensor, 399
- plane-wave
 - electric field, 199
 - standing, 199
- plasma
 - atomic, 421
 - average-atom population, 342
 - collisional-radiative, 619
 - cosmic, 421
 - diagnostics, 266
 - energy shift, 265
 - ion distribution, 342
 - ion-sphere model, 265
 - level population, 342
 - luminosity, 534
 - magnetized, 540
 - opacity, 334
 - oscillating fields, 270
 - pressure ionization, 350
 - properties, 334
 - radial distribution function, 349
 - radiation flux, 534
 - screening

- non-linear, 350
- static structure factor, 349
- transport model, 618
- Wigner-Seitz cell, 351
- plasma diagnostics
 - interferogram, 345
- plasma model
 - Debye-Hückel, 265–267
 - Ecker-Kröll, 266
 - Gordon-Kim theory, 271
 - ion-sphere, 270
 - Stewart-Pyatt, 266
- PNC, 232
 - I* dependent, 140
 - I* independent, 139
 - non-diagonal, 232
- polarimetry
 - Compton, 437
- polarizability, 295
 - dynamic, 275
 - dynamical, 292
 - electric-dipole, 275
 - multipole, 275
 - reduced tensorial, 292
 - static, 275
- polarization
 - circular, 210
 - elliptical, 202
 - linear, 210
 - topology of, 743
 - vector, 210
- polarization distribution, 743
- polarization ellipse
- eccentricity, 199
- polarization profile, 743
- polarization radiation, 744
- polynomial
 - Ince, 731
- pontential
 - double-well, 102
- positron, 492
- potential
 - atomic, 100
 - core-Hartree, 100
 - core-polarization, 101
 - Dirac-Fock-Slater, 101
 - extended-Hartree, 103
 - Gordon-Kim, 324
 - Greens, 104
 - Hartree, 101
 - Hartree-Slater, 101
 - ionization, 584
 - Kohn-Sham, 101
 - local exhange, 500
 - modified-Tietz, 103
 - multipole, 212
 - Norcross, 104
 - ponderomotive, 584
 - Tietz, 103
 - Uehling, 117, 118
 - Wichmann-Kroll, 117, 118
- principle
 - probe-before-destroy, 554
- probability
 - single ionization, 466
- process
- atomic
 - implemented, 371
 - two-electron single-Auger (TESA), 412
- pulse
 - high-intensity, 216
 - intensity, 218, 219
 - optical cycle, 217
 - shape, 217
 - vector potential, 218, 219
- QED, 163
 - implementation, 121
 - local Hamiltonian, 117
 - many-electron, 117
 - model, 121
 - model operator, 117
 - radiative potential, 120
 - self-energy potential, 119
 - Uehling potential, 118
 - Wichmann-Kroll, 118
- quantum
 - phase estimation algorithm, 190
 - variational quantum eigensolver, 190
- quantum computing
 - continuous variable, 192
 - supremacy, 190
- quantum information
 - seelight beam application, 748
- quantum phase estimation, 188
- quantum simulation, 188
- radial orbital
 - continuum, 78

- matrix elements, 68
- momentum representation, 62
- non-relativistic, 60
- relativistic, 63
- radiation field, 197
- radiation pressure, 746
- radiative correction, 163
- radiative transition
 - angular distribution, 374
 - including core-polarization, 374
 - structure function, 374
- radius
 - atomic, 690
- rate
 - ADK ionization, 614
 - tunnel ionization, 693
- Rayleigh
 - seelight scattering, 432
- RDM
 - spherically-averaged, 260
- re-coupling
 - $jj - LS$, 122
 - atomic states, 122
- recombination
 - dielectronic, 414
 - fluorescence, 480
 - negative continuum, 501
- radiataive, 395
- radiative & fluorescence, 488
- three-body, 498
- REDDA, 493
- reduced density matrix
 - 1-particle, 259
 - 2-particle, 259
- reflection
 - selective (SR), 221
- refraction index, 298, 353
- relation
 - Milne, 416
- representation
 - analytical, hydrogenic, 180
 - Berggren expansion, 174
 - CI-PT, 165
 - complex scaling, 172
 - configuration interaction, 155
 - convergent close-coupling, 176
 - coupled cluster, 181, 183
 - density functional, 180
 - DMRG, 177
 - fast CI, 167
 - Green function, 157
 - MBPT, 169
 - MCDHF, 163
 - mean-field basis, 155
 - natural-orbital functional, 180
 - qubit Hamiltonians, 185
 - Wigner distribution, 184
- RESDA, 493
- resonance
 - photoionization, 372
- resonance line
 - related quantities, 373
- resonance strength, 416
- restricted active space, 163
- rule
 - empirical Bragg, 704
- Rydberg
 - blockade, 356
 - dressing, 357
 - matter, 356
- Rydberg atom
 - binding energy, 358
 - quantum defect, 358
- scaling law
 - Compton, 93
 - pair production, 93
 - photoionization, 93
- scattering
 - Bhabha, 513
 - elastic, 499
 - Möller, 513
 - Sherman function, 501
- scattering factor, 274
- scattering function
 - incoherent, 275
- SCF, 151
- scheme
 - coherent control, 623
- Schiff theorem, 137
- screening
 - of charge impurities, 350
- selection rule
 - XMCD, 552
- shift
 - (dc) Startk, 283
- sidebands
 - two-color, 624
- Siegert state, 621

simulation
 atomic cascades, 29
slitting
 hyperfine, 234
solution
 generalized Volkov, 85
space
 chemical, 681
 Krylov, 183
space mission
 EUV, 532
 SERTS, 532
SPDC, 758
 seelight beam application, 758
spectral intensity, 463
spectroscopy
 COLTRIMS, 592
 femto-slicing, 660
 high harmonic, 597
 XANES, 549
 XMCD, 552
spin wave, 558
standard model
 CP violaton, 136
 new physics, 136
 T violaton, 136
Stark broadening
 energy shift, 705
 impact approximation, 706
 semi-empirical, 706
 spectral lines, 705
 Stark widths, 705
 temperature dependence, 705

state
 Gaussian, 194
state vector
 ASF, 155
 atomic, 151, 155
 relaxation, 151
 representation, 155
 scattering, 152
stopping power
 electron, 702
 Rohrlich-Carlson, 702
strength
 oscillator, 372
 oscillator, absorption, 372
 photoionization resonance, 372
strong-field
 amplified spontaneous emission, 624
 NSDI, 616
 superfluorescence, 624
sum rule
 Thomas-Reiche-Kuhn, 149
symmetry
 fundamental, 136
tensor
 polarization, 210
theorem
 Floquet, 620
 Hohenberg-Kohn, 180
 Kohn-Sham, 180
 Noether, 746
theory
 density functional, 180, 281
Floquet, 584
Gordon-Kim, 324
strong-field, 584, 628
three-wave mixing, 758
transform
 discrete Fourier, 184
 of OAM states, 184
transformation
 $jj - LS$, 122
 atomic states, 122
transition
 lattice clock, 278
transition array
 resolved, 376
 super, 376
 unresolved, 376
transition probabilities, 233
transition probability, 371, 372
 FON approach, 377
transport coefficients, 321
tungsten, 548
Tungsten Program, 401
tunnel ionization
 ADK rate, 692
 modified ADK rate, 692
 PPT rate, 693
uncertainties, 28
vector potential
 Bessel pulse, 737
 Bessel $\theta_k \ll 1$, 738
vector spherical harmonic, 212

vortex

circularly-polarized, 713

harmonic, 713

warm-dense matter

pair correlation function, 351

wave length

magic, 275

wavelength

magic, 315

weak-charge, 139

X-waves, 745

yield

Auger, 272

fluorescence, 272

Zeeman

splitting, 249